INSTITUT D'ASTROPHYSIQUE DE PARIS
Unité mixte de recherche 7095 CNRS - Université Pierre et Marie Curie

Mémoire d'habilitation à diriger des recherches

Mécanismes de structuration gravitationnelle : théorie et estimation

Christophe Pichon

Equipe Univers profond & Grandes Structures
Institut d'Astrophysique de Paris (CNRS –UPMC)
98 bis boulevard Arago, 75 014 Paris, France

Soutenu le 13 Mars 2009 à l'Institut d'Astrophysique de Paris devant le jury constitué de :

Prof.	Steve	Balbus	Examinateur,
Prof.	Edmund	Bertschinger	Rapporteur,
Prof.	James	Binney	Rapporteur,
Prof.	Jean	Heyvaerts	Examinateur,
Prof.	Jean-François	Giovannelli	Rapporteur.

Plan

The difference between theory and practice in practice is greater than the difference between theory and practice in theory.

Mécanismes de structuration gravitationnelle : théorie & estimation

Christophe Pichon IAP

Soutenu le 13 Mars 2009 à l'Institut d'astrophysique de Paris devant le jury :
Steve Balbus (UPMC), Ed Bertschinger (Rapporteur), James Binney (Rapporteur), Jean Heyvaerts (Examinateur), Jean-François Giovannelli (Rapporteur).

Ce document est divisé en quatre parties ; dans la première partie, le contexte de mon activité de recherche passée et en cours est décrit de manière télégraphique ; la seconde partie présente brièvement mes activités d'enseignement et d'encadrement ; la troisième partie reprend la première de manière plus détaillée, et propose aussi pour chaque thème abordé une réflexion plus personnelle ; la dernière partie correspond à ma bibliographie et un échantillon des articles publiés/soumis les plus significatifs (référés avec un symbole ¶ dans le résumé ci-dessous). Ce format de présentation atypique correspond aux contraintes imposées par une recherche transverse.

1. Contexte & Résumé

Globalement, mon activité de recherche de ces dix dernières années au CNRS s'articule autour de la dynamique gravitationnelle, avec pour point saillant la détermination dynamique de la matière noire. Quelle est sa distribution géométrique? Comment peut-elle influencer l'évolution structurelle et dynamique de son environnement ? J'ai en particulier étudié la physique des mécanismes d'instabilité appliquée aux systèmes complexes que sont les objets autogravitants. Cette physique m'a permis de m'intéresser à des sujets aussi divers que la dynamique des grandes structures de l'univers, le milieu intergalactique et interstellaire, la dynamique des galaxies et leurs trous noirs. L'acquisition des méthodes inverses utilisées dans ce contexte m'a amené à aborder d'autres problèmes connexes de l'astrophysique. La maîtrise des simulations numériques (hydrodynamique, N-corps) a constitué un autre axe de développement. En tant que théoricien, mon souci a toujours été de faire le lien entre la mesure d'une part, et la physique du *mécanisme* qui sous-tend le phénomène observé d'autre part, et ce par le biais d'une description physique et mathématique détaillée de ce phénomène.

C'est avant tout la curiosité vis-à-vis de domaines de recherches (le milieu intergalactique, la relativité générale, la physique des trous noirs, etc.) ou des outils nouveaux pour moi (la statistique, l'analyse automatique des données, les simulations numériques, les méthodes inverses) qui a guidé ma démarche. C'est aussi le sentiment que la recherche qui m'intéresse doit correspondre à cette diversité, pour inventer de nouvelles façons d'appréhender notre Univers. C'est précisément en mariant des points de vue apparemment discordants issus de thématiques différentes et en utilisant des outils originaux qu'il m'a semblé possible d'innover. Cela correspond enfin à un goût prononcé pour dégager ce qui relève du général au détriment du particulier.
A titre d'exemple, l'analyse des grandes structures s'est par essence fortement reposée sur l'analyse statistique, compte tenu de la nature des données et du modèle ; *a contrario*, la dynamique galactique a historiquement transposé une fraction des acquis de la physique des plasmas et de la mécanique céleste pour décrire de manière détaillée les systèmes gravitationnels non collisionnels. Ces deux disciplines, la cosmologie et la dynamique des galaxies, gagnent à transposer dans leurs domaines respectifs les savoir-faire de chacune. C'est cette conviction qui a été par exemple la ligne directrice du travail de thèse de mon étudiant D. Aubert (voir ci-dessous).

Afin d'atteindre les objectifs scientifiques décrits ci-dessus, je me repose sur un intérêt marqué pour des outils de l'astrophysique théorique (théorie perturbative, champs contraints, théorie WKB, représentation duale etc), des compétences en analyse numérique (simulations, calcul haute performance, parallélisme etc), et en méthodes inverses, optimisation et statistique (théorie de l'estimation, descente à mémoire limitée, régularisation auto-calibrée, etc..). Ma stratégie repose donc sur la recherche de l'innovation en travaillant de manière transverse entre la cosmologie, la dynamique gravitationnelle (relativiste ou classique), la haute résolution angulaire, la MHD, etc Ce parti pris présente toutefois peut-être l'inconvénient de compliquer quelque peu l'exposition globale de mon activité de recherche et sans doute sa visibilité *immédiate* auprès de la communauté de ces différentes disciplines.

En bref, mes principaux travaux de recherche recouvrent[1] (en % la fraction de leadership sur le projet) :

- Dynamique du centre Galactique : étude des propriétés cinématiques du centre Galactique en utilisant les mouvements propres et la photométrie IR de Genzel et al. Extraction non paramétrique du potentiel gravitationnel du centre galactique à partir d'un ajustement simultané des comptages d'étoiles et des mesures de vitesses (mouvements propres et vitesses radiales). Les mouvement propres ne sont plus compatibles avec un modèle isotrope, le trou noir Galactique se situe à 8.1 kpc du soleil et sa masse doit être révisée à la hausse de 10 % [Genzel, Pichon, Eckart, Gerhard (2000) 40%]. Profil de masse des amas : mesure non paramétrique du profil de masse de Abell 85 et Coma à partir des redshifts de leurs composantes en faisant l'hypothèse que l'amas est stationnaire et isotrope [Durret, Gerbal, Lobo, Pichon (1999) 20%]. Généralisation du formalisme de la dynamique stellaire des disques minces au cadre de la relativité d'Einstein ; construction d'une source physique interne pour la métrique de Kerr ; description détaillée d'amas stellaires relativistes en rotation différentielle localement stables ou de disques supermassifs correspondant à l'étape d'effondrement final d'un proto-quasar [Pichon, Lynden-Bell (1996) 70 %, Bicak, Lynden-Bell, Pichon (1994) 20 %].

- Stabilité des galaxies spirales : Détermination de la masse de halo nécessaire pour maintenir la stabilité dynamique globale [Pichon, Cannon (1997) 70 %] de disques galactiques proches à partir d'une analyse non-paramétrique [Pichon, Thiébaut, (1998) 50 %] de l'ensemble de leurs données cinématiques. NGC 3198 & 6503 ne sont pas maximales. Identification des configurations d'équilibre des disques minces auto-gravitants ; calcul de fonctions de distribution contraintes à des mesures cinématiques paramètrées [Pichon & Lynden-Bell (1996), financement "jeune chercheur" de l'INSU 99, encadrement de stage de DEA]. Evolution spectro-dynamique des disques : introduction de la cinématique stellaire dans les modèles de synthèse spectrale de données ; inversion non paramétrique simultanée de l'histoire de formation stellaire des disques galactiques et de leur cinématique. [Orvirk, Pichon, **et al.** 2006ab¶, 80% encadrement de stage de DEA (2001) et doctoral (2005)]. La fonction de luminosité locale : nouvelle méthode pour inverser l'équation statistique des comptages dans le voisinage local en introduisant les mouvements propres afin de tenir compte de l'autocohérence dynamique. L'inversion donne accès de manière univoque simultanément à la cinématique et à la fonction de luminosité de chaque population (sans référence à des tracés d'évolution stellaire) et conduit à un diagnostic pour distinguer cinématiquement le disque mince du disque épais ou du halo [Pichon, Siebert, Bienaymé, (2002)¶ *70%*]. Encadrement doctoral et postdoctoral].

- Environnement des halos galactiques : distribution statistique des flux cosmologiques de matière et de moment au travers des précurseurs des` halos galactiques. Mesure statistique de l'évolution temporelle des flux de masse, de gaz, ainsi que le moment advecté et les couples de marée subis par les halos identifiés de nos simulations. L'évolution dynamique (instabilités azimutales, gauchissement, accrétion, friction dynamique), physique (chauffage, refroidissement) et chimique (flux de gaz froids pauvres en métaux) des galaxies est étudiée dans le cadre des conditions aux limites imposées par leur environnement cosmologique. [Aubert, Pichon, Colombi 2004 *70%*¶, Aubert, Pichon 2007 70% ¶, Pichon Aubert, 2006 80% ¶, encadrement de stage de DEA (2001) et doctoral (2004)]. Bimodalité de l'accrétion du gaz à la surface du Viriel [Ocvirk, Pichon, Teyssier *2008.*¶ *50%,* Dekel **et al.** *2008* 5 %]. Statistique des grands arcs, et contrainte sur les sous-structures de matière noire [Peirani, Pichon, Alard, Gavazzi, Aubert, *2008 30%*].

- Cartographie du milieu intergalactique : à partir des raies d'absorption Lyman α dans le rayonnement des quasars, reproduction de la structure tri-dimensionnelle du gaz intergalactique à l'aide d'algorithmes de reconstruction non paramétriques incorporant la température et les vitesses particulières. Mesure de la température de l'IGM. Mesure de la topologie de l'univers par comparaison des fonctions de corrélation transverse et longitudinale à partir de paires de quasars. Mesure du spectre de puissance tri-dimentionnel du flux et de la densité HI par inversion simultanée de la serie Lyman. [Pichon et al. (2000) ¶ *70 %*, Rollinde, Petitjean, Pichon (2001) 30 % ; Rollinde, Petitjean, Pichon, et al. (2003) 20 %] ; encadrement doctoral. Etude des propriétés topologiques des simulations hydrodynamiques et de matière noire sondées par un faisceau de lignes de visée issues de QSO [Caucci, Colombi, Pichon et al. (2008) 30 % encadrement doctoral]. Calcul des invariants de Minkovski (surface, volume, génus) des grandes structures. Les métaux de l'IGM : classification automatique par système expert après identification des multiplets dans le spectre des Quasars ; encadrement doctoral. Mesure du clustering des systèmes CIV, SiIV, MgIV et abondance ; contrainte sur la distribution géometrique, le facteur de remplissage, et sur la nature de la source des premiers métaux. Contrainte sur l'époquede formation des premières galaxies via les abondances relatives d' OIV sur HI dans les régions les plus vides du MIG. [Pichon et al. ApJL (2004) *80 %*¶, Bergeron, Aracil, PetitJean, Pichon, (2002) 10 %, Aracil, PetitJean, Pichon, Bergeron (2004) 20 %, Scannapieco, Pichon, et

[1] sur la base d'un article, +/- une thématique de recherche.

al., ApJ (2006) *70 %*¶, encadrement doctoral].

- Caractérisation de la topologie et de la structure filamentaire de l'univers via le "*squeleton*". Analyse du squelette global et du squelette local (les "lignes de crête" du champ de densité) par segmentation ou intégration numérique des trajectoires conduisant aux points critiques (en définissant le patch gravitationnel de chaque région dans ses coordonnées lagrangiennes). Algorithme du squelette totalement connecté en dimension quelconque, correction de la distorsion en redshift [Sousbie, Colombi, Pichon. *2008 50%* ¶] sous licence CECILL CNRS. Contrainte sur le contenu en matière noire du SDSS par le squelette [Sousbie, Pichon, et al. (2007) *80 %*¶]. Nature de l'écoulement le long des filaments, alignement du spin des halos orthogonalement aux filaments [Sousbie, Pichon, et al. (2008) ¶ *80 %*]. Calcul explicite de la longueur, la courbure et la torsion différentielle dans le cadre de l'approximation du squelette "tendu" et lien avec les paramètres de forme spectrale d'un champ gaussien aléatoire. Statistique de la longueur, de la courbure et des points singuliers du squelette local [Pogosyan, Pichon **et al.** (2008) 70 %, encadrement doctoral et postdoctoral]. Statistique de l'émergence de la vorticité générée par croisement de coquilles dans des caustiques statistiquement rares lors de la formation de grandes structures de l'univers [Pichon & Bernardeau (1998) *50 %*¶].

- Physique théorique : statistique des équilibres oscillants perpétuels en rotation. Analyse des propriétés thermodynamiques du réseau formé par des particules ayant une loi d'interaction par paire avec un potentiel en r^2+1/r^2 . Etude des symétries des configurations d'équilibre en fonction du nombre de particules [Pichon, Lynden-Bell, Pichon, Lynden-Bell (2007) 50 % ¶]. Instabilités orbitales dans les disques galactiques et formation de barres; thermodynamique d'une assemblée d'orbites résonantes (modèle dit HMF pour *Hamiltonian Mean Field*), et formation adiabatique de structures barrées [Pichon & Lynden-Bell (1992) 50 %].

- Asymétrie de la convergence cosmique sur tout le ciel à partir d'une simulation à N corps de 70 milliards de particules; analyse de l'effet des masques Galactiques sur la reconstruction [Pichon, **et al.** 2008, *soumis* ¶ *80 %*, Teyssier, Pires, Prunet, Aubert, Pichon, et al. *2008 30 %*¶] *mptools* : des outils pour la génération de grosses conditions initales cosmologiques (possiblement contraintes) en architecture distribuée : validation jusqu' à 4096^3 en matière noire seule et 1024^3 en hydrodynamique AMR. Analyse des oscillations baryoniques acoustiques. [Prunet, Pichon, et al. (*2008) 50%*]. Inversion des résidus asymétriques des cartes de lentilles fortes et contrainte sur la sous structuration des halos de matière noire [Peirani, Alard, Pichon, Gavazzi, Aubert (*2008) 30%*]. Emergence du chaos dans les simulations numériques : identification d'une échelle de transition Eulerienne dans les exposants de Lyapounov variant avec l'amplitude des perturbations initiales, et d'une masse de transition pour certaines quantités lagrangiennes [Thiébaut, Pichon, Prunet, (*2008)* ¶ *80%*].

J'entends poursuivre mon investigation sur la géométrie des grandes structures, continuer à exploiter de grosses simulations hydrodynamiques pour, entre autres, étendre au gaz mes travaux sur l'accrétion de la matière noire à la surface du Viriel. J'aspire en particulier à poursuivre les travaux théoriques sur les systèmes gravitationnels ouverts. Je souhaite développer un solveur numérique de Boltzmann et faire de la sorte la synthèse entre mes travaux doctoraux théoriques sur la réponse gravitationnelle des systèmes non collisionnels d'une part, et les méthodes numériques que j'ai acquise plus récemment d'autre part. A moyenne échéance j'aimerais aussi continuer à développer un savoir-faire en MHD, et publier le fruit de mes investigations de ces dix dernières années sur la calibration automatique des méthodes inverses. Dans le contexte des grands projets de la discipline, je pense pouvoir à l'avenir contribuer à la valorisation scientifique des missions Planck, SKA et GAIA. *A moyen terme, je souhaite refocaliser ma recherche sur des aspects plus géométriques et théoriques de la dynamique gravitationnelle.* Enfin, à plus courte échéance, je souhaite mener à terme les projets/articles ci-dessous qui relèvent de près ou de loin de la dynamique gravitationnelle et des méthodes inverses :

- Théorie de la bifurcation des lignes critiques [Pichon, Pogosyan *prep. 80%*]. Profil universel des filaments [Sousbie, Pichon, Colombi. *prep.*], connectivité des filaments aux rayon du Viriel [Pichon, Sousbie, *prep.*]. Théorie variationnelle des lignes de crête d'un champ gaussien aléatoire : squelette moyen et/ou bruité [Pichon, Pogosyan et al. *prep. 50%*]. Test de Alcock-Paczynski avec le squelette sur le SDSS [Pichon, Sousbie et al. *in prep. 80%*]. Utilisation des peakpatches comme test de non-Gaussianité pour la détection des cordes cosmiques dans les cartes Planck du fond diffus cosmologique. Application du squelette à la détection des dendrites neuronales, et aux vaisseaux sanguins du foie avant opération.

- Cartographie de la convergence cosmique. Reconstruction de cartes de convergence gravitationnelle à partir de mesures d'ellipticité sur l'ensemble de la voûte céleste. Gestion des masques et de la contamination associée en modes B, de la non-linéarité du modèle, et des amas quasi ponctuels à l'échelle de la carte par une pénalisation de type L1-L2 [Pichon, et al. *soumis* ¶*80%*]. Exploitation scientifique de la simulation *HORIZON*-4π : détection des oscillations acoustiques baryoniques (BAO) à partir de la fonction de corrélation 3D des catalogues virtuels de LRG [avec Aubourg]. Détection des BAOs à partir de corrélations croisées des spectres de quasars [avec Rollinde, ANR BOSS 2008].

- Formation des galaxies par le biais de simulations numériques cosmologiques. Exploitation scientifique de la simulation MareNostrum. Evolution en redshift de la fonction de luminosité des galaxies [Devriendt, Pichon et al. *prep. 40%*]. Evolution des propriétés spectro morphologiques des galaxies en fonction de l'environnement des galaxies mesurées par la distance au squelette [Gay, Pichon, Leborgne et al. *prep. 80 %*]. Corrélation métallicité-dispersion en vitesse des systèmes dampés dans MareNostrum [avec Rollinde]. Inversion de l'histoire de la formation stellaire cosmique de MareNostrum [avec Ocvirk]. Croissance adiabatique d'un bulbe/disque/barre dans un halo autogravitant [Magorrian, Aubert, Pichon *prép. 20%*]. Evolution séculaire et perturbative du halo ouvert : [avec Aubert]. Résolution de l'équation de Boltzmann dans l'espace des phases par n-simplex ; Identification des caustiques par rectification de l'espace des phases via une transformation en variables angle-action [Macejewski, Colombi, Alard, Bouchet Pichon, *2008. 10 %*].

- Déconvolution multibande de Planck : déconvolution myope des 10 canaux polarisés de Planck pour séparer le fond diffus des autres composantes. Correction des masques et pénalisation L1L2 [Prunet, Pichon, Thiébaut *prep*]. Reconstruction en volume du champ magnétique par rotation Faraday multi-spectrale ; analyse statistique et topologique de l'hélicité du champ reconstruit [Thiébaut, Prunet, Pichon, Thiébaut *prép. 60%*]. Tomographie et optique adaptative multi-conjuguée. Déconvolution aveugle et PSF variable dans le champ [Thiébaut, Pichon *prép.*].

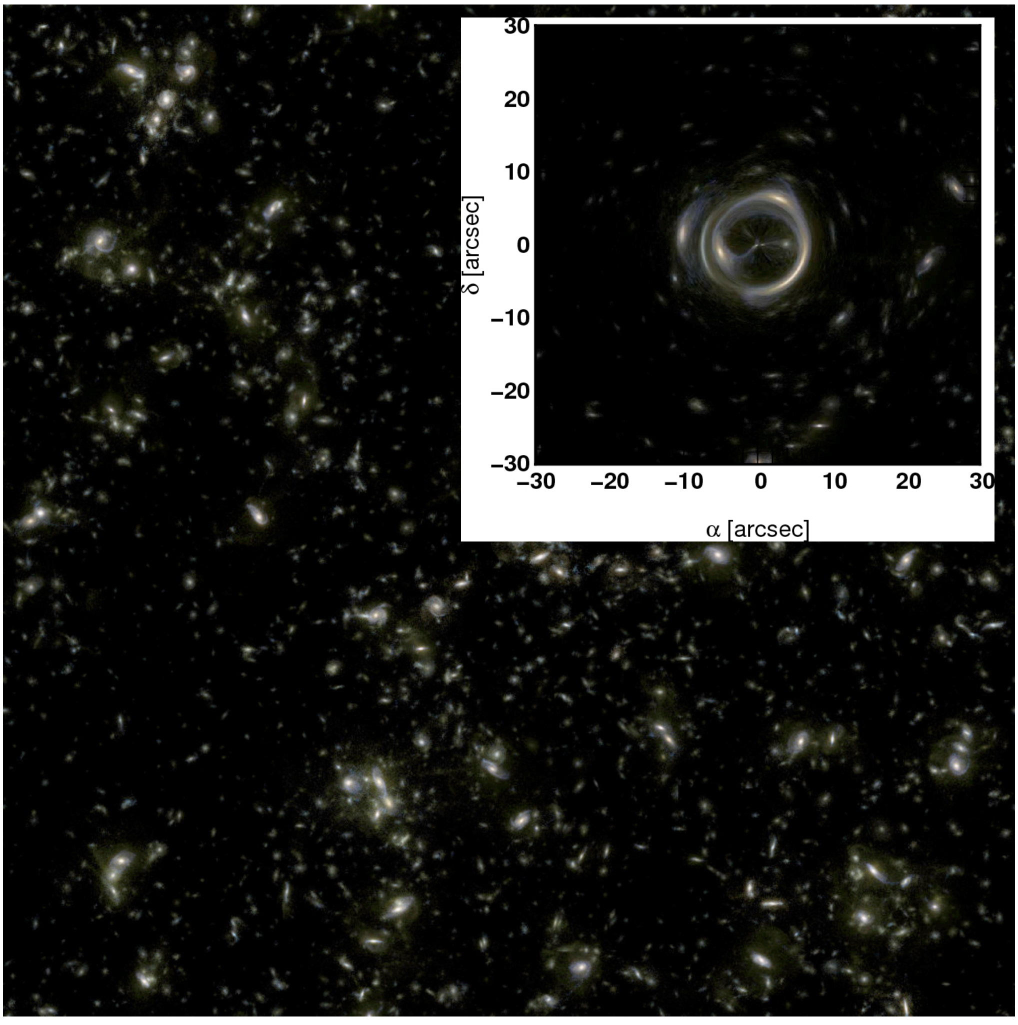

—Quelques galaxies synthétiques dans la simulation MareNostrum à z=1.55. Les couleurs sont construites à partir de la connaissance, pour chaque particule macro-étoile produite par la simulation, de la masse, la métallicité et l'âge de l'étoile, ce qui permet de lui associer un spectre [Ocvirk, Pichon, Teyssier 2008]. Encart : un exemple d'arc gravitationnel synthétique produit avec notre code de tracé de rayon [Peirani, Alard, Pichon, Gavazzi, Aubert 08].

2. Encadrement et enseignement

J'ai encadré/j'encadre dix étudiants en thèse (voir Annexe A), dont D. **Aubert** ("*Etude des flux cosmologiques au travers de la sphère du viriel d'un disque Galactique & applications*" tutelle de thèse soutenue en mai 2005) à temps plein, et avec P. Petitjean, en co-tutelle, trois étudiants sur la forêt Lyman α (E. **Rollinde** "*La physique du milieu intergalactique*", B. **Aracil** : "*Etude du milieu intergalactique à l'aide des raies d'absorption dans le spectre des quasars*" et Sara **Caucci** "*la topologie du milieu intergalactique*") sur la tomographie et la topologie des grandes structures à partir de faisceaux de lignes de visée issues de quasars), avec O. Bienaymé un sur la cinématique du voisinnage solaire (A. **Siebert** : "*Structure et dynamique des disques de la Galaxie*") et avec A. Lançon (P. **Ocvirk** "*Evolution chemo-spectro-dynamique des disques galactiques*" cotutelle de thèse soutenue en juillet 2005), avec H. Courtois (Thierry **Sousbie** "*Le Squelette de l'univers, un outil d'analyse topologique des grandes structures*" en cotutelle de thèse soutenue en décembre 2006) sur les propriétés hydrodynamiques du flot le long des filaments des grandes structures, et la détermination d'une relation de fermeture pour cet écoulement, avec S. Prunet (Jérôme **Thiébaut**, en co-tutelle depuis 2007, sur l'émergence du chaos dans les simulations numériques cosmologiques, et l'inversion des cartes de polarisation, avec R. Teyssier (Damien **Chapon** en co-tutelle depuis 2008) sur la structure et l'évolution de la Voie Lactée, et enfin avec Christophe **Gay** (depuis 2007, tutelle), sur la statistique du squelette global.

Parmi ces ex-étudiants en thèse, deux d'entre eux ont été recrutés à l'Observatoire de Strasbourg, et un à l'Institut d'astrophysique de Paris.

J'ai aussi encadré cinq stages de DEA en 2001 (D. Aubert, P. Ocvirk & M. Guenno), le troisième en co-tutelle avec A. Lançon, un stage de magistère de mathématique en 2002 (Myriam Fischer) et 2 stages de M2 en 2007 (Jérôme Thiébaut et Christophe Gay). J'ai également encadré les stages de M1 de Benjamin Depardon sur la polarisation du milieu interstellaire en 2005, de Annie Hugues sur les métaux du MIG en 2004, d'Isabelle Paris et Florence Brault en 2007 sur les effets d'environnement sur les propriétés morphologiques et spectro-photométriques des galaxies en fonction de leur position par rapport aux grandes structures.

J'ai co-encadré (avec P. Petitjean) le travail postdoctoral de E. Scannapieco sur les métaux du milieu intergalactique ; j'ai de plus co-encadré le travail postdoctoral de Pierre Ocvirk (avec R. Teyssier) sur la bimodalité de l'accrétion des métaux sur les galaxies L* (Ocvirk, Pichon, Teyssier, 2008), de Felix Stoehr (en postdoc) sur les fonctions de corrélation transverse de la forêt du MIG (Copolani et al., *2006*.), de Damien Le Borgne (postdoc) sur l'inversion du SFR cosmique à partir des comptages (Le Borgne, Elbaz, Ocvirk, Pichon 2008) et sur les caractéristiques morphologiques et spectroscopiques des galaxies dans la simulation MareNostrum (Gay, Pichon, Le Borgne, Teyssier, Sousbie *prep*.), et de Sebastien Peirani (postdoc) sur la construction et l'inversion de lentilles fortes (Peirani, Alard, Pichon, Gavazzi, Aubert 2008), et j'ai enfin encadré en postdoc *HORIZON* T. Sousbie sur le squelette de l'univers (Sousbie, Pichon et al. 2008a,b, Sousbie Colombi, Pichon 2008).

J'ai obtenu plusieurs fois du temps à l'UKAAF (centre de calcul astrophysique Britannique) financé par l'UE, et, en collaboration, au CINES, à l'IDRIS et au CCRT. J'ai eu l'occasion d'observer à l'AAT (Sidding Springs) à Hawaii (CFHT), et à Calar Alto. J'ai obtenu par le biais de mes collaborateurs du temps HST, NTT et VLT. J'ai interagi régulièrement avec P. Fernique sur l'interface d'Aladin (portail image du CDS).

J'ai été coordinateur d'une action spécifique INSU et membre d'une seconde (avec S. Colombi). J'ai participé au TMR Milieu Intergalactique. Avec mes collègues, j'ai obtenu plusieurs financement ANR (*HORIZON*, Ecostat et BOSS), PNC, PNG, GDR-galaxies. J'ai référé une bonne douzaine d'articles,[2] et j'ai été examinateur de la thèse de F. Soules (Dec. 08).

J'ai activement contribué à la mise en oeuvre du projet *HORIZON* http://www.projet-horizon.fr et de son ANR ; je suis de fait CoI IAP du projet (depuis septembre 2006) et éditeur principal du site, dans la lignée du projet INC (avec S. Colombi). J'ai été rapporteur de la commission 34, et membre du CS à l'Observatoire de Strasbourg. Je suis depuis 2005 responsable de l'équipe *Univers profond et grandes structures* de l'IAP.

J'ai enseigné en licence de statistique, et en master d'astronomie. J'ai aussi enseigné durant plusieurs écoles (Luminy, Cargèse) du CNRS, en post-DEA (simulation numérique & programmation CUDA), et j'ai écrit plusieurs articles de vulgarisation/critiques de livres pour les revues *Pour La Science* et *Science & Vie.* J'ai aussi fait des interventions dans des forums dans le cadre de la fête de la science. J'ai donné des conférence publique devant l'association des astronomes amateurs d'Alsace et la Société Française de Physique.

---

[2] ce nombre, peu élevé est un des rares avantages à mener une recherche transverse !

3. Travaux de recherche

Cette troisième partie retrace de manière plus détaillée mon activité de recherche articulée autour d'une présentation par décalage spectral vers le rouge croissant, centré sur le trou noir de notre galaxie, avec pour fil directeur la problématique de la matière noire. Elle est suivie par une sélection des articles qui m'ont semblé les plus représentatifs de mon travail. (en % la fraction de leadership sur le projet).

3.1 Matière noire compacte.

La compréhension de la dynamique des noyaux galactiques pose deux problèmes : quelle est l'influence dynamique du trou noir central sur les étoiles environnantes, et quels sont les taux de concentration et d'anisotropie induits par le trou noir sur le cuspide central ?

3.1.1 Dynamique du centre Galactique. [30 %]

Le centre de notre galaxie se prête particulièrement bien à l'étude de ces phénomènes.

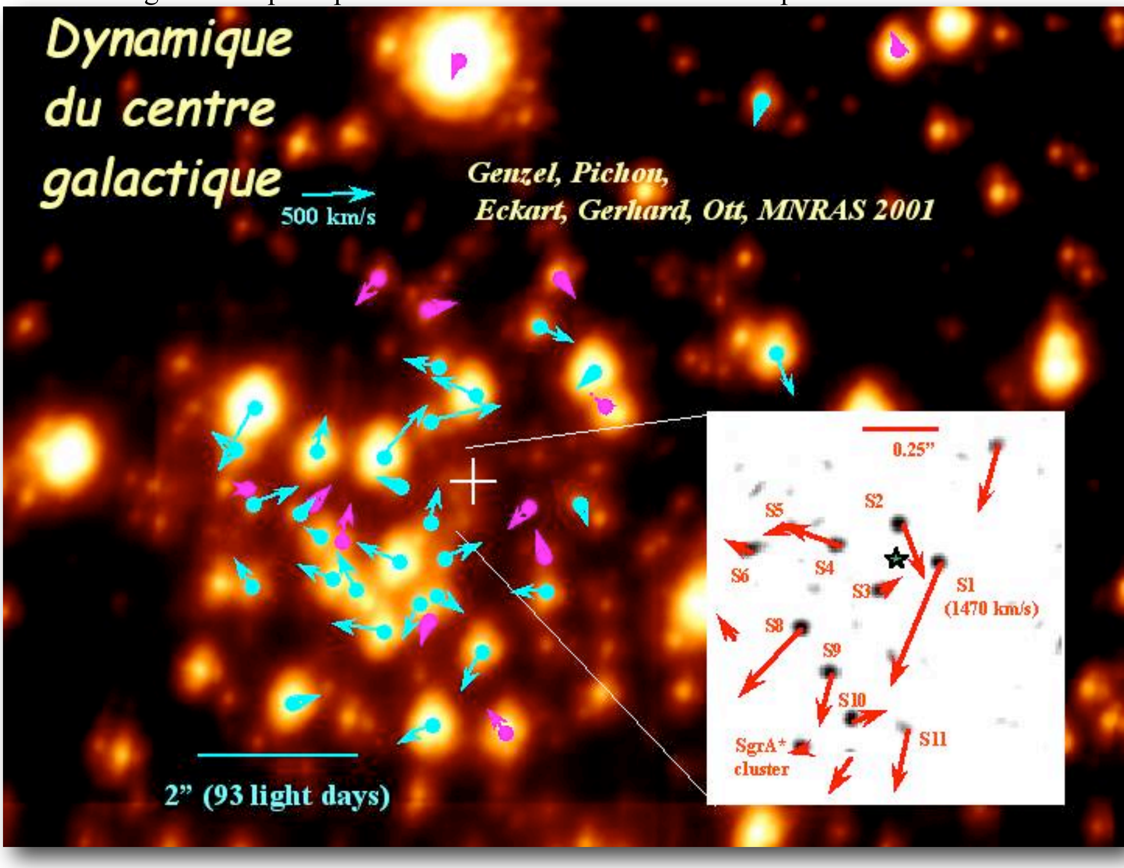

— La région du centre Galactique : le comportement asymptotique du profil de masse aux échelles du dixième de parsec traduit la présence de l'objet central massif. La cohérence dynamique entre les mouvements propres et les vitesses radiales suppose une distance au centre galactique de 8.5 kpc [Genzel, Pichon, Eckart, Gerhard, Tott 2001].

En effet, en dépit de l'extinction phénoménale aux longueurs d'onde visibles, plusieurs groupes disposent maintenant de données cinématiques très détaillées de l'amas d'étoiles central à l'aide d'observations dans l'infrarouge proche. Je me suis donc attaché à modéliser ces données.

En collaboration avec O. Gerhard, j'ai analysé les propriétés cinématiques des étoiles du voisinage du trou noir central à l'aide des vitesses radiales, des mouvements propres et de la photométrie infrarouge. J'ai développé et testé des méthodes pour estimer le degré d'anisotropie et pour extraire le potentiel gravitationnel du centre Galactique de manière non paramétrique à l'aide d'un ajustement simultané des comptages d'étoiles et des mesures de vitesse.

Il découle de cette analyse que la masse du trou noir doit être revue à la hausse et que les barres d'erreurs avaient été surestimées par le passé. Nous avons déduit un estimateur pour la distance soleil-centre Galactique indépendant de l'anisotropie de l'amas de l'ordre de 7.8-8.2 kpc (cf. Fig 2.1). J'ai par ailleurs montré que les estimateurs algébriques de Leonard-Merritt sont systématiquement biaisés d'un facteur dépendant de la pente du cuspide et de l'anistropie de la distribution au voisinage du trou noir [Genzel, Pichon, Eckart,Gerhard Tott (2001)].

En 2001, le nombre d'étoiles présentant des mesures de vitesse radiale et/ou de mouvement propre était trop faible pour mener une véritable mesure non paramétrique de la masse du trou noir, ce qui correspondait à l'objectif initial de ma contribution à ce travail. En effet, pour une telle mesure, il faut pour la méthode retenue échantillonner la distribution des étoiles (en position et énergie) sur la voûte céleste, puis la déprojeter (1/2 dérivation) et dériver le résultat de la déprojection pour calculer le gradient de pression qui s'oppose à la dispersion. Scott (92) a montré que du point de vue de l'échantillonnage non paramétrique cette opération était équivalente à un échantillonnage en dimension 5, soit 2 points de mesure indépendants. En pratique, j'avais pour ce projet développé une base analytique de splines cubiques à pas d'échantillonnage quelconque, sa transformée d'Abel inverse, et le potentiel gravitationnel induit. L'intérêt d'une telle base est sa flexibilité dans l'échantillonnage (en l'occurrence logarithmique) et l'absence d'erreur (analyticité) dans le calcul du modèle. Une alternative consiste par exemple à reparamétrer le modèle en log-log, mais la pénalité associée à l'optimisation d'une fonction de coût non-linéaire est, à mon avis trop forte quand elle peut être évitée. Cet outil m'a *in fine* servi pour la mesure du profil de masse d'Abell 85 et la mesure du Kz avec les données Hipparcos dans d'autres contextes et géométries.

Par ailleurs, pour revenir au trou noir Galactique, l'hypothèse d'isotropie spatiale de la distribution projetée des étoiles n'était pas vraiment vérifiée. Rétrospectivement, il est intéressant de noter que ma mesure, élevée, de la masse du trou noir a été confirmée spectaculairement par la mesure directe des accélérations des étoiles S_1 et S_3 (puis de 26 autres étoiles à ce jour). Le centre Galactique a fait depuis l'objet de nombreuses mesures dynamiques. Accessoirement, cette recherche m'a alors permis à titre personnel de me convaincre de la réalité du concept de trou noir!

3.1.2 Disques relativistes & formation des QSO [40%]

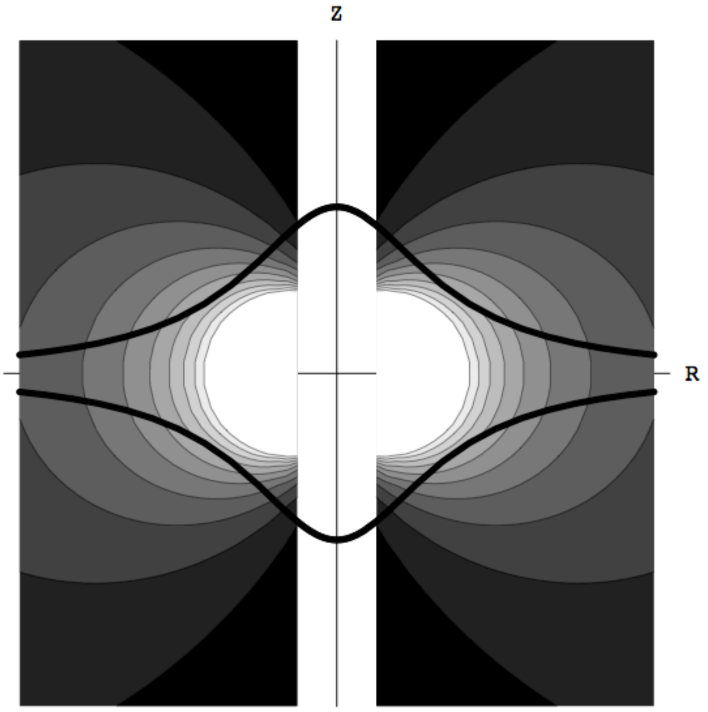

— Plongement d'une surface à courbure extrinsèque non nulle dans une métrique de Kerr. Cette courbure induit une densité d'énergie supplémentaire que l'on identifie à une pression cinétique dans le disque mince correspondant à l'identification des deux surfaces externes. [Pichon, Lynden-Bell (1996)].

Lors de l'effondrement d'un nuage baryonique de gaz, la conservation du moment angulaire conduit à son aplatissement. La contraction se poursuit jusqu'à ce qu'une description relativiste du cœur devienne nécessaire. S'il semble établi que la phase ultime de l'effondrement corresponde à un trou noir supermassif, il convient d'étudier plus en détail les étapes conduisant à la formation d'un tel objet. Pour ce faire, j'ai construit des familles de solutions analytiques exactes aux équations d'Einstein correspondant à des disques supermassifs minces. Ces solutions sont établies de manière géométrique en identifiant de part et d'autre d'un plan de symétrie les points décrivant deux surfaces de section traversant un champ du vide donné. Cette identification définit le saut des dérivées normales du champ à partir desquelles les propriétés du disque se déduisent. J'ai étudié la nature des sections conduisant à une solution physique. Pour une métrique statique, j'ai montré que le champ du vide peut être construit de manière générale par superposition linéaire de sources fictives de part et d'autre du plan de symétrie en analogie avec la démarche newtonienne. La solution correspondante peut alors être interprétée en termes de deux flots stellaires en contre rotation [Bicak, Lynden-Bell & Pichon (1994)]. Le choix d'une section à courbure extrinsèque nulle conduit à des disques dénués de pression radiale. Tout profil courbe induira au contraire un disque susceptible d'être stable vis-à-vis des instabilités radiales [Pichon, Lynden-Bell (1996)].

En raison de la complexité induite par les forces gravitomagnétiques (qui entraînent les repères inertiels), il n'existe pas de solution stationnaire générale pour laquelle la composante non diagonale de la métrique peut être choisie indépendamment. Néanmoins, il est possible de générer par transformation algébrique des familles complètes de métriques stationnaires à partir de solutions statiques connues avec une distribution d'énergie et de pression et une courbe de vitesse qui se déduit du choix de la métrique du vide dans laquelle le disque est plongé. A grande distance, ces disques deviennent newtoniens mais présentent dans leur région centrale des propriétés relativistes (décalage vers le rouge important, écoulement luminique, ergorégions, etc). J'ai transposé dans ce contexte la méthode d'inversion newtonienne présentée ci-dessus pour construire de manière univoque toutes les fonctions de distribution compatibles avec un écoulement relativiste donné.

Ce type de solutions présente un intérêt à la fois astrophysique et théorique. La généralisation du formalisme de la dynamique stellaire des disques minces au cadre de la relativité d'Einstein, et la description statistique détaillée de l'écoulement pour un ensemble très général de solutions relativistes constitue un progrès théorique important, en particulier au vu du nombre très restreint de solutions physiques aux équations d'Einstein à symétrie non sphérique. Par exemple, une des solutions que j'ai obtenu représente une source physique interne pour la métrique de Kerr qui correspond ultimement au champ généré par un trou noir en rotation.

Ces solutions sont plus généralement susceptibles de décrire des amas stellaires relativistes en rotation différentielle localement stables. Les configurations à pression isotrope correspondent éventuellement à des disques supermassifs que l'on peut associer à l'étape d'effondrement final d'un proto-quasar. J'ai calculé la fraction de l'énergie de masse qui est rayonnée lors de l'effondrement de ces objets. Celle-ci peut atteindre dix pour cent de la masse au repos du disque, ce qui suggère que ces derniers pourraient avoir une durée de vie suffisante pour avoir des conséquences observationnelles [Pichon & Lynden-Bell (1996)].

Il est rétrospectivement intéressant de noter que l'astuce utilisé pour introduire la pression dans ces disques (l'association d'une densité d'énergie supplémentaire à la courbure extrinsèque de la surface immergée) se retrouve en théorie des branes qui a été développée parallèlement en cosmologie théorique. La dérivation des fonctions de distribution pour ces disques supermassifs était une de mes premières innovations théoriques, car elle correspondait à la transposition de la formule classique pour les disques galactiques (publiée dans Pichon & Lynden-Bell 1996) mais aussi à sa généralisation imposée par l'entraînement des repères inertiels. A terme et dans ce contexte, la recherche numérique de solutions aux équations d'Einstein m'intéresserait (cf 3.6.2 ci-dessous).

3.2 Matière noire du voisinage solaire

Si l'absence de matière noire dans le voisinage local est maintenant acquise, c'est en partie grâce à la performance de la mission Hipparcos. Le lancement du satellite GAIA va dans quelques années révolutionner notre connaissance de la Voie lactée. Le voisinage solaire reste le laboratoire privilégié de la physique du milieu interstellaire, dont la structure géométrique quelconque (et notre point de vue particulier) se prête bien à la modélisation non paramétrique. Mes travaux dans ce domaine recouvrent l'estimation dynamique par le biais de méthodes inverses.

3.2.1 La densité locale de matière noire Galactique [20%]

Les nouvelles données obtenues par Hipparcos et Tycho fournissent des contraintes détaillées sur le potentiel Galactique et son aplatissement et peuvent conduire enfin à une mesure "exacte" de la distribution de masse au voisinage solaire. Les contraintes locales, fournies par Tycho et le programme complémentaire des mouvements propres tirés des plaques astrographiques, permettent aussi en principe de connaître de manière détaillée les distributions stellaires du halo et du disque épais, et de mettre en évidence une éventuelle continuité entre ces deux populations. Cette étude nous renseigne sur les véritables processus dynamiques et physiques en jeu lors de la formation galactique et conduit à des contraintes fortes sur la fonction de luminosité du halo et du disque épais et sur la distribution de la matière noire.

Dans une première étape, en collaboration avec M. Crézé et O. Bienaymé, j'ai contribué à la mesure de la masse dynamique locale dans la sphère de Hipparcos, déduite de l'ajustement simultané du profil de densité – mesuré à partir des distances issues des parallaxes, et de la distribution des vitesse orthogonales au plan du disque – mesurée à partir des mouvements propres. Ma contribution a consisté à mener une réduction non paramétrique des données Hipparcos et retrouver que ces nouvelles mesures contraignent fortement la distribution de masse totale au voisinage solaire et retrouver une densité qui exclut tout modèle de distribution aplatie pour le halo de matière noire Galactique [Crézé, Chereul, Bienaymé, Pichon (1998)].

Ce travail correspondait à la transposition de la géométrie sphérique à la géométrie plane des outils que j'avais développé pour le centre Galactique. L'intérêt de la formulation analytique tient à la flexibilité qu'elle offre du point de vue de l'échantillonnage, ce qui est un point critique pour améliorer le conditionnement du problème inverse et donc l'importance relative du biais associé au *prior*. Il n'a en pratique été implémenté que dans l'article Durret et al. décrit ci-dessous. Le satellite GAIA permettra bientôt de sonder de manière détaillé le potentiel gravitationnel de notre galaxie, et l'intérêt de ce type de modèle non paramétrique devrait alors être évident.

3.2.2 La fonction de luminosité locale [80%]

Si la photométrie et les parallaxes d'Hipparcos permettent de déterminer avec précision la partie brillante du diagramme HR dans une sphère de 100 pc, il n'est pas possible d'étudier la fonction de luminosité à plus grande échelle, car à partir des comptages seuls, nous ne savons pas distinguer une étoile brillante éloignée d'une étoile de faible luminosité plus proche.

J'ai proposé une nouvelle méthode [Pichon, Siebert, Bienaymé, (2001)], pour inverser l'équation statistique des comptages dans le voisinage local. Afin de briser la dégénérescence de cette équation, j'ai introduit les contraintes supplémentaires requises par l'autocohérence dynamique en tenant compte des mouvements propres. L'inversion donne accès simultanément à la cinématique et à la fonction de luminosité de chaque population dans au moins deux régimes : l'ellipsoïde singulier et l'ellipsoïde de Schwarzschild à rapport d'axe constant pour les modèles plans parallèles.

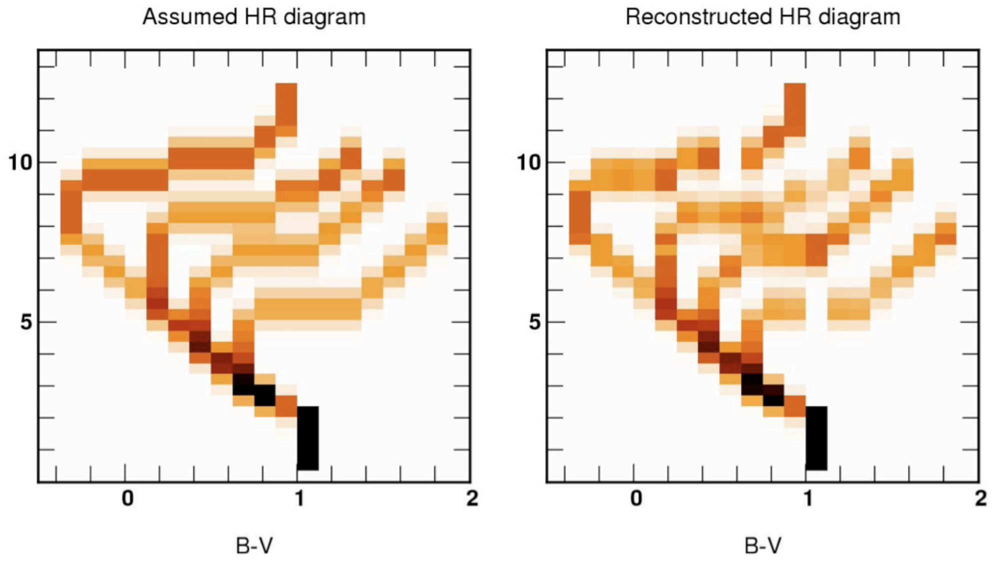

— Mise en oeuvre de la déconvolution des comptages cinématiques de données de type "Tycho". Les isocontours du diagramme HR imposé (à gauche) et reconstruit (à droite) ainsi que sa décomposition en dispersion cinématique correspondant à quatre populations distinctes caractérisées par leur rayon de décrochement à la séquence principale. [Pichon, Siebert Bienaymé, 2001].

Son application aux données telles que le catalogue de Tycho, et dans le proche avenir GAIA, conduira (en supposant connus le potentiel vertical et le courant asymétrique) à une détermination non-paramétrique de la fonction de luminosité du voisinage local sans aucune référence aux tracés d'évolution stellaire. Elle permettra aussi de déterminer la proportion d'étoiles pour chaque composante cinématique et constituera un diagnostic pour distinguer le disque mince du disque épais ou du halo.

Plus récemment, en collaboration avec A. Siebert, nous avons transposé ces travaux au régime où les vitesses radiales remplacent les mouvements propres, ce qui correspond au type de données qui seront disponible grâce au relevé RAVE.

Ce travail a eu me semble-t-il un impact en deçà de son intérêt conceptuel et technique. D'un point de vue conceptuel, il était intéressant de noter que la cohérence dynamique (l'existence d'une fonction de distribution sous-jacente qui assure à l'équilibre le lien entre les vitesses et les positions) permettait de remonter à des magnitudes absolues sans connaître la distance des étoiles mesurées, et ce même si a priori il y a une dégénérescence supplémentaire associée au mouvement propre et à la dépendance quadratique du potentiel vertical. D'un point de vue méthode, le problème inverse correspondant reste à ce jour le plus redoutable que j'ai abordé, l'espace des données ayant 5 dimensions, l'espace des paramètres 3, et le modèle nécessitant de calculer des millions d'intégrales multiples. Peut être faudra-t-il attendre GAIA pour que l'intérêt de ce type de démarche apparaisse ?

3.2.3 Magnétisme du milieu interstellaire [50%]

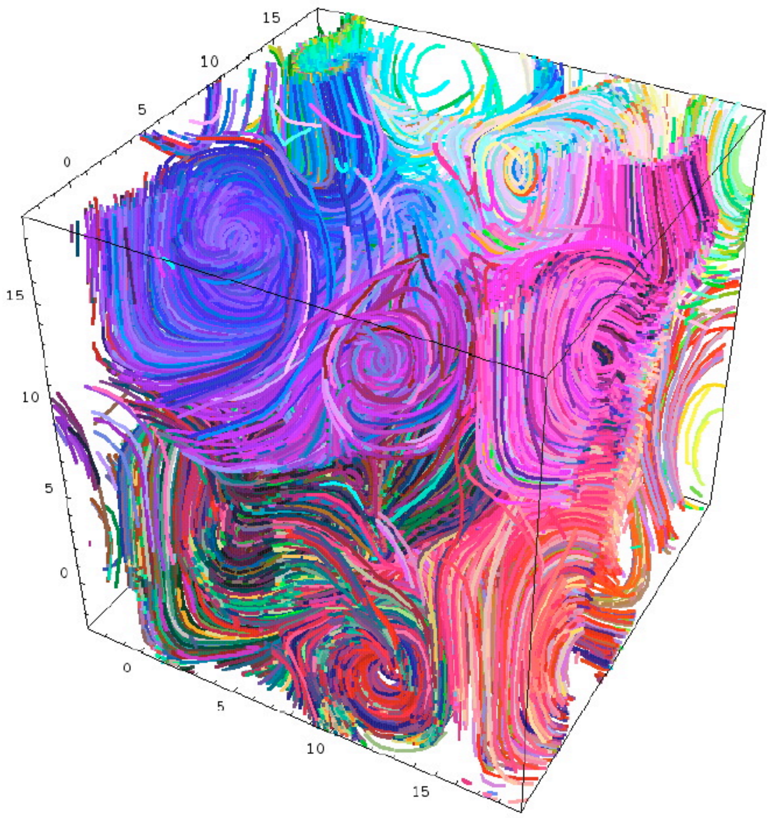

— Champ magnétique reconstruit par tomographie polarisée : le codage couleur correspond au point de départ des lignes de champ. Notez la région multiplement visitée en bas à gauche.

La structure plus ou moins turbulente du champ magnétique du milieu interstellaire reste aujourd'hui largement inexplorée. C'est pourquoi il est important d'élaborer de nouvelles méthodes pour sonder ce champ. J'ai entamé l'étude de la reconstruction tomographique du champ magnétique dans le milieu interstellaire à partir de la mesure spectrale de cartes de polarisation. Dans ce contexte, la dépendance spectrale de la longueur de Faraday permet de sonder différentiellement le milieu en profondeur et donc d'accéder au champ tridimensionnel. L'inversion permet de reconstruire le champ B en volume, et donc ses propriétés spectrales et sa topologie. C'est un problème inverse non-linéaire novateur de grande dimensionalité qui permet aussi d'étudier les propriétés statistiques d'hélicité du champ [Thiébaut, Prunet, Pichon, Thiébaut *prép*.]. L'objectif est de traiter le problème de la reconstruction du champ magnétique tridimensionnel de notre Galaxie d'une part, et de reconstruire le champ magnétique du voisinage de quasars à moyen terme en inversant aussi la densité électronique par le biais de la composante circulaire de la polarisation.

Ce problème offre la perspective de sonder en volume le champ magnétique du milieu interstellaire. Il présente néanmoins plusieurs difficultés d'ordre technique ; la première provient de la nature du noyau ; la seconde relève des hypothèses sur la distribution spatiale des électrons, et des cosmiques ; pour obtenir un problème inverse bien posé, il a été supposé que leur variation spatiale était modulée à plus basse fréquence spatiale que le champ magnétique, et pouvait donc être considéré comme constant lors de l'inversion. Deux alternatives s'offrent à nous : soit il est possible de définir une relation fonctionnelle entre ce champ et le champ magnétique, soit il doit être considéré comme un degré de liberté supplémentaire, ce qui suppose de le contraindre par un jeu supplémentaire d'observables. Une possibilité consiste à considérer la composante circulaire de la polarisation ; cependant, dans le milieu interstellaire, cette composante est typiquement plusieurs ordres de magnitudes plus faible que les composantes rectilignes. Seul le voisinage des quasars est susceptible de produire un signal suffisamment intense pour une telle détection.

3.3 Matière noire galactique.

A plus grande échelle, la problématique de la matière noire se pose de manière plus critique. En particulier, elle semble incontournable dans les régions externes des galaxies. Les enjeux actuels sont de déterminer quelle est sa distribution géométrique afin de comprendre sa nature : par exemple, quelle est sa contribution dans le disque d'une galaxie.

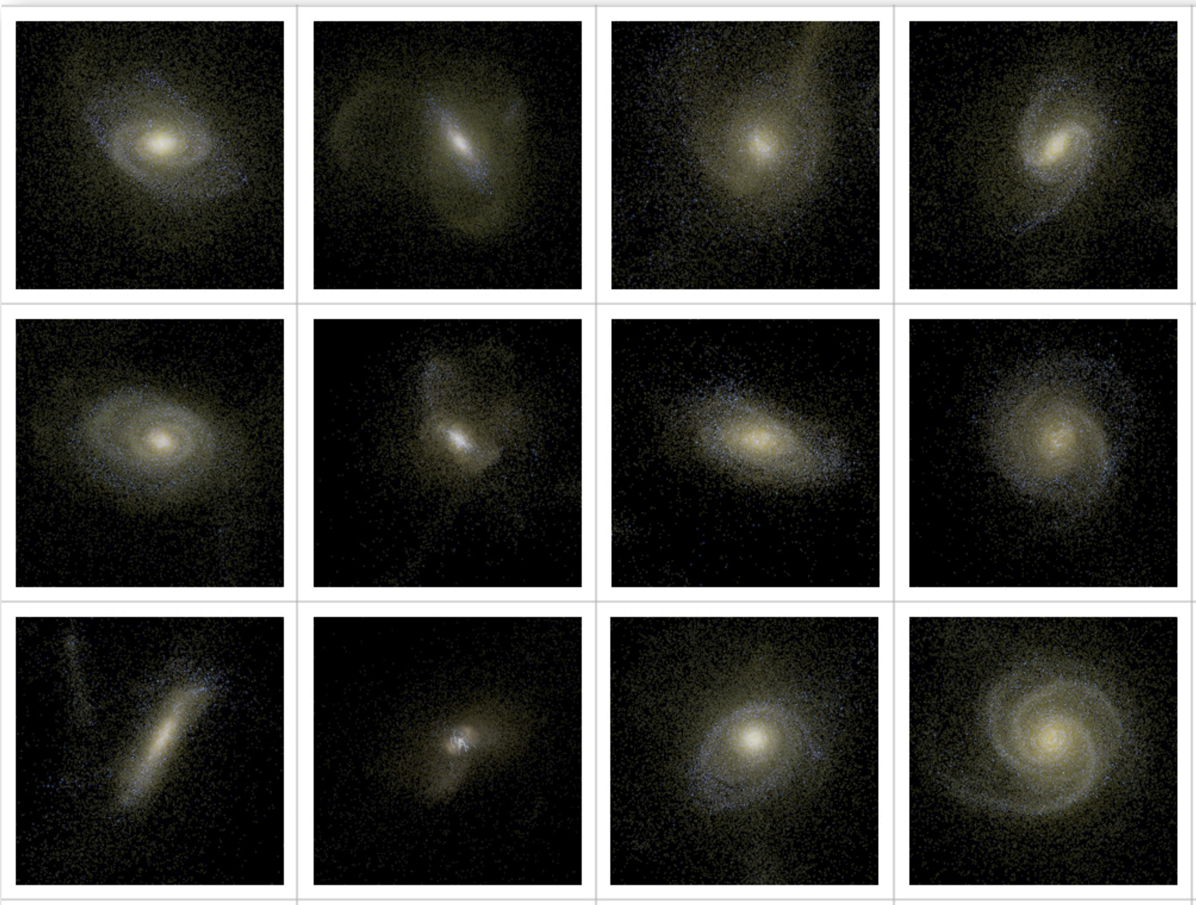

—Quelques galaxies virtuelles (parmi 160 000) apparues dans MareNostrum à z=2.4 générées par synthèse spectrale. Cette simulation “physique complète” suit la formation stellaire dans un gaz métallique d'une boîte de (50 Mpc/h)^3. La géométrie des galaxies produites et la distribution des couleurs est assez réaliste. Des simulations “zoom” conduites par R. Teyssier jusqu'à z=0 montrent que des galaxies elliptiques se forment aussi à plus bas redshift.

3.3.1 La stabilité des galaxies spirales [70%]

De par sa nature, la matière noire est difficile à observer. Néanmoins il est possible d'estimer indirectement son effet sur la matière visible voisine. Par exemple, la rotation des étoiles et/ou du gaz autour du centre d'une galaxie nous renseigne sur la distribution de masse totale, visible et invisible dans cette galaxie, et donc cette courbe de rotation peut être utilisée pour mesurer cette masse. Elle ne permet cependant pas de distinguer la composante visible de la composante noire. Pour ce faire, il faut avoir recours à un modèle plus détaillé qui tienne compte du fait que les composantes froide et lumineuse ont une dynamique assez différente. En particulier les structures observées dans de nombreux disques galactiques comme les barres, le gauchissement ou les spirales sont le résultat d'instabilités au sein de la composante froide seule mais dont la signature nous renseigne sur la distribution de la matière cinématiquement plus chaude mais invisible que constitue le halo ; par analogie, de même que l'analyse détaillée des mouvements d'un ensemble d'oscillateurs permet de déduire leur constante de raideur sans avoir accès à la nature physique des ressorts, l'analyse de la réponse d'un disque soumis à des déplacements perturbatifs virtuels permet de caractériser la "raideur" de son halo, c'est-à-dire la relative fraction de masse dans le disque.

Mes collègues et moi avons confronté directement les mécanismes d'instabilité aux observations cinématique de NGC 3198 et NGC 6503 pour fournir une estimation du rapport masse–luminosité dans ces disques. En effet une analyse détaillée des propriétés cinématiques observées permet d'induire la fonction de distribution du disque [Pichon & Thiebaut (1998)]. La connaissance de cette fonction de distribution permet de calculer le taux de croissance d'instabilités éventuelles pour ce disque qui en pratique dépend de la fraction de masse couplée dynamiquement [Pichon & Cannon (1997)].

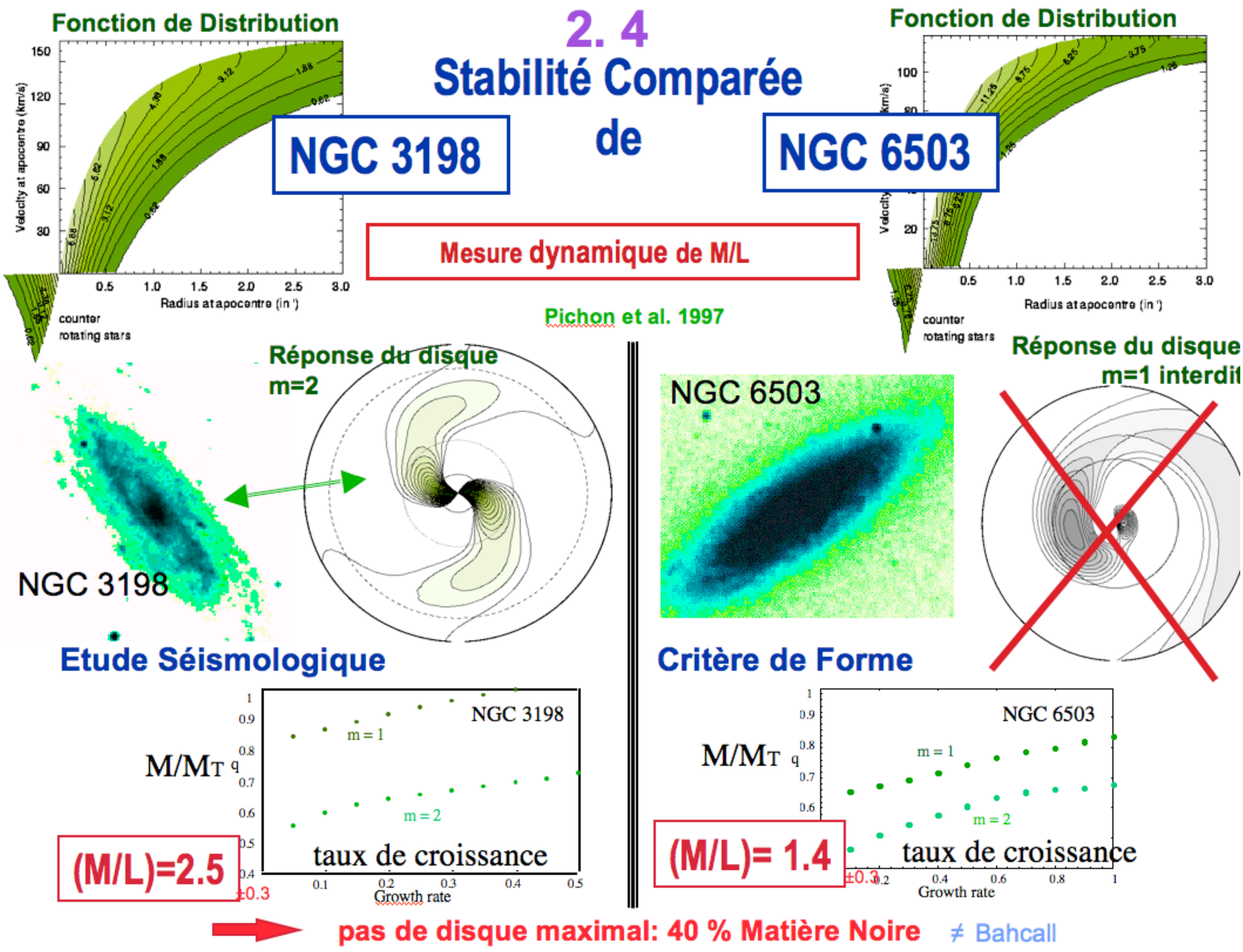

— Représentation synthétique du principe de mesure de la masse de matière noire dans le disque d'une galaxie spirale. L'ajustement de la réponse du disque ou l'absence de réponse permet de déterminer la fraction de masse dans le disque.

De la présence observée du disque sous sa forme actuelle nous pouvons inférer qu'il n'a pas subi d'instabilités rapides conduisant à la formation d'une forte spirale ou d'une barre. De ce taux de croissance maximal compatible avec les observations et de l'étude de stabilité, nous déduisons une borne inférieure pour la fraction de masse dans un halo noir stabilisant, et une borne supérieure pour la masse de la composante visible. La photométrie donnant accès à la quantité de lumière correspondante, cette analyse conduit donc à une borne supérieure pour le rapport masse–luminosité par une méthode purement dynamique, et sans hypothèse sur la chimie des étoiles.

En particulier, cette analyse permet d'apporter des éléments de réponse au problème du caractère transitoire ou intrinsèque de la formation des spirales dans les galaxies. Elle permet de plus de tester quantitativement l'hypothèse selon laquelle l'autogravité d'une galaxie spirale est dominée par le disque jusqu'au maximum de sa courbe de vitesse (hypothèse dite du disque maximal) ; NGC 3198 et NGC 6503 ne le sont pas. L'existence de modes propres d'instabilité azimutale différents pour des galaxies présentant des types morphologiques distincts constitue un lien direct entre la théorie dynamique des disques galactiques et les observations détaillées de leur cinématique.

Ce travail a fait l'objet d'une soumission de plusieurs demandes de temps de télescope (Kitt Peak, CFHT, Calar Alto), qui ont été rejetées car les TAC souhaitaient d'abord que la méthode fasse l'objet d'une validation sur des données existantes ; l'article correspondant soumis à MNRAS a été rejeté sur la base que les données existantes ne justifiaient pas une telle méthode, et que les galaxies ne pouvaient présenter d'orbite en contre-rotation ! En pratique, il conviendrait aujourd'hui de reprendre ce type d'analyse sur des échantillons plus vastes de galaxies observées (du catalogue SDSS par exemple, ou de données GIRAFFE du VLT), mais aussi issues de simulations numériques. Du point de vue de la modélisation, elle pourrait être menée avec un halo autogravitant en couplant ces résultats avec ceux obtenu dans le cadre du travail de thèse de D. Aubert (voir ci-dessous); il reste cependant à rendre compte du gauchissement possible du disque mince. Le formalisme de stabilité linéaire, qui a servi à valider le N-corps depuis, pourrait maintenant être utilisé dans le contexte des solutions numériques aux équations de Boltzmann.

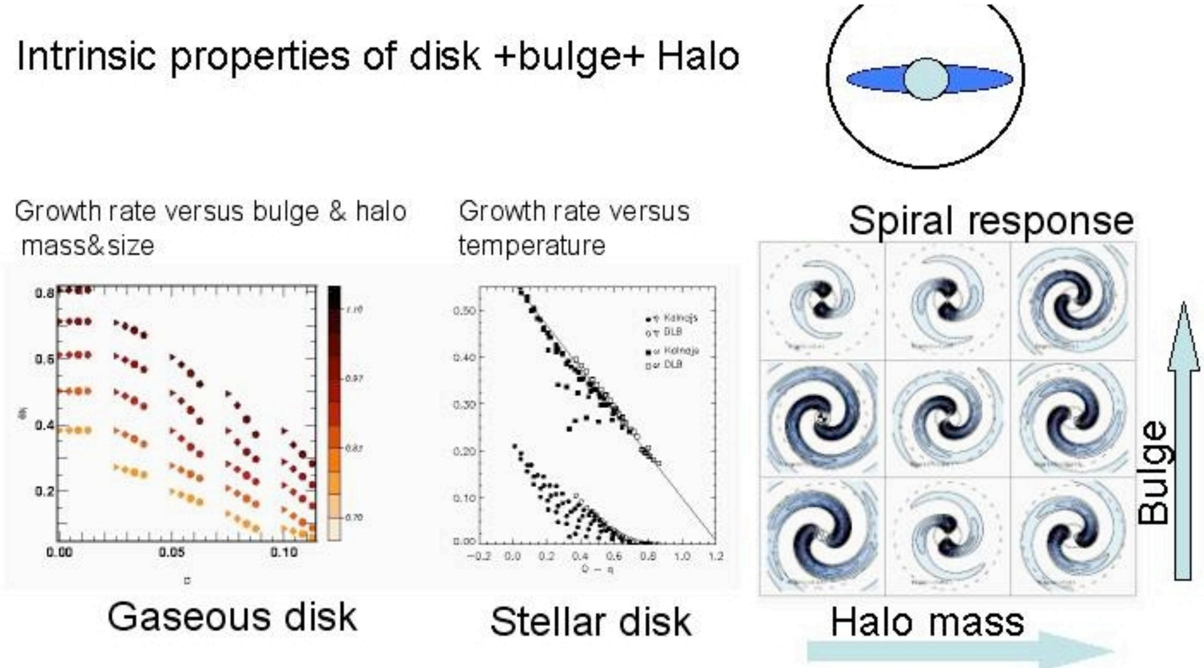

— Evolution du taux de croissance d'une instabilité linéaire et du taux de croissance en fonction d'une combinaison linéaire de la fraction de masse dans le halo, q, et de la température cinématique du disque, Q.

D'un point de vue théorique, j'ai utilisé mon code d'analyse linéaire numérique (qui calcule les modes propres d'un disque galactique quels que soient son potentiel et sa fonction de distribution) pour étudier de manière systématique les processus d'amplification de la barre en variant indépendamment le profil de température, la contribution du halo et le pic de densité central (qui détermine l'existence ou non de résonance interne de Lindblad susceptible d'absorber l'onde de densité avant amplification) [DEA de P. Ocvirk]. Ceci permet d'explorer les régimes de formation et de dissolution des barres, et en particulier le rôle du cuspide central.

J'ai enfin généralisé ce type d'analyse à l'étude de stabilité d'un disque quelconque, avec éventuellement une fraction de la masse sous forme de gaz. Dans mon algorithme, cette fraction de masse gazeuse peut être décrite soit sous forme d'un polytrope, soit comme une composante non isotrope (avec pour équation de fermeture l'annulation du tenseur de chaleur) susceptible de rendre compte de la composante nuage moléculaire du disque. L'algorithme reproduit avec succès les modes propres gazeux polytropiques publiés du disque Kuzmin-Toomre. Ces études me conduisent à des taux de précession et de croissance pour des disques mixtes.

La description du couplage gravitationnel gaz-étoile permettrait de décrire de façon réaliste les disques de type tardifs, et donc de rendre compte des propriétés de l'ensemble de la séquence de Hubble. L'objectif à terme de ce travail est de globalement reprendre les travaux de Weinberg sur l'implémentation de la méthode des matrices d'un système couplé disque-halo. Une difficulté que j'ai rencontrée dans ce contexte, et qui m'a été expliqué beaucoup plus tard par A. Kalnajs, est que les disques gazeux chauds peuvent développer des ondes *de pression* très enroulées. L'hypothèse linéaire limite cependant ce type d'analyse.

3.3.2 Evolution spectro-dynamique des disques : [70%]

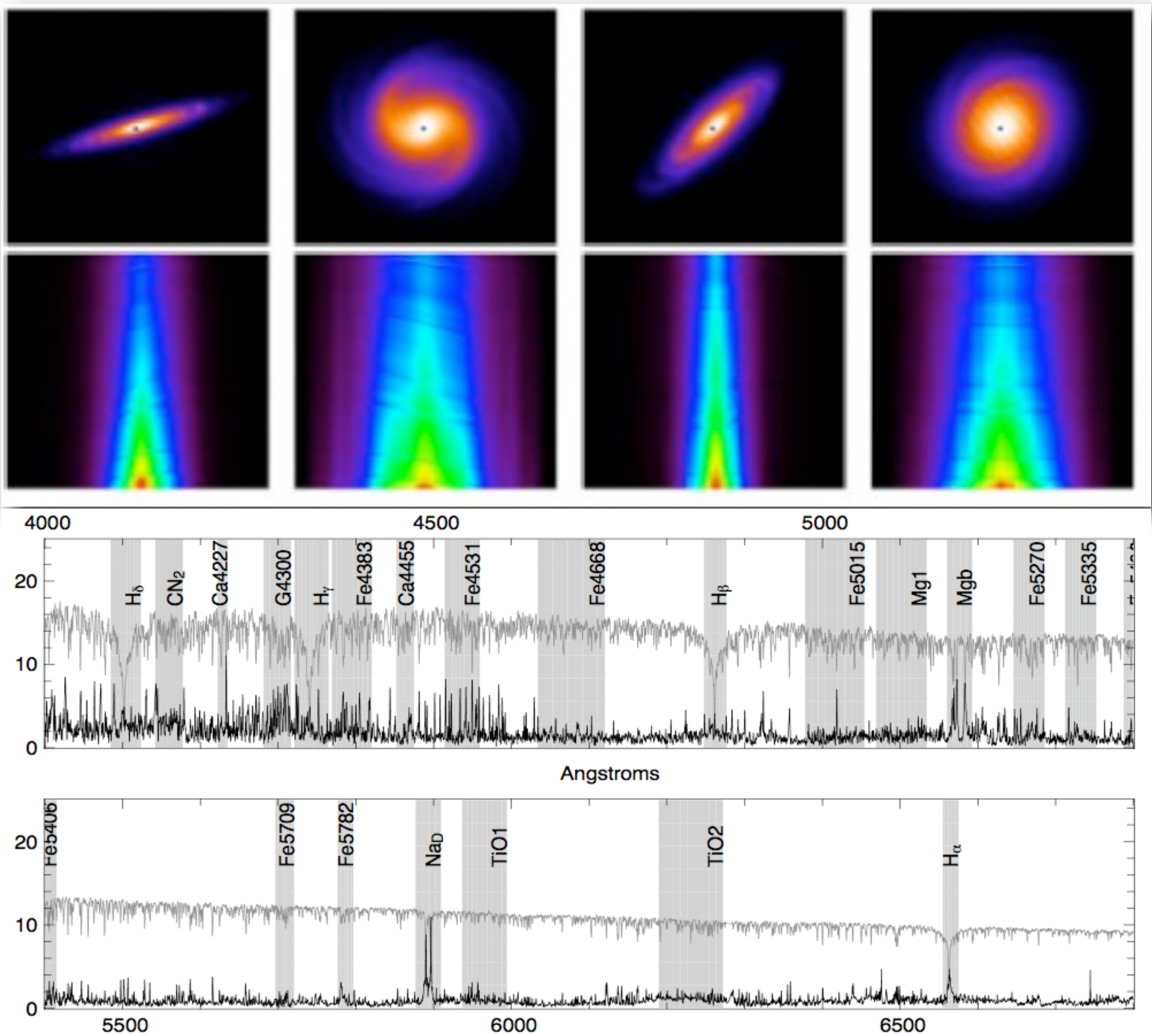

—Données synthétiques spectro-intégrales de champs de galaxies. Le panneau inférieur identifie grâce au pseudo inverse les régions du spectres pertinentes pour l'inversion.

L'étude dynamique de galaxies extérieures repose en grande partie sur la mesure, en divers points de l'objet, de la distribution de vitesses stellaires projetées sur la ligne de visée. Les vitesses moyennes et leur dispersion servent régulièrement à une première caractérisation globale du potentiel gravitationnel et de la température dynamique, mais il ressort clairement des modèles dynamiques disponibles que les moments d'ordre supérieur de la distribution des vitesses sont nécessaires à une étude plus fine (en particulier pour tenir compte des étoiles en contre rotation dans les parties centrales du disque). Récemment, il est devenu possible d'obtenir des spectres de galaxies combinant de bonnes résolutions spatiales (100 pc) et spectrales (~ 5km/s).

A. Lançon et ses collègues ont développé un code de synthèse de spectres galactiques à haute résolution spectrale. qui repose sur le modèle de synthèse de populations stellaires Pégase. En utilisant les caractéristiques instrumentales des spectrographes aujourd'hui disponibles sur les grands télescopes nous avons simulé des observations de galaxies et implémenté les méthodes d'inversion non-paramétriques que j'ai développées [Pichon, Thiébaut, 1998], pour contraindre l'évolution chémo-dynamique de la galaxie. En particulier, nous avons développé un module d'inversion qui permet de recouvrir simultanément le taux de formation stellaire, l'opacité, l'évolution en métallicité et la cinématique [Ocvirk, Pichon, Lançon, Thiébaut 2007a,b]. J'ai co-encadré la thèse de Pierre Ocvirk, qui portait sur la mise en œuvre de méthodes inverses régularisées pour le recouvrement de l'histoire de la formation stellaire et/ou des propriétés cinématiques de galaxies externes à partir de spectres haute résolution (R=10 000). En particulier, j'ai montré que l'étude du modèle inverse permet de souligner l'importance de la régularisation, de prédire les biais de l'inversion en matière de SFH, et d'identifier les régions pertinentes du spectre. Ces travaux ont trouvé un aboutissement dans la mise en oeuvre d'une variante de la méthode dans le cadre de la reconstruction de l'histoire de formation stellaire cosmique à partir des comptages de champs GOODS [Le Borgne, Elbaz, Ocvirk, Pichon *2008*] (voir ci-dessous).

Au delà de la composante astrophysique de ce travail, certains résultats sont intéressants pour les problèmes inverses linéaires en général. L'analyse de termes dominants dans la pseudo-inverse permet par exemple en principe de déterminer, en fonction du rapport signal à bruit, quelle région du spectre contraint tel ou tel paramètre physique. Couplée aux simulations hydrodynamiques cosmologiques MareNostrum (voir ci-dessous), cette méthode inverse permettrait de contraindre les biais de recouvrement de l'histoire de formation stellaire. Plus généralement, cette stratégie (génération d'un échantillon statistique de pseudo-données par le biais de simulations numériques, analyse des biais de mesure par l'intermédiaire d'une méthode inverse, validation d'un développement instrumental et déprojection des données dans l'espace du modèle pour contraindre la physique du processus) correspond à la trame de mon travail de recherche dans ce domaine.

3.3.3 Galaxies & environnement cosmologique [90%]

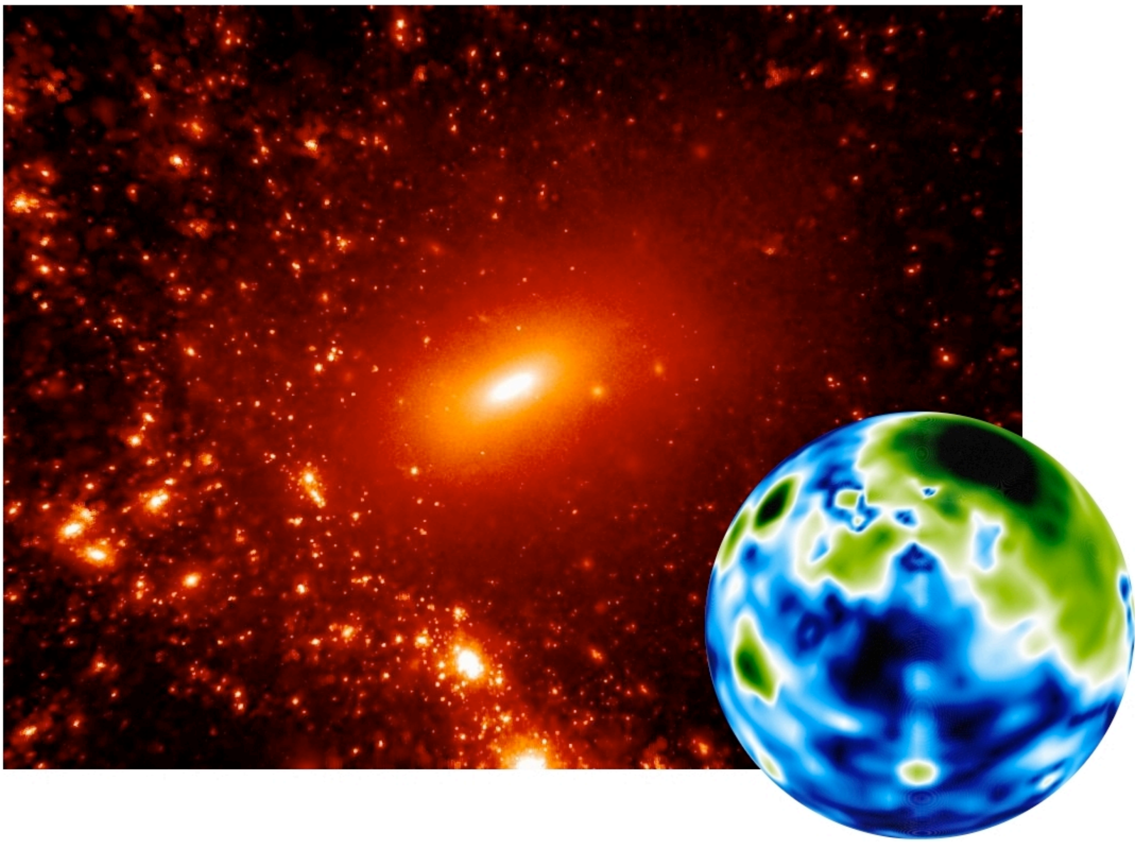

— Un exemple de simulation haute résolution 1024^3 sur laquelle la mesure des flux rentrants sur la sphère du viriel R est représentée à droite. Ces mesures permettent de caractériser la statistique de l'accrétion sur les galaxies L* pour prédire leur évolution [Aubert & Pichon 2007].

Du point de vue de son évolution dynamique, la "condition aux bords" qu'impose l'environnement cosmologique d'un disque galactique donnée est un champ temporel que nous caractérisons statistiquement, pour répondre à la question lancinante de "l'inné ou de l'acquis" des départs à l'axisymmétrie plane des disques galactiques. Dans le cadre d'un modèle cosmologique donné, je souhaite répondre à des questions du type "quel est l'effet relatif des satellites sur l'excitation spirale d'un disque (Weinberg 1998), comparé au penchant du disque à former spontanément une telle spirale (Toomre 1964)". Inversement, la confrontation statistique de ce type d'étude aux grands relevés en cours permettra de dégager des contraintes locales sur les modèles cosmologiques.

Les problèmes les plus sérieux auxquels sont confrontés les modèles hiérarchiques (la surproduction de galaxies naines dans le groupe local, la crise des cuspides de NFW, la crise du refroidissement catastrophique et la crise du moment angulaire des disques) se posent tous aux échelles galactiques Il est donc important d'étudier les effets de ce paradigme sur l'évolution galactique pour aborder ces paradoxes.

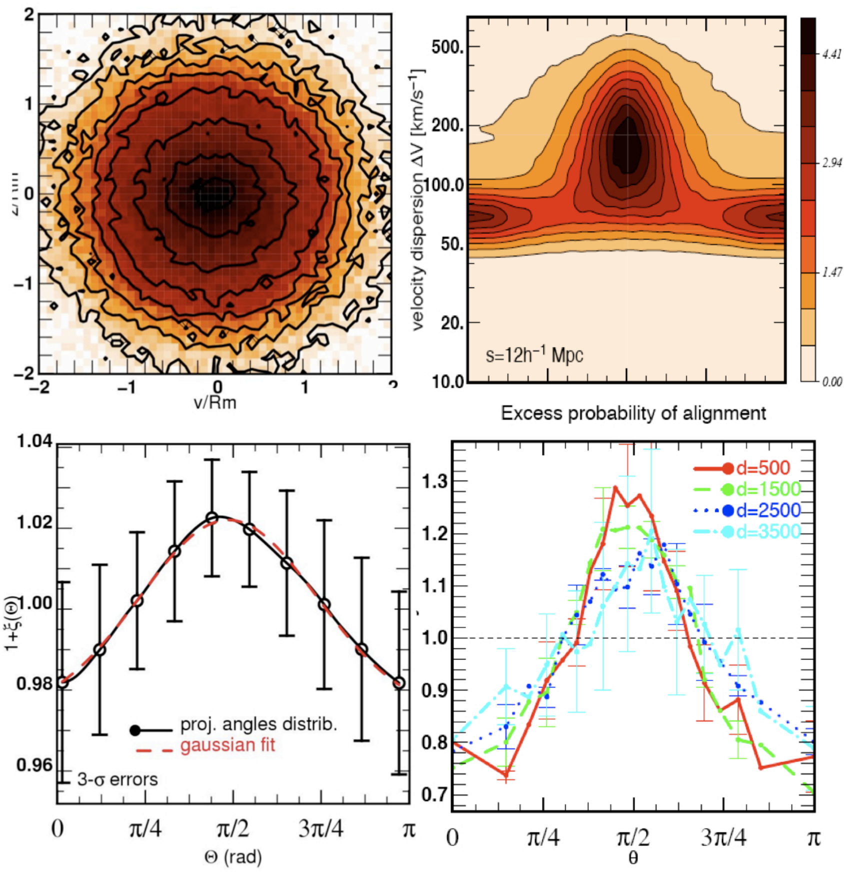

— Distribution des angles entre le spin et le moment angulaire sur la sphère mesuré à partir de 100 000 halos ; et vue en projection recentrée des satellites (*à gauche*). A droite dispersion en vitesse et orientation du spin des halos par rapport au squelette : l'accrétion est anisotrope. [Aubert, Pichon, Colombi 2004, Sousbie, Pichon et al. 2008].

Ce travail est complémentaire à l'analyse en termes d'arbres de coalescence, où l'accent est mis sur l'identification discrète de halos et le suivi des progéniteurs en fonction du décalage spectral vers le rouge. La description fluide se justifie aux échelles galactiques où une fraction dominante de la masse est accrétée sous forme d'un flux de matière non virialisée.

Elle présente de plus l'avantage de la résolution angulaire sur la sphère du viriel ; tous les mécanismes d'excitation qui dépendent de manière plus critique de la géométrie des interactions peuvent être abordés de cette façon (comme l'excitation de la structure spirale, ou encore l'accrétion prograde ou rétrograde d'un satellite, la friction dynamique...).

Spécifiquement, dans le cadre de la thèse de D. Aubert, j'ai abordé l'étude des propriétés des proches environnements des halos galactiques dans des simulations cosmologiques pour des univers ΛCDM. Par ce travail j'ai établi les liens qui peuvent exister entre les caractéristiques de la dynamique interne des galaxies (profils des halos, instabilités du disque ...) et la statistique des perturbations, qui est liée à la physique des structures à plus grandes échelle. Pour ce faire j'ai généralisé au contexte d'un système ouvert les équations de la dynamique d'un système stellaire en coordonnées sphériques. Spécifiquement, en collaboration avec J. Heyvaerts et D. Aubert, j'ai formalisé le processus de diffusion des orbites sous l'effet de la perturbation stochastique de l'environnement d'une galaxie, ainsi que l'évolution non-linéaire du couple Poisson–Boltzmann non collisionnel dans un régime ouvert ; ceci a fait l'objet d'une série de publications [Pichon, Aubert 2006, Aubert Pichon (2007)]. Cette équation de diffusion généralise le formalisme de Lennard Balescu dans le contexte de la dynamique stellaire non collisionnelle ouverte, et illustre le théoreme fluctuation-dissipation dans l'espace rectifié des angles actions du halo. Ma et Bertschinger avaient mis l'emphase sur la description des proto-halos en formation, ce qui leur permet de calculer les coefficients de diffusion qui gouvernent l'évolution galactique dans un formalisme de type champ contraint. Ici nous portons nos efforts sur les halos plus évolués subissant l'accrétion d'objets relativement moins massifs, ce qui justifie le traitement perturbatif de la dynamique interne.

Pour s'assurer une bonne représentation statistique de l'environnement des galaxies, j'ai construit une ferme de calcul de 24 processeurs pour générer, réduire et analyser environ 500 simulations cosmologiques. Pratiquement j'ai developpé un pipe-line consistant à générer des conditions initiales (GRAFIC : E. Bertschinger) et à les faire évoluer (GADGET : V. Springel) au cours du temps pour finalement les analyser avec nos propres outils parallélisés sous Yorick : mesures des flux et des densités de flux à la surface des halos, mesures des spectres de puissance et bispectres angulaires du potentiel et du flux de masse à l'interface entre le milieu galactique et inter-galactique, génération de flux synthétiques à partir des flux mesurés, reconstruction du potentiel à partir des conditions aux bords. J'ai de la sorte construit la carte d'identité de halos et de leur environnement pour environ 100 000 d'entre eux.

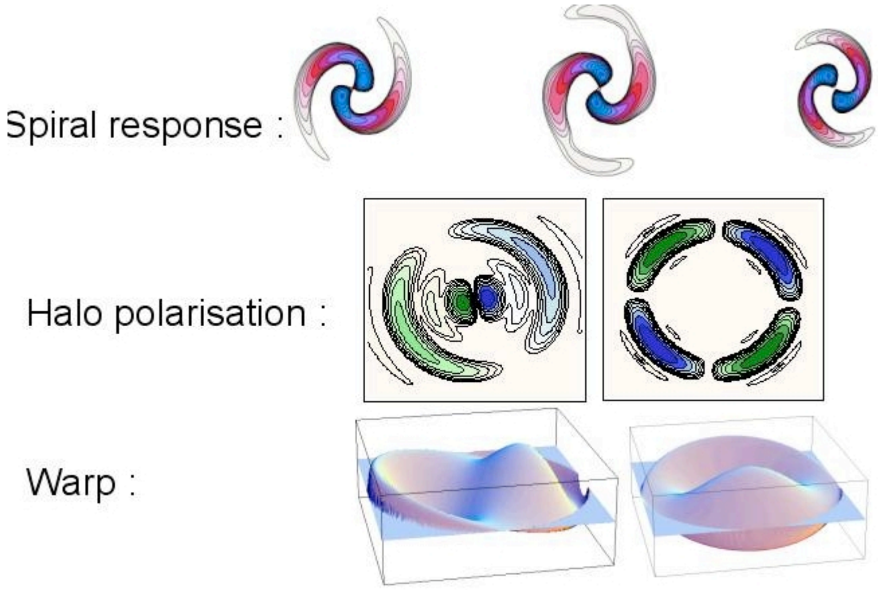

— Réponse linéaire spirale, gauchissement, et polarisation du halo en présence d'une perturbation potentielle lié à un environnement cosmologique fluctuant [Pichon & Aubert 2006].

J'ai mis en évidence la propagation des propriétés des environnements de halos vers les régions les plus internes par le biais de l'étude de la susceptibilité des halos et des disques en couplant des méthodes analytiques (réponse linéaire vis-à-vis des excitations) et numériques. Le calcul de l'opérateur de réponse en polarisation du halo me permet d'évaluer la friction dynamique exercée par le halo sur les perturbations entrantes dans la sphère du viriel (le calcul des effets non-linéaires de friction dynamique est indispensable pour tenir compte de l'amortissement de la perturbation, sans quoi les corrélations induites dans le disque et les parties internes de la galaxie sont singulières). J'ai en particulier étudié l'anisotropie de l'accrétion aux petites échelles dans l'environnement proche des halos galactiques en me reposant sur une étude statistique à un et deux points. J'en ai déduit que l'accrétion se fait préférentiellement dans le plan perpendiculaire à la direction définie par le moment angulaire du halo. [Aubert, Pichon, Colombi (2004)]. La valeur de ce spin est dominée par l'accrétion récente des sous-structures et celle-ci ne s'effectue pas de manière isotrope. Cette anisotropie peut être estimée à 15%. J'ai aussi montré que dans le référentiel du halo, les sous structures présentent un spin intrinsèque statistiquement orthogonal à leur vecteur vitesse, en accord avec l'idée d'un écoulement suivant des structures en filament, résultat qui a été confirmé depuis par la littérature et nos propres mesures avec le squelette (voir ci-dessous) [Sousbie, Pichon et al. (2008)]. Nous avons enfin mené une mesure détaillée des propriétés statistiques des processus d'accrétion de matière noire sur les halos de galaxies [Aubert, Pichon (2007)]. Le cœur de ces travaux est décrit en détail dans sa thèse.

Ce travail constitue à mon avis un des aspects les plus prometteurs de la recherche présentée dans ce document. Notamment parce qu'il devrait à terme permettre de prédire les propriétés statistiques des galaxies, moyennant sa généralisation à la physique du gaz et de la formation stellaire. Le formalisme de Vlazov-Poisson ouvert, sa résolution perturbatrice, et l'équation de Lennard-Balescu qui s'en déduit trouveront je l'espère leur audience, peut-être aussi dans le contexte de l'évolution cosmique des ceintures d'astéroïdes. La diffusion du profil moyen des halos induite par l'accrétion des sous structures cosmiques permettra il me semble d'aborder le problème de la formation des barres. L'idée est d'écrire les équations de diffusion couplées pour la composante stellaire du disque et du halo. Sous l'action de l'environnement, une fraction de l'ensemble des disques va diffuser au delà de leur seuil d'instabilité linéaire. En ce sens, le décompte de la fraction de ces objets se déduit de l'aire de la PDF du profil moyen dans la région d'instabilité. Conceptuellement, ce projet correspondait globalement à une volonté de transposer aux échelles galactiques la théorie perturbative développé entre autres par F. Bernardeau dans le contexte cosmologique.

J'étudie avec J. Magorrian et D. Aubert la polarisation d'un halo de matière noire lors de la croissance adiabatique de perturbations. Pour ce faire, nous procéderons à une comparaison entre le calcul linéaire (méthode des matrices), la réponse par la méthode dite de Young (calcul analytique), les résultats simulés du code à particules perturbatives de J. Maggorian ainsi qu'avec les résultats obtenus par intégration N-corps directs sur cartes GRAPEs. Dans le régime perturbatif, la méthode linéaire permet une description directe de la fonction de distribution dans l'espace des phases et de ses moments (densité, flux, dispersion de vitesse, moment angulaire) et adaptée au modèle à l'équilibre sous-jacent. De même, le code à particules perturbatives permet de focaliser l'intégration numérique sur les régions résonantes et constitue de fait le meilleur type de simulation pour ce type de problèmes. Enfin l'intégration à N-corps directe sur cartes dédiées constituera une référence à haute précision pour les autres méthodes, en particulier dans les études auto-gravitantes à géométrie arbitraire. A l'aide de ces méthodes, nous cherchons à comprendre la polarisation du halo liée à la croissance d'un disque, d'une spirale ou d'une barre et de sous-structures. Ceci nous permettra d'aborder les problématiques des profils NFW, des lois d'échelles type Dn-σ, de la distribution de l'émission induite par l'annihilation de particules de matière noire. D'autre part, GAIA fournira a terme des contraintes observationnelles sur le potentiel de la galaxie qui devront être interprétées en terme de croissance de perturbations [Magorrian, Aubert Pichon, *prép*]. D. Aubert et moi analysons dans l'espace des phases la réponse non-linéaire du modèle 1D plan parallèle perturbativement au second ordre avec pour objectif une comparaison avec le code simplectique de S. Colombi [Aubert, Pichon, Colombi *prép*].

Un des intérêts du formalisme perturbatif est de valider les intégrateurs numériques dans le régime symétrique où il s'applique. Une fois cette validation acquise, ce formalisme présente l'avantage d'être explicite (et peut donc être mis en oeuvre dans des méthodes inverses par exemple) alors que les intégrateurs peuvent explorer des configurations moins symétriques. La théorie des processus stochastiques (mouvement browniens etc) ouvre de plus la perspective de suivre l'évolution statistique du modèle de référence. L'inconvénient de cette formulation est de faire l'hypothèse qu'un système intégrable de référence existe, ce qui n'est pas strictement vrai en général ; cependant, les temps dynamiques dans une galaxie sont tels qu'il est raisonnable de faire l'hypothèse que si le chaos doit se développer, il le fera sauf exception (le centre galactique par exemple) sur des temps longs par rapport au temps typique entre deux perturbations dues a l'environnement.

3.3.4 Modèle HMF et formation adiabatique des barres [80%]

Une fraction importante des disques galactiques observés présente une structure barrée qui se caractérise par des isophotes allongées au-delà du bulbe central. S'il est vrai que les simulations numériques sont sujettes à de fortes instabilités bi-symétriques, seulement quarante pour cent des disques observés sont constitués d'une forte barre. Pourquoi certaines galaxies forment-elles une barre et d'autres pas?
J'ai abordé cette question en menant l'étude de la stabilité d'un système stellaire autogravitant avec pour point de vue les instabilités induites par l'alignement d'orbites résonantes. De fait, j'ai montré qu'il est possible de re-écrire les équations de la dynamique exclusivement en termes de couplage entre des flots d'étoiles décrivant une même orbite résonante. En portant mon attention sur les étoiles en résonance interne de Lindblad, j'ai montré que ce couplage conduisait à une instabilité de type instabilité de Jeans. L'instabilité de Jeans peut être interprétée comme un processus au cours duquel de plus en plus d'étoiles sont capturées par un potentiel d'amplitude croissante. Pour ce faire nous avons élaboré un modèle jouet construit sur un ensemble d'ellipses couplées par un potentiel d'interaction mutuel variant comme deux fois le cosinus de l'angle relatif d'alignement [Pichon (Knight prize 1992)].
Pour référence, ce modèle a depuis pris le nom de modèle HMF (pour *Hamiltonian Mean Field*) et est devenu une référence en physique théorique, générant beaucoup d'activité bibliographique. De la même manière, dans un disque galactique cette instabilité azimutale procède par capture du lobe des orbites résonnantes par un potentiel tournant. Le taux de précession de ce potentiel d'amplitude croissante correspond alors au taux de précession de la barre. Ce type d'instabilité n'est possible que si le moment d'inertie adiabatique des orbites piégées est positif. Ce mouvement coopératif a lieu à la résonance interne de Lindblad dans les parties centrales des galaxies. J'ai montré que le critère d'instabilité global est obtenu en considérant l'effet de toutes les résonances compatibles avec la symétrie de l'instabilité considérée [Pichon & Cannon (1997)]. J'ai par ailleurs étudié le devenir de ce type d'instabilité en construisant la fonction de distribution induite par l'alignement adiabatique d'orbites en résonance interne de Lindblad.

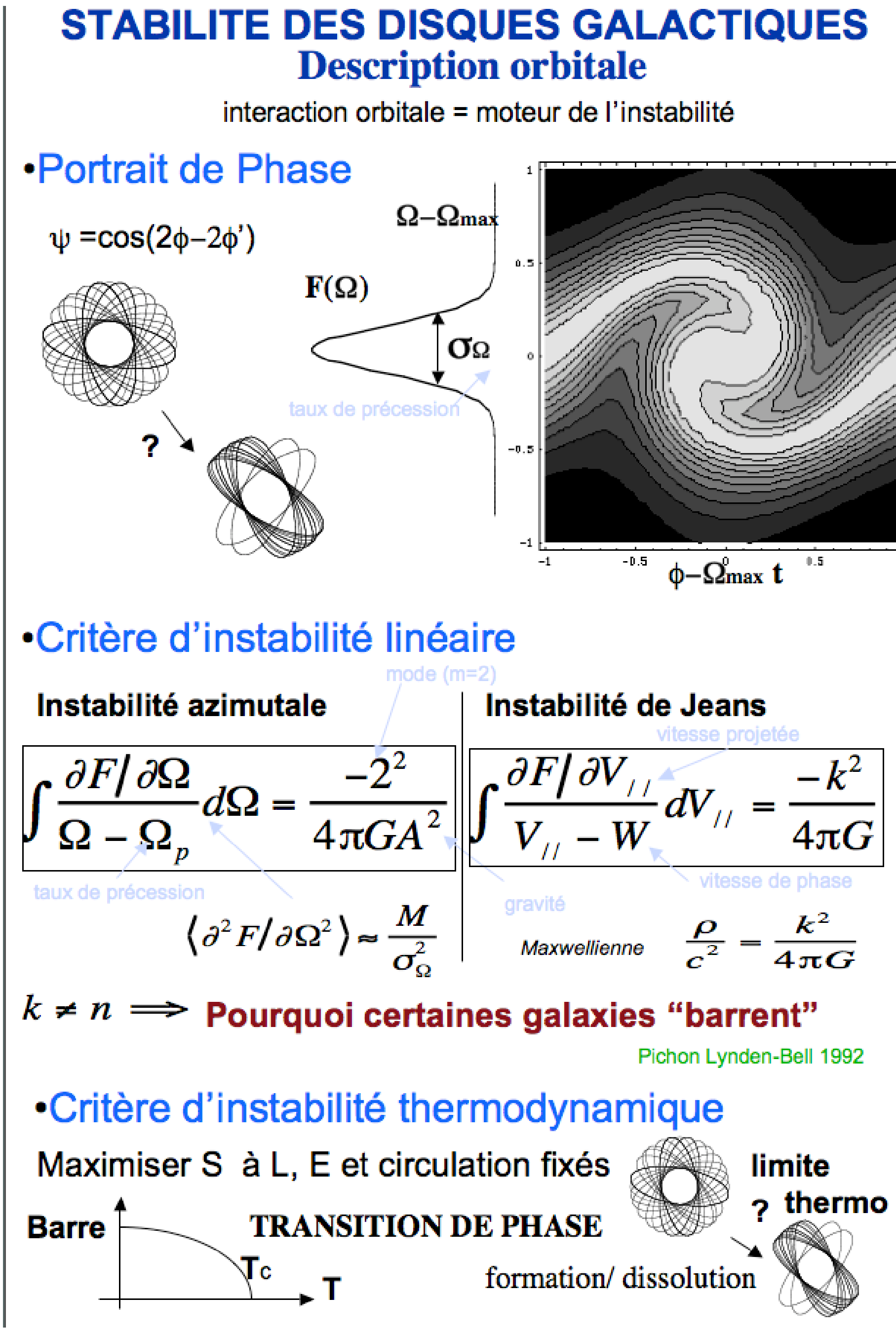

— Représentation en phase de l'instabilité azimutale de Jeans du modèle HMF expliquant pourquoi une fraction seulement des galaxies barrent. Une interprétation thermodynamique est aussi possible [Pichon, Lynden-Bell (1992)].

Cette fonction de distribution est obtenue en maximisant l'entropie du système compte tenu des contraintes de conservation du nombre d'orbites, du moment angulaire et de l'énergie totale du système, et de la conservation adiabatique détaillée de la circulation de chaque étoile décrivant son orbite. J'ai montré alors qu'il existe une température critique en deçà de laquelle le disque évolue spontanément vers un état barré avec une composante bi-symétrique naissante tournant à la fréquence prédite par l'analyse ci-dessus. Toutes les caractéristiques morphologiques de la "barre" s'en déduisent. Le système peut dans certaines configurations présenter une chaleur spécifique négative ; en considérant l'ensemble des étoiles non résonantes comme une source thermique à chaleur spécifique positive, on conçoit qu'il se produise l'équivalent d'une catastrophe gravothermale. La barre s'amplifie alors et son taux de précession décroît pendant que la température diminue encore, en accord qualitatif avec les résultats des simulations numériques. Ces résultats peuvent aussi bien rendre compte du devenir d'une barre engendrée spontanément par instabilité orbitale, mais aussi expliquer la disparition adiabatique d'une structure barrée qui posséderait une température d'équilibre en deçà de la température critique [Pichon (1992) Knight Prize, 1994 PhD].

La formulation thermodynamique de l'instabilité était une transposition assez directe de la physique du ferromagnétisme tel qu'il m'avait été enseigné en physique statistique. L'instabilité HMF est aussi la transposition au contexte galactique de l'instabilité à deux faisceaux bien connue en physique des plasmas. Elle a fait l'objet d'une étude quasi exhaustive par Chavanis en 2005. Même si dans sa formulation naïve (IRL seule) ce mécanisme prédit un taux de précession en deçà de celui mesuré dans les simulations, son extension au problème de la capture d'orbites par piégeage résonant pourrait expliquer la croissance, puis la saturation des barres galactiques, comme l'a suggéré M. Tagger en 1995.

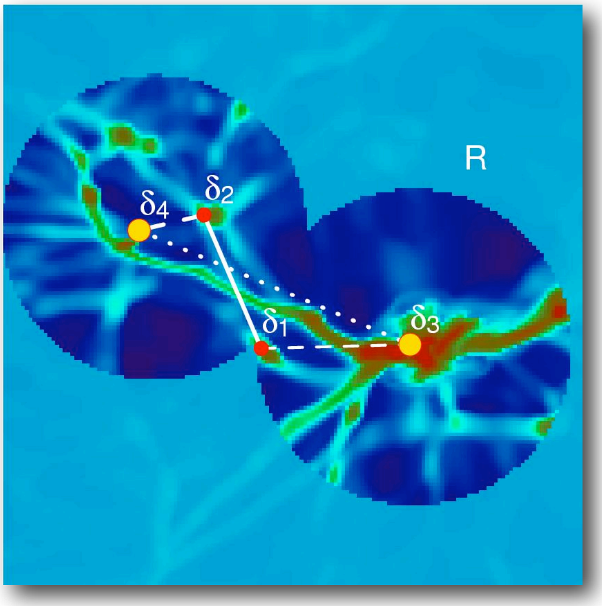

— Schéma représentant le modèle d'une pollution localisée de l'IGM : les métaux sont dans les bulles centrés sur les halos massifs. Un tel modèle permet de calculer théoriquement la fonction de corrélation attendue à la BBKS [Scannapieco, Pichon & al. 2006].

3.4 La matière noire en deçà de 10 Mpc

A plus grande échelle encore, la matière noire devient omniprésente. Elle définit le contexte de l'émergence des structures. Sa description statistique est incontournable. Elle façonne la structure du milieu intergalactique, dont nous observons indirectement la nature via les raies en absorption dans le spectre des quasars. Ce squelette définit le cadre des processus (magnéto-)hydrodynamiques qui façonnent les galaxies. Cependant, à ces échelles, la rétroaction galactique (jets, supernovae, etc.) joue aussi un role qu'il convient de définir.

3.4.1 Déconvolution de la Forêt Lymann α [70%]

Ces dernières années, un modèle cohérent de la distribution spatiale de la matière baryonique dans l'Univers a émergé de la confrontation des observations de raies d'absorption observées dans le spectre des quasars à grand décalage spectral et des résultats de simulations numériques à N-corps. Ces simulations incluent une description de l'état physique du gaz (photo-ionisation et hydrodynamique) qui apparaît confiné principalement par le potentiel gravitationnel de la matière noire. Il est ainsi possible de suivre l'évolution cosmologique du milieu inter-galactique et plus spécialement de la forêt Lymann-α. Il est apparu que la distribution spatiale des nuages de la forêt suit la structuration filamentaire de la matière noire, dont les noeuds sont les lieux où se forment de façon préférentielle les galaxies. Les simulations ont également confirmé que la forêt Lyman-α contient à grand décalage spectral une quantité de baryons très proche des prédictions de la théorie de nucléosynthèse primordiale. Elle constitue donc le réservoir de gaz qui alimente la formation des étoiles et des galaxies.

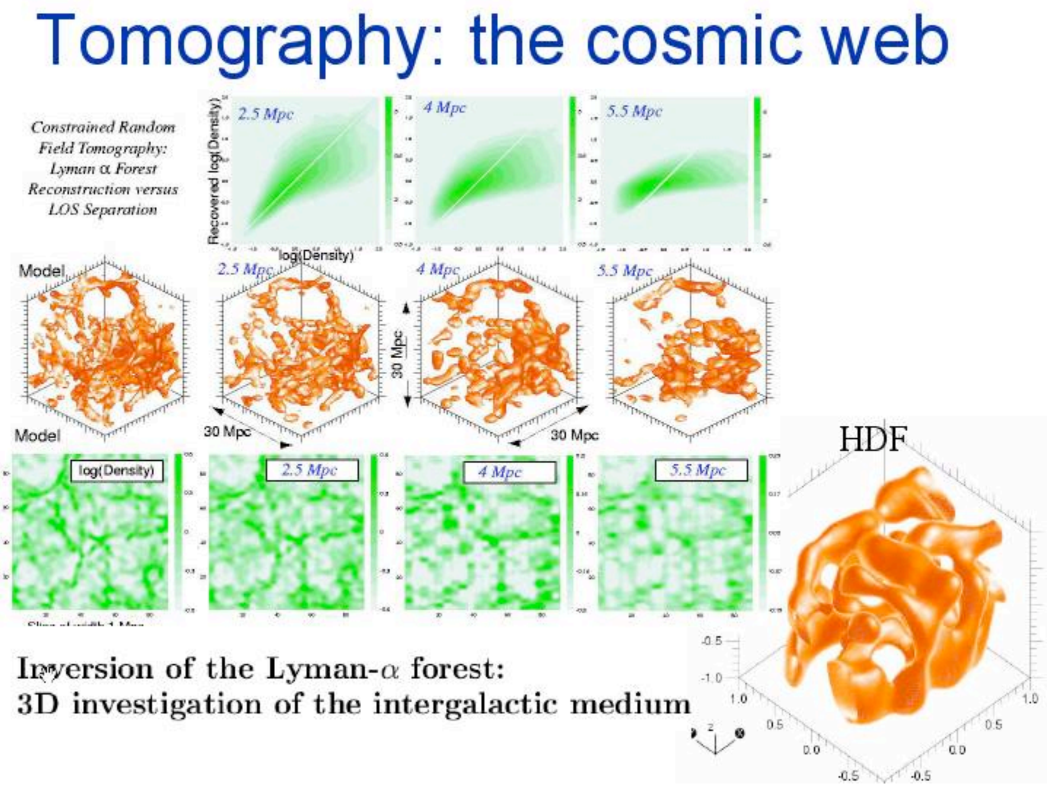

— Tomographie des grandes structures par le biais de la Forêt Ly-α des spectres de quasars les traversant. Le *prior* permet d'interpoler entre les lignes de visées. La corrélation attendue entre le champ de vitesse et le champ de densité permet de corriger partiellement de la distorsion en redshift. L'équation d'état permet de corriger de l'élargissement thermique. [Pichon & al. 2001].

Etudier la distribution spatiale du gaz absorbant à grand décalage spectral est donc un moyen unique de mettre en évidence les structures de l'Univers et de suivre leur évolution cosmologique. J. Bergeron, P. Petitjean et moi avons obtenu du temps VLT pour observer des champs contenant 25 quasars (ainsi que des paires rapprochées) afin de réaliser la cartographie 3D du milieu inter-galactique avec pour objectif la modélisation de la distribution spatiale du gaz sur toute les lignes de visée. Avec J.L. Vergely, j'ai développé et testé des méthodes statistiques d'inversion tomographique régularisée (cf. Fig 5.3) pour caractériser les structures dans ce milieu continu. En particulier, j'ai montré comment le formalisme des champs contraints permettait de relier la densité sous-jacente à la vitesse la plus probable le long de la ligne de visée, ce qui permet de corriger statistiquement les distorsions de décalage spectral vers le rouge induites par les vitesses particulières du gaz HI [Pichon, Vergely, Rollinde, Colombi, Petitjean (2001)]. S. Colombi a dans le cadre de ce projet produit une série de simulations hydrodynamiques PM correspondant à différentes résolutions et différentes cosmologies.

Ce travail fait en particulier le lien entre la théorie des champs contraints, et les méthodes inverses. Dans ce contexte, la formulation continue de Tarantola avec *prior* gaussien, s'est avérée particulièrement adaptée (de fait, elle a été développée dans un contexte de tomographie) d'autant que pour la cosmologie, l'existence a priori d'un champ log normal est motivée théoriquement. Je travaille actuellement à une extension du formalisme des champs contraints pour corriger statistiquement les distorsions de décalage spectral vers le rouge induites par les vitesses particulières du gaz HI dans des données volumétriques de type SKA ou LOFAR, ce qui correspond à une prolongation de ces travaux sur les absorbants. La technique consiste à supposer que la probabilité jointe d'avoir le logarithme du champ de densité dans l'espace réel et dans l'espace des redshifts suit une statistique non (log)Gaussienne de type Edgeworth, mais que cette correction est faible. Dans ce contexte, il est alors possible de calculer l'espérance du champ contraint, compte tenu de la donnée du champ dans l'espace des redshifts.

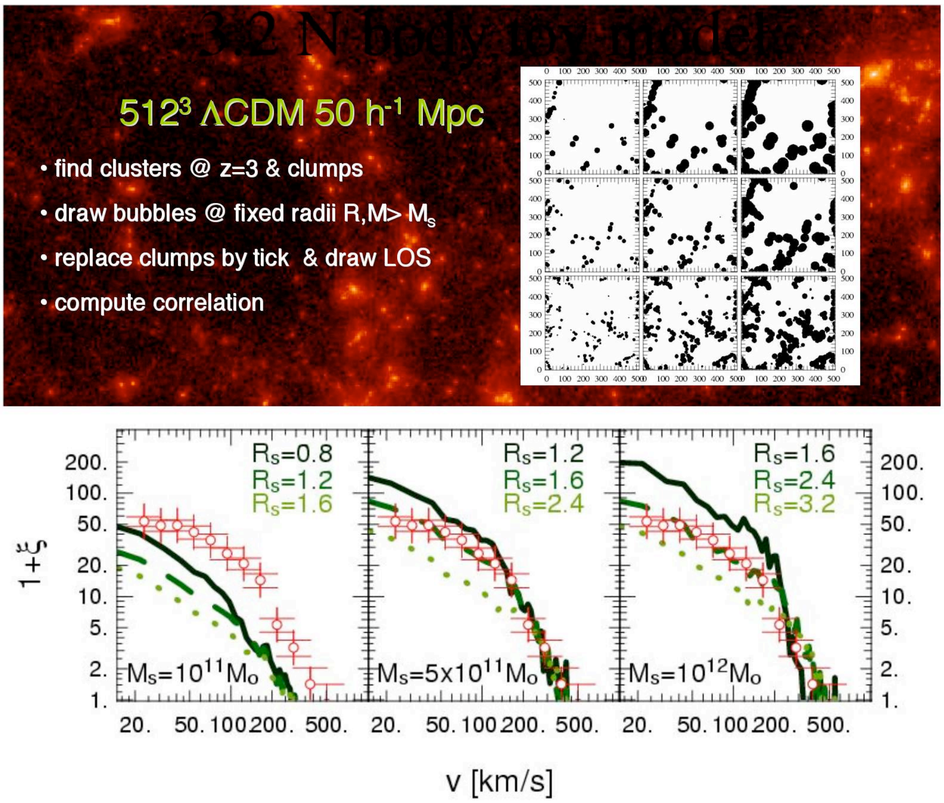

— La structuration de la fonction de corrélation du carbone dans l' IGM mesurée et modélisée par un modèle de pollueur dans des bulles ; l'amplitude du coude et sa taille permettent de contraindre la taille de bulles et la masse du progéniteur [Pichon & al. 2004].

Ces simulations m'ont permis, en collaboration avec Stéphane Colombi, Sara Caucci (que j'ai encadrée en cotutelle sur le milieu intergalactique) et Thierry Sousbie, d'étudier les propriétés topologiques du flux et ultimement de la matière noire sous-jacente [Caucci, Colombi, Pichon et al. (*2008*)]. Nous calculons en particulier les invariants de Minkovski (surface, volume, génus) des grandes structures. L'objectif est d'appliquer ces mêmes outils à des données issues de la reconstruction d'observables comme des faisceaux de lignes de visée au travers du milieu intergalactique, ou des catalogues de galaxies. Nous avons aussi comparé le squelette du champ de matière noire reconstruit à celui de la simulation de départ.

Ce travail va faire maintenant l'objet d'une étude systématique sur les simulations hydrodynamiques MareNostrum RAMSES (voir ci-dessous) et *Gadget*, où les structures du gaz en température, métallicité matière noire et densité sont systématiquement comparées par ce biais à grande et petite échelle. La géométrie de la distribution des métaux pourra être abordé en particulier avec les outils de segmentation de type peakpatch (voir ci-dessous).

3.4.2 La température du milieu intergalactique [40%]

En collaboration avec E. Rollinde, nous avons mené une première mesure de la température (12 000 K) du milieu intergalactique à décalage spectral vers le rouge de 2 à partir du QSO Q1122, et obtenu un index polytropique de l'ordre de 0,2. Nous avons montré que le rapport CIV/HI ne pouvait être constant, ce qui va à l'encontre des scenarii de mélange. Nous étudions actuellement la possibilité de contraindre l'asymétrie de la PDF du contraste en densité à partir de ces mêmes mesures afin de déterminer dynamiquement le biais cosmologique à ce décalage spectral vers le rouge [Rollinde, Petitjean, Pichon (2001)].

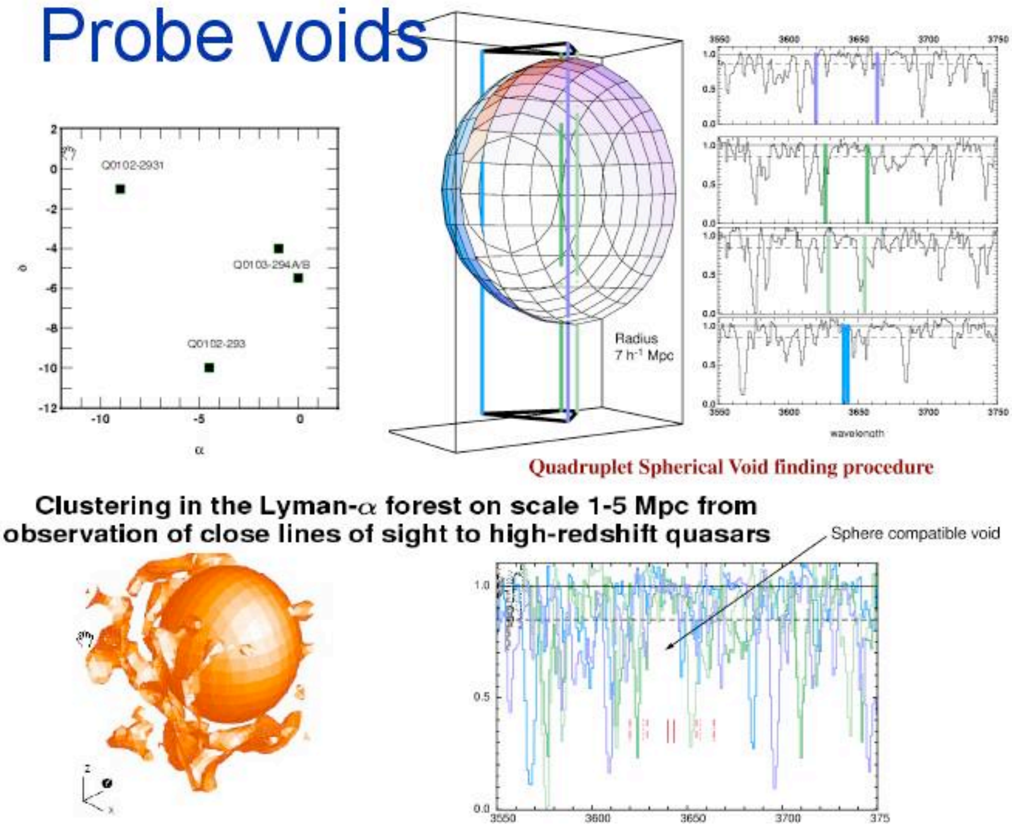

.— La taille des vides dans le milieu intergalactique par le biais de la Forêt Ly-α contrainte à partir d'un quadruplet de lignes de visée [Rollinde,Petitjean, Pichon et al., 2002].

Grâce au programme observationnel décrit ci-dessus, nous avons aussi identifié une structure vide de 25 Mpc à partir de l'observation d'un quadruplet de quasars. La confrontation de la fonction de corrélation transversale, (mesurée en comparant les positions relatives des raies d'absorption entre les deux composantes d'une paire de quasars) à la fonction de corrélation longitudinale (mesurée le long d'un spectre donné) conduit à une estimation de la constante cosmologique. En effet, la première corrélation fait intervenir une distance angulaire, alors que la seconde dépend d'une distance radiale, et le rapport de ces deux distances nous renseigne sur la topologie globale de l'univers et dépend en particulier de sa courbure [Rollinde, Petitjean, Pichon, Colombi, et al. 2002].

Depuis, des observations complémentaire de paires de quasars ont été effectuées et ont permis de compléter la première étude sur la corrélation des absorbants selon la direction transversale [Coppolani et al. 2005]. Avec Stéphane Colombi et Bastien Aracil, j'ai écrit un algorithme d'inversion de la série Lymann qui permet de reconstruire le spectre de puissance du gaz non paramétriquement (par validation croisée). Cette inversion corrigeait aussi de l'élargissement thermique des raies. L'objectif est d'inverser la forêt pour remonter au spectre de puissance de la matière noire sous-jacente.

La difficulté du travail sur l'équation d'état tient au fait qu'il convient d'inverser un champ et plusieurs paramètres simultanément (l'équation d'état), alors que l'effet des paramètres est partiellement dégénéré avec la forme du champ. Du point de vue des méthodes inverses, la difficulté consiste ausssi à éventuellement extraire à la fois un signal continu et des paramètres discrets du signal (*e.g.* l'exposant de l'équation polytropique).

3.4.3 Les métaux dans le milieu intergalactique [80%]

En parallèle, et dans l'optique d'augmenter rapidement et considérablement le nombre de mesures des paramètres physiques (température, densité, flux ionisant, turbulence, ...) du MIG, j'ai contribué à développer des outils de traitement automatique des spectres à haute résolution pris avec l'instrument UVES du Very Large Telescope en collaboration étroite avec B. Aracil. Ce travail fait partie du grand programme "QSO absorption line systems" pour lequel 30 nuits (350 heures) de VLT ont été utilisées. Nous avons automatisé l'étape primordiale et fastidieuse de normalisation des spectres et développé l'identification automatique des raies et leur ajustement physique dans les spectres à haute résolution. Enfin, nous avons mis au point une procédure d'inversion permettant d'obtenir le champ de profondeur optique pour tout multiplet métallique malgré la possible superposition fortuite d'autres absorptions [Scannapieco, Pichon et al. (2006)].

Le Large Programme VLT (PI. J. Bergeron), consiste à observer 19 quasars à haut signal sur bruit et haute résolution. Ces observations nous ont permis, grâce aux méthodes automatiques, de rassembler une statistique significative et objective sur les propriétés physiques du MIG. En particulier j'ai calculé la fonction de corrélation des systèmes carbonés (CIV et SiIV) ainsi que ferreux (FeII et MgII) des quasars du grand programme. J'ai ainsi posé une contrainte sur l'époque d'éjection des premiers métaux (ou de manière équivalente sur la masse des galaxies responsables de l'éjection) ainsi que sur le facteur de remplissage des bulles polluées par les premiers métaux (f~10%).

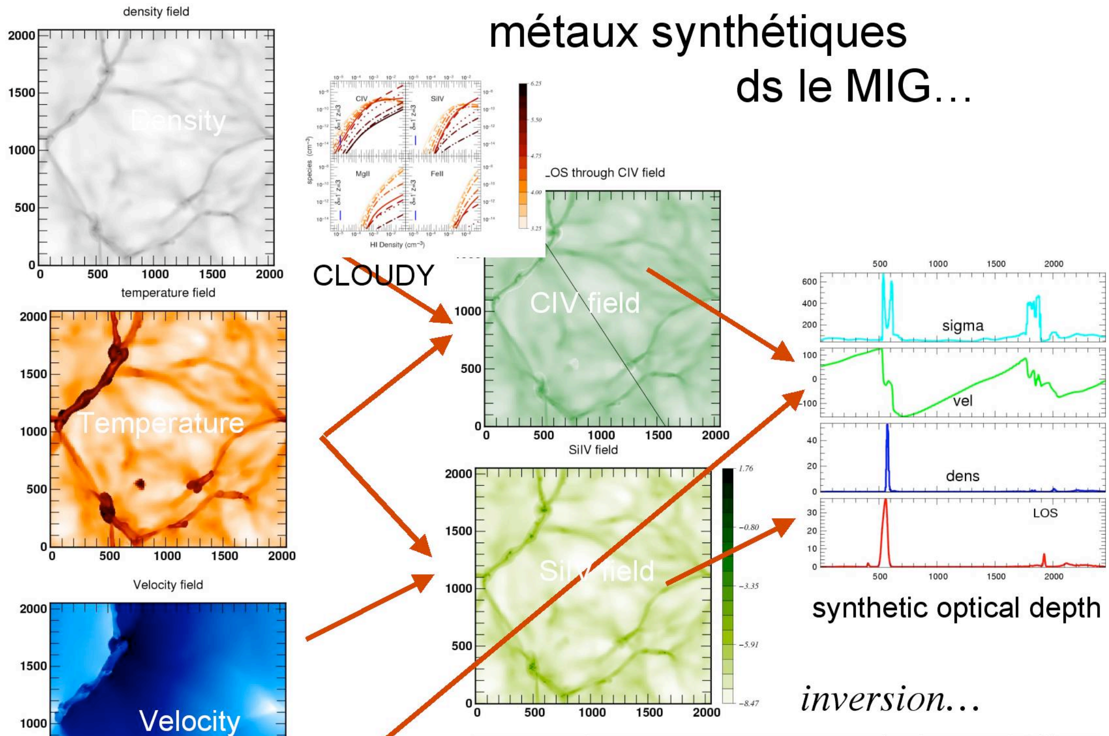

$$\tau_{\rm CIV}(x) = \int f_{\rm CIV}[n_{\rm HI}(r), T(r), Z, \alpha, J] \exp\left(- \frac{(x-r-v(r))^2}{b_{\rm CIV}(T(r))}\right) {\rm dr}$$

$$\tau_{\rm SiIV}(x) = \int f_{\rm SiIV}[n_{\rm HI}(r), T(r), Z, \alpha, J] \exp\left(- \frac{(x-r-v(r))^2}{b_{\rm SiIV}(T(r))}\right) {\rm dr}$$

— Principe de génération de spectres métalliques par le biais de simulations hydrodynamiques ΛCDM. Cet outil de synthèse a permis de valider l'estimation de la bimodalité de la fonction de corrélation des systèmes carbonés dans un modèle à bulles [Scannapieco, Pichon & al. 2004].

Cette double contrainte provient de l'amplitude de la fonction de corrélation (le biais du clustering) et de la présence d'un coude dans la fonction de corrélation correspondant à la taille de ces bulles [Pichon et al. ApJL 2004]. Avec D. Pogosyan, nous avons calculé analytiquement dans le contexte des champs contraints la fonction de corrélation des sous structures situées à l'intérieur d'une bulle de rayon R, centrée sur un amas de masse supérieure à M : ce formalisme généralise BBKS et a permis de prédire la distribution observée des systèmes FeII et MgII [Scannapieco, Pichon et al. (2006)].

Cette publication correspond à travail assez considérable de modélisation, de synthèse d'observables virtuelles, et de reduction automatisé, pour un résultat assez joli. Le résultat théorique sur la fonction de corrélation, assez pointu (il généralise à quatre points la fonction de corrélation des structures biaisées de Kaiser), a permis de *prédire* avec succès la distribution des systèmes moins ionisés (FeII, MgII), ce qui correspond à une validation de la cohérence du modèle hiérarchique. L'outil de synthèse et réduction automatique était particulièrement élaboré, et devrait être appliqué aujourd'hui à la simulation MareNostrum pour sonder les régions plus denses au voisinage des halos ; ce type d'investigation permettrait de contraindre le niveau de pollution du milieu intergalactique en métaux.

3.4.4 Profil dynamique de masse des amas [20%]

En collaboration avec F. Durret et D. Gerbal, j'ai mis en oeuvre les outils d'analyse non paramétrique que j'avais développés dans le cadre de la détermination de la masse du trou noir au centre de notre galaxie pour étudier non paramétriquement le profil de masse cumulée des amas de galaxies Abel 85 & Comas en faisant l'hypothèse que l'amas est stationnaire et isotrope. J'ai montré que ces amas étaient dynamiquement dominés par la matière noire, en accord avec les résultats du satellite X ROSAT [Durret, Gerbal, Lobo, Pichon (1999)].

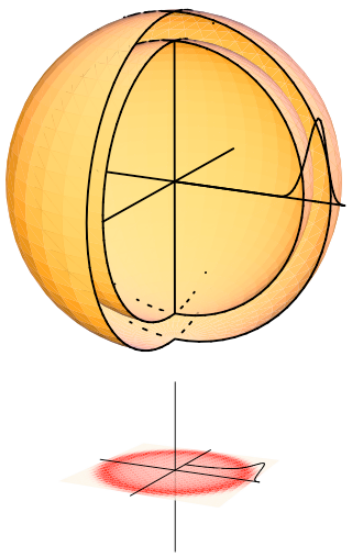

— Représentation synthétique de la projection de la base de B-spline utilisé pour la déprojection non paramétrique. Ce type de base échantillonnée logarithmiquement permet de construire avec précision un modèle mieux conditionné [Durret, Gerbal, Lobo, Pichon (1999)]

Lors des travaux d'investigation relativement à ce problème inverse, j'ai en particulier montré qu'il était possible de placer dans le noyau de la régularisation une classe entière de fonctions (solution d'une équation différentielle linéaire dont le terme de pénalisation serait la norme), ce qui permet d'utiliser l'inversion non paramétrique comme un diagnostic (ou le terme de chi^2 lève la dégénérescence). Mon rôle sur cet article s'est limité a la déprojection.

3.4.5 Cosmologie numérique et formation des galaxies [70%]

Les modèles de formation des structures dans le cadre du modèle concordant ΛCDM expliquent remarquablement bien les observations aux grandes échelles, mais semblent avoir des difficultés persistantes à bien rendre compte de la structure et l'évolution des galaxies. On peut évoquer le débat sur l'existence de cuspide de matière noire au centre des galaxies, la surproduction de galaxies naines dans le groupe local, la crise du refroidissement catastrophique et la crise du moment angulaire des disques. Tous ces débats viennent surtout d'analyses statistiques d'échantillons de galaxies qui sont confrontées aux résultats de simulations numériques. Pour faire avancer le débat, il convient, à partir des acquis des investigations numériques, d'étudier la dynamique d'une galaxie « moyenne d'ensemble » en prenant précisément en compte la réalité de son environnement, et l'histoire de son évolution.
Inversement, il est clair qu'aux échelles galactiques, les interactions avec l'environnement intergalactique peuvent prendre une forme constructive (accrétion adiabatique de gaz, moteur de l'évolution séculaire) ou destructive (chute de satellite, warp, barres, etc) en fonction de la nature détaillée du processus d'accrétion (choc d'accrétion, injection filamentaire du gaz froid, etc) Seule une analyse fine et quantitative de ces processus (paramètre d'impact, nature du fluide et des objets accrétés de la composante diffuse, orientation relative de l'accrétion) peut nous permettre de déterminer quel mécanisme l'emporte et expliquer les caractéristiques statistiques observées des galaxies et de la Voie Lactée.

Pour aborder ce problème, j'ai activement contribué à la mise en oeuvre du projet *HORIZON* http://www.projet-horizon.fr (PI Teyssier) ; je suis CoI IAP du projet depuis septembre 2006, dans la lignée du projet INC (avec S. Colombi). Ma participation s'est focalisée de manière critique dans la réalisation et la post analyse de la simulation hydrodynamique « physique complète » *Mare Nostrum (1024^3* particules dans 50 h^{-1}Mpc avec 4 niveaux de raffinement) et en particulier sur : la génération des conditions initiales ; le suivi des runs ; l'élaboration d'algorithmes d'analyses et leur parallélisation mpi (*adaptahop* : la détection des sous-structures [Aubert, Pichon, Colombi (2004)] et *powmes* : spectre de puissance multi-échelle [Colombi, Jaffe, Novikov, Pichon, *2008*] implémentés par S Colombi); la production systématique des catalogues des structures et des sous-structures ; la génération de la base de données synthétiques associée à partir des propriétés morphologiques et spectroscopiques des galaxies générées ; la production de catalogues d'observables virtuelles associées et leur mise en ligne.

Ce travail a aussi conduit à l'analyse des cartes des différents champs physiques et l'analyse des processus d'accrétion au rayon du viriel [Ocvirk, Pichon, Teyssier *2008, Dekel et al. 2008*], l'étude de fonction de luminosité et de son évolution cosmique [Devriendt, Rimes, Pichon et al. *prép.*] ; la mesure des fonctions de corrélation pondérées en flux, la construction de cartes de lentilles faibles et fortes, la génération de spectres synthétiques de QSOs et de données type spectro-intégrale de champ ; la comparaison des résultats de MareNostrum avec ceux issus d'une équipe internationale utilisant les mêmes conditions initiales et un code SPH (voir ci-dessous http://www.iap.fr/users/pichon/MareNostrum/).

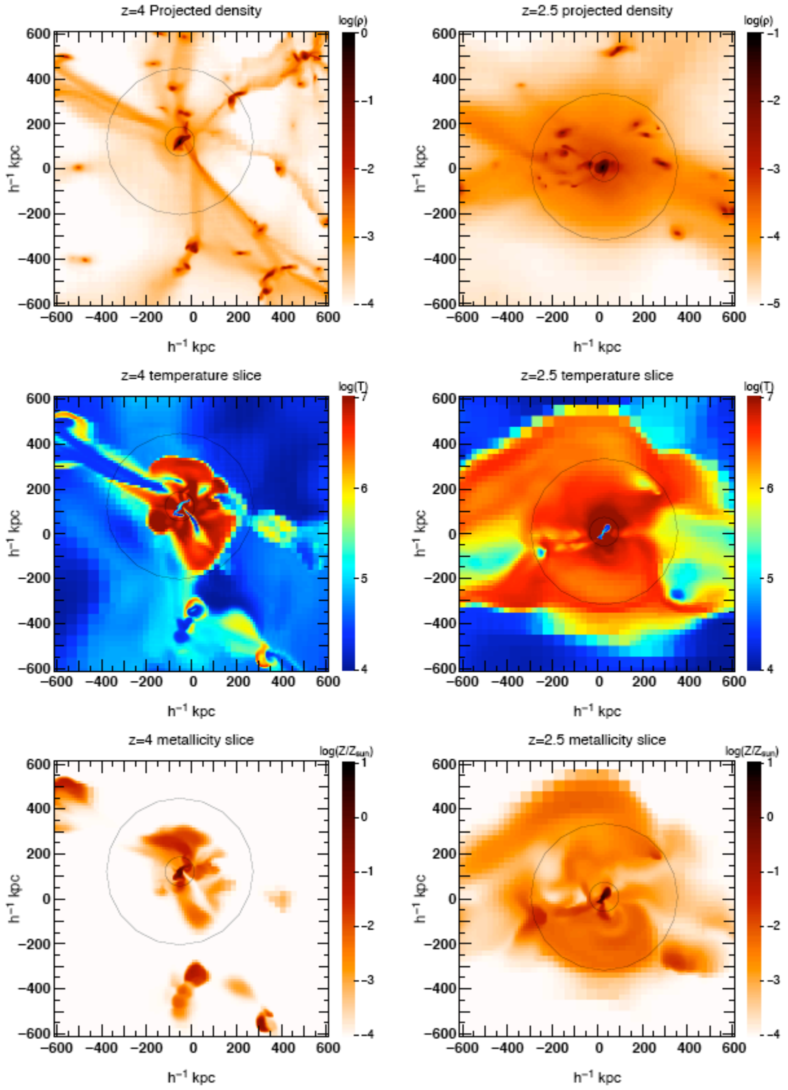

—Cartes d'accrétion dans MareNostrum à deux décalages spectraux vers le rouge différents : apparition d'une bimodalité dans la distribution des chocs en fonction de la masse du progéniteur. La nature de ces cartes est qualitativement différente pour les galaxies de fortes et de faibles masses : elle peut expliquer la rétroaction négative "anti-hiérarchique" .

Plus spécifiquement, j'ai montré avec P. Ocvirk et R. Teyssier que la bimodalité observée dans les propriétés spectro-photométriques des galaxies pouvait peut-être s'expliquer par un effet de rétroaction négative des galaxies les plus massives à redshift 2 qui, en raison de leur formation stellaire plus élevée, et compte tenu de la metallicité du gaz dans leur environnement direct, éjectent plus d'énergie thermique dans le milieu intergalactique et coupent efficacement l'accrétion filamentaire de gaz froid. *A contrario*, cette accrétion continue pour les galaxies moins massives. Les métaux jouent un rôle critique dans la définition de cette masse de transition entre accrétion diffuse chaude et accrétion froide anisotrope. Ce travail a aussi fait l'objet de la publication d'une lettre dans Nature [Dekel et al. 2008] qui argue que ce processus correspond au mode principal de régulation galactique.

Ce travail correspond au pendant hydrodynamique du travail que D. Aubert a effectué dans le cadre de sa thèse. J'ai en particulier mené la réduction systématique des clichés AMR de MareNostrum et l'extraction de tous les catalogues correspondants.

Avec J. Devriendt, nous avons montré que les fonctions de luminosité des galaxies de MareNostrum, après correction des effets d'extinction de la poussière (modélisée à partir de la métallicité) et des différences de cosmologie, étaient en accord avec celles observées dans les relevés infra rouges profonds.

En collaboration avec D. Le Borgne et P. Ocvirk, nous avons inversé les comptages par bande specrale des galaxies dans l'infra-rouge des catalogues GOODS, afin de reconstruire l'évolution cosmique de la densité de formation stellaire. L'inversion prédit aussi les fonctions de luminosité qui peuvent être comparées à bas redshift avec des catalogues existants. Nous avons trouvé que l'accord est excellent à ces redshifts. L'intérêt d'une telle inversion est de projeter dans l'espace des modèles les contraintes observationnelles relatives a la distribution "anti-hiérarchique" des galaxies observées. D'un point de vue technique, le noyau du problème inverse bi-dimensionnel est élémentaire, mais la dynamique dans les données impose une reparamétrisation logarithmique.

Cette dernière investigation, (où mon rôle a été essentiellement consultatif et rédactionnel), correspond à une première mise en oeuvre des méthodes inverses multi dimensionnelles que je développe depuis plusieurs années sur des données *observées* et non simulées. Certaines prédictions de la méthode inverse ont été confortées par des jeux de données indépendantes. Une extension possible consisterait à retrouver le taux de formation stellaire d'un échantillon de galaxies virtuelles issues de la simulation MareNostrum, pour valider les techniques d'archéologie spectrale et les biais associés. De fait, cela devrait être la motivation principale des simulations numériques couplées aux méthodes inverses.

Cet effort a aussi été accompagné par la réalisation d'un nombre important de tâches, et notamment : un gros investissement dans le hardware pour la production, le rapatriement, la gestion, et la mise en ligne des 90 To de données simulées associées à la collaboration ; la gestion de la méso machine (3 noeuds) et de la grille de calcul (7 noeuds) ; l'écriture de *mpgrafic* [Prunet, Pichon *et al. 2008.*], un code de génération de conditions initiales (incluant les oscillations baryoniques) massivement parallèle (testé jusqu'à 4096^3, pour lequel j'ai écrit le prototype de validation) et d'un code de mesure fine du spectre de puissance [Colombi, Jaffe, Novikov, Pichon *2008*] basé sur un développement sous pixel de Taylor (où j'ai fourni la simulation test) ; la production de toutes les conditions initiales cosmologiques de la collaboration : $128\text{-}1024^3$ en 20, 100 et 500 h^{-1}Mpc et jusqu'à 4096^3 pour le programme *HORIZON*-4π ; la génération de conditions initiales contraintes ; la production et la validation (spectre de puissance, fonction de masse, sous-structures) de toutes les simulations matière noire de la collaboration en 256^3, 512^3 pour 20, 100, 500 h^{-1}Mpc avec *Gadget* et 1024^3 particules pour 50, 100 et 500 h^{-1}Mpc avec *RAMSES* ; la production de simulations « zoom » issues des simulations de référence jusqu'à 4096^3, la réalisation (avec notamment R. Teyssier, S. Prunet et D. Aubert) de la simulation *HORIZON*-4π (4096^3 particules pour 2000 h^{-1}Mpc, soit presque 8 fois la Millenium), enfin la production d'outils de visualisation 2D, 3D et 4D OpenGL et stéréoscopique. Enfin, j'ai procédé à la mise en ligne de tous les produits correspondants, soit plus de 60 articles sur la partie interne et externe du site http://www.projet-horizon.fr. Cet investissement devrait profiter globalement à ma recherche sur la formation des galaxies, et à la discipline, et plus généralement à l'IAP dans le cadre du projet.

Il est paradoxal d'avoir investi autant d'énergie dans une discipline, la simulation numérique, et plus particulièrement l'hydrodynamique numérique, pour laquelle j'avais (et dans une certaine mesure j'ai encore) de sévères réserves, au moins en tant qu'outil théorique. S'il est indéniable que l'approche Monte Carlo a ses vertus dans le cadre de la génération d'observables virtuelles (ou de validations de méthodes inverses), la génération d'objets numériques fortement non-linéaires avec un ensemble d'ingrédients (algorithmiques et physiques) croissants (et rarement recoupés d'une expérience à l'autre) m'avait dans un premier temps semblé assez vaine d'un point de vue explicatif. La production d'échantillons statistiques d'objets observés, telle qu'elle est menée actuellement en cosmologie (2dF, SDSS etc) a sans doute contribué à infléchir partiellement mon jugement. Malheureusement, le mode d'évaluation actuel de la recherche biaise fortement la tendance à poursuivre cette course en avant, plutôt que de consacrer plus d'énergie à valider les outils dans ce domaine. De plus, par sa nature non-expérimentale, l'astrophysique observationnelle ne pose pas de contraintes fortes sur les modèles numériques, ce qui autorise cette dérive.

Par ailleurs, le modèle hiérarchique m'a longtemps semblé protéïforme et infalsifiable. Mais depuis 1998, date qui correspond aussi à mes premiers travaux sur le sujet, la valse des paramètres semble avoir globalement cessé. Les compétences en statistiques que j'ai acquise depuis m'ont permis de tempérer cette impression d'impunité : le modèle fait des prédictions précises pour les distributions d'observables. Dans une certaine mesure, je ne parviens cependant pas à décider si l'évolution de mon jugement correspond à une accoutumance ou à un réel progrès de la discipline !

3.5 Matière noire dans les grandes structures

A l'échelle des grandes structures, la caractérisation de la distribution de la matière noire a pour double objectif de contraindre les paramètres du modèle standard, mais aussi de définir le contexte global de la formation des *galaxies. A ces échelles, la dynamique devient relativement plus simple, mais une description intrinsèquement statistique de la formation des structures devient indispensable.*

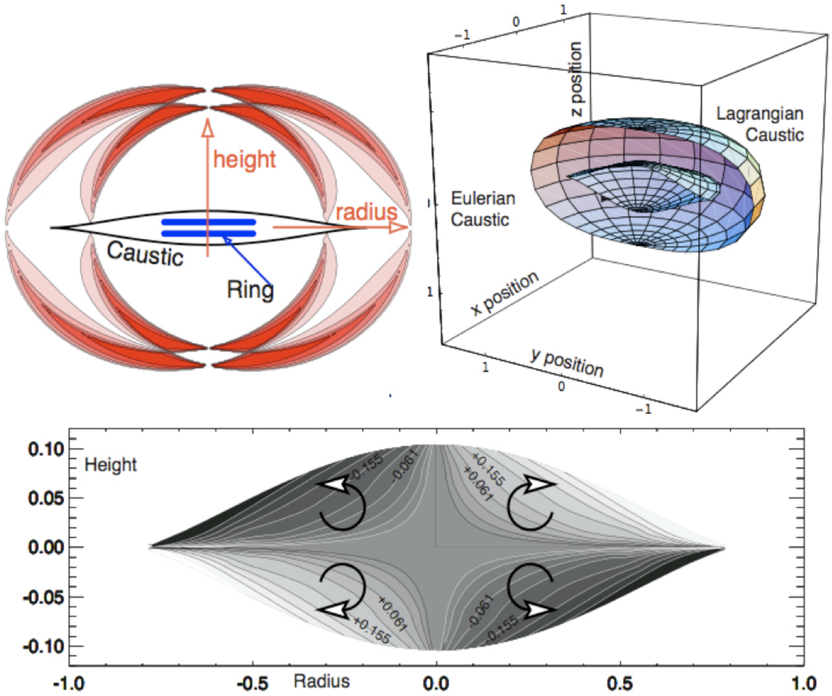

— Carte de vorticité pour la caustique la plus vraisemblable (*en bas*) ; position lagrangienne des régions contribuant au croisement de coquille (*en haut à gauche*) ; Ces cartes permettent d'estimer aux grandes échelle quelle est la contribution aux modes B de ces croisements primordiaux [Pichon, Bernardeau (1999)].

3.5.1 Emergence de la vorticité dans les grandes structures [50%]

Lors de leur formation, la dynamique des galaxies est en partie dominée par les propriétés de leurs halos. En particulier la géométrie et le taux de précession de ces halos de matière noire affectent l'évolution de la composante baryonique. Il était par conséquent souhaitable de relier statistiquement ces propriétés aux fluctuations de densité primordiale. Peebles a étudié en 1969 la distribution en moment angulaire des halos induite par effets de marée en supposant que les fluctuations à grandes et petites échelles n'étaient pas couplées. Pour aborder ce problème d'un point de vue cosmologique, le champ de vorticité constitue une grandeur macroscopique intermédiaire qu'il est possible de relier aux fluctuations élémentaires.

En collaboration avec F. Bernardeau, j'ai calculé la distribution statistique de la vorticité générée à grande échelle, c'est-à-dire la probabilité de mesurer dans une sphère donnée une vorticité supérieure à un seuil donné. Nous faisons l'hypothèse que cette vorticité est générée par croisement de coquilles dans des caustiques statistiquement rares (ce qui permet de ramener le calcul à celui d'une caustique isolée dont les propriétés statistiques se déduisent des paramètres cosmologiques par l'intermédiaire de conditions de contrainte sur la réalisation d'une surdensité correspondant à un triplet de valeurs propres pour le tenseur de déformation local). Cette approche présente un triple intérêt. Elle permet d'abord de valider le régime où le flot peut être considéré comme potentiel ; cette hypothèse d'écoulement irrotationnel est à la base de toutes les méthodes de reconstruction du champ de vitesse à partir de catalogues de décalage spectral, ou des calculs perturbatifs, qui visent tous deux à estimer les paramètres cosmologiques. La statistique du champ de vorticité est par ailleurs une quantité qu'il est possible de mesurer et d'extraire des simulations numériques en discrétisant le champ sur les cellules de Voronoi définies par la distribution des particules de la simulation. Mes travaux explorent de manière semi-analytique l'évolution et les propriétés du flot au delà du premier croisement [Pichon, Bernardeau (1999)]. Il convient maintenant de développer la théorie susceptible de relier les propriétés du champ de vorticité à la géométrie des halos primordiaux en corrélant les champs de vorticité et de densité.

Les caustiques formées lors du premier croisement de coquille sont maintenant à la limite de résolution des simulations N-corps, moyennant un échantillonnage suffisant de l'espace des vitesses. J'envisage donc de mener numériquement la mesure de cette vorticité générée par croisements.

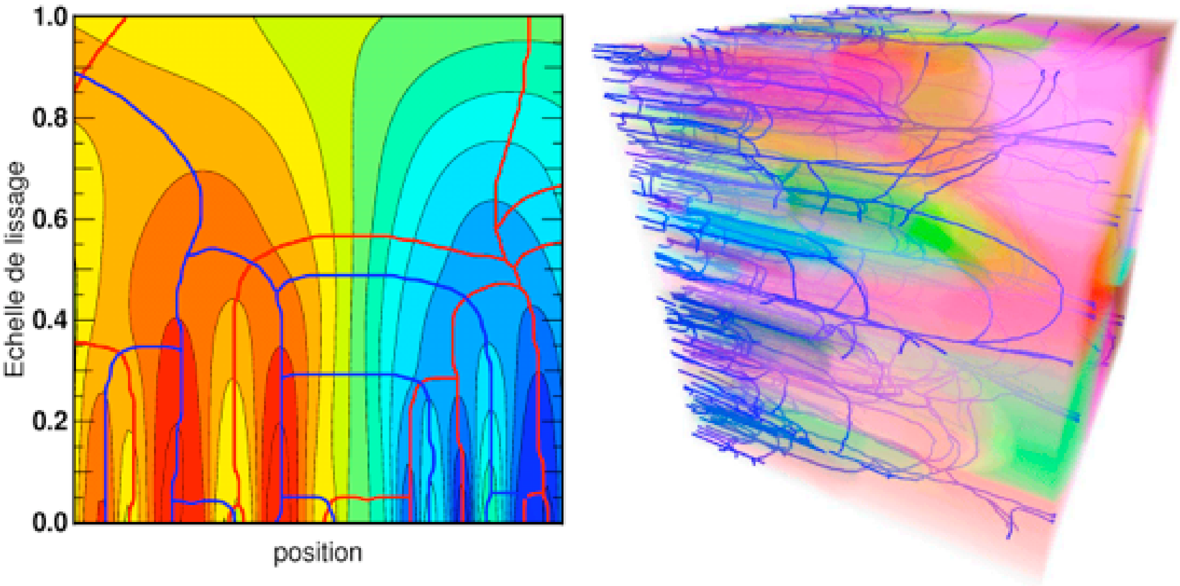

—Le squelette (*bleu*) et l'antisquelette (*rouge*) d'un champ gaussien invariant d'échelle 1D (*à gauche*) et 2D (*à droite*) dans l'espace position-lissage. Dans ces espaces abstraits, le squelette représente l'arbre de coalescence du champ. La théorie multi-échelle des peakpatches de Bond et al. et Hanami permet de faire le lien entre ces deux espaces.

3.5.2 L'émergence du chaos dans les grandes structures [80%]

S'il est acquis qu`à grande échelle, la formation des structures (filaments, vides, murs) est assez bien décrite par la physique quasi linéaire (approximation de Zeldovitch, théorie perturbative...), la question du comportement plus ou moins stochastique de la dynamique gravitationnelle à plus petite échelle se pose de manière récurrente, et notamment dans le contexte des tentatives de re-simulation de l'univers local. En collaboration avec J. Thiébaut, j'ai abordé cette question en comparant des observables Eulériennes et Lagrangiennes issues d'un jeu de simulations numériques N-corps qui ne diffèrent que du point de vue des phases des conditions initiales. J'ai montré qu'à des échelles typiquement intra amas, les exposants de Lyaponov (définis comme la dérivée du logarithme de la dispersion inter-simulation en fonction du facteur d'expansion) augmentent avec l'amplitude des fluctuation initiales, tant du point de vue Lagrangien (masses caractéristiques) qu'Eulerien (longueur caractéristique). [Thiébaut, Pichon et al. (2008)]

Ces travaux gagneraient à être étendus à plus petite échelle, notamment lors de la formation des structures virialisées, en se reposant peut-être sur la théorie KAM et en faisant intervenir des invariants adiabatiques.

3.5.3 Le *Skeleton* des grandes structures [70%]

La toile cosmique représente sans aucun doute un des exemples les plus frappants de motif géométrique. Sa complexité intrinsèque rend sa compréhension délicate, mais celle-ci est d'une grande importance car la structure filamentaire actuellement observée de la distribution de matière conserve les traces de l'évolution de notre Univers depuis sa naissance. De plus, elle définit la nature de l'environnement dans lequel se forment les galaxies et la compréhension de son influence est donc critique. D'après la théorie de Bond et. Al (1996) qui est la plus communément acceptée, la structure filamentaire de la distribution de matière a pour origine la cohérence à grande échelle des fluctuations initiales du champ de densité, accentuées par les divers effets gravitationnels non-linéaires entraînant la croissance des halos par accrétion de matière ainsi que leurs fusions.

Le Squelette local 3D, le lieu géométrique où le gradient du champ est premier vecteur propre du Hessien [Sousbie, Pichon et al. (2007)] a été développé pendant la thèse de T. Sousbie, que j'ai co-encadrée, et correspond aux lignes de crête du champ de densité : c'est un outil d'analyse de la topologie et de la géométrie des grandes structures qui permet d'une part de donner une définition mathématique de la structure filamentaire de la distribution de matière dans l'Univers, et d'autre part d'en formaliser l'extraction et la caractérisation par le biais de méthodes numériques basées sur l'intersection de surfaces critiques. Sa mise en oeuvre sur le SDSS permet de poser une contrainte sur le contenu en matière et la géométrie de l'univers (longueur totale et différentielle

[Sousbie, Pichon et al. (2007)], de mener un test de Alcock-Paczynski pour contraindre les paramètres de courbure et de contenu en énergie de l'univers [Pichon, et al., *prép*], d'étudier l'évolution dynamique des filaments et faire le lien avec la théorie des champs aléatoires pour conduire un test de non-gaussianité et la relier avec la théorie de la bifurcation [Pogosyan, Pichon, et al., *soumis*, Colombi, Pichon, Ringeval *prép.*].

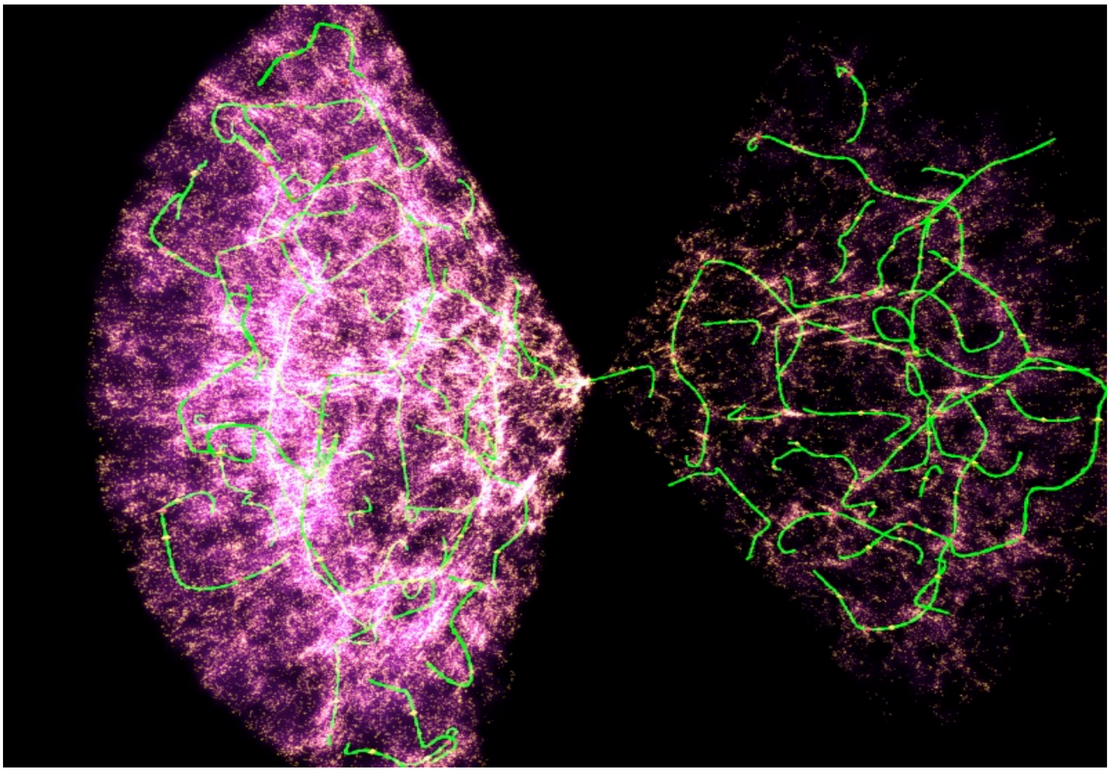

— Le squelette local de la distribution de galaxies dans le SDSS permet de contraindre le contenu en matière noire. Plus la constante cosmologique domine moins les filaments sont longs par unité de volume. [Sousbie, Pichon et al. (2007)]

Le squelette global repose sur une formulation probabiliste de la recherche de ses lignes critiques suggérée par S. Colombi. L'obtention d'un squelette continu et totalement connecté (par opposition au squelette local développé précédemment) permet de plus de se « promener » le long de la toile cosmique, rendant possible la caractérisation précise des propriétés des galaxies en fonction de la distribution de matière dans leur environnement (position dans les filaments, structure dynamique interne, distance curviligne aux halos les plus proches, anisotropie du tenseur de pression, orientation du tenseur de chaleur, etc…). Nous avons en particulier montré que le déplacement de Zeldovitch préservait la structure du squelette cosmique moyennant un lissage sur une échelle calibrée en fonction du facteur d'échelle, a, et de l'échelle de non-linéarité. En collaboration avec D. Pogosyan, T. Sousbie et S. Colombi, notre but est aussi d'étendre le formalisme du squelette aux espaces de dimension quelconque, afin d'une part d'étudier les propriétés de la distribution de matière dans un espace 6D des phases (position-vitesse) à partir de simulations numériques, et d'autre part de donner une suite à certains travaux théoriques en faisant le lien entre évolution temporelle de la distribution de la matière et squelette calculé dans un espace position-échelle de lissage, et en particulier du parallèle entre les squelettes 4D dans l'espace position-lissage et position-temps.

Enfin, en parallèle, nous explorons l'exploitation de l'outil squelette ND au delà de la thématique de l'astrophysique, et en particulier dans les domaines médicaux comme la neurologie ou le diagnostic préopératoire. Nous avons pour ce faire déposé une licence CECILL pour le logiciel de tracé de squelette ND.

En collaboration avec D. Pogosyan, j'ai étudié les caractéristiques statistiques des lignes critiques d'un champ ; j'ai en particulier mené le calcul analytique exact de la longueur différentielle du squelette local dans l'approximation dite du squelette "tendu", qui consiste à négliger les variations du hessien relativement aux variations du gradient dans le calcul du vecteur tangent au squelette. Dans ce contexte, nous avons en particulier montré que le flux d'élément de squelette est proportionnel à la courbure gaussienne moyenne de la section mono-dimensionnelle du champ. Ce calcul revient a marginaliser analytiquement une PDF de dimension 20 en se reposant sur ses symétries. Cette approximation permet aussi de calculer la distribution statistique de la courbure du squelette, et d'identifier la nature des points singuliers (vecteur tangent nul) des lignes critiques : points critiques (gradient nuls), points de bifurcation ("vecteurs propres" du tenseur des dérivées troisième du champ) et points plateaux (courbure nulle dans la direction transverse à la ligne critique) [Pogosyan, Pichon, et al. 2008]. J'étudie par ailleurs l'évolution des propriétés spectro morphologiques des galaxies en fonction de leur environnement mesurées par la distance au squelette [Gay, Pichon, Le Borgne et al. *prep.*]

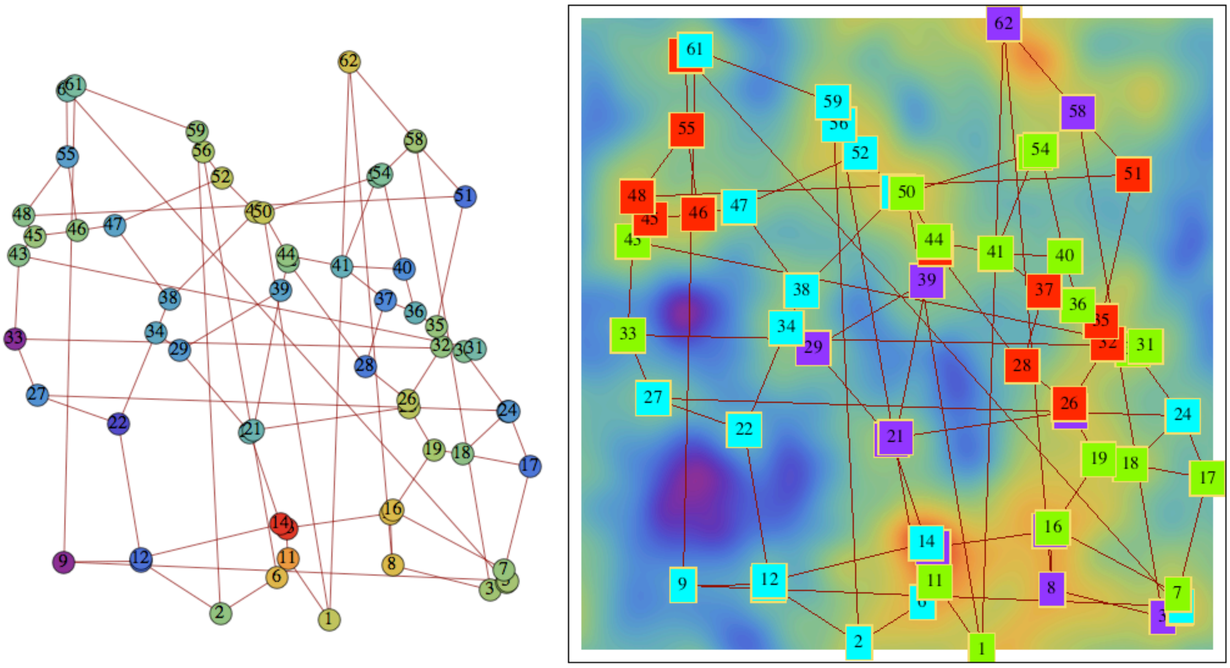

—Squelette logique extrait d'un champ gaussien aléatoire. Un développement possible de nos travaux sur le squelette d'un champ à N-D est d'en étudier la topologie et les propriétés de connexion des points critiques d'un champ au sens de la théorie des graphes discrets (diamètre, robustesse, invariance d'échelle, etc) pour la relier au continuum associé.

J'ai calculé les gradients des couleurs, de la métallicité et de l'âge des galaxies en fonction de la distance aux filaments dans la simulation hydrodynamique MareNostrum. Cette analyse conforte mes travaux sur le devenir dynamique des galaxies relativement aux grandes structures : les galaxies se forment en volume, et migrent vers les filaments pour s'écouler vers les amas. Ce mouvement est retracé dans le spin et le champs de vitesse des galaxies relativement au système de coordonnée défini par le filament. De même, la spectro-photométrie des propriétés des galaxies reflète ce mouvement. J'ai aussi formalisé le calcul de la longueur différentielle du squelette global, comme géodésique moyenne (au sens de moindre action *et* de moyenne d'ensemble) parmi toutes les trajectoires possibles et toutes les réalisations possibles d'un champ contraint.

Les perspectives de cette thématique semblent aller bien au delà de la cosmologie. En particulier sa mise en oeuvre sur des espaces abstraits dans le contexte de la théorie de la bifurcation me semble très intéressante. La segmentation dans des espaces symplectiques augmentés (espace des phases+gastrophysique) permettra peut-être d'identifier des courants d'étoiles de résidus d'accrétion, etc. Au-delà de l'astrophysique, le squelette peut servir à la détection des dendrites neuronales, et des vaisseaux sanguins du foie avant opération. Les principaux chantiers sont actuellement i) la gestion du bruit et ii) la gestion des lignes critiques secondaires, et en particulier les lignes évanescentes. Spécifiquement, je travaille actuellement à la caractérisation du profil universel des filaments, et de leur connectivité au rayon du Viriel. Je tente de formuler avec D. Pogosyan une théorie variationnelle des lignes de crête d'un champ gaussien aléatoire, avec entre autres objectifs l'identification du squelette moyen d'un champ bruité. Mon souhait est d'utiliser mes algorithmes de champ contraint pour étudier la statistique de ce squelette en fonction des propriétés des sommets. Avec S. Colombi, nous tentons enfin d'utiliser les peakpatches comme test de non gaussianité pour la détection des cordes cosmiques dans les cartes Planck du fond diffus cosmologique.

3.5.4 Astigmatisme cosmique plein ciel [80%]

J'ai plus récemment abordé le problème de la reconstruction de cartes de convergence gravitationnelle [Pichon, Thiébaut et al. *soumis*] à partir de mesures d'ellipticités sur l'ensemble de la voûte céleste. Pour ce faire, j'ai utilisé les cartes de kappa obtenues à partir de notre simulation Horizon-4π, et j'ai transposé sur la sphère les techniques d'inversion pénalisée que j'avais développées par ailleurs. Cet travail d'inversion gère en particulier les masques et la contamination associée en modes B, la non-linéarité du modèle, et les amas quasi ponctuels à l'échelle de la carte par une pénalisation adaptative. J'utilise aussi le squelette et les comptages des points sources (à l'intérieur de chaque patch) pour quantifier la qualité de la reconstruction. Je démontre que l'interpolation associée à la régularisation est extrêmement efficace pour "boucher les trous".

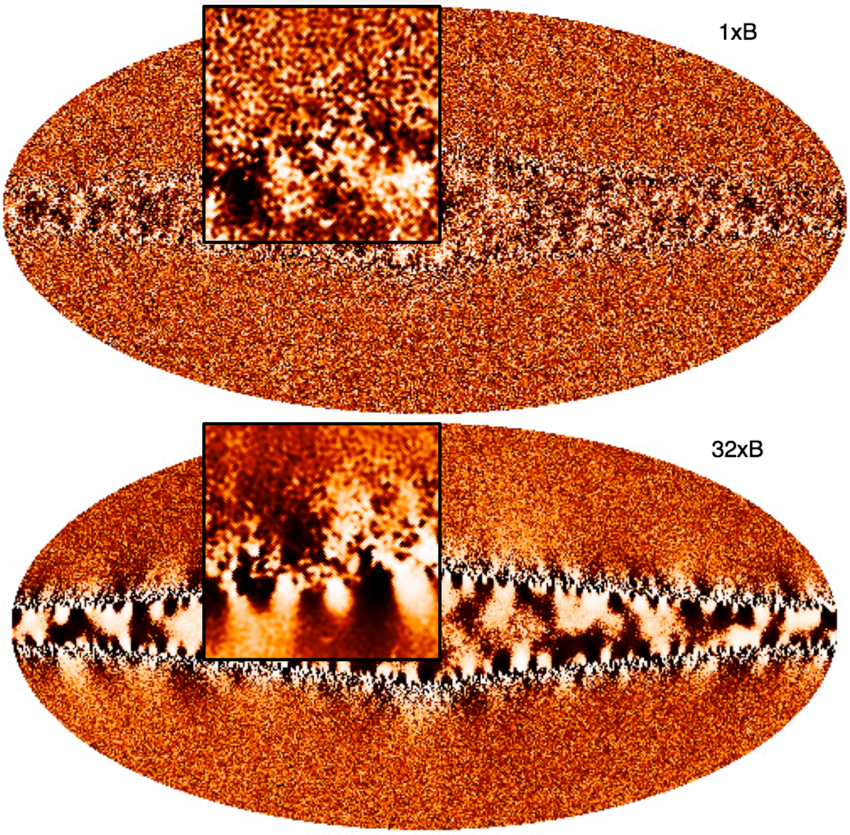

— Exemple de fuite des modes B due aux masques galactiques pour l'inversion de la convergence : la mâchoire du cosmos :-). Les modes vectoriels apparaissent dans la carte des résidus au voisinage des régions masquées.

En collaboration avec Karim Benabed, j'ai commencé à étudier l'inversion de l'équation des lentilles dans le contexte du fond diffus cosmologique, où c'est le fond diffus lui même qui subit la déflexion due à l'ensemble des grandes structures entre la surface de dernière diffusion et l'observateur à redshift zéro. C'est un problème inverse mal posé, puisque l'on dispose de trois champs observés sur la sphère et que l'on cherche à en reconstruire quatre. Il convient donc de se reposer fortement sur la forme spectrale des *a priori*. Parallèlement, en collaboration avec E. Thiébaut, nous avons développé un module de déconvolution d'images avec PSF variable dans le champ basé sur une formulation creuse du problème, avec positivité et bruit non stationnaire.
La procédure nous permet d'ittérer alternativement sur la détermination de la PSF (décrite comme une somme de B-splines) et de l'image. L'objectif scientifique est d'appliquer cette méthode aux données de type MEGACAM pour améliorer l'estimation des paramètres de forme des galaxies en vue d'une mesure de l'astigmatisme cosmique. La pénalisation de l'inversion se fait à partir d'une norme L1-L2. [Thiébaut et Pichon *prép*.]

Ce travail correspond à une synthèse de différents savoir-faire acquis dans le contexte de la simulation numérique, la cosmologie, le squelette et les méthodes inverses. Au fil de ces dix dernières années, j'ai investi une fraction importante de mon temps de recherche à l'investigation des méthodes inverses, et en particulier pour l'estimation des paramètres de régularisation optimaux en explorant différentes méthodes. Grâce à l'algorithme d'optimisation *Optimpack* de mon collègue E. Thiébaut, j'ai pu mettre en oeuvre ces méthodes inverses sur des problèmes de grande dimensionalité. A l'avenir j'aimerais étudier les perspectives de diagnostic automatique pour les méthodes inverses non-linéaires, en particulier pour établir dans quelle mesure un problème non-linéaire donné présente des symétries d'invariance qui le rendent dégénéré. En ce sens, l'exploration plus systématique de la vraisemblance semble être une option.

3.5.5 Séparation des composantes des cartes Planck [50%]

Le succès des mesures récentes des anisotropies du fond diffus (expériences WMAP, BOOMERanG, MAXIMA, DASI) pour déterminer une contrainte sur la courbure de l'univers, la densité baryonique, ou encore l'indice spectral des fluctuations de densité primordiales, a démontré tout à la fois l'importance de ces mesures pour l'étude des modèles cosmologiques, et de la maîtrise complète des méthodes inverses pour y accéder. La présence d'émissions Galactiques parasites (poussières, synchrotron, free-free) mais aussi extragalactiques (radio-galaxies, galaxies IR, effet SZ des amas), qui représentent des effets systématiques encore sous-dominants comparées aux erreurs statistiques des données actuelles, deviendront bientôt comparables (données B2K, MAP) et domineront (Planck).

Toutes les méthodes d'inversion multibande reposent dans leur forme actuelle sur une connaissance *a priori* de la structure spatiale et spectrale des diverses composantes à séparer. Avec E. Thiébaut et S. Prunet, nous avons généralisé ces méthodes en y incluant la polarisation, et nous tentons d'y inclure l'estimation de la dépendance spectrale des composantes obtenues directement à partir des données, sous forme paramétrique par une méthode non-linéaire de maximum de vraisemblance optimisé par minimisation à métrique variable et mémoire limitée. Ce choix nous permet de poser des contraintes de type masque dans l'espace des mesures, et des contraintes de type lissage adaptatif dans l'espace modèle [Prunet, Pichon, Thiébaut *prep*].

L'objectif initial de ce travail était de fonctionner en régime myope, i.e. dans un contexte où la matrice de mélange n'est que partiellement connue. Ce problème, couplé au travail sur la sphère avec un nombre très important de pixel, s'est avéré plus difficile en pratique que ce que nous avions anticipé. Ma motivation était aussi de me familiariser avec les symétries de la sphère en tant qu'espace harmonique moins trivial que la transformée de Fourier.

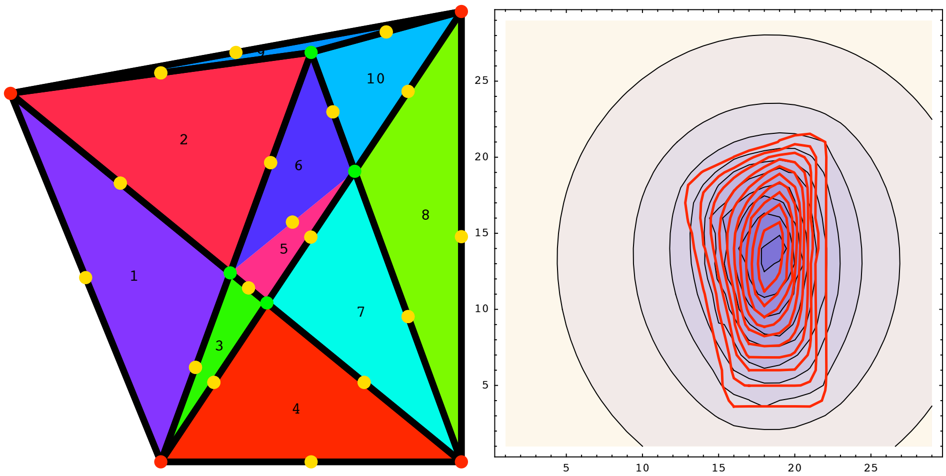

—Projection 2D d'un 4-Simplex (à gauche) permettant de résoudre le système Poisson-Boltzmann de manière symplectique (conservation de la hiérarchie des invariants de Poincaré) pour étudier les propriétés dynamiques d'un fluide autogravitant, des échelles galactiques aux échelles cosmologiques ; potentiel correspondant (à droite). Cette structure symplectique peut par exemple faciliter l'identification des queues de marée dans l'espace des phases d'un halo galactique.

3.5.6 Dynamique gravitationnelle dans l'espace des phases ; physique théorique & gravitation [60%]

La distribution observée des galaxies présente, à grande échelle, des propriétés remarquables, qui se traduisent par l'existence d'amas, de filaments et de nappes entourant de grands vides. L'étude des effets de la dynamique gravitationnelle non collisionnelle (dans un univers en expansion) est donc un élément déterminant pour interpréter les structures observées, que ce soient les "grandes", comme les amas de galaxies, ou les "petites", comme les halos de galaxies ou les galaxies elliptiques.

L'objectif est de comprendre la structure dans l'espace des phases des objets en cours d'évolution, et en particulier le comportement de la hiérarchie des équations de la dynamique, pour éventuellement dégager des relations universelles simplifiant la problématique (équations d'état : par exemple, une approximation à un, trois ou cinq flots avant thermalisation permet de tronquer la hiérarchie BBJKY à la divergence du tenseur de flux de chaleur). Dans ce but, j'ai développé un solveur de Poisson N-simplex : couplé avec les travaux de S. Colombi sur le moteur d'évolution inertiel, l'objectif est de mieux modéliser les caustiques et de tester la validité de certains résultats des simulations à N-corps (NFW…).

Je m'intéresse en particulier à l'identification des sous-structures et des caustiques dans les halos de matière noire à partir d'une formulation en termes des variables angle-action du système sous-jacent pour rectifier l'espace des phases. A cette fin, j'utilise les simulations que j'ai produites (voir ci-dessus) pour identifier ces caustiques au voisinage des plus gros halos [Macejewski, Colombi, Alard, Pichon, *2008*]. J'envisage d'améliorer l'identification de ces caustiques par rectification de l'espace des phases via une transformation en variables angle-action.

L'objectif de cette investigation à long terme est de faire la synthèse entre les analyses géométriques de type squelette et les analyses dynamiques présentés ci-dessus ; en particulier, une validation croisée avec la théorie perturbative matricielle (voir ci-dessus) appliquée à l'effondrement sphérique et aux disques est envisagée. De fait, j'ai noté que la théorie perturbative prédit la réponse d'un système gravitationnel en phase, et non seulement dans l'espace des configurations. Je souhaite aussi implémenter une formulation AMR de l'équation de Boltzmann non collisionnelle (avec un critère de raffinement basé sur la courbure du flot).

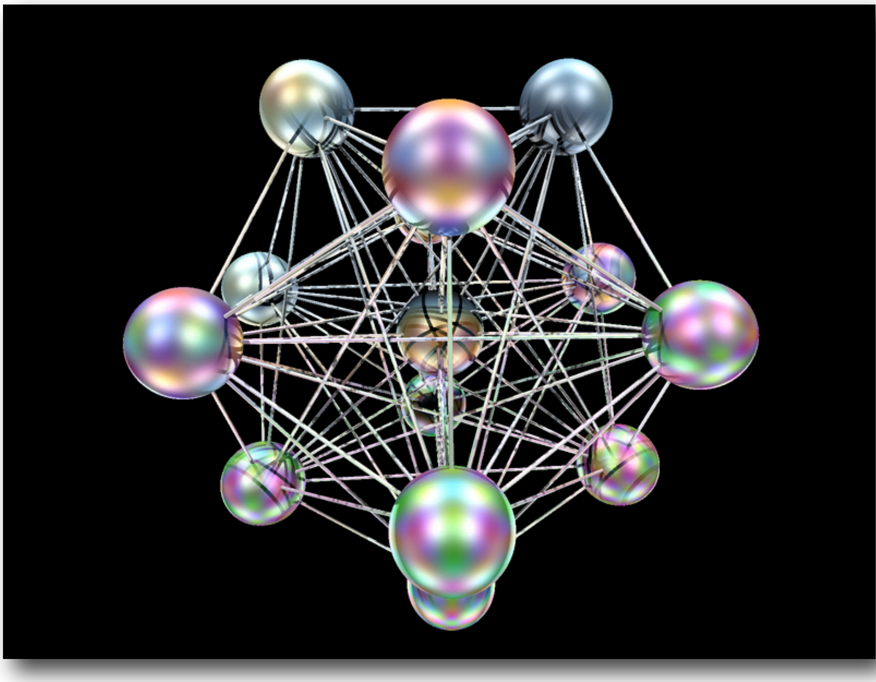

—Un exemple de quasi-cristal oscillant perpétuellement. Ces systèmes obéissent à une loi d'interaction qui a la propriété particulière de découpler leur mouvement d'échelle des mouvement internes. Ils sont construits en imposant une force de friction qui les fait se relaxer vers une configuration symétrique dépendant du nombre de particules ; [Pichon, Lynden-Bell[2] (2007)].

Avec D. Lynden-Bell [Pichon, et al. 2007], j'ai étudié les propriétés thermodynamiques du réseau formé par des particules ayant une loi d'interaction par paire avec un potentiel en r^2+1/r^2 qui ont la propriété de découpler leur mouvement radial (qui oscille perpétuellement) et azimutal/alt-azimutal (qui se thermalise). Pour une telle loi, j'ai caractérisé les symétries des configurations d'équilibre (oscillant) en fonction du nombre de particules, ainsi que leur comportement asymptotique de chaleur spécifique pour un système en rotation ou non. La description asymptotique du système dans la limite fluide est analysée, et la stratification du quasi cristal mesurée dans la limite des grands N est expliquée. L'intérêt astrophysique de ces objets est de constituer un contre exemple de relaxation violente, car un des degrés de liberté ne se relaxe jamais.

Ces axes de recherches plus ésotériques correspondent néanmoins à un intérêt de longue date pour la théorie des systèmes dynamiques, et son lien avec la physique statistique et la thermodynamique. La mise en oeuvre des outils classiques de la physique théorique dans un contexte à l'interface entre la physique du solide et la dynamique gravitationnel s'est avéré intéressante d'un point de vu conceptuel, notamment en lien avec le modèle HMF. Dans le cadre de se travail, j'ai aussi écrit mon premier programme à N corps! Depuis, je m'intéresse avec D. Aubert à l'écriture d'un code hydrodynamique (+transfert du rayonnement) sur carte graphique (CUDA tesla). L'objectif à terme est de coupler ce mode de calcul pour la partie transfert avec le reste du calcul sur le CPU de la machine hôte et fournir un modèle pour la mise en oeuvre des méthodes de rectification de distorsion des vitesses particulières (voir ci-dessus).

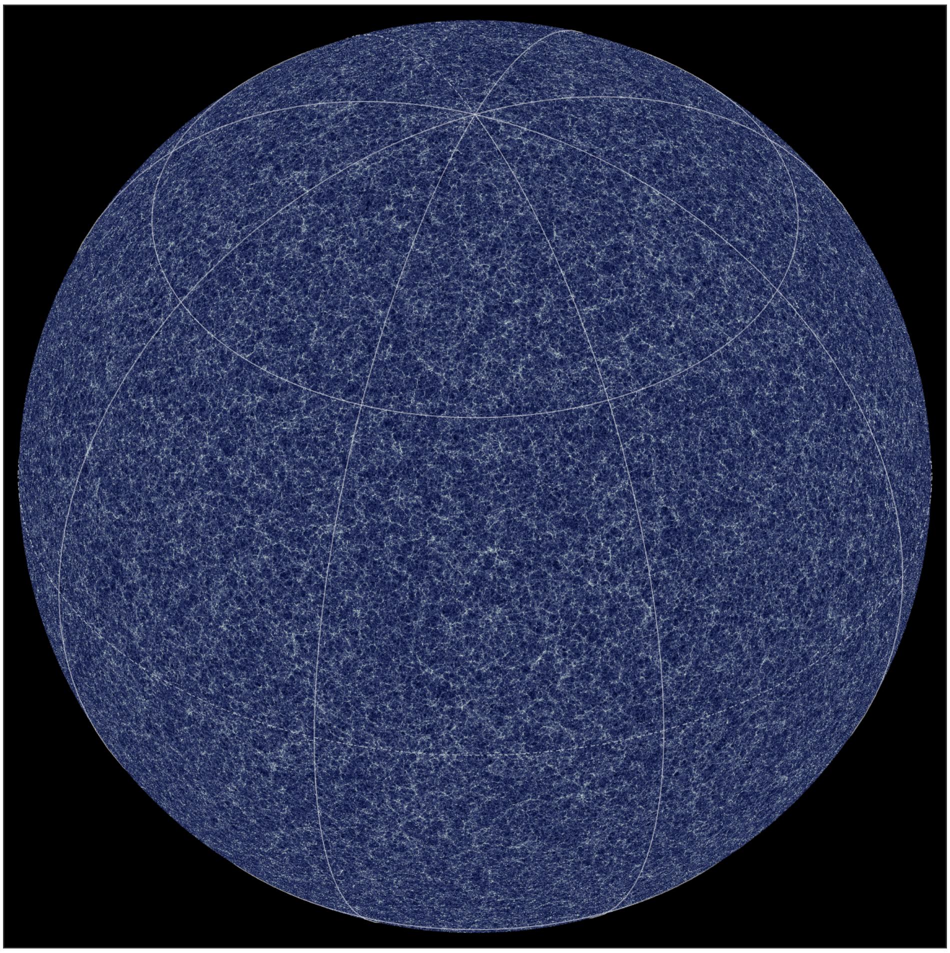

—Carte de la projection sur la voûte céleste d'une tranche de la simulation horizon-4π : 4096^3 particules de matière noire dans 2000 Mpc/h. Cette simulation peut servir à la détection des BAO, l'astigmatisme cosmique, l'identification des grands vides et amas, la distribution des sources X, SZ, la recherche de groupes locaux, etc.

3.6 Activité de recherche transverse et prospective

Ces thèmes de recherches sortent du cadre "dynamique gravitationnelle" au sens large et correspondent à des activités de recherche guidées par les affinités de mes collaborateurs ou des projets.

3.6.1 Haute résolution angulaire et optique adaptative multi -conjuguée [30%]

J'ai élaboré avec E. Thiébaut un outil de déconvolution automatique d'images grand champ, MAAD (pour *Multiscale Algorithm for Automatic Deblurring*, [Thiébaut Pichon, *prep.*], dont une version est disponible en ligne (sous forme de *webservice* *MAAD*) ce qui permet à la communauté française (et plus généralement quiconque sur le web) de procéder de manière interactive à la déconvolution soit des images accessibles par le serveur du CDS (SDSS, 2MASS DSS, Shandra, CFH, HST etc), soit de leurs propres images. Nous développons aussi deux versions plus spécialisées de MAAD, l'une faisant intervenir une description de la fonction d'étalement du point variable dans le champ, l'autre faisant intervenir une déconvolution multi-spectrale (type séparation de composantes ou spectroscopie intégrale de champ) ; voir aussi l'URL ci-dessus. J'ai travaillé sur la détermination automatique des paramètres de régularisation dans le régime à plusieurs paramètres. Je m'intéresse à la déconvolution automatisée (éventuellement myope) de cubes de données type x, y, fréquence (spectroscopie intégrale de champ), visibilités u,v, fréquence (LOFAR, SKA) ou x, y, temps (hyperrésolution).

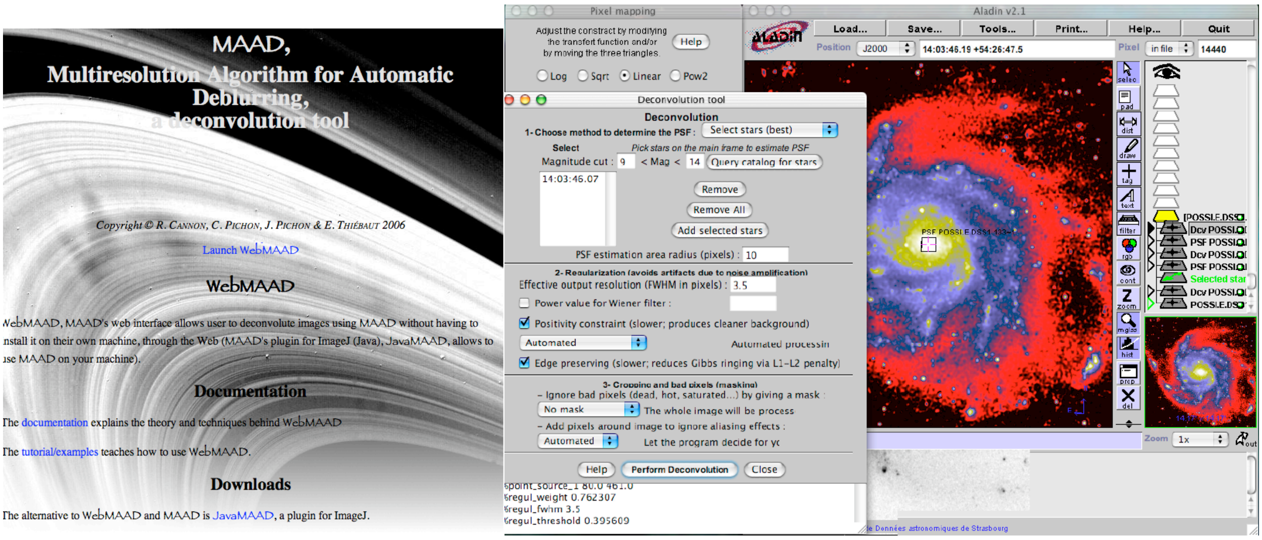

— Le webservice MAAD [Thiébaut, Pichon, *prep*.] et son intégration à ALADIN. Ce service permet de déconvoluer une image d'une PSF paramétrée, mesurée ou estimée interactivement dans l'image en imposant éventuellement la positivité du modèle avec une pénalisation quadratique ou préservant les bords (de type L1-L2).

En collaboration avec E. Thiébaut et R. Lane, j'ai transposé au contexte de l'estimation des pentes du front d'onde dans la pupille d'un télescope de grande taille mes travaux sur la tomographie des grandes structures. Dans ce contexte, plusieurs Shack Hartman (SH) sont conjugués sur différentes étoiles de référence, ce qui conduit pour chacun d'entre eux à une estimation des pentes du front d'onde dans le plan pupille. Notre objectif était d'estimer ces pentes dans une direction quelconque, afin de prédire l'évolution de la PSF optimale dans le plan image, en fonction du positionnement des étoiles de référence, de l'amplitude de la turbulence, et des caractéristiques du télescope. Ce problème nous conduit donc à déprojeter en volume l'information relative à chaque SH, interpoler au sens de la statistique *a priori* de la turbulence, et reprojeter dans le plan pupille en se reposant sur une formulation creuse des corrélations *à priori*. Cette thématique s'inscrit dans le prolongement ce qui avait fait l'objet de mon stage de DEA.

E. Thiébaut m'a fait découvrir les nombreux avantages à traiter un problème d'estimation comme un problème inverse, car seule une faible classe de problèmes en astrophysique peut être inversé explicitement, classe qui se réduit comme une peau de chagrin quand la statistique du bruit est prise en compte. Par exemple, l'estimation d'un champ, à partir d'une mesure directe mais partielle ou bruitée de ce champ, ne peut être abordée correctement que dans ce contexte.
De plus, l'inversion non paramétrique est une estimation à biais autocalibrable, c'est donc idéalement une approche optimale en termes de compromis biais-variance. Cependant, elle induit une double sanction : (i) les données en astrophysique sont souvent trop parcellaires ou bruitées pour contraindre fortement le modèle flottant et (ii) la complexité associée à la paramétrisation de ce modèle est souvent importante comparée aux méthodes paramétriques de projection du modèle dans l'espace des données. En pratique, cela induit donc beaucoup d'efforts pour un résultat cruel : l'essentiel de l'information ne provient pas des données mais du *prior*. Enfin la mise en oeuvre de *prior* explicite nécessite de régler les hyperparamètres correspondants, car en astrophysique, l'estimation du bruit n'est en général pas suffisamment précise pour intégrer des *priors* baysiens (type filtre de Wiener optimal). Cette thématique de recherche présente enfin l'inconvénient d'être très générique : il est difficile d'un point de vue bibliographie qu'elle concerne aussi bien l'astrophysique que les sciences médicales, la géophysique etc. la dissémination des connaissances sur le web compense cependant en partie cette difficulté.
Au fil des problèmes inverses linéaires que j'ai abordés dans différents contextes, j'ai pu mesurer l'importance de mener une analyse "spectrale" généralisée du problème, c'est-à-dire d'étudier son conditionnement en comparant les caractéristiques du bruit à la distribution de ses valeurs singulières, mais aussi/ et surtout d'analyser les biais du modèle en mesurant les vecteurs singuliers correspondants (pour un problème stationnaire - bruit plus modèle, la symétrie associée définit l'harmonicité de la base ; ce n'est pas génériquement le cas). J'ai aussi pu apprécier la diversité des approches possibles pour biaiser un modèle donné : *prior* explicite défini positif (e.g. de type gaussien), *prior* avec noyau contenant des classes entières de fonctions, condition initiale dans la descente d'un problème non-linéaire, choix de l'échantillonnage avant discrétisation, nature faiblement non paramétrique du modèle, choix *ad hoc* du poids de la régularisation ou de la norme correspondante. Outre le fait que le choix de ce *prior* est rarement argumenté, j'ai aussi été frappé par le fait que dans la discipline, et ce alors que les diagnostics existent (matrice de Fischer, Information, divergence de Kullback etc.), l'analyse *a posteriori* du gain associé aux données relativement au *prior* est très rarement menée !

Dans ce domaine j'aimerais à terme construire des outils de diagnostics (type calcul symbolique *etc.*) pour déterminer dans quelle mesure un problème inverse non-linéaire est intrinsèquement dégénéré (au moins dans le régime ou la source de cette dégénérescence est associée à des symétries plus ou moins triviales). Un tel outil permettrait de découpler le problème de l'optimisation numérique de la dégénérescence, ou du bogue ! Je souhaite aussi étudier le nombre de contraintes simultanées qu'il est possible de poser, et le problème du réglage des hyperparamètres correspondants. Enfin, j'aimerais élaborer des techniques de régularisation non stationnaires basées sur une segmentation a priori de l'espace (par exemple basée sur les peakpatches du module du gradient du champ) ce qui permettrait de fixer un hyperparamètre par région.

3.6.2 Etoile 2D : Evolution stellaire à deux dimensions [20%]

En collaboration avec C. Tout et R. Cannon, nous avons développé un code implicite de résolution d'équations aux dérivées partielles à deux dimensions ayant pour caractéristique une grille eulérienne flottante qui s'ajuste aux gradients des champs à déterminer. Notre objectif est la description de l'évolution stellaire d'une étoile où la rotation peut jouer un rôle important et donc aplatir l'étoile. Nous avons à ce jour vérifié que notre algorithme résout l'équation de Poisson et l'étoile polytrope à une dimension. A terme, l'algorithme serait utilisable pour tout problème bi-dimensionnel (Hydro, MHD etc.) dans la mesure où la mise en équation est entièrement automatisée à l'aide d'un module d'algèbre symbolique et que le solveur est générique.

Ce travail est un exemple parmi d'autres de l'utilisation que je fais de *Mathematica* (depuis sa version 1.2 en 1992) pour le calcul symbolique. C'est un outil particulièrement attrayant car il permet de développer ses propres "grammaires" abstraites, en prenant en charge toute la dimension fastidieuse du travail. Il m'a permis de faire souvent l'expérience à moindre frais que la "bonne" solution à un problème mathématique donné (présentant certaines symétries) est infiniment plus simple qu'une solution boguée. Je ne saurais dire si on peut en déduire que la nature préfère le beau (au sens symétrique) ; toujours est-il que la complexité (au sens combinatoire) d'une expression mathématique décrivant un phénomène physique donné dépend fortement de sa pertinence (erreur de calcul, non respect des symétries, etc.).

Pour illustrer l'intérêt d'une recherche transverse, j'ai eu l'occasion de rencontrer le problème du conditionnement et de l'échantillonnage de manière récurrente lors de ces investigations. En théorie de la stabilité des disques minces par exemple, le conditionnement est abordé indirectement dans la stratégie d'une "bonne" base sur laquelle la réponse du disque doit être projetée : c'est l' "art" du théoricien que de construire cette base, quitte à introduire un *epsilon* pour éviter la division par presque zéro lors de la recherche des modes propres projetés sur cette base (une forme *ad hoc* de régularisation). En général, ce sont les symétries du disque à l'équilibre qui imposent l'échantillonnage (ici la forme de la base).
Dans le contexte des méthodes inverses, le conditionnement correspond à un hyper-paramètre explicite (le multiplicateur de Lagrange associé à la contrainte du *prior*), qui permet de faire le meilleur compromis biais-variance. Comme je l'ai mentionné ci-dessus, le choix de la base est en principe imposé par son comportement asymptotique (il doit tendre vers un Dirac), mais en pratique la façon dont elle est échantillonnée (linéairement, logarithmiquement, symétriquement etc.) aura un impact plus ou moins considérable suivant le conditionnement du problème. Plus celui ci est mauvais, plus les biais associées à ce choix seront critiques. A *prior* donné, la non-linéarité du problème (intrinsèque ou lié au choix de la norme de pénalisation) rendra-elle la descente plus ou moins difficile?
Enfin dans le contexte des schémas de discrétisation d'équations différentielles (en hydrodynamique, MHD, dynamique symplectique, etc.) le souci de construire un algorithme causal (e.g. upwind), respectant les invariances physiques (conservation de l'énergie, du moment, des circulations ...) impose des stratégies d'échantillonnage particulières : c'est d'ailleurs un sujet de recherche en mathématiques appliqués particulièrement actif formalisé en termes de forme différentielles discrètes. On retrouve de fait dans ce domaine des contraintes (*e.g.* de courant) plus ou moins fortes suivant le schéma (explicite ou implicite).
Au sens large, ces coïncidences reflètent en fait les dualités entre les formulations différentielles (PDE ou projection en ODE) et variationnelles (intégrale) des équations de la physique, et la nécessité de préconditionner la recherche des solutions (ce n'est d'ailleurs pas un hasard si c'est ce même terme qui est utilisé dans le contexte de l'optimisation pour la recherche des solutions à la formulation variationnelle du problème, et dans celui de l'analyse différentielle, pour résoudre les PDE).
De fait, la formalisation des symétries imposées par la physique dans le langage mathématique (qui est par construction transdisciplinaire) conduit à des invariances dans les stratégies de recherche.

3.6.3 Le projet *Galactica* : la physique de la Voie Lactée dans son environnement cosmologique. [50%]

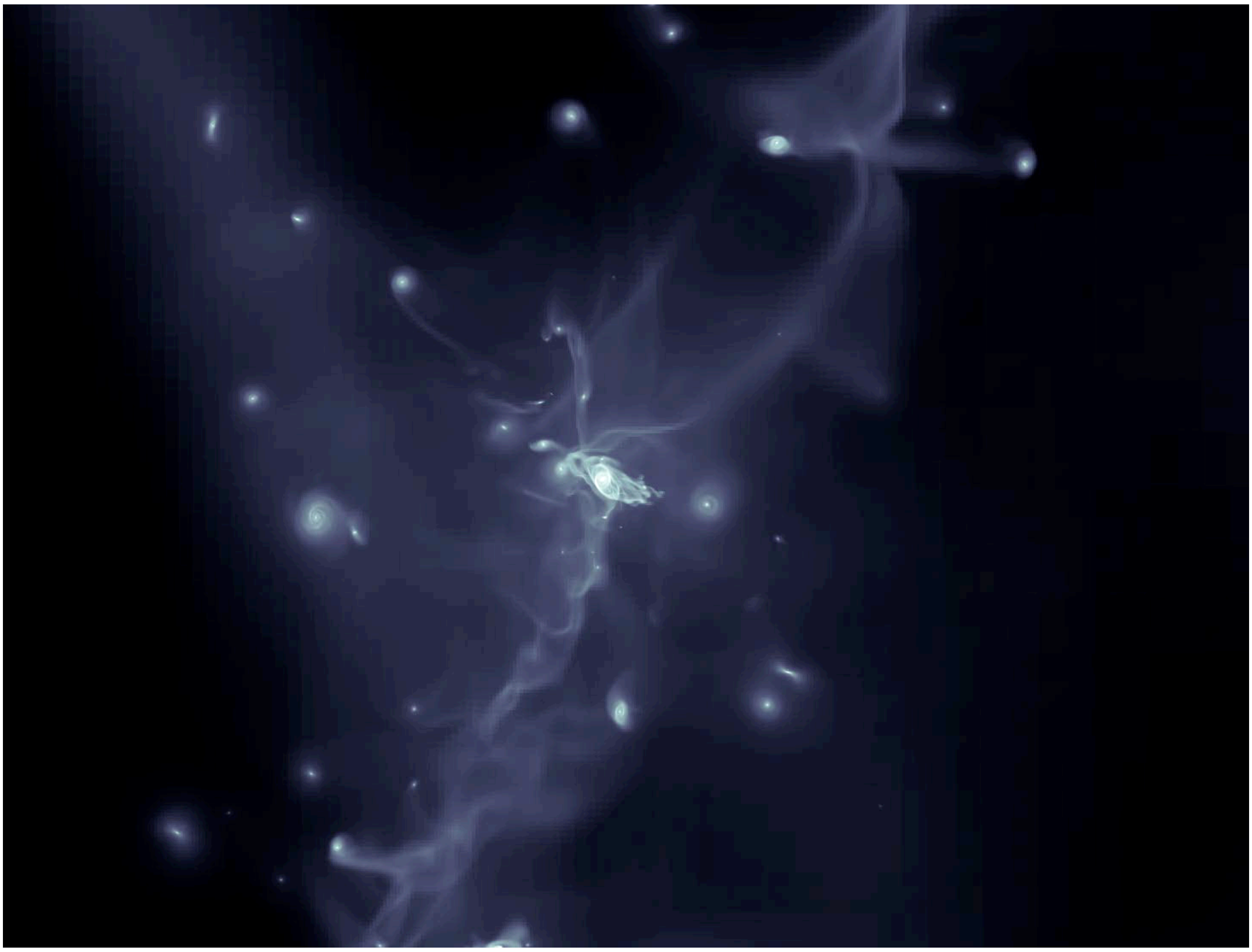

—Un exemple de formation de type Voie Lactée à z=2 avec une résolution of 80 pc. (c) *Agertz Teyssier 08*.

La question de l'inné ou de l'acquis des propriétés dynamiques des disques de galaxies reste encore largement ouverte. Si l'environnement joue une part importante dans l'établissement de ces caractéristiques (spirales, gauchissement, disques épais), son influence est modulée par la propension intrinsèque que possède un objet à réagir ou non à des perturbations. La cosmologie numérique moderne atteint aujourd'hui une dynamique qui lui permet d'aborder l'historique de la génération de galaxies de type Voie Lactée dans un contexte réaliste, avec une résolution suffisante pour explorer la structure interne de la galaxie jusqu'à la centaine de parsecs. L'objectif de ce travail est de mener une simulation dimensionnante réaliste du groupe local (Voie Lactée, Andromède, l'amas de la Vierge etc) dans une boîte de 80 Mpc/h, en mode simulation zoom contrainte, avec une résolution initiale de 4096^3 dans la région centrale, et d'utiliser 8 niveaux de raffinement de RAMSES, soit une résolution ultime de 75 pc/h au niveau de raffinement le plus élevé pour la Voie Lactée. Un tel programme présente un intérêt intrinsèque pour comprendre les mécanismes de structuration interne des galaxies sur une fraction importante de l'âge de l'univers, mais aussi dans le cadre de la phase préparatoire des missions Planck (avant plan), SDSS-3/RAVE et surtout GAIA, car la simulation produira un nombre commensurable d'étoiles avec celui mesuré par le satellite. Il sera donc possible de valider les modèles de structure Galactiques sur les données virtuelles issues de cette simulation.

Spécifiquement, ce travail permettra de résoudre l'échelle verticale du disque froid de la Voie lactée, de modéliser la détection directe des sous-structures noires dans le voisinage solaire, de sélectionner les satellites nains lumineux dans le halo, d'identifier des courants stellaires et les caustiques dans l'espace des phases étendu (mouvement propre, vitesse radiale, métallicité)... Cette modélisation des données virtuelles fera l'objet de la seconde partie du projet. Comme la simulation est dimensionnée pour résoudre l'échelle verticale du disque froid de la Voie Lactée, il sera pertinent d'étudier de manière détaillée les processus d'accrétions vers les régions centrales par instabilité spirale. Il sera aussi possible de modéliser la détection directe des sous-structures noires (des Wimps par GLAST), de sélectionner les satellites nains lumineux dans le halo (et aborder le problème de l'excédent de satellites visibles), de valider l'identification des courants stellaires et les caustiques dans l'espace des phases étendu (mouvement propre, vitesse radiale, métallicité) pour tester les méthodes archéologie stellaire. Avec T. Sousbie, nous souhaitons en particulier étendre à des dimensions abstraites la recherche du squelette (basée sur une tessellation de Voronoi) pour identifier les courants stellaires (voir ci-dessus). Enfin, la physique du gaz interstellaire et la distribution des nuages moléculaires dans le disque et des cirrus/HVC dans le halo pourra être abordée.

Dans ce contexte, j'explore actuellement l'optimisation de la recherche des conditions initiale contraintes du groupe local en temps que problème inverse pour affiner la position et la géométrie d'une sous région. J'ai aussi formulé l'inversion de MAK (Monge Ampère, Klimotovich) en tant que problème inverse non-linéaire pour tenir compte des masques et du bruit.

De fait, les analyses relatives au croisement de coquilles comme celle que j'ai menées avec F. Bernardeau pourraient ouvrir la perspective de généraliser ce formalisme aux petites échelles, où l'approximation de Zeldovitch n'est plus satisfaisante.

Plus généralement, ce *projet* de recherche me permettrait de faire la jonction d'un point de vue numérique entre plusieurs de mes thématiques de recherches principales : la structure galactique et la cosmologie, la simulation numérique et les méthodes inverses, la modélisation symplectique des systèmes gravitationnels et les problèmes d'identification dans l'espace des phases. Il présente cependant l'inconvénient d'être un peu trop à la mode à mon goût, ce qui induit des conditions de travail plus contraignante.

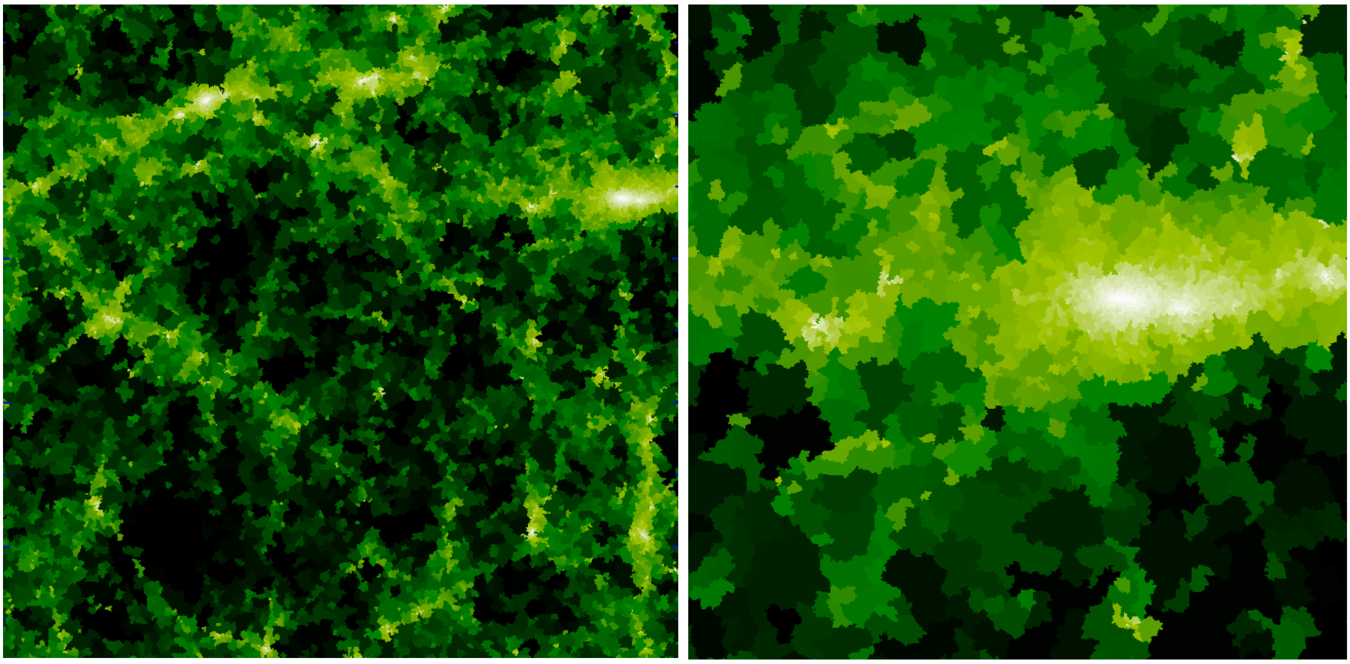

— *(à gauche)* un exemple de segmentation des peakpatches d'une tessellation de Delaunay de la projection d'une simulation CDM ; *(à droite)* un zoom sur l'amas en haut à droite. Une telle segmentation permet de calculer le squelette avec une résolution adaptative jusqu'à la particule [Soubie et al. *en prep.*].

Conclusions

Mon objectif global de recherche est de comprendre les mécanismes de structuration de l'Univers, et plus généralement d'inventer et développer des outils originaux pour confronter ces modèles aux grands relevés. Je cherche notamment à dégager ce qui relève du détail spécifique à chaque objet/thématique, des propriétés statistiques et des symétries globales au sens large. C'est pour cette raison que j'ai dans un premier temps focalisé ma recherche sur la gravitation, un processus physique classique relativement intuitif (et central en astrophysique) qui conduit néanmoins à un grand nombre de phénomènes distincts suivant le contexte (univers en expansion, faible ou grand nombre de particules, etc.). Ensuite, au fil de mes collaborations, j'ai abordé d'autres thématiques connexes.

Cet exposé a permis, je l'espère, de mettre en évidence l'intérêt de mener une recherche transverse pour stimuler l'innovation dans ce contexte. C'est une stratégie qui correspond à la fois à une formation (en tant que théoricien à Cambridge, où la théorie constitue une spécialisation en soi), et à un penchant que je retrouve parmi certains de mes collègues sur le plan international (e.g. mes rapporteurs et examinateurs, G. Miralda-Escudé, A. Nusser, P. Saha, C. Kochanek etc). C'est une stratégie que le mode de financement du CNRS autorise, ce qui a fortement motivé mon intérêt pour ce poste.[3] Le risque associé est l'émiettement et le manque de profondeur, que j'espère avoir en partie évité. Si la présentation des différentes thématiques a parfois été rapide, l'échantillon des articles qui suivent en cinquième partie permettra au lecteur d'approfondir les différents sujets abordés.

L'analyse rétrospective des travaux accomplis présentés dans ce manuscrit permet de dégager quelques avancées :

(i) dès le début des années 90, G. Gilmore soulignait les limitations du modèle de galaxies sphériques isolées et prônait la nécessité de rendre compte de l'environnement du milieu intergalactique dans le devenir dynamique d'une Voie Lactée. J'ai activement contribué à la formulation statistique de cette contrainte (Pichon, Aubert 06) et à sa quantification dans les simulations cosmologiques (Aubert, Pichon, 07, Aubert, Pichon, Colombi 08). Son extension aux flux hydrodynamiques correspondants (Ocvirk, Pichon, Teyssier 08) est maintenant devenue un sujet de recherche très dynamique (e.g. Dekel et al.).

(ii) l'analyse géométrique des lignes critiques d'un champ par le biais du squelette (Sousbie, Pichon et al. 07a, 08a,b,c) et les développements théoriques correspondants (Pogosyan, Pichon et al. 08) constituent un autre axe de contributions significatives à la discipline, rendu possible par les incitations/suggestions de Stéphane Colombi. Son extension à la connectivité de la toile cosmique aux échelles galactiques devrait me permettre de faire le lien avec le point ci-dessus.

(iii) la cosmologie observationnelle est rentrée dans les années 90 dans une époque qui se prête bien à une analyse en termes de méthodes inverses. Je pense avoir contribué à transposer le savoir-faire correspondant (issu de l'imagerie), acquis au contact d'Eric Thiébaut (voir par exemple Pichon et al. 2001, 2009 et dans le même registre, l'inversion non paramétrique des modèles de synthèse spectrale appliqués à la reconstruction de la cinématique et de l'histoire de formation stellaire des galaxies: Ocvirk, Pichon et al,a,b). La transposition systématique de ces méthodes dans le contexte de la réduction de données astrophysiques (e.g. la thèse de B. Aracil, Le Borgne et al. 09) a de beaux jours devant elle. Leur mise en oeuvre pour les données GAIA (e.g. dans l'esprit de Pichon et al. 2002) devrait me permettre de faire la synthèse entre mes différents axes de recherche (méthodes inverses, dynamique symplectique et géométrie).

(iv) d'autres travaux, plus théoriques, sur les disques relativistes, la génération de vorticité par croisement de coquilles, ou sur la formulation thermodynamique du modèle HMF ont aussi eu un impact (même si pour ce dernier, je n'ai pas été l'architecte de sa divulgation !). Globalement, à une époque où le recours systématique à la simulation numérique est une facilité illustrative à laquelle peu résistent, je me suis attaché à promouvoir une formulation analytique (e.g. Scannapieco et al. ou Pogosyan et al) qui reflète ma motivation première.

Au fil de ces 10 années de recherche au CNRS, j'ai développé un savoir faire qui recouvre une bonne fraction des différentes composantes d'un travail de modélisation : (i) génération de simulations, (ii) production de pseudo-observables (iii) automatisation des procédures de pré-reduction, (iv) estimation non paramétrique, et (v) interprétation théorique & analyse des mécanismes.

Les choix stratégiques associés à une recherche transverse (de prospection plutôt que d'ingénierie) se prêtent mal à un exercice de prospective à long terme. De fait, dans le contexte actuel, il est délicat de trouver un équilibre entre cet objectif transverse et le mode d'évaluation de la recherche qui favorise la mise en oeuvre efficace d'un savoir faire existant. Globalement, j'entends néanmoins poursuivre mon investigation sur la géométrie des grandes structures, et mes travaux théoriques sur les systèmes gravitationnels ouverts. J'aimerais aussi développer un savoir faire en hydrodynamique et en MHD (voir en relativité numérique), continuer à valoriser de grosses simulations hydrodynamiques, et publier le fruit de mes investigations de ces dix dernières années notamment sur la calibration automatique des méthodes inverses. Dans le contexte des grands projets de la discipline, je pense donc pouvoir à l'avenir contribuer à la valorisation scientifique des missions Planck, GAIA/Alma et SKA, notamment par le biais d'encadrements doctoraux.
A moyen terme, je souhaite refocaliser ma recherche sur des aspects plus géométriques et théoriques de la dynamique gravitationnelle, car c'est à mon sens la contribution la plus originale que je puisse apporter à la discipline.

[3] J'espère que c'est une possibilité que la réforme (*perpétuelle*) de la recherche française conçervera!

4. Bibliographie

Publications à comité de lecture

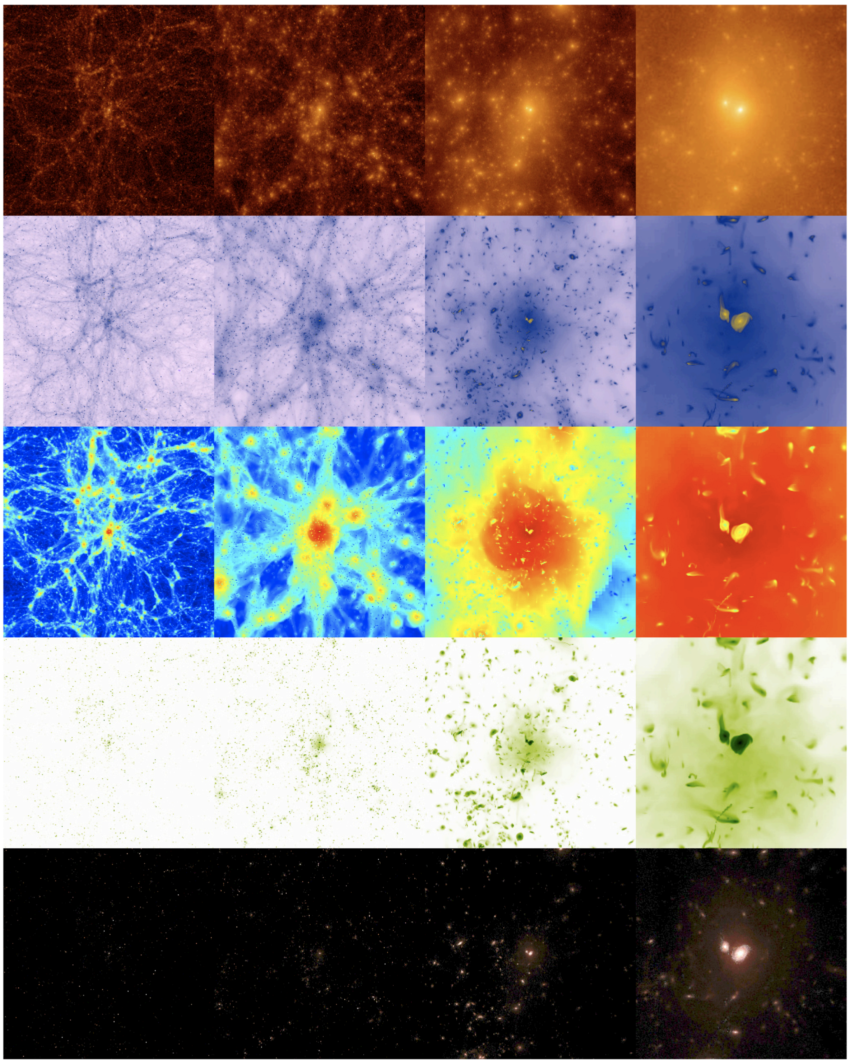

[1] B. Aracil, P. Petitjean, C. **Pichon**, and J. Bergeron. Metals in the intergalactic medium. A&A, 419:811–819, June 2004.
[2] D. Aubert and C. **Pichon**. Dynamical flows through dark matter haloes -II. One- and two-point statistics at the virial radius. MNRAS, 374:877–909, January 2007.
[3] D. Aubert, C. **Pichon**, and S. Colombi. The origin and implications of dark matter anisotropic cosmic infall on Lstar haloes. MNRAS, 352:376–398, August 2004.
[4] J. Bergeron, B. Aracil, P. Petitjean, and C. **Pichon**. The warm-hot intergalactic medium at z = 2.2: Metal enrichment and ionization source. A&A, 396:L11–L15, December 2002.
[5] J. Bicak, D. L. Bell, and C. **Pichon**. Relativistic Discs and Flat Galaxy Models. MNRAS, 265:126–+, November 1993.
[6] O. Bienayme and C. **Pichon**. Comment on the dispersion-velocity of galactic dark matter particles. A&A, 321:L43–L45, May 1997.
[7] S Colombi, A. Jaffe, D.Novikov, **C. Pichon** Accurate estimators of power-spectra in N -body simulations MN 2008
[8] S. Caucci, S. Colombi, **C. Pichon**, E. Rollinde, P. Petitjean, T. Sousbie Recovering the topology of the IGM at z~2 MN 2008
[9] F. Coppolani, P. Petitjean, F. Stoehr, E. Rollinde, C. **Pichon**, S. Colombi, M. G. Haehnelt, B. Carswell, and R. Teyssier. Transverse and longitudinal correlation functions in the intergalactic medium from 32 close pairs of high-redshift quasars. MNRAS, 370:1804–1816, August 2006.

—les différents champ physiques de la simulation “physique complète” et la dynamique correspondante: de haut en bas matière noire, gaz, température, métaux, étoiles en fausses couleur.

[10] M. Creze, E. Chereul, O. Bienayme, and C. **Pichon**. The distribution of nearby stars in phase space mapped by Hipparcos. I. The potential well and local dynamical mass. A&A, 329:920–936, January 1998.
[11] F. Durret, D. Gerbal, C. Lobo, and C. **Pichon**. The rich cluster of galaxies ABCG 85. IV. Emission line galaxies, luminosity function and dynamical properties. A&A, 343:760–774, March 1999.
[12] R. Genzel, C. **Pichon**, A. Eckart, O. E. Gerhard, and T. Ott. Stellar dynamics in the Galactic Centre: proper motions and anisotropy. MNRAS, 317:348–374, September 2000.
[13] D. Le Borgne , D. Elbaz, P. Ocvirk, **C. Pichon** Cosmic Star-formation history from the Infrared. Star-formation rate density and Luminosity Functions from direct and inverse methods. A&A 2008
[14] M. Maciejewski, C. Colombi, F. Bouchet, **C. Pichon** Phase space structures I: A comparison of 6D density estimators MNRAS 2008
[15] P. Ocvirk, A. Lançon, C. **Pichon**, P. Prugniel, D. Le Borgne, B. Rocca- Volmerange, M. Fioc, C. Soubiran, and E. Thiébaut. High resolution spectra of galaxies. Ap&SS, 284:933–936, April 2003.
[16] P. Ocvirk, C. **Pichon**, A. Lançon, and E. Thiébaut. STECKMAP: STEllar Content and Kinematics from high resolution galactic spectra viaMaximum A Posteriori. MNRAS, 365:74–84, January 2006.
[17] P. Ocvirk, C. **Pichon**, A. Lançon, and E. Thiébaut. STECMAP: STEllar Content from high-resolution galactic spectra via Maximum A Posteriori. MNRAS, 365:46–73, January 2006.
[18] P. Ocvirk, **C. Pichon,** R. Teyssier “Bimodal gas accretion in the MareNostrum galaxy formation simulation” MNRAS 2008
[19] S. Peirani , C. Alard, **C. Pichon**, R. Gavazzi and D. Aubert, Statistical signatures of substructures via strong lenses MNRAS 2008

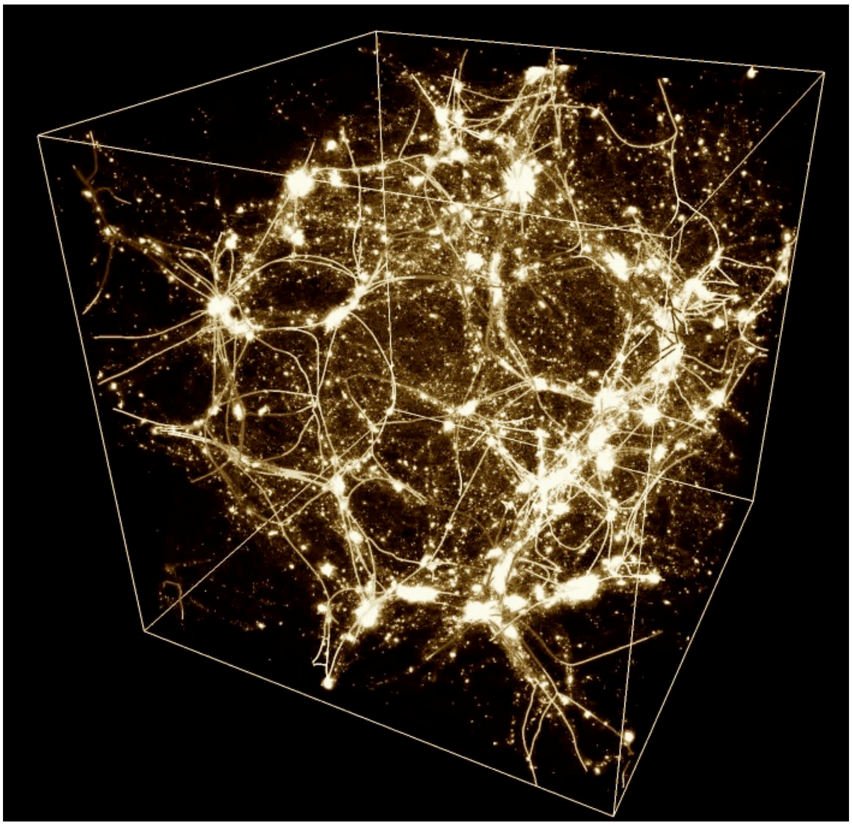

[20] C. **Pichon** and D. Aubert. Dynamical flows through dark matter haloes: inner perturbative dynamics, secular evolution and applications. MNRAS, 368:1657–1694, June 2006.
[21] C. **Pichon** and F. Bernardeau. Vorticity generation in large-scale structure caustics. A&A, 343:663–681, March 1999.
[22] C. **Pichon** and R. C. Cannon. Numerical linear stability analysis of round galactic discs. MNRAS, 291:616–+, November 1997.
[23] C. **Pichon** and D. Lynden-Bell. Equilibria of flat and round galactic discs. MNRAS, 282:1143–1158, October 1996.
[24] C. **Pichon** and D. Lynden-Bell. New sources for Kerr and other metrics: rotating relativistic discs with pressure support. MNRAS, 280:1007–1026, June 1996.
[25] C. **Pichon**, E. Scannapieco, B. Aracil, P. Petitjean, D. Aubert, J. Bergeron, and S. Colombi. The Clustering of Intergalactic Metals. ApJ, 597:L97– L100, November 2003.
[26] C. **Pichon**, A. Siebert, and O. Bienaymé. On the kinematic deconvolution of the local neighbourhood luminosity function. MNRAS, 329:181–194, January 2002.
[27] C. **Pichon** and E. Thiebaut. Non-parametric reconstruction of distribution functions from observed galactic discs. MNRAS, 301:419–434, December 1998.
[28] C. **Pichon**, J. L. Vergely, E. Rollinde, S. Colombi, and P. Petitjean. Inversion of the Lyman forest: three-dimensional investigation of the intergalactic medium. MNRAS, 326:597–620, September 2001.
[29] D. Pogosyan, C. **Pichon**, S. Prunet, C. Gay , S. Colombi , T. Sousbie & J.F. Cardoso The local theory of the cosmic skeleton MN 2008.
[30] S. Prunet, C. **Pichon,** D. Aubert, D. Pogosyan, R. Teyssier, & S. Gottloeber. Initial Conditions For Large Cosmological Simulations ApJS 2008
[31] E. Rollinde, P. Petitjean, and C. **Pichon**. Physical properties and smallscale structure of the Lyman-alpha forest: Inversion of the HE 1122-1628 UVES spectrum. A&A, 376:28–42, September 2001.
[32] E. Rollinde, P. Petitjean, C. **Pichon**, S. Colombi, B. Aracil, V. D'Odorico, and M. G. Haehnelt. The correlation of the Lyman forest in close pairs and groups of high-redshift quasars: clustering of matter on scales of 1-5 Mpc. MNRAS, 341:1279–1289, June 2003.
[33] E. Scannapieco, C. **Pichon**, B. Aracil, P. Petitjean, R. J. Thacker, D. Pogosyan, J. Bergeron, and H. M. P. Couchman. The sources of intergalactic metals. MNRAS, 365:615–637, January 2006.
[34] T. Sousbie, C. **Pichon**, S. Colombi, D. Novikov, and D. Pogosyan. The 3D skeleton: tracing the filamentary structure of the Universe. MNRAS, pages 1168–+, December 2007.
[35] T. Sousbie, C. **Pichon**, S. Colombi . The fully connected N dimensional Skeleton: probing the evolution of the cosmic web MNRAS, 2008.
[36] T. Sousbie, C. **Pichon**, H. Courtois, S. Colombi, and D. Novikov. The Three-dimensional Skeleton of the SDSS. ApJ, 672:L1–L4, January 2008.
[37] R Teyssier, S. Pires, S. Prunet, D. Aubert, **C Pichon** et al. Full-Sky Weak Lensing Simulation with 70 Billion Particles . A&A 2008
[38] J. Thiebaut, **C Pichon** , T Sousbie , S Prunet , D. Pogosyan On the Onset of Stochasticity in Cosmological Simulations MN 2008
[39] C. **Pichon** E. Thiebaut. S. Prunet, K. Benabed, S. Colombi, T. Sousbie, R. Teyssier. ASKI: towards a full sky lensing map making pipeline. MNRAS,soumis

Publication sans comité de lecture

[S1] D. Aubert and C. **Pichon**. Accretion By Dark Matter Haloes. In G. A. Mamon, F. Combes, C. Deffayet, and B. Fort, editors, EAS Publications Series, volume 20 of EAS Publications Series, pages 37–40, 2006.
[S2] D. Aubert, C. **Pichon**, and S. Colombi. Dynamical fluxes through galactic halos. In F. Combes, D. Barret, T. Contini, and L. Pagani, editors, SF2A-2003: Semaine de l'Astrophysique Francaise, pages 3–+, 2003.
[S3] J. G. Bartlett, N. Aghanim, M. Arnaud, J.-P. Bernard, A. Blanchard, M. Boer, D. J. Burke, C. A. Collins, M. Giard, D. H. Lumb, S. Majerowicz, P. Marty, D. Neumann, J. Nevalainen, R. C. Nichol, C. **Pichon**, A. K. Romer, R. Sadat, and C. Adami. The XMM-Newton Omega Project. In D. M. Neumann and J. T. V. Tran, editors, Clusters of Galaxies and the High Redshift Universe Observed in X-rays, 2001.
[S4] O. Bienayme, M. Creze, E. Chereul, and C. **Pichon**. The Potential Well and Local Dynamical Mass. In D. Zaritsky, editor, Galactic Halos, volume 136 of Astronomical Society of the Pacific Conference Series, pages 227–+,1998.
[S5] O. Bienaymé, M. Crézé, E. Chereul, and C. **Pichon**. Oort Limit from HIPPARCOS. In D. R. Merritt, M. Valluri, and J. A. Sellwood, editors, Galaxy Dynamics - A Rutgers Symposium, volume 182 of Astronomical Society of the Pacific Conference Series, pages 301–+, August 1999.
[S6] C. Boily and C. **Pichon**. The Impact of Tides on Star Cluster Formation. In R. E. Schielicke, editor, Astronomische Gesellschaft Meeting Abstracts, volume 17 of Astronomische Gesellschaft Meeting Abstracts, pages 5–+, 2000.
[S7] S. Caucci, P. Petitjean, C. **Pichon**, F. Stoehr, E. Rollinde, S. Colombi, and F. Coppolani. The topology of the intergalactic medium from multiple lines of sight to quasars. In P. Williams, C.-G. Shu, and B. Menard, editors, IAU Colloq. 199: Probing Galaxies through Quasar Absorption Lines, pages 406–408, March 2005.

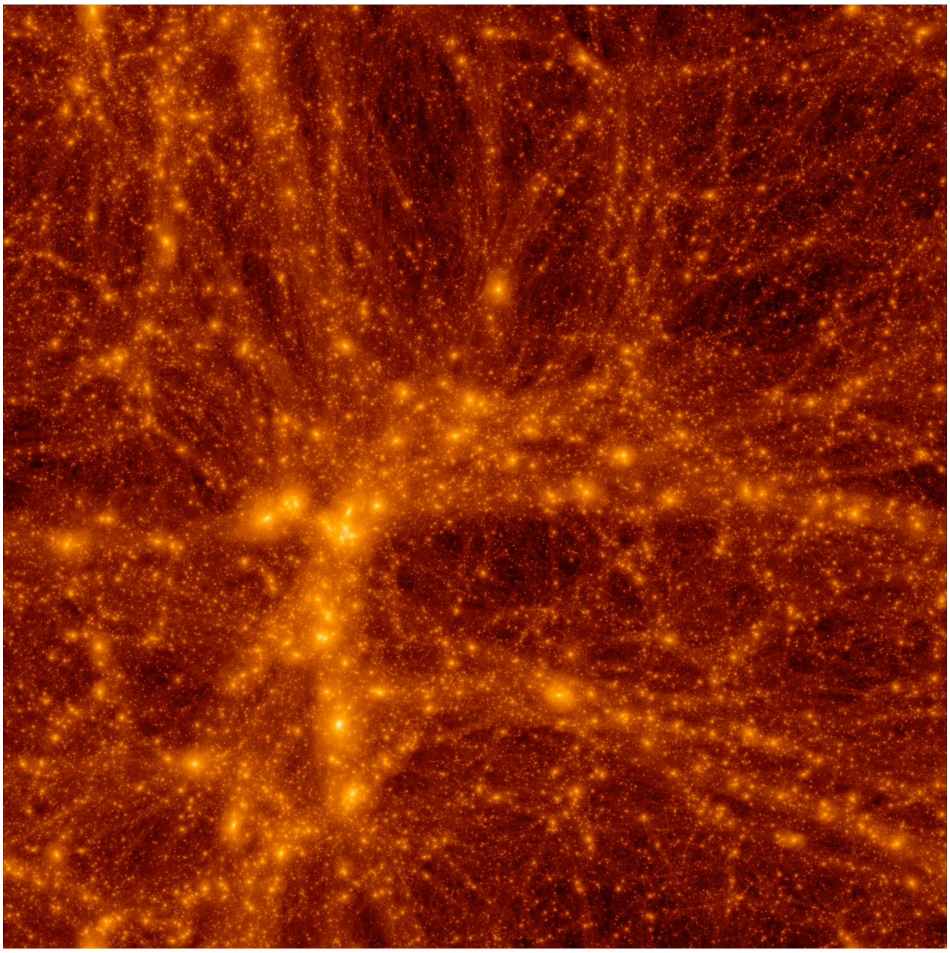

[S8] F. Coppolani. The Correlation of the Lyman-Forest and Metals in Close Pairs of High-Redshift Quasars. In V. Le Brun, A. Mazure, S. Arnouts, and D. Burgarella, editors, The Fabulous Destiny of Galaxies: Bridging Past and Present, pages 517–+, January 2006.
[S9] F. Coppolani, P. Petitjean, F. Stoehr, E. Rollinde, C. **Pichon**, S. Colombi,M. G. Haehnelt, B. Carswell, and R. Teyssier. Transverse and Longitudinal Correlation Functions in the IntergalacticMedium. The Messenger, 125:24–+, September 2006.
[S10] F. Coppolani, P. Petitjean, F. Stoehr, E. Rollinde, C. **Pichon**, S. Colombi,M. Haenelt, B. Carswell, and R. Teyssier. The correlation of the Lyman-forest and metals in close pairs of high-redshift quasars. In F. Casoli, T. Contini, J. M. Hameury, and L. Pagani, editors, SF2A-2005: Semaine de l'Astrophysique Francaise, pages 671–+, December 2005.
[S11] M. Creze, E. Chereul, O. Bienayme, and C. **Pichon**. Distribution of Nearby Stars in Phase Space Mapped by HIPPARCOS. In Hipparcos - Venice '97, volume 402 of ESA Special Publication, pages 669–674, August 1997.
[S12] A. Lançon, P. Ocvirk, D. Le Borgne, C. **Pichon**, P. Prugniel, M. Fioc, B. Rocca-Volmerange, and C. Soubiran. Modelling and interpreting optical spectra of galaxies at R=10 000. In C. C. Popescu and R. J. Tuffs, editors, The Spectral Energy Distributions of Gas-Rich Galaxies: Confronting Models with Data, volume 761 of American Institute of Physics Conference Series, pages 79–+, April 2005.
[S13] P. Ocvirk, A. Lançon, C. **Pichon**, and E. Thiébaut. Star formation history of galaxies from optical integrated light spectra. In C. C. Popescu and R. J. Tuffs, editors, The Spectral Energy Distributions of Gas-Rich Galaxies: Confronting Models with Data, volume 761 of American Institute of Physics Conference Series, pages 87–+, April 2005.
[S14] P. Ocvirk, A. Lancon, C. **Pichon**, P. Prugniel, E. Thiébaut, D. Le Borgne, B. Rocca-Volmerange, M. Fioc, and C. Soubiran. Stellar populations and their kinematics from high and medium resolution spectra: mixed inversions. In F. Combes, D. Barret, T. Contini, and L. Pagani, editors,

[S15] P. Petitjean, S. Colombi, C. **Pichon**, and J.-L. Vergely. Spatial Distribution of the Intergalactic Medium from Intervening Ly Absorption in the Spectra of High Redshift QSOs. In A. Mazure, O. Le Fèvre, and V. Le Brun, editors, Clustering at High Redshift, volume 200 of Astronomical Society of the Pacific Conference Series, pages 266–+, 2000.
[S16] C. **Pichon**. Warm Super Massive Disks: New Sources for Kerr Metric. In F. Combes and E. Athanassoula, editors, N-body Problems and Gravitational Dynamics, pages 155–161, 1993.
[S17] C. **Pichon** and R. C. Cannon. Numerical linear stability analysis of round galactic disks. ArXiv Astrophysics e-prints, April 1997.
[S18] C. **Pichon** and D. Lynden-Bell. Bar Instabilities in Galaxies. In J. Misquich, G. Pelletier, and P. Schuck, editors, Statistical Description of Transport in Plasma, Astro- and Nuclear Physics, pages 261–+, 1993.
[S19] C. **Pichon**, A. Siebert, O. Bienaymé, and R. Ibata. On the Kinematic Deconvolution of the Local Neighbourhood Luminosity Function. In S. Deiters, B. Fuchs, A. Just, R. Spurzem, and R. Wielen, editors, Dynamics of Star Clusters and the Milky Way, volume 228 of Astronomical Society of the Pacific Conference Series, pages 541–+, 2001
[S20] P. Prugniel, F. Simien, M. Fioc, D. Le Borgne, B. Rocca-Volmerange, P. Ocvirk, A. Lançon, C. **Pichon**, and C. Soubiran. The History of the Stellar Population of Bulges. In E. Perez, R. M. Gonzalez Delgado, and G. Tenorio-Tagle, editors, Star Formation Through Time, volume 297 of Astronomical Society of the Pacific Conference Series, pages 281–+, 2003.
[S21] E. Rollinde, P. Petitjean, and C. **Pichon**. Inversion of the HE 1122-1648 UVES spectrum (Rollinde+ 2001). VizieR Online [S23] E. Rollinde, P. Petitjean, C. **Pichon**, S. Colombi, B. Aracil, V. D'Odorico, and M. G. Haehnelt. The correlation of the Lyman-alpha forest in close pairs and groups of high-redshift quasars: clustering of matter on scales 1-5 Mpc. In F. Combes and D. Barret, editors, SF2A-2002: Semaine de l'Astrophysique Francaise, pages 73–+, June 2002.
[S24] A. Siebert, C. **Pichon**, O. Bienaymé, and E. Thiébaut. On the Kinematic Deconvolution of the Local Luminosity Function. In O. Bienayme and C. Turon, editors, EAS Publications Series, volume 2 of EAS Publications Series, pages 375–377, 2002.
[S25] C. **Pichon**, "The dynamics of disks" Knight Price 1992 & PhD Thesis, University of Cambridge & Clare College 1994.

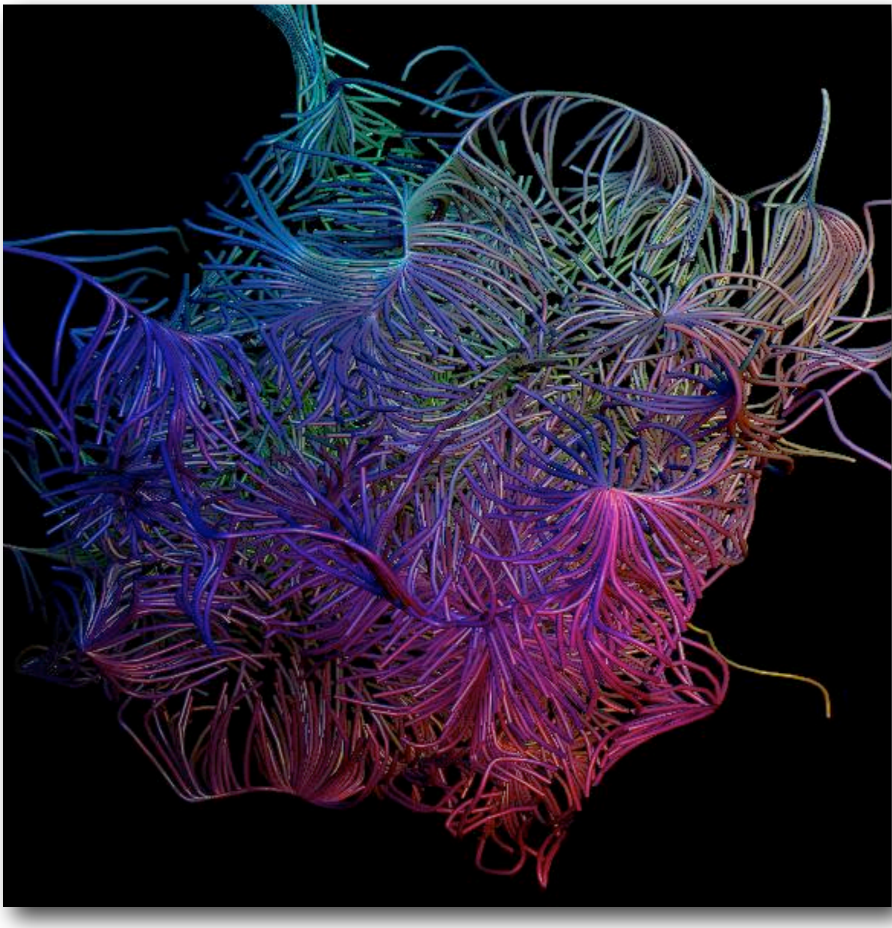

— Les lignes de champs conduisant à la segmentation tridimensionnelle de l'espace au sens des peak patches.

5. Sélection d'articles publiés et soumis

Cette partie présente un échantillon des articles publiés/soumis les plus significatifs de mon point de vue. J'ai choisi par soucie d'efficacité (et d'équité vis a vis de mes collaborateurs) de consacrer mon temps de recherche de ces derniers mois à soumettre sous forme d'article mes travaux les plus récents (en particulier les articles sur le squelette global et l'astigmatisme cosmique). Cette cinquième partie est classé en 4 sections principales : i) la dynamique galactique ii) la topologie et géométrie des grandes structures iii) physique théorique et iv) les méthodes inverses. La fin de cette partie présente la première page des autres articles.

Ces différentes sections sont séparées par des images en fausses couleurs de la simulation MareNostrum (en bleu la température, rouge la matière noire et vert la densité du gaz).

1. Dynamique galactique & formation des galaxies

- Dynamical flows through dark matter haloes I: inner perturbative dynamics, secular evolution and applications
- Numerical linear stability analysis of round galactic discs
- Dynamical flows through dark matter haloes – II. One- and two-point statistics at the virial radius
- The origin and implications of dark matter anisotropic cosmic infall on ≈ L* haloes
- Initial conditions for large cosmological simulations #
- Full-Sky Weak Lensing Simulation with 70 Billion Particles #
- Bimodal gas accretion in the MareNostrum galaxy formation simulation

2. Topologie et géométrie des grandes structures

- The 3D skeleton: tracing the filamentary structure of the Universe
- The three-dimensional skeleton of the SDSS
- The fully connected N dimensional Skeleton: probing the evolution of the cosmic web
- The local theory of the cosmic skeleton
- Vorticity generation in large-scale structure caustics

3. Physique théorique

- Lattice Melting and Rotation in Perpetually Pulsating Equilibria #
- New sources for Kerr and other metrics: rotating relativistic discs with pressure support
- On the Onset of Stochasticity in LCDM Cosmological Simulations

4. Méthodes inverses

- Non-parametric reconstruction of distribution functions from observed galactic discs
- ASKI: towards a full-sky lensing map making pipeline
- Stellar Content (& Kinematics) from high-resolution galactic spectra via Maximum A Posteriori
- On the kinematic deconvolution of the local neighbourhood luminosity function
- Inversion of the Lyman a forest: three-dimensional investigation of the intergalactic medium
- The sources of intergalactic metals#

Chaque article est présenté dans son intégralité. Les articles labelisés # correspondent à des travaux où je n'étais pas directement le porteur du projet[4], mais où mon investissement en travail/méthode justifie sa présentation.

[4] la tradition étant de faire signer les étudiants premier auteur si leur investissement le justifie.

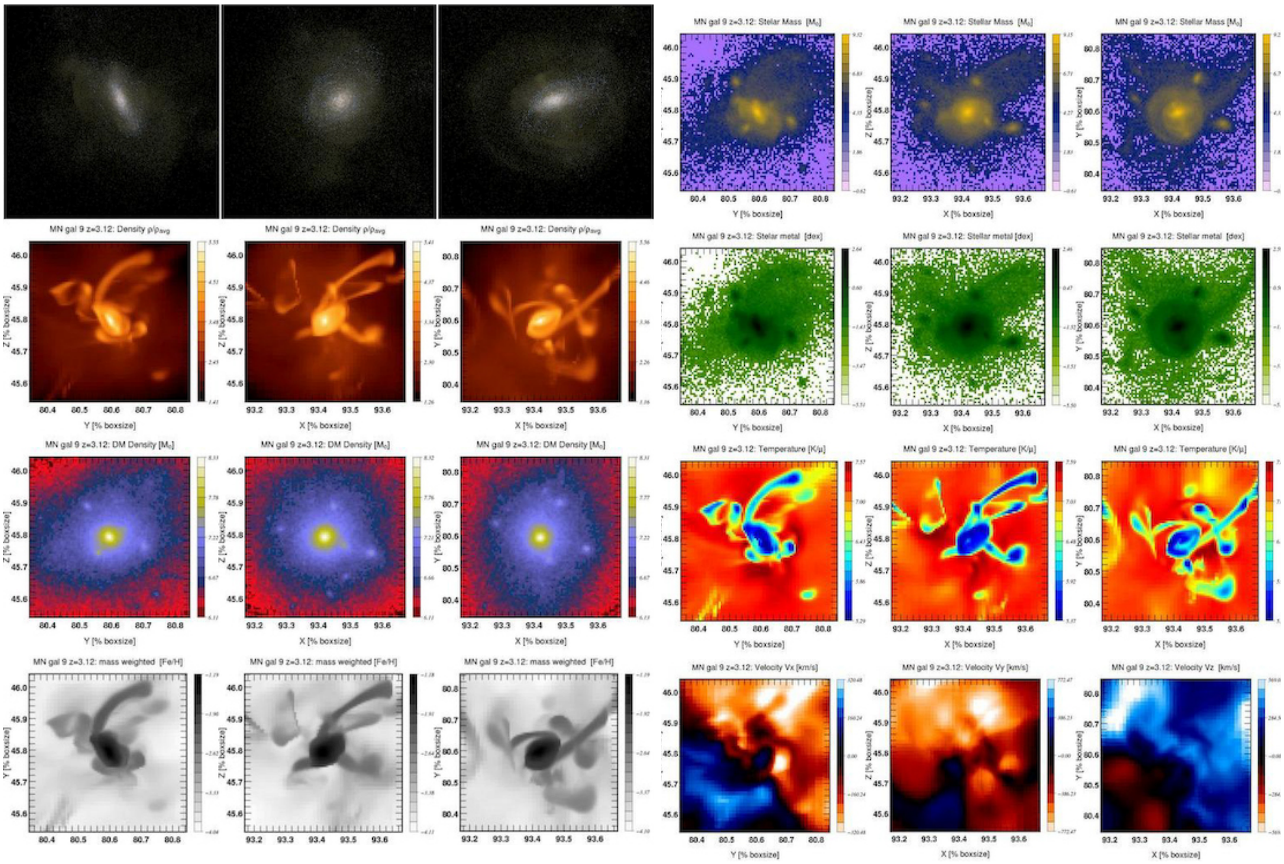

— les champs physiques d'une galaxie parmi 160 000 à redshift z=1.55 de la simulation MareNostrum ; champ stellaire, gaz, matière noire, métallicité du gaz, masse stellaire, métallicité stellaire, température ; voir http://www.iap.fr/users/pichon/ pour quelques centaines d'autres objets [Ocvirk, Pichon, Teyssier 2008].

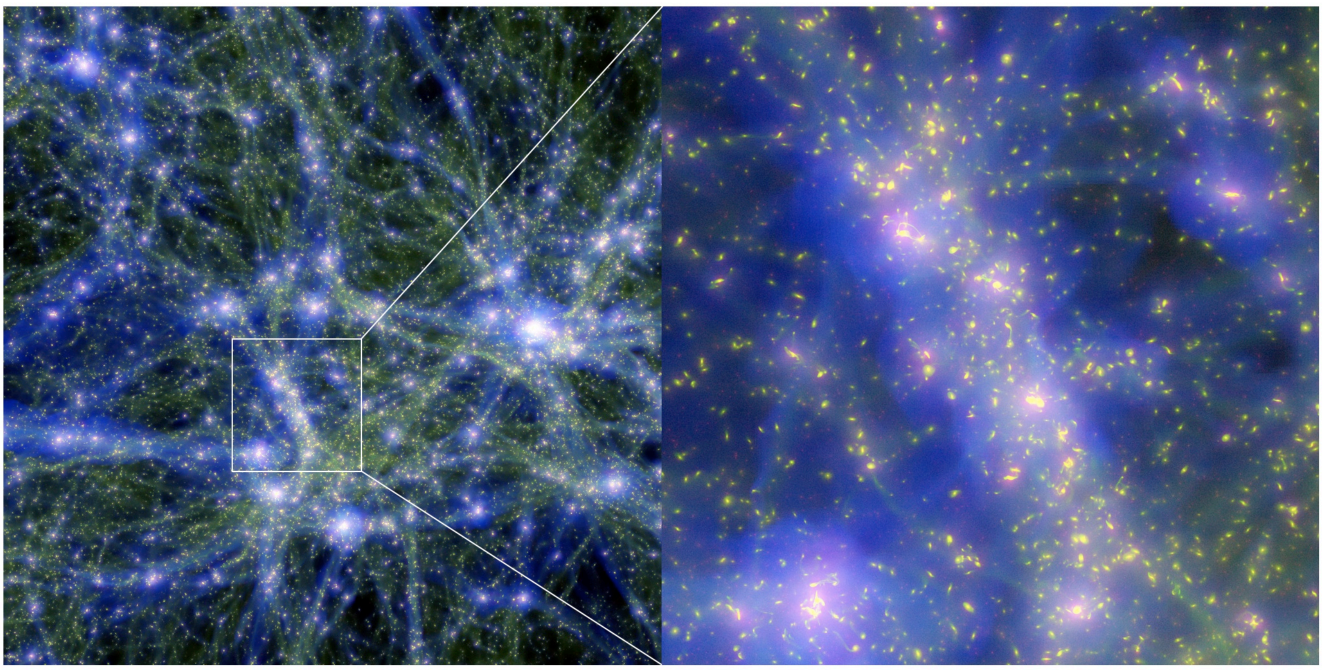

— Une vision composite globale de la simuation et un zoom d'un filament [Devriendt, Pichon, et al. *in prep.*].

Annexe A

Encadrement doctoral, post-doctoral et pré-doctoral (en % la fraction d'encadrement)

Encadrement pré-doctoral

1. D. Aubert : "*L'environnement statistique d'une galaxie L**" DEA Astronomie Paris VI 100 %
2. P. Ocvirk : "*La stabilité linéaire des disques galactiques gazeux*" DEA Astronomie Strasbourg 100 %
3. M. Guenno : "*Histoire de formation stellaire à partir de spectres HR*" DEA Astronomie Strasbourg 50 %
4. J. Thiébaut : *"Emergence du chaos à grande échelle"* M2 Astronomie Nice 100 %
5. C. Gay : "*Courbure du squelette*" M2 particule matière Paris XI 80 %
6. Myriam Fischer : "*Entropie des sphéroïdes anisotropes*" Magistère de Mathématique de Strasbourg 100 %
7. B. Depardon : "*Dépolarisation magnétique du milieu interstellaire*" Ecole des Mines de Paris 70 %
8. Annie Hugues : *"Statistique des systèmes carbonnées*" M1 Université de Melbourne 70 %
9. Isabelle Paris : "*Synthèse chromatique des galaxies de MareNostrum*" M1 Paris VI 100 %
10. Florence Brault : "*Environnement spectroscopique des galaxies de MareNostum*" M1 Paris VI 100 %

Encadrement doctoral

1. D. Aubert : "*Etude des flux cosmologiques au travers de la sphère du viriel d'un disque Galactique*" 100 %
2. E. Rollinde : "*La physique du milieu intergalactique*" avec P. Petitjean, 50 %
3. A. Siebert : "*Structure et dynamique des disques de la Galaxie*" avec O. Bienaymé 50 %
4. P. Ocvirk : "*Evolution chemo-spectro-dynamique des disques galactiques*" avec A. Lançon 70 %
5. B. Aracil :"*Etude du milieu intergalactique via les raies d'absorptions des quasars*" avec P. Petitjean 50 %
6. Sara Caucci : "*la topologie du Milieu intergalactique*" avec P. Petitjean 33 %
7. T. Sousbie : "*Le Squelette de l'univers, un outil d'analyse des grandes structures*" avec H. Courtois 50 %
8. C. Gay (2007-), sur la statistique du squelette global. 100 %
9. J. Thiébaut, sur l'inversion des cartes de polarisation, (2007-), avec S Prunet 70 %
10. D. Chapon en co tutelle (2008-) sur la structure et l'évolution de la Voie Lactée avec R. Teyssier 50 %

J'ai aussi collaboré avec J. L. Vergely et J. Petry durant leur thèse. Parmi ces ex-étudiants en thèse, deux d'entre eux ont été recrutés à l'Obervatoire de Strasbourg, et un à l'Institut d'astrophysique de Paris.

Encadrement post-doctoral

1. E. Scannapieco : *les métaux du milieu intergalactique* (Scannapieco et al. 2006 ; Pichon et al. 2005) ; 40%
2. P. Ocvirk : *la bimodalité de l'accrétion des métaux sur les galaxies* (Ocvirk, Pichon, Teyssier, 2008), 40%
3. F. Stoehr : *les fonctions de corrélation transverse de la forêt du MIG* (Copolani et al., *2006*), 20%
4. D. Le Borgne : *l'inversion du SFR cosmique à partir des comptages* (Le Borgne, et al. 2008), 10%
5. S. Peirani (postdoc) *la construction et l'inversion de lentilles fortes* (Peirani, Alard,Pichon, et al 2008), 30%
6. T. Sousbie *le squelette de l'univers* (Sousbie Pichon et al. 2008a,b, Sousbie Colombi, Pichon 2008). 70%

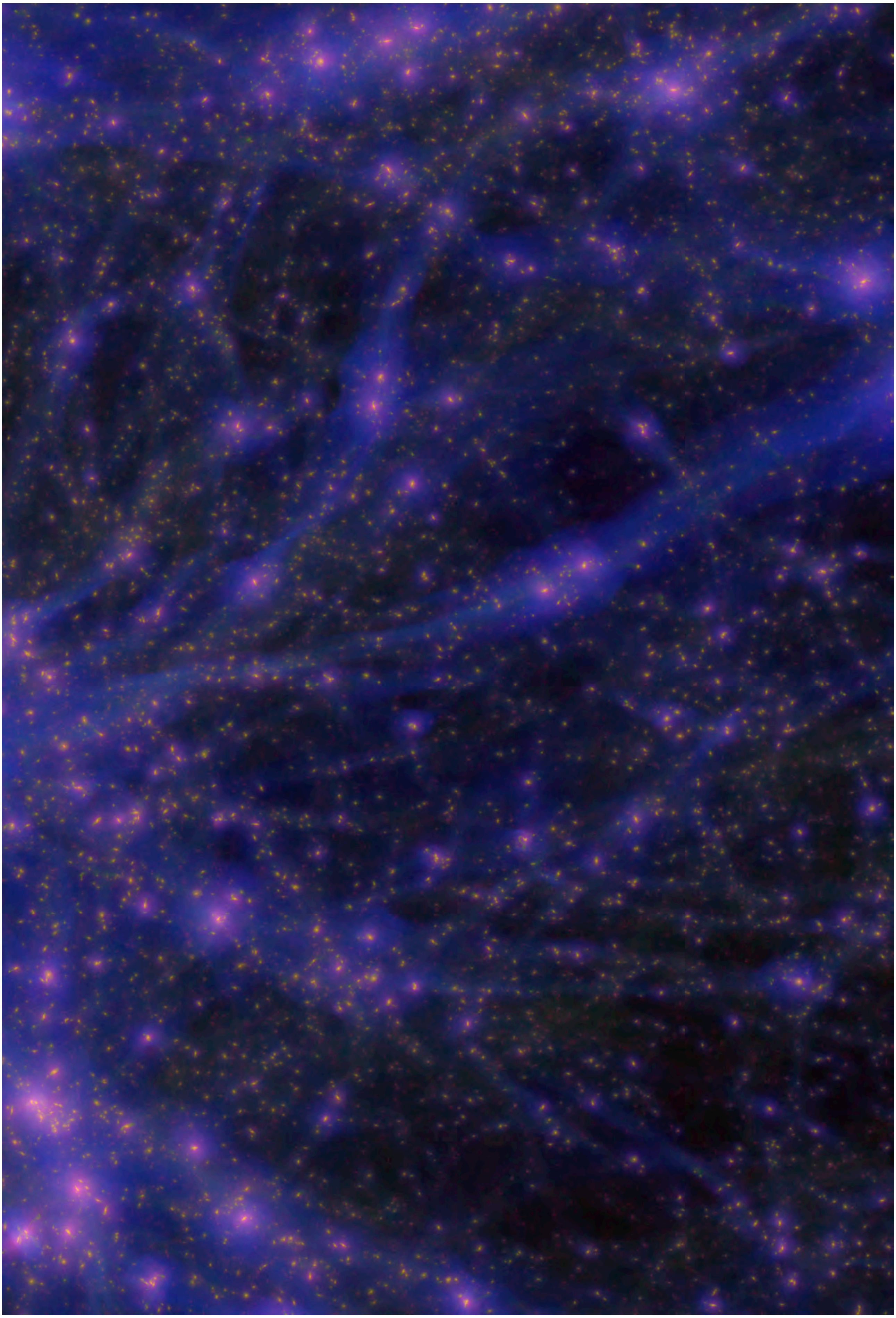

Mon. Not. R. Astron. Soc. **368,** 1657–1694 (2006) doi:10.1111/j.1365-2966.2006.10132.x

Dynamical flows through dark matter haloes: inner perturbative dynamics, secular evolution and applications

Christophe Pichon[1,2,3★] and Dominique Aubert[1,2,3,4]

[1] *Institut d'Astrophysique de Paris, 98 bis boulevard d'Arago, 75014 Paris, France*
[2] *Observatoire astronomique de Strasbourg, 11 rue de l'Universite, 67000 Strasbourg, France*
[3] *Horizon, CNRS, 98 bis boulevard d'Arago, 75014 Paris, France*
[4] *4 AIM, CEA Saclay, Orme des Merisiers, 91191 Gif Sur Yvette, France*

Accepted 2006 January 31. Received 2006 January 17; in original form 2005 August 3

ABSTRACT

We investigate statistically the dynamical consequences of cosmological fluxes of matter and related moments on progenitors of today's dark matter haloes. These haloes are described as open collisionless systems which do not undergo strong interactions anymore. Their dynamics is described via canonical perturbation theory which accounts for two types of perturbations: the tidal field corresponding to flybys and accretion of dark matter through the outer boundary of the halo.

The non-linear evolution of both the entering flux and the particles of the halo is followed perturbatively. The dynamical equations are solved linearly, order by order, projecting on a bi-orthogonal basis to consistently satisfy the field equation. Since our perturbative solution of the Boltzmann–Poisson is explicit, we obtain, as a result, expressions for the N-point correlation function of the response of the halo to the perturbative environment. It allows statistical predictions for the ensemble distribution of the inner dynamical features of haloes. We demonstrate the feasibility of the implementation via a simple example in Appendix B. We argue that the fluid description accounts for the dynamical drag and the tidal stripping of incoming structures. We discuss the realm of non-linear problems which could be addressed statistically by such a theory, such as differential dynamical friction, tidal stripping and the self-gravity of objects within the virial sphere.

The secular evolution of open galactic haloes is investigated: we derive the kinetic equation which governs the quasi-linear evolution of dark matter profile induced by infall and its corresponding gravitational correlations. This yields a Fokker–Planck-like equation for the angle-averaged underlying distribution function. This equation has an explicit source term accounting for the net infall through the virial sphere. Under the assumption of ergodicity we then relate the corresponding source, drift and diffusion coefficients for the ensemble-average distribution to the underlying cosmic two-point statistics of the infall and discuss possible applications.

The internal dynamics of substructures within galactic haloes (distortion, clumps as traced by Xray emissivity, weak lensing, dark matter annihilation, tidal streams, etc.), and the implication for the disc (spiral structure, warp, etc.) are then briefly discussed. We show how this theory could be used to (i) observationally constrain the statistical nature of the infall, (ii) predict the observed distribution and correlations of substructures in upcoming surveys, (iii) predict the past evolution of the observed distribution of clumps and finally (iv) weight the relative importance of the intrinsic (via the unperturbed distribution function) and external (tidal and/or infall) influence of the environment in determining the fate of galaxies. We stress that our theory describes the *perturbed* distribution function (mean profile removed) directly in phase space.

Key words: galaxies: haloes – galaxies: kinematics and dynamics – galaxies: statistics – dark matter.

★E-mail: pichon@iap.fr

1 INTRODUCTION

It now appears clearly that the dynamical (azimuthal instabilities, warps, accretion), physical (heating, cooling) and chemical (metal-poor cold gas fluxes) evolution of galaxies are processes which are partly driven by the boundary conditions imposed by their cosmological environment. It is therefore of prime importance to formulate the effects of such an interaction in a unified framework.

Modern digital all-sky surveys, such as the Sloan Digital Sky Survey (SDSS), two-Micron All-Sky Survey (2MASS) or the two-degree Field (2dF) provide for the first time the opportunity to build statistically relevant constraints on the dynamical states of galaxies which can be used as observational input. Other projects, like *GAIA* or *Planck*, will provide small-scale information on our Galaxy and its environment and will soon allow detailed confrontation of the predictions of models with the observations. We ought to be able to draw conclusions on the internal dynamics of the halo and its inner components and constrain their statistical properties.

Unfortunately, it is difficult to study the response of haloes to moderate amplitude perturbations. Current N-body techniques suffer from resolution limitations (due to particle number and drift in orbit integration, see e.g. Power et al. 2003; Binney 2004, for a discussion of such effects) that hide to some extent linear collective effects which dominate the response of the halo (Murali 1999; Weinberg 1998b).[1] Simulations on galactic scales are also often carried out without any attempt to represent the cosmological variety arising from the possible boundary conditions (the so-called cosmic variance problem). This is because the dynamical range required to describe both the environment and the inner structure is considerable, and can only be achieved for a limited number of simulations (e.g. Diemand, Moore & Stadel 2004; Gill et al. 2004; Knebe et al. 2004). By contrast, the method presented below circumvents this difficulty while relying on an *explicit* treatment of the inner dynamics of the halo, in the perturbative regime. Specifically, our purpose is to develop a tool to study the dynamics of an open stellar system and apply it to the dynamics of a halo which is embedded into its cosmological environment. One can think of this project as an attempt to produce a semi-analytic explicit resimulation tool, in the spirit of what is done in N-body simulations with zoomed-in initial conditions.

The concept of an initial power spectrum describing the statistical properties of the gravitational perturbations has proved very useful in cosmological studies (e.g. Peebles 1980; Bernardeau et al. 2002). The underlying paradigm, that gravity drives cosmic evolution, is likely to be a good description at the Mpc scale. We show below that a similar approach to galactic haloes is still acceptable, and marginally within the reach of our modelling capabilities. The description of the boundary is significantly more complex, but the inner dynamics of hot components is better behaved. Here, we describe a stable system which undergoes small interactions, rather than an unstable system in comoving coordinates undergoing catastrophic multiscale collapse.

The purpose of this investigation is to derive analytically the dynamical response of a galactic halo, induced by its (relatively weak) interaction with its near environment. Interaction should be understood in a general sense and involve tidal potential interactions (like that corresponding to a satellite orbiting around the galaxy), or an infall where an external quantity (virialized or not) is advected into the galactic halo.

With a suitable formalism, we derive the propagation of an external perturbation from the near galactic environment down to the scale of the galactic disc through the dark matter halo. We essentially solve the coupled collisionless Boltzmann–Poisson equations as a Dirichlet initial value problem to determine the response of the halo to infall and tidal field. The basis over which the response is projected can be customized to, say, the universal profile of dark matter haloes, which makes it possible to consistently and efficiently solve the coupled dynamical and field equations, so long as the entering fluxes of dark matter amounts to a small perturbation in mass compared to the underlying equilibrium.

In a pair of companion papers, Aubert & Pichon (in preparation) described the statistical properties of the infalling distribution of dark matter at the virial radius, R_{200} as a function of cosmic time between redshift $z = 1$ and today. These papers focused on a description of the one- and two-point statistics of the infall towards well-formed $L_\star$ dark matter haloes. All measurements were carried for 15 000 haloes undergoing minor mergers. The two-point correlations were measured both angularly and temporally for the flux densities, and over the whole 5D phase space for the expansion coefficients of the source.

Together with the measurements presented there, we show in this paper that the formalism described below will allow astronomers to address globally and coherently dynamical issues on galactic scales. Most importantly, it will allow them to tackle problems in a *statistically representative* manner. This investigation has a broad field of possible applications. Galaxies are subject to boundary conditions that reflect motions on larger scales and their dynamics may constrain the cosmology through the rate of merging events for example, or the mass distribution of satellites. Halo transmission and amplification also fosters communication between spatially separated regions (see e.g. Murali 1999) and continuously excites the disc structure. For example, spirals can be induced by encounters with satellites and/or by mass injection (e.g. Toomre & Toomre 1972; Howard & Byrd 1990), while warps results from torque interactions with the surrounding matter (Jiang & Binney 1999; López-Corredoira, Betancort-Rijo & Beckman 2002). Therefore, the proportion of spirals and warps contains information on the structure's formation and environment. The statistical link between the inner properties of galactic haloes, and their cosmic boundary can be reversed to attempt and constrain the nature of the infall while investigating the one- and two-point statistics of the induced perturbations. This is best done by transposing down to galactic scales the classical cosmic probes for the large-scale structures [lensing, Sunyaev–Zel'dovich (SZ) effect, etc.] which have been used successfully to characterize the power spectrum of fluctuations on larger scales.

[1] It has been argued that shadowing (Earn & Tremaine 1991) will in practice allow for another orbit to correct for the drift, but this is of no help to resonant processes because it requires that the *same* orbit does not diffuse for a few libration periods.

The outline of this paper is the following: we describe in Section 2 the linear response of a spherical halo which undergoes cosmological infall of dark matter, and compute the induced correlations in the inner halo; Section 3 presents the second-order perturbative response of the galactic halo to the infalling flux (Appendix D gives the higher-order corrections to the dynamics and addresses the issue of dynamical friction). Section 4 derives the Fokker–Planck equation that the cosmic mean halo profile obeys in such an open environment. Section 5 describes briefly possible astrophysical applications. In particular, it is discussed how the statistical analysis of mean and variance properties of galactic haloes and galaxies can be compared to the quantitative prediction of the concordant Lambda cold dark matter (ΛCDM) cosmogony on those scales. We also show how to revert in time observed tidal features within our Galaxy, or in external galaxies. The last section draws conclusions and discusses prospects for future work.

2 THE SPHERICAL HALO: LINEAR RESPONSE

In the following section, we extend to *open* spherical stellar systems the formalism developed by Kalnajs (1976) (for stellar discs), Aoki, Noguchi & Iye (1979) (for gaseous discs), Fridman & Poliachenko (1984), Tremaine & Weinberg (1984) and e.g. Palmer & Papaloizou (1987), Murali (1999), Vauterin & Dejonghe (1996), Bertin et al. (1994) by adding a source term to the collisionless Boltzmann equation. Since the formalism is otherwise fairly standard, we will present it relatively swiftly. In a nutshell, the dynamical equations are solved linearly while projecting over a bi-orthogonal basis to consistently satisfy the Poisson equation (e.g. Kalnajs 1971, 1976, 1977). The dynamical equation of an open system characterized by its distribution function, F, together with the field equation, read formally

$$\partial_t \mathrm{F} + \{\mathrm{H} + \psi^e, \mathrm{F}\} = s^e \quad \text{and} \quad \nabla^2 \Psi = 4\pi\mathcal{G} \int \mathrm{d}\boldsymbol{v}\mathrm{F}, \tag{1}$$

where H is the Hamiltonian of the system, $\{\ \}$ is the usual Poisson bracket and (Ψ, ψ^e, s^e) stands for the potential, the perturbing exterior potential and incoming source term. The latter, $s^e(\boldsymbol{r}, \boldsymbol{v}, t)$ accounts for the entering dark matter *at the virial radius* and is discussed in detail below (Section 2.3, see also Aubert, Pichon & Colombi 2004; Aubert & Pichon in preparation). In a somewhat unconventional manner, $\psi^e(\boldsymbol{r}, t)$ refers here to the external potential, i.e. the tidal potential created by the perturbations *outside the outer boundary of the halo* (i.e. R_{200}).

Let us expand the Hamiltonian and the distribution function, F, as

$$\mathrm{F} = F + \varepsilon f \quad \text{and} \quad \mathrm{H} = H_0 + \varepsilon\psi, \tag{2}$$

where we assume that everywhere in phase space $\varepsilon \stackrel{\triangle}{=} m/M \ll 1$ i.e. that the mass of the perturbation, m, is small compared to the mass, M, of the unperturbed halo. In equation (2), f represents the small response to the perturbations, F represents the equilibrium state and ψ the small response in potential. Putting equation (2) into (1) and reordering in ε yields the linearized Boltzmann equation

$$\frac{\partial f}{\partial t} + \frac{\partial H_0}{\partial \boldsymbol{I}} \cdot \frac{\partial f}{\partial \boldsymbol{w}} - \left(\frac{\partial \psi}{\partial \boldsymbol{w}} + \frac{\partial \psi^e}{\partial \boldsymbol{w}}\right) \cdot \frac{\mathrm{d}F}{\mathrm{d}\boldsymbol{I}} = s^e, \tag{3}$$

where $\boldsymbol{I}$ and $\boldsymbol{w}$ are conjugate canonical variables which are described in the following section.

2.1 The Boltzmann equation in action–angle

The most adequate representation of multiply-periodic integrable systems relies on the action–angle variables,[2] since resonant processes will dominate the response of the live halo, and are best expressed in those variables. We will use vector notation for simplicity. The details of the computation of these variables is discussed in Appendix B following work by Murali (1999) (see also Fig. 1). This achieves separation of variable between the phase space canonical variables (angle and actions) on the one hand, and time on the other hand. We denote as usual the set of action variables by $\boldsymbol{I}$ and angle variables by $\boldsymbol{w}$ (see Appendix B). The rates of change of angles is $\boldsymbol{\omega} \stackrel{\triangle}{=} \mathrm{d}\boldsymbol{w}/\mathrm{d}t$. Along the multiperiodic orbits, any field, Z, can be Fourier-expanded with respect to the angles as

$$Z(\boldsymbol{r}, \boldsymbol{v}, t) = \sum_{\boldsymbol{k}} Z_{\boldsymbol{k}}(\boldsymbol{I}, t) \exp\left(\mathrm{i}\boldsymbol{k} \cdot \boldsymbol{w}\right). \tag{4}$$

Conversely

$$Z_{\boldsymbol{k}}(\boldsymbol{I}, t) = \frac{1}{(2\pi)^3} \int \mathrm{d}\boldsymbol{w} \exp(-\mathrm{i}\boldsymbol{k} \cdot \boldsymbol{w}) Z(\boldsymbol{r}, \boldsymbol{v}, t), \tag{5}$$

where $\boldsymbol{k} \stackrel{\triangle}{=} (k_1, k_2, k_3)$ is the Fourier triple index conjugate to the three angles $\boldsymbol{w} \stackrel{\triangle}{=} (w_1, w_2, w_3)$. Given equations (1)–(2), the linearized Boltzmann equation in such a representation is

$$\frac{\partial f_{\boldsymbol{k}}(\boldsymbol{I}, t)}{\partial t} + \mathrm{i}\boldsymbol{k} \cdot \boldsymbol{\omega} f_{\boldsymbol{k}}(\boldsymbol{I}, t) = \mathrm{i}\boldsymbol{k} \cdot \frac{\mathrm{d}F}{\mathrm{d}\boldsymbol{I}} \left[\psi_{\boldsymbol{k}}(\boldsymbol{I}, t) + \psi^e_{\boldsymbol{k}}(\boldsymbol{I}, t)\right] + s^e_{\boldsymbol{k}}(\boldsymbol{I}, t). \tag{6}$$

[2] Note that $(\boldsymbol{w}, \boldsymbol{I})$ are canonical variables, and as such preclude nothing about the evolution of the system. They simplify the expression of the linearized equations, order by order.

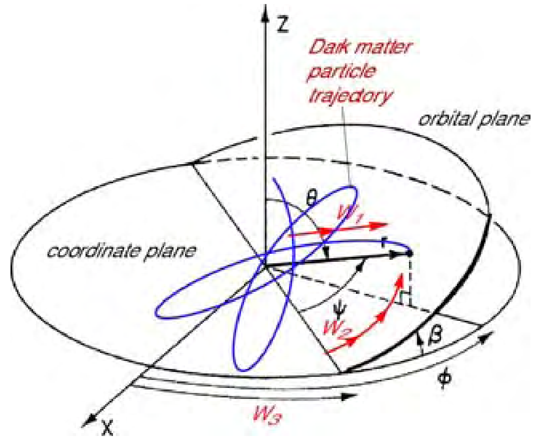

Figure 1. The action–angle ($\boldsymbol{I}$, $\boldsymbol{w}$)–spherical coordinate ($\boldsymbol{r}$, $\boldsymbol{v}$), transformation. The dark matter particle at running spherical coordinate (r, θ, ϕ) describes a rosette in the orbital plane orthogonal to its momentum, $\boldsymbol{L}$. The line of node of the orbital plane intersects the xy plane at a constant (in spherical symmetry) angle w_3 with respect to the x-axis. The orbital plane is at an angle $\beta = \mathrm{acos}\,(L_z/L)$ to the xy plane. The particle polar coordinate in the orbital plane with respect to this line of node is ψ. The angle coordinates, w_2, is measured along ψ but varies linearly with time by construction. Finally, the radial angle w_1 varies with radius between periapse and apoapse (strongly inspired from fig. 1 of Tremaine & Weinberg 1984).

Here, ψ is the potential perturbation created by the inner density fluctuations of the halo and ψ^e the potential perturbation created by external flybys. The gravitational field of incoming particles is accounted for by the source term s^e. The solution to equation (6) may then be written as

$$f_{\boldsymbol{k}}(\boldsymbol{I}, t) = \int_{-\infty}^{t} \exp(\mathrm{i}\boldsymbol{k}\cdot\boldsymbol{\omega}(\tau - t)) \left[\mathrm{i}\boldsymbol{k}\cdot\frac{\mathrm{d}F}{\mathrm{d}\boldsymbol{I}}\left[\psi_{\boldsymbol{k}}(\boldsymbol{I}, \tau) + \psi_{\boldsymbol{k}}^{e}(\boldsymbol{I}, \tau)\right] + s_{\boldsymbol{k}}^{e}(\boldsymbol{I}, \tau)\right] \mathrm{d}\tau. \tag{7}$$

Equation (7) assumes that the perturbation has been switched on a long time ago in the past so that all transients have damped out.[3]

2.2 Self-consistency

Equation (7) can be integrated over velocities and summed over $\boldsymbol{k}$ to get the density perturbation

$$\rho(\boldsymbol{r}, t) = \sum_{\boldsymbol{k}} \int_{-\infty}^{t} \mathrm{d}\tau \int \mathrm{d}\boldsymbol{v} \exp(\mathrm{i}\boldsymbol{k}\cdot\boldsymbol{\omega}(\tau - t) + \mathrm{i}\boldsymbol{k}\cdot\boldsymbol{w}) \left\{\mathrm{i}\boldsymbol{k}\cdot\frac{\mathrm{d}F}{\mathrm{d}\boldsymbol{I}}\left[\psi_{\boldsymbol{k}}(\boldsymbol{I}, \tau) + \psi_{\boldsymbol{k}}^{e}(\boldsymbol{I}, \tau)\right] + s_{\boldsymbol{k}}^{e}(\boldsymbol{I}, \tau)\right\}. \tag{8}$$

Let us expand the potential and the density over a bi-orthogonal complete set of basis functions such that

$$\psi(\boldsymbol{r}, t) = \sum_{\boldsymbol{n}} a_{\boldsymbol{n}}(t)\psi^{[\boldsymbol{n}]}(\boldsymbol{r}), \quad \rho(\boldsymbol{r}, t) = \sum_{\boldsymbol{n}} a_{\boldsymbol{n}}(t)\rho^{[\boldsymbol{n}]}(\boldsymbol{r}), \tag{9}$$

$$\nabla^2\psi^{[\boldsymbol{n}]} = 4\pi G\rho^{[\boldsymbol{n}]}, \quad \int \psi^{[\boldsymbol{n}]*}(\boldsymbol{r})\rho^{[\boldsymbol{p}]}(\boldsymbol{r})\mathrm{d}\boldsymbol{r} = \delta_{\boldsymbol{p}}^{\boldsymbol{n}}, \tag{10}$$

where $\psi^{[\boldsymbol{n}]*}(\boldsymbol{r}$ is the complex conjugate of $\psi^{[\boldsymbol{n}]}(\boldsymbol{r})$). We naturally expand the external potential on the same basis (Kalnajs 1971) as

$$\psi^{e}(\boldsymbol{r}, t) = \sum_{\boldsymbol{n}} b_{\boldsymbol{n}}(t)\psi^{[\boldsymbol{n}]}(\boldsymbol{r}). \tag{11}$$

Thus, the coefficients $a_{\boldsymbol{n}}$ are representative of the density and potential perturbations in the halo itself, at $r < R_{200}$, while the coefficients $b_{\boldsymbol{n}}$ represent the potential created in the halo by density fluctuations at $r > R_{200}$. Taking advantage of bi-orthogonality equation (8) is multiplied by $\psi_{\boldsymbol{p}}^{*}(\boldsymbol{r})$ and integrated over $\boldsymbol{r}$, which yields

$$a_{\boldsymbol{p}}(t) = \sum_{\boldsymbol{k}} \int_{-\infty}^{t} \mathrm{d}\tau \iint \mathrm{d}\boldsymbol{v}\,\mathrm{d}\boldsymbol{r} \exp(\mathrm{i}\boldsymbol{k}\cdot\boldsymbol{\omega}(\tau - t) + \mathrm{i}\boldsymbol{k}\cdot\boldsymbol{w})\psi^{[\boldsymbol{p}]*}(\boldsymbol{r}) \left\{\sum_{\boldsymbol{n}} \mathrm{i}\boldsymbol{k}\cdot\frac{\mathrm{d}F}{\mathrm{d}\boldsymbol{I}}\left[a_{\boldsymbol{n}}(\tau) + b_{\boldsymbol{n}}(\tau)\right]\psi_{\boldsymbol{k}}^{[\boldsymbol{n}]}(\boldsymbol{I}) + s_{\boldsymbol{k}}^{e}(\boldsymbol{I}, \tau)\right\}. \tag{12}$$

We may now swap from position–velocity to action–angle variables. Since this transformation is canonical $\mathrm{d}\boldsymbol{v}\mathrm{d}\boldsymbol{r} = \mathrm{d}\boldsymbol{w}\mathrm{d}\boldsymbol{I}$. In equation (12) only $\psi^{[\boldsymbol{p}]}(\boldsymbol{r})$ depends on $\boldsymbol{w}$, so we may carry the $\boldsymbol{w}$ integration over $\psi^{[\boldsymbol{p}]*}$, which yields $\psi_{\boldsymbol{k}}^{[\boldsymbol{p}]*}(\boldsymbol{I})$. Equation (12) then becomes

$$a_{\boldsymbol{p}}(t) = (2\pi)^3 \sum_{\boldsymbol{k}} \int_{-\infty}^{t} \mathrm{d}\tau \int \mathrm{d}\boldsymbol{I} \exp[\mathrm{i}\boldsymbol{k}\cdot\boldsymbol{\omega}(\tau - t)] \left\{\sum_{\boldsymbol{n}} \mathrm{i}\boldsymbol{k}\cdot\frac{\mathrm{d}F}{\mathrm{d}\boldsymbol{I}}\left[a_{\boldsymbol{n}}(\tau) + b_{\boldsymbol{n}}(\tau)\right]\psi_{\boldsymbol{k}}^{[\boldsymbol{p}]*}(\boldsymbol{I})\psi_{\boldsymbol{k}}^{[\boldsymbol{n}]}(\boldsymbol{I}) + s_{\boldsymbol{k}}^{e}(\boldsymbol{I}, \tau)\,\psi_{\boldsymbol{k}}^{[\boldsymbol{p}]*}(\boldsymbol{I})\right\}. \tag{13}$$

[3] Mathematically, we only retain the particular solution to equation (6), while assuming that the homogeneous solution did not hit long-lived resonances.

At this point, it seems natural to expand the source term on a basis too, but unlike the previous one, this basis should also describe velocity space. We admit for now that such a basis $\phi_n(\boldsymbol{r}, \boldsymbol{v})$ exists, and write

$$s^e(\boldsymbol{r}, \boldsymbol{v}, t) = \sum_{\boldsymbol{n}} c_{\boldsymbol{n}}(t)\phi^{[\boldsymbol{n}]}(\boldsymbol{r}, \boldsymbol{v}), \quad \text{so} \tag{14}$$

$$s^e_{\boldsymbol{k}}(\boldsymbol{I}, \tau) = \sum_{\boldsymbol{n}} c_{\boldsymbol{n}}(\tau)\sigma^{[\boldsymbol{n}]e}_{\boldsymbol{k}}(\boldsymbol{I}), \tag{15}$$

where $\sigma^{[\boldsymbol{n}]e}_{\boldsymbol{k}}(\boldsymbol{I})$ is the angle transform of $\phi^{[\boldsymbol{n}]}(\boldsymbol{r}, \boldsymbol{v})$ (see equation 24 below). The coefficients $c_{\boldsymbol{n}}$ are representative of the mass exchange between the halo and the external world. The sum in equation (15) spans velocity space as well as configuration space, and therefore involve significantly more terms. Such an expansion is performed in Aubert & Pichon (in preparation) to constrain the source function measured in cosmological simulations. Calling $\boldsymbol{a}(\tau) = [a_1(\tau), \ldots, a_{\boldsymbol{n}}(\tau), \ldots]$, $\boldsymbol{b}(\tau) = [b_1(\tau), \ldots, b_{\boldsymbol{n}}(\tau), \ldots]$, and $\boldsymbol{c}(\tau) = [c_1(\tau), \ldots, c_{\boldsymbol{n}}(\tau), \ldots]$, we define two matrices, $\boldsymbol{K}$ and $\boldsymbol{Q}$. The matrix $\boldsymbol{K}$ has elements $K_{\boldsymbol{p},\boldsymbol{n}}$ defined by

$$K_{\boldsymbol{p},\boldsymbol{n}}(\tau) = (2\pi)^3 \sum_{\boldsymbol{k}} \int \mathrm{d}\boldsymbol{I} \exp(\mathrm{i}\boldsymbol{k}\cdot\boldsymbol{\omega}\tau)\mathrm{i}\boldsymbol{k}\cdot\frac{\mathrm{d}F}{\mathrm{d}\boldsymbol{I}}\psi^{[\boldsymbol{p}]*}_{\boldsymbol{k}}(\boldsymbol{I})\psi^{[\boldsymbol{n}]}_{\boldsymbol{k}}(\boldsymbol{I}), \tag{16}$$

which depend only on the halo equilibrium state. The matrix $\boldsymbol{Q}$ has elements

$$Q_{\boldsymbol{p},\boldsymbol{n}}(\tau) = (2\pi)^3 \sum_{\boldsymbol{k}} \int \mathrm{d}\boldsymbol{I} \exp(\mathrm{i}\boldsymbol{k}\cdot\boldsymbol{\omega}\tau)\sigma^{[\boldsymbol{n}]e}_{\boldsymbol{k}}(\boldsymbol{I})\, \psi^{[\boldsymbol{p}]*}_{\boldsymbol{k}}(\boldsymbol{I}), \tag{17}$$

which depend only on the expansion basis of the source. Equation (13) then becomes

$$\boldsymbol{a}(t) = \int_{-\infty}^{t} \mathrm{d}\tau \left\{\boldsymbol{K}(\tau - t)\cdot[\boldsymbol{a}(\tau) + \boldsymbol{b}(\tau)] + \boldsymbol{Q}(\tau - t)\cdot\boldsymbol{c}(\tau)\right\}. \tag{18}$$

The kernels $\boldsymbol{K}$ and $\boldsymbol{Q}$ are functions of the equilibrium state distribution function, F, and of the two bases, $\phi^{[\boldsymbol{n}]}(\boldsymbol{r}, \boldsymbol{v})$, and $\psi^{[\boldsymbol{n}]}(\boldsymbol{r})$ only. They may be computed once and for all for a given equilibrium model. Assuming linearity and knowing $\boldsymbol{K}$ and $\boldsymbol{Q}$, one can see that the properties of the environments (represented by $\boldsymbol{b}$ and $\boldsymbol{c}$) are *propagated* to the inner dynamical properties of collisionless systems (described by $\boldsymbol{a}$). We may perform a 'half' Fourier transform with respect to time. In the limit where the transients may be neglected, which implies that the system should be stable, this transform amounts to a Laplace transform with $p = \mathrm{i}\omega + \epsilon^+$. Temporal convolutions are then replaced by matrix multiplications and equation (18) becomes

$$\hat{\boldsymbol{a}}(\omega) = [\mathbf{1} - \hat{\boldsymbol{K}}(\omega)]^{-1}\cdot[\hat{\boldsymbol{K}}(\omega)\cdot\hat{\boldsymbol{b}}(\omega) + \hat{\boldsymbol{Q}}(\omega)\cdot\hat{\boldsymbol{c}}(\omega)]. \tag{19}$$

In this expression, $\mathbf{1}$ is the identity matrix, and $\hat{\boldsymbol{K}}$ and $\hat{\boldsymbol{Q}}$ include Heaviside functions before Fourier transform to account for causality (see Aubert et al. 2004, for details). Section D3 gives an explicit expression for $\hat{\boldsymbol{K}}(\omega)$. Note the difference between $\boldsymbol{\omega}$, the angular frequency of the orbits, defined above equation (6), and ω, the half-Fourier transform variable associated with time which appears in equation (19). Here $\boldsymbol{b}$ and $\boldsymbol{c}$ could be given deterministic functions of time or stochastic random fields (characterized statistically in Aubert & Pichon in preparation). In contrast, $\boldsymbol{a}$ describes the detailed response of the halo in phase space within R_{200}.

2.2.1 *Higher moments*

The second moment is obtained by multiplying (7) by $\boldsymbol{v}$ and by performing an integration over velocities. Summing over $\boldsymbol{k}$ leads to

$$\rho\bar{\boldsymbol{v}}(\boldsymbol{r}, t) = \sum_{\boldsymbol{k}} \int_{-\infty}^{t} \mathrm{d}\tau \int \mathrm{d}\boldsymbol{v} \exp(\mathrm{i}\boldsymbol{k}\cdot\boldsymbol{\omega}(\tau - t) + \mathrm{i}\boldsymbol{k}\cdot\boldsymbol{w}) \left\{ \mathrm{i}\boldsymbol{k}\cdot\frac{\mathrm{d}F}{\mathrm{d}\boldsymbol{I}}\boldsymbol{v}\left[\psi_{\boldsymbol{k}}(\boldsymbol{I}, \tau) + \psi^e_{\boldsymbol{k}}(\boldsymbol{I}, \tau)\right] + \boldsymbol{v}s^e_{\boldsymbol{k}}(\boldsymbol{I}, \tau) \right\}. \tag{20}$$

Using the same bi-orthonormal expansion as above, we may express the mass flux as a function of the coefficients $a_{\boldsymbol{n}}$ and $b_{\boldsymbol{n}}$ (associated with the potential perturbations of external origin). If we define the following new tensors

$$K_{[2],\boldsymbol{n}}(\boldsymbol{r}, \tau) = \sum_{\boldsymbol{k}} \int \mathrm{d}\boldsymbol{v} \exp(\mathrm{i}\boldsymbol{k}\cdot\boldsymbol{\omega}\tau + \mathrm{i}\boldsymbol{k}\cdot\boldsymbol{w})\,\boldsymbol{v}\ \mathrm{i}\boldsymbol{k}\cdot\frac{\mathrm{d}F}{\mathrm{d}\boldsymbol{I}}\psi^{[\boldsymbol{n}]}_{\boldsymbol{k}}(\boldsymbol{I}), \tag{21}$$

and a similar expression for $Q_{[2],\boldsymbol{n}}(\boldsymbol{r}, \tau)$, involving the expansion basis of the source, the mass flux may be written as a convolution

$$\rho\bar{\boldsymbol{v}}(\boldsymbol{r}, t) = \int_{-\infty}^{t} \mathrm{d}\tau \left\{\boldsymbol{K}_2(\boldsymbol{r}, \tau - t)\cdot[\boldsymbol{a}(\tau) + \boldsymbol{b}(\tau)] + \boldsymbol{Q}_2(\boldsymbol{r}, \tau - t)\cdot\boldsymbol{c}(\tau)\right\}.$$

After half-Fourier transforming with respect to time, we get

$$\rho\hat{\bar{\boldsymbol{v}}} = \hat{\boldsymbol{K}}_{[2]}(\boldsymbol{r}, \omega)\cdot(\mathbf{1} - \hat{\boldsymbol{K}})^{-1}\cdot[\hat{\boldsymbol{b}} + \hat{\boldsymbol{Q}}\cdot\hat{\boldsymbol{c}}] + \hat{\boldsymbol{Q}}_{[2]}(\boldsymbol{r}, \omega)\cdot\hat{\boldsymbol{c}}. \tag{22}$$

We will return to equation (22) in Section 5.

2.3 Sinks, sources and tidal field

Let us now turn to an explicit description of the source term (s^e, hence $\boldsymbol{c}$), and the tidal field (ψ^e, hence $\boldsymbol{b}$) entering equation (6). We consider here a source at the virial radius corresponding to cosmic infall. Note however that we might have considered just as well sinks reflecting the presence of a super massive black hole at the centre of the host galaxy or the deflection/absorption of orbits due to a galactic disc.

2.3.1 Source of infall at R_{200}

A possible Ansatz for the source term consistent with the first two velocity moments of the entering matter has been proposed by Aubert et al. (2004). Following them $s^e(\boldsymbol{r}, \boldsymbol{v}, t)$ can be written as

$$s^e(\boldsymbol{r}, \boldsymbol{v}, t) \triangleq \sum_{\boldsymbol{m}} Y_{\boldsymbol{m}}(\boldsymbol{\Omega})\delta_D(r - R_{200})\left[\sum_{\alpha} c_{\boldsymbol{n}}(t) g_\alpha(\boldsymbol{v}) Y_{\boldsymbol{m}}(\boldsymbol{\Omega})\right],$$

where $\boldsymbol{m}$ stands for the two harmonic numbers, $(\ell, m)$and $Y_{\boldsymbol{m}}(\Omega) \triangleq Y_\ell^m(\Omega)$ is the usual spherical harmonic. The Dirac function $\delta_D(r - R_{200})$ appears because the source terms are located at the virial radius in our representation.[4] This equation corresponds to the parametrization of $\phi^{[\boldsymbol{n}]}$ as

$$\phi^{[\boldsymbol{n}]}(\boldsymbol{r}, \boldsymbol{v}) = g_\alpha(\boldsymbol{v}) Y_{\boldsymbol{m}}(\boldsymbol{\Omega})\delta_D(r - R_{200}) \triangleq g_\alpha(v) Y_{\boldsymbol{m}}(\boldsymbol{\Omega}) Y_{\boldsymbol{m}'}(\boldsymbol{\Gamma})\delta_D(r - R_{200}), \tag{23}$$

of Gaussian functions, g_α, covering the radial velocity component and spherical harmonics for the angle distribution, $\boldsymbol{\Gamma}$, of the velocity vector and orientation, $\boldsymbol{\Omega} = (\theta, \phi)$ of the infall (see Aubert & Pichon in preparation, for details). Here we have $\boldsymbol{n} \triangleq [\boldsymbol{m}, \alpha] \triangleq [\boldsymbol{m}, \boldsymbol{m}', \alpha] \triangleq [\ell, m, \ell', m', \alpha]$. From equation (15)

$$\sigma_{\boldsymbol{k}}^{[\boldsymbol{n}]e}(\boldsymbol{I}) \triangleq \frac{1}{(2\pi)^3}\int \mathrm{d}^3\boldsymbol{w} \exp(-\mathrm{i}\boldsymbol{k}\cdot\boldsymbol{w})\phi^{[\boldsymbol{n}]}(\boldsymbol{r}, \boldsymbol{v}). \tag{24}$$

With equations (23) and (24) it becomes

$$\sigma_{\boldsymbol{k}}^{[\boldsymbol{n}]e}(\boldsymbol{I}) = \frac{1}{(2\pi)^3}\int \mathrm{d}^3\boldsymbol{w} \exp(-\mathrm{i}\boldsymbol{k}\cdot\boldsymbol{w}) Y_{\boldsymbol{m}}[\boldsymbol{\Omega}(\boldsymbol{I}, \boldsymbol{w})]\, g_\alpha(\boldsymbol{v}[\boldsymbol{I}, \boldsymbol{w}])\delta_D(r(\boldsymbol{I}, \boldsymbol{w}) - R_{200}). \tag{25}$$

We can make use of the δ_D function occurring in equation (25) since $w_\mathrm{r} \triangleq \tilde{w}_\mathrm{r}(r, \boldsymbol{I})$ (given by equation B1). Therefore equation (25) reads

$$\begin{aligned}\sigma_{\boldsymbol{k}}^{[\boldsymbol{n}]e}(\boldsymbol{I}) &= \int \frac{\mathrm{d}^2\boldsymbol{w}}{(2\pi)^3}\int \mathrm{d}w_\mathrm{r} \exp(-\mathrm{i}\boldsymbol{k}\cdot\boldsymbol{w}) Y_{\boldsymbol{m}}[\boldsymbol{\Omega}(\boldsymbol{I}, \boldsymbol{w})]\, g_\alpha(\boldsymbol{v}[\boldsymbol{I}, \boldsymbol{w}])\frac{1}{|\partial\tilde{w}_\mathrm{r}/\partial r|^{-1}}\delta_D(w_\mathrm{r} - \tilde{w}_\mathrm{r}[R_{200}, \boldsymbol{I}]),\\ &= \int \frac{\mathrm{d}^2\boldsymbol{w}}{(2\pi)^3} \exp(-\mathrm{i}\boldsymbol{k}\cdot\boldsymbol{w}) Y_{\boldsymbol{m}}[\boldsymbol{\Omega}(\boldsymbol{I}, \boldsymbol{w}, \tilde{w}_\mathrm{r}[R_{200}, \boldsymbol{I}])]\, g_\alpha(\boldsymbol{v}[\boldsymbol{I}, \boldsymbol{w}, \tilde{w}_\mathrm{r}(R_{200}, \boldsymbol{I})])\frac{\omega_\mathrm{r}(\boldsymbol{I})}{|\dot{r}(R_{200}, \boldsymbol{I})|}\exp(-\mathrm{i}k_\mathrm{r}\cdot\tilde{w}_\mathrm{r}[R_{200}, \boldsymbol{I}]).\end{aligned} \tag{26}$$

In equation (26) we sum over all intersections of the orbit $\boldsymbol{I}$ with the R_{200} sphere, at the radial phase corresponding to that intersection with a weight corresponding to $\omega_\mathrm{r}/|\dot{r}|$ (see Fig. 2). Note that equation (26) involves $\mathrm{d}^2\boldsymbol{w} \triangleq \mathrm{d}w_2\mathrm{d}w_3$.

2.3.2 Tidal excitation from beyond R_{200}

The tidal potential is given as a boundary condition on the virial sphere and deprojected in volume. Let us call $b'_{\ell m}(t)$ the harmonic coefficients of the expansion of the external potential on the virial sphere. We expand the potential over the bi-orthogonal basis, $(u_n^{\ell m}, d_n^{\ell, m})$ (see Appendix B), so that

$$\psi^e(r, \boldsymbol{\Omega}, t) = \sum_{n,\ell,m} b'_{\ell m}(t) Y_\ell^m(\boldsymbol{\Omega})\left(\frac{r}{R_{200}}\right)^\ell = \sum_{\boldsymbol{n}} b_{\boldsymbol{n}}(t)\psi^{[\boldsymbol{n}]}(\boldsymbol{r}), \tag{27}$$

where $\psi^{[\boldsymbol{n}]}(\boldsymbol{r}) \triangleq Y_\ell^m(\Omega)u_j^{\ell m}(r)$. The first equality in equation (27) corresponds to the inner solution of the 3D potential whose boundary condition is given by $Y_m^\ell(\Omega)b'_{\ell m}$ on the sphere of radius R_{200} (defined below). Since the basis is bi-orthogonal, it follows that

$$b_{\boldsymbol{n}}(t) = \left[\int d_n^{\ell m}(r)\left(\frac{r}{R_{200}}\right)^\ell \mathrm{d}r\right] b'_{\ell m}(t). \tag{28}$$

It is therefore straightforward to recover the coefficient of the 3D external potential from that of the potential on the sphere.

[4] This choice is mainly justified by the measurements performed in Aubert et al. (2004) and Aubert & Pichon (in preparation) and stands as a good compromise between a relaxed halo inside this boundary and a low contribution of the orbits of relaxed particles to the flux.

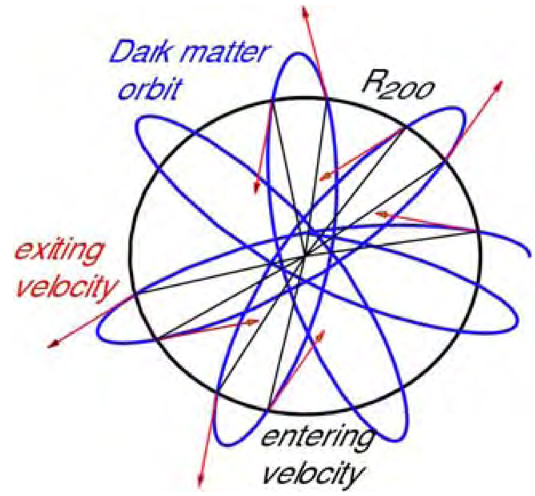

Figure 2. A typical rosette orbit in its orbital plane; the intersection with the R_{200} sphere is shown, together with the corresponding velocity vectors, both entering and exiting. The net flux of such quantities enters equation (25) and characterize the source of infall perturbing the halo. Note that by construction, in the linear regime all infalling material re-exits R_{200}, since the perturbation evolves along the unperturbed orbits. This is to be contrasted to the situation presented in Fig. 3 where dynamical friction is qualitatively accounted for.

2.4 Induced correlations in the halo

Our purpose is to characterize *statistically* the response of the dark matter halo to tidal perturbation and infall. This is best done by computing the N-point statistics of the perturbed density field. Let us start with the two-point correlation. From equation (19) the variance–covariance matrix of the response is given by

$$\langle \hat{\boldsymbol{a}} \cdot \hat{\boldsymbol{a}}^{*\top} \rangle = \langle [\hat{\boldsymbol{K}} \cdot \hat{\boldsymbol{b}} + \hat{\boldsymbol{Q}} \cdot \hat{\boldsymbol{c}}] \cdot (\mathbf{1} - \hat{\boldsymbol{K}})^{-1} \cdot (\mathbf{1} - \hat{\boldsymbol{K}})^{-1*\top} \cdot [\hat{\boldsymbol{K}} \cdot \hat{\boldsymbol{b}} + \hat{\boldsymbol{Q}} \cdot \hat{\boldsymbol{c}}]^{\top *} \rangle. \tag{29}$$

This expression of the $\boldsymbol{n} \times \boldsymbol{n}$ matrix, $\langle \hat{\boldsymbol{a}} \cdot \hat{\boldsymbol{a}}^{*\top} \rangle$ involves autocorrelation terms like the components of $\langle \hat{\boldsymbol{b}} \cdot \hat{\boldsymbol{b}}^{*\top} \rangle$ (the tidal field) and $\langle \hat{\boldsymbol{c}} \cdot \hat{\boldsymbol{c}}^{*\top} \rangle$ (the source of infall), but also cross-correlation terms such as the components of $\langle \hat{\boldsymbol{b}} \cdot \hat{\boldsymbol{c}}^{*\top} \rangle$. For a spherical harmonic basis, the induced density perturbation reads (see equation B2 in Appendix B)

$$\rho(r, \boldsymbol{\Omega}, t) = \sum_{\boldsymbol{n}} a_{\boldsymbol{n}} \rho_{\boldsymbol{n}}(\boldsymbol{r}) = \sum_{n\ell m} a^n_{\ell m}(t) Y^m_\ell(\boldsymbol{\Omega}) d^n_{\ell m}(r), \tag{30}$$

The functions $d^n_{\ell m}(r)$ depend on the chosen basis. An example is given by equation (B3). Again, $\boldsymbol{n}$ stands here for n, ℓ, m, respectively, the radial and the two angular 'quantum numbers'. As a consequence the two-point correlation function for the perturbed density reads

$$\langle \rho(r, \boldsymbol{\Omega} + \Delta\boldsymbol{\Omega}, t + \Delta t) \rho(r', \boldsymbol{\Omega}, t) \rangle = \sum_{n\ell m n'\ell' m'} Y^m_\ell(\boldsymbol{\Omega}) Y^{m'*}_{\ell'}(\boldsymbol{\Omega} + \Delta\boldsymbol{\Omega}) d^n_{\ell m}(r) d^{n'}_{\ell' m'}(r') \left\langle a^n_{\ell m}(t) a^{n'*}_{\ell' m'}(t + \Delta t) \right\rangle. \tag{31}$$

The statistical averages, $\langle a^n_{\ell m}(t)\ a^{n'*}_{\ell' m'}\ (t + \Delta t) \rangle$ are given by the temporal inverse Fourier transform of equation (29). If the perturbation is stationary and statistically rotationally invariant, $\langle a^n_{\ell m}(t)\ a^{n'}_{\ell' m'}(t + \Delta t) \rangle \stackrel{\triangle}{=} C^{nn'}_\ell(\Delta t) \delta^{m'}_m \delta^{\ell'}_\ell$. The correlation function then obeys

$$\langle \rho(r, \boldsymbol{\Omega} + \Delta\boldsymbol{\Omega}, t + \Delta t) \rho(r', \boldsymbol{\Omega}, t) \rangle = \sum_{nn'\ell m} P_\ell(\cos(\gamma)) d^n_{\ell m}(r) d^{n'}_{\ell m}(r') C^{nn'}_\ell(\Delta t), \tag{32}$$

where γ stands for the angle between $\boldsymbol{\Omega}$ and $\boldsymbol{\Omega}'$. Evaluating equation (32) for $\gamma = 0$, $\Delta t = 0$, $r = r'$ gives a measure of the cosmic variance of the amplitude of the response of the halo as a function of radius r. The full width half-maximum (FWHM) of $\langle \rho(r, \boldsymbol{\Omega} + \Delta\boldsymbol{\Omega}, t) \rho(r, \boldsymbol{\Omega}, t) \rangle$ is a measure as a function of time t and radius r, of the angular extent of the ensemble average mean polarization. Conversely, the FWHM of $\langle \rho(r, \boldsymbol{\Omega}, t) \rho(r + \Delta r, \boldsymbol{\Omega}, t) \rangle$ is a measure of its radial extent in the direction $\boldsymbol{\Omega}$. Note that equation (7) together with (18) yield a description of the response both in position and velocity. For instance, equation (22) allow us to predict the induced correlations amongst streams. Applications of equations (29)–(32) (and their non-linear generalization in Section 3.2) will be discussed in greater details in Section 5. The actual implementation of equations (29)–(32) is carried in a simplified framework in Section B4.

2.4.1 *Link with propagators*

Let us emphasize that the splitting of the gravitational field into two components, one originating outside of R_{200}, and one from the inside, via point particles obeying the distribution $s^e(\boldsymbol{r}, \boldsymbol{v}, t)$ is somewhat ad hoc from the point of view of the linear dynamics. It is convenient from the point of view of the measurements, and crucial for the non-linear evolution (described below), or the ensemble average, as shown above.[5] It allows us to specify the statistical characteristics of the infall without having to refer to the properties of the object on which this infall occurs.

We discuss in Appendix A the formulation of the response of a self-gravitating sphere in terms of a propagator (i.e. the Green function of the collisionless Boltzmann–Poisson equation). This formulation is mathematically equivalent to the approach described above, but there we relied on Gauss's theorem to reproject all the information beyond R_{200} back on to the virial sphere. This information involves two contributions: one relative to particles beyond R_{200}, which contribute to the tidal field, the other relative to particles entering R_{200} which contribute to $s^e(\Omega, \boldsymbol{v})$.

The main asset of this formulation is to localize the boundary, which is possible since the interaction is purely gravitational, at the expense of having *two* sources of different nature. In particular, this implies that the environment may be characterized once and for all, independently of the detailed nature of the inner halo.

In this section, we assumed that the polarization of the halo was *linear*. This hopefully provided some insight for some aspects of the dynamics, but effectively ignores non-linear phenomena such as dynamical friction or tidal stripping. Let us now expand perturbation theory to higher orders.

3 NON-LINEAR PERTURBATIVE RESPONSE

In the following, we describe, using perturbation theory, the non-linear response of the halo to material entering at the virial sphere. It is assumed that the perturbation is first order in the hierarchy, and that the halo is dynamically stable. This should warrant the validity of the expansion. We use the angle–action variables of the *unperturbed* system as canonical variables and investigate the non-linear evolution of the infall and the tidal excitation.

In essence, the key is to expand the potential on to the bi-orthogonal potential density basis which allows us to decouple position–velocity and time (i.e. perform a separation of variable), and solve in turns each order of the perturbation expansion.

3.1 Perturbative expansion

Recall that the dynamical equation of an open system characterized by its distribution function, F is given by equation (1). Let us expand again F as

$$\mathrm{F} = F + \sum_n \varepsilon^n f^{(n)} \quad \text{and} \quad \mathrm{H} = H_0 + \sum_n \varepsilon^n \psi^{(n)}, \tag{33}$$

where the unperturbed equilibrium is characterized by the distribution function, $F\,(\boldsymbol{I})$. Note that (n), the order of the expansion should not be confused with $\boldsymbol{n} \triangleq (n, \ell, m)$. Finally, it is assumed that the external perturbation enters as a first order only, i.e. $s^e \propto \varepsilon$ and $\psi^e \propto \varepsilon$. In short, the rewriting of equation (1) to order ε^n yields

$$\frac{\partial f_{\boldsymbol{k}}^{(n)}}{\partial t} + \mathrm{i}\boldsymbol{k}\cdot\boldsymbol{\omega} f_{\boldsymbol{k}}^{(n)} = \left(\frac{\mathrm{d}F}{\mathrm{d}\boldsymbol{I}} \cdot \mathrm{i}\boldsymbol{k}\left[\psi_{\boldsymbol{k}}^{(n)} + \delta_n^1 \psi_{\boldsymbol{k}}^e\right] - \sum_{k=1}^{n-1} \left\{\psi^{(k)}, f^{(n-k)}\right\}_{\boldsymbol{k}} + \delta_n^1 s_{\boldsymbol{k}}^e \right). \tag{34}$$

In the following, we solve equation (34) recursively, order by order, to recover the perturbative response of the halo to the tidal interaction and infall. We expand both the potentials and the source term over a bi-orthogonal basis, so that, with $^{(n)}$ referring to the order in the hierarchy and $^{[\boldsymbol{p}]}$ to the label in the basis

$$\psi_{\boldsymbol{k}}^{(n)}(\boldsymbol{I}, t) = \sum_{\boldsymbol{p}} a_{\boldsymbol{p}}^{(n)}(t)\psi_{\boldsymbol{k}}^{[\boldsymbol{p}]}(\boldsymbol{I}), \quad \psi_{\boldsymbol{k}}^e(\boldsymbol{I}, t) = \sum_{\boldsymbol{p}} b_{\boldsymbol{p}}(t)\psi_{\boldsymbol{k}}^{[\boldsymbol{p}]}(\boldsymbol{I}), \quad s_{\boldsymbol{k}}^e(\boldsymbol{I}, t) = \sum_{\boldsymbol{p}} c_{\boldsymbol{p}}(t)\sigma_{\boldsymbol{k}}^{[\boldsymbol{p}]}(\boldsymbol{I}). \tag{35}$$

Recall also that the superscript, $[\boldsymbol{p}]$, in equation (35) spans discretely a 3D or 5D space depending on the type of function basis. The first-order solution for $a_{\boldsymbol{p}}$ was given in equation (13). Let us turn to the higher-order equations.

3.1.1 Second-order perturbation theory

The second-order equation for $a_{\boldsymbol{p}}^{(2)}$ reads

$$\begin{aligned} a_{\boldsymbol{p}}^{(2)}(t) = {} & (2\pi)^3 \sum_{\boldsymbol{n}} \int_{-\infty}^{t} \mathrm{d}\tau\, a_{\boldsymbol{n}}^{(2)}(\tau) \left(\sum_{\boldsymbol{k}} \int \mathrm{d}\boldsymbol{I}\, \psi_{\boldsymbol{k}}^{[\boldsymbol{n}]}(\boldsymbol{I})\psi_{\boldsymbol{k}}^{[\boldsymbol{p}]*}(\boldsymbol{I})\, \frac{\mathrm{d}F}{\mathrm{d}\boldsymbol{I}} \cdot \mathrm{i}\boldsymbol{k} \exp(\mathrm{i}\boldsymbol{k}\cdot\boldsymbol{\omega}[\tau - t]) \right) \\ & + (2\pi)^3 \int_{-\infty}^{t} \mathrm{d}\tau \sum_{\boldsymbol{k}} \int \mathrm{d}\boldsymbol{I} \exp(\mathrm{i}\boldsymbol{k}\cdot\boldsymbol{\omega}[\tau - t]) \left\{ f^{(1)}(\tau, \boldsymbol{w}, \boldsymbol{I}), \psi^{(1)}(\tau, \boldsymbol{w}, \boldsymbol{I}) \right\}_{\boldsymbol{k}} \psi_{\boldsymbol{k}}^{[\boldsymbol{p}]*}(\boldsymbol{I}), \end{aligned} \tag{36}$$

[5] One should account for the fact that ψ_{e} should be switched on long before any particles enter R_{200} since no particle is created at the boundary.

where $\{f^{(1)}, \psi^{(1)}\}$ is the Poisson bracket of the perturbation to first order. Now for a set (f, ψ) we have

$$\{f,\psi\}_{\boldsymbol{k}} = \int \mathrm{d}\boldsymbol{w} \exp(-\mathrm{i}\boldsymbol{k}\cdot\boldsymbol{w}) \left\{ \sum_{\boldsymbol{k}_1} f_{\boldsymbol{k}_1}(\boldsymbol{I}) \exp(\mathrm{i}\boldsymbol{k}_1\cdot\boldsymbol{w}), \sum_{\boldsymbol{k}_2} \psi_{\boldsymbol{k}_2}(\boldsymbol{I}) \exp(\mathrm{i}\boldsymbol{k}_2\cdot\boldsymbol{w}) \right\}. \tag{37}$$

Therefore

$$\{f,\psi\}_{\boldsymbol{k}} = \sum_{\boldsymbol{k}_1+\boldsymbol{k}_2=\boldsymbol{k}} \left(\psi_{\boldsymbol{k}_2} \frac{\mathrm{d}f_{\boldsymbol{k}_1}}{\mathrm{d}\boldsymbol{I}} \cdot \mathrm{i}\boldsymbol{k}_2 - f_{\boldsymbol{k}_1} \frac{\mathrm{d}\psi_{\boldsymbol{k}_2}}{\mathrm{d}\boldsymbol{I}} \cdot \mathrm{i}\boldsymbol{k}_1 \right) \stackrel{\triangle}{=} \sum_{\boldsymbol{k}_1+\boldsymbol{k}_2=\boldsymbol{k}} [\![f_{\boldsymbol{k}_1}, \psi_{\boldsymbol{k}_2}]\!], \tag{38}$$

where the sum is over $\boldsymbol{k}_1$ with $\boldsymbol{k}_2 = \boldsymbol{k} - \boldsymbol{k}_1$. Given equation (7) and (36) it may be rearranged as

$$\begin{aligned} a^{(2)}_{\boldsymbol{p}}(t) =& (2\pi)^3 \sum_{\boldsymbol{q}_1} \int_{-\infty}^{t} \mathrm{d}\tau_1\, a^{(2)}_{\boldsymbol{q}_1}(\tau_1) \left\{ \sum_{\boldsymbol{k}} \int \mathrm{d}\boldsymbol{I}\, \psi^{[\boldsymbol{q}_1]}_{\boldsymbol{k}}(\boldsymbol{I}) \psi^{[\boldsymbol{p}]*}_{\boldsymbol{k}}(\boldsymbol{I}) \frac{\mathrm{d}F}{\mathrm{d}\boldsymbol{I}} \cdot \mathrm{i}\boldsymbol{k} \exp(\mathrm{i}\boldsymbol{k}\cdot\boldsymbol{\omega}[\tau_1 - t]) \right\} \\ &+ (2\pi)^3 \int^{t} \mathrm{d}\tau_1 \int^{\tau_1} \mathrm{d}\tau_2 \left\{ \sum_{\boldsymbol{k}} \int \mathrm{d}\boldsymbol{I} \exp(\mathrm{i}\boldsymbol{k}\cdot\boldsymbol{\omega}[\tau_1 - t]) \sum_{\boldsymbol{q}_1,\boldsymbol{q}_2} \left[a^{(1)}_{\boldsymbol{q}_1}(\tau_1) + b_{\boldsymbol{q}_1}(\tau_1) \right] \right. \\ &\left. \times \sum_{\boldsymbol{k}_1+\boldsymbol{k}_2=\boldsymbol{k}} \left[\!\!\left[\exp(\mathrm{i}\boldsymbol{k}_1\cdot\boldsymbol{\omega}[\tau_2-\tau_1]) \left[\frac{\mathrm{d}F}{\mathrm{d}\boldsymbol{I}} \cdot \mathrm{i}\boldsymbol{k}_1 \left[a^{(1)}_{\boldsymbol{q}_2}(\tau_2) + b_{\boldsymbol{q}_2}(\tau_2) \right] \psi^{[\boldsymbol{q}_2]}_{\boldsymbol{k}_1}(\boldsymbol{I}) + c_{\boldsymbol{q}_2}[\tau_2] \sigma^{e,[\boldsymbol{q}_2]}_{\boldsymbol{k}_1}(\boldsymbol{I}) \right], \psi^{[\boldsymbol{q}_1]}_{\boldsymbol{k}_2} \right]\!\!\right] \psi^{[\boldsymbol{p}]*}_{\boldsymbol{k}} \right\}. \end{aligned} \tag{39}$$

Note that the right-hand side (r.h.s.) of equation (39) is linear in $\boldsymbol{a}^{(2)}$ while it is quadratic in $\boldsymbol{a}^{(1)}$, $\boldsymbol{b}^{(1)}$, $\boldsymbol{c}^{(1)}$, involving products such as $\boldsymbol{a}\,\boldsymbol{a}$, $\boldsymbol{a}\,\boldsymbol{c}$, $\boldsymbol{b}\,\boldsymbol{c}$ and so on. More generally, the perturbation theory at order (n) is linear in $a^{(n)}$. Note also that equation (39) involves a double-ordered time integral over τ_1 and τ_2 of the source coefficient, $c_{\boldsymbol{q}_1}(\tau_1)$ and $c_{\boldsymbol{q}_2}(\tau_2)$, which accounts for the fact that, non-linearly, the relative phase of the accretion events matter (equation D12 gives the analogue to equation 39 in the complex frequency plane). Equation (39) includes in particular a term like

$$\exp(\mathrm{i}(\boldsymbol{k}_1+\boldsymbol{k}_2)\cdot\boldsymbol{\omega}[\tau_1-t]) \exp(\mathrm{i}\boldsymbol{k}_1\cdot\boldsymbol{\omega}[\tau_2-\tau_1]) \psi^{[\boldsymbol{p}]*}_{\boldsymbol{k}_1+\boldsymbol{k}_2} \sum_{\boldsymbol{q}_1,\boldsymbol{q}_2} \left(\frac{\mathrm{d}\sigma^{e,[\boldsymbol{q}_2]}_{\boldsymbol{k}_1}}{\mathrm{d}\boldsymbol{I}} \psi^{[\boldsymbol{q}_1]}_{\boldsymbol{k}_2} - \frac{\mathrm{d}\psi^{[\boldsymbol{q}_1]}_{\boldsymbol{k}_2}}{\mathrm{d}\boldsymbol{I}} \sigma^{e,[\boldsymbol{q}_2]}_{\boldsymbol{k}_1} \right) \left[a^{(1)}_{\boldsymbol{q}_1}(\tau_1) + b_{q_1}(\tau_1) \right] c_{\boldsymbol{q}_2}(\tau_2) \tag{40}$$

which involves the rate of change of the source term with respect to action variation (via $\partial\sigma^{e,[\boldsymbol{q}_2]}_{\boldsymbol{k}_1}/\partial I$) modulated twice over time as $\exp(\mathrm{i}(\boldsymbol{k}_1 + \boldsymbol{k}_2)\cdot\omega[\tau_1 - t]) \exp(\mathrm{i}\boldsymbol{k}_1\cdot\omega[\tau_2 - \tau_1])$.

The second-order solution can be synthetically written by introducing tensors $\boldsymbol{K}_2$ and $\boldsymbol{Q}_2$ similar to those defined in equations (16) and (17) to express the first-order solution as equation (18). These latter tensors will now be referred to as $\boldsymbol{K}_1$ and $\boldsymbol{Q}_1$. Specifically, the components of these tensors are defined as

$$(\boldsymbol{K}_1)_{\boldsymbol{p},\boldsymbol{q}_1}[\tau_1 - t] \stackrel{\triangle}{=} (\boldsymbol{K})_{\boldsymbol{p},\boldsymbol{q}_1}[\tau_1 - t] = (2\pi)^3 \sum_{\boldsymbol{k}} \int \mathrm{d}\boldsymbol{I} \exp(\mathrm{i}\boldsymbol{k}\cdot\boldsymbol{\omega}[\tau_1 - t]) \psi^{[\boldsymbol{p}]*}_{\boldsymbol{k}} \psi^{[\boldsymbol{q}_1]}_{\boldsymbol{k}} \frac{\mathrm{d}F}{\mathrm{d}\boldsymbol{I}} \cdot \mathrm{i}\boldsymbol{k}, \tag{41}$$

$$(\boldsymbol{K}_2)_{\boldsymbol{p},\boldsymbol{q}_1,\boldsymbol{q}_2}[\tau_1 - t, \tau_2 - \tau_1] = (2\pi)^3 \sum_{\boldsymbol{k}} \int \mathrm{d}\boldsymbol{I} \exp(\mathrm{i}\boldsymbol{k}\cdot\boldsymbol{\omega}[\tau_1 - t]) \sum_{\boldsymbol{k}_1+\boldsymbol{k}_2=\boldsymbol{k}} \left[\!\!\left[\exp(\mathrm{i}\boldsymbol{k}_1\cdot\boldsymbol{\omega}[\tau_2-\tau_1]) \frac{\mathrm{d}F}{\mathrm{d}\boldsymbol{I}} \cdot \mathrm{i}\boldsymbol{k}_1\, \psi^{[\boldsymbol{q}_2]}_{\boldsymbol{k}_1}, \psi^{[\boldsymbol{q}_1]}_{\boldsymbol{k}_2} \right]\!\!\right] \psi^{[\boldsymbol{p}]*}_{\boldsymbol{k}}, \tag{42}$$

while $\boldsymbol{Q}_i$ involves replacing $\psi^{[\boldsymbol{q}]}_{\boldsymbol{k}}\, \partial F/\partial\boldsymbol{I}\cdot\boldsymbol{k}$ by $\sigma^{e,[\boldsymbol{q}]}_{\boldsymbol{m}}$. For instance,

$$(\boldsymbol{Q}_2)_{\boldsymbol{p},\boldsymbol{q}_1,\boldsymbol{q}_2}[\tau_1 - t, \tau_2 - \tau_1] = (2\pi)^3 \sum_{\boldsymbol{k}} \int \mathrm{d}\boldsymbol{I} \exp(\mathrm{i}\boldsymbol{k}\cdot\boldsymbol{\omega}[\tau_1 - t]) \sum_{\boldsymbol{k}_1+\boldsymbol{k}_2=\boldsymbol{k}} \left[\!\!\left[\exp(\mathrm{i}\boldsymbol{k}_1\cdot\boldsymbol{\omega}[\tau_2-\tau_1]) \sigma^{e,[\boldsymbol{q}_2]}_{\boldsymbol{k}_1}, \psi^{[\boldsymbol{q}_1]}_{\boldsymbol{k}_2} \right]\!\!\right] \psi^{[\boldsymbol{p}]*}_{\boldsymbol{k}},$$

This implies in particular that $\boldsymbol{Q}_1 \stackrel{\triangle}{=} \boldsymbol{Q}$ given by equation (17). Note that each component of $\boldsymbol{K}_2$ has the same complexity as $\boldsymbol{K}_1$, i.e. the perturbation theory is linear order by order; on the other hand it involves *all* the couplings in configuration space, hence the double sum in $\boldsymbol{k}$. With these definitions, equations (13) and (39) read formally

$$\boldsymbol{a}^{(1)} = \boldsymbol{K}_1 \cdot \left[\boldsymbol{a}^{(1)}_1 + \boldsymbol{b} \right] + \boldsymbol{Q}_1 \cdot \boldsymbol{c}, \tag{43}$$

$$\boldsymbol{a}^{(2)} = \boldsymbol{K}_1 \cdot \boldsymbol{a}^{(2)} + \boldsymbol{K}_2 \cdot \left[\boldsymbol{a}^{(1)} + \boldsymbol{b} \right] \otimes \left[\boldsymbol{a}^{(1)} + \boldsymbol{b} \right] + \boldsymbol{Q}_2 \cdot \left[\boldsymbol{a}^{(1)} + \boldsymbol{b} \right] \otimes \boldsymbol{c}. \tag{44}$$

where the dot operator is not merely a tensor contraction, but also involves a time convolution. For example, $\boldsymbol{Z}$ being a given field,

$$(\boldsymbol{K}_1 \cdot \boldsymbol{Z})_{\boldsymbol{p}}(t) \stackrel{\triangle}{=} \sum_{\boldsymbol{q}} \int_{-\infty}^{t} \mathrm{d}\tau (K_1)_{\boldsymbol{p},\boldsymbol{q}}(\tau - t) Z_{\boldsymbol{q}}(\tau), \tag{45}$$

and similarly the higher-order contraction rule over the fields $\boldsymbol{Z}^1 \otimes \cdots \otimes \boldsymbol{Z}^n$ is defined as

$$\left(\boldsymbol{K}_n \cdot \boldsymbol{Z}^1 \otimes \cdots \otimes \boldsymbol{Z}^n \right)_{\boldsymbol{p}}(t) \stackrel{\triangle}{=} \sum_{\boldsymbol{q}_1,\ldots,\boldsymbol{q}_n} \int^{t} \mathrm{d}\tau_1 \cdots \int^{\tau_{n-1}} \mathrm{d}\tau_n (K_n)_{\boldsymbol{p},\boldsymbol{q}_1,\ldots,\boldsymbol{q}_n}(\tau_1 - t, \ldots, \tau_n - \tau_{n-1}) Z^1_{\boldsymbol{q}_1}(\tau_1) \cdots Z^n_{\boldsymbol{q}_n}(\tau_n). \tag{46}$$

Note that the order of the argument does matter (i.e. equation 46 defines a non-commutative algebra). Note also that the sum of the order in each term corresponds to the order of the perturbation. For instance, in equation (44), the second term involves the product of two first-order terms, while the first term is a single second-order term. Note finally that the contraction for the $\boldsymbol{Q}_n$ involve a summation over five indices, ℓ, m, α, ℓ', m' (whereas contraction over $\boldsymbol{K}_n$ involves only three indices: n, ℓ, m). We illustrate and discuss in Fig. 5 through synthetic diagrams the corresponding expansion. (See also Fig. D1 in Appendix D for an expansion to higher order.)

In Appendix D, we show in equations (D3)–(D4) how to rewrite equation (44) to the order of n.

As for all expansion schemes, the issue of the truncation arises. Depending on the physical process investigated, the truncation order may vary. For instance, it may be legitimate to truncate the perturbation to second order since the second order is the first order for which dynamical friction is taken into account.

3.2 Non-linear two-point correlation functions

Let us now re-address the computation of the two-point correlation function (cf. Section 2.4) of the response of the halo to tidal excitation and infall while accounting for the non-linearities described in Section 3.1.1. First, let us reshuffle the hierarchy in a format which is best suited for the statistical average of the non-linear response.

3.2.1 Reordering in $\boldsymbol{b}$ and $\boldsymbol{c}$

Let us define $\mathcal{F}(\omega, t) \triangleq \exp(\mathrm{i}\omega t)$ the Fourier operator, so that $\mathcal{F} \cdot \boldsymbol{Z}$ and $\mathcal{F}^\top \cdot \boldsymbol{Z}$ are, respectively, the half-Fourier and inverse half-Fourier transform of their argument $\boldsymbol{Z}$. Calling

$$\boldsymbol{R}_1 \triangleq \mathcal{F}^\top \cdot (\mathbf{1} - \hat{\boldsymbol{K}}_1)^{-1} \cdot \mathcal{F}, \tag{47}$$

equation (44) (and its generalization equation D3) reads like a recursion

$$\boldsymbol{a}^{(n)} \triangleq \boldsymbol{R}_1 \cdot \mathcal{K}\left[\boldsymbol{a}^{(n-1)}, \ldots, \boldsymbol{a}^{(1)}, \boldsymbol{b}, \boldsymbol{c}\right], \quad \text{for} \quad n \geqslant 2, \tag{48}$$

where $\mathcal{K}$ stands formally for some combination of $\boldsymbol{K}_n$ and $\boldsymbol{Q}_n$. Note that $\boldsymbol{K}_1$ accounts for the self-gravity of the halo. If the halo is very hot, this self-gravity may be neglected altogether and $\boldsymbol{R}_1 \to \mathbf{1}$. If not, we may define $\boldsymbol{K}'_i \triangleq \boldsymbol{R}_1 \cdot \boldsymbol{K}_i$, $\boldsymbol{Q}'_i \triangleq \boldsymbol{R}_1 \cdot \boldsymbol{Q}_i$, and rewrite the recursive relations equation (48) with $\boldsymbol{K}_1 \triangleq 0$. For instance,

$$\boldsymbol{a}^{(1)} = \boldsymbol{R}_1 \cdot (\boldsymbol{K}_1 \cdot \boldsymbol{b} + \boldsymbol{Q}_1 \cdot \boldsymbol{c}) = \boldsymbol{K}'_1 \cdot \boldsymbol{b} + \boldsymbol{Q}'_1 \cdot \boldsymbol{c}, \tag{49}$$

which we can rearrange as

$$\boldsymbol{a}^{(1)} \triangleq A_b \cdot \boldsymbol{b} + A_c \cdot \boldsymbol{c} \tag{50}$$

where $A_b \triangleq \boldsymbol{K}'_1$ and $A_c \triangleq \boldsymbol{Q}'_1$. Let us also introduce $\boldsymbol{K}''_1 = \boldsymbol{K}'_1 + \mathbf{1}$. Similarly, the contribution of b and c values to the second-order term for a can be expressed as

$$\boldsymbol{a}^{(2)} \triangleq A_{bb} \cdot \boldsymbol{b} \otimes \boldsymbol{b} + A_{cc} \cdot \boldsymbol{c} \otimes \boldsymbol{c} + A_{cb} \cdot \boldsymbol{c} \otimes \boldsymbol{b} + A_{bc} \cdot \boldsymbol{b} \otimes \boldsymbol{c}, \tag{51}$$

where

$$\begin{aligned} A_{bb} &= \boldsymbol{K}'_2 \circ \boldsymbol{K}''_1, \quad A_{cc} = \boldsymbol{K}'_2 \circ \boldsymbol{Q}'_1 + \boldsymbol{Q}'_2 \circ [\boldsymbol{Q}'_1, \boldsymbol{I}], \\ A_{cb} &= \boldsymbol{K}'_2 \circ [\boldsymbol{Q}'_1, \boldsymbol{K}''_1], \quad A_{bc} = K'_2 \circ [\boldsymbol{K}''_1, \boldsymbol{Q}'_1] + \boldsymbol{Q}'_2 \circ [\boldsymbol{K}''_1, \boldsymbol{I}]. \end{aligned} \tag{52}$$

Here the bracket, [,] accounts for the differential composition, so that,

$$A_{cb} \cdot \boldsymbol{b} \otimes \boldsymbol{b} = \boldsymbol{K}'_2 \cdot (\boldsymbol{Q}'_1 \cdot \boldsymbol{b}) \otimes (\boldsymbol{K}''_1 \cdot \boldsymbol{b}) = \boldsymbol{R}_1 \cdot \boldsymbol{K}_2 \cdot (\boldsymbol{R}_1 \cdot \boldsymbol{Q}_1 \cdot \boldsymbol{b}) \otimes ([\mathbf{1} + \boldsymbol{R}_1] \cdot \boldsymbol{K}_1 \cdot \boldsymbol{b}).$$

In Section D1.2, we also show how to write an equation similar to equation (51) for the third-order contribution and more generally for an arbitrary order (see equation D8).

3.2.2 Non-linear correlators

We may now complete the calculation of, say, the two-point correlation function of the density, C_2^ρ:

$$C_2^\rho \triangleq \langle \rho(x_1)\rho(x_2)\rangle = \sum_n \sum_{p=1}^{n} \varepsilon^n \left\langle \rho^{(p)}(x_1)\rho^{(n-p)}(x_2)\right\rangle, \tag{53}$$

where $x_i = (\boldsymbol{r}_i, \tau_i), i = 1, 2$. Following equation (35), let us also expand the response in density, ρ, over the basis function $\{\rho^{[\boldsymbol{q}]}(\boldsymbol{r})\}_{\boldsymbol{q}}$, so that

$$C_2^\rho = \sum_n \varepsilon^n \sum_{p=1}^{n} \sum_{\boldsymbol{q}_1, \boldsymbol{q}_2} \rho^{[\boldsymbol{q}_1]}(\boldsymbol{r}_1)\rho^{[\boldsymbol{q}_2]}(\boldsymbol{r}_2)\left\langle a^{(p)}_{\boldsymbol{q}_1}(\tau_1) a^{(n-p)}_{\boldsymbol{q}_2}(\tau_2)\right\rangle.$$

Now, given equations (49) and (51), we may rearrange this equation as

$$C_2^\rho = \varepsilon^2 \sum_{\boldsymbol{q}_1, \boldsymbol{q}_2} \rho^{[\boldsymbol{q}_1]}(\boldsymbol{r}_1)\rho^{[\boldsymbol{q}_2]}(\boldsymbol{r}_2) \left[C_2^{\{2\}} + \varepsilon C_2^{\{3\}} + \cdots\right], \tag{54}$$

where $C_2^{\{2\}}$ is a simple reshuffling of equation (29), i.e.

$$C_2^{\{2\}} = A_b \times A_b \cdot \langle \boldsymbol{b} \otimes \boldsymbol{b} \rangle + A_c \times A_c \cdot \langle \boldsymbol{c} \otimes \boldsymbol{c} \rangle + A_b \times A_c \cdot \langle \boldsymbol{b} \otimes \boldsymbol{c} \rangle + A_c \times A_b \cdot \langle \boldsymbol{c} \otimes \boldsymbol{b} \rangle, \tag{55}$$

and

$$\begin{aligned} C_2^{\{3\}} = {} & (A_{bb} \times A_b + A_b \times A_{bb}) \cdot \langle \boldsymbol{b} \otimes \boldsymbol{b} \otimes \boldsymbol{b} \rangle + (A_{cc} \times A_c + A_c \times A_{cc}) \cdot \langle \boldsymbol{c} \otimes \boldsymbol{c} \otimes \boldsymbol{c} \rangle + (A_{bc} \times A_c + A_b \times A_{bc}) \cdot \langle \boldsymbol{b} \otimes \boldsymbol{c} \otimes \boldsymbol{c} \rangle \\ & + (A_{bb} \times A_c + A_b \times A_{bc}) \cdot \langle \boldsymbol{b} \otimes \boldsymbol{b} \otimes \boldsymbol{c} \rangle + (A_{cb} \times A_b + A_c \times A_{bb}) \cdot \langle \boldsymbol{c} \otimes \boldsymbol{b} \otimes \boldsymbol{b} \rangle. \end{aligned} \tag{56}$$

The $\times$ operator is non-commutative and guaranties that the order is preserved in the dot contraction. Recall that $A_b \triangleq \boldsymbol{K}'_1$ and $A_c \triangleq \boldsymbol{Q}'_1$, while A_{bb}, A_{cc}, A_{cb} and A_{bc} are given by equation (53) (or in terms of the underlying distribution function, $F_0(\boldsymbol{I})$, and the basis function, $\psi^{[\boldsymbol{n}]}(\boldsymbol{r})$ via equations (41), (42) and (47) through the definitions of $\boldsymbol{K}_1, \boldsymbol{Q}_1, \boldsymbol{K}_2$ and $\boldsymbol{Q}_2$). It follows from equation (36) that the non-linear two-point correlation will involve at least the three-point correlation of the incoming flux and of the external potential. We will see in Section 5 that this is a generic consequence of mode coupling. Now the three-point correlation of the incoming flux, $\boldsymbol{c}$, and the tidal field, $\boldsymbol{b}$ may be re-expressed in terms of the mean and the two-point correlations of those fields while relying on Wick's theorem, since we showed in Aubert & Pichon (in preparation) that these fields were approximately Gaussian. Section D2 presents formally the generalization of equations (55)–(56) for the N-point correlation function to arbitrary order.

Equations such as equation (44) or its reordered version (equation 51) might look deceivingly simple. One should nevertheless keep in mind that the perturbation theory involves an exponentially growing number of terms. This is probably best realized by looking at diagrams such as Fig. D2 (presented in Appendix D) while keeping in mind that *each* straight line represents a triple sum over $\boldsymbol{k} = (k_1, k_2, k_3)$ and a time integral (see also Appendix B). The prospect of achieving resummation (in the spirit of what was achieved by e.g. Bernardeau (1992) for the gravitational instability of the large-scale structures) given the relative complexity of the double source expansion is slim. Yet it might be possible to construct scaling rules (see Fry 1984) since gravity is also here the driving force. Let us stress once again that the perturbative expansion accounts explicitly, within its convergence radius, for all aspects of the non-linear physics taking place within the R_{200} sphere.

3.3 Implication for dynamical friction and tidal stripping

One of the possible assets of this perturbative formulation is that the incoming flux may describe a virialized object which has a finite extent, and as such will undergo internal phase mixing reflecting the fact that different points in the object will describe different orbits, at different frequencies (see Fig. 3). In the perturbative regime, dynamical friction will also account for both the overall drag of the object, but also its tidal stripping (i.e. the fact that the less bound component of the object will undergo a differential more efficient friction). Specifically, the deflection of perturbed trajectories will correctly describe the balance (or lack thereof) between the self-gravity of the entering flow and its tendency to be torn by the differential gravitational field of the halo (which imposes the unperturbed different orbital trajectories). As such, the flow paradigm implemented in this paper and in Aubert et al. (2004) and Aubert & Pichon (in preparation) should allow for the appropriate level of flexibility in defining what a structure is and how time-dependent the concept is, within the self-gravitating halo (see also Section 3.3.1).

Let us briefly discuss how to identify substructures within the halo.

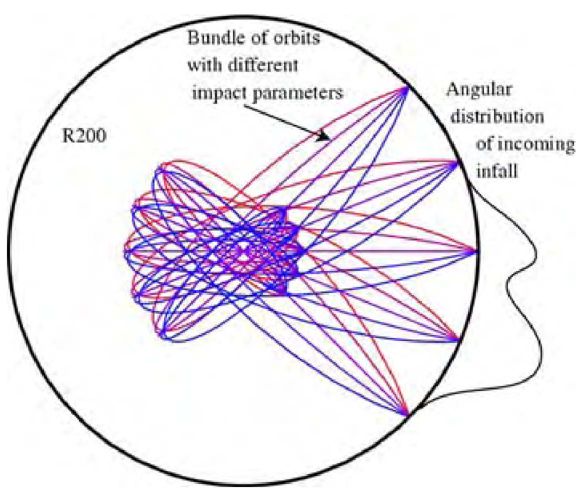

Figure 3. Displays qualitatively a bundle of orbits (in their orbital plane) which undergo dynamical friction and phase mixing within the R_{200} radius. As expected, dark matter describing orbits which initially are at the same position, but with 'slightly' different initial impact parameters will end up in quite different regions at later time. On the right-hand side the curve represents a possible angular distribution of a given entering object (for which the kinematic and angular spread has been greatly exaggerated). The caustics corresponding to the successive rebound of the orbits is clearly visible here (Fillmore & Goldreich 1984). Note that the amplitude of the friction force was ad hoc, and the self-gravity within the bundle was *not* taken into account.

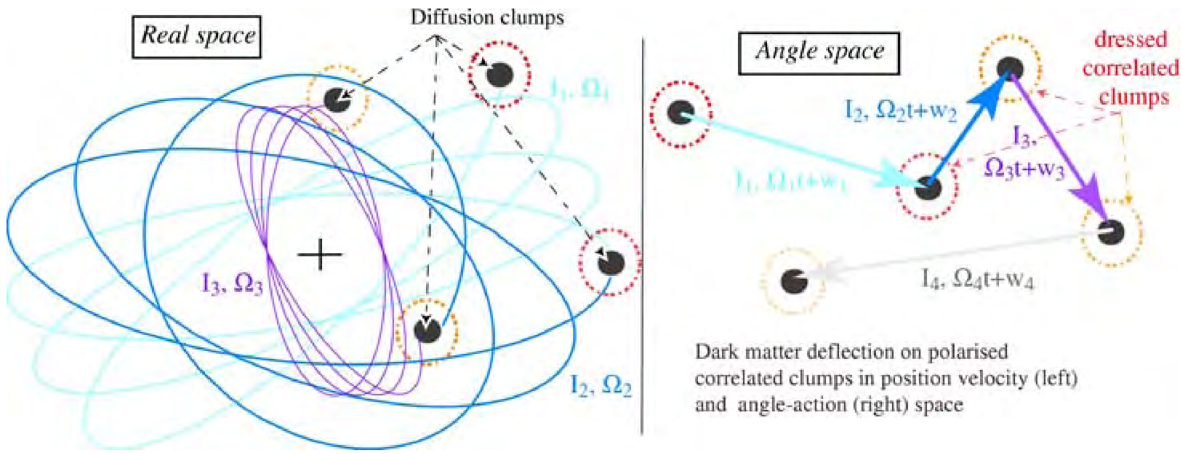

Figure 4. Left-hand panel: Schematic representation of the successive deflection of a given orbit on correlated clumps within the halo in position space. Each clump is represented with its polarization cloud. The grey-scale coding in the cloud reflects their spatial and temporal correlation within the clumps. During the deflections, the orbital parameters change (though the individual change is here grossly exaggerated). Right-hand panel: The same orbit as viewed in angle–action variables. The dynamics in these variable is straightforward (it corresponds to straight lines obeying $\boldsymbol{w} = \boldsymbol{\omega}\,(\boldsymbol{I})t + \boldsymbol{w}_0$) and the diffusion process resembles Brownian motion obeying a Langevin equation the particle receiving a random kick at each deflection, represented by a change in colour which reflects the fact that the 'collision' is instantaneous in contrast to the time interval separating two collisions.

3.3.1 Substructure counts and distribution

The identification of substructures within a given halo is a very promising but difficult topic (see e.g. Springel et al. 2001; Gill, Knebe & Gibson 2004; Aubert et al. 2004). Once the boundary flow has been propagated inwards, we have in principle access to the full distribution function of the perturbation as a function of time. When the field $f(\boldsymbol{v}, \boldsymbol{r}, t)$ is known inside R_{200}, we may attempt to identify collapsed objects and apply some form of count in cell statistics in order to characterize their spatial distribution as a function of time. This would allow us in particular to put aside objects which have been disrupted by tidal stripping or phase mixing (indeed 10 per cent of the mass of the halo is believed to remain in the form of virialized objects, while 90 per cent is disrupted by the tidal field). Recall that the disruption process is in principle well described by the perturbative expansion.

The criterion for the detection of objects must be carried while accounting for both the density contrast and the corresponding velocities (see also Arad, Dekel & Klypin 2004). Indeed, we do not wish to identify as objects local overdensities which may just correspond to caustics or local wave reinforcement. Here we are interested in the temporal coherence of objects.

For this purpose, we may coarse-grain the perturbed distribution function both in position and velocity, with some given smoothing function, $W(\boldsymbol{r}/\mathcal{R}_{\rm s}, \boldsymbol{v}/\mathcal{V}_{\rm s})$, and then apply some thresholding ($W \circ f > f_{\rm min}$ where $\circ$ stands for convolution) on the amplitude of the distribution function, defining a set of connex regions. For each of these regions, we may then compute the energy of the corresponding clump. If it is negative, the clump will be labelled as bound for the corresponding threshold ($f_{\rm min}$), and coarse-graining parameters ($\mathcal{R}_{\rm s}$, $\mathcal{V}_{\rm s}$). Note that since the response only involves the *perturbed* density, one need not subtract the mean potential (which is quite a difficult task in general).

Once the bound regions are identified, we may compute the corresponding mass and assign it to the bottom of the local potential well. This procedure may be applied for a range of threshold values, and standard statistical tools for discrete sources but in spherical geometry. We may in particular construct in this manner the mass function of satellites as a function of radius, or, say the two-point correlation function versus mass and cosmic time. Both issues are subjects of strong discussions when addressed through standard N-body simulations.

This time-dependent identification of virialized objects is useful because of biasing, i.e. the fact that most observational tracers will only be sensitive to the more massive tail of the mass function of virialized objects.

Conversely, we may want to label regions which match the thresholding but not the requirement on binding energy, i.e. identify caustics, cusps and shells (Fillmore & Goldreich 1984). We may then characterize statistically the mean distance between the apoapses (see Fig. 3), which will in general depend on $\mathcal{R}_{\rm s}$, $\mathcal{V}_{\rm s}$ and $f_{\rm min}$ but also on the underlying equilibrium, via $F(\boldsymbol{I})$ and on the statistical properties of $\boldsymbol{c}$ through, say the distribution of impact parameters. Note in closing that the competing effects of phase mixing, tidal stripping and dynamical friction all assume that the underlying basis function reaches sufficiently high spatial frequencies to resolve these phenomena. In practice, since the projection of the response (both linearly and non-linearly) is achieved over a basis which has a truncation frequency, $\ell_{\rm max}$, there is a finite time-scale, $T_{\rm max} \propto \ell_{\rm max}/\langle\omega\rangle$ above which phase mixing would induce winding at unresolved scales (here $\langle\omega\rangle$ represents the typical frequency of the dark matter in that region). Since the dynamical time is shorter in the inner region of the galaxy, such a threshold is going to be reached there first. Beyond this critical time, the dynamics is inaccurately modelled for the corresponding clump. This issue will be important for the non-linear coupling of clumps, since substructures entering the halo at later times will be dragged by streamers which are beyond the accuracy threshold.[6]

[6] These limitations are also clearly encountered in classical N-body simulations.

4 QUASI-LINEAR EVOLUTION OF HALO PROFILE

The previous sections dealt with the halo polarization while considering that perturbations were transient. In practice, a halo undergoes recursive excitations from its environment that will induce departures from its equilibrium state so that it will not remain static. In Appendix C, we derive a quasi-linear formalism for the collisionless open Boltzmann equation in order to take this effect into account. This follows in essence the work of Weinberg (1993, 2001a) or Ma & Bertschinger (2004), though the derivation differs. We introduce here an explicit expression, valid at low redshift, for the source of stochastic 'noise'. We account explicitly for the correlation induced by the entering material (as characterized by Aubert & Pichon in preparation) rather than rely on some ad hoc assumption on its nature. We also account consistently for the mean secular infall which adiabatically restructures the mean profile.

4.1 Context and derivation

Gilbert (1970) gives a very elegant derivation from first principles of the secular equation based on a $1/N$ (N being the number of particles in the system) expansion of the collisional relaxation equations presented by Bogolyubov & Gurov (1947). Weinberg (1993, 2001a) and Ma & Bertschinger (2004) rely on the same expansion scheme to derive their kinetic equation for the mean halo profile.

Weinberg (1993) focuses on the secular collective relaxation of a system induced by the finite number of particles within a multiperiodic uniform medium, hence transposing to collisionless stellar dynamics the derivation of Lenard–Balescu (Lenard 1961; Balescu 1963) applied originally to plasma physics in order to describe the secular convergence of such systems towards thermalization.

Weinberg (2001a) derives a similar result for the spherical halo in angle and action variables, while relying on the Kramers–Moyal (Risken 1989) expansion, which corresponds to a Markovian description based on the transition probability of a change in action induced by the interaction with a dressed particle cloud. His Fokker–Planck coefficients differ slightly from equations (C13)–(C14) given in Appendix C in that the spectral properties of $\langle \hat{b}_{\boldsymbol{n}} \hat{b}_{\boldsymbol{n}'} \rangle$ are postulated in his case, while $\boldsymbol{c} \stackrel{\triangle}{=} 0$.

Ma & Bertschinger (2004) construct a Fokker–Planck equation for the mean profile of a halo in a cosmic environment while relying on the constrained random field of peaks in the standard cosmological model to derive the drift and diffusion coefficients from first principles. Their derivation is dynamically accurate to second order in the perturbation theory (in position–velocity space) and relate the kinetic coefficients to the properties of the underlying linear power spectrum. In contrast to the theory presented here, their kinetic equation describes the very early phase of halo formation, whereas we focus here on the quasi-linear evolution (in angle–action space) of fully relaxed equilibria at low redshift.

In Appendix C, we account explicitly for the nature of the perturbation's power spectrum as defined in Aubert & Pichon (in preparation) and present an explicit derivation for the Fokker–Planck equation obeyed on secular time-scales by the distribution function in angle–action. It is natural to use these variables to describe a relaxed collisionless halo since they allow to split the dynamics into a secular (phase-averaged) and a fluctuating part. (See Fig. 4 for a schematic explanation.)

Even though individual dark matter particles obey a collisionless dynamics, the phase average ('ensemble average') distribution for the open system satisfies a collisional kinetic equation where the clumpiness of the *open* medium breaks the mean field approximation (see also Ma & Bertschinger 2004). Indeed, individually, clumps and tidal remnants deflect the actions of the underlying distribution in a stochastic (but correlated) manner, so that in the mean ensemble sense, the coarse-grained distribution (i.e. the distribution averaged over the angles) obeys a collisional diffusion of the Fokker–Planck type. In this formulation, the graininess of the system (as defined by the second-order closure of the Bogoliubov–Born–Green–Kirkwood–Yvon (BBGKY) hierarchy of the N-point distribution) corresponds to the mean number of clumps expected in the halo, while the detailed (kinetic and angular) power spectrum of the gravitational fluctuations is given by the cosmogony.

It is usual in plasma physics to take a two-time-scale approach to the Boltzmann equation. The short time-scale describes the dynamics of the system on the dynamical (orbital) time-scale, while the longer time-scale corresponds to the secular evolution. The action–angle variables are best suited here. This time-scale separation procedure leads to the following system of equations:

$$\frac{\partial f}{\partial t} + \boldsymbol{\omega} \cdot \frac{\partial f}{\partial \boldsymbol{w}} - \frac{\partial \psi}{\partial \boldsymbol{w}} \cdot \frac{\partial F}{\partial \boldsymbol{I}} = \frac{\partial \psi_{\mathrm{e}}}{\partial \boldsymbol{w}} \cdot \frac{\partial F}{\partial \boldsymbol{I}} + s_{\mathrm{e}}, \tag{57}$$

$$\frac{\partial F}{\partial T} = \left\langle \left[\frac{\partial \psi}{\partial \boldsymbol{w}} + \frac{\partial \psi_{\mathrm{e}}}{\partial \boldsymbol{w}} \right] \cdot \frac{\partial f}{\partial \boldsymbol{I}} \right\rangle_T - \left\langle \left[\frac{\partial \psi}{\partial \boldsymbol{I}} + \frac{\partial \psi^{e}}{\partial \boldsymbol{I}} \right] \cdot \frac{\partial f}{\partial \boldsymbol{w}} \right\rangle_T + S_{\mathrm{e}}. \tag{58}$$

In equations (57) and (58), s_{e} and S_{e} stand for the perturbative and secular advected source terms, while f stands for the fluctuating distribution and F stands for the secular distribution function (see Appendix C for details). The bracket around the quadratic terms stands for a time average over a secular time, T which is long compared to dynamical time, t (taken by a dark matter particle to describe its orbit). If we fix $F(\boldsymbol{I}, T)$, equation (57) corresponds exactly to equation (6) whose solution was described in Section 2.1. This formal solution may then be injected in the quadratic terms of equation (58). Following this route, we show in Appendix C how to rearrange equation (58) as a Fokker–Planck equation:

$$\frac{\partial F}{\partial T} = \langle D_0(\boldsymbol{I}) \rangle - \langle \boldsymbol{D}_1(\boldsymbol{I}) \rangle \cdot \frac{\partial F}{\partial \boldsymbol{I}} - \langle \boldsymbol{D}_2(\boldsymbol{I}) \rangle : \frac{\partial^2 F}{\partial \boldsymbol{I}^2}, \tag{59}$$

where D_0, $\boldsymbol{D}_1$ and $\boldsymbol{D}_2$ are given by equations (C13)–(C15), while : stands for the total contraction. Note that equation (59), in contrast to equation (58) refers this time to the driving equation for the mean halo profile since we invoked ergodicity to replace time averages by ensemble averages (see Appendix C for details). The D_0 term enters here because the halo is an open system, which may receive or lose mass. The drift term with the factor $\boldsymbol{D}_1$ accounts for the dynamical friction induced by the polarization cloud around the tidal remnants; the diffusion term with the factor $\boldsymbol{D}_2$ arises because of the fluctuations in the potential (both tidal and associated with the infalling dark matter) induced by the clumps. The diffusion term will in general induce a spreading of the energy distribution by accelerating some orbits to higher energies while decelerating some others. The polarization cloud will in general induce a drag on the clumps, represented by the $\boldsymbol{D}_1$ term. Note that the former should be independent of the mass of the clump (since the energy is exchanged via the mean field) while the latter will not (since more massive clump polarize the medium more). From the point of view of the entering dark matter, the net effect is therefore a segregation process in which the more massive clumps fall in (as discussed by Gilbert 1970).

According to Risken (1989), the corresponding Langevin (Langevin 1908) equation reads (when the source term, D_0 is *omitted*)

$$\frac{\partial \boldsymbol{I}}{\partial t} = \boldsymbol{\Delta}_1(\boldsymbol{I}) + \boldsymbol{\Delta}_2(\boldsymbol{I}) \cdot \boldsymbol{\xi}(t). \tag{60}$$

Here $\Delta_1(\boldsymbol{I})$ and $\Delta_2(\boldsymbol{I})$ are given in terms of $\boldsymbol{D}_1(\boldsymbol{I})$ and $\boldsymbol{D}_2(\boldsymbol{I})$ by

$$\boldsymbol{\Delta}_2 = \boldsymbol{D}_2^{1/2} \quad \text{and} \quad \boldsymbol{\Delta}_1 = \boldsymbol{D}_1 - \boldsymbol{D}_2^{1/2} : \nabla_{\boldsymbol{I}} \boldsymbol{D}_2^{1/2},$$

where $[\boldsymbol{D}_2]^{1/2}$ stands for the square root of the matrix $\boldsymbol{D}_2$ which is computed via diagonalization, provided the eigenvalues are positive. The 3D random field, $\boldsymbol{\xi}(t)$, should have spectral properties which reflect the stochastic properties of $\boldsymbol{b}$ and $\boldsymbol{c}$. The probability distribution of the solution to the stochastic equation (60) obeys the Fokker–Planck equation (59). In this form, the effect of diffusion on the departure from phase mixed equilibrium is easily interpreted.

4.2 Prospects for universal halo profiles

As has been suggested and illustrated by Weinberg (2001a) and Ma & Bertschinger (2004), it would be very worthwhile to use equation (59) and predict the asymptotic dark matter profile (and, say the cosmic evolution of the concentration parameter) which will be shaped in part by encounters and interlopers.

Note that the diffusion coefficients, D_i are relatively straightforward to compute for a given halo model, $F(\boldsymbol{I})$ *but* equation (59) corresponds to an evolution equation for $F(\boldsymbol{I})$ and will in practice require re-evaluating the coefficients for different values of F.

Let us now draw constraints on the stationary solutions of equation (59). Again (following Section 5), this may be done in one of two ways: take D_0, $\boldsymbol{D}_1$ and $\boldsymbol{D}_2$ as given function of the actions, and deduce what equation F should obey from requiring that equation (59) has a stationary solution (this is the route first explored by Weinberg 2001b); or, if we assume that a given model, say a universal profile, should correspond to the asymptotic solution of equation (59), we may find the relationship relating the corresponding asymptotic $\boldsymbol{D}_i$ coefficients.

For simplicity, let us illustrate this second point while neglecting here the fact that the diffusion coefficients depend on the distribution function, and restricting ourselves briefly to an isotropic distribution, $F(E, T)$. Calling

$$H(E) = \frac{\langle \boldsymbol{D}_1 \rangle \cdot \boldsymbol{\omega} + \langle \boldsymbol{D}_2 \rangle : \partial \boldsymbol{\omega}/\partial \boldsymbol{I}}{\langle \boldsymbol{D}_2 \rangle : \boldsymbol{\omega} \otimes \boldsymbol{\omega}}, \tag{61}$$

$$\text{and} \quad Q(E) = \frac{\langle D_0 \rangle}{\langle \boldsymbol{D}_2 \rangle : \boldsymbol{\omega} \otimes \boldsymbol{\omega}}, \tag{62}$$

the stationary solution ($\partial F/\partial T = 0$) to equation (59) reads formally:

$$F(E) = \int_0^E \exp\left[-\int_{e_2}^{e_3} H[e_1] \mathrm{d}e_1\right] \left\{\int^{e_3} Q[e_4] \exp\left[\int_{e_2}^{e_4} H[e_1] \mathrm{d}e_1\right] \mathrm{d}e_4\right\} \mathrm{d}e_3. \tag{63}$$

This distribution function should satisfy the self-consistency requirement that

$$\rho(r) = 2\sqrt{2} \int_{-\psi}^0 F(E)\sqrt{E+\psi}\, \mathrm{d}E, \quad \nabla^2 \psi(r) = 4\pi G \rho(r). \tag{64}$$

Imposing that F (E) obeys equations (62)–(64) yields a non-linear integral equation for the $\boldsymbol{D}_i$, i.e. a (admittedly indirect) constraint on the angular correlation of the external field. Section 5 describes other means of constraining the power spectrum of the infalling dark matter. Weinberg (2001b) found iteratively the corresponding solution while making some assumptions on the spectral properties of $\boldsymbol{b}$ in the régime where $\boldsymbol{c} = 0$. In the light of his investigation, he concluded that the tidal excitation drives the halo towards a less steep profile. It will be interesting to explore this venue with a realistic accounting of the source of infall. The setting here would be that the satellite problem and the cusp problem of dark matter haloes might be the two sides of the same coin, so that the evolution towards a universal profile might be triggered by the actual infall of substructures.

Let us now return to the perturbative dynamics described in Sections 2 and 3 and explore its implications for galaxies.

5 APPLICATIONS: HALO POLARIZATION, DISC DYNAMICS AND INVERSION

Aubert & Pichon (in preparation) provided a detailed statistical description of how dark matter falls on to a $L^\star$ galactic halo: how much mass is accreted as a function of time, how is it accreted, i.e. in what form, with what velocity distribution, along which direction and for how long? Putting the theory described here and the tabulated measurements from that paper together, allows us to address globally, and coherently dynamical issues on galactic scales in a *statistically representative* manner. With the help of the theory presented in Sections 2 and 3, we are now in a position to ask ourselves: what are the expected features of a halo/galaxy induced by their cosmic environment. Specifically, we may now 'simply' propagate the cosmological framework and its statistics to observables (describing the departure from spherical symmetry/stationarity) on galactic scales. On these scales, the realm of astrophysical applications for the perturbative open solution of the Boltzmann–Poisson equations is extremely wide. It is clearly beyond the scope of this paper to attempt an exhaustive inventory. Rather, we shall here focus on a few specific issues, for which we show how the open perturbative framework improves our understanding, and allows for a statistical investigation.

In particular, we shall restrict ourselves to settings where the detailed geometry of the infall matters, since the theory described above does account for the configuration and the time lag involved in the accretion on top of $L^\star$ galaxies.

Recall that the purpose of the statistical propagation is threefold: (i) to constrain the properties of the infall on the basis of the *observed* distribution for the properties of galaxies and their environment; (ii) to *predict* some of the statistical properties of galaxies which are not directly observable, while relying on the properties of the infall; (iii) to weigh the relative importance of the intrinsic properties of the disc plus halo compared to the strength of the environment.

We will distinguish three classes of problems; first we will describe how to transpose to galactic scales (Section 5.1) the classical probes used in cosmology to trace the large-scale structures. We will then explore in Section 5.2 the implication for the properties of external galaxies, and in Section 5.3 for the structures within the Milky Way halo. Finally, we will elaborate in Section 5.4 on the prospect of inverting the upcoming data sets for the *past* history of our own Galaxy and for field galaxies in the local group.

5.1 Cosmic probes in the neighbourhood of galaxies: $R_{200}/10 < R < R_{200}$

A series of observational probes of the statistical properties of the density field have been devised over the years, such as weak lensing, galaxy counts, the SZ effect, X-ray or γ-ray emissivity maps. In the light of large galactic surveys which are available today, it becomes quite desirable to apply these probes in the neighbourhood of galactic haloes in order to study the dark matter distribution within the R_{200} radius. Some of these tracers are only sensitive to the baryon density, which need not trace directly the dark matter density. In this section, we will systematically assume for simplicity a simple biasing, though this assumption may be lifted (at the expense of extra non-linearities, see Section E3) provided the biasing law is known (i.e. the observables are assumed to scale like the dark matter density, or some power of it); we refer to Section 3.3.1 for a brief discussion of thresholding, which is bound to be important in practice.

The calculation described in the previous sections, together with the statistical measurements described in Aubert et al. (2004) and Aubert & Pichon (in preparation) *should* allow us to make statistical predictions about observables which may be expressed in terms of the distributions of clumps within the galactic haloes, either via their gravitational potential, their projected density or even their velocity distributions (e.g. Galactic streams).

We will consider in turns observable which may be approximated as linear functions of the *perturbed* fields, either in projected coordinates on the plane of the sky, or as seen by an observer at the galactic centre of a halo. We will also consider observables which involve quadratic functions of this field (e.g. the square of the electron density), or even more non-linear functions of the dark matter distribution within the virial radius (such as the locus of virialized clumps, which dissolve at a function of time). We will in particular build the two-point statistics for these observables, since the mean of the perturber is often zero by construction. Finally, we will also consider metals lines in absorptions systems, which involve the cross-correlation of the density and the velocity fields. Note that all these measurements could in principle be carried as a function of redshift, or a function of the mass of the halo, or while varying the anisotropy of the equilibrium for the halo (by varying $F(\boldsymbol{I})$ in e.g. $\boldsymbol{K}$ in equation 41). Note finally that some tracers correspond to the scales of clusters, and we will assume here that the measurements presented in Aubert & Pichon (in preparation) could be reproduced for these objects (whereas the theory described here is scale independent provided the system is dynamically relaxed and spherical).

In this section, we will focus on a couple of probes which are supposed to scale linearly with the dark matter density in the main text (weak lensing, SZ effect), and postpone to Appendix E a presentation of other probes (X-ray emissivity, dark matter disintegration, metal lines in absorption spectra).

Note that all probes described below are a departure from the mean profile of galactic haloes (just as cosmic perturbation theory describes the growth of structure as a departure form the mean density/expansion of the Universe) and as such, assume that we have a good understanding of this profile. This will undoubtedly turn out to be a serious observational constraint when attempting to ensemble average galaxies of various size and properties.

5.1.1 Weak lensing in stacked haloes

Weak lensing corresponds to the deflection of light emitted from background galaxies by the gravitational potential of structures between those galaxies and the observer. It has recently been used quite successfully to constrain the statistical distribution of the large-scale structures. On smaller scales, the effects of substructures in haloes on the lensing measurements have been demonstrated by, for example, Dalal & Kochanek (2002) and Kochanek & Dalal (2004).

In the weak lensing regime (Peacock 1999), the relationship between the observed convergence and the underlying projected dark matter profile is approximated to be linear. Hence, we may straightforwardly propagate our statistical predictions for the clumpy dark matter distribution around a dark matter halo (or within the neighbourhood of clusters of galaxies provided some re-adjustment of the theoretical predictions described in Aubert et al. (2004) and Aubert & Pichon (in preparation) on these larger scales).

The cumulative deflection angle, $\alpha(\theta, w) \triangleq \delta \boldsymbol{x}/r_k(w)$ by which light is deflected is given by

$$\boldsymbol{\alpha}(\boldsymbol{\theta}, w) = \frac{2}{c^2}\int \mathrm{d}w' \frac{r_k(w'-w)}{r_k(w)} \nabla_\perp \psi(r_k(w')\boldsymbol{\theta}, w'), \tag{65}$$

where r_k is the angular comoving distance, $\mathrm{d}w \triangleq \mathrm{d}r/\sqrt{1-kr^2}(k=0,\pm 1)$ and $\boldsymbol{x}$ the transverse comoving distance. Defining the convergence, $\kappa(\boldsymbol{\theta})$ by

$$\kappa(\boldsymbol{\theta}) = \frac{1}{2}\nabla_{\boldsymbol{\theta}} \cdot \boldsymbol{\alpha}(\boldsymbol{\theta}), \tag{66}$$

the mean ensemble average convergence of the rescaled halo, $\langle\kappa(\theta)\rangle$, reads

$$\langle\kappa(\theta)\rangle = \frac{1}{c^2}\int \mathrm{d}w' \frac{r_k(w'-w)}{r_k(w)} \nabla_\perp^2 \psi_{\mathrm{NFW}}(r_k(w')\theta, w'). \tag{67}$$

Now recall that (cf. equation 9 where $\psi^{[\boldsymbol{n}]}$ is given by equations (B2)–(B3) in Section B2)

$$\delta\psi(\boldsymbol{r}) = \sum_{\boldsymbol{n}} a_{\boldsymbol{n}} \psi^{[\boldsymbol{n}]}(\boldsymbol{r}), \quad \text{hence} \quad \delta\kappa(\boldsymbol{\theta}) = \sum_{\boldsymbol{n}} a_{\boldsymbol{n}} \kappa^{[\boldsymbol{n}]}(\boldsymbol{\theta}), \tag{68}$$

where

$$\kappa^{[\boldsymbol{n}]}(\boldsymbol{\theta}) = \frac{1}{c^2}\int \mathrm{d}w' \frac{r_k(w'-w)}{r_k(w)} \nabla^2 \psi^{[\boldsymbol{n}]}(r_k(w')\boldsymbol{\theta}, w'). \tag{69}$$

It follows that the correlation function of the relative convergence obeys

$$\frac{\langle\delta\kappa(\boldsymbol{\theta})\delta\kappa(\boldsymbol{\theta}')\rangle}{\langle\kappa(\theta)\rangle^2} = \frac{1}{\langle\kappa(\theta)\rangle^2}\sum_{\boldsymbol{n},\boldsymbol{n}'} \langle a_{\boldsymbol{n}} a_{\boldsymbol{n}'}\rangle \kappa^{[\boldsymbol{n}]}(\boldsymbol{\theta})\kappa^{[\boldsymbol{n}']}(\boldsymbol{\theta}'). \tag{70}$$

Hence, the statistical properties of the relative convergence will depend on the statistical distribution of the clumps of the halo through the $\{a_{\boldsymbol{n}}\}$ coefficients which are given in equation (29) in terms of $b_{\boldsymbol{n}}$ and $c_{\boldsymbol{n}}$.

In practice one has to devise an observational strategy, given the expected size of the caustics of subclumps within haloes of galaxies or clusters, the number of background sources, and the expected number of foreground objects (i.e. galaxies or clusters).

Finally, it is believed that one in a hundred large ellipticals on the sky should undergo strong lensing. In the long run, the statistical properties of such a non-linear signal will be worth investigating within the framework described in this paper (following the non-linear steps described in say, Section E3).

5.1.2 *Thermal SZ effect of stacked haloes*

When the photons of the cosmic microwave background (CMB) enter the hot dense gas within the clusters and galactic haloes, they interact with the electrons of the gas. The diffusion process transfers the energy of the photons to the electrons which in turn re-emit this energy at a higher frequency. The corresponding spectral redistribution induces a local temperature decrement seen in the temperature map of the clusters, known as the thermal SZ effect (see e.g. Peacock 1999). The temperature decrement (at low frequency) reads as a function of the distance to the cluster centre, $\boldsymbol{R}$:

$$\frac{\Delta T(\boldsymbol{R})}{T_{\mathrm{CMB}}} = -2\frac{k_{\mathrm{B}}\sigma_{\mathrm{T}}}{m_{\mathrm{e}}c^2}\int \mathrm{d}z n_{\mathrm{e}}(z, \boldsymbol{R}) T_{\mathrm{e}}(z, \boldsymbol{R}), \tag{71}$$

where m_{e}, n_{e} and T_{e} are, respectively, the mass, the numerical density and the temperature of the electrons, while σ_{T} is the Thomson scattering section (6.65×10^{-25} cm^2), c the speed of light, k_{B} Boltzmann constant and T_{CMB} is the CMB temperature.

Let us assume that the variation in temperature is small compared to the variation of the electron number density.[7] Let us also assume that the electron density is proportional to the dark matter density (constant biasing) as mentioned above. Let us define the departure from the cosmic average for the profile as

$$\delta\Delta T(\boldsymbol{R}) = \Delta T(\boldsymbol{R}) - \langle\Delta T\rangle(R). \tag{72}$$

The relative fluctuation of the temperature decrement reads

$$\frac{1}{\langle\Delta T\rangle^2(R)}\langle\delta\Delta T(\boldsymbol{R})\delta\Delta T(\boldsymbol{R}')\rangle = \frac{1}{\Sigma_{\mathrm{NFW}}(R)^2}\sum_{\boldsymbol{n},\boldsymbol{n}'}\langle a_{\boldsymbol{n}} a_{\boldsymbol{n}'}\rangle \int \mathrm{d}z \int \mathrm{d}z' \rho^{[\boldsymbol{n}]}(\boldsymbol{R}, z)\rho^{[\boldsymbol{n}']}(\boldsymbol{R}', z'), \tag{73}$$

where Σ_{NFW} is the mean rescaled projected dark matter mass profile. Note that the double integral in equation (73) is carried over known functions and is just a geometric factor which will depend on R, ΔR and $\Delta\Theta$ only. Again, the knowledge of the statistics of the $\{a_{\boldsymbol{n}}\}$ (which in turn only depend on the equilibrium, F_0, and the statistics of $b_{\boldsymbol{n}}$ and $c_{\boldsymbol{n}}$ at R_{200}, see equation 19 or 20) therefore allows us to predict

[7] Note that we may lift this assumption at the cost of non-linearities, provided we may rely on an equation of state to relate it to the underlying density.

the statistical properties of the relative fluctuations in the temperature decrement. The Atacama Large Millimetre Array (ALMA) will soon provide detailed SZ maps of clusters for which it should be possible to apply these techniques.

Let us note in passing that the kinetic SZ effect of stacked haloes may also be investigated following the same route

$$\frac{\Delta T(\boldsymbol{R})}{T_{\mathrm{CMB}}} = -2\frac{k_{\mathrm{B}}\sigma_{\mathrm{T}}}{m_{\mathrm{e}}c^2}\int \mathrm{d}z n_{\mathrm{e}}(z, \boldsymbol{R}) v_z(z, \boldsymbol{R}). \tag{74}$$

In closing, let us note that maps of SZ effects within our own Galaxy will be available with the upcoming *Planck* satellite, and will provide statistical information on the small-scale distribution of local clumps. Recall finally that Appendix E presents other statistical probes of the outer structures found in galactic haloes (X-ray emissivity, dark matter disintegration, metal lines in absorption spectra). Most of these probes could be used to say, probe the shape of the density profile in the outer parts of galaxies, or the biasing law relating dark matter to stars or gas.

5.2 Galactic structure: $R < R_{200}/10$

In the previous section, we investigated the dynamical consequences of the cosmic infall in the outer region of the halo. Let us now turn to the regions of the halo where we expect to find the galaxies themselves. At lower redshift, the galaxies essentially come in two flavours, ellipticals and spirals. The response of ellipticals should follow closely that of the dark matter halo since both components are hot enough not to undergo gravitational instabilities. In effect, describing an embedded 'spherical' elliptical galaxy within a dark matter halo amounts to changing the distribution function to account for the presence of the elliptical and its possibly distinct kinematics. Note that, as mentioned before the above theory could be amended to account perturbatively for the possible triaxiality of the elliptical (Binney & Spergel 1984).

For a disc or a very flattened spheroid, the situation becomes quite different. The cooler disc is likely to be either drawn beyond its stability threshold by the perturbation, or will respond much more strongly to the perturber than its dark halo. Hence we need to model the disc component differently. The protogalactic environment is likely to be extremely noisy, particularly in outer regions, so that the halo may perturb the disc by transmitting numerous disturbances into the inner galaxy. Moreover, the inner halo may continue to oscillate as it settles after the coalescence of advected objects. Halo oscillations may easily perturb the disc through the time-dependent gravitational potential. Conversely, the structural integrity of observed discs set limits on the degree of disequilibrium in the protogalactic halo.

Within the realm of features found in galactic discs, a fraction is known to be the result of instabilities (e.g. galactic bars), while others have been shown to correspond to transients (e.g. galactic warps).

With the advent of modern systematic surveys, it is possible to construct distributions corresponding to, say, the fraction of spirals which fall within some Hubble type, or the fraction of warps whose inclination is larger than some angle. On the disc scale, we may construct the probability distribution function (PDF) of, say, the pitch angle of dynamically induced spirals, or the PDF of the extent of the bar, its amplitude, or less directly observed the PDF of pattern speeds. Some of these processes depend crucially on gas physics and will not be addressed here.

5.2.1 *Pitch angle distribution for spirals*

For stellar discs, the stars obey formally the same equation as equations (6)–(11), but this time the modes may be unstable, and sometimes the disc cannot be treated in isolation from the live halo in which it is embedded. On the other hand, it is often well approximated as an infinitely thin structure; such a 2D system becomes integrable again with two actions, $\mathrm{d}\boldsymbol{J} \triangleq \mathrm{d}J_{\mathrm{r}}\mathrm{d}L_{z,D}$. Here J_{r} is the radial action of the stars in the plane of the disc, and L_{z_D} is the momentum of the stars in the disc. Following Weinberg (1998a) and adding some source of infall at R_{200}, we may describe the coupled system disc plus halo in the complex plane as

$$\begin{pmatrix} \hat{\boldsymbol{a}}_D \\ \hat{\boldsymbol{a}}_{\mathrm{H}} \end{pmatrix} = \begin{pmatrix} \hat{\boldsymbol{K}}_{\mathrm{DD}} & \hat{\boldsymbol{K}}^*_{\mathrm{DH}} \\ \hat{\boldsymbol{K}}_{\mathrm{DH}} & \hat{\boldsymbol{K}}_{\mathrm{HH}} \end{pmatrix} \cdot \begin{pmatrix} \hat{\boldsymbol{a}}_D \\ \hat{\boldsymbol{a}}_{\mathrm{H}} + \hat{\boldsymbol{b}} \end{pmatrix} + \begin{pmatrix} 0 \\ \hat{\boldsymbol{Q}} \end{pmatrix} \cdot \begin{pmatrix} 0 \\ \hat{\boldsymbol{c}} \end{pmatrix},$$

where $\hat{\boldsymbol{K}}_{\mathrm{HH}}$ is given by equation (D15), while

$$(\hat{\boldsymbol{K}}_{\mathrm{DD}})_{\boldsymbol{p},\boldsymbol{q}} = \sum_{\boldsymbol{k}} \int \mathrm{d}\boldsymbol{J} \frac{\psi_{\boldsymbol{k}}^{D,[\boldsymbol{p}]}(\boldsymbol{J})\psi_{\boldsymbol{k}}^{D,[\boldsymbol{q}]*}(\boldsymbol{J})}{\boldsymbol{k}\cdot\boldsymbol{\omega}_D - \omega}\boldsymbol{k}\cdot\frac{\partial F_D}{\partial \boldsymbol{J}},$$

and a similar expression involving $\psi_{\boldsymbol{k}}^{[\boldsymbol{p}]}(\boldsymbol{J})\ \psi_{\boldsymbol{k}}^{D,[\boldsymbol{q}]*}(\boldsymbol{J})$ for the cross term, $\hat{\boldsymbol{K}}_{\mathrm{DH}}$. See Pichon & Cannon (1997) for details relative to the disc. Here $\hat{\boldsymbol{a}}_D$ and $\hat{\boldsymbol{a}}_{\mathrm{H}}$ are the coefficients of the expansion for the disc and the halo, respectively, F_D is the distribution function of stellar stars within the disc, $\{\psi^{D,[\boldsymbol{q}]}\ (r)\}_{\boldsymbol{q}}$ the potential basis function over which the disc response is projected and ω_D the angular frequencies of the stars in the disc.

Let us first assume that the unperturbed disc is stable. Solving the coupled equation for $[\hat{\boldsymbol{a}}_{\mathrm{H}}, \hat{\boldsymbol{a}}_D]$ yields (after inverse half-Fourier transform) the temporal evolution of the spiral response as a function of time for a given tidal field, $\boldsymbol{b}(t)$ and a given infall history, $\boldsymbol{c}(t)$. The pitch angle, $\mathcal{I}$ of the spiral, defined by $\tan(\mathcal{I}) = 1/\pi \int_0^\pi \mathrm{d}\theta \mathrm{d}\log\mathcal{R}/\mathrm{d}\theta$ (where $\mathcal{R}(\theta)$ corresponds to the crest of the spiral wave), is a non-linear function of $\boldsymbol{a}_D$, which we may write formally as $\mathcal{I}[\boldsymbol{a}_D]$. Hence we may ask ourselves what its cosmic mean, $\langle\mathcal{I}[\boldsymbol{a}_D]\rangle$ is, given that $\hat{\boldsymbol{a}}_D(\omega)$

obeys

$$\hat{\boldsymbol{a}}_D(\omega) = \hat{\boldsymbol{K}}_{\rm HD} \cdot [\boldsymbol{b} + \boldsymbol{Q} \cdot \boldsymbol{c}] \Big/ {\rm Det} \begin{vmatrix} \mathbf{1} - \hat{\boldsymbol{K}}_{\rm DD} & \hat{\boldsymbol{K}}^*_{\rm DH} \\ \hat{\boldsymbol{K}}_{\rm DH} & \mathbf{1} - \hat{\boldsymbol{K}}_{\rm HH} \end{vmatrix} .$$

Note that $\mathcal{I}[\boldsymbol{a}_D]$ will depend on the statistical properties of $\boldsymbol{b}, \boldsymbol{c}$ and also on the distribution function for the halo, $F(\boldsymbol{I})$, and the distribution function for the disc, $F_D(\boldsymbol{J})$. More generally, we may in this manner construct the full PDF of the pitch angle, as a function of say, cosmic time (or relative mass in the disc or ...), following the same route as sketched in Section E3.

If the disc is intrinsically unstable, we must then add to the driven response described above the unstable modes. The amplitude of the response will then depend on exactly when each unstable mode has been exited. Such a prescription is beyond the scope of this paper, but could be addressed statistically through the description of a phase transition.

5.2.2 Warp excitation

As mentioned earlier (Jiang & Binney 1999; López-Corredoira et al. 2002), warps are intrinsically stable modes of thin discs which respond to their environment. The action of the torque applied on the disc of a galaxy is different for different angular and radial positions of the perturbation. The orientation of the warp and its amplitude are functions of the external potential.

The work done by the presence of perturbations on the stellar system is

$$\frac{{\rm d}E}{{\rm d}t} = -\int {\rm d}\boldsymbol{r} \nabla(\psi + \psi^e) \cdot \rho \boldsymbol{v} = -\int {\rm d}\boldsymbol{r} (\psi + \psi^e) \nabla(\rho \boldsymbol{v}), \tag{75}$$

where $\psi + \psi^e$ is the total potential perturbation (self-response plus external component).

Using equations (20) and (75)

$$\left\langle \frac{{\rm d}E}{{\rm d}t} \right\rangle = -\sum_{\boldsymbol{n},\boldsymbol{n}'} \int {\rm d}\boldsymbol{r} \left\langle [a_{\boldsymbol{n}'}(t) + b_{\boldsymbol{n}'}(t)] \nabla \psi_{\boldsymbol{n}}(\boldsymbol{r}) \int_{-\infty}^{t} {\rm d}\tau K_{[2],\boldsymbol{n}}(\boldsymbol{r}, \tau - t) [a_{\boldsymbol{n}}(\tau) + b_{\boldsymbol{n}}(\tau)] + Q_{[2],\boldsymbol{n}}(\boldsymbol{r}, \tau - t) c_{\boldsymbol{n}}(\tau) \right\rangle .$$

The power spectra of potential fluctuations drive the energy rate of change through the cross-correlation between the source and the potential.

Note in closing that the framework described in this paper should allow us in the future to address the possibility of warps induced by the accretion of gas.

5.3 Substructures in our own Galactic halo

Let us now turn to the Milky Way. Our knowledge of the structure of its halo has increased dramatically in the course of the last decade with the advent of systematic imaging and spectroscopic surveys (e.g. SDSS, 2dF), both in the optical and at longer wavelengths (e.g. 2MASS), and this observational investigation will undoubtedly continue with efforts such as the Radial Velocity Experiment (RAVE), or the upcoming launch of *GAIA*. This has led to the discovery of quite a few substructures within our halo, both in projection on the plane of the sky (tidal tails) as star counts but also via kinematical features (streams). The extent of the upcoming systematic stellar surveys will allow for a systematic analysis of the dynamical properties of Galactic substructures.

5.3.1 Extent of tidal tails and streams in proper motion and galactic coordinates

The number of stars, dN, in the solid angle defined by the Galactic longitudes and latitudes $(\ell, b) \stackrel{\triangle}{=} \ell$ (within dℓd$(\sin b)$), with proper motions $(\mu_\ell, \mu_b) \stackrel{\triangle}{=} \boldsymbol{\mu}$ (within dμ_bdμ_ℓ) at time t is given by (Pichon, Siebert & Bienaymé 2002)

$${\rm d}N \stackrel{\triangle}{=} A_\lambda(\boldsymbol{\mu}, \boldsymbol{\ell}, t)\, {\rm d}\boldsymbol{\mu}\, {\rm d}\boldsymbol{\ell} = \left\{ \iint {\rm d}u_{\rm r} r^4 {\rm d}r f(\boldsymbol{r}, \boldsymbol{u}, t) \right\} {\rm d}\boldsymbol{\mu}\, {\rm d}\boldsymbol{\ell}. \tag{76}$$

The variables $\boldsymbol{r}, \boldsymbol{u}$ are the vector position and velocity coordinates $(u_{\rm r}, u_\ell, u_b)$ in phase space relative to the local standard of rest, while $\boldsymbol{r} = (R, \Phi, z)$ and $\boldsymbol{v} = (v_R, v_\Phi, v_z)$ are those relative to the Galactic centre. In particular, the radius r (within dr) corresponds to the distance along the line of sight in the direction given by the Galactic longitudes and latitudes (ℓ, b) (within the solid angle dℓcos(b)db).

These velocities are given as a function of the velocities measured in the frame of the sun by

$$\begin{aligned} v_\Phi &= \frac{1}{R}\{r_\odot \sin(b)\sin(\ell)u_b - r_\odot \cos(b)\sin(\ell)u_{\rm r} - r_\odot \cos(\ell)u_\ell + r\cos(b)[u_\ell - \sin(\ell)u_\odot] + [r_\odot + r\cos(b)\cos(\ell)]v_\odot\}, \\ v_R &= \frac{1}{R}\{[r\ \cos(b) - r_\odot\ \cos(\ell)]\ \sin(b)\, u_b - r_\odot\ \sin(\ell)\, u_\ell - \cos(b)\, [r\ \cos(b) - r_\odot\ \cos(\ell)]\, u_{\rm r} \\ &\quad + r_\odot\, u_\odot - r\ \cos(b)\cos(\ell)\, u_\odot + r\ \cos(b)\ \sin(\ell)\, v_\odot\}, \\ v_z &= \sin(b)\, u_{\rm r} + \cos(b)\, u_b + w_\odot, \end{aligned} \tag{77}$$

where

$$\Phi = \tan^{-1}\left[\frac{r\ \cos(b)\ \sin(\ell)}{R}, \frac{r_\odot - r\ \cos(b)\ \cos(\ell)}{R}\right],$$

$$R = \sqrt{r_\odot^2 - 2r_\odot r\ \cos(b)\ \cos(\ell) + r^2\cos(b)^2} \quad \text{and}$$

$$z = r\sin(b). \tag{78}$$

R measures the projected distance (in the meridional plane) to the Galactic centre, Φ the angle in the meridional plane between the star and the Galactic centre, while z is the height of the star. Here $u_\odot$, $v_\odot$, $w_\odot$ and $r_\odot$ are, respectively, the components of the Sun's velocity and its distance to the Galactic centre.

Recall that equation (7) together with equation (19) provides us with the full phase space distribution of the infall as a function of the actions of the unperturbed halo. Let us call $f_{\boldsymbol{n}}$, the phase space basis defined by

$$f_{\boldsymbol{n}}(\boldsymbol{r}, \boldsymbol{v}, \tau) \stackrel{\triangle}{=} \sum_{\boldsymbol{k}} \exp(\mathrm{i}\boldsymbol{k}\cdot\boldsymbol{\omega}\tau + \mathrm{i}\boldsymbol{k}\cdot\boldsymbol{w})\,\boldsymbol{v}\ \mathrm{i}\boldsymbol{k}\cdot\frac{\mathrm{d}F}{\mathrm{d}\boldsymbol{I}}\psi_{\boldsymbol{k}}^{[\boldsymbol{n}]}(\boldsymbol{I}), \tag{79}$$

so that the perturbation at time t and position $(\boldsymbol{r}, \boldsymbol{v})$ reads

$$f(\boldsymbol{r}, \boldsymbol{v}, t) = \sum_{\boldsymbol{n}} \int^t \mathrm{d}\tau\, f_{\boldsymbol{n}}(\boldsymbol{r}, \boldsymbol{v}, \tau - t) a_{\boldsymbol{n}}(\tau). \tag{80}$$

We may now seek the characteristic signature in observed phase space (today i.e. at $t = 0$), of a given perturbation.

$$A(\boldsymbol{\ell}, \boldsymbol{\mu}) = \sum_{\boldsymbol{n}} \int \mathrm{d}\tau a_{\boldsymbol{n}}(\tau) \int \mathrm{d}r r^4 \int \mathrm{d}u_\mathrm{r} f_{\boldsymbol{n}}(\boldsymbol{r}[\boldsymbol{\ell}, r], \boldsymbol{v}[r\boldsymbol{\mu}, u_\mathrm{r}], \tau), \tag{81}$$

where $\boldsymbol{v}\,[r\mu, u_\mathrm{r}]$ is given by equation (77), and $\boldsymbol{r}[\ell, r]$ is given by equation (78). In particular, we may compute the autocorrelation of the kinematic count defined by

$$C_\mathrm{A}^{\boldsymbol{\mu}}(\Delta\boldsymbol{\ell}, \Delta\boldsymbol{\mu}) \stackrel{\triangle}{=} \langle A(\boldsymbol{\ell} + \Delta\boldsymbol{\ell}, \boldsymbol{\mu} + \Delta\boldsymbol{\mu}) A(\boldsymbol{\ell}, \boldsymbol{\mu}). \tag{82}$$

It involves an integral over time of the autocorrelation of the coefficients, $\langle a_{\boldsymbol{n}}(\tau)\, a_{\boldsymbol{n}'}(\tau')\rangle$ as

$$C_\mathrm{A}^{\boldsymbol{\mu}} = \sum_{\boldsymbol{n},\boldsymbol{n}'} \iint \mathrm{d}\tau\, \mathrm{d}\tau' \langle a_{\boldsymbol{n}}(\tau) a_{\boldsymbol{n}'}(\tau')\rangle \iint r^4 \mathrm{d}r r'^4\, \mathrm{d}r' \iint \mathrm{d}u_\mathrm{r}\, \mathrm{d}u_\mathrm{r}' f_{\boldsymbol{n}}(\boldsymbol{r}[\boldsymbol{\ell}, r], \boldsymbol{v}[r\boldsymbol{\mu}, u_\mathrm{r}], \tau) f_{\boldsymbol{n}'}(\boldsymbol{r}[\boldsymbol{\ell} + \Delta\boldsymbol{\ell}, r], \boldsymbol{v}[r'\boldsymbol{\mu} + r'\Delta\boldsymbol{\mu}, u_\mathrm{r}'], \tau').$$

Recall that $\langle a_{\boldsymbol{n}}(\tau) a_{\boldsymbol{n}'}(\tau')\rangle$ can be re-expressed in terms of the coefficients of $\langle \hat{\boldsymbol{b}} \cdot \hat{\boldsymbol{b}}^{*\top}\rangle$, $\langle \hat{\boldsymbol{c}} \cdot \hat{\boldsymbol{c}}^{*\top}\rangle$ and $\langle \hat{\boldsymbol{b}} \cdot \hat{\boldsymbol{c}}^{*\top}\rangle$ via equation (29). The width of the correlation, $C_\mathrm{A}^{\boldsymbol{\mu}}(\Delta\ell, \Delta\mu)$, both in velocity space and in position space accounts for the expected cosmic size of structures within the Galactic halo.

5.3.2 Angular extend of tidal tails

The marginal distribution over proper motions of equation (76) yields the projection on the sky of the perturbation:

$$A(\boldsymbol{\ell}, t) \stackrel{\triangle}{=} \iint A(\boldsymbol{\ell}, \boldsymbol{\mu}, t)\, \mathrm{d}\boldsymbol{\mu} = \iiint \mathrm{d}u_\mathrm{r} r^4 \mathrm{d}r f(\boldsymbol{r}, \boldsymbol{u}, t)\, \mathrm{d}\boldsymbol{\mu}, \tag{83}$$

which can be derived from equation (81) but is also found directly via integration over the density as

$$A(\boldsymbol{\ell}, t) \ = \sum_{\boldsymbol{n}} a_{\boldsymbol{n}}(t) \int \tilde{\rho}_{\boldsymbol{n}}(\boldsymbol{r}, \boldsymbol{\ell}) r^2 \mathrm{d}r\,, \quad \text{given}$$

$$\tilde{\rho}_{\boldsymbol{n}}(\boldsymbol{r}, \boldsymbol{\ell}) \stackrel{\triangle}{=} \rho_{\boldsymbol{n}}(R(\boldsymbol{r}, \boldsymbol{\ell}), \Phi(\boldsymbol{r}, \boldsymbol{\ell}), z(r, \boldsymbol{\ell})), \tag{84}$$

where $\rho_{\boldsymbol{n}}$ is given by equation (9) and $R(\boldsymbol{r}, \ell)$ is given by equation (78). Note the generic difference between equations (81) and (84): the former involves the explicit cumulative knowledge of $a_{\boldsymbol{n}}(\tau)$ for all τ since it involves a kinematical (inertial) quantity, $\boldsymbol{\mu}$, while the latter only require the knowledge of the current $a_{\boldsymbol{n}}(t)$. This difference is weaker than it seems in practice, since self-gravity implies that $a_{\boldsymbol{n}}(t)$ depends in turn on the previous $a_{\boldsymbol{n}}(\tau)$ via equation (18). The corresponding angular correlation reads

$$C_\mathrm{A}(\Delta\boldsymbol{\ell}) \stackrel{\triangle}{=} \langle A(\boldsymbol{\ell} + \Delta\boldsymbol{\ell}) A(\boldsymbol{\ell})\rangle = \sum_{\boldsymbol{n},\boldsymbol{n}'} \langle a_{\boldsymbol{n}}(t)\, a_{\boldsymbol{n}'}(t)\rangle \iint \mathrm{d}r\, \mathrm{d}r'\, r'^2 r^2 \tilde{\rho}_n[r, \boldsymbol{\ell}] \tilde{\rho}_n[r', \boldsymbol{\ell} + \Delta\boldsymbol{\ell}]. \tag{85}$$

The FWHM of the correlation defined by equation (85) corresponds to the 'cosmic' width of tidal stream projected on the sky.

5.4 Past history of galaxies: dynamical inversion

Let us now see how the theoretical framework presented in Sections 2 and 3 may be applied to invert observed properties of galaxies back in time and constrain the past infall and the tidal field on a given dark matter halo. In short, the idea is to notice that the perturbation theory provides an explicit relationship between the response and the excitation of the inner halo which we can tackle as an integral equation for the source.[8] Let us present first the inversion for our Milky Way (Section 5.4.1), and discuss briefly extra galactic stellar streams.

[8] Since our treatment of the dynamics (including the self-consistent gravity polarization) is linear order by order, we may in principle recover the history of the excitation.

5.4.1 The Galactic inverse problem

Let us rewrite formally equation (81) as $A(\boldsymbol{\ell}, \boldsymbol{\mu}) = \mathcal{A}^{\boldsymbol{\ell},\boldsymbol{\mu}} \cdot \boldsymbol{a}$, where the dot product accounts for *both* the summation over $\boldsymbol{n}$ and the integration over τ (cf. equation 45). Let us assume that we have access to kinematic star counts, i.e. to a set of measurements $\{A_i \stackrel{\triangle}{=} A(\ell_i, \mu_i)\}_{i \leqslant n}$. We want to minimize

$$\chi^2 = \sum_i \left[A_i - \mathcal{A}_i^{\boldsymbol{\ell},\boldsymbol{\mu}} \cdot \boldsymbol{R}_1 \cdot (\boldsymbol{K} \cdot \boldsymbol{b} + \boldsymbol{Q} \cdot \boldsymbol{c})\right]^2, \tag{86}$$

subject to some penalty function. Recall that $\boldsymbol{R}_1$ is given by equation (47) and accounts for the self-gravity of the halo. Let us formally rewrite again $\mathcal{A}_i^{\boldsymbol{\ell},\boldsymbol{\mu}} \cdot \boldsymbol{R}_1 \cdot (\boldsymbol{K}_1 \cdot \boldsymbol{b} + \boldsymbol{Q}_1 \cdot \boldsymbol{c}) \stackrel{\triangle}{=} \boldsymbol{M} \cdot \tilde{\boldsymbol{b}}$, with $\tilde{\boldsymbol{b}} = [\boldsymbol{b}, \boldsymbol{c}]$. Let us also write $\boldsymbol{A} = (A_i)_{i \leqslant n}$. The solution to the linear minimization, equation (86) reads

$$\tilde{\boldsymbol{b}} \stackrel{\triangle}{=} \boldsymbol{M}_\lambda^{(-1)} \cdot \boldsymbol{A} = (\boldsymbol{M}^\top \cdot \boldsymbol{M} + \lambda \boldsymbol{P})^{-1} \cdot \boldsymbol{M}^\top \cdot \boldsymbol{A}, \tag{87}$$

where $\boldsymbol{P}$ is some penalty which should impose smoothness for $\boldsymbol{b}$ and $\boldsymbol{c}$ both angularly and as a function of time. For instance, for the $\boldsymbol{b}$ field we could use (see e.g. Pichon et al. 2002)

$$P[b_{\ell m}] = \sum_\ell [(\ell+1)\ell]^2 \int \mathrm{d}\omega \omega^2 |\hat{C}_\ell|, \quad \text{where} \quad \hat{C}_\ell(\omega) \stackrel{\triangle}{=} \langle |\hat{b}_{\ell m}|^2 \rangle$$

(so that large ω and ℓ are less likely in the solution) and a similar expression for the $\boldsymbol{c}$ field which should also impose smoothing along velocities. The penalty coefficient, λ, should be tuned so as to provide the appropriate level of smoothing. In practice, it might be necessary to impose further non-linear constraints on the solution, $\tilde{\boldsymbol{b}}$, such as requiring that the excitation is locally as compact and connex as possible on the R_{200} sphere. This can be done via some form of non-linear bandpass filter in the former, in order to limit the effective degrees of freedom in $\tilde{\boldsymbol{b}}$.

5.4.1.1 Accounting for non-linearities. The non-linear solution, equation (51) may be formally rewritten as $\boldsymbol{a}_2 \stackrel{\triangle}{=} \boldsymbol{M}_2 \cdot \tilde{\boldsymbol{b}} \otimes \tilde{\boldsymbol{b}}$, so that the perturbative inverse reads

$$\tilde{\boldsymbol{b}} \stackrel{\triangle}{=} \boldsymbol{M}_\lambda^{(-1)} \cdot \boldsymbol{A} - \boldsymbol{M}_\lambda^{(-1)} \cdot \boldsymbol{M}_2 \cdot \left(\boldsymbol{M}_\lambda^{(-1)} \cdot \boldsymbol{A}\right) \otimes \left(\boldsymbol{M}_\lambda^{(-1)} \cdot \boldsymbol{A}\right), \tag{88}$$

where $\boldsymbol{M}_\lambda^{(-1)}$ is defined by equation (87), provided the regime for the perturbative expansion applies. If not, we may still find the best non-linear solutionto the penalized likelihood problem of jointly minimizing $||\boldsymbol{A} - \boldsymbol{M} \cdot \tilde{\boldsymbol{b}} - \boldsymbol{M}_2 \cdot \tilde{\boldsymbol{b}} \otimes \tilde{\boldsymbol{b}}||^2 + \lambda \boldsymbol{P}$, while using equation (88) as a starting point.

When proper motions measurements are not available (i.e. we only have access to star counts), equations (86)–(88) still apply with some straightforward modifications, but the conditioning of the problem should decrease significantly, since the dynamics is less constrained.

For a data set such as *GAIA*, we shall have access to the full 6D description of phase space for some of the stars (via radial velocity measurements and parallax) or at least 5D measurements (ℓ, b, μ_ℓ, μ_b, u_r).

Recall that in practice, the fields, $\boldsymbol{b}$ and $\boldsymbol{c}$ are, respectively, 3D (two angles and time) and 5D (two angles, time and three velocities). Consequently, the inverse problem is generically very ill-conditioned since data space is either 2D (ℓ, b), 4D (ℓ, b, μ_ℓ, μ_b), 5D (ℓ, b, μ_ℓ, μ_b, π) or 6D (ℓ, b, μ_ℓ, μ_b, π, v_r). In fact it is anticipated that the conditioning is even poorer because the dynamical evolution involves damped modes, implying an exponential decay (which corresponds to a major challenge for extrapolation). It remains that the weakly damped modes should be tractable back in time up to some horizon, which will depend on the nature of the halo (via the conditioning of $\boldsymbol{M}_\lambda$ defined in equation 87), the volume of data, and the signal-to-noise ratio in the measurements.

Let us close this discussion of the inverse problem by emphasizing again the true complexity of the implementation: equation (87), and its non-linear counterpart, equation (88), include via the dot product large sums over $\boldsymbol{n}$ and integrals over τ. $\boldsymbol{M}$ and $\boldsymbol{M}_2$ are functions of $\mathcal{A}^{\boldsymbol{\ell},\boldsymbol{\mu}}$ (which require a couple of integrals) and A_{bb}, etc. which are themselves functions of $\boldsymbol{K}_i$ (equation 53) [which involves the underlying distribution function, $F_0(\boldsymbol{I})$, and the basis function, $\psi^{[\boldsymbol{n}]}(\boldsymbol{r})$ via equations (41), (42) and (47)].

Streamers (or tidal tails) in external galaxies may also be integrated backwards through the same procedure. It will involve the deprojection of the stream and of the underlying halo.

In contrast to the Galactic inverse problem, it will in principle be possible to reproduce the inversion process on a statistical set of haloes, which would allow us to compare directly to the predicted statistical properties of the $\boldsymbol{b}$ and the $\boldsymbol{c}$ (though clearly the bias introduced by the penalized inversion would have to be accounted for).

This completes our rapid survey of possible applications for the perturbative treatment of the dynamics of an open halo.

6 CONCLUSION

In the last few years, with the observational convergence towards the concordant cosmological model, a significant fraction of the interest has shifted towards smaller scales. Indeed, it now becomes possible to project down to these scales some of the predictions of the model. This in turn offers the prospect of transposing there what has certainly been a key asset of modern cosmology, both observationally and theoretically, statistics. This is a requirement both from the point of view of the (often understated) variety of objects falling on to an $L_\star$ galaxy, but also because of the sheer size of the configuration space for infall. It is also a requirement from the point of view of the non-linear dynamics within time-scales corresponding to the relaxation processes and the dynamical evolution decouple. Hence, we could assume a hierarchy in time so that the distribution function is constant in time when computing the polarization.

Finally, in Section 5 we considered in turn a few classical probes of the large-scale structures which had been used in the past to constrain the main cosmological parameters and the initial power spectrum, which we transposed to the galactocentric context. Note that these are built upon observables, hence they may be used to constrain the boundary power spectrum of the $a_{\boldsymbol{n}}$. Since equation (65), (71), (E1) and (E10) involve different combinations of $\langle a_{\boldsymbol{n}} a_{\boldsymbol{n}'} \rangle$, they will constrain them at different scales with different biases, which should ultimately allow us to better characterize the power spectrum. This situation is the direct analogue of the cosmic situation, where the different tracers (weak lensing, Lyα forest, CMB, etc.), constrain different scales of the cosmological power spectrum (with different biases). Note also that our knowledge of the statistical properties of the boundary (via the $b_{\boldsymbol{n}}$ and $c_{\boldsymbol{n}}$ coefficients) together with some assumptions on the equilibrium F_0 allows us to generate given realizations of the $a_{\boldsymbol{n}}$ as shown in Aubert & Pichon (in preparation) and therefore virtual observables for any of these data sets, for the purpose of, for example, validating inverse methods. We investigated the consequences of the infall down to galactic scales and showed how it could be used to account for the observed distribution of disc properties (spiral winding, warps, etc.). We demonstrated how the analytical model (both linear and non-linear) are quite useful when attempting to 'invert' the observations for the past accretion history of a given galaxy. This stems mainly from the fact that perturbation theory provides an explicit scheme for the response of the system, in contrast to the algorithmic procedure corresponding to N-body simulations.

Again, let us emphasize that equation (18) and its non-linear generalizations (D3) and (C7) yield in principle the detailed knowledge of the full *perturbed* distribution (inside R_{200}) at later times. (This is to be contrasted to the situation in N-body simulations where the response of the system is partially hidden by the mean profile of the halo, which requires first identifying substructures Aubert et al. 2004.) Hence, we should be in a position to weigh the relative importance of the environment (via s^e and ψ^e) against the inner properties of the galaxy: the unperturbed distribution function of the halo, $F(\boldsymbol{I})$ (its level of anisotropy, the presence of a central cusp, etc.), the disc (its mass, its profile, its distribution function, $F(\boldsymbol{J})$, etc.).

The work presented here derives from the fact that it was realized that the bi-orthogonal projection pioneered by Kalnajs (1976) could be applied order by order to the perturbative expansion of the dynamical equations. Yet this in turn required the knowledge of the relative phases involved in the perturbation, which involves characterizing the properties of the perturber. The characterization only made sense statistically in order to retain the generality of the approach of Kalnajs (1976). Hence the emphasis on statistics.

6.1 Discussion and prospects

Our purpose in this paper was to address in a statistically representative manner dynamical issues on galactic scales. We also advocated using perturbation theory in angle–actions in order to explicitly propagate this cosmic boundary inwards in phase space. As was demonstrated in the paper (and shown quantitatively in Section B4), this task remains in many respects quite challenging.

One of the limitations of the above method is the reliance on numerous expansions combined to the special care required in their implementation. One could argue that this level of sophistication might not be justified in the light of the weakness of some of the assumptions. Indeed, we are limited to systems with spherical geometry whereas galaxies most likely come in a variety of shapes. This assumption could be lifted provided we compute the modified actions of the flattened spheroidal equilibrium using perturbation theory for the equilibrium in the spirit of Binney & Spergel (1984), but implies a higher level of complexity (it would also require statistically specifying the orientation of the halo relative to the infall, as discussed in part in Aubert et al. 2004). We assumed here that the perturbation was relatively light, which excludes a fraction of cosmic event which might dominate the distribution of some of the observables.

Sections 4.2 and 5 and Appendix E presented a few possible applications for the framework described here and in Aubert & Pichon (in preparation). These galactic probes would need to be further investigated, in particular in terms of observational and instrumental constraints. The biasing specific to each tracer should be accounted for. The second-order perturbation theory needs to be implemented in practice together with the diffusion coefficients of Section 4, following Appendix B and extending Section B4. Similarly, the identification and evolution of substructures within the halo mentioned in Section 3.3.1 deserves more work. In Aubert et al. (2004), we showed that the accretion on to $L^\star$ haloes was anisotropic; the dynamical implication of this anisotropy will require some specific work in the future.

We will need to demonstrate against N-body simulations the relevance of perturbation theory for dynamical friction; in particular, we should explore the regime in which the second-order truncation is appropriate, and at what cost. Note that truncated perturbation theory implies that modes will ring forever. At some stage, one will therefore have to address the problem of energy dissipation.

Implementing a realistic treatment of the infalling gas will certainly be amongst the more serious challenges ahead of us. This is a requirement both from the point of view of the dynamics but also from the point of view of converting the above predictions into baryon-dependent observables. The description of the gas will require a proper treatment of the various cooling processes, which can be quite important on galactic scales. In particular, the thickening of galactic discs is most likely the result of a fine-tuning between destructive processes such as the tidal disruption of compact substructures on the one hand, and the adiabatic coplanar infall of cold gas within the disc. In fact, the non-linear theory presented in Sections 3 and 4 could be extended to the geometry of discs to account for the adiabatic polarization towards the plane of the disc.

Note that we assumed here that transients corresponding to the initial conditions where damped out so that the response of the system was directly proportional to the excitation. The underlying picture is that of a calmer past, which in fact is very much in contradiction with both our measurements and common knowledge on the more violent past accretion history of galaxies. Indeed, infalling subclumps will contribute via the external tidal potential at some earlier time, and the larger the look-back time, the relatively stronger the importance of the perturbation (since the intensity of infall is in fact an increasing function of look-back time). We are therefore facing a partially divergent boundary condition. Because of the characteristics of hierarchical clustering, the actual bootstrapping of the analytical framework is therefore challenging. This could be a problem in particular for non-linear dynamics, where the coupling of transients may turn out to be as important as the driven response. The importance of these shortcomings will need to be addressed in the future.

Finally, let us note that the theory presented in Sections 2–4 describes perturbative solutions to the collisionless Boltzmann–Poisson equation in angle–action variables, and as such are not specific to the description of dark matter haloes. It could straightforwardly be transposed to other situations or geometries provided the system remains integrable. As mentioned in Section 2.3, the stellar dynamics around a massive black hole would seem to be an obvious context in which this theory could be applied. For instance, we might want to investigate the capture of streams of stars by an infalling black hole. In a slightly different context, note in passing that the above theory could also be applied to celestial mechanics, since an angle–action expansion corresponds to an all-eccentricity scheme.

Let us close this paper by a summary of the pros and cons of the theory presented here.

Possible assets:

(i) fixed boundary: localized statistics;
(ii) fluid description: no a priori assumption on the possibly time-dependent nature of the objects;
(iii) non-linear explicit treatment of the dynamics: proper account of the self-gravity of incoming objects and statistical accounting of causality;
(iv) dynamically consistent statistically representative treatment of the cosmic environment;
(v) customized description of resonant processes within the halo via angle–action variables of universal profile;
(vi) ability to construct one- and two-point statistics for a wide range of galactic observables;
(vii) theoretical framework for dynamical inversion and secular evolution.

Possible drawbacks:

(i) weak perturbation with respect to spherical stationary equilibrium: not representative of, for example, equal mass mergers;
(ii) complex time dependent 5D boundary condition;
(iii) ad hoc position of the boundary;
(iv) no obvious truncation of two-entry perturbation theory;
(v) no account of baryonic processes;
(vi) inconsistency in relative strength of merging events versus time;
(vii) non-Gaussian environment probably untractable;
(viii) finite temporal horizon given finite $\ell_{\max}$;
(ix) no statistical accounting of linear instabilities.

ACKNOWLEDGMENTS

We are grateful to E. Bertschinger, J. Binney, S. Colombi, J. Devriendt, J. Heyvaerts, A. Kalnajs, J. Magorrian, D. Pogosyan, S. Prunet, A. Siebert, S. Tremaine and & E. Thiébaut for useful comments and helpful suggestions. We are especially grateful to J. Heyvaerts for careful reading of the manuscript and for introducing us to the quasi-linear formalism. We thank the anonymous referee for constructive remarks. Support from the France–Australia PICS is gratefully acknowledged. DA thanks the Institute of Astronomy and the MPA for their hospitality and funding from a Marie Curie studentship.

REFERENCES

Aoki S., Noguchi M., Iye M., 1979, Publ. Astron. Soc. Japan, 31, 737
Arad I., Dekel A., Klypin A., 2004, MNRAS, 353, 15
Aubert D., Pichon C., Colombi S., 2004, MNRAS, 352, 376
Balescu R., 1963, Statistical Mechanics of Charged Particles. Wiley, New York
Bernardeau F., 1992, ApJ, 392, 1
Bernardeau F., Colombi S., Gaztañaga E., Scoccimarro R., 2002, Phys. Rep., 367, 1
Bertin G., Pegoraro F., Rubini F., Vesperini E., 1994, ApJ, 434, 94
Binney J., 2004, MNRAS, 350, 939
Binney J., Spergel D., 1984, MNRAS, 206, 159
Binney J., Tremaine S., 1987, Galactic Dynamics. Princeton Univ. Press, Princeton, NJ, p. 747
Bogolyubov N., Gurov K., 1947, Zh. Eksp. Teor. Fiz., 17, 615
Dalal N., Kochanek C. S., 2002, ApJ, 572, 25
Diemand J., Moore B., Stadel J., 2004, MNRAS, 353, 624
Earn D. J. D., Tremaine S., 1991, in Sundelius B., ed., Dynamics of Disc Galaxies. Coronet Books, Philadelphia, p. 137
Fillmore J. A., Goldreich P., 1984, ApJ, 281, 9
Fridman A. M., Poliachenko V. L., 1984, Shock and Vibration. Springer, New York

Fry J. N., 1984, ApJ, 279, 499
Gilbert I. H., 1970, ApJ, 159, 239
Gill S. P. D., Knebe A., Gibson B. K., 2004, MNRAS, 351, 399
Gill S. P. D., Knebe A., Gibson B. K., Dopita M. A., 2004, MNRAS, 351, 410
Hernquist L., 1990, ApJ, 356, 359
Hernquist L., Ostriker J. P., 1992, ApJ, 386, 375
Howard S., Byrd G. G., 1990, AJ, 99, 1798
Ichimaru S., 1973, Basic Principles of Plasma Physics: A Statistical Approach. Addison-Wesley, Reading
Jiang I., Binney J., 1999, MNRAS, 303, L7
Kalnajs A. J., 1971, ApJ, 166, 275
Kalnajs A. J., 1976, ApJ, 205, 745
Kalnajs A. J., 1977, ApJ, 212, 637
Klimontovich Y., 1967, The Statistical Theory of Non-Equilibrium Processes in a Plasma. MIT Press, Cambridge
Knebe A., Gill S. P. D., Gibson B. K., Lewis G. F., Ibata R. A., Dopita M. A., 2004, ApJ, 603, 7
Kochanek C. S., Dalal N., 2004, ApJ, 610, 69
López-Corredoira M., Betancort-Rijo J., Beckman J. E., 2002, A&A, 386, 169
Langevin P., 1908, Comptes Rendu, 146, 530
Lenard A., 1961, J. Math. Phys., 2, 682
Ma C., Bertschinger E., 2004, ApJ, 612, 28
Murali C., 1999, ApJ, 519, 580
Palmer P. L., Papaloizou J., 1987, MNRAS, 224, 1043
Peacock J. A., 1999, Cosmological Physics. Cambridge Univ. Press, Cambridge, UK, ISBN: 0521422701
Peebles P. J. E., 1980, The Large-Scale Structure of the Universe. Research supported by the National Science Foundation. Princeton Univ. Press, Princeton, NJ, p. 435
Pichon C., Cannon R. C., 1997, MNRAS, 291, 616
Pichon C., Vergely J. L., Rollinde E., Colombi S., 2001, MNRAS, 326, 597
Pichon C., Siebert A., Bienaymé O., 2002, MNRAS, 329, 181
Power C., Navarro J. F., Jenkins A., Frenk C. S., White S. D. M., Springel V., Stadel J., Quinn T., 2003, MNRAS, 338, 14
Press W. H., Teukolsky S. A., Vetterling W. T., Flannery B. P., 1992, Numerical Recipes in C. The Art of Scientific Computing, 2nd ed. Cambridge Univ. Press, Cambridge
Risken H., 1989, The Fokker–Planck Equation. Methods of Solution and Applications. Springer Series in Synergetics, 2nd ed. Springer, Berlin, New York
Seguin P., Dupraz C., 1994, A&A, 290, 709
Springel V., White S. D. M., Tormen G., Kauffmann G., 2001, MNRAS, 328, 726
Stoehr F., White S. D. M., Springel V., Tormen G., Yoshida N., 2003, MNRAS, 345, 1313
Toomre A., Toomre J., 1972, ApJ, 178, 623
Tremaine S., Weinberg M. D., 1984, MNRAS, 209, 729
Vauterin P., Dejonghe H., 1996, A&A, 313, 465
Weinberg M. D., 1989, MNRAS, 239, 549
Weinberg M. D., 1993, ApJ, 410, 543
Weinberg M. D., 1998a, MNRAS, 299, 499
Weinberg M. D., 1998b, MNRAS, 297, 101
Weinberg M. D., 2001a, MNRAS, 328, 321
Weinberg M. D., 2001b, MNRAS, 328, 321

APPENDIX A: LINEAR PROPAGATOR IN ACTION–ANGLE

As mentioned in Section 2.4.1, it is useful to regard the open collisionless system as a segmentation of the source for the propagator (i.e. the Green function of the coupled Boltzmann–Poisson equation), where one distinguishes two contributions for the initial distribution: the contribution at R_{200} with $v_\mathrm{r} < 0$ (what we describe as the source term in equation 6) and the contribution beyond R_{200} or at R_{200} with $v_\mathrm{r} > 0$ (what we describe as the tidal field in the main text). In order to make this comparison, let us derive generally (without any reference to a boundary for now) the Green function satisfying the *linearized* Boltzmann–Poisson equation. Let us call $G(\boldsymbol{w}, \boldsymbol{I}, t|\boldsymbol{w}', \boldsymbol{I}', t')$ this Green function; it obeys

$$\frac{\partial G}{\partial t} + \boldsymbol{\omega}\cdot\nabla_{w} G + \frac{\partial F}{\partial \boldsymbol{I}}\cdot\nabla_{w}\int \frac{\mathrm{d}\boldsymbol{r}''}{|\boldsymbol{r}''-\boldsymbol{r}|}\, d\boldsymbol{v}'' G(\boldsymbol{r}'', \boldsymbol{v}'', t|\boldsymbol{w}', \boldsymbol{I}', t') = \delta_D(\boldsymbol{w}-\boldsymbol{w}')\delta_D(\boldsymbol{I}-\boldsymbol{I}')\delta_D(t-t'), \tag{A1}$$

so that the distribution function at $(\boldsymbol{I}, \boldsymbol{w}, t)$ reads

$$f(\boldsymbol{w}, \boldsymbol{I}, t) = \int \mathrm{d}t' \int \mathrm{d}\boldsymbol{w}' \int \mathrm{d}\boldsymbol{I}' G(\boldsymbol{w}, \boldsymbol{I}, t|\boldsymbol{w}', \boldsymbol{I}', t') f(\boldsymbol{w}', \boldsymbol{I}', t'). \tag{A2}$$

Let us define the linear propagator, $U_{\omega,\boldsymbol{k},\boldsymbol{w}_0}(\boldsymbol{I}|\boldsymbol{I}')$, as

$$U_{\omega,\boldsymbol{k},\boldsymbol{w}_0}(\boldsymbol{I}|\boldsymbol{I}') = \frac{\delta_D(\boldsymbol{I}-\boldsymbol{I}')}{\boldsymbol{k}\cdot\boldsymbol{\omega}-\omega} - \sum_{\boldsymbol{n},\boldsymbol{n}'} \frac{\partial F}{\partial \boldsymbol{I}}\cdot\boldsymbol{k}\frac{\psi_{\boldsymbol{k}}^{[\boldsymbol{n}]}(\boldsymbol{I})}{(\boldsymbol{k}\cdot\boldsymbol{\omega}-\omega)}((\mathbf{1}-\hat{\boldsymbol{K}}[\omega])^{-1})_{\boldsymbol{n},\boldsymbol{n}'} \sum_{\boldsymbol{k}'} \frac{\psi_{\boldsymbol{k}'}^{[\boldsymbol{n}']}(\boldsymbol{I}')}{(\boldsymbol{k}'\cdot\boldsymbol{\omega}'-\omega)} \exp(\mathrm{i}\boldsymbol{w}_0\cdot[\boldsymbol{k}-\boldsymbol{k}']), \tag{A3}$$

so that the distribution function, $f(\boldsymbol{I}, \boldsymbol{w}, t)$, at time t, with action $\boldsymbol{I}$ and angles $\boldsymbol{w}$ induced by the propagation of the distribution at earlier time t', with action $\boldsymbol{I}'$, and angles $\boldsymbol{w}'$ reads

$$f(\boldsymbol{I}, \boldsymbol{w}, t) = \int \mathrm{d}t' \int \mathrm{d}\boldsymbol{I}' \int \mathrm{d}\boldsymbol{w}' \sum_{\boldsymbol{k}} \int \mathrm{d}\omega \exp(\mathrm{i}\omega[t-t'] - \mathrm{i}\boldsymbol{k}\cdot[\boldsymbol{w}-\boldsymbol{w}'])U_{\omega,\boldsymbol{k},\boldsymbol{w}_0}(\boldsymbol{I}|\boldsymbol{I}')f(\boldsymbol{I}', \boldsymbol{w}', t'). \tag{A4}$$

It is interesting to contrast equation (A3) to the propagator found by Ichimaru (1973) for the uniform plasma. In particular, the gradient of the density profile breaks the stationarity in $\boldsymbol{w} - \boldsymbol{w}_0$ of the propagator, equation (A3). Note also that the first term on the r.h.s. of equation (A3) corresponds to free streaming inside the halo (i.e. dark matter particles describing their unperturbed orbits), and reads in real space

$$G_{\mathrm{free}}(\boldsymbol{I}, \boldsymbol{w}, t|\boldsymbol{I}', \boldsymbol{w}', t') = \sum_{\boldsymbol{k}} \int \mathrm{d}\omega \exp(\mathrm{i}\omega[t-t'] - \mathrm{i}\boldsymbol{k}\cdot[\boldsymbol{w}-\boldsymbol{w}'])\frac{\delta_D(\boldsymbol{I}-\boldsymbol{I}')}{\boldsymbol{k}\cdot\boldsymbol{\omega}-\omega} = \delta_D(\boldsymbol{I}-\boldsymbol{I}')\delta_D(\boldsymbol{w}-\boldsymbol{w}'-\boldsymbol{\omega}[t-t']),$$

while the second term in equation (A4) corresponds to the self-gravitating polarization of the halo induced by the perturbation. Note that since the field dynamical equation is solved with a right-hand side (i.e. a source breaking the mass conservation in phase space), Liouville's theorem is not obeyed anymore: a new fluid is injected into the halo. We may now assume that in equation (A2), $f(\boldsymbol{r}', \boldsymbol{v}', t') = f(\boldsymbol{w}', \boldsymbol{I}', t')$ is split in two: one contribution from dark matter particles exiting R_{200} or beyond R_{200}; another contribution describing particles on R_{200} with negative radial velocity. The former component may then be resumed over the corresponding region of phase space with a $1/|\boldsymbol{r}-\boldsymbol{r}'|$ weight, and yields ψ^e. The latter corresponds to $s^e(t')$.

APPENDIX B: IMPLEMENTATION

Let us describe in this appendix in greater details how Section 2 are implemented in practice, while focusing here on a simple isotropic halo (i.e. $F(\boldsymbol{I}) = F(E)$, where $E = v^2/2 + \Psi(r)$ is the energy, and $\Psi(r)$ the unperturbed potential). We will show here how to compute the operator, $\boldsymbol{K}$ (defined by equation 16) and elements of $\boldsymbol{Q}$ (defined by equation 17), for the corresponding basis, following, e.g. Tremaine & Weinberg (1984), Murali (1999) and Seguin & Dupraz (1994). We will then implement in practice the average induced correlation triggered by some ad hoc coloured radial perturbation. Similarly, one could compute the non-linear coefficients, $[\![\ ]\!]$ entering equation (39), but the implementation of the non-linear formalism of Sections 3 and 4 are beyond the scope of this paper.

B1 Detailed angle–action linear response for isotropic spheres

The 3D nature of galactic halo makes the implementation slightly more complicated than one would think at first sight. The assumption that the halo is spherical allow us to assume that the equilibrium is integrable. Hence, the action space is effectively at most 2D, but configuration space remains 3D (though one angle is mute). In practice, this implies that integration over action space, occurring in, for example, equation (41) is effectively 2D. On the other hand, the sum over $\boldsymbol{k}$ involves three indices, each corresponding to a degree of freedom.

Let us define I_1 as the radial action, $I_2 \triangleq L$ as the total angular momentum and $I_3 \triangleq L_z$ as the z-component of the angular momentum, so that

$$I_1 = \frac{1}{\pi}\int_{r_\mathrm{p}}^{r_\mathrm{a}} \mathrm{d}r \sqrt{2[E-\Psi(r)] - I_2^2/r^2}.$$

Here r_a and r_p are, respectively, the apoapses and periapses of dark matter particles. This defines $\boldsymbol{I} \triangleq (I_1, I_2, I_3)$ introduced in Section 2.1. Similarly, let us define the corresponding angles, $\boldsymbol{w} \triangleq (w_1, w_2, w_3)$ (see Fig. 1) given by

$$w_1 = \omega_1 \int_{r_\mathrm{p}(\boldsymbol{I})}^{r} \frac{\mathrm{d}r}{\sqrt{2[E-\Psi(r)] - I^2/r^2}}, \quad w_2(\boldsymbol{I}, w_1) = \chi - \int_{r_\mathrm{p}(\boldsymbol{I})}^{r(\boldsymbol{I}, w_1)} \frac{\mathrm{d}r(\omega_2 - I_2/r^2)}{\sqrt{2[E-\Psi(r)] - I_2^2/r^2}}, \quad w_3 = \phi - \mathrm{asin}(\cot(\beta)\,\cot(\theta)), \tag{B1}$$

where $\cos\beta = L_z/L$.

B2 Computing the linear response operator

Following *very* closely the notation of Murali (1999), let us introduce a bi-orthogonal basis constructed around spherical harmonics

$$\rho(\boldsymbol{r}, t) = \sum_{\ell m n} a_{\ell m n}(t) d_n^{\ell m}(r) Y_{\ell m}(\boldsymbol{\Omega}) \quad \text{and} \quad \psi(\boldsymbol{r}, t) = \sum_{\ell m n} a_{\ell m n}(t) u_n^{\ell m}(r) Y_{\ell m}(\boldsymbol{\Omega}) \tag{B2}$$

for, respectively, the density and the potential. Weinberg (1989) suggests the following potential–density pair

$$u_n^{\ell m}(r) = -\frac{4\pi G\sqrt{2}}{\alpha_{\boldsymbol{n}}|j_\ell(\alpha_{\boldsymbol{n}})|} R^{-1/2} j_\ell(\alpha_{\boldsymbol{n}} r/R) \quad \text{and} \quad d_n^{\ell m}(r) = -\frac{\alpha_{\boldsymbol{n}}\sqrt{2}}{|j_\ell(\alpha_{\boldsymbol{n}})|} R^{-5/2} j_\ell(\alpha_{\boldsymbol{n}} r/R), \tag{B3}$$

where j_ℓ stands for the spherical Bessel function and where $\alpha_{\boldsymbol{n}}$ obeys the relation $\alpha_{\boldsymbol{n}} j_{\ell-1/2}(\alpha_{\boldsymbol{n}}) = 0$. Here R is the truncation radius of the basis. Hernquist & Ostriker (1992) suggest another set of (non-normalized) bi-orthogonal functions defined by

$$u_n^{\ell m}(r) = -\frac{-r^\ell}{(1+r)^{2\ell+1}}\sqrt{4\pi} C_n^{2\ell+3/2}(\xi) \quad \text{and} \quad d_n^{\ell m}(r) = \frac{K_{n\ell}}{2\pi}\frac{r^{\ell-1}}{(1+r)^{2\ell+3}}\sqrt{4\pi} C_n^{2\ell+3/2}(\xi), \tag{B4}$$

where $K_{n\ell} = n/2(n+4\ell+3)+(\ell+1)(2\ell+1)$, $\xi = (r-1)/(r+1)$ and $C_n^\ell(x)$ stand for ultraspherical polynomials.

The action–angle transform of the potential basis is given by

$$W_{\boldsymbol{k}}^{\ell n}(\boldsymbol{I}) \triangleq \psi_{\boldsymbol{k}}^{\boldsymbol{n}}(\boldsymbol{I}) = \frac{1}{2\pi}\int_{-\pi}^{\pi} \mathrm{d}w_1 \exp(-\mathrm{i}k_1 w_1) u_n^{\ell k_3}(r) \exp[\mathrm{i}k_2(\chi - w_2)]. \tag{B5}$$

We may now rewrite equation (16) as

$$K_{\boldsymbol{n}}^{\boldsymbol{n}'}(\tau - t) = -\delta_{\ell'}^{\ell}\delta_{m'}^{m}\frac{(2\pi)^3}{4\pi G}\iint \mathrm{d}E\frac{L\mathrm{d}L}{\omega_1}\frac{\mathrm{d}F}{\partial E}\sum_{\boldsymbol{k}} C_{\ell k_2}\mathrm{i}\boldsymbol{k}\cdot\boldsymbol{\omega}\exp[\mathrm{i}\boldsymbol{k}\cdot\boldsymbol{\omega}(\tau - t)]W_{\boldsymbol{k}}^{*\ell n'}(\boldsymbol{I})\left[W_{\boldsymbol{k}}^{\ell n}(\boldsymbol{I}) + \frac{4\pi}{3}\delta_\ell^1 p_n^{\ell m} X_{\boldsymbol{k}}(\boldsymbol{I})\right], \tag{B6}$$

where

$$p_n^{1m} = \int \mathrm{d}r r^2 d_n^{1m}(r)\frac{\partial\Psi}{\partial r} \tag{B7}$$

and

$$C_{\ell k_2} = \frac{2^{2k_2-1}}{\pi^2}\frac{(\ell-k_2)!}{(\ell+k_2)!}\frac{\Gamma^2[1/2(\ell+k_2+1)]}{\Gamma^2[1/2(\ell-k_2)+1]}, \quad \text{if} \quad \ell+k_2 \quad \text{even, else} \quad 0. \tag{B8}$$

Here Γ is the standard Gamma function. Note that $X_{\boldsymbol{k}}(\boldsymbol{I})$ accounts for the fact that the response is computed in a non-inertial referential frame. To take into account the barycentric drift of the halo, the perturbed Hamiltonian should include the induced inertial potential $\boldsymbol{a}_b\cdot\boldsymbol{r}$, where $\boldsymbol{a}_b$ is the acceleration of the barycentre in the frame of the unperturbed halo. Its action–angle transform is given by

$$X_{\boldsymbol{k}}(\boldsymbol{I}) = \frac{1}{2\pi}\int_{-\pi}^{\pi}\mathrm{d}w_1\exp(-ik_1w_1)r\exp[ik_2(\psi - w_2)]. \tag{B9}$$

As can be seen from equation (B6), this inertial contribution is limited to the dipole component ($\ell = 1$) of the response: as expected, it is equivalent to a spatially homogeneous field force.[9]

B3 Implementation and validation

The actual computation of the linear response of the halo to a tidal field is a two-step procedure. First, the kernel $\boldsymbol{K}$ must be computed via equation (B6). It involves an integration over the orbits' space and requires to Fourier transforms the bi-orthogonal basis (W and X quantities) along orbits. It can be done by 'throwing orbits' in the equilibrium potential and finding the associated sets of $(\boldsymbol{I}, \boldsymbol{\omega})$ in the halo's model: such a procedure provides the angle dependence of the functions of the basis for a given action. Knowing $W(\boldsymbol{I})$, $X(\boldsymbol{I})$, $\omega(\boldsymbol{I})$ over a given sampling of the $\boldsymbol{I}$ space, equation (B6) can be computed. In order to achieve high computing efficiency and accurate responses, we implemented the calculation of equation (B6) in a parallel fashion, where the integrals in each subspace of the action space are computed by a different processor.

Secondly, the expansion $\boldsymbol{a}(t)$ of the halo's response is computed either by iteration or by means of a Volterra's equation solver (e.g. Press et al. 1992). We found that both methods give very similar results and differ only by their time consumption. The iterative method can be very fast if a proper initial guess is available but if it is not the case it may take a significant amount of time to achieve convergence. Conversely, the Volterra solver's time consumption is fixed for a given time resolution.

In order to validate our implementation, we set up two tests. The first one is suggested by Weinberg (1989). A Plummer's halo is embedded in a homogeneous force field and should experience a global drift described by the response of the potential:

$$\psi(\boldsymbol{r}, t) = -\boldsymbol{r}_b(t)\cdot\nabla\Phi(\boldsymbol{r}), \tag{B10}$$

where $\boldsymbol{r}_b$ stands for the barycentre position and Φ stands for the equilibrium potential. We chose the force field to have a $a_0\sin(\nu t)$ time dependence with $a_0 = 0.01$ and $\nu = 0.01$. The Plummer model has a unit mass M and characteristic radius b. The response was computed using a 60×60 sampling in (E, L) and 20 radial terms of the basis given by equation (B3). We switched off the drift compensation modelled by the X term in equation (B6). Fig. B1 shows the response computed at $t = 10$ (in units of $\sqrt{b^3/GM}$) along with the prediction given by equation (B10). Clearly the two responses coincide, providing a first validation of our implementation.

A second test involves reproducing the contraction of a Hernquist's halo induced by a central spherical mass (which would model the presence of a galaxy, for example). This central mass is assumed to follow a Hernquist's profile, whose potential is given by

$$\Phi(r) = -\frac{GM}{r+a}. \tag{B11}$$

The halo has a unit mass M and characteristic radius a, while the central object has a final mass of $m_\mathrm{p} = 0.001$ and $a_\mathrm{p} = 0.25$ as a constant characteristic radius. The perturber is turned on at $t = 0$ and follows a $m_\mathrm{p}(t) = m_\mathrm{p}(t_\mathrm{f})(3(t/t_\mathrm{f})^2 - 2(t/t_\mathrm{f})^3)$ temporal evolution, where t_f is the final time-step. We compare the linear response at $t = t_\mathrm{f}$ with the simulation of the same test case using a perturbative particle code (Magorrian private communication). The response was computed using a 60×60 sampling in 13 subregions of the whole (E, L) space and 21 radial terms of the basis given by equation (B4). Self-gravity of the response is *not* taken in account in both methods. Fig. B2 shows the comparisons between the two type of calculations, made for two different growing time t_f. Clearly, the two methods are in good agreement. One can see that matter is dragged towards the centre and the longer it takes to grow the perturber, the further from the centre are the affected regions.

[9] Technically speaking, the $\delta_{\ell1}$ dependence arise from the fact that $\boldsymbol{r}$ is expressed as a function of $Y_{1m}(\boldsymbol{\Omega})$ spherical harmonics.

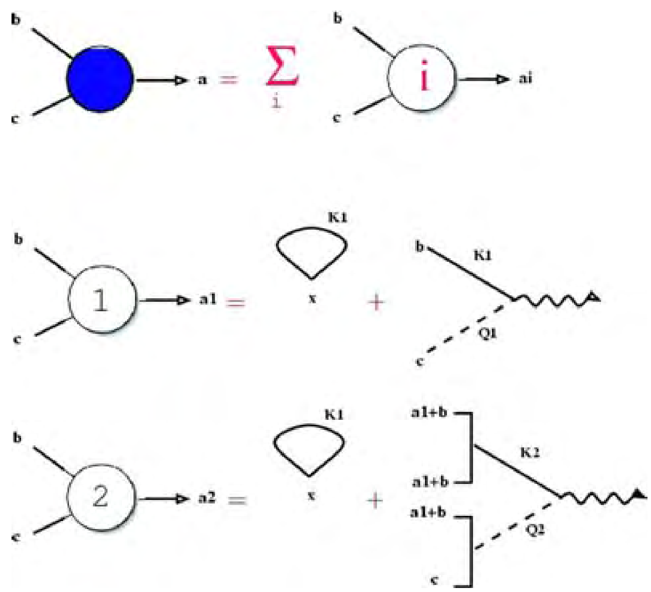

Figure 5. Diagrammatic representation of the expansion to second order given in equations (43)–(44). The top diagram states that one should sum over all orders in the coupling in order to model the non-linear response of the halo; the second diagram from the top stands for equation (43) and the third for equation (44). The loops correspond to the self-coupling, i.e. the self-gravity response of the halo to the perturbing flow. The second diagram corresponds to the 'propagation' of the double excitation (see also Appendix A for a discussion of the distribution function propagator in angle–action variables): the input are the external potential, ψ^e (through its $\boldsymbol{b_n}$ coefficients) and the source, s^e (expanded over the $c_{\boldsymbol{n}}$ coefficients); the output is the coefficient of the expansion of the inner potential. The coupling is achieved via the operator K_i and Q_i defined by equations (42) (Section 3.1.1) and (D4), while the contraction is achieved by equations (45) and (46) and is represented by the wiggly horizontal line.

the dark matter halo in order to account for the relative time ordering of accretion events. It was pointless to describe continuous infall, haloes are typically not in fully phase-mixed equilibria, and the resulting fluctuation spectrum may seed or excite the observed properties of galaxies.

In this paper, we aimed at constructing a self-consistent description of dynamical issues for dark matter haloes embedded in a moderately active cosmic environment. It relied entirely on the assumption that the statistics of the infall is well characterized, as described in Aubert & Pichon (in preparation), and that the mass of the infalling material (or to a lesser extend that of the flyby) should be small compared to the mass of the halo. It also assumed that the halo was spherical and static or evolving adiabatically (Section 4). The emphasis was on the theoretical framework, rather than the details of the actual implementation. In other words, we aimed at describing a self-consistent setting which allows us to propagate the cosmological environment into the core of galactic haloes.

In Section 2, we derived the dynamical equations governing the linear evolution of the induced perturbation by direct infall or tidal excitation of a spherically symmetric (integrable) stationary dark matter halo. The simplified geometry of the initial state allowed us to focus on the specificities of an open system. Specifically, we revisited the influence of the external perturbations on the spherical halo, and extended the results of the literature by considering an advection term in the Boltzmann equation. This approach was compared to the classical Green solution in Appendix A. Note that both the intrinsic properties of the halo, via the distribution function, F (equation 16), and the environment, via (s^e, ψ^e) (equation 17), of the infall and the tidal distortion were accounted for. Clearly, the subclass of problems corresponding to tidal perturbations only will turn out to be easier to implement at first. Appendix B presents the details of the angle–action variables on the sphere together with an explicit expression for the kernel, $\boldsymbol{K}$, and carried out a test case implementation of the statistical propagation of an ensemble of radial excitations with a power-spectrum scaling like ν^{-2}.

In Section 3, we derived the non-linear response of the galactic halo to second order (equation 44) in the perturbation (and to order n in Appendix D together with the corresponding N-point correlation function) to account for tidal stripping and dynamical friction. The dynamics was 'solved' iteratively, in the spirit of the successful approach initiated in cosmology by Fry (1984) and considerably extended by Bernardeau (1992). In particular, we presented and illustrated a set of diagrams (Figs 5 and D1), each corresponding to the contribution of the perturbation expansion. Though the actual implementation of the non-linear theory is going to be CPU intensive, we argue that it will improve our understanding of the competing dynamical processes within a galactic halo. In particular, we discussed how this explicit theory of non-linear dynamics provides the setting in which substructure evolution (and destruction) will have to be carried, in order to account for, e.g. tidal stripping.

In Section 4, we presented the Fokker–Planck equation governing the quasi-linear evolution of the mean profile of the ensemble-averaged halo embedded in its cosmic environment. Specifically, we showed how the infall, drift and diffusion coefficients (equations C13–C15) are related to the two-point correlation of the tidal field and incoming fluxes. Appendix C gives a derivation of this equation from first principles, while in the main text, we focused on the bibliographic context and possible applications. The key physical ingredient behind this secular evolution theory was the stochastic fluctuation caused by the incoming cosmic substructures. The key technical assumption was that the two

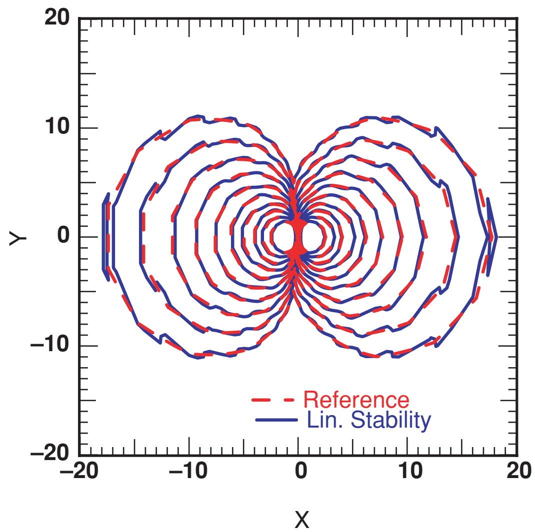

Figure B1. Isocontours in the xy plane of the potential's response of a Plummer sphere embedded in a homogeneous force field (see text for details). The force field is aligned along the x-axis. The dashed line stands for the prediction and the solid line stands for the linear calculation presented in this paper.

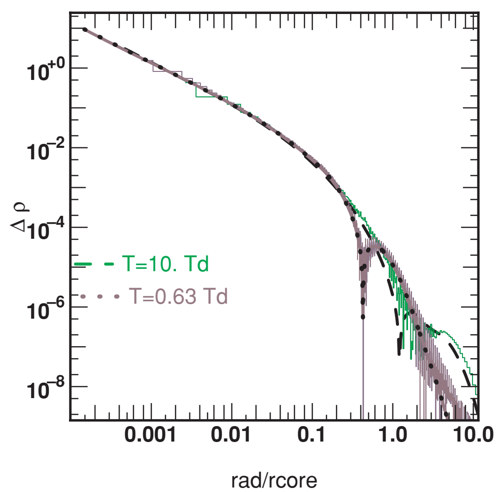

Figure B2. The radial profile of the density response of a Hernquist's halo due to a central perturber. Lines stand for the linear response of the halo as the central perturber grows over a $t = 0.63t_{\rm d}$ (dotted line) and $t = 10t_{\rm d}$ time-scale (dashed line). $t_{\rm d}$ is the dynamical time of the main halo within its core radius. Radii are given in units of the main halo's core radius. Density units are in code units. Superimposed are the calculations of the same response using a perturbative particle simulation (Magorrian private communication). No scaling has been applied and the two methods agree quantitatively.

B4 Statistical propagation: a test case

In this section, we compute the two-point statistics of a halo responding to a simple type of tidal perturbation as an illustration of statistical propagation. Without any assumption on the type of perturbation, we recall that the two-point statistics of the halo's response is given by equation (29) and can be derived directly from the perturbations statistics. Let us simplify the computation of the correlation by assuming that the halo is only tidally perturbed, so that equation (29) reduces to

$$\langle \hat{\boldsymbol{a}} \cdot \hat{\boldsymbol{a}}^{*\top} \rangle = \langle [\hat{\boldsymbol{K}} \cdot \hat{\boldsymbol{b}}] \cdot (\mathbf{1} - \hat{\boldsymbol{K}})^{-1} \cdot (\mathbf{1} - \hat{\boldsymbol{K}})^{-1*\top} \cdot [\hat{\boldsymbol{K}} \cdot \hat{\boldsymbol{b}}]^{\top *} \rangle. \tag{B12}$$

Furthermore, let us also (rather crudely) assume that the tidal field is monopolar, and has a radial dependence equals to the Nth element of the radial basis which diagonalize the Poisson equation. Then, the coefficient of the tidal perturber can be written as

$$b^n_{\ell m}(t) = b(t)\delta_{nN}\delta_{\ell 0}\delta_{m0}, \tag{B13}$$

where the perturbing tidal field is described by

$$\psi^e(r, \boldsymbol{\Omega}, t) = b(t)u^N_{00}(r). \tag{B14}$$

Since no radial coupling occurs, the halo's response can be simply written as

$$\psi(r, \boldsymbol{\Omega}, t) = a(t)u^N_{00}(r). \tag{B15}$$

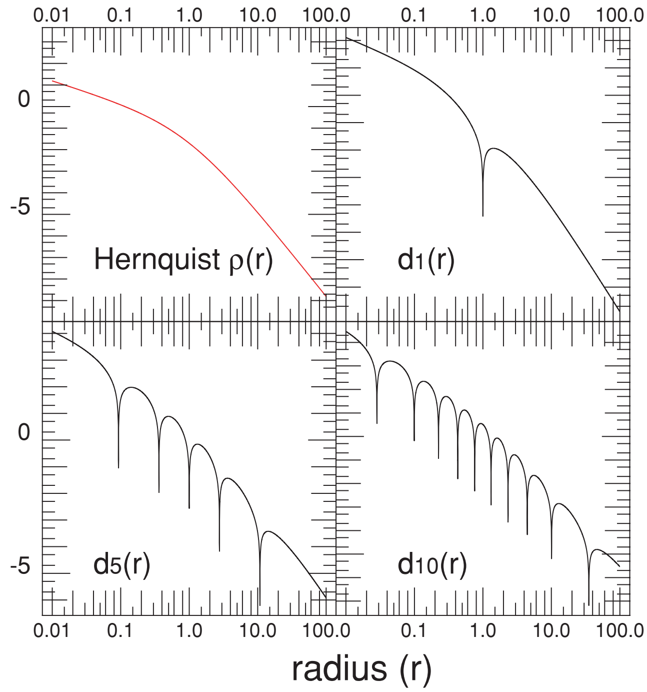

Figure B3. The halo's density profile chosen for the statistical propagation's example follows a hernquist model (top left-hand panel). We apply a monopolar tidal field $\psi^e(r)$ with a radial structure given by the $d^N(r)$ function of the bi-orthogonal basis of Hernquist & Ostriker (1992). Here are shown the corresponding density profiles $\rho^e(r) = \Delta\psi^e/4\pi G$ for $N = 1, 5, 10$.

Consequently, the only remaining degree of freedom is the temporal variation of the tidal field. If we consider an *ensemble* of tidal environments and if we assume stationarity and Gaussianity of the induced perturbations, it will be described by the temporal two-point correlation function of $b(t)$ coefficients, or equivalently by their temporal power spectrum $P_b(\nu)$:

$$P_b(\nu) = \langle \hat{b}(\nu)\hat{b}^*(\nu)\rangle, \tag{B16}$$

where ν stands for the frequency. If the temporal power spectrum of the response is given by $P_a(\nu)$ then equation (B12) reduces to

$$P_a(\nu) = \langle \hat{a}(\nu)\hat{a}^*(\nu)\rangle = \frac{\left|\hat{K}^{00}_{NN}(\nu)\right|^2}{\left|1 - \hat{K}^{00}_{NN}(\nu)\right|^2} P_b(\nu). \tag{B17}$$

Equation (B17) simply states that the frequency structure of the 'tidal noise' is transmitted to haloes via a (scalar) transfer function given by the response kernel.

Let us further describe our test halo again by a Hernquist's model (Hernquist 1990). The corresponding kernel is computed following the procedure described by Section B2 using the Hernquist & Ostriker (1992) potential–density pair (see Fig. B3). Further details can be found in Murali (1999) and Seguin & Dupraz (1994). The radial dependence of the tidal perturber is given by the Nth potential function $u_N(r) = u^{00}_N(r)$ of the basis described by Hernquist & Ostriker (1992). The associated density function is given by $d_N(r) = d_N(r)^{00} = \Delta u_N(r)/4\pi G$ and examples of such profiles are given in Fig. B3 along with the halo's profile. For simplicity, the tidal frequency distribution has been chosen to follow a power law:

$$P_b(\nu) \sim \nu^{-2}. \tag{B18}$$

This power law describes the *ensemble* frequency behaviour and therefore a single realization of the tidal noise may deviate from this relation as long as statistical convergence is achieved. Fig. B4 shows both an example of the time dependence of such a perturber and the time dependence of the induced response. One can see that the halo acts as a low-pass frequency filter and do not recover all the high-frequency features present in the tidal field. Also, the halo response appears as delayed in time, reflecting the effect of the halo's own inertia.

The same computation was performed for an ensemble of 1000 different tidal perturbations. Fig. B5 shows the power spectrum $P_b(\nu)$ averaged over all the realizations along with $P_a(\nu)$ averaged over the 1000 haloes' responses (shown as symbols with error bars). $P_b(\nu)$ departs from a power law at low frequencies ($\nu < 50$ in code units) because of the finite time range over which the tidal field is applied (not shown here). At higher frequencies, the frequency distribution of the perturbers follows exactly equation (B18). Independently, $P_a(\nu)$ is directly predicted from $P_b(\nu)$ using equation (B17), without relying on the computations of individual responses, and shown on the same plot as solid lines. Clearly, the predicted power spectrum of the response matches the statistically averaged one and even reproduces 'bumpy' features seen at various frequencies. The filtering effect of the halo response can still be seen in the predicted spectra: $P_a(\nu)$ follows the ν^{-2} law at low frequencies but exhibits a steeper slope at higher frequencies. This cut-off effect is more important for large-scale perturbations (low N) and

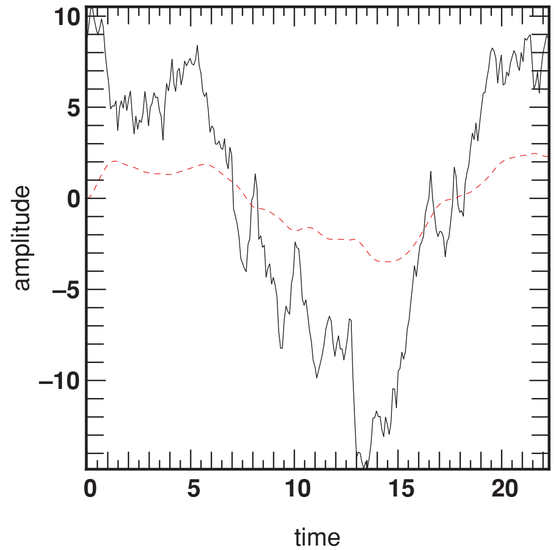

Figure B4. An example of time evolution of the tidal field's amplitude $b(t)$ (plain line). Its power spectrum $P_b(\nu)$ follows a ν^{-2} law. Assuming an $N = 2$ radial dependence, the amplitude $a(t)$ of the induced halo's response can be computed (dashed line). The halo does not respond to high-frequency features and globally its response is slightly delayed, reflecting its own inertia.

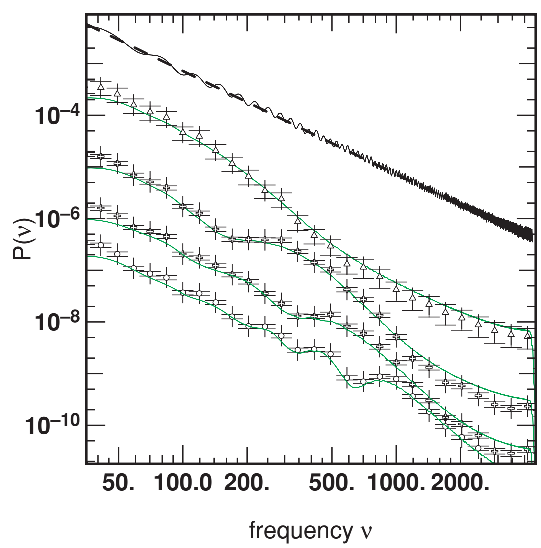

Figure B5. An example of statistical propagation. The average power spectrum of the 1000 tidal perturbations applied to the Hernquist halo (top curve) follows a ν^{-2} law (dashed thick curve). Symbols stand for power spectrum of the halo's response averaged over the 1000 realizations of $\psi^e(r, t)$ with four different radial dependences (with $N = 1, 3, 5, 10$, from top to bottom). The superimposed curves show the direct predictions on the power spectra, following equation (B17). For clarity, these curves have been divided, respectively, by 1, 20, 40 and 70. Frequencies are in code units.

reflects the fact that perturbations at high frequencies are unable to 'resonnate' efficiently with the halo's large-scale modes. Conversely, tidal perturbations with features on small spatial scales (large N) are more likely to induce large frequencies and preserve the frequency structure of the perturbation. Moreover, the 'bumps' seen in the $P_a(\nu)$ curves reflect the eigenfrequencies of the halo. The scale-free spectrum of the perturber hits resonances which react in a stronger fashion than any other frequency. Again, these resonances occur at larger frequencies as the radial order N increases: smaller radial-scale perturbations relate to shorter characteristic time-scales.

The illustration presented in this section is admittedly simplistic but hints at the possibilities which can be foreseen for statistical propagation: for a given set of constrained environment, predictions on the statistics of the induced response can be made without relying on the computation of individual realizations. Predictions on spatial or spatiotemporal correlations of the halo's response can be made following the same procedure. It will possibly allow us to study the impact of the different scales of accretion or potential, the influence of the rate of change of these perturbations and their relative relevance on the statistical properties of matter within the halo as discussed in Section 5.

APPENDIX C: SECULAR EVOLUTION WITH INFALL

Let us derive in this appendix the secular equation for the evolution of the ensemble average halo embedded in a typical cosmic environment (with infall and tidal field). This follows the pioneering work of Weinberg (2001a) and Ma & Bertschinger (2004). The settings in which they derive their coefficients differ: their starting point is the kinetic closure relation given by Klimontovich (1967), Ichimaru (1973) and Gilbert (1970) who note that the BBGKY hierarchy may be closed while assuming that the two-point correlation function will relax on a shorter dynamical time-scale, whereas the one-point distribution function evolves on a longer secular time-scale.[10] Hence, if one assumes that the distribution function F entering the linearized equation (6) can be considered to be constant, then the second-order equation in the BBGKY hierarchy is automatically satisfied while the r.h.s. of the first equation is proportional to the propagated (via equation A3) excess correlation induced by the dressed clumps. This kinetic theory has been successfully applied in plasma physics, leading to the so called Lenard–Balescu (Lenard 1961; Balescu 1963) collision term, and was also transposed by Weinberg (1993) for a multiperiodic 'stellar' system.

Note that the BBGKY hierarchy is a $1/N$ expansion, where N is the number of particles in the system. Formally, it would make sense here to identify N as a measure of the clumpiness of the medium, but this definition is qualitative only. We rely here on the *same* time-ordering hierarchy, but the degree of clumpiness in the system is explicitly imposed by the boundary condition. In this appendix, the derivation is carried from first principles, while relying on an explicit infall and tidal field.

C1 Quasi-linear equations in angle–action variables

The collisionless Boltzmann equation of an open system may be written as

$$\frac{\partial \mathrm{F}}{\partial t} + \{H, \mathrm{F}\} = S^e + s^e, \quad \text{with} \quad H = \frac{v^2}{2} + \Psi(\boldsymbol{I}, \boldsymbol{w}, t, T), \tag{C1}$$

where F is defined by

$$\mathrm{F}(\boldsymbol{I}, \boldsymbol{w}, t, T) = F(\boldsymbol{I}, T) + f(\boldsymbol{I}, \boldsymbol{w}, t) \quad \text{and} \quad \Psi(\boldsymbol{I}, \boldsymbol{w}, t, T) = \Psi_0(\boldsymbol{I}, \boldsymbol{w}, T) + \psi(\boldsymbol{I}, \boldsymbol{w}, t) + \psi^e(\boldsymbol{I}, \boldsymbol{w}, t), \tag{C2}$$

with F describing the secular evolution of the DF and f describing the fluctuations of the DF over this secular evolution. In equation (C1), the r.h.s. stands for the incoming infall, both fluctuating ($s^e[\boldsymbol{I}, \boldsymbol{w}, t]$) and secular ($S^e(\boldsymbol{I}, T)$). Since this system evolves secularly because of its environment, these actions are not conserved. The last two terms on the r.h.s. of equation (C2) represents the fluctuating component tracing the motions of clumps within the environment of the halo.[11] Note that since $F(\boldsymbol{I}, T)$ is assumed to depend here only on the action, it represents a coarse-grained distribution function (averaged over the angles) for which we make no attempt to specify where each star is along its orbit nor how oriented the orbit is. Note also that the canonical variables $\boldsymbol{I}$ and $\boldsymbol{w}$ are the actions and the angles of the *initial* system. Developing the collisionless Boltzmann equation, equation (C1), over the secular and the fluctuating expansion leads to

$$\frac{\partial F}{\partial t} + \frac{\partial f}{\partial t} + \boldsymbol{\omega} \cdot \frac{\partial f}{\partial \boldsymbol{w}} - \frac{\partial \psi}{\partial \boldsymbol{w}} \cdot \left(\frac{\partial F}{\partial \boldsymbol{I}} + \frac{\partial f}{\partial \boldsymbol{I}} \right) - \frac{\partial \psi^e}{\partial \boldsymbol{w}} \cdot \left(\frac{\partial F}{\partial \boldsymbol{I}} + \frac{\partial f}{\partial \boldsymbol{I}} \right) + \left[\frac{\partial \psi}{\partial \boldsymbol{I}} + \frac{\partial \psi^e}{\partial \boldsymbol{I}} \right] \cdot \frac{\partial f}{\partial \boldsymbol{w}} = S^e + s^e. \tag{C3}$$

This equation involves two time-scales, t and T. On the fluctuation time-scale, t, secular quantities can be described as static, leaving only the linearized open collisionless Boltzmann equation (6):

$$\frac{\partial f}{\partial t} + \boldsymbol{\omega} \cdot \frac{\partial f}{\partial \boldsymbol{w}} - \left(\frac{\partial \psi}{\partial \boldsymbol{w}} + \frac{\partial \psi^e}{\partial \boldsymbol{w}} \right) \cdot \frac{\partial F}{\partial \boldsymbol{I}} = s^e, \tag{C4}$$

where the amplitude of f is of first order compared to F and involves only the fluctuating part of the external forcing, $s^e(\boldsymbol{I}, \boldsymbol{w}, t)$. On a longer time-scale, T, the Boltzmann equation, equation (C3) can be T-averaged, considering that the average of fluctuations are zero on such time-scales. This leads to a second equation:

$$\frac{\partial \langle F \rangle}{\partial T} = \left\langle \left[\frac{\partial \psi}{\partial \boldsymbol{w}} + \frac{\partial \psi^e}{\partial \boldsymbol{w}} \right] \cdot \frac{\partial f}{\partial \boldsymbol{I}} \right\rangle_T - \left\langle \left[\frac{\partial \psi}{\partial \boldsymbol{I}} + \frac{\partial \psi^e}{\partial \boldsymbol{I}} \right] \cdot \frac{\partial f}{\partial \boldsymbol{w}} \right\rangle_T + \langle S^e \rangle_T \, . \tag{C5}$$

The brackets denotes averaging over a time longer than the typical time-scale of fluctuations:

$$\langle Y \rangle_T \triangleq 1/\Delta T \int_{T-\Delta T/2}^{T+\Delta T/2} \mathrm{d}t Y(t).$$

The time interval, ΔT, should be chosen so that a given dark matter particle describing its orbit will encounter a few times the incoming clump at various phases along its orbit. Because the incoming clump is subject to dynamical friction, the resonance will only last so long, and induce a finite but small kick, $\Delta \boldsymbol{I}$ during ΔT. Because the infall displays some degree of temporal and spatial coherence, we may not assume that the successive kicks are uncorrelated, in contrast to the situation presented by Weinberg (2001a), Ma & Bertschinger (2004) or the classical image described in Brownian motion. In other words, when we write an effective microscopic Langevin counterpart to the corresponding Fokker–Planck equation, it will involve a coloured 3D random variable (see equation 60).

[10] This time ordering is originally due to Bogolyubov & Gurov (1947).
[11] We neglect here the secular drift of the external potential which should slowly shift the frequencies, $\boldsymbol{\omega}$ in equation (C3).

Derivative and averaging may be exchanged considering that F and Ψ evolve slowly with respect to time. Terms involving the product of two first-order quantities survive to the time averaging because we cannot presume that the response in distribution function and potential within R_{200} are uncorrelated. In order to evaluate those quadratic terms, we may integrate equation (C4), while assuming that $F(\boldsymbol{I}, T)$ is effectively constant with respect to time t. The solution, equation (7), may then be re-injected into the quadratic terms in equation (C5) so that they involves terms such as

$$\frac{\partial f}{\partial \boldsymbol{I}} \cdot \frac{\partial \psi}{\partial \boldsymbol{w}} = -\left(\sum_{\boldsymbol{k}_1, \boldsymbol{k}_2} \mathrm{e}^{\mathrm{i}(\boldsymbol{k}_1+\boldsymbol{k}_2)\cdot \boldsymbol{w}} \psi_{\boldsymbol{k}_2}(\boldsymbol{I}, t) \int_{-\infty}^{t} \mathrm{d}\tau \mathrm{e}^{\mathrm{i}\boldsymbol{k}_1\cdot\boldsymbol{\omega}(\tau-t)} \psi_{\boldsymbol{k}_1}(\boldsymbol{I}, \tau) \boldsymbol{k}_1 \otimes \boldsymbol{k}_2\right) : \frac{\partial^2 F}{\partial \boldsymbol{I}^2}$$
$$-\left(\sum_{\boldsymbol{k}_1, \boldsymbol{k}_2} \mathrm{e}^{\mathrm{i}(\boldsymbol{k}_1+\boldsymbol{k}_2)\cdot \boldsymbol{w}} \boldsymbol{k}_1 \psi_{\boldsymbol{k}_2}(\boldsymbol{I}, t) \boldsymbol{k}_2 \cdot \frac{\partial}{\partial \boldsymbol{I}} \int_{-\infty}^{t} \mathrm{d}\tau \mathrm{e}^{\mathrm{i}\boldsymbol{k}_1\cdot\boldsymbol{\omega}(\tau-t)} \psi_{\boldsymbol{k}_1}(\boldsymbol{I}, \tau)\right) \cdot \frac{\partial F}{\partial \boldsymbol{I}}, \tag{C6}$$

where we may factor the action derivative of $F(\boldsymbol{I}, T)$ out of the τ-time integral because the secular distribution is assumed to be constant over a few dynamical times. Since the hand-hand side of equation (C5) does not depend on $\boldsymbol{w}$, we may average its r.h.s. over $\mathrm{d}\boldsymbol{w}$. This implies that in equation (C6), only the $\boldsymbol{k}_1 = -\boldsymbol{k}_2$ terms remain. We rely effectively on the averaging theorem (Binney & Tremaine (1987)) to convert orbit averages into angle average. The corresponding evolution equation hence depends on the actions only, as expected. Note that in doing so, we assume that no other resonances matter. The secular equation, equation (C5), becomes finally after some similar algebra for the other contributions[12]:

$$\frac{\partial F}{\partial t} = \langle D_0(\boldsymbol{I})\rangle - \langle \boldsymbol{D}_1(\boldsymbol{I})\rangle \cdot \frac{\partial F}{\partial \boldsymbol{I}} - \langle \boldsymbol{D}_2(\boldsymbol{I})\rangle : \frac{\partial^2 F}{\partial \boldsymbol{I}^2}, \tag{C7}$$

where

$$\langle D_0(\boldsymbol{I})\rangle = \frac{1}{(2\pi)^3}\int \langle S_\mathrm{e}\rangle_T \mathrm{d}\boldsymbol{w} + \left\langle \sum_{\boldsymbol{k}} \mathrm{i}\boldsymbol{k} \cdot \frac{\partial}{\partial \boldsymbol{I}}\left(\left[\psi^*_{\boldsymbol{k}}(\boldsymbol{I}, t) + \psi^{e*}_{\boldsymbol{k}}(\boldsymbol{I}, t)\right] \int_{-\infty}^{t} \mathrm{e}^{\mathrm{i}\boldsymbol{k}_1\cdot\boldsymbol{\omega}(\tau-t)} s_\mathrm{e}(\boldsymbol{k}, \boldsymbol{I}, \tau)\mathrm{d}\tau\right)\right\rangle_T, \tag{C8}$$

while the drift coefficient, $\boldsymbol{D}_1$, obeys

$$\langle \boldsymbol{D}_1(\boldsymbol{I})\rangle = \left\langle \sum_{\boldsymbol{k}} \boldsymbol{k}\ \boldsymbol{k} \cdot \frac{\partial}{\partial \boldsymbol{I}}\left(\left[\psi^*_{\boldsymbol{k}}(\boldsymbol{I}, t) + \psi^{e*}_{\boldsymbol{k}}(\boldsymbol{I}, t)\right] \int_{-\infty}^{t} \mathrm{e}^{\mathrm{i}\boldsymbol{k}\cdot\boldsymbol{\omega}(\tau-t)} [\psi_{\boldsymbol{k}}(\boldsymbol{I}, \tau) + \psi^{e}_{\boldsymbol{k}}(\boldsymbol{I}, \tau)]\mathrm{d}\tau\right)\right\rangle_T, \tag{C9}$$

and the diffusion coefficient, $\boldsymbol{D}_2$, is given by

$$\langle \boldsymbol{D}_2(\boldsymbol{I})\rangle = \left\langle \sum_{\boldsymbol{k}} \boldsymbol{k} \otimes \boldsymbol{k}\left[\psi^*_{\boldsymbol{k}}(\boldsymbol{I}, t) + \psi^{e*}_{\boldsymbol{k}}(\boldsymbol{I}, t)\right] \int_{-\infty}^{t} \mathrm{e}^{\mathrm{i}\boldsymbol{k}\cdot\boldsymbol{\omega}(\tau-t)} \left[\psi_{\boldsymbol{k}}(\boldsymbol{I}, \tau) + \psi^{e}_{\boldsymbol{k}}(\boldsymbol{I}, \tau)\right] \mathrm{d}\tau\right\rangle_T. \tag{C10}$$

Note that the infall coefficient, D_0, includes both the secular infall, and a contribution arising from the possible correlation between the fluctuating tidal field and the fluctuating infall. It may be an explicit function of time, T, reflecting the fact that, as more mass is accreted, the profile of dark matter changes with time. The coefficients D_0, $\boldsymbol{D}_1$ and $\boldsymbol{D}_2$ are also an implicit function of time because of the time average, $\langle\ \rangle_T$ and via the secular distribution function, $F(\boldsymbol{I}, T)$, which occurs in $\psi_{\boldsymbol{k}}(\boldsymbol{I}, t)$ through equation (18). Clearly, if the potential and/or the source term are completely decorrelated in time, so that $\langle \psi^*_{\boldsymbol{k}}(\boldsymbol{I}, t)\ \psi^*_{\boldsymbol{k}}(\boldsymbol{I}, \tau)\rangle_T \propto \delta_\mathrm{D}(t-\tau)$ and $\langle \psi^*_{\boldsymbol{k}}(\boldsymbol{I}, t)\ s^{e*}_{\boldsymbol{k}}(\boldsymbol{I}, \tau)\rangle_T \propto \delta_D(t-\tau)$, equation (C10) or (C9) would vanish. Provided ΔT is long compared to the typical correlation time of the potential (and/or the source term), we may take the limit $t \to \infty$ in the integrals entering equations (C8)–(C10). Note, finally, that equation (C7) does not derive from a kinetic theory in the classical sense, in that it does not rely on a diffusion process in velocity space induced by the discrete number of particles in the system.

C2 Linking the infall, drift and diffusion to the cosmic two-point correlations

Up to this point we investigated the secular evolution of a *given* (phase-averaged) halo, undergoing a given inflow and tidal field accretion history. Let us now invoke ergodicity so as to replace temporal averages by ensemble averages in equations (C8)–(C10). In doing so, we now try and describe a *mean* galactic halo embedded in the typical environment presenting the most likely correlations. This involves replacing $\langle\ \rangle_T$ with $\langle\ \rangle \stackrel{\triangle}{=} E\{\ \}$. Let us use equation (10) to expand equation (C10). This yields

$$\langle \boldsymbol{D}_2(\boldsymbol{I}, T)\rangle = \sum_{\boldsymbol{k}} \boldsymbol{k} \otimes \boldsymbol{k} \sum_{\boldsymbol{n}, \boldsymbol{n}'} \left(\int_{-\infty}^{\infty} \left\langle \mathrm{a}^*_{\boldsymbol{n}'}(t)\mathrm{a}_{\boldsymbol{n}}(\tau)\right\rangle \mathrm{e}^{\mathrm{i}\boldsymbol{k}\cdot\boldsymbol{\omega}(\tau-t)}\mathrm{d}\tau\right) \psi^{[\boldsymbol{n}']*}_{\boldsymbol{k}}(\boldsymbol{I})\psi^{[\boldsymbol{n}]}_{\boldsymbol{k}}(\boldsymbol{I}), \tag{C11}$$

where $\mathrm{a}_{\boldsymbol{n}}(t) \stackrel{\triangle}{=} a_{\boldsymbol{n}}(t) + b_{\boldsymbol{n}}(t)$ corresponds to the coefficient of the total (self-consistent plus external) potential. If the first-order perturbations are stationary, let us write the two-point cross-correlation of the temporal fields, $\langle \mathrm{a}_{\boldsymbol{n}}(t), \mathrm{a}_{\boldsymbol{n}'}(\tau)\rangle$ as $\mathrm{C}[\mathrm{a}_{\boldsymbol{n}}, \mathrm{a}_{\boldsymbol{n}'}](t-\tau)$ so that the integral in equation (C11) may be carried as (assuming parity for the correlation function)

$$\int_0^{\infty} \mathrm{C}[\mathrm{a}_{\boldsymbol{n}}, \mathrm{a}_{\boldsymbol{n}'}](\Delta\tau)\mathrm{e}^{\mathrm{i}\boldsymbol{k}\cdot\boldsymbol{\omega}\Delta\tau}\mathrm{d}\Delta\tau = P^{\boldsymbol{n},\boldsymbol{n}'}_{\mathrm{a}}[\boldsymbol{k}\cdot\boldsymbol{\omega}], \tag{C12}$$

[12] Note that when $S^e = s^e = 0$ this equation is conservative by construction.

giving the temporal power spectrum evaluated at the temporal frequency, $\boldsymbol{k}\cdot\boldsymbol{\omega}$. Consequently, the diffusion coefficient becomes

$$\langle \boldsymbol{D}_2(\boldsymbol{I})\rangle = \sum_{\boldsymbol{k}} \boldsymbol{k}\otimes\boldsymbol{k}\sum_{\boldsymbol{n},\boldsymbol{n}'}\psi_{\boldsymbol{k}}^{[\boldsymbol{n}']*}(\boldsymbol{I})\psi_{\boldsymbol{k}}^{[\boldsymbol{n}]}(\boldsymbol{I})P_{\mathrm{a}}^{\boldsymbol{n},\boldsymbol{n}'}[\boldsymbol{k}\cdot\boldsymbol{\omega}]. \tag{C13}$$

The same procedure may be applied to the other coefficient:

$$\langle \boldsymbol{D}_1(\boldsymbol{I})\rangle = \sum_{\boldsymbol{k}} \boldsymbol{k}\sum_{\boldsymbol{n},\boldsymbol{n}'}\boldsymbol{k}\cdot\frac{\partial}{\partial \boldsymbol{I}}\left(\psi_{\boldsymbol{k}}^{[\boldsymbol{n}']*}(\boldsymbol{I})\psi_{\boldsymbol{k}}^{[\boldsymbol{n}]}(\boldsymbol{I})P_{\mathrm{a}}^{\boldsymbol{n},\boldsymbol{n}'}[\boldsymbol{k}\cdot\boldsymbol{\omega}]\right), \tag{C14}$$

while, for the secular correlation (equation C8):

$$\langle D_0(\boldsymbol{I})\rangle = \frac{1}{(2\pi)^3}\int\langle S_{\mathrm{e}}\rangle_T\,\mathrm{d}\boldsymbol{w} + \sum_{\boldsymbol{k}} \boldsymbol{k}\sum_{\boldsymbol{n},\boldsymbol{n}'}\boldsymbol{k}\cdot\frac{\partial}{\partial \boldsymbol{I}}\left(\psi_{\boldsymbol{k}}^{[\boldsymbol{n}']*}(\boldsymbol{I})\sigma_{\boldsymbol{k}}^{[\boldsymbol{n}],e}(\boldsymbol{I})P_{\mathrm{ac}}^{\boldsymbol{n},\boldsymbol{n}'}[\boldsymbol{k}\cdot\boldsymbol{\omega}] \qquad big\right), \tag{C15}$$

where $P_{\mathrm{ac}}^{\boldsymbol{n},\boldsymbol{n}'}[\omega]$ is the mixed power spectrum given by $\langle \hat{a}_{\boldsymbol{n}}^*\hat{c}_{\boldsymbol{n}}\rangle = \langle[\hat{a}_{\boldsymbol{n}}^* + \hat{b}_{\boldsymbol{n}}^*]\hat{c}_{\boldsymbol{n}}\rangle$. Hence

$$P_{\mathrm{ac}}^{\boldsymbol{n},\boldsymbol{n}'}[\boldsymbol{k}\cdot\boldsymbol{\omega}] = \left((\hat{A}_b+1)\times(1)\cdot\langle\hat{\boldsymbol{b}}^*\otimes\hat{\boldsymbol{c}}\rangle + \hat{A}_c\times(1)\cdot\langle\hat{\boldsymbol{c}}^*\otimes\hat{\boldsymbol{c}}\rangle\right)[\boldsymbol{k}\cdot\boldsymbol{\omega}]. \tag{C16}$$

Recall also that (given equations 19 and 49)

$$P_{\mathrm{a}}^{\boldsymbol{n},\boldsymbol{n}'}[\boldsymbol{k}\cdot\boldsymbol{\omega}] = \left((\hat{A}_b+1)\times\left(\hat{A}_b^*+1\right)\cdot\langle\hat{\boldsymbol{b}}\otimes\hat{\boldsymbol{b}}^*\rangle + \hat{A}_c\times\hat{A}_c^*\cdot\langle\hat{\boldsymbol{c}}\otimes\hat{\boldsymbol{c}}^*\rangle + (\hat{A}_b+1)\times\hat{A}_c^*\cdot\langle\hat{\boldsymbol{b}}\otimes\hat{\boldsymbol{c}}^*\rangle + \hat{A}_c\times\left(\hat{A}_b^*+1\right)\cdot\langle\hat{\boldsymbol{c}}\otimes\hat{\boldsymbol{b}}^*\rangle\right)[\boldsymbol{k}\cdot\boldsymbol{\omega}], \tag{C17}$$

where A_b and A_c involve $\boldsymbol{K}$ and therefore the secular distribution function, F, via equation (16). Recall that A_b and A_c involve $(\mathbf{1}-\hat{\boldsymbol{K}})^{-1}$, which reflects the fact that the perturbation is dressed by the self-gravity of the halo. Equation (C7), together with equations (C13)–(C14) and (C17) provides a consistent framework in which to evolve secularly the mean distribution of a galactic halo within its cosmic environment. Note that it is possible via equation (51) to apply non-linear corrections to the induced correlation within R_{200}.

APPENDIX D: PERTURBATION THEORY TO HIGHER ORDER

D1 Perturbative dynamical equations

In this section, we 'solve' the dynamical equation to order *n*, which will allow us in the next section to present the *N*-point correlation to order *n*.

D1.1 Perturbation theory to all orders

Recall that for $n \geqslant 2$, $f_{\boldsymbol{k}}^{(n)}(\boldsymbol{I},t)$obeys equation (34). Given equation (15), it follows that

$$\begin{aligned} a_{\boldsymbol{p}}^{(n)}(t) = &\sum_{\boldsymbol{q},\boldsymbol{k}}\int \mathrm{d}\tau\,\exp(\mathrm{i}\boldsymbol{k}\cdot\boldsymbol{\omega}[\tau-t])\left[a_{\boldsymbol{q}}^{(n)}(\tau)+\delta_1^n\,b_{\boldsymbol{q}}(\tau)\right]\left((2\pi)^3\int\mathrm{d}\boldsymbol{I}\,\psi_{\boldsymbol{k}}^{[\boldsymbol{n}]}(\boldsymbol{I})\psi_{\boldsymbol{k}}^{[\boldsymbol{p}]*}(\boldsymbol{I})\frac{\partial F}{\partial \boldsymbol{I}}\cdot\mathrm{i}\boldsymbol{k}\right)\\ &-\sum_{k=1}^{n-1}\sum_{\boldsymbol{q},\boldsymbol{k}}\int\mathrm{d}\tau\,\exp(\mathrm{i}\boldsymbol{k}\cdot\boldsymbol{\omega}[\tau-t])\left[a_{\boldsymbol{q}}^{(k)}(\tau)+\delta_1^k\,b_{\boldsymbol{q}}(\tau)\right]\left((2\pi)^3\int\mathrm{d}\boldsymbol{I}\left\{\psi^{[\boldsymbol{q}]}(\boldsymbol{w},\boldsymbol{I}),\,f^{(n-k)}(\boldsymbol{w},\boldsymbol{I},t)\right\}_{\boldsymbol{k}}\psi_{\boldsymbol{k}}^{[\boldsymbol{p}]*}(\boldsymbol{I})\right), \end{aligned} \tag{D1}$$

where the first term in equation (D1) corresponds to the usual self-gravity coupling at order *n*, and the sum corresponds to the feed of lower-order potential coupling into the *n*th order equation. Here $f_{\boldsymbol{k}}^{(n)}(\boldsymbol{I},t)$ obeys

$$\begin{aligned} f_{\boldsymbol{k}}^{(n)}(\boldsymbol{I},t) = &\sum_{\boldsymbol{q}}\int\mathrm{d}\tau\,\exp(\mathrm{i}\boldsymbol{k}\cdot\boldsymbol{\omega}[\tau-t])\times\left[\frac{\partial F}{\partial\boldsymbol{I}}\cdot\mathrm{i}\boldsymbol{k}\,\psi_{\boldsymbol{k}}^{[\boldsymbol{q}]}\left[a_{\boldsymbol{q}}^{(n)}(\tau)+\delta_1^n\,b_{\boldsymbol{q}}(\tau)\right]+\sum_{k=1}^{n-1}\left[a_{\boldsymbol{q}}^{(k)}(\tau)+\delta_1^k\,b_{\boldsymbol{q}}(\tau)\right]\left\{f^{(n-k)},\,\psi_{\boldsymbol{k}}^{[\boldsymbol{q}]}\right\}_{\boldsymbol{k}}\right]\\ &+\sum_{\boldsymbol{q}}\int\mathrm{d}\tau\,\exp(\mathrm{i}\boldsymbol{k}\cdot\boldsymbol{\omega}[\tau-t])c_{\boldsymbol{q}}(\tau)\delta_{\boldsymbol{n}}^1\sigma_{\boldsymbol{k}}^{e,[\boldsymbol{q}]}. \end{aligned} \tag{D2}$$

Note that the response in equation (D2) is, as expected, out of phase with respect to the potential excitation, $a_{\boldsymbol{n}}(\tau)$ because of inertia (hence the modulation in $\exp\,(\mathrm{i}\boldsymbol{k}\cdot\omega(\tau-t))$). Now, to *n*th order equation (D1), (D2) may be rewritten formally as (using the contraction rule equation 46)

$$\begin{aligned} \boldsymbol{a}^{(n)} = &\boldsymbol{K}_1\cdot\boldsymbol{a}^{(n)} + \boldsymbol{K}_2\cdot\left(\sum_{i_1+i_2=n}\left[\boldsymbol{a}^{(i_1)}+\delta_{i_1}^1 b\right]\otimes\left[\boldsymbol{a}^{(i_2)}+\delta_{i_2}^1\boldsymbol{b}\right]\right)+\cdots+\boldsymbol{K}_j\cdot\left(\sum_{i_1+\cdots+i_j=n}\bigotimes_j\left[\boldsymbol{a}^{(i_1)}+\delta_{i_1}^1\boldsymbol{b}\right]\right)+\cdots+\boldsymbol{K}_n\cdot\bigotimes_n\left[\boldsymbol{a}^{(1)}+\boldsymbol{b}\right]\\ &+\boldsymbol{Q}_2\cdot\left(\boldsymbol{a}^{(n-1)}\otimes\boldsymbol{c}\right)+\cdots+\boldsymbol{Q}_j\cdot\left(\sum_{i_1+\cdots+i_j=n-1}\left[\bigotimes\left[\boldsymbol{a}^{(i_1)}+\delta_{i_1}^1\boldsymbol{b}\right]\right]\otimes\boldsymbol{c}\right)+\cdots+\boldsymbol{Q}_n\cdot\left[\bigotimes_{n-1}\left[\boldsymbol{a}^{(1)}+\boldsymbol{b}\right]\right]\otimes\boldsymbol{c}, \end{aligned} \tag{D3}$$

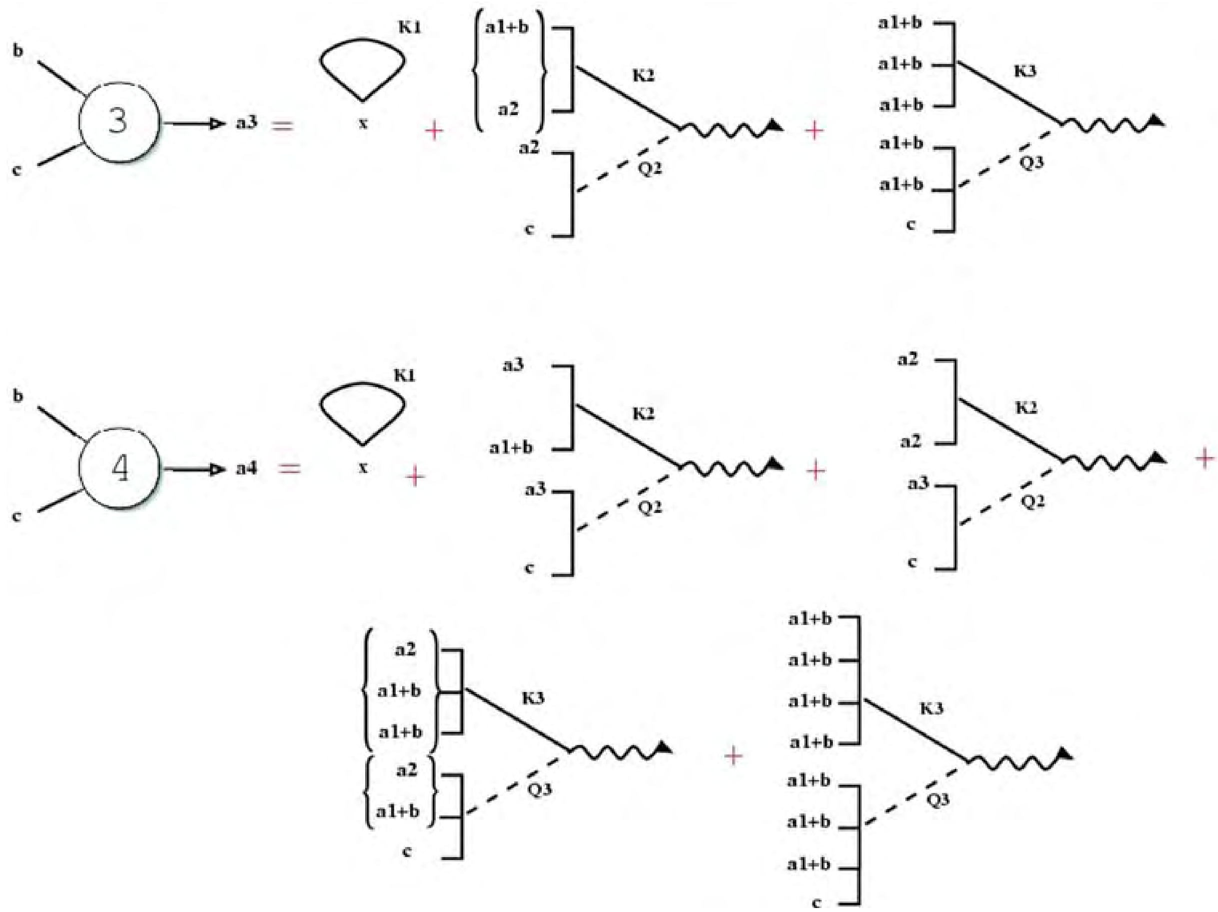

Figure D1. Diagrammatic representation of the expansion to third order (top diagram, corresponding to equation D5) and fourth order (bottom diagram, given equation D6); again (see Fig. 5 for details) the coupling of the tidal interaction (through the b_n coefficients) and the incoming infall (expanded over the c_n coefficients) yields the coefficient of the response inside R_{200}. The coupling is achieved via the operator $\boldsymbol{K}_i$ and $\boldsymbol{Q}_i$ as explained in Fig. D2; the curly brace in front of the diagrams account for the number of such diagrams entering the expansion, corresponding to the permutation of the input (recalling that the order matters). Note also for each branch the sum of the order of the subbranch correspond to the order of the expansion.

where the kernels $\boldsymbol{K}_1$ and $\boldsymbol{K}_2$ are given by equations (41)–(42), while $\boldsymbol{K}_n$, $n \geqslant 2$ obey formally

$$(\boldsymbol{K}_n)_{\boldsymbol{p},\boldsymbol{q}_1,\boldsymbol{q}_2,\ldots,\boldsymbol{q}_n}[\tau_1 - t, \tau_2 - \tau_1, \ldots, \tau_n - \tau_{n-1}] = [2\pi]^3 \sum_{\boldsymbol{k}} \int \mathrm{d}\boldsymbol{I} \exp(\mathrm{i}\boldsymbol{k}\cdot\boldsymbol{\omega}[\tau_1 - t]) \sum_{\boldsymbol{k}_1+\boldsymbol{k}_2=\boldsymbol{k}} \left\llbracket \exp(\mathrm{i}\boldsymbol{k}_1\cdot\boldsymbol{\omega}[\tau_2-\tau_1]) \cdots \right.$$
$$\left. \times \sum_{\boldsymbol{k}_{2n-1}+\boldsymbol{k}_{2n}=\boldsymbol{k}_n} \left\llbracket \exp(\mathrm{i}\boldsymbol{k}_{2n-3}\cdot\boldsymbol{\omega}[\tau_n-\tau_{n-1}]) \frac{\partial F}{\partial \boldsymbol{I}} \cdot \mathrm{i}\boldsymbol{k}_{2n-3}\psi^{[\boldsymbol{q}_n]}_{\boldsymbol{k}_{2n-3}}, \psi^{[\boldsymbol{q}_{n-1}]}_{\boldsymbol{k}_{2n-2}} \right\rrbracket \cdots, \psi^{[\boldsymbol{q}_2]}_{\boldsymbol{k}_4} \right\rrbracket, \psi^{[\boldsymbol{q}_1]}_{\boldsymbol{k}_2} \right\rrbracket \psi^{[\boldsymbol{p}]*}_{\boldsymbol{k}}. \qquad \text{(D4)}$$

Note that the nth order Kernel involves 'only' one integral over action space, but n couplings in configuration space and $n+1$ time-ordered instants $(t, \tau_1, \ldots, \tau_n)$. Note also that equation (D1) implies that secular perturbation theory accounts for both the rate of change in frequency of the system, via $\partial^n\omega/\partial\boldsymbol{I}^n$, the rate of change in equilibrium via $\partial^n F/\partial\boldsymbol{I}^n$ but also the rate of change in the incoming flow via $\partial^n\sigma^{[p],e}/\partial\boldsymbol{I}^n$. Note, finally, that the relative phases (causality) are accounted for via the ordered time integrals. For instance, equation (D3) reads to third order as

$$\boldsymbol{a}^{(3)} = \boldsymbol{K}_1\cdot\boldsymbol{a}^{(3)} + \boldsymbol{K}_2\cdot\left(\left[\boldsymbol{a}_1^{(1)}+\boldsymbol{b}\right]\otimes\boldsymbol{a}^{(2)} + \boldsymbol{a}^{(2)}\otimes\left[\boldsymbol{a}^{(1)}+\boldsymbol{b}\right]\right)$$
$$+\boldsymbol{K}_3\cdot\left(\left[\boldsymbol{a}^{(1)}+\boldsymbol{b}\right]\otimes\left[\boldsymbol{a}^{(1)}+\boldsymbol{b}\right]\otimes\left[\boldsymbol{a}^{(1)}+\boldsymbol{b}\right]\right) + \boldsymbol{Q}_3\cdot\left(\left[\boldsymbol{a}_1^{(1)}+\boldsymbol{b}\right]\otimes\left[\boldsymbol{a}_1^{(1)}+\boldsymbol{b}\right]\otimes\boldsymbol{c}\right) + \boldsymbol{Q}_2\cdot\boldsymbol{a}^{(2)}\otimes\boldsymbol{c}, \qquad \text{(D5)}$$

and is illustrated in Fig. D1 together with $\boldsymbol{a}^{(4)}$

$$\boldsymbol{a}^{(4)} = \boldsymbol{K}_1\cdot\boldsymbol{a}^{(4)} + \boldsymbol{K}_2\cdot\left(\boldsymbol{a}^{(3)}\otimes\left[\boldsymbol{a}^{(1)}+\boldsymbol{b}\right] + \left[\boldsymbol{a}^{(1)}+\boldsymbol{b}\right]\otimes\boldsymbol{a}^{(3)} + \boldsymbol{a}^{(2)}\otimes\boldsymbol{a}^{(2)}\right)$$
$$+\boldsymbol{K}_3\cdot\left(\boldsymbol{a}^{(2)}\otimes\left[\boldsymbol{a}^{(1)}+\boldsymbol{b}\right]\otimes\left[\boldsymbol{a}^{(1)}+\boldsymbol{b}\right] + \left[\boldsymbol{a}^{(1)}+\boldsymbol{b}\right]\otimes\boldsymbol{a}^{(2)}\otimes\left[\boldsymbol{a}^{(1)}+\boldsymbol{b}\right] + \left[\boldsymbol{a}^{(1)}+\boldsymbol{b}\right]\otimes\left[\boldsymbol{a}^{(1)}+\boldsymbol{b}\right]\otimes\boldsymbol{a}^{(2)}\right)$$
$$+\boldsymbol{K}_4\cdot\left[\boldsymbol{a}^{(1)}+\boldsymbol{b}\right]\otimes\left[\boldsymbol{a}^{(1)}+\boldsymbol{b}\right]\otimes\left[\boldsymbol{a}^{(1)}+\boldsymbol{b}\right]\otimes\left[\boldsymbol{a}^{(1)}+\boldsymbol{b}\right]$$
$$+\boldsymbol{Q}_2\cdot\left(\boldsymbol{a}^{(3)}\otimes\boldsymbol{c}\right) + \boldsymbol{Q}_3\cdot\left(\boldsymbol{a}^{(2)}\otimes\left[\boldsymbol{a}^{(1)}+\boldsymbol{b}\right]\otimes\boldsymbol{c} + \left[\boldsymbol{a}^{(1)}+\boldsymbol{b}\right]\otimes\boldsymbol{a}^{(2)}\otimes\boldsymbol{c}\right) + \boldsymbol{Q}_4\cdot\left[\boldsymbol{a}^{(1)}+\boldsymbol{b}\right]\otimes\left[\boldsymbol{a}^{(1)}+\boldsymbol{b}\right]\otimes\left[\boldsymbol{a}^{(1)}+\boldsymbol{b}\right]\otimes\boldsymbol{c}. \qquad \text{(D6)}$$

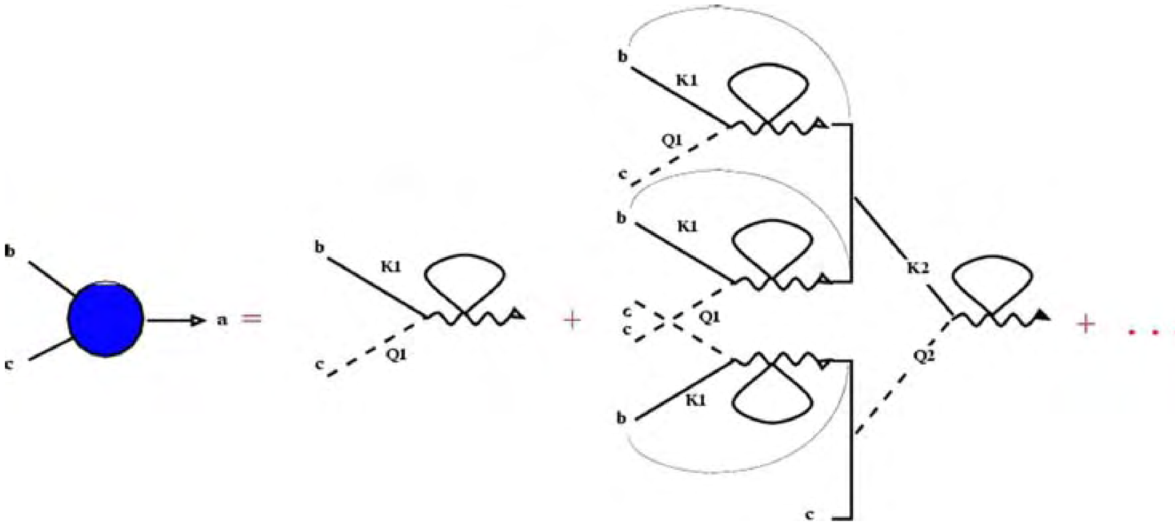

Figure D2. Reordered diagrammatic representation to second order (first order included) of the expansion given in equations (43)–(44). This time only b_n and c_n are inputs. The closed loop accounts for the self-gravity and represents $(1-\hat{\boldsymbol{K}}_1)^{-1}$. The thin loop traces the fact that the perturbed potential contributes also directly to the second-order term via $\boldsymbol{a}_1 + \boldsymbol{b}$ (see equation 44 for details). Note that in each diagram, each oblique line represents a sum over $\boldsymbol{k}$ and a time integral. The dashed line stands for infall coupling, while the thick line stands for the tidal coupling.

Note that equation (D6) depends recursively on equation (D5) and both depends recursively on equations (44) and (43). When the recursion is carried through (see Fig. D2) the expected relative complexity of the non-linear evolution appears clearly.

D1.2 Reordering to higher order

In the main text, we give in equation (53) and above the first- and second-order reshuffling of the perturbation in $\boldsymbol{b}$ and $\boldsymbol{c}$. Similarly, the third-order term reads in terms of products of $\boldsymbol{b}$ and $\boldsymbol{c}$ as

$$\boldsymbol{a}^{(3)} = A_{bbb}\cdot\boldsymbol{b}\otimes\boldsymbol{b}\otimes\boldsymbol{b} + A_{ccc}\cdot\boldsymbol{c}\otimes\boldsymbol{c}\otimes\boldsymbol{c} + A_{bbc}\cdot\boldsymbol{b}\otimes\boldsymbol{b}\otimes\boldsymbol{c} + A_{ccb}\cdot\boldsymbol{c}\otimes\boldsymbol{c}\otimes\boldsymbol{b}$$
$$+ A_{bcb}\cdot\boldsymbol{b}\otimes\boldsymbol{c}\otimes\boldsymbol{b} + A_{cbb}\cdot\boldsymbol{c}\otimes\boldsymbol{b}\otimes\boldsymbol{b} + A_{bcc}\cdot\boldsymbol{b}\otimes\boldsymbol{c}\otimes\boldsymbol{c} + A_{cbc}\cdot\boldsymbol{c}\otimes\boldsymbol{b}\otimes\boldsymbol{c},$$

where (following the same convention as in the main text for the brackets)

$$A_{bbb} = \boldsymbol{K}'_3\circ\boldsymbol{K}''_1 + \boldsymbol{K}'_2\circ[\boldsymbol{K}''_1, \boldsymbol{K}'_2\circ\boldsymbol{K}''_1] + \boldsymbol{K}'_2\circ[\boldsymbol{K}'_2\circ\boldsymbol{K}''_1, \boldsymbol{K}''_1],$$

$$A_{ccc} = \boldsymbol{K}'_3\circ\boldsymbol{Q}'_1 + \boldsymbol{K}'_2\circ\{[\boldsymbol{Q}'_1, \boldsymbol{K}'_2\circ\boldsymbol{Q}'_1 + \boldsymbol{Q}'_2\circ[\boldsymbol{Q}'_1,\mathbf{1}]] + [\boldsymbol{K}'_2\circ\boldsymbol{Q}'_1 + \boldsymbol{Q}'_2\circ[\boldsymbol{Q}'_1,\mathbf{1}], \boldsymbol{Q}'_1]\} + \boldsymbol{Q}'_3\circ[\boldsymbol{Q}'_1,\boldsymbol{Q}'_1,\mathbf{1}]$$
$$+ \boldsymbol{Q}'_2\circ[\boldsymbol{K}'_2\circ\boldsymbol{Q}'_1 + \boldsymbol{Q}'_2\circ\boldsymbol{Q}'_1,\mathbf{1}],\mathbf{1}],$$

$$A_{bbc} = \boldsymbol{K}'_3\circ[\boldsymbol{K}''_1,\boldsymbol{K}''_1,\boldsymbol{Q}'_1] + \boldsymbol{Q}'_3\circ[\boldsymbol{K}''_1,\boldsymbol{K}''_1,\mathbf{1}] + \boldsymbol{K}'_2\circ[\boldsymbol{K}''_1, \boldsymbol{K}'_2\circ[\boldsymbol{K}''_1,\boldsymbol{Q}'_1] + \boldsymbol{Q}'_2\circ[\boldsymbol{K}''_1,\mathbf{1}]],$$

$$A_{bcb} = \boldsymbol{K}'_3\circ[\boldsymbol{K}''_1,\boldsymbol{Q}'_1,\boldsymbol{K}''_1] + \boldsymbol{K}'_2\circ[\boldsymbol{K}'_2\circ[\boldsymbol{K}''_1,\boldsymbol{Q}'_1] + \boldsymbol{Q}'_2\circ[\boldsymbol{K}''_1,\mathbf{1}],\boldsymbol{K}''_1],$$

$$A_{ccb} = \boldsymbol{K}'_3\circ[\boldsymbol{Q}'_1,\boldsymbol{Q}'_1,\boldsymbol{K}''_1] + \boldsymbol{K}'_2\circ[\boldsymbol{Q}'_1,\boldsymbol{K}'_2\circ[\boldsymbol{Q}'_1,\boldsymbol{K}''_1]],$$

$$A_{cbb} = \boldsymbol{K}'_3\circ[\boldsymbol{Q}''_1,\boldsymbol{K}''_1,\boldsymbol{K}''_1] + \boldsymbol{K}'_2\circ[\boldsymbol{Q}'_1,\boldsymbol{K}'_2\circ\boldsymbol{K}''_1],$$

$$A_{bcc} = \boldsymbol{K}'_3\circ[\boldsymbol{K}''_1,\boldsymbol{Q}'_1,\boldsymbol{Q}'_1] + \boldsymbol{Q}'_3\circ[\boldsymbol{K}''_1,\boldsymbol{Q}'_1,\mathbf{1}] + \boldsymbol{K}'_2\circ[\boldsymbol{K}''_1,\boldsymbol{K}'_2\circ\boldsymbol{Q}'_1 + \boldsymbol{Q}'_2\circ[\boldsymbol{Q}'_1,\mathbf{1}]] + \boldsymbol{K}'_2\circ[\boldsymbol{K}''_1,\boldsymbol{K}'_2\circ\boldsymbol{Q}'_1 + \boldsymbol{Q}'_2\circ[\boldsymbol{Q}'_1,\mathbf{1}]]$$
$$+ \boldsymbol{Q}'_2\circ[\boldsymbol{K}'_2\circ[\boldsymbol{K}''_1,\boldsymbol{Q}'_1] + \boldsymbol{Q}'_2\circ[\boldsymbol{K}''_1,\mathbf{1}],\mathbf{1}],$$

$$A_{cbc} = \boldsymbol{K}'_3\circ[\boldsymbol{Q}'_1,\boldsymbol{K}''_1,\boldsymbol{Q}'_1] + \boldsymbol{Q}'_3\circ[\boldsymbol{Q}''_1,\boldsymbol{K}'_1,\mathbf{1}] + \boldsymbol{K}'_2\circ[\boldsymbol{K}'_2\circ[\boldsymbol{Q}'_1,\boldsymbol{K}''_1],\boldsymbol{K}''_1] + \boldsymbol{K}'_2\circ[\boldsymbol{Q}'_1,\boldsymbol{K}'_2\circ[\boldsymbol{K}''_1,\boldsymbol{Q}'_1] + \boldsymbol{Q}'_2\circ[\boldsymbol{K}''_1,\mathbf{1}]]$$
$$+ \boldsymbol{Q}'_2\circ[\boldsymbol{K}'_2\circ[\boldsymbol{Q}'_1,\boldsymbol{K}''_1],\mathbf{1}]. \tag{D7}$$

Generically, after reordering, equation (53) becomes

$$a^{(n)}_{\boldsymbol{p}}(t) = \left(\sum_{\boldsymbol{i}_1,\ldots,\boldsymbol{i}_n\in[\boldsymbol{b},\boldsymbol{c}]} A_{\boldsymbol{i}_1\cdots\boldsymbol{i}_n}\cdot(\boldsymbol{i}_1\otimes\cdots\otimes\boldsymbol{i}_n)\right)_{\boldsymbol{p}}(t),$$
$$= \sum_{\boldsymbol{i}_1,\ldots,\boldsymbol{i}_n\in[\boldsymbol{b},\boldsymbol{c}]}\int_{-\infty}^{t}\mathrm{d}\tau_1\cdots\int_{-\infty}^{\tau_n-1}\mathrm{d}\tau_n\sum_{\boldsymbol{q}_1\cdots\boldsymbol{q}_n}\left[A_{\boldsymbol{i}_1\cdots\boldsymbol{i}_n}\right]_{\boldsymbol{p},\boldsymbol{q}_1,\ldots,\boldsymbol{q}_n}(t-\tau_1,\ldots,\tau_n-\tau_{n-1})[\boldsymbol{i}_1]_{\boldsymbol{q}_1}(\tau_1)\cdots[\boldsymbol{i}_n]_{\boldsymbol{q}_n}(\tau_n), \tag{D8}$$

which involves 2^n terms. Here $[A_{\boldsymbol{i}_1\ldots\boldsymbol{i}_n}]_{\boldsymbol{p},\boldsymbol{q}_1,\ldots,\boldsymbol{q}_n}(\theta_1,\ldots,\theta_n)$ is some linear tensor of order $n+1$ which returns the nth order response to the excitation $b_i(\theta)$, $c_j(\theta)$ at various times $\theta_1,\theta_2,\ldots,\theta_\mathrm{p}$. Note that it involve the equilibrium distribution function, F_0 and its derivatives with respect to the actions, $\boldsymbol{I}$, together with the properties of the basis function.

D2 The *N*-point correlation function

In the main text, we presented the calculation of the two-point correlation of the fields within the R_{200} sphere. More generally, we are interested in the N-point correlation of, say, the density (at various times):

$$
\begin{aligned}
C_N &\stackrel{\triangle}{=} \langle \rho(x_1)\rho(x_2)\cdots\rho(x_N)\rangle = \sum_{n=N}^{\infty} \varepsilon^n \sum_{p_1+p_2+\cdots+p_N=n} \left\langle \rho^{(p_1)}(x_1)\rho^{(p_2)}(x_2)\cdots\rho^{(p_N)}(x_N)\right\rangle \\
&= \sum_{n=N} \varepsilon^n \sum_{p_1+p_2+\cdots+p_N=n} \sum_{\boldsymbol{q}_1,\ldots,\boldsymbol{q}_N} \rho^{[\boldsymbol{q}_1]}(\boldsymbol{r}_1)\cdots\rho^{[\boldsymbol{q}_N]}(\boldsymbol{r}_N)\left\langle a^{(p_1)}_{\boldsymbol{q}_1}(\tau_1)\cdots a^{(p_N)}_{\boldsymbol{q}_N}(\tau_N)\right\rangle.
\end{aligned} \tag{D9}
$$

Now, solutions to the nth order perturbation theory are given by equation (D8). It follows that

$$
\begin{aligned}
\left\langle a^{(p_1)}_{\boldsymbol{q}_1}(\tau_1)\cdots a^{(p_N)}_{\boldsymbol{q}_N}(\tau_N)\right\rangle = &\sum_{\boldsymbol{i}_1,\ldots,\boldsymbol{i}_{p_1}\in[\boldsymbol{b},\boldsymbol{c}]}\cdots\sum_{\boldsymbol{i}_1,\ldots,\boldsymbol{i}_{p_N}\in[\boldsymbol{b},\boldsymbol{c}]}\ \sum_{\boldsymbol{q}_{1,1},\ldots,\boldsymbol{q}_{p_N,p_N}} \int \mathrm{d}^{p_1}\theta\left[A_{\boldsymbol{i}_1\cdots\boldsymbol{i}_{p_1}}\right]_{\boldsymbol{q}_1,\boldsymbol{q}_{1,1},\ldots,\boldsymbol{q}_{1,p_1}}(\tau_1,\theta_{1,1},\ldots,\theta_{1,p_1})\cdots \\
&\times\int \mathrm{d}^{p_N}\theta\left[A_{\boldsymbol{i}_1\cdots\boldsymbol{i}_{p_N}}\right]_{\boldsymbol{q}_N,\boldsymbol{q}_{p_N,1},\ldots,\boldsymbol{q}_{p_N,p_N}}(\tau_N,\theta_{1,p_1},\ldots,\theta_{p_N,p_N}) \\
&\times\langle[\boldsymbol{i}_1]_{\boldsymbol{q}_{1,1}}(\theta_{1,1})\cdots[\boldsymbol{i}_{p_1}]_{\boldsymbol{q}_{1,p_1}}(\theta_{p_N,1})\cdots[\boldsymbol{i}_{p_N}]_{\boldsymbol{q}_{1,p_N}}(\theta_{1,p_N})\cdots[\boldsymbol{i}_{p_N}]_{\boldsymbol{q}_{p_N p_N}}(\theta_{p_N,p_N})\rangle.
\end{aligned} \tag{D10}
$$

If the perturbation is a centred Gaussian random field, Wick's theorem states that

$$
\begin{aligned}
&\langle[\boldsymbol{i}_1]_{\boldsymbol{q}_{1,1}}(\theta_{1,1})\cdots[\boldsymbol{i}_{p_1}]_{\boldsymbol{q}_{1,p_1}}(\theta_{p_N,1})\cdots[\boldsymbol{i}_{p_N}]_{\boldsymbol{q}_{1,p_N}}(\theta_{1,p_N})\cdots[\boldsymbol{i}_{p_N}]_{\boldsymbol{q}_{p_N p_N}}(\theta_{p_N,p_N})\rangle \\
&\quad=\sum_{\text{all permutations}}\prod\langle[\boldsymbol{i}_1]_{\boldsymbol{q}_{1,1}}(\theta_{1,1})[\boldsymbol{i}_{p_1}]_{\boldsymbol{q}_{1,p_1}}(\theta_{p_N,1})\rangle\cdots\langle[\boldsymbol{i}_{p_N}]_{\boldsymbol{q}_{1,p_N}}(\theta_{1,p_N})[\boldsymbol{i}_{p_N}]_{\boldsymbol{q}_{p_N p_N}}(\theta_{p_N,p_N})\rangle.
\end{aligned} \tag{D11}
$$

Putting equations (D10)–(D11) into (D9) yields formally the N-point correlation function to arbitrary order. A special case in given in the main text corresponding to third-order expansion of the two-point correlation, equation (34). The N-point correlation of other (possibly mixed) moments of the distribution function may be computed following the same route.

D2.1 Synthetic hierarchy

D3 Perturbation theory in the complex Fourier plane

Let us close this appendix by a presentation of the perturbative solutions in the complex Fourier plane. In frequency space, equation (39) reads

$$
\begin{aligned}
\hat{a}^{(2)}_{\boldsymbol{p}}(\omega) = &\sum_{\boldsymbol{q}_1}\hat{a}^{(2)}_{\boldsymbol{q}_1}(\omega)\left([2\pi]^3\sum_{\boldsymbol{k}}\int \mathrm{d}\boldsymbol{I}\,\psi^{[\boldsymbol{q}_1]}_{\boldsymbol{k}}(\boldsymbol{I})\psi^{[\boldsymbol{p}]}_{\boldsymbol{k}}(\boldsymbol{I})\,\frac{\partial F}{\partial \boldsymbol{I}}\cdot\boldsymbol{k}\frac{1}{\boldsymbol{k}\cdot\boldsymbol{\omega}-\omega}\right) \\
&+[2\pi]^3\sum_{\boldsymbol{k}}\int \mathrm{d}\boldsymbol{I}\sum_{\boldsymbol{q}_1,\boldsymbol{q}_2}\int \mathrm{d}\omega'\left[\hat{a}^{(1)}_{\boldsymbol{q}_1}(\omega')+\hat{b}_{\boldsymbol{q}_1}(\omega')\right]\frac{\mathrm{i}}{\boldsymbol{k}\cdot\boldsymbol{\omega}-\omega'} \\
&\times\sum_{\boldsymbol{k}_1+\boldsymbol{k}_2=\boldsymbol{k}}\left[\!\!\left[\frac{\mathrm{i}}{\boldsymbol{k}_1\cdot\boldsymbol{\omega}-(\omega-\omega')}\left[\frac{\partial F}{\partial \boldsymbol{I}}\cdot\mathrm{i}\boldsymbol{k}_1\psi^{[\boldsymbol{q}_2]}_{\boldsymbol{k}_1}(\boldsymbol{I})\left[\hat{a}^{(1)}_{\boldsymbol{q}_2}(\omega')+\hat{b}_{\boldsymbol{q}_2}(\omega')\right]+\sigma^{e,[\boldsymbol{q}_2]}_{\boldsymbol{k}_1}(\boldsymbol{I})\hat{c}_{\boldsymbol{q}_2}[\omega']\right],\psi^{[\boldsymbol{q}_1]}_{\boldsymbol{k}_2}\right]\!\!\right]\psi^{[\boldsymbol{p}]}_{\boldsymbol{k}}.
\end{aligned} \tag{D12}
$$

Following equation (45), let us also define in frequency space the contraction rule:

$$
(\hat{\boldsymbol{K}}\cdot\hat{\boldsymbol{Z}})_{\boldsymbol{p}}(\omega)\stackrel{\triangle}{=}\sum_{\boldsymbol{q}}\hat{K}_{\boldsymbol{p},\boldsymbol{q}}(\omega)\hat{Z}_{\boldsymbol{q}}(\omega) \tag{D13}
$$

(note that equations D13 only involve a sum and no integral) and the higher-order contraction rule (cf. equation 46):

$$
\left(\hat{\boldsymbol{K}}_n\cdot\hat{\boldsymbol{Z}}^1\otimes\cdots\otimes\hat{\boldsymbol{Z}}^n\right)_{\boldsymbol{p}}(\omega)\stackrel{\triangle}{=}\sum_{\boldsymbol{q}_1,\ldots,\boldsymbol{q}_n}\int \mathrm{d}\omega_1\cdots\int \mathrm{d}\omega_n\hat{K}_{\boldsymbol{p},\boldsymbol{q}_1,\ldots,\boldsymbol{q}_n}(\omega_1,\ldots,\omega_n)\delta_D\left(\omega-\sum_{i=1}^{n}\omega_i\right)\hat{Z}^1_{\boldsymbol{q}_1}(\omega_1)\cdots\hat{Z}^n_{\boldsymbol{q}_n}(\omega_n). \tag{D14}
$$

The operator, $\hat{\boldsymbol{K}}_n[\omega_1,\omega_2,\ldots,\omega_n]$, obeys

$$
\begin{aligned}
(\hat{\boldsymbol{K}}_n)_{\boldsymbol{p},\boldsymbol{q}_1,\boldsymbol{q}_2,\ldots,q_n}[\omega_1,\omega_2,\ldots,\omega_{\boldsymbol{n}}] = &[2\pi]^3\sum_{\boldsymbol{k}}\int \mathrm{d}\boldsymbol{I}\frac{\mathrm{i}}{\boldsymbol{k}\cdot\boldsymbol{\omega}-\omega_1} \\
\times\sum_{\boldsymbol{k}_1+\boldsymbol{k}_2=\boldsymbol{k}}\left[\!\!\left[\frac{\mathrm{i}}{\boldsymbol{k}_1\cdot\boldsymbol{\omega}-\omega_2}\cdots\sum_{\boldsymbol{k}_{2n-1}+\boldsymbol{k}_{2n}=\boldsymbol{k}_n}\left[\!\!\left[\frac{\mathrm{i}}{\boldsymbol{k}_{2n-3}\cdot\boldsymbol{\omega}-\omega_n}\frac{\partial F}{\partial\boldsymbol{I}}\cdot\mathrm{i}\boldsymbol{k}_{2n-3}\psi^{[\boldsymbol{q}_n]}_{\boldsymbol{k}_{2n-3}},\psi^{[\boldsymbol{q}_{n-1}]}_{\boldsymbol{k}_{2n-2}}\right]\!\!\right]\cdots,\psi^{[\boldsymbol{q}_2]}_{\boldsymbol{k}_4}\right]\!\!\right],\psi^{[\boldsymbol{q}_1]}_{\boldsymbol{k}_2}\right]\!\!\right]\psi^{[\boldsymbol{p}]}_{\boldsymbol{k}}.&
\end{aligned} \tag{D15}
$$

APPENDIX E: OTHER COSMOLOGICAL PROBES

In this appendix, we discuss other non-linear statistical probes of the cosmic environment of haloes, expanding over Section 5.1.

E1 Dark matter disintegration

It has been claimed that dark matter could be made of neutralinos which can be traced indirectly via their disintegration signature, which scales like the square of the local dark matter density (Stoehr et al. 2003). The total number of γ photons received during integration time, t_γ reads

$$N_{\rm a}(\boldsymbol{\Omega}, t_\gamma) = D_{\rm eff}\, t_\gamma\, \frac{N_{\rm cont}}{2}\frac{\langle\sigma v\rangle}{m_\chi^2}\frac{\Delta\Omega}{4\pi}\frac{1}{\Delta\Omega}\int {\rm d}\boldsymbol{\Omega}\int {\rm d}r\, \rho_{\rm DM}^2(r) \stackrel{\triangle}{=} W_\chi \int {\rm d}\boldsymbol{\Omega}\int {\rm d}r\, \rho_{\rm DM}^2(r), \tag{E1}$$

where $D_{\rm eff}$ is the effective size of the telescope, $\Delta\Omega$ the angular resolution of the telescope, and $N_{\rm cont}(E_\gamma)$ is the number of continuum photons and $\langle\sigma v\rangle$ is the continuum cross-section of neutralinos of mass, m_χ. The integral accounts for measured flux of γ photons arising from neutralinos disintegrating in the direction, $\boldsymbol{\Omega}$. (See Stoehr et al. 2003 for details about the computation of $N_{\rm cont}$, $D_{\rm eff}$ and $\langle\sigma v\rangle$). Since the $N_{\rm a}(\boldsymbol{\Omega}, T)$ scales like the line integral of the square of the density along the line of sight, it is straightforward to propagate the statistical properties of the density fluctuations to that of $N_{\rm a}$. For instance, the cosmic mean will scale like

$$\langle N_{\rm annih}(\boldsymbol{\Omega})\rangle = W_\chi \int {\rm d}r\, \langle\rho_{\rm DM}(\boldsymbol{r})\rangle^2 + W_\chi \int {\rm d}r \left\langle \delta\rho_{\rm DM}^2(\boldsymbol{r})\right\rangle, \tag{E2}$$

where

$$\left\langle \delta\rho_{\rm DM}^2(\boldsymbol{r})\right\rangle = \sum_{\boldsymbol{n},\boldsymbol{n}'} \langle a_{\boldsymbol{n}} a_{\boldsymbol{n}'}\rangle \rho^{[\boldsymbol{n}]}(\boldsymbol{r})\rho^{[\boldsymbol{n}']}(\boldsymbol{r}). \tag{E3}$$

Hence, we expect an excess of annihilation because of the polarized clumps within the halo. Similarly, we may predict the angular correlation function, or the related variance as a function of smoothed angular scale as

$$\begin{aligned}\langle \delta N_{\rm a}(\boldsymbol{\Omega})\delta N_{\rm a}(\boldsymbol{\Omega}')\rangle &= W_\chi^2 \iint {\rm d}r\,{\rm d}r' \left\langle \delta\rho_{\rm DM}^2(\boldsymbol{\Omega}, r)\delta\rho_{\rm DM}^2(\boldsymbol{\Omega}', r')\right\rangle \\ &= W_\chi^2 \sum_{\boldsymbol{n}_1,\boldsymbol{n}_2,\boldsymbol{n}_3,\boldsymbol{n}_4} \langle a_{\boldsymbol{n}_1} a_{\boldsymbol{n}_2} a_{\boldsymbol{n}_3} a_{\boldsymbol{n}_4}\rangle \iint {\rm d}r\,{\rm d}r' \rho^{[\boldsymbol{n}_1]}(r,\boldsymbol{\Omega})\rho^{[\boldsymbol{n}_2]}(r,\boldsymbol{\Omega})\rho^{[\boldsymbol{n}_3]}(r',\boldsymbol{\Omega}')\rho^{[\boldsymbol{n}_4]}(r',\boldsymbol{\Omega}'),\end{aligned} \tag{E4}$$

where $\delta N_{\rm annih}(\boldsymbol{\Omega}) \stackrel{\triangle}{=} N_{\rm annih}(\boldsymbol{\Omega}) - \langle N_{\rm annih}(\boldsymbol{\Omega})\rangle$. Note that we assumed here that the resolution of the telescope was effectively infinite (i.e. $\Delta\Omega \to 0$ in equations E1). Now we may rely on Wick's theorem to express the four-point correlation entering equation (E4) as products of two-point correlations. Calling $\delta a \stackrel{\triangle}{=} a - \langle a\rangle$, we have $\langle \delta a_{\boldsymbol{n}_1}\delta a_{\boldsymbol{n}_2}\delta a_{\boldsymbol{n}_3}\rangle = 0$ and

$$\begin{aligned}\langle \delta a_{\boldsymbol{n}_1}\delta a_{\boldsymbol{n}_2}\delta a_{\boldsymbol{n}_3}\delta a_{\boldsymbol{n}_4}\rangle &= \langle \delta a_{\boldsymbol{n}_1}\delta a_{\boldsymbol{n}_2}\rangle\langle \delta a_{\boldsymbol{n}_3}\delta a_{\boldsymbol{n}_4}\rangle \\ &\quad + \langle \delta a_{\boldsymbol{n}_1}\delta a_{\boldsymbol{n}_3}\rangle\langle \delta a_{\boldsymbol{n}_2}\delta a_{\boldsymbol{n}_4}\rangle + \langle \delta a_{\boldsymbol{n}_2}\delta a_{\boldsymbol{n}_3}\rangle\langle \delta a_{\boldsymbol{n}_1}\delta a_{\boldsymbol{n}_4}\rangle.\end{aligned} \tag{E5}$$

If the infall is statistically isotropic, equation (E4) may be averaged over the direction, $\boldsymbol{\Omega}$ and reads

$$\langle \delta N_{\rm annih}(\boldsymbol{\Omega})\delta N_{\rm annih}(\boldsymbol{\Omega}')\rangle_\Omega = \sum_\ell C_\ell^{\rm annih} P_\ell[\boldsymbol{\Omega}\cdot\boldsymbol{\Omega}'], \tag{E6}$$

where

$$C_\ell^{\rm annih} = W_\chi^2 \sum_\ell C_{\ell_1}^{\rm DM} C_{\ell_2}^{\rm DM} U_{\ell_1,\ell_2}^\ell. \tag{E7}$$

Note that the geometric factor, U_{ℓ_1,ℓ_2}^ℓ, only depends on the basis function, $\rho^{[\boldsymbol{n}]}(\boldsymbol{r})$ and possibly the resolution of the telescope if it is not assumed to be infinite:

$$U_{\ell_1,\ell_2}^\ell = \sum_{\boldsymbol{n}_1,\boldsymbol{n}_2,\boldsymbol{n}_3,\boldsymbol{n}_4} \int {\rm d}\boldsymbol{\Omega} Y_\ell^{m*}(\boldsymbol{\Omega}') \int {\rm d}\boldsymbol{\Omega}' Y_\ell^{m*}(\boldsymbol{\Omega}') \iint {\rm d}r\,{\rm d}r' \rho^{[\boldsymbol{n}_1]}(r,\boldsymbol{\Omega})\rho^{[\boldsymbol{n}_2]}(r,\boldsymbol{\Omega})\rho^{[\boldsymbol{n}_3]}(\boldsymbol{\Omega}', r')\rho^{[\boldsymbol{n}_4]}(\boldsymbol{\Omega}', r'), \tag{E8}$$

given that $\rho^{[\boldsymbol{n}]}_{(\boldsymbol{r})} = u_{\ell m}^n(r)\, Y_\ell^m(\boldsymbol{\Omega})$ and given the properties of spherical harmonics, the integral $\int {\rm d}\boldsymbol{\Omega} Y_{\ell_1}^{m_1}(\boldsymbol{\Omega}) Y_{\ell_2}^{m_2}(\boldsymbol{\Omega}) Y_{\ell_3}^{m_3}(\boldsymbol{\Omega}') Y_{\ell_4}^{m_4}(\boldsymbol{\Omega}'){\rm d}\boldsymbol{\Omega}$ can be re-expressed iteratively in terms of Clebsch–Jordan coefficients. Ensemble average and comparison with the observation is possible at the high-ℓ limit corresponding to the small-scale structure of the dark matter halo, for which we may expect independent angular regions of the Galactic halo to be representative of an ensemble average.

E2 Bremsstrahlung X-ray emission of stacked haloes

Assuming that the gas traces the dark matter, we may reproduce the thought experiment of Section E1, though the ensemble average is constructed while staking projections of haloes on the sky rather than in a galactocentric framework.

The emissivity per unit volume at frequency ν, $\varepsilon_\nu(\boldsymbol{r})$, for a hydrogen plasma is given by (Peacock 1999)

$$\varepsilon_\nu(\boldsymbol{r}){\rm d}\boldsymbol{r}\,{\rm d}\nu = \frac{\epsilon_{\rm X} n_{\rm e}^2(\boldsymbol{r})}{\sqrt{T_{\rm e}(\boldsymbol{r})}}\left\{1 + \log_{10}\left[\frac{k_{\rm B}T_{\rm e}(\boldsymbol{r})}{h\nu}\right]\right\}\exp\left[-\frac{h\nu}{k_{\rm B}T_{\rm e}(\boldsymbol{r})}\right]\,{\rm d}\boldsymbol{r}\,{\rm d}\nu, \tag{E9}$$

where T_e is the temperature in K, ν the frequency in Hz, k_B the Boltzmann constant, h the Planck constant, and $\epsilon_\mathrm{X} \triangleq 6.8 \times 10^{-32}$ for an emissivity in $\mathrm{W\,m^{-3}\,Hz^{-1}}$. Let us assume here that the cluster is isothermal, hence the variation of T_e with z are neglected compared to that of n_e squared.[13] Let us also assume that M/L is the mass-to-light ratio of the cluster is constant. Hence the emissivity per unit surface, σ_ν, is given by

$$\sigma_\nu(\boldsymbol{R}) = \int \mathrm{d}z\,(\mathrm{M/L})^2\,\varepsilon_\nu(\boldsymbol{R}, z) \triangleq W_X \int \mathrm{d}z \rho^2_\mathrm{DM}(\boldsymbol{R}, z). \tag{E10}$$

Hence, taking an ensemble average yields

$$\langle\sigma_\nu(\boldsymbol{R})\rangle = W_X \int \mathrm{d}z\,\langle\rho_\mathrm{DM}\rangle^2(\boldsymbol{R}, z) + W_X \int \mathrm{d}z\,\langle\delta\rho^2_\mathrm{DM}\rangle(\boldsymbol{R}, z), \tag{E11}$$

where

$$\left\langle\rho^2_\mathrm{DM}\right\rangle(\boldsymbol{R}, z) = \sum_{\boldsymbol{n},\boldsymbol{n}'} \langle a_{\boldsymbol{n}} a_{\boldsymbol{n}'}\rangle \rho^{[\boldsymbol{n}]}(\boldsymbol{r})\rho^{[\boldsymbol{n}']}(\boldsymbol{r}). \tag{E12}$$

The two-point correlation of the cosmic fluctuation of the emissivity is given by

$$\frac{\langle\delta\sigma_\nu(\boldsymbol{R})\delta\sigma_\nu(\boldsymbol{R}')\rangle}{\langle\sigma_\nu(R)\rangle^2} = \frac{\iint \mathrm{d}z\mathrm{d}z'\left\langle\delta\rho^2_\mathrm{DM}(\boldsymbol{R}, z)\delta\rho^2_\mathrm{DM}(\boldsymbol{R}', z')\right\rangle}{\langle\sigma_\nu(R)\rangle^2},$$

where

$$\left\langle\delta\rho^2_\mathrm{DM}(\boldsymbol{R}, z)\delta\rho^2_\mathrm{DM}(\boldsymbol{R}', z')\right\rangle = \sum_{\boldsymbol{n}_1,\boldsymbol{n}_2,\boldsymbol{n}_3,\boldsymbol{n}_4} \langle a_{\boldsymbol{n}_1} a_{\boldsymbol{n}_2} a_{\boldsymbol{n}_3} a_{\boldsymbol{n}_4}\rangle \rho^{[\boldsymbol{n}_1]}(\boldsymbol{R}, z)\rho^{[\boldsymbol{n}_2]}(\boldsymbol{R}, z)\rho^{[\boldsymbol{n}_3]}(\boldsymbol{R}', z')\rho^{[\boldsymbol{n}_4]}(\boldsymbol{R}', z'). \tag{E13}$$

Note the cancellation of the dependence on W_X (hence T or M/L) in equation (E13). Relying again on Wick's theorem, equation (E5), we may express the four-point correlations as products of known (cf. equation E5) two-point correlations.

E3 Galactic halo's ellipticity

More generally, let us consider a problem which depends non-trivially on the perturbed distribution function, e.g. the ellipticity, e_H, of the departure from sphericity of the substructures induced by the environment around a given halo. The ellipticity is defined as

$$e_\mathrm{H} = \frac{3\lambda_1}{\sum_i \lambda_i} - 1 \triangleq \mathcal{G}(\delta\rho(\boldsymbol{r})), \quad \text{with } \{\lambda_i\} = \mathrm{Eigenval}(\boldsymbol{I}_\mathrm{H}) \tag{E14}$$

and

$$\boldsymbol{I}_{\mathrm{H},i,j} = \frac{\int_{\leqslant R_{200}} \mathrm{d}\boldsymbol{r}\,\delta\rho(\boldsymbol{r})x_i x_j}{\int_{\leqslant R_{200}} \mathrm{d}\boldsymbol{r}\,\rho_\mathrm{NFW}(\boldsymbol{r})}, \tag{E15}$$

so that λ_1 is the largest eigenvalue of $\boldsymbol{I}_\mathrm{H}$ and $e_\mathrm{H} = 0$ if the halo's perturbation is spherical. Since we know the statistical properties of $\delta\rho(\boldsymbol{r})$, we may predict the statistical properties of e_H. In practice, assuming $\mathcal{G}$ is a well-behaved function of its arguments, we may Taylor-expand e_H with respect to $\delta\rho$ as

$$e_\mathrm{H} = \sum_n \left(\frac{\partial^n \mathcal{G}}{\partial\delta\rho^n}\right) \cdot [\delta\rho(\boldsymbol{r}_1) - \langle\delta\rho(\boldsymbol{r}_1)\rangle] \cdots [\delta\rho(\boldsymbol{r}_n) - \langle\delta\rho(\boldsymbol{r}_n)\rangle]\,. \tag{E16}$$

Note that the derivative in equation (E16) is a Frechet functional derivative, so that the dot involves an integration over $\boldsymbol{r}$. Hence the ensemble average, $\langle e_\mathrm{H}\rangle$ will involve N-point correlations, and reads

$$\langle e_\mathrm{H}\rangle = \sum_n \sum_{\boldsymbol{i}_1\cdots\boldsymbol{i}_n} \langle a_{i_1}\cdots a_{i_n}\rangle \left(\frac{\partial^n \mathcal{G}}{\partial\delta\rho^n}\right) \cdot \rho^{[i_1]}(\boldsymbol{r}) \cdots \rho^{[i_n]}(\boldsymbol{r}_n), \tag{E17}$$

where, once again, we may rely on Wick's theorem to re-express $\langle a_{i_1}\cdots a_{i_n}\rangle$ as products of two-point correlations. Since the relationship between the density perturbation and the ellipticity is not linear, we expect a non-zero ellipticity on average.

Note that in principle, we may reconstruct the full PDF of e. Formally, calling $z \triangleq (e, a_2, \ldots, a_{\boldsymbol{n}})$ (so that $z = (\mathcal{G}(a_1, \ldots, a_{\boldsymbol{n}}), a_2, \ldots, a_{\boldsymbol{n}}) = g(a_1, \ldots, a_{\boldsymbol{n}})$), inverting for z as a function of $\{a_i\}$ (provided the ellipticity is not degenerate in a_1), and marginalizing over the other coefficients yields

$$\mathrm{PDF}(e) = \frac{\int \mathrm{d}a_2\cdots\mathrm{d}a_{\boldsymbol{n}}\mathrm{PDF}(g^{-1}(z))}{|\partial z/\partial a_{\boldsymbol{n}}|}.$$

Now in practice, equation (E17) might not be the simplest procedure to compute $\langle e_\mathrm{H}\rangle$, and Monte Carlo resimulation may turn out to be more practical.

[13] This is a better approximation than for the SZ effect.

E4 Metal lines in quasi-stellar object (QSO) damped Lyman α systems

Let us, finally, consider a more convolved observable, which will depend on both the clump distribution within the haloes, but also on their velocities.

In the red part of a high-resolution spectrum of quasars, groups of absorption features are found, corresponding to the physical situation where the light emitted by the quasar is partially absorbed by the metal-rich[14] clumps which the line of sight happens to intercept. Formally, the normalized flux in a QSO is proportional to minus the log of the optical depth along the line of sight. The optical depth in the metal transition is (Pichon et al. 2001)

$$\tau(w, \boldsymbol{R}) = \frac{c\,\sigma_0}{H(\bar{z})\sqrt{\pi}} \int_{-\infty}^{+\infty} \frac{n_Z(v, \boldsymbol{R})}{b(v, \boldsymbol{R})} \exp\left\{-\frac{[w - v - v_z(v, \boldsymbol{R})]^2}{b(v, \boldsymbol{R})^2}\right\} \mathrm{d}v, \tag{E18}$$

where c is the velocity of light, σ_0 is the metal absorption cross-section, $H(\bar{z})$ is the Hubble constant at redshift $\bar{z}$, $n_Z(v, \boldsymbol{R})$ the ionized metal number density field, $b(v, \boldsymbol{R})$ the Doppler parameter (accounting for the thermal broadening of the line), and $v_p(v, \boldsymbol{R})$ is the peculiar velocity, at impact parameter, $\boldsymbol{R}$ from the centre of the cluster. The observed normalized flux, F, is simply $F = \exp(-\tau)$. If we assume here again constant biasing, so that $n_Z \propto \rho_{\mathrm{DM}}$. This assumption may be lifted once the identification of virialized substructure described in Section 3.3.1 is carried through. The two-point correlation of the optical depth fluctuation will involve statistical properties of both the density and the velocity field in a non-trivial manner.

$$\frac{1}{\langle\tau\rangle^2(w, R)} \langle \delta\tau(w, \boldsymbol{R}) \delta\tau(w', \boldsymbol{R})\rangle, \tag{E19}$$

with

$$\delta\tau(w, \boldsymbol{R}) = \tau(w, \boldsymbol{R}) - \langle\tau\rangle(w, R). \tag{E20}$$

Note that the distance to the halo centre, $\boldsymbol{R} \stackrel{\triangle}{=} b(\cos[\vartheta_b], \sin[\vartheta_b])$ still occurs in equation (E20). Since we do not know in general the impact parameter of the line of sight with respect to the halo centre, let us marginalize over its a priori probability distribution, which we may infer from, for example, the PT model (which at these scales corresponds essentially to the autocorrelation of the unperturbed universal halo profile). Given that we consider systems at the redshift of a damped Lyα, we may assume that we fall close to a galactic structure. Calling $p_b(b, \bar{z}, M)\mathrm{d}b\mathrm{d}\bar{z}$ the probability of a given point in space to be at a distance, b within d b of an object of mass larger than M, which is at redshift $\bar{z}$ within $\mathrm{d}\bar{z}$, we may construct the weighted sum

$$C_\tau(\Delta w) = \int_0^\infty \mathrm{d}b \int_0^\infty \mathrm{d}\bar{z} \int_0^{2\pi} \mathrm{d}\vartheta_b\, p_b(b, z, M)\, \langle \delta\tau(w, b\cos[\vartheta_b], b\sin[\vartheta_b]) \delta\tau(w + \Delta w, b\cos[\vartheta_b], b\sin[\vartheta_b])\rangle_w\,. \tag{E21}$$

This quantity may now be compared to the observable. Let us assume some equation of state for the metal phase, so that $b(\boldsymbol{R}, z) = b_0\,(\rho(\boldsymbol{R}, z)/\bar{\rho})^\gamma$. Equation (E18) may then be written formally as $\delta\tau(w, \boldsymbol{R}) = \mathcal{T}[\delta\rho(v, \boldsymbol{R}), v_z(v, \boldsymbol{R})]$. Let us Taylor-expand this expression in the neighbourhood of the mean density fluctuation as

$$\delta\tau(w, \boldsymbol{R}) = \sum_n \left(\frac{\partial^n \mathcal{T}}{\partial\delta\rho\,\cdots\,\partial\delta v_z}\right) [\delta\rho(\boldsymbol{r}_1) - \langle\delta\rho(\boldsymbol{r}_1)\rangle] \cdots [\delta v_z(\boldsymbol{r}_n) - \langle\delta v_z(\boldsymbol{r}_n)\rangle]\,. \tag{E22}$$

Again the derivative in equation (E22) is a functional derivative (cf. Section E3). Equations (E21)–(E22) together with equation (29) yield the expected correlation as a function of the statistical environment.

[14] Since we make predictions at lower redshift we need to concentrate on metals such as Mg II or Fe II which are found typically at redshift $z \leqslant 1.5$ in the visible.

This paper has been typeset from a TEX/LATEX file prepared by the author.

Mon. Not. R. Astron. Soc. **291,** 616–632 (1997)

Numerical linear stability analysis of round galactic discs

C. Pichon[1,2] and R. C. Cannon[3,4]

[1]*Astronomisches Institut Universitaet Besel, Venusstrasse 7, CH-4102 Binningen, Switzerland*
[2]*CITA, McLennan Labs, University of Toronto, 60 St George Street, Toronto, Ontario M5S 1A7, Canada*
[3]*Observatoire de Lyon, 9 Avenue Charles André 69 561 Saint Genis Laval, France*
[4]*University of Southampton, Bassett Crescent East, Southampton SO16 7PX*

Accepted 1997 April 28. Received 1997 April 10; in original form 1996 September 16

ABSTRACT

The method originally developed by Kalnajs for a numerical linear stability analysis of round galactic discs is implemented in the regimes of non-analytic transformations between position space and angle–action space, and of vanishing growth rates. This allows effectively any physically plausible disc to be studied, rather than only those having analytic transformations into angle–action space which have formed the primary focus of attention to date. The transformations are constructed numerically using orbit integrations in real space, and the projections of orbit radial actions on a given potential density basis are Fourier-transformed to obtain a dispersion relation in matrix form. Nyquist diagrams are used to isolate modes growing faster than a given fraction of the typical orbital period, and to assess how much extra mass would be required to reduce the growth rate of the fastest mode below this value. To verify the implementation, the fastest $m=2$ growth rates of the isochrone and the Kuzmin–Toomre discs are recovered, and the weaker $m=2$ modes are computed. The evolution of those growth rates as a function of the halo mass is also calculated, and some $m=1$ modes are derived as illustration. Algorithmic constraints on the scope of the method are assessed, and its application to observed discs is discussed.

Key words: instabilities – methods: analytical – methods: numerical – galaxies: kinematics and dynamics – galaxies: structure.

1 INTRODUCTION

Theoretical studies of the stability of thin stellar discs provide useful constraints on models of galactic formation and dynamics. Disc models can be excluded as unrealistic if they are found to be very unstable, and the results of galaxy formation studies can be clarified where they lead to models close to marginal stability. When applied to observed discs, stability analysis provides a unique tool to probe what fraction of the mass is in luminous form via the requirement that there be enough extra matter to make the observed distribution stable over a period comparable to the age of the galaxy.

Three main approaches have been adopted for disc stability analysis: direct N-body simulations, N-body simulations where the bodies are smeared on to a biorthonormal basis, thereby solving Poisson's equation implicitly, and linear modal analysis. The first has been widely used, initially by Hohl (1971), and more recently by, e.g., Athanassoula & Sellwood (1985). It provides a flexible tool of investigation which can be carried into the non-linear regime. These simulations, however, provide insight into instabilities only in the statistical sense, and generally probe poorly the marginal stability regime. This drawback has recently been addressed by Earn & Sellwood (1995), who developed the second approach of solving Poisson's equation through a biorthonormal basis. The stability of stellar systems has also been explored for spherical systems via a global 'energy principle' (see Sygnet & Kandrup 1984), but this approach has not been successfully implemented for discs because of resonances (Lynden-Bell & Ostriker 1967). Moreover, the method usually provides stability statements which are of little practical use, since no time-scale for the astrophysically relevant growth rates is available.

The third method, linear modal analysis (Kalnajs 1977; Zang 1976; Hunter 1993), is used here. In spite of the obvious limitation to perturbations of small amplitudes, it has several potential advantages. In this approach the integro-differential equation resulting from self-consistent solutions of the Boltzmann and Poisson equations is recast into a non-linear eigenproblem using an appropriately defined orthonormal basis. The method, pioneered by Kalnajs (1971, 1976, 1977) on the linear stability of galactic discs, involves the formulation of the dynamical perturbed equations in angle–action coordinates and the restriction to a (finite) set of perturbed densities which diagonalize Poisson's equation in position space. Kalnajs' original work (Kalnajs 1971) concerned the stability of the isochrone disc, for which explicit transformations between angle–action and position–velocity coordinates exist. Zang (1976) studied the self-similar Mestel discs in the same way. More recently, the method was implemented by Hunter (1993) (via repeated evaluation of elliptical integrals) for the infinite Kuzmin–Toomre disc. The approach of these authors involved calculating explicit transformations between angle–action variables and position–velocity variables, and was therefore restricted to a very limited set of simple analytic discs. Also recently, the relevant angle–action integrals were computed by quadrature by Weinberg (1991), and by Bertin (1994) while studying the stability of spherical systems for which the Hamiltonian is separable. Finally, Vauterin & Dejonghe (1996) carried out a similar analysis for discs while performing the whole investigation in position space.

Here, the first step of mapping the distribution function into angle–action space is implemented numerically by calculating the appropriate transformations from the results of integrating unperturbed orbits in the mean field of the galaxy. This then allows considerable freedom in the initial equilibrium to be studied, including the prospect of applying linear stability analysis to distribution functions recovered for observed galaxies. This method is not restricted to integrable potentials, and it could be generalized to three dimensions. It can, in particular, be implemented for *measured* distribution functions, where the potential is deduced from the rotation curve.

In Section 2, Kalnajs' matrix method is recovered following an indirect route corresponding to a rewriting of Boltzmann's and Poisson's equations directly in action space. The stability criteria are then reformulated in a form suitable for numerical evaluation of the matrix elements in Section 3. Details of the numerical method are presented, and its range of validity is discussed. Section 4 contains results of calculations for the isochrone and the Kuzmin–Toomre discs. These are in agreement with those found by Kalnajs (1978), Athanassoula & Sellwood (1985), Hunter (1993) and Earn & Sellwood (1995). Prospects and applications to observed data as probes of dark matter are sketched in Section 5.

2 LINEAR STABILITY ANALYSIS REVISITED

Linear stability analysis concerns the dynamical evolution of initially small perturbations in their own self-consistent field. The derivation (see, e.g., Kalnajs 1977 and Sellwood & Wilkinson 1993) of the resulting integro-differential equation is sketched here, putting the emphasis on a coherent description in action space. This analysis is to be contrasted with that of Vauterin & Dojonghe (1996), who chose to implement stability analysis for discs in position space alone. The resulting dispersion relation, equation (2.17), is fully equivalent to Kalnajs' equation K-15, but the intermediate integral equation, equation (2.11), also provides a connection with orbital stability analysis (Lynden-Bell 1979; Pichon & Lynden-Bell 1992; Collett 1995).

2.1 The integral equation

The Boltzmann–Vlasov equation,

$$\partial F/\partial t + [H, F] = 0, \tag{2.1}$$

governs the dynamical evolution of an ensemble of collisionless stars. Here H is the Hamiltonian for the motion of one star, F is the mass-weighted distribution function in phase space, and the square bracket denotes the Poisson bracket. Writing $F = F_0 + f$, and $\Psi = \psi_0 + \psi$, where F_0 and ψ_0 are the unperturbed distribution function and potential respectively, and linearizing equation (2.1) in f and ψ, the perturbed distribution function and potential, yields

$$\partial f/\partial t + [H_0, f] - [\psi, F_0] = 0. \tag{2.2}$$

According to Jeans's theorem, the unperturbed equation, $[H_0, F_0] = 0$, is solved if F_0 is any function only of the specific energy, ε, and the specific angular momentum, h.

Following Lynden-Bell & Kalnajs (1972), angle and action variables of the unperturbed Hamiltonian H_0 are chosen here as canonical coordinates in phase space. The unperturbed Hamilton equations are quite trivial in these variables, which makes them suitable for perturbation theory in order to study quasi-resonant orbits. The actions are defined in terms of the polar coordinates, (R, θ), by $\boldsymbol{J} = (J_R, J_y)$, where

$$J_R = (2\pi)^{-1} \oint [\dot{R}]\, \mathrm{d}R \qquad \textit{and} \qquad J_\theta = h = R^2 \dot{\theta}. \tag{2.3}$$

Here $[\dot{R}]$ is a function of the radius, R, the specific energy, ε, and the specific angular momentum, h, given by $[\dot{R}]=\sqrt{2\varepsilon+2\psi_0(R)-h^2/R^2}$. The angle between apocentres is $\Theta=\oint h/R^2[\dot{R}]^{-1}\,\mathrm{d}R$. For a radial period T_R, and a pair of azimuthal and radial epicyclic frequencies Ω and κ, given by $\Omega=\Theta/T_R$ and $\kappa=2\pi/T_R$ the phase-angles conjugate to J_R and h are $\varphi=(\varphi_R, \varphi_\theta)$, where

$$\varphi_R=\kappa\int^R [\dot{R}]^{-1}\,\mathrm{d}R \qquad \text{and} \qquad \varphi_\theta=\theta+\int^R (h/R^2-\Omega)[\dot{R}]^{-1}\,\mathrm{d}R. \tag{2.4}$$

The stationary unperturbed Boltzmann equation (2.1) is solved by any distribution function of the form $F=F_0(\boldsymbol{J})$, since $[H_0, \boldsymbol{J}]=0$.

For growing instabilities, f and ψ are both taken to be proportional to $\mathrm{e}^{-i\omega t}$, ω having a positive imaginary part. When expanded in Fourier series with respect to the angles φ, equation (2.2) becomes, after simple algebra (Kalnajs 1977),

$$f_{\boldsymbol{m}}=\frac{m^{-1}\boldsymbol{m}\cdot\partial F_0/\partial\boldsymbol{J}}{\Omega_\ell-\Omega_p}\,\psi_{\boldsymbol{m}}, \tag{2.5}$$

where $\boldsymbol{m}$ is a integer vector with components (ℓ, m), $\Omega_\ell=m^{-1}\boldsymbol{m}\cdot\boldsymbol{\Omega}=\Omega+\ell\kappa/m$, $\boldsymbol{\Omega}$ stands for (κ, Ω), and $\Omega_p=\omega/m$. Here $\psi_{\boldsymbol{m}}$ and $f_{\boldsymbol{m}}$ are the Fourier transforms of ψ and f with respect to $(\varphi_R, \varphi_\theta)$; for instance,

$$\psi_{\boldsymbol{m}}(\boldsymbol{J})=\frac{1}{4\pi^2}\int \psi(R, \theta)\exp[-\mathrm{i}(\boldsymbol{m}\cdot\boldsymbol{\varphi})]\,\mathrm{d}^2\varphi. \tag{2.6}$$

Poisson's integral relates the potential, ψ, to the density perturbation:

$$\psi(R', \theta')=4\pi G\int \frac{f(\boldsymbol{R}, \boldsymbol{v})}{|\boldsymbol{R}-\boldsymbol{R}'|}\,\mathrm{d}R\,\mathrm{d}\theta\,\mathrm{d}v_R\,\mathrm{d}v_\theta. \tag{2.7}$$

This equation may be written in order to make explicit the contribution from the interaction of orbits. Here again angle–action variables are useful, as a given unperturbed orbit is entirely specified by its actions. It is therefore straightforwrd to identify in Poisson's integral the contribution corresponding to the interaction of given orbits. Re-expressing this equation in terms of angles and actions $(\boldsymbol{\varphi}, \boldsymbol{J})$, using Parseval's theorem and taking its Fourier transform with respect to $\boldsymbol{\varphi}$, leads to

$$\psi_{\boldsymbol{m}}(\boldsymbol{J})=4\pi G\sum_{\boldsymbol{m}'}\int f_{\boldsymbol{m}'}(\boldsymbol{J}')A_{\boldsymbol{m}\boldsymbol{m}'}(\boldsymbol{J}, \boldsymbol{J}')\,\mathrm{d}^2J', \tag{2.8}$$

where $\psi_{\boldsymbol{m}}$ and $f_{\boldsymbol{m}}$ are given by equation (2.6), and

$$A_{\boldsymbol{m}\boldsymbol{m}'}=\frac{1}{(2\pi)^4}\int \frac{\exp\mathrm{i}(\boldsymbol{m}'\cdot\boldsymbol{\varphi}'-\boldsymbol{m}\cdot\boldsymbol{\varphi})}{|\boldsymbol{R}-\boldsymbol{R}'|}\,\mathrm{d}^2\varphi'\,\mathrm{d}^2\varphi. \tag{2.9}$$

The double sum in equation (2.8) extends in both ℓ and m from minus infinity to infinity, where the radii $\boldsymbol{R}(\boldsymbol{\varphi}, \boldsymbol{J})$ and $\boldsymbol{R}(\boldsymbol{\varphi}', \boldsymbol{J}')$ are re-expressed as functions of these variables. Now $|\boldsymbol{R}-\boldsymbol{R}'|$ depends on φ_θ and φ'_θ in the combination $\varphi'_\theta-\varphi_\theta\equiv\Delta\varphi$ only. As $|\partial(\varphi'_\theta\varphi_\theta)/\partial(\Delta\varphi\varphi_\theta)|=1$, the order of integration in equation (2.9) may then be reversed, doing the φ_θ integration with $\Delta\varphi$ fixed. This yields $2\pi\delta_{mm'}$, so $\boldsymbol{m}'$ becomes (ℓ', m) in the surviving terms. This gives for equation (2.9)

$$A_{\boldsymbol{m}\boldsymbol{m}'}=\frac{2\pi\delta_{mm'}}{(2\pi)^4}\int \frac{\exp\mathrm{i}(m\Delta\varphi-\ell'\varphi'_R+\ell\varphi_R)}{|\boldsymbol{R}-\boldsymbol{R}'|}\,\mathrm{d}\Delta\,\mathrm{d}\varphi'_R\,\mathrm{d}\varphi_R. \tag{2.10}$$

Each m mode therefore evolves independently. The dependence on m will be implicit from now on. So, for example, ψ_ℓ is the Fourier transform of $\psi(R, \theta)$ with respect to both φ_R and φ_θ.

Putting equation (2.5) into equation (2.8) leads to the integral equation

$$\psi_{\ell_1}(\boldsymbol{J}_1)=4\pi G\sum_{\ell_2}\int A_{\ell_1\ell_2}(\boldsymbol{J}_1, \boldsymbol{J}_2)\,\frac{m_2^{-1}\boldsymbol{m}_2\cdot\partial F_0/\partial\boldsymbol{J}_2}{\Omega_{\ell_2}-\Omega_p}\,\psi_{\ell_2}(\boldsymbol{J}_2)\,\mathrm{d}^2\boldsymbol{J}_2. \tag{2.11}$$

This equation is the integral equation for the linear growing mode with an m-fold symmetry of a thin disc. Equation (2.11) was later approximated by Pichon & Lynden-Bell (1992), Collet (1995) and Lynden-Bell (1994) to analyse the growth of the perturbation in terms of a Landau instability.

2.2 The dispersion relation

The perturbed distribution function and potential are now expanded over a potential-distribution basis $\{f^{(n)}\}_n$, $\{\psi^{(n)}\}_n$ as

$$f(R, V)=\sum_n a_n f^{(n)}(R, V), \qquad \text{and} \qquad \psi(R)=\sum_n a_n \psi^{(n)}(R), \tag{2.12}$$

where the basis is assumed to satisfy Poisson's equation (2.7), which when written in action space has Fourier components obeying (following equation 2.8 and given equation 2.10)

$$\psi_\ell^{(n)}(\boldsymbol{J})=4\pi G \sum_{\ell'} \int f_{\ell'}^{(n)}(\boldsymbol{J}')A_{\ell\ell'}(\boldsymbol{J}, \boldsymbol{J}')\, \mathrm{d}^2\boldsymbol{J}'. \tag{2.13}$$

For basis functions scaling like $\exp(\mathrm{i}m'\theta)$ (preserving the axial symmetry described above), equation (2.6) applied to, say, $\psi^{(n)}(R)\exp(\mathrm{i}m'\theta)$ gives for the Fourier mode ℓ:

$$\psi_\ell^{(n)}(\boldsymbol{J})=\frac{1}{2\pi}\int_0^{2\pi} \mathrm{e}^{-\mathrm{i}\ell\varphi_R}\psi^{(n)}(R[\varphi_R])\,\mathrm{e}^{\mathrm{i}m\delta\theta(\varphi_R)}\, \mathrm{d}\varphi_R, \tag{2.14}$$

where equation (2.4) has been used to define the relative azimuthal increment $\delta\theta(\varphi_R)\equiv\varphi_\theta-\theta$.

Expanding ψ over this basis (using the *same* expansion for all ℓs) according to equation (2.12), inserting this expansion into equation (2.11), multiplying by $f_\ell^{(p)*}(\boldsymbol{J})$, integrating over $\boldsymbol{J}$, and summing over ℓ yields

$$\sum_n a_n\left[\sum_{\ell_1}\int \psi_{\ell_1}^{(n)}(\boldsymbol{J}_1)f_{\ell_1}^{(p)*}(\boldsymbol{J}_1)\, \mathrm{d}^2\boldsymbol{J}_1\right]=\sum_{n'} a_{n'}\left[4\pi G\sum_{\ell_2,\ell_1}\int\!\!\int f_{\ell_1}^{(p)*}(\boldsymbol{J}_1)A_{\ell_1\ell_2}(\boldsymbol{J}_1,\boldsymbol{J}_2)\,\frac{\boldsymbol{m}_2^{-1}\boldsymbol{m}_2\cdot\partial F_0/\partial \boldsymbol{J}_2}{\Omega_{\ell_2}-\Omega_p}\,\psi_{\ell_2}^{(n')}(\boldsymbol{J}_2)\, \mathrm{d}^2\boldsymbol{J}_2\, \mathrm{d}^2\boldsymbol{J}_1\right]. \tag{2.15}$$

Since $f_{\ell_1}^{(p)}$ belongs to the basis, it satisfies equation (2.13), and consequently

$$\sum_n a_n\left[\sum_{\ell_1}\int \psi_{\ell_1}^{(n)}(\boldsymbol{J}_1)f_{\ell_1}^{(p)*}(\boldsymbol{J}_1)\, \mathrm{d}^2\boldsymbol{J}_1\right]=\sum_{n'} a_{n'}\left[\sum_{\ell_2}\int \psi_{\ell_2}^{(p)*}(\boldsymbol{J}_2)\,\frac{\boldsymbol{m}_2^{-1}\boldsymbol{m}_2\cdot\partial F_0/\partial \boldsymbol{J}_2}{\Omega_{\ell_2}-\Omega_p}\,\psi_{\ell_2}^{(n')}(\boldsymbol{J}_2)\, \mathrm{d}^2\boldsymbol{J}_2\right]. \tag{2.16}$$

Requiring that equation (2.16) has non-trivial solutions in $\{a_n\}$ leads to the dispersion relation

$$D(\omega)=\det|\boldsymbol{\Lambda}-\mathbf{M}(\omega)|=0, \tag{2.17}$$

where the matrix $\mathbf{M}$ is defined in terms of its components (n', p) by the bracket on the right-hand side of equation (2.16), while the matrix $\boldsymbol{\Lambda}$ corresponds to the identity if the basis (ψ_n, f_n) is biorthonormal, or to a matrix with components (n, p) by the bracket on the left-hand side of equation (2.16) otherwise. Equation (2.17) was first derived in this context by Kalnajs (1977). In order to approximate the behaviour of a halo, a supplementary parameter $q\in]0, 1]$ is introduced:

$$D_q(\omega)=\det|\boldsymbol{\Lambda}-q\mathbf{M}(\omega)|=0, \tag{2.18}$$

as discussed below.

2.3 Unstable modes and Nyquist diagrams

The dispersion relations (2.18) give, for each m, the criterion for the existence of exponentially growing unstable modes of the form $\exp(-\mathrm{i}\omega t+\mathrm{i}m\theta)$. They are functions of a free complex parameter ω corresponding in its real part to m times the pattern speed of the growing mode, Ω_p, and in its imaginary part to the growth rate of the perturbation. The search for the growing modes is greatly facilitated by the use of Nyquist diagrams. Consider the complex ω plane and a contour that traverses along the real axis and then closes around the circle at ∞ with $\mathrm{Im}(\omega)$ positive. The determinant D_q is a continuous function of the complex variable ω; so, as ω traces out the closed contour, $D_q(\omega)$ traces a closed contour in the complex D_q plane. If the $D_q(\omega)$ contour encircles the origin, then there is a zero of the determinant inside the original contour, and the system is unstable. In fact, a simple argument of complex analysis shows that the number of loops around the origin corresponds to the number of poles above the line $\mathrm{Im}(\omega)\equiv\eta=$constant. An intuitive picture of how the criterion operates on equation (2.17) is provided by the following thought experiment. Imagine turning up the strength of qG for the disc (i.e., turn on self-gravity, which is physically equivalent to allowing for the gravitational interaction to play its role; alternatively, vary q, the ratio of relative halo support). Starting with small qG, all the M^{np} are small, so for all ωs the determinant $D_q(\omega)$ remains on a small contour close to $\det|\Lambda|$. As qG is increased to its full value, either the D_q contour passes through the origin to give a marginal instability or it does not. If it does not, then continuous change of qG does not modify the stability, and therefore the self-gravitating system has the same stability as in the zero qG case: it is stable. If, however, it crosses, and remains circling the origin, then it has passed beyond the marginally stable case and is unstable. This picture is illustrated in the next sections, where the image of the complex line $m\Omega_p + \mathrm{i}\eta$, $\Omega_p \in]-\infty, \infty[$, is plotted for various values of η.

3 NUMERICAL IMPLEMENTATION

3.1 Method

Stability analysis, as implemented in the previous section, allows the treatment of a wide range of potentials and distribution functions which, in general, will not afford the explicit transformations between angle–action variables and velocity–position variables.

Spline interpolation for tabulated potentials and distribution functions is used to compute the transformation of variables by numerically integrating orbits in the given potential. The whole calculation is performed on a grid of points in (R_0, V_0) space, where R_0 is the radius at apocentre, and V_0 is the corresponding tangential velocity. As may be seen from Fig. 4 in Section 3.2, a 40×40 grid is adequate for the discs considered here.

For each point in this grid, three orbits are calculated, one starting at the grid-point itself, and the others at small deviations in $h_0 = R_0 V_0$, and along $h_0 =$ constant. The angles and actions for these orbits are used later to calculate numerical derivatives of the distribution function. A fourth-order Runge–Kutta integration scheme is employed for the orbits, stopping at the first pericentre for all but the most eccentric orbits where more than one oscillation is needed to give sufficient accuracy in the actions. Further points on the orbits corresponding to grid vertices are then calculated at exact subintervals of the orbital period. The Fourier components ψ_l^n of a particular basis element along an orbit equation (2.14) are then given by

$$\psi_\ell^{(n)}(R_0, V_0) = \frac{1}{T_R} \int_0^{T_R} \mathrm{e}^{-2\pi \mathrm{i}\ell t/T_R} \psi^{(n)}(R[t]) \, \mathrm{e}^{\mathrm{i}m\delta\theta(t)} \, \mathrm{d}t, \tag{3.1}$$

where $t = \varphi_R/\kappa$, and

$$\delta\theta(\varphi_R) = \kappa^{-1} \int^{\varphi_R} \frac{h}{5R^2} \, \mathrm{d}\varphi_R - \kappa^{-1} \frac{\varphi_R}{2\pi} \oint \frac{h}{R^2} \, \mathrm{d}\varphi_R = \theta(t) - \langle \dot{\theta}(t) \rangle t. \tag{3.2}$$

Numerically, this simply corresponds to taking a discrete Fourier transform (DFT) over the resampled points. The symmetry of an orbit means that although the argument is complex, the result is purely real.

The matrix element defined in equation (2.16) is rewritten in terms of (R_0, V_0) and truncated in ℓ:

$$M^{(n)(n')}(\omega) = \sum_{\ell=-L}^{\ell=L} \int\!\!\int \psi_\ell^{(n)*} \frac{(\partial F/\partial h \cdot m + \partial F/\partial J \cdot \ell)}{\Omega \cdot m + \kappa \cdot \ell - m\Omega_p - \mathrm{i}\eta} \psi_\ell^{(n')} \left| \frac{\partial J \partial h}{\partial R_0 \partial V_0} \right| \mathrm{d}R_0 \, \mathrm{d}V_0, \tag{3.3}$$

where the $\psi_\ell^{(n')}$ are now surfaces in (R_0, V_0) space given by the ℓth-order term of the DFT of the orbit at R_0, V_0.

The inclusion of retrograde stars may be effected transparently by specifying a grid in R_0, V_0 which includes negative V_0 or, more efficiently, by noting that

$$\psi_\ell^{(n)}(-h) = \frac{1}{\pi} \int_0^{\pi} \cos[\ell\varphi_R(-h) - m\delta\varphi(-h)] \psi^{(n)}\{R[\varphi_R(-h)]\} \, \mathrm{d}\varphi_R, \tag{3.4a}$$

$$= \frac{1}{\pi} \int_0^{\pi} \cos[\ell\varphi_R(h) + m\delta\varphi(h)] c^{(n)}\{R[\varphi_R(h)]\} \, \mathrm{d}\varphi_R, \tag{3.4b}$$

$$= \psi_{-\ell}^{(n)}(h); \tag{3.4c}$$

so, with the appropriate sign switching, the same set of orbits and Fourier modes may be used as for prograde stars.

Having calculated the derivatives of the distribution function with respect to J and h by finite differences across the slightly displaced orbits described earlier and the Jacobian $\partial(Jh)/\partial(R_0 V_0)$ in the same manner, the problem of computing the matrix elements of equation (3.3) reduces to one of integrating quotients of surfaces on the R_0, V_0 grid. It is worth noting that, although it is the steps of the calculation up to this point which provide the generality of the implementation, their computational cost is relatively slight, amounting in total, for example, to about 1 min on a workstation with a specFp92 of 100.

For vanishing growth rates, the integrand in equation (3.3) is a quotient of surfaces with a real numerator but a denominator which may vanish along a line within the region of integration. The integral then exists only as a principal-value integral. Rather than attempting a brute-force discretization, we approximate both numerator and denominator by continuous piecewise flat surfaces and employ analytic formulae, or their power-series expansions, for each flat subsection. Each square of the R_0, V_0 grid is treated as two triangles. According to the magnitudes and slopes of the two surfaces over a given triangle there are six different approximations to be used for each component of the integral. For modes with finite growth rates, the integrand in equation (3.3) is of a quotient of surfaces with a real numerator but a complex denominator, and this prescription still holds. The extra generality afforded yields a solution which handles transparently the marginal stability case, where the resonances can be infinitely sharp.

The integration and summation then yields, for each Ω_p and η, an $n \times n$ matrix $\mathbf{M}$. Marginal stability corresponds to the vanishing of $\det|\mathbf{I}-\mathbf{M}|$. As described in Section 2.3, it is convenient to use Nyquist diagrams to locate the critical points: matrices corresponding to about 100 values of ω are calculated for lines of constant η. Provided that the sampling is good enough, the number of times the line $\det|\mathbf{I}-\mathbf{M}|$ encircles the origin in the complex plane gives the number of zeros above the initial line $m\Omega_p + \mathrm{i}\eta$. An example of Nyquist diagrams for the isochrone/9 disc (Section 4) is illustrated in Fig. 1 and shown more quantitatively in Figs 2 and 3. The three-dots-dashed curve corresponds to $\eta = 0.16$ and does not encircle the origin (or rather it loops once clockwise and once anticlockwise), whereas the other two curves ($\eta = 0.12$ and 0.14) do, indicating that the growth rate for the fastest growing bisymmetric instability of this disc is between 0.14 and 0.16.

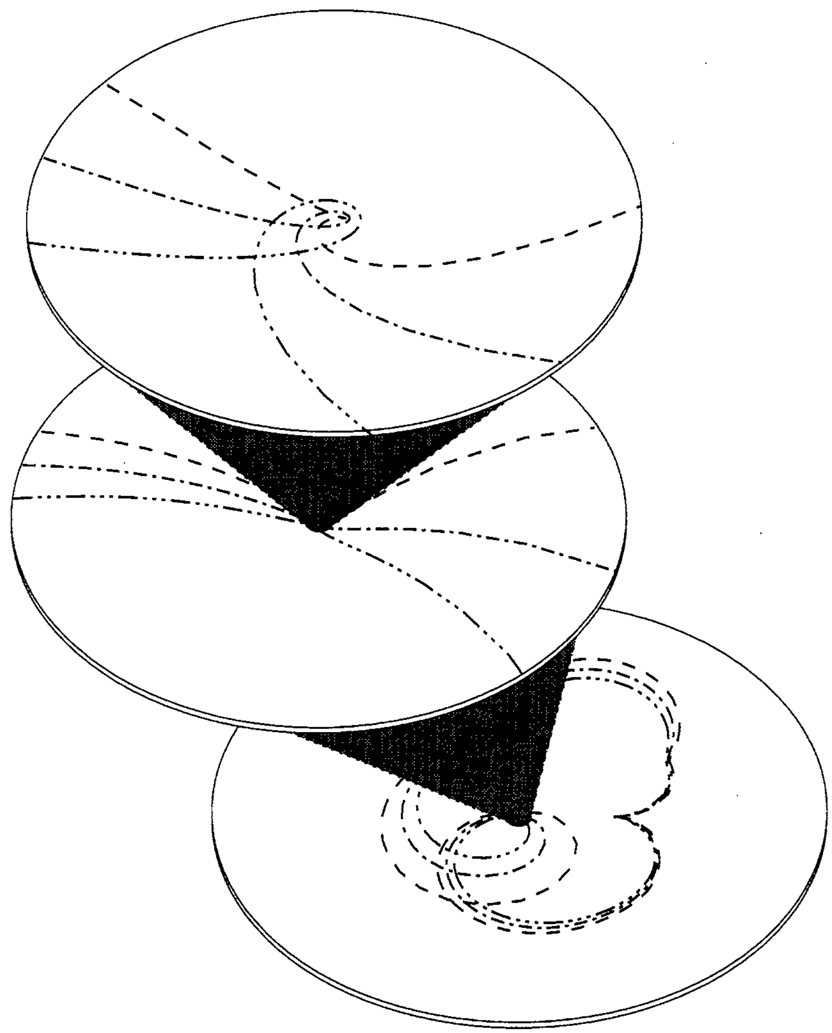

Figure 1. Nyquist diagram for the fastest growing mode of an isochrone/9 model for growth rates $\eta = 0.12$ (dashed curve), $\eta = 0.14$ (dot–dashed curve) and $\eta = 0.16$ (dot–long-dashed curve). The magnification shows that the first two curves do enclose the origin, whereas the third does not, indicating that the true growth rate is between 0.14 and 0.16.

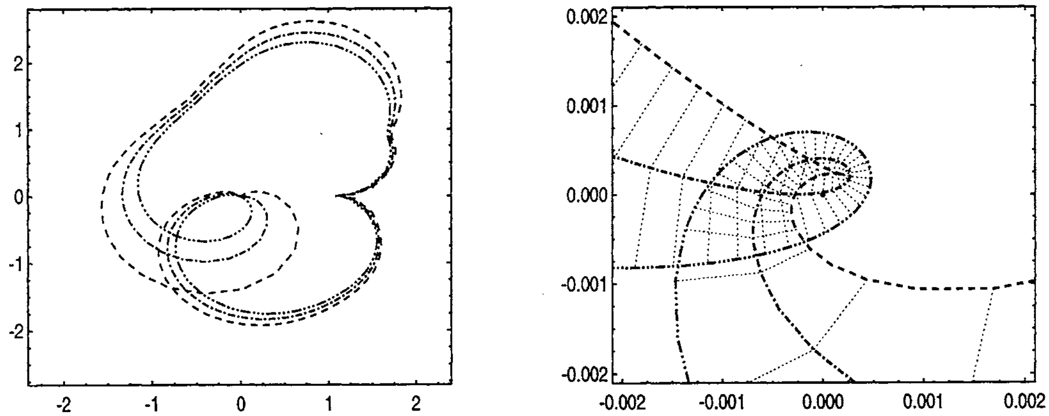

Figure 2. Nyquist diagram for the fastest growing mode of an isochrone/9 disc with curves labelled as in Fig. 1. The dotted lines join points for the same ω.

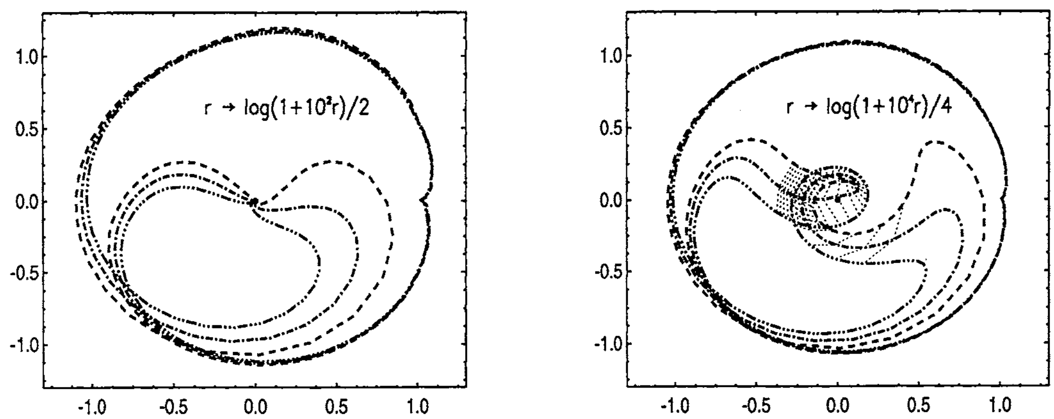

Figure 3. Nyquist diagram for the fastest growing mode of an isochrone/9 as in Figs 1 and 2. A logarithmic scaling has been applied near the origin mapping $r \rightarrow \log_{10}(1 + 10^{\alpha}r)/\alpha$, allowing the full topology to be seen more easily.

This method is easy to apply to verify calculations where the growth rate and pattern speed are already known, but becomes more time-consuming when treating discs with unknown properties. Many automatic schemes can be envisaged for locating zeros in the complex plane but, since computing the matrices is the slowest part of the calculation, we have found it most efficient to manage the search by hand with an interactive tool for examining Nyquist diagrams for different values of q (Section 2.3). With a little experience, the zeros can be efficiently located even from poorly sampled diagrams with spurious loops which would easily lead to confusion in automated procedures.

3.2 Validation

There are two distinct types of errors to be assessed in this analysis: numerical errors arising from the discretization of integrals and from machine rounding, and truncation errors relating to the use of small finite bases, limited Fourier expansions and the calculation of only the inner parts of infinite discs.

While, in principle, constraining the first type of errors is purely routine, it is worth noting that both the bases considered here require the use of arbitrary precision languages (such as **bc**) for their evaluation. As noted by Earn & Sellwood (1995), Kalnajs' basis requires the use of about 50 figures precision to get the first 30 basis elements to five figures. The problem, however, lies only in evaluating the polynomial terms, because the coefficients are large and induce substantial cancellations. Qian's basis (1992) not only requires extended precision to evaluate a single element, but it is also extremely close to being singular.

Besides evaluation of the basis elements, the only other part requiring special care is in the numerical derivatives of the distribution function with respect to J and h, where a tight compromise must be made between the desire for a small interval to give an accurate derivative, and the loss of significance in the differences between angles and actions calculated for very close orbits. Nevertheless, a straightforward Runge–Kutta scheme for the orbits remains adequate in all the cases studied here.

The second class of errors – those arising from the truncation of equations (2.17) – are best assessed by simply recomputing the same quantity with more basis functions, more Fourier harmonics, or a larger disc. The results of these tests for all the truncated quantities can be seen in Figs 4 and 5. All these results are for the isochrone/9 model first studied by Kalnajs (1976) with the $n=7$ series of Kalnajs' basis functions, which is further discussed in Section 4. Since the calculation of the matrix $\mathbf{M}(\omega)$ in equation (2.18) is the most computationally intensive operation, the self-gravity parameter q is taken instead of the growth rate η as a convergence criterion. The q plotted in the figures is that which satisfies equation (2.18). It is found by bisection with respect to the winding number of the Nyquist diagram. A value $q=1$ for the expected exact growth rate (given by Kalnajs 1978) is the asymptote towards which the calculation should converge when the appropriate range of parameters have been found.

Fig. 4 shows how the sampling affects the result when the initial R_0, V_0 grid has the same number of points in each direction. The different lines in this and subsequent figures indicate how q converges for different sizes of basis. The figure shows that for this disc, a sampling with a 40×40 grid reduces the sampling errors well below those from the basis truncation. The right-hand panel shows how the truncation of the disc influences convergence for different sizes of basis. If the instability is localized to the inner parts of the disc, including more of the outer regions should not affect the result. The behaviour seen here is due to stretching of the basis when $R_{\max}$ is increased, so more functions are required to sample the inner regions to the same resolution. If, however, enough functions are used, no change is seen beyond about $R_{\max}=4.5$.

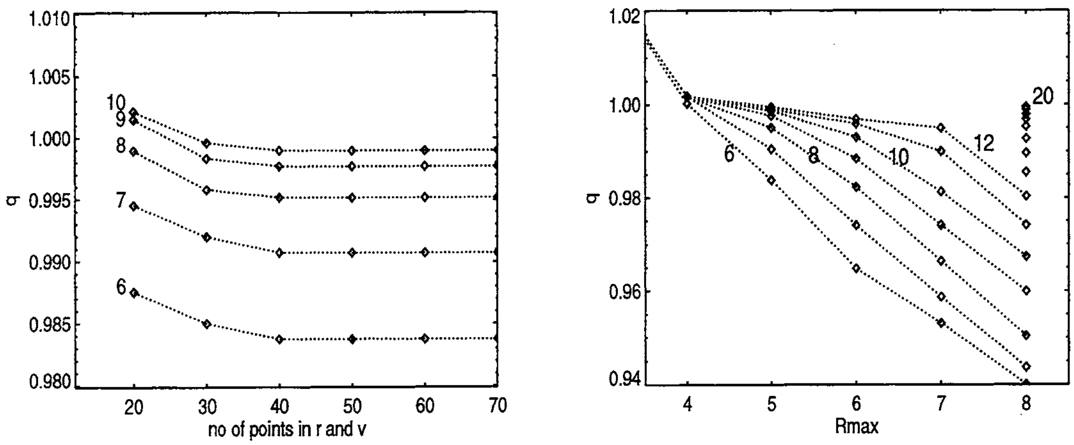

Figure 4. The self-gravity parameter, q, as a function of the grid sampling, and the disc truncation. Data are shown for bases of various sizes as labelled. In the right-hand panel, q is shown as a function of the truncation radius of the disc for different sizes of basis as labelled. More functions are needed for convergence with larger R, because the inner, dominant, part of the disc is less well sampled when the basis is stretched over a larger domain. As with all the figures in this section, the disc is Kalnajs' isochrone/9 model. The basis is Kalnajs' biorthonormal set with $k=7$.

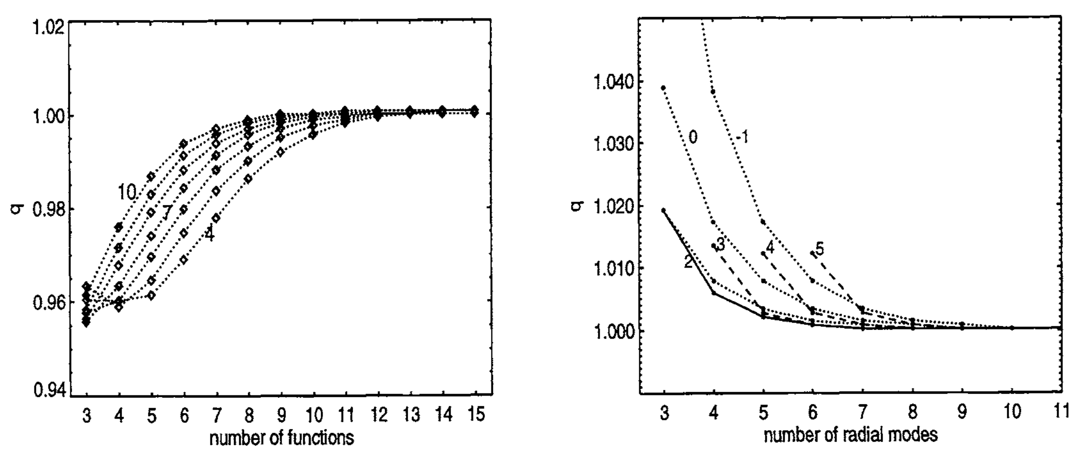

Figure 5. The dependence of the self-gravity parameter, q, upon the order of the basis, the number of functions used in the calculation, and the number of radial harmonics. The left-hand panel shows q against the basis size for different bases from Kalnajs' set, labelled by the corresponding k parameter. In the right-hand panel, 12 functions were used, with the number of radial harmonics on the abscissa taken on either side of a central value as labelled on the lines. Centring the harmonics on 2 (when looking for bisymmetric instabilities) shows appreciably better convergence than taking equal numbers of positive and negative harmonics (centre 0).

As remarked by Earn & Sellwood (1995), choosing an appropriate basis for a given instability has a significant effect on the number of basis functions necessary to resolve the mode. This may be seen in Fig. 5 for Kalnajs' set of biorthonormal bases with $4 \leq k \leq 10$. 10 functions with the $k=4$ basis are required to give the same error in q as achieved with only six functions in the $k=10$ basis. Kalnajs remarks that some economies may be made by not using the same number of positive and negative radial Fourier modes but by centring the range on m, the order of the instability. This is illustrated in the right-hand panel, where the abscissa gives the number of radial modes on each side of a central value as labelled. The computational load is almost directly proportional to the number of radial modes to be used, so this effect is well worth exploiting. Developing a specific basis for different thin discs also speeds up the calculation, by reducing the number of functions required for convergence, but it is not necessary. Any reasonable basis will get there in the end, and the feasibility of the resulting computations considerably enhances the generality of this approach. Finally, Fig. 6 illustrates the convergence of the shape of the mode as a function of the number of basis functions.

4 APPLICATION: THE ISOCHRONE AND KUZMIN–TOOMRE DISCS

The versatility of the algorithm for linear stability described above is now illustrated while recovering growth rates and pattern speeds of previously studied discs with old and new distribution functions, finding the modal response – in position space and in action space – of these discs both for bisymmetric and lopsided modes.

4.1 The equilibria

Three families of discs are studied here: two corresponding to equilibria for the isochrone disc (Hénon 1961), and one for the Kuzmin–Toomre mass model (Kuzmin 1956). The isochrone disc is defined by its potential, $\psi = GM/(b+r_b)$, where $r_b^2 = R^2 + b^2$. The corresponding surface density is $\Sigma = Mb\{\ln[(R+r_b)/b] - R/r_b\}/(2\pi R^3)$. The Kuzmin–Toomre potential is defined by $\psi = GM/r_b$, and the corresponding surface density is $\Sigma = Mb/2\pi r_b^3$. Miyamoto (1974), followed by Kalnajs (1976), Athanassoula & Sellwood (1985) and Pichon & Lynden-Bell (1996), chose specific forms of distribution functions, assuming simple algebraic Ansatz for its expression in (ε, h) space. Historically, these models were first used to construct families of maximally rotating discs (e.g., the Miyamoto/m_{M} disc models – Hunter 1993), while for others, counter-rotating stars were re-introduced by simple, though somewhat arbitrary, tricks (Kalnajs 1978) described by Earn & Sellwood (1995). In this paper, the Kalnajs isochrone/m_{K} models are implemented in order to recover Kalnajs' (1978) first linear stability results on differentially rotating discs. To demonstrate the flexibility of the method, the truncated version of Hunter's Kuzmin–Toomre/m_{M} models is also constructed, and the stability of the equilibria given by Pichon & Lynden-Bell (1996) is analysed.

Kalnajs' distribution family reads (in units of b and $G=1$)

$$f_{\mathrm{K}}(\varepsilon, h) = 2^{2m-1}(\sqrt{-2\varepsilon}h)^{-m}\pi^{-1}(-\varepsilon)^{m-1}g(\sqrt{-2\varepsilon}h), \tag{4.1}$$

where

$$g(x) = x\frac{\partial[x^m\tau_m(x)]}{\partial x} + \int_0^1 (tx)^m\tau_m(tx)P''_{m-1}(t)\,\mathrm{d}t - \tfrac{1}{2}(m-1)mx^m\tau_m(x), \tag{4.2}$$

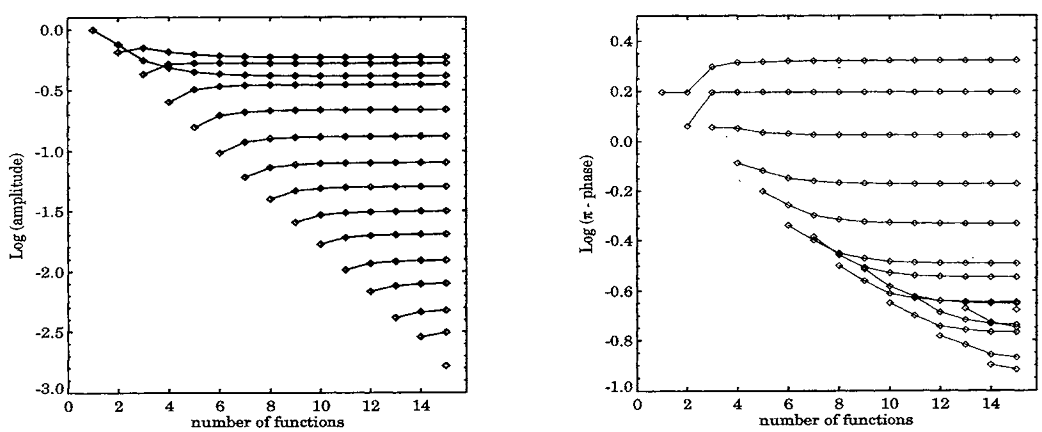

Figure 6. The amplitude (left-hand panel) and the phase (right-hand panel) of components of the critical eigenvectors as a function of the number of basis functions. The rapid convergence of the shape of the mode appears clearly.

and

$$\tau_m(x) = \left. \frac{\log(r+\sqrt{1+r^2}) - r/\sqrt{1+r^2}}{2\pi r^3(-1-\sqrt{1+r^2})^{-m}} \right|_{r=2x/(x^2-1)}. \tag{4.3}$$

Here P_m stands for the Legendre polynomial of order m. Pichon & Lynden-Bell's distribution family for the isochrone disc is given by

$$f_{\mathrm{P}}(\varepsilon, h) = \frac{(-\varepsilon)^{m+1/2}}{4\pi^2(m+1/2)!!} \frac{h}{\sqrt{2}} \left(\frac{\partial}{\partial s}\right)^{m+2} [(s^2-1)_m L(s)] \bigg|_{s=1+h^2/2}, \tag{4.4}$$

with $L(s) = \log(\sqrt{s^2-1}+s) + \sqrt{s^2-1}/s$. Its contours for $m_{\mathrm{P}}=4$ are illustrated in Fig. 7, while the Q profiles are given by Pichon & Lynden-Bell (1996, fig. 5). Finally, Miyamoto's distribution is

$$f_{\mathrm{M}}(\varepsilon, h) = \frac{(2m+3)}{2\pi^2} (-\varepsilon)^{2+2m} {}_2F_1\left(-m, -2-2m, \frac{1}{2}, \frac{-h^2}{2\varepsilon}\right), \tag{4.5}$$

where ${}_2F_1$ is a terminating hypergeometric function of the second kind.

4.2 Characteristics of the linear wave

4.2.1 Bisymmetric $m=2$ modes

The pitch angle of the spiral response is commonly defined as $\cot(i) = \langle \partial\theta/\partial \log(R) \rangle_\theta$, where $\theta = \theta(R)$ at the crest of the spiral wave. In practice, it is best to calculate $\tan(i) = \langle \partial \log(R)/\partial\theta \rangle_R$ since $R = R(\theta)$ is a bijection in $[0, 2\pi/m[$. Another useful set of quantities are defined by the radius, $R_{1/2}$, (resp. the angle $\theta_{1/2}$) at which the spiral response has decreased to half its maximum amplitude. The winding number $n_{1/2} = \theta_{1/2}/(2\pi)$ yields a measure of the winding of the wave: the larger $n_{1/2}$ is, the more wound it is. Comparing the position of the resonances and $R_{\max}$ to $R_{1/2}$ provides the means to assess whether the truncation of the disc is likely to have generated spurious cavity waves. Specifically, it is required that $R_{1/2} < R_{\mathrm{OLR}} < R_{\max}$, so that the wave is well damped by the outer Lindblad resonance before the disc is truncated. Numerical simulations have suggested that $R_{1/2} \sim R_{\mathrm{COR}}$. Both statements are verified here for instance in Fig. 10 (resp. Fig. 11), which gives the linear response of a $m_{\mathrm{K}}=7$ and a $m_{\mathrm{K}}=11$ isochrone disc (resp. $m_{\mathrm{K}}=5$ Kuzmin disc) for its first growing mode. These perturbations display the usual bar-shaped

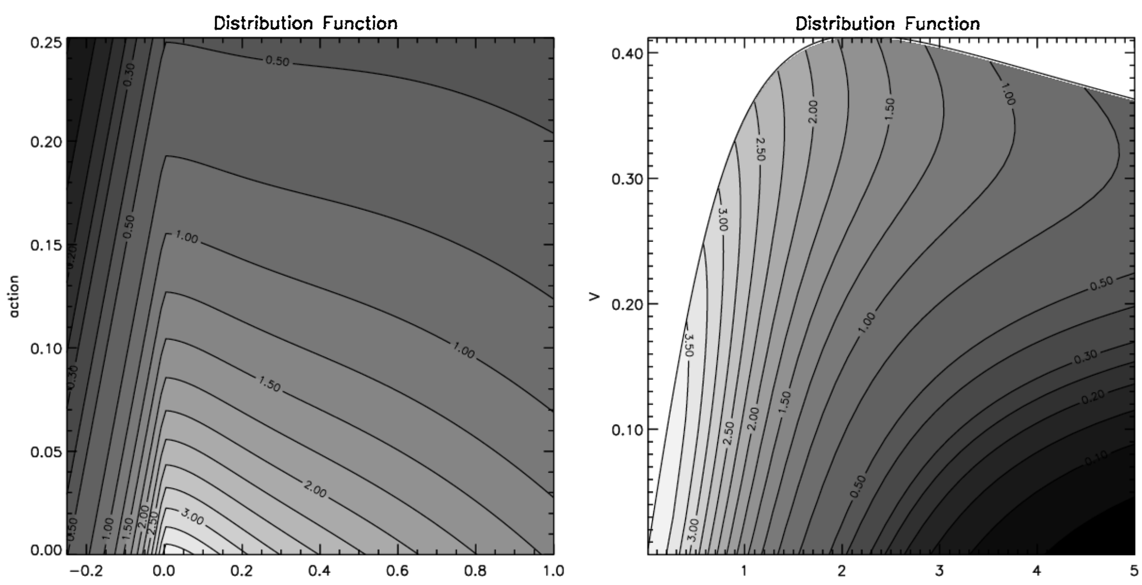

Figure 7. Left-hand panel: isocontours of the $m_{\mathrm{P}}=4$ distribution function in action space. The sharp break at zero momentum is an artefact of Kalnajs' trick which was used here to incorporate counter-rotating stars; right-hand panel: same isocontours for the prograde stars only in (R_0, V_0) – apocentre, velocity at apocentre – space. These variables are those used throughout the calculation to label the orbits. Note the envelope corresponding to the rotation curve of that galaxy. It appears clearly in this parametrization that in this galaxy most orbits are of low ellipticity.

central response with a loosely wound spiral response further out. Fig. 12 gives the evolution of cot(i), $R_{1/2}$, $n_{1/2}$, Ω_p and η as a function of the Toomre number Q of the Kalnajs /m_K discs. Tables 1–3 give the growth rates and pattern speeds of the /m_K, /m_P and /m_M families. Note that for the new /m_P family the bar modes given in Table 2 again have pattern speeds well above the maximum of $\Omega - \kappa/2$, and hence do not display inner Lindblad resonance. Note also that the more compact Kuzmin–Toomre potential has larger growth rates and pattern speeds, as expected since the dynamical time is shorter and the self-gravity is enhanced for those discs. Table 4 gives the growth rates for the second and the third growth rate of the m_K discs. Note that the growth rate of the second fastest growing mode of a $m_K=12$ model was found by this method to equal $\omega + i\eta = 0.461 + 0.145i$, roughly within the error bars given by Earn & Sellwood (1995). Note that the number of radial nodes for these slower modes increase with the rank in stability (as illustrated in Fig. 16 for an $m=1$ mode discussed in the next subsection), which is consistent in so far as winding decreases self-gravity. Note also the small relative error between the growth rates recovered for the Myamoto/Hunter models and those given by Hunter (1993) for the Kuzmin–Toomre discs. Small residual discrepancies are expected, given that Hunter's discs are infinite, whereas those studied here are truncated at $R=5$. Fig. 8 gives for the m_K and m_P families the evolution of the first growing mode as a function of the Toomre Q number (mass-averaged in the inner region $R<2$) of these discs and 'the mass in the halo' as parametrized by q. An *new* attempted fit of a combination of Q and q is also given in Fig. 9 for both distributions; the relative dispersion illustrates the well-known

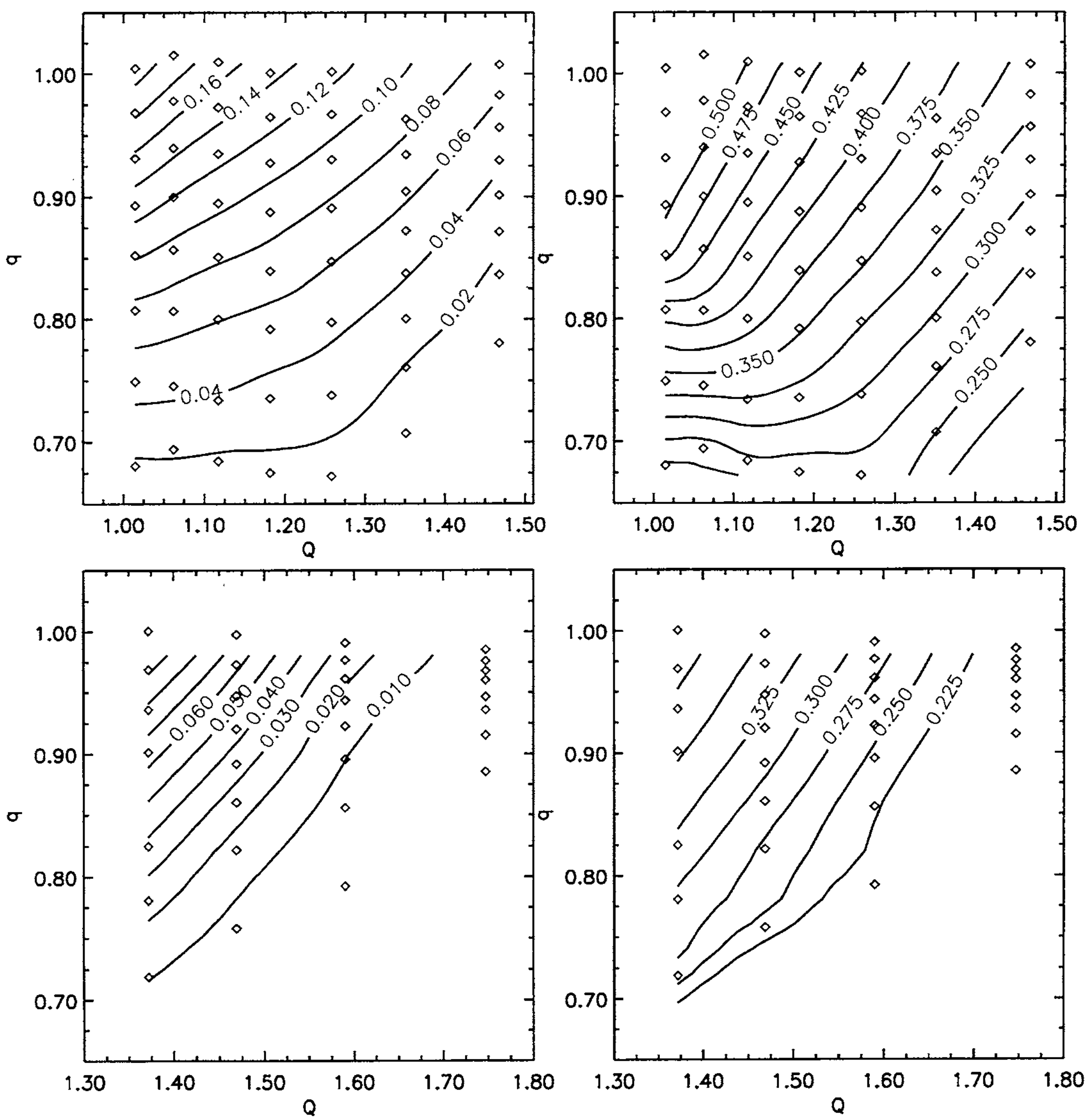

Figure 8. The variation of the $m=2$ growth-rate (top-left panel) and the pattern speed (top-right panel) of an isochrone/m_K family as a function of the self-gravity parameter q and the Toomre number Q. The bottom panels show the same results for the isochrone/m_P family. The precision in the growth-rates – at fixed truncation in the basis – drops for lower values of Q, since these modes are more centrally concentrated.

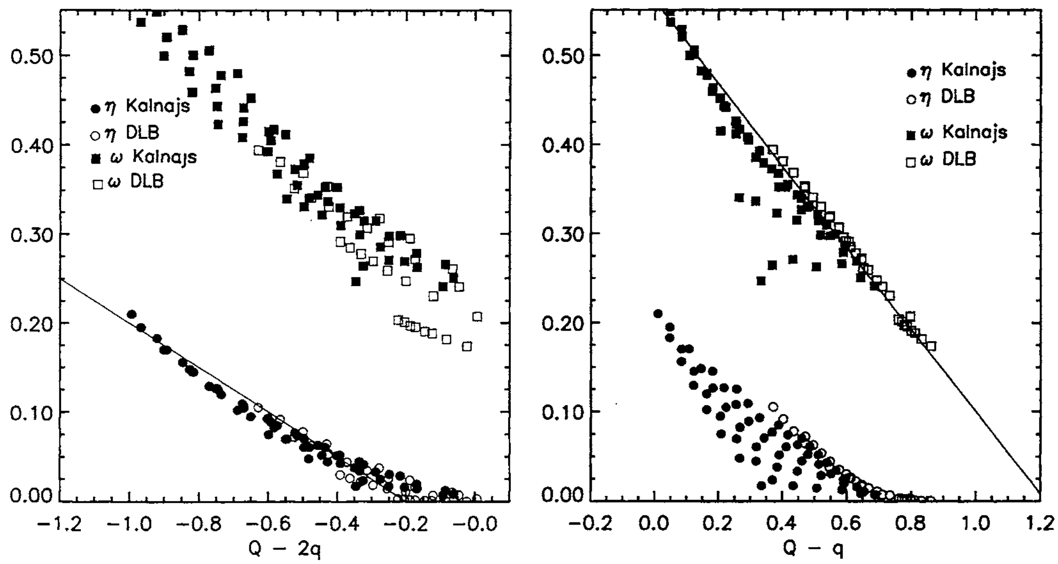

Figure 9. Fits to the evolution of the $m=2$ growth rate and the pattern speed of an isochrone/m_K (marked Kalnajs) and an isochrone/m_P (marked DLB) family as a function of a linear combination of the self-gravity parameter q and the Toomre number Q. The left-hand panel minimizes the dispersion in η, whereas the right-hand panel minimizes that in ω. The best fits are obtained for different linear combinations of Q and q. The solid line for η is $\eta=-0.05-0.25(Q\xi q)$ and that for ω: $\omega=0.56-0.46(Q-q)$.

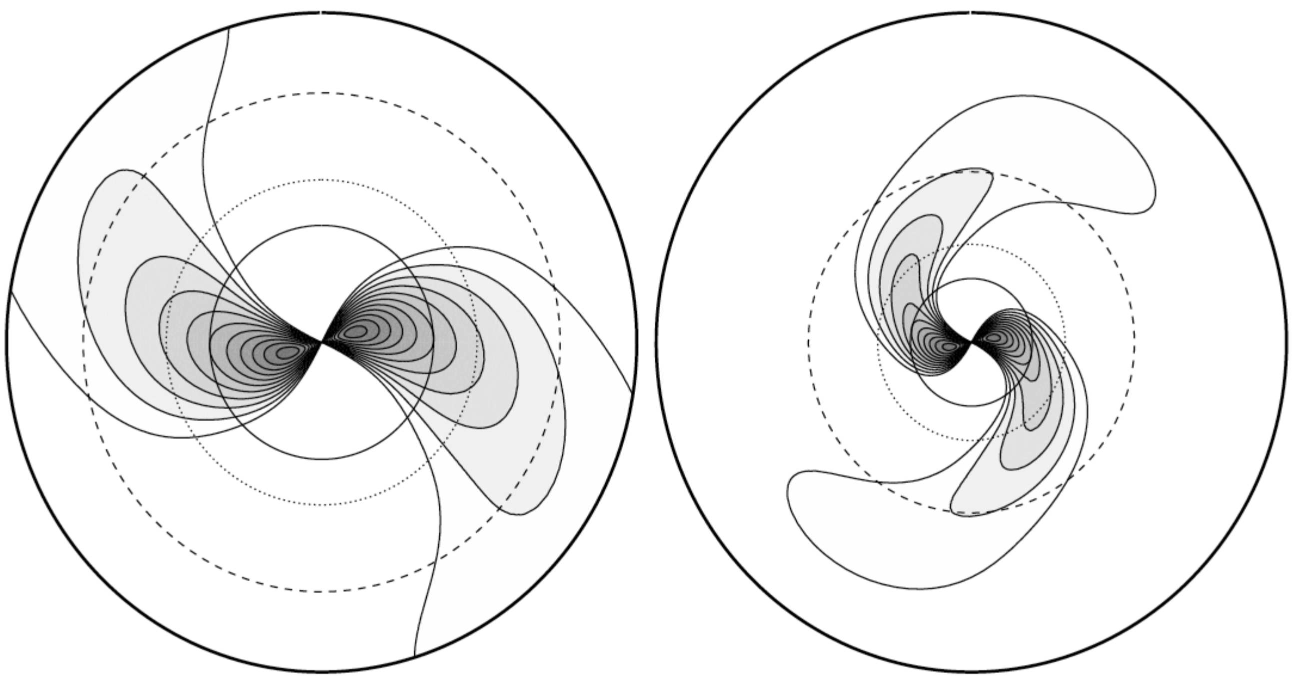

Figure 10. The density response corresponding to the fastest $m=2$ growing mode of the isochrone/7 and isochrone/11 model. Note that the colder /11 model yields a more tightly wound spiral, as shown quantitatively in Fig. 12. This is expected, since in the locally marginally radially unstable regime, the disc response should asymptotically match that of unstable rings. Its spiral response is also more centrally concentrated than that of its hotter counterpart. The solid circle corresponds to $R_{1/2}$, the radius at which the wave has damped by a factor of 2, the dotted circle to corotation resonance, the dashed circle to the outer Lindblad resonance, and the outer circle to $R_{\max}=5$.

fact that the stability does not depend only on a simple combination of these numbers. These curves seem to be in qualitative agreement with those given by Vauterin & Dejonghe (1996) for different disc models. Here, too, the pattern speed at fixed growth rate is a decreasing function of the Q number ($\partial\Omega_p/\partial Q_\eta<0$). The conjecture of Athanassoula & Sellwood (1985) of an asymptotic value of $Q\approx 2$ for marginal stability of *fully self-gravitating discs* seems also consistent with these results.

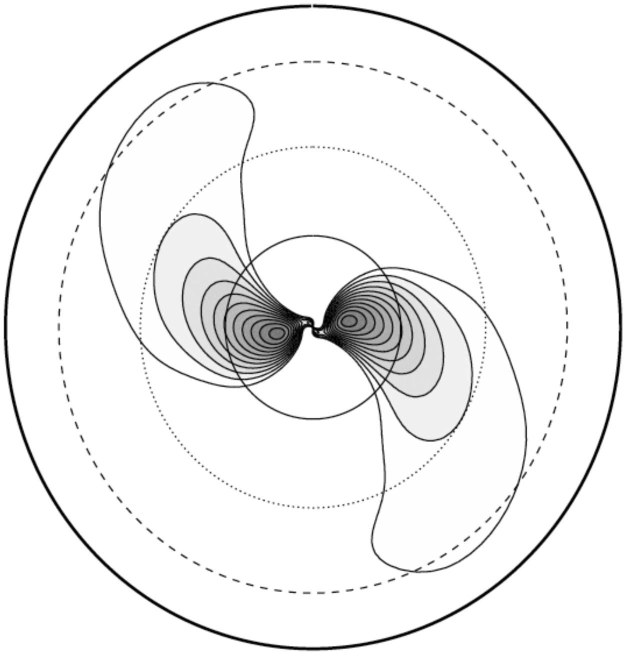

Figure 11. Same as Fig. 10 for a Myamoto–Hunter/3 model. Note that the response is much more centrally concentrated, since the outer circle is $R_{max}=3$. This is expected, since the Kuzmin–Toomre potential is more compact than the isochrone.

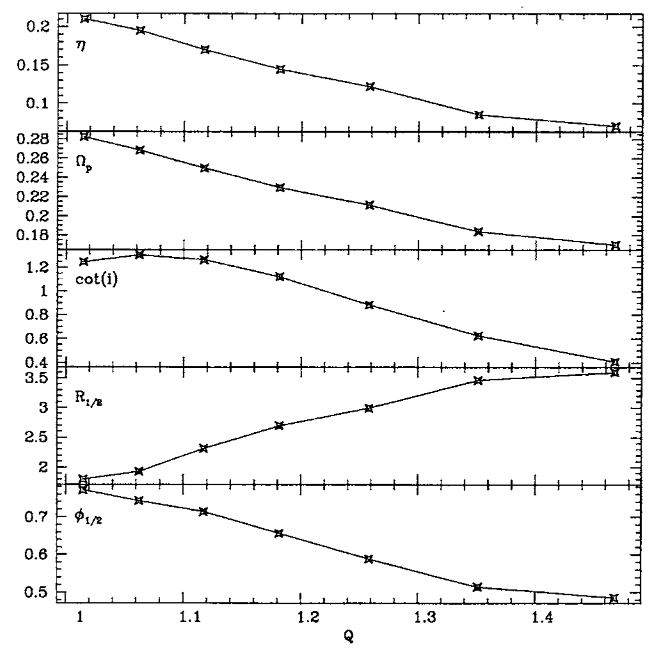

Figure 12. The evolution of η, Ω_p, $\cot(i)$, $R_{1/2}$ *and* $n_{1/2}$, as a function of the Toomre number Q of the isochrone/m_K discs. Note that the hotter disc have less wound spiral response.

Table 1. $m=2$ growth rates and pattern speed of the isochrone/m_K model.

The isochrone/m_K model: bisymmetric mode

Model	$m\Omega_p$	η
6	0.34	0.075
7	0.37	0.085
8	0.43	0.125
9	0.47	0.145
10	0.50	0.170
11	0.53	0.195
12	0.59	0.210

Table 2. $m=2$ growth rates and pattern speed of the isochrone/m_P model.

The isochrone/m_P model: bisymmetric mode

Model	$m\Omega_p$	η
3	0.21	0.003
4	0.29	0.032
5	0.35	0.072
6	0.40	0.105

Table 3. $m=2$ growth rates and pattern speed of the Toomre/m_M model.

The Toomre/m_M model: bisymmetric mode

Model	$m\Omega_p$	η
2	0.598	0.204
3	0.714	0.294
4	0.810	0.371
5	0.916	0.445

Table 4. Second and third fastest $m=2$ growing modes of the isochrone/m_K model.

The isochrone/m_K model: bisymmetric mode

Model	Second mode	Third mode
7	0.29(4) + 0.04(1)i	0.22(0) + 0.008(8)i
10	0.39(7) + 0.10(5)i	0.27(3) + 0.039(5)i
11	0.42(8) + 0.12(8)i	0.34(7) + 0.091(5)i
12	0.46(1) + 0.14(5)i	0.26(4) + 0.051(2)i

4.2.2 *Lopsided m = 1 modes*

The algorithm presented in Section 3 is, in principle, inadequate to address the growth of $m=1$ perturbations which for purely self-gravitating discs are forbidden, since the perturbation does not conserve momentum. Following Zang (1976), it is assumed here that the disc is embedded in some sufficiently massive halo to compensate its infinitesimal centre of mass shift. Fig. 15 gives the $m=1$ modal response of the isochrone/$m_{10,11}$ discs, while the corresponding pattern speeds and growth rates are given

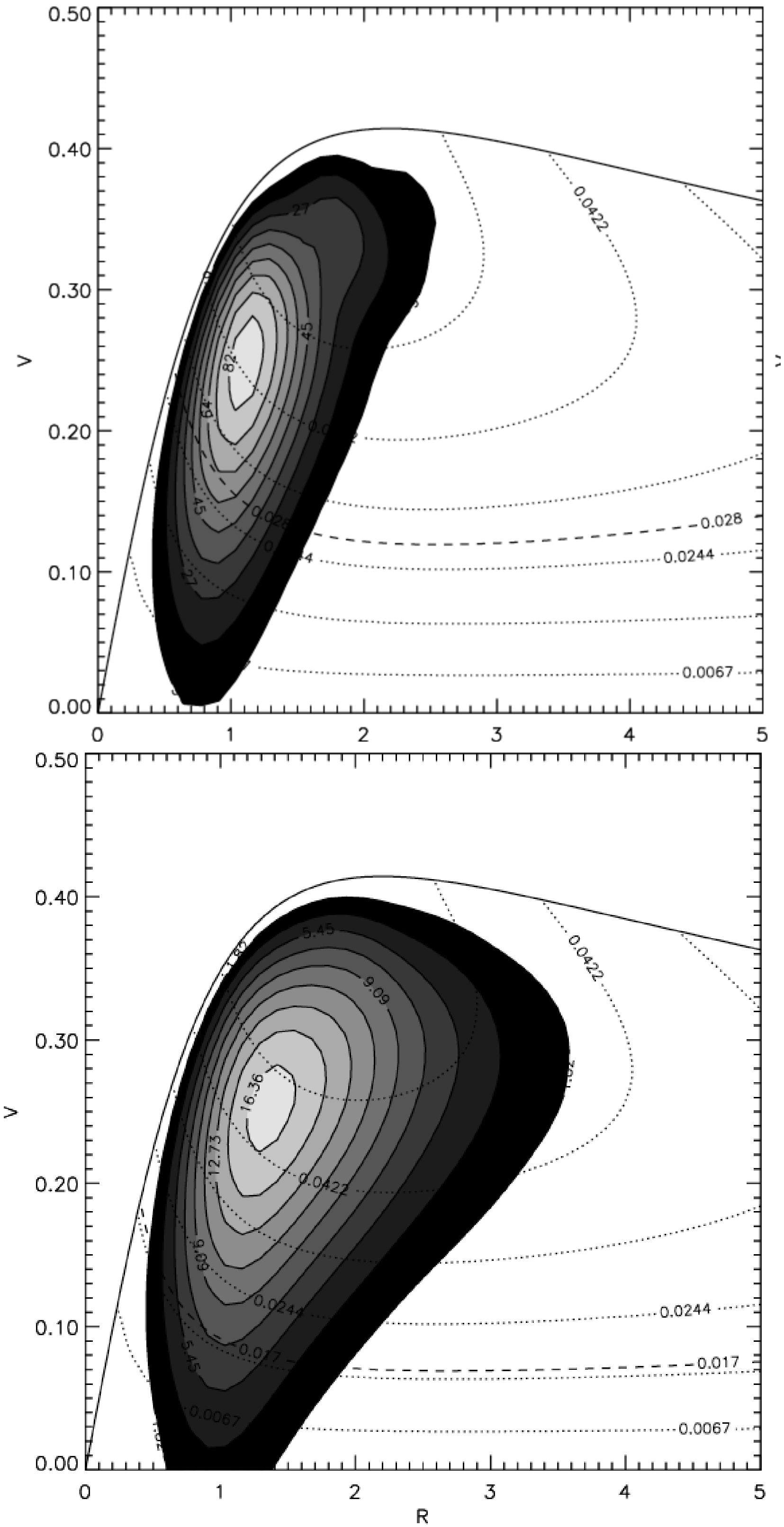

Figure 13. The orbital response in action space corresponding to the fastest growing mode described in Fig. 4. The amplitude of the left-hand side of equation (2.5) is plotted for the $\ell = -1$ (ILR) fastest growing mode of an isochrone/12 model (left-hand panel), and an isochrone/6 model (right-hand panel). Superimposed are the isocontours of the corresponding resonance $\Omega - \kappa/2$. The dashed line corresponds to the isocontour of a tenth of the pattern of the wave. Note that the hotter disc forms a Grand Design structure involving more eccentric orbits.

Table 5. First and second growth rates and pattern speeds of the $m=1$ isochrone/m_K model.

The isochrone/m_K model: lopsided mode

Model	Pattern speed	Growth rate
9	0.135	0.0325
10	0.17	0.065
11	0.20	0.095
12	0.23	0.125

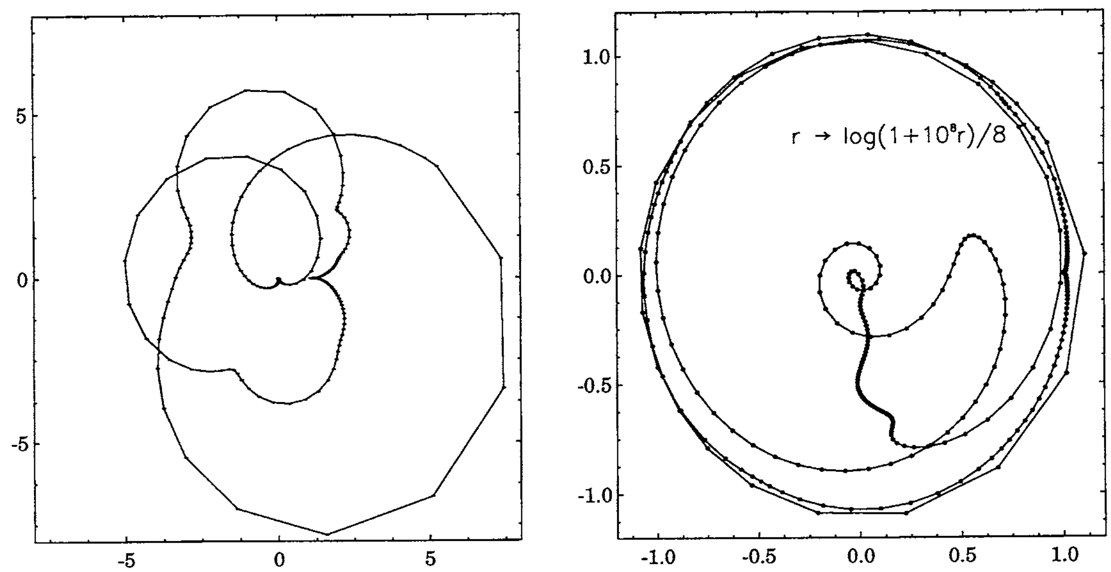

Figure 14. Nyquist diagram for the second $m=1$ modes of an isochrone/12 disc. There are more large loops than are seen for the bisymmetric modes, and also more structure at small scales: in the right-hand panel, the origin is shown enlarged under the mapping $r \rightarrow (1+10^8 r)/8$. All the space within the innermost of the three large concentric loops corresponds to the tiny cusp at the centre of the left-hand panel.

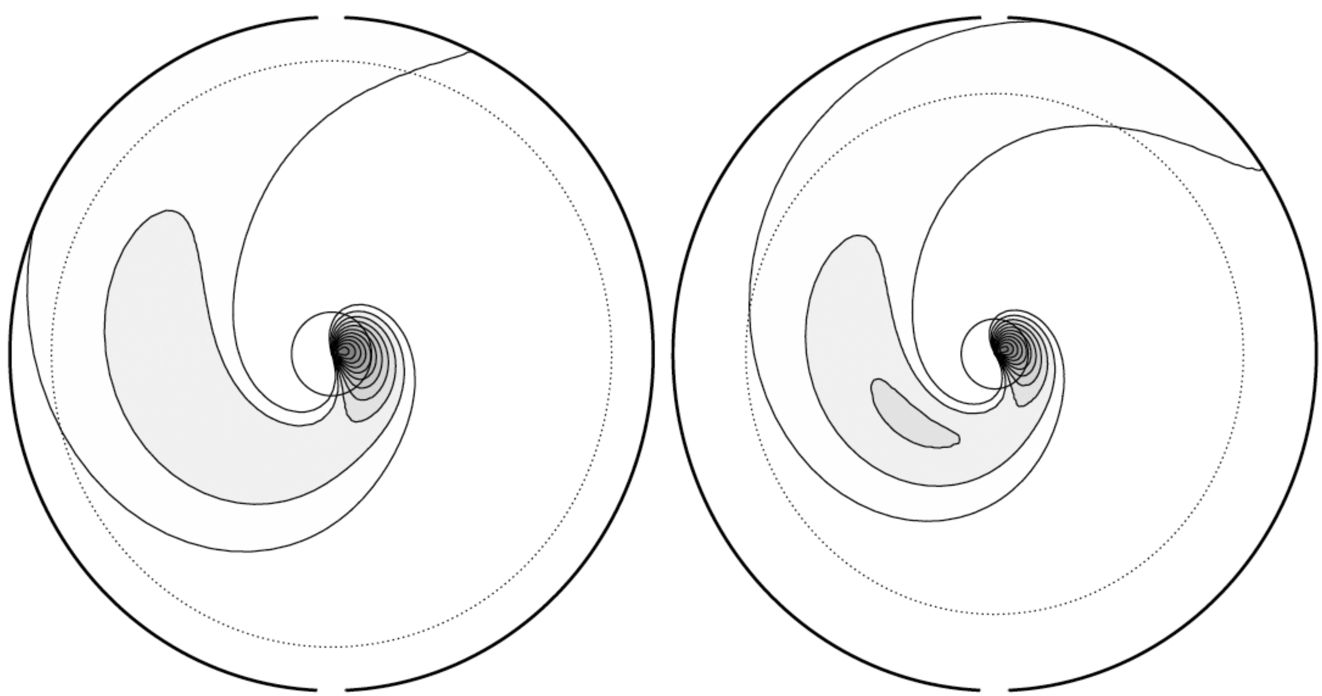

Figure 15. The $m=1$ density response corresponding to the growing mode of the isochrone/10 and isochrone/11 model. The lopsided mode, which has a smaller growth rate, has a much more centrally concentrated response than its bisymmetric counterpart.

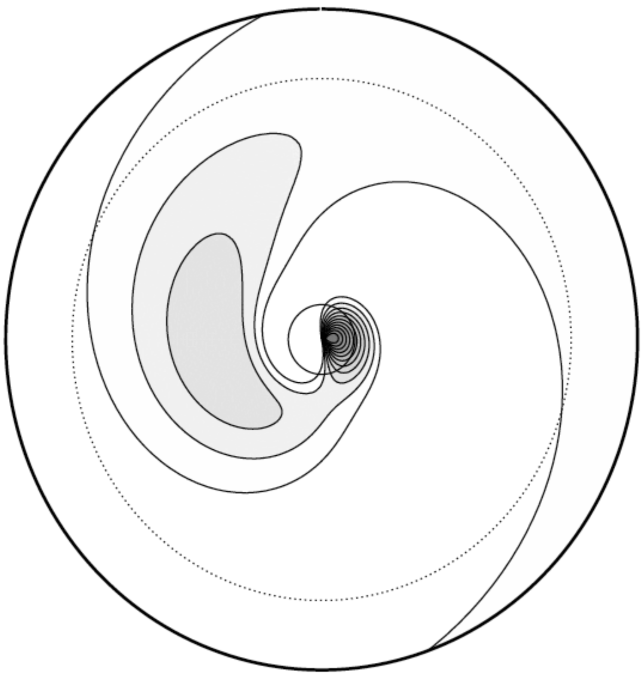

Figure 16. The $m=1$ density response corresponding to the second faster growing mode ($\Omega_p + i\eta = 0.18 + i0.075$) of the isochrone/12 model. The number of radial nodes in the response has increased by one compared to the corresponding faster mode illustrated on Fig. 15 for an isochrone/11 disc.

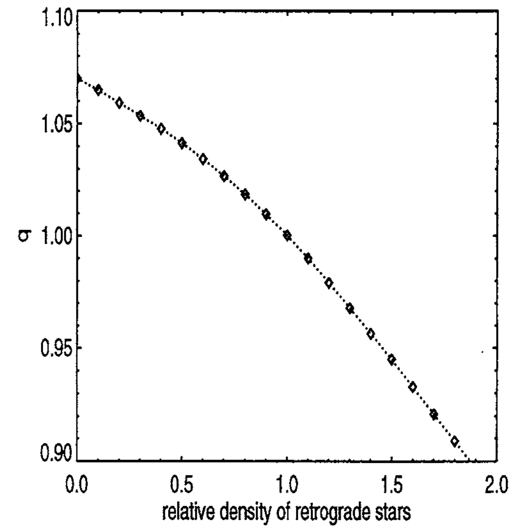

Figure 17. The effect on q of artificially modifying the density of retrograde stars in Kalnajs' isochrone/9 distribution function. The retrograde part of the distribution function has been multiplied by the factor on the ordinate, keeping the prograde stars the same. Although in Kalnajs' model stars on retrograde orbits only account for a few per cent of the total mass, they play a significant role in stabilizing the disc.

in Table 5. These modes have smaller growth rates than their bisymmetric counterparts, and are practically more difficult to isolate because they are close to other modes which grow almost as fast; the Nyquist diagrams show many large loops, all of which must be properly sampled to avoid spurious contours encircling the origin, as illustrated in Fig. 14. Indeed, when investigating weaker and weaker modes, the amount of looping in the corresponding Nyquist diagrams should increase, since modes always occur in pairs ($\omega \pm \eta$), so that when η is small, one is always in a regime corresponding to at least two (a growing and a decaying) modes.

The physical mechanism leading to the appearance of these modes needs to be clarified, but presents little practical interest when their growth rates do not correspond to the fastest growing mode. The detailed analysis of $m=1$ modes for the isochrone disc is therefore delayed until models of distribution functions which display weaker $m=2$ modes are designed.

4.3 Application to observed discs

The procedure described in Section 3 makes no assumption on the nature of the distribution function or the potential of the disc. In particular, it is well adapted to distribution functions recovered from measured discs, where the radial derivative of the potential follows from H I rotation curve of the disc, while the distribution function itself is inverted from line-of-sight velocity profiles. The technique was tested on tables generated from equation (4.5). The agreement between the 'theoretical' and 'measured' (i.e., derived from a discretized representation of the distribution) growth rates was found to be in better than 1 per cent. One peculiarity in this context lies in the finite difference chosen in the numerical derivatives of the distribution function with respect to J and h. While applying this analysis to observed data, special care should be taken in handling measurements relative to the core of the galaxy, since the relative fraction of counter-rotating stars plays a crucial role in determining the growth rates of the disc, as pointed out already by Kalnajs and illustrated in Fig. 17. This appears clearly when recalling that counter-rotating stars add up to an effective azimuthal pressure in the inner core, which therefore prevents the self-gravity of the disc to build up by orbit alignment. A non-parametric inversion technique has been devised by Pichon & Thiébaut (1997) to recover the best distribution accounting for all the measured kinematics while handling specifically the counter-rotating stars.

5 CONCLUSION AND PROSPECTS

A numerical investigation of linear stability of round galactic discs has proven successful in recovering known growth rates for the isochrone disc and the Kuzmin–Toomre discs. The method is fast and versatile, and can be applied to realistic discs with arbitrary density and velocity profiles, and relative 'halo' support. Unstable bisymmetric growing modes for *new* equilibria, and the fastest growing lopsided modes for Kalnajs' distribution function have also been isolated to demonstrate the code's versatility. The authors are currently applying the method in a study of the stability to families of discs parametrized by their relative temperature, compactness, fraction of counter-rotating stars and halo support in order to identify the orbits responsible for the instability, and to probe the intrinsic (orbital or wave-like) nature of the $m=2$ bar instability. The nature of lopsided $m=1$ instabilities in disc galaxies is also under investigation. The implementation of linear stability analysis for observed galactic disc, yielding a direct relationship between the growth rate of the instability, the measured kinematical characteristics of the disc and the relative mass in the halo, is also being investigated. The requirement of marginal stability will provide an estimate of the minimum halo mass. All ingredients will then be in place to probe the amount of dark matter required to stabilize observed galactic discs.

ACKNOWLEDGMENTS

CP thanks J. Collett, D. Lynden-Bell, S. Tremaine, J. F. Sygnet and O. Gerhard for useful conversations. Many thanks are due to the referee, J. Sellwood, for positive criticism, to J. Binney for reading the manuscript, and to P. Englemaier for his help with **sm**. Funding from the Swiss NF and computer resources from the IAP are gratefully acknowledged.

REFERENCES

Athanassoula E., Sellwood J., 1985, MNRAS, 221, 213
Bertin G., 1994, ApJ, 434, 94
Collett J., 1995, PhD thesis, Univ. Cambridge
Earn D., Sellwood J., 1995, ApJ, 451, 533
Hénon M., 1960, Ann. d'Astrophys., 23, 668
Hohl F., 1971, ApJ, 168, 343
Hunter C., 1993, in Dermott S. F., Hunter J. H., Wilson R. E., eds, Astrophysical Disks. New York Academy of Sciences
Kalnajs A., 1971, ApJ, 166, 275
Kalnajs A., 1976, ApJ, 205, 745
Kalnajs A., 1977, ApJ, 212, 637
Kalnajs A., 1978, in Berkhuisjen E., Wielebinski R., eds, Proc. IAU Symp. 77, Structures and Properties of Nearby Galaxies. Reidel, Dordrecht, p. 113
Kuzmin G. G., 1956, Astron Zh., 33, 27
Lynden-Bell D., 1979, MNRAS, 187, 101
Lynden-Bell D., 1994, in Contopoulos G., Spyrou N. K., Vlahos L., eds, Galactic Dynamics and N-body Simulations: lectures at the EADN Astrophysical School, Thessaloniki. Springer-Verlag, Berlin, p. 3
Lynden-Bell D., Kalnajs A., 1972, MNRAS, 157, 1
Lynden-Bell D., Ostriker J., 1967, MNRAS, 136, 293
Miyamoto, 1974, A&A, 30, 441
Pichon C., Lynden-Bell D., 1992, Orbital instabilities in galaxies, contribution to the Ecole de Physique des Houches on: Transport Phenomena in Astrophysics, Plasma Physics and Nuclear Physics
Pichon C., Lynden-Bell D., 1996, MNRAS, 282, 1143
Pichon C., Thiébaut E., 1997, MNRAS, submitted
Qian E., 1992, MNRAS, 257, 581
Sellwood J., Wilkinson A., 1993, Rep. Prog. Phys., 56, 173
Sygnet J. F., Kandrup H. E., 1984, ApJ, 276, 737
Vauterin P., Dejonghe H., 1996, A&A, 313, 465
Weinberg M. D., 1991, ApJ, 368, 66
Zang T., 1976, PhD thesis, MIT

Mon. Not. R. Astron. Soc. **374,** 877–909 (2007) doi:10.1111/j.1365-2966.2006.11203.x

Dynamical flows through dark matter haloes – II. One- and two-point statistics at the virial radius

Dominique Aubert[1,2,3]★ and Christophe Pichon[1,3]

[1] *Observatoire Astronomique de Strasbourg, 11 rue de l'Universite, 67000 Strasbourg, France*
[2] *Service d'Astrophysique, CEA Saclay, 91191 Gif-Sur-Yvette, France*
[3] *Institut d'Astrophysique de Paris, 98 bis boulevard Arago, 75014 Paris, France*

Accepted 2006 October 12. Received 2006 October 9; in original form 2006 July 23

ABSTRACT

In a series of three papers, the dynamical interplay between environments and dark matter haloes is investigated, while focusing on the dynamical flows through the virtual virial sphere. It relies on both cosmological simulations, to constrain the environments, and an extension to the classical matrix method to derive the responses of the halo. A companion paper (Paper I) showed how perturbation theory allows us to propagate the statistical properties of the environment to an ensemble description of the dynamical response of the embedded halo. The current paper focuses on the statistical characterization of the environments surrounding haloes, using a set of large-scale simulations; the large statistic of environments presented here allows us to put quantitative and statistically significant constrains on the properties of flows accreted by haloes.

The description chosen in this paper relies on a 'fluid' halocentric representation. The interactions between the halo and its environment are investigated in terms of a time-dependent external tidal field and a source term characterizing the infall. The former accounts for fly bys and interlopers. The latter stands for the distribution function of the matter accreted through the virial sphere. The method of separation of variables is used to decouple the temporal evolution of these two quantities from their angular and velocity dependence by means of projection on a 5D basis.

It is shown that how the flux densities of mass, momentum and energy can provide an alternative description to the 5D projection of the source. Such a description is well suited to regenerate synthetic time lines of accretion which are consistent with environments found in simulations as discussed in the Appendix. The method leading to the measurements of these quantities in simulations is presented in detail and applied to 15 000 haloes, with masses between 5×10^{12} and $10^{14}\,\mathrm{M}_{\odot}$ evolving between $z = 1$ and 0. The influence of resolution, class of mass, and selection biases are investigated with higher resolution simulations. The emphasis is put on the one- and two-point statistics of the tidal field, and of the flux density of mass, while the full characterization of the other fields is postponed to Paper III.

The net accretion at the virial radius is found to decrease with time. This decline results from both an absolute decrease of infall and a growing contribution of outflows. Infall is found to be mainly radial and occurring at velocities $\sim$0.75 times the virial velocity. Outflows are also detected through the virial sphere and occur at lower velocities $\sim 0.6V_{\mathrm{c}}$ on more circular orbits. The external tidal field is found to be strongly quadrupolar and mostly stationary, possibly reflecting the distribution of matter in the halo's near environment. The coherence time of the small-scale fluctuations of the potential hints a possible anisotropic distribution of accreted satellites. The flux density of mass on the virial sphere appears to be more clustered

★E-mail: aubert@astro.u-strasbg.fr

than the potential, while the shape of its angular power spectrum seems stationary. Most of these results are tabulated with simple fitting laws and are found to be consistent with published work, which rely on a description of accretion in terms of satellites.

Key words: methods: *N*-body simulations – galaxies: formation – galaxies: kinematics and dynamics.

1 GALAXIES IN THEIR ENVIRONMENT

Examples of galaxies interacting with their environments are numerous. The Antennae, the Cartwheel Galaxy and M51 are among the most famous ones. One of our closest neighbours, M31, exhibits a giant stellar stream which may be associated with its satellites (e.g. McConnachie et al. 2003). Even the Milky Way shows relics of past interactions with material coming from the outskirts, such as the Sagittarius dwarf (Ibata, Gilmore & Irwin 1995). It appears clearly that the evolution of galactic systems cannot be understood only by considering their internal properties but also by taking into account their environment. From a dynamical point of view, it is still not clear, for example, if spirals in galaxies are induced by intrinsic unstable modes (e.g. Lynden-Bell & Kalnajs 1972; Kalnajs 1977) or if they are due to gravitational interactions with satellites or other galaxies (e.g. Toomre & Toomre 1972). Similarly, normal mode theories of warps have been proposed (Hunter & Toomre 1969; Sparke & Casertano 1988) but failed to reproduce long-lived warps in a live halo for example (e.g. Binney, Jiang & Dutta 1998). Since warped galaxies are likely to have companions (Reshetnikov & Combes 1998), it is natural to suggest satellite tidal forcing as a generating mechanism (e.g. Weinberg 1998; Tsuchiya 2002). Another possibility is angular momentum misalignment of infalling material (e.g. Ostriker & Binney 1989; Jiang & Binney 1999). The existence of the thick disc may also be explained by past small mergers (e.g. Quinn et al. 1993; Walker, Mihos & Hernquist 1996; Velazquez & White 1999). Conversely, very thin discs put serious constraints on the amplitude of the interactions they may have experienced in the past.

On a larger scale, dark matter haloes are built in a hierarchical fashion within the cold dark matter (CDM) model. Some of the most serious challenges these models are now facing – the overproduction of dwarf galaxies in the Local Group (e.g. Klypin et al. 1999; Moore et al. 1999), the cuspide crisis of Navarro–Frenk–White (NFW)-like haloes (e.g. Flores & Primack 1994; Moore 1994), the overcooling problem and the momentum crisis for galactic discs (e.g. Navarro & Steinmetz 1997) – occur at these scales; it is therefore important to study the effects of the cosmological paradigm on the evolution of galaxies in order to address these issues.

In fact, the properties of galaxies naturally present correlations with their environments. For example, Tormen (1997) showed that the shape of haloes tends to be aligned with the distribution of surrounding satellites. Also, the halo's spin is sensitive to recently accreted angular momentum (e.g. van Haarlem & van de Weygaert 1993; Aubert, Pichon & Colombi 2004). More generally, haloes inherit the properties of their progenitors.

At this point, a question naturally arises; 'what is the dynamical response of a galactic system (halo + disc) to its environment?'. One way to address this issue is to compute high-resolution simulations of galaxies into a given environment (e.g. Abadi et al. 2003; Gill et al. 2004; Knebe et al. 2004). However, if one is interested in reproducing the variety of dynamical responses of galaxies to various environments, the use of such simulations becomes rapidly tedious. An alternative way to investigate this topic is presented here, which should complement both high-resolution simulations and large cosmological simulations. In a series of three papers, a hybrid approach is presented to investigate the interplay between environments and haloes. It relies on both cosmological simulations (to constrains the environments) and a straightforward extension of the classical tools of galactic dynamics (to derive the haloes' response). A companion paper (Pichon & Aubert 2006, hereafter Paper I) describes the analytic theory which allows us to assess the dynamics of haloes in the open, secular and non-linear regimes. The purpose of the current paper is to set out a framework in which to describe statistically the environments of haloes and present results on the tidal field and the flux density of matter. Paper III (Aubert & Pichon, in preparation) will conclude the complete description of the environments of dark haloes.

1.1 Galactic infall as a cosmic boundary

Clearly, a number of problems concerning galactic evolution can only be tackled properly via a detailed statistical investigation. Let us briefly make an analogy to the cosmological growth of density fluctuations. Under certain assumptions, one can solve the equations of evolution of those overdensities in an expanding universe (e.g. Peebles 1980, see Bernardeau et al. 2002 for an extensive review). Their statistical evolution due to gravitational clustering follows, given the statistical properties of the initial density field. For example, the power spectrum, $P(z, k)$, may be computed for various primordial power spectra, $P_{\mathrm{prim}}(k)$, and for various cosmologies. In other words, the statistical properties of the initial conditions are *propagated* to a given redshift through an operator $\aleph$ given by the non-linear dynamical equations of the clustering:

$$P(z, k) = \aleph(P_{\mathrm{prim}}(k), z). \tag{1}$$

In a similar way, how would the statistical properties of environments be propagated to the dynamical properties of galactic systems? This is clearly a daunting task: the previous analogy with the cosmological growth of perturbation is restricted to its principle. For example, the assumption of a uniform and cold initial state cannot be sustained for galaxies and haloes. While spatial isotropy is clearly not satisfied by discs, and hot, possibly triaxial haloes, the velocity tensor of galaxies may also be anisotropic. Environments also share these inhomogeneous and anisotropic features since they are also the product of gravitational clustering and cannot be simply described as Gaussian fields. These boundary conditions are not pure 'initial conditions' since they evolve with time and in a non-stationary manner (e.g. the accretion rate decreases with time). A whole range of mass must be taken into account, each with different statistical properties. Finally, trajectories cannot be considered as ballistic (even in the linear regime) and must be integrated over long periods. Notwithstanding the above specificities of the galactic framework, two questions have to be answered.

(i) What is the 'galactic' equivalent of $P_{\rm prim}(k)$, i.e. how does one describe statistically the boundary conditions?

(ii) What is the 'galactic' equivalent of $\aleph$, i.e. how does one describe the inner galactic dynamics?

The second point is discussed extensively in Paper I and is briefly summarized in Section 2. In that paper, it is shown how a perturbative theory can describe the dynamics of haloes which experience both accretion and tidal interactions (see also Aubert et al. 2004). Within this formalism, the environment is described by the external gravitational potential and a source function. The former describes fly bys and the tidal field of neighbouring large-scale structures. The latter describes the flows of dark matter, i.e. the exchanges of material between the halo and the 'interhalo' mediums. The knowledge of these two quantities fully characterizes the boundary condition. The focus here is on well-formed haloes which do not undergo major merger between $z = 1$ and 0. This bias is consistent with a galactocentric description in which a perturbative description of the inner dynamics is appropriate and equal mass mergers are explicitly ignored. As briefly explained in Section 2, this formalism provides a link between the statistical properties of environments to the statistical distributions of the responses of haloes: this link is referred to as statistical propagation. In this manner, the distribution of haloes' dynamical state can be directly inferred from the statistical properties of environments, without relying on the follow up of individual interacting haloes. The observed distributions of dynamical features provide information on the cosmic boundaries which influence haloes. This, together with the perturbative formalism described in Paper I, should allow us to address statistically the recurrent 'nurture or nature' problem of structure formation within galactic systems.

This statistical formalism is complementary to methods based on merger trees (which also couple environment and inner properties of galactic systems; see e.g. Kauffmann & White 1993; Roukema et al. 1997; Somerville & Kolatt 1999). These 'analytic' or 'semi-analytic' models, with prescription for the baryons contained in haloes, angular momentum transfer, cooling and star formation, may predict properties of galaxies given in their formation history (e.g. Cole et al. 1994). This history may be provided analytically using extended Press–Schechter formalism (see e.g. Bond et al. 1991; Lacey & Cole 1993) or using simulations (e.g. Kauffmann et al. 1999; Benson et al. 2001). Even though this technique now extends its field of application to subhaloes (see e.g. Blaizot et al. 2006), it remains somewhat limited for the purpose of dynamical applications. These require a detailed description of the geometrical configuration of the perturbations, and of the dynamical response of the halo. Both of these are difficult to reduce to simple recipes. Conversely, full analytic theories of the inner dynamics of interacting haloes were developed in e.g. Tremaine & Weinberg (1984), Weinberg (1998) and Murali (1999). Relying on the matrix method, these theories do take properly into account the resonant processes that occur when the halo is perturbed by an external potential. However, they usually do not account for the perturbations induced by the accretion of matter, while these authors generally considered test cases where a halo responds to a given configuration (or statistics; see e.g. Weinberg 2001) of perturbations. Paper I extended these theories to open stellar systems and, while relying on numerical simulations to constrain the environments, it reformulated them in terms of the statistics of the inner dynamics of a representative population of haloes.

Paper I presents a list of possible applications. For instance, gravitational lensing by haloes is affected by inner density fluctuations, which are induced by the halo's environment: hence the statistics of the lensing signal are be related to the statistics of halo's perturbations, therefore to the cosmological growth of structures. Paper I showed how this approach could be extended to other observables, such as X-ray temperature maps, SZ surveys or direct detection of dark matter. Statistical propagation allows us to relate cosmology to the inner properties of cluster and galaxies. Conversely, it should be possible to show if the perturbations measured in simulations are consistent with a secular drift towards a universal profile of haloes. Closer to us, the correlation of the numerous artefacts of past accretion in the Local Group, such as streams or tidal tails, can be understood in terms of statistics of environments. All processes which depend critically on the geometry of the interactions may be tackled in this framework.[1]

The statistical propagation relies on the knowledge of the properties of the environment and is stated by the point (i) mentioned above. This question is investigated the current paper by using a large set of simulations, where each halo provides a realization of the environment. From this large ensemble of interacting haloes, the aim is to extract the global properties of their 'cosmic neighbourhood'. Such a task requires an appropriate description of the source and the surrounding tidal field. It is the purpose of this work to implement this description which should both provide insights on the generic properties of cosmic environments and be useful in a 'dynamical' context. Specifically, a method is presented to constrain the exchanges between the halo and its neighbourhood, via the properties of accretion and potential measured on the virial sphere. The advantages, specificities and caveats (and the methods implemented to overcome them) provided by this *halocentric* approach will be presented in this paper.

As shown in the following sections, the source function is given by the phase-space distribution function (DF hereafter) of the advected material. As a consequence, its full characterization is a complex task since it involves sampling a five-dimensional space and relies on the projection of its DF on a suitable 5D basis. In particular, it is shown that how such a description can be used to constrain the kinematic properties of accretion by dark matter haloes in cosmological simulations. The detailed statistical characterization of the higher moments of the source is postponed to Paper III. An alternative description of the source is also presented; it relies on flux densities through the virial sphere, i.e. the moments of the source DF. Even though it is less suited to the dynamical propagation, this alternative description is easier to achieve numerically and to interpret physically. In particular, it illustrates how the source term may be characterized statistically via its moments. The link between these flux densities and the 5D projection of the source is discussed together with the one- and two-point statistics of the flux densities of mass through haloes in simulations. Also, the mean of reprojecting the effect of the external gravitational potential inside the halo (through Gauss's theorem) while knowing its properties on the virial sphere is discussed. The potential's one- and two-point statistics are also investigated around simulated haloes and interpreted.

Finally, Appendix F provides means of regenerating such flows *ab initio* from its tabulated statistical properties. Such tools yield a way to embed idealized simulations of galaxies into realistic cosmological environments.

[1] However, all departure to angular isotropy on the sphere will be ignored here (in contrast to what was stressed in Aubert et al. 2004), and its implications will be postponed to the discussions in Section 8.

 110

The outline of the paper is as follows. Section 2 presents briefly the dynamics of open collisionless systems and states the principle of statistical propagation. Section 3 presents the procedure used to compute the source term, and illustrates its implementation on a given halo. The simulations and the corresponding selection biases of our sample are then described in Section 4.2. Sections 5 and 6 present the statistical measurements for one- and two-point statistics, respectively. Section 7 draws a global picture of galactic infall on $L^\star$ galaxies, while a discussion and conclusions follow in Section 8.

Among the different results described in this paper, the reader will find the following.

(i) A statistical description of the external gravitational field felt by haloes: the potential is found to be quadrupolar and stationary.

(ii) A study of the evolution of accretion: accretion by dark matter haloes decreases with time, while the outflows become more significant at recent times.

(iii) Constrains on the trajectory of infalling material: accretion is found to be essentially radial, while outflows are found to be more circular.

(iv) Results on the two-point statistics of the external potential measured on the viral sphere: the potential provides hints of an anisotropic perturbation of the halo.

(v) Results on the two-point statistics of the accretion's distribution on the virial sphere: accretion is dominated by small-scale fluctuations and has a shorter coherence than the external gravitational field.

2 DYNAMICS OF OPEN COLLISIONLESS SYSTEMS

The exchanges occurring between a halo and its environment can be characterized in several ways. One of the classical method involves building a merger tree where the whole history of formation of a halo is expressed in terms of global properties of its progenitors (e.g. Kauffmann & White 1993; Lacey & Cole 1993; Somerville & Kolatt 1999). While well suited to study the evolution of those characteristics, it cannot be directly applied to predict in detail the haloes' inner dynamic because of the lack of spatial information on these interactions. One could track the whole (six-dimensional) phase-space history of all the progenitors, but not only would it be difficult to store in practice it would also not give information on the influence of large-scale structures through their gravitational potential. In the present paper, following Aubert et al. (2004), it is suggested to measure the relevant quantities on a surface at the interface between the halo and the intergalactic medium. Accretion is described as a flux of particles through the haloes' external boundaries.

This section presents an extension of the formalism developed by e.g. Tremaine & Weinberg (1984) and Murali (1999) to open spherical collisionless systems. The dynamics of a dark matter spherical halo is obtained by solving the collisionless Boltzmann equation coupled with the Poisson equation

$$\partial_t F + \boldsymbol{v}\cdot\partial_{\boldsymbol{r}} F - \nabla\Psi\cdot\partial_{\boldsymbol{v}} F = 0, \tag{2}$$

$$\Delta\Psi = 4\pi G\int \mathrm{d}^3 v F(\boldsymbol{v}), \tag{3}$$

where $F(\boldsymbol{r}, \boldsymbol{v}, t)$ is the system's DF coupled to $\Psi(\boldsymbol{r}, t) \equiv \psi + \psi_{\mathrm{e}}$, the total gravitational potential (self-gravitating + external perturbation). Note that, in a somewhat unconventional manner, ψ^{e} refers here to the external potential, i.e. the tidal potential created by the perturbations *outside* the boundary. The gravitational field of incoming particles is accounted for by the source term. Equation (2) coupled with Hamilton's equations is a conservation equation

$$\partial_t F + \tilde{\nabla}(\boldsymbol{u}F) = 0, \tag{4}$$

where $\boldsymbol{u} \equiv (\boldsymbol{v}, -\nabla\Psi)$ and $\tilde{\nabla} \equiv (\partial_{\boldsymbol{r}}, \partial_{\boldsymbol{v}})$. As a consequence, considering a 'source of material' described by $f_{\mathrm{e}}(\boldsymbol{w})$ located on a surface $S(\boldsymbol{w})$ implies

$$\partial_t F + \tilde{\nabla}(\boldsymbol{u}F) = -\delta_{\mathrm{D}}[S(\boldsymbol{w}) - a]\boldsymbol{u}\cdot\frac{\nabla S}{|\nabla S|} f_{\mathrm{e}}(\boldsymbol{w}), \tag{5}$$

where $\boldsymbol{w} \equiv (\boldsymbol{r}, \boldsymbol{v})$ describes the phase space and a defines the surface boundary of the studied system (here δ_{D} stands for the Dirac delta function). If this boundary is defined as a spherical surface with radius R, then equation (5) becomes (e.g. Appel 2002)

$$\partial_t F + \tilde{\nabla}(\boldsymbol{u}F) = -\delta_{\mathrm{D}}(r - R) v_{\mathrm{r}} f_{\mathrm{e}}(\boldsymbol{w}) \tag{6}$$

$$\equiv -\delta_{\mathrm{D}}(r - R) s^{\mathrm{e}}(\boldsymbol{w}). \tag{7}$$

The function s^{e} will be hereafter referred to as the 'source' function. Formally, the right-hand side of equation (7) can be seen as an additional local rate of change of the system's DF. Note that equation (7) involves the external potential, ψ^{e}, via $\boldsymbol{u}$.

2.1 Moments of the source term

Integrating equation (7) over velocities leads to the mass conservation relation

$$\partial_t\rho + \nabla(\boldsymbol{v}\rho) = -\delta_{\mathrm{D}}(r - R)(\rho v_{\mathrm{r}})_{\mathrm{e}} \equiv -\delta_{\mathrm{D}}(r - R)\varpi_\rho, \tag{8}$$

where the source appears as an external flux density of matter $(\rho\overline{v_{\mathrm{r}}})_{\mathrm{e}}$ or ϖ_ρ. Taking the next moment of equation (7) leads us to the Euler–Jeans equation

$$\partial_t\rho\boldsymbol{v} + \nabla\cdot(\rho\boldsymbol{v}\boldsymbol{v}) + \rho\nabla\Psi = -\delta_{\mathrm{D}}(r - R)(\rho v_{\mathrm{r}}\boldsymbol{v})_{\mathrm{e}}, \tag{9}$$

where the source adds a flux density of momentum, $\varpi_{\rho\boldsymbol{v}}$, to the conventional Jeans equation. Taking the successive moments of equation (7) will generically include a new term in the resulting equations.

2.2 Propagating the dynamics

Following Tremaine & Weinberg (1984), equation (7) can be solved along with Poisson's equation in the regime of small perturbations. In the spirit of Paper I, let us define the system's environment by the external perturbative potential $\psi^{\mathrm{e}}(\boldsymbol{r}, t)$ and the source $s^{\mathrm{e}}(\boldsymbol{r}, \boldsymbol{v}, t)$. Given this environment, the system's linear potential response $\psi(\boldsymbol{r}, t)$ can be computed. Writing the following expansions:

$$\psi(\boldsymbol{r}, t) = \sum_{\boldsymbol{n}} a_{\boldsymbol{n}}(t)\psi^{[\boldsymbol{n}]}(\boldsymbol{r}), \tag{10}$$

$$\psi^{\mathrm{e}}(\boldsymbol{r}, t) = \sum_{\boldsymbol{n}} b_{\boldsymbol{n}}(t)\psi^{[\boldsymbol{n}]}(\boldsymbol{r}), \tag{11}$$

$$s^{\mathrm{e}}(\boldsymbol{r}, \boldsymbol{v}, t) = \sum_{\boldsymbol{n}} c_{\boldsymbol{n}}(t)\phi^{[\boldsymbol{n}]}(\boldsymbol{r}, \boldsymbol{v}), \tag{12}$$

where $\phi^{[\boldsymbol{n}]}(\boldsymbol{r}, \boldsymbol{v})$ and $\psi^{[\boldsymbol{n}]}(\boldsymbol{r})$ are suitable basis functions, and solving the Boltzmann and Poisson's equations for $a_{\boldsymbol{n}}$, one finds (Aubert et al. 2004)

$$\boldsymbol{a}(t) = \int_{-\infty}^{\infty}\mathrm{d}\tau\boldsymbol{K}(\tau - t)\cdot[\boldsymbol{a}(\tau) + \boldsymbol{b}(\tau)] + \boldsymbol{H}(\tau - t)\cdot\boldsymbol{c}(\tau). \tag{13}$$

Table 1. Description of the various flux densities. The first 10, together with the external potential, are sufficient to characterize fully the environment as shown in Section 3.3.

	Flux density, ϖ	Flux, Φ	Motivation
Mass	ρv_r	$\mathrm{d}m/\mathrm{d}t$	Heating and cooling
Angular momentum	$\rho v_\mathrm{r}\, \boldsymbol{r} \times \boldsymbol{v}$	$\mathrm{d}L/\mathrm{d}t$	Warp, shape of haloes
Kinetic energy	$\rho v_\mathrm{r}\, \sigma_i \sigma_j$	$\mathrm{d}E/\mathrm{d}t$	Virialized objects
Shear	$\rho v_\mathrm{r}(\partial v_j/\partial x_I + \partial v_i/\partial x_j)$	$\mathrm{d}c/\mathrm{d}t$	Tidal field
Vorticity	$\rho v_\mathrm{r}\, \nabla \times \boldsymbol{v}$	$\mathrm{d}\omega/\mathrm{d}t$	Anisotropic accretion

The kernels $\boldsymbol{K}$ and $\boldsymbol{H}$ are functions of the equilibrium state DF, F_0, and of the two bases, $\phi^{[\boldsymbol{n}]}(\boldsymbol{r}, \boldsymbol{v})$ and $\psi^{[\boldsymbol{n}]}(\boldsymbol{r})$ only (see Paper I). As a consequence, they may be computed once and for all for a given equilibrium model. Since the basis function, $\psi^{[\boldsymbol{n}]}$, can be customized to the NFW-like profile of dark matter haloes, it solves consistently and efficiently the coupled dynamical and field equations so long as the entering fluxes of dark matter amount to a small perturbation in mass compared to the underlying equilibrium.

Assuming the linearity and knowledge of $\boldsymbol{K}$ and $\boldsymbol{H}$, one can see that the properties of the environments (through $\boldsymbol{b}$ and $\boldsymbol{c}$) are *propagated* exactly to the inner dynamical properties of collisionless systems. Note in particular that the whole phase-space response of the halo follows from the knowledge of $\boldsymbol{a}$. For example, taking the temporal Fourier transform of equation (13), the cross-correlation matrix is easily deduced:

$$\langle \hat{\boldsymbol{a}} \cdot \hat{\boldsymbol{a}}^{*\top} \rangle = \langle (\boldsymbol{I} - \hat{\boldsymbol{K}})^{-1} \cdot [\hat{\boldsymbol{K}} \cdot \hat{\boldsymbol{b}} + \hat{\boldsymbol{H}} \cdot \hat{\boldsymbol{c}}] \cdot [\hat{\boldsymbol{K}} \cdot \hat{\boldsymbol{b}} + \hat{\boldsymbol{H}} \cdot \hat{\boldsymbol{c}}]^{\top *} \cdot (\boldsymbol{I} - \hat{\boldsymbol{K}})^{-1*\top} \rangle, \quad (14)$$

where $\hat{\boldsymbol{x}} = \hat{\boldsymbol{x}}(\omega)$ is the Fourier transform of $\boldsymbol{x}(t)$. The environment's two-points statistic, via $\langle \hat{\boldsymbol{b}} \cdot \hat{\boldsymbol{b}}^{*\top} \rangle$, $\langle \hat{\boldsymbol{c}} \cdot \hat{\boldsymbol{c}}^{*\top} \rangle$ and $\langle \hat{\boldsymbol{b}} \cdot \hat{\boldsymbol{c}}^{*\top} \rangle$, modifies the correlation of the response of the inner halo.

Linear dynamics do not take into account the effects on the perturbation induced by dynamical friction. More generally the damping of incoming fluxes will ultimately require non-linear dynamics (since the relative temporal phases of the infall do matter in that context). It is also assumed in equation (13) that the incoming material does not modify the equilibrium state of the system. The secular evolution of the system should also be ultimately taken into account, through a quasi-linear theory for example (see e.g. Paper I).

Let us emphasize that, since the addressed problem is linear, the response, equation (13), can be recast into a formulation which only involve an 'external potential', namely the sum of ψ^e and the potential created by the entering particles described by s^e. While formally simpler at the linear deterministic level, this alternative formulation does not translate well non-linearly or statistically (since it would require the full knowledge of the perturbation everywhere in space in a manner which is dependent upon the inner structure of the halo).

In the following sections, our aim is to describe how the two fields $\psi^\mathrm{e}(\boldsymbol{r}, t)$ and $s^\mathrm{e}(\boldsymbol{r}, \boldsymbol{v}, t)$ can be extracted from haloes in cosmological simulations. Then it will be shown how to characterize their statistical properties as a function of time via their expansion coefficients, $b_{\boldsymbol{n}}(t)$ and $c_{\boldsymbol{n}}(t)$.

2.3 Convention and notations

In what follows, let us characterize the properties of two fields, either angularly, kinematically, statistically or temporally, or any combination (for various classes of masses). For a given field, X, let us introduce the following notations for clarity:

$$\overline{X} \equiv \frac{1}{4\pi} \int X(\theta, \phi)\, \mathrm{d}\sin(\theta)\, \mathrm{d}\phi, \quad (15)$$

which represents the angular average of X over the sphere. Alternatively, let us define the temporal average over ΔT as

$$\underline{X} \equiv \frac{1}{\Delta T} \int_T^{T+\Delta T} X(t)\, \mathrm{d}t. \quad (16)$$

Finally, let us define the ensemble average as

$$\langle X \rangle \equiv \int X\, \mathcal{F}(X)\, \mathrm{d}X = E\{X\}, \quad (17)$$

where $\mathcal{F}$ is the density probability distribution of X. Here $E\{X\}$ stands for the expectation of X. In practice, in Section 5, an estimator for ensemble average of X measured for N haloes is given:[2]

$$\langle X \rangle_{N} = \frac{1}{N} \sum_{i}^{N} X_i. \quad (18)$$

The underlying probability distributions are sometimes very skewed (when e.g. corresponding to a strong or weak accretion event around massive or smaller haloes), which requires special care when attempting to define statistical trends. Hence, let us also define $\langle\langle X \rangle\rangle$ as the *mode* (or most probable value) of the fitting distribution of $\mathcal{F}$.

All external quantities (flux densities, potential, etc.) will generally be labelled as X^e. Let us introduce moments of the source over velocities, which correspond to flux densities, noted ϖ_X, and their corresponding fluxes, noted Φ_X. Table 1 gives a list of such flux densities and flux pairs. Finally, the harmonic transform of the field, X, will be written as $a^X_{\ell,m}$ and its corresponding power spectrum C^X_ℓ, while the parameters relative to fitting the statistics of the field will be written as q_X. Note that the contrast of the field, X, was also introduced as

$$\delta_X \equiv \frac{X - \overline{X}}{\langle \overline{X} \rangle}, \quad (19)$$

and its corresponding harmonic transform, $\tilde{a}^X_{\ell m}$. A summary of all the notations can be found in Appendix H.

3 THE SOURCE OF INFALL

Let us first describe our strategy to fully characterize the source of cosmic infall at the virial radius via collisionless dark matter simulations, and enumerate the corresponding biases. In particular, let us illustrate our procedure on a template halo.

[2] An alternative would be to weight the sum by the relative number of objects in each halo, hereby down-weighting light haloes. It is found that this alternative estimator did not significantly affect our measurements.

3.1 Describing the source

As argued in Section 2, computing the response of an open system to infalling material requires the knowledge of the source function, $s^{\mathrm{e}}(\boldsymbol{r}, \boldsymbol{v}, t)$. Given the particles accreted by a halo, one possibility involves storing those phase-space properties for all particles. While feasible for a limited number of haloes, this task would become rapidly intractable for our large number of simulations. In order to compress the information, the accreted DF is projected here on a basis of function, following equation (12).

Since the measurement is carried at a fixed radius, the phase space is reduced from six to five degrees of freedom: two for the angular position on the sphere, described by two angles $(\theta, \phi) \equiv \boldsymbol{\Omega}$, and three for the velocity space described in spherical coordinates by $(v, \Gamma_1, \Gamma_2) = (v, \boldsymbol{\Gamma})$, where v is the velocity modulus and $\boldsymbol{\Gamma}$ are the two angles describing its orientation (see Fig. 1). The angle, Γ_1, indicates how radial is the velocity, with $\Gamma_1 > \pi/2$ for infalling dark matter and $\Gamma_1 < \pi/2$ for outflows. Γ_2 indicates the orientation of the tangential motion of the infall.

Recall that the two fields, $c_{\boldsymbol{n}}$ (hence $s^{\mathrm{e}}(\boldsymbol{\Omega}, \boldsymbol{\Gamma}, v, t)$) and $b_{\boldsymbol{n}}$ (hence $\psi^{\mathrm{e}}(\boldsymbol{\Omega}, t)$) are, respectively, five and two dimensional (as a function of mass and time). Note also that both s^{e} and ψ^{e} are statistically stationary with respect to $\boldsymbol{\Omega}$, while s^{e} is partially isotropic and not stationary with respect to $\boldsymbol{\Gamma}$; neither ψ^{e} and s^{e} is stationary with respect to the cosmic time.

3.1.1 Harmonic expansion of the incoming fluxes

The $\boldsymbol{\Omega}$ and $\boldsymbol{\Gamma}$ dependences are naturally projected on a basis of spherical harmonics, $Y_{\ell m}(\boldsymbol{\Omega})$ and $Y_{\ell' m'}(\boldsymbol{\Gamma})$. The velocity amplitude dependence is projected on a basis of Gaussian functions, $g_\alpha(v)$, with mean μ_α and a given rms σ. One can write

$$\phi^{[\boldsymbol{n}]}(\boldsymbol{r}, \boldsymbol{v}) = Y_{\boldsymbol{m}}(\boldsymbol{\Omega}) Y_{\boldsymbol{m}'}(\boldsymbol{\Gamma}) g_\alpha(v), \tag{20}$$

where $\boldsymbol{n} \equiv (\ell, m, \alpha, \ell', m') = (\boldsymbol{m}, \alpha, \boldsymbol{m}')$. The expansion coefficients, $c_{\boldsymbol{m}'}^{\boldsymbol{m}\alpha}(t)$, are given by

$$c_{\boldsymbol{m}'\alpha}^{\boldsymbol{m}}(t) = \left(\boldsymbol{G}^{-1} \cdot \boldsymbol{s}_{\boldsymbol{m}'}^{\boldsymbol{m}}\right)_\alpha, \tag{21}$$

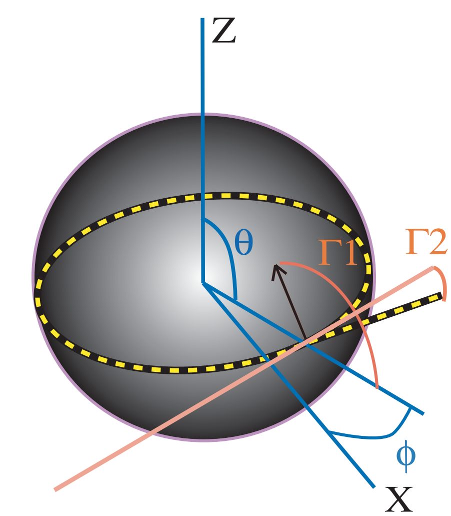

Figure 1. The angles $\boldsymbol{\Omega}$ and $\boldsymbol{\Gamma}$. The dot indicates the position of the particle on the sphere. The dashed ellipse represents the plane which contains both the particle and the sphere centre. X and Z are arbitrary directions defined by the simulation box. $(\theta, \phi) = \boldsymbol{\Omega}$ are the particle's angular coordinates on the sphere. $\boldsymbol{\Gamma} = (\Gamma_1, \Gamma_2)$ define the orientation of the particle's velocity vector (shown as an arrow).

where

$$\left(\boldsymbol{s}_{\boldsymbol{m}'}^{\boldsymbol{m}}\right)_\beta = \int \mathrm{d}\boldsymbol{\Omega} \mathrm{d}\boldsymbol{\Gamma} \mathrm{d}v v^2 g_\beta(v) Y_{\boldsymbol{m}}^*(\boldsymbol{\Omega}) Y_{\boldsymbol{m}'}(\boldsymbol{\Omega}) s^{\mathrm{e}}(v, \boldsymbol{\Omega}, \boldsymbol{\Gamma}, t), \tag{22}$$

given

$$\boldsymbol{G}_{\alpha,\beta} = \int \mathrm{d}v v^2 g_\alpha(v) g_\beta(v). \tag{23}$$

Note that the expansion defined in equation (12), where the coefficients are given by equation (21), involves five subscripts spanning the five-dimensional phase space, while the expansion in equation (10) only involves three subscripts. This description of the source term is reduced to a set of coefficients which depends on time only. Furthermore, this procedure requires parsing the particles only once, and all the momenta (e.g. mass flux density, probability distribution function, hereafter PDF, of impact parameter, etc.) of the source terms can be computed directly from these coefficients. As a consequence, the statistics of momenta follow linearly from the *statistics* of coefficients only, as shown in Section 4.2.

3.1.2 Harmonic expansion of the external potential

Let us call $b'_{\ell m}(t)$ the harmonic coefficients of the expansion of the external potential on the virial sphere. Following Murali (1999), let us expand the potential over the biorthogonal basis $(u_n^{\ell m}, d_n^{\ell, m})$, so that

$$\psi^{\mathrm{e}}(r, \boldsymbol{\Omega}, t) = \sum_{n,\ell,m} b'_{\ell m}(t) Y_\ell^m(\boldsymbol{\Omega}) \left(\frac{r}{R_{200}}\right)^\ell,$$
$$= \sum_{\boldsymbol{n}} b_{\boldsymbol{n}}(t) \psi^{[\boldsymbol{n}]}(\boldsymbol{r}), \tag{24}$$

where $\psi^{[\boldsymbol{n}]}(\boldsymbol{r}) \equiv Y_\ell^m(\boldsymbol{\Omega}) u_j^{\ell m}(r)$. The first equality in equation (24) corresponds to the inner solution of the three-dimensional potential whose boundary condition is given by $Y_m^\ell(\boldsymbol{\Omega}) b'_{\ell m}$ on the sphere of radius R_{200} (defined below). Since the basis is biorthogonal, it follows that

$$b_{\boldsymbol{n}}(t) = \left[\int d_n^{\ell m}(r) \left(\frac{r}{R_{200}}\right)^\ell \mathrm{d}r\right] b'_{\ell m}(t). \tag{25}$$

It is therefore straightforward to recover the coefficient of the 3D external potential from that of the potential on the sphere.

3.2 From simulations to expansion coefficients

Once a halo is detected, its outer 'boundary' is defined as a sphere centred on its centre of mass with a radius, R_{200} (or virial radius), defined implicitly by $3M/(4\pi R_{200}^3) = 200\rho_0$. This choice of radius is the result of a compromise between being a large distance to the halo centre, to limit the contribution of halo's inner material to fluxes, and being still close enough to the halo's border, to limit the simulation's fraction to be processed and avoid contributions of fly by objects. Let us emphasize that several definition of the virial radius can be found in the literature, involving e.g. the critical density, or a different contrast factor, where the latter may or may not depend on the cosmology. Hence, one should keep in mind that all the quantitative results presented in this article depend on our specific choice of a definition.

The time evolution of accretion is measured backwards in time by following the biggest progenitor of each halo detected at redshift $z = 0$. The positions and velocities of particles passing through the virial sphere between snapshots are then stored. All positions are measured

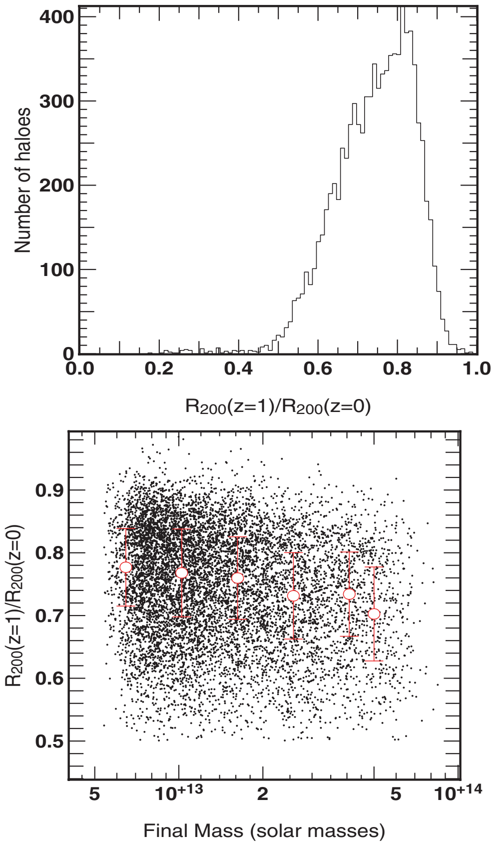

Figure 2. Top: the distribution of the ratio between the virial radii measured at $z = 1$ and 0. Bottom: the distribution of $R_{200}(z = 1)/R_{200}(z = 0)$ as a function of the halo's final mass. Each point represents one halo. Symbols stand for the median value of $R_{200}(z=1)/R_{200}(z=0)$ in six different classes of masses. Bars stand for the interquartile. The two measurements were performed on 9023 haloes which satisfy the selection criteria defined in Section 4.2.

relative to the biggest progenitor centre of mass, while velocities are measured relative to its average velocity, for each redshift z. In one of the simulation described below, the total comoving drift distance of the centre of mass was compared to the distance between the halo's positions measured at $z = 1$ and 0. The haloes were chosen to satisfy the criteria described in Section 4.2. It is found that the scattering of the motion of the centre of mass represents less than 10 per cent of the distance covered in 8 Gyr. The centre of mass of the biggest progenitor seems stable enough to be a reference.

Sticking to the previous definition of R_{200} would imply a changing outer boundary, and an 'inertial' flux through a moving surface would have to be taken into account. To overcome this effect, the sphere was kept constant in time at a radius equals to $R_{200}(z = 0)$. This choice corresponds to a reasonable approximation since the actual virial radius does not change significantly with time between $z < 2$ for a reasonably smooth accretion history. As shown in Fig. 2, the virial radius at $z = 1$ is only 20 per cent smaller than R_{200} measured at $z = 0$. Larger haloes have larger variations, but the median value of the difference between the two radii remains smaller than 30 per cent for final masses smaller than $10^{14}\,\mathrm{M}_\odot$. Finally, measurements were done using physical coordinates (and not comoving coordinates). These choices were partly guided by the fact that they simplify future applications of these results to the inner dynamic of the haloes (see Paper I).

3.2.1 *Sampling on the sphere*

As shown in Section 2, the source function s^{e} reads

$$s^{\mathrm{e}} \equiv f(\boldsymbol{r}, \boldsymbol{v}, t) v_{\mathrm{r}} = \sum_i \delta_{\mathrm{D}}^3[\boldsymbol{r} - \boldsymbol{r}_i(t)]\delta_{\mathrm{D}}^3[\boldsymbol{v} - \boldsymbol{v}_i(t)] v_{\mathrm{r},i}. \tag{26}$$

Switching to spherical coordinates leads us to

$$s^{\mathrm{e}} = \sum_i^N \frac{\delta_{\mathrm{D}}[R_{200} - r_i(t)]}{R_{200}^2} \frac{\delta_{\mathrm{D}}[v - v_i(t)]}{v^2} \tag{27}$$

$$\times \frac{\delta_{\mathrm{D}}[\boldsymbol{\Omega} - \boldsymbol{\Omega}_i(t)]}{\sin \Omega_1} \frac{\delta_{\mathrm{D}}[\boldsymbol{\Gamma} - \boldsymbol{\Gamma}_i(t)]}{\sin(\Gamma_1)} v_{\mathrm{r},i}(t),$$

where i is the particle index. Now,

$$v_{\mathrm{r},i}\delta_{\mathrm{D}}[R_{200} - r_i(t)] = \sum_k v_{\mathrm{r},k,i} \left| \frac{\mathrm{d}t}{\mathrm{d}r} \right| \delta_{\mathrm{D}}(t - t_{200,k,i}),$$

$$= \sum_k w_{k,i}\delta_{\mathrm{D}}(t - t_{200,k,i}), \tag{28}$$

where $t_{200,k,i}$ corresponds to the kth passage of the ith particle through the virtual boundary R_{200} (and $v_{\mathrm{r},k,i}$ is the corresponding radial velocity). In our conventions, the weight function $w_{k,i}$ takes the value 1 if the particle is entering and -1 if it is exiting the virial sphere. Given that our time resolution is finite, let us consider a time interval ΔT around t and define the (temporal) average phase-space flux density over ΔT:

$$\underline{s}^{\mathrm{e}}(t) \equiv \frac{1}{\Delta T} \int_t^{t+\Delta T} \mathrm{d}\tau s^{\mathrm{e}}(\tau). \tag{29}$$

Equation (28) becomes

$$\underline{s}^{\mathrm{e}}(t) = \sum_{i,k}^N \frac{\delta(v - v_{i,k})}{v^2 \Delta T R_{200}^2} \frac{\delta(\boldsymbol{\Omega} - \boldsymbol{\Omega}_{i,k})}{\sin \Omega_1} \frac{\delta(\boldsymbol{\Gamma} - \boldsymbol{\Gamma}_{i,k})}{\sin(\Gamma_1)} w_{i,k}. \tag{30}$$

The simulations were sampled in time regularly in $\ln(z)$ [i.e. $\Delta\ln(z) =$ constant]. From $z = 2$ to 0.1, 23 snapshots were taken (and a $z = 0$ snapshot was added to the sample). If Δt is small, the sum over k should mostly involve one passage, i.e.

$$\underline{s}^{\mathrm{e}}(t) \sim \frac{1}{\Delta T R_{200}^2} \sum_i^N \frac{\delta(v - v_i)}{v^2} \frac{\delta(\boldsymbol{\Omega} - \boldsymbol{\Omega}_i)}{\sin \Omega_1} \frac{\delta(\boldsymbol{\Gamma} - \boldsymbol{\Gamma}_i)}{\sin(\Gamma_1)} w_i. \tag{31}$$

Now, these measurements only give access to (v, $\boldsymbol{\Omega}$, $\boldsymbol{\Gamma}$) at fixed redshift, z, and at every varying redshift Δz. Consequently, these values need to be interpolated at the sought $t_{200,i}$ approximated by

$$t_{200,i} = t_i(z_n) + \frac{t(z_{n+1}) - t(z_n)}{r_i(z_{n+1}) - r_i(z_n)}[R_{200} - r_i(z_n)]. \tag{32}$$

Given these 'crossing' instant, the positions, $\boldsymbol{r}$, and velocities, $\boldsymbol{v}$, are also linearly interpolated. For instance, one gets for the x component of the velocity

$$v_{x,i}(t_{200}) = v_{x,i}(z_n) + \frac{v_{x,i}(z_n + 1) - v_{x,i}(z_n)}{t(z_{n+1}) - t(z_n)}[t_{200} - t(z_n)]. \tag{33}$$

Such an interpolation is not strictly self-consistent since a ballistic motion requires a constant velocity along the trajectory. The worst-case scenario would correspond to particles which have entered the virial sphere with an outflowing velocity vector and vice versa. As a simple but important check, the distribution of interpolated radial velocities was plotted (see Fig. 3). Those were computed from the whole history of accretion of a typical halo ($R_{200} = 860$ kpc,

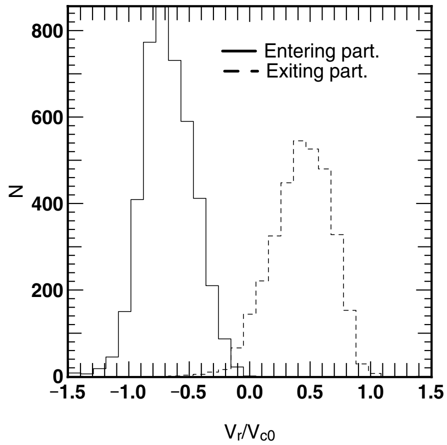

Figure 3. The distribution of interpolated radial velocities $v_{\rm r}$ of particles passing through the virial radius. Those particles were taken from the whole history of accretion of a typical halo [$R_{200} = 860$ kpc, $M(z = 0) = 3 \times 10^{13}\,{\rm M}_\odot$]. Entering particles (solid line) have $v_{\rm r} < 0$, while exiting particles (dashed line) have $v_{\rm r} > 0$, as it should be.

$M_{z=0} = 3 \times 10^{13}\,{\rm M}_\odot$). The two types of particles (entering/exiting) are confined in their radial velocity plane: entering (respectively exiting) particles have negative (respectively positive) radial velocities. Velocities are correctly interpolated. It also means that our time-steps are small enough to ensure a small variation of positions/velocities of particles, validating a posteriori our assumptions. A fraction of exiting particles do have a negative radial velocity but represent less than a few per cent of the total population. For safety, those particles are rejected from the following analysis.

One should note that the measured angular scales are sensitive to the time sampling (see Fig. 4). Increasing the sampling time tends to increase the apparent size of objects as measured in the sphere. Since this increase depends on the shape or the orientation of the objects, this effect *cannot* be simply time averaged. As a consequence, a varying time-step would induce a variation of typical spatial scale. The interpolation given by equation (32) allows also for a constant time-step resampling of the source term $\underline{s}^{\rm e}$. All reference to the time average will be dropped from now on.

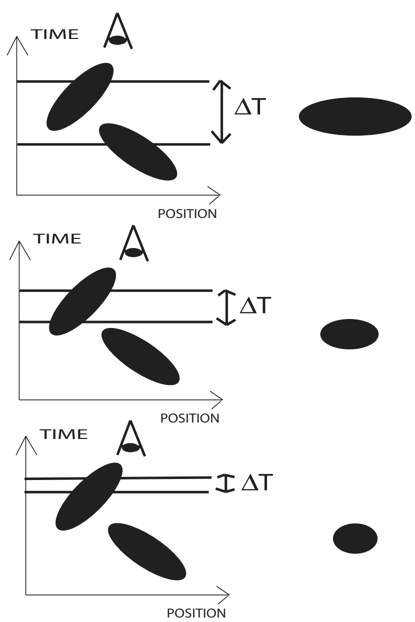

Figure 4. The impact of time averaging on the measured scales of dark matter passing through the sphere. On the left-hand side, time–position diagram of dark matter (black ellipses) as they pass through the sphere. Time integration is performed during ΔT (the two horizontal lines). On the right-hand side, the accreted dark matter as seen on the sphere. A longer integration time increases the length-scale of the incoming blob. If ΔT gets very large, different blobs may be seen as one (upper diagram).

Given equation (30), computing the expansions coefficients of $s_{\rm e}$ is straightforward:

$$c^{\boldsymbol{m}}_{\alpha,\boldsymbol{m}'} = \left[\boldsymbol{G}^{-1}\sum_i^N w_i \frac{\boldsymbol{g}(v_i) Y^*_{\boldsymbol{m}}(\boldsymbol{\Omega}_i) Y^*_{\boldsymbol{m}'}(\boldsymbol{\Gamma}_i)}{\Delta T\, R^2_{200}}\right]_\alpha . \tag{34}$$

It is expected that the above procedure is more accurate than the strategy presented in Aubert et al. (2004), where the flux densities were smoothed over a shell of finite thickness ($R_{200}/10$).

The harmonic expansion $b'_{\boldsymbol{m}}$ of the external potential $\psi^{\rm e}(R_{200}, \boldsymbol{\Omega})$ is computed directly from the positions of external particles (e.g. Murali & Tremaine 1998):

$$b'_{\ell,m}(t) = -\frac{4\pi G}{2\ell+1}\sum_j^N Y^*_{\ell m}[\boldsymbol{\Omega}_j(t)] \frac{R^\ell_{200}}{r_j^{\ell+1(t)}}, \tag{35}$$

where r_j and $\boldsymbol{\Omega}_j$ are the distance and the two angles defining the position of the jth external particles, respectively. The quantities $r_j(t)$ and $\boldsymbol{\Omega}_j(t)$ at time t are obtained by linear interpolation between two snapshots. Using equation (24), $\psi^{\rm e}(r < R_{200}, \boldsymbol{\Omega})$ can be reconstructed from the coefficients $b'_{\boldsymbol{m}}$.

Section 4.2 makes extensive use of equations (34) and (35) for *each* halo in our simulations to statistically characterize these two fields.

3.3 From flux densities to the 5D source

The description of the source term $s^{\rm e}$ involves time-dependent coefficients $c^{\ell m}_{\alpha \ell' m'}(t)$. Their computation from the particle coordinates is quite straightforward and as shown in the previous sections, the different margins can be recovered through the manipulation of these coefficients. Yet a projection of the source on an a priori basis is a complex operation. Here this projection aims at describing a 5D space for which little is known. As shown in the following sections, the distribution of incidence angles is quite smooth, while the distribution of velocities appears to be easily parametrized by Gaussians. The 5D basis presented in the current paper induces little bias, but it is very likely that a more compact basis exists and that the size of the expansions chosen can be reduced in the future.

Because of this large amount of information contained in the source, it is not always convenient to relate coefficients or their correlations to physical quantities, like the mass flux or the flux density of energy. An alternate description of the source term was presented in Aubert et al. (2004) with the following ansatz:

$$s^{\rm e}(\boldsymbol{r}, \boldsymbol{v}, t) = \sum_{\boldsymbol{m}} Y_{\boldsymbol{m}}(\boldsymbol{\Omega}) \frac{\hat{\varpi}_{\rho,\boldsymbol{m}}(2\pi)^{-3/2}}{\det(\hat{\varpi}_{\rho\sigma\sigma,\boldsymbol{m}}/\hat{\varpi}_{\rho,\boldsymbol{m}})} \times \exp\left[-\frac{1}{2}\left(\boldsymbol{v} - \frac{\hat{\varpi}_{\rho v,\boldsymbol{m}}}{\hat{\varpi}_{\rho,\boldsymbol{m}}}\right)^\top \left(\frac{\hat{\varpi}_{\rho\sigma\sigma,\boldsymbol{m}}}{\hat{\varpi}_{\rho,\boldsymbol{m}}}\right)^{-1}\left(\boldsymbol{v} - \frac{\hat{\varpi}_{\rho v,\boldsymbol{m}}}{\hat{\varpi}_{\rho,\boldsymbol{m}}}\right)\right]. \tag{36}$$

This representation of the source is by construction consistent with the first two velocity moments

$$\int {\rm d}^3\boldsymbol{v} s^{\rm e}(\boldsymbol{r}, \boldsymbol{v}) = \varpi_\rho(\boldsymbol{r}), \qquad \int {\rm d}^3\boldsymbol{v}\boldsymbol{v} s^{\rm e}(\boldsymbol{r}, \boldsymbol{v}) = \varpi_{\rho v}(\boldsymbol{r}), \tag{37}$$

while

$$\int \mathrm{d}^3\boldsymbol{v}\left(v_i - \frac{\varpi_{\rho v,i}}{\varpi_\rho}\right)\left(v_j - \frac{\varpi_{\rho v,j}}{\varpi_\rho}\right)s^{\mathrm{e}}(\boldsymbol{r},\boldsymbol{v})$$
$$= \varpi_{\rho\sigma_i\sigma_j}(\boldsymbol{r}) - \frac{\varpi_{\rho v}(\boldsymbol{r})^2}{\varpi_\rho(\boldsymbol{r})} + \sum_{\boldsymbol{m}} Y_{\boldsymbol{m}}(\boldsymbol{\Omega})\delta(r - R_{200})\frac{\hat{\varpi}_{\rho v,\boldsymbol{m}}(t)^2}{\hat{\varpi}_{\rho,\boldsymbol{m}}(t)},$$
$$\approx \varpi_{\rho\sigma_i\sigma_j}(\boldsymbol{r}). \tag{38}$$

Obviously, the third moment is not fully recovered from the ansatz given by equation (36). This example should be taken as an illustration and highlights the possibility of building a source term from its moments. It is not unique and more realistic expressions could be found, which satisfies higher moments of the source. Still, the successive measurements on the sphere of the flux density of mass ϖ_ρ, momentum $\varpi_{\rho v}$ and velocity dispersion $\varpi_{\rho\sigma\sigma}$ allow a coherent description of the infall of matter. Unlike the coefficients, these flux densities are easier to interpret since they describe physical quantities and are directly involved in specific dynamical processes (see Table 3.3). Furthermore, these three flux densities are easily expressed in terms of coefficients, $c^{\ell m}_{\alpha\ell' m'}(t)$, or more precisely in terms of *a subset* of the source's coefficients, implying a smaller number of computations relative to a complete calculation of $c^{\ell m}_{\alpha\ell' m'}(t)$. Finally, these flux densities are particularly suited to the regeneration of synthetic environments. As shown in Appendix F, synthetic spherical maps can be generated from the two-point correlations and cross-correlations of these fields. Such environments would be consistent with the measurements in simulations and will allow us to easily embed simulated galaxies or haloes in realistic environments as a function of time.

The expression given in equation (36) has one important drawback: it is not of the form of equation (12), i.e. it would require a reprojection over a linear expansion for a dynamical propagation. Nevertheless, its capacity makes it easier to compute than the full set of coefficients and the associated strategy would be (i) to measure the flux densities from the simulation, (ii) to build a source term from e.g. equation (36) and (iii) to project over an appropriate 5D basis when needed, i.e. when the source is used as an input to the analytic description of the haloes' dynamics.

The following sections will make intensive use of the coefficients described by equations (34) and (35). In particular, it will show how the manipulation of these coefficients allows us to recover relevant physical quantities. In the current paper, only the first moment of the source, the flux density of mass ϖ_ρ, together with the external potential, will be fully assessed. The kinematical properties of the accreted material will in particular be investigated. The complete characterization of the $\boldsymbol{c}(t)$ coefficients is beyond the scope of the current paper and will be completed in Paper III. The full measurements of these 11 fields required by equation (36) and the comparisons between the two expressions of the source will also be assessed in the future paper as well. Appendices G1 and G2 describe how the other moments, the flux density of momentum $\varpi_{\rho v}$ or the flux density of energy $\varpi_{\rho\sigma^2}$ may be recovered from the source expansion.

3.4 A template halo

As an illustration, let us first apply the whole machinery to one typical halo. At $z = 0$, this 'template' halo has a mass M of $3.4 \times 10^{13}\,\mathrm{M}_\odot$, with a virial radius R_{200} of $800\,h^{-1}$ kpc. The corresponding circular velocity is $V_{c0} = 600$ km s^{-1}. Its accretion history is shown in Fig. 5 for $z < 1$. Each point on the azimuth–time diagram represents one particle of the simulation passing through the virial sphere at a given azimuth and at a given time. Temporal space has been sampled using 15 equally spaced bins between $z = 1$ and 0 (see bottom panel in Fig. 5). For each time-step, the expansion coefficients $c^{\boldsymbol{m}'}_{\alpha,\boldsymbol{m}}(t)$ are computed from equation (34). The Gaussian basis $g_\alpha(v)$ involved 25 functions with mean μ_α equally distributed from $v = 0$ to 1.5 in V_{c0} units and with a rms $\sigma = 0.03$. The harmonic expansions were carried up to $\ell = 50$ in position space and $\ell' = 25$ in velocity space.

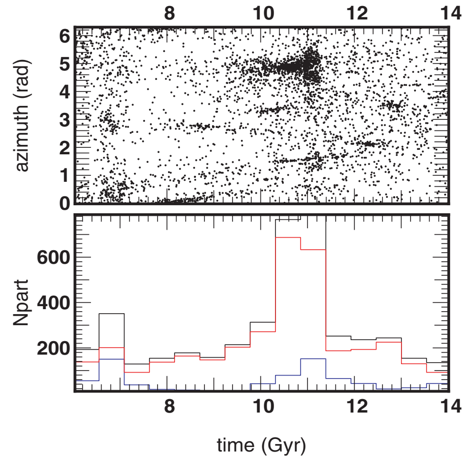

Figure 5. An example of accretion history. Top: azimuth–time diagram. Each point in the diagram represents one particle passing through the virial sphere at a given azimuth (y-axis) at a given time measured from the big bang (x-axis). Bottom: the distribution of crossing instances of particles (in black). Time increases from left to right. The infalling (respectively outflowing) particles distribution is shown in red (respectively blue).

3.4.1 *Advected mass: angular space (ϖ_ρ)*

The template halo accretes an object at $t_{\mathrm{s}} = 11$ Gyr (where $t = 14$ Gyr stands for $z = 0$) adding $7.5 \times 10^{12}\,\mathrm{M}_\odot$ to the system during a ~1-Gyr interval. The corresponding spherical flux density field, $\varpi_\rho(\boldsymbol{\Omega}, t_{\mathrm{s}})$, is shown in Fig. 6. It represents the distribution of accreted particles as seen from a halocentric point of view. The field $\varpi_\rho(\boldsymbol{\Omega}, t_{\mathrm{s}})$ has been reconstructed from the coefficients (see equation 34). It reads

$$\varpi_\rho(\boldsymbol{\Omega}, t) = \int \mathrm{d}\boldsymbol{\Gamma}\mathrm{d}v v^2 s^{\mathrm{e}}(v, \boldsymbol{\Omega}, \boldsymbol{\Gamma}, t) = \sum_{\boldsymbol{m}} a_{\boldsymbol{m}}(t) Y_{\boldsymbol{m}}(\boldsymbol{\Omega}). \tag{39}$$

Since

$$\int \mathrm{d}\boldsymbol{\Gamma}\, Y_{\ell',m'} = \sqrt{4\pi}\delta_{\ell'0}\delta_{m'0}\,, \quad \text{and} \quad \int \mathrm{d}v v^2 g_\alpha(v) = \mu_\alpha^2 + \sigma^2. \tag{40}$$

It follows that

$$a_{\boldsymbol{m}}(t) = \sqrt{4\pi}\sum_\alpha (\mu_\alpha^2 + \sigma^2) c^{\boldsymbol{m}}_{\alpha,\boldsymbol{0}}(t), \tag{41}$$

allowing us to recover $\varpi_\rho(\boldsymbol{\Omega}, t_{\mathrm{s}})$. Also shown is the same field, but computed this time using directly the angular distribution of particles as described in Aubert et al. (2004) (see below). All the major features are well reproduced by the expansion coefficients (equations 34–41). Clearly, an object is 'falling' through the virial sphere. It is straightforward to obtain the angular power spectrum $C_\ell^{\varpi_\rho}$ from the $c^{\boldsymbol{m}}_{\alpha,\boldsymbol{m}'}$ coefficients via the definition of $a_{\ell m}$ in equation (41):

$$C_\ell^{\varpi_\rho} = \frac{1}{4\pi}\frac{1}{2\ell+1}\sum_m |a_{\ell m}|^2. \tag{42}$$

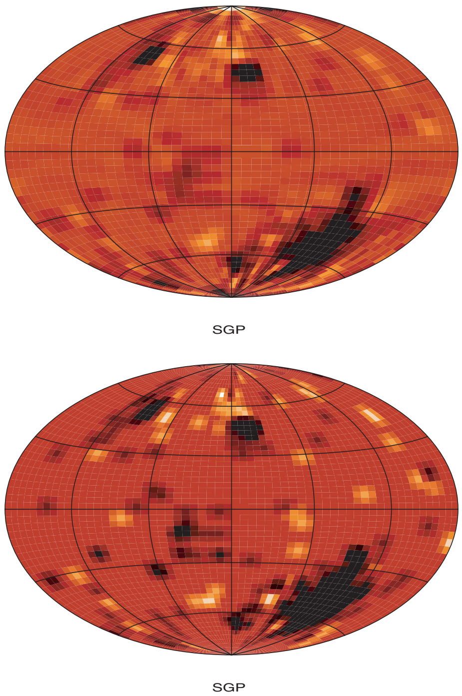

Figure 6. An example of a flux density reconstructed from the coefficients $c^{\boldsymbol{m}}_{l\alpha,\boldsymbol{m}}$: the mass flux density, $\rho v_{\rm r}(\boldsymbol{\Omega})$. It represents the angular distribution of incoming mass as seen from a halocentric point of view. Here $t_{\rm s} \sim$ 11 Gyr. Light regions correspond to strong infall, while darker regions stand for low accretion and outflows. Top: the spherical field obtained directly from the spatial distribution of particles. Bottom: the reconstructed spherical field from the coefficients (equation 34).

The angular power spectrum of $\varpi_\rho(\boldsymbol{\Omega}, t_{\rm s})$, derived from the expansion (equation 34), is shown in Fig. 7. From the positions and velocities of particles, it is also possible to evaluate $\varpi_\rho(\boldsymbol{\Omega}, t_{\rm s})$ on an angular grid and recover the angular power spectrum 'directly'. The agreement between the two $C^{\varpi_\rho}_\ell$ is good, though for the smallest scales ($\ell \geqslant 30$), the power spectrum computed from the coefficients is slightly larger than the one derived directly from the particles.

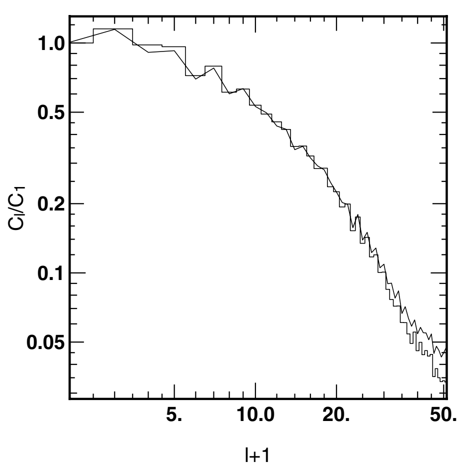

Figure 7. The angular power spectrum, C_ℓ/C_1 (equation 42), of the distribution of incoming matter, $\varpi_\rho(\boldsymbol{\Omega})$ (shown in Fig. 6) at $t\sim$ 11 Gyr, for our template halo. For a given ℓ, the corresponding angular scale is π/ℓ. The histogram corresponds to the power spectrum derived directly from the angular distribution of particles. The solid line is the power spectrum reconstructed from the coefficients.

This may be explained by the fact that a grid sampling tends to smooth the actual ϖ_ρ field. As a consequence, the amplitude of small-scale fluctuations is decreased, leading to a smaller $C^{\varpi_\rho}_\ell$. A more complete discussion on harmonic convergence can be found in Appendix A. For a given ℓ, the corresponding angular scale is π/ℓ in radians.

Note that the coefficients a_{00} are closely related to the accretion field averaged over all directions, $\Phi^{\rm M}(t)$, defined by

$$\Phi^{\rm M}(t) \equiv \overline{\varpi_\rho} = \frac{1}{4\pi}\int {\rm d}\boldsymbol{\Omega}\rho v_{\rm r}(\boldsymbol{\Omega}, t) = \frac{a_{00}}{\sqrt{4\pi}}. \tag{43}$$

Measuring $a_{00}(t)$ amounts to measuring the accretion flux density, i.e. the quantity of dark matter accreted per unit surface and per unit time.

3.4.2 Advected mass: velocity space

Integration over the sphere leads us to the distribution of accreted matter in velocity space:

$$\rho v_{\rm r}(\boldsymbol{\Gamma}, v, t) = \int {\rm d}\boldsymbol{\Omega} s^{\rm e}(v, \boldsymbol{\Omega}, \boldsymbol{\Gamma}, t), \tag{44}$$

$$= \sqrt{4\pi}\sum_{\alpha,\boldsymbol{m}'} c^0_{\alpha,\boldsymbol{m}'} g_\alpha(v) Y_{\boldsymbol{m}'}(\boldsymbol{\Gamma}). \tag{45}$$

Projections over Γ_2 and v give the probability distribution of the incidence angle Γ_1, $\vartheta(\Gamma_1, t)$, defined as

$$\begin{aligned}\vartheta(\Gamma_1, t) &= \int {\rm d}\Gamma_2 {\rm d}v v^2 \rho v_{\rm r}(\boldsymbol{\Gamma}, v, t),\\ &= 2\pi\sqrt{4\pi}\sum_{\alpha,\ell'} c^0_{\alpha,\{\ell',0\}}\left(\mu_\alpha^2 + \sigma^2\right) Y_{\ell',0}(\boldsymbol{\Gamma}).\end{aligned} \tag{46}$$

The impact parameter b of an incoming particle (measured in units of the virial radius) is related to Γ_1 by

$$\frac{b}{R_{200}} = \sin(\Gamma_1), \tag{47}$$

therefore the probability distribution of impact parameters, $\vartheta(b)$, is easily deduced from equation (46). At $t \sim 11$ Gyr, the $\vartheta(b)$ computed from the source coefficients is compared to that derived directly from the velocities of particles in Fig. 8. Note that for pure geometrical reasons small impact parameter b is less likely since there is only one trajectory passing through the centre, while there is a whole cone of trajectories with $b \neq 0$. As a consequence, errors are intrinsically larger for small values of b. The reconstruction from the source coefficients is clearly adequate. In this example, the high probability for infalling particles to have a small impact parameter ($b < 0.5$) implies that velocities are strongly radial. The object 'dives' into the halo's potential well.

Projection over Γ_1 leads to the probability distribution of particle velocities, $\varphi(v, t_{\rm s})$, as they pass through the virial sphere. The PDF $\varphi(v, t)$ is defined as

$$\varphi(v, t) \equiv v^2 \int {\rm d}\boldsymbol{\Omega}\, {\rm d}\boldsymbol{\Gamma} s^{\rm e}(v, \Omega, \boldsymbol{\Gamma}, t). \tag{48}$$

Here the v^2 weighting accounts for the fact that the probability distribution of measuring a velocity, v, within ${\rm d}v$ is of interest here. Using coefficients, it follows that

$$\varphi(v, t) = 4\pi\sum_\alpha v^2 g_\alpha(v) c^0_{\alpha,0}. \tag{49}$$

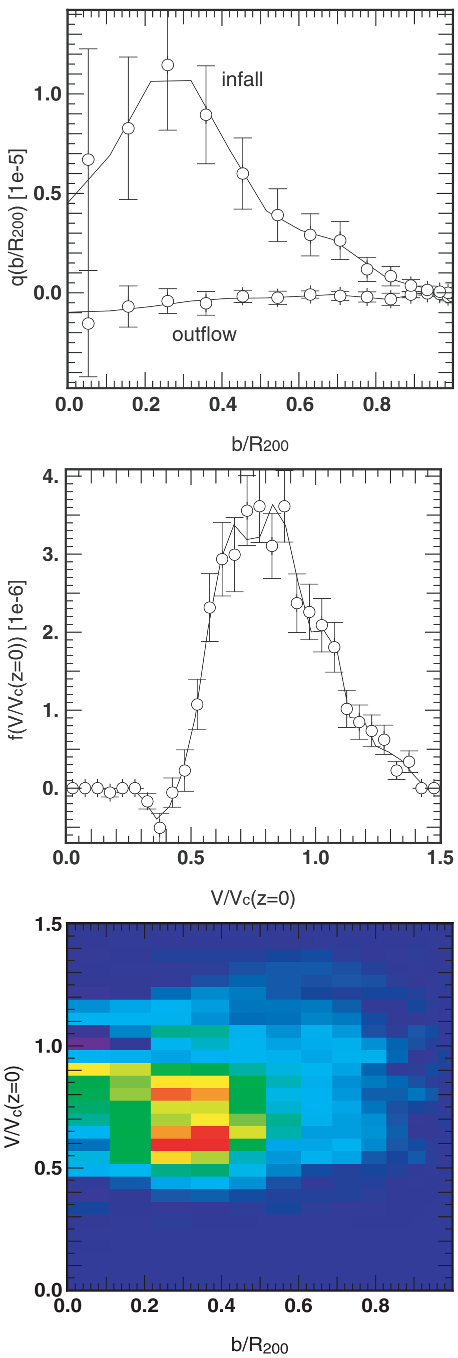

Figure 8. Top: excess probability distribution of impact parameters b and $\vartheta(b)$, derived from the $c^{\boldsymbol{m}}_{\alpha,\boldsymbol{m}'}(t)$ source coefficients (equation 34) of our template halo at $t_{\mathrm{s}} \sim 11$ Gyr (line). The histogram corresponds to the same distribution derived directly from the positions and velocities of particles. Error bars stand for 3σ errors. The impact parameters are given in units of R_{200}. The unit in y-axis is $5 \times 10^9\ \mathrm{M}_{\odot}\,\mathrm{kpc}^{-2}\,\mathrm{Myr}^{-1}$. Infall is mainly radial. Middle: the velocity distribution of particles, $\varphi(v)$, accreted at $t_{\mathrm{s}} \sim 11$ Gyr, for our template halo. Velocities are expressed in terms of the circular velocity at $z = 0$. The unit in y-axis is $5 \times 10^9\ \mathrm{M}_{\odot}\,\mathrm{kpc}^{-2}\,\mathrm{Myr}^{-1}$. The histogram corresponds to the velocity distribution obtained directly from the velocities of the particles. The solid line is the reconstructed distribution from the source coefficients. Bottom: the probability distribution, $\wp(b, v)$, of particles in the $b - v$ subspace. Units are the same as above. Red/blue stands for high/low densities. No correlation is found between b and v for this specific example.

The reconstructed velocity distribution is also shown in Fig. 8. It reproduces well the actual velocity distribution. For this specific halo, the satellite is being accreted with a velocity of 0.75 V_{c0}.

The correlation between the incidence angle Γ_1 and the velocity's amplitude v may be studied by integrating $\rho v_{\mathrm{r}}(\Gamma, v, t)$ over Γ_2 only. The DF, $\wp(\Gamma_1, v)$, of particles in the (Γ_1, v) subspace is defined by

$$\wp(\Gamma_1, v) \equiv \int \mathrm{d}\Gamma_2 \mathrm{d}v v^2 \rho v_{\mathrm{r}}(\boldsymbol{\Gamma}, v, t)\,,$$
$$= 2\pi\sqrt{4\pi}\sum_{\alpha,\ell'} c^{\boldsymbol{0}}_{\alpha,\{\ell',0\}} g_\alpha(v) Y_{\ell',0}(\Gamma_{1,0}). \qquad (50)$$

Given the relation (equation 47), the correlation $\wp(b, v)$ between the impact parameter and the velocity's amplitude is easily obtained. The $\wp(b, v)$ distribution is shown in Fig. 8. Again, note that $\wp(b, v)$ represents an excess probability of finding an impact parameter b (with a velocity v) compared to isotropy. In this specific example, no real correlation may be found between the two quantities. Finally, the integration of $\wp(b, v)$, $\varphi(v, t)$ and $\vartheta(\Gamma_1)$ over their respective space leads to the same quantity, namely the integrated flux $\Phi^{\mathrm{M}}(t)$.

3.4.3 *External potential*

The final field needed on the virial sphere is the external tidal field created by the dark matter distribution around the halo.

Using equation (35), the external potential $\psi^{\mathrm{e}}(\boldsymbol{\Omega}, t)$ is easily computed from the positions of external particles, having restricted the sampling to particles within a 4 Mpc (physical) sphere centred on the halo. The position of external particles is linearly interpolated at a given measurement of time. The coefficients $b_{\boldsymbol{m}}$ for the template halo are computed at $t_{\mathrm{s}} \sim 7$ Gyr (measured from the big bang). The reconstructed field $\psi^{\mathrm{e}}(\boldsymbol{\Omega}, t)$ is shown in Fig. 9 along with the modulus of the advected mass $|\rho v_{\mathrm{r}}(\boldsymbol{\Omega})|$. The two reconstructions were restricted to harmonics $\ell \leqslant 20$.

The two spherical fields show the same main features. However, almost no small-scale feature is seen in the map of the external potential even though they have the same resolution. Since the gravitational potential is known to be smoother than the associated density and is dominated by the global tidal field, it is not surprising that $\psi^{\mathrm{e}}(\boldsymbol{\Omega}, t)$ appears smoother than the advected mass field $|\varpi_\rho(\boldsymbol{\Omega})|$.

The potential's angular power spectrum may also be computed by replacing $a_{\ell m}$ by $b_{\ell m}$ in equation (42) (see Fig. 10). The power spectrum of the potential, $C_\ell^{\varpi_\rho}$, sharply decreases with ℓ, while $C_\ell^{\varpi_\rho}$ has a gentler slope. Large scales are clearly more important for the potential than for the advected mass. Furthermore, C_ℓ^{ψ} systematically peaks for even ℓ values, reflecting the 'even' symmetry of the potential measured on the sphere.

4 SIMULATION SAMPLE AND STATISTICAL BIASES

Section 3.4 details the measurement strategy for a given typical halo. It is now possible to reproduce the above measurements for all the haloes of the simulation sample. Let us first describe in turn the construction of our sample, and the corresponding biases, which constrain our ability to convert a large set of simulations into the statistics of the source.

4.1 Simulations

In order to achieve a sufficient sample and ensure a convergence of the measurements, a set of ~500 simulations was produced

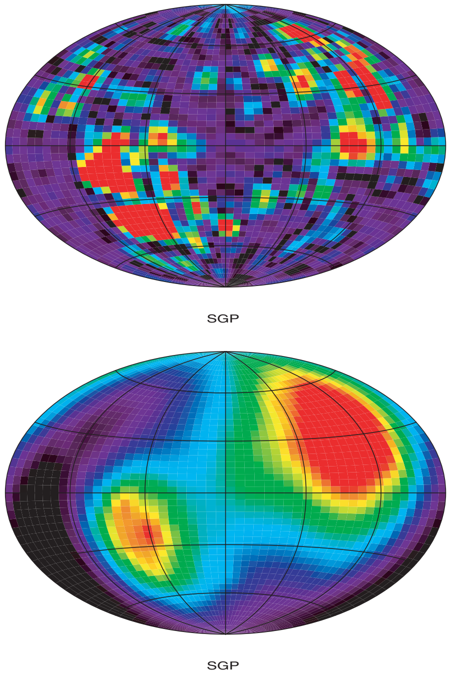

Figure 9. A comparison between the external potential, $\psi^{\mathrm{e}}(\mathbf{\Omega})$ and the modulus of the flux density of matter, $|\rho v_{\mathrm{r}}(\mathbf{\Omega})|$. The measurement is made at $t \sim 7$ Gyr (measured from the big bang) on our template halo. The two fields were, respectively, reconstructed from $c^{\boldsymbol{m}}_{\alpha,\boldsymbol{m}'}$ and $b_{\boldsymbol{n}}$ coefficients with $\ell_{\max} \leqslant 20$. Even though the two fields are similar and exhibit a strong quadrupolar component, $\psi^{\mathrm{e}}(\mathbf{\Omega})$ is smoother than $\rho v_{\mathrm{r}}(\mathbf{\Omega})$. It is expected that the corresponding expansion coefficients be statistically correlated.

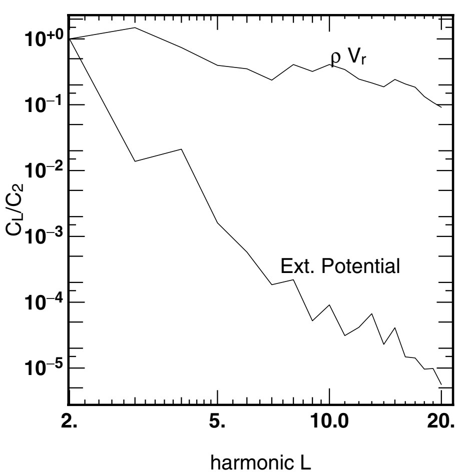

Figure 10. A comparison between the angular power spectrum of $\rho v_{\mathrm{r}}(\mathbf{\Omega})$ and $\psi^{\mathrm{e}}(\mathbf{\Omega})$ for our template halo (the two fields are shown in Fig. 9). The two power spectra C_ℓ are normalized by C_2, i.e. the quadrupole contribution. The slope of the potential's power spectrum is clearly stronger. Large scales (i.e. small-ℓ values) dominate the angular distribution of $\psi^{\mathrm{e}}(\mathbf{\Omega})$, as expected.

as discussed in Aubert et al. (2004). Each of them consists of a $50\,h^{-1}$ Mpc^3 box containing 128^3 particles. The mass resolution is 5×10^9 M$_\odot$. A ΛCDM cosmogony ($\Omega_{\mathrm{m}} = 0.3$, $\Omega_\Lambda = 0.7$, $h = 0.7$ and $\sigma_8 = 0.928$) is implemented with different initial conditions. These initial conditions were produced with GRAFIC (Bertschinger 2001), where a BBKS (Bardeen–Bond–Kaiser–Szalay; Bardeen et al. 1986) transfer function was chosen to compute the initial

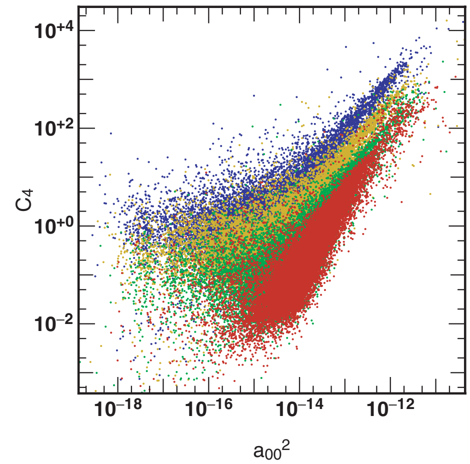

Figure 11. Scatter plot of $C_4^{\varpi_\rho}$ versus a_{00}^2 measured at lookback times $t = 7.8$ (red), 5.6 (green), 4.0 (yellow) and 2.9 (blue) Gyr. The quantity a_{00} scales as the average accretion rate of the haloes while $C_4^{\varpi_\rho}$ scales as the contribution of $\ell = 4$ structures in the flux density of mass measured on the sphere. This plot illustrates how a threshold on the accretion rate affects in a non-trivial way the typical clustering measured for ϖ_ρ. In particular, one should note how $C_4^{\varpi_\rho}$ remains constant at recent times for low accretion rates.

power spectrum. The initial conditions were used as inputs to the parallel version of the tree code GADGET (Springel, Yoshida & White 2001). The softening length was set to 19 h^{-1} kpc.[3] The halo detection was performed using the halo finder HOP (Eisenstein & Hut 1998). The density thresholds suggested by the authors ($\delta_{\mathrm{outer}} = 80$, $\delta_{\mathrm{saddle}} = 2.5\delta_{\mathrm{outer}}$, $\delta_{\mathrm{peak}} = 3.\delta_{\mathrm{outer}}$) were used.

4.2 Selection criteria

As shown in Aubert et al. (2004), the completion range in mass of the simulations spans from 3×10^{12} to 3×10^{14} M$_\odot$. Since the emphasis is on $L_\star$ galaxies, the survey is focused mainly on galactic haloes and light clusters, only haloes with a mass smaller than 10^{14} M$_\odot$ at $z = 0$ were considered. The interest is for haloes already 'formed', i.e. which will not experience major fusions anymore. To satisfy these requirements, the focus is on the last 8 Gyr (redshifts $z < 1$ in a ΛCDM cosmogony). Since the history of a given halo is followed by finding its most massive progenitor, it is required not to accrete more than half its mass in a two-body fusion. As a final safeguard, a halo is rejected if it accretes more than 5×10^{12} M$_\odot$ between two time-steps (i.e. per 500 Myr, see the next section). This mass corresponds approximately to the smallest haloes considered at $z = 0$. The final range of mass of haloes which satisfy these criteria is $\sim 5 \times 10^{12}$–10^{14} M$_\odot$, the fraction of rejected haloes being $\sim$20 per cent. Clearly, such a priori selection criteria will modify the distributions of measured values and the related biases may be difficult to predict. For instance, Fig. 11 shows the scatter plot of the contribution of $\pi/(\ell = 4) = 45°$ fluctuations to ϖ_ρ field versus a_{00}, i.e. the accretion rate. It appears from this plot that modifying the threshold for the accretion will modify the average angular scale of ϖ_ρ in a non-trivial way. Since only a small fraction of haloes are rejected, the biases are expected to be moderate, but as for now their

[3] A second set of simulations with a resolution increase by a factor of 2^3 (respectively 2^6) was carried in order to investigate the convergence of some measurements (see Section 6.2.2).

impact cannot be estimated accurately on the average source or its moments.

Let us emphasize that the above selection criteria should be added to those corresponding to the simulations themselves. Aside from the fact that a 50 $\mathrm{Mpc}^3\,h^{-1}$ box size implies a limited range of mass, the universe described in these simulations is more homogeneous than it should be, since each box must satisfy a given mean density. In other words, the probability of rare events is reduced. This effect should not influence the number of haloes with high accretion rate, since strong accretions are rejected a priori. On the other hand, it should influence the number of objects which experience low accretion history, which are probably less numerous in our simulations than in larger simulated volumes since voids are less likely. Furthermore, the intrinsic mass resolution sets a minimum accretion rate equals to one particle mass ($5 \times 10^9\,\mathrm{M}_\odot$) per time interval. One could imagine an object with a mass smaller than the particle's mass which would not be included in the simulation at the current resolution. Furthermore, an object with a mass equals to a few times the minimum mass is to be considered as diffuse accretion. Finally, this mass resolution is related to the spatial resolution, which limits intrinsically the angular description of fluxes on the virial sphere. For a given type of simulation, all these effects cannot be avoided and reduce the representability of the following measurements.

In short, this strategy involves a bias in mass, redshift, resolution and strength of a merging event. However, these biases should only influence somewhat extreme realizations (related to e.g. very low accretion or equal mass mergers) of the source or the external potential and since the focus is on the typical scales, presumably related to moderate interactions, hopefully they should not significantly affect the measurements.

4.3 Reduction procedure

In the following discussion, most of the distances (respectively velocities) will be expressed as functions of the virial radius R_{200} (respectively the circular velocity V_c) measured at $z = 0$. These quantities are related to the halo's virial mass by

$$V_\mathrm{c} = \sqrt{\frac{G M_{200}}{R_{200}}}. \tag{51}$$

Here $M_{200} = M(r < R_{200})$. The mass dependence of R_{200} and V_c is given in Fig. 12 and may be fitted by

$$R_{200} = 537 M^{1/3}\ , \quad V_\mathrm{c} = 400 M^{1/3}, \tag{52}$$

where R_{200} is expressed in (h^{-1} kpc), V_c in km s^{-1} and M in units of $10^{13}\,\mathrm{M}_\odot$. Here M stands for the total mass of the halo, returned by the halo finder HOP. In equation (52), R_{200} and V_c appear to be strongly correlated to the final masses of haloes, the few outliers being related to external subhaloes or peculiar halo geometries. Since the selection criteria are quite restrictive, most of the haloes experience the same relatively quiet history of accretion and account for the lack of scatter.

The simulations in that redshift interval involved 15 snapshots sampled with $\Delta(\log z) = \mathrm{cst}$ for $z \leqslant 1$ down to $z = 0.1$ plus a snapshot at $z = 0$. The gap between the last snapshot and the second to the last is nearly 1.4 Gyr. As a consequence, the assumption of ballistic trajectories is not valid anymore (see the Appendix). Simulations were resampled in 15 bins distributed regularly in *time* (i.e. not in redshift) using the procedure described in Section 3.2: the corresponding time-step is ∼500 Myr. To take into account the last gap, results obtained from the last three 'new' bins (which cover the last 1.4 Gyr) were averaged into a single bin centred on 0.8 Gyr.

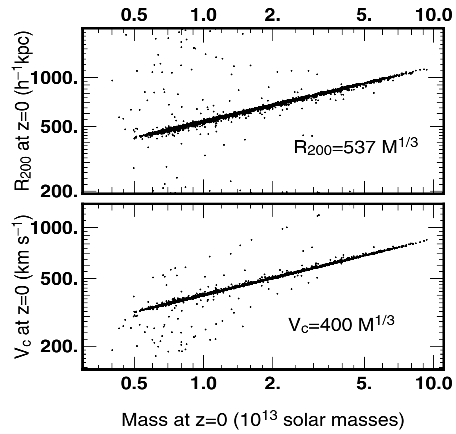

Figure 12. Virial radii (R_{200}) and circular velocities (V_c) as functions of haloes final masses. The quantities have been measured at redshift $z = 0$. Scaling relations between R_{200} or V_c and the final mass are also given.

The source coefficients, $c^{\boldsymbol{m}}_{\alpha,\boldsymbol{m}'}(t)$, were computed following the procedure described in Section 3.4. Maximum harmonic orders were set to $\ell_{\max} = 50$ for the position–angular description. For a typical halo with $R_{200} = 500$ kpc, $\ell_{\max} = 50$ corresponds to a spatial scale of 30 kpc, i.e. equals to 1.5 times the spatial resolution of the simulation. The harmonic description of the velocities angular dependence is restricted to $\ell'_{\max} = 15$. The velocity amplitude is projected on a Gaussian basis which involves 25 functions regularly spaced from $v/v_\mathrm{c} = 0$ to 1.5 with a rms of 0.03. These parameters allow a satisfying reproduction of distributions computed from particles.

The external potential coefficients, $b_{\boldsymbol{m}}(t)$, were computed following the procedure described in Section 3.4. Only particles within a 4-Mpc physical sphere centred on the halo are taken into account. Maximum harmonic orders were set to $\ell_{\max} = 20$.

A set of 100 simulations have been fully reduced allowing us to compute $c^{\boldsymbol{m}}_{\alpha,\boldsymbol{m}'}(t)$ and $b_{\boldsymbol{m}}(t)$ for 15 000 haloes. Since a well-defined (if only biased) sample of histories of haloes was constructed in our simulations, it may be projected on our basis, to compute the external potential and the flux density of mass, following Section 3.4. Let us now characterize the corresponding coefficients, via one-point (Section 5) and two-point (Section 5) statistics.

5 ONE-POINT STATISTICS

In this section, let us first describe the evolution and the statistical distributions of the global properties (i.e. integrated over the sphere) of the source and the potential. Let us discuss the evolution of the mean potential, of the mass flux $\Phi^\mathrm{M}(t)$ and the kinematical properties of s^e via the velocity distribution $\phi(v)$ and the impact parameter distribution $\vartheta(b)$.

Let us then describe in turn the statistical PDF, mean and variance of the integrated fluxes, their corresponding flux densities and finally their mean kinematical features, following the steps of Section 3.4.

5.1 Mean external potential

The mean external potential on the sphere is actually somewhat meaningless but is being used as a normalization value for potential

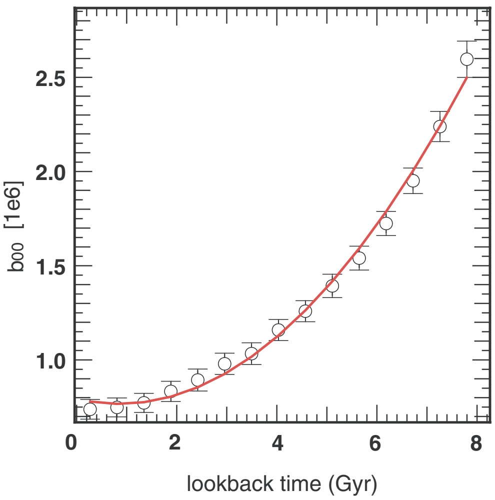

Figure 13. The time evolution of the monopole component of the external potential, $b_{00}(t)$. The time evolution is fitted by a second-order polynomial – $b_{00}(t) = 35\,948 * t^2 - 61\,480.7 * t + 793\,067$. Lookback time t is expressed in Gyr, while b_{00} coefficients are expressed in units of GM/R. M is expressed in $10^{10}\,\mathrm{M}_{\odot}$, R in kpc h^{-1} and $G = 43\,007$ in internal units.

fluctuations (see Section 6.1). Because of isotropy, the mean potential is seen as a monopole and only the $b_{00}(t)$ coefficient is statistically different from zero. Furthermore, following equation (24), the three-dimensional potential component induced by the monopole is a constant potential throughout the sphere volume. As a consequence, it influences the halo's dynamics only through its temporal variation.

The time evolution of the $\langle\langle b_{00}\rangle\rangle$ coefficient is given in Fig. 13. The $b_{00}(t)$ distribution exhibits a tail due to large $-\,b_{00}$ values and is better fitted with a lognormal distribution than with a normal distribution (see Fig. C1). Hence, $\langle\langle b_{00}\rangle\rangle$ stands for the most probable value of the lognormal fitting distribution.[4] The evolution shown in Fig. 13 reflects the measurement procedure. Given that the potential is computed from all the particles contained within a fixed physical volume, the overall expansion implies that particles tend to exit the measurement volume with time. In other words, the average density in the measurement volume decreases with time. This effect leads naturally to the decline of the average potential within the virial sphere due to external material.

5.2 Mass flux: $\Phi^M(t)$

At each time-step, the $a_{0,0}$ distribution is fitted by a Gaussian function with mean $\langle a_{0,0}\rangle$ (see also Fig. C3). This Gaussian hypothesis is clearly verified for low redshifts while strong accretion events give rise to a tail in the $a_{0,0}$ distribution at high z. At these epochs (lookback time $t > 7$ Gyr), the Gaussian fit tends to slightly overestimate the mode position. Yet the Gaussian hypothesis remains a good approximation of the distribution, while the time evolution of the Gaussian mean value $\langle a_{0,0}\rangle$ (t) represents well the evolution of the mode of $a_{0,0}$.

The time evolution of the average flux of matter through the sphere, $\Phi^{\mathrm{M}}(t) = \overline{\varpi_\rho}$, is directly derived from the evolution of the

[4] Since the measured distribution is quite peaked, fits made with a normal distribution (not shown here) return a very similar time evolution of the mode position.

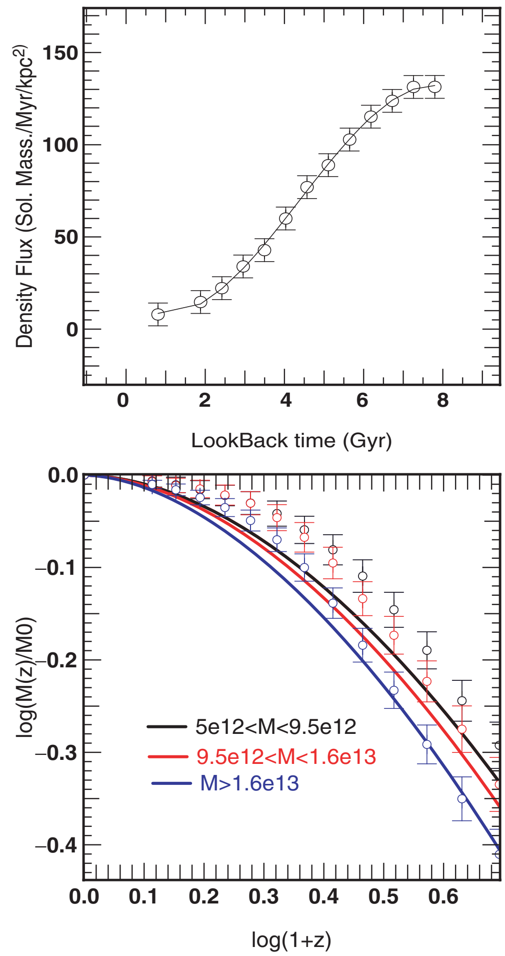

Figure 14. Top: the time evolution of the average flux density of matter through the virial sphere, $\langle\Phi^{\mathrm{M}}(t)\rangle = \langle\overline{\varpi_\rho}\rangle(t)$ (*symbols*). Bars stand for 3σ errors. Here Φ^{M} (t) is computed directly from a_{00} coefficients following equation (56). Its time evolution is fitted by a third-order polynomial (solid line). Bottom: the MAH $\log M(z)/M(z=0)$ for three different classes of masses. Masses are expressed in solar masses. Symbols represent the median value of $\log M(z)/M(z=0)$ within each classes. Lines represent the fitting function suggested by van den Bosch (2002b). Even though the global behaviour is reproduced by the fitting functions, the measured accretion rate is systematically smaller. This discrepancy has already been noted by van den Bosch (2002b).

monopole (see equation 43) and is shown in Fig. 14. It can be fitted by

$$\Phi^{\mathrm{M}}(t) \equiv \langle\overline{\varpi_\rho}\rangle(t) = -0.81t^3 + 10.7t^2 - 19.3t + 17.57, \tag{53}$$

where $\Phi^{\mathrm{M}}(t)$ is in units of $\mathrm{M}_{\odot}\,\mathrm{Myr}^{-1}\,\mathrm{kpc}^{-2}$ and lookback time t is expressed in Gyr. As expected, the average quantity of material accreted by haloes decreases with time. For $z < 1$, a large fraction of the objects of interest are already 'formed' and only gain matter through the accretion of small objects or diffuse material. In a hierarchical scenario, such a source of matter becomes scarcer, inducing a decrease in the accretion rate. Furthermore, recall that $\Phi^{\mathrm{M}}(t)$ is measured as a net flux, i.e. the outflowing material may cancel a fraction of the infalling flux. Therefore, the decrease with time may also be the consequence of an increasing contribution of outflows: the measurement radius $R_{200}(z=0)$ becomes the actual virial radius of the halo as time goes by, i.e. the radius where the inner material is reprocessed and where outflows are susceptible to be detected.

As a check, the average mass accretion history (hereafter MAH) of the haloes was computed. The MAH $\Psi(t)$ is defined as

$$\Psi(t) \equiv \frac{M(t)}{M(z=0)}, \tag{54}$$

where $M(z)$ is the halo's mass at a given instant. Using the extended Press–Schechter formalism, van den Bosch (2002b) showed that haloes have an universal MAH, fitted by the following formula:

$$\log[\Psi(M(z=0), t)] = -0.301 \left[\frac{\log(1+z)}{\log(1+z_f)}\right]^{\nu}, \tag{55}$$

where z_f and ν are two parameters which depend on the considered class of mass only. These two parameters are found to be correlated and for instance Wechsler et al. (2002) found a similar relation using a single parameter. For each halo, its mass evolution $M(t)$ was computed from its final mass $M(z=0)$ and its integrated flux of matter $\Phi^{\mathrm{M}}(t)$:

$$M(t) = M(t=0) - 4\pi R_{200}^2 \int_{t=0}^{t} \mathrm{d}t\,\Phi^{\mathrm{M}}(t). \tag{56}$$

From equation (54), $\Psi(t)$ was computed for each halo. The *median* value of $\Psi(t)$ for three classes of mass was compared to the fit suggested by van den Bosch (2002b) (see Fig. 14). For the three classes, the agreement with the fitting formula is qualitatively satisfying: the three measurements evolve in the expected manner while their relative positions are the same as the relative positions of the three fits. However, our measurements are quantitatively inconsistent with the three curves. At low redshift, $\Psi(t)$ is systematically larger than the expected value (i.e. the accretion rate is *smaller*). The median mass at $z = 1$ is well recovered even though the two methods disagree slightly quantitatively. In other words, our measurements overestimate the accretion at high redshift and underestimates at low redshift. This may be related to the measurement procedure through the sphere: at higher redshift, accreted material is assumed to be added to the biggest progenitor, even though it has not yet reached the central object and its mass is overestimated. Still, this material ends up in the most massive progenitor and the final mass is recovered. Note that since specific selection criteria were applied, these haloes may not be completely representative of the whole halo population. Finally, recall that the *median* value of $\Psi(t)$ was represented here because of strong outliers, while the fitting formula is given for the *average* MAH (extracted from merger trees). A similar discrepancy between the extended Press–Schechter theory and the results obtained from numerical simulations had already been noticed by van den Bosch (2002b) and Wechsler et al. (2002). In particular, van den Bosch (2002b) found that the Press–Schechter models tend to underestimate the formation time haloes compared to simulations. Clearly, our measurements seem to confirm this discrepancy. Since the global behaviour of MAHs is recovered and since the median mass at $z = 1$ is recovered, it is concluded that the measure of $\Phi^{\mathrm{M}}(t)$ through the virial sphere reproduces the accretion history of haloes.

5.3 Mean kinematics

Let us now turn to the kinematical properties of the flow, while averaging the source over the virial sphere.

5.3.1 probability distribution of the modulus of velocities

Given the source coefficients $c_{\alpha,\boldsymbol{m}'}^{\boldsymbol{m}}$, the average velocity distribution $\langle\varphi(v,t)\rangle$ (defined by equation 19) is easily computed since it only involves $\langle c_{\alpha,0}^{0}(t)\rangle$. The ensemble average of $\langle c_{\alpha,0}^{0}\rangle$ and the related ensemble dispersion $\sigma(c_{\alpha,0}^{0})(t) \equiv \langle (c_{\alpha,0}^{0} - \langle c_{\alpha,0}^{0}\rangle)^2\rangle$ are derived by fitting the $c_{\alpha,0}^{0}(t)$ distribution by a Gaussian function. From these two quantities, it follows

$$\langle\varphi(v,t)\rangle = 4\pi v^2 \sum_{\alpha} g_\alpha(v)\left\langle c_{\alpha,0}^{0}\right\rangle, \tag{57}$$

and

$$\sigma[\varphi(v,t)] = 4\pi v^2 \sqrt{\sum_{\alpha} g_\alpha(v)^2 \sigma\left(c_{\alpha,0}^{0}\right)^2}, \tag{58}$$

which are, respectively, the ensemble average and rms of the velocity distribution. The time evolution of $\langle\varphi(v,t)\rangle$ is given in Figs 15 and 16. Errors on $\langle\varphi(v,t)\rangle$ are computed as

$$\Delta[\langle\varphi(v,t)\rangle] = 3\frac{\sigma[\varphi(v,t)]}{\sqrt{N_{\mathrm{haloes}}}}. \tag{59}$$

At 'early times' ($t > 5$ Gyr), the distribution is unimodal with a maximum around $0.7V_{\mathrm{c}}\,(z=0)$. No outflows can be detected at

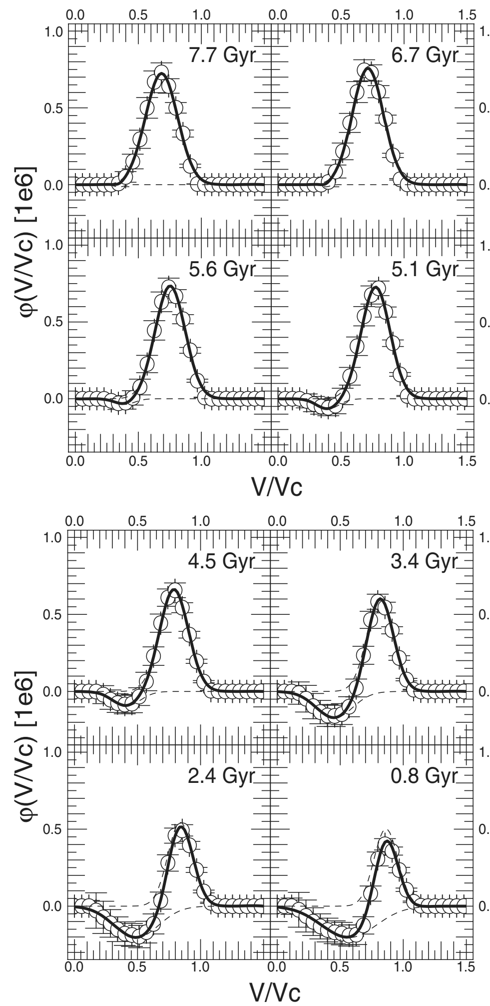

Figure 15. The time evolution of the average velocity distribution, $\langle\varphi(v, t)\rangle$, defined in equation (19), for $z < 1$ (*symbols*). Ages are expressed as lookback times (i.e. $t = 0$ for $z = 0$). Velocities are given relative to the halo's circular velocity at $z = 0$. The unit in y-axis is $5 \times 10^9\,\mathrm{M}_\odot\,\mathrm{kpc}^{-2}\,2\,\mathrm{Myr}^{-1}/V_{\mathrm{c}}$. Error bars stand for 3σ errors. Here $\varphi(v)$ is fitted by the sum of two Gaussians with opposite signs (solid line). Each Gaussian contribution is also shown (dashed lines).

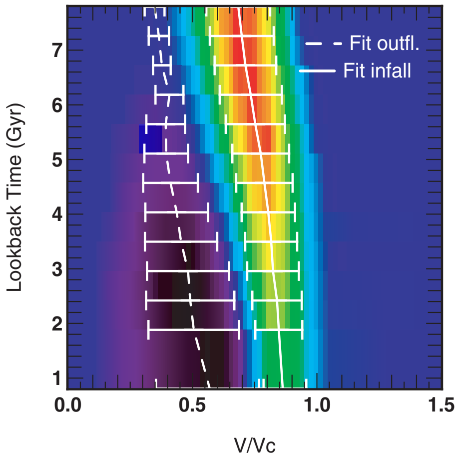

Figure 16. The time evolution of the average velocity distribution in the t–$V/V_{\rm c}$ plane. Red (online) colours stand for positive values of the distribution (i.e. infall), while blue (online) colours stand for negative ones (i.e. outflows). Each of these components is fitted by a Gaussian function in the $V/V_{\rm c}$ space. The time evolutions of the mean of the Gaussians are given by the two lines (*solid* for infall, *dashed* for outflows). The rms of Gaussians are also shown as bars.

any velocity and the infalling dark matter dominates. At later times, $\langle\varphi(v, t)\rangle$ drops below zero for velocities around $0.4V_{\rm c}$ $(z = 0)$. Outflows dominate at 'low' velocities. Meanwhile, the amplitude of the previous peak decreases and shifts to higher velocities. The fraction of infall relative to the total amount of material passing through the sphere drops from 1. to 0.6 between $t = 8$ and 0.8 Gyr.

This behaviour is likely to be due to our measurement at a *fixed* radius, $R_{200}(z = 0)$. At 'early times', this measurement radius is bigger than the actual virial radius of haloes. Thus no sign of 'virialization' (outflows consecutive to accretion) is detected. Later, the actual R_{200} gets closer to the measurement radius. Outflows pass through the measurement radius as a sign of internal dynamical reorganization. The fact that accretion intrinsically decreases with time would provide another explanation of this trend. This decrease can actually be traced in Figs 15, 16 and D1.

The global behaviour of $\langle\varphi(v, t)\rangle$ can be modelled by summing two Gaussians representing the infalling and outflowing components:

$$\langle\varphi(v,t)\rangle = \frac{q_{\iota,3}(t)}{q_{\iota,2}(t)\sqrt{2\pi}}\exp\left\{-\frac{[v-q_{\iota,1}(t)]^2}{2q_{\iota,2}(t)^2}\right\} + \frac{q_{o,3}(t)}{q_{o,2}(t)\sqrt{2\pi}}\exp\left\{-\frac{[v-q_{o,1}(t)]^2}{2q_{o,2}(t)^2}\right\}. \quad (60)$$

Subscripts ι and o stand for infall and outflow. Note that $q_{\iota,3}(t) \geqslant 0$ and $q_{o,3}(t) \leqslant 0$. The coefficient time evolution is given in Fig. D1, where t can be expressed in Gyr and $\varphi(v, t)$ in $5 \times 10^9\,{\rm M}_\odot\,{\rm kpc}^{-2}\,{\rm Myr}^{-1}/V_{\rm c}$. Examples of fits are shown as solid lines in Fig. 15. Note that all the six coefficients evolve roughly linearly with time (see Fig. D1). Their linear fitting parameters are given in Table D1. Using equation (60) and the linear parametrization of the Gaussian coefficients, $\langle\varphi(v, t)\rangle$ is reproduced accurately. The only restriction concerns the negative amplitude of the Gaussian $(q_{o,3})$ which should not be greater than 0. Since this condition is not naturally satisfied by a linear fit, it should be set manually.

The evolution of the relative positions of two Gaussians is given in Fig. 16. For $t > 5$ Gyr, it is consistent with the 'no outflow' hypothesis, the amplitude of the negative Gaussian being close to zero at this epoch. Both Gaussians mean values seem to drift to higher velocities as a function of time. Even though the relative velocity of accreted material is determined by the initial conditions (namely large-scale clustering), the velocity of an infalling satellite should partly reflect the properties of the accreting body. A dense massive halo will not accrete like a fluffy light one. In other words, the velocity of infalling material should reflect the actual circular velocity of the accreting body. As a consequence, it is expected that accretion velocity drifts with time towards $V_{\rm c}$ $(z = 0)$.

Furthermore, the mean values of both Gaussians evolve roughly linearly over the whole time range with comparable rate of change (see Fig. D1 and the following discussion). As a consequence, their relative positions remain roughly constant (see Fig. 16). This indicates that these two components may be physically related, outflows being the consequence of a past accretion. Mamon et al. (2004) mention the existence of a *backsplash* population, rebounding through the virial radius and this population is known to have a different velocity (e.g. Gill et al. 2004). The outflows detected via our description of the source are consistent with this backsplash component. The difference in velocity may be explained if outflows are representative of an earlier accretion with a velocity typical of earlier times. Also past accreted material is influenced by the halo's internal dynamics. Its velocity distribution would be 'reprocessed' (e.g. via dynamical friction, tidal stripping or phase mixing) to lower velocities as the material exits through the measurement radius.

However, recall that the distribution shown here is a 'net' distribution. In other words, it is quite plausible that an outflowing component may be completely cancelled by an infalling component which has an exact opposite distribution. This effect is illustrated in Fig. 17, where the velocity distribution of infall and outflows is being shown separately. This distribution has been computed from 300 haloes at $t = 2.3$ Gyr. This distribution is quite representative of the average ones, except a few high velocities events which skew the distribution of the infalling component and which are induced by outliers. If the Gaussian fits are removed from these two separate distributions, two almost identical distributions appear for the two components, centred on $V/V_{\rm c} \sim 0.6$. These two identical distributions are related to the virialized component of infall, which already interacted with the inner region of the halo. The overall shape of these two distributions may provide insights on the typical dynamical state in the haloes' inner regions.

5.3.2 *Impact parameters and incidence angles*

The average distribution of incidence angle, $\langle\vartheta(\Gamma_1, t)\rangle$ has been computed following the same procedure described above for $\langle\varphi(v, t)\rangle$. Defining $\tilde{c}_{\ell'}(t)$ as

$$\tilde{c}_{\ell'}(t) = 2\pi\sqrt{4\pi}\sum_\alpha c_{\alpha,0,\{\ell',0\}}\left(\mu_\alpha^2+\sigma^2\right), \quad (61)$$

yields

$$\langle\vartheta(\Gamma_1,t)\rangle = \sum_{\ell'} Y_{\ell',0}(\mathbf{\Gamma})\langle\tilde{c}_{\ell'}(t)\rangle \quad (62)$$

and

$$\sigma(\vartheta(\Gamma_1,t)) = \sqrt{\sum_{\ell'} Y_{\ell',0}(\mathbf{\Gamma})^2\sigma(\tilde{c}_{\ell'}(t))^2}, \quad (63)$$

where $\langle\vartheta(\Gamma_1, t)\rangle$ and $\sigma(\vartheta(\Gamma_1, t))$ are derived by fitting the $\tilde{c}_{\ell'}(t)$ distribution by a Gaussian function. Errors on $\langle\vartheta(\Gamma_1, t)\rangle$ are computed

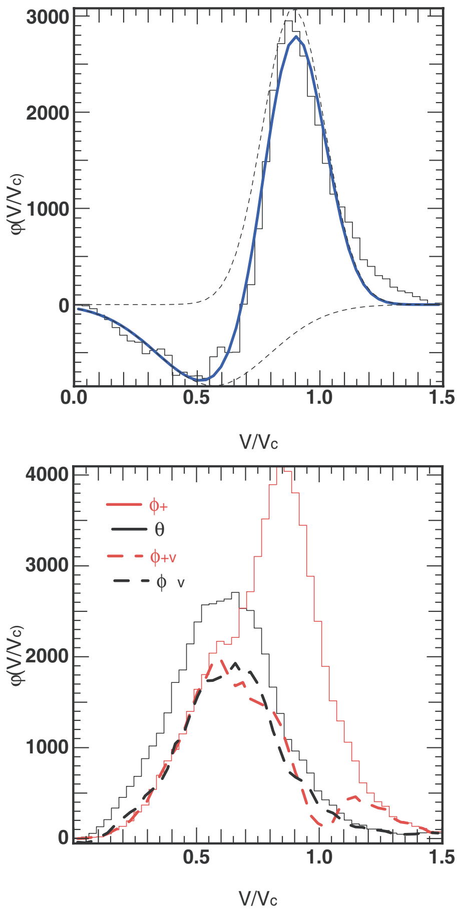

Figure 17. Top: the net velocities distribution (histogram) measured from 300 haloes at t = 3.4 Gyr. This distribution is the representative of the distribution computed from coefficients and averaged over 15 000 haloes. Velocities are given in circular velocity units, while units in y-axis are arbitrary. The two components are fitted by two Gaussians (dashed lines). Bottom: the separate velocities distribution of accretion (red histogram) and outflows (black histogram). The dashed curves represent the difference between these two distributions and their respective fits shown above. It results in two residual distributions, centred on the same velocity and displaying nearly the same shape. These two residual distributions describe the material which already experienced one passage through the virial sphere.

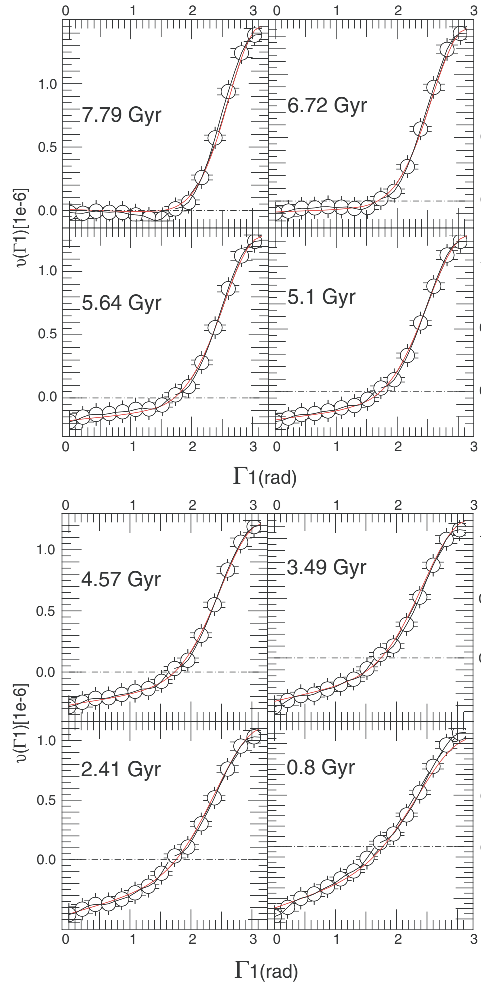

Figure 18. The time evolution (symbols) of the distribution of the average incidence angle Γ_1 $\langle\vartheta(\Gamma_1)\rangle$ is defined by equation (46). Ages are expressed as lookback time. Bars stand for 3σ errors. The unit in y-axis is 5 $\times$ 10^9 $\mathrm{M_\odot}$ kpc^{-2} Myr^{-1}. Outflows are counted negatively, leading to negative values of $\langle\vartheta(\Gamma_1)\rangle$ for $\Gamma_1 < \pi/2$. The result of the model described in equation (64) is also shown (red line).

similarly to errors on $\langle\varphi(v, t)\rangle$ (see equation 59). The time evolution of $\langle\vartheta(\Gamma_1, t)\rangle$ is shown in Fig. 18. Since the impact parameter and the incidence angle are simply related by $b/R_{200} = \sin(\Gamma_1)$, $\langle\vartheta(b, t)\rangle$ is also easily computed (Fig. 19).

The infall ($\Gamma_1 > \pi/2$ or the upper branch in $\langle\vartheta(b, t)\rangle$ diagrams) is clearly mostly radial. The infalling part of the distribution peaks for $\Gamma_1 \sim \pi$ instead of having a uniform behaviour and this trend can be observed for all redshifts below 1. The distribution slightly widens with but remains skewed towards large values of Γ_1. In the $\langle\vartheta(b, t)\rangle$ representation, the higher branch becomes flatter with time. The outflows ($\Gamma_1 < \pi/2$ or lower branch in $\langle\vartheta(b, t)\rangle$ diagrams) are mainly undetectable at early times, as mentioned earlier. As time increases, the outflow contribution becomes stronger and radial orbits ($\Gamma_1 \sim 0$) also appear to be dominant. However, the behaviour of the 'outflowing' part of the $\langle\vartheta(\Gamma_1, t)\rangle$ distribution is almost linear and does not peak. Tangential orbits cannot be neglected for this component.

The evolution of $\langle\vartheta(\Gamma_1, t)\rangle$ can be fitted by the following parametrization:

$$\langle\vartheta(\Gamma_1, t)\rangle = \frac{p_0}{\sqrt{2\pi}p_1(t)} \exp\left[-\frac{(\Gamma_1 - \pi)^2}{2p_1(t)^2}\right] + p_2(t)\Gamma_1 + p_3(t), \tag{64}$$

where $p_0 = 2 \times 10^{-6}$ in our units. The 'infalling' part is modelled as a Gaussian, while the 'outflowing' part is fitted linearly. The time evolution of the three parameters $p_k(t), k = 1, 2, 3$, can be fitted by a linear evolution and the related linear parameters are given in Table D2. The evolution of $p_1(t)$ confirms that the 'infalling' part of the distribution, $\langle\vartheta(\Gamma_1, t)\rangle$ widens with time.

This result implies that the material experiences a circularization as it interacts with the halo. Consequently, orbits are more tangential as particles *exit* and *re-enter* the halo's sphere. Such an effect has already been measured by e.g. Gill et al. (2004). Dynamical friction would provide a natural explanation for this evolution of the orbits, but this argument is refuted by e.g. Colpi, Mayer & Governato (1999) or Hashimoto, Funato & Makino (2003). Gill et al. (2004) mention the secular evolution of haloes to explain this circularization: the time evolution of the potential well induced by the halo would affect the orbits of infalling material and satellites. Other processes, such as tidal stripping or satellite–satellite interactions, may also modify the orbital parameters of dark matter fluxes. Clearly, the interactions between the infall and the halo drive this circularization, but the detailed process still has to be understood.

This dynamical circularization could also explain why the 'outflowing' part of the $\langle\vartheta(\Gamma_1)\rangle$ (or $\langle\vartheta(b)\rangle$) is flatter than the infalling one: by definition this component interacted with the halo in the past, unlike most of the infall. Finally, the Γ_1 or b representation explicitly separates infall and outflows. It implies that *virialized* particles which pass through the sphere do not 'cancel' each other and do contribute to the distributions. Such a 'relaxed' material is likely to have a non-zero tangential motion, flattening the distributions as its contribution becomes important. Since the actual size of the halo gets closer to the measurement radius as time advances, this component contributes more with time and its flattening effect on the incidence angle (or impact parameter) distributions should increase as well.

Fig. 20 presents a correlation between the velocity amplitude v and the impact parameter b, at four different instances and for both the infall and the outflow components. Considering these two components separately, no correlation can be found: the incidence does not depend on the amplitude of the first approximation. The only notable result comes from the fact that accreted material has systematically a higher velocity than outflows, which confirms the results obtained from the distribution of velocities only. Again, this effect is related to the separate origin of these two fluxes, accretion, being dominated by newly accreted material, and outflows, which were processed by the inner dynamics of haloes.

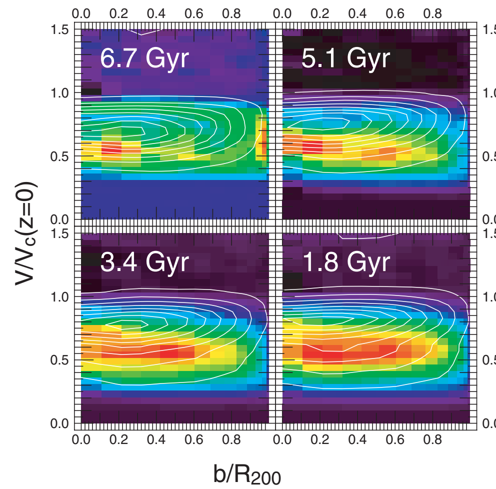

Figure 20. Top: the distribution, $\langle\wp(b, v)\rangle$, of particles in the (b, v) subspace at lookback time t = 1.8, 3.4, 5.1 and 6.7 Gyr; the infall (contour plot) and outflow (density plot) are represented separately. Beyond the bimodal feature, no residual correlation appears.

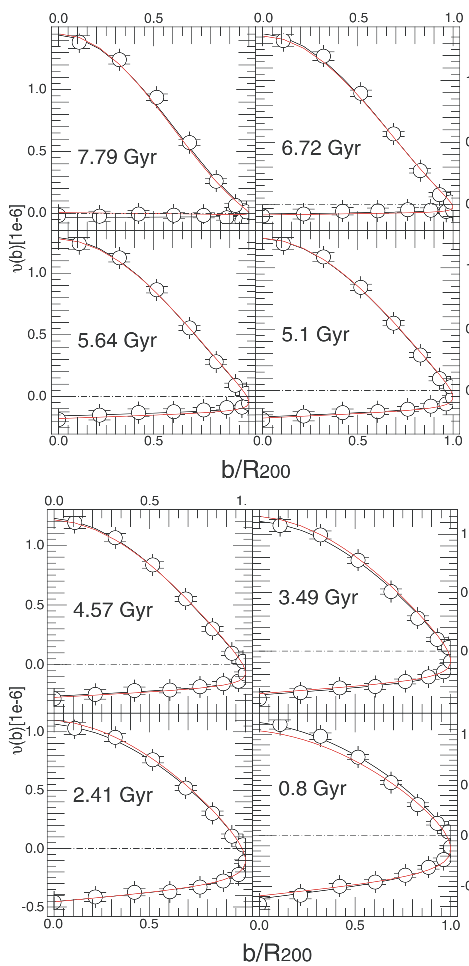

Figure 19. The time evolution (symbols) of the impact parameter b distribution $\langle\vartheta(b,\, t)\rangle$ is defined by equation (46). Ages are expressed as lookback time. Bars stand for 3σ errors. The unit in y-axis is 5×10^9 $M_\odot\,\mathrm{kpc}^{-2}\,\mathrm{Myr}^{-1}$. The lower (respectively higher) branch is the $\langle\vartheta(b,\, t)\rangle$ distribution for outflows (respectively infall). The result of the model described in equation (64) is also shown (red line).

6 TWO-POINT STATISTICS

Let us now focus on the second-order statistics, through the correlations on the virial sphere. The two-point correlations are assessed through the angular power spectrum and the angulo-temporal correlation function for both the external potential, ψ^{e} and the first moment of the source term, i.e. the flux density of mass, ϖ_ρ.

6.1 External potential

6.1.1 Angular power spectrum

The potential's angular power spectrum $C_\ell^{\psi^{\mathrm{e}}}$ is computed for each halo from the $\tilde{b}_{\ell,m}$ coefficients (Aubert et al. 2004),

$$\tilde{b}_{\ell,m} \equiv \sqrt{4\pi}\left(\frac{b_{\ell,m}}{\langle b_{00}\rangle} - \delta_{\ell 0}\frac{b_{0,0}}{\langle b_{00}\rangle}\right), \tag{65}$$

related to the potential contrast

$$\delta_{[\psi^{\mathrm{e}}]}(\boldsymbol{\Omega}) \equiv \frac{\psi^{\mathrm{e}}(\boldsymbol{\Omega}) - \overline{\psi^{\mathrm{e}}}}{\langle\overline{\psi^{\mathrm{e}}}\rangle} = \sum_{\ell,m}\tilde{b}_{\ell,m}Y_{\ell,m}(\boldsymbol{\Omega}). \tag{66}$$

The probability distribution of $C_\ell^{\psi^{\mathrm{e}}}(t)$ was weighted as described in Appendix A. For each time-step and each harmonic ℓ, $C_\ell^{\psi^{\mathrm{e}}}$ was fitted by a lognormal distribution (see Fig. C2). Let us define $\langle\!\langle C_\ell^{\psi^{\mathrm{e}}}\rangle\!\rangle(t)$ as the mode of the fitting distribution. The time evolution of the external potential's power spectrum is shown in Fig. 21. Globally, the power spectrum is dominated by large scales and is quite insensitive to time evolution. However, two regimes may be distinguished. For

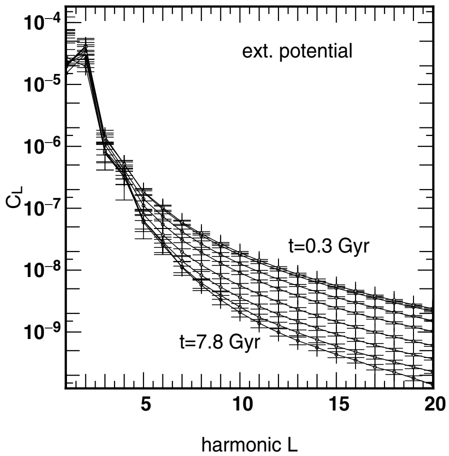

Figure 21. The angular power spectrum of the external gravitational potential $\psi^{\mathrm{e}}(\mathbf{\Omega}, t)$. Symbols represent the *mode* of the $C_\ell^{\psi^{\mathrm{e}}}$ distribution for each harmonic ℓ and each time-step. Times are lookback times. Bars stand for 3σ errors on the mode value. The large-scale contribution remains constant with time, while the small-scale contribution smoothly increases with time. The bump for the $\langle C_2 \rangle$ component indicates a strong quadrupolar configuration for $\psi^{\mathrm{e}}(\mathbf{\Omega}, t)$.

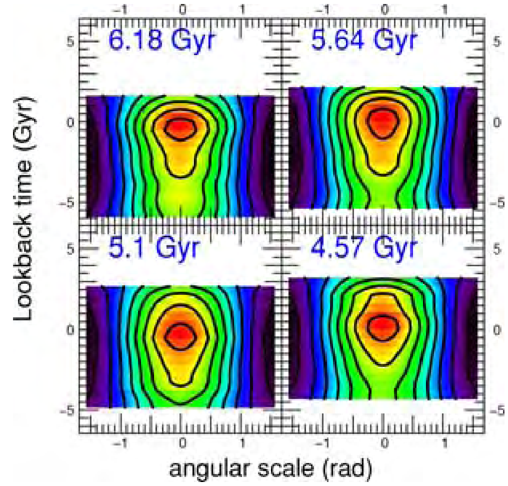

Figure 22. The angulo-temporal correlation function, $w^{\mathrm{e}}(\theta, \Delta t) = \langle \delta_{[\psi^{\mathrm{e}}]}(\mathbf{\Omega}, t)\delta_{[\psi^{\mathrm{e}}]}(\mathbf{\Omega} + \Delta\mathbf{\Omega}, t + \Delta t)\rangle$. Blue (respectively red) colours stand for low (respectively high) values of the correlation. Isocontours are also shown. Large angular scale isocontours ($\theta \sim \pi/2$) have large temporal extent, due to the quadrupole dominance over the potential seen in the virial sphere.

low-order harmonics, $\langle\langle C_\ell^{\psi^{\mathrm{e}}} \rangle\rangle(t)$ remains mostly constant. For smaller scales ($\ell > 5$), $\langle\langle C_\ell^{\psi^{\mathrm{e}}} \rangle\rangle(t)$ increases along time. As a consequence, the power spectrum's amplitude does not change but its shape evolves while smaller scales become more important relative to larger scales.

These two regimes reflect the two-fold nature of tidal interactions of a halo with its environment. Small angular variations of the potential relate to small spatial scales and presumably track the presence of objects which are getting closer or going through the virial sphere. Since small-scale contribution increases, it suggests that these objects tend to get smaller with time. It would be consistent with the global decrease of the accretion rate, as long as the merger rate does not increase strongly during this epoch. However, the rise of small scales may also be related to an increasing contribution of weak and poorly resolved accretion events. In such a case, the isolated particles' contribution to the potential should be measured. This possibility is investigated in Section 6.2.

Meanwhile, large-scale fluctuations of potential ($\ell \leqslant 4$) may reflect the 'cosmic tidal field' resulting from the distribution of matter around the halo on scales larger than the radius of the halo. The amplitude of such a tidal field should remain fairly constant, as indeed measured. Furthermore, the peripheral distribution of matter is not spherically distributed but is rather elongated along some direction: haloes tend to be triaxial with their ellipsoid aligned with the surrounding distribution of satellites. The intersection of an elongated distribution of matter with the virial sphere would induce a quadrupolar component, as detected in our measurements. These two effects cannot be easily disentangled, since they actually are two sides of the same effect. Large-scale distribution of matter is responsible for both the 'cosmic tidal field' and the halo triaxiality (via the distribution of satellites). In other words, it is not clear whether the large-scale behaviour of $\langle\langle C_\ell^{\psi^{\mathrm{e}}} \rangle\rangle(t)$ reflects the tidal field or the reaction of the halo to this tidal field.

6.1.2 Angulo-temporal correlation

6.1.2.1 Correlations and coherence time. To further investigate these two regimes of tidal interactions, let us compute the angulo-temporal correlation function of the external potential contrast, defined as

$$\langle\langle w^{\mathrm{e}}(\theta, t, t + \Delta t)\rangle\rangle = \langle\langle \delta_{[\psi^{\mathrm{e}}]}(\mathbf{\Omega}, t)\delta_{[\psi^{\mathrm{e}}]}(\mathbf{\Omega} + \Delta\mathbf{\Omega}, t + \Delta t)\rangle\rangle, \quad (67)$$

which is related to $T_\ell^{\psi^{\mathrm{e}}}$ (t, t + Δt) coefficients by

$$w^{\mathrm{e}}(\theta, t, t + \Delta t) = \sum_\ell T_\ell^{\psi^{\mathrm{e}}}(t, t + \Delta t)(2\ell + 1)P_\ell[\cos(\theta)], \quad (68)$$

where

$$T_\ell^{\psi^{\mathrm{e}}}(t, t + \Delta t) \equiv \frac{1}{4\pi}\frac{1}{2\ell + 1}\sum_m \tilde{b}_{\ell m}(t)\tilde{b}^*_{\ell m}(t + \Delta t). \quad (69)$$

Here, θ stands for the angular distance between two points on the sphere located at $\mathbf{\Omega}$ and $\mathbf{\Omega} + \Delta\mathbf{\Omega}$. The $T_\ell^{\psi^{\mathrm{e}}}(t, t + \Delta t)$ coefficients were computed for each halo and each pair of time-step, for each harmonic. The $T_\ell^{\psi^{\mathrm{e}}}(t, t + \Delta t)$ distributions were fitted by a lognormal distribution and $\langle\langle T_\ell^{\psi^{\mathrm{e}}}(t, t + \Delta t)\rangle\rangle$ was deduced from it. The corresponding $\langle\langle w^{\mathrm{e}}(\theta, t, t + \Delta t)\rangle\rangle$ are shown in Fig. 22.

For large angular scales (>45°), isocontours remain open during the whole time range. Large scales have a long coherence time (∼5 Gyr) and are consistent with a 'cosmic tidal field' resulting from the large-scale distribution of matter. The latter is not expected to evolve significantly with time at our redshifts and the triaxiality of the halo is also a fairly constant feature. The innermost isocontours are closed around the measurement time t_1. Small angular scales (<45°) have shorter coherence time (∼1.5 Gyr). This is consistent with a contribution to the potential due to objects, where satellites pass by or dive into the halo and apply a tidal field only for a short period.

This difference between large and small scales can also be investigated through the time matrices of the $T_\ell^{\psi^{\mathrm{e}}}(t, t + \Delta t)$ coefficients (see Fig. 23). The diagonal terms describe the time evolution of the angular power spectrum, $T_\ell^{\psi^{\mathrm{e}}}(t, t) = C_\ell^{\psi^{\mathrm{e}}}(t)$. A smooth (respectively peaked) distribution of values around the diagonal indicates a long (respectively short) coherence time. Clearly, different scales have different characteristic time-scales. The non-diagonal elements of the quadrupole matrix ($\ell = 2$) decrease slowly with the distance to the diagonal while the T_{20} matrix is almost diagonal. Not surprisingly, the smaller the angular scale, the smaller is the coherence

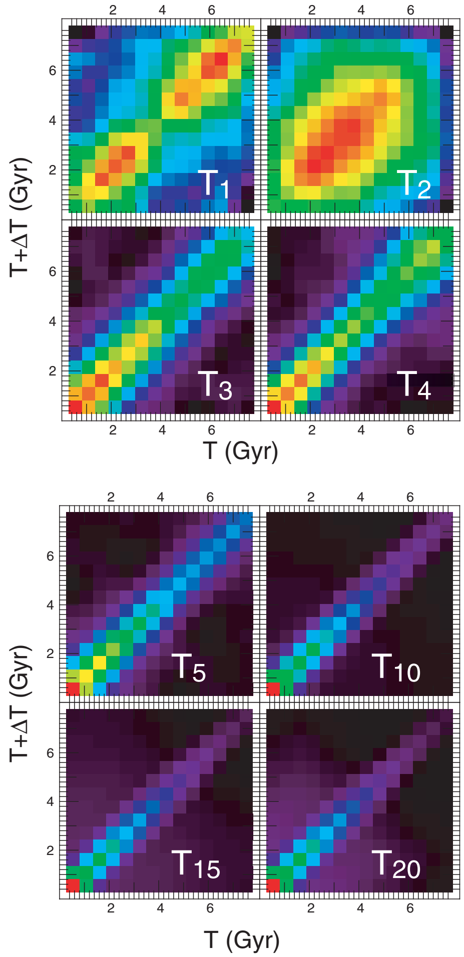

Figure 23. The time matrices of the $T_\ell^{\psi^e}(t, t+\Delta t)$ coefficients. Blue (respectively red) colours stand for low (respectively high) values of the coefficients. The diagonal terms are equal to the angular power spectrum, i.e. $T_\ell^{\psi^e}(t,t) = C_\ell^{\psi^e}(t)$. As can be seen from Fig. 21, fluctuations observed for T_1 are within the error bars. A smooth (respectively sharp) decrease of $T_\ell^{\psi^e}(t, t+\Delta t)$ with the distance to the diagonal implies a long (respectively short) coherence time. Here, coherence time decreases with angular scale.

time: a small 3D object passing through the sphere is likely to have a small angular size on the sphere.

For a given ℓ and a given t, the correlation coefficients $T_\ell^{\psi^e}$ can be fitted by a Lorentzian function defined by

$$T_\ell(t, t+\Delta t) = \frac{q_3^{\mathrm{Te}}(t)}{2/\pi} \frac{q_2^{\mathrm{Te}}(t)}{\left[\Delta t - q_1^{\mathrm{Te}}(t)\right]^2 + \left[q_2^{\mathrm{Te}}(t)/2\right]^2} + q_4^{\mathrm{Te}}(t), \tag{70}$$

where the characteristic time-scale, $\Delta T_{T_\ell^e}$, is given by $q_2^{\mathrm{Te}}(t)$ and the reference time t is equal to $q_1^{\mathrm{Te}}(t)$. Examples of fits are shown in Fig. 24.

For example, the time evolution of $\Delta T_{T_\ell^e} = q_2^{\mathrm{Te}}(t)$ is given in Fig. 24 for different ℓ values. Given the error bars, the characteristic time-scales are constant over time (except for the $\ell = 4$ mode). In the prospect of the regeneration of the potential, the stationary hypothesis can then be considered as valid for most of the angular scales. Meanwhile, the $\ell = 4$ potential fluctuations display a decreasing $\Delta T_{T_\ell^e}$ with time. The same effect exists at a 1σ level for $\ell = 5$. One interpretation would be that satellites achieve higher velocities along time: for a given typical size, a faster satellite would

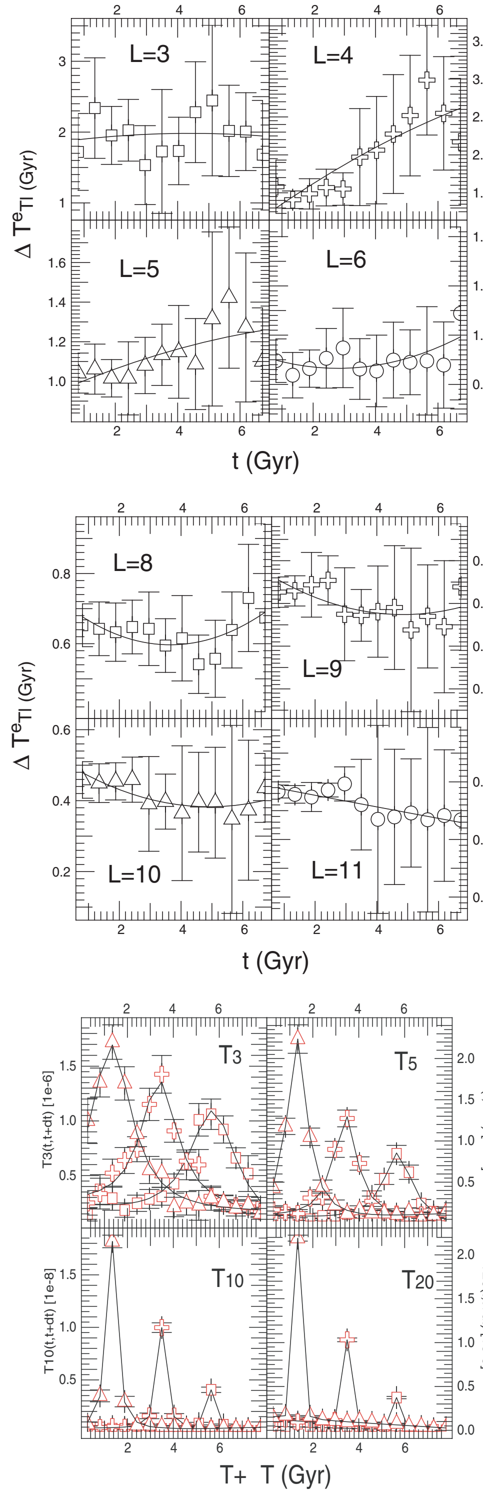

Figure 24. Top and middle: the time evolution of the characteristic time-scale $\Delta T_{T_\ell^e}$, obtained by fitting $T_\ell^{\psi^e}(t, t+\Delta t)$ with equation (70). Symbols are the measurements while bars stand for 3σ fitting error bars. The second-order fit of the time evolution of each $T_\ell^{\psi^e}$ is also shown. Except for the $\ell = 4$ and (marginally) for the $\ell = 5$ modes, no time evolution is observed. The time resolution is 0.53 Gyr. Bottom: examples of $T_\ell^{\psi^e}(t, t+\Delta t)$ fitted by Lorentzian functions.

spend less time to be accreted and the associated potential would be detected on a smaller time-scale. This picture is supported by the results shown in Section 5.3.1, where the mean velocity of infalling material increases along time. Another possibility would be that $\ell = 4$ fluctuations had a longer radial extent in the past. Since there is no reason for potential fluctuations to have such a property, one could imagine *successive* potential fluctuations which overlapped, leading to an apparent longer radial extent. This possibility is further investigated in the following paragraphs, by comparing the coherence time variation of the potential fluctuations to the evolution of the typical velocity of the infall.

6.1.2.2 Correlations without the dipole and the quadrupole. In order to focus on the coherence time of small angular scales, the correlation function $\langle\!\langle w^{\mathrm{e}}(\theta, t, \Delta t)\rangle\!\rangle$ was also computed without the dipole ($\ell = 1$) and the quadrupole ($\ell = 2$) component of the potential (see also equation 68). The angulo-temporal correlation function is shown in Fig. 25. Again, the isocontours of the correlation function are closed around $\Delta t = 0$. This shows that the potential on the sphere has a finite coherence time. In contrast to coherence times measured on the $T_\ell^{\psi^{\mathrm{e}}}$ coefficients, all the angular scales are mixed and the typical time-scales are those of structures as they are 'really' seen from a halocentric point of view, where 'potential blobs' appear and disappear on the sphere. To evaluate the related typical time-scale $\Delta T_{\psi^{\mathrm{e}}}$, $\langle\!\langle w^{\mathrm{e}}(\Delta\Omega, t, \Delta t)\rangle\!\rangle$ was fitted with a 2D function for different values of t. The model used is given by

$$\langle\langle w^{\mathrm{e}}(\theta, t, \Delta t)\rangle\rangle = q_6^{\mathrm{we}}(t) + \frac{q_5^{\mathrm{we}}(t)}{2\pi}\frac{q_4^{\mathrm{we}}(t)}{\left[\Delta t - q_3^{\mathrm{we}}(t)\right]^2 + \left[\frac{q_4^{\mathrm{we}}(t)}{2}\right]^2} \times \frac{\sin\left\{2\pi\left[\Delta\Omega - q_1^{\mathrm{we}}(t)\right]/q_2^{\mathrm{we}}(t)\right\}}{\Delta\Omega}, \tag{71}$$

where the angular dependence is fitted by a cardinal sine function while the time dependence is fitted by a Lorentzian function. Examples of 2D fits are shown in Fig. 25. The correlation function was also computed using only harmonics with $\ell \geqslant 4$, 5, 6, 7 and the same fitting procedure is applied. The evolution of the resulting characteristic time-scales $\Delta T_{\mathrm{w^e}} = q_4^{\mathrm{we}}(t)$ is shown in Fig. 26. Bars stand for 3σ fitting errors.

Note that $\Delta T_{\mathrm{w^e}}$ tends to decrease with time for every truncation order. The $\ell \geqslant 3$ and 4 correlation function displays a rise of $\Delta T_{\mathrm{w^e}}$ before it drops to lower values. Furthermore, $\Delta T_{\mathrm{w^e}}$ tends to decrease with $\ell_{\min}$, suggesting that the $\ell_{\min}$ contribution dominates each w^{e} reconstruction. Correlation functions with $\ell_{\min} \geqslant 5$ show marginal $\Delta T_{\mathrm{w^e}}$ variation but recall that our time resolution is 0.53 Gyr, hence any fluctuations on smaller scales should be taken in caution. Still, the 0.81-Gyr variation observed for $\ell \geqslant 3$ between $t = 5.1$ and 0.8 Gyr is significant and so is the variation observed for $\ell \geqslant 4$ (1.3 Gyr).

6.1.2.3 A longer coherence length. As mentioned above, the variation of the characteristic time-scale can be explained by the measured increase in mean velocity. Conversely, the decrease of coherence time may be the consequence of smaller potential blobs as time passes: a 'large' (three-dimensional) potential takes longer to

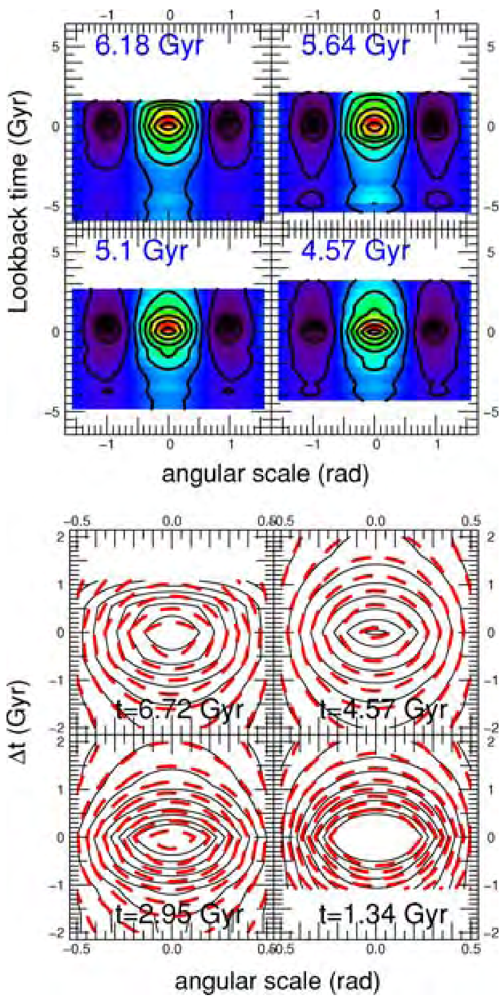

Figure 25. Top: the angulo-temporal correlation function, $w^{\mathrm{e}}(\theta, \Delta t) = \langle\delta_{[\psi^{\mathrm{e}}]}(\boldsymbol{\Omega}, t)\delta_{[\psi^{\mathrm{e}}]}(\boldsymbol{\Omega} + \Delta\boldsymbol{\Omega}, t + \Delta t)\rangle$. The dipole ($\ell = 1$) and the quadrupole ($\ell = 2$) components were removed. Blue (respectively red) colours stand for low (respectively high) values of the correlation. Isocontours are also shown. The main axes of the 'ellipses' centred on ($\Delta\boldsymbol{\Omega} = 0$, $\Delta t = 0$) give indications on the characteristic time and angular scales of $\psi^{\mathrm{e}}(\boldsymbol{\Omega}, t)$. Bottom: comparison between the measured 2D correlation function (solid lines) and the fit obtained using equation (71) (dashed lines).

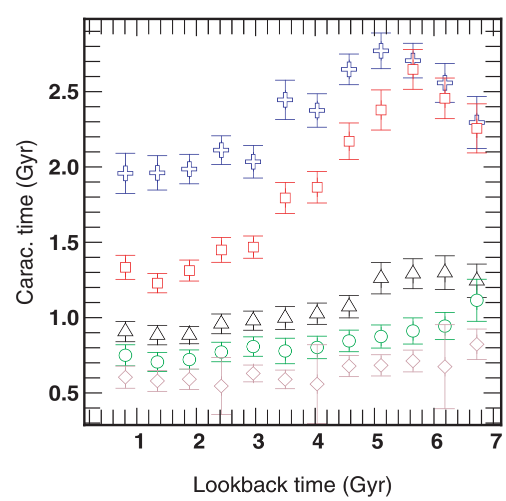

Figure 26. The cosmic evolution of the potential's coherence time. This characteristic time-scale is obtained by fitting the 2D correlation function w^{e} (θ, Δt) with the function given in equation (71). The correlation function is computed using harmonics coefficients with $\ell \geqslant 3$ (*crosses*), $\ell \geqslant 4$ (*squares*), $\ell \geqslant 5$ (*triangle*), $\ell \geqslant 6$ (*circle*) and $\ell \geqslant 7$ (*diamonds*). Bars stand for 3σ fitting errors. The time resolution is 0.53 Gyr.

disappear than a smaller one. One crude approximation could be

$$\frac{L_1}{L_2} = \frac{V_1 \Delta T_1}{V_2 \Delta T_2}, \tag{72}$$

where L is the radial size, V is the radial velocity and ΔT is the coherence time of the potential blob. It is assumed that the $\ell \geqslant 4$ truncation is the representative of the potential due to infalling objects, i.e. $\Delta T_1/\Delta T_2 \sim 1.95$. Let us also consider that the radial velocity variation is equal to the one measured for the mean velocity of infall (see Section 5.3.1): $V_1/V_2 = 0.77$. Following equation (72), it suggests that $L_1 \sim 1.5 L_2$, i.e. the radial size decreases with time. The same calculation with $\ell \geqslant 3$ leads us to $L_1 \sim 1.1 L_2$: the results remain qualitatively the same. In other words, the coherence length was longer in the past and the velocity variation cannot explain the variation of coherence time. The only other way to explain a longer coherence length involves potential blobs falling successively through the sphere, coming from roughly the same direction. To induce a decreasing coherence time, these blobs would have to be either bigger before or more numerous. Such a crude picture is coherent with the measured decrease of accretion with time and the anisotropic nature of accretion by haloes (see e.g. Aubert et al. 2004; Knebe et al. 2004; Zentner et al. 2005).

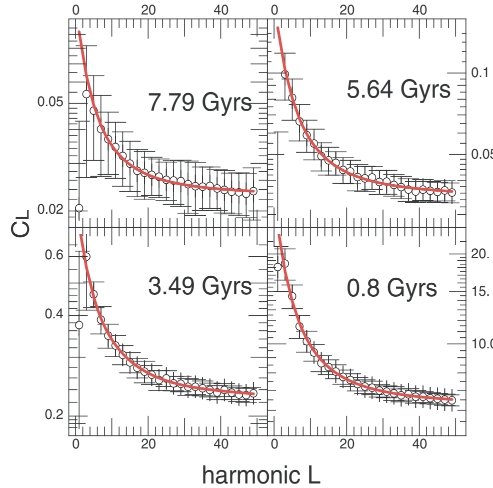

Figure 27. The average angular power spectrum, $\langle\langle C_\ell^{\varpi_\rho} \rangle\rangle$ (t), at $t = 0.8$, 3.5, 5.7, 7.8 Gyr (symbols). $\langle\langle C_\ell^{\varpi_\rho} \rangle\rangle$ (t) is taken as the mode of the lognormal function used to fit the C_ℓ distribution. Bars stand for 3σ errors. For a given ℓ, the corresponding angular scale is π/ℓ. $\langle\langle C_\ell^{\varpi_\rho} \rangle\rangle$ (t) may be fitted by a generic model given by equation (75) (solid line).

6.2 Flux density of mass: $\varpi_\rho \equiv \rho v_r$

The mode $\langle\langle C_\ell^{\varpi_\rho} \rangle\rangle$ of the distribution of the ϖ_ρ angular power spectrum is computed using equations (41) and (42). In order to deal with adimensional quantities, the reduced harmonic coefficients, $\tilde{a}_{\ell,m}$, are defined as

$$\tilde{a}_{\ell,m} \equiv \sqrt{4\pi} \left(\frac{a_{\ell,m}}{\langle a_{00} \rangle} - \delta_{\ell 0} \frac{a_{0,0}}{\langle a_{00} \rangle} \right). \tag{73}$$

The accretion contrast, $\delta_{[\varpi_\rho]}$, and the $\tilde{a}_{\ell,m}$ coefficients are linked by

$$\delta_{[\varpi_\rho]}(\mathbf{\Omega}) \equiv \frac{\varpi_\rho(\mathbf{\Omega}) - \overline{\varpi_\rho}}{\langle \overline{\varpi_\rho} \rangle} = \sum_{\ell,m} \tilde{a}_{\ell,m} Y_{\ell,m}(\mathbf{\Omega}). \tag{74}$$

6.2.1 *Angular power spectrum*

Given $\langle a_{00} \rangle(t)$, the angular power spectrum $C_\ell^{\varpi_\rho}(t)$ is computed for each halo. At each time-step and for each harmonic order ℓ, the $C_\ell^{\varpi_\rho}(t)$ distribution was fitted by a lognormal distribution (see Fig. C4). The probability distribution of $C_\ell^{\varpi_\rho}(t)$ is weighted as described in Appendix A.

The evolution of $\langle\langle C_\ell^{\varpi_\rho}(t) \rangle\rangle$ with time is shown in Fig. 27. The shape of $\langle\langle C_\ell^{\varpi_\rho}(\mathrm{t}) \rangle\rangle$ remains mostly the same with time and is fitted by a simple function

$$\langle\langle C_\ell^{\varpi_\rho} \rangle\rangle(t) = q_1^{\varpi_\rho}(t) + \frac{q_2^{\varpi_\rho}(t)}{\left[\ell + q_3^{\varpi_\rho}(t)\right]^2}. \tag{75}$$

The time evolutions of $q_1^{\varpi_\rho}$, $q_2^{\varpi_\rho}$ and $q_3^{\varpi_\rho}$ are shown in Fig. D2 and can be fitted by decreasing the exponential

$$q^{\varpi_\rho}(t) = h + k \exp\left(-\frac{t}{u^2}\right). \tag{76}$$

Only the dipole ($\ell = 1$) harmonic does not fit with the previous functional form and is systematically lower than the contribution of the other harmonics. If particle velocities were measured in an absolute referential, the dipole strength would reflect the motion of the halo in the surrounding matter. Also strong mergers may cover a 180° angle on the sphere and would contribute to the dipole. Since velocities are measured in the rest frame of the halo and strong mergers are excluded, the dipole strength is substantially lowered, as is measured.

The values for h, k and u are given in Table D3. The offset $q_1^{\varpi_\rho}$ of $\langle\langle C_\ell^{\varpi_\rho}(t) \rangle\rangle$ increases with time. From equation (73), one can see that $\langle\langle C_\ell^{\varpi_\rho}(t) \rangle\rangle$ is proportional to the square of the accretion contrast. If the power spectrum experiences a global shift towards higher values with time, it implies that the accretion contrast increases with time. Since the average velocity does not vary strongly with time, this suggests that objects are getting denser with time. This effect is similar to the global increase of the 3D power spectrum $P(k)$ with time due to the density growth. Also, the $q_2^{\varpi_\rho}$ coefficient is found to evolve as $q_1^{\varpi_\rho}$. This illustrates the fact that the amplitude of $\langle\langle C_\ell^{\varpi_\rho}(t) \rangle\rangle$ remains mainly constant. The $q_3^{\varpi_\rho}$ coefficient should be seen as a typical scale and varies slightly from $q_3^{\varpi_\rho} = 6$ at $z = 1$ to $q_3^{\varpi_\rho} = 11$ at $z = 0.1$. $\langle\langle C_\ell^{\varpi_\rho}(t) \rangle\rangle$ becomes marginally 'flatter' as time passes, implying that small scales contribute more to the spatial distribution of $\varpi_\rho(\mathbf{\Omega}, t)$, consistently with the evolution of $\langle\langle C_\ell(t)^{\psi^e} \rangle\rangle$. The flat power spectrum measured for ϖ_ρ on small scales suggests that isolated particles contribute significantly and increasingly with time. In other words, the accretion becomes low enough to be poorly resolved in terms of particles.

6.2.2 *Resolution in mass and particle number*

In order to assess these environments/resolution effects, $\langle\langle C_\ell^{\varpi_\rho}(t) \rangle\rangle$ was computed for three different classes of mass (see Fig. 28) at a lookback time of 800 Myr. For the heaviest haloes, the power spectrum is peaked towards low-ℓ values. The contribution of large scales is quite important. For smaller masses, the power spectrum gets flatter and all scales almost contribute equally for the lightest class of mass. Recall that the harmonic decomposition of a Dirac function leads to C_ℓ = constant, thus a flat power spectrum indicates that isolated particles contribute significantly to the distribution of matter on the sphere. The relative behaviour of the three $\langle\langle C_\ell^{\varpi_\rho}(t) \rangle\rangle$ confirms that larger haloes still experience important mergers (i.e. on large scales) while small ones are in quiet environments at our simulation resolution. The effect of the mass resolution on the

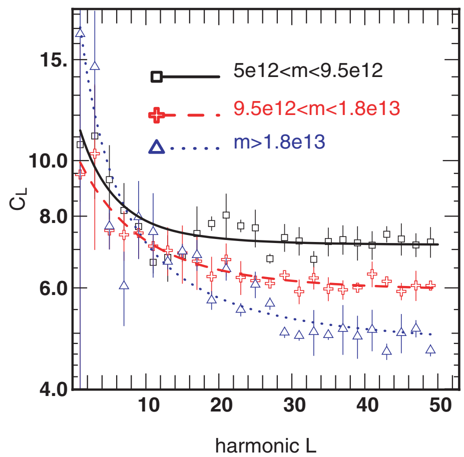

Figure 28. The average angular power spectrum, $\langle\!\langle C_\ell^{\varpi_\rho} \rangle\!\rangle\ (t)$, at $t = 0.8$ Gyr (symbols) for three different classes of masses. $\langle\!\langle C_\ell^{\varpi_\rho} \rangle\!\rangle\ (t)$ is taken as the mode of the lognormal function used to fit the $C_\ell^{\varpi_\rho}$ distribution. Bars stand for 3σ errors. Masses are expressed in solar masses. For a given ℓ, the corresponding angular scale is π/ℓ. The three measurements are fitted by equation (75) (solid line). The power spectrum gets flatter for small haloes. Accretion by small haloes is dominated by small objects or even isolated particles.

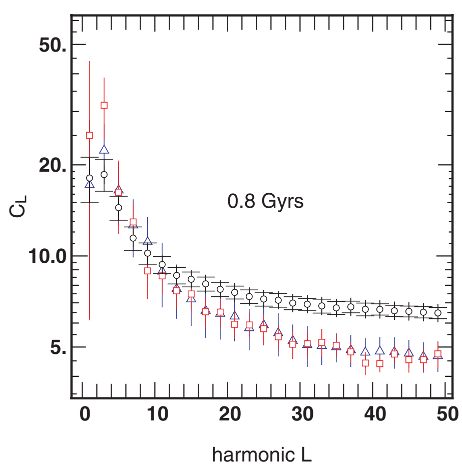

Figure 29. The average angular power spectrum, $\langle\!\langle C_\ell^{\varpi_\rho} \rangle\!\rangle\ (t)$, at $t = 0.8$ Gyr for three different mass resolutions in the simulations. $\langle\!\langle C_\ell^{\varpi_\rho} \rangle\!\rangle\ (t)$ is taken as the mode of the lognormal function used to fit the $C_\ell^{\varpi_\rho}$ distribution. For a given ℓ, the corresponding angular scale is π/ℓ. Circles stand for the measurements performed on the main set of simulations (50 Mpc h^{-1}, 128^3 particles), while error bars stand for 3σ errors. Square and triangles stand for measurements performed on simulation with higher mass resolution, respectively, 50 Mpc h^{-1} for 256^3 particles (1532 haloes analysed) and 20 Mpc h^{-1} for 256^3 particles (545 haloes analysed). In these two cases, error bars stand for 1σ errors.

angular structure of accretion was also investigated with two smaller sets of simulations: the first one involves 10 simulations with 256^3 particles in 50 Mpc h^{-1} boxes and the second in five simulations with the 256^3 particles in 20 Mpc h^{-1} boxes. The related $\langle\!\langle C_\ell^{\varpi_\rho} \rangle\!\rangle$ measured at a lookback time of 800 Myr are shown in Fig. 29. Here, 1532 and 545 haloes satisfying the conditions described in Section 4.2 were detected in these two additional sets of simulations. For clarity, 1σ error bars are shown for the two high-resolution measurements, while the 'larger statistics' power spectrum is still represented with 3σ bars. For large scales ($\ell < 10$), the three power spectra are consistent, thus suggesting that convergence was achieved there. On smaller scales, the two higher resolution spectra differ significantly from the one measured using the other set of simulations (50 Mpc/128^3 particles): high-ℓ holds significantly less power. This confirms that the lack of resolution tends to overestimate the importance of small scales and implies that the study of ϖ_ρ requires simulations at higher resolution in order to understand, e.g., the detailed statistics of small infalling objects. Interestingly, the two higher resolution simulations have identical $\langle\!\langle C_\ell^{\varpi_\rho} \rangle\!\rangle$, given the admittedly large error bars. This suggests that statistical convergence at scales $\ell <$ 50 does not require extremely resolved simulations and simulation boxes with a mass resolution only 8–10 times greater than that used in this paper should suffice.

Finally, it clearly appears from Figs 27 and D2 that the angulo-temporal correlation function related to $\langle\!\langle C_\ell^{\varpi_\rho} \rangle\!\rangle(t)$ is dominated by the overall shift of the angular power spectrum towards higher values and consequently no coherence time should be detectable. It is shown in Appendix E that how the evolution of $\langle\!\langle C_\ell^{\varpi_\rho} \rangle\!\rangle(t)$ is related to mass biases and possible resolution effects. The previous measurements on the potential were not sensitive to these effects because of the smoother nature of the field.

In Appendix E, the measured secular evolution is avoided by using an alternative definition of $\langle\!\langle C_\ell^{\varpi_\rho} \rangle\!\rangle(t)$. It is found that the angular power spectrum of ϖ_ρ can be fitted by a simple power law (see Fig. E1) at every time:

$$\left\langle\!\left\langle C_\ell^{'\varpi_\rho} \right\rangle\!\right\rangle(t) \sim \ell^{-1.15}. \tag{77}$$

The corresponding angulo-temporal correlation function is given in Fig. E3. As expected, there is a shorter coherence time for the ϖ_ρ field than that for the potential, because of the 'sharper' nature of the former. Overall, these results strongly suggest that the class of mass and resolution biases should be systematically investigated beyond what was shown here.

7 A SCENARIO FOR THE ACCRETION OF A TYPICAL HALO AT $z \leqslant 1$

Let us draw a summary of the previous results, in order to get a synthetic picture of the flux properties at the virial radius. A typical halo in our sample has a mass of $10^{13}\,\mathrm{M}_\odot$ and a radius $R_{200} \sim$ 500 kpc at $z = 0$. It is embedded in a quasi-stationary gravitational potential, ψ^{e}. Such a potential is highly quadrupolar and is likely to be induced by the large-scale distribution of matter around the halo. The halo accretes material between $z = 1$ and 0 at a rate which declines with time. At high redshift, only accretion is detected at R_{200}. It is mainly radial and occurs at a velocity close to 75 per cent times the circular velocity. As time advances, accretion of new material decreases, while outflows become significant. Outflows occur at lower velocities and on more circular orbits. A fraction of the outflowing component is due to a backsplash population made of material which already passed through the virial sphere. Another fraction of outflows corresponds to 'virialized' material of the halo which goes further than R_{200} and is being 'cancelled' by its infalling counterpart. The clustering on the sphere of the gravitational potential drifts towards smaller scales, while the clustering of matter follows marginally the same trend at our level of resolution. It reflects the increasing contribution with time of weak/diffuse accretion, poorly sampled at our resolution. In parallel, the coherence time of potential fluctuations is found to be decreasing with time by the halocentric observer. This decrease may be related with the accretion of satellites, where objects were numerous enough to 'overlap' in the past, which implies that accretion occurs mainly in the same direction on the virial sphere.

This scenario seems consistent with most of the past studies made on the subject using the full 3D information contained in simulations. The decline of accretion rate has been already measured by e.g. van den Bosch (2002a) even though our measurements are in a slight quantitative disagreement. The 'rebound' of matter through the virial sphere has already been measured by e.g. Mamon et al. (2004) or Gill et al. (2004). Furthermore, the velocity bimodality is recovered together with the circularization of orbits measured by Gill et al. (2004) in high-resolution simulations. Finally, the variation of the coherence time of the potential is found to be related to the anisotropy of accretion, already demonstrated by e.g. Aubert et al. (2004), Knebe et al. (2004) or Zentner et al. (2005).

8 SUMMARY AND DISCUSSION

This paper, the second in a series of three, presents measurements of the detailed statistical properties of dark matter flows on small scales ($\leqslant$ 500 kpc) in the near environment of haloes using a large set of ΛCDM cosmological simulations. The purpose of this investigation was two-fold: (i) characterize statistically (via one- and two-point statistics) the detailed (angular and kinematic) incoming fluxes of dark matter entering the virial sphere of a biased (described in Section 4.2) sample of haloes undergoing minor mergers for the broader interest of astronomers concerned with the environment of galaxies; (ii) compute the first two moments of the linear coefficients, $c_{\boldsymbol{n}}$ (respectively $b_{\boldsymbol{n}}$), of the source term (respectively external potential) entering equations (13) and (14) (Paper I).

We concentrated on flows at the haloes' virial radius while describing the infalling matter via flux densities through a spherical shell. In parallel, we measured the statistical properties of the tidal potential reprojected back on to the boundary. The statistical one- and two-point expectations of the inflow were tabulated both kinematically and angularly on the R_{200} virtual sphere. All measurements were carried for 15 000 haloes undergoing minor (as defined) mergers between redshifts $z = 1$ and 0. The two-point correlations are carried both angularly and temporally for the flux densities and the tidal field. We also provided a method to regenerate realization of the field, via equations (37) and (F6).

We briefly demonstrated how a perturbative description of the dynamics of haloes could propagate the statistical properties of environments down to the statistical properties of the halo's response. The description of the environment involved the projection of the potential and the source on a basis of functions. This basis allowed us to decouple the time evolution from the angular and velocity dependence of these two quantities. Hence, the accretion and the tidal potential were completely described by the projection coefficients and their statistical properties, which depend on time only. We also discussed how the flux densities of matter, momentum and energy could be related to the source and its expansion coefficients. We restricted ourselves to the one- and two-statistical descriptions of the tidal field $\psi^{\rm e}$ and the flux density of mass ϖ_ρ and postponed to Paper III (Aubert & Pichon, in preparation), the full description of the higher moments. Since these measurements will be used as an entry to a perturbative description of the inner dynamics of haloes, only objects with quiet accretion history were selected as discussed in Section 4.2. Throughout this biased sample of haloes, we made statistical measurements of the kinematic properties of accretion and derived results on the following quantities.

(i) The evolution of the accretion rate at the virial sphere: the net accretion is found to decrease with time, probing both the increasing contribution of outflows and the decline of strong interactions.

(ii) The evolution of the net velocity distribution of the accretion: infall exhibits a typical velocity of $0.75V_{\rm c}$. A backsplash component is detected at recent times with a significant outflowing component at a lower velocity ($\sim 0.6V_{\rm c}$).

(iii) The evolution of the impact parameters/incidence angle distribution of the infall. The infall is found to be mainly radial while outflows are on more circular orbits.

(iv) The angulo-temporal two-point correlation of the external potential on virial sphere. The potential appears to be mainly dominated by a strong and constant quadrupole. The coherence time of smaller angular scales provides hints of an anisotropic accretion.

(v) The angular power spectrum of accreted matter. The clustering is dominated by small angular scales, possibly at the resolution limit.

(vi) The angulo-temporal correlation of the flux density of mass. The coherence time appears shorter than that for potential fluctuations, as expected.

These results can be interpreted in terms of properties of accreted objects or of smooth accretion and are coherent with previous studies (e.g. Ghigna et al. 1998; van den Bosch 2002a; Aubert et al. 2004; Gill et al. 2004; Knebe et al. 2004; Mamon et al. 2004; Benson 2005). These studies were mainly focused on to the properties of accreted satellites. Properties of accreted subhaloes could also be directly derived from these results, once a clear definition allows us to distinguish structures within the general flow of matter. Substructures are expected to form a distinct 'phase' of the accreted fluid: for instance, the velocity dispersion is expected to be quite different in compact objects than in the smooth accreting component. This phase separation will be assessed in Paper III where a systematic comparison of the current approach with an analysis in terms of pre-identified satellites will be carried, in the spirit of Aubert et al. (2004). The contribution of outflows, the lack of a standard definition for subhaloes, resolution issues and the fact that properties are measured at one radius (which could be statistically propagated towards inner regions) are all issues which must be assessed before a complete and rigorous comparison can be performed. Yet, the current agreement between a fluid description of the environment and these above mentioned published results is clearly encouraging hits for the reliability of the method presented here.

These kinematic signatures provide insights in the processes which occur in the inner regions of haloes. In particular, the kinematic discrepancies between the different components of the mass flux should be understood in terms of dynamical friction, tidal stripping or even satellite–satellite interactions within the halo. The kinematical properties of accreted matter may be transposed to the kinematical properties of satellites observed around galaxies. Newly accreted material exhibits kinematic signatures (radial, high-velocity trajectories) different from the ones measured for matter which already interacted with the halo (tangential, low-velocity orbits). Admittedly, it is not straightforward to apply directly these results to the luminous component (see Paper I, for a discussion of thresholding), and to see how projection effects may affect the distributions. Nevertheless, the corresponding observational measurements on satellites should provide information on the past history of these objects.

As discussed in Paper I, these measurements can be used as an entry to the perturbative theory of the response of the open halo. Phenomena related to accretion can be consistently assessed via this framework: dynamical friction, tidal stripping and phase mixing. With the statistical description of the tidal field presented in this paper only, we may already implement the theory presented in Paper I in the regime of pure tidal excitation. The complete knowledge of the source (which will be completed in Paper III) should considerably extend the realm of application provided by this theory. Specifically, we have shown in Paper I that the internal dynamics of substructures within galactic haloes (distortion, clumps as traced by X-ray emissivity, weak lensing, dark matter annihilation, tidal streams, etc.) and the implication for the disc (spiral structure, warp, etc.) could be predicted within this framework. Conversely, the knowledge of the observed properties of a statistical sample of galactic haloes could be used to (i) constrain observationally the statistical nature of the infall (ii) predict the observed distribution and correlations of upcoming surveys, (iii) time reverse the observed distribution of clumps, and finally (iv) weight the relative importance of the intrinsic (via the unperturbed DF) and external (tidal and/or infall) influence of the environment in determining the fate of galaxies.

The current measurements reduce the degree of freedom that still exists in the setting of numerical experiments in a galactic context. For instance, given that the structure of the external tidal field is found to be simple, it can easily be modelled as an external component in numerical simulations (or even in analytical studies). It would provide a simple but statistically relevant contribution of the large-scale structure to the dynamical states of haloes. The temporal coherence of the first $\ell > 2$ angular harmonics of the tidal field should allow one to draw more accurate representations of external contribution to the field that would include the fluctuations due to smaller structures. The kinematics of accretion is not random as well and the distribution of velocities at R_{200} follows a Gaussian-shaped curve which characteristics evolve with time and exhibit a certain distribution of the impact parameter. These results put prescriptions that could be used to generate encounters between satellites and galactic discs that follow the ones measured in cosmological simulations at large radii. We also presented first constrains on the angulo-temporal correlation function of the accretion. Even though it is not completely clear yet how resolution will eventually affect these results, such functions contain some glimpses of information regarding the angular distribution of encounters with external systems but also regarding the frequency of accretion events. This frequency can also be probed by the temporal coherence of the fluctuations in the tidal field. The apparent contradiction that exists between the observed number of discs and the predicted large number of mergers may be solved by a better knowledge of the frequency of the latter: it may be low enough to solve this contradiction. In this context, simulations of successive mergers between a galaxy and satellites should be consistent with large-scale simulations and we provide first constrains on the rate of minor encounters at the outer boundary of the halo.

As argued in Paper I, we emphasize that an a priori discrimination between 'objects' and diffuse matter may not constitute the best way to describe accretion: it is not clear that luminous matter is always attached to dark matter overdensities, there is no unambiguous definition of substructures and their state change with time under the influence of tidal shocks or dynamical friction. The generation of objects that follow the current results is admittedly the easiest way to proceed but should be followed by a more general description of matter in terms of 'fluid approach', where 'objects' only constitute a specific phase of such a fluid. The statistical measurements on both ψ^{e} and ϖ_ρ allow the regeneration of synthetic environments. Knowing the average evolution and the angular power spectra of these quantities, the generation of spherical maps in the Gaussian regime is straightforward. We describe such a regeneration procedure in Appendix F. Such maps would efficiently provide realistic environments of haloes, consistent (up to two-point statistics) with those measured in cosmological simulations and could be 'embedded' into simulation of galaxies. Again, virialized structures would be naturally included (since they have their own statistical signature on the virial sphere) without relying on any ad hoc prescription on their nature.

Extensions to non-Gaussian fields are also possible (following e.g. Contaldi & Magueijo 2001) but would rely on higher order correlations. It was assumed throughout these investigations that fields could be approximated as Gaussian fields, fully described by their two-point statistics. Yet a simple visual inspection of ϖ_ρ maps reveals that they are not strictly Gaussian, a finding confirmed by preliminary analysis of their bispectrum. Furthermore, Paper I demonstrated that a dynamical description which takes into account non-linear effects, such as dynamical friction, requires higher order correlations. Therefore, extensions to non-Gaussian fields are in order in the long run.

It should again be emphasized that some aspects of the present work are exploratory only, in that the resolution achieved ($M_{\mathrm{halo}} > 5 \times 10^{12}\,\mathrm{M}_\odot$) is somewhat high for $L_\star$ galaxies. In fact, it will be interesting to confirm that the properties of infall do not asymptote for lower mass ($M_{\mathrm{halo}} < 5 \times 10^{12}\,\mathrm{M}_\odot$) together with the intrinsic properties of galaxies. In addition, a systematic study of biases induced by our estimators of angular correlations should be conducted. For a fixed halo mass, our lack of resolution implies that we overestimate the clumsiness of the infall.

As demonstrated in Section 6.2.2, the limited resolution (both spatially and in mass) of our simulations appeared to be an issue for some of the results presented here (e.g. the angular power spectrum of ϖ_ρ). The systematic use of higher resolution simulations (in the spirit of Section 6) will be required to fully assess these limitations. In particular, a fraction of the accretion detected as a weak/diffuse component may be associated with unresolved objects; the influence of small-mass satellites should therefore be explored. With the prospect of deducing the properties of galaxy from haloes environments, lower mass haloes are more likely to host only one galaxy, making them more suitable for such a study. Cosmological simulation of small volumes also tends to prevent the formation of rare events which may be relevant for the representativity of the study: for example, some discs seem to indicate that they were formed in 'very quiet' environments. The right balance between resolution and volume should be found. Aside from these biases induced by simulations, we also introduced selection criteria on both the mass or the accretion history of haloes and the influence of these arbitrary choices on our statistical distribution should be assessed precisely.

Eventually using hydrodynamical codes which include baryonic effects in simulations and introducing the physics of gas in our model, we would construct a complete semi-analytic tool to study the detailed inner dynamics of galaxies.

ACKNOWLEDGMENTS

We are grateful to S. Colombi and J. Devriendt for useful comments and helpful suggestions. We would like to thank D. Munro for freely distributing his YORICK programming language (available at ftp://ftp-icf.llnl.gov:/pub/Yorick), together with its MPI interface, which we used to implement our algorithm in parallel. DA thanks the Institute of Astronomy for its hospitality and funding from a Marie Curie studentship. We acknowledge support from the

Observatoire de Strasbourg computer facility and the *HORIZON* project (http://www.projet-horizon.fr). Finally, we would like to thank the anonymous referee for useful remarks on the manuscript.

REFERENCES

Abadi M. G., Navarro J. F., Steinmetz M., Eke V. R., 2003, ApJ, 597, 21
Appel W., 2002, Mathematiques Pour la Physique et les Physiciens. H&K Editions, Paris
Aubert D., Pichon C., Colombi S., 2004, MNRAS, 352, 376
Bardeen J. M., Bond J. R., Kaiser N., Szalay A. S., 1986, ApJ, 304, 15
Benson A. J., 2005, MNRAS, 358, 551
Benson A. J., Frenk C. S., Baugh C. M., Cole S., Lacey C. G., 2001, MNRAS, 327, 1041
Bernardeau F., Colombi S., Gaztañaga E., Scoccimarro R., 2002, Phys. Rep., 367, 1
Bertschinger E., 2001, ApJS, 137, 1
Binney J., Jiang I., Dutta S., 1998, MNRAS, 297, 1237
Blaizot J. et al., 2006, MNRAS, 369, 1009
Bond J. R., Cole S., Efstathiou G., Kaiser N., 1991, ApJ, 379, 440
Cole S., Aragon-Salamanca A., Frenk C. S., Navarro J. F., Zepf S. E., 1994, MNRAS, 271, 781
Colpi M., Mayer L., Governato F., 1999, ApJ, 525, 720
Contaldi C. R., Magueijo J., 2001, Phys. Rev. D, 63, 103512
Eisenstein D. J., Hut P., 1998, ApJ, 498, 137
Flores R. A., Primack J. R., 1994, ApJ, 427, L1
Ghigna S., Moore B., Governato F., Lake G., Quinn T., Stadel J., 1998, MNRAS, 300, 146
Gill S. P. D., Knebe A., Gibson B. K., Dopita M. A., 2004, MNRAS, 351, 410
Hashimoto Y., Funato Y., Makino J., 2003, ApJ, 582, 196
Hunter C., Toomre A., 1969, ApJ, 155, 747
Ibata R. A., Gilmore G., Irwin M. J., 1995, MNRAS, 277, 781
Jiang I., Binney J., 1999, MNRAS, 303, L7
Kalnajs A. J., 1977, ApJ, 212, 637
Kauffmann G., White S. D. M., 1993, MNRAS, 261, 921
Kauffmann G., Colberg J. M., Diaferio A., White S. D. M., 1999, MNRAS, 303, 188
Klypin A., Kravtsov A. V., Valenzuela O., Prada F., 1999, ApJ, 522, 82
Knebe A., Gill S. P. D., Gibson B. K., Lewis G. F., Ibata R. A., Dopita M. A., 2004, ApJ, 603, 7
Lacey C., Cole S., 1993, MNRAS, 262, 627
Lynden-Bell D., Kalnajs A. J., 1972, MNRAS, 157, 1
Mamon G. A., Sanchis T., Salvador-Solé E., Solanes J. M., 2004, A&A, 414, 445
McConnachie A. W., Irwin M. J., Ibata R. A., Ferguson A. M. N., Lewis G. F., Tanvir N., 2003, MNRAS, 343, 1335
Moore B., 1994, Nat, 370, 629
Moore B., Ghigna S., Governato F., Lake G., Quinn T., Stadel J., Tozzi P., 1999, ApJ, 524, L19
Murali C., 1999, ApJ, 519, 580
Murali C., Tremaine S., 1998, MNRAS, 296, 749
Navarro J. F., Steinmetz M., 1997, ApJ, 478, 13
Ostriker E. C., Binney J. J., 1989, MNRAS, 237, 785
Peacock J. A., 1999, Cosmological Physics. Cambridge Univ. Press, Cambridge
Peebles P. J. E., 1980, The Large-Scale Structure of the Universe. Princeton Univ. Press, Princeton, NJ, p. 435
Pichon C., Aubert D., 2006, MNRAS, 368, 1657 (Paper I)
Quinn P. J., Hernquist L., Fullagar D. P., 1993, ApJ, 403, 74
Reshetnikov V., Combes F., 1998, A&A, 337, 9
Roukema B. F., Quinn P. J., Peterson B. A., Rocca-Volmerange B., 1997, MNRAS, 292, 835
Somerville R. S., Kolatt T. S., 1999, MNRAS, 305, 1
Sparke L. S., Casertano S., 1988, MNRAS, 234, 873
Springel V., Yoshida N., White S. D. M., 2001, New. Astron., 6, 79
Toomre A., Toomre J., 1972, ApJ, 178, 623
Tormen G., 1997, MNRAS, 290, 411
Tremaine S., Weinberg M. D., 1984, MNRAS, 209, 729
Tsuchiya T., 2002, New. Astron., 7, 293
van den Bosch F. C., 2002a, MNRAS, 331, 98
van den Bosch F. C., 2002b, MNRAS, 332, 456
van Haarlem M., van de Weygaert R., 1993, ApJ, 418, 544
Velazquez H., White S. D. M., 1999, MNRAS, 304, 254
Walker I. R., Mihos J. C., Hernquist L., 1996, ApJ, 460, 121
Wechsler R. H., Bullock J. S., Primack J. R., Kravtsov A. V., Dekel A., 2002, ApJ, 568, 52
Weinberg M. D., 1998, MNRAS, 299, 499
Weinberg M. D., 2001, MNRAS, 328, 321
Zentner A. R., Kravtsov A. V., Gnedin O. Y., Klypin A. A., 2005, ApJ, 629, 219

APPENDIX A: HARMONIC CONVERGENCE

As explained in Section 3.1, the angular dependence of the source function is expanded over a basis of spherical harmonics $Y_{\ell m}(\boldsymbol{\Omega})$. In order to set the maximal order of this expansion, $\ell_{\max}$, we compared the two-point correlation function of the spherical field $\rho v_{\mathrm{r}}(\boldsymbol{\Omega})$ to the one inferred from harmonic coefficients, $a_{\ell m}$, and power spectrum C_ℓ (see equations 41 and 42). Within a set of randomly distributed particles, let $d_{\mathrm{poisson}}(\theta)$ be the probability of finding two particles with an angular separation θ. If $d(\theta)$ is the same probability for a given distribution of particles then its two-point correlation function $\xi(\theta)$ is defined as

$$\xi(\theta) \equiv \frac{d(\theta)}{d_{\mathrm{poisson}}(\theta)} - 1. \tag{A1}$$

The correlation function $\xi(\theta)$ and the $a_{\ell m}$ coefficients are related by (e.g. Peacock 1999)

$$\xi(\theta) = \sum_{\ell=0}^{\ell_{\max}} C_\ell (2\ell + 1) P_\ell(\cos\theta), \tag{A2}$$

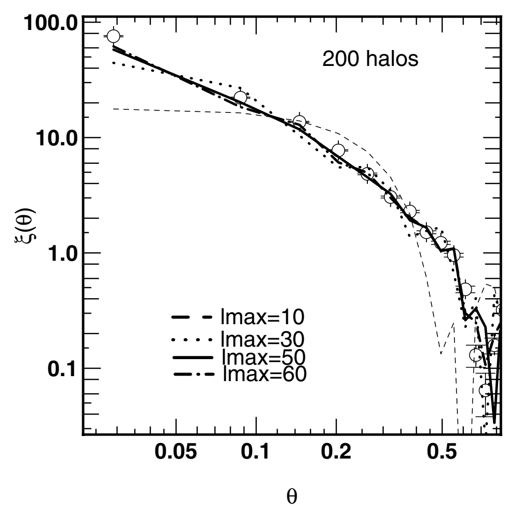

Figure A1. The average angular two-point correlation function, $\langle\langle\xi(\theta)\rangle\rangle$, of the advected mass spherical field $\rho v_{\mathrm{r}}(\boldsymbol{\Omega})$. The correlation function is shown as a function of the angular distance on the sphere θ given in radians. Using the positions of accreted particles around 200 haloes at $z = 1$, the average correlation function can be computed (*dots*). Lines represent the correlation function deduced from the harmonic coefficients of the $\rho v_{\mathrm{r}}(\boldsymbol{\Omega})$ fields around the same 200 haloes, with $\ell_{\max} = 10, 30, 50, 60$. The convergence is ensured for $\ell_{\max} \geqslant 50$.

where θ is an angular distance of the sphere and $P_\ell(x)$ is a Legendre function. The average angular correlation function $\langle\langle\xi(\theta)\rangle\rangle_{\rm pair}$ is defined as

$$\langle\langle\xi(\theta)\rangle\rangle_{\rm pair} \equiv \frac{1}{\sum_p n_p^2} \sum_p n_p^2 \xi_p(\theta), \tag{A3}$$

where $\xi_p(\theta)$ is the two-point correlation function of the pth halo computed using n_p particles passing through the virial sphere. From a set of 200 haloes extracted from a simulation, we computed $\langle\langle\xi(\theta)\rangle\rangle$ using different values for $\ell_{\max}$ (see Fig. A1). From the same set of haloes, we also computed the average two-point correlation function directly from the particles' positions using equation (A1).

From Fig. A1, it clearly appears that $\langle\langle\xi(\theta)\rangle\rangle_{\rm pair}$ has not converged for $\ell_{\max} \leqslant 30$. For $\ell_{\max} \geqslant 50$, the actual two-point correlation function is well reproduced. Since no real difference can be distinguished between $\ell_{\max} = 50$ and 60, we chose to limit the harmonic expansion of the source term to $\ell \leqslant 50$. Note that the truncation in $\ell_{\max}$ defines an effective resolution beyond which the distribution is effectively coarse grained.

APPENDIX B: ANGULO-TEMPORAL CORRELATION

Let us consider a spherical field $X(\boldsymbol{\Omega}, t)$ which can be expanded over the spherical harmonic basis

$$X(\boldsymbol{\Omega}, t) = \sum_{\ell m} x_{\ell m}(t) Y_{\ell m}(\boldsymbol{\Omega}). \tag{B1}$$

The correlation w^X between two successive realizations of X is defined as

$$w^X(\boldsymbol{\Omega}, \boldsymbol{\Omega}', t, t') \equiv \langle X(\boldsymbol{\Omega}, t) X(\boldsymbol{\Omega}', t')\rangle, \tag{B2}$$

where $\langle\cdot\rangle$ stands for the statistical average. If $X(\boldsymbol{\Omega}, t)$ is *isotropic*, the correlation should not depend on $\boldsymbol{\Omega}$ or $\boldsymbol{\Omega}'$ but only on the distance θ between the two points. It implies that w^X can be expanded on the basis of Legendre polynomials, $P_{\rm L}(y)$,

$$w^X(\boldsymbol{\Omega}, \boldsymbol{\Omega}', t, t') = w^X(\theta, t, t') = \sum_{\rm L} (2L+1) T_{\rm L} P_{\rm L}[\cos(\theta)]. \tag{B3}$$

How are $T_{\rm L}$ and $x_{\ell m}$ related? Rewriting equation (B2) as

$$w^X(\theta, t, t') = \sum_{\ell m} \sum_{\ell' m'} \langle x_{\ell m}(t) x^*_{\ell' m'}(t')\rangle Y_{\ell m}(\boldsymbol{\Omega}) Y^*_{\ell' m'}(\boldsymbol{\Omega}'), \tag{B4}$$

one can write

$$\int {\rm d}\boldsymbol{\Omega}{\rm d}\boldsymbol{\Omega}' Y^*_{\ell_1 m_1}(\boldsymbol{\Omega}) Y_{\ell_2 m_2}(\boldsymbol{\Omega}') w^X = \left\langle x_{\ell_1 m_1}(t) x^*_{\ell_2 m_2}(t')\right\rangle. \tag{B5}$$

Meanwhile, assuming isotropy, one can also write

$$\begin{aligned}
&\int {\rm d}\boldsymbol{\Omega}{\rm d}\boldsymbol{\Omega}' Y^*_{\ell_1 m_1}(\boldsymbol{\Omega}) Y_{\ell_2 m_2}(\boldsymbol{\Omega}') w^X \\
&\quad = \sum_{\rm L} (2L+1) T_{\rm L} \int {\rm d}\boldsymbol{\Omega}{\rm d}\boldsymbol{\Omega}' Y^*_{\ell_1 m_1}(\boldsymbol{\Omega}) Y_{\ell_2 m_2}(\boldsymbol{\Omega}') P_{\rm L}[\cos(\theta)] \\
&\quad = \sum_{\rm LM} (4\pi) T_{\rm L} \int {\rm d}\boldsymbol{\Omega}{\rm d}\boldsymbol{\Omega}' Y^*_{\ell_1 m_1}(\boldsymbol{\Omega}) Y_{\ell_2 m_2}(\boldsymbol{\Omega}') Y_{\rm LM}(\boldsymbol{\Omega}) Y^*_{\rm LM}(\boldsymbol{\Omega}') \\
&\quad = \sum_{\rm LM} (4\pi) T_{\rm L} \delta_{{\rm L}\ell_1} \delta_{{\rm L}\ell_2} \delta_{M m_1} \delta_{M m_2},
\end{aligned} \tag{B6}$$

where $P_{\rm L}$ is expressed in terms of spherical harmonics using the spherical harmonics addition theorem. In the end, we get

$$T_\ell = \frac{1}{4\pi} \left\langle x_{\ell m}(t) x^*_{\ell m}(t')\right\rangle. \tag{B7}$$

For a given realization of $X(\boldsymbol{\Omega}, t)$, T_ℓ can be estimated by

$$T_\ell = \frac{1}{4\pi} \frac{1}{2\ell+1} \sum_m x_{\ell m}(t) x^*_{\ell m}(t'). \tag{B8}$$

APPENDIX C: DISTRIBUTIONS

In this appendix, we present the various distributions fitted either by normal or by lognormal PDF. For each quantity, the mode (or most probable value) of the distribution has been obtained from these fits. The Gaussian distribution is defined by

$$\mathrm{N}(x) = \frac{A}{\sigma\sqrt{2\pi}} \exp\left[-\frac{(x-\mu)^2}{2\sigma^2}\right], \tag{C1}$$

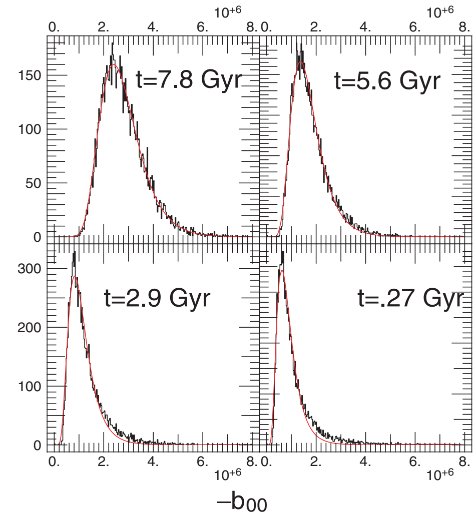

Figure C1. The probability distribution of b_{00} at four different times. This coefficient is proportional to the external potential averaged on the sphere. The lognormal fit is also shown.

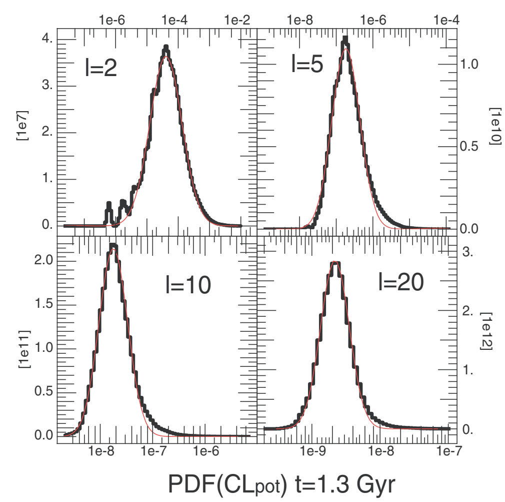

Figure C2. The probability distribution of $C_\ell^{\psi^{\rm e}}$ for $\ell = 2, 5, 10, 20$ at the lookback time $t = 1.9$ Gyr. Note that x-axis is sampled logarithmically; the corresponding lognormal fit of the mode is also shown.

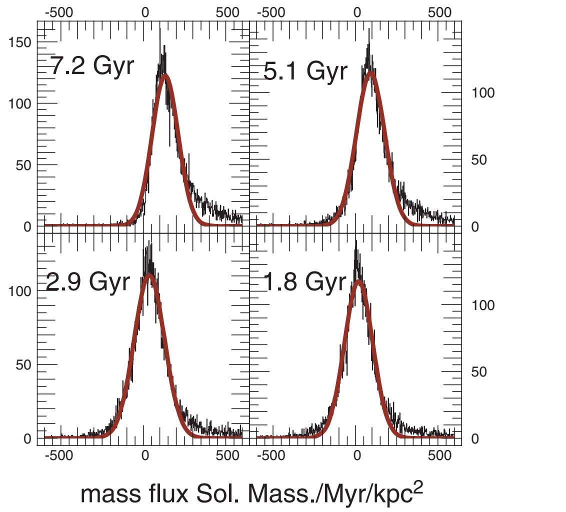

Figure C3. The probability distribution of the mean flux $\Phi^{\rm M}$ (t) for four different times. The normal fit is also shown.

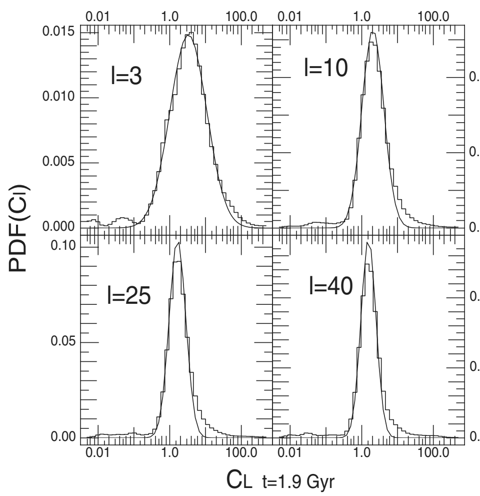

Figure C4. The probability distribution of the C_ℓ for $\ell = 3$, 10, 25, 40 at the lookback time $t = 1.9$ Gyr. Note that x-axis is sampled logarithmically; the corresponding lognormal fit of the mode is also shown.

while the mode is equivalent to the mean μ. The lognormal distribution is given by

$$\mathrm{LN}(x) = \frac{A}{\sigma\sqrt{2\pi}} \exp\left\{-\frac{[\log(x/\mu)]^2}{2\sigma^2}\right\}, \tag{C2}$$

while the mode is given by $\mu \exp(-\sigma^2)$. The different fits mentioned in the main text are described in the following figures.

(i) Fig. C1 shows the distributions of the harmonic coefficient $b_{00}(t)$ which is proportional to the potential averaged on the sphere. It is expressed in units of GM/R, where M is expressed in 10^{10} M$_\odot$, R in kpc h^{-1} and $G = 43\,007$ in internal units.

(ii) Fig. C2 shows the distributions of the external potential's power spectrum for four different harmonics $\ell = 2$, 5, 10, 20 at $t = 1.3$ Gyr. The distribution has been fitted by a lognormal function.

(iii) Fig. C3 shows the distributions of the mean flux $\Phi^{\rm M}(t)$. The mean flux is proportional to the harmonic coefficient a_{00}. The distribution is fitted by a normal distribution. The normal model agrees well with the measured distribution at recent times but fails to reproduce the outliers' tail at high redshift. Consequently, the mode position is underestimated at these times.

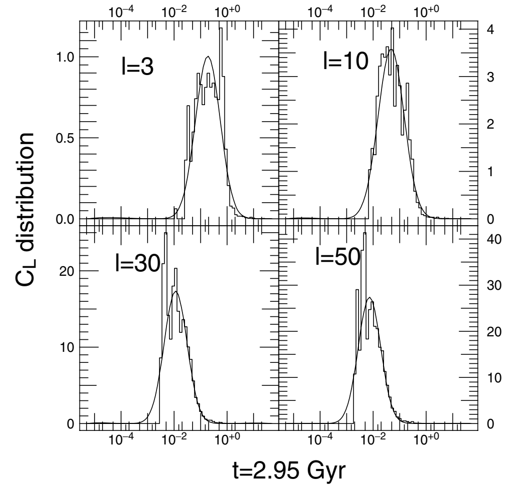

Figure C5. The probability distribution of $C_\ell^{\varpi_\rho'}$ for $\ell = 3$, 10, 25, 40 at the lookback time $t = 1.9$ Gyr. Note that x-axis is sampled logarithmically; the corresponding lognormal fit of the mode is also shown.

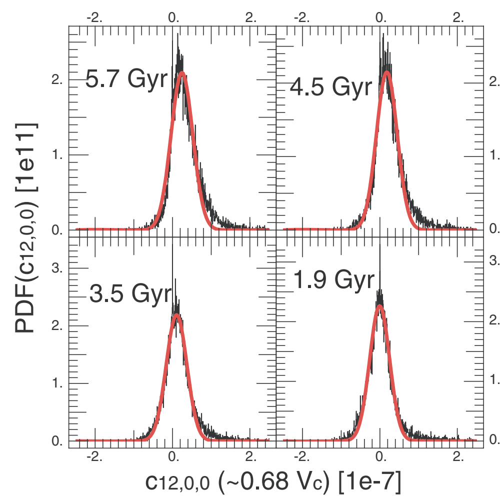

Figure C6. The probability distribution of the $c^{0,0}_{12,0,0}$ for the lookback times $t = 1.9$, 3.5, 4.5 and 5.7 Gyr. Note that x-axis is sampled linearly; the corresponding fit of the mode is also shown.

(iv) Fig. C6 shows the distributions of one of the coefficients involved in the computation of the velocity distribution $\phi(v)$. Four different times are being represented. The coefficient distribution has been fitted by a Gaussian distribution.

(v) Fig. C4 shows the distributions of the power spectrum values $C_\ell^{\varpi_\rho}$ for four different harmonic orders, ℓ. The fits were made at $t = 1.9$ Gyr. This distribution has been fitted by a lognormal distribution.

(vi) Fig. C5 shows the distributions of the power spectrum values $C_\ell^{\varpi_\rho'}$ for four different harmonic orders, ℓ. The fits were made at $t = 2.95$ Gyr. This distribution has been fitted by a lognormal distribution.

APPENDIX D: FITS AND TABLES

In the main text, some statistics are fitted by simple laws and the time evolution of these statistics can be described by the time evolution of

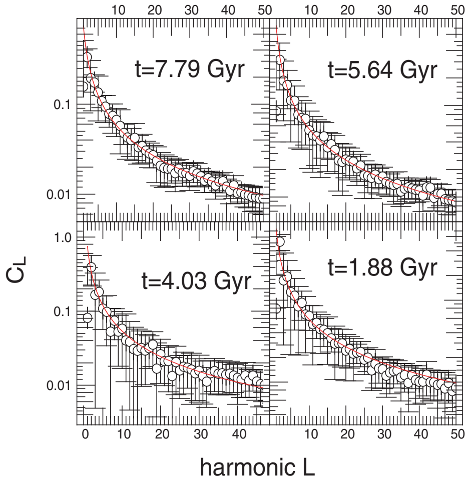

Figure E1. The angular power spectrum of the external potential, $\langle\!\langle C'^{\varpi_\rho}_\ell \rangle\!\rangle$ (t), at four different lookback times (symbols). Harmonics coefficients were normalized using equation (E2), halo by halo. $\langle\!\langle C'^{\varpi_\rho}_\ell \rangle\!\rangle$ (t) is taken as the mode of the lognormal function used to fit the $C'^{\varpi_\rho}_\ell$ distribution. Bars stand for 3σ errors. For a given ℓ, the corresponding angular scale is π/ℓ. The power spectra maybe fitted by a generic model given by equation (E3) (solid line). Unlike $\langle\!\langle C'^{\varpi_\rho}_\ell \rangle\!\rangle$ (t), $\langle\!\langle C'^{\varpi_\rho}_\ell \rangle\!\rangle$ (t) remains the same with time because of a different normalization.

Still, the angular power spectrum $\langle\!\langle C'^{\varpi_\rho}_\ell \rangle\!\rangle$ (t) of $\delta'_{[\varpi_\rho]}(\mathbf{\Omega})$ is much more regular than the one obtained from the previous definition. Its overall amplitude remains constant over the last 8 Gyr, while its shape seems to be less dominated by small-scale contributions. This alternative power spectrum is well fitted by a single power law

$$\langle\langle C'^{\varpi_\rho}_\ell \rangle\rangle(t) = 0.75\ell^{-1.15}, \tag{E3}$$

for the whole time range covered by the current measurements. This constant shape suggests that harmonic coefficients scale like a_{00}, i.e. the mass flux. Such a scaling is not obvious, since a strongly clustered ϖ_ρ field may coexist with a nil net flux (i.e. $a_{00} \sim 0$). It also implies that the evolution measured on the previous definition of the power spectrum, $\langle\!\langle C^{\varpi_\rho}_\ell \rangle\!\rangle(t)$, is more related to the evolution of the average flux (traced by a_{00}) than to the modification of the fluctuations amplitude (traced by the others $a_{\ell m}$). Still, the evolution of $\langle a_{00}\rangle$ spans over one magnitude, while the evolution of $\langle\!\langle C^{\varpi_\rho}_\ell \rangle\!\rangle(t)$ spans over several order of magnitudes: this strongly suggests that two different populations of haloes contribute to the two types of power spectrum. In Fig. E2, the scatter plot of C_{40} and C'_{40} as a function of a_{00} shows that the haloes which experience strong accretion dominate the peak of the C'_{40} distribution, while haloes with low accretion dominate the peak of the C_{40}. Furthermore, C_{40} does not scale anymore like a_{00} as it drops below some level, providing hints of resolution and isolated particles' effects. To conclude, $\delta'_{[\varpi_\rho]}(\mathbf{\Omega})$ appears as better way to rescale the fluctuations' amplitude since it provides a more regular behaviour of the power spectrum, but it is a more complex quantity to manipulate. Meanwhile, $\delta_{[\varpi_\rho]}(\mathbf{\Omega})$ is probably the correct way to proceed but is clearly more sensitive to resolution effects, which should be assessed with bigger simulations in the future.

Since the behaviour of $\delta'_{[\varpi_\rho]}(\mathbf{\Omega})$ is more regular than the previous contrast definition, the angulo-temporal correlation function of the flux density of mass has been computed from this new definition. Since this definition is different from that used for the potential, we restrict ourselves to a qualitative description. The correlations are

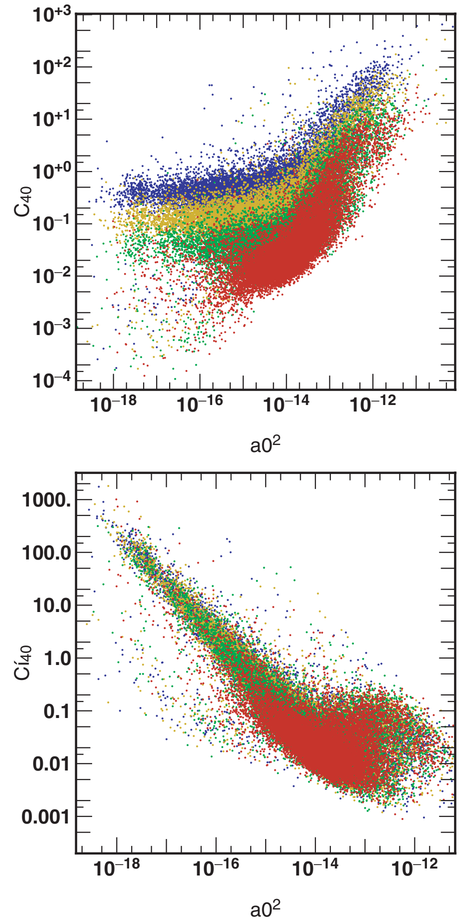

Figure E2. Scatter plots of the power spectra $C^{\varpi_\rho}_{40}$ (top) and $C'^{\varpi_\rho}_{40}$ (bottom) as a function of a^2_{00}. The four colours stand for different lookback times: t = 7.8 (red), 5.6 (green), 4.0 (yellow) and 2.8 Gyr (blue). The monopole a_{00} scales like the integrated flux of matter. The quantities $C^{\varpi_\rho}_{40}$ and $C'^{\varpi_\rho}_{40}$ differ by the normalization applied to the harmonic coefficients $a_{\ell m}$. See the main text for more details.

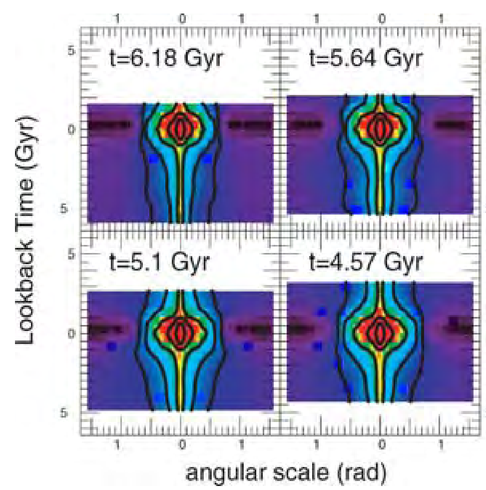

Figure E3. The angulo-temporal correlation function, $w'^{\varpi}(\theta, \Delta t) = \langle \delta_{[\varpi]}(\mathbf{\Omega}, t)\delta_{[\varpi]}(\mathbf{\Omega} + \Delta\mathbf{\Omega}, t + \Delta t)\rangle$. Blue (respectively red) colours stand for low (respectively high) values of the correlation. Isocontours are also shown. Large angular scale isocontours ($\Delta\mathbf{\Omega} \sim \pi/2$) have large temporal extent, due to the quadrupole dominance over the potential seen in the virial sphere.

given in Fig. E3. Clearly, the correlation is more peaked around $\Delta t = 0$ and more generally w^{ϖ_ρ} is sharper than w^{ψ}. Note that no multipole ℓ has been removed during the computation of w^{ϖ_ρ}, implying that the quadrupole effect measured in the potential correlation is simply not detected for this field. This strongly suggests a large-scale 'cosmic' origin for the quadrupolar tidal field rather than an artefact of the spherical intersection of an ellipse. Furthermore, the correlation time is smaller than the one measured for the potential, even compared to the correlation time of the potential without the $\ell = 2$ component. This is coherent with the fact that density blobs should be 'sharper' than potential blobs as they pass through the sphere.

APPENDIX F: REGENERATING GALACTIC TIME LINES

Given the measurements in Sections 5 and 6, let us describe here how to regenerate realizations of the history of the environment of haloes, first for the tidal field only, and then for the full accretion history.

F1 Regenerating tidal fields

Let us first focus on the generation of the potential tidal field generated by fly bys, hence neglecting the influence of the infall through the virial sphere.[5]

First, we consider two time variables: T (the 'slow time') which describes the secular evolution of the field and $t_{\rm f}$ (the 'fast time') which describes the temporal evolution around a given value of T, hence describing high-frequency variations. We assume that correlations exist only on small time-scales, while variations on the 'slow time' scale describe secular drifts. Therefore, the field's regeneration should include both correlations on short time-scales and long-term evolution.

Let us call $\hat{\boldsymbol{\Psi}} = \hat{\psi}_{\boldsymbol{m},\omega}(T)$ the temporal (with respect to the fast time) and angular Fourier transforms of the potential, at fixed slow time, T. The probability distribution of $\hat{\boldsymbol{\Psi}}$, $p(\hat{\boldsymbol{\Psi}})$ is given by

$$p(\hat{\boldsymbol{\Psi}}) = \frac{\exp\left[-\frac{1}{2}(\hat{\boldsymbol{\Psi}} - \langle\hat{\boldsymbol{\Psi}}\rangle)^{\top}\cdot\boldsymbol{C}_{\hat{\Psi}}^{-1}\cdot(\hat{\boldsymbol{\Psi}} - \langle\hat{\boldsymbol{\Psi}}\rangle)\right]}{(2\pi)^{1/2}\det^{1/2}|\boldsymbol{C}_{\hat{\Psi}}|}, \tag{F1}$$

where the variance reads

$$\boldsymbol{C}_{\Psi}(T) = \langle(\hat{\Psi}_{\boldsymbol{m},\omega} - \langle\hat{\Psi}_{\boldsymbol{m},\omega}\rangle).(\hat{\Psi}_{\boldsymbol{m},\omega} - \langle\hat{\Psi}_{\boldsymbol{m},\omega}\rangle)\rangle, \tag{F2}$$

and the mean field obeys

$$\langle\hat{\boldsymbol{\Psi}}\rangle(T) = \left\langle\hat{\Psi}_{\boldsymbol{m},\omega}\right\rangle. \tag{F3}$$

Since the potential is isotropic, $\langle\hat{\boldsymbol{\Psi}}\rangle(T)$ is essentially zero (see also Fig. F1), while $\boldsymbol{C}_{\Psi}$ stands for the angular power spectrum described in Section 6.1. Let us call $\{\hat{\boldsymbol{\Psi}}_{\boldsymbol{m},\omega}(T_i)\}_{i\leqslant N}$, the set of sampled $\hat{\boldsymbol{\Psi}}$ a fixed slow time, T_i. Relying on a linear interpolation between two such realizations, the corresponding external potential reads in real space

$$\psi^{\rm e}(t, \boldsymbol{\Omega}) = \sum_i \sum_{\boldsymbol{m}} \int {\rm d}\omega \exp\left(\imath\boldsymbol{m}\cdot\boldsymbol{\Omega} + \imath\omega t\right)\mathcal{K}_i^{\boldsymbol{m}}(t, \omega), \tag{F4}$$

[5] Note that this assumption is not coherent with the way the measurements are carried, since it implies that the infalling material somehow disappears after crossing R_{200}.

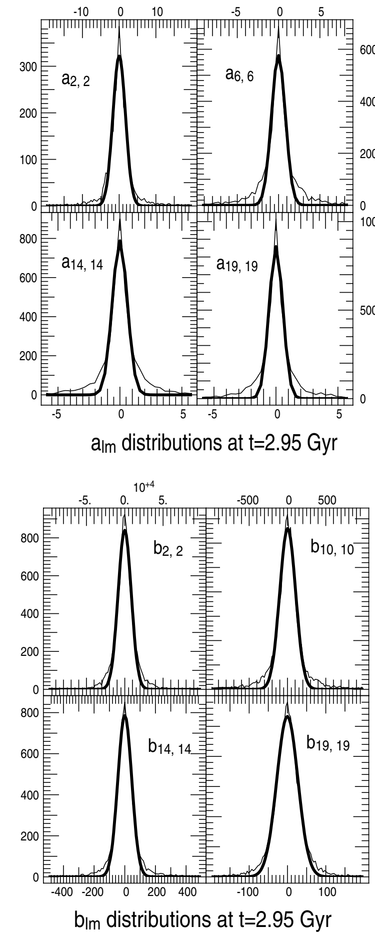

Figure F1. Probing the Gaussianity of the harmonic expansions $a_{\ell m}$, describing the flux density of mass (top) and $b_{\ell m}$, describing the potential $\psi^{\rm e}$ (bottom). Units are arbitrary. Only the real part of the coefficients is shown here, but the imaginary parts have similar distributions. Clearly, the distributions are quasi-Gaussians.

where the kernel, $\mathcal{K}_i^{\boldsymbol{m}}(t, \omega)$, reads

$$\mathcal{K}_i^{\boldsymbol{m}}(t, \omega) = \left[\hat{\Psi}_{\boldsymbol{m},\omega}(T_{i+1})\frac{t - T_i}{T_{i+1} - T_i} + \hat{\Psi}_{\boldsymbol{m},\omega}(T_i)\frac{T_{i+1} - t}{T_{i+1} - T_i}\right] \times \Theta(T_{i+1} - t)\Theta(t - T_i), \tag{F5}$$

recalling that $\Theta(x)$ is the Heaviside function.

To sum up, the computation of $\hat{\Psi}_{\boldsymbol{m},\omega}$ following F1 and F3 ensures that correlations on short periods are reproduced, while the interpolation procedure allows us to take into account the long-period evolution of the field. This procedure can be repeated for an arbitrary number of virtual tidal histories.

F2 Regenerating tidal fields and infall history

Let us assume briefly that the fields are stationary both in time and angle, and that their statistics is Gaussian. As shown in Fig. F1, this assumption is essentially valid for the expansions of the potential and the flux density of mass. Let us call the 11-dimensional vector $\boldsymbol{\Pi}(t) \equiv (\varpi_{\rho}, \varpi_{\rho v}, \varpi_{\rho\sigma\sigma}, \psi^{\rm e})$; and $\hat{\boldsymbol{\Pi}}_{\boldsymbol{m},\omega}$ the temporal and angular Fourier transforms of the fields. The joint probability of the field,

$p(\hat{\mathbf{\Pi}}_{\boldsymbol{m},\omega})$, reads

$$p(\hat{\mathbf{\Pi}}_{\boldsymbol{m},\omega}) = \frac{\exp\left[-\frac{1}{2}(\hat{\mathbf{\Pi}} - \langle\hat{\mathbf{\Pi}}\rangle)^{\top}\cdot \boldsymbol{C}_{\hat{\Pi}}^{-1}\cdot(\hat{\mathbf{\Pi}} - \langle\hat{\mathbf{\Pi}}\rangle)\right]}{(2\pi)^{11/2}\det^{1/2}|\boldsymbol{C}_{\hat{\Pi}}|}, \tag{F6}$$

where

$$\boldsymbol{C}_{\Pi} = \left[\left\langle(\hat{\Pi}^{i}_{\boldsymbol{m},\omega} - \langle\hat{\Pi}^{i}_{\boldsymbol{m},\omega}\rangle)\cdot\left(\hat{\Pi}^{j}_{\boldsymbol{m},\omega} - \left\langle\hat{\Pi}^{j}_{\boldsymbol{m},\omega}\right\rangle\right)\right\rangle\right]_{i,j\leqslant 11} \tag{F7}$$

and

$$\langle\hat{\mathbf{\Pi}}\rangle = \left[\left\langle\hat{\Pi}^{i}_{\boldsymbol{m},\omega}\right\rangle\right]_{i\leqslant 11}. \tag{F8}$$

Since these fields are mostly isotropic, their expansion coefficients are nil on average. Hence, the quantity $\boldsymbol{C}_{\Pi}$ stands for the angular power spectrum of the 11 fields. For, respectively, the potential and the flux density of mass, its *temporal* evolution is described in Sections 6.1 and 6.2. These measured power spectra are sufficient to generate environments restricted to the flux density of mass and the potential. We emphasize that these two fields would not be coherent if no cross-correlations is specified. These cross-correlations and the power spectra for higher moments of the source are postponed to Paper III.

Assuming the full knowledge of these 11 fields and their cross-correlation, it is therefore straightforward to generate for each ($\boldsymbol{m}$, ω) a 11-dimensional vector which satisfies equation (F6), and repeat the draw for all modes (both $\boldsymbol{\omega}$ and $\boldsymbol{m}$). Inverse Fourier transform yields $\Pi(t)$. Once $\Pi(t)$ is known, we can regenerate the whole five-dimensional phase-space source as a function of time via equation (37). This process can also be repeated for an arbitrary number of virtual halo histories. The assumption of stationarity in time can be lifted following the same route as that sketched in Section F1 (see equation F5).

APPENDIX G: FROM EXPANSION COEFFICIENTS TO FLUX DENSITIES

G1 From expansion coefficients to advected momentum

The phase-space distribution of advected momentum is given by

$$\varpi_{\rho\boldsymbol{v}}(\boldsymbol{\Omega}, v, \boldsymbol{\Gamma}, t) \equiv s^{\mathrm{e}}(\boldsymbol{\Omega}, v, \boldsymbol{\Gamma}, t)\boldsymbol{v} \tag{G1}$$

$$= \sum_{\alpha,\boldsymbol{m},\boldsymbol{m}'} c^{\boldsymbol{m}}_{\alpha\boldsymbol{m}'}(t) g_{\alpha}(v) Y_{\boldsymbol{m}}(\boldsymbol{\Omega}) Y_{\boldsymbol{m}'}(\boldsymbol{\Gamma})\boldsymbol{v}, \tag{G2}$$

where the velocity vector may be written as a function of spherical harmonics

$$\begin{aligned}\boldsymbol{v} = &-v\sqrt{\frac{2\pi}{3}}\left[-Y^{*}_{1-1}(\boldsymbol{\Gamma}) + Y^{*}_{11}(\boldsymbol{\Gamma})\right]\boldsymbol{e}_{\theta}\\ &-\mathrm{i}v\sqrt{\frac{2\pi}{3}}\left[Y^{*}_{1-1}(\boldsymbol{\Gamma}) + Y^{*}_{11}(\boldsymbol{\Gamma})\right]\boldsymbol{e}_{\phi}\\ &v\sqrt{\frac{\pi}{3}}Y^{*}_{10}(\boldsymbol{\Gamma})\boldsymbol{e}_{\mathrm{r}}.\end{aligned} \tag{G3}$$

Then, one can write

$$\varpi_{\rho\boldsymbol{v}}(\boldsymbol{\Omega}, t) \equiv \int \mathrm{d}v\mathrm{d}\boldsymbol{\Gamma} v^{2} s^{\mathrm{e}}(\boldsymbol{\Omega}, v, \boldsymbol{\Gamma}, t)\boldsymbol{v} \tag{G4}$$

$$= \sum_{\alpha,\boldsymbol{m},\boldsymbol{m}'} [\varpi_{\rho\boldsymbol{v}}]_{\boldsymbol{m}}(t) Y_{\boldsymbol{m}}(\boldsymbol{\Omega}), \tag{G5}$$

where

$$[\varpi_{\rho\boldsymbol{v}}]_{\boldsymbol{m}}(t) = \sum_{\alpha}\left(3\sigma^{2}\mu_{\alpha} + \mu_{\alpha}^{3}\right)\boldsymbol{T}_{\boldsymbol{m}}(t), \tag{G6}$$

and

$$\begin{aligned}\boldsymbol{T}_{\boldsymbol{m}}(t) = &\sqrt{\frac{2\pi}{3}}\left[c^{\boldsymbol{m}}_{\alpha,1,-1}(t) - c^{\boldsymbol{m}}_{\alpha,1,1}t\right]\boldsymbol{e}_{\theta}\\ &+\mathrm{i}\sqrt{\frac{2\pi}{3}}\left[-c^{\boldsymbol{m}}_{\alpha,1,-1}(t) - c^{\boldsymbol{m}}_{\alpha,1,1}t\right]\boldsymbol{e}_{\phi}\\ &+2\sqrt{\frac{\pi}{3}}c^{\boldsymbol{m}}_{\alpha,1,0}(t)\boldsymbol{e}_{\mathrm{r}}.\end{aligned} \tag{G7}$$

G2 From coefficients to advected velocity dispersion

The distribution of advected velocity dispersion is given by

$$\varpi_{\rho\sigma_i\sigma_j}(\boldsymbol{\Omega}, v, \boldsymbol{\Gamma}, t) = s^{\mathrm{e}}(\boldsymbol{\Omega}, v, \boldsymbol{\Gamma}, t)[\boldsymbol{v} - \boldsymbol{V}(\boldsymbol{\Omega}, t)]_{i}[\boldsymbol{v} - \boldsymbol{V}(\boldsymbol{\Omega}, t)]_{j}, \tag{G8}$$

where the subscripts i and j stand for r, θ, ϕ and

$$\boldsymbol{V}_{i}(\boldsymbol{\Omega}, t) \equiv \frac{\int \mathrm{d}v\,\mathrm{d}\boldsymbol{\Gamma} v^{2} s^{\mathrm{e}}(\boldsymbol{\Omega}, v, \boldsymbol{\Gamma}, t) v_{i}}{\int \mathrm{d}v\,\mathrm{d}\boldsymbol{\Gamma} v^{2} s^{\mathrm{e}}(\boldsymbol{\Omega}, v, \boldsymbol{\Gamma}, t)} = \frac{\varpi_{\rho v_i}(\boldsymbol{\Omega}, t)}{\varpi_{\rho}(\boldsymbol{\Omega}, t)}. \tag{G9}$$

Using equations (G8) and (G9), we find

$$\varpi_{\rho\sigma_i\sigma_j}(\boldsymbol{\Omega}, t) + \frac{\varpi_{\rho v_i}(\boldsymbol{\Omega}, t)\varpi_{\rho v_j}(\boldsymbol{\Omega}, t)}{\varpi_{\rho}(\boldsymbol{\Omega}, t)} = \int \mathrm{d}v\mathrm{d}\boldsymbol{\Gamma} v^{2} s^{\mathrm{e}}(\boldsymbol{\Omega}, v, \boldsymbol{\Gamma}, t) v_i v_j \tag{G10}$$

$$= \sum_{\boldsymbol{m}} [\boldsymbol{q}_{ij}(t)]_{\boldsymbol{m}} Y_{\boldsymbol{m}}(\boldsymbol{\Omega}). \tag{G11}$$

The six independent elements of the symmetric tensor $\boldsymbol{q}(t)$ can be computed from $c^{\boldsymbol{m}}_{\alpha\boldsymbol{m}'}(t)$ coefficients using equation (G3) and recalling that

$$\int \mathrm{d}\boldsymbol{\Omega} Y_{\ell_1,m_1} Y_{\ell_2,m_2} Y_{\ell_3,m_3} = \sqrt{\frac{(2\ell_1+1)(2\ell_2+1)(2\ell_3+1)}{4\pi}} \times \begin{pmatrix}\ell_1 & \ell_2 & \ell_3\\ 0 & 0 & 0\end{pmatrix}\begin{pmatrix}\ell_1 & \ell_2 & \ell_3\\ m_1 & m_2 & m_3\end{pmatrix}, \tag{G12}$$

where $\begin{pmatrix}\ell_1 & \ell_2 & \ell_3\\ m_1 & m_2 & m_3\end{pmatrix} = W^{\ell_1,\ell_2,\ell_3}_{m_1,m_2,m_3}$ is the Wigner 3j symbol. One can find

$$\begin{aligned}
[\boldsymbol{q}_{rr}(t)]_{\boldsymbol{m}} &= \sum_{\alpha\boldsymbol{m}'} \mathcal{H}^{\boldsymbol{m}}_{\alpha\boldsymbol{m}'}(t) 2 W^{11\ell'}_{000} W^{11\ell'}_{00m'}\\
[\boldsymbol{q}_{r\phi}(t)]_{\boldsymbol{m}} &= \sum_{\alpha\boldsymbol{m}'} \mathcal{H}^{\boldsymbol{m}}_{\alpha\boldsymbol{m}'}(t)\mathrm{i}\sqrt{2} W^{11\ell'}_{000}\left(W^{11\ell'}_{1-1m'} + W^{11\ell'}_{11m'}\right)\\
[\boldsymbol{q}_{r\theta}(t)]_{\boldsymbol{m}} &= \sum_{\alpha\boldsymbol{m}'} \mathcal{H}^{\boldsymbol{m}}_{\alpha\boldsymbol{m}'}(t)\sqrt{2} W^{11\ell'}_{000}\left(W^{11\ell'}_{1-1m'} - W^{11\ell'}_{11m'}\right)\\
[\boldsymbol{q}_{\phi\phi}(t)]_{\boldsymbol{m}} &= \sum_{\alpha\boldsymbol{m}'} \mathcal{H}^{\boldsymbol{m}}_{\alpha\boldsymbol{m}'}(t)(-1) W^{11\ell'}_{000}\left(W^{11\ell'}_{11m'} + 2W^{11\ell'}_{1-1m'} + W^{11\ell'}_{-1-1m'}\right)\\
[\boldsymbol{q}_{\phi\theta}(t)]_{\boldsymbol{m}} &= \sum_{\alpha\boldsymbol{m}'} \mathcal{H}^{\boldsymbol{m}}_{\alpha\boldsymbol{m}'}(t)\mathrm{i} W^{11\ell'}_{000}\left(W^{11\ell'}_{-1-1m'} - W^{11\ell'}_{11m'}\right)\\
[\boldsymbol{q}_{\theta\theta}(t)]_{\boldsymbol{m}} &= \sum_{\alpha\boldsymbol{m}'} \mathcal{H}^{\boldsymbol{m}}_{\alpha\boldsymbol{m}'}(t) W^{11\ell'}_{000}\left(W^{11\ell'}_{11m'} - W^{11\ell'}_{-1-1m'} - 2W^{11\ell'}_{1-1m'}\right),
\end{aligned} \tag{G13}$$

where $\mathcal{H}^{\boldsymbol{m}}_{\alpha\boldsymbol{m}'}(t) = \sqrt{4\pi(2\ell'+1)}(6\sigma^{2}\mu_{\alpha}^{2} + \mu_{\alpha}^{4}) c^{\boldsymbol{m}}_{\alpha\boldsymbol{m}'}(t)$.

APPENDIX H: NOTATIONS

Table H1. A summary of the notations used throughout the paper.

Symbol	Meaning
$(\boldsymbol{r}, \boldsymbol{v})$	Position and velocity
t, τ	Lookback time variables
R_{200}	Virial radius measured at $z = 0$
V_{c}	Circular velocity measured at R_{200}
F	The phase-space DF of the halo
ψ	The self-gravitating potential
ψ^{e}	The external potential, induced by external perturbations
s^{e}	The source function in phase space
ϖ_x	The flux density of x
ϖ_ρ	The flux density of mass
$\varpi_{\rho \boldsymbol{v}}$	The flux density of momentum
$\varpi_{\rho\sigma\sigma}$	The flux density of velocity dispersion
$\psi^{[n]}(\boldsymbol{r})$	3D projection basis of the potential
$\phi^{[n]}(\boldsymbol{r})$	6D projection basis of the source term
$\boldsymbol{a}(t)$	Expansion coefficients of the potential/density response
$\boldsymbol{b}(t)$	Expansion coefficients of the external potential perturbation
$\boldsymbol{c}(t)$	Expansion coefficients of the source perturbation
$\boldsymbol{\Omega}$	Angular position on the virial sphere (two angles)
$\boldsymbol{\Gamma}$	Angular orientation of the velocity vector on the virial sphere (two angles)
v	Velocity's amplitude
$\bar{X}$	Angular average of X
$\underline{\mathrm{X}}$	Temporal average of X
$\langle X \rangle$	Statistical expectation (or average value) of X
$\langle\!\langle X \rangle\!\rangle$	Most probable value (or mode) of X
$\delta_{[X]}(\boldsymbol{\Omega})$	Contrast density of X measured on the virial sphere
$\boldsymbol{m} = (\ell, m)$	Harmonic coefficients related to $\underline{0}$
$\boldsymbol{m}' = (\ell', m')$	Harmonic coefficients related to $\boldsymbol{\Gamma}$
$a_{\ell,m}(t)$	Harmonic expansion coefficients of $\delta_{[\varpi_\rho]}$
$b_{\ell,m}(t)$	Harmonic expansion coefficients of $\delta_{[\psi^{\mathrm{e}}]}$
$C_\ell(t)$	Angular power spectrum
$T_\ell(t, t + \Delta t)$	Angular-temporal power spectrum
$w(\theta, t, t + \Delta t)$	Angulo-temporal correlation function measured on the sphere for an angulo-temporal separation θ and Δt
$\Phi^{\mathrm{M}}\ (t)$	Accretion rate measured at the virial radius (averaged over all directions)
$\vartheta(\Gamma_1, t)$	PDF of the velocity's incidence angle
b	Impact parameter
$\varphi(v, t)$	PDF of the velocity's amplitude
$\wp(v, t)$	Joint PDF of the velocity's incidence angle and amplitude

This paper has been typeset from a TEX/LATEX file prepared by the author.

Mon. Not. R. Astron. Soc. **352,** 376–398 (2004) doi:10.1111/j.1365-2966.2004.07883.x

The origin and implications of dark matter anisotropic cosmic infall on $\approx L_\star$ haloes

D. Aubert,[1,3]⋆ C. Pichon[1,2,3] and S. Colombi[2,3]

[1] *Observatoire Astronomique de Strasbourg, 11 Rue de l'Université, 67000 Strasbourg, France*
[2] *Institut d'Astrophysique de Paris, 98 bis Boulevard d'Arago, 75014 Paris, France*
[3] *Numerical Investigations in Cosmology (NIC), CNRS, France*

Accepted 2004 March 26. Received 2004 March 26; in original form 2003 December 22

ABSTRACT

We measure the anisotropy of dark matter flows on small scales (∼500 kpc) in the near environment of haloes using a large set of simulations. We rely on two different approaches to quantify the anisotropy of the cosmic infall: we measure the flows at the virial radius of the haloes while describing the infalling matter via fluxes through a spherical shell; and we measure the spatial and kinematical distributions of satellites and substructures around haloes detected by the subclump finder ADAPTAHOP described for the first time in the appendix. The two methods are found to be in agreement both qualitatively and quantitatively via one- and two-point statistics.

The peripheral and advected momenta are correlated with the spin of the embedded halo at levels of 30 and 50 per cent. The infall takes place preferentially in the plane perpendicular to the direction defined by the spin of the halo. We computed the excess of equatorial accretion both through rings and via a harmonic expansion of the infall.

The level of anisotropy of infalling matter is found to be ∼15 per cent. The substructures have their spin orthogonal to their velocity vector in the rest frame of the halo at a level of about 5 per cent, suggestive of an image of a flow along filamentary structures, which provides an explanation for the measured anisotropy. Using a 'synthetic' stacked halo, it is shown that the positions and orientations of satellites relative to the direction of spin of the halo are not random even in projection. The average ellipticity of stacked haloes is 10 per cent, while the alignment excess in projection reaches 2 per cent. All measured correlations are fitted by a simple three-parameter model.

We conclude that a halo does not see its environment as an isotropic perturbation, we investigate how the anisotropy is propagated inwards using perturbation theory, and we discuss briefly the implications for weak lensing, warps and the thickness of galactic discs.

Key words: galaxies: formation – galaxies: haloes – dark matter.

1 INTRODUCTION

Isotropy is one of the fundamental assumptions in modern cosmology and is widely verified on very large scales, both in large galaxy surveys and in numerical simulations. However, on scales of a few megaparsecs, the matter distribution is structured in clusters and filaments. The issue of anisotropy down to galactic and cluster scales has long been studied, as it is related to the search for large-scale structure in the near environment of galaxies. For example, both observational studies (e.g. West 1994; Plionis & Basilakos 2002; Kitzbichler & Saurer 2003) and numerical investigations (e.g. Faltenbacher et al. 2002) showed that galaxies tend to be aligned with their neighbours and support the vision of anisotropic mergers along filamentary structures. On smaller scales, simulations of rich clusters showed that the shape and velocity ellipsoids of haloes tend to be aligned with the distribution of infalling satellites, which is strongly anisotropic (Tormen 1997). However, the point is still moot and recent publications did not confirm such an anisotropy using resimulated haloes; they proposed 20 per cent as a maximum for the anisotropy level of the distribution of satellites (Vitvitska et al. 2002).

When considering preferential directions within the large-scale cosmic web, the picture that comes naturally to mind is one involving these long filamentary structures linking large clusters to one other. The flow of haloes within these filaments can be responsible

⋆E-mail: aubert@astro.u-strasbg.fr

for the emergence of preferential directions and alignments. Previous publications showed that the distributions of spin vectors are not random. For example, haloes in simulations tend to have their spin pointing orthogonally to the direction of the filaments (Faltenbacher et al. 2002). Furthermore, down to galactic scales, the angular momentum remains mainly aligned within haloes (Bullock et al. 2001). Combined with the results suggesting that the spins of haloes are mostly sensitive to recent infall (van Haarlem & van de Weygaert 1993), these alignment properties fit well with accretion scenarios along special directions: angular momentum can be considered as a good marker to test this picture.

Most of these previous studies focused on the fact that alignments and preferential directions are consequences of the formation process of haloes. However, the effects of such preferential directions on the inner properties of galaxies have been less addressed. It is widely accepted that the properties of galaxies partly result from their interactions with their environments. While the amplitude of the interactions is an important parameter, some issues cannot be studied without taking into account the spatial extension of these interactions. For example, a warp may be generated by the torque imposed by infalling matter on the disc (Ostriker & Binney 1989; López-Corredoira, Betancort-Rijo & Beckman 2002): not only the direction but also the amplitude of the warp are a direct consequence of the spatial configuration of the perturbation. Similarly, it is likely that disc thickening due to infall is not independent of the incoming direction of satellites (e.g. Quinn, Hernquist & Fullagar 1993; Huang & Carlberg 1997; Velazquez & White 1999).

Is it possible to observe the small-scale alignment? In particular, weak lensing deals with effects as small as the level of detected anisotropy (if not smaller) (e.g. Croft & Metzler 2000; Heavens, Refregier & Heymans 2000; Hatton & Ninin 2001); hence it is important to put quantitative constraints on the existence of alignments on small scales. Therefore, the present paper also addresses the issue of detecting preferential projected orientations on the sky of substructures within haloes.

Our main aim is to provide quantitative measurements to study the consequences of the existence of preferential directions on the dynamical properties of haloes and galaxies, and on the observation of galaxy alignments. Hence our point of view is more galactocentric (or cluster-centric) than previous studies. We search for local alignment properties on scales of a few hundred kiloparsecs. Using a large sample of low-resolution numerical simulations, we aim to extract quantitative results from a large number of halo environments. We reach a higher level of statistical significance while reducing the cosmic variance. We applied two complementary approaches to study the anisotropy around haloes: the first one is particulate and uses a new substructure detection tool ADAPTAHOP; the other one is the spherical galactocentric fluid approach. Using two methods, we can assess the self-consistency of our results.

After a brief description of our set of simulations (Section 2), we describe the galactocentric point of view and study the properties of angular momentum and infall anisotropy measured at the virial radius (Section 3). In Section 4 we focus on anisotropy in the distribution of discrete satellites and substructures, and we study the properties of the satellites' proper spins, which provide an explanation for the detected anisotropy. In Section 5 we discuss the level of anisotropy as seen in projection on the plane of the sky. We then investigate how the anisotropic infall is propagated inwards and discuss the possible implications of our results to weak lensing and to the dynamics of the disc through warp generation and disc thickening (Section 6). Conclusions and prospects follow. The Appendix describes the substructures detection tool ADAPTAHOP together with the relevant aspects of one-point centred statistics on the sphere. We also formally derive there the perturbative inward propagation of infalling fluxes into a collisionless self-gravitating sphere.

2 SIMULATIONS

In order to achieve a sufficient sample and ensure convergence of the measurements, we produced a set of $\sim$500 simulations. Each of them consists of a 50 h^{-1} Mpc^3 box containing 128^3 particles. The mass resolution is 5×10^9 M$_\odot$. A ΛCDM cosmogony ($\Omega_\mathrm{m} = 0.3$, $\Omega_\Lambda = 0.7$, $h = 0.7$ and $\sigma_8 = 0.928$) is implemented with different initial conditions. These initial conditions were produced with GRAFIC (Bertschinger 2001), where we chose a BBKS (Bardeen et al. 1986) transfer function to compute the initial power spectrum. The initial conditions were used as inputs to the parallel version of the tree code GADGET (Springel, Yoshida & White 2001b). We set the softening length to 19 h^{-1} kpc. The halo detection was performed using the halo finder HOP (Eisenstein & Hut 1998). We employed the density thresholds suggested by the authors ($\Delta_\mathrm{outer} = 80$, $\delta_\mathrm{saddle} = 2.5\delta_\mathrm{outer}$, $\delta_\mathrm{peak} = 3\delta_\mathrm{outer}$) As a check, we computed the halo mass function at $z = 0$ defined as (Jenkins et al. 2001):

$$f(\sigma(M)) = \frac{M}{\rho_0}\frac{\mathrm{d}n}{\mathrm{d}\ln\sigma^{-1}}. \tag{1}$$

Here $n(M)$ is the abundance of haloes with a mass less than M and ρ_0 is the average density, while $\sigma^2(M)$ is the variance of the density field smoothed with a top-hat filter at a scale that encloses a mass M. The simulations mass function is shown in Fig. 1 and compared to the Press–Schechter model (see Press & Schechter 1974) and to the fitting formula given by Jenkins et al. (2001). The Press–Schechter model overestimates the number of small haloes by a factor of 1.7 as already demonstrated by, for example, Gross et al. (1998). The fitting formula seems to be in better agreement with the measured mass function with an accuracy of $\sim$10 per cent for masses below 3×10^{14} M$_\odot$.

As another means to check our simulations and to evaluate the convergence ensured by our large set of haloes, we computed the probability distribution of the spin parameter λ', defined as (Bullock et al. 2001)

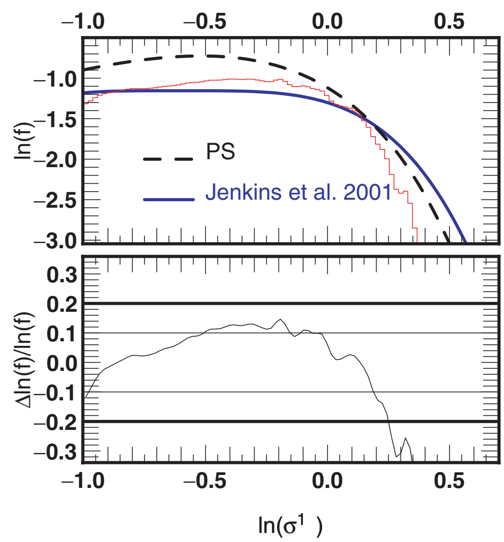

Figure 1. Top: the mass function $f(\sigma(M))$ of haloes (thin full line) compared to the Press–Schechter model (thick dashed line) and to the fitting formula of Jenkins et al. (2001) (thick full line). Bottom: relative residuals between the fitting formula and the mass function.

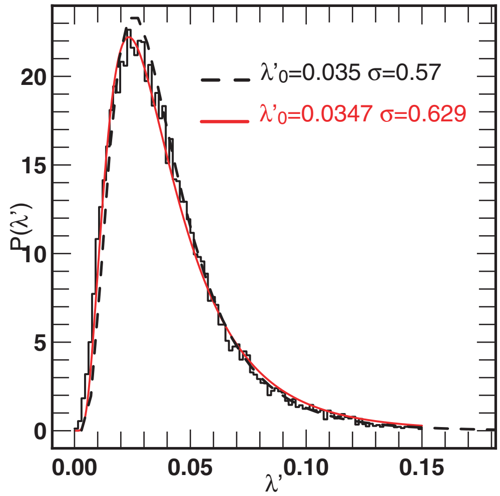

Figure 2. The distribution of the spin parameter λ' defined as $\lambda' \equiv J/(\sqrt{2}MVR_{200})$ computed using 100 000 haloes with a mass greater than 5×10^{12} M$_\odot$. The distribution can be fitted with a log-normal function with parameters $\lambda'_0 = 0.0347 \pm 0.0006$ and $\sigma = 0.63 \pm 0.02$ (solid line). The curve parametrized by $\lambda'_0 = 0.035$ and $\sigma = 0.57$ is also shown (dashed line). The two results are almost coincident, indicating that the value of σ is not so strongly constrained using a log-normal distribution.

$$\lambda' \equiv \frac{J}{\sqrt{2}MVR_{200}}. \tag{2}$$

Here J is the angular momentum contained in a sphere of virial radius R_{200} with a mass M and $V^2 = GM/R_{200}$. The measurement was performed on 100 000 haloes with a mass larger than 5×10^{12} M$_\odot$ as explained in the next section. The resulting distribution for λ' is shown in Fig. 2. The distribution $P(\lambda')$ is well fitted by a log-normal distribution (e.g. Bullock et al. 2001):

$$P(\lambda')\,\mathrm{d}\lambda' = \frac{1}{\lambda'\sqrt{2\pi}\sigma}\exp\left[-\frac{\ln^2(\lambda'/\lambda'_0)}{2\sigma^2}\right]\mathrm{d}\lambda'. \tag{3}$$

We found $\lambda'_0 = 0.0347 \pm 0.0006$ and $\sigma = 0.63 \pm 0.02$ as best-fitting values, consistent with the parameters ($\lambda' = 0.035$ and $\sigma = 0.57$) found by Peirani, Mohayaee & De Freitas Pacheco (2004), but our value of σ is slightly larger. However, using $\sigma = 0.57$ does not lead to a significantly different result. The value of σ is not strongly constrained and no real disagreement exists between our and their best-fitting values. The halo's spin, on which some of the following investigations are based, is computed accurately.

3 A GALACTOCENTRIC POINT OF VIEW

The analysis of exchange processes between the haloes and the intergalactic medium will be carried out using two methods. The first one can be described as 'discrete'. The accreted objects are explicitly counted as particles or particle groups. This approach will be applied and discussed later in this paper. The other method relies on measuring directly relevant quantities on a surface at *the interface* between the halo and the intergalactic medium. In this approach, the measured quantities are scalar, vector or tensor fluxes, and we assign to them *flux densities*. The flux density representation allows us to describe the angular distribution and temporal coherence of infalling objects or quantities related to this infall. The formal relation between a flux density, $\varpi(\mathbf{\Omega})$, and its associated total flux, Φ, through a region S is

$$\Phi \equiv \int_S \varpi(\mathbf{\Omega}) \cdot \mathrm{d}\mathbf{\Omega}, \tag{4}$$

where $\mathbf{\Omega}$ denotes the position on the surface where ϖ is evaluated and $\mathrm{d}\mathbf{\Omega}$ is the surface element normal to this surface. Examples of flux densities are mass flux density, $\rho \boldsymbol{v}_r$, or accreted angular momentum, $\rho \boldsymbol{v}_r \cdot \boldsymbol{L}$. In particular, this description in terms of a spherical boundary condition is well suited to study the dynamical stability and response of galactic systems. In this section, these fields are used as probes of the environment of haloes.

3.1 Halo analysis

Once a halo is detected, we study its environment using a galactocentric point of view. The relevant fields $\varpi(\mathbf{\Omega})$ are measured on the surface of a sphere centred on the halo's centre of mass with radius R_{200} [where $3M/(4\pi R_{200}^3) \equiv 200\overline{\rho}$] (cf. Fig. 3). There is no exact, nor unique, definition of the halo's outer boundary and our choice of R_{200} (also called the virial radius) is the result of a compromise between a large distance to the halo's centre and a good signal-to-noise ratio in the determination of spherical density fields.

We used 40×40 regularly sampled maps in spherical angles $\mathbf{\Omega} = (\vartheta, \phi)$, allowing for an angular resolution of 9°. We take into account haloes with a minimum number of 1000 particles, which gives a good representation of high-density regions on the sphere. This minimum corresponds to 5×10^{12} M$_\odot$ for a halo, and allows us to reach a total number of 10 000 haloes at $z = 2$ and 50 000 haloes at $z = 0$. This range of mass corresponds to a somewhat high value for a typical $L_\star$ galaxy but results from our compromise between resolution and sample size. Detailed analysis of the effects of resolution is postponed to Aubert & Pichon (2004).

The density, $\rho(\mathbf{\Omega})$, on the sphere is computed using the particles located in a shell with a radius of R_{200} and a thickness of $R_{200}/10$ (this is quite similar in spirit to the counts-in-cells techniques widely used in analysing large-scale structures, but in the context of a sphere the cells are shell segments). Weighting the density with quantities such as the radial velocity or the angular momentum of each particle contained within the shell, the associated spherical fields, $\rho \boldsymbol{v}_r(\mathbf{\Omega})$ or $\rho \boldsymbol{L}(\mathbf{\Omega})$, can be calculated for each halo. Two examples of spherical maps are given in Fig. 3. They illustrate a frequently observed discrepancy between the two types of spherical fields, $\rho(\mathbf{\Omega})$ and $\rho \boldsymbol{v}_r(\mathbf{\Omega})$. The spherical density field, $\rho(\mathbf{\Omega})$, is strongly quadrupolar, which is due to the intersection of the halo triaxial three-dimensional density field by our two-dimensional virtual sphere. By contrast the flux density of matter, $\rho \boldsymbol{v}_r(\mathbf{\Omega})$, does not have such a quadrupolar distribution. The contribution of halo particles to the net flux density is small compared to the contribution of particles coming from the outer intergalactic region.

3.2 Two-point statistics: advected momentum and the halo's spin

The influence of infalling matter on the dynamical state of a galaxy depends on whether or not the infall occurs inside or outside the galactic plane. If the infalling matter is orbiting in the galactic plane, its angular momentum is aligned with the angular momentum of the disc. Taking the halo's spin as a reference for the direction of the 'galactic' plane, we want to quantify the level of alignment of the orbital angular momentum of peripheral structures (i.e. as measured on the virial sphere) relative to that spin. The inner spin $\boldsymbol{S}$ is calculated using the positions and velocities ($\boldsymbol{r}_{\mathrm{part}}$, $\boldsymbol{v}_{\mathrm{part}}$) of the

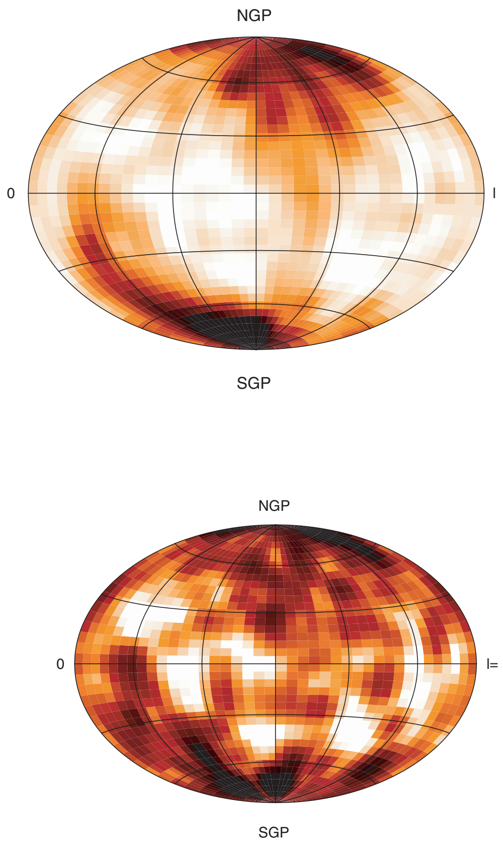

Figure 3. A galactocentric point of view of the density field, $\rho(\boldsymbol{\Omega})$ (top), and of the flux density of mass, $\rho v_r(\boldsymbol{\Omega})$, surrounding the same halo (bottom). This measurement was extracted from a ΛCDM cosmological simulation. The considered halo contained about 10^{13} $M_\odot$ or 2000 particles. The high-density zones are darker. The density's spherical field shows a strong quadrupolar component with high-density zones near the two poles while this component is less important for the mass flux density field measured on the sphere. This discrepancy between the two spherical fields is common and reflects the shape of the halo as discussed in the main text.

particles inside the R_{200} sphere in the centre-of-mass rest frame $(\boldsymbol{r}_0, \boldsymbol{v}_0)$:

$$\boldsymbol{S} = \sum_{\text{part}} (\boldsymbol{r}_{\text{part}} - \boldsymbol{r}_0) \times (\boldsymbol{v}_{\text{part}} - \boldsymbol{v}_0). \tag{5}$$

Here $\boldsymbol{r}_0$ is the position of the halo centre of mass, while $\boldsymbol{v}_0$ stands for the average velocity of the halo's particles. This choice of rest frame is not unique; another option would have been to take the most bounded particle as a reference. Nevertheless, given the considered mass range, no significant alteration of the results is to be expected. The total angular momentum, $\boldsymbol{L}_\text{T}$ (measured at the virial radius, R_{200}) is computed for each halo using the spherical field $\rho\boldsymbol{L}(\boldsymbol{\Omega})$:

$$\boldsymbol{L}_\text{T} = \int_{4\pi} \rho\boldsymbol{L}(\boldsymbol{\Omega}) \cdot \mathrm{d}\boldsymbol{\Omega}. \tag{6}$$

The angle, θ, between the spin of the inner particles $\boldsymbol{S}$ and the total orbital momentum $\boldsymbol{L}_\text{T}$ of 'peripheral' particles is then easily computed:

$$\theta = \cos^{-1}\left(\frac{\boldsymbol{L}_\text{T}\cdot\boldsymbol{S}}{|\boldsymbol{L}_\text{T}||\boldsymbol{S}|}\right). \tag{7}$$

Measuring this angle θ for all the haloes of our simulations allow us to derive a raw probability distribution of angle, $d_\text{r}(\theta)$. An isotropic distribution corresponds to a non-uniform probability density $d_\text{iso}(\theta)$. Typically d_iso is smaller near the poles (i.e. near the region of alignment), leading to a larger correction for these angles and to larger error bars in these regions (see Fig. 4): this is the consequence of smaller solid angles in the polar regions (which scales like $\sim\sin\theta$) than in equatorial regions for a given θ aperture. The true anisotropy is estimated by measuring the ratio:

$$d_\text{r}(\theta)/d_\text{iso}(\theta) \equiv 1 + \xi_{LS}(\theta), \tag{8}$$

Here, $1 + \xi_{LS}(\theta)$ measures the excess probability of finding $\boldsymbol{S}$ and $\boldsymbol{L}_\text{T}$ away from each other, while $\xi_{LS}(\theta)$ is the cross-correlation of the angles of $\boldsymbol{S}$ and $\boldsymbol{L}_\text{T}$. Thus having $\xi_{LS}(\theta) > 0$ (respectively, $\xi_{LS}(\theta) < 0$) implies an excess (respectively, a lack) of configurations with a θ separation relative to an isotropic situation.

To take into account the error in the determination of θ, each count (or Dirac distribution) is replaced with a Gaussian distribution and contributes to several bins:

$$\delta(\theta - \theta_0) \rightarrow \mathcal{N}(\theta_0, \sigma_0) = \frac{1}{\sigma_0\sqrt{2\pi}} \exp\left[-\frac{(\theta-\theta_0)^2}{2\sigma_0^2}\right], \tag{9}$$

where $\mathcal{N}$ stands for a normalized Gaussian distribution and where the angle uncertainty is approximated by $\sigma_0 \sim (4\pi/N)^{1/2}$ using N particles as suggested by Hatton & Ninin (2001). If N_v is equal to the number of particles used to compute $\rho\boldsymbol{L}(\boldsymbol{\Omega})$ on the virial sphere and if N_h is the number of particles used to compute the halo's spin, the error we associated to the angle between the angular momentum at the virial sphere and the halo's spin is

$$\sigma_0 = \sqrt{(4\pi/N_\text{v}) + (4\pi/N_\text{h})} \sim \sqrt{(4\pi/N_\text{v})}, \tag{10}$$

because we have $N_\text{v} \ll N_\text{h}$. Note that this Gaussian correction introduces a bias in mass: a large infall event (large N_v, small σ_0) is weighted more for a given θ_0 than a small infall (small N_v, large σ_0). All the distributions are added to give the final distribution:

$$d_\text{r}(\theta) = \sum_p^{N_p} \mathcal{N}(\theta_p, \sigma_p), \tag{11}$$

where N_p stands for the total number of measurements (i.e. the total number of haloes in our set of simulations). The corresponding isotropic angle distribution is derived using the same set of errors randomly redistributed:

$$d_\text{iso}(\theta) = \sum_p^{N_p} \mathcal{N}\left(\theta_p^\text{iso}, \sigma_p\right). \tag{12}$$

Fig. 4 shows the excess probability, $1 + \xi_{LS}(\theta)$, of the angle between the total orbital momentum of particles at the virial radius $\boldsymbol{L}_\text{T}$ and the halo's spin $\boldsymbol{S}$. The solid line is the correlation deduced from 40 000 haloes at redshift $z = 0$. The error bars were determined using 50 subsamples of 10 000 haloes extracted from the whole set of available data. An average Monte Carlo correlation and a Monte Carlo dispersion σ is extracted. In Fig. 4, the symbols stand for the average Monte Carlo correlation, while the vertical error bars stand for the 3σ dispersion.

The correlation in Fig. 4 shows that all angles are not equivalent since $\xi_{LS}(\theta) \neq 0$. It can be fitted with a Gaussian curve using the following parametrization:

$$1 + \xi_{LS}(\theta) = \frac{a_1}{\sqrt{2\pi}a_3} \exp\left(-\frac{\theta - a_2^2}{2a_3^2}\right) + a_4. \tag{13}$$

The best-fitting parameters are $a_1 = 2.351 \pm 0.006$, $a_2 = -0.178 \pm 0.002$, $a_3 = 1.343 \pm 0.002$ and $a_4 = 0.6691 \pm 0.0004$. The

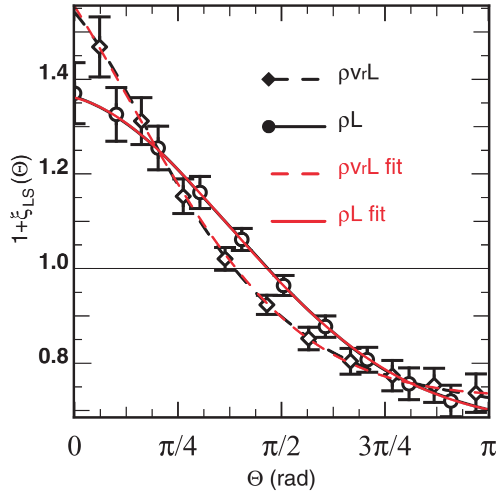

Figure 4. Excess probability, $1 + \xi_{LS}(\theta)$, of the angle, θ, between the halo's spin ($\boldsymbol{S}$) and the angular momentum ($\boldsymbol{L}_{\rm T}$ for total, or $\boldsymbol{L}_{\rm A}$ for accreted) measured on the virial sphere using the fluid located at the virial radius. Here $\boldsymbol{L}_{\rm T}$ represents the *total* angular momentum measured on the virial sphere (solid line and circles) and $\boldsymbol{L}_{\rm A}$ the *total accreted* angular momentum measured on the sphere (dashed line and diamonds). The error bars represent the 3σ dispersion measured on subsamples of 10 000 haloes. The correlation takes into account the uncertainty on the angle determination due to the small number of particles at the virial radius. Here $\xi_{LS}(\theta) \equiv 0$ would be expected for an isotropic distribution of angles between $\boldsymbol{S}$ and $\boldsymbol{L}$ while the measured distributions indicate that the aligned configuration ($\theta \sim 0$) is significantly more likely. The two excess probability distributions are well fitted by Gaussian functions (almost coincident red curves in *Synergy*: see main text).

maximum being located at small angles, the aligned configuration, $\widehat{\boldsymbol{L}_{\rm T}\cdot\boldsymbol{S}} \sim 0$, is the most enhanced configuration (relative to an isotropic distribution of angle θ). The aligned configuration of $\boldsymbol{L}_{\rm T}$ relative to $\boldsymbol{S}$ is 35 per cent [$\xi_{LS}(0) = 0.35$], more frequent in our measurements than for a random orientation of $\boldsymbol{L}_{\rm T}$. As a consequence, matter is preferentially located in the plane perpendicular to the spin, which is hereafter referred to as the 'equatorial' plane.

The angles, (ϑ, ϕ), are measured relative to the z- and x-axes of the simulation boxes and not relative to the direction of the spin. Thus we do not expect artificial $\boldsymbol{L}_{\rm T}$–$\boldsymbol{S}$ correlations due to the sampling procedure. Nevertheless, it is expected on geometrical grounds that the aligned configuration is more likely since the contribution of *recent* infalling dark matter to the halo's spin is important. As a check, the same correlation was computed using the total *advected* orbital momentum:

$$\boldsymbol{L}_{\rm A} = \int_{4\pi} \boldsymbol{L}\rho \boldsymbol{v}_r(\boldsymbol{\Omega}) \cdot {\rm d}\boldsymbol{\Omega}. \tag{14}$$

The resulting correlation (see Fig. 4) is similar to the previous one but the slope towards small values of θ is even stronger and for example the excess of aligned configuration reaches the level of 50 per cent [$\xi_{LS}(0) \sim 0.5$]. The correlation can be fitted following equation (13) with $a_1 = 3.370 \pm 0.099$, $a_2 = -0.884 \pm 0.037$, $a_3 = 1.285 \pm 0.016$ and $a_4 = 0.728 \pm 0.001$. This enhancement confirms the relevance of advected momentum for the build-up of the halo's spin, though the increase in amplitude is limited to 0.2 for $\theta = 0$. The halo's inner spin is dominated by the orbital momentum of infalling clumps (given the larger lever arm of these virialized clumps and their high radial velocities) that have just passed through the virial sphere, as suggested by Vitvitska et al. (2002) (see also Appendix D). It reflects a temporal coherence of the infall of matter and thus of angular momentum, and a geometrical effect: a fluid clump that is just being accreted can intersect the virtual virial sphere, being in part both 'inside' and 'outside' the sphere. Finally a small fraction of the accreted momentum may come from material that has already passed once through the R_{200} sphere. This component would be aware of the dynamical properties of the inner halo. Thus it is expected that the halo's spin $\boldsymbol{S}$ and the momenta $\boldsymbol{L}_{\rm T}$ and $\boldsymbol{L}_{\rm A}$ at the virial radius are correlated since the halo's spin is dominantly set by the properties of the angular momentum in its outer region. The anisotropy of the two fields $\boldsymbol{L}_{\rm T}$ and $\boldsymbol{L}_{\rm A}$ do not have the same implication. The spatial distribution of advected angular momentum, $\boldsymbol{L}_{\rm A}$, contains stronger dynamical information. In particular, the variation of the angular momentum of the halo plus disc is induced by tidal torques but also by accreted momentum for an open system. For example, the anisotropy of $\boldsymbol{L}\rho\boldsymbol{v}_r$ should be reflected in the statistical properties of warped discs as discussed later in Sections 6.1 and 6.2.

3.3 One-point statistics: equatorial infall anisotropy

The previous measurement does not account for dark matter falling into the halo with a very small angular momentum (radial orbits). We therefore measured the excess of equatorial accretion, $\delta_{\rm m}$, defined as follows. We can measure the average flow density of matter, Φ_r, in a ring centred on the equatorial plane:

$$\Phi_r \equiv \frac{1}{S_r} \int_{-\pi/8<\theta-\pi/2<\pi/8} \rho \boldsymbol{v}_r(\boldsymbol{\Omega}) \cdot {\rm d}\boldsymbol{\Omega}, \tag{15}$$

where $S_r = \int_{-\pi/8<\theta-\pi/2<\pi/8} {\rm d}\boldsymbol{\Omega}$. The ring region is defined by the area where the polar angle satisfies $\theta_{\rm pol} = \pi/2 \pm \pi/8$, which corresponds to about 40 per cent of the total covered solid angle. The larger this region is, the better the convergence of the average value of Φ_r, but the lower the effects of anisotropy, since averaging over a larger surface leads to a stronger smoothing of the field. This value of $\pm\pi/8$ is a compromise between these two contradictory trends. In the next section and in the Appendix, we discuss more general filtering involving spherical harmonics that are related to the dynamical evolution of the inner component of the halo. We also measure the flow averaged over all the directions $\overline{\Phi}$:

$$\overline{\Phi} \equiv \overline{\rho \boldsymbol{v}_r} \equiv \frac{1}{4\pi} \int_{4\pi} \rho \boldsymbol{v}_r(\boldsymbol{\Omega}) \cdot {\rm d}\boldsymbol{\Omega}. \tag{16}$$

Since we are interested in accretion, we computed Φ_r and $\overline{\Phi}$ using only the infalling part of the density flux of matter, where $\rho\boldsymbol{v}_r(\boldsymbol{\Omega}) \cdot {\rm d}\boldsymbol{\Omega} < 0$, ignoring the outflows. The fraction of outflowing material decreases from 20 per cent of the total integrated flux at $z = 0$ to 10 per cent at $z = 2$. We define $\delta_{\rm m}$ as

$$\delta_{\rm m} \equiv \frac{\Phi_r - \overline{\Phi}}{\overline{\Phi}}. \tag{17}$$

This number quantifies the anisotropy of the infall. It is positive when infall is in excess in the galactic equatorial plane, while for isotropic infall $\delta_{\rm m} \equiv 0$. The quantity $\delta_{\rm m}$ can be regarded as being the 'flux density' contrast of the infall of matter in the ring region (formally it is the centred top-hat-filtered mass flux density contrast as shown in Appendix C1). This measurement, in contrast to those of the previous section, does not rely on some knowledge of the inner region of the halo but only on the properties of the environment.

Fig. 5 displays the normalized distribution of $\delta_{\rm m}$ measured for 50 000 haloes with a mass in excess of 5×10^{12} $\mathrm{M}_\odot$ and for different redshifts ($z = 1.8, 1.5, 0.9, 0.3, 0.0$). The possible values for

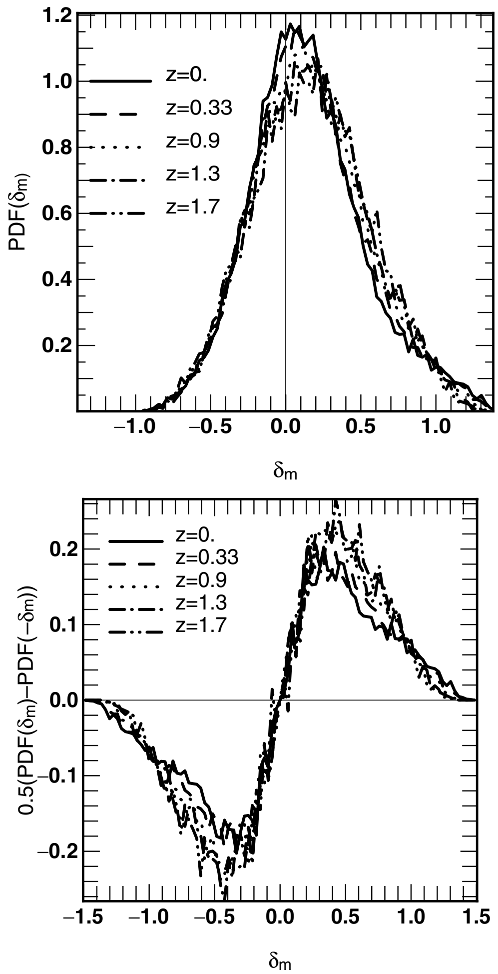

Figure 5. Top: normalized probability distributions (PDF) of the excess of equatorial infall, $\delta_{\rm m}$, measured at the virial radius. The quantity $1+\delta_{\rm m}$ stands for the ratio between the flux of matter through the equatorial subregion of the R_{200} sphere and the average flux of matter through the whole R_{200} sphere. The equatorial subregion is defined as being perpendicular to the direction of the halo's spin. It formally corresponds to the top-hat-smoothed mass flux density contrast. The value $\delta_{\rm m}=0$ is expected for an isotropic infall of matter through the virial sphere. The average value of $\delta_{\rm m}$ is always greater than zero, indicating that the infall of matter is, on average, more important in the direction orthogonal to the halo's spin vector than in other directions. Bottom: the antisymmetric part of the $\delta_{\rm m}$ distribution. Being positive for positive values of $\delta_{\rm m}$, the antisymmetric part of the $\delta_{\rm m}$ distributions shows that accretion in the equatorial plane is in excess relative to that expected from isotropic accretion of matter.

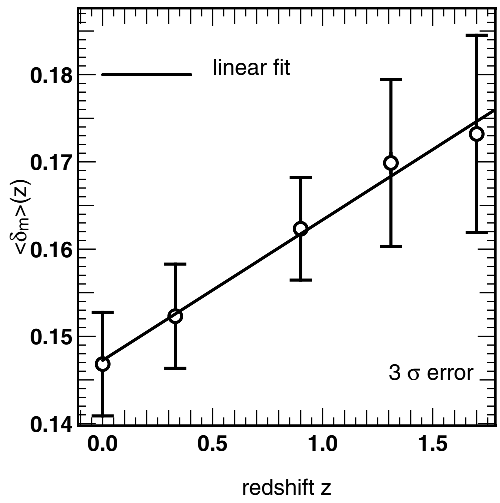

Figure 6. The redshift evolution of $\langle\delta_{\rm m}\rangle$. The average $\langle\rangle$ is performed on a set of 40 000 haloes at $z=0$ and 10 500 haloes at $z=1.8$. The error bars stand for the error on the estimation of $\langle\delta_{\rm m}\rangle$ with $\Delta=\sigma(\delta_{\rm m})/\sqrt{N}$, where N is the number of haloes needed to compute $\langle\delta_{\rm m}\rangle$. The value of $\langle\delta_{\rm m}\rangle$ is always positive and indicates an excess of accretion in the equatorial plane. This redshift evolution can be fitted as $\langle\delta_{\rm m}\rangle\,(z)=0.0161(\pm\,0.0103)z+0.147(\pm\,0.005)$. This excess is detected for every redshift smaller than $z=2$, which indicates an excess of accretion in the equatorial region. We applied a mass threshold of $5\times10^{12}\,{\rm M}_\odot$ to our haloes for every redshift. Then, the halo population is different from one redshift to another. This selection effect may dominate the observed time evolution.

$\delta_{\rm m}$ range between $\delta_{\rm m}\sim-1$ and $\sim$1.5. The average value $\langle\delta_{\rm m}\rangle$ of the distributions is statistically larger than zero (see also Fig. 6). Here $\langle\rangle$ stands for the statistical expectation, which in this paper is approximated by the arithmetic average over many haloes in our simulations. The antisymmetric part of the distribution of $\delta_{\rm m}$ is positive for positive $\delta_{\rm m}$. The probability distribution function (PDF) of $\delta_{\rm m}$ is skewed, indicating an excess of accretion through the equatorial ring. The median value for $\delta_{\rm m}$ is $\delta_{\rm med}=0.11$, while the first 25 per cent haloes have $\delta_{\rm m}<\delta_{25}\equiv-0.11$ and the first 75 per cent haloes have $\delta_{\rm m}<\delta_{75}\equiv0.37$. Therefore we have $(\delta_{75}-\delta_{\rm med})/(\delta_{25}-\delta_{\rm med})=1.13$, which quantifies how the distribution of $\delta_{\rm m}$ is positively skewed. The skewness $S_3=\langle(\delta-\bar\delta)^3\rangle/\langle(\delta-\bar\delta)^2\rangle^{3/2}$ is equal to 0.44. Combined with the fact that the average value $\langle\delta_{\rm m}\rangle$ is always positive, this shows that the infall of matter is larger in the equatorial plane than in the other directions.

This result is robust with respect to time evolution (see Fig. 6). At redshift $z=1.8$, we have $\langle\delta_{\rm m}\rangle=0.17$, which falls to $\langle\delta_{\rm m}\rangle=0.145$ at redshift $z=0$. This redshift evolution can be fitted as $\langle\delta_{\rm m}\rangle\,(z)=0.0161(\pm\,0.0103)z+0.147(\pm\,0.005)$. This trend should be taken with caution. For *every* redshift z we take in account haloes with a mass bigger than $5\times10^{12}\,{\rm M}_\odot$. Thus the population of haloes studied at $z=0$ is not exactly the same as the one studied at $z=2$. Actually, at $z=0$, there is a strong contribution of small haloes (i.e. with a mass close to $5\times10^{12}\,{\rm M}_\odot$) that have just crossed the mass threshold. The accretion on small haloes is more isotropic as shown in more details in Appendix D2. One possible explanation is that they experienced less interactions with their environment and have since had time to relax, which implies a smaller correlation with the spatial distribution of the infall. Also bigger haloes tend to lie in more coherent regions, corresponding to rare peaks, whereas smaller haloes are more evenly distributed. The measured time evolution of the anisotropy of the infall of matter therefore seems to result from a competition between the trend for haloes to become more symmetric and the bias corresponding to a fixed mass cut.

In short, the infall of matter measured at the virial radius in the direction orthogonal to the halo's spin is larger than expected for an isotropic infall.

3.4 Harmonic expansion of anisotropic infall

As mentioned earlier (and demonstrated in Appendix A), the dynamics of the inner halo and disc is partly governed by the statistical properties of the flux densities at the boundary. Accounting for the gravitational perturbation and the infalling mass or momentum requires projecting the perturbation over a suitable basis such as the spherical harmonics:

$$\varpi(\mathbf{\Omega}) = \sum_{\ell,m} \alpha_\ell^m Y_\ell^m(\mathbf{\Omega}). \tag{18}$$

Here, ϖ stands for the mass flux density, the advected momentum flux density, or the potential perturbation, for example. The resulting α_ℓ^m coefficients correspond to the spherical harmonic decomposition in an *arbitrary* reference frame. The different m correspond to the different fundamental orientations for a given multipole ℓ. A spherical field with no particular orientation gives rise to a field averaged over the different realizations that appear as a monopole, i.e. $\langle \alpha_{\ell m} \rangle = 0$ for $\ell \neq 0$. Having constructed our virial sphere in a reference frame attached to the simulation box, we effectively performed a randomization of the orientation of the sphere. However, since the direction of the halo's spin is associated to a general preferred orientation for the infall, it should be traced through the $\alpha_{\ell m}$ coefficients. Let us define the rotation matrix, $\mathcal{R}$, which brings the z-axis of the simulation box along the direction of the halo's spin. The spherical harmonic decomposition centred on the spin of the halo, $a^m{}_\ell$, is given by (e.g. Varshalovich, Moskalev & Khersonskii 1988):

$$a_\ell^m = \mathcal{R}\left[\alpha_{\ell'}^{m'}\right] \equiv \sum_{\ell' m'} \mathcal{R}_{\ell,\ell'}^{m,m'}(\vartheta, \varphi)\alpha_{\ell'}^{m'}. \tag{19}$$

If the direction of the spin defines a preferential plane of accretion, the corresponding a_ℓ^m will be systematically enhanced. We therefore expect the equatorial direction (which corresponds to $m = 0$ for every ℓ) not to converge to zero.

We computed the spherical harmonic decomposition of $\rho v_r(\vartheta, \varphi)$ given by equation (18) for the mass flux density of 25 000 haloes at $z = 0$, up to $\ell = 15$. For each spherical field of the mass density flux, we performed the rotation that brings the halo's spin along the z-direction to obtain a set of 'centred' a_ℓ^m coefficients. We also computed the related angular power spectra C_ℓ:

$$C_\ell \equiv \frac{1}{4\pi}\frac{1}{2\ell+1}\sum_{m=-\ell}^{\ell}\left|a_\ell^m\right|^2 = \frac{1}{4\pi}\frac{1}{2\ell+1}\sum_{m=-\ell}^{\ell}\left|\alpha_\ell^m\right|^2. \tag{20}$$

Let us define the normalized $\tilde{a}_\ell^m$ (or harmonic contrast, see Appendix C1),

$$\tilde{a}_\ell^m \equiv \sqrt{4\pi}\frac{a_\ell^m}{a_0^0} = \frac{a_\ell^m}{\mathrm{sign}\left(a_0^0\right)\sqrt{C_0}}. \tag{21}$$

This compensates for the variations induced by our range of masses for the halo. For each ℓ, we present in Fig. 7 the median value, $|\langle \mathrm{Re}\{\tilde{a}_\ell^m\}\rangle|$ for $\ell = 2, 4, 6, 8$ computed for 25 000 haloes. All the $\tilde{a}_\ell^m$ have converged towards zero, except for the $\tilde{a}_{\ell 0}$ coefficients. The imaginary parts of $\tilde{a}_\ell^m$ have the same behaviour, except for the $\mathrm{Im}\{\tilde{a}_{\ell 0}\}$ coefficients, which vanish by definition (not shown here). The $m = 0$ coefficients are statistically non-zero. We find $\langle \tilde{a}_2^0 \rangle = -0.65 \pm 0.04$, $\langle \tilde{a}_4^0 \rangle = 0.12 \pm 0.02$, $\langle \tilde{a}_6^0 \rangle = -0.054 \pm 0.015$ and $\langle \tilde{a}_8^0 \rangle = 0.0145 \pm 0.014$. Errors stand for the distance between the 5th and the 95th percentile. The typical pattern corresponding to an $m = 0$ harmonic is a series of rings parallel to the equatorial plane. This confirms that accretion occurs preferentially in a plane perpendicular to the direction of the halo's spin.

The spherical accretion contrast $\langle \delta_{[\rho v_r]}(\vartheta, \phi) \rangle$ can be reconstructed using the $\langle \tilde{a}_\ell^m \rangle$ coefficients (as shown in the Appendix):

$$\delta_{[\rho v_r]}(\vartheta, \varphi) = \sum_{\ell,m} \tilde{a}_\ell^m Y_\ell^m(\vartheta, \varphi) - 1. \tag{22}$$

In Fig. 8, the polar profile

$$\left\langle \delta_{[\rho v_r]}(\vartheta) \right\rangle \equiv \sum_{\ell,m} \left\langle \tilde{a}_\ell^m \right\rangle Y_\ell^m(\vartheta, 0) - 1 \tag{23}$$

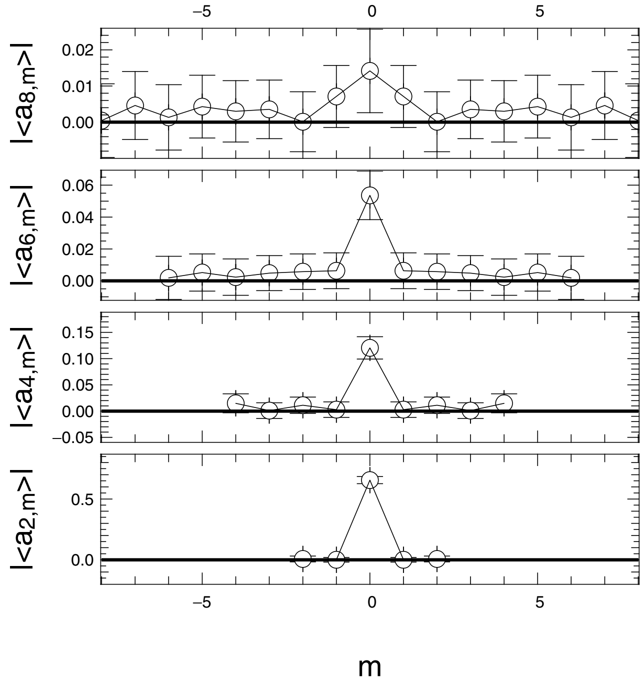

Figure 7. The convergence of the modulus of the real part of $\langle \tilde{a}_\ell^m \rangle$, for $\ell = 2, 4, 6, 8$. The $\tilde{a}_\ell^m$ decomposition was computed for 25 000 haloes, and each coefficient has been normalized with the corresponding C_0 (see text for details). Here, $\langle\rangle$ stands for the median while the error bars stand for the distance between the 5th and 95th percentiles. The median value of $\langle \tilde{a}_\ell^m \rangle$ is zero except for the $\langle \tilde{a}_\ell^0 \rangle$ coefficient: this is a signature of a field invariant to azimuthal rotations.

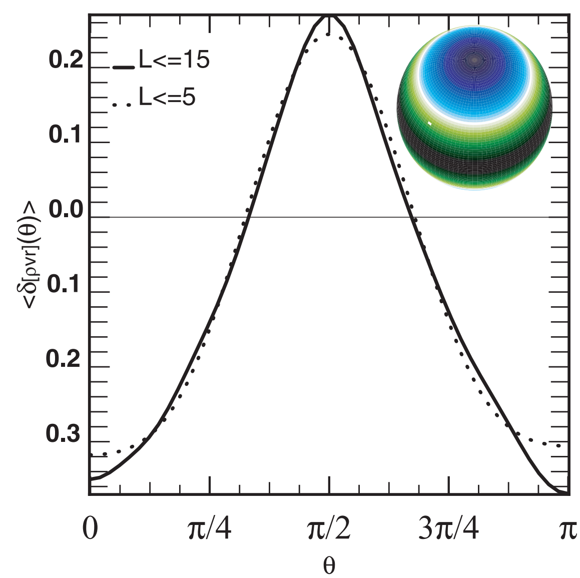

Figure 8. An illustration of the convergence of $\tilde{a}_{\ell m}$ presented in Fig. 7. The solid line stands for the azimuthal average of the spherical contrast of accretion computed using equation (23), the dotted line for the spherical field reconstructed with $\ell \leqslant 5$. The insert represents the reconstructed spherical field using the expansion of the $\tilde{a}_{\ell m}$ of the mass flux measured at the virial sphere. The sphere presents an excess of accretion in the equatorial region because of the non-zero average value of $\tilde{a}_{\ell 0}$ coefficients (for even values of ℓ).

of this reconstructed spherical contrast is shown. This profile has been obtained using the $\langle \tilde{a}_\ell^m \rangle$ coefficients with $\ell \leqslant 5$ and $\ell \leqslant 15$. The contrast is large and positive near $\vartheta = \pi/2$ as expected for an equatorial accretion. The profile reconstructed using $\ell \leqslant 5$ is quite similar to the one using $\ell \leqslant 15$. This indicates that most of the energy involved in the equatorial accretion is contained in a typical angular scale of 36° (a scale that is significantly larger than $\pi/20$ corresponding to the cut-off frequency in our sampling of the sphere as mentioned earlier).

Using a spherical harmonic expansion of the incoming mass flux density (equation 8), we confirmed the excess of accretion in the equatorial plane found above. This similarity was expected since these two measurements (using a ring or using a spherical harmonic expansion) can be considered as two different filterings of the spherical accretion field as demonstrated in Appendix C. The main asset of the harmonic filtering resides in its relevance for the description of the inner dynamics as discussed in Section 6.

3.5 Summary

To sum up, the two measurements of Sections 3.2 and 3.3 (or 3.4) are not sensitive to the same effects. The first measurement (involving the angular momentum $\rho \boldsymbol{L}$ at the virial radius) is mostly a measure of the importance of infalling matter in building the halo's proper spin. The second and the third measurements (involving the excess of accretion in the equatorial plane, $\delta_{\rm m}$, using rings and harmonic expansion) are quantitative measures of coplanar accretion. The equatorial plane of a halo is favoured relative to the accretion of matter (compared to an isotropic accretion) to a level of ~12 per cent between $z = 2$ and $z = 0$. Down to the halo scale (~500 kpc), anisotropy is detected and is reflected in the spatial configuration of infalling matter.

4 ANISOTROPIC INFALL OF SUBSTRUCTURES

To confirm and assess the detected anisotropy of the matter infall on haloes in our simulations, let us now move on to a discrete framework and measure related quantities for satellites and substructures. In the hierarchical scenario, haloes are built up by successive mergers of smaller haloes. Thus if an anisotropy in the distribution of infalling matter is to be detected, it seems reasonable that this anisotropy should also be detected in the distribution of satellites. The previous galactocentric approach for the mass flow does not discriminate between an infall of virialized objects and a diffuse material accretion, and therefore is also sensitive to satellites merging: one would need to consider, say, the energy flux density. However, it is not clear if satellites are markers of the general infall and Vitvitska et al. (2002) did not detect any anisotropy at a level greater than 20 per cent.

The detection of substructures and satellites is performed using the code ADAPTAHOP, which is described in detail in the Appendix. This code outputs trees of substructures in our simulations, by analysing the properties of the local dark matter density in terms of peaks and saddle points. For each detected halo we can extract the whole hierarchy of subclumps or satellites and their characteristics. Here we consider the leaves of the trees, i.e. the most elementary substructures that the haloes contain. Each halo contains a 'core', which is the largest substructure in terms of particle number, and 'satellites', corresponding to the smaller ones. We call the ensemble of core plus satellites the 'mother' or the halo. Naturally the number of substructures is correlated with the mother's mass. The bigger the number of substructures, the bigger the total mass. Because the resolution in mass of our simulations is limited, smaller haloes tend to have only one or two satellites. Thus in the following sections we will discriminate cases where the core has less than four satellites. A total of 50 000 haloes have been examined, leading to a total of about 120 000 substructures.

4.1 Core spin–satellite orbital momentum correlations

In the mother–core–satellite picture, it is natural to regard the core as the central galactic system, while satellites are expected to join the halo from the intergalactic medium. One way to test the effect of large-scale anisotropy is to compare directly the angle between the core's spin, $\boldsymbol{S}_{\rm c}$, and the satellites' angular momentum, $\boldsymbol{L}_{\rm s}$, relative to the core. These two angular momenta are chosen since they should be less correlated with each other than, for example, the halo's spin and the angular momentum of its substructures. Furthermore, particles that belong to the cores are strictly distinct from those that belong to satellites, thus preventing any 'self-contamination' effect. As a final safeguard, we took into account only satellites with a distance relative to the core larger than the mother's radius. The latter quantity is computed using the mean square distance of the particles belonging to the mother, and thus we focus only on 'external' satellites. The core's spin is

$$\boldsymbol{S}_{\rm c} = \sum_p (\boldsymbol{r}_p - \boldsymbol{r}_{\rm c}) \times (\boldsymbol{v}_p - \boldsymbol{v}_{\rm c}), \tag{24}$$

where $\boldsymbol{r}_p$ and $\boldsymbol{v}_p$ (respectively $\boldsymbol{r}_{\rm c}$ and $\boldsymbol{v}_{\rm c}$) stand for the particles' positions and velocities (respectively the core's centre-of-mass position and velocity) and where

$$r_p < d_{\rm c}, \tag{25}$$

where $d_{\rm c}$ is the core's radius. The angular momentum for a satellite is computed likewise, with a different selection criterion on particles, namely

$$|\boldsymbol{r}_p - \boldsymbol{r}_{\rm s}| < d_{\rm s}, \tag{26}$$

where $\boldsymbol{r}_{\rm s}$ stands for the satellite's centre-of-mass position and $d_{\rm s}$ is its radius.

Fig. 9 displays the reduced distribution of the angle, $\theta_{\rm cs}$, between the core's spin and the satellites' orbital momentum, where $\theta_{\rm cs}$ is defined by

$$\theta_{\rm cs} = \cos^{-1}\left(\frac{\boldsymbol{L}_{\rm s}\cdot\boldsymbol{S}_{\rm c}}{|\boldsymbol{L}_{\rm s}||\boldsymbol{S}_{\rm c}|}\right). \tag{27}$$

The Gaussian correction was applied as described in Section 3.2, to take into account the uncertainty on the determination of $\theta_{\rm cs}$.

The correlation of $\theta_{\rm cs}$ indicates a preference for the aligned configuration with an excess of ~12 per cent of aligned configurations relative to the isotropic distribution. We ran Monte Carlo realizations using 50 subsamples of 10 000 haloes extracted from our whole set of substructures to constrain the error bars. We found a 3σ error of 6 per cent: the detected anisotropy exceeds our errors, i.e. $\xi_{\rm cs}(\theta_{\rm cs})$ is not uniform with a good confidence level. The variations with the fragmentation level (i.e. the number of satellites per system) remains within the error bars. The best-fitting parameters for the measured distributions of systems with at least one satellite are $a_1 = 0.3993 \pm 0.0038$, $a_2 = 0.0599 \pm 0.0083$, $a_3 = 0.8814 \pm 0.0055$ and $a_4 = 0.9389 \pm 0.0002$ (see equation 13 for parametrization). Not surprisingly, a less structured system shows a stronger alignment of its satellites' orbital momentum relative to the core's spin. In the extreme case of a binary system (one core plus a satellite), it is common for the two bodies to have similar masses. Since

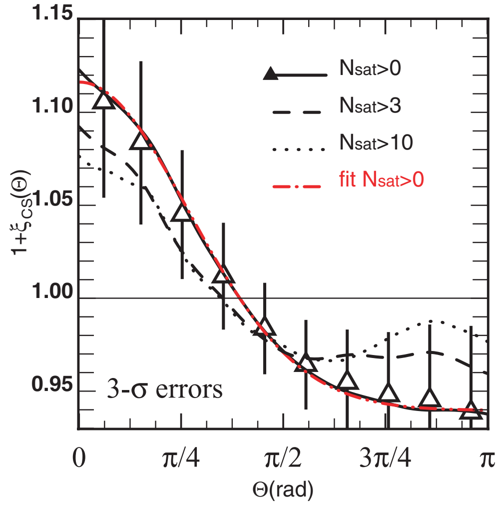

Figure 9. Excess probability, $1+\xi_{\rm cs}(\theta_{\rm cs})$, of the angle between the core's spin and the orbital momentum of satellites. Cores have at least one satellite (solid line), four satellites (dashed line) and 10 satellites (dotted line). These curves have been normalized by the expected isotropic distribution and the Gaussian correction was applied to account for errors on the angle determination. Here $\xi_{\rm cs}(\theta)=0$ is expected for an isotropic distribution of angles between the core's spin and the orbital momentum. All satellites are external to the core, yet an excess of alignment is present. The triangles represent the angle distribution, the error bars stand for the 3σ dispersion for 50 subsamples of 10 000 satellites (out of 35 000) while the dash-dotted curve (red in the online version of this article on *Synergy*) stands for the best Gaussian fit of the distribution for systems with at least one satellite (see equation 13 for parametrization). The best-fitting parameters are: $a_1 = 0.3993 \pm 0.0038$, $a_2 = 0.0599 \pm 0.0083$, $a_3 = 0.8814 \pm 0.0055$ and $a_4 = 0.9389 \pm 0.0002$. The isotropic case is excluded with a good confidence level, even for systems with a large number of satellites.

the two bodies are revolving around each other, a natural preferential plane appears. The core's spin will be likely to be orthogonal to this plane. Increasing the number of satellites increases the isotropy of the satellites' spatial distribution (the distribution's maxima are lower and the slope towards low values of $\theta_{\rm cs}$ is gentler), but switching from at least four satellites to at least 10 satellites per system does not change significantly the overall shape distribution. This suggests that convergence, relative to the number of satellites, has been reached for the $\theta_{\rm cs}$ distribution.

As the measurements of the anisotropy factor $\delta_{\rm m}$ indirectly suggested, satellites have an anisotropic distribution of their directions around haloes. Furthermore the previous analysis of the statistical properties of δ (Section 3.3) indicated an excess of aligned configuration of 15 per cent, which is consistent with the current method using substructures. While the direction of the core's spin should not be influenced by the infall of matter, we still find the existence of a preferential plane for this infall, namely the core's equatorial plane.

4.2 Satellite velocity–satellite spin correlation

The previous sections compared the properties of haloes with those of satellites. In a galactocentric framework, the existence of this preferential plane could only be local. In the extreme each halo would then have its own preferential plane without any connection to the preferential plane of the next halo. Taking the satellite itself as a reference, we have analysed the correlation between the satellite's average velocity in the core's rest frame and the structure's spin. Since part of the properties of these two quantities are consequences of what happened outside the galactic system, the measurement of their alignment should provide information on the structuration on scales larger than the halo scale, while sticking to a galactocentric point of view.

For each satellite, we extract the angle, $\theta_{\rm vs}$, between the velocity and the proper spin and derive its distribution using the Gaussian correction (see Fig. 10). The satellite's spin $\boldsymbol{S}_{\rm s}$ is defined by

$$\boldsymbol{S}_{\rm s} = \sum_p (\boldsymbol{r}_p - \boldsymbol{r}_{\rm s}) \times (\boldsymbol{v}_p - \boldsymbol{v}_{\rm s}), \tag{28}$$

where $\boldsymbol{r}_{\rm s}$ and $\boldsymbol{v}_{\rm s}$ stands for the satellite's position and velocity in the halo core's rest frame. The angle $\theta_{\rm vs}$ between the satellite's spin and the satellite's velocity is

$$\theta_{\rm vs} = \cos^{-1}\left(\frac{\boldsymbol{S}_{\rm s}\cdot\boldsymbol{v}_{\rm s}}{|\boldsymbol{S}_{\rm s}||\boldsymbol{v}_{\rm s}|}\right). \tag{29}$$

Only satellites external to the mother's radius are considered while computing the distribution of angles. This leads to a sample of about 40 000 satellites, at redshift $z=0$. The distribution $\xi(\theta_{\rm vs})$ was calculated as sketched in Section 2. An isotropic distribution of $\theta_{\rm vs}$ would as usual lead to a uniform distribution $\xi(\theta_{\rm vs}) = 0$. The result is shown in Fig. 10. The error bars were computed using the same Monte Carlo simulations described before with 50 subsamples of 10 000 satellites.

We obtain a peaked distribution with a maximum for $\theta_{\rm vs}=\pi/2$ corresponding to an excess of orthogonal configuration of 5 per cent compared to a random distribution of satellite spins relative to their

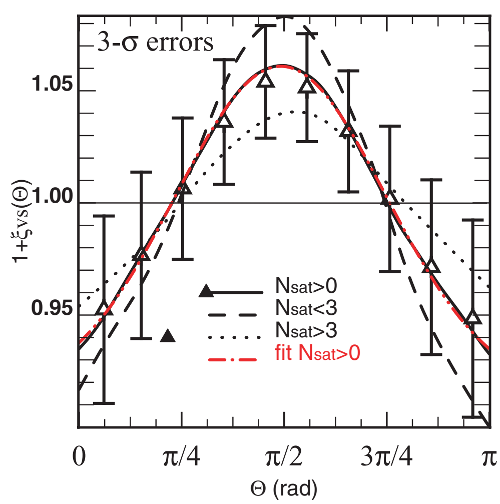

Figure 10. Excess probability, $1+\xi_{\rm vs}$, of the angle between the substructures' spin and their velocities in the mother's rest frame. The Gaussian correction was applied to take into account uncertainty on the angle determination. The distribution was measured for all mothers (solid line), mothers with at least four substructures (dotted line) and mothers with at most three substructures (dashed line). The triangles represent the mean angle distribution. The error bars represent the Monte Carlo 3σ dispersion for 50 subsamples of 10 000 haloes (out of 35 000). The dash-dotted curve (red in the online version of this article on *Synergy*) stands for the best fit of the distribution with a Gaussian function for systems with at least one satellite (see equation 13 for parametrization). The best-fitting parameters are: $a_1 = 0.2953 \pm 0.0040$, $a_1 = 1.5447 \pm 0.0015$, $a_2 = 0.8045 \pm 0.0059$ and $a_3 = 0.9144 \pm 0.0010$. In the core's rest frame, the satellites' motion is orthogonal to the direction of the satellites' spin. This configuration would fit in a picture where structures move along filamentary directions.

velocities. The substructure's motion is preferentially perpendicular to their spin. This distribution of angles for systems with at least one satellite can be fitted by a Gaussian function with the following best-fitting parameters (see equation 13): $a_1 = 0.2953 \pm 0.0040$, $a_1 = 1.5447 \pm 0.0015$, $a_2 = 0.8045 \pm 0.0059$ and $a_3 = 0.9144 \pm 0.0010$. The variation with the mother's fragmentation level is within the error bars. However, the effect of an accretion orthogonal to the direction of the spin is stronger for satellites that belong to less structured systems. This may again be related to the case where two comparable bodies revolve around each other, but from a satellite point of view. The satellite spin is likely to be orthogonal to the revolution plane and consequently to the velocity's direction.

This result was already known for haloes in filaments (Faltenbacher et al. 2002), where their motion occurs along the filaments with their spins pointing outwards. The current results show that the same behaviour is measured down to the satellite's scale. However, this result should be taken with caution since Monte Carlo tests suggest that the error (deduced from the 3σ dispersion) is about 4 per cent.

This configuration where the spins of haloes and satellites are orthogonal to their motion fits with the image of a flow of structures along the filaments. Larger structures are formed out of the merging of smaller ones in a hierarchical scenario. Such small substructures should have small relative velocities in order eventually to merge while spiralling towards each other. The filaments correspond to regions where most of the flow is laminar, hence the merging between satellites is more likely to occur when one satellite catches up with another, while both satellites move along the filaments. During such an encounter, shell crossing induces vorticity perpendicular to the flow as was demonstrated in Pichon & Bernardeau (1999). This vorticity is then converted to momentum, with a spin orthogonal to the direction of the filament.

Finally, the flow of matter along the filaments may also provide an explanation for the excess of accretion through the equatorial regions of the virial sphere. If a sphere is embedded in a 'laminar' flow, the density flux detected near the poles should be smaller than that detected near the 'equator' of the sphere. The flux measured on the sphere is larger in regions where the normal to the surface is collinear with the 'laminar' flow, i.e. the 'equator'. On the other hand, a nil flux is expected near the poles since the vector normal to the surface is orthogonal to the direction of the flow. The same effect is measured on Earth, which receives the Sun's radiance: the temperature is larger in the tropics than near the poles. Our observed excess of accretion through the equatorial region supports the idea of a filamentary flow orthogonal to the direction of the halo's spin down to scales $\leqslant$500 kpc.

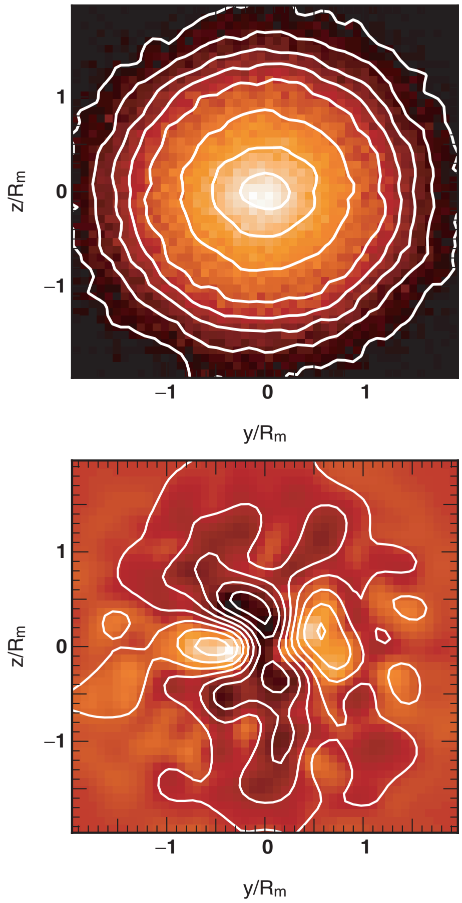

Figure 11. The projected distribution of satellites around the core's centre of mass. We used the position of 40 000 satellites around their respective core to produce a synthetic halo plus satellites (a 'mother') system. The projection is performed along the x-axis. The y and z coordinates are given in units of the mother's radius. The z-axis is collinear to the direction of the core's spin. Top: the isocontours of the number density of satellites around the core's centre of mass present a flattened shape. The number of satellites is lower in darker bins than in lighter bins. The flattened isocontours indicate that satellites lie preferentially in the plane orthogonal to the direction of the spin. Bottom: the excess number of satellites surrounding the core. We compared the distribution of satellites measured in our simulations to an isotropic distribution of satellites. Light zones stand for an excess of satellites in these regions (compared to an isotropic distribution) while dark zones stand for a lack of satellites. The satellites are more numerous in the equatorial region than expected in an isotropic distribution of satellites around the core. Also, there are fewer satellites along the spin's axis than expected for an isotropic distribution of satellites.

5 PROJECTED ANISOTROPY

5.1 Projected satellite population

We looked directly into the spatial distributions of satellites surrounding the cores of the haloes to confirm the existence of a preferential plane for the satellite locations in projection. In Fig. 11, we show the compilation of the projected positions of satellites in the core's rest frame. The result is a synthetic galactic system with 100 000 satellites in the same rest frame. We performed suitable rotations to bring the spin axis collinear to the z-axis for each system of satellites, and then we added all these systems to obtain the actual synthetic halo with 100 000 satellites. The positions were normalized using the mother's radius (which is of the order of the virial radius). A quick analysis of the isocontours of the satellite distributions indicates that satellites are more likely to be found in the equatorial plane, even in projection. The axial ratio measured at one mother's radius is $\epsilon(R_\mathrm{m}) \equiv a/b - 1 = 0.1$ with $a > b$. We compared this distribution to an isotropic 'reference' distribution of satellites surrounding the core. This reference distribution has the same average radial profile as the measured satellite distributions but with isotropically distributed directions. The result of the subtraction of the two profiles is also shown in Fig. 11. The equatorial plane (perpendicular to the z-axis) presents an excess in the number of satellites (light regions). Meanwhile, there is a lack of satellites along the spin direction (dark regions). This confirms our earlier results obtained using the alignment of orbital momentum of satellites with the core's spin, i.e. satellites lie more likely in the plane orthogonal to the halo's spin direction. Qualitatively, these results have already been obtained by Tormen (1997), where the major axis of the ellipsoid defined by the satellites' distribution is found to be aligned with the cluster's major axis. This synthetic halo is more directly comparable to observables since, unlike the dark matter halo itself, the satellites should emit light. Even though ΛCDM predicts too many satellites, its relative geometrical distribution might still be correct. In the following sections, our intent is to quantify this effect more precisely.

The propensity of satellites to lie in the plane orthogonal to the direction of the core's spin appears as an 'anti-Holmberg' effect. Holmberg (1974) and more recently Zaritsky et al. (1997) have found observationally that the distribution of satellites around discs is biased towards the pole regions. Thus if the orbital momentum vector of galaxies is aligned with the spin of their parent haloes, our result seems to contradict these observations. One may argue that satellites are easier to detect out of the galactic plane. Furthermore our measurements are carried far from the disc while its influence is not taken in account. Huang & Carlberg (1997) have shown that the orbital decay and the disruption of satellites are more efficient for coplanar orbits near the disc. This would explain the lack of satellites in the disc plane. Thus our distribution of satellites can still be made consistent with the 'Holmberg effect'.

5.2 Projected satellite orientation and spin

In addition to the known alignment on large scales, we have shown that the orientation of structures on smaller scales should be different from that expected for a random distribution of orientations. Can this phenomenon be observed? The previous measurements were carried in 3D while this latter type of observation is performed in projection on the sky. The projection 'dilutes' the anisotropy effects detected using 3D information. Thus an effect of 15 per cent may be lowered to a few per cent by projecting on the sky. However, even if the deviation from isotropy is as important as a few per cent, as we will suggest, this should be relevant for measurements involved in extracting a signal just above the noise level, such as weak lensing.

To see the effect of projection on our previous measurements, we proceed in two steps. First, every mother (halo core plus satellites) is rotated to bring the direction of the core's spin to the z-axis. Secondly, every quantity is computed using only the y and z components of the relevant vectors, corresponding to a projection along the x-axis.

The first projected measurement involves the orientation of satellites relative to their position in the core's rest frame. The spin of a halo is statistically orthogonal to the main axis of the distribution of matter of that halo (Faltenbacher et al. 2002), and assuming that this property is preserved for satellites, their spin $\boldsymbol{S}_{\rm s}$ is an indicator of their orientation. The angle, $\theta_{\rm P}$ (*in projection*), between the satellites' spin and their position vector (in the core's rest frame) is computed as follows:

$$\theta_{\rm P} = \cos^{-1}\left(\frac{\boldsymbol{S}_{\rm s}^{y,z}\cdot\boldsymbol{r}_{\rm sc}^{y,z}}{\left|\boldsymbol{S}_{\rm s}^{y,z}\right|\left|\boldsymbol{r}_{\rm sc}^{y,z}\right|}\right), \tag{30}$$

with

$$\boldsymbol{r}_{\rm sc} = \boldsymbol{r}_{\rm s} - \boldsymbol{r}_{\rm c}, \tag{31}$$

where $\boldsymbol{r}_{\rm s}$ and $\boldsymbol{r}_{\rm c}$ stand respectively for the position vector of the satellite and the core's centre of mass. Two extreme situations can be imagined. The 'radial' configuration corresponds to a case where the satellite's main axis is aligned with the radius joining the core's centre of mass to the satellite centre of mass (spin perpendicular to the radius, or $\theta_{\rm P} \sim \pi/2$). The 'circular' configuration is the case where the satellite main axis is orthogonal to the radius (spin parallel to the radius, $\theta_{\rm P} \sim 0$ [π]). These reference configurations will be discussed in what follows.

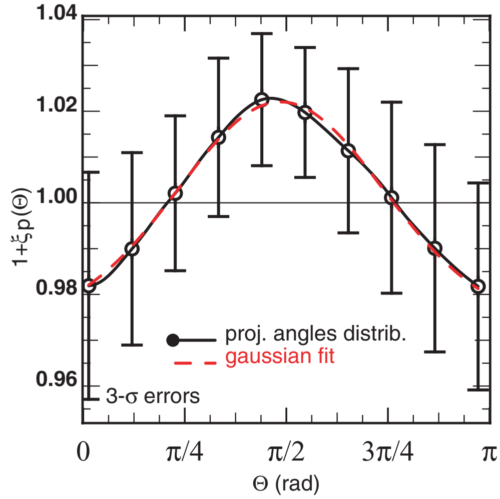

Figure 12. Excess probability, $1+\xi_{\rm P}$, of the projected angles between the direction of the spin of substructures and their position vector in the core's rest frame. The projection is made along the x-axis where the z-axis is coincident with the core's spin direction. The solid line represents the average distribution of projected angles of 50 subsamples of 50 000 substructures (out of 100 000 available substructures). The error bars represents the 3σ dispersion relative to these 50 subsamples. An isotropic distribution of orientation would correspond to a value of 1 for $1+\xi_{\rm P}$. The projection plus the reference to the position vector instead of the velocity's direction lowers the anisotropy effect. The dashed curve stands for the best Gaussian fit of the excess probability (see equation 13 for parametrization). The best-fitting parameters are: $a_1 = 0.0999 \pm 0.0030$, $a_2 = 1.5488 \pm 0.0031$, $a_3 = 0.8259 \pm 0.0131$ and $a_4 = 0.9737 \pm 0.0007$. It seems that on average the projected orientation of a substructure is orthogonal to its projected position vector.

The resulting distribution, $1+\xi_{\rm P}(\theta_{\rm P})$, is shown in Fig. 12. As before, an isotropic distribution of orientations would lead to $\xi_{\rm P}(\theta_{\rm P}) = 0$. The distribution is computed with 100 000 satellites, without the cores, while the error bars result from Monte Carlo simulations on 50 subsamples of 50 000 satellites each. As compared to the distribution expected for random orientations, the orthogonal configuration is present in excess of $\xi_{\rm P}(\pi/2) \sim 0.02$. If the spin of satellites is orthogonal to their principal axis, the direction vector in the core's rest frame is more aligned with the satellites' principal axes than one would expect for an isotropic distribution of satellite orientations. This configuration is 'radial'. The peak of the distribution is slightly above the error bars: $\Delta\xi_{\rm P}(\theta_{\rm P} \sim \pi/2) \sim 0.02$. The distribution can be fitted by the Gaussian function given in equation (13) with the following parameters: $a_1 = 0.0999 \pm 0.0030$, $a_2 = 1.5488 \pm 0.0031$, $a_3 = 0.8259 \pm 0.0131$ and $a_4 = 0.9737 \pm 0.0007$. The alignment seems to be difficult to detect in projection. With 50 000 satellites, we barely detect the enhancement of the orthogonal configuration at the 3σ level, and thus we do not expect a detection of this effect at the 1σ level for less than 6000 satellites. Nevertheless, the distribution of the satellites' orientation in projection seems to be 'radial' on dynamical grounds, without reference to a lensing potential.

Our previous measurement was 'global' since it does not take into account the possible change of orientation with the relative position of the satellites in the core's rest frame. In Fig. 13, we

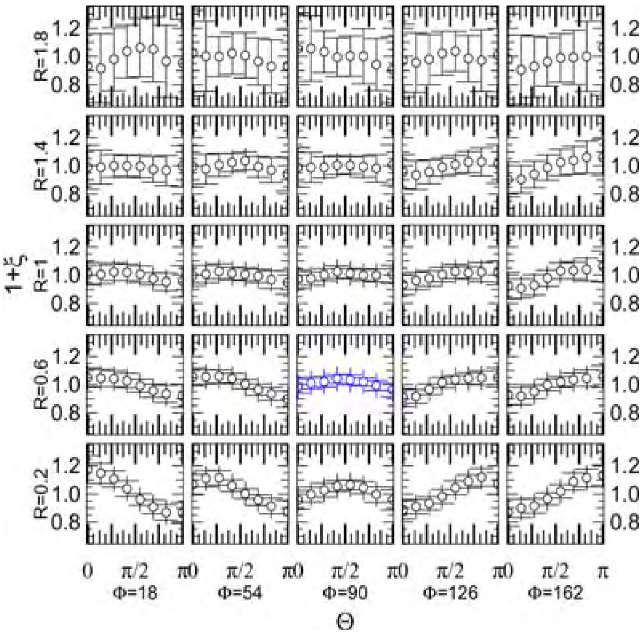

Figure 13. Radial and azimuthal grid of the excess probability, $1+\xi_{\rm P}$, of the projected angles between the direction of the spin of substructures and their direction relative to the central position of the core (as shown on average in Fig. 12). The projection is made along the x-axis where the z-axis is coincident with the direction of the core's spin. Each row represents a distance relative to the central core in the mother's radius units (from bottom to top): $R \in [0, 0.4[$, $R \in [0.4, 0.8[$, $R \in [0.8, 1.2[$, $R \in [1.2, 1.6[$ and $R \in [1.6, 2[$. Each column represents an angular distance (in degrees) relative to the direction of the core's spin (z-axis): $\phi_{\rm s} \in]0, 36]$, $\phi_{\rm s} \in [36, 72[$, $\phi_{\rm s} \in [72, 108[$, $\phi_{\rm s} \in [108, 144[$ and $\phi_{\rm s} \in [144, 180[$. The isotropic orientation distribution corresponds to a value of 1. Each sector presents a preferential direction that depends on its position relative to the spin direction of the central core. The distributions are computed using 50 samples of 50 000 satellites each. In each sector, the points represents the distribution averaged over the 50 samples. The error bars represent the 3σ Monte Carlo dispersion of the distribution over these 50 samples.

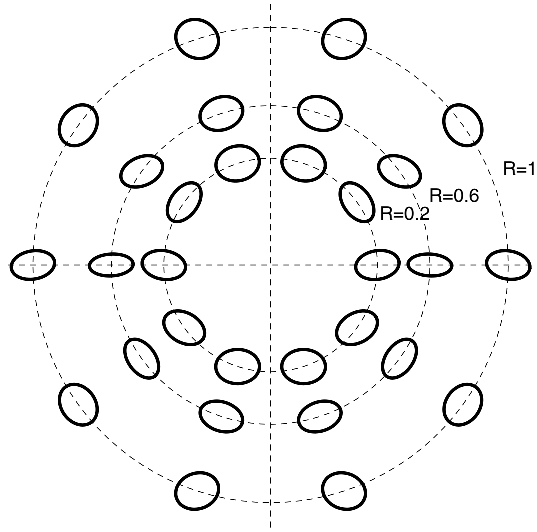

Figure 14. Geometric configuration of mean satellites around their core galaxy; each panel of Fig. 13 is represented by an ellipse at its log radius and angle around the core galaxy. The axial ratio of the ellipses is proportional to the peak-to-peak amplitude of the corresponding correlation (accounting for the relative signal-to-noise ratio), while its orientation is given by the orientation of the maximum of $1+\xi_{\rm P}$.

explore the evolution of $1+\xi_{\rm P}$ with the radial distance relative to the core's centre of mass and with the angular distance relative to the z-axis, i.e. relative to the direction of the core's spin. The previous synthetic halo was divided into sectors and, for each sector, $1+\xi_{\rm P}$ can be computed. The sectors are thus defined by their radius (in the mother's radius units): $R \leqslant 0.4$, $0.4 < R \leqslant 0.8$, $0.8 < R \leqslant 1.2$, $1.2 < R \leqslant 1.6$ and $1.6 < R \leqslant 2$; and by their polar angle relative to the direction of the core's spin (in degrees): $\phi_{\rm s} \leqslant 36$, $36 < \phi_{\rm s} \leqslant 72$, $72 < \phi_{\rm s} \leqslant 108$, $108 < \phi_{\rm s} \leqslant 144$ and $144 < \phi_{\rm s} \leqslant 180$. Each of the previous Monte Carlo subsamples can also be divided into sectors in order to compute the dispersion σ for the distributions within the subsamples. The error bars still represent the 3σ dispersions.

Fig. 14 is a qualitative representation of the results presented in Fig. 13. Each sector with $R \leqslant 1$ in Fig. 13 is represented by an ellipse at its actual position. The orientation of the ellipse is given by the angle of the maximum of the corresponding $1+\xi_{\rm P}(\theta_{\rm P})$ function. We chose to represent the spin's direction perpendicular to the ellipse's major axis. We also chose to scale the ellipse axial ratio with the signal-to-noise ratio of $1+\xi_{\rm P}(\theta_{\rm P})$. Indeed large errors lead to weak constraints on the spin orientation and the galaxy would be seen as circular on average. Conversely a strongly constrained orientation leads to a typical axial ratio of 0.5.

Two effects seem to emerge from this investigation. For some sectors, the orthogonal configuration is in excess compared to an isotropic distribution of satellites' orientation relative to the radial vector. This seems to be true especially for radii smaller than the mother's radius but the effect is still present at larger distances, especially near $\phi_{\rm s} \sim \pi/2$. Switching from low values to high values of $\phi_{\rm s}$ changes the slope of the $1+\xi_{\rm P}(\theta)$ distribution. This may be a marker of a 'circular configuration' of the orientation of satellites.

The existence of a 'radial' component in the orientation of the satellites was expected, both from the unprojected measurements made in the previous sections and from the global distribution extracted from the projected data. The fact that the 'radial' signature is stronger around the equatorial plane ($72 < \phi_{\rm s} < 108$ in Fig. 13) may be further evidence for a filamentary flow of satellites, even in projection. It seems that the existence of a 'circular' component was mostly hidden in the previous measurements by the dominant signature of the 'radial' flow. Nevertheless, the dominance of 'circular' orientations near the poles fits with the picture of a halo surrounded by satellites with their spin pointing orthogonally to the filament directions.

The 'circular' flow may alternatively be related to the flow of structures around clusters located at the connection between filaments. There are observations of such configurations (Kitzbichler & Saurer 2003), where galaxies have their spin pointing along their direction of accretion, and these observations could be consistent with our 'circular' component.

6 APPLICATIONS

Let us give here a quick overview of the implications of the previous measurements for the inner dynamics of the halo down to galactic scales. In particular, let us see how the self-consistent dynamical response of the halo propagates anisotropic infall inwards, and then briefly and qualitatively discuss the implications of anisotropy on galactic warps, disc thickening and lensing.

6.1 Linear response of galaxies

In the spirit of Kalnajs (1971) or Tremaine & Weinberg (1984), for example, we show in Appendix A and elsewhere (Aubert & Pichon 2004) how to propagate dynamically the perturbation from the virial radius into the core of the galaxy using a self-consistent combination of the linearized Boltzmann and Poisson eqnarrays under the assumption that the mass of the perturbation is small compared to the mass of the host galaxy. Formally, we have

$$\boldsymbol{r}(\boldsymbol{x}, t) = \boldsymbol{R}[F, \boldsymbol{\Omega}, \boldsymbol{x}, t - \tau](\varpi(\boldsymbol{\Omega}, \tau)), \tag{32}$$

where $\boldsymbol{R}$ is a linear operator that depends on the equilibrium state of the galactic halo (plus disc) characterized by its distribution function F, and $\boldsymbol{r}(\boldsymbol{x}, t)$ represents the self-consistent response of the inner halo at time t due to a perturbation $\varpi(\boldsymbol{\Omega}, \tau)$ occurring at time τ. Here ϖ represents formally the perturbed potential on the virial sphere and the flux density of advected momentum, mass and kinetic energy at R_{200}. A 'simple' expression for $\boldsymbol{R}$ is given in Appendix A for the self-consistent polarization of the halo. The linear operator, $\boldsymbol{R}$, follows from eqnarrays (A6), (A13) and (A16). These eqnarrays generalize the work of Kalnajs (1971) in that it accounts for a consistent infall of advected quantities at the outer edge of the halo. It is shown in particular in Appendix A that self-consistency requires the knowledge of all 10 (scalar, vector and symmetric tensor) fields $\varpi_\rho(\boldsymbol{\Omega}, \tau)$, $\varpi_{\rho v}(\boldsymbol{\Omega}, \tau)$ and $\varpi_{\rho\sigma_i\sigma_j}(\boldsymbol{\Omega}, \tau)$.

When dealing with disc broadening, $\boldsymbol{R}$ could be the velocity orthogonal to the plane of the disc, or, for the warp, its amplitude, as a function of position in the disc, $\boldsymbol{x}$ (or the orientation of each ring if the warp is described as concentric rings). More generally, it could correspond to the perturbed distribution function of the disc plus halo. The whole statistics of $\boldsymbol{R}$ is relevant. The average response $\langle \boldsymbol{r}(\boldsymbol{x}, t)\rangle$ can be written as

$$\langle \boldsymbol{r}(\boldsymbol{x}, t)\rangle = \boldsymbol{R}\langle \varpi(\boldsymbol{\Omega}, \tau)\rangle = \sum_{\ell m} \boldsymbol{R} Y_\ell^m(\boldsymbol{\Omega})\left\langle a_\ell^m\right\rangle. \tag{33}$$

Since the accretion is anisotropic, $\langle a_\ell^m\rangle$ do not converge towards zero (see Section 3.4) inducing a non-zero average response. Most importantly the two-point correlation of the response will tell us qualitatively what the correlation length and the rms amplitude of the response will be. For the purpose of this section, and to keep things simple, we will ignore temporal issues (discussed in Appendix A) altogether, for both the mean field and the cross-correlations. The two-point correlation of $\boldsymbol{r}(\boldsymbol{x})$ then depends linearly on the two-point correlation of ϖ:

$$\langle \boldsymbol{r}(\boldsymbol{x}) \cdot \boldsymbol{r}^{\mathrm{T}}(\boldsymbol{y})\rangle = \boldsymbol{R}\langle \varpi(\boldsymbol{\Omega}) \cdot \varpi^{\mathrm{T}}(\boldsymbol{\Omega}')\rangle \boldsymbol{R}^{\mathrm{T}}, \tag{34}$$

where $^{\mathrm{T}}$ stands for the transposition. Clearly, if the infall, $\varpi(\boldsymbol{\Omega})$, is anisotropic, the response will be anisotropic. As was discussed in Section 3.4, when the infall is not isotropic, we have

$$\left\langle \left|\tilde{a}_\ell^m\right|^2\right\rangle \neq \left\langle \left|\tilde{\alpha}_\ell^m\right|^2\right\rangle = \frac{1}{2\ell+1}\sum_{m=-\ell}^{m=\ell}\left\langle \left|\tilde{a}_\ell^m\right|^2\right\rangle. \tag{35}$$

Let us therefore introduce

$$\Delta \tilde{R}_\ell^m \equiv \left\langle \left|\tilde{a}_\ell^m\right|^2\right\rangle - \left\langle \left|\tilde{\alpha}_\ell^m\right|^2\right\rangle, \tag{36}$$

which would be identically zero if the field were stationary on the sphere. Here $\Delta \tilde{R}_\ell^m$ represents the anisotropic excess for each harmonic correlation. In particular, the excess polarization of the response induced by the anisotropy reads

$$\Delta\langle \boldsymbol{r}(\boldsymbol{x}) \cdot \boldsymbol{r}^{\mathrm{T}}(\boldsymbol{y})\rangle = \sum_{\ell m} \boldsymbol{R} Y_\ell^m(\boldsymbol{\Omega}) \Delta \tilde{R}_\ell^m Y_\ell^m(\boldsymbol{\Omega}')\boldsymbol{R}^{\mathrm{T}}. \tag{37}$$

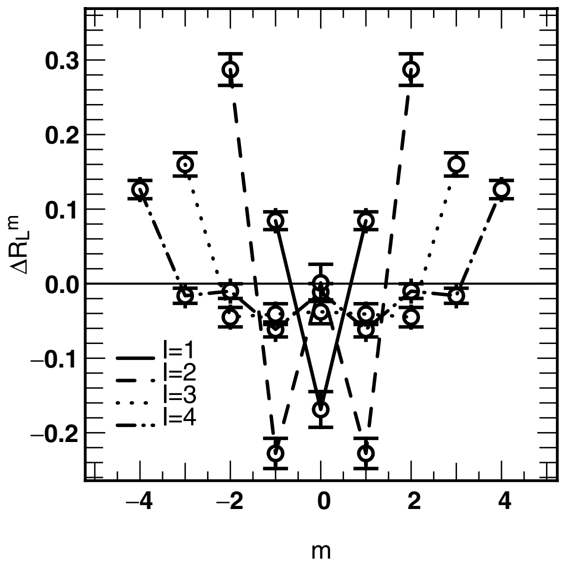

Figure 15. The residual anisotropic harmonic power spectra, $\Delta \tilde{R}_\ell^m$, introduced in equation (36) as a function of m for $\ell = 1, 2, 3, 4$. These residuals will serve as input to the computation of the dynamical response of the halo.

Fig. 15 displays $\Delta \tilde{R}_\ell^m$, for $\ell = 1, 2, 3, 4$. The different $\Delta \tilde{R}_\ell^m$ clearly converge towards different non-zero values. Consequently the response should reflect the anisotropic nature of the external perturbations.

It is beyond the scope of this paper to pursue the quantitative exploration of the response of the inner halo to a given anisotropic infall, since this would require an explicit expression of the response operator, $\boldsymbol{R}$, for each dynamical problem investigated.

6.2 Implication for warps, thick discs and lensing

In this paper, the main emphasis is on measured anisotropies. It turns out that it never exceeds 15 per cent in accretion. For a whole class of dynamical problems where anisotropy is not the dominant driving force, it can be ignored at that level. Here we now discuss qualitatively the implication of the previous measurements to galactic warps, thick discs and weak lensing where anisotropy is essential.

6.2.1 Galactic warps

The action of the torque applied on the disc of a galaxy is different for different angular and radial positions of the perturbation. Consequently the warp's orientation and its amplitude are functions of the spatial configuration of the external potential. For example, López-Corredoira et al. (2002) found that the warp's amplitude due to an intergalactic flow is dependent on the direction of the incoming 'beam' of matter. Having modelled the intergalactic flow applied to the Milky Way, they found that the warp amplitude rises steeply as the beam leaves the region coplanar to the disc and this warp amplitude reaches a maximum for an inclination of 30 degrees relative to the disc's plane. As the beam direction becomes perpendicular to the galactic plane, the warp amplitude decreases slowly. In this context, the existence of a typical spatial configuration for the incoming intergalactic matter or infalling satellites may induce a kind of 'typical' warp in the disc of galaxies.

The existence of a preferential plane for the accretion of angular momentum also implies that the recent evolution of the halo's spin has been rather smooth. Bullock et al. (2001) have shown that the angular momentum tends to remain aligned within haloes. Furthermore, the accretion of matter by haloes is preferentially performed on plunging radial orbits; thus the inner parts of haloes are aware of the properties of the recently accreted angular momentum. Therefore, a disc embedded in the halo would also 'feel' this anisotropic accretion. Ostriker & Binney (1989) have shown that the misalignment of the accreted angular momentum and the disc's spin forces the latter to slew the symmetry axis of its inner parts. The warp line of nodes is also found to be aligned with the axis of the torque applied to the disc. As stressed by Binney (1992), a non-straight line of nodes can be associated with changes in the direction of the accreted angular momentum. Using a sample of 12 galaxies, Briggs (1990) established rules of thumb for galactic warps, one of them being that the line of nodes is straight in the inner region of a disc while it is wound in the outer parts. If the angular momentum is accreted along a stationary preferential direction, as we suggest, the warp line of nodes should remain mostly straight. However, if the accretion plane differs slightly from the disc plane, more than one direction of accretion become possible (by symmetry around the vector defining the disc plane) and, as a consequence, different directions are possible for the torque induced by accreted matter. We may then consider a varying torque along accretion history, with an accreted angular momentum 'precessing' around the halo's spin but close to its direction. In this scenario, the difference in the behaviour of the warp line of nodes between the inner and outer regions of the galaxies may be explained.

6.2.2 *Galactic disc thickening*

Thin galactic discs put serious constraints on merging scenarios, since their presence implies a fine tuning between the cooling mechanisms (e.g. coplanar infall of gas) and the heating processes (merging of small virialized objects, deflection of spirals on molecular clouds). It has been shown that small mergers can produce a thick disc (e.g. Quinn, Hernquist & Fullagar 1993; Walker, Mihos & Hernquist 1996). However, the presence of old stars within the thin disc cannot be explained in the framework of the merging scenario unless a fraction of the accretion took place within the equatorial plane of the galaxy. Furthermore, the geometric characteristic of the infall is essential in the formation process of a thick disc. In Velazquez & White (1999), numerical simulations of interactions between galactic discs and infalling satellites show that the heating and thickening is more efficient for coplanar satellites. They also stressed the differences between the effect of prograde or retrograde orbits of infalling satellites (relative to the rotation of the disc): prograde orbits induce disc heating while retrograde orbits induce disc tilting. Our results indicate that the infall is preferentially prograde and coplanar relative to the halo's spin: if we consider an alignment between the halo's spin and the galaxy's angular momentum, the thickening process may be more efficient than that expected in an isotropic configuration of infalling matter. Furthermore, our estimate of the fraction of coplanar accretion at the virial scale may be considered as a lower bound near the disc since the presence of a disc will focus the infall closer to the galactic plane. In fact, Huang & Carlberg (1997) found that the disc tends to tilt towards the orbital plane of infalling prograde low-density satellites. This effect would also contribute to enhance the excess of coplanar accretion down to galactic scales.

However, the nature of infalling virialized objects was shown to affect their ability to heat or destroy the disc. Huang & Carlberg (1997) found that the presence of low-density satellites should induce preferentially a tilting of the disc instead of a thickening: one needs to enhance the relative mass of the satellite (∼30 per cent of the disc mass) to produce an observable thickening in the inner parts of the galaxy. Unfortunately such a massive satellite has a destructive impact on the outer parts of the disc. The relationship between the excess of accretion and the satellite mass should be constrained but our limited mass resolution prevents us from performing such a quantitative analysis. We should therefore aim at achieving higher angular resolution of the virial sphere and higher mass resolution in order to describe rather compact virialized objects.

6.2.3 *Gravitational lensing*

The first detection of cosmic shear was reported by four different groups in 2000 (Bacon, Refregier & Ellis 2000; Kaiser, Wilson & Luppino 2000; Van Waerbeke et al. 2000; Wittman et al. 2000). One of the basic assumptions made by cosmic shear studies is that the intrinsic ellipticities of galaxies are expected to be uncorrelated, and that the observed correlations are the results of gravitational lensing induced by the large-scale structures between those galaxies and the observer. Hence, the detection of a weak lensing signal assumes a gravitationally induced departure from a random distribution of galactic shapes. Consequently, if there exists intrinsic alignments or preferential patterns in galactic orientations, this would potentially affect the interpretation from weak lensing measurements. Several papers have already considered the 'contamination' of the weak lensing signal by intrinsic galactic alignment. Using analytic arguments, Catelan, Kamionkowski & Blandford (2001) have shown that such alignments should exist. The issue of the amplitude of the intrinsic correlations compared to the correlation induced by the cosmic shear has also been explored by Croft & Metzler (2000) and Heavens et al. (2000). The 'intrinsic' correlations may overcome the shear-induced signal in surveys with a narrow redshift range. We have shown that the orientation of satellites around haloes is not randomly distributed, which is a clear indication of intrinsic correlations for our considered scales (∼500 kpc). Taking $z_{\rm m} = 1$ as a typical median redshift for large lensing surveys, the corresponding angular scale is 1 arcmin in the cosmogony of our simulations. Furthermore, the prospect of studying the redshift evolution of gravitational clustering via shear measurements will require the investigation of narrower redshift bins and, as such, small-scale dynamically induced polarization might become an issue. As recommended by Catelan et al. (2001), our measurement may also be used as a 'numerical' calibration of the relation between ellipticity and tidal fields. Interestingly, they suggested to compensate for the finite number of galaxies around clusters by 'stacking' several clusters, which is precisely the procedure we followed to extract signal from our simulations. Finally, weak lensing predicts no 'curl' component in the shear field (e.g. Pen, Lee & Seljak 2000) and such 'curl' configurations would serve to extract the intrinsic signal. Even though satellites exhibit both 'circular' and 'radial' configurations in our simulations, we do not observe a clear signature of a 'curl' component of orientations at our level of detection.

7 CONCLUSION AND PROSPECTS

7.1 Conclusion

Using a set of 500 ΛCDM simulations, we investigated the properties of the spatial configuration of the cosmic infall of dark matter around galactic $\approx L_\star$ haloes. The aim of the present work was to find out if the existence of preferential directions existing on large scales (such as filaments) is reflected in the behaviour of matter accreted by haloes, and the answer is a clear quantitative yes.

Two important assumptions were made in the present paper. We did not consider different classes of halo mass (except for Fig. D2), but instead applied normalizations to includes all haloes in our measurements (considering, for example, the statistical average of contrasts). We also did not take into account outflows and focused on accreted quantities.

First we looked at the angular distribution of matter at the interface between the intergalactic medium and the inner regions of the haloes. We measured the accreted mass and the accreted angular momentum at the virial radius, describing these quantities as spherical fields.

(i) The total (respectively, advected) angular momentum measured at the virial radius is strongly aligned with the inner spin of the halo with a proportion of aligned configuration 30 per cent (respectively, 50 per cent) more frequent than expected in an isotropic distribution of accreted angular momentum $[1 + \xi_{LS}(0) \sim 1.5]$. This result reflects the importance of accreted angular momentum in the building of the inner spin of the haloes.

(ii) The accretion of mass measured at the virial radius in the ring-like region perpendicular to the direction of the halo's spin is $\sim$15 per cent larger than the one expected in the case of an isotropic infall of matter. We also detected the excess of accretion at the same level in the equatorial plane using a spherical harmonic expansion of the mass density flux.

(iii) In the spin's frame, the average of the harmonic $a_{\ell 0}$ coefficients does not converge towards zero, indicating that there is a systematic accretion structured in rings parallel to the equatorial plane. Using the substructure detection code ADAPTAHOP, we confirmed that the existence of a preferential plane for the infalling mass is reflected in the distribution of satellites around haloes.

(iv) Investigating the degree of alignment between the orbital momentum of satellites and the central spin of the halo, it is shown that the aligned configuration is present in excess of $\sim$12 per cent. Satellites tend to revolve in the plane orthogonal to the direction of the halo's spin. The two methods (using spherical fields and detection of satellites) yield consistent results and suggest that the image of a spherical infall on haloes should be reconsidered at the quoted level. We studied the distribution of the angle between the direction of accretion of satellites and their own spin.

(v) An orthogonal configuration is 5 per cent more frequent than would be expected for an isotropic distribution of spin and directions of accretion. Satellites tend to be accreted in the direction orthogonal to their own spin. These findings are interpreted as the results of the filamentary flows of structures, where satellites and haloes are accreted along the main direction of filaments with their spins orthogonal to this preferential direction. The flow along filaments also explains why matter is accreted preferentially in the equatorial plane at the virial radius. The halo points its spin perpendicular to the flow and sees a larger flux in the regions normal to the flow direction, i.e. near the equator. Thus, it appears that the existence of preferential directions on large scales is still relevant on galactic scales and should have consequences for the inner dynamics of the halo. We addressed the issue of observing these alignments in projection.

(vi) The distribution of satellites projected on to the sky is flattened, with an axial ratio of 1.1 at the virial radius.

(vii) It seems that the orientation of satellites around their haloes is not random, even if the 2D representation dilutes the effects of alignments. The 'radial' orientation, where the satellites main axis is aligned with the line joining the satellite to the halo centre, is $\sim$5 per cent more frequent than the one expected in a completely random distribution of orientation. The 'circular' configuration, where the satellites main axis is perpendicular to the line joining the satellite to the halo centre, is also present in excess compared to a random distribution near the pole of the host galaxy.

Table 1. Summary of the fitting parameters[a] for the angular correlations.

Angle	a_1	a_2	a_3	a_4
$\theta_{\rho\mathrm{L}}$	2.351 ± 0.006	-0.178 ± 0.002	1.343 ± 0.002	0.669 ± 0.000
$\theta_{\rho\mathrm{vrL}}$	3.370 ± 0.099	-0.884 ± 0.037	1.285 ± 0.016	0.728 ± 0.001
θ_{cs}	0.399 ± 0.003	0.059 ± 0.008	0.881 ± 0.005	0.938 ± 0.000
θ_{vs}	0.295 ± 0.004	1.544 ± 0.001	0.804 ± 0.005	0.914 ± 0.001
θ_{P}	0.099 ± 0.003	1.548 ± 0.003	0.825 ± 0.013	0.973 ± 0.000

Note. [a]Here $\theta_{\rho\mathrm{L}}$ is the angle between the halo's spin and the angular momentum measured on the virial sphere; $\theta_{\rho\mathrm{vrL}}$ is the angle between the halo's spin and the accreted angular momentum measured on the virial sphere; θ_{cs} is the angle between the core's spin and the satellite's orbital momentum; θ_{vs} is the angle between the satellite's velocity in the core's rest frame and the satellite's spin; θ_{P} is the projected angle between the satellite's spin and its direction relative to the core's position. The fitting model we used is $1 + \xi(\theta) = [a_1/(\sqrt{2\pi}a_3)]\exp[-(\theta - a_2)^2/(2a_3^2)] + a_4$.

Table 2. Summary of other quantities[a] related to anisotropic accretion.

$\langle\delta_{\mathrm{m}}\rangle(z)$	$0.0161(\pm 0.0103)z + 0.147(\pm 0.005)$
$S_3(\delta_{\mathrm{m}})$	0.44
$\epsilon(R_{\mathrm{m}})$	0.1
$\tilde{a}_{20}$	-0.65 ± 0.04
$\tilde{a}_{40}$	0.12 ± 0.02
$\tilde{a}_{60}$	-0.054 ± 0.015
$\tilde{a}_{80}$	0.0145 ± 0.0014

Note. [a]Here $\langle\delta_{\mathrm{m}}\rangle(z)$ is the redshift evolution of the average excess of accretion in the plane orthogonal to the direction of the spin; $S_3(\delta_{\mathrm{m}})$ is the skewness of the distribution of excess of accretion; $\epsilon(R_{\mathrm{m}})$ is the axial ratio $a/b - 1$ with $a > b$ of the projected satellite distribution; and $\tilde{a}_{20}$, $\tilde{a}_{40}$, $\tilde{a}_{60}$ and $\tilde{a}_{80}$ are the normalized harmonic coefficients of the 'equatorial' modes.

All corresponding fits are summarized in Tables 1 and 2, while Fig. 16 gives a schematic view of the measurements we carried out.

We investigated how the self-consistent dynamical response of the halo would propagate anisotropic infall down to galactic scales. In particular, we gave the corresponding polarization operator in the context of an open system. We have shown in Appendix A that accounting for dark matter infall required knowledge of the first three moments of the flux densities, $\varpi_\rho(\boldsymbol{\Omega}, \tau)$, $\varpi_{\rho v}(\boldsymbol{\Omega}, \tau)$ and $\varpi_{\rho\sigma_i\sigma_j}(\boldsymbol{\Omega}, \tau)$.

It is suggested that the existence of a preferential plane of accretion of matter, and thus of angular momentum, should have an influence on warp generation and disc thickening. If the anisotropic properties of infalling matter measured in the outer parts of haloes are conserved in the inner region of galaxies, there may exist a 'typical' warp amplitude and this anisotropic accretion of matter may explain the properties of warp line of nodes. In the same spirit, the efficiency of the thickening of the disc may be enhanced or reduced by equatorial accretion. Finally, our finding of intrinsic alignments

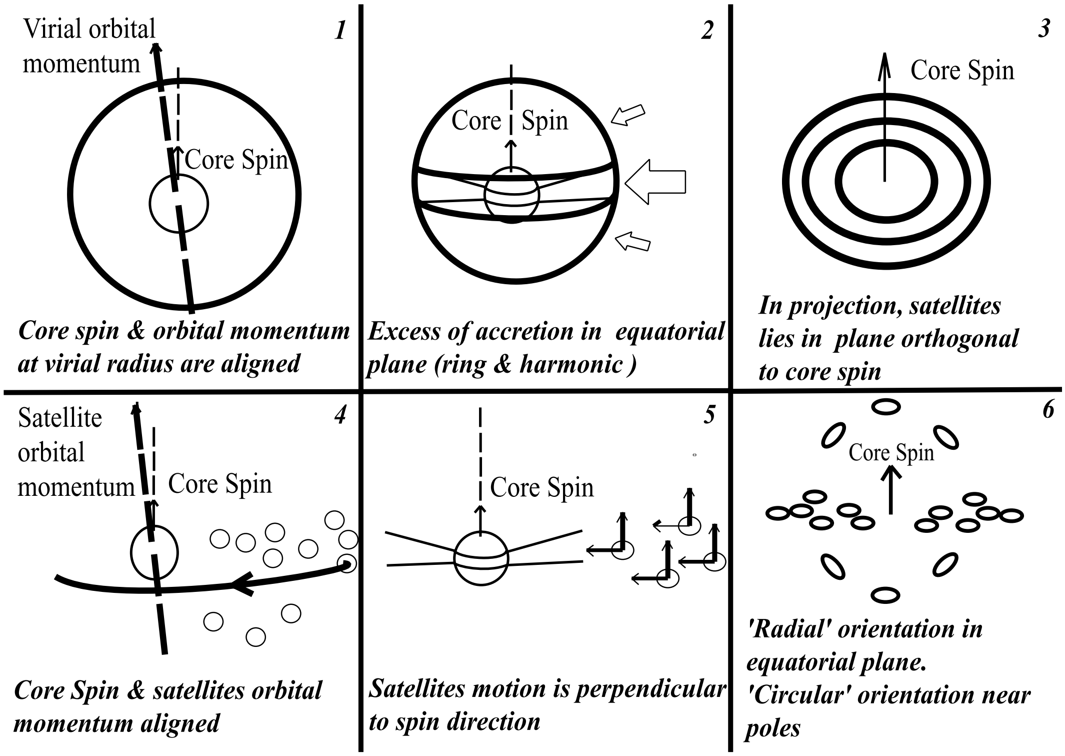

Figure 16. A schematic representation of all estimates of anisotropic accretion considered in this paper. (1) We measured the distribution of the angle between the orbital momentum on the virial sphere and the halo's spin. The average orbital momentum measured on the virial sphere is mostly aligned with the spin of the halo embedded in the virial sphere (discussed in Section 3.2). (2) We compared the accretion in the plane orthogonal to the direction of the halo's spin with the average accretion on the sphere. On the virial sphere, we detected an excess of ring-like or harmonic accretion in the equatorial plane (discussed in Sections 3.3 and 3.4). (3) In projection, we used a 'synthetic' halo to look at the distribution of satellites detected with ADAPTAHOP and at the orientation of their spin around the direction of the spin. In projection, satellites lie preferentially in the projected equatorial plane (discussed in Section 5.1). (4) We measured the angle between the halo's spin and the orbital momentum of each satellite. The orbital momentum of satellites is preferentially aligned with the spin of their hosting core (discussed in Section 4.1). (5) We compared the orientation of each satellite velocity vector (in the core's rest frame) with the orientation of their own spin. The velocity vector of satellites (in the core's rest frame) is orthogonal to the direction of their spin (discussed in Section 4.2). (6) In the equatorial plane, the projected orientation of satellites is more 'radial', while near the direction of the spin a 'circular' configuration of orientation seems to emerge (discussed in Section 5.2).

on small scales as well as specific orientations of structures should be relevant for cosmic shear studies on wide and shallow surveys.

7.2 Prospects

The main purpose of our investigation was to provide quantitative measurements of the level of anisotropy involved in the infall on scales ∼500 kpc. The next step should clearly involve working out quantitatively their implications for warp, disc heating, etc., as discussed in Section 6.

Our measurements were carried out at R_{200}, which on galactic scales is a long way from the inner region of the galaxy. One should clearly propagate the infall (and its anisotropy) towards the centre of the galaxy, and more radial infalling components will play a more important role and should be weighted accordingly. It should also be stressed that we did not take into account the extra polarization induced by the presence of an embedded disc, which will undoubtedly reinforce the polarization and the anisotropy of the infall. We also concentrated on mass accretion, as the lowest-order moment of the underlying 'fluid' dynamics. Clearly higher moments involving the anisotropically accreted momentum, the kinetic energy, etc., are dynamically relevant for the evolution of the central object as is discussed in Section 6 and in the Appendix. The time evolution of the statistics of these flux densities is also essential for the inner dynamics of the halo and should be addressed systematically as well. It will be worth while to explore different cosmologies and their implications on small-scale dynamics, and on the characteristics of infalling clumps, though we hope that the qualitative results sketched here should persist.

It should be emphasized that some aspects of the present work are exploratory only, in that the resolution achieved ($M_{\rm halo} > 5 \times 10^{12}$ M$_\odot$) is somewhat high for $L_\star$ galaxies. In fact, it would be interesting to see if the properties of infall changes for lower mass ($M_{\rm halo} < 5 \times 10^{10}$ M$_\odot$) together with the intrinsic properties of galaxies. In addition, a systematic study of biases induced by the estimators of angular correlations should be conducted, e.g. the mass-weighted errors we introduced in Section 3.2.

Observationally, the synthetic halo described in Section 5.1 could be compared to stacked satellite distributions relying on galactic surveys such as the SDSS. Once the anisotropy has been propagated to the inner regions of the galactic halo following the method sketched in Section 6, we should be in a position to compile a synthetic edge-on galactic disc and compare the flaring of the disc with the corresponding predictions. The residual preferred orientation of galactic discs around more massive objects discussed in Section 5.2 should be observed on the scales ⩽500 kpc.

Using larger simulations will allow us to combine high resolution with the statistics required to detect the anisotropic accretion of mass and angular momentum. A wide range of halo masses will become accessible and the halo mass dependence of our findings will be constrained without suffering from the lack of statistics. Better angle determinations will naturally follow from a better resolution and will improve the accuracy of our quantitative results. Resimulations (zoom simulations) should give access to a larger range of satellite masses, while we were here mostly sensitive to the biggest substructures. Large infalling objects are likely to feel differently the effects of tidal forces or dynamical friction than smaller satellites. Resimulated haloes allow us to investigate the dependence on the spatial distribution of satellites with their masses corresponding to a given cosmological environment. However, using only a few resimulations may not be sufficient to overcome cosmic variance and, given the difficulty to produce a large number of high-resolution haloes, such a project remains challenging.

The inclusion of gas physics in these simulations and their impact on the results is the natural following step. For example, gas filaments are known to be narrower than dark matter filaments, thus we would expect to see a higher level of anisotropy in the distribution of gas accreted by the haloes. Furthermore, the transmission of angular momentum from one parcel of gas to another (or to the underlying dark matter) may be highly effective and would lead to higher homogeneity of the properties of the accreted angular momentum direction, enhancing the effect of spin alignments. The loss of angular momentum from the gas to the halo will lead to a modification of our pure dark matter findings. Yet, the inclusion of gas physics in simulations would force us to address issues such as overcooling, and the requirement to take star formation and related feedback processes into account. It remains that, in the longer term, the inclusion of gas physics cannot be avoided and will give new insights into the anisotropic accretion of matter by haloes.

ACKNOWLEDGMENTS

We are grateful to J. Devriendt, J. Heyvaerts, A. Kalnajs, D. Pogosyan, E. Scannapieco, F. Stoehr, R. Teyssier and E. Thiébaut for useful comments and helpful suggestions. DA would like to thank C. Boily for reading early versions of this paper. CP would like to thank F. Bernardeau for stimulating discussions during the early part of this work. We would like to thank D. Munro for freely distributing his Yorick[1] programming language, together with its MPI interface, which we used to implement our algorithm in parallel. The simulations were carried out on the 'Pleiades' cluster, Strasbourg, at the CINES, Montpellier, and at the UKAFF, Leicester. Finally we would like to thank the referee for useful remarks on the manuscript.

REFERENCES

Aubert D., Pichon C., 2004, MNRAS, submitted
Bacon D. J., Refregier A. R., Ellis R. S., 2000, MNRAS, 318, 625
Bardeen J. M., Bond J. R., Kaiser N., Szalay A. S., 1986, ApJ, 304, 15
Bertschinger E., 2001, ApJS, 137, 1
Binney J., 1992, ARA&A, 30, 51
Briggs F. H., 1990, ApJ, 352, 15
Bullock J. S., Dekel A., Kolatt T. S., Kravtsov A. V., Klypin A. A., Porciani C., Primack J. R., 2001, ApJ, 555, 240
Catelan P., Kamionkowski M., Blandford R. D., 2001, MNRAS, 320, L7
Croft R. A. C., Metzler C. A., 2000, ApJ, 545, 561
Eisenstein D. J., Hut P., 1998, ApJ, 498, 137
Faltenbacher A., Gottlöber S., Kerscher M., Müller V., 2002, A&A, 395, 1
Goldstein H., 1950, Addison-Wesley World Student Series, Classical Mechanics. Addison-Wesley, Reading, MA
Gross M. A. K., Somerville R. S., Primack J. R., Holtzman J., Klypin A., 1998, MNRAS, 301, 81
Hatton S., Ninin S., 2001, MNRAS, 322, 576
Heavens A., Refregier A., Heymans C., 2000, MNRAS, 319, 649
Holmberg E., 1974, Arkiv Astron., 5, 305
Huang S., Carlberg R. G., 1997, ApJ, 480, 503
Jenkins A., Frenk C. S., White S. D. M., Colberg J. M., Cole S., Evrard A. E., Couchman H. M. P., Yoshida N., 2001, MNRAS, 321, 372
Jost J., 2002, Riemannian Geometry and Geometric Analysis. Springer, Berlin
Kaiser N., Wilson G., Luppino G., 2000, preprint (astro-ph/0003338)
Kalnajs A. J., 1971, ApJ, 166, 275
Kitzbichler M. G., Saurer W., 2003, ApJ, 590, L9
López-Corredoira M., Betancort-Rijo J., Beckman J. E., 2002, A&A, 386, 169
Monaghan J. J., 1992, ARA&A, 30, 543
Murali C., 1999, ApJ, 519, 580
Ostriker E. C., Binney J. J., 1989, MNRAS, 237, 785
Peirani S., Mohayaee R., De Freitas Pacheco J. A., 2004, MNRAS, 348, 921
Pen U., Lee J., Seljak U., 2000, ApJ, 543, L107
Pichon C., Bernardeau F., 1999, A&A, 343, 663
Plionis M., Basilakos S., 2002, MNRAS, 329, L47
Press W. H., Schechter P., 1974, ApJ, 187, 425
Quinn P. J., Hernquist L., Fullagar D. P., 1993, ApJ, 403, 74
Springel V., 1999, PhD thesis Ludwig-Maximilians Univ.
Springel V., White S. D. M., Tormen G., Kauffmann G., 2001a, MNRAS, 328, 726
Springel V., Yoshida N., White S. D. M., 2001b, New Astron., 6, 79
Tormen G., 1997, MNRAS, 290, 411
Tremaine S., Weinberg M. D., 1984, MNRAS, 209, 729
van Haarlem M., van de Weygaert R., 1993, ApJ, 418, 544
Van Waerbeke L. et al., 2000, A&A, 358, 30
Varshalovich D. A., Moskalev A. N., Khersonskii V. K., 1988, Quantum Theory of Angular Momentum. World Scientific, Singapore
Velazquez H., White S. D. M., 1999, MNRAS, 304, 254
Vitvitska M., Klypin A. A., Kravtsov A. V., Wechsler R. H., Primack J. R., Bullock J. S., 2002, ApJ, 581, 799
Walker I. R., Mihos J. C., Hernquist L., 1996, ApJ, 460, 121
West M. J., 1994, MNRAS, 268, 79
Wittman D. M., Tyson J. A., Kirkman D., Dell'Antonio I., Bernstein G., 2000, Nat, 405, 143
Zaritsky D., Smith R., Frenk C. S., White S. D. M., 1997, ApJ, 478, L53

APPENDIX A: LINEAR RESPONSE OF A SPHERICAL HALO TO INFALLING DARK MATTER FLUXES

In the following section, we extend to open spherical stellar systems the formalism developed by Tremaine & Weinberg (1984) and Murali (1999) by adding a source term to the collisionless Boltzmann eqnarray.[2] For an open system, the dark matter dynamics within the R_{200} sphere is governed by the collisionless Boltzmann equation coupled with the Poisson eqnarray:

$$\frac{\mathrm{d}F}{\mathrm{d}t} \equiv \frac{\partial F}{\partial t} + \{F, H\} = s^{\mathrm{e}}(\boldsymbol{r}, \boldsymbol{v}, t), \quad \text{and}$$
$$\nabla^2\Psi = 4\pi G \int \mathrm{d}^3 v F(\boldsymbol{v}), \tag{A1}$$

[1] Available at ftp://ftp-icf.llnl.gov/pub/Yorick/doc/index.html

[2] This is formally equivalent to summing the response of the halo to a point-like particle for all entering particles.

where { } is the standard Poisson bracket, $F(\boldsymbol{r}, \boldsymbol{v}, t)$ is the system's distribution function (DF) submitted to $\Psi(\boldsymbol{r}, t)$, the total gravitational potential (self-gravity plus external perturbation). The right-hand side of (A1) is non-zero because of infalling fluxes from the environment, which require adding a source term, $s^{\mathrm{e}}(\boldsymbol{r}, \boldsymbol{v}, t)$, to the Vlazov eqnarray. We may now discriminate between a stationary part corresponding to the unperturbed state from a weak time-dependent perturbation induced by the environment. Thus the DF can be written as $F = F_0 + f$. Provided the mass of the incoming flux of dark matter is small compared to the mass of the halo, we may assume that f is small compared to F_0. Similarly, the Hamiltonian H of the system can be expanded as $H_0 + \Delta H$, with $\Delta H = \psi^{\mathrm{e}} + \psi$ where ψ^{e} and ψ stand respectively for the external perturbative potential and for the small response in potential of the open system.

A1 The Boltzmann equation in action–angle

Given the periodicity of the system, the most adequate representation of a spherical halo corresponds to action–angle variables (Goldstein 1950). The linearized Boltzmann equation in such a representation is

$$\frac{\partial f_{\boldsymbol{k}}(\boldsymbol{I}, t)}{\partial t} + \mathrm{i}\boldsymbol{k}\cdot\boldsymbol{\omega}\, f_{\boldsymbol{k}}(\boldsymbol{I}, t) = \mathrm{i}\boldsymbol{k}\cdot\frac{\mathrm{d}F_0}{\mathrm{d}\boldsymbol{I}}\Delta H_{\boldsymbol{k}}(\boldsymbol{I}, t) + s^{\mathrm{e}}_{\boldsymbol{k}}(\boldsymbol{I}, t). \quad \text{(A2)}$$

The new variables are the actions $\boldsymbol{I}$ and the angles $\boldsymbol{w}$ together with the angular rates $\boldsymbol{\omega} \equiv \mathrm{d}\,\boldsymbol{w}/\mathrm{d}t$. In equation (A2) we have Fourier-expanded the linearized equation (A1) over the periodic angles:

$$X(\boldsymbol{r}, \boldsymbol{v}, t) = \sum_{\boldsymbol{k}} X_{\boldsymbol{k}}(\boldsymbol{I}, t)\exp\left(\mathrm{i}\boldsymbol{k}\cdot\boldsymbol{w}\right), \qquad \text{with}$$

$$X_{\boldsymbol{k}}(\boldsymbol{I}, t) \;=\frac{1}{(2\pi)^3}\int \mathrm{d}^3\boldsymbol{w}\,\exp(-\mathrm{i}\boldsymbol{k}\cdot\boldsymbol{w})X(\boldsymbol{r}, \boldsymbol{v}, t), \quad \text{(A3)}$$

where X is any function of $(\boldsymbol{r}, \boldsymbol{v}, t)$ with $\boldsymbol{k}$ being the Fourier triple index corresponding to the three degrees of freedom on the sphere. The equilibrium state F_0 does not depend on time or angles since it is assumed to be stationary. Then the solution to (A2) can be written as

$$f_{\boldsymbol{k}}(\boldsymbol{I}, t) = \int_{-\infty}^{t}\mathrm{d}\tau\,\exp[\mathrm{i}\boldsymbol{k}\cdot\boldsymbol{\Omega}(\tau - t)] \times\left[\mathrm{i}\boldsymbol{k}\cdot\frac{\mathrm{d}F_0}{\mathrm{d}\boldsymbol{I}}\left[\psi_{\boldsymbol{k}}(\boldsymbol{I}, \tau) + \psi^{\mathrm{e}}_{\boldsymbol{k}}(\boldsymbol{I}, \tau)\right] + s^{\mathrm{e}}_{\boldsymbol{k}}(\boldsymbol{I}, \tau)\right], \quad \text{(A4)}$$

where we have written $\Delta H_{\boldsymbol{k}}(\boldsymbol{I}, \tau) = \psi_{\boldsymbol{k}}(\boldsymbol{I}, \tau) + \psi^{\mathrm{e}}_{\boldsymbol{k}}(\boldsymbol{I}, \tau)$. We can integrate (A4) over velocities and sum over $\boldsymbol{k}$ to recover the density perturbation:

$$\rho(\boldsymbol{r}, t) = \sum_{\boldsymbol{k}}\int_{-\infty}^{t}\mathrm{d}\tau\int\mathrm{d}^3\boldsymbol{v}\Bigg\{\exp[\mathrm{i}\boldsymbol{k}\cdot\boldsymbol{\omega}(\tau - t) + \mathrm{i}\boldsymbol{k}\cdot\boldsymbol{w}] \times\left[\mathrm{i}\boldsymbol{k}\cdot\frac{\mathrm{d}F_0}{\mathrm{d}\boldsymbol{I}}\left[\psi_{\boldsymbol{k}}(\boldsymbol{I}, \tau) + \psi^{\mathrm{e}}_{\boldsymbol{k}}(\boldsymbol{I}, \tau)\right] + s^{\mathrm{e}}_{\boldsymbol{k}}(\boldsymbol{I}, \tau)\right]\Bigg\}. \quad \text{(A5)}$$

Let us expand the potential and the density over a biorthogonal complete basis function $\{\psi^{[\boldsymbol{n}]}, \rho^{[\boldsymbol{n}]}\}$ such that

$$\psi(\boldsymbol{r}, t) = \sum_{\boldsymbol{n}} a_{\boldsymbol{n}}(t)\psi^{[\boldsymbol{n}]}(\boldsymbol{r});$$

$$\rho(\boldsymbol{r}, t) = \sum_{\boldsymbol{n}} a_{\boldsymbol{n}}(t)\rho^{[\boldsymbol{n}]}(\boldsymbol{r});$$

$$\nabla^2\psi^{[\boldsymbol{n}]} = 4\pi G\rho^{[\boldsymbol{n}]};$$

$$\int\mathrm{d}^3\boldsymbol{r}\,\psi^{[\boldsymbol{n}]*}(\boldsymbol{r})\rho^{[\boldsymbol{p}]}(\boldsymbol{r}) = \delta^{\boldsymbol{n}}_{\boldsymbol{p}}. \quad \text{(A6)}$$

The external potential can be expanded along the same basis as

$$\psi^{\mathrm{e}}(\boldsymbol{r}, t) = \sum_{\boldsymbol{n}} b_{\boldsymbol{n}}(t)\psi^{[\boldsymbol{n}]}(\boldsymbol{r}). \quad \text{(A7)}$$

Note that in equation (A6) the expansion runs over a triple index $\boldsymbol{n} \equiv (n, \ell, m)$ corresponding to the radial, azimuthal and altazimuthal degrees of freedom, while in equation (A6) the three coefficients are not independent since the radial variation of the external potential is fixed by its boundary value on the sphere R_{200}. Making use of the biorthogonality, multiplying (A5) by $\psi^{[\boldsymbol{p}]*}(\boldsymbol{r})$ for some given $\boldsymbol{p}$ and integrating over $\boldsymbol{R}$ yields

$$a_{\boldsymbol{p}}(t) = \sum_{\boldsymbol{k}}\int_{-\infty}^{t}\mathrm{d}\tau\iint\mathrm{d}^3\boldsymbol{v}\,\mathrm{d}^3\boldsymbol{r}\,\exp[\mathrm{i}\boldsymbol{k}\cdot\boldsymbol{\omega}(\tau - t) + \mathrm{i}\boldsymbol{k}\cdot\boldsymbol{w}]\psi^{[\boldsymbol{p}]*}(\boldsymbol{r}) \times\left[\sum_{\boldsymbol{n}}\mathrm{i}\boldsymbol{k}\cdot\frac{\mathrm{d}F_0}{\mathrm{d}\boldsymbol{I}}\left[a_{\boldsymbol{n}}(\tau) + b_{\boldsymbol{n}}(\tau)\right]\psi^{[\boldsymbol{n}]}_{\boldsymbol{k}}(\boldsymbol{I}) + s^{\mathrm{e}}_{\boldsymbol{k}}(\boldsymbol{I}, \tau)\right]. \quad \text{(A8)}$$

A2 Self-consistency of the response

We may now swap from position–velocity to angle–action variables since $\mathrm{d}^3\boldsymbol{v}\,\mathrm{d}^3\boldsymbol{r} = \mathrm{d}^3\boldsymbol{w}\,\mathrm{d}^3\boldsymbol{I}$. In (A8) only $\psi^{[\boldsymbol{p}]}(\boldsymbol{r})$ depends on $\boldsymbol{w}$ so we may carry the $\boldsymbol{w}$ integration over $\psi^{[\boldsymbol{p}]}*$, yielding $\psi^{[\boldsymbol{p}]}*_{\boldsymbol{k}}(\boldsymbol{I})$, which leads to

$$a_{\boldsymbol{p}}(t) = \sum_{\boldsymbol{k}}\int_{-\infty}^{t}\mathrm{d}\tau\int\mathrm{d}^3\boldsymbol{I}\,\exp[\mathrm{i}\boldsymbol{k}\cdot\boldsymbol{\omega}(\tau - t)] \times\Bigg[\sum_{\boldsymbol{n}}\mathrm{i}\boldsymbol{k}\cdot\frac{\mathrm{d}F_0}{\mathrm{d}\boldsymbol{I}}\left[a_{\boldsymbol{n}}(\tau) + b_{\boldsymbol{n}}(\tau)\right]\psi^{[\boldsymbol{p}]*}_{\boldsymbol{k}}(\boldsymbol{I})\psi^{[\boldsymbol{n}]}_{\boldsymbol{k}}(\boldsymbol{I}) + s^{\mathrm{e}}_{\boldsymbol{k}}(\boldsymbol{I}, \tau)\psi^{[\boldsymbol{p}]*}_{\boldsymbol{k}}(\boldsymbol{I})\Bigg]. \quad \text{(A9)}$$

Note that the last term of equation (A9) corresponds to the modulated potential along the unperturbed trajectories weighted by the number of particles entering with $(\boldsymbol{v}, \boldsymbol{\Omega})$ at time τ. This is expected since it just reflects the fact that we could have linearly summed over all incoming individual particles (since the interaction between particles in a collisionless fluid is purely gravitational). In this sense, this term corresponds to a ray tracing problem in a variable index medium. Note also that equation (A9) does not account for dynamical friction since we integrate over the unperturbed trajectories. At this point, we expand the source term over a complete basis; this basis should also describe (known) velocity space variations. We assume that such a basis $\phi^{[\boldsymbol{n}]}(\boldsymbol{r}, \boldsymbol{v})$ exists. We write

$$s^{\mathrm{e}}(\boldsymbol{r}, \boldsymbol{v}, t) = \sum_{\boldsymbol{n}} c_{\boldsymbol{n}}(t)\phi^{[\boldsymbol{n}]}(\boldsymbol{r}, \boldsymbol{v}) \text{ so } s^{\mathrm{e}}_{\boldsymbol{k}}(\boldsymbol{I}, \tau) = \sum_{\boldsymbol{n}} c_{\boldsymbol{n}}(\tau)\sigma^{[\boldsymbol{n}]\mathrm{e}}_{\boldsymbol{k}}(\boldsymbol{I}) \text{ where } \sigma^{[\boldsymbol{n}]\mathrm{e}}_{\boldsymbol{k}}(\boldsymbol{I}) \equiv \frac{1}{(2\pi)^3}\int\mathrm{d}^3\boldsymbol{w}\exp(-\mathrm{i}\boldsymbol{k}\cdot\boldsymbol{w})\phi^{[\boldsymbol{n}]}(\boldsymbol{r}, \boldsymbol{v}). \quad \text{(A10)}$$

Calling $\boldsymbol{a}(\tau) = [a_{\boldsymbol{1}}(\tau), \ldots, a_{\boldsymbol{n}}(\tau)]$, $\boldsymbol{b}(\tau) = [b_{\boldsymbol{1}}(\tau), \ldots, b_{\boldsymbol{n}}(\tau)]$, $\boldsymbol{c}(\tau) = [c_{\boldsymbol{1}}(\tau), \ldots, c_{\boldsymbol{n}}(\tau)]$ and $\Theta(\tau)$ the Heaviside function, we define two tensors:

$$K_{\boldsymbol{pn}}(\tau) = [1 - \Theta(\tau)] \times\sum_{\boldsymbol{k}}\int\mathrm{d}^3\boldsymbol{I}\,\exp(\mathrm{i}\boldsymbol{k}\cdot\boldsymbol{\omega}\tau)\mathrm{i}\boldsymbol{k}\cdot\frac{\mathrm{d}F_0}{\mathrm{d}\boldsymbol{I}}\psi^{[\boldsymbol{p}]*}_{\boldsymbol{k}}(\boldsymbol{I})\psi^{[\boldsymbol{n}]}_{\boldsymbol{k}}(\boldsymbol{I}), \quad \text{(A11)}$$

which depends only on the halo equilibrium state via F_0, and

$$H_{pn}(\tau) = [1 - \Theta(\tau)] \times \sum_{k} \int \mathrm{d}^3\boldsymbol{I} \exp(\mathrm{i}\boldsymbol{k}\cdot\boldsymbol{\omega}\tau)\sigma_{\boldsymbol{k}}^{[n]\mathrm{e}}(\boldsymbol{I})\psi_{\boldsymbol{k}}^{[p]*}(\boldsymbol{I}), \tag{A12}$$

which depends only on the expansion basis. Then equation (A9) becomes

$$\boldsymbol{a}(t) = \int_{-\infty}^{\infty} \mathrm{d}\tau\{\boldsymbol{K}(\tau - t)\cdot[\boldsymbol{a}(\tau) + \boldsymbol{b}(\tau)] + \boldsymbol{H}(\tau - t)\cdot\boldsymbol{c}(\tau)\}. \tag{A13}$$

We now perform a Fourier transform with respect to time. Hence convolutions become multiplications and we get

$$\hat{\boldsymbol{a}}(p) = [\boldsymbol{I} - \hat{\boldsymbol{K}}(p)]^{-1}\cdot[\hat{\boldsymbol{K}}(p)\cdot\hat{\boldsymbol{b}}(p) + \hat{\boldsymbol{H}}(p)\cdot\hat{\boldsymbol{c}}(p)], \tag{A14}$$

where p stands for the frequency conjugate to time. The computation of the variance–covariance matrix is straightforward:

$$\langle\hat{\boldsymbol{a}}\cdot\hat{\boldsymbol{a}}^{*\mathrm{T}}\rangle = \langle(\boldsymbol{I} - \hat{\boldsymbol{K}})^{-1}\cdot[\hat{\boldsymbol{K}}\cdot\hat{\boldsymbol{b}} + \hat{\boldsymbol{H}}\cdot\hat{\boldsymbol{c}}]\cdot[\hat{\boldsymbol{K}}\cdot\hat{\boldsymbol{b}} + \hat{\boldsymbol{H}}\cdot\hat{\boldsymbol{c}}]^{\mathrm{T}*}\cdot(\boldsymbol{I} - \hat{\boldsymbol{K}})^{-1*\mathrm{T}}\rangle, \tag{A15}$$

where $\boldsymbol{I}$ is the identity matrix. Note that $\langle\hat{\boldsymbol{a}}\cdot\hat{\boldsymbol{a}}^{*\mathrm{T}}\rangle$ involves autocorrelation like $\langle\hat{\boldsymbol{b}}\cdot\hat{\boldsymbol{b}}^{*\mathrm{T}}\rangle$ and $\langle\hat{\boldsymbol{c}}\cdot\hat{\boldsymbol{c}}^{*\mathrm{T}}\rangle$ but also cross-correlation terms such as $\langle\hat{\boldsymbol{b}}\cdot\hat{\boldsymbol{c}}^{*\mathrm{T}}\rangle$. In other words, recalling that $\boldsymbol{b}$ and $\boldsymbol{c}$ stand respectively for the expansion coefficients of the external potential, equation (A7), and the parametrized velocity distribution, equation (A10), their cross-correlation will modify the correlation of the response of the inner halo. Two-point statistics are sufficient to characterize stationary perturbations and therefore the induced response. Nevertheless, higher statistics of the response can be easily expressed in terms of higher-order correlations of the perturbation if needed. For example, it can be shown that the three-point correlation function of the response's coefficients can be written as a function of the two- and three-point correlation of the perturbation coefficients. There are still quite a few caveats involved; for instance, it is not completely clear today that we have a good understanding of what the unperturbed distribution function of a halo plus disc should be.

A3 The source term

A possible choice[3] for the source term consistent with the first two velocity moments of the entering matter involves constructing $s^{\mathrm{e}}(\boldsymbol{r}, \boldsymbol{v}, t)$ in the following manner:

$$\begin{aligned} s^{\mathrm{e}}(\boldsymbol{r}, \boldsymbol{v}, t) &= \sum_{\boldsymbol{m}} Y_{\boldsymbol{m}}(\boldsymbol{\Omega})\frac{\delta_{\mathrm{D}}(r - R_{200})\hat{\varpi}_{\rho,\boldsymbol{m}}(t)(2\pi)^{-3/2}}{\det|\hat{\varpi}_{\rho\sigma_i\sigma_j,\boldsymbol{m}}(t)/\hat{\varpi}_{\rho,\boldsymbol{m}}(t)|} \\ &\quad\times\exp\left[-\frac{1}{2}\left(\boldsymbol{v} - \frac{\hat{\varpi}_{\rho v,\boldsymbol{m}}(t)}{\hat{\varpi}_{\rho,\boldsymbol{m}}(t)}\right)^{\mathrm{T}}\right. \\ &\quad\times\left.\left(\frac{\hat{\boldsymbol{\varpi}}_{\rho\sigma_i\sigma_j,\boldsymbol{m}}(t)}{\hat{\varpi}_{\rho,\boldsymbol{m}}(t)}\right)^{-1}\left(\boldsymbol{v} - \frac{\hat{\varpi}_{\rho v,\boldsymbol{m}}(t)}{\hat{\varpi}_{\rho,\boldsymbol{m}}(t)}\right)\right] \\ &\equiv \sum_{\boldsymbol{m}} Y_{\boldsymbol{m}}(\boldsymbol{\Omega})\delta_{\mathrm{D}}(r - R_{200})\mathcal{C}_{\boldsymbol{m}}(\boldsymbol{v}, t), \end{aligned} \tag{A16}$$

where $\boldsymbol{m}$ stands for the two harmonic numbers, (ℓ, m) and $Y_{\boldsymbol{m}}(\boldsymbol{\Omega}) \equiv Y_\ell^m(\boldsymbol{\Omega})$. Here the Dirac function $\delta_{\mathrm{D}}(r - R_{200})$ is introduced since we measure the source terms at the virial radius. The global form is Gaussian and is constructed using $\hat{\varpi}_{\rho,\boldsymbol{m}}$, $\hat{\varpi}_{\rho v,\boldsymbol{m}}$, $\hat{\varpi}_{\rho\sigma_i\sigma_j,\boldsymbol{m}}$, the harmonic components of respectively the mass flux density field, velocity flux density vector field and the specific kinetic energy flux density tensor field measured on the R_{200} sphere. When taking the successive moments of this flux distribution over velocity, we get

$$\begin{aligned} \int \mathrm{d}^3\boldsymbol{v}s^{\mathrm{e}}(\boldsymbol{r}, \boldsymbol{v}) &= \varpi_\rho(\boldsymbol{r}), \\ \int \mathrm{d}^3\boldsymbol{v}\boldsymbol{v}s^{\mathrm{e}}(\boldsymbol{r}, \boldsymbol{v}) &= \varpi_{\rho v}(\boldsymbol{r}), \end{aligned} \tag{A17}$$

while

$$\begin{aligned} &\int \mathrm{d}^3\boldsymbol{v}\left(v_i - \frac{\varpi_{\rho v,i}}{\varpi_\rho}\right)\left(v_j - \frac{\varpi_{\rho v,j}}{\varpi_\rho}\right)s^{\mathrm{e}}(\boldsymbol{r}, \boldsymbol{v}) \\ &= \varpi_{\rho\sigma_i\sigma_j}(\boldsymbol{r}) + \left[\sum_{\boldsymbol{m}} Y_{\boldsymbol{m}}(\boldsymbol{\Omega})\delta(r - R_{200})\frac{\hat{\varpi}_{\rho v,\boldsymbol{m}}(t)^2}{\hat{\varpi}_{\rho,\boldsymbol{m}}(t)} - \frac{\varpi_{\rho v}(\boldsymbol{r})^2}{\varpi_\rho(\boldsymbol{r})}\right] \\ &\approx \varpi_{\rho\sigma_i\sigma_j}(\boldsymbol{r}), \end{aligned} \tag{A18}$$

so that the Ansatz, equation (A16), satisfies the first two moments, and approximately the third moment of the fluid eqnarrays. Let us now expand $\mathcal{C}_{\boldsymbol{m}}(\boldsymbol{v}, t)$ over a linear complete basis, say b-splines covering the radial velocity component and spherical harmonics for the angle distribution of the velocity vector:

$$\mathcal{C}_{\boldsymbol{m}}(\boldsymbol{v}, t) = \sum_\alpha C_{\boldsymbol{m},\alpha}(t)b_\alpha(\boldsymbol{v}). \tag{A19}$$

The particular choice of equation (A16) has led to the parametrization

$$c_{\boldsymbol{n}}(t) = C_{\boldsymbol{m},\alpha}(t) \quad \text{and} \quad \phi^{[\boldsymbol{n}]}(\boldsymbol{r}, \boldsymbol{v}) = b_\alpha(\boldsymbol{v})Y_{\boldsymbol{m}}(\boldsymbol{\Omega})\delta_{\mathrm{D}}(r - R_{200}), \tag{A20}$$

while equation (A10) becomes

$$\sigma_{\boldsymbol{k}}^{[\boldsymbol{n}]\mathrm{e}}(\boldsymbol{I}) = \frac{1}{(2\pi)^3}\int \mathrm{d}^3\boldsymbol{w}\exp(-\mathrm{i}\boldsymbol{k}\cdot\boldsymbol{w})Y_{\boldsymbol{m}}[\boldsymbol{\Omega}(\boldsymbol{I}, \boldsymbol{w})]b_\alpha \times(\boldsymbol{v}[\boldsymbol{I}, \boldsymbol{w}])\delta_{\mathrm{D}}(r(\boldsymbol{I}, \boldsymbol{w}) - R_{200}). \tag{A21}$$

Note that we can make use of the δ_{D} function occurring in equation (A21) since $w_r \equiv \tilde{w}_r(r, \boldsymbol{I})$. Therefore equation (A21) reads:

$$\begin{aligned} \sigma_{\boldsymbol{k}}^{[\boldsymbol{n}]\mathrm{e}}(\boldsymbol{I}) &= \int\frac{\mathrm{d}^2\boldsymbol{w}}{(2\pi)^3}\int \mathrm{d}w_r\exp(-\mathrm{i}\boldsymbol{k}\cdot\boldsymbol{w})Y_{\boldsymbol{m}}[\boldsymbol{\Omega}(\boldsymbol{I}, \boldsymbol{w})]b_\alpha \\ &\quad\times(\boldsymbol{v}[\boldsymbol{I}, \boldsymbol{w}])\frac{1}{|\partial\tilde{w}_r/\partial r|^{-1}}\delta_{\mathrm{D}}(w_r - \tilde{w}_r[R_{200}, \boldsymbol{I}]), \\ &= \int\frac{\mathrm{d}^2\boldsymbol{w}}{(2\pi)^3}\exp(-\mathrm{i}\boldsymbol{k}\cdot\boldsymbol{w})Y_{\boldsymbol{m}}[\boldsymbol{\Omega}(\boldsymbol{I}, \boldsymbol{w}, \tilde{w}_r[R_{200}, \boldsymbol{I}])]b_\alpha \\ &\quad\times(\boldsymbol{v}[\boldsymbol{I}, \boldsymbol{w}, \tilde{w}_r(R_{200}, \boldsymbol{I})])\frac{\omega_r(\boldsymbol{I})}{|\dot{r}(R_{200}, \boldsymbol{I})|} \\ &\quad\times\exp(-\mathrm{i}k_r\cdot\tilde{w}_r[R_{200}, \boldsymbol{I}]). \end{aligned} \tag{A22}$$

In equation (A22) we sum over all intersections of the orbit $\boldsymbol{I}$ with the R_{200} sphere, at the radial phase corresponding to that intersection (with a weight corresponding to $\omega_r/|\dot{r}|$).

Given eqnarrays (A6), (A16) and (A22), equation (A13) can be recast formally as

$$\rho(\boldsymbol{r}, t) = \boldsymbol{R}\{F_0, t, \tau, \boldsymbol{\Omega}\} \times[\psi_{\mathrm{e}}(\boldsymbol{\Omega}, \tau), \varpi_\rho(\boldsymbol{\Omega}, \tau), \varpi_{\rho v}(\boldsymbol{\Omega}, \tau), \varpi_{\rho\sigma_i\sigma_j}(\boldsymbol{\Omega}, \tau)], \tag{A23}$$

which corresponds to the form given in the main text in equation (32). It should be emphasized once again that the splitting of the gravitational field into two components, one outside of R_{200}, and one inside, via point particles obeying the distribution $s_{\mathrm{e}}(\boldsymbol{r}, \boldsymbol{v}, t)$ is completely arbitrary from the point of view of the dynamics. In fact,

[3] An alternative choice is made in Aubert & Pichon (2004) to account for the bimodality of the velocity distribution.

one should account that $\psi_{\rm e}(\boldsymbol{\Omega}, t)$ should be switched on long before any particles enter R_{200} since no particle is created at the boundary. This last constraint is clearly satisfied by our simulations.

APPENDIX B: ADAPTAHOP: A SUBSTRUCTURE FINDER BASED ON SADDLE POINT HANDLING

Dark matter haloes can contain a hierarchy of subhaloes, which can be viewed as a tree of structures and substructures. Given a mass resolution (a finite number of particles such as in our N-body simulations), there is a limit to this hierarchy, which can be formalized as an ensemble of leaves in a tree. The goal here is to draw this tree by applying the simplest principles of Morse theory (e.g. Jost 2002). Morse theory basically involves relating the topology of an excursion, e.g. the regions of space with density above a given threshold, $\rho > \rho_{\rm t}$, to the set of critical points it contains, $\{\boldsymbol{x}, \nabla\rho(\boldsymbol{x}) = 0\}$, and to the field lines connecting these points together, i.e. the curves obtained by following the gradient of the density field. In that approach, the smallest substructures, which are the leaves of the tree, can be identified as peak patches, i.e. ensembles of field lines converging to the same local maximum. The connectivity between substructures is ruled by the saddle points, which are local maxima in the surfaces defining the contours of the peak patches: from the knowledge of these saddle points and the local maxima they connect, it is possible to extract the full tree of structures (haloes) and substructures (subhaloes) in four steps:

(i) In order to eliminate, at least partly, the effects of Poisson noise and to have an estimate of the local density as close as possible to a Morse function,[4] while conserving as much as possible details of the distribution, we perform adaptive smoothing of this distribution with the standard SPH technique (smooth particle hydrodynamics, e.g. Monaghan 1992). This smoothing assumes that each particle is a smooth spherical cloud of given radius R, e.g. a spline $S(r)$. For each particle, the list of its $N_{\rm SPH}$ closest neighbours is found, typically $N_{\rm SPH}$ of a few tens (here we take $N_{\rm SPH} = 64$). The distance from the furthest neighbour fixes R, while the SPH density at the particle of interest is estimated by a summation over its neighbours with weight $S(r)$. To find rapidly the closest neighbours of each particle, we use a standard Oct-tree algorithm, which decomposes hierarchically space in subcells until they contain zero or one particle.

(ii) The leaves of the tree of structures and substructures are identified while associating each particle to the peak patch to which it belongs. This is performed by a simple walk from particle to particle, while following the gradient until convergence: at each step of the walk, the SPH density of the particle is compared to its $N_{\rm HOP}$ closest neighbours (which were stored during the SPH smoothing step), the particle for the next step of the walk being the one with the largest SPH density. We take $N_{\rm HOP} = 16$, as advocated by Eisenstein & Hut (1998).

(iii) For each leaf of the tree, the connections with the other leaves are created by searching the saddle points on the intersecting surfaces $\mathcal{S}_{ij}$ between peak patches i and j. Each surface $\mathcal{S}_{ij}$ is made of particles belonging to one of the peak patches and having at least one of their closest neighbours among $N_{\rm HOP}$ in the other peak patch, and vice versa. If the set $\mathcal{S}_{ij}$ contains only particles belonging to i or only particles belonging to j, the connection between i and j is considered as non-significant (because non-symmetric) and eliminated. Saddle points are local maxima in $\mathcal{S}_{ij}$. To establish the connectivity as a function of a density threshold, only the highest saddle point matters, when there are several. The search for this saddle point involves finding the maximum of the SPH density among particles belonging to S_{ij}. We proceed as follows to estimate accurately the SPH density in S_{ij}. For each particle A in S_{ij}, say belonging to peak patch i and with density ρ_A, we consider the list of its closest neighbours among $N_{\rm HOP}$ belonging to peak patch j, with density ρ_k, $k = 1, \ldots, N_j \leqslant N_{\rm HOP}$. The density associated to this particle in $\mathcal{S}_{ij}$ is then given by $\rho = \min(\rho_A, \rho_k)$. By applying this procedure, we locate accurately S_{ij} and avoid slight overestimation of the SPH density at the saddle point.

(iv) It is possible to build the tree of structures and substructures when the list of neighbouring leaves to which a given leaf is connected is given, as well as the corresponding saddle points. This is performed recursively by increasing progressively a threshold parameter, $\rho_{\rm t}$, from an initial value, $\rho_{\rm TH}$, corresponding to the typical overdensity used to select galaxy haloes, here called structures. A typical choice for $\rho_{\rm TH}$ is $\rho_{\rm TH} = 81$, which corresponds approximately to friends-of-friends haloes selected with a linking parameter $b = 0.2$ (e.g. Eisenstein & Hut 1998). Suppose we are at step n of the process and let us compute step $n + 1$. At this point, we are sitting on a branch of the tree – a structure or a substructure – and we aim to draw the details of this branch. This (sub)structure contains a number of peak patches connected by saddle points of densities $\rho_{\rm s}$. For the considered value of $\rho_{\rm t}$, the connections inside that (sub)structure are examined and destroyed when $\rho_{\rm s} < \rho_{\rm t}$. The (sub)structure is then broken into as many components as necessary. During the process, the particles above $\rho_{\rm t}$ belonging to each subcomponent are tagged, which allows us to determine at any time various properties of a given (sub)structure, namely the number of particles it contains, its mass, its average and maximum SPH density, for possible application to various morphological criteria of selection. One such criterion is Poisson noise. In order to assess if a given substructure containing N particles should be considered as statistically significant compared to Poisson noise, its average density must be sufficiently significant compared to $\rho_{\rm t}$:

$$\langle\rho\rangle_{\rm substructure} > \rho_{\rm t}\left(1 + \frac{f_{\rm Poisson}}{\sqrt{N}}\right), \tag{B1}$$

where $f_{\rm Poisson}$ is a '$f_{\rm Poisson}\sigma$' detection parameter, typically a few units. A good choice is $f_{\rm Poisson} = 4$. If the substructure is below this threshold, it disappears, i.e. it is not considered in the next step of the recursion. At the end of the selection, two situations are possible: (i) two substructures or more are detected and new nodes are created in the tree; (ii) the (sub)structure was not broken into multiple components and nothing happens at this step. The process is then repeated on the new substructures by increasing locally the threshold $\rho_{\rm t}$:

$$\rho_{\rm t} \rightarrow \rho_{\rm t}\left(1 + \frac{f_{\rm Poisson}}{\sqrt{N}}\right), \tag{B2}$$

until there is only one peak patch in the (sub)structure. Note that the Poisson noise selection, equation (B1) is not applied to the haloes when $\rho_{\rm t} = \rho_{\rm TH}$.

At the end of the process, one obtains a tree of structures and substructures, each node of the tree corresponding to a (sub)structure, with its position, its number of particles, its mean square radius, its average and maximum SPH density, and the density $\rho_{\rm s}$ of the highest saddle point that connects it to another substructure. In addition, a flag is given to each particle. This flag is a pointer to the

[4] That is, a smooth function such that the ensemble of critical points is discrete and the matrix of second derivatives in their neighbourhood is non-degenerate.

closest possible node to a leaf (if not a leaf), which allows one to find recursively the list of particles belonging to any (sub)structure and thus perform some more elaborate post-treatment, such as some relying on dynamical prescriptions (boundedness). The difficulty in that case is to estimate accurately the gravitational potential. Its computation can be rather costly, since 'peeling' the (sub)haloes requires iterating several forward and backward walks in the tree of structures and substructures with corresponding calculations of the gravitational potential. Our prescription is therefore at the present time purely morphological and does not involve the estimate of the gravitational potential. The current implementation is rather fast, most of the CPU time being taken by the SPH smoothing, e.g. 1–3 h on 16 million particles on current fast scalar processors.

Our algorithm is called ADAPTAHOP since we aim to improve HOP Eisenstein & Hut (1998): the first two steps above are exactly the same as in HOP, but the last two are different. Indeed, in HOP, the idea is to combine information on the saddle point densities, ρ_s, on the local maxima, $\rho_{\max}$, inside a connected set of peak patches to decide whether it has to be broken into multiple *disjoint haloes*. The aim of HOP is indeed to improve standard friends-of-friends methods in order to obtain more compact and spherical haloes. The goal of ADAPTAHOP is quite different since it focuses on substructure detection.

In spirit, ADAPTAHOP is in fact very similar to the substructure finder of Springel (1999): SUBFIND (see also Springel et al. (2001a)). Of course, there is a major difference, since SUBFIND has in addition a sophisticated dynamical prescription involving exact calculation of the gravitational potential. Springel uses also a slightly more elegant method to construct the tree of structures and substructures prior to dynamical post-treatment. After step one above, the idea is to rank the particles by decreasing density and treat them in this order. Investigating the distribution of particles in such a way is equivalent to examining isocontours of decreasing density. It uses (as in ADAPTAHOP) the closest neighbours of a particle to decide if the particle examined during the process (i) creates a new (sub)structure since it is isolated, (ii) belongs to an existing substructure or (iii) connects two substructures, which makes the construction of the tree of structures and substructures much simpler than in ADAPTAHOP and more accurate, since there is no need to use the threshold parameter ρ_t. In SUBFIND, no treatment is made to account for the local Poisson noise: it is not necessary because of the dynamical post-processing, which destroys unbounded structures.

It is important to note that since ADAPTAHOP has no dynamical post-treatment, it gives slightly different results compared to SUBFIND in its present form. In particular, for a given sufficiently massive dark matter halo, SUBFIND (Springel et al. 2001a) describes it in terms of a large, smooth central component, and a bunch of much less massive subhaloes. In ADAPTAHOP, the result is quite similar, except that the central component is much less spatially extended (it is extended up to the isocontour level corresponding to the saddle point connecting it to a subhalo), and it is therefore less massive.

Fig. B1 illustrates how well ADAPTAHOP performs in one of the simulations we realized for this work, for the most massive halo detected in this realization.

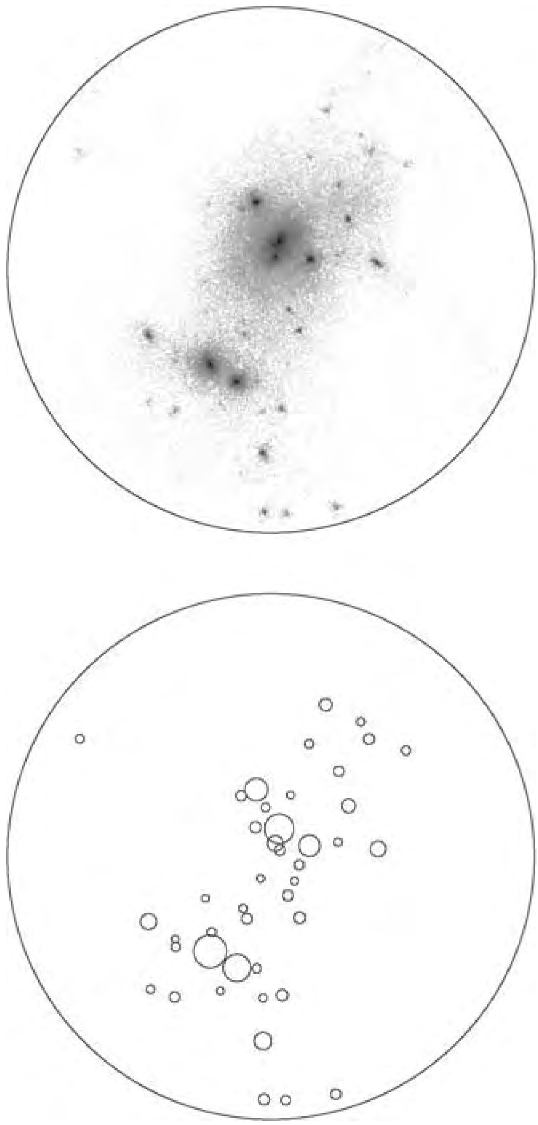

Figure B1. Illustration of the output of ADAPTAHOP for one of the simulations of this work. A sphere of radius 5 Mpc centred on the most massive halo is represented. In the upper panel, the dark matter density is shown using a logarithmic scale. Darker regions correspond to higher density contrasts. The lower panel displays the detected subhaloes (i.e. the most elementary structures corresponding to the peak patches or the leaves of the tree). The size of the circle scales with $M^{1/3}$, where M is the mass of the subhalo. Most of the subhaloes seen on the figure belong to the most massive halo. Clearly, ADAPTAHOP is rather successful at detecting all the significant substructures.

APPENDIX C: STATISTICS ON THE SPHERE

When dealing with spherical fields, there are different ways to characterize their angular structure. In the present paper, we essentially deal with centred statistics, i.e. we describe the angular structuration of scalar or vector fields relative to a specific direction, defined by the halo or satellite's spin $\boldsymbol{S}$. Let us first formally introduce filtering on the sphere, statistical and angular averages, and present one-point statistics (probability distribution functions) while postponing two-point statistics (correlation functions, or excess probability of joint events) to Aubert & Pichon (2004).

C1 One-point statistics

For any field, x, on the sphere, let us introduce the smoothed field, $(x)_\alpha$ (filtered on scale α), as

$$(x)_\alpha(\boldsymbol{\Omega}) \equiv \frac{1}{\int \Theta_\alpha(\boldsymbol{\Omega}')\,\mathrm{d}\boldsymbol{\Omega}'} \int \Theta_\alpha(\boldsymbol{\Omega}' - \boldsymbol{\Omega}) x(\boldsymbol{\Omega}')\,\mathrm{d}\boldsymbol{\Omega}' \quad \text{(C1)}$$

$$\equiv \int w_\alpha(\boldsymbol{\Omega} - \boldsymbol{\Omega}') x(\boldsymbol{\Omega}')\,\mathrm{d}\boldsymbol{\Omega}', \quad \text{(C2)}$$

where Θ_α stands for the top-hat function,

$$\Theta_\alpha(\boldsymbol{\Omega}) = 1 \qquad \text{if} \qquad |\vartheta| \leqslant \alpha, \tag{C3}$$

and w_α is defined by equation (C7), the standard top-hat filter on the sphere.

Consider now the centred top-hat-filtered (on scale α) field, $[x]_\alpha$, defined by

$$[x]_\alpha \equiv (x)_\alpha(\pi/2), \tag{C4}$$

$$\equiv \frac{1}{\int \Theta_\alpha(\boldsymbol{\Omega}')\,\mathrm{d}\boldsymbol{\Omega}'}\int \Theta_\alpha(\vartheta' - \pi/2) x(\boldsymbol{\Omega}')\,\mathrm{d}\boldsymbol{\Omega}', \tag{C5}$$

$$\equiv \int W_\alpha(\boldsymbol{\Omega}') x(\boldsymbol{\Omega}')\,\mathrm{d}\boldsymbol{\Omega}'. \tag{C6}$$

Note that equation (C6) defines W_α. Our filtering is now centred, in that the average is carried out on a window that is centred at the equatorial plane (since in this paper we are interested in the polarization of accretion processes with respect to that plane). Let us also introduce the average of x on the sphere, as

$$\bar{x} \equiv (x)_{\pi/2} = \frac{1}{\int\,\mathrm{d}\boldsymbol{\Omega}}\int x(\boldsymbol{\Omega})\,\mathrm{d}\boldsymbol{\Omega}. \tag{C7}$$

We may also for a given x define its contrast as

$$\delta_x \equiv \frac{x}{\bar{x}} - 1. \tag{C8}$$

Note that, in contrast to standard cosmology, we expect that $\bar{x} \neq \langle x \rangle$, (i.e. no ergodicity) since the angular average over one virial sphere is not representative of the whole cosmological set, and since $\langle x \rangle$ depends on ϑ whereas $\bar{x}$ does not. As a consequence,

$$\langle \delta_x \rangle = \left\langle \frac{x}{\bar{x}} \right\rangle - 1 \neq \frac{\langle x \rangle}{\langle \bar{x} \rangle} - 1.$$

Consider now the top-hat-filtered centred flux density contrast, $[\delta_\varpi]_\alpha$, defined by

$$[\delta_\varpi]_\alpha \equiv (\delta_\varpi)_\alpha(\pi/2) = \frac{1}{\bar{\varpi}}\int W_\alpha(\boldsymbol{\Omega})\varpi\,\mathrm{d}\boldsymbol{\Omega} - 1. \tag{C9}$$

Since, by construction, $[\delta_\varpi]_\alpha$ is a filtered version of δ_ϖ, it inherits some of it statistical properties. In particular, the PDFs of $\delta_\varpi(\pi/2)$ and $[\delta_\varpi]_\alpha$ should be quite similar provided α is small enough.

In the main text, we consider the anisotropic parameter, $\delta_\mathrm{m} \equiv [\delta_{\rho v_r}]_{\pi/8}$, which therefore corresponds formally to the centred top-hat-smoothed (on scales of $\pi/8$) mass flux density contrast. Following the same spirit, we could also consider quantities such as $[\delta_{\rho v_r v^2}]_{\pi/8}$, which would measure the anisotropy in the accreted kinetic energy: the excess of accreted kinetic energy should allow us to track the excess of incoming virialized objects in the equatorial plane without performing their explicit identification. One should also consider $[\delta_{\rho v_r L}]_{\pi/8}$, the anisotropy in the accreted momentum, since this quantity is directly related to the torque applied to the system by the infall. More generally still we could investigate $(\delta_\varpi)_\alpha(\vartheta)$, the flux density contrast top-hat-smoothed on a ring of size α centred on ϑ.

Note that we can think of the harmonic coefficients, a_ℓ^m, introduced in Section 3.4, as a specific type of filtering, where the window function, W_α, is replaced by an axisymmetric spherical harmonic, $Y_\ell^0(\boldsymbol{\Omega})$:

$$[\delta_\varpi]_\ell = \frac{1}{\bar{\varpi}}\int Y_\ell^{0*}(\boldsymbol{\Omega})\varpi(\boldsymbol{\Omega})\,\mathrm{d}\boldsymbol{\Omega} = \frac{a_\ell^0}{\bar{\varpi}}. \tag{C10}$$

We can also write $\bar{\varpi}$ in terms of spherical harmonics:

$$\bar{\varpi} \equiv \frac{1}{4\pi}\int \varpi\,\mathrm{d}\boldsymbol{\Omega} = \frac{1}{\sqrt{4\pi}}\int Y_0^{0*}(\boldsymbol{\Omega})\varpi\,\mathrm{d}\boldsymbol{\Omega} = \frac{a_0^0}{\sqrt{4\pi}}. \tag{C11}$$

Therefore we obtain

$$[\delta_\varpi]_\ell = \frac{a_\ell^0}{\mathrm{sign}\left(a_0^0\right)\sqrt{C_0}}, \tag{C12}$$

where $C_0 = |a_0^0|^2/4\pi$ is the $\ell = 0$ component of the angular power spectrum C_ℓ.

Since a step function can be expanded along spherical harmonics as

$$\Theta_\alpha(\vartheta - \pi/2) = \sum_\ell b_\ell Y_\ell^0(\vartheta, 0), \tag{C13}$$

then $[\delta_\varpi]_\alpha$ defined by equation (C9) obeys

$$[\delta_\varpi]_\alpha = \sum_\ell b_\ell [\delta_\varpi]_\ell - 1. \tag{C14}$$

Taking $x = \rho v_r$ for example, we have

$$\delta_{[\rho v_r]}(\vartheta, \varphi) = \sum_{\ell, m} d_\ell^m Y_\ell^m(\vartheta, \varphi) = \frac{\rho v_r(\vartheta, \varphi)}{\overline{\rho v_r}} - 1, \tag{C15}$$

where

$$\overline{\rho v_r} = \frac{1}{4\pi}\int \mathrm{d}\vartheta\,\mathrm{d}\varphi \rho v_r(\vartheta, \varphi)\sin\vartheta = \frac{a_0^0}{\sqrt{4\pi}}. \tag{C16}$$

Since

$$\int \mathrm{d}\vartheta\,\mathrm{d}\varphi Y_\ell^m(\vartheta, \varphi)\sin\vartheta = \sqrt{4\pi}\delta_{l0}\delta_{m0}$$

(e.g. Varshalovich et al. 1988), we find

$$d_\ell^m = \tilde{a}_\ell^m - \sqrt{4\pi}\delta_{l0}\delta_{m0}. \tag{C17}$$

We finally obtain

$$\delta_{[\rho v_r]}(\vartheta, \varphi) = \sum_{\ell, m} \tilde{a}_\ell^m Y_\ell^m(\vartheta, \varphi) - 1. \tag{C18}$$

APPENDIX D: CONVERGENCE ISSUES

D1 Substructures and spins of haloes

For each tree of substructure satellites, we computed the total spin inside the mother structure, $\boldsymbol{S}_\mathrm{M}$, and the momentum of each substructure inside the mother structure, $\boldsymbol{L}_\mathrm{s}$. Then we compared the inner satellites and the contribution of the core to the mother's spin. The comparison is only made on the components of the substructures' momentum parallel to $\boldsymbol{S}_\mathrm{M}$. The results are shown in Fig. D1. We plotted the *total* contribution of satellites to the mother's spin versus the core's contribution. From the barycentre of the distribution shown in Fig. D1, it appears that substructures contain about 80 per cent of the total host's spin, with a satellites' contribution of 50 per cent and about 30 per cent for the core. The bottom panel shows the total contribution of substructures to the mother's mass versus the contribution of the core. As expected, given the definition of the core, we found that the relative proportions are almost reversed compared to the previous plot. A core contains about half of the total mass while satellites represent about 40 per cent of the total mass. Clearly the specific angular momentum is larger in satellites than in the core. The distance of satellites relative to the mother's centre and their velocities induce a 'lever arm' effect. Even if satellite remnants are light in terms of mass they are important if not dominant for the spin of the galactic system. This effect also suggests that

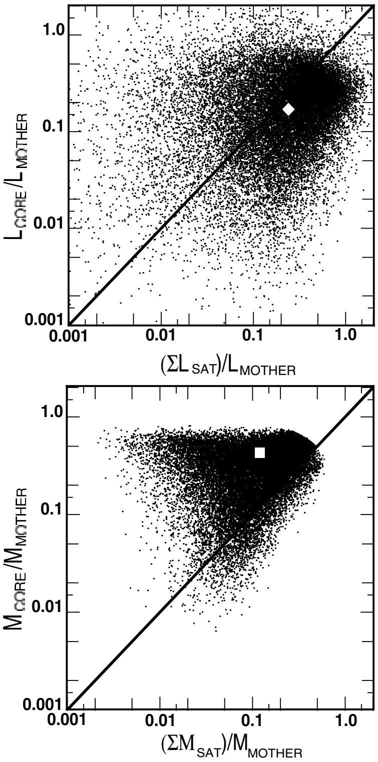

Figure D1. Comparison of the substructure's and the core's contributions to the amplitude of the mother's spin and to the mother's mass. Top: Comparison of the core's contribution to the mother's spin compared to the contribution of all the satellites for each mother detected in our simulations. Bottom: Same comparison but for the core's and satellites' mass relative to the mother's total mass. In both figures, the open square symbol indicates the barycentre of the cloud of points while the thick line's slope is unity. While the total mass is dominated by the core's contribution, the mother's spin is dominated by satellites, showing that their specific orbital momentum is more important than that of the core.

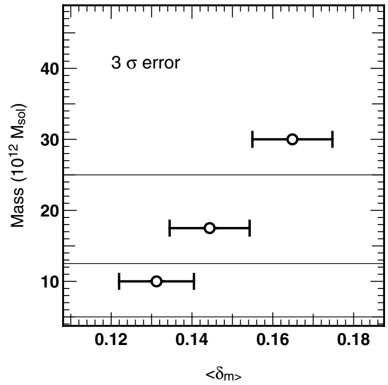

Figure D2. Comparison of $\langle\delta_{\rm m}\rangle$ for different classes of halo mass at $z = 0$. The error bars stand for the 3σ error. The thin lines separate the three classes of mass: 5×10^{12} $M_\odot < m < 1.25 \times 10^{13}$ $M_\odot$, 1.25×10^{13} $M_\odot < m < 2.5 \times 10^{13}$ $M_\odot$ and $m > 2.5 \times 10^{13}$ $M_\odot$. Each class contains 16 500 haloes.

the mother's spin is aligned with the orbital momentum of infalling satellites because they determine the direction of the halo's spin.

D2 Mass dependence of $\langle\delta_{\rm m}\rangle$

We measured the average excess of accretion $\langle\delta_{\rm m}\rangle$ (see Section 3.3) for three different class of masses at redshift $z = 0$: 5×10^{12} $M_\odot < m < 1.25 \times 10^{13}$ $M_\odot$, 1.25×10^{13} $M_\odot < m < 2.5 \times 10^{13}$ $M_\odot$ and $m > 2.5 \times 10^{13}$ $M_\odot$. Each class contains approximately 16 500 haloes. The results are shown in Fig. D2. It is found that $\langle\delta_{\rm m}\rangle$ increases with mass but does not change significantly even if the three classes cover different mass magnitudes. Consequently, no class of mass dominates when all the haloes are being used in the computation of $\langle\delta_{\rm m}\rangle$.

This paper has been typeset from a TEX/LATEX file prepared by the author.

Draft version April 22, 2008
Preprint typeset using LaTeX style emulateapj v. 03/07/07

INITIAL CONDITIONS FOR LARGE COSMOLOGICAL SIMULATIONS

S. Prunet,[1] C. Pichon,[1,4] D. Aubert,[2,1] D. Pogosyan[3], R. Teyssier,[4] & S. Gottloeber[5]

Draft version April 22, 2008

ABSTRACT

This technical paper describes a software package that was designed to produce initial conditions for large cosmological simulations in the context of the Horizon collaboration. These tools generalize E. Bertschinger's `Grafic1` software to distributed parallel architectures and offer a flexible alternative to the `Grafic2` software for "zoom" initial conditions, at the price of large cumulated cpu and memory usage. The codes have been validated up to resolutions of 4096^3 and were used to generate the initial conditions of large hydrodynamical and dark matter simulations. They also provide means to generate constrained realisations for the purpose of generating initial conditions compatible with, e.g. the local group, or the SDSS catalog.

Subject headings: Cosmology: numerical methods

1. INTRODUCTION

Numerical simulations have proved to be valuable tools in the field of cosmology and galaxy formation. They provide a mean to test theoretical assumptions, to predict the properties of large scale structures (and galaxies within) and give access to synthetic observations without sacrifying the whole complexity that arise from non-linearities. Thanks to the recent progresses in terms of numerical techniques and available hardware, numerical cosmology has become one of the most important (and CPU consumming) field among the scientific topics that require extreme computing. Over the last few years, a series of large simulations have been produced by, among others, Cen and Ostriker (2000), the Virgo Consortium (Frenk et al. 2000, the Millenium: Springel et al. 2005), Weinberg et al. (2002), the Gasoline team (Wadsley et al. 2004). Following the same route, the purpose of the Horizon Project[6] is to federate numerical simulations activities within the french comunity on topics such as : the large scale structure formation in a cosmological framework, the formation of galaxies and the prediction of its observational signatures. The collaboration studies the influence on the predictions of the resolution, the numerical codes, the self-consistent treatment of the baryons and of the physics included.

These investigations are performed on initial conditions (ICs thereafter) that share the same phases and their production is described in the current paper. The large Horizon ICs involves two boxes of 50 and 2000 Mpc/h comoving size with respectively 1024^3 and 4096^3 initial resolution elements (particles or grid points), following a ΛCDM concordance cosmogony. They were generated from an existing set of initial conditions created for the 'Mare Nostrum' simulation (Gottlöber and Yepes 2007): they share the same phases but with different box sizes and resolutions. The ($50h^{-1}$Mpc,1024^3) ICs were used as inputs to the AMR code RAMSES (Teyssier 2002) in a simulation that included dark matter dynamics, hydrodynamics, star formation, metal enrichment of the gas and feedback. This simulation directly compares to the MareNostrum simulation in terms of cosmology and physics and it will be refered as the Horizon-MareNostrum simulation hereafter(Ocvirk, Pichon and Teyssier 2008). The ($2000h^{-1}$Mpc,4096^3) ICs served as a starting point for the Horizon-4Π simulation(Teyssier et al. 2007, `http://www.projet-horizon.fr`): it is a pure dark matter simulation and assumes a cosmology constrained by WMAP3. It is currently used to investigate the full-sky gravitational lensing signal that could be observed by the DUNE experiment (hence the 4Π).

The paper is organised as follows: first, we briefly explain the principle of the ICs' generation. Then we describe how the phases were extracted from the MareNostrum ICs in order to make the Horizon ICs consistent with this reference. We describe next the features of a series of codes used to generate and process the different Horizon ICs:

- `mpgrafic`: ICs generation with optional low-frequency constraints
- `constrfield`: Low-frequency ICs generation with point-like constraints.
- `degraf`: Low-pass filtering and resampling of ICs
- `powergrid`: ICs empirical power spectrum estimation.
- `splitgrafic`: Estimation of matter density on a grid from a set of particle positions, and Peano-Hilbert domain decomposition.

Finally we illustrate how these codes were implemented on the two Horizon simulations.

2. RANDOM FIELD FOR COSMOLOGICAL INITIAL CONDITIONS

[1] Institut d'Astrophysique de Paris, UMR 7095, 98bis Boulevard Arago, 75014 Paris, France
[2] Observatoire Astronomique de Strasbourg, UMR 7550, 11 rue de l'Universite, 67000 Strasbourg, France
[3] Department of Physics, University of Alberta, Edmonton, Alberta, T6G 2G7, Canada
[4] CEA/DAPNIA/SAP, l'Orme des Merisiers, 91170, Gif sur Yvette, France
[5] AIP, An der Sternwarte 16, 14 482, Potsdam, Germany
[6] http://www.projet-horizon.fr

2.1. *Grid-based initial conditions*

For completeness, we quickly review the principle of ICs generation. Most of the following has been strongly inspired from articles by Pen (1997) and Bertschinger (2001). Let us consider the initial 3D gaussian random field $\delta(\mathbf{x})$, representing the density or the displacements, and let us define its Fourier transform $\delta(\mathbf{k})$. If we consider zero-mean fields, they are completely defined by their correlation function or, equivalently, by their power spectra, $P(k)$:

$$P(k)\delta_D(\mathbf{k}-\mathbf{k}') = \langle \delta(\mathbf{k})\delta^*(\mathbf{k}')\rangle. \quad (1)$$

All the statistical information in a gaussian homogeneous and isotropic realization is contained in this quantity and the difficulty of generating initial conditions resides in obtaining a field which has the correct power spectrum.
We chose to follow the convolution-based method described by e.g Pen (1997) and define the correlation kernel in Fourier space as:

$$A(k) = \sqrt{P(k)}. \quad (2)$$

To reproduce the correlation function accurately one may need to first convolve the power spectrum with the window that describes the simulation box, as advocated by Pen (1997). The influence of the box size on rms density in spheres of given radius (which are relevant for mass function estimates of collapsed objects), is negligible for sphere radii much smaller than the box length, even for simulations designed to study galaxy cluster scales.

Then the ICs generation is a two-step procedure. First a normal, uncorrelated random field of unit variance is generated in position space[7]. This *white noise* $n_1(\mathbf{x})$ has a constant power spectrum, e.g.:

$$\langle |n_1(\mathbf{k})|^2\rangle = 1. \quad (3)$$

The second step involves convolving the white noise with the correlation kernel in order to obtain the initial fluctuation field:

$$\delta(\mathbf{x}) = n_1(\mathbf{x}) * A(\mathbf{x}), \quad (4)$$

or in Fourier space

$$\delta(\mathbf{k}) = n_1(\mathbf{k})A(\mathbf{k}). \quad (5)$$

It can be easily seen that $\langle |\delta(\mathbf{k})^2|\rangle = P(k)$ and the initial field automatically has the correct power spectrum.

One of the main virtue of the method resides in the possibility of using the same white noise for different power spectra. In other words, it decouples explicitely the phases (which contain the specificities of a given realization in terms of relative positions) from the amplitudes of the fluctuations (corresponding to one's favorite choice of cosmological model). A change in the physics or in the box size results in a change of the convolution kernel, but the underlying structure of the field will remain globally the same for a given white noise realization. Conversely, Eq. 5 implies that the initial phases can be recovered from a set of ICs, provided that the convolution operation can be inverted. In other words, it is possible to generate a new set of ICs from an old one (see Section 4) and such a set would share the same overall structures with e.g. a modified cosmology or box size.

[7] We could have directly generated the real and imaginary part of each $\delta(\mathbf{k})$ following a $\mathcal{N}(0, 1/\sqrt{2})$ law, saving the cost of an extra Fourier transform, but we chose to remain compatible with the `Grafic` code.

2.2. *Grid-based versus particle-based initial conditions*

In numerical simulations, the dark matter distribution is almost exclusively described in terms of particles and this discretized description is also applied to the gas in SPH-like hydrodynamical codes. Consequently, dealing with 'particle-type' data is the most frequent case while the current procedure naturally deals with densities and velocities sampled on a grid. This can be easily tackled by recalling the density-velocity relation that is valid in the linear regime :

$$\frac{1}{aH}\nabla_{\mathbf{x}}\mathbf{u} = -f(\Omega_m, \Omega_\Lambda)\delta(\mathbf{x}). \quad (6)$$

Here $\mathbf{u}$ stands for the comoving peculiar velocity, $\mathbf{x}$ for the comoving position, H for the Hubble constant, a for the scale factor and f is defined as the logarithmic time derivative of the growth factor:

$$f(\Omega_m, \Omega_\Lambda) \equiv \frac{\mathrm{d}\log D^+}{\mathrm{d}\log a}. \quad (7)$$

Functional fits for f can be found in the literature (e.g. Lahav et al. 1991) or be directly computed for a given cosmology. Hence, assuming that particles were displaced from a regular grid and knowing their velocities, the initial density field can be directly recovered from Eq. (6). One can see that the (eulerian) positions of particles are not directly involved in this procedure; however, their lagrangian coordinates are used to remap the particle velocities to grid cells.

3. GRID-BASED ICS: TECHNICAL IMPLEMENTATION

Once the "phases" (the white noise) are chosen on a grid of a given size, it is possible to use them to generate initial density and velocity realizations with the desired cosmology and power spectrum, at resolutions that can differ from the initial white noise realization.

According to linear theory, which applies for initial conditions [8], density and velocity divergence are related through Eq. (6), so that a single white noise realization determines both density and velocities on a grid of equal size (see e.g. Bertschinger 2001).
A first numerical implementation of this algorithm was made by E. Bertschinger in the package `Grafic1`. We extend here his code using the Message Passing Interface (MPI) library to deal with large simulation cubes on distributed memory platforms. Another implementation of MPI-based Initial Conditions generator in the context of the GRACOS code is described in Shirokov (2007), `http://www.gracos.org`.
We also develop a few tools (low-pass filtering and resampling, power spectrum estimation, estimation of matter density on a grid from a set of particle positions) that work as well in parallel environments. We describe these tools and their usage in the following subsections.

3.1. *`Mpgrafic`: a parallel version of `Grafic1`*

Generating initial conditions for cosmological simulations on a grid from an initial white noise realization

[8] actually, the validity of the linear theory is enforced by chosing the starting redshift in such a way that the resulting variance of the discrete density field is significantly less than unity

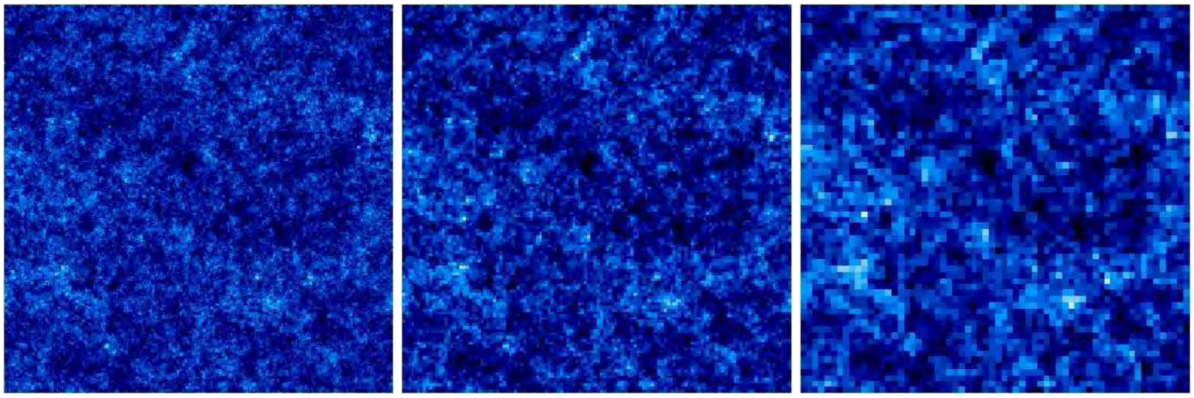

Fig. 1.— The left image shows a slice of a density field realization of size 256^3. The middle and right images show respectively slices of the cubes of size $128^3$and 64^3obtained from the first density field by lowpass filtering and subsampling. The images have been rescaled to the same size to ease their comparison. The initial density field was obtained using `mpgrafic` with the parameters of Table 2. The low-frequency, resampled fields were obtained with the `degraf` utility.

is theoretically quite simple, as it involves a straightforward implementation of Equations (5) and (6) in Fourier space. Indeed, the main issues in the `Grafic1` code involve getting the normalization right (in terms of σ_8 or $Q_{\rm rms}$, which are input parameters), and therefore in the cosmology routines.

3.1.1. *Description*

Difficulties of a more technical nature appear as the size of the desired cubes (and/or the number of particles) grow and that a single cube does not fit into a computer's memory. An elegant answer to this problem, in the context of multi-resolution ("zoom") initial conditions was designed by Bertschinger (2001) and implemented in the `Grafic2` package. This solution involves generating a low resolution cube first, and successively adding higher frequencies in nested sub-regions, constrained by the phases of the already existing low frequency modes. Strictly speaking, the exact solution to this problem is (naively) as costly as the direct generation of the full cube at the highest resolution, but approximate, less costly solutions based on anti-aliasing kernels can be designed. This is precisely what is done in the `Grafic2` package.

The main advantage of this solution is to produce multi-resolution initial conditions with a very reasonable memory usage, but it also has drawbacks, namely its complexity, and its built-in restrictions on the nested cubes structure of a given maximum size. Given the growing size of computer clusters, our "brute force" approach to the problem based on parallelism becomes possible, and it is also in some ways more flexible. First of all, it allows for a direct generation of global initial conditions for very large cosmological simulations. Secondly, it also allows, together with associated tools for low-pass filtering and resampling, to create multi-resolution simulations of a more general structure by simply extracting the desired sub-regions from the series of "downgraded" cubes (obtained by low-pass filtering and resampling of the initial large high-resolution cube).

There are two issues that arise when implementating a parallel (MPI-based) version of the `Grafic1` software. The first involves performing efficient three-dimensional fast fourier transforms (FFTs thereafter); this difficulty is solved by using the parallel version of the FFTW [9] library, which uses a slab domain decomposition. The second difficulty lies in the input/output. Indeed, we decided to keep the binary (Fortran) structure of the files in the `Grafic1` format. In a parallel environment where each MPI process is responsible for one chunk of data, this lead us to write part of the I/O subroutines in C using reentrant read/write routines, wrapped in fortran90 to be callable from the main program.

Finally, apart from the parallelism of `mpgrafic`, we have added a few new features to the original `Grafic1` code. An implementation of the matter power spectrum with baryon oscillations was introduced, as described in Eisenstein and Hu (1998). Secondly, the possibility of constraining the low frequency phases of the density and velocity realizations was implemented, with the input of a given white noise cube of lower resolution. This allowed us to use the same set of initial condition phases for cosmological simulations at different resolutions. Lastly, we have implemented the possibility of constraining the value of the density or velocity field values, as well as their gradients and hessians at a chosen set of positions. We will come back in more details on this last point in a following section, as it is a non-trivial extension of the code.

3.1.2. *Code installation and parameter file structure*

A prerequisite to use `mpgrafic` is to have (of course) a valid MPI library installed, including a fortran90 compiler. A second prerequisite is to have the `fftw-2.1.5` library installed, with the `--enable-mpi --enable-type-prefix` options at the configure step. The first option builds the static and shared FFTW MPI-based libraries, the second is for the type (float or double) naming scheme of the libraries.

Note that the default build of FFTW corresponds to double precision, whereas the default type in `mpgrafic` is single precision. To change to single precision realizations, you need to make the single precision FFTW MPI libraries by adding the `--enable-float` at configure time. To compile `mpgrafic` in double precision mode, you need to configure with the `--enable-double` keyword.

The code usage has been kept as close as possible to the `Grafic1` code interface, except of course for the few additional options to the code. In table 2 we show an

[9] `http://www.fftw.org`

example of parameter file of `mpgrafic`.

Compared to the original `Grafic1` parameter files, the only differences lie in the possibility of an input power spectrum with baryonic oscillations (Eisenstein and Hu 1998), and in the optional input of a small noise file to constrain the large scale phases. Otherwise, the code is called in the following way:

`mpirun -np` < #proc> `mpgrafic` < `parameter_file`

Like `Grafic1`, it produces seven data cubes (one density file, three dark matter velocity files, and three baryon velocity files). In the file `grafic1.inc`, the offsets of the velocity fields is controlled by the parameters `offvelb, offvelc`. The redshift of the realizations is controlled by the variance of the density field on the grid, as specified by `sigstart`. Finally, the size of the cubes is controlled by the parameters `np1,np2,np3`, that can take different values and are set in `grafic1.inc`. Note that when these parameters are changed the code needs recompilation.

3.1.3. *Illustration on a small example, power spectrum estimate*

In figure 1 we show a slice of a density file realization with the parameter file displayed in Table 2, but without large scale constraints, and for `np1=np2=np3=256`. In the same figure, we show the density files of linear grid size 128 and 64 obtained from this realization, by low-pass filtering and subsampling. This operation has been done using the utility called `degraf`, that makes use of the FFTW parallel Fourier transform routines. Written in fortran90, it takes as input a collection of files in `Grafic1` format, as well as some parameters in a namelist file. These parameters include the list of the input file names, the target resolution of the output files, as well as an optional shift vector allowing a global translation of the output files (with periodic initial conditions).

Finally, another utility, `powergrid`, uses the FFTW parallel Fourier transform routines to compute the periodogram estimate of a density field power spectrum. It allows correction for nearest grid point (NGP) or cloud in cell (CIC, linear) interpolation of a particles set to the computation grid. Note that this resampling of a discrete density field given by particles onto grid cells leads not only to a smoothing of the grid Fourier modes (this can be corrected by the code) but also to some power aliasing, that cannot be corrected, unless prior knowledge of the density power spectrum is available. These points will be illustrated in the next section, for the Horizon simulations. Of course, none of these problems appear if one is only interested in computing the periodogram of the IC grid-sampled density fields. Figure 2 shows the theoretical power spectrum corresponding to the density field realization shown in Figure 1, together with its periodogram estimate, as well as the periodograms of its low-passed, resampled versions.

3.2. *Constrained initial conditions*

Since `mpgrafic` opens the opportunity of generating ICs which are consistent with a given low frequency cube, it is interesting to build such a cube of phases so that the overall cube satisfy (low frequency) point like constraints on a given set of points. These constraints fix the mean value of the density or velocity field, as well as their gradients and hessians, computed at a chosen set of positions, for a given smoothing length R_p (see Equation 11 below).

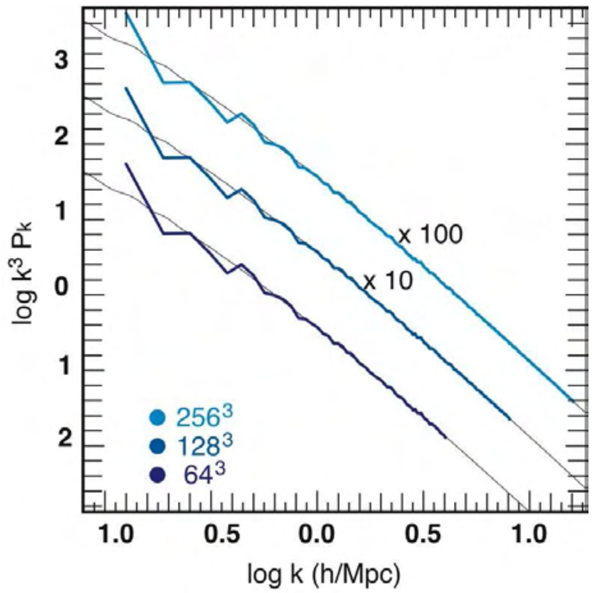

Fig. 2.— Theoretical power spectrum (solid line, as output in the file power.dat by `mpgrafic`), together with the periodogram estimates (computed by powergrid), of the 256^3density realization (top thick line), and its downgraded versions produced by degraf (middle and bottom lines for $128^3$and 64^3 respectively).

Once such a low-frequency cube has been generated, it is then whitened, and set as an input to `mpgrafic`, which is then used to add small scale power and to resample the field according to the new Nyquist frequency [10].

This procedures allows for instance to generate initial conditions which are consistant with, say a given merging event, or the structure of the Local Group, the large scale structures derived from large surveys such as the SDSS (Adelman-McCarthy and for the SDSS Collaboration 2007), the 2dF (Percival et al. 2001), 2Mass (Jarrett et al. 2003), the Local Group (Mohayaee and Tully 2005), etc.

The ensemble of unconstrained gaussian random fields is defined by all possible realizations of the field values $\delta(\mathbf{x})$, or their Fourier amplitudes $\delta(\mathbf{k})$, for a given power spectrum. If we impose the constraints on the field, the statistical ensemble narrows down to a subset of realizations, those that have the constraints satisfied. In particular, for a discrete representation of the field on a grid of size N^3, this means that not all N^3 values of $\delta(\mathbf{x})$ are real degrees of freedom. Averaging over the constrained ensemble $\langle \ldots \rangle_c$ makes both the mean $\langle \delta(\mathbf{x}) \rangle_c$ and the variance dependent on position $\mathbf{x}$.

We shall be dealing with linear constraints each of which, in general, sets a linear functional relation $V_a[\delta(\mathbf{x})]$ (we will use latin letters to index the constraints where each constraint is defined by a grid position $\mathbf{x}_a$ and a constraint operator Y_a, see below) between field values to a given value, $V_a[\delta(\mathbf{x})] = \tilde{V}_a$.

Alternatively, we can take a point of view that such a restricted ensemble defines a new (constrained) random

[10] In principle, adding small scale power with `mpgrafic`, while keeping the same low-frequency phases, violates the point-like constraints imposed by `constrfield`. However, if the smoothing kernel $W(kR_p)$ and its associated smoothing length are chosen in such a way that it cuts all modes with wave vectors above the initial Nyquist frequency, the constraints are not violated by adding small scale power.

Fourier space	Configuration space	Physical meaning
$Y(\mathbf{k}) = 1$	$V[\delta] = \delta$	density value
$Y(\mathbf{k}) = -\imath\mathbf{k}_i/k^2$	$V[\delta] = -\nabla_i\Delta^{-1}\delta$	linear displacement
$Y(\mathbf{k}) = \mathbf{k}_i\mathbf{k}_j/k^2 - \frac{1}{3}\delta_{ij}$	$V[\delta] = (\nabla_i\nabla_j\Delta^{-1} - \frac{1}{3}\delta_{ij})\delta$	flow shear
$Y(\mathbf{k}) = \imath\mathbf{k}_i$	$V[\delta] = \nabla_i\delta$	density gradient
$Y(\mathbf{k}) = -\mathbf{k}_i\mathbf{k}_j$	$V[\delta] = \nabla_i\nabla_j\delta$	density curvature

TABLE 1
Different type of point -like constraints

field $\delta_c(\mathbf{x})$ which is still gaussian (due to the linearity of imposed relations) but is statistically inhomogeneous. Under these conditions, the well known way to construct a constrained field from unconstrained realizations is

$$\delta_c(\mathbf{x}) = \delta(\mathbf{x})+\sum_{ab}\langle\delta(\mathbf{x})V_a[\delta]\rangle\langle V_a[\delta]V_b[\delta]\rangle^{-1}\left(\tilde{V}_b - V_b[\delta]\right) . \tag{8}$$

(see e.g. Bardeen et al. 1986; Hoffman and Ribak 1991). In this expression, the random quantities on the right-hand side are unconstrained $\delta(x)$. Here $\tilde{V}_b$ is a numerical value of the constraint b, while $\langle\delta(\mathbf{x})V_a[\delta]\rangle$ is the covariance between the field and a constraint, and $C_{ab} = \langle V_a[\delta]V_b[\delta]\rangle$ is the convariance matrix between the constraint functionals.

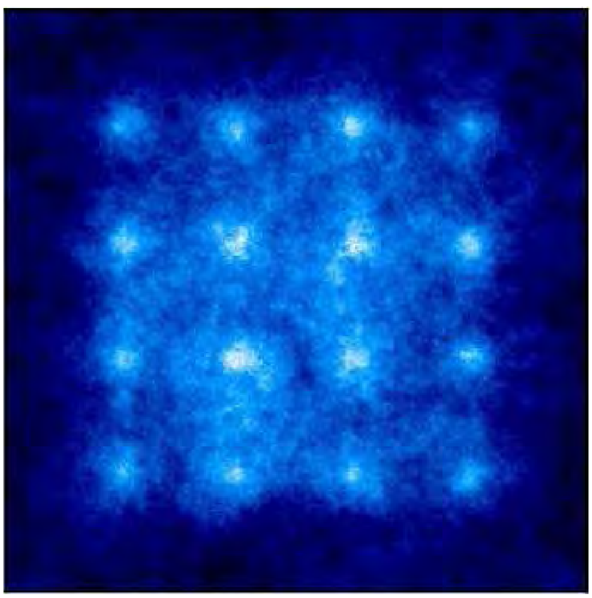

Fig. 3.— Example of contrained realization generated using CONSTRFIELD and extended at a 1024^3resolution using `mpgrafic`. Here a regular grid of $4 \times 4 \times 4$ density peaks is imposed within a ΛCDM cosmological simulation in a box of length $100h^{-1}$Mpc. Here the constraints are of the density type, so that $Y(\mathbf{k}) = 1$ for each constraint; in such a case, $V_a(\delta) = \delta(\mathbf{x}_a)$, where $delta(x_a)$ is the chosen constraint at position x_a.

This recipe reproduces the mean (note, the averaging is taken over all unconstrained realizations)

$$\langle\delta_c(\mathbf{x})\rangle = \langle\delta(\mathbf{x})V_a\rangle\langle V_aV_b\rangle^{-1}\tilde{V}_b\,, \tag{9}$$

and the correlation function

$$\begin{aligned}\langle\delta_c(\mathbf{x})\delta_c(\mathbf{x}')\rangle = &\xi(\mathbf{x},\mathbf{x}') - \langle\delta(\mathbf{x})V_a\rangle\langle V_aV_b\rangle^{-1}\langle\delta(\mathbf{x}')V_b\rangle\\ &+\langle\delta_c(\mathbf{x})\rangle\langle\delta_c(\mathbf{x}')\rangle\,,\end{aligned} \tag{10}$$

which define all statistical properties for the gaussian case.

In cosmology the primary interest is to define constraints that describe the physical properties of a patch (see e.g. Bond and Myers 1996; van de Weygaert 1996) of the density field - density, density derivatives, shear flow, averaged over the volume of the patch. Such constraints can be represented in Fourier space as

$$V_a[\delta] = \int d^3k\delta(\mathbf{k})Y_a(\mathbf{k})W(kR_p)e^{-\mathbf{ikx}_a}\,, \tag{11}$$

where $\mathbf{x}_a$ is the position of the patch, $W(kR_p)$ is a averaging filter over the patch size R_p, and $Y_a(\mathbf{k})$ is the Fourier representation of the operator that specifies the constraint functional. In particular, we use the constraint types given in Table 1. Using constrained field formalism Bond et al. (1996) have demonstrated that the observed filamentary Cosmic Web of matter distribution in the Universe can be understood as dynamical enhancement of the geometrical properties of intial density field. The web is largely defined by the position and primordial tidal fields of rare events in the medium, such as precursors of large galaxies at high redshifts or clusters of galaxies at present time, with the strongest filaments between nearby clusters whose tidal tensors are nearly aligned.

The code `constrfield` implements the same cosmology as `mpgrafic` (including baryon wiggles) and offers the possibility of whitening [11] the resulting field in order to feed it to `mpgrafic` as a low frequency input. An example of this procedure is illustrated in Fig. 3.

3.3. *Splitting the ICs*

Starting a parallel computation requires the initial conditions to be dispatched over all the computing processes. Two alternatives exist to perform this operation. The first one involves having the initial conditions to be read by a 'master' process and the data to be broadcasted to all the other processes, and then keep or reject the broadcasted data according to the topology of the computation's domain split. While simple to implement, this option happens to be difficult to use in practice since broadcasting over a large number of processes can be technically problematic and time consuming.

We present an alternative option which involves having the processes upload their own set of data only. Because it is wasteful for each process to parse the whole set of initial conditions to get the relevant subset of data, this option implies that initial conditions are pre-split according to the domain decomposition strategy of the integrator.

[11] Here we understand by whitening the operation that transforms an unconstrained field into a white noise, i.e. a collection of independent indentically distributed random variables $\mathcal{N}(0,1)$. Note that the presence of constraints breaks the independence of the grid cells even after "whitening" (see Equation 10).

This splitting is both a domain boundary assignment, a procedure for distributing particles among the processes, and a per process file dump.

It results in a faster procedure, since each process reads its own set of data, instead of having one process reading the full initial conditions. A possible drawback lies in the fact that a splitting is defined a priori; changing the number of processes dedicated to the computation therefore requires the production of a whole new set of split initial conditions. However splitting can be performed on a single process, prior to any parallel computation, and exhibits a negligible cost in terms of CPU-time. Such a procedure can thus be applied an arbitrary number of times at almost no expense.

Horizon simulations were started from split initial conditions, where each process uploaded its own set of data. The splitting scheme followed the domain decomposition's strategy of the cosmological calculations performed with RAMSES. It relies on a 3D Peano-Hilbert space filling curve (Salmon and Warren 1997; MacNeice et al. 2000) which provides a complete mapping between the 3D position of a grid point and a 1D coordinate on this curve. A two-dimensionnal example of such a curve is shown in figure 4. By using this piecewise linear representation of the computation domain, each process is being given a continuous portion of this curve and load balancing is achieved by 'sliding' the limits of the local data sets along the space-filling curve. In particular, the initial conditions are by construction well-balanced, therefore the splitting among all the processes involves a set of even subdivisions of the Peano-Hilbert curve. A (i, j, k) grid point maps to a single *key* q. A set of successive $(q_1, q_2, ..., q_n)$ corresponds to a single process p.

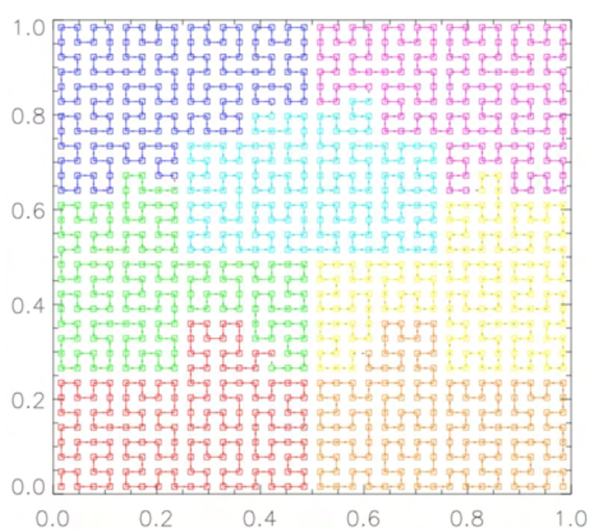

FIG. 4.— Example of a ICs splitting following a Peano-Hilbert domain decomposition in two dimensions.

Note that all sub-domains are simply connected, i.e. within there are no isolated sub-regions owned by a process in the middle of another region owned by another process. For instance, in 3D, if the curve is split in 2^r sections, each section fits in a 3D rectangle of different sizes and orientations (see figure 5). Moreover, if the curve is split in 8^r parts, all the sections fit in a cube of the same volume. This type of domain decomposition is known to be most efficient if we consider the ensemble of all the refined grids configurations. It may be surpassed by other strategies (e.g. layer splitting, angular splitting) on specific situations, but Peano-Hilbert domain decomposition remains the best strategy *on average*.

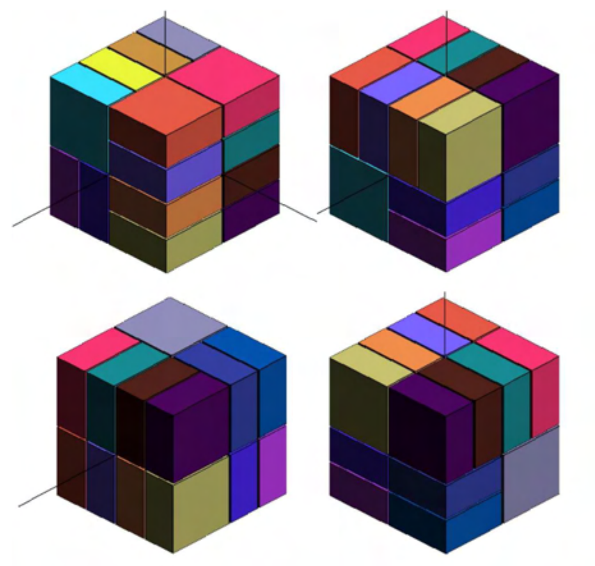

FIG. 5.— Example of a ICs splitting in 16 subvolumes following a Peano-Hilbert domain decomposition as seen from four different directions.

Here we implemented a fast and simple algorithm which performs the splitting of initial conditions according to the Peano-Hilbert domain decomposition. It relies on a plane-by-plane investigation of the data cube which limits the memory consumption. Let n^3 be the number of cells in the initial conditions data cube, $F(i, j, k)$ the value of the 3D field at grid indices $1 \leq i, j, k \leq n$ and f a 2D slice of F at index k. We assume that the number of processes nproc is a *power of two* (even though this constraint can be lifted as explained below); it ensures that each process domain is a 3D rectangle. Consequently the extent of the sub-domain corresponding to a process p is given by two triplets $(i_m, j_m, k_m)^p$ and $(i_M, j_M, k_M)^p$ which correspond to the two extreme corners of the rectangle. The algorithm described below runs on one process only, and involves two distinct steps:

- do $k = 1, n$: loop over data planes
  - read $f = F(1 : n, 1 : n, k)$: the 2D data is uploaded.
  - initialisations:
    - process(1 : nproc) =.false.,
    - $(i_m, j_m, k_m)^p = -1$, $(i_M, j_M, k_M)^p = -1$, $\forall p \in [1 : \text{nproc}]$
  - do $j = 1, n$, $i = 1, n$
    - Peano-Curve mapping : (i,j,k) $\rightarrow$ q $\rightarrow$ p
    - process p is found in the k plane: process(p)=.true.
    - if process p found for the 1st time set the minimum position : if $(i_m, j_m, k_m)^p = -1$ then $(i_m, j_m, k_m)^p = (i, j, k)$

  - ∗ update the maximum position: if $(i, j, k) > (i_M, j_M, k_M)^p$ then $(i_M, j_M, k_M)^p = (i, j, k)$
- – do $p = 1$, nproc
  - ∗ if process(p)=.false. skip : only processes detected in the plane are taken in account.
  - ∗ write f($i_m^p : i_M^p, j_m^p : j_M^p$) in the file of the process p.

First, initial conditions fields are parsed plane by plane and for each plane, the process map is achieved through the space-filling curve mapping. Then for each process found in the current plane the subset of data is written in the relevant files. Because of the compacity of the sub-domains, a significant speedup can be obtained by parsing the i and j indexes of the second loop with steps larger than 1 : this procedure is safe as long as the step remains smaller than the smallest extent of the sub-domains along one direction. We call this step the speedup step. Finally the nproc= 2^r constraint can be lifted if a set of processes upload the same set of data. Each process would load a small initial condition file and would retain only its 'sub-sub-domain' within a sub-domain. For instance the HORIZON 4Π simulation ran on $6144 = 3 \times 2048$ processes: the splitting was performed over 2048 sub-domains and each sub-file was uploaded by three processes. Overall, this algorithm can be quite effective and as an illustration, the 4096^3 initial conditions fields of this simulation were split in 15 minutes on a single process of the CCRT computing center using a speedup step of 256. The code ran on Itanium2 processors (double-core, but only a single core has been used here) with a 1.6 GHz frequency.

4. APPLICATION TO LARGE HORIZON SIMULATIONS

Let us now illustrate on a couple of large scale simulation how `mpgrafic` was used. We will consider in turn a hydrodynamical and a dark matter only simulation.

4.1. *Horizon-MareNostrum*

The first major application of the `mpgrafic` code was the generation of ICs for a simulation of a cosmological hydrodynamical simulation of linear size $50h^{-1}$Mpc on a grid of size 1024^3.

For the Mare Nostrum simulation, we started for technical reasons with external ICs (given as a set of particle velocities), as one of the goals was to compare two n-body plus hydro codes (namely the RAMSES and GADGET2 codes) on similar ICS. The particle velocities were therefore read from external ICs and we performed the derivation of the density field samples on the grid from the particle velocities in Fourier space, using the JMFFT Fourier Transform package[12]. The f factor involved in Eq. (7) was computed using routines provided in the original `Grafic1` package. Once the velocity divergence and $f$are known, the initial density field is easily recovered and ready to be used as an input for simulations (especially for the hydrodynamical part of RAMSES), or as a source for a specific set of initial phases.

[12] `http://www.idris.fr/data/publications/JMFFT/`

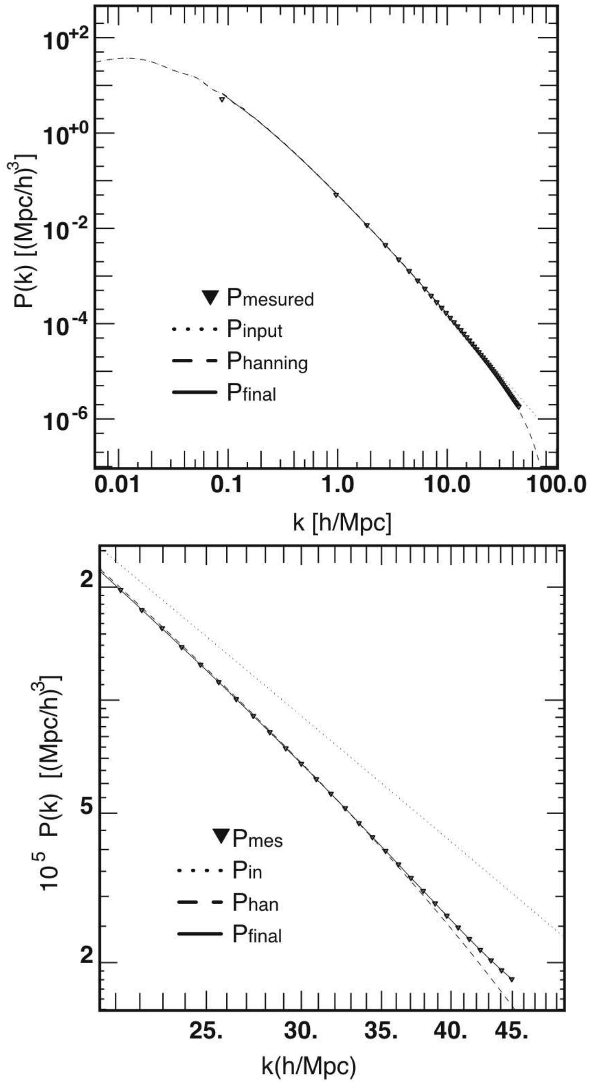

FIG. 6.— The power spectrum $P(k)$ of the 'Mare Nostrum' initial conditions. Symbols stand for the measured power spectrum, $P_{\rm mes}(k)$, while the dotted line stands for the theoretical power spectrum $P_{\rm in}(k)$. The dashed line, $P_{\rm Han}(k)$, stand for the theoretical power spectra plus a Hanning filter contribution. The solid line, $P_{\rm final}(k)$ stand for our best fit of the power spectrum. The bottom panel represents a zoomed version of the top one where only the small scales are shown.

4.1.1. *Power Spectrum Extraction from Mare Nostrum Initial Conditions*

The master equation (Eq. (5)) can only be inverted knowing the convolution kernel, i.e. the power spectrum $P(k)$. In principle, the knowledge of the cosmology and the included physics should be sufficient to derive $P(k)$ prior to the deconvolution. Let us call $P_{\rm in}(k)$, this theoretical power spectrum constrained only by physics. In practice, this theoretical power spectrum differs from the effective power spectrum used to draw the (external, particle based) ICs. Our goal in this section is to define a power spectrum $P_{\rm final}(k)$ that should accurately represent the ensemble averaged power spectrum of the external ICs (so that $\langle P_{\rm mes}(k)\rangle \approx P_{\rm final}(k))$), based on the available theoretical and measured power spectra. $P_{\rm final}(k)$ will then be used in the deconvolution.

Using an inaccurate spectrum to deconvolve Eq. (5) would lead to a 'colored' noise for the initial phases, i.e.

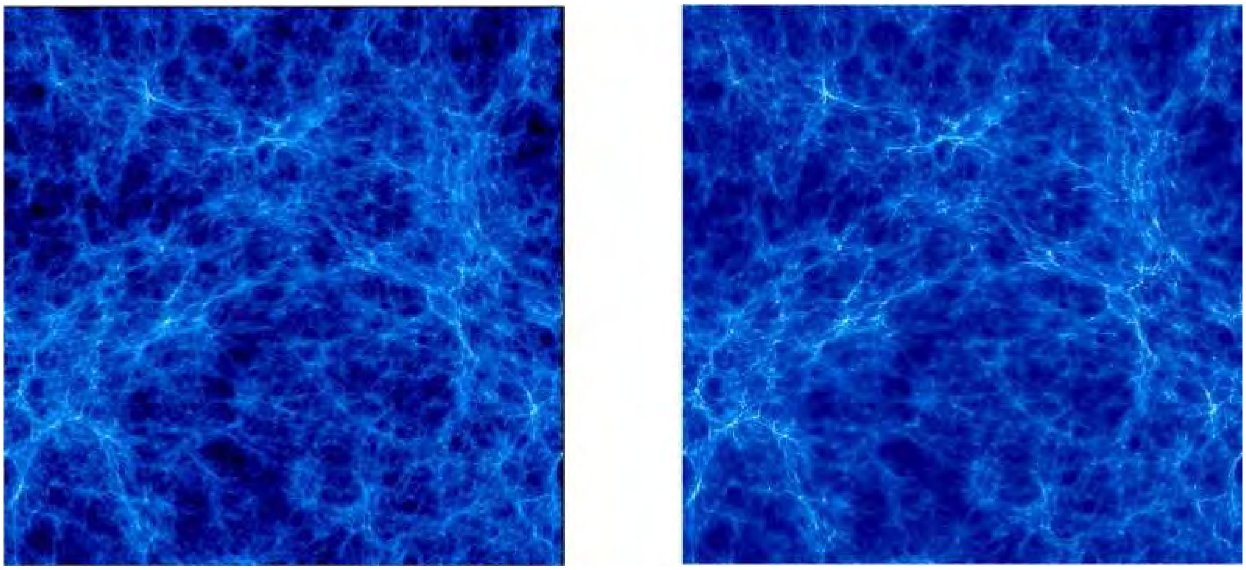

FIG. 7.— Comparison between the gas in the SPH MARENOSTRUM simulation at redshift $z = 5.7$ (*left*) from which ICs the Horizon white noise was extracted, and the Horizon-MARENOSTRUM simulation (*right*) for which the initial conditions were generated with `mpgrafic`. This figure demonstrates that on large scales the phases are indeed reproduced by the procedure. It also shows that on these scales, the two code produce quite similar features.

with spurious characteristic length scales.

Let us illustrate the discrepancy between the theoretical and the measured $P(k)$ by describing the power spectrum of the Mare Nostrum ICs. The measured $P(k)$ is shown in figure 6 as triangles. The theoretical $P(k) = P_{\rm in}(k)$ (i.e. the one used to generate this set of ICs) is also shown as a dotted line and unsurprisingly, the two curves disagree.

At low k, the finite volume of the simulation implies that the empirical power spectrum of large scale modes has large sampling variance and thus departs from the theoretical curve. The high k discrepancy is of different nature: clearly the sampling variance is negligible, but now the discreetness of the grid and anisotropy of very high k mode representation play role. $P(k)$ departs significantly from $P_{\rm in}(k)$ as easily seen when zooming on the large k regions, where $P(k)$ lacks power compared to the expected behavior. Therefore, $P_{\rm in}(k)$ cannot be used without corrections to whiten the external IC set. In the following, we rely on the fact that Gaussian initial conditions are statistically characterized by power spectrum only.

The exact set of corrections depends on how the field have been generated. For Mare Nostrum IC's we must first include a Hanning filter defined in the Fourier space by

$$W_H(k) = \cos(\frac{\pi k}{2k_N}), \tag{12}$$

Here the Nyquist frequency is given by $k_N = 2\pi/L \times N/2$, where $L = 50$ Mpc/h is the size of the box of the Mare Nostrum ICs and N stands for the (linear) number of grid elements. Such a filtering is frequently encountered when dealing with initial conditions: because Fourier modes are sampled on a cartesian grid, the two conditions $k < \pi N\sqrt{3}/L$ and $(k_x, k_y, k_z) < \pi N/L$ imply that anisotropies arise on the smallest scales along the diagonals. The Hanning filter damps high frequency modes, and reduces the small scales contributions and consequently the anisotropies. In Fig. 6, we display the $P_{\rm Han}$ curve as a dashed line, where:

$$P_{\rm Han} = W_H(k)^2 P_{\rm in}(k). \tag{13}$$

Clearly, $P_{\rm Han}(k)$ reproduces well the measured power spectrum (except at high frequencies, see below), with $N = 2048$, which corresponds to the original resolution of the external ICs, prior to some (external) degradation procedure. This modification of the spectrum corresponds to the most favorable case where an analytic expression is known or can be found for the filtering applied on the data.

Secondly, Fig. 6 shows that $P_{\rm Han}(k)$ still lack some power for $k > 40$ h/Mpc. This feature corresponds to the external degradation procedure: one particle out of eight was provided, out of the original 2048^3 particles, resulting in power aliasing at high frequency. This part of the power spectrum was fitted by a smoothed version of the measured power spectrum. We call $P_{\rm final}(k)$ this final power spectrum that includes the effect of the Hanning Filter and corrects the high frequencies effects due to the degradation:

$$P_{\rm final}(k) = \quad P_{\rm Han}(k) \quad {\rm k} \leq 40{\rm h/Mpc}, \tag{14}$$

$$S[P_{mes}(k)]\, {\rm k} > 40{\rm h/Mpc}, \tag{15}$$

where $S[X]$ stands for a smoothing operator. By using a smoothed version of the spectrum, we avoid overfitting of the fluctuations in the spectrum, which would artificially reduce the variance at these scales.

To conclude, $P_{\rm final}(k)$ combines both an analytic expression of the filtered theoretical spectrum at low frequencies and a numerical evaluation at high frequencies, based on the measured power spectrum. We emphasize that these choices are by no means unique but were found to provide phases with the proper spectrum.

4.1.2. *Whitening*

The "whitening" operation (i.e. getting the white noise $n_1(\mathbf{x})$ from $\delta(\mathbf{x})$ and $P_{\rm final}(k)$) is then performed by deconvolution as in Eq. (5). For the Horizon Mare Nostrum

ICs, the power spectrum of the resulting white noise is shown in Fig. 8. The whitened ICs are now ready to be processed into new initial conditions: the whitened ICs serve as low frequency constraints when generating the refined ICs using `mgrafic`

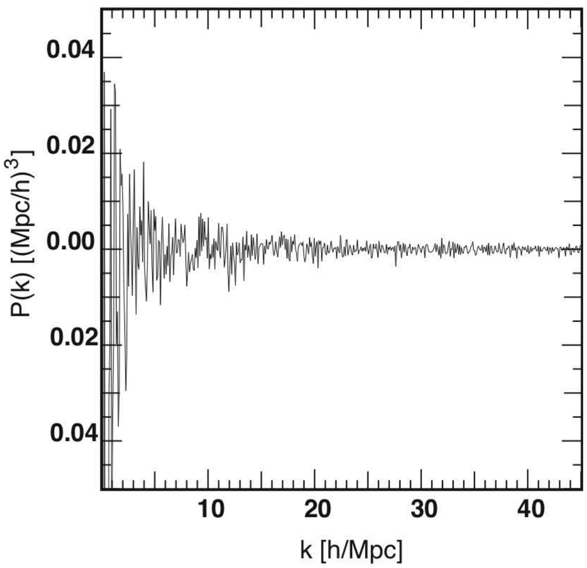

FIG. 8.— The power spectrum of the phases contained in the 'Mare Nostrum' initial conditions, with the expectation value of the power of a white noise of unit variance substracted . As expected from a white noise's realisation, the spectrum fluctuates around an overall flat line.

The code `mpgrafic` was then used to generate the ICs of a ΛCDM hydrodynamical "full physics" simulation (with star formation and metals) with a boxsize of $50h^{-1}$Mpc on a grid of 1024^3 using the HORIZON reference white noise. The comparison between the input phases and the reproduced phases with `mpgrafic` is illustrated in Figure 7 which shows both simulations at redshift 5.7.

4.2. HORIZON 4Π

As mentionned earlier, the code `mpgrafic` was also used to generate the ICs of HORIZON-4Π a ΛCDM dark matter only simulation based on cosmological parameters inferred by the WMAP three-years results, with a boxsize of $2h^{-1}$Gpc on a grid of size 4096^3. The purpose of this simulation is to investigate full sky weak lensing and baryonic accoustic oscillations. The 70 billions particles were evolved using the Particle Mesh scheme of the RAMSES code on an adaptively refined grid (AMR) with about 140 billions cells. Each of the 70 billions cells of the base grid was recursively refined up to 6 additional levels of refinement, reaching a formal resolution of 262144 cells in each direction (roughly 7 kpc/h comoving).

The corresponding power spectrum was measured using `powergrid`, and is shown in Figure 11. Since the simulation snapshots involves a collection of particles, we had to resample them on a grid using a convolution kernel before estimating the power spectrum. The resulting (analytical) bias in the power spectrum was corrected; however, this resampling procedure leads to some power aliasing close to the Nyquist frequency that cannot be corrected without additional information. Finally, note

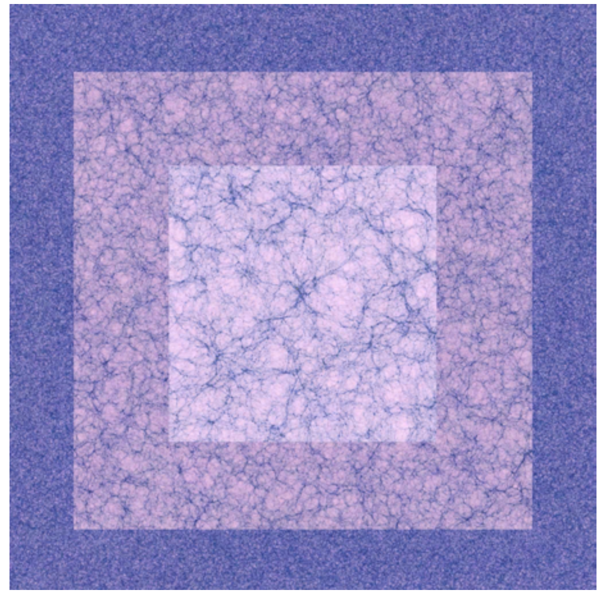

FIG. 9.— A multi resolution view of HORIZON 4Π. The outer region corresponds to a view of the universe on scales of $16h^{-1}$Gpc: it is generated by unfolding the simulation while cuting a slice obliquely through the cube in order to preserve the continuity of the field thanks to the periodicity. The intermediate region corresponds to a slice of $2h^{-1}$Gpc, while the inner region is at the original resolution the initial conditions. RAMSES has refined 6 times over the course of the run from that resolution.

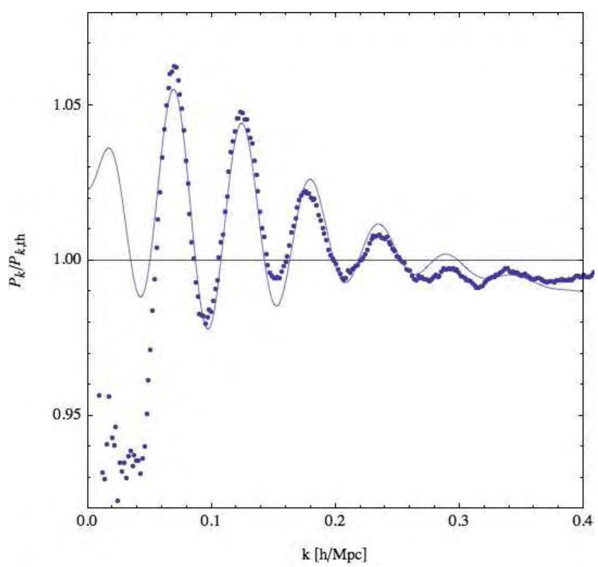

FIG. 10.— The measured baryon wiggles at $z = 0$ together with the corresponding fit (scaling like $\exp(-[k/0.1]^{1.4}) \sin(2\pi k/k_A)$ plus some linear drift in k), which finds that $2\pi/k_A = 113h^{-1}$Mpc.

that the AMR structure of the RAMSES code leaves the opportunity of measuring the power spectrum at frequencies beyond the Nyquist frequency of the 4096^3 grid. Such measurements are outside the scope of this paper, and the power spectrum tool `powergrid` should be viewed primarily as a diagnosis tool. Here, as a check of both the initial condition generation algorithm, including the implementation of the baryon wiggles, a novelty of this implementation, figure 10 displays the measured baryon wiggles in the $z = 0$ snapshot, together with the corresponding fit.

Parameters	Description
4	Power spectrum parametrization: 4 is Eisenstein & Hu
$0.24, 0.76, 73.0$	$\Omega_m, \Omega_\Lambda, H_0$
0.042	Ω_b
0.96	n_S
-0.92	Normalization: $-\sigma_8$ if negative, Q_{rms} if positive
$0.01, 100.0$	k_{min} and k_{max} in $h^{-1}Mpc$ for analytical PS output
-50.0	Box length in $h^{-1}Mpc$ if negative, mesh length in Mpc if positive
1	`Grafic1` mode: no choice here
0	`Grafic1` mode: no choice here
1	1: Generate noise file and save it / 2: Read from noise file
1234	Initial seed (useful if 1 is set above)
white-256.dat	Noise file name
1	1: Constraint of large scale phases with small noise file / 2: No padding
white-128.dat	Small (constraint) noise file name

TABLE 2
`MPGRAFIC` PARAMETER FILE EXAMPLE.

5. CONCLUSION

A series of tools to construct and validate initial conditions for large ($n \geq 1024^3$) cosmological simulations in parallel were presented and illustrated. These tools involve ICs generation with optional constraints, low-pass filtering and resampling, power spectrum estimation, estimation of matter density on a grid from a set of particle positions and Peano-Hilbert domain decomposition. As illustrated in section 4, they allowed us to produce very large cosmological simulations. From these high-resolution ICs, one can then create at will, zoom-like initial conditions and constrained ICs with the help of the resampling tool. Let us emphasize that `mprafic` provides an alternative route to initial condition generation such as `Grafic2`. It is more versatile as it does not impose any relationship between resolution and boundaries for the refined sub volumes. The remaining limitation is the total amount of memory available on distributed architectures. A logical extension of this work will be to generate initial conditions corresponding to the local group. Note finally that with simple amendments, the above mentionned code could be used in the context of vector field generation (magnetic field with a given helicity), or turbulence.

We warmly thank the Barcelona Supercomputing Center and the CCRT staff for their help in producing the Horizon-MareNostrum and the Horizon-4Π simulations. We also thank the referee for his careful reading of the manuscript, G. Yepes for his help with the MareNostrum initial conditions, Stephane Colombi, Karim Benabed, Julien Devriendt, Thierry Sousbie for advices, and D. Munro for freely distributing his `Yorick` programming language and opengl interface (available at `http://yorick.sourceforge.net`). This work was carried within the framework of the HORIZON project: `http://www.projet-horizon.fr`. All codes described in this paper are available at `ftp://ftp.iap.fr/pub/from_users/prunet/`.

APPENDIX

MPGRAFICS PARAMETER FILE

REFERENCES

J. K. Adelman-McCarthy and for the SDSS Collaboration. The Sixth Data Release of the Sloan Digital Sky Survey. *ArXiv e-prints*, 707, July 2007.

J. M. Bardeen, J. R. Bond, N. Kaiser, and A. S. Szalay. The statistics of peaks of gaussian random fields. *ApJ*, 304:15–61, May 1986.

E. Bertschinger. Multiscale Gaussian Random Fields and Their Application to Cosmological Simulations. *ApJS*, 137:1–20, November 2001.

J. R. Bond, L. Kofman, and D. Pogosyan. How filaments of galaxies are woven into the cosmic web. *Nature*, 380:603–+, April 1996.

J. R. Bond and S. T. Myers. The Peak-Patch Picture of Cosmic Catalogs. I. Algorithms. *ApJS*, 103:1–+, March 1996.

R. Cen and J. P. Ostriker. Physical Bias of Galaxies from Large-Scale Hydrodynamic Simulations. *ApJ*, 538:83–91, July 2000.

D. J. Eisenstein and W. Hu. Baryonic Features in the Matter Transfer Function. *ApJ*, 496:605–+, March 1998.

C. S. Frenk, J. M. Colberg, H. M. P. Couchman, G. Efstathiou, A. E. Evrard, A. Jenkins, T. J. MacFarland, B. Moore, J. A. Peacock, F. R. Pearce, P. A. Thomas, S. D. M. White, and N. Yoshida. Public Release of N-body simulation and related data by the Virgo consortium. *ArXiv Astrophysics e-prints*, July 2000.

S. Gottlöber and G. Yepes. Shape, Spin, and Baryon Fraction of Clusters in the MareNostrum Universe. *ApJ*, 664:117–122, July 2007.

Y. Hoffman and E. Ribak. Constrained realizations of Gaussian fields - A simple algorithm. *ApJ*, 380:L5–L8, October 1991.

T. H. Jarrett, T. Chester, R. Cutri, S. E. Schneider, and J. P. Huchra. The 2MASS Large Galaxy Atlas. *AJ*, 125:525–554, February 2003.

P. MacNeice, K.M. Olson, C. Mobarry, R. de Fainchtein, and C. Packer. PARAMESH: A parallel adaptive mesh refinement community toolkit. *Computer Physics Communications*, 126(3): 330–354, 2000.

R. Mohayaee and R. B. Tully. The Cosmological Mean Density and Its Local Variations Probed by Peculiar Velocities. *ApJ*, 635:L113–L116, December 2005.

P. Ocvirk, C. Pichon and R. Teyssier. Bimodal gas accretion in the Mare Nostrum galaxy formation simulation. submitted to *MNRAS*

U.-L. Pen. Generating Cosmological Gaussian Random Fields. *ApJ*, 490:L127+, December 1997.

W. J. Percival, C. M. Baugh, J. Bland-Hawthorn, T. Bridges, R. Cannon, S. Cole, M. Colless, C. Collins, W. Couch, G. Dalton, R. De Propris, S. P. Driver, G. Efstathiou, R. S. Ellis, C. S. Frenk, K. Glazebrook, C. Jackson, O. Lahav, I. Lewis, S. Lumsden, S. Maddox, S. Moody, P. Norberg, J. A. Peacock, B. A. Peterson, W. Sutherland, and K. Taylor. The 2dF Galaxy Redshift Survey: the power spectrum and the matter content of the Universe. *MNRAS*, 327:1297–1306, November 2001.

J. Salmon and MS Warren. Parallel, out-of-core methods for N-body simulation. *Conference: 8. SIAM conference on parallel processing for scientific computing, Minneapolis, MN (United States), 14-17 Mar 1997*, 1997.

A. Shirokov. GRAvitational COSmology (GRACOS) code release announcement, for version 1.0.1a9. *ArXiv e-prints*, 711, November 2007.

R. E. Smith, J. A. Peacock, A. Jenkins, S. D. M. White, C. S. Frenk, F. R. Pearce, P. A. Thomas, G. Efstathiou, and H. M. P. Couchman. Stable clustering, the halo model and non-linear cosmological power spectra. *MNRAS*, 341:1311–1332, June 2003.

V. Springel, S. D. M. White, A. Jenkins, C. S. Frenk, N. Yoshida, L. Gao, J. Navarro, R. Thacker, D. Croton, J. Helly, J. A. Peacock, S. Cole, P. Thomas, H. Couchman, A. Evrard, J. Colberg, and F. Pearce. Simulations of the formation, evolution and clustering of galaxies and quasars. *Nature*, 435: 629–636, June 2005.

R. Teyssier. Cosmological hydrodynamics with adaptive mesh refinement. a new high resolution code called ramses. *A&A*, 385:337–364, April 2002.

R. Teyssier, S. Pires, D. Aubert, C. Pichon, S. Prunet, A. Amara, K. Benabed, S. Colombi, A. Refregier, J.-L. Starck. Full-Sky Weak Lensing Simulation with 70 Billion Particles. submitted to *A&A*, 2007.

R. van de Weygaert. Tidal Fields and Structure Formation. In P. Coles, V. Martinez, and M.-J. Pons-Borderia, editors, *Mapping, Measuring, and Modelling the Universe*, volume 94 of *Astronomical Society of the Pacific Conference Series*, pages 49–+, 1996.

J. W. Wadsley, J. Stadel, and T. Quinn. Gasoline: a flexible, parallel implementation of TreeSPH. *New Astronomy*, 9:137–158, February 2004.

D. H. Weinberg, L. Hernquist, and N. Katz. High-Redshift Galaxies in Cold Dark Matter Models. *ApJ*, 571:15–29, May 2002.

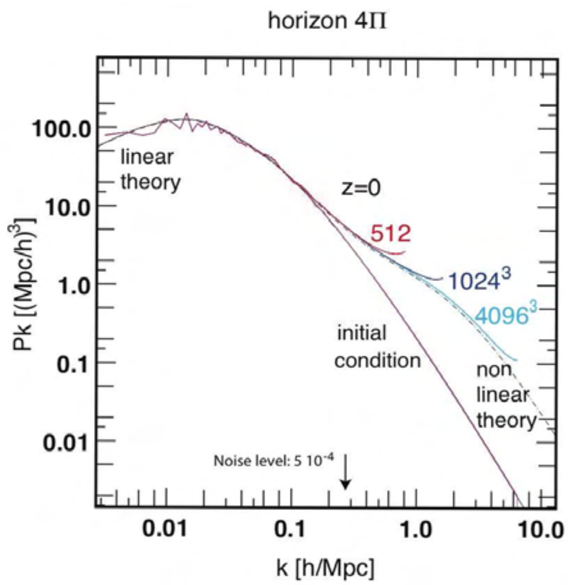

FIG. 11.— A Measure of the power spectrum with `powergrid` of the HORIZON-4Π in the `mpgrafic` generated initial condition (*bottom curve*) and at redshift zero for different samplings (*top curves* for resp. $512^3, 1024^3$and 4096^3 as labeled), with the modes k in units of h^{-1}Mpc. Here the density is resampled on the grids using the nearest grid point kernel (NGP) whose bias is corrected. However, the shot noise bias was not corrected in this figure, and no attempt was made to correct the power aliased by the resampling procedure. Both measurements are compared to resp. the linear theory and the theoretical predictions of Smith et al. (2003). Note that the agreement between the linear theory and the generated initial conditions is excellent for all measured scales.

Astronomy & Astrophysics manuscript no. article2
July 24, 2008

Full-Sky Weak Lensing Simulation with 70 Billion Particles

Romain Teyssier[1,4], Sandrine Pires[1,2], Simon Prunet[4], Dominique Aubert[3], Christophe Pichon[1,4], Adam Amara[1], Karim Benabed[4], Stéphane Colombi[4], Alexandre Refregier[1], and Jean-Luc Starck[1,2]

[1] Service d'Astrophysique, CEA Saclay, Batiment 709, 91191 Gif–sur–Yvette Cedex, France
[2] Service d'Electronique, de Detection et d'Informatique, CEA Saclay, Batiment 141, 91191 Gif–sur–Yvette Cedex, France
[3] Observatoire Astronomique, Université de Strasbourg, UMR 7550, 11 rue de l'Université, 67000, Strasbourg, France
[4] Institut d'Astrophysique de Paris, 98 bis, boulevard Arago, 75014 Paris, France

Accepted; Received; in original form;

ABSTRACT

We have performed a 70 billion dark matter particles N–body simulation in a 2 h^{-1} Gpc periodic box, using the concordance cosmological model as favored by the latest WMAP3 results. We have computed a full sky convergence map with a resolution of $\Delta\theta \simeq 0.74$ arcmin^2, spanning 4 orders of magnitude in angular dynamical range. Using various high-order statistics on a realistic cut sky, we have characterized the transition from the linear to the non–linear regime at $\ell \simeq 1000$ and shown that realistic galactic masking only affect high–order moments below $\ell < 200$. Each domain (Gaussian and non–Gaussian) spans 2 decades in angular scale. This map is therefore an ideal tool to test map–making algorithms on the sphere. As a first step in addressing the full map reconstruction problem, we have benchmarked in this paper two denoising methods: 1) Wiener filtering applied on the Spherical Harmonics decomposition of the map and 2) a new method, called MRLens, based on the modification of the Maximum Entropy Method on a Wavelet decomposition. While the latter is optimal on large scales, where the signal is Gaussian, MRLens outperforms Wiener on small scales, where the signal is highly non–Gaussian. The simulated Full-Sky convergence map is freely available to the community to help the development of new map–making algorithms dedicated to the next generation weak–lensing surveys.

Key words. Methods: N–body simulations; Cosmology: observations; Techniques: image processing

1. Introduction

Weak gravitational lensing, or 'cosmic shear', provides a unique tool for mapping the matter density distribution in the Universe (for reviews, see Refregier 2003; Hoekstra 2003; Munshi et al. 2006). Current weak lensing surveys together cover about 100 square degrees and have been used to measure the amplitude of the matter power spectrum and other cosmological parameters (see Benjamin et al. 2007, and references therein). A number of new instruments are being planned to carry out these surveys over larger sky fractions (PanSTARRS, DES, SNAP and LSST)[1] or even over the full extra-galactic sky (DUNE[2]). Such wide field surveys will yield cosmic shear measurements on both large scales, where gravitational dynamics is in the linear regime, and small scales, where the dynamics is highly non-linear. The comparison of these measurements with theoretical predictions of the evolution of the density field will place strong constraints on the cosmological parameters including dark energy parameters (eg. Hu & Tegmark 1999; Huterer 2002; Amara & Refregier 2006; Albrecht & Bernstein 2007). On small scales, the highly non-linear nature of the density field makes predictions based on analytic calculations prohibitively difficult and requires the use of numerical simulations. N-body simulations have thus been used to simulate weak lensing maps on small patches using the flat sky approximation (eg. Jain et al. 2000; Hamana et al. 2001; White & Vale 2004). The simulation of full-sky maps required for future surveys involve a wide dynamical range in both mass and length scales and is quite challenging for current N body simulations. The range of scales involved also requires the development of efficient algorithms for deriving a mass map from real noisy data sets. These algorithms need to be well–suited to both the large–scale signal, essentially a Gaussian random field, and that at small–scales, where it is highly non–Gaussian and exhibits localized features.

In this paper, we use a high resolution N-body simulation to construct, for the first time, a full sky weak lensing map and test a new map reconstruction method based on the multiresolution technique. For this purpose, we use the Horizon simulation, a 70 billion particles N–body simulation, featuring more than 140 billion cells in the AMR grid of the RAMSES code (Teyssier 2002). The simulation covers a sufficiently large volume ($L_{box} = 2h^{-1}$Gpc) to compute a full sky convergence map, while resolving Milky-Way size halos with more than 100 particles, and exploring small scales deeply into the non–linear regime (see Section 2). This unprecedented computational effort allows us, for the first time, to close the gap between scales close to the cosmological horizon and scales deep inside virialized dark matter haloes.

The dark matter distribution in the simulation was integrated in a light cone out to redshift 1, around an observer located at the center of the simulation box (see Section 3). This light cone was then used to calculate the corresponding Full Sky lensing convergence field, which we map using the Healpix pixelisation scheme (Górski et al. 2005) with a pixel resolution of $\Delta\theta \simeq 0.74$ arcmin^2 ($n_{\rm side} = 4096$), and add "instrumental" noise for a typical all–sky survey with 40 galaxies per arcmin^2, as expected for example for the DUNE mission (Réfrégier et al. 2006). Using an Undecimated Isotropic Wavelet Decomposition of this real-

Send offprint requests to: romain.teyssier@cea.fr
[1] http://pan-starrs.ifa.hawaii.edu, https://www.darkenergysurvey.org, http://snap.lbl.gov and http://www.lsst.org
[2] http://www.dune-mission.net

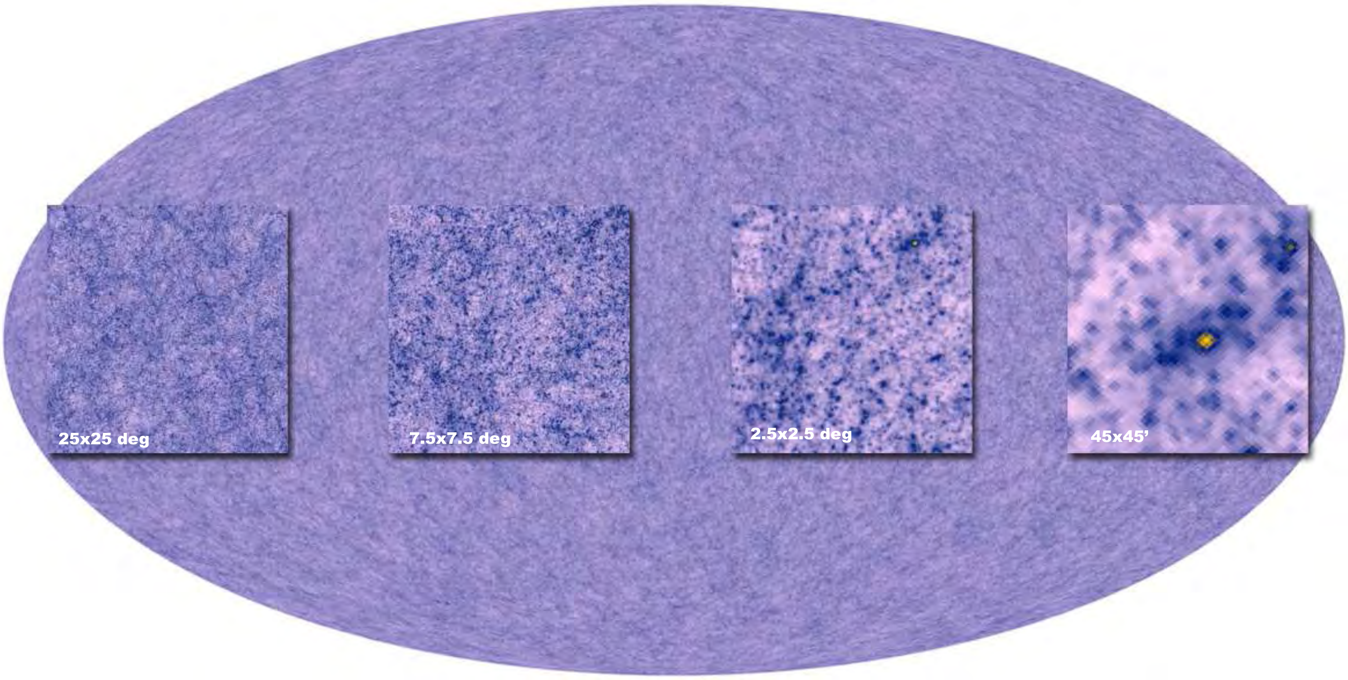

Fig. 1. Full-sky simulated convergence map derived from the Horizon Simulation. Its resolution of 200 million pixels has been downgraded to fit the page. The various inserts display a zoom sequence into smaller and smaller areas of the sky. The pixel size is 0.74 arcmin^2.

istic simulated weak-lensing map on the sphere, we analyze the statistics of each wavelet plane using second, third and fourth order moments estimator (Section 4). We then apply, in Section 5, a multiresolution algorithm to filter a fictitious simulated κ data set based on an extension of the wavelet filtering technique of Starck et al. (2006b). We characterise the quality of the reconstruction using the power spectrum of the error map and compare this to the result of standard Wiener filtering on the sphere. Our results, summarised in Section 6, illustrate the virtue of high resolution simulations such as the one reported here to prepare for future weak lensing surveys and to design new map–making technics.

2. The Horizon N Body Simulation

This large N body simulation was carried out using the RAMSES code (Teyssier 2002) for two months on the 6144 Itanium2 processors of the CEA supercomputer BULL Novascale 3045 hosted in France by CCRT[3]. RAMSES is a parallel hydro and N body code based on the Adaptive Mesh Refinement (AMR) technics. Using a parallel version of the `grafic` package (Bertschinger 2001), we generated the initial displacement field on a 4096^3 grid for the cosmological parameters from the WMAP 3rd year results (Spergel et al. 2007), namely $\Omega_m = 0.24$, $\Omega_\Lambda = 0.76$, $\Omega_b = 0.042$, $n = 0.958$, $H_0 = 73$ km/s/Mpc and $\sigma_8 = 0.77$. We used the Eisenstein & Hu (1999) transfer function, which includes baryon oscillations. The box size was set to 2 Gpc/h, which corresponds roughly to a comoving distance to an object at $z \simeq 0.8$. We use 68.7 billion particles to sample the dark matter density field, yielding a particle mass of $7.7 \times 10^9\ M_\odot$ and 130 particles per Milky Way halo. This large particle distribution was split across 6144 individual files, one for each processor, according to the RAMSES code domain decomposition strategy (Prunet et al. 2007). Starting with a base (or coarse) grid with 4096^3 grid points, each AMR cell is individually refined if the number of particles in the cell exceeds 40. In this way, the number of particles per cell varies between 5 and 40, so that the particle shot noise is ensured to remain at an acceptable level. This refinement strategy was applied recursively, with a factor of 2 in linear size between each level of refinement. At the end of the simulation, we reached 6 levels of refinement with a total of 140 billion AMR cells. This corresponds to a formal resolution of 262144^3 or 7.6 h^{-1} kpc comoving spatial resolution. Parallel computing is perfomed using the MPI message passing library, with a domain decomposition based on the Peano–Hilbert space–filling curve. The work and memory load was dynamically adjusted by reshuffling particles and grid points from each processor to its neighbors. The simulation required 737 main (or coarse) time steps and more than 10^4 fine time steps for completion.

[3] Centre de Calcul Recherche et Technologie

3. Light Cone and Convergence Map

We constructed a light cone by storing, at each main time step, the positions of all the particles lying within the boundaries of a photon plane moving at the speed of light towards an observer located at the center of the box, based on technics presented in Hamana et al. (2001). This lead to 348 slices in the light cone, spanning the redshift range [0,1]. Thanks to the large size of the simulated volume, the effect of periodic replications of the computational box are minimised. Each slice was then converted into a full-sky Healpix map ($nside = 4096$) of the average overdensity using a simple "Nearest Grid Point" mass projection scheme. We assumed that the background galaxies are on a single source plane located at redshift $z_s = 1$. The final convergence map has been finally computed using a new ray-tracing scheme described in Appendix A and based on a multiple lens plane approach (see Jain et al. 2000; Hamana et al. 2001; White & Vale 2004, for other approaches). Using Born approximation for all neighboring light rays is a good approximation

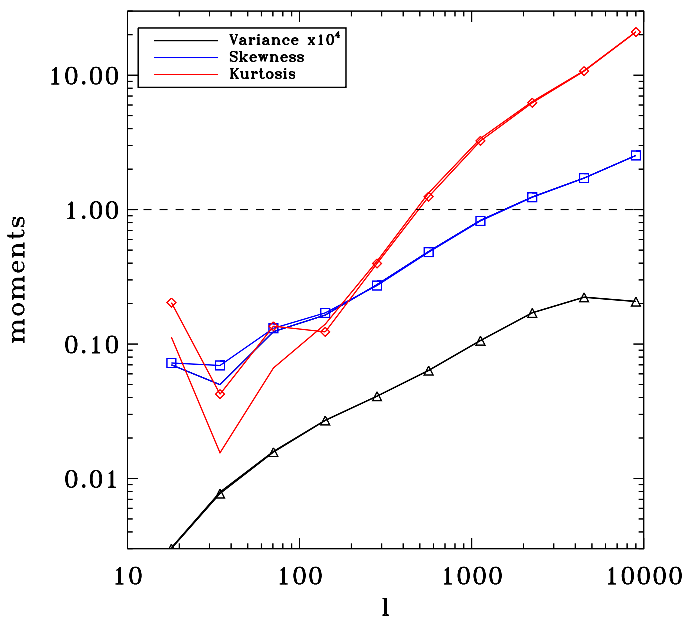

Fig. 2. Moments of the convergence as a function of the average multipole moment for each wavelet scale. The variance, skewness and kurtosis are shown as black, blue and red lines, respectively. Solid lines are for a full sky analysis while symbols correspond to our realistic sky cut analysis.

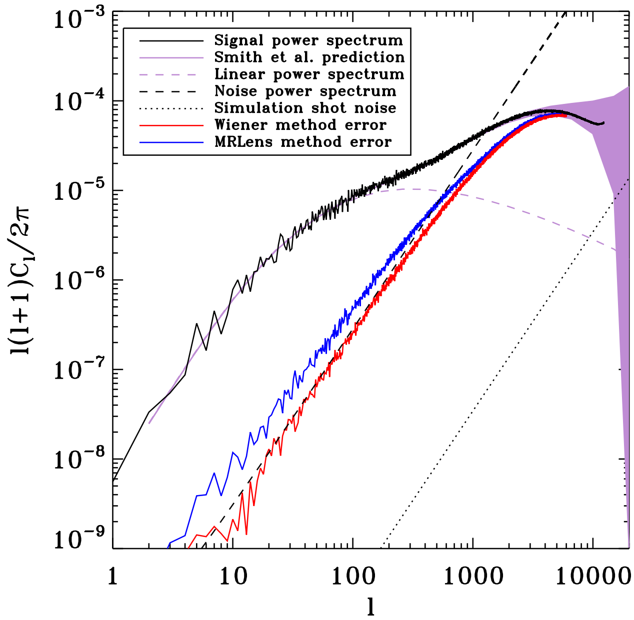

Fig. 3. Angular power spectrum of the simulated convergence map (black solid line), compared to a fit based on the Smith et al. (2001) analytical model with error bars corresponding to our noise model (pink area). Also shown is the prediction from linear theory (pink dashed curve). The noise power spectrum is plotted as the dashed black line. The green solid line is the power spectrum of the error map obtained with the Wiener filter method, while the blue solid line are that for the MRLens method.

in the linear regime of structure formation, but certainly fails in the non-linear regime. Consequently, distortion effects of lensing beyond the first order cannot be reliably simulated. Moreover, as shown by Van Waerbeke et al. (2001), the Born approximation introduces a relative error in the skewness of the signal of the order of 10% on large scales where the convergence is Gaussian, and around 1% on small scales in the non–linear regime.

The resulting full sky Healpix map, with a pixel size of $\Delta\theta \simeq 0.74$ arcmin^2 is shown in Figure 1, with small inserts to highlight the large dynamical range achieved. Higher resolution images are available at `http://www.projet-horizon.fr`. The shot noise corresponding to our 70 billion particles has a small impact on the map. As shown in Figure 3, the shot noise is well below the expected instrumental noise, and even low enough to be negligeable in the spectral analysis of the signal.

4. High–Order Moments and Realistic Sky Cut

In Figure 1 the signal appears as a typical Gaussian random field on large scales, similar to the Cosmic Microwave Background map seen by the WMAP satellite (Spergel et al. 2007). On small scales, the signal is clearly dominated by clumpy structures (dark matter halos) and is therefore highly non-Gaussian. To characterize this quantitatively, we have performed a wavelet decomposition of our map using the Undecimated Isotropic Wavelet Transform on the sphere (Starck et al. 2006a), and, for each wavelet scale, we have computed its second-, third- and fourth-order moment. We used 11 wavelet scales with central multipole ℓ_0 = 9000, 4500, 2250, 1125, 562, 282, 141, 71, 35, 18. For each of these maps, we have computed the variance $\sigma^2 = <\kappa^2>$, the normalized skewness $S = <\kappa^3> / \sigma^3$ and the normalized kurtosis $K = <\kappa^4> / \sigma^4$. Results are plotted in Figure 2 as solid lines with various colors. We see that the variance of the signal steadily rises for higher and higher multipoles, and saturates at a fraction of 10^{-4}, corresponding to the value predicted from the non–linear gravitational clustering for $\ell \geq 6000$. The variance of each wavelet plane can be considered as a band power estimate of the angular power spectrum, as can be checked using Figure 3. In the same figure, we have also plotted for comparison the *linear* power spectrum, in order to highlight the scale below which non–linear clustering contributes significantly, i.e. for $\ell > 750$ or equivalently $\theta < 15'$, as first pointed out by Jain & Seljak (1997). The skewness and the kurtosis are more direct estimators of the non–Gaussianity of the signal: departure from Gaussianity occurs around $\ell \simeq 750 - 1500$, where both statistics cross unity. Thanks to the large dynamical range of the Horizon simulation, we have computed a map spanning two decades in angular scales in the linear, Gaussian regime and two additional decades in angular scales deep into the non–linear, non–Gaussian regime.

It is clear from Figure 2 that at small ℓ, the skewness and the kurtosis of the map are strongly affected by cosmic variance. Moreover, the statistics of the convergence field cannot be measured in practice over the entire sky because of sky cuts imposed by the presence of saturated stars and by absorption in the galactic plane. We have estimated the impact of this sky cut on the accuracy of our multiresolution statistical analysis. For this purpose, we have computed the expected number of bright stars that would typically saturate the CCD's of a wide field survey (B-magnitude< 20) , and removed from our analysis each pixel contaminated by at least 3 bright stars, based on a random Poisson realization of bright stars in our Galaxy (according to the model of Bahcall & Soneira (1980), Appendix B). We obtain a mask with 40% of the sky removed, corresponding roughly to a

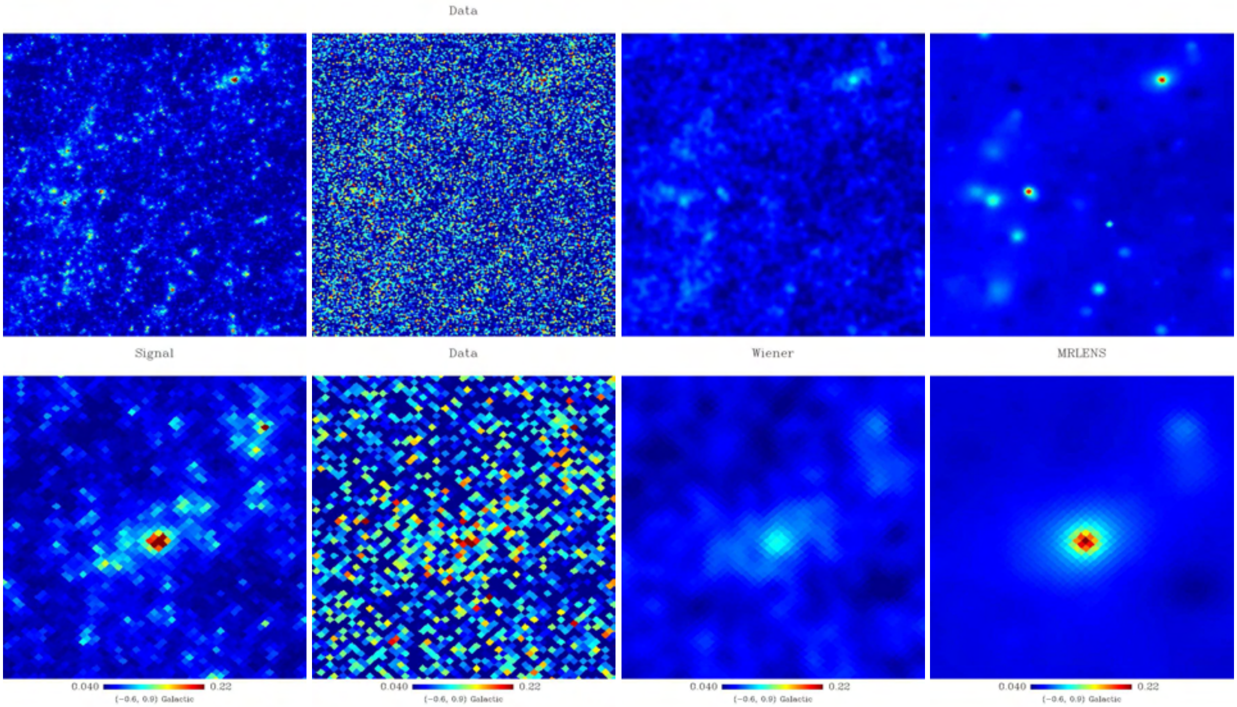

Fig. 4. Reconstruction of convergence maps with our 2 filtering techniques. The top panels show the $2.5^o \times 2.5^o$ square map corresponding to first zoom sequence of Figure 1. The bottom panels are subset of the corresponding top images with linear size $45'$. From left to right, we show the original signal, the noisy image, the Wiener-filtered image and the the MRLens-filtered image.

$\pm 20^o$ Galaxy cut. The resulting statistics are overplotted as lines with symbols in Figure 2. The transition scale, for which the departure from Gaussianity is significant, can still be reliabily estimated around $\ell \simeq 750 - 1500$. We conclude that the cosmic variance of the cut sky affects high–order moments only below $\ell \simeq 200$.

5. Map–Making using Multiresolution Filtering

The full-sky simulated convergence maps described above can be used to analyze and compare denoising (or map–making) methods on the sphere. For this purpose, we have considered a purely white instrumental noise, typical of the next generation all–sky surveys, with root mean square per pixel of area A_p given by $\sigma_N = 0.3/\sqrt{n_{gal} A_p}$ with $n_{gal} = 40$ background galaxies per arcmin^2. Recovering the best convergence map from noisy data will be an important step in future surveys. The reconstructed map can indeed be used to construct a mass selected halo catalog, measure its statistical properties to constrain cosmological parameters, as well as to compare it to cluster catalogues detected via other techniques (X-ray, galaxy counts or SZ). Note that we restrict ourselves to the full sky denoising of a convergence map already reconstructed from the shear derived from galaxy ellipticities.

A straightforward filtering method is the Wiener filtering scheme, which is optimal for Gaussian random fields, and is thus expected to work effectively at large scales. Defining S_ℓ as the power spectrum of the input signal (see Figure 3) and N_ℓ the power spectrum of the noise, this method involves convolving the noisy map by the Wiener filter defined as $W_\ell = S_\ell/(S_\ell + N_\ell)$. The results of the Wiener filtering approach are shown in Figure 4. Comparing with the input signal map, we conclude that, although the agreement is satisfactory on large scales, the dense clumps clearly visible in the image are poorly recovered as they have been over-smoothed.

A dedicated weak lensing wavelet restoration method, called MRLens, has recently been presented (Starck et al. 2006b). It can be seen as an extension of the Maximum Entropy Method (MEM), but with a different concept of information. In MRLens, the entropy constraint is not applied on the pixels of the solution, but rather on its wavelet coefficients. This allows us to take into account more efficiently the multi-scale behavior of the information. MRLens was however designed for weak lensing maps with smaller surface on the sky, for which the non–Gaussian signal is stronger. MRLens has been extended here to the sphere by considering independently each of the 12 Healpix base pixels covering the sphere as 12 independent Cartesian maps, on which we applied the MRLens algorithm of Starck et al. (2006b). Full sky denoising performed with MRLens is shown in Figure 4. It performs much better than Wiener on small scales, with dense clumps more accurately estimated, but less efficient than Wiener at large scale when recovering low frequency waves in the map. We have also computed the angular power spectrum of the error map (see Figure 3) for both cases (Wiener and MRLens). We see that Wiener filtering outperforms MRLens on large scales.

Interestingly, the MRLens errors decrease significantly above the transition scale we have identified in the last section around $\ell \simeq 1000$ (see Fig. 3). This strongly suggests that new methods should be developed using a multiresolution formulation; for instance using spherical harmonics on large scales, while exploiting wavelets coefficients on small scales. The methodology of such a combined approach could be based on the idea of Combined Filtering introduced by Starck et al. (2006a).

6. Conclusion

Using the 70 billion particles of the Horizon N–body Simulation, we have computed for the first time a realistic full sky convergence map with a pixel resolution of $\Delta\theta \simeq 0.74$ arcmin^2. We have analyzed the resulting map using multiresolution statistics (variance, skewness and kurtosis) and angular power spectrum analysis. We have shown that this simulated map spans 4 decades of usefull signal in angular scale, with 2 decades within the linear, Gaussian regime and 2 decades well into the non–linear, non–Gaussian regime. We have shown that, when considering a realistic sky cut, we can reliabily estimate high–order moments of the map above $\ell \simeq 200$. Using even higher resolution maps, angular scales smaller than $\theta \simeq 1'$ could be explored in future works, although the mass ditribution at these scales might be affected by baryons physics (Jing et al. 2006), so that the present map might already cover all cosmologically relevant scales.

As a first step towards a realistic map–making procedure, we have tested two denoising schemes on a simplified fictitious dataset derived from the full sky map, namely Wiener filtering and the MRLens method (Starck et al. 2006b). We have shown quantitatively that Wiener filtering is the best method on large scales, but some signal is lost at small scales. MRLens performs better on small scales and recovers the dense clumps associated to dark matter halos, but deals less accurately with low frequency waves in the map. Hence this work demonstrates the need for an hybrid multiresolution approach, e.g. by combining spherical harmonics and wavelet coefficients. The present analysis will be extended in future works to map–making algorithms dealing directly with galaxy shears. The simulated convergence map is freely available for download at `http://www.projet-horizon.fr`. It may prove to be an effective tool for the design of new map–making methods and for the preparation of the next generation weak–lensing surveys.

Acknowledgements. We would like to thank Julien Devriendt, Pierre Ocvirk, Arthur Petitpierre and Philippe Lachamp for their unvaluable help during the course of this project. The Horizon Simulation presented here was supported by the "Centre de Calcul Recherche et Technologie" (CEA, France) as a "Grand Challenge project". This work was supported by the Horizon Project.

Appendix A: Computing the convergence maps from simulations

We first recall how to compute the convergence in the Born approximation, and then we present our new ray-tracing scheme.

A.1. Born approximation

We start from the convergence formula relating it to the density contrast:

$$\kappa(\hat{n}) = \frac{3}{2}\Omega_m \int_0^{z_s} \frac{dz}{E(z)} \frac{\mathcal{D}(z)\mathcal{D}(z,z_s)}{\mathcal{D}(z_s)} \frac{1}{a(z)} \delta(\frac{c}{H_0}\mathcal{D}(z)\hat{n}, z)$$

which is valid for sources at a single redshift z_s, and $\mathcal{D}(z) = \frac{H_0}{c}\chi(z)$is the adimensional comobile radial coordinate ($d\mathcal{D} = dz/E(z)$). We will now rewrite this formula in a form that is more suited to integration over redshift slices in a simulation.

$$\kappa(\theta_{pix}) \approx \frac{3}{2}\Omega_m \sum_b W_b \frac{H_0}{c} \int_{\Delta z_b} \frac{cdz}{H_0 E(z)} \delta(\frac{c}{H_0}\mathcal{D}(z)\hat{n}_{pix}, z)$$

where

$$W_b = \left(\int_{\Delta z_b} \frac{dz}{E(z)} \frac{\mathcal{D}(z)\mathcal{D}(z,z_s)}{\mathcal{D}(z_s)} \frac{1}{a(z)}\right) / \left(\int_{\Delta z_b} \frac{dz}{E(z)}\right)$$

is a slice-related weight, and the integral over the density contrast reads

$$\begin{aligned} I &= \int_{\Delta z_b} \frac{cdz}{H_0 E(z)} \delta(\frac{c}{H_0}\mathcal{D}(z)\hat{n}_{pix}, z) \\ &= \int_{\Delta \chi_b} d\chi \delta(\chi \hat{n}_{pix}, \chi) \\ &\approx \frac{V(simu)}{N_{part}(simu)} \left(\frac{N_{part}(\theta_{pix}, z_b)}{S_{pix}(z_b)} - \Delta\chi_b\right) \end{aligned}$$

where

$$S_{pix}(z_b) = \frac{4\pi}{N_{pix}} \frac{c^2}{H_0^2} \mathcal{D}^2(z_b)$$

is the comoving surface of the spherical pixel. Putting all together, we get the following formula for the convergence map (forgetting the $\Delta\chi_b$ term that leads to a constant term):

$$\kappa(\theta_{pix}) = \frac{3}{2}\Omega_m \frac{N_{pix}}{4\pi} \left(\frac{H_0}{c}\right)^3 \frac{V(simu)}{N_{part}(simu)} \sum_b W_b \frac{N_{part}(\theta_{pix}, z_b)}{\mathcal{D}^2(z_b)} \quad \text{(A.1)}$$

This is the equation used to get the convergence map in the Born approximation.

A.2. Ray–tracig using multiple planes

We will discuss here the formulae needed for the multi-plane computations, where we consider the lensing by a number of thin lenses located at $\{z_b\}$. Let us define

$$\kappa_{fac} = \frac{3}{2}\Omega_m \frac{N_{pix}}{4\pi} \left(\frac{H_0}{c}\right)^3 \frac{V(simu)}{N_{part}(simu)}$$

and

$$\zeta(z_b, \theta) = \kappa_{fac}\omega(z_b) \frac{N_{part}(\theta, z_b)}{\mathcal{D}^2(z_b)} \quad \text{(A.2)}$$

with

$$\omega(z_b) = \left(\int_{\Delta z_b} \frac{dz}{E(z)} \frac{\mathcal{D}(z)}{a(z)}\right) / \left(\int_{\Delta z_b} \frac{dz}{E(z)}\right)$$

To follow the light rays, we are interested in computing the angular displacement field for each ray i due to a slice at z_b. We then define

$$\alpha_i^b = \left(-2\nabla\Delta^{-1}\left(\zeta(z_b)\right)\right)(\theta_i) \quad \text{(A.3)}$$

where the gradient and Laplacien are computed using angular covariant derivatives on the (unit) sphere, and $\theta_i$is the current direction of light ray i when it hits the slice b. Now, let us start from light rays being back-propagated from the observer at z=0 towards the source (here at z=1). Let us denote by $\{\theta^1\}$ the location of the Healpix centers, which corresponds to the initial directions of the back-propagated rays emanating from the observer. The tangent vectors to each light ray will be modified by the deflection field at each lens plane, defined by equation A.3. Then, computing the displacement of the rays at slice b reads

$$\boldsymbol{\alpha}_i^b = \left(-2\nabla\Delta^{-1}(\zeta(z_b)\right)(\theta_i^b)$$

We then update the direction $\boldsymbol{\beta}_i^b$ of the rays according to

$$\boldsymbol{\beta}_i^b = R(\boldsymbol{n}_i^b \times \boldsymbol{\alpha}_i^b, ||\boldsymbol{\alpha}_i^b||)\boldsymbol{\beta}_i^{b-1} \quad \text{(A.4)}$$

where $\boldsymbol{\beta}_i^0 = \boldsymbol{n}_i^1$ (light rays are shot from observer, thus perpendicularly to the first slice), and $\boldsymbol{n}_i^b$is the vector normal to slice b at the intersection of light-ray i on slice b. Equation A.4 can be simplified by noting that $\boldsymbol{\alpha}$ is naturally expressed in the local $(\boldsymbol{e}_{\theta,}\boldsymbol{e}_{\phi})$ basis of the tangent plane at position (θ, ϕ):

$$\boldsymbol{\alpha} = ||\boldsymbol{\alpha}||(\cos\delta\boldsymbol{e}_\theta + \sin\delta\boldsymbol{e}_\phi)$$

Once the new value of $\boldsymbol{\beta}$ has been calculated, one needs to compute the intersection of the light rays with the next shell. Let us call $\boldsymbol{x}_i^b$the cartesian position of the intersection of light ray i with slice b, then the next intersection will be given by

$$\begin{aligned} \boldsymbol{x}_i^{b+1} &= \boldsymbol{x}_i^b + \lambda\boldsymbol{\beta}_i^b \\ \lambda^2 + 2\lambda(\boldsymbol{x}_i^b.\boldsymbol{\beta}_i^b) + R_b^2 - R_{b+1}^2 &= 0\,,\ \lambda > 0 \end{aligned}$$

assuming that $\boldsymbol{\beta}$ is kept strictly unitary, and R_b is the comoving radius of slice b. Once $\boldsymbol{x}_i^{b+1}$is known, it is easy to compute the new θ_i^{b+1}positions. The contributions to κ are then calculated following Equation A.1, but where the slice contributions are interpolated at the displaced positions:

$$\kappa(\theta_{i=pix}) = \frac{3}{2}\Omega_m \frac{N_{pix}}{4\pi}\left(\frac{H_0}{c}\right)^3 \frac{V(simu)}{N_{part}(simu)} \sum_b W_b \frac{N_{part}(\theta_i^b, z_b)}{\mathcal{D}^2(z_b)}$$

References

Albrecht, A. & Bernstein, G. 2007, Phys. Rev. D, 75, 103003
Amara, A. & Refregier, A. 2006, ArXiv Astrophysics e-prints
Bahcall, J. N. & Soneira, R. M. 1980, ApJS, 44, 73
Bartelmann, M. & Schneider, P. 2001, Phys. Rep., 340, 291
Benjamin, J., Heymans, C., Semboloni, E., et al. 2007, ArXiv Astrophysics e-prints
Bertschinger, E. 2001, ApJS, 137, 1
Eisenstein, D. J. & Hu, W. 1999, ApJ, 511, 5
Górski, K. M., Hivon, E., Banday, A. J., et al. 2005, ApJ, 622, 759
Hamana, T., Colombi, S., & Suto, Y. 2001, A&A, 367, 18
Hoekstra, H. 2003, ArXiv Astrophysics e-prints
Hu, W. & Tegmark, M. 1999, ApJ, 514, L65
Huterer, D. 2002, Phys. Rev. D, 65, 063001
Jain, B. & Seljak, U. 1997, ApJ, 484, 560
Jain, B., Seljak, U., & White, S. 2000, ApJ, 530, 547
Jing, Y. P., Zhang, P., Lin, W. P., Gao, L., & Springel, V. 2006, ApJ, 640, L119
Munshi, D., Valageas, P., Van Waerbeke, L., & Heavens, A. 2006, ArXiv Astrophysics e-prints
Prunet, S., Pichon, C., Aubert, D., Pogosyan, D., & Teyssier, R. 2007, in preparation
Refregier, A. 2003, ARA&A, 41, 645
Réfrégier, A., Boulade, O., Mellier, Y., et al. 2006, in Presented at the Society of Photo-Optical Instrumentation Engineers (SPIE) Conference, Vol. 6265, Space Telescopes and Instrumentation I: Optical, Infrared, and Millimeter. Edited by Mather, John C.; MacEwen, Howard A.; de Graauw, Mattheus W. M.. Proceedings of the SPIE, Volume 6265, pp. 62651Y (2006).
Spergel, D. N., Bean, R., Doré, O., et al. 2007, ApJS, 170, 377
Starck, J.-L., Moudden, Y., Abrial, P., & Nguyen, M. 2006a, A&A, 446, 1191
Starck, J.-L., Pires, S., & Réfrégier, A. 2006b, A&A, 451, 1139
Teyssier, R. 2002, A&A, 385, 337
Van Waerbeke, L., Hamana, T., Scoccimarro, R., Colombi, S., & Bernardeau, F. 2001, MNRAS, 322, 918
White, M. & Vale, C. 2004, Astroparticle Physics, 22, 19

Mon. Not. R. Astron. Soc. **000**, 000–000 (0000) Printed 31 March 2008 (MN LATEX style file v2.2)

Bimodal gas accretion in the MareNostrum galaxy formation simulation

P. Ocvirk[1,2], C. Pichon[3,2] & R. Teyssier[2]
[1] *Astrophysikalisches Institut Potsdam, An der Sternwarte 16, D-14482 Potsdam, Germany.*
[2] *Institut de Recherches sur les lois Fondamentales de l'Univers, DSM, l'Orme des Merisiers, 91198 Gif-sur-Yvette, France.*
[3] *Institut d'Astrophysique de Paris (UMR7095) et UPMC, 98 bis boulevard Arago, 75014 Paris, France.*

Typeset 31 March 2008; Received / Accepted

ABSTRACT
The physics of diffuse gas accretion and the properties of the cold and hot modes of accretion onto proto-galaxies between z=2 and z=5.4 are investigated using the large cosmological simulation performed with the RAMSES code on the MareNostrum supercomputing facility. Galactic winds, chemical enrichment, UV background heating and radiative cooling are taken into account in this very high resolution simulation. Using *accretion–weighted temperature histograms*, we have perfomed two different measurements of the thermal state of the gas accreted towards the central galaxy.

The first measurement, performed using accretion–weighted histograms on a spherical surface of radius $0.2\mathrm{R_{vir}}$ centred on the densest gas structure in the vicinity of the halo centre of mass, is a good indicator of the presence of an accretion shock in the vicinity of the galactic disc. We define the hot shock mass, $\mathrm{M_{shock}}$, as the typical halo mass separating cold dominated from hot dominated accretion in the vicinity of the galaxy.

The second measurement is performed by radially averaging histograms between $0.2\mathrm{R_{vir}}$ and $\mathrm{R_{vir}}$, in order to detect radially extended structures such as gas filaments: this is a good proxy for detecting cold streams feeding the central galaxy. We define $\mathrm{M_{stream}}$ as the transition mass separating cold dominated from hot dominated accretion in the outer halo, marking the disappearance of these cold streams.

We find a hot shock transition mass of $\mathrm{M_{shock}} = 10^{11.6}\mathrm{M_\odot}$, with no significant evolution with redshift. Conversely, we find that $\mathrm{M_{stream}}$ increases sharply with z. This is in striking agreement with the analytical predictions of Birnboim & Dekel (2003) and Dekel & Birnboim (2006), *if we correct their metallicity assumptions to those we measure when computing radiative cooling rates*. We therefore find that metal enrichment of the intergalactic medium (IGM) is a key ingredient in determining the transition mass from cold to hot dominated diffuse gas accretion.

We find that the diffuse cold gas supply at the inner halo stops at z=2 for objects with stellar masses of about $10^{11.1}\mathrm{M_\odot}$, which is close to the quenching mass determined observationally by Bundy et al. (2006). However, its evolution with z is not well constrained, making it difficult to rule out or confirm the need for an additional feedback process such as AGN.

Key words: methods: Numerical simulations, N-body, hydrodynamical, adaptive mesh refinement galaxies: formation

1 INTRODUCTION

It is currently accepted that the ΛCDM theory provides a framework with which a large number of observed galaxy properties can be interpreted. This framework is referred to as the "hierarchical scenario of galaxy formation". Most importantly, this framework explains why many of these properties (physical sizes, black hole mass, bulge mass...) are found to correlate simply with galaxy mass (Kauffmann & Haehnelt 2000). Amidst this apparently simple scaling of galaxy properties with mass, the discovery of a bimodality in the colour distribution of Sloan Digital Sky Survey (SDSS) galaxies (Kauffmann et al. 2003) stood unexpected and at odds with the predictions of hierarchical galaxy formation. Galaxy bimodality can indeed appear to be anti-hierarchical, as can be grasped from the following simple argument. Under the assumption (common in early semi-anlytical models, hereinafter SAMs) that the star formation rate (hereafter SFR) is proportional to the gas accretion rate, the latter being proportional to the halo mass to some power (van den Bosch 2002), one expects that, at all times, objects with the highest SFR should be the largest galaxies. In this framework, massive elliptical galaxies would still be blue and forming stars at $z = 0$. The fact that observed elliptical galaxies do not obey this fundamental prediction of the hierarchical scenario is the origin of the so-called "anti-hierarchical" behaviour of massive red galaxies (Rasera & Teyssier 2006). This observation is further supported by the analysis of spectroscopic data, using star formation history reconstruction methods (Reichardt et al. 2001; Panter et al. 2003; Cid Fernandes et al. 2004; Ocvirk et al. 2006b,a). Since these giant galaxies are in the form of apparently "dead" (i.e. no ongoing star formation) red elliptical galaxies, the quest has been ongoing for several years to find the origin of this halt in the star formation process (also refered to as "star formation quenching").

A substantial part of astrophysical research nowadays is devoted to searching for new physical mechanisms able to prevent cold gas accreted at $R_{\rm vir}$ from falling into the galactic disc, condensing into molecular clouds and forming stars. The heating of the infalling gas from virialization and feedback from supernovae and hot stars has been considered as a serious candidate for more than a decade but seems insufficient to explain the drop in star formation of massive systems in recent times (Rasera & Teyssier 2006), leading the authors to suggest a superwind phase for the high mass end of the galaxy population.

Active Galactic Nuclei (AGN) feedback has been proposed by several authors (Bower et al. 2006; Hopkins et al. 2007) as the origin of this quenching, and has the additional desirable propery of preventing cooling flows in the core of the most massive cluster galaxies (De Lucia et al. 2006; Cattaneo & Teyssier 2007). However, AGN physics are still poorly understood, both theoretically (because of the intrinsic complexity of relativistic magnetohydrodynamic flows around black holes, see for instance Proga (2007)), and observationally (because of the small physical extent of the region of interest). Moreover, the mechanism involved in transferring the energy from the black hole accretion flow to the surroundings remains elusive. Jets have been proposed, and have the advantage of being supported by observations, but shock waves arising from the interaction of the jet with the interstellar medium would tend to push away the hot gas while leaving surrounding clumps of cold gas rather unchanged (Slyz et al. 2005). However, this would depend on the position of the clumps with respect to the jet origin and the violence of the shock, and for instance, with a Mach number ≈ 10 and density contrast ≈ 10, Nakamura et al. (2006) do indeed predict cloud destruction.

A jet-driven turbulence is another alternative, and to assess its relevance one has to repeat experiments such as those of Banerjee et al. (2007) and cattaneo07 at the galactic scale. The balance between the mechanical power output of bubble-carving jets (estimated from radio luminosity at 1.4 GHz) and the radiative losses of the hot gas halo of galaxy clusters has been proposed as a signature of the global control of gas cooling by interaction with a central black hole jet (Best et al. 2006). However, a necessary requirement for this scenario to work for galaxies is that the energy available in the jet remains in the galaxy, while observations show that radio sources have linear sizes significantly larger than their host galaxies. It is thus not clear how jets can prevent star formation to happening, and it has also been argued that they might actually *enhance* star formation (Silk 2005). More generally, the causal relation between AGNs and star formation is unclear: does the starburst trigger AGN activity and a subsequent quenching or does the AGN activity trigger the starburst ? As a matter of fact, strong AGN activity is seen in galaxies with intense star formation activity (Wild et al. 2007; Cid Fernandes et al. 2001), demonstrating that AGN and star formation co-exist, although this could be just a short-lived phase (Kauffmann et al. 2003; Schawinski et al. 2007; Ciotti & Ostriker 2007). Finally, purely radiative feedback from the accretion disc around the black hole might be an alternative (Fabian et al. 2006, 2008), but the mechanical coupling through which the dust phase being blown away drags the cold gas along is uncertain. Hence, it is worth investigating possible quenching mechanisms other than AGN feedback. In this respect, the detailed analysis of diffuse gas accretion around star forming galaxies is of great interest because it can provide a form of self-regulation. The seminal paper of Birnboim & Dekel (2003) (hereinafter BD03) investigates the stability of hot accretion shocks around disc galaxies, showing that such shocks can exist only for haloes more massive than $\approx 10^{11.5} M_\odot$. In an ideal spherical flow, this hot shock would prevent cold gas from reaching the disc (or at least slow it down) and thus is likely to affect star formation. Dekel & Birnboim (2006) (hereinafter DB06) extended this approach to the study of the stability of cold streams ("filaments") within the shock–heated halo gas. They showed that the observed transition mass from blue to red galaxies at $z \simeq 0$ could be matched to the critical mass at which a stable accretion shock can exist and that stable filaments would disappear around z=1.5. These findings were also driven and further confirmed by numerical simulations of high redshift galaxy formation based on adaptive mesh refinement techniques (AMR) as in Kravtsov (2003), or smoothed particle hydrodynamics (SPH), as in Kereš et al. (2005). DB06 actually presented the rise of stable hot shocks not as the origin of the quenching but only as a necessary condition for an efficient AGN feedback.

However, it is too early to discard the existence of stable hot shocks or the destruction of the gas filaments as the origin of the galaxy bimodality. Indeed, no numerical study has considered the influence of chemical enrichment, which was shown in DB03 and DB06 to have a crucial impact on shock stability, since metallicity, along with gas density, determines the cooling rate (Sutherland & Dopita 1993). More recently, Cattaneo et al. (2007) checked the good behaviour of SAMs with respect to hot and cold accretion modes by comparing GalICS (Hatton et al. 2003) results to the Kereš et al. (2005) simulation, which does not take into account chemical enrichment.

In this paper, we address these very issues using the results of a very large cosmological simulation performed on the MareNostrum supercomputer at the Barcelona Supercomputer Centre. It was performed within the Horizon collaboration (`http://www.projet-horizon.fr`) using the RAMSES code (Teyssier 2002), which now includes a detailed treatment of metal–dependent gas cooling, UV heating, star formation, supernovae feedback and metal enrichment.

The simulation parameters ($L_{\rm box} = 50\ h^{-1}$Mpc, 1024^3 dark matter particles and a spatial resolution of about 1 h^{-1}kpc) are optimal to capture the most important properties of gas accretion around typical Milky Way–like galaxies. The large box size allows us to have a large (more than 100) sample of $L_\star$ galaxies at $z \geqslant 2$ and above, with a strong statistical significance. For this mass scale, the main transitions in the accretion regime (appearance of hot accretion shocks, disappearance of cold filaments) effectively takes place between $2 \leqslant z \leqslant 6$. Moreover, the AMR method adopted in RAMSES allows us to investigate the flow in an Eulerian framework, in contrast to the Lagrangian approach adopted by Kereš et al. (2005). Finally, it was recently observed that the apparent bimodality mass scale might increase with redshift (Juneau et al. 2005; Bundy et al. 2006; Hopkins et al. 2007), an intriguing behaviour that has yet to be checked against models.

The outline of this paper is as follows: first we describe in Sec. 2 our methodology, in terms of numerical techniques and statistical measurements. We specifically introduce a new estimator to analyse the thermodynamical properties of accretion, namely *accretion–weighted histograms*. We then present in Sec. 3 our main results concerning the physical properties of the accreted gas. Our findings are then discussed in the framework of earlier theoretical modelling in Sec. 4, and recent observations in Sec. 5.

2 METHODOLOGY

In this section, we first describe the MareNostrum simulation: a cosmological N body and hydrodynamics simulation of unprecedented scale with most of the physical processes involved in galaxy formation theory. We then describe our dark matter halo catalogue and its corresponding properties, present our statistical tool – accretion–weighted temperature histograms, and discuss our criterion for separating diffuse gas accretion from satellite merging.

2.1 The MareNostrum simulation

We have performed a cosmological simulation of unprecedented scale, using 2048 processors of the MareNostrum computer installed at the Barcelona Supercomputing Centre in Spain. We have used intensively the AMR code RAMSES (Teyssier 2002) for 4 weeks dispatched over one full year. This effort is part of a consortium between the Horizon project in France (`http://www.projet-horizon.fr`) and the MareNostrum galaxy formation project in Spain (`http://astro.ft.uam.es/∼marenostrum`). The main asset of this project relies on using a quasi exhaustive number of physical ingredients that are part of the current theory of galaxy formation, and at the same time covering a large enough volume to provide a fair sample of the universe, especially at redshifts above one. Specifically, we have considered metal-dependent cooling and UV heating using the Hardt and Madau background model. We have incorporated a simple model of supernovae feedback and metal enrichment using the implementation decribed in Dubois & Teyssier (2008). For high–density regions, we have considered a polytropic equation of state to model the complex, multi-phase and turbulent structure of the ISM (Yepes et al. 1997; Springel & Hernquist 2003) in a simplified form (see Schaye & Dalla Vecchia (2007); Dubois & Teyssier (2008)): the ISM is defined as gas with a density greater than $n_0 \simeq 0.1$ H/cm^3. Star formation has also been included, for ISM gas only ($n_{\rm H} > n_0$), by spawning star particles at a rate consistent with the Kennicutt law derived from local observations of star forming galaxies. Technically, we have $\dot{\rho}_* = \rho_{gas}/t_*$ where $t_* = t_0(n_{\rm H}/n_0)^{-1/2}$ and $t_0 = 8$ Gyr. Recast in units of the local free-fall time, this corresponds to a star formation efficiency of 5%. The simulation was started with a base grid of 1024^3 cells and the same number of dark matter particles, and the grid was progressively refined, on a cell–by–cell basis, when the local number of particles exceeded 10. A similar citerion was used for the gas, implementing what is called a Quasi-Lagrangian refinement strategy. Five additional levels of refinement were considered, but the maximum level of refinement was adjusted so that the minimum cell size in *physical units* never exceeded one kpc. In this way, our spatial resolution is consistent with the angular resolution used to derived the Kennicutt law from observations. On the other hand, we are not in a position to resolve the scale height of thin cold discs so the detailed galactic dynamics are likely to be be affected by resolution effects.

The simulation was run for a ΛCDM universe with $\Omega_M = 0.3$, $\Omega_\Lambda = 0.7$, $\Omega_B = 0.045$, $H_0 = 70$ km/s/Mpc, $\sigma_8 = 0.9$ in a periodic box of 50 h^{-1}Mpc. Our dark matter particle mass ($m_{\rm part.} \simeq 8 \times 10^6\ M_\odot$), our spatial resolution (1 kpc *physical*) and our box size make this simulation ideally suited to study the formation of galaxies within dark matter haloes, from dwarf– to Milky Way–sized objects at high redshift. For large galaxies, we can nicely resolve the radial extent of the disc, but not its vertical extent, while for small galaxies, we can resolve the gravitational contraction of the cooling gas, but barely the final disc. The simulation was stopped at redhift $z \simeq 1.5$ the allocated time ran out. The total number of star particles at the end of the simulation was more than 2×10^5, and the total number of AMR cells was greater than 5×10^9.

2.2 Virial spheres at rest

In order to analyse the physical properties around high redshift galaxies, we have built from our simulation data a Friend–Of–Friend (FOF) halo catalogue (Efstathiou et al. 1988). For each snapshot and for each halo, we compute its mass and its centre of mass. The Virial radius is defined here as R_{200b}, the radius at which the average mass density in the halo is 200 times the background matter density. We then define the Bright Central Galaxy (BCG) of the halo as the highest gas density peak in a sphere centred on the halo centre of mass and of radius $0.5{\rm R_{vir}}$. This position will serve as our reference point for computing radial accretion rates. We checked a posteriori that this position also also to the most massive substucture in the halo. We subtract from the gas velocity the mass-averaged velocity of the gas inside the Virial radius in order to put the system at rest. The basic physical properties of the gas are then mapped onto concentric shells centred on the BCG position.

2.3 A new tool: accretion–weighted histograms

It is quite common in cosmological simulations including gas physics to analyse the thermodynamical state of baryons using so–called "phase space diagrams"[1] (Cen & Ostriker 1993; Katz et al. 1996; Rasera & Teyssier 2006), for which the total mass fraction in a given gas density and temperature range is given as 2D histograms. This sort of diagram yields only a static view and does not include any reference to mass or energy fluxes. Instead, we propose to gain insight into the accretion regimes of cosmological haloes by using a new tool: accretion–weighted phase space diagrams. We still use temperature and density probability distribution functions, but we weight the contribution to each temperature and density bin by the local accretion rate. In this way, static regions will be discarded from the analysis, while large radial velocity regions will dominate the signal. Since the accretion is towards the BCG in the halo centre, we define concentric shells where the temperature, density, velocity and metallicity are computed by smoothing the underlying 3D fields with a window function of scale R:

$$T_R(r,\theta,\phi) = \int T(\mathbf{x}')W_R(\mathbf{x}-\mathbf{x}')\mathrm{d}^3\mathbf{x}' \,. \tag{1}$$

We then sample this 3D field on various spherical surfaces of radius $0.2R_{\rm vir} < r < R_{\rm vir}$, with an angular resolution $\Delta\theta \simeq R/r$. In the current analysis, we fix $R \simeq 2$kpc, twice our spatial resolution, so that for our largest haloes, the sphere was sampled with 400×400 pixels. We obtained for each halo angular maps of each smoothed gas variables (density, velocity, temperature, metallicity). We then define the local accretion rate $\dot{m}_R$ as (see e.g. Aubert et al. (2004), Aubert & Pichon (2007))

$$\dot{m}_R(r,\Omega) = \frac{\partial\dot{\mathrm{M}}}{\partial\Omega} = \rho_R\,\mathbf{v}_R\cdot\mathbf{n}\,r^2 \,, \tag{2}$$

where the solid angle is defined by $\mathrm{d}\Omega = \sin\theta\mathrm{d}\theta\mathrm{d}\phi$ in the direction $\Omega = (\theta,\phi)$ and the total accretion rate across the sphere is recovered using $\dot{\mathrm{M}} = \int \dot{m}_R\,\mathrm{d}\Omega$. For most of this paper, we will omit the density variable, ρ, to focus on the thermal and chemical properties of the accretion flow, described here by T and Z. At a given radius, r, we can marginalize Eq. (2) over all cells which have a given temperature, T, and obtain the accretion rate per unit temperature as

$$\dot{m}_R(r,T) = \int \delta_{\rm D}(T-T(\Omega))\,\dot{m}_R\,\mathrm{d}\Omega = \frac{\partial\dot{\mathrm{M}}}{\partial T}\,, \tag{3}$$

where $\delta_{\rm D}$ is the Dirac function. The total accretion rate across the sphere is recovered using $\dot{\mathrm{M}} = \int \dot{m}\,\mathrm{d}T$. Similarly, while marginalizing over all angles which have a given temperature, T, and a given metallicity, Z, we may introduce our main tool, the accretion-weighted temperature–metallicity two-dimensional probability density function (hereinafter PDF)

$$\dot{m}_R(r,T,Z) = \int\delta_{\rm D}(T-T(\Omega))\delta_{\rm D}(Z-Z(\Omega))\dot{m}_R\mathrm{d}\Omega = \frac{\partial^2\dot{\mathrm{M}}}{\partial T\partial Z}\,. \tag{4}$$

From now on, we drop the subscript R, since in the present analysis it is fixed to the physical resolution of the simulation.

2.4 Diffuse accretion versus clumpy satellites

In this paper, we are interested in characterizing the accretion of diffuse intergalactic gas rather than the accretion of galaxy satellites. We therefore need to separate the contribution of infalling gaseous discs from the smooth accretion through filaments or other diffuse components. In our model, the star–forming dense ISM is defined as $n_{\rm H} \geqslant 0.1\mathrm{H/cm}^3$. We remove from our spherical analysis all pixels whose density exceeds this theshold. Although this truncation may seem brutal, infalling satellites are frequently embedded in diffuse filaments. As such, the filament is the natural surrounding of the infalling satellite, and deciding where the boundary lies is difficult yet critical. In this context, a density criterion is still the most straightforward separation method. In the future, a possible alternative could be to use a segmentation algorithm to separate the filament from the satellites on topological grounds, in the spirit of the skeleton reconstructions of Sousbie et al. (2008).

2.5 Entire halo versus galaxy vicinity

We use two distinct estimators, $\dot{m}$ and $\langle\dot{m}\rangle$, to characterize the diffuse gas accretion around the central galaxy.

The first one, $\dot{m}$ is directly related to the gas properties close to the galactic disc: we compute the accretion-weighted T-Z histogram, Eq. (4), at radius $r = 0.2R_{\rm vir}$, which turned out to be close enough to, but not intersecting, the neutral HI disc. This region defines the disc vicinity, for which we would like to analyse the thermal properties of the accreted gas. We easily detect the presence of an accretion shock upwind of the disc if the accreted gas is predominantly in a hot phase. On the other hand, if the accreted gas is predominantly in a cold phase, it means that no accretion shock is present above $0.2R_{\rm vir}$.

The second estimator, $\langle\dot{m}\rangle$, is based on averaging the accretion-weighted histograms measured at different radii between $0.2R_{\rm vir}$ and $R_{\rm vir}$.

$$\langle\dot{m}\rangle(T,Z) = \int_{0.2R_{\rm vir}}^{R_{\rm vir}} \dot{m}(r,T,Z)\frac{\mathrm{d}r}{\Delta r}\,, \tag{5}$$

where $\Delta r \equiv 0.8R_{\rm vir}$ and $\dot{m}(r,T,Z)$ is given by Eq. (4). Coadding different histograms at different radii increases the weight of coherent radial structures such as filaments or cold streams that eventually extend out to (or beyond) the Virial radius. Indeed, if the velocity flow is chemo-thermodynamically similar between two neighbouring shells, the corresponding histograms will add up consistently. Note that under the assumption of a steady spherically symmetric flow, the accretion rate does not depend on radius. As we will see later on, even in the presence of an accretion shock, cold streams can persist in the halo and directly feed the central galaxy with fresh cold gas. This phenomenon will appear in

[1] as in different physical phases, *not* position-velocity phase space

our histograms as a dominant cold phase. If on the other hand these filaments are destroyed, the histograms will be dominated by the hot phase out to the halo Virial radius.

3 PROPERTIES OF DIFFUSE GAS ACCRETION

We computed the accretion-weighted PDFs for several hundred haloes spanning dark matter masses between $10^{10}\mathrm{M}_\odot$ and $4\times10^{12}\mathrm{M}_\odot$ between $2\leqslant z\leqslant 5$. We then co-added (stacked) these histograms for haloes of the same mass range in order to produce an "average" PDF for a given mass scale. We use these to study the typical temperature and metallicity distribution of the accretion flow, and the transition mass between the hot dominated and the cold dominated accretion regimes.

3.1 Bimodality in the temperature distribution

The top panels of Fig. 1 shows several radially–averaged accretion–weighted stacked–histograms (following Eq. (5)) for haloes of mass $\mathrm{M_{DM}} = 2\times10^{10}$, 2×10^{11} and $2\times10^{12}\mathrm{M}_\odot$ taken from the $z = 4$ snapshot of the simulation. We see that the accretion pattern involves two main distinct components:

(i) A cold, metal-rich component associated with the close vicinity of galaxy satellites
(ii) A hot, metal-poor component, the temperature and contribution of which increases sharply with halo mass

As such, accretion itself is clearly bimodal in temperature. Indeed, at any halo mass, little mass is ever accreted around $T\approx 2.5\times10^5$ K. Instead, most of the mass is accreted either below or above this temperature. As already noted by BD03 and Kereš et al. (2005), this involves a link with the physics of cooling: little mass will be accreted at temperatures where the cooling is efficient, since gas cannot remain at this temperature for very long. This provides a natural temperature threshold that allows us to separate the cold and the hot accretion modes, associated with low and high mass haloes respectively. The middle and bottom rows of Fig. 1 show that this bimodality in temperature is also seen at $z = 2.5$, in the whole halo as well as the inner halo.

A third component is seen as the low-metallicity tail of the cold metal-rich component. It is very prominent at $z = 4$ and disappears at $z = 2.5$ in the inner and outer halo. It can be identified with the dense, cold, metal poor gas filaments seen in Fig. 5. This is best seen at $z = 4$, where the filaments are better defined. Their density is somehow intermediate between the galaxy discs and the background. The left bottom panel clearly shows a cold metal-poor filament tunneling down all the way from almost $2\mathrm{R_{vir}}$ to the central galaxy's disc. On the other hand, the cold *metal-rich* denser phase makes up the galaxy discs. The hot phase, with intermediate density and metallicity, is distributed in a large bubble, of radius smaller than $\mathrm{R_{vir}}$ at $z = 4$ but significantly larger than $\mathrm{R_{vir}}$ at later times.

The accretion-weighted PDFs can be normalized using the total diffuse gas accretion at the Virial radius. Figure 2 shows that the accretion rate decreases with cosmic time for all masses and increases with mass at fixed redshift. This evolution is very similar to that reported in Kereš et al. (2005); Rasera & Teyssier (2006); Guo & White (2007); Neistein & Dekel (2008), in trend and normalization.

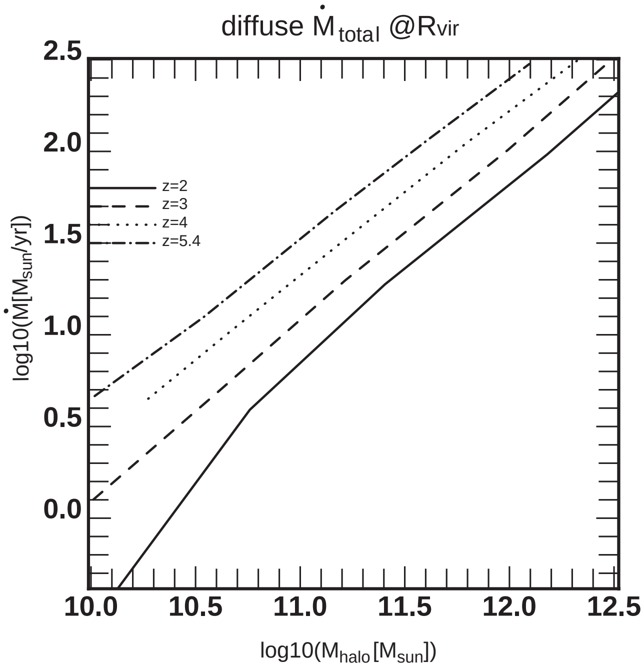

Figure 2. Diffuse gas accretion rate measured at $\mathrm{R_{vir}}$ versus mass at various epochs between redshift 2 and 5.4

3.2 Metallicity of the hot mode

The top panels of Fig. 1 show that the metallicity of the hot and cold phase can differ by up to 3 decades. This gap involves a huge difference in the ability for the gas to cool down radiatively, further aggravated by the relative densities of the two phases. This bimodal metallicity distribution is also seen at the inner halo radius. This has important consequences for semi-analytical models, and highlights the necessity of treating the gas as being composed of two phases with widely different metallicities. Moreover, at a given temperature, the large spread of the PDF in metallicity shows that the gas is not well mixed. Indeed, a perfectly well mixed accreted gas would show up as a narrow peak in metallicity. This suggests that for cooling modelling purposes, the metallicity of the maximum of the PDF of the hot accreted gas may be more relevant than the accretion-weighted average of the metallicity. Hence, in the following, we define $\mathrm{Z_{hot}}$ as the metallicity of the maximum of the accretion–weighted PDF of the hot gas.

A good criterion for establishing the existence of a well-developed hot phase is to require the existence of a saddle point in the accretion–weighted PDFs of Fig. 1, as a local minimum in temperature and a local maximum in metallicity. According to this criterion, the hot phase of the $\mathrm{M_{DM}} = 2\times10^{10}\mathrm{M}_\odot$ haloes is not well-developed at any redshift between $z = 2$–4. However, for the 2 other mass bins, when the hot phase is well-developped, its metallicity $\mathrm{Z_{hot}}$ does not depend on halo mass. Moreover, comparing the highest mass bins at $z = 2$ and $z = 4$ in Fig. 1, shows that it

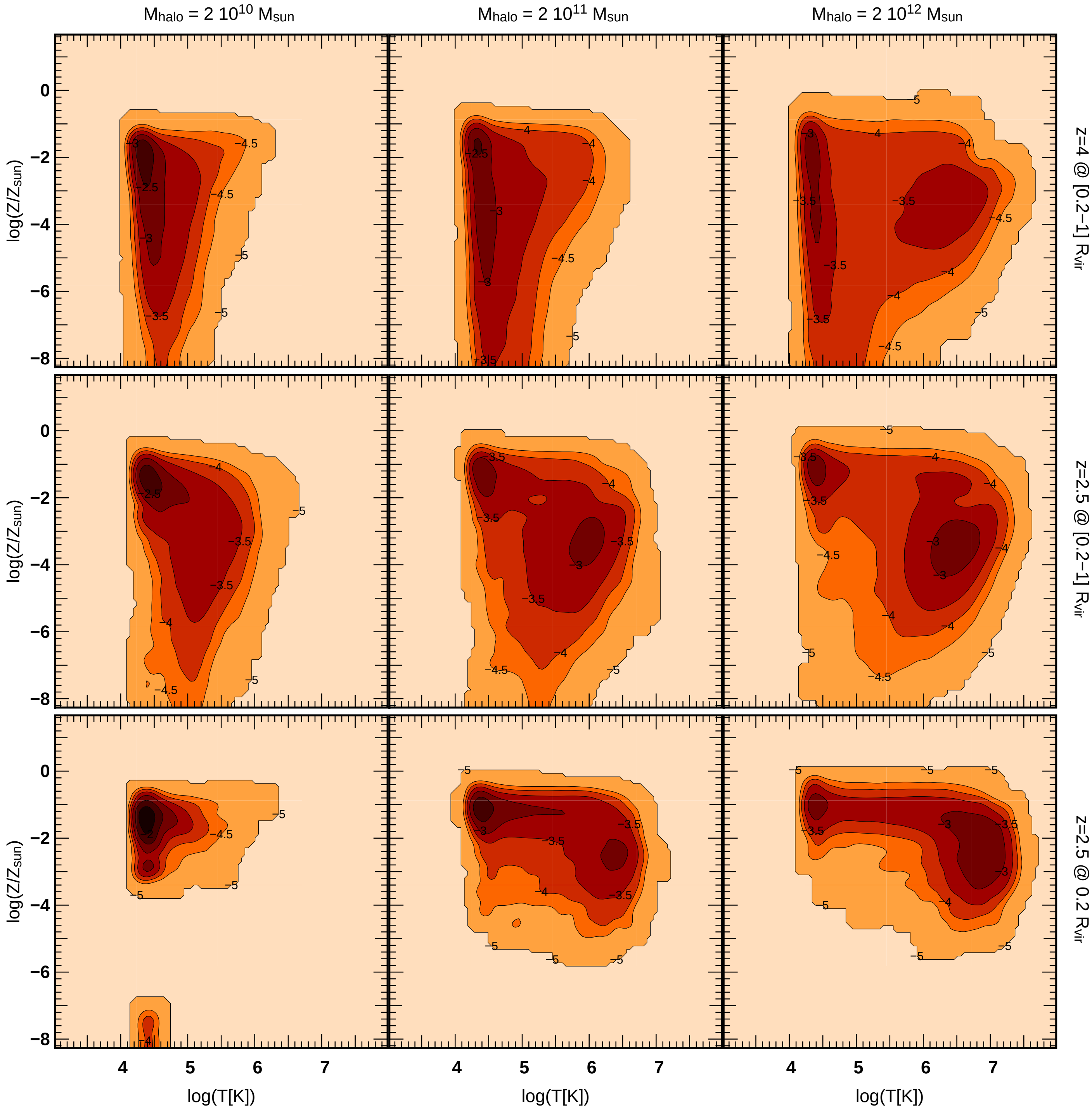

Figure 1. Accretion–weighted PDFs for 3 mass bins $[2\times10^{10}\mathrm{M}_\odot, 2\times10^{11}\mathrm{M}_\odot, 2\times10^{12}\mathrm{M}_\odot]$ (from left to right). *Top:* z=4, radially averaged. *middle:* z=2.5, radially averaged. *bottom:* z=2.5, $0.2\mathrm{R}_{\mathrm{vir}}$. The numbered labels on the contours give the $\log_{10}$ value of the PDF. When the hot phase is well developed, there is a clear bimodality in temperature and metallicity.

also does not evolve with redshift. On the other hand, $\mathrm{Z}_{\mathrm{hot}}$ does depend on the distance to the halo centre. Fig. 3 shows the evolution with radius of $\mathrm{Z}_{\mathrm{hot}}$, computed as:

$$\mathrm{Z}_{\mathrm{hot}}(\mathrm{r}) = \frac{\int_{\mathrm{T}_0}^{\infty} \dot{\mathrm{m}}(\mathrm{r},\mathrm{T},\mathrm{Z}) \log_{10}(\mathrm{Z})\,\mathrm{dT}}{\int_{\mathrm{T}_0}^{\infty} \dot{\mathrm{m}}(\mathrm{r},\mathrm{T},\mathrm{Z})\,\mathrm{dT}} \qquad (6)$$

We find that the dependency of $\mathrm{Z}_{\mathrm{hot}}$ with radius is well fit

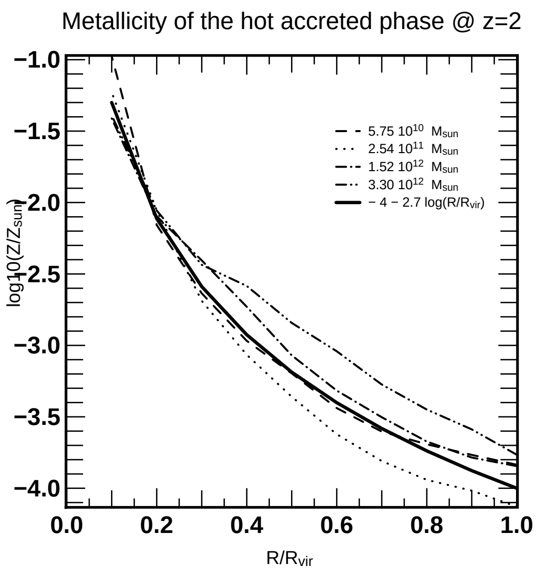

Figure 3. Metallicity of the hot accreted gas as a function of the normalized radius $R/\mathrm{R_{vir}}$ at z=2 for halo mass between $5\,10^{10} - 3\,10^{12}\mathrm{M}_\odot$. The thick line shows the analytical fit of equation 7. The dependence with respect to radius is very strong, while no clear trend in mass is seen.

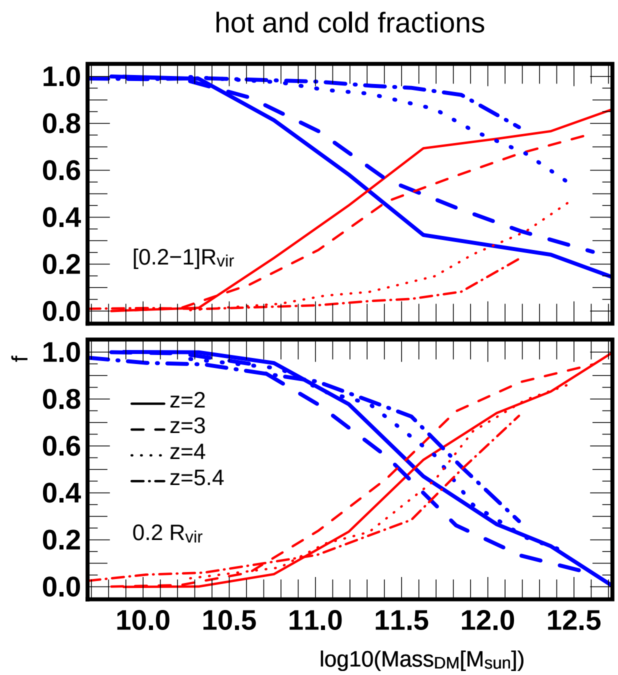

Figure 4. Evolution of the hot and cold accreted mass fractions versus $\mathrm{M_{DM}}$ for $z \in [5.4, 2]$. Top: $\langle \mathrm{f_{cold}} \rangle$ and $\langle \mathrm{f_{hot}} \rangle$ (integrated inwards down to $0.2\mathrm{R_{vir}}$). Bottom: $\mathrm{f_{cold}}$ and $\mathrm{f_{hot}}$ on the $0.2\mathrm{R_{vir}}$ sphere.

by the following law:

$$Z/\mathrm{Z}_\odot = -4 - 2.7 \log_{10}\left(\frac{R}{\mathrm{R_{vir}}}\right), \tag{7}$$

where $\mathrm{R_{vir}}$ is the Virial radius as defined in Sec. 2. This fit is mainly independent of mass and redshift in the 2×10^{10} - $2 \times 10^{12}\mathrm{M}_\odot$ range and between redshift $2 \leqslant z \leqslant 5$. The dependence with respect to mass is only implicit through $\mathrm{R_{vir}}$. This fit can be useful for analytical approaches performed in this context (see Sec. 4) or for semi-analytical models of galaxy formation.

3.3 Two critical masses for diffuse gas accretion

To allow for comparison with previous work (Kereš et al. 2005) we set the temperature threshold between the hot and cold modes at $T_0 = 250\,000$ K. Marginalizing the accretion rate over metallicity and integrating over temperature on the hot and cold temperature domains yields the hot and cold accretion rate respectively. Dividing by the total accretion rate at the chosen radius gives the contributions of the hot and cold mode to the total accretion rate:

$$\mathrm{f_{cold}}(\mathrm{r}) = \frac{1}{\dot{\mathrm{M}}(r)} \int_{T=0}^{T=T_0} \int_{Z=0}^{Z=\infty} \dot{m}(r,T,Z)\mathrm{d}T\mathrm{d}Z\,, \tag{8}$$

$$\mathrm{f_{hot}}(\mathrm{r}) = \frac{1}{\dot{\mathrm{M}}(r)} \int_{T=T_0}^{\infty} \int_{Z=0}^{Z=\infty} \dot{m}(r,T,Z)\mathrm{d}T\mathrm{d}Z \tag{9}$$

where $\dot{m}(r,T,Z)$ is given by Eq. (4). A similar definition involving $\langle \dot{m}(T,Z) \rangle$ and Eq. (5) allow us to define $\langle \mathrm{f_{cold}} \rangle$ and $\langle \mathrm{f_{hot}} \rangle$. The top panel of Fig. 4 displays the fractions computed from the accretion-weighted histograms averaged over the entire halo (between $0.2\mathrm{R_{vir}}$ and $\mathrm{R_{vir}}$). The bottom panel of Fig. 4 shows these fractions measured at radius $0.2R_{\mathrm{vir}}$ (galaxy vicinity) as a function of mass for various redshifts. A common feature of these plots is the increasing importance of the hot accretion mode with increasing mass, and the corresponding decreasing contribution of the cold mode, as could be foreseen from the top panels of Fig. 1. The mass at which $\langle \mathrm{f_{cold}} \rangle = \langle \mathrm{f_{hot}} \rangle$ defines the critical mass marking the transition between the two accretion regimes.

This critical mass seems to increase sharply with redshift, if the entire halo is considered (radially averaged case, top panel of Fig. 4). Note that at redshift 5.4, it can only be guessed since no halo in the simulation is massive enough to have $\langle \mathrm{f_{hot}} \rangle \geqslant 0.5$. This evolution is the signature of a gradual disappearance of cold radially extended features, like filaments, in the massive haloes between $z = 5.4$ and $z = 2$. To illustrate this point, we show in Fig. 5 maps of a typical halo of mass $\mathrm{M_{DM}} = 2 \times 10^{12}\mathrm{M}_\odot$ at $z = 4$ (left) and another halo of the same mass at redshift z =2 (right). While the former features clear filaments streaming into the inner halo, the latter lies at the centre of a hot bubble, with no apparent filaments inside the Virial radius (large black circle). The critical mass defined by the accretion transition in the entire halo marks the disappearance of cold streams. It is therefore called here $\mathrm{M_{stream}}$.

On the contrary, the critical mass defined using accretion–weighted histograms in the vicinity of the central galaxy for which $\mathrm{f_{hot}} \geqslant 0.5$ shows only a slow variation with redshift, if any. It indicates that accretion in the inner parts of the halo switches to the hot mode as soon as $\mathrm{M_{DM}} \geqslant 10^{11.5-12}\mathrm{M}_\odot$, while the outer part of the halo can still be dominated by the cold mode. Again, this is well illustrated by Fig. 5. The inner part of the halo (inner circle) has been shock heated in both case, although the radius of the accretion shock is much larger in the low redhift case. At high redshift, the accretion shock coexists with cold streams coming from the outer parts of the halo. The critical mass defined in the galaxy vicinity marks the appearance of an accretion shock around the galaxy. It is therefore called here $\mathrm{M_{shock}}$.

An important parameter in our approach is the density threshold we used to remove clumpy satellites from the analysis. We checked that our conclusions in terms of transition masses and average metallicity of the hot phase are robust to changes of this parameter by repeating our measurements with a lower density threshold. The main effect of this extra gas removal is to reduce the fraction of high metallicity, cold gas in the vicinity of galaxy satellites, without any noticeable effect on the metallicity of the hot phase and on the critical masses.

4 COMPARISON TO EARLIER THEORETICAL MODELLING

The physics of accretion has been investigated by several authors in the past. It is insightful to review their results in light of our measurements. Fig. 4 shows the evolution of $\mathrm{M_{stream}}$ for several redshifts. For $z = 2$ it is approximately $10^{11.5}\mathrm{M_\odot}$ and it increases sharply with redshift. Indeed, at $z \geqslant 4$ and above, even the most massive haloes in the simulation are still dominated by cold accretion. However, a rough extrapolation of the $z = 4$ curves yields a transition mass of about $\approx 10^{12.7}\mathrm{M_\odot}$. Qualitatively, this behaviour is in agreement with the evolution of $\mathrm{M_{stream}}$ with redshift as derived by DB06. According to their study, filaments exist only in $\mathrm{M} \leqslant \mathrm{M_{stream}}$ haloes. However, their figure 7 shows that $\mathrm{M_{streamDB06}}(z = 2) = 10^{12.4}\mathrm{M_\odot}$, which is significantly larger than what we find. We will now show that correcting the metallicity assumptions of DB06 to the metallicity we measure in the simulation can reconcile these discrepant values. Taking the log of their equation (40), we see that $\mathrm{M_{stream}}$ is defined with respect to a critical mass for shock stability, $\mathrm{M_{shock}}$,

$$\log(\mathrm{M_{stream}}) = 2\log(\mathrm{M_{shock}}) - \log(\mathrm{M_\star}) - \log(3)\,, \quad (10)$$

where $\mathrm{M_\star}$ is the typical dark matter halo mass at a given redshift as computed using the formalisms of Lahav et al. (1991); Carroll et al. (1992); Mo & White (2002) and following Appendix 3 of DB06. $\mathrm{M_{shock}}$ in turn is calculated at 0.1 $\mathrm{R_{vir}}$. However, it is clear from Fig. 5 that for steady cold streams to be stable in a hot gas bubble they need to be stable all the way up to $\mathrm{R_{vir}}$. Moreover, $\mathrm{M_{shock}}$ strongly depends on metallicity via the cooling function, as also shown by Fig. 10 of BD03 and Fig. 2 of DB06. Although the lowest metallicity assumed by the authors is 0.03 $\mathrm{Z_\odot}$ at $\mathrm{R_{vir}}$, the fit we provide in equation (7) at $z = 2.5$ gives $\log(Z(\mathrm{R_{vir}}, z = 2.5)/\mathrm{Z_\odot}) = -4$, which translates to $\log(Z(\mathrm{R_{vir}}, z = 0)/\mathrm{Z_\odot}) = -3.6$ assuming an average chemical enrichment rate $s = 0.17$ as in DB06 and De Lucia et al. (2004). Analysing the dependence of $\mathrm{M_{shock}}$ with respect to the problem parameters in equation (34) of DB06, we can isolate the dependence in metallicity as:

$$\mathrm{M_{shock}}(R, Z_0, z) = 0.7\log(Z_0) + A(R, z)\,, \quad (11)$$

where $Z_0 = Z/\mathrm{Z_\odot}$ at z=0, and $A(R, z)$ can be tabulated from Fig. 2 of DB06. On the one hand, using our value $Z_0 = 10^{-3.5}$, we get $\mathrm{M_{streamDB06}}$ shown in Fig. 6, which agrees well with our measurements. On the other hand, they rule out the $Z_0 = 0.1$ hypothesis, as shows Fig. 6. This difference can be entirely attributed to a lower efficiency of the radiative cooling with decreasing metallicity. The value given for $\mathrm{M_{stream}}$ at z=5.4 is an extrapolation and is given only as a lower limit (indicated by the arrow). On the other hand, the metallicity assumption of DB06 $Z_0 = 0.1$ is quite close to the metallicity we measure at the inner halo: our fit from equation (7) gives $\log(Z(0.1\mathrm{R_{vir}}, z = 2.5)/\mathrm{Z_\odot}) = -1.3$, which translates into $\log(Z(0.1\mathrm{R_{vir}}, z = 2.5)/\mathrm{Z_\odot}) = -0.9$ assuming the same chemical enrichment rate $s = 0.17$. As a consequence, we expect the critical hot shock masses $\mathrm{M_{shock}}$ computed by DB06 to match our measurements well, provided that we compute and measure $\mathrm{M_{shock}}$ at the same depth in the halo, i.e. at 0.2 $\mathrm{R_{vir}}$. Equation (7) and the chemical enrichment rate yields $Z_0 = 0.02$ at $0.2\mathrm{R_{vir}}$. Fig. 6 shows that a good agreement is indeed achieved. We also agree with a quasi constant $\mathrm{M_{shock}}$ as found by Kereš et al. (2005); Birnboim et al. (2007) in SPH simulations, although the absolute normalization seems to differ. However, their methodology is quite different (they analyse the temperature history of their gas particles) and their metallicity was uniform and constant throughout the whole simulation. We conclude that while the high metallicity assumption of DB06 at the inner halo is reasonable, a hundredfold lower metallicity must nonetheless be assumed when investigating the stability of the gas filaments in order to reconcile this with our measurements. Once the importance and the effect of these assumptions has been accounted for, the consistency between the MareNostrum measurements and the theory of DB06 is remarkably good, and shows that their analytical approach indeed seems to capture the essence of our (nonetheless limited) understanding of the processes involved in gas accretion physics as modelled by this simulation.

The agreement on $\mathrm{M_{stream}}$ also suggests that the main process driving the stability of cold filaments in a hot halo is the competition between a compressive increase of temperature in the filament on the one hand, and radiative cooling on the other hand. This is an important point since several other hydrodynamical processes are expected to be at work, such as Kelvin-Helmholtz instabilites, which are not modelled in DB06. However, this simulation is not tailored to resolve them. Klein et al. (1994) showed that at least 100 cells per cloud radius are needed to resolve interface instabilities involved in cloud destruction by shock waves. However, it has been argued that the gas filaments can be stabilized by the underlying dark matter stream, and could totally prevent Kelvin-Helmholtz instability from appearing. The density contrast of the cold gas stream and the average density at the Virial radius is also an important parameter, and DB06 note that it could range from 1 to 10. In the calculations shown here it is ≈ 3. Increasing this ratio could have a similar effect to decreasing the metallicity, in making the cold filaments disappear earlier.

Finally, in DB06, the metallicity of the cold streams is linked to the metallicity of the gas as a whole. While this simplification makes the problem analytically more tractable (it allows the authors to circumvent mixing issues, together with the fact that the mass rate in the cold and hot phase may differ significantly), it is in strong disagreement with the results shown in Fig. 1. Allowing the two gas phases

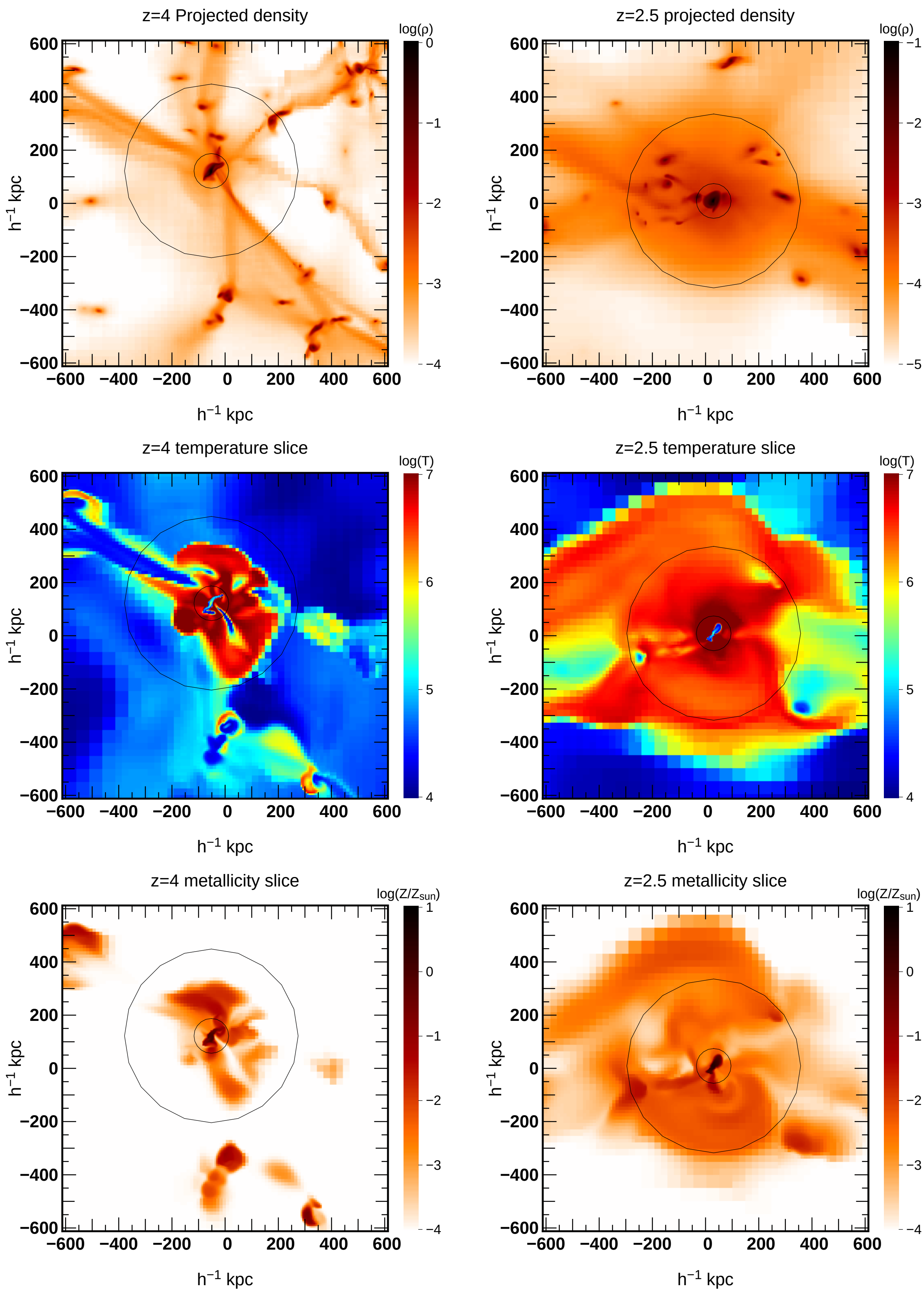

Figure 5. Maps of the physical properties of the gas for a typical $M = 2 \times 10^{12} \mathrm{M}_{\odot}$. *Left:* $z = 4$, *right:* $z = 2.5$. *Top:* Projected density, *middle:* temperature slice, *bottom:* metallicity slice. The large (small) black circle shows the location of $\mathrm{R_{vir}}$ ($0.2\mathrm{R_{vir}}$) for the central galaxy. Note the disappearance of filaments at low redshift.

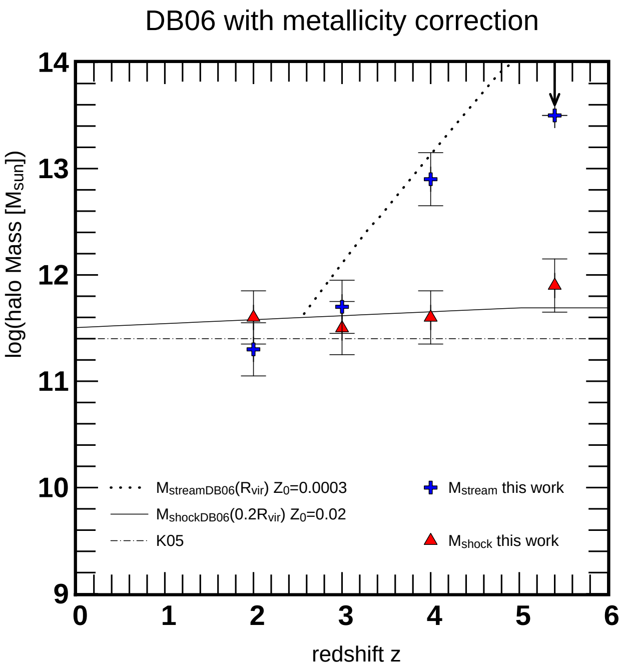

Figure 6. Evolution of $\mathrm{M_{shock}}$ and $\mathrm{M_{stream}}$ with redshift, from our measurements and comparison to analytical modelling. The solid line shows DB06 prediction for $\mathrm{M_{shock}}(0.2\mathrm{R_{vir}})$ with a metallicity assumption $Z_0 = 0.02$, while the dotted line shows their prediction for $\mathrm{M_{stream}}$ with a metallicity assumption $Z_0 = 0.0003$. Finally, the dash dotted line shows the constant transition mass reported by Kereš et al. (2005). The error bars on our measurements are equal to the widths of the mass bins used. The arrow pointing to the $\mathrm{M_{stream}}(z = 5.4)$ indicates that this point is given as a lower limit only, as can be estimated from Fig. 4.

to have different metallicities could lead to a significant improvement of the DB06 model.

5 COMPARISON TO OBSERVATIONS

It is difficult to find observables to compare our measurements to since our measurements "only" reach down to $z = 2$ while observational studies of the galaxy bimodality are generally restricted to $z \leqslant 1.5$, and the bimodality becomes clear only at later times. Also, the definition of the critical masses constrained by theoreticians and observers have little in common: theoreticians have access to quantities that are in general impossible to measure with existing or even future observing facilities (for instance the mass accretion rate of cold gas at $\mathrm{R_{vir}}$), while observers have access to enormous volumes of the universe and events which would be impossible to simulate with the sufficiently high spatial and temporal resolution required for imposing useful constraints. Hence, shortcuts are taken. They always involve external assumptions, and the relevance of the quantities being compared must be carefully examined. Here we discuss our results in the light of the observed transition and quenching masses measured by Bundy et al. (2006), hereinafter B06.

The $\mathrm{M_\star/M_{DM}}$ ratio used to estimate the observed stellar mass from the halo mass and its evolution with redshift is subject to large uncertainties and is a hotly debated topic. It is linked to the evolution of the Tully-Fisher relation (Tully & Fisher 1977; Bell & de Jong 2001). It seems reasonable to expect that the ratio increases with decreasing redshift (Rettura et al. 2006; Kannappan & Gawiser 2007), as more gas is turned into stars. However, a non-evolving stellar-to-total mass ratio could also be in agreement with both observations (Bamford et al. 2006; Böhm & Ziegler 2007; Atkinson et al. 2007) and numerical studies (Portinari & Sommer-Larsen 2007). In our simulation a stellar to dark matter halo mass ratio of about ≈ 50 seems reasonable at $z = 2$ for structures in the mass range considered here.

B06 measured the evolution with redshift of the transitional mass $\mathrm{M_{tr}}$ marking the transition from the blue to red sequence of galaxies. This study is based on a sample of 8000 DEEP2 galaxies between $0.4 \leqslant\leqslant 1.4$. The galaxies are divided into two groups (star forming and passive), ideally according to their SFR, with a limiting SFR$=0.2\mathrm{M_\odot}$/yr. However, the [OII] emission line generally used to derive the SFR (Kewley et al. 2004) falls in the DEEP2 survey wavelength range only for $z \geqslant 0.75$. As a consequence, the colour index (U-B) is also used as a proxy for the SFR as measured from [OII], and an absolute magnitude-dependent colour cut is made as an alternative to the SFR cut (van Dokkum et al. 2000). The authors show that indeed, very few galaxies with (U-B)$\geqslant 0.2$ are forming stars. However, there is a large fraction ($\approx 30\%$) of galaxies with (U-B)$\leqslant 0.2$ which are passive. This means that the sample of passive galaxies will suffer only limited pollution from star-forming galaxies, while the star-forming sample contains a significant fraction of passive galaxies ($\approx 30\%$ at $z = [0.75 - 1]$ as can be seen from their Fig. 1). Once the red and blue galaxy groups are defined (through the colour or SFR criterion), the authors compute the mass functions of the blue and red groups and the contribution of blue and red galaxies to the total mass function. They show that the massive end of the mass function is dominated by red galaxies while the fainter end is dominated by blue galaxies. They then define two transition masses:

(i) $\mathrm{M_{tr}}$ is the mass for which the mass function of red galaxies equals that of the blue galaxies, i.e. both groups contribute equally to the total mass function. $\mathrm{M_{tr}}$ shows only a moderate dependence on the red/blue separation criterion. It is found to increase from $10^{10.5}\mathrm{M_\odot}$ to $10^{10.8}\mathrm{M_\odot}$ between $0.4 \leqslant z \leqslant 1.4$.

(ii) $\mathrm{M_{quenchB06}}$ is the mass for which the fraction of blue galaxies drops below 1/3 (which means the contribution of blue galaxies is half the contribution of the red galaxies to the total mass function). The authors claim it represents the mass at which star formation "quenches". It increases from $10^{10.73}\mathrm{M_\odot}$ to $10^{11.23}\mathrm{M_\odot}$ between $0.4 \leqslant z \leqslant 1.4$.

Various other investigations consider different photometric filters, colour cuts, SFR estimates or mass estimates, but relie on similar methodology (Arnouts et al. 2007; Hopkins et al. 2007). Given the complexity of the method and the number of steps and assumptions involved, it is clear that the physical meaning of the observed transition masses can be quite far from that of the transition masses we compute from our gas accretion measurements. However, it is admitted that they correspond to a real change in the evolution of SFR or specific SFR with galaxy mass. The details are difficult to assess, for instance, does the transition mass signify a total shutdown of star formation or a smooth decline. Such details are bound to be fuzzy because we are looking at populations whose properties have an intrinsic dispersion, as they have different histories, environment etc... Having recalled these difficulties, we now proceed to make a number of remarks:

(i) Using a stellar to dark matter mass ratio of $\mathrm{M}_\star/\mathrm{M}_{\mathrm{DM}} = 50$ we get $M^\star_{\mathrm{shock}} \approx 10^{9.9}\mathrm{M}_\odot$ at $z = 2$, which is significantly smaller than M_{tr} found in B06 at any epoch. Moreover, since M_{tr} increases with z, the disagreement is bound to be stronger if we were to observe $\mathrm{M}_{\mathrm{tr}}(z = 2)$. A similar disagreement is seen for $\mathrm{M}_{\mathrm{stream}}$.

(ii) On the other hand, we can define a mass $\mathrm{M}_{\mathrm{quench}}$ where the cold gas accretion rate on the central galaxy drops to zero, also corresponding to the mass where $\mathrm{f}_{\mathrm{cold}} = 0$ at the inner halo, instead of $\mathrm{f}_{\mathrm{cold}} = 0.5$ as for $\mathrm{M}_{\mathrm{shock}}$. We find $\mathrm{M}_{\mathrm{quench}} = 10^{12.8}\mathrm{M}_\odot$, which translates to $\approx 10^{11.1}\mathrm{M}_\odot$ in stellar mass. Although $\mathrm{M}_{\mathrm{quenchB06}}$ is expected to increase between $z = 1.4$ and $z = 2$, the agreement is remarkable. It is also roughly consistent with the results of Pozzetti et al. (2003); Fontana et al. (2004), based on the K20 survey.

(iii) This raises the question as to what we should adopt as threshold in $\mathrm{f}_{\mathrm{cold}}$. Indeed we see that moving this threshold can results in a shift of more than a decade in the masses obtained. There is actually little reason for expecting $\mathrm{f}_{\mathrm{cold}} = 0.5$ haloes to match observed transition masses precisely.

(iv) We find a difference between $\mathrm{M}_{\mathrm{shock}}$ and $\mathrm{M}_{\mathrm{quench}}$ of about $1.2 - 1.3$ dex. This is actually a measure of the sharpness of the transition from cold to hot accreting haloes. This contrasts with the finding of B06 where $\mathrm{M}_{\mathrm{tr}} - \mathrm{M}_{\mathrm{quenchB06}} \approx 0.2 - 0.4$, which suggests a much sharper transition. In future modelling works and observational studies, computing the sharpness in mass of the transition from blue to red galaxies could help constraining the mechanism responsible for the transition.

(v) We find a quasi-constant $\mathrm{M}_{\mathrm{shock}}$, with only very slight evolution with z, compatible with the findings of earlier theoretical works, both numerical and analytical. In contrast, both M_{tr} and $\mathrm{M}_{\mathrm{quenchB06}}$ evolve strongly with z. On the other hand, it is difficult to check the evolution of $\mathrm{M}_{\mathrm{quench}}$ with redshift, since the only epoch where $\mathrm{f}_{\mathrm{cold}} \approx 0$ haloes exist in the simulation is $z = 2$. A naive linear extrapolation of the evolution of $\mathrm{f}_{\mathrm{cold}}$ at larger redshifts suggests a quasi-constant $\mathrm{M}_{\mathrm{quench}}$, but this is simply impossible to check and would require simulating a larger box in order to get haloes massive enough to reach $\mathrm{f}_{\mathrm{cold}} = 0$ earlier in the life of the universe.

(vi) If we believe that $\mathrm{M}_{\mathrm{quench}}$ has a physical meaning similar to $\mathrm{M}_{\mathrm{quenchB06}}$ this apparent difference in their evolution with redshift is problematic. Moreover, a stellar to dark matter ratio $\mathrm{M}_\star/\mathrm{M}_{\mathrm{DM}}$ evolving with z would make this issue even worse. Indeed, a constant $\mathrm{M}_{\mathrm{quench}}$ combined with a decreasing $\mathrm{M}_\star/\mathrm{M}_{\mathrm{DM}}$ with z would lead to a *decreasing* $\mathrm{M}_{\mathrm{quench}}(\mathrm{z})$, which would then be in even stronger disagreement with observations.

(vii) On the other hand, $\mathrm{M}_{\mathrm{stream}}$ does evolve with z, with a slope similar to that of M_{tr} and $\mathrm{M}_{\mathrm{quenchB06}}$. It would be interesting to compute the mass at which the cold fraction $\mathrm{f}_{\mathrm{cold}}$ drops to zero at the outer halo because such a mass may be comparable in absolute normalisation *and* in slope to $\mathrm{M}_{\mathrm{quenchB06}}$. However, this is difficult to even estimate from the current simulation, and the corresponding masses are clearly out of reach as can be seen on Fig. 4.

Finally, it becomes clear that in order to compare our theoretical transition masses to observed ones, one should use the same mass definitions in the simulation as in the observations. This involves building catalogues of galaxies (rather than dark matter haloes), computing their luminosities and colours according to the age and metallicity distributions of their stars using stellar population models such as Bruzual & Charlot (2003); Fioc & Rocca-Volmerange (1997); Le Borgne et al. (2004); Coelho et al. (2007). The resulting colour-magnitude diagrams of the galaxy population could then be compared directly to observations such as the SDSS $M_r/(u-r)$ distribution (Baldry et al. 2004). This is the approach adopted in SAMs such as those of Cattaneo et al. (2006). The same colour cuts as in the observations (Arnouts et al. 2007; van Dokkum et al. 2000) could then be applied and the corresponding red and blue galaxy mass functions constructed, along with the desired transition masses. Since the colour bimodality of galaxies falls into place only after $z \leqslant 1.5$ (the last redshift bin of Arnouts et al. (2007) shows no bimodality in (NUV-r')/K at all), it should not be expected that the bimodality can be clearly seen in a colour-magnitude diagram even at the lowest redshift of the simulation. Moreover, since the AGN feedback now often proposed as the origin of the galaxy bimodality has not been implemented in the MareNostrum simulation, it might never appear even if we could continue the simulation down to lower redshifts. In any case, the above colour-magnitude diagram synthesis and the corresponding colour cuts have to be carried out quantitatively to check for the presence/absence of a galaxy bimodality in the MareNostrum simulation.

6 CONCLUSIONS

We used the MareNostrum galaxy formation simulation to study the processes involved in gas accretion on galaxies. We introduced mass accretion rate weighted statistics that allow us to quantify the mass accretion rates as a function of gas temperature and metallicity.

Gas accretion is bimodal both in temperature and in metallicity, defining a hot and a cold accretion mode. The cold accretion mode is associated with a combination of metal poor filamentary accretion and dense metal-rich galaxy disc surroundings, while the hot accretion mode is mostly metal-poor but features strongly heterogeneous metallicity.

The cooling properties of the hot gas are affected by this inhomogeneity and deviate strongly from those of a gas having the average metallicity of the hot accreted phase. We give an analytical fit to the metallicity of the maximum hot mass accretion rate as a function of radius, which will hopefully be relevant for future SAMs.

We define $\mathrm{M}_{\mathrm{shock}}$ and $\mathrm{M}_{\mathrm{stream}}$, the halo masses for which cold and hot accretion contribute equally, at the inner halo and within the whole halo, respectively. Haloes more massive than $\mathrm{M}_{\mathrm{shock}}$ develop stable hot shocks, but may still possess cold gas filaments nourishing the galaxy disc. For halo masses larger than M_{stream}, these filaments disappear.

M_{shock} is found to be quasi-constant with z, while on the other hand, M_{stream} increases sharply. These results are in good agreement with the analytical stability calculations of DB06, provided that their metallicity assumption for the outer halo is adjusted to the metallicity measured in the simulation. This agreement suggests that, as long as the stability of hot shocks and cold streams is assumed to be mainly driven by a competition between compression and radiative cooling, their analytical modelling is accurate within this model; it then depends critically on assumptions made about the metallicity, via the cooling function. In this respect the fit to the metallicity of the hot phase given here could be an important input to such analytical models.

We propose that in addition to the transition masses, two other observables should always be considered by future SAMs or numerical investigations of the origin of the galaxy bimodality:

(i) the sharpness of the transition $\log_{10}(M_{quench}/M_{shock})$, whose observable counterpart could for instance be the log ratio of the quenching mass to the transition mass as defined in B06.

(ii) The evolution of transition/quenching masses with redshift.

Modelling these two quantities should be helpful to pinpoint the nature of star formation quenching in galaxies.

Comparing the transition masses we obtain to observed transition masses is a difficult task, and we found only marginal agreement. The diffuse cold gas supply drops to zero at the inner halo for an estimated stellar mass $M^{\star}_{\rm quench} \approx 10^{11.1} M_{\odot}$ at $z = 2$, which is remarkably close to the quenching masses observed by B06. Unfortunately, we are not able to constrain the evolution of M_{quench}. However, we note that the evolution of the observed quenching mass is similar to the evolution of M_{stream}. In this respect, the agreement between measured and observed quenching masses suggests that one does not necessarily require more ingredients to simulate galaxy populations than the physics already modelled in the MareNostrum simulations. We recall here that no AGN feedback has been taken into account in this work. To be more conclusive, one will need to better constrain M_{quench} and its evolution. One therefore needs to zoom-simulate smaller boxes centred on massive haloes to lower z. Since M_{quench} is determined mostly by the few most massive haloes of the simulation, one would also need a larger box or more realizations of a box of the same size to improve the statistics.

Conversely, one may need additional ingredients in order to prevent clumpy gas accretion from reaching the galaxy centre when it is significant (a study of the contribution of clumpy gas accretion will be carried out in a forthcoming paper). But they need not be in the form of AGN feedback. Although stripping of the hot halo of infalling satellite galaxies is properly resolved in the MareNostrum simulation, the interface instabilities cold disc/hot gas and cold filaments/hot gas are not. These could be the missing physics.

Similarly, some energy input into the hot component might be required to maintain its temperature and avoid cooling flows at later stages. Dekel & Birnboim (2008) proposed that "gravitational quenching" could be a solution. It involves keeping the inner halo gas hot through interactions with cold dense gas clumps (drag), allowing to transfer the potential energy of these infalling clouds to the inner halo. A crucial step arising from our study is that of the interplay between the hot gas bubble and cold streams/clouds. Are hot gas bubbles able to disrupt filaments connected to the disc via electronic conduction, turbulence, Kelvin-Helmhotz instability ? Are cold streams immune to disruption thanks to increased pressure (feeling pressure of the hot gas) and thus higher density and consequently higher radiative cooling efficiency or the underlying dark matter stream ? Can electronic conduction be impeded by local magnetic fields of suitable intensity ? Is there a pressure/temperature/halo mass for which a given cold stream of given density/velocity/DM flux will be disrupted by these instabilities ? It will be decades before cosmological simulations with the same size as the MareNostrum simulation will have the resolution required to resolve interface instabilities. Hence, as a first step, more restricted, idealised experiments are needed in order to investigate these phenomena.

ACKNOWLEDGEMENTS

The authors thankfully acknowledge the computer resources, technical expertise and assistance provided by the Barcelona Supercomputing Centre - Centro Nacional de Supercomputacion. This work was performed within the framework of the Horizon collaboration (`http://www.projet-horizon.fr`). We thank D. Aubert, A. Dekel, P. Clark, S. Colombi, J. Devriendt, J. Forero-Romero, S. Glover, N. Maddox and D. Leborgne for useful comments and helpful suggestions. We would also like to thank D. Munro for freely distributing his Yorick programming language (available at `http://yorick.sourceforge.net/`) PO was supported by a grant from the Centre National de la Recherche Scientifique (CNRS) and a grant from the Deutsches Zentrum für Luft und Raumfahrt (DLR).

REFERENCES

Arnouts S., Walcher C. J., Le Fèvre O., Zamorani G., Ilbert O., Le Brun V., Pozzetti L., Bardelli S., Tresse L., Zucca E., Charlot S., Lamareille F., McCracken 2007, A&A, 476, 137

Atkinson N., Conselice C. J., Fox N., 2007, ArXiv e-prints, 712

Aubert D., Pichon C., 2007, MNRAS, 374, 877

Aubert D., Pichon C., Colombi S., 2004, MNRAS, 352, 376

Baldry I. K., Glazebrook K., Brinkmann J., Ivezić Ž., Lupton R. H., Nichol R. C., Szalay A. S., 2004, ApJ, 600, 681

Bamford S. P., Aragón-Salamanca A., Milvang-Jensen B., 2006, MNRAS, 366, 308

Banerjee R., Klessen R. S., Fendt C., 2007, ApJ, 668, 1028

Bell E. F., de Jong R. S., 2001, ApJ, 550, 212

Best P. N., Kaiser C. R., Heckman T. M., Kauffmann G., 2006, MNRAS, 368, L67

Birnboim Y., Dekel A., 2003, MNRAS, 345, 349

Birnboim Y., Dekel A., Neistein E., 2007, MNRAS, 380, 339
Böhm A., Ziegler B. L., 2007, ApJ, 668, 846
Bower R. G., Benson A. J., Malbon R., Helly J. C., Frenk C. S., Baugh C. M., Cole S., Lacey C. G., 2006, MNRAS, 370, 645
Bruzual G., Charlot S., 2003, MNRAS, 344, 1000
Bundy K., Ellis R. S., Conselice C. J., Taylor J. E., Cooper M. C., Willmer C. N. A., Weiner B. J., Coil A. L., Noeske K. G., Eisenhardt P. R. M., 2006, ApJ, 651, 120
Carroll S. M., Press W. H., Turner E. L., 1992, ARAA, 30, 499
Cattaneo A., Blaizot J., Weinberg D. H., Kereš D., Colombi S., Davé R., Devriendt J., Guiderdoni B., Katz N., 2007, MNRAS, 377, 63
Cattaneo A., Dekel A., Devriendt J., Guiderdoni B., Blaizot J., 2006, MNRAS, 370, 1651
Cattaneo A., Teyssier R., 2007, MNRAS, 376, 1547
Cen R., Ostriker J. P., 1993, ApJ, 417, 404
Cid Fernandes R., Heckman T., Schmitt H., Delgado R. M. G., Storchi-Bergmann T., 2001, ApJ, 558, 81
Cid Fernandes R., Mateus A., Sodre L., Stasinska G., Gomes J. M., 2004, astro-ph/0412481
Ciotti L., Ostriker J. P., 2007, ApJ, 665, 1038
Coelho P., Bruzual G., Charlot S., Weiss A., Barbuy B., Ferguson J. W., 2007, MNRAS, 382, 498
De Lucia G., Kauffmann G., White S. D. M., 2004, MNRAS, 349, 1101
De Lucia G., Springel V., White S. D. M., Croton D., Kauffmann G., 2006, MNRAS, 366, 499
Dekel A., Birnboim Y., 2006, MNRAS, 368, 2
Dekel A., Birnboim Y., 2008, MNRAS, 383, 119
Dubois Y., Teyssier R., 2008, A&A, 477, 79
Efstathiou G., Frenk C. S., White S. D. M., Davis M., 1988, MNRAS, 235, 715
Fabian A. C., Celotti A., Erlund M. C., 2006, MNRAS, 373, L16
Fabian A. C., Vasudevan R. V., Gandhi P., 2008, MNRAS, pp L13+
Fioc M., Rocca-Volmerange B., 1997, A&A, 326, 950
Fontana A., Pozzetti L., Donnarumma I., Renzini A., Cimatti A., Zamorani G., Menci N., Daddi E., Giallongo E., Mignoli M., Perna C., Salimbeni S., Saracco P., Broadhurst T., Cristiani S., D'Odorico S., Gilmozzi R., 2004, A&A, 424, 23
Guo Q., White S. D. M., 2007, ArXiv e-prints, 708
Hatton S., Devriendt J. E. G., Ninin S., Bouchet F. R., Guiderdoni B., Vibert D., 2003, MNRAS, 343, 75
Hopkins P. F., Bundy K., Hernquist L., Ellis R. S., 2007, ApJ, 659, 976
Juneau S., Glazebrook K., Crampton D., McCarthy P. J., Savaglio S., Abraham R., Carlberg R. G., Chen H.-W., Le Borgne D., Marzke R. O., Roth K., Jørgensen I., Hook I., Murowinski R., 2005, ApJL, 619, L135
Kannappan S. J., Gawiser E., 2007, ApJL, 657, L5
Katz N., Weinberg D. H., Hernquist L., 1996, ApJS, 105, 19
Kauffmann G., Haehnelt M., 2000, MNRAS, 311, 576
Kauffmann G., Heckman T. M., Tremonti C., Brinchmann J., Charlot S., White S. D. M., Ridgway S. E., Brinkmann J., Fukugita M., Hall P. B., Ivezić Ž., Richards G. T., Schneider D. P., 2003, MNRAS, 346, 1055
Kereš D., Katz N., Weinberg D. H., Davé R., 2005, MNRAS, 363, 2
Kewley L. J., Geller M. J., Jansen R. A., 2004, AJ, 127, 2002
Klein R. I., McKee C. F., Colella P., 1994, ApJ, 420, 213
Kravtsov A. V., 2003, ApJL, 590, L1
Lahav O., Lilje P. B., Primack J. R., Rees M. J., 1991, MNRAS, 251, 128
Le Borgne D., Rocca-Volmerange B., Prugniel P., Lançon A., Fioc M., Soubiran C., 2004, A&A, 425, 881
Mo H. J., White S. D. M., 2002, MNRAS, 336, 112
Nakamura F., McKee C. F., Klein R. I., Fisher R. T., 2006, ApJS, 164, 477
Neistein E., Dekel A., 2008, MNRAS, 383, 615
Ocvirk P., Pichon C., Lançon A., Thiébaut E., 2006a, MNRAS, 365, 74
Ocvirk P., Pichon C., Lançon A., Thiébaut E., 2006b, MNRAS, 365, 46
Panter B., Heavens A. F., Jimenez R., 2003, MNRAS, 343, 1145
Portinari L., Sommer-Larsen J., 2007, MNRAS, 375, 913
Pozzetti L., Cimatti A., Zamorani G., Daddi E., Menci N., Fontana A., Renzini A., Mignoli M., Poli F., Saracco P., Broadhurst T., Cristiani S., D'Odorico S., Giallongo E., Gilmozzi R., 2003, A&A, 402, 837
Proga D., 2007, in Ho L. C., Wang J.-W., eds, The Central Engine of Active Galactic Nuclei Vol. 373 of Astronomical Society of the Pacific Conference Series, Theory of Winds in AGNs. pp 267–+
Rasera Y., Teyssier R., 2006, A&A, 445, 1
Reichardt C., Jimenez R., Heavens A. F., 2001, MNRAS, 327, 849
Rettura A., Rosati P., Strazzullo V., Dickinson M., Fosbury R. A. E., Rocca-Volmerange B., Cimatti A., di Serego Alighieri S., Kuntschner H., 2006, A&A, 458, 717
Schawinski K., Thomas D., Sarzi M., Maraston C., Kaviraj S., Joo S.-J., Yi S. K., Silk J., 2007, MNRAS, 382, 1415
Schaye J., Dalla Vecchia C., 2007, MNRAS, pp 1159–+
Silk J., 2005, MNRAS, 364, 1337
Slyz A. D., Devriendt J. E. G., Bryan G., Silk J., 2005, MNRAS, 356, 737
Sousbie T., Pichon C., Colombi S., Novikov D., Pogosyan D., 2008, MNRAS, 383, 1655
Springel V., Hernquist L., 2003, MNRAS, 339, 289
Sutherland R. S., Dopita M. A., 1993, ApJS, 88, 253
Teyssier R., 2002, A&A, 385, 337
Tully R. B., Fisher J. R., 1977, A&A, 54, 661
van den Bosch F. C., 2002, MNRAS, 331, 98
van Dokkum P. G., Franx M., Fabricant D., Illingworth G. D., Kelson D. D., 2000, ApJ, 541, 95
Wild V., Kauffmann G., Heckman T., Charlot S., Lemson G., Brinchmann J., Reichard T., Pasquali A., 2007, MNRAS, 381, 543
Yepes G., Kates R., Khokhlov A., Klypin A., 1997, MNRAS, 284, 235

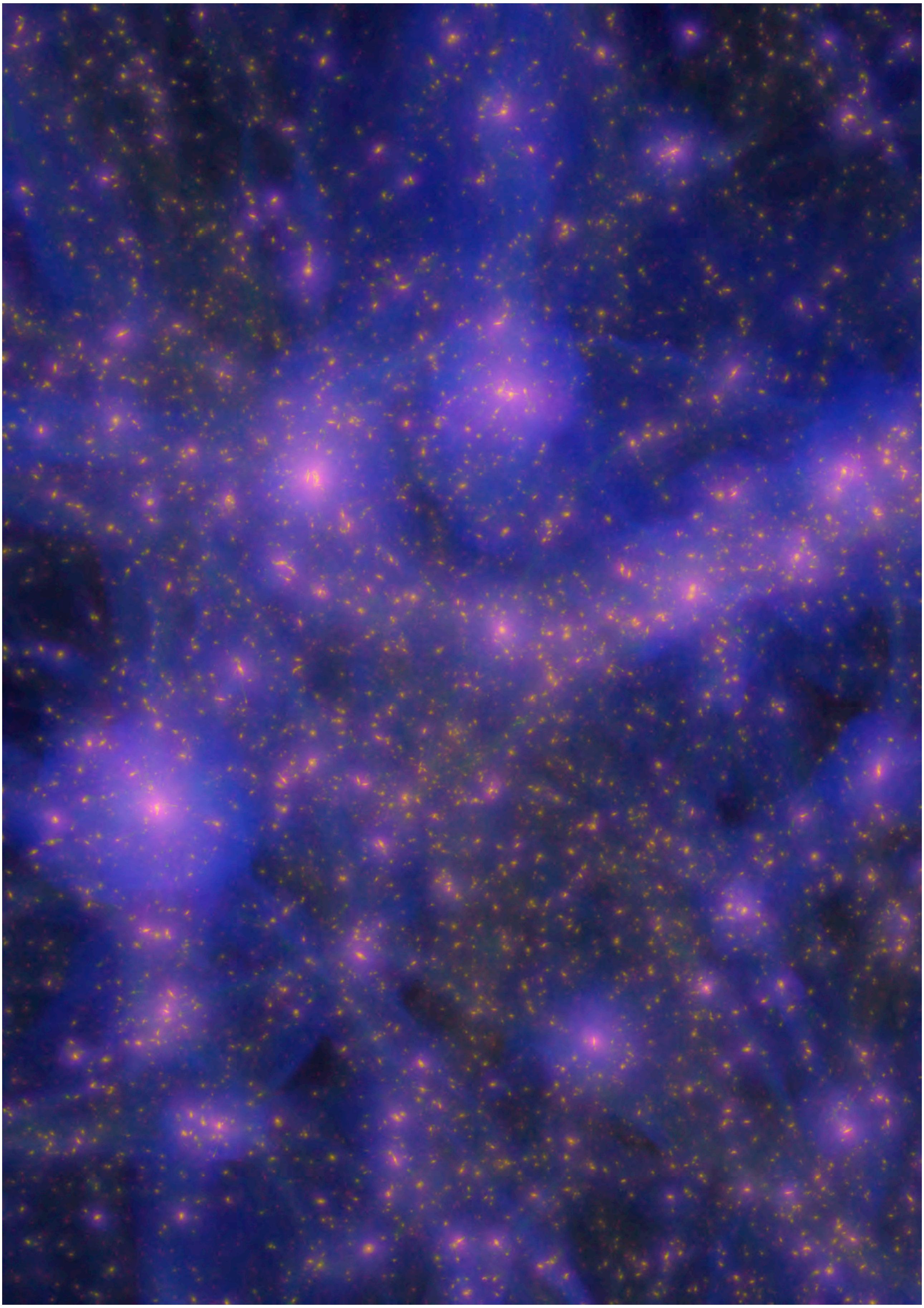

Mon. Not. R. Astron. Soc. (2007) doi:10.1111/j.1365-2966.2007.12685.x

The 3D skeleton: tracing the filamentary structure of the Universe

T. Sousbie,[1,2]★ C. Pichon,[1,2]★ S. Colombi,[1]★ D. Novikov[3]★ and D. Pogosyan[4]★

[1]*Institut d'Astrophysique de Paris & UPMC, 98 bis boulevard Arago, 75014 Paris, France*
[2]*Centre de Recherche Astrophysique de Lyon, 9 avenue Charles Andr é, 69561 Saint Genis Laval, France*
[3]*Astrophysics, Blackett Laboratory, Imperial College London, London SW7 2AZ*
[4]*Department of physics, University of Alberta, 11322-89 Avenue, Edmonton, Alberta, Canada T6G 2J1*

Accepted 2007 November 5. Received 2007 September 12; in original form 2007 July 15

ABSTRACT

The skeleton formalism, which aims at extracting and quantifying the filamentary structure of our Universe, is generalized to 3D density fields. A numerical method for computing a local approximation of the skeleton is presented and validated here on Gaussian random fields. It involves solving equation $(\mathcal{H}\nabla\rho \times \nabla\rho) = 0$, where $\nabla\rho$ and $\mathcal{H}$ are the gradient and Hessian matrix of the field. This method traces well the filamentary structure in 3D fields such as those produced by numerical simulations of the dark matter distribution on large scales, and is insensitive to monotonic biasing.

Two of its characteristics, namely its length and differential length, are analysed for Gaussian random fields. Its differential length per unit normalized density contrast scales like the probability distribution function of the underlying density contrast times the total length times a quadratic Edgeworth correction involving the square of the spectral parameter. The total length-scales like the inverse square smoothing length, with a scaling factor given by $0.21\ (5.28 + n)$ where n is the power index of the underlying field. This dependency implies that the total length can be used to constrain the shape of the underlying power spectrum, hence the cosmology.

Possible applications of the skeleton to galaxy formation and cosmology are discussed. As an illustration, the orientation of the spin of dark haloes and the orientation of the flow near the skeleton is computed for cosmological dark matter simulations. The flow is laminar along the filaments, while spins of dark haloes within 500 kpc of the skeleton are preferentially orthogonal to the direction of the flow at a level of 25 per cent.

Key words: cosmology: theory – dark matter – large-scale structure of Universe.

1 INTRODUCTION

Recent galaxy surveys like 2dF (Colless et al. 2003) or Sloan Digital Sky Survey (SDSS) (Gott et al. 2005) emphasized the complexity of the matter distribution in the Universe which presents large-scale structures such as filaments, clusters or walls on the boundaries of low-density bubbles (voids). On the theoretical side, the currently favoured scenario suggests that the Universe evolved from Gaussian initial conditions to form the structures that are observed nowadays. Numerical simulations have successfully captured the main features of the observed filamentary distribution, both statistically and visually. The skeleton formalism in 2D was introduced in (Novikov, Colombi & Doré 2006) (NCD) and aims at making possible the extraction and analysis of these filamentary structures. This paper extends it to three dimensions in order to describe the Universe's large-scale matter distribution and its dynamical environment.

In the literature, various steps towards a quantitative description of the large structures have been suggested. Statistical tools such as correlation functions (e.g. Peebles 1980) and power spectra (e.g. Peacock 1998) have been widely used and have been successful in describing matter distribution and constraining cosmological parameter. Recently, fast algorithms have been designed for first and second order (Szapudi et al. 2005), as well as higher order statistics (counts in cells etc.) as in Croton et al. (2004) or Kulkarni et al. (2007). The Minkowski functionals have also been very popular since their first applications to matter density field topology (see e.g. Gott, Melott & Dickinson 1986). By studying the average properties of excursion sets, they allow the extraction of characteristic numbers that reflect the topology of the field such as the genus, computed from the mean curvature of isodensity surfaces (see Hamilton, Gott & Weinberg 1986). This approach is in fact very powerful and has been used to test various properties of matter distribution such as its Gaussianity in Doroshkevich (1970), Gott et al. (1986), Winitzki

★E-mail: sousbie@iap.fr (TS); pichon@iap.fr (CP); colombi@iap.fr (SC); novikov@astro.ox.ac.uk (DN); pogosyan@phys.ualberta.ca (DP)

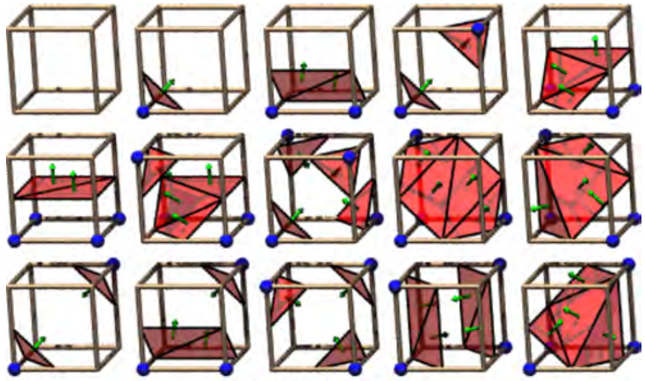

Figure A1. Illustration of the different possible configurations of a grid cell used for marching cube algorithm. Given a field *f* and isocontour $f = 0$, a blue ball represents a vertex where $f > 0$. It is then easy to build the isocontour by linearly interpolating the value of *f* along the edges. This picture was borrowed from James Sharman's web site, http://www.exaflop.org/docs/marchcubes/ind.html.

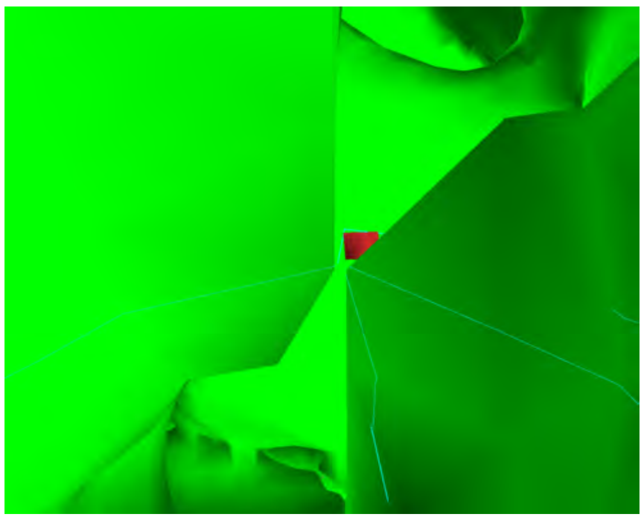

Figure A2. Illustration of a drawback of marching cubes algorithm. The green surface is an isosurface solution of equation (7) and the light blue line is the resulting skeleton. The red diamond represent a field maximum. It is clear on this picture that the algorithm misses the part close to that maximum, thus creating a spurious hole in the skeleton.

The next step involves solving the system of equations (8); the solution of this system corresponding to the intersection of two of the three solutions of equations (7). This is done by computing the 3D meshes of the 2D surfaces that are solution to these equations: the skeleton is at the intersection of two of them, depending on the value of the gradient at the point considered. Solving equation (7) is equivalent to finding the null isocontour of field $\mathcal{S}_i$, which can be done using the marching cube algorithm (Lorensen & Harvey 1987). The basic idea is to consider every cell of the grid as an individual cube. One can then compute the value of every $\mathcal{S}_i$ for the eight vertices and it is easy to check whether the isosurface intersects the cube or not. In fact, every vertex is above or below a threshold value (in this case 0), which gives a total of $2^8 = 256$ types of intersections (only 15 of them being intrinsically different) that can be pre-computed as illustrated in Fig. A1. The exact positions of the intersections are computed using quadratic interpolation. This yields the position of the intersections of the grid and the isocontour, and defines triangles that smartly link those intersection vertices: one can then reconstruct a very good approximation of what the isocontour is.

Which surfaces should be used for each cell is decided by computing $d_k = \det(\boldsymbol{r}_i, \boldsymbol{r}_j, \nabla\boldsymbol{\rho}), i \neq j \neq k \in \{1, 2, 3\}$ and selecting only the two $\mathcal{S}_k$ for which d_k is maximal. This gives two surfaces defined by triangles whose intersection can be efficiently computed: it amounts to computing the intersection of triangle pairs only. It is then straightforward to compute the eigenvalue of the Hessian for every segment and keep or reject them depending on the previously defined criteria (equation 10) in order to draw the *local* skeleton. The exact same method was used for efficiently and consistently finding the extrema and saddle points of the field. Indeed, if one defines three fields $f_i = \partial\rho/\partial r_i$, those critical points are the intersections of the three isocontour surfaces $f_i = 0$. One can then decide if a critical point is a maximum, minimum or saddle point by checking the value of eigenvalues of the Hessian (i.e. the curvature). Although marching cubes algorithms are very efficient for computing isodensity contour, they present some drawbacks for ambiguous configurations. Indeed, as illustrated on Fig. A2, some configurations are degenerate and one cannot decide where the isosurface should pass. This problem happens most of the time around critical points where the value of the field can go above and below the threshold within one cell. It induces the loss of small skeleton segments.

In order to obtain a smooth skeleton that does not present holes and to retrieve the connectivity information (i.e. to be able to follow the skeleton from one point to another), a three steps post-processing is applied. Here the algorithm is based on a weighted marking system to

& Kosowsky (1998) or more recently in Hikage, Komatsu & Matsubara (2006). They can also be used as so-called 'shape finders' (Sahni, Sathyaprakash & Shandarin 1998) and have been successfully applied to observed data sets (see e.g. Hikage et al. 2002; Sheth & Sahni 2005; James, Lewis & Colless 2007 for application to the SDSS and other galaxy distribution surveys). A large number of good reviews on the subject can be found (e.g. Melott 1990 or Kerscher 2000 and references therein).

These topological and statistical estimators analyse the distribution of observed galaxies globally and uniformly, and make little attempt at recovering the precise geometry of the matter distribution, i.e. they do not focus on specific regions (such as clumps, voids and filaments). Focusing on the identifiable regions of the Universe, the peak patches theory (Bond & Myers 1996a) attempts to describe cosmic structures formation through the identification of the collapse of the dense regions near the density peak and surrounding patches. In this framework, the evolution of patches hierarchy can be understood

from the measurement of only a few characteristics of the patches, while assuming that their flow does not depend on their internal non-linear dynamics.

This line of thought has been extended in the Cosmic Web paradigm (Bond, Kofman & Pogosyan 1996), which has emphasized that the large-scale spatial distribution of galaxy clusters and the filaments between them can be understood as mildly non-linear enhancements of the high-density peaks and filamentary ridges already present in the initial Gaussian density field. Recently, Hanami (2001) presented the so-called skeleton tree formalism: it analyses the process of hierarchical merging and extends the language of the peak patch through the analysis of the ridges of the density field in an abstract space corresponding to the usual three dimensions augmented by the smoothing length. The structure of voids in the large-scale dark matter distribution also has an extended history of theoretical modelling – see e.g. Hoffman & Shaham (1982), Icke (1984) or Bertschinger (1985) – while various void identifiers have been designed (see e.g. Platen, van de Weygaert & Jones 2007 and references therein).

One of the first attempts to develop an algorithm to detect and trace the filaments in the particle distribution has been the minimal spanning tree technique proposed by Doroshkevich in Doroshkevich (1970) and Barrow, Bhavsar & Sonoda (1985). Starting from a point distribution (a galaxy survey or a dark matter simulation), this method constructs the graph that connects all the dots with the property of never forming closed paths and being of minimal total lengths. Interesting statistical features can be extracted from it like the shape of the clusters or the length of the trunk (the longest path) and branches which are characteristic of the filamentarity of the distribution (Pearson & Coles 1995). More recently, other techniques with the same aim have been developed, such as Stoica et al. (2005), which uses a marked point process in order to recover the filament locations or Aragon-Calvo et al. (2007a) which provides an automatic segmentation of the different galactic distribution components using multiscale morphology filtering.

The 3D skeleton described in this paper focuses on the critical lines of a distribution, i.e. the set of lines joining the critical points in order to be able to compute the characteristic features of the underlying field (such as the total length of the filaments in a cosmological dark matter distribution). The skeleton provides a simple mathematical definition of the filaments of a density field based on Morse theory – see e.g. Milnor (1963), Colombi, Pogosyan & Souradeep (2000), Jost (2002) or Novikov, Colombi & Doré (2006) – and thus allows their extraction as well as their characterization.

Section 2 defines the local skeleton of large-scale structures. Section 3 introduces the numerical algorithm for constructing the local skeleton, and discusses its properties near the critical points (Appendix A gives a more detailed description of the algorithm). Section 4 investigates the evolution of its differential and total length as a function of the properties of the underlying field. Appendix C sketches the derivation of this differential length. Possible applications to cosmology and galaxy formation are discussed in Section 5, where two illustrations regarding the nature of the dark matter flow near the skeleton are given.

2 THE LOCAL SKELETON: THEORY

A comprehensive definition of the skeleton and how its local approximation in two dimensions is derived can be found in Novikov et al. (2006). To sum up, the so-called 'real' skeleton is by definition the subset of critical lines joining the saddle points of a field to its maxima while following the gradient's direction (while critical lines link *all* kinds of critical points together). It is easy to picture that applying this definition to a 2D field (an altitude map in a mountainous region for instance) allows the extraction of the ridges of that distribution. Although simple in appearance, this definition presents the drawback that it is in essence non-local: the presence of the skeleton in a given subregion may depend on the presence of a saddle point in a different subregion. In order to enforce locality, an approximation can in fact be derived using Taylor expansion in the vicinity of the critical points (i.e. local maxima and saddle points), leading to a second-order approximation of the skeleton: the local skeleton.

2.1 The 2D local skeleton

Defining the *local critical lines* as the set of points where the gradient of the field is an extremum along an isodensity contour, it can be shown (Novikov et al. 2006) that this set of points obeys the equation

$$\mathcal{S} \equiv \frac{\partial\rho}{\partial r_1}\frac{\partial\rho}{\partial r_2}\left(\frac{\partial^2\rho}{\partial r_1^2}-\frac{\partial^2\rho}{\partial r_2^2}\right) + \frac{\partial^2\rho}{\partial r_1\partial r_2}\left(\left[\frac{\partial\rho}{\partial r_2}\right]^2-\left[\frac{\partial\rho}{\partial r_1}\right]^2\right) = 0, \tag{1}$$

where r_1 and r_2 denote space coordinates and $\rho(r_1, r_2)$ is the density field. Equation (1) can be rewritten as

$$\mathcal{S} = \det(\mathcal{H}\nabla\rho, \nabla\rho) = 0, \tag{2}$$

where $\mathcal{H} \equiv \partial^2\rho/\partial r_1\partial r_2$ is the Hessian (second derivatives matrix) of the field. The solution to equation (2) can be interpreted mathematically as the set of points where the gradient of the field is an eigenvector of the Hessian (i.e. gradient and main curvature axis are aligned), which is clearly a local property of the field.

The local skeleton is defined as the subset of the local critical lines that is an approximation of the skeleton. Selecting this subset can be achieved by enforcing an additional condition: the gradient should be *minimal* [i.e. every point of the local skeleton of coordinates $\boldsymbol{r}$ should also be a local minimum of the isodensity contour at density $\rho(\boldsymbol{r})$]. That is, the second eigenvalue of the Hessian should be negative:

$$\lambda_2 < 0, \quad \text{and} \quad \mathcal{H}\,\nabla\rho = \lambda_1\nabla\rho, \tag{3}$$

where λ_i are the eigenvalues of the Hessian and $\lambda_2 < \lambda_1$.

2.2 The 3D local skeleton

Let us now derive the generalization of the notion of the local skeleton to a 3D space. The philosophy is essentially the same but minor differences arise.

Starting from the same definition as in 2D, the local skeleton should be the set of points where the density is an extremum along an isodensity contour. Let (u, v) be a coordinate system along an isocontour $(r_1(u, v), r_2(u, v), r_3(u, v))$ where $r_i, i \in \{1..3\}$ are the three space coordinates. The definition of an isocontour implies that

$$\begin{cases} \dfrac{\partial\rho}{\partial r_1}\dfrac{\mathrm{d}r_1}{\mathrm{d}u} + \dfrac{\partial\rho}{\partial r_2}\dfrac{\mathrm{d}r_2}{\mathrm{d}u} + \dfrac{\partial\rho}{\partial r_3}\dfrac{\mathrm{d}r_3}{\mathrm{d}u} = 0 \\ \\ \dfrac{\partial\rho}{\partial r_1}\dfrac{\mathrm{d}r_1}{\mathrm{d}v} + \dfrac{\partial\rho}{\partial r_2}\dfrac{\mathrm{d}r_2}{\mathrm{d}v} + \dfrac{\partial\rho}{\partial r_3}\dfrac{\mathrm{d}r_3}{\mathrm{d}v} = 0. \end{cases} \tag{4}$$

Moreover, as the gradient of the field ρ has to be an extremum:

$$\frac{\mathrm{d}}{\mathrm{d}u}(|\nabla\rho|^2) = 0 \quad \text{and} \quad \frac{\mathrm{d}}{\mathrm{d}v}(|\nabla\rho|^2) = 0. \tag{5}$$

Using equations (4) and (5), let us derive the equation of the local critical lines, which should only depend on the field and its first- and second-order spatial derivatives, similarly to equation (1). To do so, a coordinate system along the isocontour is needed but, as opposed to the 2D case, any coordinate system defined on an isocontour will be singular in some place as an isocontour is a closed surface. In order to avoid this problem, we choose to define three coordinates systems and swap from one to another when it becomes singular.

Defining three 1D coordinate systems s_i (see Fig. 1) so that for different values of s_i, one remains in the plane $(\boldsymbol{r}_j, \boldsymbol{r}_k)$ where $i \neq j \neq k$ and $i, j, k \in \{1..3\}$. The coordinate system s_i is singular wherever $\nabla\rho$ is proportional to $\boldsymbol{r}_i$. The 3D local critical lines satisfy equations (4) and (5) for $u \equiv s_i$ and $v \equiv s_j$ with $i \neq j$. For any s_i, these read

$$\frac{\mathrm{d}}{\mathrm{d}s_i}(|\nabla\rho|^2) = 0, \quad \text{and} \quad \frac{\partial\rho}{\partial r_1}\frac{\mathrm{d}r_1}{\mathrm{d}s_i} + \frac{\partial\rho}{\partial r_2}\frac{\mathrm{d}r_2}{\mathrm{d}s_i} + \frac{\partial\rho}{\partial r_3}\frac{\mathrm{d}r_3}{\mathrm{d}s_i} = 0. \tag{6}$$

Choosing $i \neq j \neq k \in \{1..3\}$, this system becomes after doing some algebra

$$\begin{aligned} \mathcal{S}_i \equiv\ & \frac{\partial^2\rho}{\partial r_j \partial r_k}\left(\frac{\partial\rho}{\partial r_j}^2 - \frac{\partial\rho}{\partial r_k}^2\right) \\ & + \frac{\partial\rho}{\partial r_j}\frac{\partial\rho}{\partial r_k}\left(\frac{\partial^2\rho}{\partial r_k^2} - \frac{\partial^2\rho}{\partial r_j^2}\right) \\ & - \frac{\partial\rho}{\partial r_i}\left(\frac{\partial\rho}{\partial r_k}\frac{\partial^2\rho}{\partial r_i \partial r_j} - \frac{\partial\rho}{\partial r_j}\frac{\partial^2\rho}{\partial r_i \partial r_k}\right) = 0. \end{aligned} \tag{7}$$

One can check that equation (7) reduces to equation (1) in the 2D case, assuming that the field is constant in the third dimension [the first two terms of equation (7) are the same as in equation (1)]. The local critical lines are thus the set of points that satisfies

$$\boldsymbol{\mathcal{S}} \equiv \begin{pmatrix} \mathcal{S}_i \\ \mathcal{S}_j \end{pmatrix} = \boldsymbol{0}, \; i \neq j \in \{1, 2, 3\}. \tag{8}$$

It is interesting to note that, as in the 2D case, equation (8) defines the local critical line as the set of points where the gradient of the density is an eigenvector of its Hessian matrix (the gradient and the principal curvature axis are collinear):

$$\mathcal{S} = (\mathcal{H} \cdot \nabla\rho \times \nabla\rho) = \boldsymbol{0}. \tag{9}$$

Once again, in order to require that the skeleton traces only the ridges of the distribution (i.e. the filaments in 3D), retrieving the subset of local critical lines that define the local skeleton can be achieved by

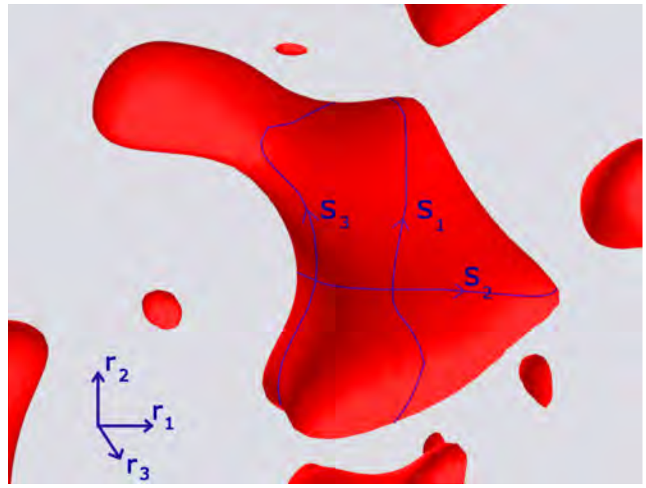

Figure 1. Definition of the coordinate system on an isocontour.

enforcing a negativity condition on the weakest eigenvalues of the Hessian:

$$\lambda_2 < 0, \quad \lambda_3 < 0, \quad \mathcal{H}\nabla\rho = \lambda_1\nabla\rho. \tag{10}$$

That is, the local skeleton is the subset of the local critical where the norm of the 3D gradient is minimal along the 2D isodensity contours (as opposed to simply extremal). Note that from equation (8) it is straightforward to show that any monotonic function of the field will have exactly the same skeleton as the field itself.

3 IMPLEMENTATION AND FEATURES

3.1 Implementation

Equation (8) is at the basis of the numerical implementation of the local skeleton determination developed here. The details of the algorithm are described in Appendix A, while the optimal choice of resolution and smoothing is presented in Appendix B. All the computations were performed using a specially developed C package: SKELEX[1] (Skeleton Extractor). This package also includes a flexible OpenGL visualization tool that was used for making the figures in this paper.

Fig. 2 presents the skeleton obtained for a density field sampled from a numerical simulation of dark matter distribution on a $50\,h^{-1}$ Mpc box with 512^3 particles using GADGET-2 (Springel 2005). The lighter colours represent denser regions and the blue skeleton appears to match quite well what one could identify as the filaments by eye. Note that the skeleton is both a tracer of the topology (it links a subset of the critical points) and the geometry of its underlying density. Hence it can be used to compare the geometrical and topological properties of various fields, e.g. the temperature and the dark matter distribution in hydrodynamical simulations. See also Fig. A3 for a graphical description of how the local skeleton is drawn.

3.2 The local skeleton branching properties

Let us now describe some global branching properties of the critical lines and the local skeleton. Important ingredients of the skeleton

[1] Available on request from the authors.

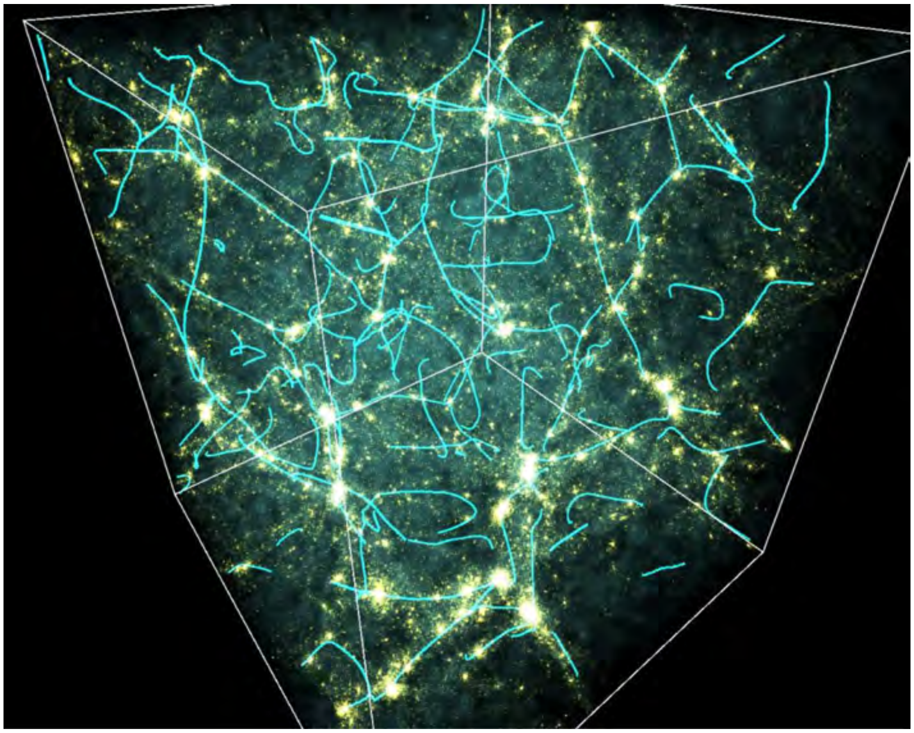

Figure 2. The final 3D skeleton derived from a 50-Mpc standard ΛCDM simulation run with sc gadget-2 using 512^3 particles. This result is obtained after post treating the skeleton using the method described in Appendix A.

are the extrema of the field. Indeed, the 'real skeleton' is defined as a set of critical lines that connect maxima to saddle points. Much of the topological behaviour of the skeleton is related to the distribution of such extremal points. For the *local* skeleton described this paper, the role of the extrema is similar but the whole set of critical lines encompass additional branches linking all kind of field extrema together.

Since the local skeleton is based on a local second-order approximation of the density field, ρ, its properties can be understood through the properties of the gradient $\nabla\rho$ and Hessian matrix $\mathcal{H}(\rho)$ only. The eigenvalues of $\mathcal{H}$ define the local curvature at any point, thus separating space into distinct regions depending on the sign of these eigenvalues λ_i. Within a 3D space, as by definition $\lambda_j < \lambda_i$ if $j > i$, there exist four of these regions. Let I be the number of negative eigenvalues, then the regions where I is equal to 0, 1, 2 and 3. This classification applies to critical points of the field in particular, where $\nabla\rho = 0$, the maxima ($I = 3$) and minima ($I = 0$) existing within local clumps and voids, respectively, while two types of saddle points can be distinguished: the filaments type saddle points (for $I = 2$) and the pancake type ones (for $I = 1$).

Fig. 3 illustrates a second-order approximation of the density field in the vicinity of the field extrema. The total set of critical lines form a fully connected path linking all the critical points together and exactly six branches pass through each of them in the direction of the three eigenvectors of the Hessian. Empirically, it is possible to picture the typical behaviour of the whole set of critical lines. Defining $E = \{0, 1, 2, 3\}$ and considering a given critical point where $I = n$, if $i < j < k \in E - \{n\}$, this critical point C_n is usually linked to three other pairs of critical points C_i, C_j and C_k (where $I = i, j$ and k, respectively) by critical lines aligned with eigenvectors associated with eigenvalues λ_1, λ_2 and λ_3, respectively, at point C_n. Most of the time, each of these branches connect to critical points C_i, C_j and C_k along the eigenvectors associated with eigenvalues λ_1, λ_2 and λ_3, respectively, evaluated at points C_i, C_j and C_k, respectively. In this picture, the critical lines can be seen as a fully connected path linking all the different regions defined by the sign of the eigenvalues of $\mathcal{H}$.

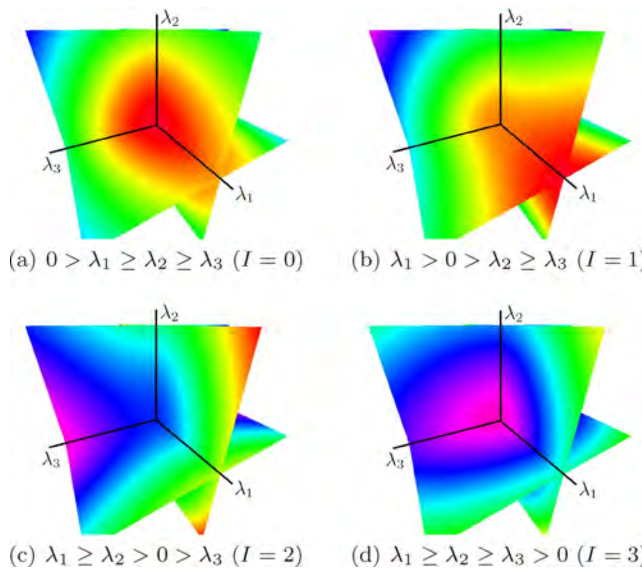

Figure 3. Illustration of a second-order approximation of the density field around a maximum ($I = 0$), filament ($I = 1$) and pancake ($I = 2$) saddle point and a minimum ($I = 3$). The colour stands for the density, ranging from purple in low-density regions to red in high-density regions. The axes are the eigenvectors of the Hessian, and give the direction of the six branches of the local critical lines going through these critical points (i.e. where the gradient of the field and the eigenvectors of H are aligned). The skeleton is the subset of these critical lines linking maxima (Fig. 3a) and filament saddle points (Fig. 3b), in the direction of the eigenvector associated with λ_1.

The overdense filamentary structure correspond to the subset of the critical lines that constitute an approximation of the 'real' skeleton (i.e. the 'ridges' of the distribution). This part is the one which links maxima ($I = 3$) and filamentary saddle points ($I = 2$). The typical behaviour of such lines is the following: in the immediate vicinity of a non-degenerate maximum, two branches of the skeleton exist, stretching in the eigendirection that corresponds to λ_1. Following one of the branches, denoting as $\lambda_{||}$ an eigenvalue whose eigenvector is parallel to the skeleton and $\lambda_{\perp,1,2}$ as two eigenvalues associated to eigenvectors in the perpendicular directions. Near the maximum, $0 > \lambda_{||} = \lambda_1 > \lambda_{\perp,1} > \lambda_{\perp,2}$. As one follows a branch one probable outcome is the change of sign of $\lambda_{||}$, in which case the branch will typically end in a saddle point of a filamentary type along its λ_1 direction. There is always another branch that starts from this saddle point on the other side, thus this type of branches have a fully connected structure. However, another possible outcome is that one of the orthogonal eigenvalues changes faster than $\lambda_{||}$ as one moves away from the maximum and becomes positive before the saddle point is reached. In this case the branch of the local skeleton formally terminates, which however in reality often means that the skeleton splits at this point in two new branches.

Such branching of the skeleton is especially frequent near the maxima of the field, where it accounts for how multiple filamentary sections can end up in a single dark matter halo. Studying how skeleton segments merge is relevant for questions such as the multipole structure of matter inflow on to dark haloes (Aubert, Pichon & Colombi 2004; Pichon & Aubert 2006). This property of skeleton segments to end outside of the critical points is specific to the local definition of the skeleton, in contrast to the 'real' skeleton whose segments are always connected on both ends.

4 THE SKELETON LENGTH FOR SCALE-FREE GAUSSIAN RANDOM FIELDS

Before considering general cosmological density fields, the local skeleton of scale-free Gaussian random fields ρ with null average value $\langle\rho\rangle = 0$ will be investigated. For convenience, it is useful to define some spectral parameters that depend on the spectral index n and on the smoothing length. In the statistical description of the skeleton of a random density field (Appendix C), the following spectral parameters appear to play a role:

$$\sigma_0^2 = \langle\rho^2\rangle, \tag{11}$$

$$\sigma_1^2 = \langle(\nabla\rho)^2\rangle, \tag{12}$$

$$\sigma_2^2 = \langle(\Delta\rho)^2\rangle, \tag{13}$$

$$\sigma_3^2 = \langle(\nabla\Delta\rho)^2\rangle. \tag{14}$$

This introduces three linear scales into the skeleton theory

$$R_0 = \frac{\sigma_0}{\sigma_1}, \quad R_* = \frac{\sigma_1}{\sigma_2}, \quad \tilde{R} = \frac{\sigma_2}{\sigma_3}, \tag{15}$$

where the first two have a well-known meaning of typical separation between zero crossing of the field R_0 and mean distance between extrema, R_* (Bardeen et al. 1986), while the third one, $\tilde{R}$ is, by analogy, the typical distance between the inflection points.

Out of three scales two dimensionless ratios may be constructed that are intrinsic parameters of the theory

$$\gamma \equiv \frac{R_*}{R_0} = \frac{\sigma_1^2}{\sigma_0\sigma_2}, \quad \tilde{\gamma} \equiv \frac{\tilde{R}}{R_*} = \frac{\sigma_2^2}{\sigma_3\sigma_1}, \tag{16}$$

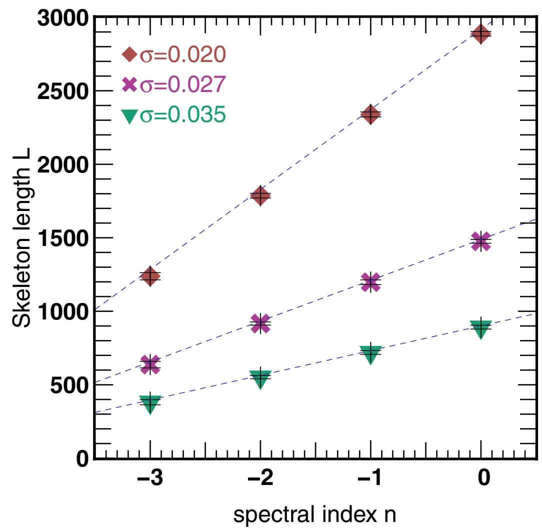

Figure 4. Total length L of the skeleton per unit box size for different smoothing lengths $\sigma = 0.020, 0.027, 0.035$; measured over 25 realizations of Gaussian random fields as a function of the spectral index n. While L depends linearly on the spectral index n, it grows as a power of σ. The dotted lines represent the fits obtained using the function: $L \approx 0.21(n + 5.28)\sigma^{-2}$.

where γ says how frequent encountering a maximum between two zero crossings of the field is, while $\tilde{\gamma}$ describes, on average, how many inflection points are between two extrema. For Gaussian fields, these parameters can be easily calculated from the power spectrum. Both γ and $\tilde{\gamma}$ range from 0 up to 1. For reference, for the power-law spectra with index $n > -3$, smoothed at small scales with a Gaussian window,

$$\gamma = \sqrt{\frac{n+3}{n+5}}, \quad \tilde{\gamma} = \sqrt{\frac{n+5}{n+7}}. \tag{17}$$

Note that cosmologically relevant density power spectra have $n > -3$ and thus, while γ can attain low values, $\tilde{\gamma}$ are always close to unity.[2]

Appendix C introduces a statistical description of the skeleton for the Gaussian and non-Gaussian random field. This section presents the numerical measurements of the properties of the skeleton for scale-free Gaussian fields.

The first quantity of interest is the total length of the skeleton, $L_{\rm tot}$. In the context of cosmology, $L_{\rm tot}$ can be linked to the total length of the filaments linking clusters together and in that sense reflects the history of matter accretion as well as the initial distribution of matter (which is supposed to be similar to a Gaussian random field with a scale-dependent effective spectral index similar to the ones considered here). Fig. 4 presents the result of the measurement of the total length $L_{\rm tot}$ of the skeleton per unit box size as a function of the spectral index and for different smoothing lengths σ (within the range of validity of the algorithm as described in Appendix B). These measurements are carried over 25 realizations of scale-free 256^3 Gaussian random fields as a function of the spectral index n. The sensitivity of the skeleton to the value of the spectral index is clear on this plot and, if $L_{\rm tot}$ appears to be a linear function of the

[2] Cosmological density fields, therefore, have of order one inflection point per extremum, unlike, e.g. a mountain range, where one encounters many inflection points on a way from a mountain top to the bottom.

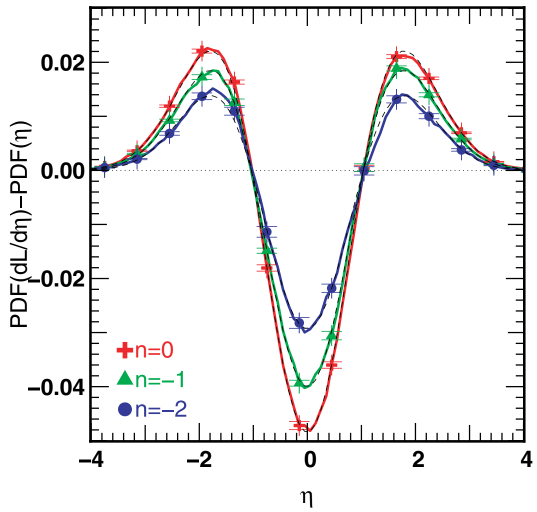

Figure 5. Difference between the PDF of the density field and the normalized differential length of the skeleton $\mathrm{d}L/\mathrm{d}\eta$ as a function of the density contrast $\eta = \rho/\sigma_0$. Each curve represents the average value and variance of the measured value of $\mathrm{d}L/\mathrm{d}\eta$ over 25 different realizations of scale-free Gaussian fields, for different values of the spectral index $n = 0, -1, -2$. The dotted curves represent the estimation obtained by fitting data using equation (19) (see Table 1 for values of the parameters).

spectral index, it is also clear that it grows as a power law of the smoothing length. The dotted lines on Fig. 4 shows the result of such a fit of the data and seems to work very well. A very good approximation of $L_{\rm tot}$ per unit box size is thus given by the function:

$$L_{\rm tot} = 0.21(n + 5.28)\sigma^{-2.00}. \quad (18)$$

As expected, the exponent of σ is measured to be exactly 2. It can be proved with a simple argument that this should be the case for scale-free Gaussian fields. In fact, for such fields, computing the skeleton over a grid of volume l^3 and smoothed on a scale σ is equivalent to computing the skeleton on a grid of volume $(\alpha\ l)^3$ while smoothing on a scale $(\alpha\sigma)$ and rescaling the result by a factor of $1/\alpha$. Because of the scale invariance, we also have $L(\sigma) = \alpha^{-3} L(\alpha\sigma)$ and so $L(\sigma) \propto \sigma/\sigma^3 = \sigma^{-2}$.

Interestingly, the dependence on the spectral index n is close to $n + 5$ which argues for filaments being relatively straight between extrema, see Appendix C. A visual examination of the filaments confirms this picture.

Now consider the differential length of the skeleton, $\mathrm{d}L/\mathrm{d}\eta(\eta)$ where $\eta \equiv \rho/\sigma_0$ is the normalized density contrast. This quantity represents the expected length of skeleton that can be measured in a given distribution between density contrasts η and $\eta + \mathrm{d}\eta$. Fig. 5 shows the normalized function $\mathrm{d}L/\mathrm{d}\eta(\eta)$ as a function of the normalized density contrast η from which was subtracted the probability distribution function (PDF) of the field (which, within the range of sampling and finite volume effects approximations, is a Gaussian function). These values were also averaged over 25 realizations of Gaussian fields with spectral index $n = 0, -1, -2$ sampled on 256^3 pixel grids and for a smoothing length $\sigma = 0.027$. This value was chosen as a compromise between finite volume effect and differentiability of the field on a grid discussed in Appendix B. Considering the error bars, it is clear that the value of $\mathrm{d}L/\mathrm{d}\eta(\eta)$ is directly linked to the spectral index n.

It is shown in Appendix C that $\mathrm{d}L/\mathrm{d}\eta\,(\eta)$ can be written using an Edgeworth expansion (see also Novikov et al. 2005 for the corresponding proof and fit in 2D):

$$\frac{\mathrm{d}L}{\mathrm{d}\eta}(\eta) = \frac{L_{\rm tot}}{\sqrt{2\pi}} \exp(-\eta^2/2) \left(\sum_{n \geqslant 0} C_{2n} \gamma^{2n} H_{2n} \left(\eta/\sqrt{2}\right) \right), \quad (19)$$

where $L_{\rm tot}$ is the total length of the skeleton, $C_0 = 1$ and H_{2n} are Hermite polynomials (using the Probabilist's convention). Fig. 4 demonstrates that this expansion also works very well in the 3D case. Remarkably, equation (19) does not depend on $\tilde{\gamma}$ which again argues for the picture of a stiff behaviour of the skeleton for cosmological scale-invariant density fields (see Appendix C). Table 1 presents the values of the first three coefficients C_{2n} obtained by fitting the measurements presented in Fig. 5 (the dotted line of Fig. 5 are the result of these fits). Not only does equation (19) allows a very good fit of the measured data, but it also appears that only the first-order term is non-null and the differential length of the skeleton of a Gaussian random field with spectral parameter γ is thus given by

$$\frac{\mathrm{d}L}{\mathrm{d}\eta}(\eta) = \frac{L_{\rm tot}}{\sqrt{2\pi}} \exp(-\eta^2/2) \left[1 + 0.21\gamma^2(\eta^2 - 1)\right]. \quad (20)$$

The only non-null coefficients in the expansion are thus $C_0 = 1$ and $C_2 = 0.21$, to be contrasted to $C_2 = 0.17$ in the 2D case. Equation (20) can be used as a test of non-Gaussianity like any other topological estimator, such as the genus, the PDF, etc. as discussed in Novikov et al. (2006), since departure from the shape of equation (20) must appear when the skeleton's differential length is computed while the underlying field is not Gaussian.[3]

For the matter distribution in the Universe, the filaments are overdense regions along which matter flows. In that sense, they are less subject to numerical or observational noise and contain most of the information about the underlying matter distribution. The skeleton length can thus be seen as a method for measuring the power spectrum which naturally weights information in different regions according to their importance.

Table 1. Measured values of the first three non-null terms in the Edgeworth expansion, equation (19), for three different values of the spectral index $n = 0, -1, -2$. These results are obtained by fitting equation (19) on the data presented in Fig. 5 on which the dotted lines represent the fitted function. The measurements show very good agreement, whatever the value of n.

	C_2	C_4	C_6
$n = 0$	0.219	0.006	−0.001
$n = -1$	0.212	0.002	−0.002
$n = -2$	0.206	−0.005	−0.008
	0.21 ± 0.005	0.001 ± 0.005	-0.004 ± 0.003

5 ILLUSTRATION: DYNAMICAL ENVIRONMENT OF FILAMENTS

Drawing the skeleton allows us to pin down the nature of the flow around the filaments. Indeed one may roughly define three dynamically distinct regions in large-scale structures: voids, clusters and filaments. The first two have been investigated in some detail. The filaments represent a fairly unexplored venue. Beyond the kinematics (velocity distribution, spin, etc.), the photometric and spectroscopic properties of galaxies (colour, age, metallicity, etc.), their morphology (ellipticals versus spirals, Gini number, asymmetry) or

[3] Of course, given the properties of the skeleton, this will not apply if the non-Gaussianity involves only a (monotonic) bias.

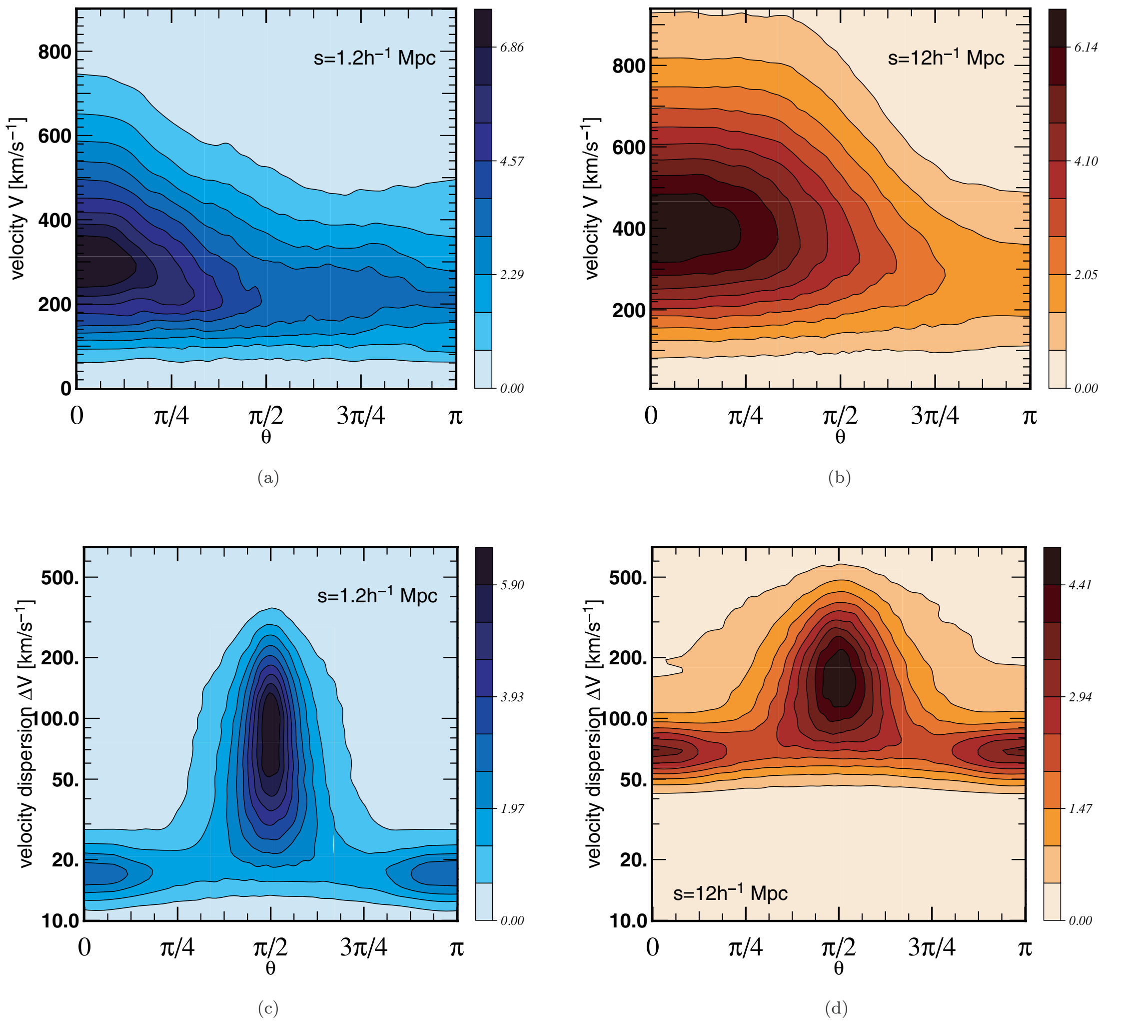

Figure 6. Top panels: PDF of the velocity field V of the dark matter along the skeleton as a function of its angle θ with the skeleton and its norm. The measurements were achieved on a $100\,h^{-1}$ Mpc and $1000\,h^{-1}$ Mpc dark matter simulation featuring 512^3 particles and a standard ΛCDM model, smoothed over a scale $s = 1.2$ and $12\,h^{-1}$ Mpc (left- and right-hand panels, respectively). The skeleton is oriented in the direction of increasing density. Dark matter appears to be flowing along the filaments in the direction of higher density regions (i.e. haloes). Bottom panels: PDF of main eigenvector of the velocity dispersion tensor ΔV_{ij} as a function of its angle θ with the skeleton and its eigenvalue amplitude. The peak of the PDF corresponds to high velocity dispersion orthogonal to the filaments, which is coherent with the picture of dark matter being accreted orthogonally by the filaments before flowing along them. Note the increase in velocity dispersion with scale (left- and right-hand panels) as well as the larger angular dispersion in the dark matter flow. This trend is also found while considering the same simulation at higher z.

the IGM (gas temperature, WHIM detection, fraction of gas/metals in the filaments, etc.), could also be investigated as a function of the distance to, and along the filaments.

In this section, two examples simply illustrate how the skeleton can be used to explore the environment of filaments in cosmological simulations.

5.1 Dark matter flow near the skeleton

Fig. 6 displays PDF of different characteristics of the dark matter flow along the skeleton. In order to understand the correlations between the filaments and the velocity field, we computed the PDF of its angle relative to the skeleton as a function of its intensity (top panels), and the PDF of the angle between its largest eigenvector and the skeleton as a function of the norm of the corresponding eigenvalue (bottom panels). These measurements were achieved by first sampling the field characteristics on a grid, averaging particles velocities $V \equiv \langle v \rangle$ and dispersion tensor, $\Delta V_{ij}^2 \equiv \langle (v_i - \langle v_i \rangle)(v_j - \langle v_j \rangle) \rangle$ over each cell, and then computing for each segment the distance-weighted average of their PDF. Left- and right-hand panels yield the resulting PDF computed in a $100\,h^{-1}$ and $1000\,h^{-1}$ Mpc dark matter standard Lambda cold dark matter (ΛCDM) model simulation, respectively, at redshift $z = 0$ and using 512^3 particles. In both cases, the density and velocity fields where sampled on a 512^3 pixels grid and smoothed over $\sigma_{\rm p} = 6$ pixels (i.e. $s = 1.2\,h^{-1}$ Mpc and $s = 12\,h^{-1}$ Mpc, respectively). The skeleton segments being oriented in the direction of increasing density, an angle of $\theta = 0$ means that dark matter is flowing along the filament in the direction of higher density regions.

The flows appears to be laminar and its amplitude increases with scale: this is expected since on larger scales the clusters are more massive, the potential difference is larger, hence the flow towards them is faster. Most dark matter particles have a mean velocity of about 300 (respectively 400) km s^{-1} along the filament and a dispersion of about 100 (respectively 150) km s^{-1} orthogonal to the filaments for the two scales considered here. The angular spread

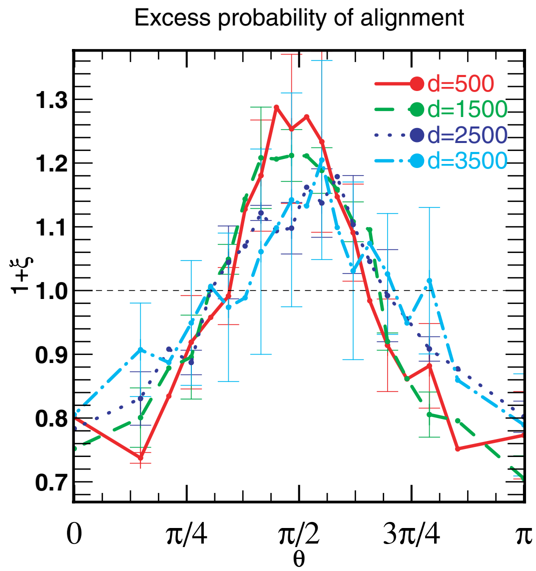

Figure 7. Excess probability of spin alignment with the local skeleton computed from the average of three 512^3 50 h^{-1} Mpc ΛCDM simulations at different distances: $d \in [0, 500], [500, 1500], [1500, 2500]$ and $[2500, 3500]$ h^{-1} kpc from the closest skeleton segments. This figure demonstrates that on average the spin of dark matter haloes tends to be orthogonal to the local filaments at a level of 25 per cent for distances shorter than 500 kpc. The simulation is analysed at redshift zero.

(panels 6a and b) also increases with scale, from about 30° to about 45°, reflecting the larger internal heat of the filament, also seen in Figs 6(c) and (d).

The qualitative shape of this PDF may be explained by the advection of new haloes on to the 'highways' corresponding to the mean flow. The first eigenvector of the dispersion tensor is on average clearly orthogonal to the filament, reflecting the velocity of dark matter falling on to the filaments. Note that the distribution is decreasing monotonously with θ in Fig. 6(a): some dark matter particles statistically even move downhill, and their relative fraction decreases with scale. The filaments are collecting matter away from the underdense regions. Smaller filaments empty smaller voids, which tend to get depleted earlier than larger ones; hence this may explain why the flow becomes more orderly at smaller scale as accretion diminishes.

Note that the redshift evolution (not shown here) of this distribution follows closely its scale evolution, the $z = 15$ PDF over 100 h^{-1} Mpc resembling the $z = 0$ PDF over 1000 h^{-1} Mpc (Sousbie 2006).

The detailed nature of the flow should eventually be investigated in a smoothing scale-independent manner, in order to derive universal features which would only depend on the cosmology and the initial power spectrum. Its evolution with redshift or with the cosmology should also be systematically analysed.

5.2 Dark matter spin-skeleton connection

The geometric orientation of the spin of dark matter haloes corresponds to another feature of the large-scale structure which can be characterized using the skeleton. The spin of dark haloes was computed using the classical friend-of-friend algorithm with 0.2 times the interparticle distance as linking length and retaining only haloes containing more than 100 particles. Fig. 7 displays the excess probability of alignment of the haloes' spins with the closest skeleton segment for different distances [0, 0.5], [0.5, 1.5], [1.5, 2.5] and [2.5, 3.5] h^{-1} Mpc. This probability reaches 25 per cent for an angle $\theta = \pi/2$ between the spin and the skeleton: the spin of dark matter haloes is preferentially orthogonal to the filament they belong to. This trend accounts for the fact that the filaments are the locus of laminar flow where haloes coalesce along the direction of the filaments parallel to the mean flow, hence acquiring momentum orthogonal to the flow, as observed in Aubert et al. (2004) and Aragon-Calvo et al. (2007b).

6 CONCLUSION AND PERSPECTIVES

The 3D skeleton formalism is a well-defined framework for studying the filamentary structure of a distribution. The 'real' skeleton is defined as the set of critical lines joining saddle points to maxima of the field along the gradient. A local approximation of it was introduced in Section 2 along with a numerical method allowing a fast retrieval of the locus of the filaments from a sampled field (see also Appendix A). This method involves computing the null isodensity surfaces of each component of a function $\mathcal{S} = (\mathcal{H} \cdot \nabla\rho \times \nabla\rho)$ of the gradient, $\nabla\rho$, and Hessian matrix, $\mathcal{H}$ of this field.

The ability to localize and characterize the filamentary structure of matter distribution in the Universe opens the prospect of many applications for the skeleton as discussed in Sections 4 and 5. It has been shown in Section 4 that for a Gaussian random field, the total length of the skeleton per unit volume depended only of the chosen smoothing length σ and spectral index n, with a specific functional from which was both fitted from simulations and motivated in Appendix C. In this sense, the local skeleton provides a direct measurement of the local shape of the power spectrum, $P(k)$, on various scales depending on the smoothing applied to the underlying field. Though there exist other ways to measure the power spectrum of a given distribution, the skeleton length is promising as it relies only on the filamentary structure of the distribution. A forthcoming paper will investigate in more details the expected scalings on the shape of the power spectrum. The analysis of the length of the skeleton of the galaxy distribution in the SDSS as a measurement of cosmological parameter Ω_m can be found in Sousbie et al. (2007). This paper addresses the issue of implementing the present algorithm on observational data sets and mock catalogues. In particular, it is shown there that the effect of redshift distortion is well accounted for by comparing data from large-scale surveys to such catalogues.

The skeleton may also be used as an isotropy probe. It corresponds in fact to a good candidate for the Alcock–Paczynski (Alcock & Paczynski 1979) test, since the apparent longitudinal to transverse length of skeleton segments should directly constrain the curvature of space in a manner which is bias independent. This test will be presented in a forthcoming paper.

It was demonstrated in Section 4 that the dark matter flow in the vicinity of filaments was dominantly laminar along the filaments and shows signs of orthogonal accretion corresponding to the infall of dark matter collected from the voids. It was also shown that the spin of dark matter haloes were preferentially orthogonal to the filament's direction, a feature which can be understood as a consequence of merger events taking place along these filaments. A clear virtue of the local skeleton is that since it relies on a local expansion of the field, it can deal with truncated/masked fields, segmented or vanishing ridges or isolated structures. Note finally that the fit, equation (20), opens the prospect of using the local skeleton to estimate the bias in observed surveys. The idea is to compute the PDF of galaxies on the one hand, which depends on the mass to light ratio of the sample, and the differential length (equation 20) on the other hand. Since the former depends on the bias, whereas the later does not, comparing the two should give an estimate of the bias. On the other hand, the local formulation of the skeleton presents some limitations. Mainly, it is not fully connected: it has by construction (since it is drawn from a second-order Taylor expansion of the field) only two segments per maxima whereas full connection would require three or more. A consequence is that it cannot represent merging filaments.

One could also use the curvature and torsion of filaments as cosmological probes, since the acceleration of the Universe induced by the cosmological constant is likely to straighten the filaments, though the fact that the local skeleton has only two segments near its maxima (the other segments must branch out) is likely to introduce some artefacts. The topology and geometry of the skeleton near the density peaks and the redshift evolution of the skeleton of the large-scale structures may prove of interest, for instance to study the frequency of reconnection, though again the local skeleton is not ideal in this respect. It would also be interesting to construct the skeleton in higher dimensions, for instance in space–time, to trace the events lines, but again connection is critical. In a forthcoming paper, an alternative algorithm for the identification of the skeleton, loosely based on a least action formulation, will be presented. It is complementary to the solution presented in this paper and will allow us to tackle those points for which the local skeleton is less efficient. Finally, the 3D skeleton algorithm could possibly be applied to other fields of research, such as neurology, in order to trace the neural network.

ACKNOWLEDGMENTS

We thank the anonymous referee, H. Courtois, D. Aubert and S. Prunet for comments and D. Munro for freely distributing his Yorick programming language and OpenGL interface (available at http://yorick.sourceforge.net/). This work was carried within the framework of the Horizon project, www.projet-horizon.fr.

REFERENCES

Alcock C., Paczynski B., 1979, Nat, 281, 358
Aragon-Calvo M. A., Jones B. J. T., van de Weygaert R. M. J., der Hulst V., 2007a, preprint (arXiv:0705.2072)
Aragon-Calvo M. A., van de Weygaert R., Jones B. J. T., van der Hulst J. M., 2007b, ApJ, 655, L5
Aubert D., Pichon C., 2007, MNRAS, 374, 877
Aubert D., Pichon C., Colombi S., 2004, MNRAS, 352, 376A
Bardeen J. M., Bond J. R., Kaiser N., Szalay A. S., 1986, ApJ, 304, 15
Barrow J. D., Bhavsar S. P., Sonoda D. H., 1985, MNRAS, 216, 17
Bertschinger E., 1985, ApJS, 58, 1
Bond J. R., Kofman L. A., Pogosyan D., 1996, Nat, 380, 63
Colless M. et al., 2003, preprint (astro-ph/0306581)
Colombi S., Pogosyan D., Souradeep T., 2000, Phys. Rev. Lett., 85, 5515
Croton D. J. et al., 2004, MNRAS, 352, 1232
Doroshkevich A. G., 1970, Astrofizica, 6, 581 (Astrophys., 6, 320)
Doroshkevich A. G., Tucker D. L., Lin H., Turchaninov V., Fong R., 2001, MNRAS, 322, 369
Gott J. R., III, Melott A. L., Dickinson M., 1986, ApJ, 306, 341
Gott J. R., III, Jurić M., Schlegel D., Hoyle F., Vogeley M., Tegmark M., Bahcall N., Brinkmann J., 2005, ApJ, 624, 463
Hamilton A. J. S., Gott J. R., III, Weinberg D., 1986, ApJ, 309, 1
Hanami H., 2001, MNRAS, 327, 721
Hikage C. et al., 2002, PASJ, 54, 707
Hikage C., Komatsu E., Matsubara T., 2006, ApJ, 653, 11
Hoffman Y., Shaham J., 1982, ApJ, 262, L23
Icke V., 1984, MNRAS, 206, 1
James J. B., Lewis, G. F., Colless M., 2007, MNRAS, 375, 128
Jost J., 2002, Riemannian Geometry and Geometric Analysis, 3rd edn. Springer-Verlag, Berlin
Kerscher M., 2000, Lecture Notes in Physics, 554, 36
Kulkarni G. V., Nichol R. C., Sheth R. K., Seo H.-J., Eisenstein D. J., Gray A., 2007, MNRAS, 378, 1196
Lorensen W., Harvey E., 1987, Cline. Marching Cubes: A High Resolution 3D Surface Construction Algorithm. Computer Graphics (SIGGRAPH 87 Proceedings), p. 163
Melott A. L., 1990, Phys. Rep., 193, 1
Milnor J., 1963, Morse Theory. Princeton Univ. Press, Princeton, NJ
Novikov D., Colombi S., Doré O., 2006, MNRAS, 366, 1201
Peacock J. A., 1998, Cosmological Physics. Cambridge Univ. Press, Cambridge
Pearson R. C., Coles P., 1995, MNRAS, 272, 231
Peebles P. J. E., 1980, The Large-Scale Structure of the Universe. Princeton Univ. Press, Princeton, NJ
Platen E., van de Weygaert R., Jones B. J. T., 2007, MNRAS, 380, 551
Sahni V., Sathyaprakash B. S., Shandarin S. F., 1998, ApJ, 495, L5
Sheth J. V., Sahni V., 2005, preprint (astro-ph/0502105)
Springel V., 2005, MNRAS, 364, 1105
Sousbie T., 2006, PhD thesis, http://hal-insu.archives-ouvertes.fr/
Sousbie T., Pichon C., Courtois H., Colombi S., Novikov D., 2007, ApJL, in press, preprint (astro-ph/0602628)
Stoica R. S., Martínez V. J., Mateu J., Saar E., 2005, A&A, 434, 423
Szapudi I., Pan, J., Prunet S., Budavári T., 2005, ApJ, 631, L1
Winitzki S., Kosowsky A., 1998, New Astron., 3, 75

APPENDIX A: NUMERICAL IMPLEMENTATION

All the computations were performed using a specially developed C package: SKELEX[4] (Skeleton Extractor). This package also includes a flexible OpenGL visualization tool that was used for making the figures in this paper.

The first step before computing the skeleton requires obtaining a density field from a discrete point-like distribution. This is achieved by smoothing appropriately the density field on a grid so that it is not singular (i.e. is sufficiently differentiable) but still contains all the topological information. The density field is computed using cloud-in-cell interpolation and convolving the result with Gaussian windows of different widths. As was shown in section B, the grid size and smoothing length are decisive parameters. It is then necessary to compute first and second derivatives of the field on the grid, which can be done using finite difference or Fourier transform method. Choosing one method or the other does not seem to have any influence on the resulting skeleton if the field is smooth enough (which is anyway a necessary condition).

[4] Available on request from the authors.

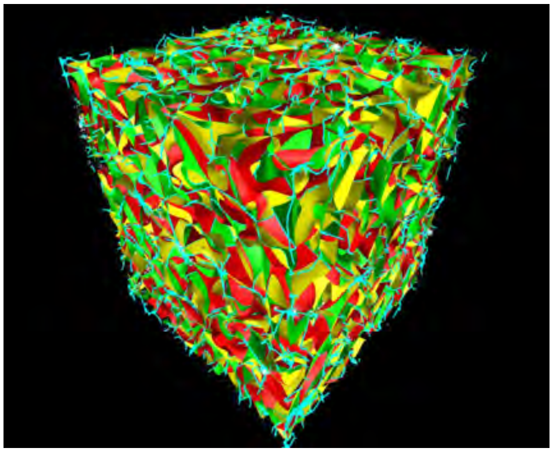

(a) The three fields isosurfaces the intersection of which constitutes the critical lines

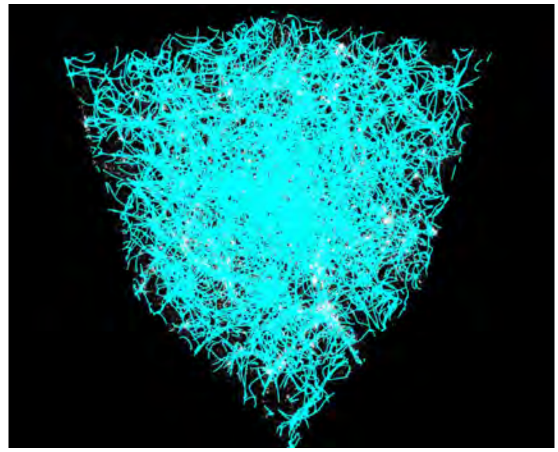

(b) The resulting critical lines made of all the intersection of any two of the three isosurfaces shown in 3(a).

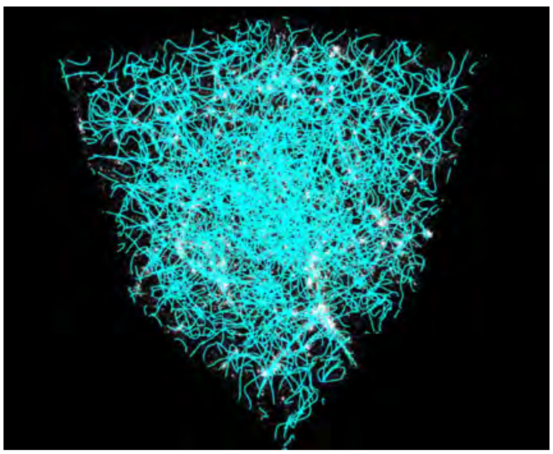

(c) The local critical lines obtained by selecting only the two least degenerate fields depending on the value of the gradient.

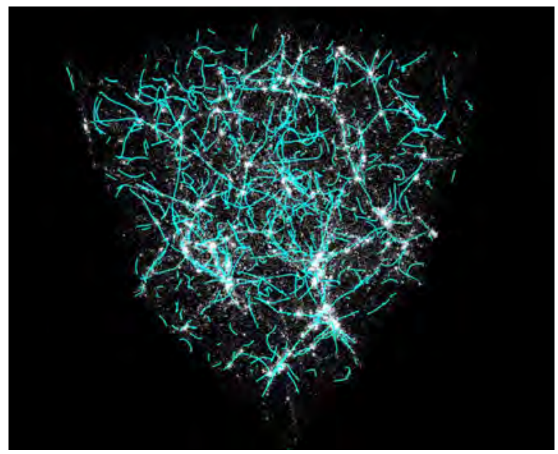

(d) The skeleton obtained after enforcing condition 10 on the local critical lines: $\lambda_1 > 0$ and $\lambda_2, \lambda_3 < 0$.

Figure A3. Illustration of the process of the skeleton computation. White points are dark matter particles extracted from a standard ΛCDM simulation run using sc gadget-2. The skeleton is defined as the intersection of two (among three) isosurfaces (Fig. 3a). Defining the curvature as λ_i with $H\nabla\rho = \lambda_i \nabla\rho$ and $\forall\, j > i, \lambda_j < \lambda_i$($\rho$ being the density and H its Hessian), it is possible to select only some parts of the skeleton depending on the value of λ_i and retrieve only the filaments (Fig. 3d). Using a simple post treatment, it is then possible to remove insignificant pieces and obtain the precise locus of the filaments (Fig. 2).

achieve this result (where the weights are assigned depending on the relative importance of the selection criteria). (i) The branches that were missed around the extrema are regenerated using the fact that the skeleton around an extremum is along the main curvature axis (i.e. along the first eigenvector of the Hessian). So for each extremum, marks are given to all skeleton segment, favouring those at small distances and with similar orientation as the main eigenvector of $\mathcal{H}$. Each extremum is eventually connected to the segment with the highest mark. (ii) The gaps between segments in the sequence of skeleton branches are filled. Starting from segments connected to extrema, all segments are visited iteratively: for the running segment, a mark is now assigned to all other unprocessed segments, based upon their relative distance, their relative angle and relative orientation. Note that the corresponding cost functions are non-linear: for instance segments with too large a relative angle are given an exponentially negative mark. (iii) Finally, all segments which have not been considered during step (ii) are dropped. The process is illustrated on Fig. A3, and the resulting skeleton is shown on Fig. 2. A detailed accounting of all stages of the skeleton extraction, including the post treatment is given in Sousbie (2006) (which gives the exact marking scheme described above), while the code is available upon request from the authors.

From a performance point of view, this method presents the advantage of being both fast and robust. The computational cost in fact mainly scales as the number of pixels in grid $N_{\rm g}^3$; the cost of computing the isosurfaces intersections is negligible given the possibility of computing only the intersections of faces belonging to the same pixel. It is moreover memory efficient and can be trivially parallelized: the computation can be done on subgrid regions and then merged. On a modern computer, the memory requirement corresponds to the requirement to store one subgrid and its three isosurface, which can be arbitrarily small, and the computational time for a 128^3 pixel grid is of the order of a few seconds on a modern desktop computer while only a few tens of minutes is necessary for a grid of 1024^3 pixel.

APPENDIX B: SMOOTHING LENGTH AND RESOLUTION

One aspect of the numerical implementation that deserves special attention is the issue of smoothing. In the main text, we consider the total skeleton of Gaussian random fields, focusing mainly on two of its properties: its length L and differential length $\mathrm{d}L/\mathrm{d}\eta$. The algorithm

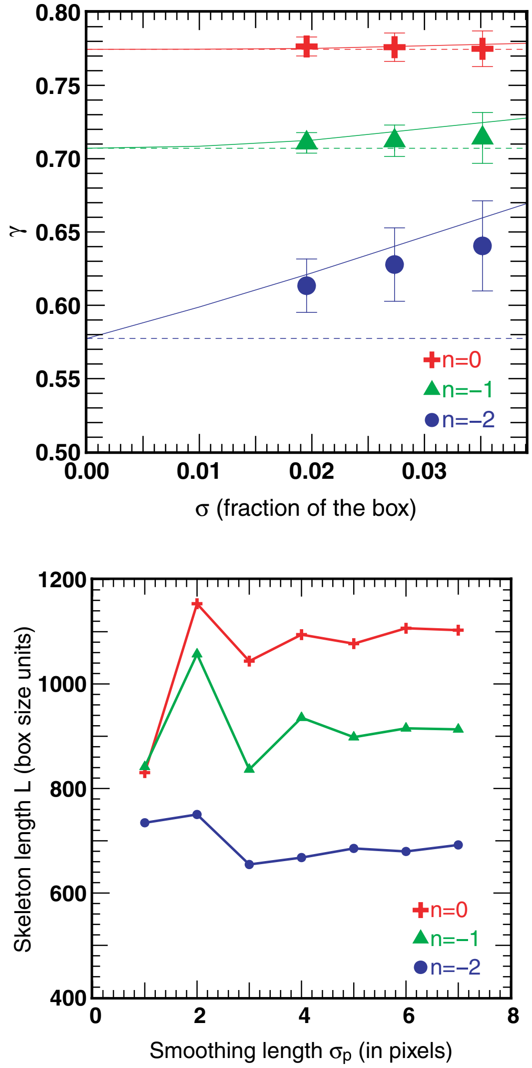

Figure B1. Top: evolution of the measured spectral parameter γ (see equation 16) for 25 realizations of Gaussian random fields with spectral index $n = 0$ (red crosses), $n = -1$ (green triangles) and $n = -1$ (blue discs) as a function of the smoothing scale σ expressed in box size units. The three continuous lines represent the expected theoretical values, measured by integrating the power spectrum truncated to grid limit frequencies. The dotted lines are the theoretical expectations (equation 17) without accounting for finite volume effects. For higher values of σ, the finite box size effects have more influence and the measured value of γ tends to differ from the correct one, thus limiting the maximal smoothing scale Bottom: evolution of the measured length of the total skeleton in box size units as a function of the smoothing length in pixels σ_{p}, for different values of the spectral index n and while keeping the smoothing scale to a constant fraction of the box size $\sigma \approx 0.031$. The measurements are obtained by resampling one initial realization of a Gaussian random field (generated over a 256^3 pixel grid) on smaller resolution grids and smoothing the resulting fields over the appropriate number of pixels. The measured length of the total skeleton appears to become stable for values of σ_{p} above a limit of 4 to 5 pixels at least, which corresponds to $\sigma > 0.19$ for a field sampled on a 256^3 pixels grid.

presented in this paper deals with the numerical computation of the skeleton of a discretized realization of a given field. It is thus important in the first instance to be able to deal with the influence of this discretization on the measured skeleton properties (see e.g. Colombi et al. 2000).

The statistical properties of a scale-free Gaussian random field can be described using only two numbers: its spectral index n and the amplitude A of its power spectrum $P(k) = Ak^n$, where k is the wavenumber. The skeleton formalism is totally independent of the amplitude of the field, so only the value of n is of interest to us. Consider a realization of a 3D scale-free Gaussian random field with spectral index n on a N_{g}^3 pixel grid. In order to ensure sufficient differentiability, this field is convolved to a Gaussian kernel whose scale σ is expressed per unit box size. The value of σ limits the size of the smallest scale that can be considered, while the finite size of the grid imposes an upper limit. Fig. B1 presents the measured value of the spectral parameter $\gamma^2 = (n+3)/(n+5)$ as a function of σ, for 25 realizations of Gaussian random fields with spectral index $n \in \{0, -1, -2\}$, together with the theoretical value, measured by integrating the power spectrum truncated to grid limit frequencies. As expected, a departure from theory is observed for higher values of σ, especially for fields with lower spectral index where most of the power is concentrated on small values of k (i.e. on large scales). This sets an upper limit on the value of the smoothing scale and so we will only be considering fields smoothed on scales $\sigma \leqslant 0.035$.

The other constraint on the value of σ arises from the fact that the skeleton computation algorithm requires a field that is continuously differentiable twice in the finite difference scheme sense. This means that the smoothing length should be large enough for the computational errors on field derivatives to be negligible. These considerations imply a lower limit on the smoothing length value expressed in number of pixels $\sigma_{\rm p} = \sigma\, N_{\rm g}$. In order to estimate this limit, we again generated Gaussian random fields with different spectral indices over a 256^3 ($N_{\rm g} = 256$) pixels grid and downsampled them on grids with eight different values of $N_{\rm g}$ ranging from $N_{\rm g} = 64$ up to $N_{\rm g} = 224$. Fig. B1 presents the evolution of the measured skeleton length for these realizations, each of them being computed for a smoothing scale corresponding to a constant fraction of the box size $\sigma \approx 0.031$ but to different values of $\sigma_{\rm p}$ ranging from $\sigma_{\rm p} = 1$ up to $\sigma_{\rm p} = 7$. One would clearly expect the length of the skeleton to depend only on the value of σ as long as the numerical approximations are negligible, which seems to be the case only for values of $\sigma_{\rm p}$ at least of order 5 pixels. For a given sampling $N_{\rm g}$, this limits the possible smoothing scale to $\sigma > 5/N_{\rm g}$. As was noted previously, this exact value depends on the considered spectral index, so we chose to consider the worst case, $n = 1$, where the fluctuations of the field do not dampen on small scales thus making the field naturally not smooth on any scale.

In this paper, all fields considered are sampled over $N_{\rm g} = 256$ cubic grids, so in order to respect the constraints described above, the fields are smoothed on scales in the range $0.02 < \sigma < 0.035$.

APPENDIX C: THE THEORETICAL DIFFERENTIAL LENGTH OF THE SKELETON

C1 Average length of the skeleton per unit volume

To find the average length per unit volume, $\mathcal{L}(\rho_{\rm th})$, of the critical lines[5] that are above the threshold $\rho_{\rm th}$ consider the vicinity of the points through which the local critical line passes, $S_i = 0, S_j = 0$. (Since the sets of conditions $(\mathcal{S}_i, \mathcal{S}_j) = (0, 0),\ i \neq j$ is degenerate, without loss of generality one can assume a particular choice for i and j). Define the set of points, $\mathcal{E}$, in the excursion $\rho > \rho_{\rm th}$ near the critical line solutions that satisfy $-\Delta\mathcal{S}_i/2 \leqslant S_i \leqslant \Delta\mathcal{S}_i/2$ and $-\Delta\mathcal{S}_j/2 \leqslant S_j \leqslant \Delta\mathcal{S}_j/2$ where ΔS_i and ΔS_j are sufficiently small so that the linear expansion $\Delta S_i \approx \nabla S_i \cdot {\rm d}\,\boldsymbol{r}$, $\Delta S_j \approx \nabla S_j \cdot {\rm d}\,\boldsymbol{r}$ holds.[6] The fraction of the total volume the set $\mathcal{E}$ occupies (the filling factor) is

$$\mathcal{V}(\rho_{\rm th}, \Delta\mathcal{S}_i, \Delta\mathcal{S}_j) = \int_{\rho>\rho_{\rm th}} {\rm d}\rho \int_{-\Delta\mathcal{S}_i/2}^{\Delta\mathcal{S}_i/2} {\rm d}\mathcal{S}_i \int_{-\Delta\mathcal{S}_j/2}^{\Delta\mathcal{S}_j/2} {\rm d}\mathcal{S}_j \int {\rm d}^3(\nabla\mathcal{S}_i)\, {\rm d}^3(\nabla\mathcal{S}_j) \mathcal{P}(\rho, \mathcal{S}_i, \mathcal{S}_j, \nabla\mathcal{S}_i, \nabla\mathcal{S}_j), \tag{C1}$$

where $\mathcal{P}(\rho, \mathcal{S}_i, \mathcal{S}_j, \nabla\mathcal{S}_i, \nabla\mathcal{S}_j)$ is the joint PDF of the quantities $(\rho, \mathcal{S}_i, \mathcal{S}_j, \nabla\mathcal{S}_i, \nabla\mathcal{S}_j)$. Here the seemingly redundant distribution of the gradients ∇S_i and ∇S_j was introduced to have the expression for the fraction of the total volume occupied by a differential subset of $\mathcal{E}$ that has specific values of the gradients $\nabla S_i, \nabla S_j$ [within ${\rm d}^3(\nabla\mathcal{S}_i)$ and ${\rm d}^3(\nabla\mathcal{S}_j)$]:

$${\rm d}\mathcal{V}(\rho_{\rm th}, \Delta S_i, \Delta\mathcal{S}_j, \nabla S_i, \nabla S_j) = {\rm d}^3(\nabla\mathcal{S}_i)\, {\rm d}^3(\nabla\mathcal{S}_j) \int_{\rho>\rho_{\rm th}} {\rm d}\rho \int_{-\Delta\mathcal{S}_i/2}^{\Delta\mathcal{S}_i/2} {\rm d}\mathcal{S}_i \int_{-\Delta\mathcal{S}_j/2}^{\Delta\mathcal{S}_j/2} {\rm d}\mathcal{S}_j \mathcal{P}(\rho, \mathcal{S}_i, \mathcal{S}_j, \nabla\mathcal{S}_i, \nabla\mathcal{S}_j). \tag{C2}$$

Since the area, Σ, of a section locally orthogonal to the such subset, is simply (modulo some trigonometry) given by

$$\Sigma(\Delta\mathcal{S}_i, \Delta\mathcal{S}_j, \nabla\mathcal{S}_i, \nabla\mathcal{S}_j) = \Delta\mathcal{S}_i \Delta\mathcal{S}_j / |\nabla\mathcal{S}_i \times \nabla\mathcal{S}_j|,$$

dividing ${\rm d}\mathcal{V}$ by Σ, integrating over all possible gradients $\nabla S_i, \nabla S_j$ and then taking the limit $(\Delta\mathcal{S}_i, \Delta\mathcal{S}_j) \to (0, 0)$ yields the length per unit volume of the skeleton that is above the threshold $\rho_{\rm th}$:

$$\begin{aligned}\mathcal{L}(\rho_{\rm th}) &= \lim_{(\Delta\mathcal{S}_i,\Delta\mathcal{S}_j)\to(0,0)} \int \frac{{\rm d}\mathcal{V}(\rho_{\rm th}, \Delta\mathcal{S}_i, \Delta\mathcal{S}_j, \nabla\mathcal{S}_i, \nabla\mathcal{S}_j)}{\Sigma(\Delta\mathcal{S}_i, \Delta\mathcal{S}_j, \nabla\mathcal{S}_i, \nabla\mathcal{S}_j)} \\ &= \int_{\rho>\rho_{\rm th}} {\rm d}\rho \int {\rm d}^3(\nabla\mathcal{S}_i)\, {\rm d}^3(\nabla\mathcal{S}_j)\, |\nabla\mathcal{S}_i \times \nabla\mathcal{S}_j| \mathcal{P}(\rho, \mathcal{S}_i = 0, \mathcal{S}_j = 0, \nabla\mathcal{S}_i, \nabla\mathcal{S}_j).\end{aligned} \tag{C3}$$

This generalizes the calculation of NCD to three dimensions: the length of the local skeleton is defined by the properties of the density field and its partial derivatives up to third order, as expected.

In order to understand the scalings involved in the computation of $\mathcal{L}$, let us rewrite this equation in terms of dimensionless quantities

$$\sigma_0\eta \equiv \rho_{th}, \quad \sigma_0 x \equiv \rho, \quad \sigma_1 x_i \equiv \frac{\partial\rho}{\partial r_i}, \quad \sigma_2 x_{ij} \equiv \frac{\partial^2\rho}{\partial r_i \partial r_j}, \quad \sigma_3 x_{ijk} \equiv \frac{\partial^3\rho}{\partial r_i \partial r_j \partial r_k}, \quad \sigma_2\sigma_1^2 s_i \equiv \mathcal{S}_i, \quad \sigma_3\sigma_1^2 \nabla s_i \equiv \nabla\mathcal{S}_i, \tag{C4}$$

with, following Bardeen et al. (1986),

$$\sigma_n^2 \equiv \int \frac{k^2{\rm d}k}{2\pi^2} P(k) k^{2n}, \tag{C5}$$

where $P(k)$ is the power spectrum of ρ. Equation (9) and its gradient can be written more conveniently using the totally antisymmetric tensor, ϵ^{ijk}, as

$$s_i = \sum_{jkl} \epsilon^{ijk} x_{jl} x_l x_k, \quad \text{and} \quad \nabla_m s_i \equiv \nabla\hat{s}_i(x_k, x_{kl}, x_{klm}) = \sum_{jkl} \epsilon^{ijk} \left(x_{jlm} x_l x_k + \tilde{\gamma}[x_{jl} x_{lm} x_k + x_{jl} x_{km} x_l] \right). \tag{C6}$$

[5] the distinction is made here between the theoretical expectation, $\mathcal{L}(\rho_{\rm th})$, in this section and the estimator, L, in the main text.

[6] In such small neighbourhood of a critical line there are no other critical lines since the solution for linearized skeleton equations is unique. Note that the linear expansion of S_i breaks near the extrema of the field, where $\nabla S_i = 0$, which allows several critical lines to intersect at such points. However, extremal points are of measure zero as far as the computation of the length of the skeleton is concerned.

The variances of all the random quantities defined in equation (C4) do not depend on spectral parameters (they are pure numbers) except for ∇s_i. Keeping that in mind, in this new notation, equation (C3) becomes

$$\mathcal{L}(\eta) = \left(\frac{\sigma_3}{\sigma_2}\right)^2 \int_{x>\eta} \mathrm{d}x \int \mathrm{d}^3(\nabla s_i)\,\mathrm{d}^3(\nabla s_j)\,|\nabla s_i \times \nabla s_j| \mathcal{P}(x, s_i = 0, s_j = 0, \nabla s_i, \nabla s_j). \tag{C7}$$

Equation (C7) is the formal expression for the length per unit volume of the total set of critical lines above the threshold η.

Let us express the joint distribution function $\mathcal{P}(\eta, s_i, s_j, \nabla s_i, \nabla s_j)$ in terms of the joint distribution function of the underlying field and its derivatives $P(x, x_k, x_{km}, x_{klm})$. Expressions (C6) for s_i and ∇s_i involve up to third derivatives of the field x, thus, accounting for the symmetries in the derivative tensors of the second and third order is, one deals with a set of 20 independent variables $(x, x_k, x_{kl}, x_{klm})$. $\mathcal{P}$ is obtained as a marginalization over the field distribution

$$\mathcal{P}(\eta, s_i, s_j, \nabla s_i, \nabla s_j) = \int \mathrm{d}x\mathrm{d}^3x_k\mathrm{d}^6x_{kl}\mathrm{d}^{10}x_{klm}\, P(x, x_k, x_{kl}, x_{klm})\delta_D(x-\eta)\delta_D(\hat{s}_i(x_k, x_{kl}) - s_i)\delta_D(\hat{s}_j(x_k, x_{kl}) - s_j)$$

$$\times\delta_D(\nabla\hat{s}_i(x_k, x_{kl}, x_{klm}) - \nabla s_i)\delta_D(\nabla\hat{s}_j(x_k, x_{kl}, x_{klm}) - \nabla s_j), \tag{C8}$$

which yields the appropriate 9D probability density. Substituting the expression (C8) into equation (C7), differentiating with respect to η, and accounting for two delta functions in ∇s_i and ∇s_j yields

$$\frac{\partial\mathcal{L}}{\partial\eta} = \left(\frac{1}{\tilde{R}}\right)^2 \int \mathrm{d}^3x_k\mathrm{d}^6x_{kl}\mathrm{d}^{10}x_{klm}\,|\nabla\hat{s}_i \times \nabla\hat{s}_j| P(\eta, x_k, x_{kl}, x_{klm})\,\delta_D(\hat{s}_i(x_k, x_{kl}))\delta_D(\hat{s}_j(x_k, x_{kl})), \tag{C9}$$

where σ_3/σ_2 is rewritten in terms $\tilde{R}$ with the help of equation (16).

Expression (C9) gives the differential length per unit volume of the total set of critical lines. Note that $\nabla\hat{s}_i$ and $\nabla\hat{s}_j$ are now functions of (x_k, x_{kl}, x_{klm}) and $\hat{s}_i$ and $\hat{s}_j$ are function of (x_k, x_{kl}) given by equation (C6). The two delta functions couple the different x_k, x_{kl}, accounting for the fact that the integral should be restricted to the intersection of the two isosurfaces, i.e. along the critical lines. The modulus in $|\nabla\hat{s}_i \times \nabla\hat{s}_j|$ makes the summation of skeleton segments non-algebraic, which complicates the further reduction of equation (C9). For the set of local critical lines, there are no restriction to the region of integration. If one is interested in the local skeleton, the integration should be restricted to regions where the condition given by equation (10) holds.

The total length of the critical lines per unit volume is

$$\mathcal{L}_{tot} = \int_{-\infty}^{\infty} \mathrm{d}\eta \frac{\partial\mathcal{L}}{\partial\eta} = \left(\frac{1}{\tilde{R}}\right)^2 \int \mathrm{d}^3x_k\mathrm{d}^6x_{kl}\mathrm{d}^{10}x_{klm}\,|\nabla\hat{s}_i \times \nabla\hat{s}_j| P(x_k, x_{kl}, x_{klm})\delta_D(\hat{s}_i(x_k, x_{kl}))\delta_D(\hat{s}_j(x_k, x_{kl})). \tag{C10}$$

C2 $\partial\mathcal{L}/\partial\eta$ for a Gaussian random field

Since at a point the value of a Gaussian field does not correlate with its derivatives of odd orders (this is easy to understand using symmetries in Fourier space), the joint distribution function $P(x, x_k, x_{kl}, x_{klm})$ can be factorized as

$$P(x, x_k, x_{kl}, x_{klm}) = P_0(x, x_{kl})P_1(x_k, x_{klm}). \tag{C11}$$

In P_0, the only dependence on the power spectrum of the underlying field is in the parameter γ (cf. equation 16) that describes the correlation between the field and its second derivatives. Similarly, $P_1(x_i, x_{ijk})$ only involves $\tilde{\gamma}$ which describes the correlation between the gradient of the field and its third derivatives. Therefore $\partial\mathcal{L}/\partial\eta$ depends only on η, $\tilde{R}$, γ and $\tilde{\gamma}$, as argued in the main text. Note that, by symmetry, $\partial\mathcal{L}/\partial\eta$ for the total set of critical lines should be an even function of η. The total length of the skeleton, $\mathcal{L}_{\rm tot}$, which follows from marginalization of the equation (C9) over η may depend only on $\tilde{\gamma}$ and $\tilde{R}$ since the integration of $P_0(\eta, x_{kl})$ over all η cancels the dependency on γ.

C2.1 The 'stiff' filament approximation

The $1/\tilde{R}^2$ scaling in equation (C9) reflects the basic fact that, by definition, the local skeleton lines are almost straight within a volume, $\sim \tilde{R}^3$, that contains one inflection point. A straight segment through such volume has the length $\sim \tilde{R}$, thus, the expected length per unit volume is $\sim 1/\tilde{R}^2$. The dependence on the spectral index is then $1/\tilde{R}^2 \propto (n+7)/\sigma^2$, where σ is the smoothing length. Is this the scaling with n that one should expect in the simulations? Let us write formally

$$\nabla s_i \times \nabla s_j = \boldsymbol{A}(x_k, x_{kl}, x_{klm}) + \tilde{\gamma}\boldsymbol{B}(x_k, x_{kl}, x_{klm}) + \tilde{\gamma}^2\boldsymbol{C}(x_{k,}x_{kl}). \tag{C12}$$

Suppose the last term dominates statistically.[7] Then, since $\tilde{\gamma}/\tilde{R} = 1/R_*$, and given that $\boldsymbol{C}(x_{k,}\ x_{lm})$ does not depend on the third derivative of the field (which can then be integrated out), equation (C12) becomes

$$\frac{\partial\mathcal{L}}{\partial\eta} \approx \left(\frac{1}{R_*}\right)^2 \int \mathrm{d}^3x_k\mathrm{d}^6x_{kl}\,|\boldsymbol{C}(x_{k,}x_{lm})|\ P_0(\eta, x_{kl})\ P_1(x_k)\delta_D(\hat{s}_i(x_k, x_{kl}))\delta_D(\hat{s}_j(x_k, x_{kl})). \tag{C13}$$

It is easy to foresee when this regime is valid. The same argument as before implies that the $1/R_*^2$ scaling arises when the skeleton is almost straight within a volume that contains one extremum, $\sim R_*^3$, rather than one inflection point. This is supported by the fact that the integral

[7] Or equivalently assume that the magnitude of derivative of the Hessian is negligible relative to the magnitude of the Hessian.

does not depend on the third derivatives, thus inflection points play no role, and no dependence on $\tilde{\gamma}$ remains. This picture corresponds to a skeleton connecting extrema with relatively straight segments. The scaling is then $1/R_*^2 \propto (n+5)/\sigma^2$. We call this regime and the expression (C13) that describes it 'the stiff approximation'.

For the total length of the critical lines, integration over η gives

$$\mathcal{L}_{tot} \approx \left(\frac{1}{R_*}\right)^2 \int \mathrm{d}^3 x_k \mathrm{d}^6 x_{kl}\ |\boldsymbol{C}(x_{k,}x_{lm})|\ P_0(x_{kl}) P_1(x_k) \delta_D(\hat{s}_i(x_k, x_{kl})) \delta_D(\hat{s}_j(x_k, x_{kl})) \propto (n+5)\sigma^{-2} \tag{C14}$$

strictly, since the integral is just a pure number. This is very close to the scaling with n that was found in the numerical fit, equation (18). The differential length in the stiff regime is then only the function of γ times $\mathcal{L}_{\rm tot}$. This demonstrates theoretical consistency between the scaling $\sim (n+5)\,\sigma^{-2}$ of $\mathcal{L}_{\rm tot}$ and insensitivity of $\partial\mathcal{L}/\partial\eta$ to $\tilde{\gamma}$ for scale-free Gaussian random fields that was observed in the simulations.

C2.2 Joint distribution of the field and its derivatives for a Gaussian random field

The full expression $P_0(x, x_{kl})$ is given in Bardeen et al. (1986). Introducing variables

$$u \equiv -\Delta x = -(x_{11} + x_{22} + x_{33}), \quad v \equiv \frac{1}{2}(x_{33} - x_{11}), \quad w \equiv \sqrt{\frac{1}{12}}(2x_{22} - x_{11} - x_{33}), \tag{C15}$$

in place of diagonal elements of the Hessian (x_{11}, x_{22}, x_{33}) one finds that $u, v, w, x_{12}, x_{13}, x_{23}$ are uncorrelated. Importantly, the field, x is only correlated with $u = \Delta x$ and

$$\langle xu \rangle = \gamma, \quad \langle xv \rangle = 0, \quad \langle xw \rangle = 0, \quad \langle x x_{kl} \rangle = 0,\ k \neq l, \tag{C16}$$

where γ is the same quantity as in equation (16). The full expression of $P_0(x, x_{kl})$ is then

$$P_0(x, x_{kl})\, \mathrm{d}x\, \mathrm{d}^6 x_{kl} = \frac{(15)^{5/2}}{(2\pi)^{7/2}(1-\gamma^2)^{1/2}} \exp\left[-\frac{(x-\gamma u)^2}{2(1-\gamma^2)} - \frac{u^2}{2}\right] \exp\left[-\frac{15}{2}(v^2 + w^2 + x_{12}^2 + x_{13}^2 + x_{23}^2)\right] \mathrm{d}x\, \mathrm{d}u\, \mathrm{d}v\, \mathrm{d}w\, \mathrm{d}x_{12}\, \mathrm{d}x_{13}\, \mathrm{d}x_{23},$$

and is described by only one correlation parameter γ.

A similar procedure can be performed for the joint probability of the first and third derivatives of the fields, $P_1(x_i, x_{ijk})$, by defining the following nine parameters (see also Hanami 99):

$$u_i \equiv \nabla_i u, \quad v_i \equiv \frac{1}{2}\epsilon^{ijk}\nabla_i(\nabla_j\nabla_j - \nabla_k\nabla_k)x, \ \text{ with } \ j < k, \quad \text{ and } \quad w_i \equiv \sqrt{\frac{5}{12}}\nabla_i\left(\nabla_i\nabla_i - \frac{3}{5}\Delta\right)x, \tag{C17}$$

and replacing the variables $(x_{i11}, x_{i22}, x_{i33})$ with (u_i, v_i, w_i). In that case, the only cross-correlations in the vector $(x_1, x_2, x_3, u_1, v_1, w_1, u_2, v_2, w_2, u_3, v_3, w_3, x_{123})$ which do not vanish are between the same components of the gradient and the gradient of the Laplacian of the field:

$$\langle x_i u_i \rangle = \tilde{\gamma}/3, \quad i = 1, 2, 3, \tag{C18}$$

where $\tilde{\gamma}$ is the same quantity as in equation (16).

This allows us to write

$$P_1(x_i, x_{ijk}) \mathrm{d}^3 x_i\, \mathrm{d}^{10} x_{ijk} = \frac{105^{7/2} 3^3 \mathrm{d}^3 w_i\, \mathrm{d}^3 v_i\, \mathrm{d}x_{123}}{(2\pi)^{13/2}(1-\tilde{\gamma}^2)^{3/2}} \exp\left[-\frac{105}{2}\left(x_{123}^2 + \sum_{i=1}^{3}(v_i^2 + w_i^2)\right)\right] \prod_{i=1}^{3} \mathrm{d}u_i\, \mathrm{d}x_i \exp\left[-\frac{3(u_i - \tilde{\gamma}x_i)^2}{2(1-\tilde{\gamma}^2)} - \frac{3x_i^2}{2}\right].$$

C2.3 Dependence of the differential length on threshold and spectral parameters

What is the dependence of the skeleton differential length on the parameter γ and the threshold η? Let us look at the structure of the integrals involved with respect to the variable u. Importantly, the arguments of the delta functions $S_i \neq S_i(u)$ and $\nabla S_i \times \nabla S_j$, given by equation (C12), is $\sim \sqrt{Q_4(u)}$ where $Q_4(u)$ is a positive quartic in u. Inserting the expressions for P_1 and P_0 into equation (C9) one sees that the integral over u in $\partial\mathcal{L}/\partial\eta$ has the form

$$\mathcal{I}(\gamma, \eta) = \int_{-\infty}^{\infty} \frac{\sqrt{Q_4(u)}\exp\left(-u^2/2\right)}{(2\pi)^{1/2}(1-\gamma^2)^{1/2}} \exp\left[-\frac{(\eta - \gamma u)^2}{2(1-\gamma^2)}\right] \mathrm{d}u, \tag{C19}$$

where $Q_4(u)$, of course, also depends on $v, w, u_k, v_k, w_k, x_{123}, x_{k<l}$ and possibly $\tilde{\gamma}$, but not on γ.

In the trivial limit $\gamma \to 0$ the coupling between u and the field value η vanishes and the differential length is reduced to the PDF of η:

$$\mathrm{d}\mathcal{L}/\mathrm{d}\eta \propto \exp\left[-\frac{\eta^2}{2}\right] = \frac{\mathcal{L}_{\rm tot}}{(2\pi)^{1/2}} \exp\left[-\frac{\eta^2}{2}\right]. \tag{C20}$$

For non-vanishing γ, following NCD, the differentiation of equation (C19) shows that $\mathcal{I}(\gamma, \eta)$ obeys the equation

$$\gamma\frac{\partial\mathcal{I}}{\partial\gamma} = -\frac{\partial}{\partial\eta}\left[\eta\mathcal{I}(\gamma, \eta) + \frac{\partial\mathcal{I}}{\partial\eta}\right],$$

whose solution involve even Hermite polynomials (retaining only the convergent solution at large η):

$$\mathcal{I}(\gamma,\eta)=\sum_{n=0}^{\infty}c_{2n}\gamma^{2n}H_{2n}(\eta/\sqrt{2})\exp\left[-\frac{\eta^2}{2}\right]. \tag{C21}$$

Due to the orthogonality property of Hermite polynomials, c_{2n} is given by

$$c_{2n}=\lim_{\gamma\to 1}\int \mathrm{d}x\,H_{2n}(x/\sqrt{2})\exp(-x^2/2)\mathcal{I}(x,\gamma)=\int \mathrm{d}x\,H_{2n}(x/\sqrt{2})\exp(-x^2/2)\sqrt{Q_4(x)}=c_{2n}(v,w,u_i,u_i,w_i,x_{123},x_{ij}). \tag{C22}$$

The integration of equation (C21) over v, w, u_k, u_k, w_k, x_{123}, $x_{k<l}$ (while accounting for the rest of the integrant corresponding to P_0 and P_1 together with the two delta functions) yields the functional form of $\mathrm{d}\mathcal{L}/\mathrm{d}\eta$, equation (19), where C_{2n} is a pure number in the stiff approximation, but may depend on $\tilde{\gamma}$ in general.

In the stiff approximation, equation (C13) can be investigated semi-analytically. This analysis is the subject of a subsequent paper.

This paper has been typeset from a TEX/LATEX file prepared by the author.

THE ASTROPHYSICAL JOURNAL, 672: L1–L4, 2008 January 1

THE THREE-DIMENSIONAL SKELETON OF THE SDSS

T. SOUSBIE,[1] C. PICHON,[1,2] H. COURTOIS,[3,4] S. COLOMBI,[2] AND D. NOVIKOV[5]
Received 2006 February 15; accepted 2007 September 14; published 2007 December 11

ABSTRACT

The length of the three-dimensional filaments observed in the fourth public data release of the SDSS is measured using the "local skeleton" method. This consists of defining a set of points where the gradient of the smoothed density field is extremal along its isocontours, with some additional constraints on local curvature to probe actual ridges in the galaxy distribution. A good fit to the mean filament length per unit volume, $\mathcal{L}$, in the SDSS survey is found to be $\mathcal{L} = (52500 \pm 6500)\ (L/\mathrm{Mpc})^{-1.75\pm0.06}\,\mathrm{Mpc}/(100\ \mathrm{Mpc})^3$ for 8.2 Mpc $\leq L \leq$ 16.4 Mpc, where L is the smoothing length in Mpc. This result, which deviates only slightly, as expected, from the trivial behavior $\mathcal{L} \propto L^{-2}$, is in excellent agreement with a ΛCDM cosmology, as long as the matter density parameter remains in the range $0.25 < \Omega_{\mathrm{matter}} < 0.4$ at the 1 σ confidence level, considering the universe is flat. These measurements, which are in fact dominated by linear dynamics, are not significantly sensitive to observational artifacts such as redshift distortion, edge effects, incompleteness, and biasing. Hence it is argued that the local skeleton is a rather promising and discriminating tool for the analysis of filamentary structures in three-dimensional galaxy surveys.

Subject headings: large-scale structure of universe — methods: data analysis — methods: statistical

Online material: color figures, mpeg animation

1. INTRODUCTION

From the Great Wall of CFA1 (Geller & Huchra 1989) to the very long filaments seen in the SDSS (Gott et al. 2005) and the 2DF (Colless et al. 2001), the ever growing size of the largest structures observed in the three-dimensional galaxy distribution has often been considered a challenge to models of large-scale structure formation. It is therefore of prime importance to find a robust way to identify filaments in the universe and to characterize them, e.g., through their length, thickness, and/or average density. To achieve that, one usually relies on the analysis of the morphological properties—e.g., through structure functions (Babul & Starkman 1992), Minkowski functionals (Mecke et al. 1994), shape finders (Sahni et al. 1998)—of an excursion's connected components in overdense regions of the catalog, which can be obtained using friends-of-friends algorithms (Zel'dovich et al. 1982), the minimum spanning tree technique (Barrow et al. 1985; Doroshkevich et al. 2004), or percolation on a grid where the density field has been smoothly interpolated (Gott et al. 1986; Dominik & Shandarin 1992).

This Letter works instead in the framework of Morse theory (Milnor 1963; Jost 2002), which establishes a rigorous although simple relationship between the number and distribution of critical points of a field and its general topology (Colombi et al. 2000). It uses the approach proposed recently by Novikov et al. (2006) and Sousbie et al. (2008b), where filaments are seen as a set of special field lines, departing from saddle points and converging to local maxima while following the gradient of the density field, $\nabla\rho \equiv \partial\rho/\partial x_i \equiv \rho_i$. However, the "skeleton" thus defined remains nonlocal, which makes analytical calculations challenging and edge effects difficult to cope with in real catalogs. In fact, its detection at a given location depends on the detection of an arbitrarily distant maximum or saddle point of the field. To solve these issues, a local approximation of the skeleton was proposed by Novikov et al. (2006) in the 2D case, and generalized to 3D by Sousbie et al. (2008b). Given the Hessian, $\mathcal{H} \equiv \partial^2\rho/\partial x_i \partial x_j \equiv \rho_{ij}$, and its eigenvalues, λ_i, ranked in decreasing order, the "local skeleton" is defined as the set of points where $\mathcal{H}\cdot\boldsymbol{\nabla}\rho = \lambda_1\boldsymbol{\nabla}\rho$ and $\lambda_2, \lambda_3 < 0$, to ensure that ridges of the density field are probed.

In this Letter, the local skeleton is extracted from the SDSS DR4 galaxy catalog. Its total length per unit volume is measured and compared to that obtained in ΛCDM cosmologies. Relying on realistic mock catalogs, various effects such as incompleteness, survey geometry, cosmic variance, redshift distortions, biasing, and nonlinear dynamics are extensively tested.

2. OBSERVATIONAL AND MOCK DATA SAMPLES

A complete description of the Fourth Data Release of the Sloan Digital Sky Survey (DR4 SDSS) can be found in Adelman-McCarthy et al. (2006). The main sample used in this Letter is extracted from the Catalog Archive Server facility. To ensure proper spectral identification of galaxies, objects with *specclass* = 2 and *zconf* > 0.35 are selected in the *specphoto* table. This yields a main sample containing 459,408 galaxies. The completeness in apparent magnitude was investigated and is achieved for $U_{\mathrm{SDSS}} < 19$. Two subsamples were extracted: a sample cut at distance $d < 350$ Mpc containing 148,012 galaxies (hereafter DR4-350), and a homogeneous, volume-limited sample (hereafter DR4-VL350) containing 25,843 galaxies selected on the basis of their absolute magnitude $M_{\mathrm{absU}} < -17$ and $d < 350$ Mpc. The distance of the cut was chosen as it empirically represent a good compromise between the level of completeness, which ensures that different populations of galaxies are fairly represented, and the total number of galaxies in the sample.

To test the robustness of the measurements and compare observational results to theoretical predictions, a large ΛCDM simulation was performed, using the publicly available tree code GADGET-2 (Springel 2005), involving 512^3 particles in a 1024 h^{-1} Mpc box, and with the following cosmological

[1] CRAL, Observatoire de Lyon, 69561 Saint Genis Laval Cedex, France; sousbie@obs.univ-lyon1.fr.
[2] Institut d'Astrophysique de Paris, UMR 7595, UPMC, 98 bis boulevard d'Arago, 75014 Paris, France.
[3] IFA, University of Hawaii, 2680 Woodlawn Drive, Honolulu, HI 96822.
[4] IPNL, Université Lyon I, 4 rue Enrico Fermi, 69622 Villeurbanne Cedex, France.
[5] Astrophysics Group, Imperial College, Blackett Laboratory, Prince Consort Road, London SW7 2AZ, UK.

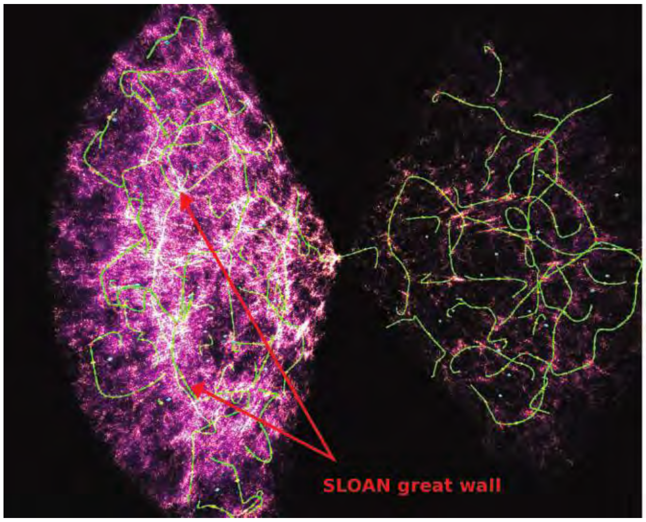

FIG. 1.—Derived 3D skeleton in a slice of the SDSS for a smoothing length $L = 16.4$ Mpc. This animation still frame shows how well structures are captured, notably the SLOAN Great Wall. [*This figure is available as an mpeg animation in the electronic edition of the Journal.*]

parameters: $H_0 = 70$ km s^{-1} Mpc^{-1}, $\Omega_{\rm baryons} = 0.05$, $\Omega_{\rm matter} = 0.3$, $\Omega_\Lambda = 0.7$, and normalization $\sigma_8 = 0.92$. Various mock catalogs were extracted from this simulation, using MoLUSC (Sousbie et al. 2008a). This tool is designed to build realistic mock galaxy catalogs from dark matter simulations of large volume but poor mass resolution, by reprojecting, as functions of local phase-space density, the statistical properties of the galaxy distribution (type, spectral features, number density, etc.) derived from semianalytic models applied to simulations of higher mass resolution. Here, the results calculated by GalICS (Hatton et al. 2003) on a tree code simulation with 256^3 particles in a cube of 150 Mpc on a side are used as inputs of MoLUSC. According to the analyses of Blaizot et al. (2006), this simulation should provide sufficient mass resolution to describe realistically the statistical properties of SDSS galaxies with $U_{\rm SDSS} < 19$. The advantage of using MoLUSC is that it allows one to probe a realistic volume of the universe without worrying about finite volume or replication effects in the realization of mock catalogs themselves (Blaizot et al. 2005).

For the purpose of testing the skeleton properties, three different kinds of mock catalogs were built, all cut at a distance of 350 Mpc: (1) the main catalog is called MOCK and attempts to reproduce all the characteristics of DR4-350 (redshift space distortion, incompleteness, survey geometry, etc.); (2) MOCK-PS is identical to MOCK but uses the exact positions of the galaxies to test the effect of redshift distortion; (3) MOCK-AS is an all-sky version of MOCK aimed to test the influence of survey geometry; and finally, (4) MOCK-NB is identical to MOCK but with dark matter particles (without density biasing). The volume of our simulation is approximately 30 times that covered by DR4-350, which yields an error bar reflecting cosmic variance from the dispersion among 25 random realizations of MOCK. Note finally that measurements were also performed directly on the dark matter distribution simulation boxes and on the initial conditions of the simulation, to test the effects of nonlinear clustering.

3. THE 3D SKELETON: ALGORITHM

The details of the algorithm used to draw the local skeleton defined in § 1 are given in Sousbie et al. (2008b), so only a brief sketch of it is given here:

1. *Interpolation and smoothing.*—The first step consists of performing cloud-in-cell interpolation (Hockney & Eastwood 1981) on a 512^3 grid covering a 700 Mpc cube embedding the survey. To avoid extra degeneracies while drawing the skeleton, the empty regions of the cube are filled with a random distribution of galaxies with 1000 times smaller average density than inside the survey. At the end of the process, only the parts of the skeleton belonging to the original survey are kept. To warrant sufficient differentiability, convolution with a Gaussian window of size L is performed prior to computing the gradient and the Hessian using a finite difference method. As argued in Novikov et al. (2006), in order to avoid contamination by the grid, discreteness, and finite volume effects, respectively, the smoothing scale should verify $L/\Delta \gtrsim 4$, $L/\lambda \gtrsim 1$, and $L/V^{1/3} \lesssim 20$, where Δ is the grid step, λ is the mean interparticle distance, and V is the survey volume. As a result, the following conservative scale range, 8.2 Mpc $\leq L \leq$ 16.4 Mpc, will be used for the measurements performed in this Letter.

2. *Surface intersection modeling.*—The second step of the algorithm consists of drawing the skeleton, noting that it is embedded in the set of points verifying $\mathcal{H} \cdot \boldsymbol{\nabla}\rho \times \boldsymbol{\nabla}\rho = 0$. This leads to three conditions, $S_i(x_1, x_2, x_3) = 0$, that define three surfaces intersecting along a common line. The actual method used to compute the surfaces $S_i = 0$ as an assemblage of triangles and their intersections as a set of connected lines relies on the classical marching cube algorithm (Lorensen & Cline 1987), as detailed further in Sousbie et al. (2008b). Additional conditions, namely that the gradient should be aligned with the major axis of curvature—in practice, $|\boldsymbol{\nabla}\rho \cdot \boldsymbol{u}_1| > \max(|\boldsymbol{\nabla}\rho \cdot \boldsymbol{u}_2|, |\boldsymbol{\nabla}\rho \cdot \boldsymbol{u}_3|)$, where $\boldsymbol{u}_i$ are the eigenvectors of $\mathcal{H}$—and $\lambda_2, \lambda_3 < 0$ are enforced locally after diagonalizing the Hessian.

3. *Cleaning.*—Some additional treatment has to be performed in regions where the field becomes degenerate (e.g., in the vicinity of critical points, $\nabla\rho = 0$), as explained in detail in Sousbie et al. (2008b). Finally, the parts of the local skeleton which do not pass through any critical point are removed. As argued in Sousbie et al. (2008b), these parts are mostly irrelevant as they do not, in general, correspond to real filaments. The derived 3D skeleton is shown in Figure 1.

4. MEASUREMENTS AND ROBUSTNESS VERSUS OBSERVATIONAL BIASES

Figure 2 shows the skeleton measured in DR4-350 for three smoothing scales $L = 16.4$, 10.9, and 8.2 Mpc (*top left and bottom left and right panels*; note that each panel comprises the two hemispheres), while the measurements of its length $\mathcal{L}$ as a function of L are summarized in Table 1.

As expected, the skeleton matches the intuitive visual definition of what a filament is, and its length and complexity increase with the inverse of L. Note in Figure 2 that the prominent features of the skeleton remain mostly independent of smoothing: decreasing L essentially adds new branches to the skeleton, corresponding to finer structures in the galaxy distribution. In other words, the skeleton grows like a tree, while L decreases. The overall scale dependence of the measured length, $\mathcal{L} = (52500 \pm 6500)$ $(L/{\rm Mpc})^{-1.75\pm0.06}$ Mpc/(100 Mpc)^3, is in good qualitative agreement with the expected trivial power law in the scale-free case, $\mathcal{L} \propto L^{-2}$ (Sousbie et al. 2008b).

These results match very well the predictions of the standard ΛCDM model (compare MOCK to DR4-350). This allows one to use the mock catalogs as a solid baseline to test possible

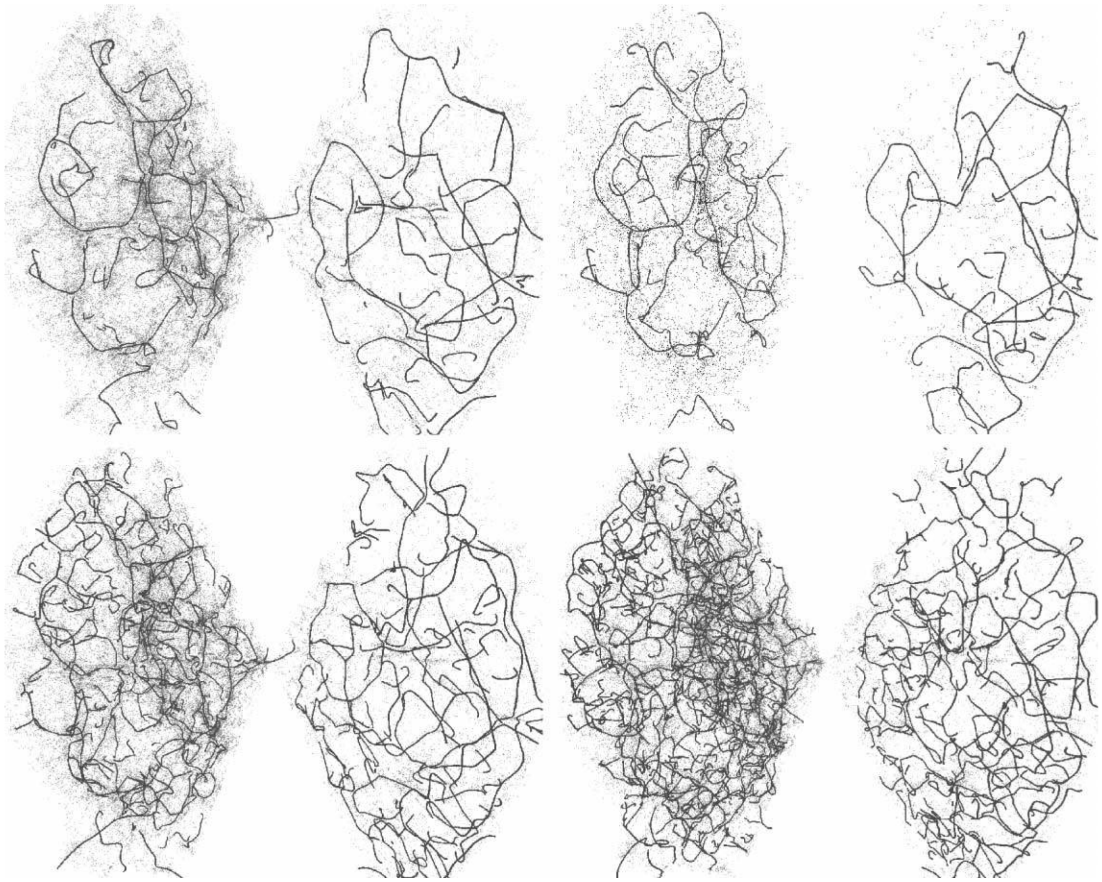

FIG. 2.—Skeleton of the SDSS compared to the corresponding galaxy distribution. Each panel comprises the two hemispheres. *Top left and right panels*: The galaxy distribution, respectively in DR4-350 and its volume-limited counterpart, DR4-VL350, with the superimposed skeleton measured for a smoothing scale $L = 16.4$ Mpc. *Bottom left and right panels*: The skeleton measured in DR4-350, for $L = 10.9$ and 8.2 Mpc, respectively. The difference in appearance between the northern and southern hemispheres reflects the geometry of the survey: while the northern part is made of one large slice, the southern part is composed of three thin slices, making it almost two-dimensional. The corresponding bias on the skeleton length is taken into account as we reproduce this exact same geometry in the mock catalogs. See the Fig. 1 legend regarding our mpeg movie, where the skeleton is measured on the full SDSS-DR4 data for $L = 16.4$ Mpc. [*See the electronic edition of the Journal for a color version of this figure.*]

observational and dynamical effects on the skeleton, as discussed now, using Table 1 as a guideline. *Incompleteness and discreteness* effects can simultaneously be tested by comparing DR4-350 to its volume-limited counterpart, DR4-VL350, which probes only 15% of the galaxies available in DR4-350 (see Fig. 2, *top panels*). They have little impact on the skeleton, changing its length by at most 3%. *Edge effects* arise from the particular geometry of the SDSS. They can be probed by comparing MOCK to MOCK-AS. They have a small but systematic impact on the measured length of the skeleton, which is increasingly overestimated with scale, from about 1% for $L = 8.2$ Mpc to 8% for $L = 16.4$ Mpc. In terms of scaling behavior, $\mathcal{L} \propto L^{-\alpha}$, α is therefore slightly underestimated, which explains partly the slight deviation from the expectation $\alpha = 2$, in addition to the scale dependence of the power spectrum of the density fluctuations. *Cosmic variance* should be small: when estimated from the dispersion among 25 realizations of MOCK, it increases with smoothing scale, as expected, from a 2% error for $L = 8.2$ and $L = 10.9$ to a 5% error for $L = 16.4$. *Redshift distortion* effects, discussed at length in Sousbie et al. (2008b), can be tested by comparing MOCK to MOCK-PS. They have negligible impact on the measurements, well within the cosmic variance. Finally, since the skeleton probes overdense regions of the universe and large smoothing scales are considered, the measurements are expected to be rather insensitive to effects of *biasing* and to be dominated by the predictions of *linear* dynamics. This has been fully confirmed when comparing the skeleton of simulations at $z = 0$ and in the initial conditions, at least in the ΛCDM cosmogony framework. Moreover, the small amplitude of the change of length of the skeleton when nonlinear biasing is applied can be checked in Table 1 (compare MOCK-NB and MOCK).

5. DISCUSSION: A TEST OF LARGE-SCALE STRUCTURE FORMATION MODELS

In this Letter a method to probe the filamentary structure in the galaxy distribution, involving the extraction of the local skeleton from the data and measuring its length per unit volume, $\mathcal{L}$, was tested on the SDSS and mock catalogs. The length of the skeleton was found to be a robust statistic in the scaling regime 8.2 Mpc $\leq L \leq$ 16.4 Mpc, rather insensitive to nonlinearities, biasing, redshift distortion, incompleteness, and cosmic variance. The results were, however, slightly affected by edge effects due to the geometry of the SDSS (see Table 1, col. [6]). Still, one observes a good agreement with the ΛCDM concordant model, which pleads in favor of consistency (within the quoted error bars) between this model and observed large-scale structures (see Fig. 3, *top panel*).

One question remains: is the length of the skeleton a discriminant measure of large-scale structure? In theory, the answer is positive: for a Gaussian field, $\mathcal{L}$ depends on the shape

TABLE 1
LENGTH PER UNIT VOLUME OF THE SKELETON FOR DIFFERENT SDSS AND MOCK SAMPLES

	LENGTH DENSITY [Mpc/(100 Mpc)^3]					
L (1)	DR4-350 (2)	DR4-VL350 (3)	MOCK (4)	MOCK-PS (5)	MOCK-AS (6)	MOCK-NB (7)
16.4	372	363	390 ± 19	395 ± 16	362	403 ± 17
10.9	795	772	796 ± 18	815 ± 19	740	790 ± 24
8.2	1271	1299	1272 ± 25	1308 ± 27	1285	1204 ± 25

of the power spectrum of density fluctuations, $P(k)$, through its moments of order $2m$, $\int k^{2m+2}P(k)\exp(-k^2L^2)dk$, up to $m = 3$, leading to the approximate scaling $\mathcal{L} \propto (5.2 + n)L^{-2}$ for $P(k) \propto k^n$ (Sousbie et al. 2008b). To demonstrate that this spectral dependence can be used to constrain models of large-scale structure in practice, nine flat-universe simulations were carried out with GADGET-2, involving 256^3 particles and with the same cosmological parameters as previously used except that $\Omega_{\rm matter}$ was left as a free variable in the range $0.1 \le \Omega_{\rm matter} \le 0.9$. From each of the simulations, 25 mock catalogs were extracted, in which $\mathcal{L}$ was estimated. These measurements were used to perform standard χ^2 analysis to find the best matching value of $\Omega_{\rm matter}$ for the SDSS, using MOCK as the reference. The final 1 σ constraint is $0.25 < \Omega_{\rm matter} < 0.4$ (see Fig. 3).

This clearly demonstrates that the length of the skeleton is a discriminant estimator, which might prove to be a real alternative to traditional two-point statistics estimators which are extremely sensitive to the bias in the nonlinear stage of gravitational instability. The local skeleton extraction also opens new paths of investigation for the structure analysis of galactic or dark matter distribution, with the prospect of defining quantitatively the locus of filaments. In particular, it will allow astronomers to carry measurements (velocity, pressure, etc.) along the main motorways of galactic infall (Aubert et al. 2004).

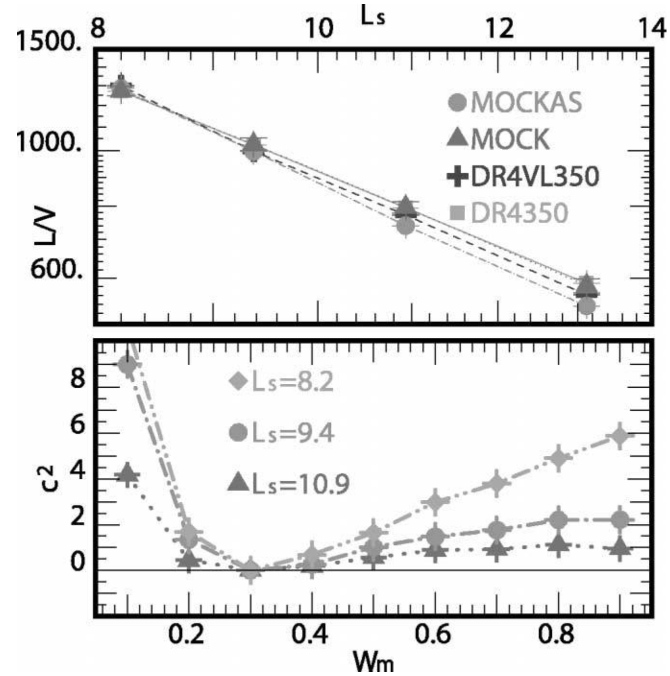

FIG. 3.—*Top*: Skeleton length per unit volume [in Mpc/(100 Mpc)^3] as a function of smoothing length for mock catalogs and SDSS showing the very good agreement (as explained in the text). The error bars correspond to the cosmic variance, which is estimated via 25 realizations of the mock. *Bottom*: χ^2 corresponding to the squared difference between the total length per unit volume of the mock catalog and that of the SDSS, in units of the rms of the mock; these χ^2 curves yield a confidence interval for $\Omega_{\rm matter}$ (for a flat universe) of [0.25, 0.4] at the 1 σ level and [0.15, 0.75] at the 2 σ level. The simulations are 256^3 dark matter particles of a given $H_0 = 70$ km s^{-1} Mpc^{-1} using an Eke prescription (Eke et al. 1996) for the normalization of the spectrum. [*See the electronic edition of the Journal for a color version of this figure.*]

This work was carried out within the Horizon Project, http://www.projet-horizon.fr. We thank the SDSS Collaboration, http://www.sdss.org, for publicly releasing the DR4 data. The computational means used to perform the 512^3 simulation (IBM POWER4) were made available to us by IDRIS. We thank S. Prunet, D. Aubert, J. Devriendt, and D. Pogosyan for useful comments. We thank the referee for constructive comments.

REFERENCES

Adelman-McCarthy, J. K., et al. 2006, ApJS, 162, 38
Aubert, D., Pichon, C., & Colombi, S. 2004, MNRAS, 352, 376
Babul, A., & Starkman, G. D. 1992, ApJ, 401, 28
Barrow, J. D., Bhavsar, S. P., & Sonoda, D. H. 1985, MNRAS, 216, 17
Blaizot, J., et al. 2005, MNRAS, 360, 159
———. 2006, MNRAS, 369, 1009
Colless, M., et al. 2001, MNRAS, 328, 1039
Colombi, S., Pogosyan, D., & Souradeep, T. 2000, Phys. Rev. Lett., 85, 5515
Dominik, K. G., & Shandarin, S. F. 1992, ApJ, 393, 450
Doroshkevich, A., Tucker, D. L., Allam, S., & Way, M. J. 2004, A&A, 418, 7
Eke, V. R., Cole, S., & Frenk, C. S. 1996, MNRAS, 282, 263
Geller, M. J., & Huchra, J. P. 1989, Science, 246, 897
Gott, J. R., III, Melott, A. L., & Dickinson, M. 1986, ApJ, 306, 341
Gott, J. R., III, et al. 2005, ApJ, 624, 463
Hatton, S., et al. 2003, MNRAS, 343, 75
Hockney, R. W., & Eastwood, J. W. 1981, Computer Simulation Using Particles (New York: McGraw-Hill)
Jost, J. 2002, Riemannian Geometry and Geometric Analysis (3rd ed.; Berlin: Springer)
Lorensen, W. E., & Cline, H. E. 1987, Computer Graphics, 21(4), 163
Mecke, K. R., Buchert, T., & Wagner, H. 1994, A&A, 288, 697
Milnor, J. 1963, Morse Theory (Princeton: Princeton Univ. Press)
Novikov, D., Colombi, S., & Doré, O. 2006, MNRAS, 366, 1201
Sahni, V., Sathyaprakash, B. S., & Shandarin, S. 1998, ApJ, 495, L5
Sousbie, T., Bryan, G., Devriendt, J., & Courtois, H. 2008a, ApJ, in press
Sousbie, T., et al. 2008b, MNRAS, in press
Springel, V. 2005, MNRAS, 364, 1105
Zel'dovich, Ya. B., Einasto, J., & Shandarin, S. F. 1982, Nature, 300, 407

Mon. Not. R. Astron. Soc. **000**, 000–000 (0000) Printed 19 November 2008 (MN LATEX style file v2.2)

The local theory of the cosmic skeleton

D. Pogosyan[1], C. Pichon[2,3], C. Gay[2],
S. Prunet[2], J.F. Cardoso[4,2], T. Sousbie[2] & S. Colombi[2]
[1] *Department of Physics, University of Alberta, 11322-89 Avenue, Edmonton, Alberta, T6G 2G7, Canada*
[2] *Institut d'Astrophysique de Paris & UPMC, 98 bis boulevard Arago, 75014 Paris, France*
[3] *Service d'Astrophysique, IRFU, CEA-CNRS, L'orme des merisiers, 91 470, Gif sur Yvette, France,*
[4] *Laboratoire de Traitement et Communication de l'Information, LTCI/CNRS 46, rue Barrault, 75013 Paris, France.*

19 November 2008

ABSTRACT

The local theory of the critical lines of 2D and 3D Gaussian fields that underline the cosmic structures is presented. In the context of cosmological matter distribution the subset of critical lines of the 3D density field serves to delineate the skeleton of the observed filamentary structure at large scales. A stiff approximation used to quantitatively describe the filamentary skeleton shows that the flux of the skeleton lines is related to the average Gaussian curvature of the (N-1)D sections of the field, much in the same way as the density of the peaks. The distribution of the length of the critical lines with threshold is analyzed in detail, while the extended descriptors of the skeleton - its curvature and its singular points, are introduced and briefly described. Theoretical predictions are compared to measurements of the skeleton in realizations of Gaussian random fields in 2D and 3D. It is found that the stiff approximation predicts accurately the shape of the differential length, allows for analytical insight, and explicit closed form solutions. Finally, it provides a simple classification of the singular points of the critical lines: i) critical points; ii) bifurcation points; iii) slopping plateaux.

1 INTRODUCTION

The concept of random fields is central to cosmology. Random fields both provide initial conditions for the evolution of the matter distribution in the Universe, and represent how the observed signals manifest themselves in 3D, (e.g., in the galaxy or matter density inhomogeneities that form the Large Scale Structure (LSS)), or on the 2D sky (e.g. for the Cosmic Microwave Background (CMB) temperature and polarization, the convergence or shear in weak lensing maps). In the modern cosmological theories where initial seeds for inhomogeneities observed as cosmic structures have quantum origin, the fields of initial density fluctuations (and velocities) are Gaussian. Subsequent evolution retains Gaussianity for the observables that evolve linearly (CMB, very Large Scale Structure) while developing non-Gaussian signature if non-linear effects are involved (*e.g.* lensing and LSS at smaller scales).

While comparing the observational data to cosmological theory, in particular in order to estimate parameters of cosmological models, the emphasis is traditionally placed on the statistical descriptors of the random fields. For Gaussian fields the two-point correlation function or the power spectrum provide full statistical information, while non-Gaussian properties may be reflected in multi-point correlations. The understanding and the description of the morphology of structures in our Universe, on the other hand, calls for the studies of the *geometry* and *topology* of random fields. This subject has an extensive history from the early description of the one-dimensional radio signal time-streams in 1940's, to the study of the 2D ocean wave patterns in 1960's (Longuet-Higgins 1957) to 3D dimensional fields (Adler 1981) that found the most fruitful application in cosmology (Arnol'd et al. 1981; Bardeen et al. 1986). The most prominent geometrical objects in a typical realization of a random field are rear events - regions of unusually high or low values of the field. The rare events are usually related to the most spectacular observed objects – clusters of galaxies at low z, large protogalaxies at high-z or extensive voids. They are associated with the neighbourhoods of extrema – maxima or minima – making studies of such *critical* points the first step in understanding typical geometry of a field (Kaiser 1984; Bardeen et al. 1986; Regos & Szalay 1995; Scannapieco et al. 2006). The behaviour of the field in the neighbourhood of a rare peak is highly correlated with the peak properties, which allows to describe not only extrema but the extended peak-patch region (Bond & Myers 1996a) as a point process that involves the field and its successive derivatives. Including the shear flow into consideration gives a compelling application of the geometry of rare events to the description of cluster formation through the peak-patch collapse (Bond & Myers 1996b).

The rare events reflect the organization of the field around them and by and large determine the way the high (low) field regions are interconnected by the bridges of enhanced field values. In application to cosmology, the "Cosmic Web" picture emerges, which relates the observed clusters of galaxies, and filaments that link them, to the geometrical properties of the initial density field that are enhanced but not yet destroyed by the still mildly non-linear evolution on supercluster scales (Bond et al. 1996). The study of the connectivity of filamentary structures reveal the role of the remaining type of critical points, the saddle extrema, in establishing, in particular, the percolation properties of the Web (Colombi et al. 2000). The next step naturally involves describing the statistical properties of these filamentary structures (Pogosyan et al. 1998; Schmalzing et al. 1999) and developing techniques for mapping the filaments in the simulation and data. Novikov et al. (2006) presented a 2D algorithm to trace the filaments of a density field while introducing the *skeleton* as the set of locally defined critical lines emanating from the critical points. Sousbie et al. (2008) (hereafter SPCNP) extended the local theory and algorithm to three dimensions and provided the foundation for this work while introducing the "stiff" approximation. Recently, Sousbie et al. (2008) presented an algorithm to map out a fully connected version of the skeleton that is defined according to the global properties as the lines of intersections of the patches (see also Aragón-Calvo et al. (2007), Platen et al. (2007) for alternative algorithms). This approach connects the study of the filamentary structure to the geometrical and topological aspects of the theory of gradient flows (Jost 2008) and returns the focus to the notions of peak and void patches.

This paper presents a consistent local theory for the cosmic skeleton, while focusing on the stiff approximation to compute the differential length of the skeleton as a function of the contrast and modulus of the gradient of the field. It allows us to define precisely how the properties of the skeleton depend analytically on the underlying spectral parameters, and understand what type of line prevails where. The crucial advantage of the local approach to the critical lines is that it allows to cast the statistical treatment of the linear objects as a point process that involves the field and its derivatives, which allows for analytical insight, and explicit closed form solutions. Our purpose is to construct the theory of critical lines of a given field corresponding to an intermediate representation of the field, which is more extended than the knowledge of the critical points.

The organization of the paper is the following. Section 2 classifies the various critical lines in 2D and 3D, connects the average length in a unit volume to the flux of the skeleton lines and, within the stiff approximation, to the average Gaussian curvature of the field in transverse sections. It also discusses the meaning of this approximation. Section 3 calculates the differential length of all sets of critical lines in 2D, while Section 4 investigates the corresponding 3D set of critical lines. More generally, the expression for the differential length of the N dimensional skeleton is sketched in Appendix A. Section 5 introduces the extended descriptors of the skeleton, Section 5.3 describes their singular points, while Section 6 provides the discussion and the summary. Appendix D gives the general method for obtaining in close form the joint distribution of the field and any combination of its derivative tensors in arbitrary dimensions. In particular, it exhibits all the statistical invariants and their dependence on the spectral parameters.

2 THE CRITICAL LINES AND THE SKELETON OF A 3D RANDOM FIELD

2.1 Local definition and classification

The subject of our investigation is a random field, $\rho(\mathbf{r})$, that in a cosmological setting describes, for example, the density of the matter in the Universe, or the projected distribution of Cosmic Microwave light on the celestial sphere. Our focus is on the geometrical properties of the critical lines, that connect extrema of the field mapping out the filamentary ridges and valleys of the field. SPCNP have introduced the definition of the *local critical lines* as the set of points where the gradient of the density, $\nabla\rho$, is an eigenvector of its Hessian matrix, $\mathcal{H}$, $\mathcal{H}\cdot\nabla\rho = \lambda\nabla\rho$ i.e, the gradient and one of the principal curvature axes are collinear. Formally, this can be specified by a set of equations

$$\mathbf{S} \equiv (\nabla\rho\cdot\mathcal{H})\cdot\boldsymbol{\epsilon}\cdot(\nabla\rho) = \mathbf{0}\ , \tag{1}$$

where $\boldsymbol{\epsilon}$ is the fully antisymmetric (Levi-Civita) tensor of rank N. In general $\mathbf{S}$ is an antisymmetric $N-2$ tensor.

In 3D, the function $\mathbf{S}$ is vector-valued, $S^i = \sum_{klm}\epsilon^{ikl}(\nabla_m\rho)\mathcal{H}^m{}_k(\nabla_l\rho)$. However, zeroes of $\mathbf{S}$ determine a set of lines rather than isolated points. Let us consider the behaviour of $\mathbf{S}$ function in the neighbourhood of a point $\mathbf{r}=\mathbf{0}$ that satisfies criticality condition $\mathbf{S}(\mathbf{0})=\mathbf{0}$:

$$\mathbf{S}(\delta\mathbf{r}) \approx \mathbf{0} + \sum_k (\nabla_k\mathbf{S})\,\delta r^k\ . \tag{2}$$

In our case, under the condition $S^i=0$, the matrix $\nabla_k S^i$ by definition possesses the *left* null-vector, furnished by the density gradient, $\sum_i \nabla_i\rho\left(\nabla_k S^i\right)=0$; hence the gradients ∇S^i are not linearly independent. Consequently, there is a non-trivial solution for the *right* null-vector $\sum_k\left(\nabla_k S^i\right)\delta r^k = \mathbf{0}$, which determines the local direction of the line along which the criticality condition is maintained, $\mathbf{S}(\delta\mathbf{r})=\mathbf{0}$. The critical lines intersect where $\nabla_k S^i$ admits more than one independent *right* null-vector.

When we take the eigenvalues of the Hessian to be sorted, $\lambda_1\geqslant\lambda_2\geqslant\lambda_3$, the gradient of the field at the critical line may be found aligned with the first, second, or third eigenvector. This gives rise to the classification of the critical lines based on the choice of the eigenvector aligned with the gradient, that becomes more fine grained when the magnitudes of the eigenvalues are taken into account. Namely, we distinguish *primary* critical lines, which correspond to $\nabla\rho$ being aligned with the direction in which the field is the least curved, i.e where the eigenvalue is the smallest in magnitude, and *secondary* critical lines at which $\nabla\rho$ is aligned with the eigenvalues of larger magnitude. The primary type consists of

Type		Alignment	Condition
Primary	Skeleton:	$\mathcal{H}\cdot\nabla\rho=\lambda_1\nabla\rho$	$\lambda_1+\lambda_2\leqslant 0$
	Inter-skeleton:	$\mathcal{H}\cdot\nabla\rho=\lambda_2\nabla\rho$	$\lambda_1+\lambda_2>0$ and $\lambda_3+\lambda_2<0$
	Anti-skeleton:	$\mathcal{H}\cdot\nabla\rho=\lambda_3\nabla\rho$	$\lambda_3+\lambda_2\geqslant 0$
Secondary		$\mathcal{H}\cdot\nabla\rho=\lambda_2\nabla\rho$	$\lambda_1+\lambda_2\leqslant 0$
		$\mathcal{H}\cdot\nabla\rho=\lambda_3\nabla\rho$	$\lambda_1+\lambda_2\leqslant 0$
		$\mathcal{H}\cdot\nabla\rho=\lambda_1\nabla\rho$	$\lambda_1+\lambda_2>0$ and $\lambda_3+\lambda_2<0$
		$\mathcal{H}\cdot\nabla\rho=\lambda_3\nabla\rho$	$\lambda_1+\lambda_2>0$ and $\lambda_3+\lambda_2<0$
		$\mathcal{H}\cdot\nabla\rho=\lambda_1\nabla\rho$	$\lambda_3+\lambda_2\geqslant 0$
		$\mathcal{H}\cdot\nabla\rho=\lambda_2\nabla\rho$	$\lambda_3+\lambda_2\geqslant 0$

Table 1. the classification of the critical lines in 3D.

(i) The *skeleton*, that has the gradient in the λ_1 direction and is limited to the region $|\lambda_1|\leqslant|\lambda_2|$, which translates to the condition $\lambda_1+\lambda_2\leqslant 0$. The skeleton has always eigenvalues in the directions transverse to $\nabla\rho$ negative, $\lambda_3\leqslant\lambda_2\leqslant 0$ and corresponds to the filamentary ridges spreading from the maxima in the direction of the slowest descent.

(ii) The *anti-skeleton*, that has the gradient in the λ_3 direction and is restricted to the region $|\lambda_3|\leqslant|\lambda_2|$, i.e $\lambda_3+\lambda_2\geqslant 0$. In the directions transverse to $\nabla\rho$ the anti-skeleton has always positive curvature $\lambda_1\geqslant\lambda_2\geqslant 0$. It corresponds to the filamentary valleys spreading from the minima in the direction of the slowest ascent. Anti-skeleton can be viewed as a skeleton of the $-\rho$ field.

(iii) The *intermediate skeleton* along which the gradient is aligned with the middle eigen-direction of the Hessian where this direction is the shallowest $|\lambda_2|<|\lambda_1|,|\lambda_3|$, i.e $-\lambda_1<\lambda_2<-\lambda_3$. This conditions is only possible in saddle-like regions where $\lambda_1>0$ and $\lambda_3<0$.

The formal classification of the critical lines is summarized in Table 1.

2.2 The average flux (length per unit volume) of the critical lines

As the average number density is the fundamental quantity that describes point events, e.g. extrema of a field, conversely the most important characterization of the critical lines or skeleton is their flux, *i.e.* the number of critical lines intersecting a given oriented surface[1]. This flux is equivalent to the length of the lines per unit volume. Following NCD and SPCNP we shall preferentially use the latter terminology as it highlights that we deal with the first geometrical parameter, the length, of the lines. The subsequent parameters of these linear objects are the curvature, and, in 3D, the torsion.

In this paper we consider ρ to be a homogeneous and isotropic Gaussian random field of zero mean, described by the power spectrum $P(k)$. In the statistical description of the skeleton of the field ρ, several linear scales are involved

$$R_0=\frac{\sigma_0}{\sigma_1},\quad R_*=\frac{\sigma_1}{\sigma_2},\quad \tilde{R}=\frac{\sigma_2}{\sigma_3},\quad \hat{R}=\frac{\sigma_3}{\sigma_4}\,, \tag{3}$$

$$\text{where}\quad \sigma_0^2=\langle\rho^2\rangle,\quad \sigma_1^2=\langle(\nabla\rho)^2\rangle,\quad \sigma_2^2=\langle(\Delta\rho)^2\rangle,\quad \sigma_3^2=\langle(\nabla\Delta\rho)^2\rangle\,,\quad\text{and generally}\quad \sigma_p^2=\frac{2\pi^{D/2}}{\Gamma[D/2]}\int_0^\infty k^{2p}P(k)k^{D-1}dk\,. \tag{4}$$

These scales are ordered $R_0\geqslant R_*\geqslant\tilde{R}\geqslant\ldots$. The first two have well-known meanings of typical separation between zero-crossing of the field R_0 and mean distance between extrema, R_* (Bardeen & al. 1986), and the third one, $\tilde{R}$ is, by analogy, the typical distance between the inflection points. These three are the only ones that are involved in determination of the length of the critical lines. The higher order scale $\hat{R}$ appear only in computation of the curvature and the torsion (see Section 5).

Let us define a set of spectral parameters that depend on the shape of the underlying power spectrum. Out of these five scales four dimensionless ratios may be constructed that are intrinsic parameters of the theory

$$\gamma\equiv\frac{R_*}{R_0}=\frac{\sigma_1^2}{\sigma_0\sigma_2},\quad \tilde{\gamma}\equiv\frac{\tilde{R}}{R_*}=\frac{\sigma_2^2}{\sigma_3\sigma_1}\,,\quad \hat{\gamma}\equiv\frac{\hat{R}}{\tilde{R}}=\frac{\sigma_3^2}{\sigma_4\sigma_2}\,,\quad\text{and generally}\quad \gamma_{p,q}=\frac{\sigma^2_{(p+q)/2}}{\sigma_p\sigma_q}\,. \tag{5}$$

From the geometrical point of view γ specifies how frequently one encounters a maximum between two zero crossings of the field, while $\tilde{\gamma}$ describes, on average, how many inflection points are between two extrema. From a statistical perspective, γ's are the cross-correlation coefficients between the field and its derivatives at the same point (see Appendix D).

$$\gamma=\frac{\langle\rho\Delta\rho\rangle}{\sigma_0\sigma_2},\quad \tilde{\gamma}=\frac{\langle\nabla\rho\cdot\nabla\Delta\rho\rangle}{\sigma_1\sigma_3},\quad\ldots \tag{6}$$

[1] For M dimensional objects in N dimensional space, in general, one counts the average number of intersections between objects M and N-M dimensional surfaces, per unit N-M volume. From a statistical point of view this constitutes a *point* process that can be evaluated knowing the distribution of the field and some of its derivatives at one arbitrary point only.

For Gaussian fields, these parameters can be easily calculated from the power spectrum. All γ's range from zero to one. For reference, for the power-law spectra with index $n > -3$, smoothed at small scales with a Gaussian window, $\gamma = \sqrt{(n+3)/(n+5)}$, $\tilde{\gamma} = \sqrt{(n+5)/(n+7)}$. Note that cosmologically relevant density power spectra have $n > -3$ and, thus, while γ can attain low values, $\tilde{\gamma}$ are always close to unity[2] .

Let us introduce the dimensionless quantities for the field and its derivatives as well as for the functions S^i and their gradients ∇S^i:

$$\sigma_0 x \equiv \rho, \quad \sigma_1 x_k \equiv \nabla_k \rho, \quad \sigma_2 x_{kl} \equiv \nabla_k \nabla_l \rho, \quad \sigma_3 x_{klm} \equiv \nabla_m \nabla_l \nabla_k \rho, \quad \sigma_2 \sigma_1^2 s^i \equiv \mathcal{S}^i, \quad \sigma_2^2 \sigma_1 \nabla s^i \equiv \nabla \mathcal{S}^i, \quad \sigma_4 \sigma_1^2 \nabla\nabla s^i \equiv \nabla\nabla \mathcal{S}^i, \tag{7}$$

giving

$$s^i = \sum_{klm} \epsilon^{imk} x_{ml} x_l x_k \,, \quad \text{and} \quad \nabla_m s^i = \sum_{kln} \epsilon^{ink} \left(\tilde{\gamma}^{-1} x_{nlm} x_l x_k + [x_{nl} x_{lm} x_k + x_{nl} x_{km} x_l] \right) . \tag{8}$$

Note the specific choice of scaling for ∇S which is convenient in view of the subsequent development of the so-called "stiff" approximation. SPCNP has shown that in terms of these dimensionless quantities, the *cumulative* length per unit volume of the total set of critical lines below the threshold η is given by

$$\mathcal{L}(\eta) = \left(\frac{1}{R_*}\right)^2 \int_{-\infty}^{\eta} dx \int d^3x_k d^6x_{kl} d^{10}x_{klm} \, |\nabla s^i \times \nabla s^j| P(x, x_k, x_{kl}, x_{klm}) \delta_{\rm D} \left(s^i(x_k, x_{kl}, x_{klm})\right) \delta_{\rm D} \left(s^j(x_k, x_{kl}, x_{klm})\right) , \tag{9}$$

where a pair $\nabla s^i, \nabla s^j$ can be chosen arbitrarily as long as it is linearly independent. In this equation $|\nabla s^i \times \nabla s^j|$ reflects the inverse characteristic area orthogonal to a critical line per one such line while the two $\delta_{\rm D}$-functions account for the critical line condition (1). For the complete set of critical lines, there are no restriction to the region of integration. If one is interested in a particular type of the critical lines, the integration should be restricted to the regions consistent with Table 1. The *differential* length (per unit volume) is simply given by the derivative of equation (9) with respect to η:

$$\frac{\partial \mathcal{L}}{\partial \eta} = \left(\frac{1}{R_*}\right)^2 \int d^3x_k d^6x_{kl} d^{10}x_{klm} \, |\nabla s^i \times \nabla s^j| P(\eta, x_k, x_{kl}, x_{klm}) \delta_D \left(s^i(x_k, x_{kl}, x_{klm})\right) \delta_D \left(s^j(x_k, x_{kl}, x_{klm})\right) , \tag{10}$$

while the total length of critical lines is

$$L \equiv \mathcal{L}(\infty) = \int_{-\infty}^{\infty} d\eta \frac{\partial \mathcal{L}}{\partial \eta} \quad . \tag{11}$$

Since for Gaussian field, the derivatives of even order are uncorrelated with the odd orders, the joint distribution function $P(x, x_k, x_{kl}, x_{klm})$ entering equation (9) is factorized as

$$P(x, x_k, x_{kl}, x_{klm}) = P_0(x, x_{kl}) P_1(x_k, x_{klm}). \tag{12}$$

In P_0, the only dependence on the power spectrum of the field is through the parameter γ (c.f. equation (5)) that describes the correlation between the field and its second derivatives. Similarly $P_1(x_k, x_{klm})$ only involves $\tilde{\gamma}$ which describes the correlation between the gradient of the field and its third derivatives. Therefore, $\partial\mathcal{L}/\partial\eta$ depends only on η, $\tilde{R}$ γ and $\tilde{\gamma}$. The integrated length, L may depend only on $\tilde{\gamma}$ and $\tilde{R}$ since the marginalization of $P_0(\eta, x_{kl})$ over η eliminates the dependency over γ.

2.3 The "stiff" filament approximation

Let us look at the dependence of the length of the critical lines on characteristic scales of the field in more detail. The R_*^{-2} factor that appeared in equation (10) reflect our choice of dimensionless variables (8) and is suggestive but not yet conclusive since $|\nabla s^i \times \nabla s^j|$ that includes third derivative terms, depends also on the other scale, $\tilde{R}$. Let us write formally

$$\nabla s^i \times \nabla s^j = \tilde{\gamma}^{-2} \mathbf{A}(x_k, x_{kl}, x_{klm}) + \tilde{\gamma}^{-1} \mathbf{B}(x_k, x_{kl}, x_{klm}) + \mathbf{C}(x_k, x_{kl}) \, . \tag{13}$$

If the third derivatives are important and the first term dominates, then the length scaling $L \propto \tilde{\gamma}^{-2} R_*^{-2} = \tilde{R}^{-2}$ would reflect the mean separation between the inflection points, $\tilde{R}$. Indeed, by definition the local skeleton is almost straight within a volume that has one inflection point $\sim \tilde{R}^3$. A straight segment through such volume has length $\sim \tilde{R}$, thus the expected length per unit volume is $\sim 1/\tilde{R}^2$. But if the last term dominates statistically, the length per unit volume of the skeleton will scale as $L \propto R_*^{-2}$ that can be interpreted that the critical lines are almost straight within a large volume volume $\sim R_*^3$ containing one extremum. This is consistent with observation that the integral term does not depend on the third derivatives, thus inflection points play no role, and any dependence on $\tilde{\gamma}$ drops out.

Which regime holds can be established by measuring the dependence of the critical lines length in the simulations as a function of smoothing length for different spectral indexes. For the power-law spectra with Gaussian smoothing at the radial scale σ, in 3D, $R_* = \sqrt{2}\sigma/\sqrt{n+5}$, while $\tilde{R} = \sqrt{2}\sigma/\sqrt{n+7}$. The measurements in SPCNP found that $L \propto (n+5.5)\sigma^{-2}$ over the range of spectral indexes relevant to cosmology, which points at the subdominant nature played by the third derivatives. In the "stiff" approximation we omit the third derivative, effectively assuming that the Hessian can be treated as constant

[2] Cosmological density fields, therefore, have of order one inflection point per extremum, unlike, for, example, a mountain range, where one encounters many inflection points on a way from a mountain top to the bottom; see also Section 4.4.

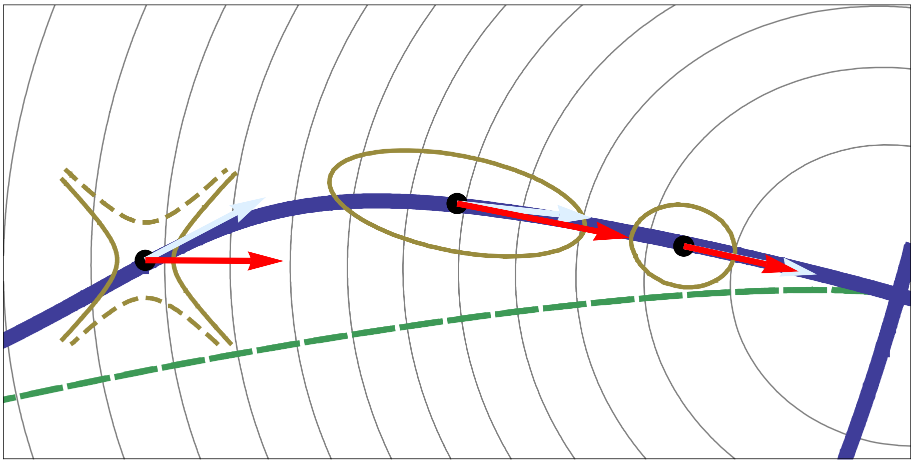

Figure 1. The neighbourhood of a local critical line (thick blue line). This is a zoomed section of the wide patch shown in Figure 3. Thin lines are isocontours of the field. Three sample points are investigated in detail. The signature, orientation and the magnitude of the local Hessian are represented by the golden shapes. Near the maximum on the right edge, the signature of the eigenvalues of the Hessian is (-1,-1), which is shown by ellipses oriented according to eigen-directions with longer semi-axis along the direction of the least curvature. At the leftmost point the eigenvalue signature is "saddle-like", (1,-1), which is represented by a pair of hyperbolae, also oriented with respect to eigen-directions. By definition, on the critical line the gradient of the field $\nabla\rho$, shown by red arrows, is aligned with one of the eigen-directions (i.e the axis of the ellipse or hyperbola in the graph). The light cyan arrows are the tangent vectors to the critical line $\propto \boldsymbol{\epsilon}\cdot\nabla S$, while stiff approximation to them would be parallel to the gradient. The direction of the critical line is close to the gradient when it follows the ridge near the maximum, but slides at an angle in the "saddle-like" region, before joining the saddle extremal point beyond the left edge of the plot (see Figure 3). Note that the gradient line that takes us to the same saddle as a segment of the global skeleton (dashed green) does not follow the ridge too closely in this instance.

during the evaluation of ∇s. This picture corresponds to a skeleton connecting extrema with relatively straight segments. In the "stiff" approximation, equation (10) becomes

$$\frac{\partial\mathcal{L}}{\partial\eta} \approx \left(\frac{1}{R_*}\right)^2 \int d^3x_k d^6x_{kl}\ |\mathbf{C}(x_k,x_{lm})|\ P_0(\eta,x_{kl})\ P_1(x_k)\delta_D\left(s^i(x_k,x_{kl})\right)\delta_D\left(s^j(x_k,x_{kl})\right). \tag{14}$$

The differential length is then only the function of γ times L.

The "stiff" approximation can be looked at from another perspective. By definition at a point on a local critical line, two of the characteristic directions defined for the field, namely, the direction of the gradient, $\nabla\rho$, and one chosen eigen direction of the Hessian, $\mathcal{H}$, must coincide. But the direction of the critical line itself, given by $\nabla S^i \times \nabla S^j$, is not, in general, aligned with the gradient of the field. Local critical lines are not the gradient lines, and in this sense they differ from the skeleton lines defined globally as void-patch intersections (Sousbie et al. 2008). In the "stiff" approximation, however, $\left(\nabla_m s^i\right)_{\rm stiff} \approx \sum_{kln} \epsilon^{ink}\left[x_{nl}x_{lm}x_k + x_{nl}x_{km}x_l\right]$ and $\left[\left(\nabla s^i\right)_{\rm stiff} \times \left(\nabla s^j\right)_{\rm stiff}\right] \times \nabla\rho = 0$, *i.e.* it is parallel to the gradient. Figure **??** shows the details of the calculations for the high-resolution segment of the 2D field. Thus, the essence of the stiff approximation lies in the assumption that the mismatch between the critical lines and gradient directions is statistically small. As Figure 3, which contains an extended view of the same field, illustrates, this assumption holds particularly well for the primary critical lines which more closely correspond to the intuitive picture of sharp ridges and deep valleys. Indeed, at a primary line the gradient points to the least curved direction, i.e, in some sense in the direction in which the changes of the field properties are the slowest. Therefore one can expect that this is the direction in which the condition of criticality will be maintained, i.e which the critical line itself will follow. Figure 3 shows that the primary lines start to deviate from the gradient flow mostly towards their end points when the curvature of the field along the line becomes comparable in magnitude to the transverse one. Secondary critical lines are much less certain to follow the gradient, sometimes exhibiting a "sliding" behaviour, on occasion almost orthogonal to the gradient, as a loop-like secondary line near the right saddle in Figure 3 exhibits. So the stiff approximation for the secondary lines should be taken with more caution, although we include them for completeness.

The stiff approximation provides a framework to compute the total differential length of the critical lines and the local skeleton almost completely analytically. In the next two sections we will carry this calculation in two and three dimensions and argue that it can straightforwardly be extended in N dimensions (see Appendix A). In what follows we shall omit in the derivation for brevity the $1/R_*$ (in 2D) and $1/R_*^2$ (in 3D) factors, but keep in mind that all the length quantities below scale accordingly. In section 4.4, after the computational machinery is developed, we return to the role the third derivative may play in description of the critical lines.

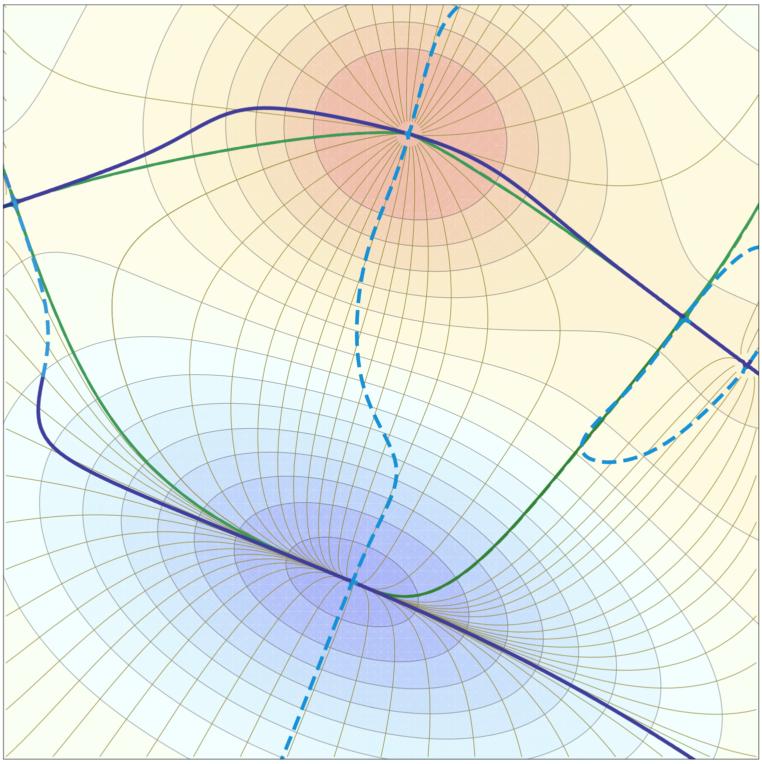

Figure 2. An example of a generic patch of a 2D field. The underlying isocontours correspond to the density field. The thin gold lines are the gradients lines of the field. The blue lines is the local set of critical lines, given by the solution of $\mathcal{S} \equiv (\mathcal{H} \cdot \nabla\rho) \times \nabla\rho = \mathbf{0}$. Primary lines are shown in solid and the secondary lines are dashed. The green lines correspond to global critical lines: the skeleton and the anti skeleton, which delineate a special bundle of gradient lines (Jost 2008) at the intersection of a peak patch and a void patch. The primary local lines follow fairly well the gradient lines, noticeably near the extrema, where the "stiff" approximation holds best. In contrast, the approximation worsens for the secondary critical lines. The main distinction between the global and local skeletons is that the global one follows the everywhere smooth gradient line that uniquely connects a maximum to a saddle, at the cost of deviating from being exactly on the ridge (see how in the vicinity of the minimum at the bottom, the right green line does not follow the trough) The local skeleton tries to delineate the ridges as far from extrema as possible, but then the lines that follow this local procedure from different extrema do not meet and have to rather suddenly reconnect. A particularly striking example is the loop on the right hand side. A zoomed view of the area left to the top maximum is shown in Figure **??**.

Type		Alignment	Condition
Primary	Skeleton:	$\mathcal{H} \cdot \nabla\rho = \lambda_1 \nabla\rho$	$\lambda_1 + \lambda_2 \leqslant 0$
	Anti-skeleton:	$\mathcal{H} \cdot \nabla\rho = \lambda_2 \nabla\rho$	$\lambda_1 + \lambda_2 > 0$
Secondary		$\mathcal{H} \cdot \nabla\rho = \lambda_2 \nabla\rho$	$\lambda_1 + \lambda_2 \leqslant 0$
		$\mathcal{H} \cdot \nabla\rho = \lambda_1 \nabla\rho$	$\lambda_1 + \lambda_2 > 0$

Table 2. the classification of the critical lines in 2D.

3 CRITICAL LINES OF 2D FIELDS

Even though the large scale structures of the universe are three dimensional, other important observed data sets involve 2D maps such as the cosmic microwave background or lensing convergence maps. Hence analyzing the local statistical properties of filaments in two dimensions is astrophysically well motivated. The 2D case is also a convenient starting point to introduce the details of the calculations that can be generalized to 3D and higher dimensions.

The 2D case affords several simplifications over the 3D case. In 2D, S is a (pseudo) scalar function and its zero level, orthogonal to ∇S, determines the critical lines. The expression for the differential length simplifies to

$$\frac{\partial \mathcal{L}}{\partial \eta} = \frac{1}{R_*} \int d^2 x_k d^3 x_{kl} d^4 x_{klm} \, |\nabla s| P(\eta, x_k, x_{kl}, x_{klm}) \delta_D \left(s(x_k, x_{kl}) \right) . \tag{15}$$

There are just four types of critical lines: two primary, the skeleton and the anti-skeleton, and two corresponding secondary ones. The classification of the 2D critical lines is summarized in Table 2. We shall focus on the most interesting primary lines in the main text, leaving the secondaries to the Appendix B. In Figure 3 the critical lines of different types are shown for an example generic patch of a 2D field.

3.1 The differential length of the critical lines of 2D fields

For 2D Gaussian fields, the calculation of the length of the critical lines can be carried almost completely analytically in the stiff approximation.

3.1.1 Direct derivation in the field's frame

Let us first proceed in the original coordinate frame. Defining

$$s = x_1 x_2 \left(x_{11} - x_{22}\right) + x_{12}\left(x_2^2 - x_1^2\right) = 2w x_1 x_2 + x_{12}\left(x_2^2 - x_1^2\right) , \tag{16}$$

the stiff approximation to ∇s involves only up to second derivatives of the field

$$|\nabla s|^2 = \left(x_1^2 + x_2^2\right)\left(w^2 + x_{12}^2\right)\left(u^2 + 4\left(w^2 + x_{12}^2\right) - 4\frac{2x_1 x_2 x_{12} + w\left(x_1^2 - x_2^2\right)}{x_1^2 + x_2^2} u\right) , \tag{17}$$

and equation (15) becomes explicitly

$$\frac{\partial \mathcal{L}}{\partial \eta} = \frac{16}{(2\pi)^3\sqrt{1-\gamma^2}} \exp\left[-\frac{\eta^2}{2}\right] \iiiint\!\!\int du dw dx_{12} dx_1 dx_2 \, |\nabla s| \, \delta_{\rm D}(s) \exp\left[-\frac{(u-\gamma\eta)^2}{2(1-\gamma^2)} - 4w^2 - 4x_{12}^2 - x_1^2 - x_2^2\right] , \tag{18}$$

where the second derivatives are described using $u = -(x_{11} + x_{22})$, $w = (x_{11} - x_{22})/2$ and x_{12}. Let us integrate over x_{12} using the $\delta_{\rm D}$-function, which leads to a substitution $x_{12} \to (2x_1 x_2 w)/(x_1^2 - x_2^2)$ with the Jacobian $|1/(x_1^2 - x_2^2)|$. Then equation (18) becomes

$$\frac{\partial \mathcal{L}}{\partial \eta} = \frac{16}{(2\pi)^3\sqrt{1-\gamma^2}} \exp\left[-\frac{\eta^2}{2}\right] \iiiint du dw dx_1 dx_2 \frac{|\nabla s|}{|x_1^2 - x_2^2|} \exp\left[-\frac{(u-\gamma\eta)^2}{2(1-\gamma^2)} - 4w^2\frac{(x_1^2 + x_2^2)^2}{(x_1^2 - x_2^2)^2} - x_1^2 - x_2^2\right] , \tag{19}$$

where

$$|\nabla s|^2 = w^2 \frac{(x_1^2 + x_2^2)^3}{(x_1^2 - x_2^2)^2}\left(u + 2w\frac{(x_1^2 + x_2^2)}{(x_1^2 - x_2^2)}\right)^2 . \tag{20}$$

Let us now substitute[3]

$$\tilde{w} = w\frac{(x_1^2 + x_2^2)}{(x_1^2 - x_2^2)}, \quad \text{noting that} \quad \tilde{w}^2 = (w^2 + x_{12}^2) , \tag{21}$$

to obtain

$$\frac{\partial \mathcal{L}}{\partial \eta} = \frac{16}{(2\pi)^3\sqrt{1-\gamma^2}} \exp\left[-\frac{\eta^2}{2}\right] \iiiint du d\tilde{w} dx_1 dx_2 \frac{|\tilde{w}(u + 2\tilde{w})|}{\sqrt{x_1^2 + x_2^2}} \exp\left[-\frac{(u-\gamma\eta)^2}{2(1-\gamma^2)} - 4\tilde{w}^2 - x_1^2 - x_2^2\right] . \tag{22}$$

The integration over the first derivatives is now easily performed in the polar coordinates of the x_1, x_2 plane to give

$$\frac{\partial \mathcal{L}}{\partial \eta} = \frac{2}{\pi^{3/2}\sqrt{1-\gamma^2}} \exp\left[-\frac{\eta^2}{2}\right] \int_{-\infty}^{\infty}\int_{-\infty}^{\infty} du d\tilde{w} \, |\tilde{w}(u + 2\tilde{w})| \exp\left[-\frac{(u-\gamma\eta)^2}{2(1-\gamma^2)} - 4\tilde{w}^2\right] . \tag{23}$$

This is the final integral form which can be easily investigated in the $u, \tilde{w}$ plane.

3.1.2 Derivation in the Hessian eigenframe

To generalize the derivation to higher dimensions we note that one can just perform all the calculations in the Hessian eigenframe. We shall denote all quantities *evaluated* in the eigenframe with tilde, e.g., $\tilde{x}_{11}(=\lambda_1), \tilde{x}_{22}(=\lambda_2), \tilde{u}, \tilde{w}, \tilde{x}_1, \tilde{x}_2$. What must be taken into account is that, in general, these quantities are not Gaussian random variables (while the corresponding ones in the fixed frame are), since the transformation from the fixed to eigenframe is non-linear. The Gaussian nature is only preserved for $\tilde{u}, \tilde{x}_1, \tilde{x}_2$. In the Hessian eigenframe $\tilde{x}_{12} = 0$. From equations (16-17)

$$\tilde{s} = \tilde{x}_1\tilde{x}_2(\tilde{x}_{11} - \tilde{x}_{22}) = \tilde{x}_1\tilde{x}_2(\lambda_1 - \lambda_2) = 2\tilde{x}_1\tilde{x}_2\tilde{w} , \quad \left|\tilde{\nabla} s\right| = |\tilde{w}|\sqrt{(\tilde{u} + 2\tilde{w})^2\tilde{x}_1^2 + (\tilde{u} - 2\tilde{w})^2\tilde{x}_2^2} . \tag{24}$$

In equation (15) the averaging is now carried over the distribution of the eigenvalues with the measure $\pi(\lambda_1 - \lambda_2)$ (Doroshkevich 1970) that accounts for eigenvalues being sorted, $\lambda_1 \geqslant \lambda_2$:

$$\frac{\partial \mathcal{L}}{\partial \eta} = \frac{8\cdot 2\cdot\pi}{(2\pi)^3\sqrt{1-\gamma^2}} \exp\left[-\eta^2/2\right] \iiiint (\lambda_1 - \lambda_2) d\lambda_1 d\lambda_2 d\tilde{x}_1 d\tilde{x}_2 \left|\tilde{\nabla} s\right| \delta_{\rm D}(\tilde{s}) \exp\left[-\frac{(\tilde{u}-\gamma\eta)^2}{2(1-\gamma^2)} - 4\tilde{w}^2 - \tilde{x}_1^2 - \tilde{x}_2^2\right] , \tag{25}$$

[3] here we made a choice of sign. Now in the coordinate frame that has the first direction aligned with the gradient of the field, i.e. $x_2 = 0$, $\tilde{w} = (x_{11} - x_{22})/2$, while in the frame that has gradient aligned with the second direction, $x_1 = 0$, $\tilde{w} = (x_{22} - x_{11})/2$

or in terms of $\tilde{u}, \tilde{w}$

$$\frac{\partial \mathcal{L}}{\partial \eta} = \frac{16}{(2\pi)^2\sqrt{1-\gamma^2}} \exp\left[-\eta^2/2\right] \iiiint |\tilde{w}| d\tilde{u} d\tilde{w} d\tilde{x}_1 d\tilde{x}_2 \left|\tilde{\nabla} s\right| \delta_{\rm D}(\tilde{s}) \exp\left[-\frac{(\tilde{u}-\gamma\eta)^2}{2(1-\gamma^2)} - 4\tilde{w}^2 - \tilde{x}_1^2 - \tilde{x}_2^2\right] . \tag{26}$$

In the argument of the delta-function in equation (26) $\tilde{w}$ can be zero only at special field points , not at a generic point on a skeleton. So vanishing $\tilde{s}$ requires either $\tilde{x}_1 = 0$ or $\tilde{x}_2 = 0$ which describes, as expected, that in the Hessian eigenframe one of the component of the gradient vanishes on the critical line. Since we have already chosen the coordinates so that the direction "1" is aligned with the largest eigenvalue and the critical lines can go in both eigen-directions, these two possibilities add up:[4]

$$\frac{\partial \mathcal{L}}{\partial \eta} = \frac{4\sqrt{2}}{(2\pi)^{3/2}\sqrt{1-\gamma^2}} \exp\left[-\eta^2/2\right] \int_0^\infty d\tilde{w}\tilde{w} \int_{-\infty}^\infty d\tilde{u} \left(|2\tilde{w}+\tilde{u}| + |2\tilde{w}-\tilde{u}|\right) \exp\left[-\frac{(\tilde{u}-\gamma\eta)^2}{2(1-\gamma^2)} - 4\tilde{w}^2\right] \quad . \tag{27}$$

Note that $|\tilde{w} - \tilde{u}/2| = |\lambda_1| = |\tilde{x}_{11}|$ and $|\tilde{u}/2 + \tilde{w}| = |\lambda_2| = |\tilde{x}_{22}|$. That is, the length of the critical lines per unit volume is given by the average absolute value of the Gaussian curvature of the field in the space orthogonal to the skeleton, given that in stiff approximation the direction of the skeleton is assumed to coincide with the gradient of the field. The reason for this is clear - the higher the curvature, the closer the next neighbouring segment of the skeleton can be, thus increasing the flux *i.e.* the length per unit volume. If we replace $\tilde{w} \to -\tilde{w}$ in the second integral, we return to the formula (23) with integration over both positive and negative $\tilde{w}$. The integrated length of the critical lines is reduced to

$$L = \frac{2\sqrt{2}}{\pi} \int_0^\infty \tilde{w} d\tilde{w} \int_{-\infty}^\infty d\tilde{u} \left(|2\tilde{w}+\tilde{u}| + |2\tilde{w}-\tilde{u}|\right) \exp\left[-\frac{\tilde{u}^2}{2} - 4\tilde{w}^2\right] . \tag{28}$$

equations (27) and (28) are the results of the stiff approximation for the threshold dependent differential and the integrated lengths of the critical lines in 2D respectively.

3.2 Primary critical lines in 2D: Skeleton and anti-Skeleton.

The local skeleton is the subset of all the critical lines, which includes the parts that appear as the ridges in the field profile, rather than the valleys. This subset is described by the constraints that the skeleton lines should go along the largest eigenvalue λ_1 and, in addition, that this direction has the smallest curvature, $|\lambda_1| \leqslant |\lambda_2|$. The anti-skeleton is a mirror structure describing the valley of the field and in all the results can be obtained by replacing $\eta \to -\eta$ in the formulae for the skeleton.

To derive the expression for the skeleton differential length let us return to equation (27). The critical lines with $\nabla\rho$ aligned with the largest eigenvalue direction have $\tilde{x}_2 = 0$. Thus, only one term is selected by the $\delta_{\rm D}$-function: it is $\propto 2|\lambda_2| = |2\tilde{w} + \tilde{u}|$. The magnitude restrictions translates into $\tilde{u} \geqslant 0$, thus

$$\frac{\partial \mathcal{L}^{\rm skel}}{\partial \eta} = \frac{4\sqrt{2}}{(2\pi)^{3/2}\sqrt{1-\gamma^2}} \exp\left[-\eta^2/2\right] \int_0^\infty d\tilde{w}\tilde{w} \int_0^\infty d\tilde{u} \left(2\tilde{w}+\tilde{u}\right) \exp\left[-\frac{(\tilde{u}-\gamma\eta)^2}{2(1-\gamma^2)} - 4\tilde{w}^2\right] \quad . \tag{29}$$

This result should not be confused with equation (28), where $\tilde{w}$ is integrated over full range of negative and positive values and which is strictly equivalent to equation (27), counting critical lines aligned both with the lowest and the largest eigen-directions. Performing the last two integrals one obtains for the differential length in closed form

$$\frac{\partial \mathcal{L}^{\rm skel}}{\partial \eta} = \frac{1}{\sqrt{2\pi}} \exp\left[-\frac{\eta^2}{2}\right] \left[\frac{1}{8}\left(1 + \frac{2}{\sqrt{\pi}}\gamma\eta\right)\left(1 + {\rm Erf}\left[\frac{\gamma\eta}{\sqrt{2}\sqrt{1-\gamma^2}}\right]\right) + \frac{\sqrt{1-\gamma^2}}{2\sqrt{2\pi}} \exp\left(-\frac{\gamma^2\eta^2}{2(1-\gamma^2)}\right)\right] , \tag{30}$$

and for the integrated skeleton length[5]

$$L^{\rm skel} = \frac{1}{8} + \frac{\sqrt{2}}{4\pi} = 0.23754 \ (\times R_*^{-1}) \quad . \tag{31}$$

Note that modulo the stiff approximation, equation (31) gives a universal, spectral parameter independent, scaling. Figure 4 demonstrates the threshold behaviour of the differential lengths for several values of the spectral parameter γ.

The most important and robust result of our theory is the behaviour of the differential length at high density thresholds

$$\frac{\partial \mathcal{L}^{\rm skel}}{\partial \eta} \overset{\gamma\eta\to\infty}{\sim} \frac{1}{\sqrt{2\pi}} \exp\left[-\frac{\eta^2}{2}\right] \times \frac{1}{4}\left(1 + \frac{2}{\sqrt{\pi}}\gamma\eta\right) , \tag{32}$$

It represents a bias similar to the one found in Kaiser (1984) for the clustering of high critical points - maxima. According to the latter, the number density of peaks in regions above high thresholds is higher than on average. Similarly, the length density of critical lines above high threshold is enhanced relative to the mean. From the point of view of measurements, perhaps a

[4] If we do not sort the eigenvalues and, thus, do not restrict the $\tilde{w}$ to be non-negative, then the notions of first and second direction are undefined, and we could choose now that the skeleton goes in, say, the first direction and $\tilde{x}_2 = 0$. We will loose here factor of two which is recovered by having to extend $\tilde{w}$ integration to negative values

[5] In other words, one expect to find one segment of skeleton per linear section of $\approx (4.2 R_*)$.

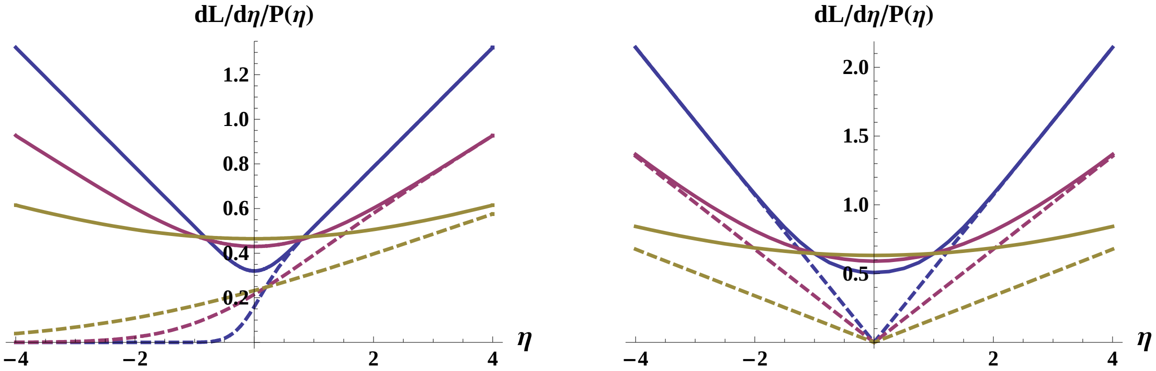

Figure 3. *left*: $\partial\mathcal{L}^{\rm skel}/\partial\eta/P(\eta)$ (dashed) and $\partial\mathcal{L}^{\rm skel+antiskel}/\partial\eta/P(\eta)$ (solid) in 2D for the spectral parameter values $\gamma = 0.3, 0.6, 0.95$. *Right:* $\partial\mathcal{L}/\partial\eta/P(\eta)$ (solid) and its asymptotic behaviour (dashed) in 2D for the same spectral parameter values

more interesting quantity than the differential length is the length per unit volume within the regions of high excursions of the field $\mathcal{L}(>\eta)$. In terms of the cumulative length given by equation (9), $\mathcal{L}(>\eta) = L - \mathcal{L}(\eta)$. Its asymptotic behaviour at high η for the skeleton is found by direct integration of equation (32)

$$\mathcal{L}^{\rm skel}(>\eta) \sim \frac{1}{2}{\rm Erfc}\left(\frac{\eta}{\sqrt{2}}\right) \times \frac{1}{4}\left(1 + \frac{2}{\sqrt{\pi}}\gamma\eta\right) . \tag{33}$$

The first factor here is the fractional volume occupied by these high excursions of the field. Note that, at large η the differential length divided by the PDF scales like $\eta\gamma/R_* = \eta/R_0$ once the proper scaling with $1/R_*$ is introduced. Hence the differential length as a function of η together with the total length give access to two characteristic scales R_0 and R_*. See Appendix A for a general proof of this result in N dimensions.

The threshold dependence of the statistics of critical lines in the stiff approximation is determined solely by the spectral parameter γ. In the limit $\gamma = 0$, when the distribution of the second derivatives of the field ρ is completely independent on the threshold, the length of the skeleton per unit volume within the regions with ρ/σ_0 in the interval $\eta, \eta + d\eta$ is just proportional to the fraction of the unit volume that these regions occupy. Completely generally, for any type of critical line,

$$\frac{\partial\mathcal{L}}{\partial\eta}(\gamma = 0) = \frac{L}{\sqrt{2\pi}} \exp\left[-\frac{\eta^2}{2}\right] . \tag{34}$$

When $\gamma \to 1$ the trace of the Hessian u becomes uniquely determined by the field level η (recall equation (6)). For over-dense regions with positive η equation (32) is exact for $\gamma = 1$, while no skeleton exists in under-dense regions in this limit.

Near zero (mean density) threshold the dependence of $\partial\mathcal{L}^{\rm skel}/\partial\eta$ is

$$\frac{\partial\mathcal{L}^{\rm skel}}{\partial\eta} \overset{\eta\to 0}{\sim} \frac{1}{\sqrt{2\pi}} \exp\left[-\frac{\eta^2}{2}\right] \times \frac{1}{4}\left(\frac{1}{2} + \frac{\sqrt{2}\sqrt{1-\gamma^2}}{\pi} + \frac{1}{\sqrt{\pi}}\frac{1+\sqrt{1-\gamma^2}}{\sqrt{1-\gamma^2}}\gamma\eta\right) . \tag{35}$$

Its details, in particular a step-like cutoff at negative η when $\gamma \to 1$, are sensitive to the definition of the primary lines. In under-dense regions with large negative densities the skeleton is exponentially suppressed.

Starting from equation (30) with $\eta \to -\eta$ for anti-skeleton, we obtain for the union of both primary critical lines

$$\frac{\partial\mathcal{L}^{\rm skel+antiskel}}{\partial\eta} = \frac{1}{\sqrt{2\pi}} \exp\left[-\frac{\eta^2}{2}\right]\left[\frac{1}{4} + \frac{1}{2\sqrt{\pi}}{\rm Erf}\left(\frac{\gamma\eta}{\sqrt{2}\sqrt{1-\gamma^2}}\right)\gamma\eta + \frac{\sqrt{1-\gamma^2}}{\sqrt{2\pi}}\exp\left(-\frac{\gamma^2\eta^2}{2(1-\gamma^2)}\right)\right] , \tag{36}$$

with twice the integrated length

$$L^{\rm skel+antiskel} = \frac{1}{4} + \frac{1}{\sqrt{2\pi}} = 0.47508 \; (\times R_*^{-1}) \quad . \tag{37}$$

This function is now symmetric in η with the skeleton providing the dominant contribution described by equation (32) in over-dense regions of space, and the anti-skeleton dominating the under-dense regions. Near the mean, zero, threshold of the field, both critical lines are present

$$\frac{\partial\mathcal{L}^{\rm skel+antiskel}}{\partial\eta} \overset{\eta\to 0}{\sim} \frac{1}{\sqrt{2\pi}} \exp\left[-\frac{\eta^2}{2}\right]\left(\frac{1}{4} + \frac{\sqrt{1-\gamma^2}}{\sqrt{2\pi}} + \frac{\gamma^2\eta^2}{2\sqrt{2\pi}\sqrt{1-\gamma^2}}\right) . \tag{38}$$

3.3 Secondary critical lines in 2D

Secondary critical lines do not allow for a full analytical treatment and are investigated in Appendix B. They are particularly important near zero threshold, since at this transitional regime the exact behaviour of primary or secondary lines depends significantly on our somewhat arbitrary separation of the critical lines in types. In this paper we are tracking the skeleton — density ridges — as primary lines emanating from the maxima, until the largest eigenvalue ceases to be the shallowest. Alternative definition may, for example, somewhat extend the skeleton at the expense of secondary lines at lower densities as long as all the eigenvalues transverse to the gradient are negative, i.e until λ_2 becomes positive. As an advantage, the differential length of the skeleton and the corresponding secondary lines defined this way would not exhibit inflections at low densities that can be seen in Figures 4 and B1 for high γ's. But the downside is that then one looses the ability to describe the primary lines analytically in a closed form. At the high density excursions the properties of the skeleton remain robust with respect to the variations in their exact definition.

However the important advantage of the definition of the primary lines adopted in this paper lies deeper. The magnitude of the eigenvalue along the direction transverse to the gradient is connected to the stability of these trajectories near the critical lines and to their possible bifurcations. This is discussed in part in Section 5.3.

Let us summarize the results for the total set of critical lines, primary and secondary combined, which are, of course, universal whatever the definition of the separate types. Summing up the results of this Section with the corresponding ones in Appendix B

$$L = \frac{\sqrt{2}+\mathrm{acot}(\sqrt{2})}{\pi} = 0.646071\ (\times R_*^{-1})\,. \tag{39}$$

$$\frac{\partial \mathcal{L}}{\partial \eta} \overset{\eta\to\infty}{\sim} \frac{1}{\sqrt{2\pi}}\exp\left[-\frac{\eta^2}{2}\right]\times\frac{\gamma\eta}{\sqrt{\pi}}\,, \tag{40}$$

$$\frac{\partial \mathcal{L}}{\partial \eta} \overset{\eta\to 0}{\sim} \frac{1}{\sqrt{2\pi}}\exp\left[-\frac{\eta^2}{2}\right]\times\left(\frac{\sqrt{2(1-\gamma^2)}+\mathrm{acot}\left(\sqrt{2(1-\gamma^2)}\right)}{\pi}+\frac{\sqrt{2(1-\gamma^2)}}{\pi(3-2\gamma^2)}(\gamma\eta)^2\right)\,. \tag{41}$$

The full behaviour of the total differential length is presented in Figure 4. One should note the linear asymptotic behaviour at high density levels and the regular quadratic behaviour near zero density threshold[6]. Finally recall that in the section 3 we have omitted almost everywhere a $1/R_*$ factor for the quoted lengths and differential lengths.

4 CRITICAL LINES OF 3D FIELDS

In three dimensions, we carry the computations directly in the eigenframe of the Hessian, following closely the derivation of Sections 3.1 and 3.2. We present the formalism first for all the critical lines and then narrow our focus to the primary ones.

4.1 The length of the critical lines of 3D fields

In 3D, let us use the variables $\tilde u=-(\lambda_1+\lambda_2+\lambda_3), \tilde w=(\lambda_1-\lambda_3)/2, \tilde v=(2\lambda_2-\lambda_1-\lambda_3)/2$. In the Hessian eigenframe

$$\tilde s^1=(\lambda_2-\lambda_3)\tilde x_2\tilde x_3=(\tilde w+\tilde v)\tilde x_2\tilde x_3\,,\quad \tilde s^2=(\lambda_3-\lambda_1)\tilde x_1\tilde x_3=-2\tilde w\tilde x_1\tilde x_3\,,\quad \tilde s^3=(\lambda_1-\lambda_2)\tilde x_1\tilde x_2=(\tilde w-\tilde v)\tilde x_1\tilde x_2\,, \tag{43}$$

and

$$\begin{aligned}
\widetilde{\nabla s}^1 &= \{0,\ \lambda_2(\lambda_2-\lambda_3)\tilde x_3,\ \lambda_3(\lambda_2-\lambda_3)\tilde x_2\}=\left\{0,\ -\frac{1}{3}(\tilde u-2\tilde v)(\tilde w+\tilde v)\tilde x_3,\ -\frac{1}{3}(\tilde u+\tilde v+3\tilde w)(\tilde w+\tilde v)\tilde x_2\right\}\,,\\
\widetilde{\nabla s}^2 &= \{\lambda_1(\lambda_3-\lambda_1)\tilde x_3,\ 0,\ \lambda_3(\lambda_3-\lambda_1)\tilde x_1\}=\left\{\frac{2}{3}(\tilde u+\tilde v-3\tilde w)\tilde w\tilde x_3,\ 0,\ \frac{2}{3}(\tilde u+\tilde v+3\tilde w)\tilde w\tilde x_1\right\}\,,\\
\widetilde{\nabla s}^3 &= \{\lambda_1(\lambda_1-\lambda_2)\tilde x_2,\ \lambda_2(\lambda_1-\lambda_2)\tilde x_1,\ 0\}=\left\{-\frac{1}{3}(\tilde u+\tilde v-3\tilde w)(\tilde w-\tilde v)\tilde x_2,\ -\frac{1}{3}(\tilde u-2\tilde v)(\tilde w-\tilde v)\tilde x_3,\ 0\right\}\,.
\end{aligned} \tag{44}$$

In the eigenvalue space the measure is $2\pi^2|(\lambda_1-\lambda_2)(\lambda_2-\lambda_3)(\lambda_3-\lambda_1)|$ and the eigenvalues are considered sorted. For sorted eigenvalues the choice of the directions has been fixed and the $(s^2,s^3),(s^1,s^3)$ and (s^1,s^2) pairs of surfaces describe different possibilities for the critical line. Those choices add together in the average integrated length. Using the variable $\tilde w,\tilde v$ the condition of eigenvalues being sorted is $\tilde w\geqslant 0,\ \ -\tilde w\leqslant\tilde v\leqslant\tilde w$.

Let us consider the critical lines that are the intersections of (s^2,s^3). Their differential length is given by

$$\begin{aligned}
\frac{\partial \mathcal{L}}{\partial \eta} = 2\pi^2\cdot\frac{3}{2}\cdot\frac{3^{3/2}15^2 5^{1/2}}{(2\pi)^5\sqrt{1-\gamma^2}}\exp\left[-\frac{1}{2}\eta^2\right]\int|(\lambda_1-\lambda_2)(\lambda_2-\lambda_3)(\lambda_3-\lambda_1)|\,d\lambda_1 d\lambda_2 d\lambda_3 d\tilde x_1 d\tilde x_2 d\tilde x_3\left|\widetilde{\nabla s}^2\times\widetilde{\nabla s}^3\right|\delta_{\rm D}(\tilde s^2)\delta_{\rm D}(\tilde s^3)\\
\times\exp\left[-\frac{(\tilde u-\gamma\eta)^2}{2(1-\gamma^2)}-\frac{15}{2}\tilde w^2-\frac{5}{2}\tilde v^2-\frac{3}{2}\tilde x_1^2-\frac{3}{2}\tilde x_2^2-\frac{3}{2}\tilde x_3^2\right]\,.
\end{aligned} \tag{45}$$

[6] For all γ but $\gamma=1$, for which

$$\frac{\partial \mathcal{L}}{\partial \eta}(\gamma\to 1,\eta\to 0)\sim\frac{1}{\sqrt{2\pi}}\exp\left[-\eta^2/2\right]\left(\frac{1}{2}+\frac{1}{3\sqrt{\pi}}|\eta|^3-\frac{1}{10\sqrt{\pi}}|\eta|^5\dots\right)\,. \tag{42}$$

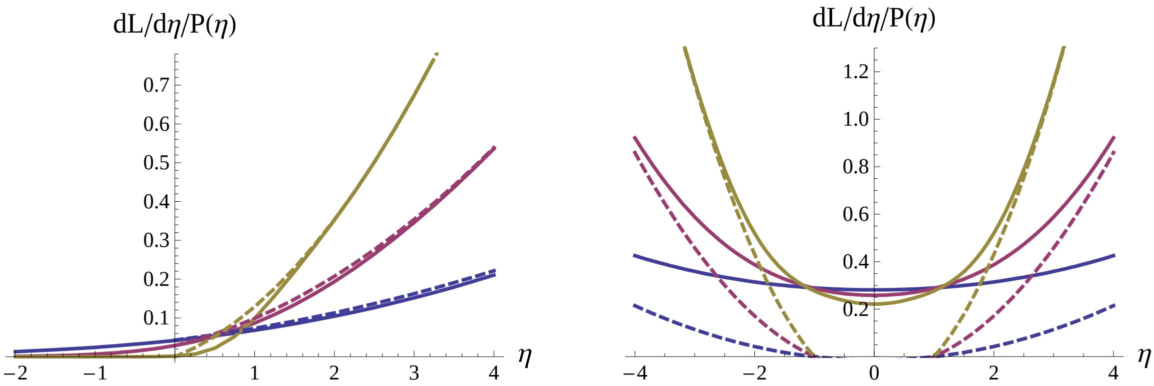

Figure 4. *Left:* The skeleton $\partial\mathcal{L}^{\rm skel}/\partial\eta/P(\eta)$ (solid) and its asymptotic behaviour at high density thresholds (dashed) in 3D. The anti-skeleton is described by the curves symmetric with respect to a reflection of η. *Right:* $\partial\mathcal{L}/\partial\eta/P(\eta)$ its asymptotic behaviour for the total set of critical lines. The spectral parameter values are (from bottom to top at high η) $\gamma = 0.3, 0.6, 0.95$.

Integration over $\delta_{\rm D}(\tilde{s}_2)$ and $\delta_{\rm D}(\tilde{s}_3)$ leads to the only possibility $\tilde{x}_2 = 0, \tilde{x}_3 = 0$. That is, the choice of the surface S_2 and S_3 in the Hessian eigenframe describes the skeleton along which the gradient is aligned with the direction 1, correspondent to the largest eigenvalue, while in the directions 2 and 3 the components of the gradient of the field vanish. With $\tilde{x}_2 = \tilde{x}_3 = 0$ we get a simple expression for

$$\left|\widetilde{\nabla s_2} \times \widetilde{\nabla s_3}\right| = |\lambda_2\lambda_3(\lambda_3-\lambda_1)(\lambda_1-\lambda_2)|\,\tilde{x}_1^2 = \frac{2}{9}\,|(\tilde{u}-2\tilde{v})(\tilde{u}+\tilde{v}+3\tilde{w})(\tilde{w}-\tilde{v})\tilde{w}|\,\tilde{x}_1^2\,, \tag{46}$$

while the subsequent integration over $\tilde{x}_2$ and $\tilde{x}_3$ using $\delta_{\rm D}$-functions and afterwards over $\tilde{x}_1$ gives

$$\frac{\partial\mathcal{L}^1}{\partial\eta} = \frac{3^4 5^{5/2}}{16\pi^2\sqrt{2\pi(1-\gamma^2)}}\exp\left[-\frac{1}{2}\eta^2\right]\int d\lambda_1 d\lambda_2 d\lambda_3 (\lambda_1-\lambda_2)(\lambda_2-\lambda_3)(\lambda_3-\lambda_1)|\lambda_2\lambda_3|\exp\left[-\frac{(\tilde{u}-\gamma\eta)^2}{2(1-\gamma^2)} - \frac{15}{2}\tilde{w}^2 - \frac{5}{2}\tilde{v}^2\right]. \tag{47}$$

Notice again that what the integrand involves the Gaussian curvature in the direction orthogonal to the gradient, which in stiff approximation is the direction of the filament itself. The contributions of the critical lines directed along the second and third eigen-direction is given by similar considerations and are added together when all critical lines are considered. Changing variables one finally obtains

$$\frac{\partial\mathcal{L}}{\partial\eta} = \frac{3^3 5^{5/2}\exp\left[\eta^2/2\right]}{4\pi^2\sqrt{2\pi(1-\gamma^2)}}\int d\tilde{u}d\tilde{w}d\tilde{v}\;\tilde{w}(\tilde{w}^2-\tilde{v}^2)\left(|\lambda_2\lambda_3|+|\lambda_1\lambda_3|+|\lambda_1\lambda_2|\right)\exp\left[-\frac{(\tilde{u}-\gamma\eta)^2}{2(1-\gamma^2)} - \frac{15}{2}\tilde{w}^2 - \frac{5}{2}\tilde{v}^2\right], \tag{48}$$

while the integrated length is

$$L = \frac{3^3 5^{5/2}}{4\pi^2}\int d\tilde{u}d\tilde{w}d\tilde{v}\;\tilde{w}(\tilde{w}^2-\tilde{v}^2)\left(|\lambda_2\lambda_3|+|\lambda_1\lambda_3|+|\lambda_1\lambda_2|\right)\exp\left[-\frac{1}{2}\tilde{u}^2 - \frac{15}{2}\tilde{w}^2 - \frac{5}{2}\tilde{v}^2\right], \tag{49}$$

with [7]

$$|\lambda_2\lambda_3|+|\lambda_1\lambda_3|+|\lambda_1\lambda_2| = \frac{1}{9}\left[|(\tilde{u}-2\tilde{v})(\tilde{u}+\tilde{v}+3\tilde{w})| + |(\tilde{u}+\tilde{v}+3\tilde{w})(\tilde{u}+\tilde{v}-3\tilde{w})| + |(\tilde{u}-2\tilde{v})(\tilde{u}+\tilde{v}-3\tilde{w})|\right]. \tag{50}$$

The equations (48) and (49) account for all the critical lines. In Figure 5 (right panel) the results for 3D critical lines are plotted while the discussion of the corresponding asymptotics is given in the Appendix C. We shall now turn our attention to the study of the primary lines and, in particular, the 3D skeleton that delineates the over dense filamentary structure and is of more direct observational interest.

4.2 Primary critical lines of 3D fields: Skeleton and Anti-Skeleton

The subset of critical lines identified with the skeleton correspond to the lines with the gradient aligned with the largest eigenvalue λ_1 while having $\lambda_1 + \lambda_2 \leqslant 0$. In equation (48) such lines are described by the first term $\sim |\lambda_2\lambda_3|$. The differential

[7] One should note the correspondence with the well-known result for the number density of extrema of the field (Bardeen et al. 1986)

$$N_{\rm ext} \propto \int d\tilde{u}d\tilde{w}d\tilde{v}\;\tilde{w}(\tilde{w}^2-\tilde{v}^2)|\lambda_1\lambda_2\lambda_3|\exp\left[-\frac{1}{2}\tilde{u}^2 - \frac{15}{2}\tilde{w}^2 - \frac{5}{2}\tilde{v}^2\right].$$

which is determined by the mean three-dimensional Gaussian curvature $|\lambda_1\lambda_2\lambda_3|$.

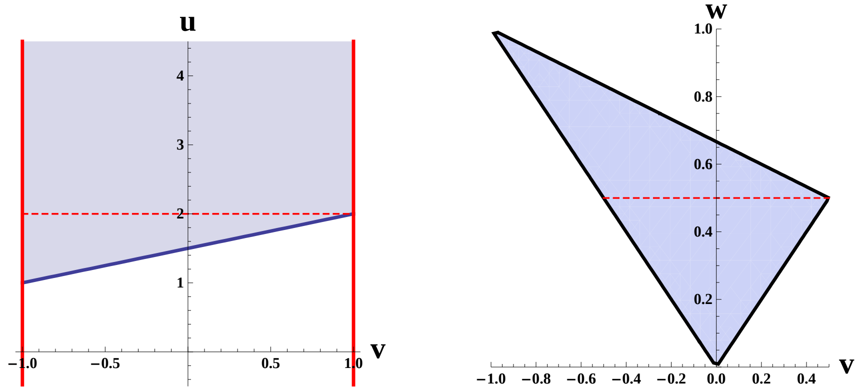

Figure 5. *Left*: Integration zones in the $\tilde{v},\tilde{u}$ plane for the 3D skeleton analysis. Variables are given in units of $\tilde{w}$. $\tilde{v}$ varies from $-\tilde{w}$ to $+\tilde{w}$, while $\tilde{u}$ must be greater than $\frac{1}{2}(\tilde{v}+3\tilde{w})$. In the allowed shaded region $0>\lambda_2\geqslant\lambda_3$ everywhere. Horizontal lines mark the further subdivision of the integration space if the order of integration is changed according to equation (53). *Right*: Integration zones in the $(\tilde{v},\tilde{w})$ plane after $\tilde{u}$ has been mapped to the $[0-\infty]$ interval. Variables are given in the units of $\tilde{u}$. The lower triangular zone corresponds to the semi-open rectangular band above the red dashed line in the left panel. In this region the integrand is given by the first term of equation (53). It dominates the high η asymptotics.

length of the skeleton is then

$$
\begin{aligned}
\frac{\partial \mathcal{L}^{\rm skel}}{\partial \eta} &= \frac{3^3 5^{5/2}\exp\left[-\eta^2/2\right]}{4\pi^2\sqrt{2\pi(1-\gamma^2)}}\int_0^\infty d\tilde{w}\int_{-\tilde{w}}^{\tilde{w}} d\tilde{v}\int_{\frac{1}{2}(\tilde{v}+3\tilde{w})}^{\infty} d\tilde{u}\;\tilde{w}(\tilde{w}^2-\tilde{v}^2)\lambda_2\lambda_3\exp\left[-\frac{(\tilde{u}-\gamma\eta)^2}{2(1-\gamma^2)}-\frac{15}{2}\tilde{w}^2-\frac{5}{2}\tilde{v}^2\right], \qquad (51)\\
&= \frac{3\cdot 5^{5/2}\exp\left[-\eta^2/2\right]}{4\pi^2\sqrt{2\pi(1-\gamma^2)}}\int_0^\infty d\tilde{w}\int_{-\tilde{w}}^{\tilde{w}} d\tilde{v}\int_{\frac{1}{2}(\tilde{v}+3\tilde{w})}^{\infty} d\tilde{u}\;\tilde{w}(\tilde{w}^2-\tilde{v}^2)(\tilde{u}-2\tilde{v})(\tilde{u}+\tilde{v}+3\tilde{w})\exp\left[-\frac{(\tilde{u}-\gamma\eta)^2}{2(1-\gamma^2)}-\frac{15}{2}\tilde{w}^2-\frac{5}{2}\tilde{v}^2\right].
\end{aligned}
$$

The integration in $\tilde{v}$–$\tilde{u}$ plane is limited to the region $\tilde{u}>\frac{1}{2}(\tilde{v}+3\tilde{w})$, as shown in the left panel of Figure 6. The integrated length of the skeleton is

$$
L^{\rm skel} = 0.046186\ (\times R_*^{-2})\,, \qquad (52)
$$

that is, one expect on average one skeleton line crossing a random $\approx (5R_*)^2$ surface element. The results of integration of equation (51) are presented in the left panel of Figure 5.

4.2.1 *Asymptotic behaviour at $\gamma\eta\to\infty$*

To study high η asymptotes it is useful to change the order of integration to have the $\tilde{u}$ integral as the outmost one. The inner integration in $\tilde{v}$–$\tilde{w}$ plane is then carried out over the region shown in the right panel of Figure 6.

$$
\int_0^\infty d\tilde{w}\int_{-\tilde{w}}^{\tilde{w}} d\tilde{v}\int_{\frac{1}{2}(\tilde{v}+3\tilde{w})}^{\infty} d\tilde{u} \;\to\; \int_0^\infty d\tilde{u}\int_0^{\tilde{u}/2} d\tilde{w}\int_{-\tilde{w}}^{\tilde{w}} d\tilde{v} + \int_0^\infty d\tilde{u}\int_{\tilde{u}/2}^{\tilde{u}} d\tilde{w}\int_{-\tilde{w}}^{2\tilde{u}-3\tilde{w}} d\tilde{v} \qquad (53)
$$

The last term is exponentially suppressed as $\eta\to\infty$ while the first one gives

$$
\begin{aligned}
\frac{\partial \mathcal{L}^{\rm skel}}{\partial \eta} &\overset{\gamma\eta\to\infty}{\sim} \frac{3\cdot 5^{5/2}\exp\left[-\eta^2/2\right]}{4\pi^2\sqrt{2\pi(1-\gamma^2)}}\int_0^\infty d\tilde{u}\int_0^\infty d\tilde{w}\int_{-\tilde{w}}^{\tilde{w}} d\tilde{v}\;\tilde{w}(\tilde{w}^2-\tilde{v}^2)(\tilde{u}-2\tilde{v})(\tilde{u}+\tilde{v}+3\tilde{w})\exp\left[-\frac{(\tilde{u}-\gamma\eta)^2}{2(1-\gamma^2)}-\frac{15}{2}\tilde{w}^2-\frac{5}{2}\tilde{v}^2\right]\\
&\overset{\gamma\eta\to\infty}{\sim} \frac{1}{\sqrt{2\pi}}\exp\left[-\frac{1}{2}\eta^2\right]\frac{(\gamma\eta)^2+9(\gamma\eta)/\sqrt{10\pi}+(9/10-\gamma^2)}{6\pi}\,. \qquad (54)
\end{aligned}
$$

The leading quadratic and the next linear terms can be recovered found by replacing $\tilde{u}\to\gamma\eta$ in the pre-exponential factor and treating the exponent as the $\delta_{\rm D}$-function. A more detailed asymptotic study of this Laplace-type integral is required to recover the third-order constant term, that also contributes to the accuracy of the expansion at the level demonstrated in Figure 5.

One finds that in the leading order in η the skeleton has the differential length growing as $(\gamma\eta)^2$ (see also Appendix A) and involves, as expected, a third of all the critical lines (compare with Appendix C) in the regions of high excursions concentrated around the maxima of the field. However, at intermediated thresholds, the skeleton constitutes more than a half of all critical lines, highlighting enhanced importance of the filamentary dense ridges among other critical lines. [8]

[8] Note the appearance of the linear in $\gamma\eta$ term in the next to leading order for the skeleton, that canceled out for the critical lines.

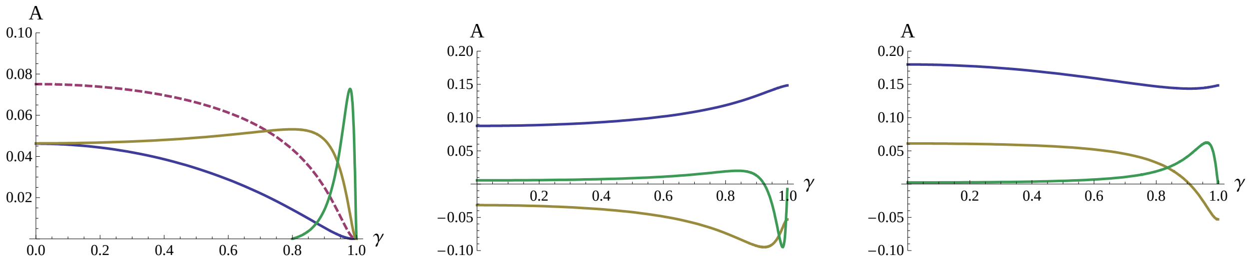

Figure 6. First coefficients of low-η power expansion (A_0 – blue, A_2 – yellow, A_4 – green) of the differential lengths of the 3D skeleton (*left*), inter-skeleton (*middle*) and total set of primary critical lines (*right*). The odd terms (e.g. A_1 – dashed) are present only for the asymmetric case of the primary lines.

4.2.2 Power series at $\eta \to 0$ and Hermite expansion

Using two alternative series representations of the shifted Gaussian form that encodes the dependence of the skeleton on the threshold η

$$\frac{1}{\sqrt{2\pi(1-\gamma^2)}}\exp\left[-\frac{(u-\gamma\eta)^2}{2(1-\gamma^2)}\right] = \frac{1}{\sqrt{2\pi}}\exp\left[-\frac{u^2}{2}\right]\sum_{k=0}^{\infty}\gamma^k H_k(\eta)H_k(u)\,, \tag{55}$$

$$= \frac{1}{\sqrt{2\pi(1-\gamma^2)}}\exp\left[-\frac{u^2}{2(1-\gamma^2)}\right]\sum_{k=0}^{\infty}\frac{1}{\sqrt{k!}}\left(\frac{\gamma}{\sqrt{1-\gamma^2}}\eta\right)^k H_k\left(\frac{u}{\sqrt{1-\gamma^2}}\right)\,, \tag{56}$$

we obtain either power series or Hermite[9] (Novikov et al. 2006) expansion of the differential length

$$\frac{\partial\mathcal{L}^{\rm skel}}{\partial\eta} = \frac{1}{\sqrt{2\pi}}\exp\left[-\eta^2/2\right]\times\begin{cases}\sum_{k=0}^{\infty}A_k(\gamma)(\gamma\eta)^k\,,\\ \sum_{k=0}^{\infty}B_k\gamma^k H_k(\eta)\,,\end{cases} \tag{57}$$

where

$$A_k(\gamma) \equiv \frac{3\cdot 5^{5/2}}{4\pi^2\sqrt{k!}(1-\gamma^2)^{\frac{k+1}{2}}}\int_0^\infty d\tilde w\int_{-\tilde w}^{\tilde w}d\tilde v\int_{\frac12(\tilde v+3\tilde w)}^\infty d\tilde u\;\tilde w(\tilde w^2-\tilde v^2)(\tilde u-2\tilde v)(\tilde u+\tilde v+3\tilde w)$$
$$\times\;\exp\left[-\frac{\tilde u^2}{2(1-\gamma^2)}-\frac{15}{2}\tilde w^2-\frac52\tilde v^2\right]H_k\left(\frac{\tilde u}{\sqrt{1-\gamma^2}}\right)\quad, \tag{58}$$

and

$$B_k \equiv \frac{3\cdot 5^{5/2}}{4\pi^2}\int_0^\infty d\tilde w\int_{-\tilde w}^{\tilde w}d\tilde v\int_{\frac12(\tilde v+3\tilde w)}^\infty d\tilde u\;\tilde w(\tilde w^2-\tilde v^2)(\tilde u-2\tilde v)(\tilde u+\tilde v+3\tilde w)\exp\left[-\frac{\tilde u^2}{2}-\frac{15}{2}\tilde w^2-\frac52\tilde v^2\right]H_k\left(\tilde u\right)\quad. \tag{59}$$

These two expansions are similar but distinct. The power-law expansion is suitable for an accurate analysis of the differential length near zero threshold for all $\gamma < 1$. On the other hand, the expansion in orthogonal Hermite polynomials is useful as an approximation over an extended range of thresholds. Both series are improper for $\gamma = 1$.

Although these coefficients can be computed analytically, their expressions are too cumbersome. Instead, we plot several leading ones in Figure 7. Remarkably, the power in Hermite expansion is concentrated in a few low order terms, in particular, $k = 0, 1, 2, 3$ for the skeleton, with subsequent terms forming a slowly decaying oscillating series. This finding confirms in 3D the conjecture of Novikov et al. (2006). The contribution of the first three most dominant terms, $\sum_{k=0}^{2} B_k H_k(\eta) = 0.0462 + 0.0751\gamma\eta + 0.0464\gamma^2(\eta^2 - 1)$ has the same structure and remarkably similar coefficients as the high η asymptotics of equation (54) which evaluates to $0.0477 + 0.0852\gamma\eta + 0.0531\gamma^2(\eta^2 - 1)$. This explains why the high η asymptotics provides a visually good fit through all thresholds when γ is not too high. At $\gamma \to 1$, the oscillatory tail of Hermite series provides the correction that reflects the irregular nature of the expansion in this limit.

The power series expansion reflects the features of the Hermite expansion. Starting, by definition, at $A_0(0) = B_0 = \mathcal{L}^{\rm skel}_{\rm tot} = 0.0462$, A_0 behaves as $A_0(\gamma) \approx \mathcal{L}_{\rm tot}(1-\gamma^2)$ over most of the γ range. Coupled with $A_2(\gamma) \approx {\rm const} = \mathcal{L}_{\rm tot}$ and $A_1(\gamma) \approx 0.0751\sqrt{1-\gamma^2}$ we get for the first three orders $\sum_{k=0}^{2} A_k(\gamma)(\gamma\eta)^k \approx 0.0462 + 0.0751\sqrt{1-\gamma^2}\gamma\eta + 0.0462\gamma^2(\eta^2-1)$, close both to the Hermite expansion and to the high η law for moderate γ. On the other hand, the power series expansion explicitly demonstrates the increasing importance of higher-order terms for $\gamma > 0.8$.

[9] we use here the *normalized* Hermite polynomials following probabilistic definition, $1/\sqrt{2\pi}\int_{-\infty}^{\infty}du\exp\left[-\frac12 u^2\right]H_k(u)H_m(u) = \delta_{mk}$

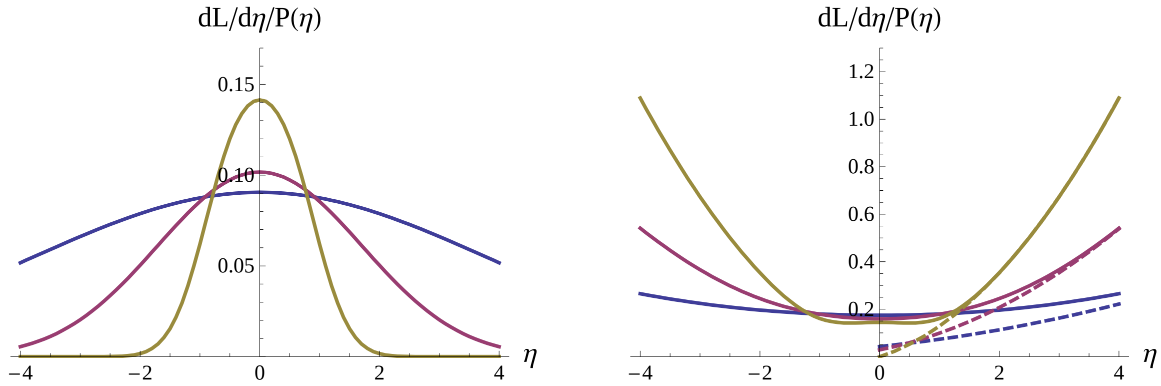

Figure 7. Differential length $\partial\mathcal{L}/\partial\eta/P(\eta)$ of the intermediate (*left panel*) and combined primary lines (*right panel*) as function of the threshold η in 3D. Different curves from blue to yellow correspond to the spectral parameter values $\gamma = 0.3, 0.6, 0.95$. The dashed curves, drawn only for positive η, correspond to high-η asymptotic solutions.

4.3 Primary critical lines of 3D fields: Inter-Skeleton and the overall behaviour

The intermediate primary critical lines are associated with saddle-like regions where the largest eigenvalues in magnitude are $\lambda_1 \geqslant 0$ and $\lambda_3 \leqslant 0$, and have opposite signs, and the shallowest direction aligned with the gradient is the second one with $-\lambda_1 < \lambda_2 < -\lambda_3$. Their appearance reflects the complexity of critical lines in space of more than two dimensions.

The differential length of the intra-skeleton computed in the stiff approximation is presented in Figure 8. The conditions for intermediate lines are prevalent for the regions of the field of moderate values - within 2σ ($|\eta| < 2$ of the zero mean for $\gamma > 0.6$. Although the occurrence of the intra-skeleton within these regions is never large ($\partial\mathcal{L}/\partial\eta/P(\eta)$ is relatively small), the regions corresponding to a near mean density occupy large fractions of the total volume, and as the result the total length of the intermediate skeleton is almost twice that of the skeleton or the anti-skeleton:

$$L^{\mathrm{inter}} = 0.087533\ (\times R_*^{-2})\,. \tag{60}$$

It constitutes nearly a half of the total length of the primary critical lines

$$L^{\mathrm{prim}} = L^{\mathrm{skel}} + L^{\mathrm{antiskel}} + L^{\mathrm{inter}} = 0.179905\ (\times R_*^{-2})\,. \tag{61}$$

At high $|\eta|$ thresholds, in very dense regions near maxima or under-dense regions near minima of the field, the intermediate skeleton is rare.

The total set of the primary critical line is even more than the skeleton dominated by the low order terms in Hermite expansion. Indeed, Figure 7 demonstrates that just the first two terms (odd orders are absent due to symmetry) in Hermite series are dominant, $\sum_{k=0}^{\infty} B_k H_k(\eta) \approx \mathcal{L}_{\mathrm{tot}}^{\mathrm{prim}}\left(1 + 0.340\gamma^2(\eta^2 - 1)\right)$.

4.4 Validity of the stiff approximation

Let us consider the opposite to "stiff" regime, when the derivatives of the Hessian dominate the ∇s,

$$(\nabla_m s^i)^{\mathrm{lax}} \approx \tilde{\gamma}^{-1} \sum_{jkl} \epsilon^{ijk} x_{jlm} x_l x_k\,. \tag{62}$$

Although not natural for cosmology-inspired spectra, such a situation arises when the power spectrum has an extended short wave tail with spectral index[10] n between -9 and -5. Such spectra have small $\tilde{\gamma}$, $\tilde{R} \ll R_*$ and there are many inflection points of the field per extremum. Interestingly, this regime also automatically means that the correlation between the gradient and third derivatives of the field is small.

Using the Hessian eigenframe formalism, we can obtain the important results without explicit computation of the differential length. Let us focus on the critical lines corresponding to the first eigenvalue. Equations (43) for $\mathcal{S}$-surfaces gives rise to two δ_{D}-functions, $\delta_{\mathrm{D}}(2\tilde{w}\tilde{x}_1\tilde{x}_3)\delta_{\mathrm{D}}((\tilde{w}-\tilde{v})\tilde{x}_1\tilde{x}_2)$ that after integration over the transverse gradient components $\tilde{x}_2$ and $\tilde{x}_3$ enforce $\tilde{x}_2 = \tilde{x}_3 = 0$, with the Jacobian factor $1/|2\tilde{w}(\tilde{w}-\tilde{v})\tilde{x}_1^2|$. The length element in this frame obeys

$$|\nabla s^2 \times \nabla s^3|^{\mathrm{lax}} \approx \tilde{\gamma}^{-2} x_1^4 \left| \sum_{ijmn} \epsilon_{kmn} \epsilon^{2i1} \epsilon^{3j1} x_{i1m} x_{j1n} \right| \equiv \tilde{\gamma}^{-2} x_1^4 \psi(x_{klm})\,, \tag{63}$$

[10] In a cosmological framework this takes place when the density field with $n < -1$ spectrum is smoothed with a top-hat window.

where the last expression defines the $\psi(x_{klm})$ function. The differential length is now given by

$$\frac{\partial \mathcal{L}^{\rm lax}}{\partial \eta} = \frac{1}{\tilde{R}^2}\left\{\frac{3^3 5^{5/2}}{8\pi^3\sqrt{1-\gamma^2}}\exp\left[-\frac{1}{2}\eta^2\right]\int d\tilde{u}d\tilde{w}d\tilde{v}\,(\tilde{w}+\tilde{v})\exp\left[-\frac{(\tilde{u}-\gamma\eta)^2}{2(1-\gamma^2)}-\frac{15}{2}\tilde{w}^2-\frac{5}{2}\tilde{v}^2\right]\right\} \times$$
$$\times\left\{\int x_1^2 dx_1 d^{10}x_{klm}\psi(x_{klm})P_1(x_1,x_2=x_3=0,x_{klm})\right\} \tag{64}$$

The last integral, with P_1 given by equation (D6), is a function of $\tilde{\gamma}$ only. The first term shows that, since the integrand prefactor is independent on $\tilde{u}$, the differential length does not depend on the threshold η at large η (it does at small η only because of non-trivial integration boundaries dependent on the exact type of critical lines). This is not surprising, since in this limit, there is little link between the skeleton length and the second derivatives, the only ones that are correlated with the field value. Such threshold independent behaviour is not observed in simulations with cosmological spectra, which argues once again for the statistical validity of the "stiff" approximation.

4.5 Measurements

In this section we compare the predictions of the local theory in stiff approximation with the measurements of the statistical properties of the critical lines done on realizations of the Gaussian fields with different power spectra.

We perform the measurements on critical lines found according to the global definition. The measurements are carried as follows: a set (typically ~ 100) of scale-invariant Gaussian random field of a N-D maps (typically 1024^2) or cubes (typically 256^3) is generated with a given power index of $n = 0$, -1 or -2. The N-D cube is then smoothed via convolution with a Gaussian kernel of width 6 pixels. The spectral parameters, γ, $\tilde{\gamma}$ *etc...* are computed through the second moments of the derivative of the smoothed field. The set of critical lines is then extracted as the intersection of the peak patches and void patches (see Sousbie et al. (2008) for details). In Figure 2 an example realization of the primary critical lines in 3D cube is shown. Since the algorithm produces a set of segments describing those critical lines tagged by the underlying (smoothed) density field, it is straightforward to compute the total and differential length per unit volume of the whole set. The differential length per unit modulus gradient is extracted by tagging the critical lines with this modulus (obtained via Fourier transform differentiation) and proceeding as before. Finally, the curvature of the skeleton is measured by computing the local curvature of a set of adjacent segments via finite difference.

Let us emphasize that these measurements correspond to properties of the global skeleton, whereas the theory developed in this paper is focused on the local skeleton. Hence even more remarkable is the match between the measured and the theoretical differential lengths for all values of γ, that is exhibited in Figure 9. This accuracy should be considered as indicative of the correspondence between the stiff approximation to the local theory and the global set of critical lines.

5 OTHER STATISTICS AND SPECTRAL PARAMETERS

In the previous sections, the emphasis has been on the differential length of the critical lines as a function of the excursion in density. As argued in Sousbie et al. (2008) and demonstrated here, it provides means of constraining the shape parameter, γ. Let us now explore other statistics which will allow us to constraint other shape parameters. In particular, let us demonstrate that the differential length as a function of the excursion in the modulus of the *gradient* of the density and the differential curvature depend on the second shape parameter, $\tilde{\gamma}$. Finally, we investigate the number density of singular points on the critical lines.

5.1 Differential length versus the gradient modulus

The differential length of the skeleton with respect to the threshold η carries information on the spectral parameter γ thanks to the correlation between the value η and the Hessian of the field. In the stiff approximation the Hessian curvature completely determines the length of the critical lines. For the exact formulation, the length also depends on the third derivatives, that are correlated with the first derivatives via the parameter $\tilde{\gamma}$. Thus, measuring length as a function of the modulus of the gradient should carry information on $\tilde{\gamma}$ and provide an estimate of an impact the third derivatives have on the length statistics of the critical lines.

To demonstrate the dependence of the skeleton length on the gradient of the field in "stiff" approximation let us return to equation (45) which we take integrated over all density thresholds. As before, we perform the integration over the δ-functions that enforces alignment of the gradient with the first eigen-direction, $x_2 = x_3 = 0$, however this time we do not integrate over but rather take the differential of the result with respect to x_1. Noting that $|x_1| = X \equiv \sqrt{x_1^2+x_2^2+x_3^2}$. we obtain in place of equation (47)

$$\frac{\partial \mathcal{L}}{\partial X} = \frac{3}{2}\cdot\frac{3^{3/2}15^2 5^{1/2}}{(2\pi)^{5/2}}\exp\left[-\frac{3}{2}X^2\right]\int|(\lambda_1-\lambda_2)(\lambda_2-\lambda_3)(\lambda_3-\lambda_1)|\,d\lambda_1 d\lambda_2 d\lambda_3|\lambda_2\lambda_3|\exp\left[-\frac{1}{2}\tilde{u}^2-\frac{15}{2}\tilde{w}^2-\frac{5}{2}\tilde{v}^2\right], \tag{65}$$

where the last integral does not depend on X. Dividing by the integrated length, $L = \int_0^\infty \partial\mathcal{L}/\partial X dX$, and generalizing the

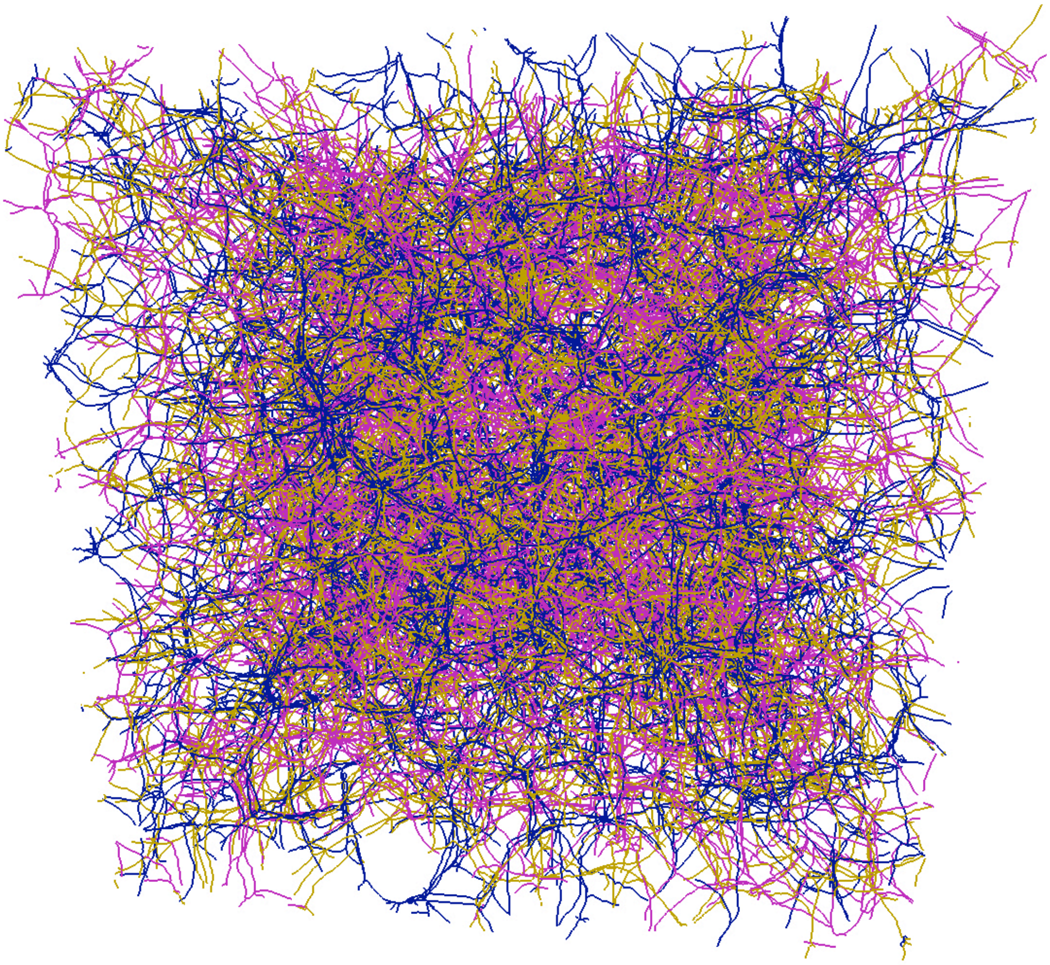

Figure 8. An example of set of primary critical lines (resp. skeleton in blue, intermediate in magenta and anti skeleton in gold) for a scale invariant power spectrum with $\gamma = 0.6$ in a 256^3 box smoothed over 5 pixels.

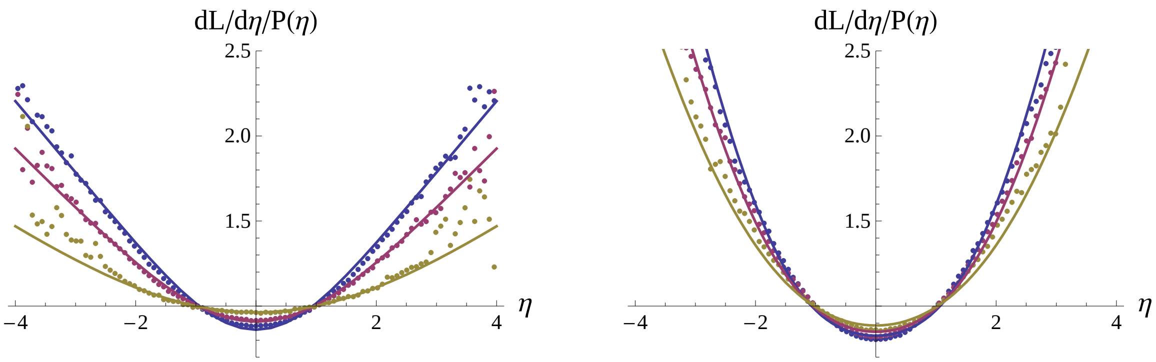

Figure 9. The relative differential length, $\partial\mathcal{L}/\partial\eta/\mathrm{PDF}$, measured in simulation of 2D (*left*) and 3D (*right*) Gaussian random fields with scale invariant power-law spectra versus predictions of the local theory in stiff approximation (solid curves). The spectral parameter $\gamma = 0.71, 0.59, 0.39$ for the 2D and $\gamma = 0.77, 0.70, 0.60$ for the 3D simulations.

result to fields in arbitrary N dimensions we conclude that

$$\left(\frac{1}{L}\frac{\partial\mathcal{L}}{\partial X}\right)^{\mathrm{stiff}} = \sqrt{\frac{2N}{\pi}}\exp\left[-\frac{N}{2}X^2\right]. \tag{66}$$

The exact dependence of the differential lengths will deviate from this form in a $\tilde{\gamma}$ -dependent way. It is natural to

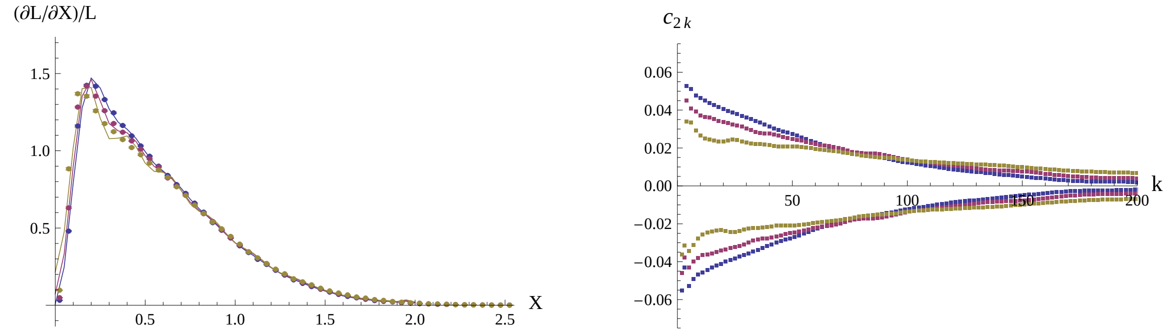

Figure 10. *left*: measured $\partial\mathcal{L}/\partial X/L$ as a function of $X \equiv |\nabla\rho|$ for $\tilde\gamma = 0.71, 0.58$ and 0.38 using the set of 25 2D simulations of 1024^2 Gaussian random fields with scale invariant spectra smoothed over 7 pixels. *Right*: value of the fit parameters c_k (see equation (67)). Note that $c_0 = 1$.

parameterize such deviation expanding the true statistics in Hermite series around the stiff approximation

$$\frac{1}{L}\frac{\partial\mathcal{L}}{\partial X} = \sqrt{\frac{2N}{\pi}}\exp\left[-\frac{N}{2}X^2\right]\left(\sum_{k=0}^{\infty}\frac{c_{2k}(\tilde\gamma)}{\sqrt{(2k)!}}H_{2k}(\sqrt{N}X)\right). \tag{67}$$

This choice of expansion is dictated by the orthogonality of the Hermite polynomials with the weight $\propto \exp[-\sqrt{N}X^2/2]$ on the interval $X \geqslant 0$. Thus, $c_0 = 1$. If the deviation from the stiff approximation is small, one expects the expansion to be dominated by the $n = 0$ term, while the subsequent terms should quickly fall in a orderly fashion.

To gain understanding on how the coefficients $c_{2k}(\tilde\gamma)$ behave with $\tilde\gamma$, let us consider again the lax situation, opposite to the stiff case, when the third derivatives of the field dominate the length statistics. Our starting point is equation (64) which has the following structure when we consider the differential length with respect to the $|x_1| = X$

$$\frac{\partial\mathcal{L}}{\partial X}^{\rm lax} \propto X^2\exp\left[-\frac{3}{2}X^2\right]\int du_1\left\{\frac{\exp\left[-\frac{3}{2}\frac{(u_1-\tilde\gamma X)^2}{1-\tilde\gamma^2}\right]+\exp\left[-\frac{3}{2}\frac{(u_1+\tilde\gamma X)^2}{1-\tilde\gamma^2}\right]}{\sqrt{2\pi(1-\tilde\gamma^2)}}\right\}\int d^9x_{ijk}\psi(x_{ijk})\bar{P}_1(x_2=x_3=0,x_{ijk}/u_1) \tag{68}$$

where $\bar{P}_1$ is given by equation (D6) with the dependence on u_1 factored out. The difference with the stiff approximation is large even for $\tilde\gamma = 0$ as the gradient's dependence becomes $\propto X^2\exp[-3/2X^2]$ in place of the stiff scaling $\propto \exp[-3/2X^2]$. Using now this factor as the weight, for $\tilde\gamma \neq 0$ we expand the expression in the brackets in generalized Laguerre polynomials. The expansion coefficients are of the form $\tilde\gamma^{2k}\exp[-3u_1^2/2]\sum_{m=0}^{k}d_m\tilde\gamma^{2m}H_{2m}(\sqrt{3}u_1)$; denoting the result of the integration of the expansion coefficients and all of the residual factors over the third derivatives by $\Psi_k(\tilde\gamma)$ we obtain

$$\frac{1}{L}\frac{\partial\mathcal{L}}{\partial X}^{\rm lax} = 3\sqrt{\frac{6}{\pi}}X^2\exp\left[-\frac{3}{2}X^2\right]\sum_{k=0}^{\infty}\frac{2^k k!}{(2k+1)!!}\tilde\gamma^{2k}L_k^{(1/2)}\left(3X^2/2\right)\Psi_k(\tilde\gamma), \tag{69}$$

where, again, $\Psi_0(\tilde\gamma) = 1$. With the help of the relation between the Laguerre and Hermite polynomials

$$3X^2k!L_k^{(1/2)}\left(3/2X^2\right) = (-1)^k2^{-k}\left(H_{2k+2}(\sqrt{3}X)+(2k+1)H_{2k}(\sqrt{3}X)\right),$$

we can cast equation (69) in the form of equation (67)

$$\begin{aligned}\frac{1}{L}\frac{\partial\mathcal{L}}{\partial X}^{\rm lax} &= \sqrt{\frac{6}{\pi}}\exp\left[-\frac{3}{2}X^2\right]\sum_{k=0}^{\infty}\frac{(-1)^k}{(2k+1)!!}\tilde\gamma^{2k}\left(H_{2k+2}(\sqrt{3}X)+(2k+1)H_{2k}(\sqrt{3}X)\right)\Psi_k(\tilde\gamma),\\ &= \sqrt{\frac{6}{\pi}}\exp\left[-\frac{3}{2}X^2\right]\left[1+\sum_{k=1}^{\infty}\frac{(-1)^{k-1}}{(2k-1)!!}\left[\tilde\gamma^{2k-2}\Psi_{k-1}(\tilde\gamma)-\tilde\gamma^{2k}\Psi_k(\tilde\gamma)\right]H_{2k}(\sqrt{3}X)\right].\end{aligned} \tag{70}$$

The coefficients $c_{2k}(\tilde\gamma)$ are

$$c_0 = 1\,,\quad c_2 = \sqrt{2}\left(1-\tilde\gamma^2\Psi_1(\tilde\gamma)\right)\,,\quad c_{2k} = \left((-1)^{k-1}\sqrt{(2k)!}/(2k-1)!!\right)\tilde\gamma^{2k-2}\left(\Psi_{k-1}(\tilde\gamma)-\tilde\gamma^2\Psi_k(\tilde\gamma)\right). \tag{71}$$

In particular, in the limit $\tilde\gamma \to 0$ the first two coefficients remain finite and of equally significant magnitude $c_0 = 1$, $c_2 = \sqrt{2}$, while all the other ones vanish.

Figure 10 and Figure 11 present the measurements of $\partial\mathcal{L}/\partial X/L$ in 2 and 3D respectively, together with the corresponding coefficients given by equation (67). It is found that these coefficients are significantly smaller in two dimensions, a clear indication that the stiff approximation holds better in 2D.

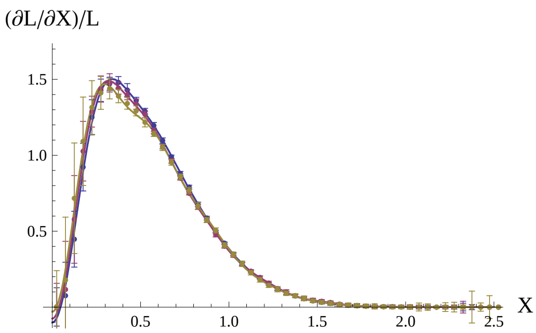

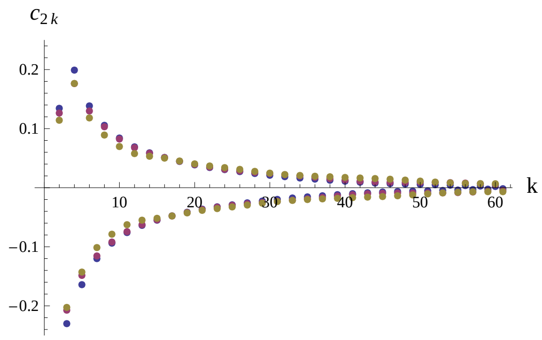

Figure 11. *left*: measured $\partial\mathcal{L}/\partial X/L$ as a function of $X \equiv |\nabla\rho|$ for $\tilde\gamma = 0.86, 0.83$ and 0.79 using the set of 3D simulation of 128^3 Gaussian random fields with scale invariant spectra smoothed over 7 pixels. *Right*: value of the fit parameters c_k, Note its faster convergence combined with a larger amplitude relative to the 2D case.

5.2 Statistics of the curvature of the critical lines

The local curvature, κ, at a point on a curve specified by the tangent vector $\mathbf{u} = d\mathbf{r}/dt$ is determined by the acceleration of the tangent vector $\dot{\mathbf{u}} \equiv d\mathbf{u}/dt = \mathbf{u}\cdot(\partial\mathbf{u}/\partial\mathbf{r})$ transverse to the curve direction:

$$\kappa = \frac{|\mathbf{u}\times\dot{\mathbf{u}}|}{|\mathbf{u}|^3} = \frac{|\mathbf{u}\times((\nabla\mathbf{u})\cdot\mathbf{u})\,|}{|\mathbf{u}|^3}\,. \tag{72}$$

Importantly, the curvature does not depend on parameterization t, nor on normalization of the tangent vector $\mathbf{u}$. In the local theory, the tangent vector to a critical line is orthogonal to $\nabla s^i(x_k, x_{kl})$ and can be taken to be

$$\mathbf{u} = \boldsymbol{\epsilon}\cdot\nabla s \quad (2D)\,, \qquad \mathbf{u} = \nabla s^i\cdot\boldsymbol{\epsilon}\cdot\nabla s^j = \nabla s^i\times\nabla s^j \quad (3D)\,; \tag{73}$$

so the curvature κ is the random quantity which involves the derivatives of the field up to fourth order,

$$(2D)\quad \kappa \;=\; |\nabla s\cdot(\nabla\nabla s)\cdot\nabla s|/|\nabla s|^3\quad, \tag{74}$$

$$(3D)\quad \kappa \;=\; \left|\left(\nabla s^i\times\nabla s^j\right)\times\left[\left(\nabla s^i\times\nabla s^j\right)\cdot\nabla\left(\nabla s^i\times\nabla s^j\right)\right]\right|/\left|\nabla s^i\times\nabla s^j\right|^3. \tag{75}$$

The curvature of the critical lines fundamentally reflects the derivatives of the field higher than the second. If they are neglected, the curvature is identically zero. Explicitly, the contributions that do not involve higher derivatives, in 2D

$$(2D)\quad (\mathbf{u}\times\dot{\mathbf{u}})^2 \;=\; 4x_1^2x_2^2\lambda_1^4\,(\lambda_1-\lambda_2)^6\,\lambda_2^4+\ldots\,, \tag{76}$$

$$(3D)\quad (\mathbf{u}\times\dot{\mathbf{u}})^2 \;=\; \left(x_2^2\lambda_3^2+x_3^2\lambda_2^2\right)(\lambda_1-\lambda_2)^4\,(\lambda_1-\lambda_3)^4\,\lambda_1^2\left(3x_1^2\lambda_2^2\lambda_3^2+\left(x_2^2\lambda_3^2+x_3^2\lambda_2^2\right)\lambda_1^2\right)^2+\ldots\,, \tag{77}$$

vanish when the correspondent critical line conditions $x_2 = 0$ or $x_2 = x_3 = 0$ are applied[11].

The integrated curvature over the length of the line, $C = \int \kappa dL$ is a useful dimensionless characteristics of the overall extend a line is curved. We have seen that the critical line length in volume dV is $dL \propto |\nabla s|\delta_{\rm D}(s)dV$ and $dL \propto |\nabla s^i\times\nabla s^j|\delta_{\rm D}(s^i)\delta_{\rm D}(s^j)dV$ in 2D and 3D respectively. Averaging over statistical distribution in regions above threshold η we obtain the mean density of the integrated critical line curvature $\mathcal{C} = \langle dC/dV\rangle$

$$(2D)\quad \mathcal{C}(\eta_>) \;=\; \frac{1}{R_*\tilde R}\int_{\eta>x} dx d^2x_k d^3x_{kl} d^4x_{klm} d^5x_{klmn}\,\kappa(x_k,x_{kl},\cdots)|\nabla s|\delta_{\rm D}(s)P(x,x_k,x_{kl},\cdots)\,, \tag{78}$$

$$(3D)\quad \mathcal{C}(\eta_>) \;=\; \frac{1}{R_*^2\tilde R}\int_{\eta>x} dx d^3x_k d^6x_{kl} d^{10}x_{klm} d^{15}x_{klmn}\,\kappa(x_k,x_{kl},\cdots)\left|\nabla s^i\times\nabla s^j\right|\delta_{\rm D}(s^i)\delta_{\rm D}(s^j)P(x,x_k,x_{kl}\cdots)\,, \tag{79}$$

where the integration is carried over all the derivatives up to the fourth order. The required joint probability function is given in equations (D19) and (D21).

Let us consider 2D case and estimate the curvature by using stiff approximation for the tangent vector u while following its local variation which involve higher derivatives of the underlying field. In the Hessian eigenframe, assuming the skeleton lies along 1, if $\mathbf{u}$ is approximated by its stiff counterpart we have:

$$\left(\frac{|\mathbf{u}\times\dot{\mathbf{u}}|}{|\mathbf{u}|^2}\right)^{\rm stiff} = |x_1|\,|(\lambda_1+\lambda_2)x_{112}|\,, \tag{80}$$

[11] Note that by construction, the torsion: $\tau = |\mathbf{u}\cdot(\dot{\mathbf{u}}\times\ddot{\mathbf{u}})|/|\mathbf{u}\times\dot{\mathbf{u}}|^2$ contains only the terms proportional to at least the third derivatives of the field.

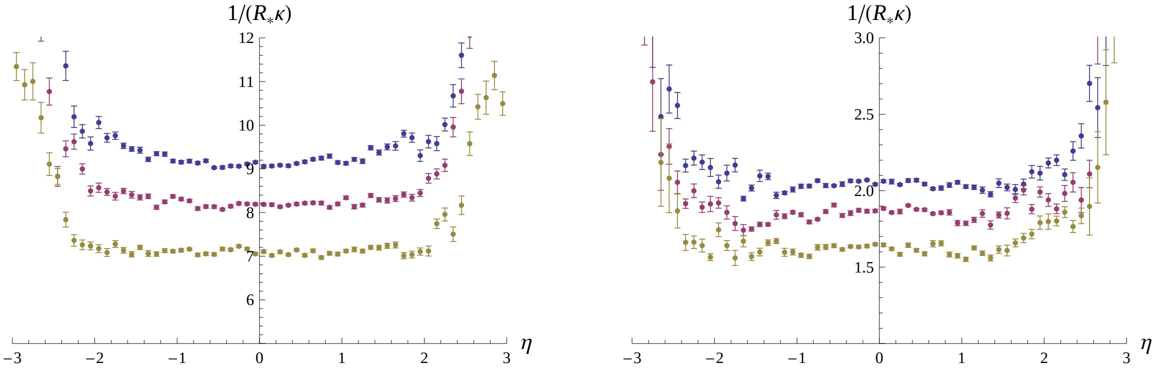

Figure 12. $1/(R_*\langle\kappa\rangle)$, the mean curvature *radius* in units of R^* as a function of η measured in simulation of 2D (*left*) and 3D (*right*) Gaussian random fields with scale invariant power-law spectra. The top curves correspond to spectra with more power at small scales and higher γ and $\tilde\gamma$ spectral parameters.

so that (taking into account the measure in the eigenframe and the $\delta_{\rm D}$ function of S in x_2):

$$\begin{aligned}\frac{\partial \mathcal{C}^{\rm stiff}}{\partial \eta} &= \pi \int d\lambda_1 d\lambda_2 d^4 x_{ijk}\,|(\lambda_1+\lambda_2)x_{112}|\,P_0(\eta,x_{kl})P_1(x_{ijk}) \\ &= \frac{\sqrt{2-\tilde\gamma^2}}{4\pi R_*\tilde R}\left(\sqrt{2(1-\gamma^2)}\exp\left[-\frac{\gamma^2\eta^2}{2(1-\gamma^2)}\right]+\sqrt{\pi}\mathrm{Erf}\left[\frac{\gamma\eta}{\sqrt{2(1-\gamma^2)}}\right]\gamma\eta\right)\frac{1}{\sqrt{2\pi}}\exp\left[-\frac{\eta^2}{2}\right],\end{aligned} \tag{81}$$

the last evaluation being done for the primary critical lines.

We have measured the mean curvature of the skeleton lines at the threshold η,

$$\langle\kappa\rangle \equiv \frac{\partial\mathcal{C}/\partial\eta}{\partial\mathcal{L}/\partial\eta}, \tag{82}$$

in simulations of the Gaussian random fields of different spectra, using the global skeleton techniques. Figure (12) displays the 2D (left panel) and 3D (right panel) results in terms of the curvature radius, $R_{\rm curv} = 1/\langle\kappa\rangle$. The measurements show that for the spectra we consider, the averaged curvature is insensitive to the density threshold for low-to-moderate threshold values showing a plateau in the interval $-2<\eta<2$. This indicates that in this regime the curvature of the skeleton does not depend on γ, but rather on $\tilde\gamma$ and perhaps $\hat\gamma$. It follows that in 3D the critical lines are relatively more wiggly than in 2D. If we use the lower value of $R^{\rm 3D}_{\rm curv}$ as a guidance, it seems the stiff approximation is less accurate in 3D that in 2D, as could be expected. The stiff estimate (81) gives the threshold-averaged mean density of the integrated curvature $\mathcal{C}^{\rm stiff}$ and, using equation (37), the mean curvature radius, $R^{\rm stiff}_{\rm curv}$, as

$$\mathcal{C}^{\rm stiff} = \frac{\sqrt{1-\tilde\gamma^2/2}}{2\pi R_*\tilde R}, \quad R^{\rm stiff}_{\rm curv} \equiv \frac{L}{\mathcal{C}} = \frac{\sqrt{2}+\pi/2}{\sqrt{1-\tilde\gamma^2/2}}\tilde R \approx 2.985\frac{\tilde\gamma}{\sqrt{1-\tilde\gamma^2/2}}R_*. \tag{83}$$

This result captures the qualitative dependence on $\tilde\gamma$ observed in simulations, but is a factor of three smaller in the magnitude of the curvature radius. This shows that the global skeleton, used in the numerical measurement, is notably straighter than the local critical lines, although the dependence of curvature on the spectral parameters seems similar.

Note in closing that in 2D, (resp. 3D) the knowledge of the differential length, curvature (resp. length, curvature and torsion) corresponds to an exhaustive global statistical description of the critical lines.

5.3 Singular points of critical lines

Let us now ask ourselves the following question: are there any special points along the skeleton? The obvious ones are the extrema of the field itself where critical lines intersect. Beyond this, one can anticipate two other types of singular points. The first type corresponds to points where the curvature transverse to the direction of the critical line vanishes along at least one axis: typically, in 2D, they mark regions where a crest becomes a trough, or vanish into a plateau. The second type correspond to points where the critical lines would split, even though the field does not go through an extremum: a bifurcation of the lines occurs along the slope; the occasional skier or mountaineer will be familiar with a crest line splitting in two, even though the gradient of the field has not vanished. From the point of view of the theory of random fields, the frequency of such points is an interesting venue: indeed we expect that steep power spectrum present relatively more bifurcation points as $\tilde R$, the distance between inflection points (see Sec. 2.2), becomes much shorter than R_*, the distance between extrema. In an astrophysical context, the statistical properties of the first type of points, and in particular their clustering properties are of interest for understanding the geometry of galactic infall, which in turn is believed to play an important role in defining the morphological properties of galaxies. The multiplicity of the maxima (*i.e.* the number of connected skeleton segments) is also of interest in the context of galaxy formation and feedback. In more abstract spaces, such as position-time, identifying bifurcations is important to pin down merging events (see e.g. Hanami (2001) and Appendix A).

5.3.1 Defining the skeleton singular points

Formally a singular condition along the skeleton occurs when at some point the determination of the critical line direction fails. It means that at this point the matrix $\nabla_k S^i$ of equation (2) has more than one distinct *right* null-vector, or, equivalently, all M^k defined by equation (A7) are zero. The only case when it happens exactly is at the extremal points of the field $\nabla\rho = 0$. There are no other formal singularities on the local critical lines, since when $\nabla\rho \neq 0$, the requirement $M^k = 0$ sets N relations between the field gradient, second and third derivatives which have vanishing probability to be simultaneously satisfied along a line in a random field.

The failure of the formal definition to identify all the physically interesting situations primarily reflects the inadequacy of the local skeleton construction, which only utilizes locally quadratic approximation to the field, to map the field near the singular points. [12] Figure 13 gives a 2D example. In 2D, the critical lines are zero levels of the scalar S-function, while $\nabla S = 0$ at the extrema of S field. In Figure 13 the region where a ridge splits into two is shown. One expect two critical lines cross there, with three branches following the ridges, and one following the through between two of the split branches. Instead, the locally defined critical lines are not allowed two join at the bifurcation point since the formal condition $\nabla S = 0$ is satisfied just *off* $S = 0$ contour, rather they artificially reconnect near the bifurcation point into two non-intersecting segments.

We conjecture that the critical lines experience a qualitative change in behaviour in the vicinity of the points where either the Hessian eigenvalue of the orthogonal to the gradient direction vanish, or becomes equal to the one along the gradient. Namely, if, for definiteness, $\nabla\rho$ is taken to be along the first eigen-direction, $\lambda_2 = 0$, or $\lambda_2 = \lambda_1$. We call the first case the "sloping plateau" as it designates the entering of a flat region, and the second, tentatively, the "bifurcation" as it designates the places of possible reconnection of critical lines. In particular, at the $\lambda_2 = \lambda_1$ points most of the transitions from primary to secondary behaviour take place. Remarkably, these special points on the critical lines are recovered by the formal singular condition $|M^k| = 0$ if $\nabla_k S^i$ is evaluated in the stiff approximation. As given in equation (A12), along the ND critical line defined by $x_2 = \ldots = x_N = 0$, $|M^{\rm stiff}| = x_1^{N-1}\prod_{i>1}\lambda_i\,(\lambda_1-\lambda_i) = 0$ gives rise to three classes of situations: (i) $x_1 = 0$ corresponding to extremal points; (ii) one of $\lambda_i = 0$ corresponding to slopping flattened tubes; and (iii) one of $\lambda_i = \lambda_1$, corresponding to an isotropic bifurcation.

Since it is beyond the scope of this paper to develop the full theory of these special points, we will focus here on their number density for isotropic 2D Gaussian random fields, leaving more detailed investigation to future work.

5.3.2 Number density of the singular points of the 2D critical lines

In 2D, the skeleton's singular points correspond to points where $S_k \equiv \nabla_k S = \mathbf{0}$. The number density, $n_{\rm B}(\eta)$ of singular points below the threshold η is equal to

$$n_{\rm B}(\eta) = \int_{\eta>x} dx d^2x_k d^3x_{kl} d^4x_{klm} d^5x_{klmn} P(x, x_k, x_{kl}, \cdots)|\det\left(\nabla_k\nabla_l s\right)|\delta_{\rm D}(s_1)\delta_{\rm D}(s_2)\,. \tag{84}$$

The simplest case of the skeleton singular points $\nabla S = \mathbf{0}$ are, according to equation (8), the extrema of the field itself, $x_1 = x_2 = 0$. Indeed when both x_1 and x_2 vanish

$$|\det\left(\nabla_k\nabla_l s\right)|\delta_{\rm D}(s_1)\delta_{\rm D}(s_2) = |x_{kl}|\delta_{\rm D}(x_1)\delta_D(x_2)\,, \tag{85}$$

which is exactly the integrand involved in the number density of *extrema* of the field. The extrema number densities, for reference, are given in 2D by (Longuet-Higgins 1957)

$$\frac{\partial n_{\rm saddle}}{\partial\eta} = \frac{1}{{R_*}^2}\frac{1}{4\sqrt{3}}\left[\frac{1}{\sqrt{2\pi}\sqrt{1-2\gamma^2/3}}\exp\left(-\frac{\eta^2}{2(1-2\gamma^2/3)}\right)\right]\,, \tag{86}$$

$$\frac{\partial n_{\rm min+max}}{\partial\eta} = \frac{\partial n_{\rm saddle}}{\partial\eta} + \frac{1}{4R_*^2}\gamma^2(-1+\eta^2)\frac{1}{\sqrt{2\pi}}\exp\left(-\frac{\eta^2}{2}\right)\,. \tag{87}$$

The singularity of the extrema from the points of view of the critical line theory is manifest in the fact that at extrema several critical lines intersect.

The gradient of S, evaluated in the stiff approximation, in the Hessian eigenframe has the components

$$s_1^{\rm stiff} = x_2\lambda_1\left(\lambda_1-\lambda_2\right)\,, \quad \text{and} \quad s_2^{\rm stiff} = x_1\lambda_2\left(\lambda_1-\lambda_2\right)\,. \tag{88}$$

and involves only second derivatives of the field. Remarkably, within this approximation, there are new singular points that lie *on* the (local) critical lines. The reason is that among two conditions needed for ∇S to vanish, one is already automatically satisfied by being on a critical line.

To be specific, let us consider the critical line that corresponds to the $x_2 = 0$ condition in the Hessian eigenframe. Then $s_1^{\rm stiff}$ vanishes everywhere along this line. The requirement $s_2^{\rm stiff} = 0$ has a solution at the extremal points, $x_1 = 0$, but also in two other cases, namely $\lambda_2 = 0$ or $\lambda_2 = \lambda_1$, that we conjectured to be of interest.

[12] Similarly, the bifurcation points for the global fully-connected skeleton (Sousbie et al. 2008) also formally merge with critical points in the strict sense due to sharp topological theorems (Jost 2008). However they appear if the skeleton is viewed with a finite resolution.

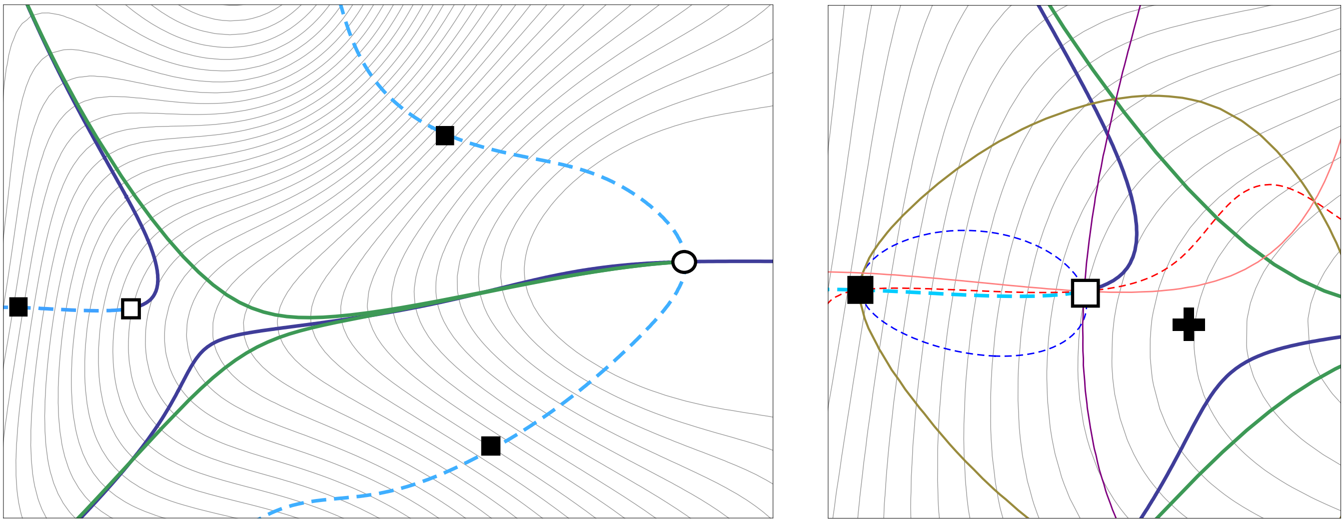

Figure 13. *Left:* the three types of singular point on the critical lines (in solid blue: primary; dashed: secondary; green: gradient lines of the global skeleton): an extremum (*open circle*), a "bifurcation" (*white square*), and "slopping plateaux" (*black squares*). The thin lines are the isocontours of the field. *Right:* Detailed view of the bifurcation region: The pink and purple lines mark the conditions $x_{11} = x_{22}$ and $x_{12} = 0$, which when intersect give the point where $\lambda_1 = \lambda_2$. This point is a singular point of the critical line (*white square*). The gold line is the condition $\lambda_2 = 0$ that marks the "sloping plateau" on the critical lines. The red and blue dashed lines are zero isocontours of two components of $\nabla S^{\rm stiff}$. The $\nabla S^{\rm stiff} = 0$ criterium pin-points exactly all types of the singular points on the critical lines. The black cross marks the position of the point $\nabla S = 0$.

The first situation, *the sloping plateau* with a flat transverse gradient, only occurs on secondary critical lines since it implies $\lambda_1 > 0$, and corresponds to

$$\left|\det\left(\nabla_{(k} s_{l)}^{\rm stiff}\right)\right| \delta_{\rm D}(s_1)\delta_{\rm D}(s_2) = \left|\frac{x_1 x_{112} x_{222}}{(\lambda_1-\lambda_2)}\right| \delta_{\rm D}(\lambda_2)\delta_{\rm D}(x_2)\,, \tag{89}$$

hence

$$\begin{aligned}
\frac{\partial n_{\rm B}^{\rm F}}{\partial \eta} &= \frac{1}{\tilde R^2}\int d\lambda_1 P_0(\eta,\lambda_1,\lambda_2=0)\times\int dx_1 d^4x_{klm} P_1(x_1,x_2=0,x_{klm})|x_1x_{112}x_{222}| \;+\; (1\to 2,\ \eta\to-\eta)\,,\\
&= \frac{1}{\sqrt{3}\pi^2\tilde R^2}\left[\frac{1}{\sqrt{2\pi}\sqrt{1-2\gamma^2/3}}\exp\left(-\frac{\eta^2}{2(1-2\gamma^2/3)}\right)\right]\left[\sqrt{1-\tilde\gamma^2}+\frac{1}{4}(2-3\tilde\gamma^2)\mathrm{atan}\left(\frac{2-3\tilde\gamma^2}{4\sqrt{1-\tilde\gamma^2}}\right)\right]\,,\\
&\equiv \frac{4}{\tilde\gamma^2\pi^2}\mathcal{G}_B^F(\tilde\gamma)\frac{\partial n_{\rm saddle}}{\partial\eta}\,.
\end{aligned} \tag{90}$$

The second situation (isotropic Hessian) corresponds to

$$\left|\det\left(\nabla_{(k} s_{l)}^{\rm stiff}\right)\right| \delta_{\rm D}(s_1)\delta_{\rm D}(s_2) = \frac{1}{4}\left|\frac{x_1(u_2^2-16(w_1^2+w_2^2))}{(\lambda_1-\lambda_2)}\right| \delta_{\rm D}(\lambda_1-\lambda_2)\delta_{\rm D}(x_2)\,,$$

therefore

$$\begin{aligned}
\frac{\partial n_{\rm B}^{\rm I}}{\partial \eta} &= \frac{1}{\tilde R^2}\int d\lambda_1 P_0(\eta,\lambda_1,\lambda_2=\lambda_1)\times\int dx_1 d^4x_{klm} P_1(x_1,x_2=0,x_{klm})\left|x_1(u_2^2/4-4(w_1^2+w_2^2))\right| \;+\; (1\to 2,\ \eta\to-\eta)\,,\\
&= \frac{1}{\pi\tilde R^2}\left[\frac{1}{\sqrt{2\pi}}\exp\left(-\frac{\eta^2}{2}\right)\right]\left[\frac{2}{\sqrt{2-\tilde\gamma^2}}-\frac{1}{2}(1+\tilde\gamma^2)\right]\equiv\frac{1}{\tilde\gamma^2\pi R_*^2}\mathcal{G}_B^I(\tilde\gamma)P(\eta)\,.
\end{aligned} \tag{91}$$

Both $\mathcal{G}_B^F(\tilde\gamma)$ and $\mathcal{G}_B^I(\tilde\gamma)$ are weak functions of $\tilde\gamma$ of order unity. The main $\tilde\gamma$ dependence $\propto \tilde\gamma^{-2}$ reflects $\tilde R$ as the fundamental scale for the singular points.

We note that the number density of the "sloping plateaux" is proportional to the density of the saddle points, hence this type of singular points is predominantly concentrated near mean field values (small η). In contrast, the number density of "bifurcation" points is proportional just to the PDF of the field and, hence, the bifurcation points are as frequent in the regions of high field values as in the low ones. This may provide explanation for the observed insensitivity of the curvature of the skeleton to the threshold, if we conjecture that most of the curvature accumulates near the "bifurcation" points.

2D		3D	
Skeleton	$4.21R_*$	Skeleton:	$(4.65R_*)^2$
Anti-skeleton	$4.21R_*$	Anti-skeleton:	$(4.65R_*)^2$
		Inter-skeleton:	$(3.38R_*)^2$
All primary	$2.11R_*$	All primary	$(2.36R_*)^2$
All secondary	$5.54R_*$	All secondary	$(3.02R_*)^2$
Total	$1.55R_*$	Total	$(1.86R_*)^2$

Table 3. Inverse average integrated flux (the characteristic area (3D) or length (2D) per critical line) of the critical lines of different types.

6 CONCLUSION & PERSPECTIVES

The filamentary structure is a dramatic feature of the observed or simulated Cosmic Web. This paper investigated how the set of critical lines of a given field corresponds to an intermediate representation of the field, which is more extended than the knowledge of the critical points, but nevertheless much more compact than the field itself. It introduced the stiff approximation, which states that the tangent vector to the critical lines only involves up to the the second derivative of the fields. Within its framework it has been demonstrated that, for stationary Gaussian random fields, ergodicity allows one to recast the description of the ND critical lines into a point process, which only involve the first spectral parameter, γ, when considering the differential length as a function of the contrast, and the second spectral parameter, $\tilde{\gamma}$, when considering it as a function of the modulus of the gradient. The former probability distribution was shown to involve the average flux of the Gaussian curvature of the 1D sections. In turn, these averages can be carried out analytically almost to the last integral in 2D and 3D, and provide simple asymptotics at large and small contrast. The detailed contribution of all types of critical lines as a function of thresholding was described. The main results of this investigation corresponds to equations (27) and (28) for the differential length of the skeleton and the total set of critical lines in 2D and equations (48) and (51) in 3D. Their generalization to N dimensions is given by equation (A18) in Appendix A. Table 3 summarizes the average integrated fluxes (i.e length per unit volume) of the critical lines. For instance in 3D one expect on average one skeleton line crossing a random $\approx (5R_*)^2$ surface element.

These findings were illustrated on scale free power spectra with spectral parameters which are relevant to cosmology[13]. The prediction of the stiff approximation was checked against measurements for global skeletons (Sousbie et al. 2008) on realizations of these fields in two and three dimensions and was found to be in good qualitative agreement. The differential curvature of the corresponding lines was also measured (section 5.2) and the corresponding radii were found to be $\approx 8R_*$ and $\approx 2.5R_*$ near $\eta = 0$ in two and three dimensions respectively. Hence an access to both the curvature and the length of the skeleton provides the means of constraining two shape parameters, γ and $\tilde{\gamma}$. The stiff approximation is also implemented to compute the differential curvature in 2D. Finally (section 5.3), the stiff theory of the singular points of the critical lines was laid out in general, identifying generically three types of points: critical points of the underlying field, bifurcation points and slopping plateaux. Again, the stiff approximation provide means of computing the number density of these points. Appendix D derived the general joint probability of the field and its successive derivative in arbitrary dimensions, which come into play when computing these higher order statistics.

Clearly the formalism developed in this paper will be useful in the context of the upcoming surveys such as the LSST, or the SDSS-3 BAO surveys since it yields access to the shape of the power-spectrum without artifacts related to varying light to mass ratio. For instance, Sousbie et al. (2008) first applied the corresponding theory to the SDSS-DR4 catalogue in order to constraint the global dark matter content of the universe, since the cosmological parameters are directly a function of the spectral parameter, γ. Its application to CMB related full sky data, such as WMAP or Planck should provide insight into, e.g. the level of non-Gaussianity in these maps (see SPCNP for a discussion). Similarly, upcoming large scale weak lensing surveys could be analyzed in terms of these tools (Pichon et al. 2009).

A natural extension of the theoretical component of this work would be to investigate the properties of the bifurcation points in anisotropic settings and extend beyond the stiff approximation the preliminary results of Section 5.3. This will be the topic of a forthcoming paper. Another natural venue would be to also investigate the statistical properties of, *e.g.* the peak patch walls (surface, curvature) defined as $x_3 = 0$ in the eigenframe of the Hessian. Eventually, a global theory of the critical manifolds beyond the local approximation should also be developed to provide a framework to study the connectivity of the critical lines.

ACKNOWLEDGMENTS

We thank D. Aubert and K. Benabed for comments and D. Munro for freely distributing his Yorick programming language and opengl interface (available at `http://yorick.sourceforge.net/`). DP thanks the CNRS (France) for support through a

[13] in other fields, the stiff approximation might be less well motivated (see Section 4.4), but the calculations hold.

"poste rouge" visiting position during Summer 2007 when this investigation was originated. CP, TS, SP and CG also thank the hospitality of the University of Alberta, and the "Programme National de Cosmologie" for funding. Finally, CP and DP thank the Canadian Institute for Theoretical Astrophysics for hosting the work involved in finalizing this paper. This investigation carried within the framework of the Horizon project, `www.projet-horizon.fr`.

REFERENCES

Adler R. J., 1981, The Geometry of Random Fields. The Geometry of Random Fields, Chichester: Wiley, 1981
Aragón-Calvo M. A., Jones B. J. T., van de Weygaert R., van der Hulst J. M., 2007, aap, 474, 315
Arnol'd V. I., Zel'dovich Y. B., Shandarin S. F., 1981, Usp. Mat. Nauk, Tom 36, p. 244 - 245, 36, 244
Bardeen J. M., Bond J. R., Kaiser N., Szalay A. S., 1986, *ApJ*, 304, 15
Bond J. R., Kofman L., Pogosyan D., 1996, *Nature*, 380, 603
Bond J. R., Myers S. T., 1996a, *ApJ Sup.*, 103, 1
Bond J. R., Myers S. T., 1996b, *ApJ Sup.*, 103, 63
Cardoso J.-F., 2009, In preparation
Colombi S., Pogosyan D., Souradeep T., 2000, Physical Review Letters, 85, 5515
Doroshkevich A. G., 1970, Astrophysics, 6, 320
Hanami H., 2001, *MNRAS*, 327, 721
Jost J., 2008, Riemannian Geometry and Geometric Analysis, Fifth Edition. Berlin ; New York : Springer, c2008.
Kaiser N., 1984, *ApJ Let.*, 284, L9
Longuet-Higgins M. S., 1957, Royal Society of London Philosophical Transactions Series A, 249, 321
Novikov D., Colombi S., Doré O., 2006, *MNRAS*, 366, 1201
Pichon C., Bernardeau F., 1999, Astronomy and Astrophysics, 343, 663
Pichon C., Thibaut E., Prunet S., Benabed K., Sousbie T., Teyssier R., 2009, MNRAS, 0, 0
Platen E., van de Weygaert R., Jones B. J. T., 2007, *MNRAS*, 380, 551
Pogosyan D., Bond J. R., Kofman L., Wadsley J., 1998, in Colombi S., Mellier Y., Raban B., eds, Wide Field Surveys in Cosmology Cosmic Web: Origin and Observables. pp 61–66
Regos E., Szalay A. S., 1995, *MNRAS*, 272, 447
Scannapieco E., Pichon C., Aracil B., Petitjean P., Thacker R. J., Pogosyan D., Bergeron J., Couchman H. M. P., 2006, *MNRAS*, 365, 615
Schmalzing J., Buchert T., Melott A. L., Sahni V., Sathyaprakash B. S., Shandarin S. F., 1999, *ApJ*, 526, 568
Sousbie T., Colombi S., Pichon C., 2008, *MNRAS*
Sousbie T., Pichon C., Colombi S., Novikov D., Pogosyan D., 2008, *MNRAS*, 383, 1655
Sousbie T., Pichon C., Courtois H., Colombi S., Novikov D., 2008, *ApJ Let.*, 672, L1

APPENDIX A: THE STIFF SKELETONS OF ND FIELDS

The emphasis in this paper is on developing the analytical theory of the critical lines of a given GRF in two and three dimensions. Yet the critical lines in higher dimensions are of interest in more abstract spaces such as space-time or space-smoothing etc. . In 3+1 Dimensions, corresponding to 3D space+time, the 4D critical lines are the dynamical tracks of critical points in 3D. An alternative view is to think of the 4D skeleton as event lines of over densities, while the critical points correspond to the position and time of merging events. In fact Hanami (2001) explored sloping saddles (i.e. points in position-smoothing space corresponding degenerate saddle points) as a mean of identifying merging events, and argued that the ridges (the path of the maxima in position-smoothing space as a function of smoothing) form a 4D skeleton. Clearly these higher dimensional spaces would typically not be strictly isotropic, stationary nor Gaussian. As a first step, let us nonetheless investigate these N dimensional lines.

A1 Critical Lines in ND

The local critical lines in N dimensions are defined as the points where the condition

$$\mathcal{H} \cdot \nabla\rho = \lambda_i \nabla\rho \,, \tag{A1}$$

is satisfied. This can be expressed as the condition of the vanishing of the $N-2$ antisymmetric tensor

$$\mathbf{S} = S^{i_1,i_2,\ldots,i_{N-2}} \equiv \sum_{klm} \nabla_k \rho H^k{}_l \epsilon^{i_1,\ldots,i_{N-2},l,m} \nabla_m \rho = 0 \tag{A2}$$

as defined in equation (1). In spaces of dimension $N > 4$ it is more compact to consider the Hodge-dual rank 2 tensor

$$(*\mathbf{S}) = (*S)^{ij} = \frac{1}{(N-2)!} \sum_{i_1,\ldots,i_{N-2}} S^{i_1,i_2,\ldots,i_{N-2}} \epsilon_{i_1,\ldots,i_{N-2},i,j} = 0 \quad . \tag{A3}$$

Local direction of the filament corresponds to the *right* null-vector δr^k of the $N-2+1$-rank tensor of the derivatives of $\mathbf{S}$

$$\sum_k \left(\nabla_k S^{i_1,i_2,\ldots,i_{N-2}}\right)\delta r^k = 0 \quad . \tag{A4}$$

A non-trivial solution of this set of C_N^2 homogeneous equations generally exists, since the existence of the *left* null-vector $\sum_{i_1} \nabla_{i_1}\rho\left(\nabla_k S^{i_1,i_2,\ldots,i_{N-2}}\right) = 0$ imposes C_{N-1}^2 linear relations leaving exactly $C_N^2 - C_{N-1}^2 = N-1$ independent equations to define a line.

The notion of *primary* skeleton lines is automatically generalized for N D as the subset of critical lines obeying

$$\mathcal{H}\cdot\nabla\rho = \lambda_1\nabla\rho\,, \quad \text{and} \quad \lambda_1+\lambda_2 \leqslant 0\,, \tag{A5}$$

where λ_1 is the largest and λ_2 is the second largest of the sorted eigenvalues.

Let us derive the general expression for the statistical average of the flux of the lines arbitrarily defined over the properties of the ND random field by $N-1$ equations $S^i = 0$, $i = 1\cdots N-1$, where $S^i(x, x_k, x_{kl}, \ldots)$ are functions of the field and it's derivatives. We can shortcut the procedure of flux evaluation by marking each line with one intersection point with a fiducial surface Σ, orthogonal to it, and finding the N-1 number density of the intersection points on the surface $\Sigma = 0$. The average number density of the points defined as the intersection of n non degenerate hypersurfaces $\sigma^i, \ldots, \sigma^N$ is given by

$$n = \int dx d^N x_k \cdots P(x, x_k, \cdots)\delta_{\rm D}(\sigma^1)\cdots\delta_{\rm D}(\sigma^n)|\det(\nabla\sigma^1, \cdots \nabla\sigma^n)|\,. \tag{A6}$$

Let us choose $S^1\cdots S^{N-1}$ as $\sigma^2\cdots\sigma^n$ and Σ to be σ^N. Expanding the determinant $|\det(\nabla S^1, \cdots, \nabla S^{N-1}, \nabla\Sigma)|$ along its last row we obtain

$$n = \int dx d^N x_k \cdots P(x, x_k, \cdots)\delta_{\rm D}(S^1)\cdots\delta_{\rm D}(S^{N-1})\delta_{\rm D}(\Sigma)\left|\sum_k M^k\ \nabla_k\Sigma\right|\,, \tag{A7}$$

where

$$M^k = (-1)^{k+1}\det\left(\nabla_l S^i\right)_{l=1,\ldots,k-1,k+1,\ldots,N}^{i=1,\ldots,N-1} = \sum_{l_1,\ldots,l_{N-1}} \epsilon^{k,l_1,\ldots,l_{N-1}}\nabla_{l_1}S^1\ldots\nabla_{l_{N-1}}S^{N-1} \tag{A8}$$

are the corresponding minors. By design the $\Sigma = 0$ surface is to be orthogonal to the line and therefore its normal $\boldsymbol{\nabla}\Sigma$ and the "vector" $\mathbf{M} \equiv (M^k)$ are parallel,

$$\left|\sum_k M^k\ \nabla_k\Sigma\right| = |\mathbf{M}|\,|\boldsymbol{\nabla}\Sigma| \quad .$$

Without loss of generality, we can consider the intersection point to be at $\mathbf{r} = 0$ and take $\Sigma = \mathbf{e}_\Sigma\cdot\mathbf{r}$ where $\mathbf{e}_\Sigma$ is the unit vector in the local direction of the filament, hence $|\boldsymbol{\nabla}\Sigma| = 1$. The average (N-1)D number density of intersection points on Σ surface that gives us the average flux $\mathcal{L}$ is obtained by integrating the volume number density over the coordinate along $\mathbf{e}_\Sigma$, $z = \mathbf{e}_\Sigma\cdot\mathbf{r}$, with $\delta_D(\Sigma)$ in equation (A7) properly counting exactly one intersection per line

$$\mathcal{L} \equiv \int n\ d(\mathbf{e}_\Sigma\cdot\mathbf{r}) = \int dx d^N x_k \cdots P(x, x_k, \cdots)\delta_{\rm D}(S^1)\cdots\delta_{\rm D}(S^{N-1})\,|\mathbf{M}| \quad . \tag{A9}$$

To apply this general formula to the critical lines one must choose an arbitrary subset of $N-1$ linearly independent $\nabla S^{i_1,i_2,\ldots,i_{N-2}}$ from the set of all C_N^2 of them.

Note that one can also think of $\mathcal{L}$ as the average length of lines per unit volume, which is the interpretation we focus on in the main text.

A2 Stiff critical lines in ND

In the theory of ND critical lines, the N-1 independent functions S^i that define the critical condition (A2) acquire the following simple form in the eigenframe of the Hessian of the field

$$s^i = x_a x_i\,(\lambda_a - \lambda_i) = 0, \quad i \neq a \quad . \tag{A10}$$

Here a is the index of the Hessian eigenvector that the gradient is aligned with, as is obvious from the solution $x_i = 0$, $i \neq a$.

In the stiff approximation, the gradients ${s^i}_k \equiv \nabla s^i$ have just two non-zero components, ${s^i}_a = x_i\lambda_a(\lambda_a - \lambda_i)$ (which vanishes on the critical line) and ${s^i}_i = x_a\lambda_i(\lambda_a - \lambda_i)$. The vector that determines the direction of the critical line becomes

$$M^k = x_a^{N-2}x_k\prod_{i\neq k}\lambda_i\prod_{i\neq a}(\lambda_a - \lambda_i) \quad . \tag{A11}$$

On the critical line, it has just one non-vanishing component

$$M^a = x_a^{N-1}\prod_{i\neq a}\lambda_i\,(\lambda_a - \lambda_i) = |\mathbf{M}|\,, \tag{A12}$$

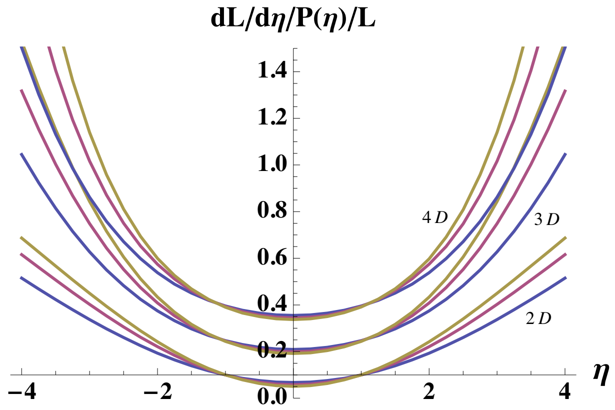

Figure A1. $\partial\mathcal{L}/\partial\eta/P(\eta)/L$ in 2D, 3D and 4D as labeled for the spectral parameter values $\gamma = 0.57, 0.65, 0.70$ (*from bottom to top*). These quantities are derived here by direct numerical integration of equation (A18). The different bundles corresponding to different dimensions have been shifted down (by 0.3 for 2D and 0.15 for 3D) for clarity. Note the change in the power of the asymptotic curves.

which shows that in the stiff approximation we equate the direction of the line with the gradient of the field. Substituting this expression into equation (A9) and integrating over $\delta_{\rm D}(s^i) = \delta_{\rm D}(x_i)/(x_a(\lambda_a - \lambda_i))$ we obtain a simple expression for the flux of the critical lines in the stiff approximation

$$\mathcal{L} = \int dx dx_{kl} P(x, 0, x_{kl}) \left|\prod_{i\neq a} \lambda_i\right| \quad . \tag{A13}$$

i.e the flux of critical lines (or the length per unit volume) is given by the average absolute value of the Gaussian curvature of the field in the space orthogonal to the skeleton.

Let us write the probability of measuring the set $\{\lambda_i\}$ as

$$\prod_{i\leqslant \rm N} d\lambda_i \prod_{i<j} (\lambda_i - \lambda_j) \exp\left(-\frac{1}{2} Q_\gamma(\eta, \{\lambda_i\})\right) , \tag{A14}$$

where Q_γ is a quadratic form in λ_i and η which functional form is

$$Q_\gamma(\eta, \{\lambda_i\}) = \eta^2 + \frac{\left(\sum_i \lambda_i + \gamma\eta\right)^2}{(1-\gamma^2)} + \mathcal{Q}_N(\{\lambda_i\}) , \tag{A15}$$

and $\prod_{i<j}(\lambda_i - \lambda_j)$ is the Jacobian of the transformation to the Hessian eigenframe. Here $\mathcal{Q}_N$ involves polynomial combinations of the eigenvalues of the traceless part of the Hessian (see Appendix D):

$$\mathcal{Q}_N(\{x_{ij}\}) = \frac{N(N+2)}{2} \sum_{ij} \overline{x}_{ij}\overline{x}_{ij} , \quad \text{with} \quad \overline{x}_{ij} = x_{ij} - \delta_{ij}\frac{1}{N}\sum_i x_{ii} , \tag{A16}$$

which can be rearranged explicitly in terms of λs as:

$$\mathcal{Q}_N(\{\lambda_i\}) = (N+2)\left[\frac{1}{2}(N-1)\sum_i \lambda_i^2 - \sum_{i\neq j}\lambda_i\lambda_j\right] . \tag{A17}$$

It now follows that the differential length of the ND-critical lines is for the stiff approximation:

$$\frac{\partial \mathcal{L}^{\rm ND}}{\partial \eta} \propto \left(\frac{1}{R_*}\right)^{N-1} \frac{1}{\sqrt{1-\gamma^2}} \int \cdots \int \prod_{i\leqslant n} d\lambda_i \prod_{i<j}(\lambda_i - \lambda_j) \left|\prod_{i>1}\lambda_i\right| \exp\left(-\frac{1}{2}Q_\gamma(\eta, \{\lambda_i\})\right) . \tag{A18}$$

Equation (A18) is the formal generalization of equations (30) and (49). For the ND-skeleton, equation (A18) also holds but the integration region should be restricted to the corresponding condition on the sign of the eigenvalues. Since the argument of Q_γ is extremal as a function of η when $\gamma\eta \sim \sum_i \lambda_i$, the largest contribution at large $\gamma\eta$ in the integral should arise when $\lambda_i \propto \gamma\eta$ since near the maximum at high contrast all eigen values are equal (Pichon & Bernardeau 1999). Hence given that $\prod_{i<j}(\lambda_i - \lambda_j)$ is the measure, the only remaining contribution in the integrand comes from $\left|\prod_{i>1}\lambda_i\right| \propto (\lambda\eta)^{N-1}$, and the dominant term at large η is given by

$$\frac{\partial \mathcal{L}^{\rm ND}}{\partial \eta} \overset{\gamma\eta\to\infty}{\sim} \frac{1}{\sqrt{2\pi}} \exp\left[-\frac{1}{2}\eta^2\right] \left(\frac{\eta}{R_0}\right)^{N-1} ,$$

where $R_0 = R_*/\gamma$ is defined in equation (3).

APPENDIX B: SECONDARY CRITICAL LINES IN 2D

In this Appendix we present a study of asymptotic behaviour of the lengths statistics of secondary critical lines for 2D Gaussian field. Secondary critical lines are the ones that have a gradient of the field aligned with the Hessian eigenvector that corresponds to the largest by magnitude eigenvalue, i.e with the direction of maximum curvature of the field. In 2D, this is the direction of λ_2 in the skeleton region, $|\lambda_1| < |\lambda_2|$, and is the direction of λ_1 in the anti-skeleton region. We shall explicitly consider the first type, realizing that the second type is a mirror case with $\eta \to -\eta$.

Our starting point is the part of expression (27) that corresponds to the lines where the gradient is aligned with the second eigen-direction, in the region when they are secondary, $\tilde{u} > 0$

$$\frac{\partial \mathcal{L}^{\rm sec}}{\partial \eta} = \frac{4\sqrt{2}}{(2\pi)^{3/2}\sqrt{1-\gamma^2}} \exp\left[-\eta^2/2\right] \int_0^\infty d\tilde{w}\tilde{w} \int_0^\infty d\tilde{u}\, |2\tilde{w}-\tilde{u}| \exp\left[-\frac{(\tilde{u}-\gamma\eta)^2}{2(1-\gamma^2)} - 4\tilde{w}^2\right] \quad . \tag{B1}$$

The absolute value of the transverse to the gradient curvature $2\lambda_1 = 2\tilde{w} - \tilde{u}$ is evaluated differently for $\tilde{u} \leqslant 2\tilde{w}$ and $\tilde{u} > 2\tilde{w}$. It is convenient to make the inner integration to be over $\tilde{w}$, since it can be carried out analytically. The integral splits into two terms

$$\frac{\partial \mathcal{L}^{\rm sec}}{\partial \eta} = \frac{4\sqrt{2}}{(2\pi)^{3/2}\sqrt{1-\gamma^2}} \exp\left[-\eta^2/2\right] (I_1 + I_2) \ , \tag{B2}$$

where

$$I_1 = \int_0^\infty d\tilde{u} \exp\left[-\frac{(\tilde{u}-\gamma\eta)^2}{2(1-\gamma^2)}\right] \int_{\tilde{u}/2}^\infty \tilde{w}(2\tilde{w}-\tilde{u}) d\tilde{w} e^{-4\tilde{w}^2} = \frac{\sqrt{\pi}}{16} \int_0^\infty d\tilde{u} \exp\left[-\frac{(\tilde{u}-\gamma\eta)^2}{2(1-\gamma^2)}\right] \mathrm{Erfc}(\tilde{u})\,, \tag{B3}$$

$$I_2 = \int_0^\infty d\tilde{u} \exp\left[-\frac{(\tilde{u}-\gamma\eta)^2}{2(1-\gamma^2)}\right] \int_0^{\tilde{u}/2} \tilde{w}(\tilde{u}-2\tilde{w}) d\tilde{w} e^{-4\tilde{w}^2} = \frac{\sqrt{\pi}}{16} \int_0^\infty d\tilde{u} \exp\left[-\frac{(\tilde{u}-\gamma\eta)^2}{2(1-\gamma^2)}\right] \left[\frac{2}{\sqrt{\pi}}\tilde{u} - \mathrm{Erf}(\tilde{u})\right] . \tag{B4}$$

so that finally

$$\frac{\partial \mathcal{L}^{\rm sec}}{\partial \eta} = \frac{1}{4\pi^{3/2}\sqrt{1-\gamma^2}} \exp\left[-\eta^2/2\right] \int_0^\infty d\tilde{u}\, \exp\left[-\frac{(\tilde{u}-\gamma\eta)^2}{2(1-\gamma^2)}\right] \left[\tilde{u} - \sqrt{\frac{\pi}{4}}\mathrm{Erf}(\tilde{u}) + \sqrt{\frac{\pi}{4}}\mathrm{Erfc}(\tilde{u})\right] \quad . \tag{B5}$$

The integrated length of critical lines $L^{\rm sec}$ is obtained by marginalization over all threshold values η. Performing this integration first

$$L^{\rm sec} = \frac{1}{2\sqrt{2\pi}} \int_0^\infty d\tilde{u} \exp\left[-\frac{\tilde{u}^2}{2}\right] \left[\tilde{u} - \sqrt{\frac{\pi}{4}}\mathrm{Erf}(\tilde{u}) + \sqrt{\frac{\pi}{4}}\mathrm{Erfc}(\tilde{u})\right] = \frac{\sqrt{2} - \mathrm{ArcCot}(2\sqrt{2})}{4\pi} = 0.08550 \tag{B6}$$

Thus secondary critical lines are on average almost three times rarer that the primary ones.

B1 Special cases: $\eta \to \infty$

At high density thresholds the leading asymptotic behaviour for $\gamma\eta \gg 1$ is obtained by using $\frac{1}{\sqrt{2\pi(1-\gamma^2)}} \exp\left[-\frac{(\tilde{u}-\gamma\eta)^2}{2(1-\gamma^2)}\right] \stackrel{\eta\to\infty}{\to} \delta_{\rm D}(\tilde{u}-\gamma\eta)$. Therefore

$$\frac{\partial \mathcal{L}^{\rm sec}}{\partial \eta} \stackrel{\eta\to\infty}{\sim} \frac{1}{\sqrt{2\pi}} \exp\left[-\eta^2/2\right] \frac{1}{4} \left(\frac{2}{\sqrt{\pi}}\gamma\eta - 1\right) \quad . \tag{B7}$$

B2 Special cases: $\eta \to 0$

At small threshold η series representation

$$\exp\left[-\frac{(\tilde{u}-\gamma\eta)^2}{2(1-\gamma^2)}\right] = \exp\left[-\frac{\tilde{u}^2}{2(1-\gamma^2)}\right] \sum_{n=0}^\infty \frac{1}{n!(1-\gamma^2)^{n/2}} H_n\left(\frac{\tilde{u}}{\sqrt{1-\gamma^2}}\right) (\gamma\eta)^n \ , \tag{B8}$$

where Hermite polynomials H_{2n} are taken in probabilistic notation, gives

$$\frac{\partial \mathcal{L}^{\rm sec}}{\partial \eta}(\eta \to 0) = \frac{1}{\sqrt{2\pi}} \exp\left[-\eta^2/2\right] \sum_{n=0}^\infty A_n (\gamma\eta)^n \quad \text{where}$$

$$A_n \equiv \frac{1}{2\sqrt{2\pi}n!(1-\gamma^2)^{n/2}} \int_0^\infty d\bar{u} \exp\left[-\bar{u}^2/2\right] H_n(\bar{u}) \left(\sqrt{1-\gamma^2}\bar{u} - \sqrt{\frac{\pi}{4}}\mathrm{Erf}\left[\sqrt{1-\gamma^2}\bar{u}\right] + \sqrt{\frac{\pi}{4}}\mathrm{Erfc}\left[\sqrt{1-\gamma^2}\bar{u}\right]\right) \tag{B9}$$

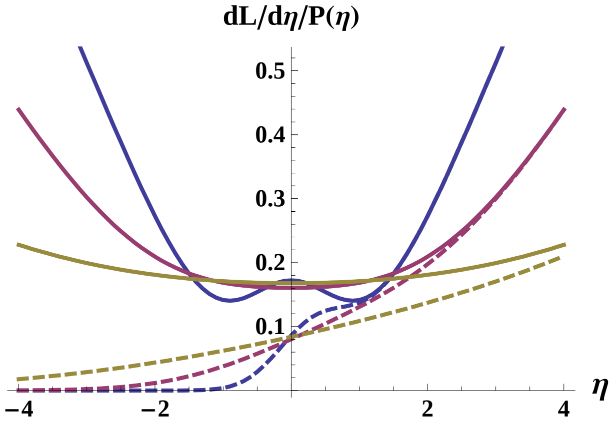

Figure B1. Differential length of the secondary critical lines $\partial\mathcal{L}/\partial\eta/\mathrm{PDF}$ in 2D for the complete set (solid) and the ones with $\nabla\rho$ aligned with λ_2 direction in the skeleton $|\lambda_1| \leqslant |\lambda_2|$ region (dashed). Different curves from purple to green correspond to the spectral parameter values $\gamma = 0.3, 0.6, 0.95$.

The first three coefficients are

$$
\begin{aligned}
A_0 &= \frac{\sqrt{2(1-\gamma^2)} + \mathrm{acot}[\sqrt{2(1-\gamma^2)}] - \mathrm{atan}[\sqrt{2(1-\gamma^2)}]}{4\pi} , \\
A_1 &= \frac{1}{4\sqrt{\pi}} \left(1 + \frac{1}{\sqrt{2(1-\gamma^2)}} - \frac{2}{\sqrt{(3-2\gamma^2)}} \right) , \\
A_2 &= \frac{\sqrt{2}}{8\pi} \frac{1-2\gamma^2}{3-2\gamma^2} (1-\gamma^2)^{-\frac{1}{2}} ,
\end{aligned}
\tag{B10}
$$

If we add all secondary critical lines, the odd power terms of the expansion (B8) cancel, while the even double recovering symmetrical behaviour of the differential length with the threshold. In Figure B1 this behaviour is illustrated.

Under our definition of the secondary critical lines, for $\gamma > 1/\sqrt{2}$ there is an excess of critical lines near zero threshold. The curvature at $\eta = 0$ is positive and diverges in the limit $\gamma \to 1$ when our series expansion formally fails. This divergence in the second derivative of the differential length is exactly opposite the one the primary lines demonstrate in this limit. We should emphasize, that near $\eta = 0$ the behaviour of critical lines of individual type depend significantly on how exactly they are defined.

APPENDIX C: ASYMPTOTIC BEHAVIOUR OF CRITICAL LINES IN 3D

There are four regions with the different signs of sorted eigenvalues in 3D: I — ($0 > \lambda_1 \geqslant \lambda_2 \geqslant \lambda_3$), II — ($\lambda_1 \geqslant 0, 0 > \lambda_2 \geqslant \lambda_3$), III — ($\lambda_1 \geqslant \lambda_2 \geqslant 0, 0 > \lambda_3$) and IV — ($\lambda_1 \geqslant \lambda_2 \geqslant \lambda_3 \geqslant 0$). Since $\tilde{w}$ is non-negative, the correspondent zones of integration for equations (48) and (49) are easy to visualize in $(\tilde{v}, \tilde{u})$ plane (see Figure C1). The integration limits and the integrand acquire the following form

$$
\left.
\begin{aligned}
I: &\int_0^\infty d\tilde{w} \int_{-\tilde{w}}^{\tilde{w}} d\tilde{v} \int_{-\tilde{v}+3\tilde{w}}^{\infty} d\tilde{u} \left[\frac{1}{3}\tilde{u}^2 - \frac{1}{3}\tilde{v}^2 - \tilde{w}^2 \right] \\
II: &\int_0^\infty d\tilde{w} \int_{-\tilde{w}}^{\tilde{w}} d\tilde{v} \int_{2\tilde{v}}^{-\tilde{v}+3\tilde{w}} d\tilde{u} \left[\tilde{w}^2 - \frac{1}{9}(\tilde{u}+\tilde{v})^2 + \frac{2}{3}\tilde{w}(\tilde{u}-2\tilde{v}) \right] \\
III: &\int_0^\infty d\tilde{w} \int_{-\tilde{w}}^{\tilde{w}} d\tilde{v} \int_{-\tilde{v}-3\tilde{w}}^{2\tilde{v}} d\tilde{u} \left[\tilde{w}^2 - \frac{1}{9}(\tilde{u}+\tilde{v})^2 - \frac{2}{3}\tilde{w}(\tilde{u}-2\tilde{v}) \right] \\
IV: &\int_0^\infty d\tilde{w} \int_{-\tilde{w}}^{\tilde{w}} d\tilde{v} \int_{-\infty}^{-\tilde{v}-3\tilde{w}} d\tilde{u} \left[\frac{1}{3}\tilde{u}^2 - \frac{1}{3}\tilde{v}^2 - \tilde{w}^2 \right]
\end{aligned}
\right\} \times \tilde{w}\left(\tilde{w}^2 - \tilde{v}^2\right) \exp\left[-\frac{(\tilde{u}-\gamma\eta)^2}{2(1-\gamma^2)} - \frac{15}{2}\tilde{w}^2 - \frac{5}{2}\tilde{v}^2 \right] .
\tag{C1}
$$

Changing variables $\tilde{u} \to -\tilde{u}, \tilde{v} \to -\tilde{v}$ in III and IV one can combine the last two cases with the first two

$$
\left.
\begin{aligned}
I+IV: &\int_0^\infty d\tilde{w} \int_{-\tilde{w}}^{\tilde{w}} d\tilde{v} \int_{3\tilde{w}-\tilde{v}}^{\infty} d\tilde{u} \left[\frac{1}{3}\tilde{u}^2 - \frac{1}{3}\tilde{v}^2 - \tilde{w}^2 \right] \\
II+III: &\int_0^\infty d\tilde{w} \int_{-\tilde{w}}^{\tilde{w}} d\tilde{v} \int_{2\tilde{v}}^{3\tilde{w}-\tilde{v}} d\tilde{u} \left[\tilde{w}^2 - \frac{1}{9}(\tilde{u}+\tilde{v})^2 + \frac{2}{3}\tilde{w}(\tilde{u}-2\tilde{v}) \right]
\end{aligned}
\right\} \times \tilde{w}\left(\tilde{w}^2 - \tilde{v}^2\right) \exp\left[-\frac{15}{2}\tilde{w}^2 - \frac{5}{2}\tilde{v}^2 \right] \Phi_\gamma(\tilde{u}, \eta) .
\tag{C2}
$$

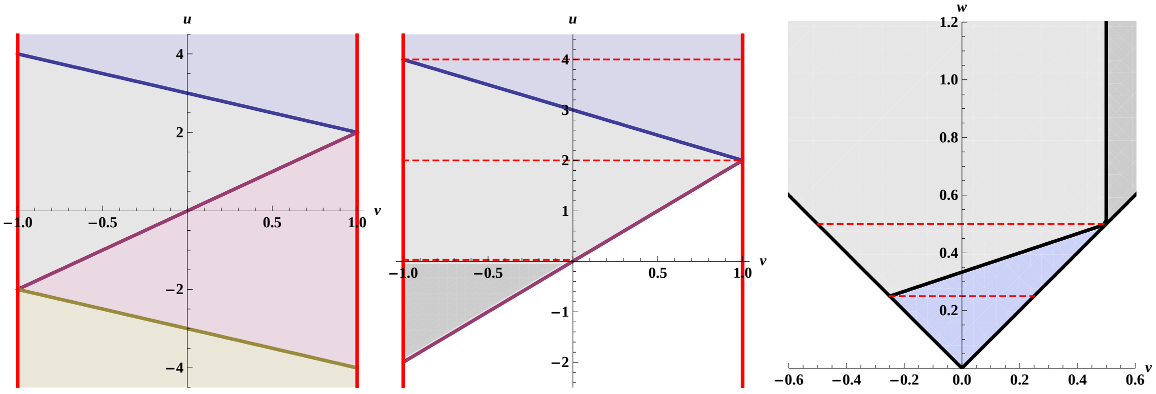

Figure C1. *Left*: Integration zones in $\tilde{v}, \tilde{u}$ plane based on the signs of the eigenvalues. Variables are given in units of $\tilde{w}$. Here $\tilde{v}$ varies from $-\tilde{w}$ to $+\tilde{w}$, while $\tilde{u}$ is unrestricted. Three inclined lines are (from top to bottom) a) $\lambda_1 = 0 \Rightarrow \tilde{u} = -\tilde{v} + 3\tilde{w}$, b) $\lambda_2 = 0 \Rightarrow \tilde{u} = 2\tilde{v}$ and c) $\lambda_3 = 0 \Rightarrow \tilde{u} = -\tilde{v} - 3\tilde{w}$. In the upper sector I (that stretches to infinity in $\tilde{u}$) $(0 > \lambda_1 \geqslant \lambda_2 \geqslant \lambda_3)$, next is the zone II $(\lambda_1 \geqslant 0, 0 > \lambda_2 \geqslant \lambda_3)$, then III $(\lambda_1 \geqslant \lambda_2 \geqslant 0, 0 > \lambda_3)$, and, finally extending to minus infinity in $\tilde{u}$ is the sector IV where $(\lambda_1 \geqslant \lambda_2 \geqslant \lambda_3 \geqslant 0)$. *Centre*: two zones of integration after variable change leading to equation (C2). Horizontal dashed lines mark the further subdivision of the integration space if the order of integration is changed according to equation (C5). *Right*: Integration zones in the $(\tilde{v}, \tilde{w})$ plane after $\tilde{u}$ has been mapped to the $[0-\infty]$ interval. Variables are given in units of $\tilde{u}$. The lower triangular zone corresponds to semi-open upper band in $\tilde{v} - \tilde{u}$ of the centre panel. In this region, the integrand is given by the terms I+III of equation (C2). Vice-versa, the open upper band in the $(\tilde{v}, \tilde{w})$ plane corresponds to the II+IV integration over the lower triangular zone in the $\tilde{v} - \tilde{u}$ space. The right-most sector of this region, however, corresponds to negative $\tilde{u}$, so the integrand in this sector has coordinate change $\tilde{u} \to -\tilde{u}, \tilde{v} \to -\tilde{v}$ The dashed lines show the subdivided integrals given in equation (C5), which corresponds to subdivisions in the centre panel.

where

$$\Phi_\gamma(\tilde{u}, \eta) = \exp\left[-\frac{(\tilde{u} - \gamma\eta)^2}{2(1-\gamma^2)}\right] + \exp\left[-\frac{(\tilde{u} + \gamma\eta)^2}{2(1-\gamma^2)}\right] .$$

Direct evaluation of the integrated length gives

$$L = 0.289627 \; (\times R_*^{-2}) \quad . \tag{C3}$$

To study high threshold regime it is advantageous to make the $\tilde{u}$ integration the outmost one, since it depends on the variable threshold

$$I + IV: \quad \int_0^\infty d\tilde{w} \int_{-\tilde{w}}^{\tilde{w}} d\tilde{v} \int_{3\tilde{w}-\tilde{v}}^\infty d\tilde{u} \to \int_0^\infty d\tilde{u} \int_0^{\tilde{u}/4} d\tilde{w} \int_{-\tilde{w}}^{\tilde{w}} d\tilde{v} + \int_0^\infty d\tilde{u} \int_{\tilde{u}/4}^{\tilde{u}/2} d\tilde{w} \int_{3\tilde{w}-\tilde{u}}^{\tilde{w}} d\tilde{v} \tag{C4}$$

$$II + III: \quad \int_0^\infty d\tilde{w} \int_{-\tilde{w}}^{\tilde{w}} d\tilde{v} \int_{2\tilde{v}}^{3\tilde{w}-\tilde{v}} d\tilde{u} \to \int_0^\infty d\tilde{u} \int_{\tilde{u}/4}^{\tilde{u}/2} d\tilde{w} \int_{-\tilde{w}}^{3\tilde{w}-\tilde{u}} d\tilde{v} + \int_0^\infty d\tilde{u} \int_{\tilde{u}/2}^\infty d\tilde{w} \int_{-\tilde{w}}^{\tilde{u}/2} d\tilde{v} + \int_0^\infty d\tilde{u} \int_{\tilde{u}/2}^\infty d\tilde{w} \int_{\tilde{u}/2}^{\tilde{w}} d\tilde{v} (\tilde{u}, \tilde{v} \to -\tilde{u}, -\tilde{v}) \quad .$$

The parenthesis in the last term indicate the substitution that must be performed in the integrand. Right panel in Figure C1 illustrates the integration zones now in the $(\tilde{v}, \tilde{w})$ plane.

Although one can perform the $\tilde{v}$ integral analytically and reduce the problem to two-dimensional integration, the resulting expression is too cumbersome. We can obtain useful limits already from unreduced formulae. In particular, at high density threshold, $\gamma\eta \to \infty$, only the first integral in the term (C4), which contains $\tilde{w}, \tilde{v} \sim 0$ neighbourhood, is not exponentially small. Moreover, in the leading order the upper limit of the integral over $\tilde{w}$ can be set to infinity.

$$\frac{\partial \mathcal{L}}{\partial \eta} \overset{\gamma\eta\to\infty}{\sim} \frac{3^2 5^{5/2}}{4\pi^2 \sqrt{2\pi(1-\gamma^2)}} \exp\left[-\frac{1}{2}\eta^2\right] \int_0^\infty d\tilde{u} \int_0^\infty d\tilde{w} \int_{-\tilde{w}}^{\tilde{w}} d\tilde{v} \tilde{w}(\tilde{w}^2 - \tilde{v}^2) \left[\tilde{u}^2 - \tilde{v}^2 - 3\tilde{w}^2\right] \exp\left[-\frac{(\tilde{u}-\gamma\eta)^2}{2(1-\gamma^2)} - \frac{15}{2}\tilde{w}^2 - \frac{5}{2}\tilde{v}^2\right]$$

$$\overset{\gamma\eta\to\infty}{\sim} \frac{1}{\sqrt{2\pi}} \exp\left[-\frac{1}{2}\eta^2\right] \frac{(\gamma\eta)^2 - \gamma^2}{2\pi} . \tag{C5}$$

APPENDIX D: JOINT DISTRIBUTION OF THE FIELD AND ITS DERIVATIVES FOR A GRF

The joint point distribution functions that are needed for the study of the critical lines in this paper are $P_0(x, x_{kl})$ and $P_1(x_i, x_{ijk})$, taking into account that for Gaussian random field there is no cross-correlation between odd order derivatives and the field itself or even order derivatives. When considering the curvature of the critical lines, fourth order derivatives, and, thus, more general $P_0(x, x_{kl}, x_{klmn})$ have to be considered. Some well known results in 2D and 3D are first summarized in section D1. More general results can be obtained by resorting to a general framework which is sketched in section D2 and applied in section D3 for the various cases of interest.

D1 Lower order joint distributions

Distribution of the Gaussian field and its second derivative in 3D. The full expression for $P_0(x, x_{kl})$ for the Gaussian field is given in Bardeen et al. (1986). Introducing the variables

$$u \equiv -\Delta x = -(x_{11} + x_{22} + x_{33}) , \quad w \equiv \frac{1}{2}(x_{11} - x_{33}) , \quad v \equiv \frac{1}{2}(2x_{22} - x_{11} - x_{33}) , \tag{D1}$$

in place of diagonal elements of the Hessian (x_{11}, x_{22}, x_{33}) one finds that $u, v, w, x_{12}, x_{13}, x_{23}$ are uncorrelated. Importantly, the field, x is only correlated with $u = \Delta x$ and

$$\langle xu \rangle = \gamma, \quad \langle xv \rangle = 0, \quad \langle xw \rangle = 0, \quad \langle x x_{kl} \rangle = 0, \ k \neq l, \tag{D2}$$

where γ is the same quantity as in equation (5). The full expression of $P_0(x, x_{kl})$ is then

$$P_0(x, x_{kl}) dx d^6 x_{kl} = \frac{5^{1/2} 15^2}{(2\pi)^{7/2}(1-\gamma^2)^{1/2}} \exp\left(-\frac{1}{2} \left[Q_0(x,u) + Q_2(v, w, x_{12}, x_{13}, x_{23}) \right] \right) dx\, du\, dv\, dw\, dx_{12}\, dx_{13}\, dx_{23} \,,$$

with the quadratic forms Q_0 and Q_2 given by

$$Q_0 = x^2 + \frac{(u-\gamma x)^2}{(1-\gamma^2)} \qquad Q_2 = 5v^2 + 15(w^2 + x_{12}^2 + x_{13}^2 + x_{23}^2). \tag{D3}$$

It depends only one a single correlation parameter: γ.

First and third derivatives of the Gaussian field in 3D. A similar procedure can be performed for the joint probability of the first and third derivatives of the fields, $P_1(x_i, x_{ijk})$ by defining the following nine parameters (see also (Hanami 2001)):

$$u_i \equiv \nabla_i u, \quad v_i \equiv \frac{1}{2} \epsilon^{ijk} \nabla_i \left(\nabla_j \nabla_j - \nabla_k \nabla_k \right) x \,, \ \text{with} \ j < k \,, \quad \text{and} \quad w_i \equiv \sqrt{\frac{5}{12}} \nabla_i \left(\nabla_i \nabla_i - \frac{3}{5} \Delta \right) x \,, \tag{D4}$$

and replacing the variables $(x_{i11}, x_{i22}, x_{i33})$ with (u_i, v_i, w_j). In that case, the only cross-correlations in the vector $(x_1, x_2, x_3, u_1, v_1, w_1, u_2, v_2, w_2, u_3, v_3, w_3, x_{123})$ which do not vanish are between the same components of the gradient and the gradient of the Laplacian of the field:

$$\langle x_i u_i \rangle \quad = \quad \tilde\gamma/3, \quad i = 1, 2, 3, \tag{D5}$$

where $\tilde\gamma$ is the same quantity as in equation (5). This allows us to write:

$$P_1(x_i, x_{ijk}) d^3 x_i \, d^{10} x_{ijk} = \frac{105^{7/2} 3^3}{(2\pi)^{13/2}(1-\tilde\gamma^2)^{3/2}} \ \exp\left(-\frac{1}{2} \left(Q_1 + Q_3 \right) \right) d^3 x_i \, d^3 u_i \, d^3 w_i \, d^3 v_i \, dx_{123}. \tag{D6}$$

with the quadratic forms:

$$Q_1 = 3 \sum_i \left(\frac{(u_i - \tilde\gamma x_i)^2}{(1-\tilde\gamma^2)} + x_i^2 \right) , \qquad Q_3 = 105 \left(x_{123}^2 + \sum_{i=1}^{3} (v_i^2 + w_i^2) \right) . \tag{D7}$$

The Gaussian field and its second derivative in 2D. Introducing the variables

$$u \equiv -\Delta x = -(x_{11} + x_{22}) , \quad w \equiv \frac{1}{2}(x_{11} - x_{22}) , \tag{D8}$$

one finds again that u, w, x_{12} are uncorrelated. The expression for $P_0(x, x_{kl})$ is then

$$P_0(x, x_{kl}) dx d^3 x_{kl} = \frac{8}{(2\pi)^2 (1-\gamma^2)^{1/2}} \exp\left(-\frac{1}{2} \left[Q_0(x,u) + Q_2(w, x_{12}) \right] \right) dx\, du\, dw\, dx_{12} \,,$$

where the quadratic forms Q_0 and Q_2 are

$$Q_0 = x^2 + \frac{(u-\gamma x)^2}{(1-\gamma^2)} , \qquad Q_2 = 8(w^2 + x_{12}^2). \tag{D9}$$

First and third derivatives of the Gaussian field in 2D. Defining the following 4 uncorrelated parameters:

$$u_i \equiv \nabla_i u, \quad w_i \equiv \nabla_i \left(\nabla_i \nabla_i - \frac{3}{4} \Delta \right) x \,, \tag{D10}$$

yields

$$P_1(x_i, x_{ijk}) d^2 x_i \, d^4 x_{ijk} = \frac{128}{(2\pi)^3 (1-\tilde\gamma^2)} \exp\left(-\frac{1}{2} \left(Q_1 + Q_3 \right) \right) d^2 x_i \, d^2 u_i d^2 w_i \ . \tag{D11}$$

with the quadratic forms:

$$Q_1 = 2\sum_{i=1}^{2}\left(\frac{(u_i-\tilde\gamma x_i)^2}{(1-\tilde\gamma^2)}+x_i^2\right), \qquad Q_3 = 32\sum_{i=1}^{2} w_i^2\,. \tag{D12}$$

It is the purpose of the next section to elucidate the nature of these quadratic forms and to show how similar expressions can be obtained for any combination of derivatives in a space of any dimension.

D2 Theory

To proceed further, a more systematic way of computing the correlations between the field derivatives is needed. This can be provided by the harmonic decomposition of symmetric tensors (such as derivative tensors). The main results are outlined hereafter, the reader being referred to Cardoso (2009) for a detailed exposition.

Harmonic decomposition of symmetric tensors. The harmonic decomposition of symmetric tensors amounts to projection onto the irreducible representations of $\mathrm{SO}(n)$. It is obtained in close form as follows. A symmetric tensor T of rank n is associated with a set $\{T^{(\ell)} \mid 0\leqslant \ell\leqslant n,\ n-\ell \text{ even}\}$ of "harmonic components" where each $T^{(\ell)}$ is a symmetric trace-free tensor of rank ℓ. Index ℓ can be understood as an *angular frequency*. We refer to it as the "frequency" of the component. The harmonic component at frequency $\ell = n-2k$ of a rank n tensor is obtained as

$$T^{(n-2k)} = \overline{\mathrm{tr}^k\, T}\,,$$

where ($\mathrm{tr}^k\cdot$) means applying k times the trace operator (contraction over any pair of indices) and where $\overline{T}$ denotes the traceless part of tensor T. In indexed notations, the first (ranks $0,\ldots,5$) de-traced tensors on R^3 are given by $\bar t = t$, $\bar t_i = t_i$, $\bar t_{ij} = t_{ij} - \frac{1}{3}t_{aa}\delta_{ij}$,

$$\bar t_{ijk} = t_{ijk} - \frac{3}{5}\,t_{aa(j}\delta_{kl)},\quad \bar t_{ijkl} = t_{ijkl} - \frac{6}{7}\,t_{aa(ij}\delta_{kl)} + \frac{3}{35}\,t_{aabb}\delta_{(ij}\delta_{kl)},\quad \bar t_{ijklm} = t_{ijklm} - \frac{10}{9}\,t_{aa(ijk}\delta_{lm)} + \frac{5}{21}\,t_{aabb(i}\delta_{jk}\delta_{lm)}\,, \tag{D13}$$

with an implicit summation over repeated indices and symmetrization between parenthesized indices (for instance: $t_{aa(j}\delta_{kl)} = [t_{aaj}\delta_{kl} + t_{aak}\delta_{lj} + t_{aal}\delta_{jk}]/3$ and so on).

Invariant statistics. Let $\mathcal{T} = \{T_0, T_1, \ldots\}$ be a set of symmetric tensors which are jointly isotropically distributed. A consequence of isotropy is frequency decoupling: $T_a^{(\ell)}$ is uncorrelated with $T_b^{(\ell')}$ if $\ell\neq\ell'$. Further, at any frequency ℓ, the scalar product $\langle T_a^{(\ell)} \mid T_b^{(\ell)}\rangle$ is invariant under rotations. It is convenient to arrange these products at frequency ℓ into a $m_\ell\times m_\ell$ Gram matrix $\widehat{R}_\ell$ where m_ℓ denotes the number of tensors in $\mathcal{T}$ having an harmonic component at frequency ℓ (this occurs whenever $\mathrm{rank}(T)-\ell$ is a non-negative even integer):

$$[\widehat{R}_\ell]_{ab} = \langle T_a^{(\ell)} \mid T_b^{(\ell)}\rangle\,,$$

where indices a and b run only over the m_ℓ relevant values (the specific ordering does not matter). A further consequence of isotropy is that, in the Gaussian case, these matrices form a set of sufficient statistics: the joint distribution of $\mathcal{T}$ can be expressed as a function of those matrices and nothing else, as seen next.

Spectral matrices. The 'spectral matrix' R_ℓ at frequency ℓ is defined as the expected value of $\widehat{R}_\ell$, that is, $R_\ell = \mathrm{E}(\widehat{R}_\ell)$. For a set $\mathcal{T}$ of symmetric random tensors with a rotationally invariant joint distribution, one finds

$$\mathcal{T}^\dagger\,\mathrm{Cov}(\mathcal{T})^{-1}\mathcal{T} = \sum_\ell w_\ell\,\mathrm{tr}\big(\widehat{R}_\ell R_\ell^{-1}\big)\,,$$

where w_ℓ is a positive scalar, which is equal to $2\ell+1$ for tensors in R^3.

Spectral matrices for a GRF. Now, we consider the case when in $\mathcal{T} = \{T_0,\ldots,T_Q\}$, the q-th tensor T_q is the q-th derivative at a given point: $t_{i_1\cdots i_n} = \partial^n\rho/\partial r_{i_1}\cdots\partial r_{i_n}$ of a stationary random field ρ with spectrum $P(\nu)$. Then $\mathcal{T}$ is a set of isotropically distributed symmetric tensors and each spectral matrix R_ℓ can be expressed as a function of the spectrum. Indeed, if $\ell-q$ and $\ell-q'$ are non negative even integers, matrix R_ℓ has an entry $[R_\ell]_{qq'}$ related to the derivatives of orders q and q' given by

$$[R_\ell]_{qq'} = (-1)^{\frac{q-q'}{2}}\, g_\ell\,\sigma^2_{\frac{q+q'}{2}}\,,$$

with the spectral moments σ_p^2 defined at eq. (4). The geometric factor g_ℓ is the squared ratio $g_\ell = (\|\overline{\xi^\ell}\|/\|\xi^\ell\|)^2$ by which the norm of the ℓ-th tensor product ξ^ℓ of any vector ξ is decreased upon detracing. It is equal to $g_\ell = \ell!/(2\ell-1)!!$ in dimension $D=3$. We do not provide explicit expressions for w_l and g_ℓ in arbitrary dimension since only their ratio w_ℓ/g_ℓ is needed and turns out to have a simpler expression than either w_ℓ or g_ℓ:

$$\frac{w_\ell}{g_\ell} = \frac{(2\ell+D-2)!!}{\ell!\ (D-2)!!}\,. \tag{D14}$$

Some precomputed values are listed in Table D1.

	$\ell=0$	$\ell=1$	$\ell=2$	$\ell=3$	$\ell=4$	$\ell=5$
D=2	1	2	4	8	16	32
D=3	1	3	15/2	35/2	315/8	693/8
D=4	1	4	12	32	80	192
D=5	1	5	35/2	105/2	1155/8	3003/8

Table D1. Values of $w_\ell/g_\ell=(2\ell+D-2)!!/(\ell!\ (D-2)!!)$ in dimensions $D=2,3,4,5$ for $0\leqslant\ell\leqslant 5$.

Summary and rescaled forms. We collect all previous results into a normalized form. Using the normalized spectral shape parameters of def. (5) and normalized derivative tensors X_n defined as:

$$X_n=\frac{1}{\sigma_n}\nabla^n\rho\,,\qquad i.e.\qquad x_{i_1\cdots i_n}=\sigma_n^{-1}\frac{\partial^n\rho}{\partial r_{i_1}\cdots\partial r_{i_n}}\,,$$

one finds that

$$\mathcal{X}^\dagger\,\mathrm{Cov}(\mathcal{X})^{-1}\mathcal{X}=\sum_\ell\frac{(2\ell+D-2)!!}{\ell!\ (D-2)!!}\ \mathrm{tr}\big(\widehat{\Gamma}_\ell\Gamma_\ell^{-1}\big)\,,\quad\text{with}\quad[\widehat{\Gamma}_\ell]_{pq}=\big\langle X_p^{(\ell)}\mid X_q^{(\ell)}\big\rangle\quad\text{and}\quad[\Gamma_\ell]_{pq}=(-1)^{\frac{p-q}{2}}\gamma_{p,q}\,.\tag{D15}$$

Note that the diagonal entries of Γ_ℓ are always equal to 1.

Special cases and smaller statistics. Our approach compresses a set of derivative tensors into a set $\widehat{\Gamma}_\ell$ of symmetric matrices of size $m_\ell\times m_\ell$, yielding $\sum_\ell m_\ell(m_\ell+1)/2$ invariant scalars. There are two special cases where even smaller invariant sufficient statistics can be found.

First, at angular frequency $\ell=0$, the detraced tensors are just scalars so that, for $\ell=0$, one has $[\widehat{\Gamma}_0]_{pq}=\big\langle X_p^{(0)}\mid X_q^{(0)}\big\rangle=X_p^{(0)}X_q^{(0)}$. Therefore $\widehat{\Gamma}_0$ actually is a rank-one matrix: $\widehat{\Gamma}_0=vv^\dagger$ where the entries of vector v are $v_p=X_p^{(0)}$. Hence, at the null frequency, we can further compress the $m_0(m_0+1)/2$ statistics (the non-redundant entries of $\widehat{\Gamma}_0$) into m_0 scalars (the entries of v). Of course, the $\ell=0$ term in the quadratic form also reads:

$$\mathrm{tr}\big(\widehat{\Gamma}_0\Gamma_0^{-1}\big)=v^\dagger\Gamma_0^{-1}v.\tag{D16}$$

Second, there are several cases of interest where $m_\ell=2$. This happens for instance at $\ell=0$ with derivative orders 0 and 2, at $\ell=1$ when considering derivatives of order 1 and 3, at $\ell=2$ with derivatives of orders 0,2 and 4, etc. Then, for such an ℓ,

$$\mathrm{tr}\big(\widehat{\Gamma}_\ell\Gamma_\ell^{-1}\big)=\mathrm{tr}\Big(\begin{bmatrix}\langle a\mid a\rangle & \langle a\mid b\rangle\\ \langle b\mid a\rangle & \langle b\mid b\rangle\end{bmatrix}\begin{bmatrix}1 & -\gamma\\ -\gamma & 1\end{bmatrix}^{-1}\Big)$$

where a and b are rank-ℓ tensors and γ is a scalar. Simple algebra yields

$$\mathrm{tr}\big(\widehat{\Gamma}_\ell\Gamma_\ell^{-1}\big)=\|a\|^2+\frac{\|b+\gamma a\|^2}{1-\gamma^2}\,,\tag{D17}$$

that is, a form ubiquitous in this paper. However, an equivalent, more regular form is

$$\mathrm{tr}\big(\widehat{\Gamma}_\ell\Gamma_\ell^{-1}\big)=\frac{1}{1-\gamma^2}\left(\|a\|^2+\|b\|^2\right)+\frac{2\gamma}{1-\gamma^2}\ \langle a\mid b\rangle\,,$$

which has the benefit of stressing that, at such ℓ, a sufficient statistic is only made of *two* invariant scalars, namely $\|a\|^2+\|b\|^2$ and $\langle a\mid b\rangle$. In the limit of weak correlation $\gamma\to 0$, one has, of course, $\mathrm{tr}\big(\widehat{\Gamma}_\ell\Gamma_\ell^{-1}\big)=\|a\|^2+\|b\|^2$. An even more symmetric form, which stresses the decorrelation between $a+b$ and $a-b$ is

$$\mathrm{tr}\big(\widehat{\Gamma}_\ell\Gamma_\ell^{-1}\big)=\frac{\|a+b\|^2}{2(1-\gamma)}+\frac{\|a-b\|^2}{2(1+\gamma)}.$$

D3 Some applications

We now work out these expressions in some cases of interest.

Derivative of orders 0+2 in 3D. The case $\mathcal{X}=\{X_0,X_2\}$ is the simplest non-trivial case. The theory sketched at sec. D2 applies straightforwardly. In the notations of section D2], we are concerned with frequencies $\ell=0$ and $\ell=2$ for which, in 3D, $w_0/g_0=1$, $w_2/g_2=15/2$ (see table D1). The quadratic form (D15) then reduces to $\mathrm{tr}\big(\widehat{\Gamma}_0\Gamma_0^{-1}\big)+\frac{15}{2}\,\mathrm{tr}\big(\widehat{\Gamma}_2\Gamma_2^{-1}\big)$. For $\ell=0$, we have here $m_0=2$ and we can use the specific form (D17) to work out $\mathrm{tr}\big(\widehat{\Gamma}_0\Gamma_0^{-1}\big)$ with $[a,b]=[X_0^{(0)},X_2^{(0)}]=[x,x_{aa}]$, that is the (normalized) field and the trace of its Hessian. For $\ell=2$, we have here $m_2=1$: we need only scalars. Following expressions (D15) again, we have $\widehat{\Gamma}_2=\|X_2^{(2)}\|^2=\|\bar{X}_2\|^2=\bar{x}_{ab}\bar{x}_{ab}$ and $\Gamma_2=(-)^{(2-2)/2}\gamma_{2,2}=1$. In summary:

$$Q_0+Q_2=\mathrm{tr}\big(\widehat{\Gamma}_0\Gamma_0^{-1}\big)+\frac{15}{2}\,\mathrm{tr}\big(\widehat{\Gamma}_2\Gamma_2^{-1}\big)=x^2+\frac{(x_{aa}+\gamma x)^2}{1-\gamma^2}+\frac{15}{2}\,\bar{x}_{ab}\bar{x}_{ab}\,,\tag{D18}$$

This is, of course, identical to equation (D3) using the local definitions there. It also shows that the complicated expression for Q_2 in (D3) is nothing but the the squared Euclidean norm of the detraced Hessian (with a 15/2 prefactor).

Result for orders 1+3 in 3D. We take $\mathcal{X} = \{X_1, X_3\}$, that is, the first and third order derivatives of the field. The rescaled harmonic components are

$$\left[\sigma_1^{-1} X_1^{(1)}\right]_i = x_i\,, \qquad \left[\sigma_3^{-1} X_3^{(1)}\right]_i = x_{iaa}\,, \qquad \left[\sigma_3^{-1} X_3^{(3)}\right]_{ijk} = x_{ijk} - \frac{3}{5} x_{aa(i}\delta_{jk)} = \overline{x}_{ijk}.$$

We need frequencies $\ell = 1$ and $\ell = 3$ for which, in 3D, $w_1/g_1 = 3$, $w_3/g_3 = 35/2$ (see table D1). For frequency $\ell = 1$, we have $m_\ell = 2$; matrix Γ_1 is 2×2 with entries given by equation (D15), that is, diagonal entries equal to 1 (as always) and off-diagonal entries given by $(-1)^{(1-3)/2}\gamma_{1,3} = -\tilde\gamma$. Since Γ_1 is 2×2, we can still use equation (D17) and finally obtain In summary:

$$\frac{w_1}{g_1}\,\mathrm{tr}\big(\widehat\Gamma_1\Gamma_1^{-1}\big) + \frac{w_3}{g_3}\,\mathrm{tr}\big(\widehat\Gamma_3\Gamma_3^{-1}\big) = 3\ \mathrm{tr}\left\{\begin{bmatrix} 1 & -\tilde\gamma \\ -\tilde\gamma & 1\end{bmatrix}^{-1}\begin{bmatrix} x_i x_i & x_i x_{iaa} \\ x_i x_{ibb} & x_{icc}x_{idd}\end{bmatrix}\right\} + \frac{35}{2}\,\overline{x}_{ijk}\overline{x}_{ijk} \tag{D19}$$

$$= 3\left(x_i x_i + \frac{(x_{iaa} - \tilde\gamma x_i)(x_{ibb} - \tilde\gamma x_i)}{1-\tilde\gamma^2}\right) + \frac{35}{2}\,\overline{x}_{ijk}\overline{x}_{ijk}\,. \tag{D20}$$

This is consistent with equation (D6) and reveals the meaning of $x_{123}^2 + \sum_{i=1}^3 (v_i^2 + w_i^2)$ as equal to $\frac{1}{6}\overline{x}_{ijk}\overline{x}_{ijk}$ *i.e.* the squared norm of the detraced third derivative tensor (with a prefactor 1/6).

The results for other combinations of derivatives can be derived in the same way. A few results are listed below without going into much detail.

Result for orders 0+2+4 in 3D. We consider $\mathcal{X} = \{X_0, X_2, X_4\}$. Hoping to improve clarity, we denote $y_{ij} = [\sigma_4^{-1} X_4^{(2)}]_{ij}$, that is, the de-traced contraction of the 4th-order derivative tensor. Explicitly, in 3D:

$$y_{ij} = x_{ijaa} - \frac{1}{3} x_{aabb}\delta_{ij}\,,$$

With this notation and recalling that $\overline{x}_{ijkl}$ denotes the traceless part of x_{ijkl} (the rescaled 4th-order derivative tensor) computed according to the prescription (D13), the quadratic form is

$$\begin{bmatrix} x \\ x_{aa} \\ x_{aabb}\end{bmatrix}^\dagger \begin{bmatrix} 1 & -\gamma & \breve\gamma \\ -\gamma & 1 & -\hat\gamma \\ \breve\gamma & -\hat\gamma & 1\end{bmatrix}^{-1}\begin{bmatrix} x \\ x_{aa} \\ x_{aabb}\end{bmatrix} + \frac{15}{2}\,\mathrm{tr}\left\{\begin{bmatrix} 1 & -\hat\gamma \\ -\hat\gamma & 1\end{bmatrix}^{-1}\begin{bmatrix} \overline{x}_{ij}\overline{x}_{ij} & \overline{x}_{ij}y_{ij} \\ \overline{x}_{ij}y_{ij} & y_{ij}y_{ij}\end{bmatrix}\right\} + \frac{315}{8}\,\overline{x}_{ijkl}\overline{x}_{ijkl}\,, \tag{D21}$$

where yet another spectral shape parameter has to be defined:

$$\breve\gamma = \frac{\sigma_2^2}{\sigma_0\sigma_4} = \frac{\tilde R \hat R}{R_0 R_\star} = \frac{\gamma\tilde\gamma^2}{\hat\gamma}\,,$$

Needless to say that expression (D18) obtained for $\mathcal{X} = \{X_0, X_2\}$ is recovered by cutting the irrelevant terms from equation (D21).

Result for orders 1+3+5 in 3D. To simplify the notations, we introduce local definitions for the derivative tensors and their contractions:

$$y_a = x_{abb}\,, \qquad z_a = x_{abbcc}\,, \qquad t_{abc} = x_{abcdd}\,,$$

and, proceeding as above, we obtain the quadratic form:

$$3\ \mathrm{tr}\left\{\begin{bmatrix} 1 & -\gamma_{1,3} & \gamma_{1,5} \\ -\gamma_{1,3} & 1 & -\gamma_{3,5} \\ \gamma_{1,5} & -\gamma_{3,5} & 1\end{bmatrix}^{-1}\begin{bmatrix} x_a x_a & x_a y_a & x_a z_a \\ y_a x_a & y_a y_a & y_a z_a \\ z_a x_a & z_a y_a & z_a z_a\end{bmatrix}\right\} + \frac{35}{2}\,\mathrm{tr}\left\{\begin{bmatrix} 1 & -\gamma_{3,5} \\ -\gamma_{3,5} & 1\end{bmatrix}^{-1}\begin{bmatrix} \bar x_{ijk}\bar x_{ijk} & \bar x_{ijk}\bar t_{ijk} \\ \bar t_{ijk}\bar x_{ijk} & \bar t_{ijk}\bar t_{ijk}\end{bmatrix}\right\} + \frac{693}{8}\,\overline{x}_{ijklm}\overline{x}_{ijklm} \tag{D22}$$

The 2D case. The theory applies to isotropic fields in any dimension. We have already provided expressions for the spectral moments (4) and the coefficients w_ℓ/g_ℓ of equation (D14). It remains to find detracing coefficients. In the 2D case, the first (ranks $0, \ldots, 5$) de-traced tensors on R^2 are given by $\overline{y} = y$, $\overline{y}_i = y_i$, $\overline{y}_{ij} = y_{ij} - \frac{1}{2} y_{aa}\delta_{ij}$,

$$\overline{y}_{ijk} = y_{ijk} - \frac{3}{4}\,y_{aa(i}\delta_{jk)}, \quad \overline{y}_{ijkl} = y_{ijkl} - y_{aa(ij}\delta_{kl)} + \frac{1}{8}\,y_{aabb}\delta_{(ij}\delta_{kl)}, \quad \overline{y}_{ijklm} = y_{ijklm} - \frac{5}{4}\,y_{aa(ijk}\delta_{lm)} + \frac{5}{16}\,y_{aabb(i}\delta_{jk}\delta_{lm)}\,. \tag{D23}$$

For the correlation between the field and its Hessian, we proceed as above in 3D with $w_0/g_0 = 1$ and $w_2/g_2 = 4$ given in table D1. Therefore the quadratic form is

$$Q_0 + Q_2 = \mathrm{tr}\big(\widehat\Gamma_0\Gamma_0^{-1}\big) + 4\,\mathrm{tr}\big(\widehat\Gamma_2\Gamma_2^{-1}\big) = x^2 + \frac{(x_{aa} + \gamma x)^2}{1-\gamma^2} + 4\,\overline{x}_{ab}\overline{x}_{ab}\,,$$

in agreement with equation (D9). For the case of first and third order derivatives, we read $w_1/g_1 = 2$ and $w_3/g_3 = 8$ from table D1 so that, similar to equation (D19), one finds

$$\frac{w_1}{g_1}\,\mathrm{tr}\big(\widehat{\Gamma}_1\Gamma_1^{-1}\big) + \frac{w_3}{g_3}\,\mathrm{tr}\big(\widehat{\Gamma}_3\Gamma_3^{-1}\big) = 2\,\mathrm{tr}\left\{\begin{bmatrix}1 & -\tilde{\gamma}\\ -\tilde{\gamma} & 1\end{bmatrix}^{-1}\begin{bmatrix}x_ix_i & x_ix_{iaa}\\ x_ix_{ibb} & x_{icc}x_{idd}\end{bmatrix}\right\} + 8\,\overline{x}_{ijk}\overline{x}_{ijk}\,, \tag{D24}$$

$$= 2\left(x_ix_i + \frac{(x_{iaa}-\tilde{\gamma}x_i)(x_{ibb}-\tilde{\gamma}x_i)}{1-\tilde{\gamma}^2}\right) + 8\,\overline{x}_{ijk}\overline{x}_{ijk}\,, \tag{D25}$$

with $\overline{x}_{ijk} = x_{ijk} - \frac{3}{4}\,x_{aa(i}\delta_{jk)}$ so that $8\overline{x}_{ijk}\overline{x}_{ijk}$ can be checked to equal Q_3 in equation (D12).

The d-dimensional case. We outline some results in the d-dimensional case. The de-tracing formulae can be extended to the d-dimensional case but, in this paper, we will content ourselves with the correlations between the field and its Hessian: $\mathcal{X} = \{X_0, X_2\}$. Therefore, we need only $\ell = 0$ and $\ell = 2$ so that de-tracing remains trivial: the normalized de-traced Hessian given by $\bar{x}_{ij} = x_{ij} - \frac{1}{d}\,\delta_{ij}\,x_{aa}$. Hence for the correlation between the field and its Hessian, we obtain the quadratic form

$$\begin{bmatrix}x\\ x_{aa}\end{bmatrix}^{\dagger}\begin{bmatrix}1 & -\gamma\\ -\gamma & 1\end{bmatrix}^{-1}\begin{bmatrix}x\\ x_{aa}\end{bmatrix} + \frac{d(d+2)}{2}\,\overline{x}_{ab}\overline{x}_{ab}\,, \tag{D26}$$

which is a straightforward extension of the 3D case of equation (D18). Just recall that γ is now defined in terms of the spectral moments (5) and that de-tracing the Hessian requires a factor $1/d$ instead of $1/3$.

Mon. Not. R. Astron. Soc. **000**, 000–000 (0000) Printed 6 September 2008 (MN LATEX style file v2.2)

The fully connected N dimensional Skeleton and its peak patch hierarchy: probing the evolution of the cosmic web

T. Sousbie[1], C. Pichon[1,2] & S. Colombi[1]
[1] *Institut d'Astrophysique de Paris, CNRS UMR 7095 & UPMC, 98 bis boulevard Arago, 75014 Paris, France*
[2] *Institut de Recherches sur les lois Fondamentales de l'Univers, DSM, l'Orme des Merisiers, 91198 Gif-sur-Yvette, France*
sousbie@iap.fr, pichon@iap.fr, colombi@iap.fr

6 September 2008

ABSTRACT

A method to compute the full hierarchy of critical subsets from a density field within spaces of arbitrary dimensions and geometry is presented. It is based on an improved watershed technique and uses a probability propagation scheme which improves the quality of the segmentation by circumventing the discreteness of the sampling. This recursive segmentation of space yields, for a d-dimensional space, a succession of $d-1$ n-dimensional subspaces that characterize the topology of the density field. The method applies whatever the pixelisation provided a distance to neighbours can be computed. The final 1D manifold of the hierarchy is the fully connected network of the primary critical lines of the field. The skeleton, which correspond to the subset of lines linking maxima to saddle points, provides a definition of the cosmic web as a precise physical object, which makes it possible to compute any of its properties such as its length, curvature, connectivity etc...

When the skeleton extraction is applied to initial conditions of cosmological N-body simulations and their present day non linear counterparts, it is shown that the time evolution of the cosmic web, as traced by the skeleton, is well accounted for by the Zel'dovich approximation, provided the initial field is smoothed over a scale given by $L_{\rm cor} = \sqrt{1.00 - 0.16\,(a - a_i)}$ in units of the non linear scale, and then distorted before the skeleton is computed (a is the expansion factor). Comparing this skeleton to the initial skeleton undergoing the Zel'dovich mapping shows that two effects are competing during the formation of the cosmic web: a general dilation of the larger filaments that is captured by a simple deformation of the skeleton of the initial conditions on the one hand, and the shrinking, fusion and disappearance of the more numerous smaller filaments on the other hand. The net result corresponds to a decrease of the cosmic skeleton's length with time.

Other applications of the N dimensional skeleton and its peak patch hierarchy are discussed.

Key words: Cosmology: simulations, statistics,observations Galaxies: formation, dynamics.

1 INTRODUCTION

The web-like pattern certainly is the most striking feature of matter distribution on megaparsecs scale in the Universe. The existence of the "cosmic web" (Zel'Dovich 1970) (Bond & Myers 1996) has been confirmed more than twenty years ago by the first CfA catalog (de Lapparent et al. 1986) and the more recent catalogs such as SDSS (Adelman-McCarthy et al. 2008) or 2dFGRS (Colless et al. 2003). These observations, together with the dramatic improvement of computer simulations (e.g. Teyssier et al. (2008) Ocvirk et al. (2008)) have largely improved the picture of a Universe formed by an intricate network of voids (*i.e.* globular under-dense regions) embedded in a complex filamentary web which nodes are the location of denser halos. The traditional way of understanding large scale structures (LSS) formation and evolution relies on Friedman equations and assumes that LSS are the outcome of the growth of very small primordial quantum fluctuations by gravitational instability (see *e.g.* Peebles (1980) or Peebles (1993) and references therein). In this theory, the solution for structure formation is described in terms of a mass distribution that one needs to grasp (*i.e.* by following the evolution of its most important features) and compare these to observations. Comprehending the mass distribution as a whole, especially at non-linear stages, is a very difficult task. A possible solution therefore consists in extracting and studying simple characteristic features of matter distribution such as voids, halos and filaments as individual physical objects. So far, mainly because of the relatively higher complexity of the filaments, most theoretical and computational researches have focused on the voids and halos.

The dark matter halos have arguably been the most studied component of the cosmic web. Their density profiles for instance are very well described by so-called NFW profiles (Navarro et al. 1997) and non-parametric models are still under investigation (Merritt et al. 2006). The dependence of these density profiles on the halos mass (*e.g.* Bond & Myers (1996), Lacey & Cole (1993)) has also been investigated thoroughly and its relationship with redshift and environmental properties are a very active topics (*e.g.* Harker et al. (2006), Aubert & Pichon (2006), Wang et al. (2007), Aragón-Calvo et al. (2007), Sousbie et al. (2008) or Hahn et al. (2007)). From a computational point of view, much effort has been put into the development of various algorithms to identify halos in simulations and galaxies in spectroscopic redshift galaxy surveys. The friend-of-friend algorithm (Huchra & Geller 1982) is now widely spread, as well as more complex hierarchical sub-structures identifiers such as HFOF (Gottloeber 1998), SUBFIND (Springel et al. 2001), VOBOZ (Neyrinck et al. 2005) or ADAPTAHOP (Aubert et al. 2004).

Voids are another feature of cosmological matter distribution that also have a long history of theoretical and computational modeling. The first voids were observed by Kirshner et al. (1981) and are in some sense the counterpart of halos: the initial quantum perturbations collapsing into halos at non-linear stages leave room to voids in the under-dense regions. The first theoretical voids models where developed by Hoffman & Shaham (1982), Icke (1984) or Bertschinger (1985) among others, while numerical void finders exist, such as the one described in El-Ad & Piran (1997), ZOBOV (Neyrinck 2008), based on Voronoi tessellation, or the recent Watershed Void Finder, based on the Watershed transform (*e.g.* Beucher & Lantuejoul (1979), Beucher & Meyer (1993)), by Platen et al. (2007) (see the introduction and references therein for a more complete review of the subject). The improvements in our understanding of voids and halos properties led to the formulation of powerful theories such as the patches theory (Bond & Myers 1996) the extended Press-Schechter theory (*e.g.* Bond et al. (1991) and Sheth (1998)) or the skeleton-tree formalism (Hanami 2001).

But our investigation of the filaments as individual objects is not yet as thorough as for the halos and voids: the definition of a well established mathematical framework for their study could therefore lead to significant improvements in our understanding of matter distribution in the Universe. The first attempts date from Barrow et al. (1985), who used a graph-theory construction: the minimal spanning tree (MST). This method defines the cosmic web as the network linking galaxies (or particles from a numerical simulation), having the property of being loop-free and of minimal total length. This technique was later developed in order to try quantifying in an objective way the properties of the cosmic web (see *e.g.* Graham et al. (1995), Colberg (2007) and a review on the subject can be found in Martinez & Saar (2002)). Another method, based on the CANDY model, commonly used to detect road networks, uses a marked point process and a simulated annealing algorithm to trace the filaments (Stoica et al. 2005). More recently, the skeleton formalism and its local approximation, that describe the filaments as particular field lines of the density field, was introduced by Novikov et al. (2006) and Sousbie et al. (2008) with the advantage of framing a well-defined mathematical ground for theoretical predictions of the filaments properties as well as an efficient numerical identification algorithm. Finally, an interesting first attempt to unify halos, voids and filaments identification using the Multiscale Morphology Filter (MMF) technique was also proposed by Aragón-Calvo et al. (2007).

In this paper, we introduce a framework and algorithm to identify the full hierarchy of critical lines, surfaces, volumes... of density distribution in the general case of d-dimensional spaces. For 3D space, these critical subspaces can be identified to the void and peak patches, as well as filaments and other primary critical lines of the distribution. The algorithm extracts the filaments as a differentiable and, by definition, fully connected networks that traces the backbone of the cosmic web. This method is closely related to the skeleton formalism presented in Novikov et al. (2006) and Sousbie et al. (2008) and is also based on both Morse theory (see *e.g.* Milnor (1963) or Jost (1995)) and an improved Watershed segmentation algorithm that uses a probability propagation scheme.

This paper is organized as follows. In section 2, we present a general definition of the critical sub-spaces that we use as well as a method to extract them from sampled density field with a sub-pixel precision (focusing more specifically on the filaments in the 2D and 3D case). In section 3, we use this formalism to study the time evolution of the cosmic web, and understand the change of its properties as a specific object via the truncated Zel'dovich approximation (Zel'Dovich 1970). Finally, in section 4, we summarize our findings and discuss a few possible applications to N-body simulations and observational spectroscopic galaxy surveys. The details of a general simplex minimization algorithm used in section 2 are presented in Appendix A while the general behavior of the inter-skeleton pseudo-distance as defined in section 3 is given in appendix B.

2 METHOD

The main goal of the algorithm presented here is to allow a robust extraction of the non-local primary critical lines (among which the skeleton) as introduced in Novikov et al. (2006) and Sousbie et al. (2008). In these papers, the skeleton was defined as the set of points that can be reached by following the gradient of the field, starting from the filament type saddle points (i.e. those where only one eigenvalue of the Hessian is positive). Let $\rho(\mathbf{x})$ be the density field, and $\nabla\rho$ its gradient at position $\mathbf{x}$, the skeleton can be retrieved by solving the following differential Equation:

$$\frac{d\mathbf{x}}{dt} \equiv \mathbf{v} = \nabla\rho\,, \tag{1}$$

using the "filament" type saddle points as initial boundary conditions. Because of the difficulty of designing a robust algorithm to solve this equation, it was achieved only in $2D$ in Novikov et al. (2006) and a solution to a local approximation in $3D$ was proposed in Sousbie et al. (2008). This local approximation allowed the extraction of a more general set of critical lines linking critical points together, the subset of this lines linking saddle points and maxima together corresponding to the skeleton (i.e. the "filaments" in the large scale distribution of matter in the universe). See Pogosyan et al. (in prep.) for a discussion of these various sets.

This method works in a very general framework and allows the extraction of a fully connected *non-local* skeleton as well as an extension of the primary critical lines introduced in Novikov et al. (2006) and Sousbie et al. (2008) to a hierarchy of critical surface. Following the idea, already present in Equation (1), that the topology of a field can be expressed in terms of the properties its field lines, it takes ground in Morse theory (Jost 1995) and is roughly based on an extension of the patches theory (Bond & Myers 1996). For any C^2 scalar field of dimension d, the peak patches – PP hereafter – (*resp.* void patches – VP hereafter) are defined as the set of points from which the field lines solution of Equation (1) all converge to the same maximum (*resp.* minimum) of the field. Within this framework, we show that in a d-dimensional space, the skeleton can be thought of as the result of $d-1$ successive identifications of VPs or, equivalently, as the one dimensional interface between at least d VPs. Using this definition, extracting the skeleton of a distribution thus simply amounts to finding a way of robustly and consistently identifying the patches.

Whether considering a particle distribution obtained from a numerical simulation or a density field sampled on a grid, the major difficulty arises from the discrete nature of the data. In fact, even if the underlying density field is supposedly smooth and continuous, the discreteness of the sampling implies a relatively large uncertainty on the precise location of the patches boundaries, as sampling is limited by computational power, which is even more true when considering higher dimensions space. The algorithm we use is an improved version of the Watershed transform method (Beucher & Lantuejoul 1979), based on a probability propagation scheme and aims at attributing a probability of belonging to a given patch to every sampled point of the density field. This scheme is very general and efficient as it allows dealing with discrete dataset in a naturally continuous fashion and on manifolds of arbitrary dimensions.

2.1 Probabilistic patches extraction

The initial idea beyond our patches identification algorithm is that a patch can be defined as the set of field lines (i.e. curves that follow the gradient of a field) that originate from a given minimum (VP) or maximum (PP) of a field. Considering a sampled field, being able to identify the patches thus amounts to being able to decide, for any given pixel p, from which extremum all field lines that cross p originate. It is therefore easy to understand that the discrete nature of the sampling rapidly plagues such a task: for each pixel, considering the measured gradient, one has to decide from which, in the fixed number of neighbouring pixels, the field line comes from. Within a d-dimensional space, having to select between only 3^d possibly different direction for field lines is a crude approximation that leads, because of accumulation, to a largely wrong answer for pixels located far away from the extrema.

Although we present the algorithm in the general case here, the reader can refer to figure 1 and its legend for a simpler and more visual explanation of the algorithm in the $2D$ case. More generally, our algorithm involves considering each pixel of a sampled field in the order of their increasing (*resp.* decreasing) value, depending on whether we want to compute the VPs or PPs and, for each of them, computing the probability that it belongs to a given VP (*resp.* PP). This probability map is simply computed by scanning the probability distribution of its 3^d-1 neighbours (within a d-dimensional space, here $d=2$) and deducing the current pixel patch probability distribution from it. Two cases are possible:

(i) none of the neighbours has already been considered (i.e their respective densities are all higher -*resp.* lower- than that of the current pixel). This means that the pixel is a local minimum (*resp.* maximum) of the field: a new VP (*resp.* PP) index is created and the probability that the current pixel belongs to it is set to 100%.

(ii) At least one neighbour has already been considered (i.e its density is lower -*resp.* higher- than that of the current pixel). The current pixel probability distribution is computed as an inverse gradient weighted average of its lower -*resp.* higher- density neighbours' probability distributions.

Once all pixels have been visited, a number N of patches have thus been created and a list of N probabilities P_i^k,$k \in \{1,..,N\}$, has been computed for each pixel, i. These probabilities quantify the odds that a given pixel i belongs to a given patch k. Figure 2 illustrates the advantages of our probability list scheme compared to the naive approach: without it, the patches borders have a strong tendency to be aligned with the sampling grid and the problem tend to get much worse when considering lower sampling and of course higher dimensions.

Figure 3(c) presents the results obtained by applying this algorithm to the $2D$ Gaussian random field of Figure 3(a). On this picture, each patch is assigned a different shade, and the colour of each pixel is the probability weighted average colour of its possible patches. As expected, a majority of pixels seems to belong to a definite void patch with high probability (close to 100%). In fact, considering two neighbouring void patches A and B, all the pixels that belong to one of these patches and have a value lower than that of the first kind saddle point(s) on their border (i.e. where the Hessian only has one positive eigenvalue)

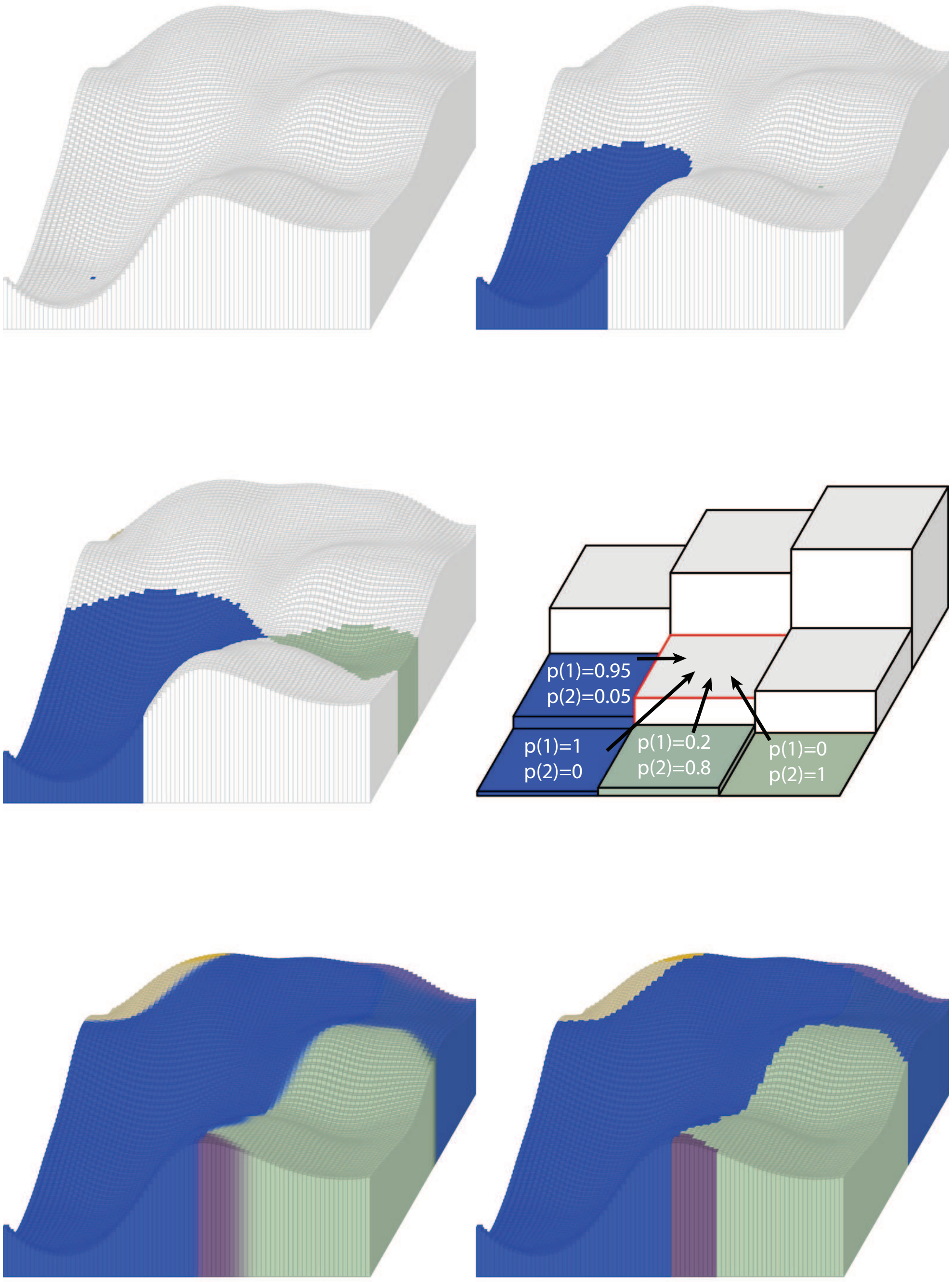

Figure 1. The different steps of the probabilistic algorithm for finding the patches. The height of the histograms is proportional to the density at each pixel of a $2D$ random field. *Top-left*: the pixel with lowest density is identified and tagged as belonging to the void-patch number 1 (blue colour) with probability $P(1) = 1$. *Top-right*: the pixels are then considered in ascending order and are tagged according to the tag of their already visited surrounding pixels. This is repeated until the level of the minimum with second lowest density is reached. As this pixel does not have any tagged neighbour, a new void-patch index is added and the pixel is tagged as belonging to it (green colour) with probability $P(2) = 1$. *Middle-left and middle-right*: the process is repeated until one reaches the saddle point with lowest density, located at the border of two patches (middle-left). Above this threshold, a pixel can have several neighbours, each tagged with different patch indexes (middle-right). A list of probabilities associated to the different patch index of the neighbouring pixels is attributed to the current pixel by computing the density difference weighted average of the respective patches probabilities of the surrounding pixels. *Bottom-left*: repeating the process until all pixels have been visited, one obtains for each pixel a list of possible patches index together with their respective probabilities (hence the blurred borders between patches on the picture). *Bottom-right*: a clean border between the patches can be found by defining the index of the patch a pixel belongs to as the one with highest probability. It is very straightforward to extend this method to spaces with arbitrary number of dimensions.

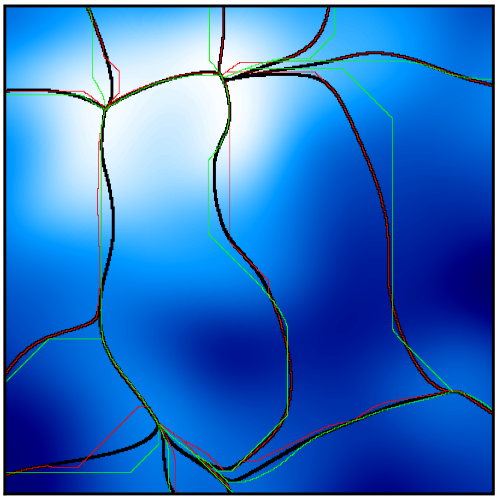

Figure 2. Illustration of the virtue of the probabilistic algorithm. These three curves represent the borders of the void patches obtained with the probabilistic algorithm, by limiting the maximum number of probabilities recorded for each pixel. The black line was derived without any limitation, while for the red one two probabilities were kept and only one for the green one. This last case is equivalent to not using any probability list, as only the values of neighbouring pixels is taken into account. Also note the tendency of the borders to be aligned with the sampling grid when not taking advantage of the probabilistic algorithm.

have a 100% probability of belonging to either A or B. Hence, the probabilities of belonging to different patches only starts mixing above first kind saddle points. This can be seen on the top right zoomed panel of Figure 3(c) where probabilities only start blending mildly for densities above this threshold (the saddle point are represented by the probability "nodes" on the picture). This results in a complex distribution of patch index probabilities in the vicinity of higher density borders (see upper left panel of Figure 3(c)), and thus a higher uncertainty of the location of the void patches border. This uncertainty on the precise patch index is directly linked to the location of the skeleton. In fact, as explained in the next section, the skeleton can also be defined as the set of field lines that do not belong to any patch, or in other terms, where sampled pixels have an equal probability of belonging to several distinct patches.

2.2 The d-dimensional skeleton

As one can easily see, the major strengths of this simple patch extraction algorithm are that it is robust and can be trivially extended to spaces of any dimensions and topology, the only requirement being that one needs to be able to define neighbouring relationships between pixels and measure distances between them. So we now have a robust algorithm for extracting the VP and PP of arbitrary scalar fields. In this subsection, we show that it is possible to generalize the definition of the skeleton (Novikov et al. 2006) to spaces of arbitrary dimension and present a simple method to compute the skeleton, as well as critical lines and surfaces, based on our patches extraction algorithm.

2.2.1 *Definition*

Let us first present important results of the Morse theory without demonstrating them. The more thorough reader can refer to Jost (1995) for a mathematical demonstration.

Let us consider the general case of a d-dimensional C^2 scalar field $\Phi_d(\mathbf{x})$, with $\mathbf{x} \in M_d$ and M_d a manifold (i.e $\mathbb{R}^d$, the sphere S^2, ...)[1]. Following Jost (1995), the field lines of $\Phi_d(\mathbf{x})$ fill M_d and a VP can be defined as the set of points that can be reached by following the field lines originating from a given minimum of $\Phi_d(\mathbf{x})$. The VPs of $\Phi_d(\mathbf{x})$ thus segment a set of d-dimensional volumes that completely fill M_d, each of them encompassing exactly one minimum of $\Phi_d(\mathbf{x})$. The interface of the VPs, M_{d-1}, defines a $(d-1)$-surface (i.e. a surface of dimension $d-1$ embedded in M_d). It is therefore possible to apply our probabilistic algorithm to $\Phi_{d-1}(\mathbf{x})$, the restriction of $\Phi_d(\mathbf{x})$ to M_{d-1}, in order to extract the VPs on this interface. For clarity, we will call the VPs of $\Phi_{d-1}(\mathbf{x})$ the first order VPs of $\Phi_d(\mathbf{x})$, noted 1-VPs hereafter. Recursively, the 1-VPs define $(d-1)$-dimensional volumes that pave M_{d-1}, each of them encompassing, by definition of a VP, exactly one minimum of $\Phi_{d-1}(\mathbf{x})$, with coordinates $\mathbf{m} \in M_{d-1} \subset M_d$, and the reasoning can be applied to the whole hierarchy of α-VPs, $\alpha \in \{0, .., d-1\}$.

Starting from a d-dimensional C^2 scalar field $\Phi_d(\mathbf{x})$, it is thus possible to define a complete hierarchy of sets of α-VPs, $\alpha \in \{0, .., d-1\}$. These α-VPs are $(d-\alpha)$-dimensional volumes that partition $M_{d-\alpha}$, where $M_{d-\alpha}$ is defined as the $(d-\alpha)$-dimensional interface of the $(d-\alpha+1)$-patches. Each set of α-VPs is defined as the set of void patches of $\Phi_{d-\alpha}(\mathbf{x})$, the restriction of $\Phi_d(\mathbf{x})$ to $M_{d-\alpha}$. Let us call a critical point,$\mathbf{x}$, of kind n a critical point with Morse index $\mu(\mathbf{x}) = n$ (*i.e.* where the Hessian $\mathcal{H}(\mathbf{x})$ has exactly n positive eigenvalues). Then, $M_{d-\alpha}$ encompasses the whole set of saddle points of kind $n \leqslant d-\alpha$, of $\Phi_d(\mathbf{x})$, the minima of $\Phi_{d-\alpha}(\mathbf{x})$ associated to each α-patch being the saddle points of $\Phi_d(\mathbf{x})$ of kind $d-\alpha$. The interface M_1 is thus a curve embedded in M_d that links the maxima of $\Phi_d(\mathbf{x})$ to its saddle points of kind 1: the skeleton of $\Phi_d(\mathbf{x})$. It is interesting to note that this approach also allows a rigorous definition of the whole set of critical lines similar to the one introduced with the local approximation of the skeleton in Sousbie et al. (2008), as well as their extension to critical hyper-surfaces of any number of dimensions.

Although we have only addressed the α-VPs case so far, the exact same argumentation holds for the whole hierarchy of α-PPs, which leads to M_d being the skeleton of the voids that links minima to saddle points of kind $d-1$. Moreover, alternating a selection of n_v α_v-VPs and n_p α_p-VPs, $n_v + n_p = d$, leads to M_d being the curve that links

[1] It will be assumed throughout this paper that the field satisfy the Morse condition (Jost 1995) in the lose sense, so that it does not contain extended singular regions (*i.e.* the critical points are isolated and non-degenerate).

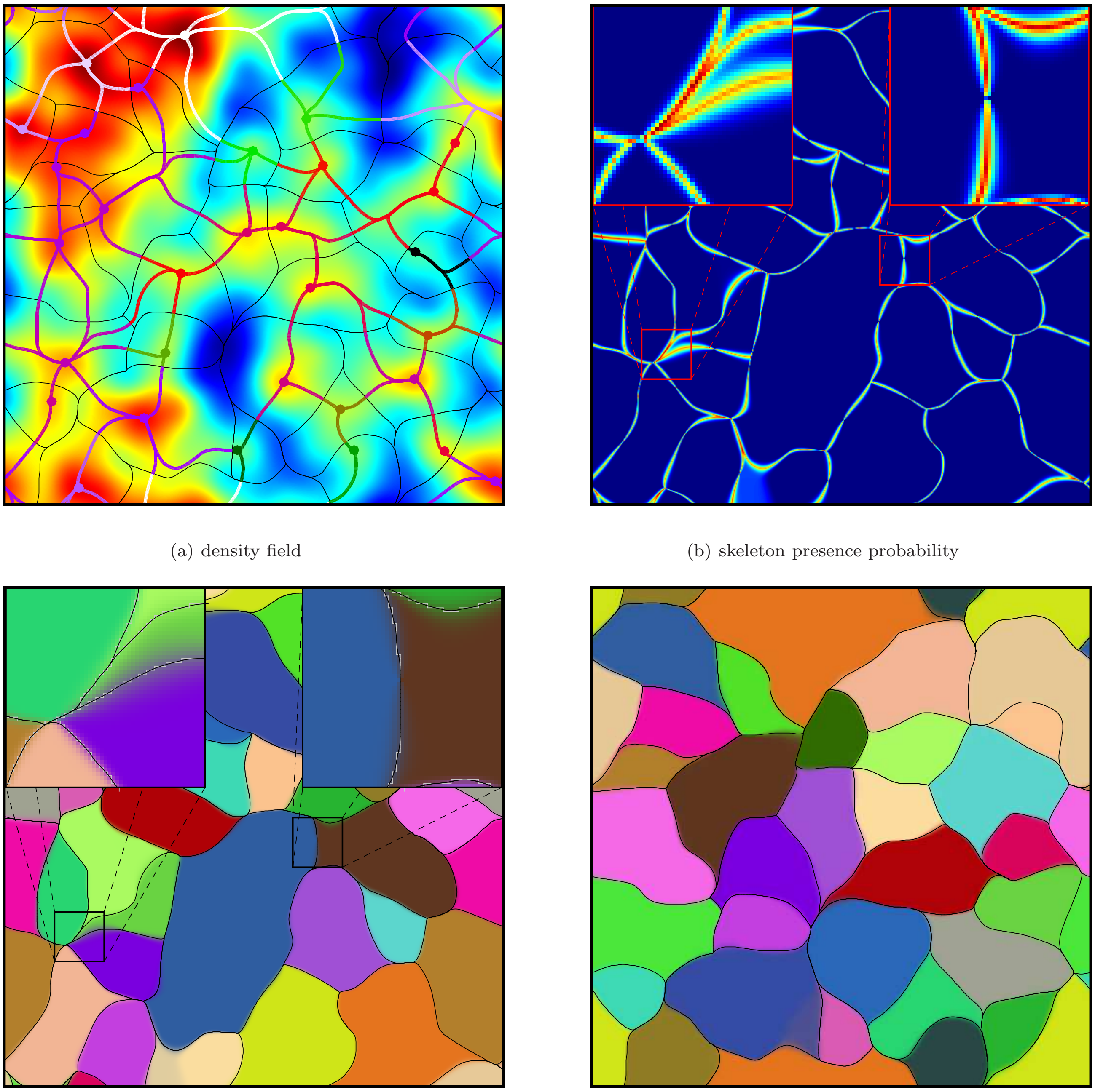

(a) density field

(b) skeleton presence probability

(c) void patches

(d) peak patches

Figure 3. Figure 3(a) represents a 2D density field together with its anti-skeleton (black curve) and skeleton (thick coloured curve). The skeleton is coloured according to the value of the index of the underlying void patch, which allows the detection of the saddle points (intersection of the skeleton and void patch borders). A skeleton branch starts from a field maximum (large dots) and goes through one saddle point before reaching another maximum. Figure 3(b) represents, for each pixel, the value of the probability that it belongs to its most probable patch. By definition, the skeleton is the set of points that do not belong to any patch so the lowest this value, the more probable the pixel belongs to the skeleton. Figure 3(c) was obtained by attributing a given random colour to each patch index and representing each field with the colour resulting of the probability weighted blend of all patches colours. The zoomed parts show patches borders where the uncertainty on the index of the most probable patch index is maximal. The skeleton is represented in white, together with its smoothed counterpart (black). Figure 3(d) represent the peak patches of the same field.

saddle points of kind n_p to saddle points of kind $n_p + 1$: a peculiar set of critical lines of the field. One can note that, as rigorously demonstrated in Morse theory (Jost 1995), critical lines defined in such a way can only link critical points whose Morse index only differ by unity.

2.2.2 Implementation

The representation of the critical lines of a given scalar field as a peculiar limit of a peak or void patches hierarchy certainly has some mathematical appeal. From a practical point of view, although apparently straightforward, its direct numerical implementation can nevertheless to be somewhat problematic. Let G be an initial sampling grid and $\bar{G}$ its reciprocal (i.e. G shifted by half the size of the pixels in every direction). Using our patch computation algorithm on a scalar field $\Phi_d(\mathbf{x})$ sampled over G, we obtain for every pixel, i, of G a probability P_i^k that it belongs to a given patch, k. Those sets of probability distributions could be used to define a border between the patches and thus to compute the 1-PPs and 1-VPs. Nevertheless, this is in general not an easy task: one in fact first needs a very precise localization of the 1-PPs and 1-VPs (those living on the (hyper-)surface of the initial VPs or PPs) to be able to compute the following segmentation of the hierarchy (as opposed to a density probability). In order to overcome this issue, we chose first to base our implementation on a subset only of the different patches probabilities and only keep for every pixel the index of its most probable patch. This way, we are able to simply define the borders between patches as the set of pixels of $\bar{G}$ that overlap at least 2 pixels of G with different most probable patch index. The patches extraction algorithm can then be applied again over that border, restraining pixels examination to the ones that lie on its surface. Identifying pixels of G that overlap at least 2 pixels of $\bar{G}$ with different most probable patch index, one can thus identify the 2-PP or 2-VP and, repeating this procedure, all orders of the patches hierarchy.

For 2D Gaussian random fields, as pictured on figure 3(d) and 3(c), the skeleton (*resp.* anti-skeleton) are identical to the VP (*resp.* PP) borders and the direct implementation of this algorithm leads to a very precise and smooth skeleton. But the implementation in spaces of higher dimensions raises a critical issue with this simplified method, due to the fact that the borders of the α-PPs and α-VPs are only defined by the index of the pixels they cross: thus they are jagged and considered locally flat (on the scale of one pixel and its direct neighbourhood). Figure 4(a) presents the 1-VPs obtained by applying this algorithm to a 3D Gaussian random field, each colour corresponding to a different 1-VP index. The 1-VPs live on the 2D surface which is the border between the cells formed by the void patches of the field, each of this cell encompassing exactly one minimum of the field. This surface is complex: it can be multiply connected at the interface of more than two different void patches and its curvature is locally significant. Although neighbouring relationships between pixels are easily obtained even where the surface is multiply connected, only a rough approximation of the actual distances along the surface can be computed, as the local curvature is not taken into account. Figure 4(b) shows the corresponding skeleton, computed as the border of the 1-VPs of Figure 4(a). This skeleton is clearly not very well defined, the uncertainty in distance computation leading to errors in the probability propagation algorithm. This bias results in multiple skeleton branches that seem to oscillate and cross each other along the true skeleton location.

In the end, it appears that dropping the full probability distribution and approximating borders between patches is too coarse an approximation. One solution would involve trying to compute the precise location of the α-VPs and α-PPs using the full set of probabilities, but, as it will be discussed in section 2.3, this raises complex issues. As it is the patches interface computation that seems to be difficult, the alternative we chose to implement involves computing directly the skeleton from the $0-$VPs and $0-$PPs of the field, without having to consider the full hierarchy of α-VPs and α-VPs. A close examination of Figure 4(a) led us to formulate the conjecture that the $(d-1)$-VPs or $(d-1)$-PPs interface corresponds in fact to the subspace of M_{d-1} where the manifold is sufficiently multiply connected (i.e. where the $(d-1)$-surface defined by M_{d-1} folds onto itself). Equivalently, this locus can be defined in $3D$ as the interface of at least 3 different PPs or VPs (see Figure 4(a)). This is formally demonstrated in Jost (1995). In the general case of $M_{d>3}$, the skeleton should thus be the 1D interface between at least d VPs or PPs of $\Phi_d(\mathbf{x})$. Figure 4(c) presents the skeleton obtained using this method on the same Gaussian random field as the one used for Figures 4(a) and 4(b). As expected, as there is no need to recursively compute the full hierarchy of VPs, the resulting skeleton is much more precise and well defined. Moreover, a quick comparison to Figure 4(b) confirms that it is in fact the approximation of the α-patches interfaces by individual pixels that plagues the algorithm, each recursive step exponentially increasing the error.

2.2.3 The skeleton as a set of individual filaments

The concepts introduced above allow the definition and extraction of the skeleton as a *fully connected* network that continuously link maxima and saddle-points of a scalar field together. It is certainly of interest to try understanding the topological and geometrical properties of this scalar field through the connectivity and hierarchy relationship that it introduces between the critical points. Applied to cosmology, it also allows a formal definition of the concept of individual filaments. Considering matter distribution on large scales in the Universe, a natural definition of a *single* filament would be a subset of the cosmic web that directly links two halos together. The transposition of such a definition to the skeleton would allow the introduction of useful concepts such as neighbouring relationship between halos in the cosmic web sense. It would also make possible the study of filaments as individual physical objects, similarly to what has been done for years in the literature with the halos and voids.

On Figure 3(a), the skeleton (coloured thick network, where the colour corresponds to the underlying PP index) and anti-skeleton (black network) are superimposed on the density field from which they where extracted. Let us define

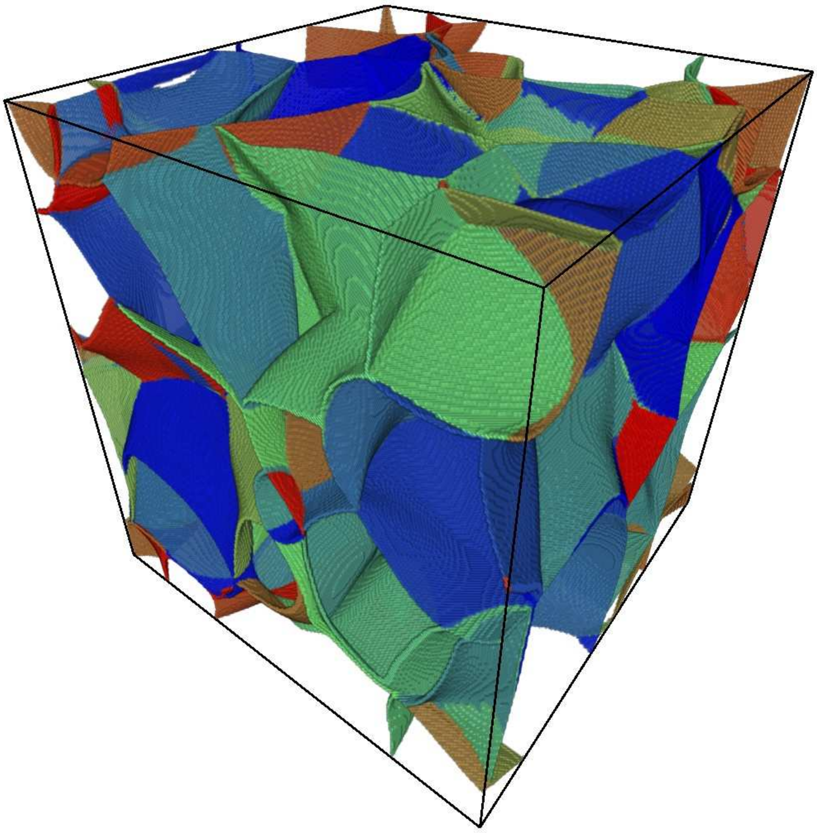

(a) The 1-VPs of a 3D Gaussian random field

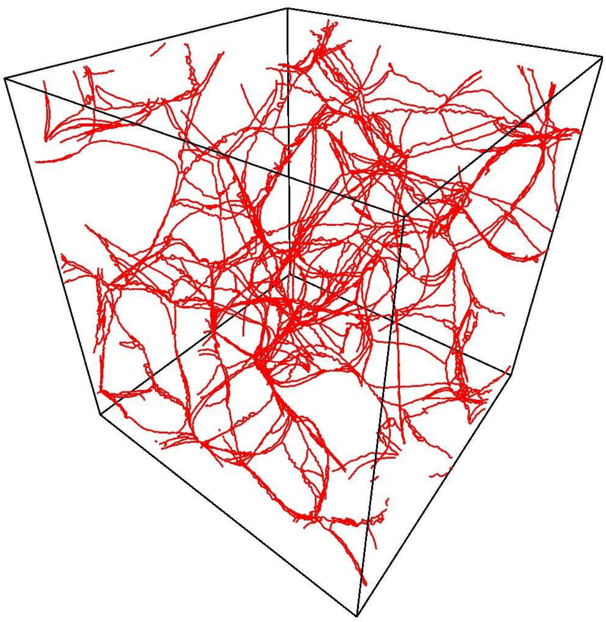

(b) Recursive algorithm

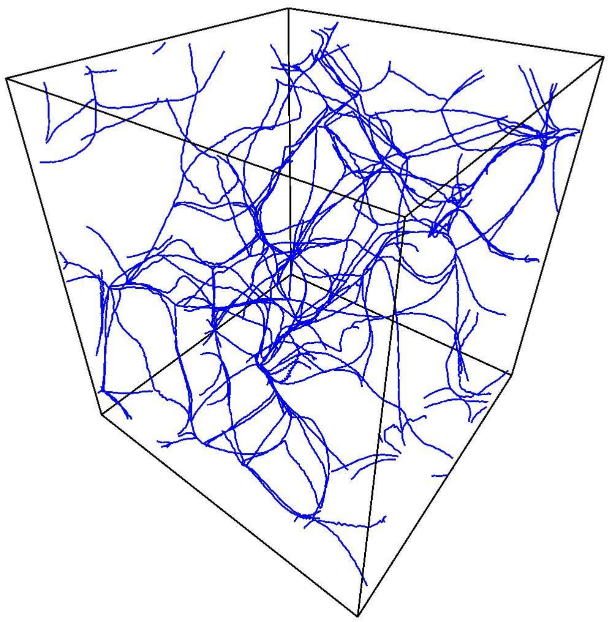

(c) Direct algorithm

Figure 4. Illustration of the computation of the skeleton as the 1D interface of the 1-VPs for a 3D field, $\Phi_3(\mathbf{x})$. Figure 4(a) presents the 1-VPs of $\Phi_3(\mathbf{x})$. The 2D surface, M_2, is computed as the interface of the VPs of $\Phi_3(\mathbf{x})$. The 1-VPs are the void patches of the restriction, $\Phi_2(\mathbf{x})$, of $\Phi_3(\mathbf{x})$ to M_2. Similarly to picture 3, each colour corresponds to a given 1-VP of $\Phi_2(\mathbf{x})$, associated to a given minimum of $\Phi_2(\mathbf{x})$ (which is also a saddle point of kind 1 of $\Phi_3(\mathbf{x})$). The rough appearance of M_2 is due to the fact that it is approximated by the set of pixels of the sampling grid crossed by the interface of the VPs. The skeleton of Figure 4(b) is defined as the interface of the 1-VPs of Figure 4(a): its location is not very precise and it seems to oscillate around its "true" location, mainly because only a locally flat approximation of M_2 is computed. Conversely, the skeleton of picture 4(c) is computed as the border between at least 3 PPs of $\Phi_3(\mathbf{x})$ or equivalently as the set of points of the surface M_2 (pictured on Figure 4(a)) which are multiply connected (i.e. where M_2 folds onto itself). This algorithmically simpler definition leads to a much better defined skeleton.

a filament as a subset of the skeleton continuously linking two maxima together while going through one - and only one - first kind saddle point. These saddle points can be easily extracted as they are located on the skeleton, at the border between the peak (*resp.* void) patches (i.e where the patch index along the skeleton changes, this definition being valid for any number of dimensions). This way, all the filaments of an N-dimensional distribution can be extracted individually by starting from each maximum of the field, following all the branches of the skeleton, and storing only the paths that cross one saddle point before reaching another maximum. This algorithm thus allows the individual extraction of filaments as well as a continuous wander of the filamentary structure of a distribution, which should be very useful in a wide range of applications in cosmology.

2.3 Sub-pixel resolution and skeleton smoothing

Let us first consider for simplicity a Cartesian sampling grid (even though this sub pixel smoothing does not critically depend on this geometry, see below). The implementation of the procedure of Section 2.2 naturally leads to a skeleton that lives along pixel edges and is thus jagged at the pixels scale. The differentiability of the skeleton is nonetheless a feature which may be critical for a number of its characteristics: its length, curvature, general connectivity ... In order to enforce this differentiability, we developed two smoothing methods which we use in practice in turn. The first one is based on a multi-linear interpolation of the patches probability distribution which flows naturally from the original algorithm used to create the skeleton. It provides sub-pixel resolution consistently with the probabilistic framework, thus allowing a precise extraction of the skeleton even when the sampling is low. The other is used to control the level of smoothness away from fixed points (the maxima or the bifurcation points) and can be used to enforce sufficient differentiability.

2.3.1 Multi-linear sub-pixel skeleton

Let us first find a way to obtain a sub-pixel resolution on the skeleton position based on the patches probability distribution of each pixel. The raw skeleton is made of individual segments located on the edges of the pixels of a Cartesian grid G. Each segment is defined by its two end points, and each of them is surrounded by 2^d pixels with a full list of possible patches index, together with their respective probabilities. Recall that the probabilistic algorithm we use works on individual pixels so the resulting skeleton position, defined as the position of the border between several patches, is computed with a precision of one pixel. This implies that the smoothing procedures may not move the skeleton on more than half the size of a pixel. In other words, if we consider the dual sampling grid, $\bar{G}$, of G, the skeleton can be freely moved within the pixels of $\bar{G}$ that its jagged approximation crosses. So it is sufficient to consider individually each of these pixels. Let $\bar{p}$ be one of these pixels. We then know for each of its vertices, p_i with $i \in 1..2^d$, the probability distribution of the different VPs, P_i^k, where k is the index of a VP. In order to obtain sub-pixel resolution, these probabilities can be interpolated within $\bar{p}$.

For simplicity, we will only use a multi-linear interpolation and define $P^k(\mathbf{x})$, the probability distribution of patch k, interpolated at point $\mathbf{x} = (x_1, .., x_d) \in [0, 1]^d$ within $\bar{p}$ as:

$$P^k(\mathbf{x}) = \sum_{i=1}^{2^d} P_i^k \prod_{j=1}^{d} \epsilon_j^i(x_j), \tag{2}$$

where $\epsilon_j^i(x) = x$ if the j^{th} coordinate of p_i within $\bar{p}$ is 1 and $\epsilon_j^i(x) = (1 - x)$ if it is 0. Ideally, the skeleton should not belong to any VP, so it should be located where all the non null values of $P^k(\mathbf{x})$ are equal. Let us define the arithmetic mean of the probability (over the VPs with index k) over the pixel

$$\langle P(\mathbf{x})\rangle = 1/N \sum_{k}^{N} P^k(\mathbf{x}), \tag{3}$$

and its root mean square,

$$\tilde{P}(\mathbf{x}) = \sqrt{\sum_{k}^{N} \left(P^k(\mathbf{x}) - \langle P(\mathbf{x})\rangle\right)^2}, \tag{4}$$

where the sum is over all the N subscripts k such that there exist a pixel p_i where $\forall l \neq k, P_i^k > P_i^l$. Clearly, all patches with dominating probabilities $P^k(\mathbf{x})$ in $\bar{p}$ are equal when

$$\tilde{P}(\mathbf{x}) = 0. \tag{5}$$

Equation (5) is of fourth order and is thus difficult to solve in general.

2.3.2 Approximate quadrics sub-pixel smoothing

Insights into the solution of Equation (5) can be found while considering the intersection sets of points where pairs of probabilities are equal instead of equating them all at the same time. These sets are solution of the set of equations

$$P^k(\mathbf{x}) = P^{k\prime}(\mathbf{x}), \quad k \neq k\prime \tag{6}$$

where k and $k\prime$ are subscripts of the patches that dominate on at least one vertex of $\bar{p}$.

For clarity, let us consider the $d = 2$ case first. With a proper indexing of the four pixels p_i,

$$\begin{aligned} P^k(\mathbf{x}) \quad = \quad & P_1^k(1 - x_1)(1 - x_2) + P_2^k(x_1)(1 - x_2) \\ & + P_3^k(1 - x_1)(x_2) + P_4^k(x_1)(x_2), \end{aligned} \tag{7}$$

Equation (6) writes in this case:

$$A\, x_1 x_2 + B\, x_1 + C\, x_2 + D = 0\,, \tag{8}$$

where A, B, C and D only depend on the values of P_i^k. Equation (8) is quadratic and its solutions are well known curves of dimension $d - 1 = 1$ called quadrics. Figure 5 illustrates solutions of Equation (8) when $\bar{p}$ is located at the intersection of $N_p = 2$, $N_p = 3$ or $N_p = 4$ different VPs. In the most frequent configuration where $\bar{p}$ is at the intersection of 2 VPs, Equation (8) directly gives the first order approximation of the intersection of the skeleton and $\bar{p}$, and we may approximate it by a straight segment. Finding the end points of this segment is easily achieved by computing the location of equal probability along the two sides of $\bar{p}$ that link vertices with different patches (Figure 5(a)). The $N_p = 3$ configuration is rarer, and concerns only the maxima of the field as well as all bifurcation points of the skeleton. In

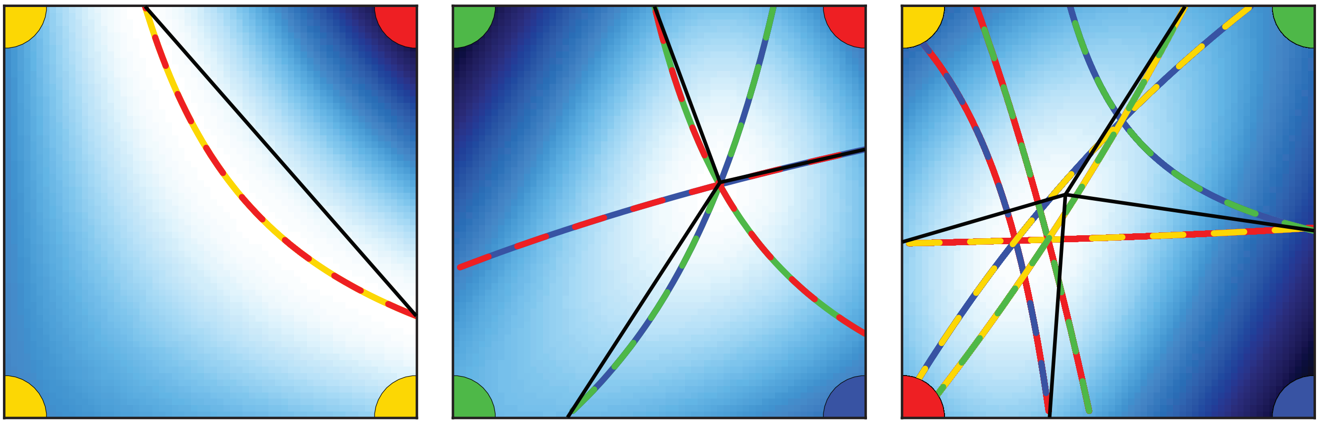

(a) Intersection of 2 patches (b) Intersection of 3 patches (c) Intersection of 4 patches

Figure 5. Illustration of the computation of the sub-pixel skeleton in the case of a 2D bi-linearly interpolated pixel located at the border of 2, 3 and 4 different patches. The colour of the pixels vertices represent the index of the dominant patch, while the two-coloured dotted lines are the quadrics, solutions of Equation (6). These lines are the regions where the probabilities corresponding to the patches with similar colours are equal. The underlying blue gradient corresponds to the value of $\tilde{P}(\mathbf{x})$ (Equation (4)), light colours encoding lower value. Finally, the black lines represent our approximation of the smoothed intersection of the skeleton with the pixel.

this case, we know that three different branches of the skeleton merge within the pixel, at a point where all probabilities are equal. So, we may set the bifurcation point as the locus where all the $C_2^3 = 3$ quadrics of Equation (6) intersect (note that the three of them always intersect in a single point as $P^1(\mathbf{x}) = P^2(\mathbf{x})$ and $P^1(\mathbf{x}) = P^3(\mathbf{x})$ implies $P^2(\mathbf{x}) = P^3(\mathbf{x})$). The three branches of the skeleton in $\bar{p}$ are thus obtained by linking the bifurcation point to the iso-probability along the three sides of $\bar{p}$ that link vertices associated to different patches (Figure 5(b)). Finally, the $N_p = 4$ configuration is very rare[2] and also more problematic. As previously, we know that there exist a bifurcation point within $\bar{p}$, but this time with 4 different skeleton branches. Since there are now $C_2^3 = 6$ different Equations (6), and given that the solution of each of them is a 1D quadric, this system is clearly over constrained to find the precise location of the bifurcation point. A solution may well be to use a higher order interpolation, allowing more complex curves than quadrics for equal probabilities regions, or to try solving directly Equation (5). As this case is clearly rare, it would also be possible to approximate the bifurcation point as the barycenter of the three points of intersection of the subsets of Equations (6) taken in pairs. Again, the smoothed skeleton would therefore be derived by linking the bifurcation point to the four iso-probability points along the four sides of $\bar{p}$ (Figure 5(c)).

2.3.3 *Actual recursive implementation*

Having discussed the underlying geometry of the sub-pixel multi linear interpolation, let us now turn to our actual sub-pixel smoothing algorithm. Indeed, in d-dimensions, Equation (6) is of order d and is linear in each of the d space coordinates x_i. Its solutions are thus $d-1$ dimensional quadrics whose intersections, as in $2D$, can be used to recover the skeleton position down to a sub-pixel precision. Finding intersections of quadrics in general remains nonetheless a highly difficult (or even untractable!) problem and even state-of-the-art solvers can only achieve such a performance for $d = 3$ at most. To circumvent this difficulty, we thus opted in practice for a different solution that consists in a recursive numerical minimization of the value of $\tilde{P}(\mathbf{x})$ over the hierarchy of n-cubes (i.e hypercubes of dimension n), $n \in \{1, .., d\}$, that are the faces of each cell of the sampling grid. The trick is to always reduce the problem to a 1D minimization of a polynomial of order d (see appendix A). Figure 6 illustrates the full process in 3D. Let us consider the grid cell of Figure 6(a), located at the interface of 4 different patches. The skeleton extraction algorithm produces the jagged skeleton represented in red. In order to improve its resolution, we first consider each of the 12 edges individually (see Figure 6(b)) and determine for each of them the point of equal probability for the two patches that dominate at the end points of segment. Of course this point only exists if different patches dominate at the end points of a segment and we thus obtain at most 12 new points (7 in this instance, represented by the red crosses). The edges of a cube can be considered as its "one dimensional faces" or 1-faces. The following step consists in examining the configuration of its 2-faces, usually called faces for a 3D cube. Figure 6(c) illustrates the configuration of these 6 faces together with the iso-probability points computed over their edges. We know that at least 3 different patches have to dominate on at least one of the 4 vertices of each face for a skeleton branch to enter the cell through this face. Using the minimization algorithm presented in Appendix A and the iso-probability points on the edges, it is thus possible to compute, over these faces, the location of the minimum of $\tilde{P}(\mathbf{x})$ (represented as blue crosses on Figure 6(c)). Finally, considering the 3-face of the cell (i.e. the cube itself), one can determine the point of minimal value of $\tilde{P}(\mathbf{x})$ over the cube, which is the point where the

[2] note that the scarcity of these points is directly related to resolution, i.e. whether or not the skeleton is featureless at the sub-pixel scale. Hence these points may occur more often in higher dimensions, which for computational reasons may be relatively under-sampled.

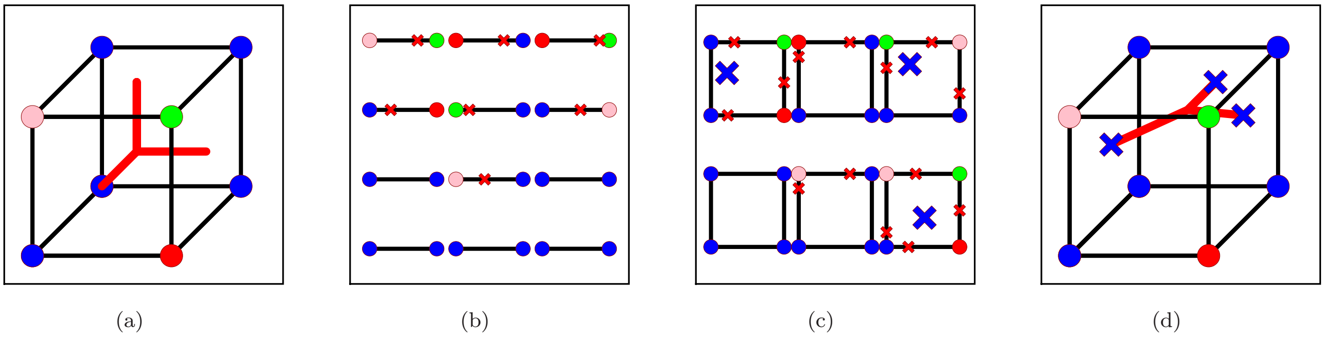

Figure 6. Illustration of different steps of the recursive algorithm used to obtain sub-pixel resolution for the skeleton, in 3D. The colour of the balls represent the index of the patch with maximal probability while the intersection of the skeleton and the cell is displayed in red. The algorithm consists in recursively considering the n-dimensional faces of the sampling unit volume (here an hypercube). For a 3D Cartesian sampling grid, one starts equating dominant probabilities on the vertices of edges, then faces and finally the cube.

skeleton branches connect (see figure 6(d)).

The generalization of this algorithm is relatively straightforward. Let us again consider a cell that is a hypercube of dimension d. We know that the skeleton intersects this cell if at least d of its vertices have different maximal probability patches index. In that case, the sub-pixel resolved skeleton can be recovered by considering all the n-faces of the hypercube, $n \in \{1, .., d-1\}$, in ascending order of their dimension n. When considering a p-face, we minimize the value of $\tilde{P}(\mathbf{x})$ in order to obtain the point where its vertices respective patches have equal probability, using the points obtained from the $(p-1)$-faces. This point only exist for a p-face if at least $(p+1)$ vertices most probably belong to different patches. In the end, one thus obtains a number of points from the $(d-1)$-faces that are the points where the skeleton enters the cell and one point for the d-face (i.e. the cell itself), which gives the location where different branches of the skeleton connect. Figure 7 illustrates the result of applying this algorithm in the $2D$ case.

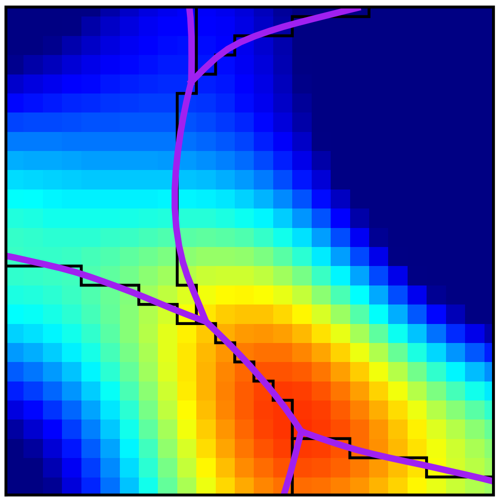

Figure 7. Illustration of the skeleton with a sub-pixel resolution in 2D. The background pixels colour represent the sampled density field while the black skeleton was obtained using our probabilistic algorithm. The purple skeleton is the post-treated version of the black one. Note how any sampling grid influence disappeared, especially in the originally vertical segment located in the upper-left corner of the image.

2.3.4 Artifacts correction and differentiability

Though the method presented above to obtain sub-pixel resolution works most of the time, there nonetheless exist situations where it can fail due to sampling effects. Figure 8 illustrates such a situation, which can sometimes occur when the sampling grid pixel size is not totally negligible compared to the average extension of the patches. When the thickness of a peak or void patch is smaller than a pixel size, it can in fact lead to mistakingly isolated subregions of size one pixel, implying the creation of spurious loops in the skeleton (in red). This phenomenon, although rare, occurs in spaces of arbitrary dimension and triggers artifacts when applying our sub-pixel resolution algorithm. The green skeleton on Figure 8 presents such an example of a spurious skeleton loop.

In order to fix these anomalous segments, we chose to post-treat the skeletons by opening-up all one-pixel sized loops (i.e. of at most $2d$ segments) and smooth the resulting skeleton to enforce a desired level of differentiability in the skeleton trajectory (see the blue skeleton of Figure 8). The smoothing method that we use presents the advantage of being quite robust, and involve fixing some specific points of the skeleton, and averaging the position of each non-fixed segments end points with the position of its closest neighbouring end points a number of times. Let x_j^i be the j^{th} coordinates of the i^{th} sampled skeleton location (among N) between two fixed points. Before smoothing, all x_j^i are located on the edges of G and we can define their smoothed counterparts as y_j^i, computed as:

$$y_k^i = A^{ij} x_k^j, \tag{9}$$

with

$$A^{ij} = \begin{cases} 3/4 & \text{if} \quad i = j = 0 \quad \text{or} \quad i = j = N, \\ 1/2 & \text{if} \quad i = j, \\ 1/4 & \text{if} \quad i = j + 1 \quad \text{or} \quad i = j - 1, \\ 0 & \text{elsewhere}, \end{cases} \tag{10}$$

where Equation (9) is applied s times in order to smooth

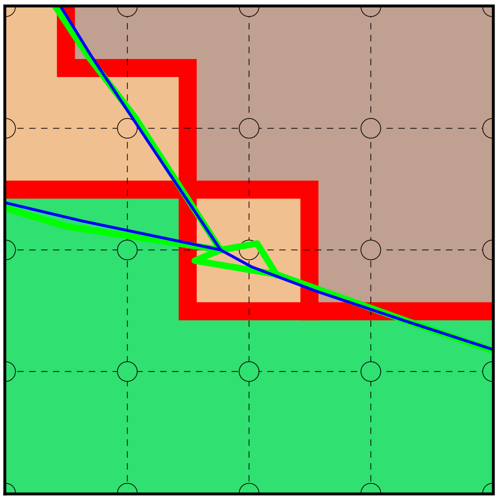

Figure 8. A failure of the skeleton sub-pixel algorithm due to the lack of sampling resolution. The dotted grid represents the reciprocal sampling grid, $\bar{G}$, while the pixels colour represents their dominating patches and the initial raw skeleton is represented in red. The green skeleton is the result of applying the sub-pixel resolution algorithm while the blue one was obtained from the green one, after removing one pixel sized loops and smoothing.

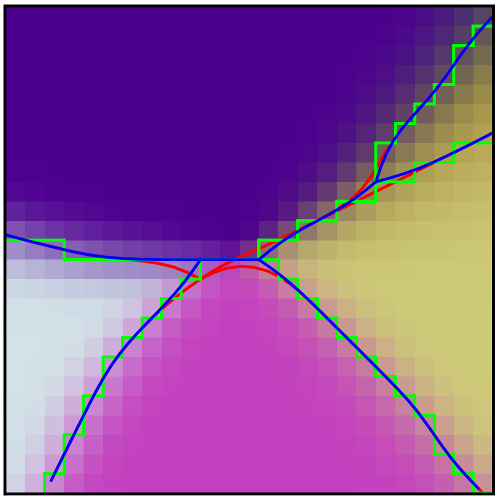

Figure 9. Influence of the choice of fixed points on the shape of the smoothed skeleton. The original skeleton is represented in green, while the red and blue skeletons are smoothed $s = 6$ times, while fixing the field maxima and the bifurcation (i.e multiply connected) points respectively. In both cases, the smoothed versions always stay within half the size of a pixel distance from the original non-smoothed skeleton. On this illustration, the smoothed skeleton was computed *directly* from its raw jagged version to emphasize the effect of the choice of different fixed points. This discrepancy between the two options is considerably weakened if the skeleton is previously post-treated. The background colour corresponds to the weighted probability each pixel has to belong to a definite patch.

over s segments. Basically, Equation (9) is used to compute smoothed coordinates y^i_j as a weighted average of the original coordinates x^i_j together with the coordinates of its 2 direct neighbours, x^{i-1}_j and x^{i+1}_j. Applying this scheme s times thus produces the final smoothed coordinates y^i_j to be a weighted average of x^i_j and its s closest neighbours along the skeleton.

This smoothing technique introduces two parameters of importance: the skeleton smoothing length s, and the type of fixed points. In order to determine the optimal value of s, it is possible to minimize the reduced χ^2 corresponding to the discrepancy between y^i_j and x^i_j supplemented by a penalty corresponding to the total length of the skeleton (over-smoothing will increases the discrepancy, under-smoothing will increase the total length). In practice, though, as a post treatment to an already smooth skeleton (using the sub pixel probabilities), this choice is not critical.

The choice of the skeleton points that should be fixed before smoothing depends of the planned application; in practice, we implemented two possibilities: (i) fixing the field extrema, or (ii) the bifurcation points of the skeleton (i.e the points of the skeleton where two filaments merge into one). Figure 9 illustrates the influence of this choice on the shape of the smoothed skeleton. By fixing the extrema of the field, one ensures that the skeleton subsets that link these extrema are treated independently: this is the solution used to study the properties of individual filaments in the dark matter distribution on cosmological scales. One should note that, in this case, the parts of the skeleton that belong to several individual filaments are duplicated (see the red skeleton on Figure 9), affecting global properties of the skeleton such as its total skeleton length. In contrast, fixing bifurcation points enforces the differentiability of the skeleton while conserving its global properties.

2.4 Summary

Let us finally recap the main steps involved in the extraction of the fully connected skeleton in a d-dimensional space.

(i) The density field is sampled and smoothed in order to ensure sufficient differentiability. A smoothing scale of at least 5 pixels is recommended when using a Cartesian grid.

(ii) All pixels are considered in the order of their ascending (or descending) density. Depending on their neighbours, they are labelled as minima (or maxima), or assigned a list of probability to belong to a given VP (or PP) following the algorithm of section 2.1.

(iii) Considering only the patch index with highest probability for each pixel, skeleton segments are created on pixel edges when at least d surrounding pixels among 2^d have a different most probable patch index.

(iv) Calling a vertex connected to more than two segments a node of the skeleton and considering each node, the sets of connected segments that link them to other nodes are recorded in order to later recover the information on the skeleton connectivity (and allow a continuous wander along the fully connected skeleton).

(v) The sub-pixel smoothing procedure of Sec. 2.3.3 is implemented. All the vertices of the skeleton segments are considered one by one together with the value of the probability distribution in the center of the surrounding pixels. According to the sub-pixel algorithm, the extremities are moved in order to obtain a differentiable skeleton.

(vi) Configurations that are identified as problematic are corrected for following the method described in section 2.3.4,

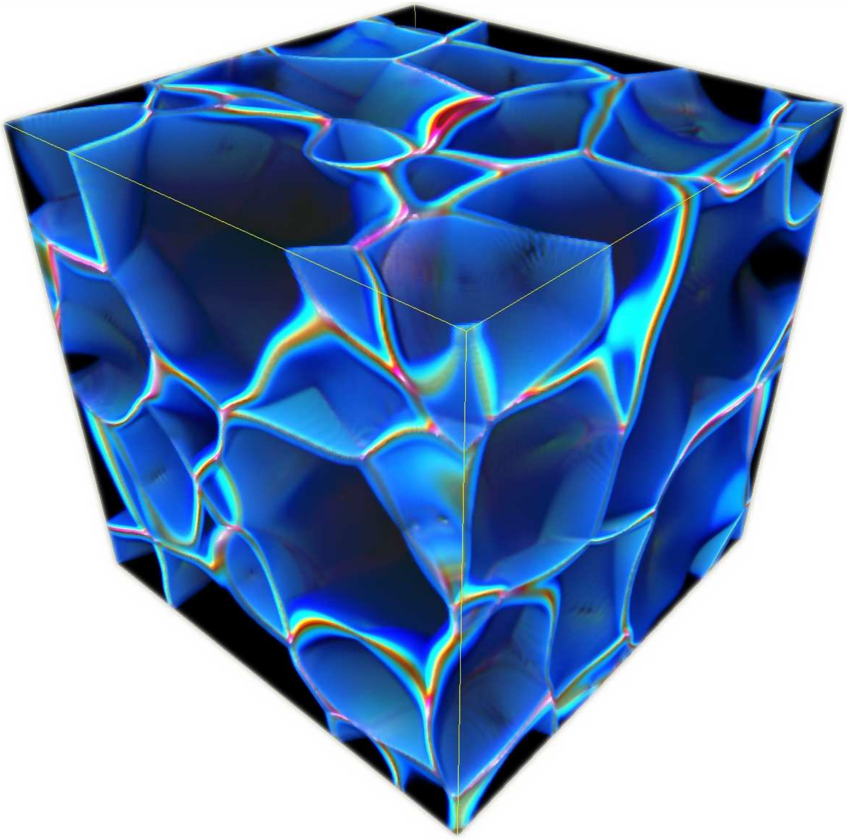

Figure 10. the 3D peakpatch colour coded probability function: warm colours correspond to equiprobability regions, dark colours to regions where one probability dominates (see also Figure 3(b)). This supplementary map complements the peakpatch map in the present algorithm and allow for a precise sub pixel segmentation and skeleton extraction. Note the extended equiprobability sheets corresponding to places where the exact position of the filament will be more uncertain.

and the resulting skeleton is smoothed over a few pixels (usually d of them) while fixing either bifurcation points or maxima/minima.

(vii) Eventually, individual filaments can be extracted (and tagged) following the method of section 2.2.3.

Figures 11 and 12 show a 3D skeleton computed from a simulated density field at $z = 0$, sampled over only 128^3 pixels.

Note that in this paper, we did not address the issue of shot noise that has for long been known to be a problem for most segmentation algorithms, and in particular for Watershed techniques (see *e.g.* Roerdink (1995) for a review on the subject). In fact, shot noise often leads to over segmentation, and numerous complex techniques have been developed to try and compensate for it. Instead, we chose here to follow the approach used in Novikov et al. (2006), Sousbie et al. (2008) and Sousbie et al. (2008), that involve simply filtering the sampled fields using a Gaussian kernel on large enough scales (in terms of number of sampled pixels) so that it is possible to consider that the sampled field is a smooth enough representation of the underlying field. A clear disadvantage of this method is that it introduces a particular smoothing scale and thus adds one parameter (the smoothing scale) to take into account when considering sets of critical lines an surfaces computed on a field. Improvements over this shortcoming are postponed to further investigations.

Regarding performance, the computing time and memory consumption for the extraction of the skeleton mainly depends on three parameters: the number of pixels N_p, the smoothing length L in units of pixel size and the number of dimensions N_d. Most of the computational power is spent during the first step of the process: the propagation of the probabilities to compute the patches. For a constant value of L and N_d, the algorithm speed is linear in N_p, and so is the memory consumption. A smaller value of L implies more smaller patches, which therefore have proportionally more borders with each other thus increasing the number of different probabilities to propagate. Indeed, for very small values of L, memory consumption is largely increased as well as the computational time; it seems reasonable to keep L above a minimal threshold of $L \geqslant 5$ pixels (which in any case is also necessary to ensure sufficient differentiability of the sampled field). Finally, the value of N_d is most critical to memory consumption and speed, not only because N_p should increase with N_d to keep a constant sampling resolution, but also because the number of neighbours for each pixels scales as 3^{N_d} for a Cartesian grid. The computational time and the memory consumption follows, as the number of different probabilities to keep track of is also much increased (each pixels having many more neighbours, the ra-

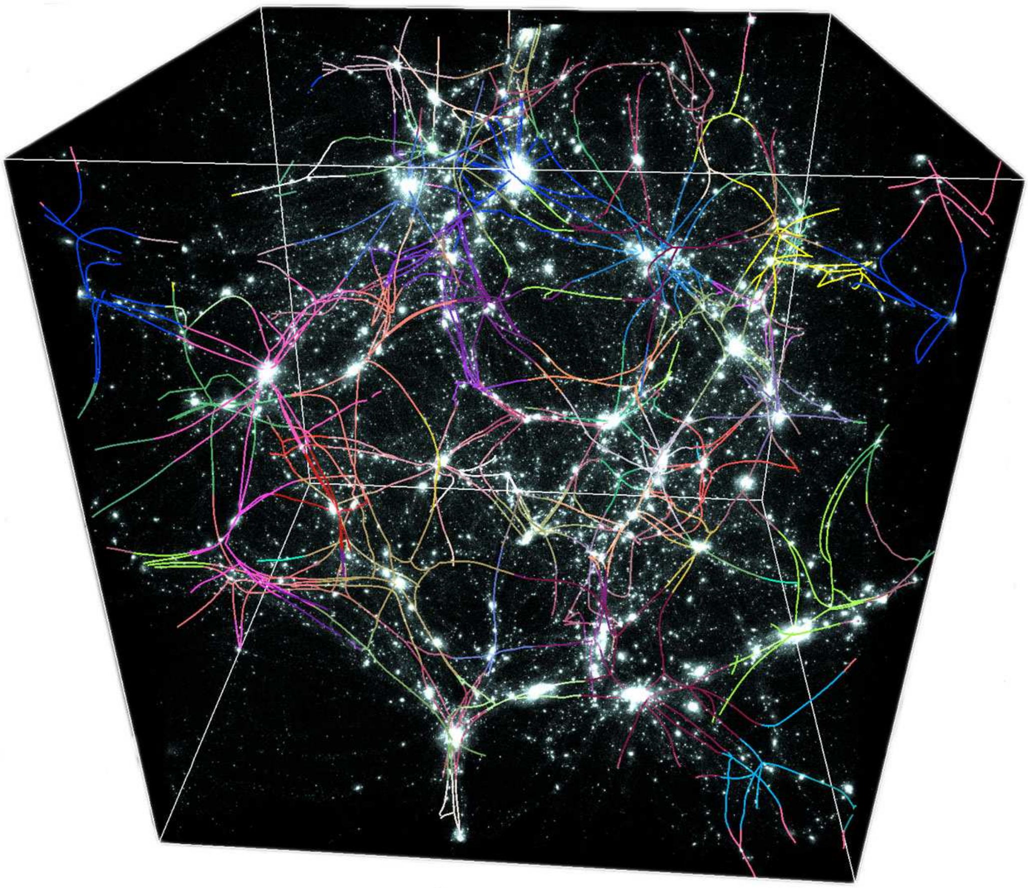

Figure 12. The 3D skeleton of the simulation of the cosmological density density field in a $50h^{-1}$ Mpc box with `gadget-2` (see also Figure 11). This skeleton was computed from a 128^3 pixels sampling grid smoothed over 5 pixels ($\approx 2h^{-1}$ Mpc). The skeleton colour represents the index of the peak patch. which provide by construction the natural segmentation of filaments attached to the different clusters.

tio of patches interface surface to their volume increases and so does the number of different probabilities to propagate, on larger distances). For the different skeletons presented in this paper, to give and order of magnitude, for a single modern CPU, $2D$ skeletons of 1024^2 pixels smoothed over $l \approx 10$ pixels are computed in a matter of few seconds and the memory needed is of order ≈ 10 MBytes. Computing a $3D$ skeleton on a 128^3 pixels grid with $L \approx 6$ takes approximately 1 minute and a hundred of MegaBytes of memory, while for a 512^3 grid, it takes about an hour and around 14 GBytes of memory are used. While $4D$ skeletons are still tractable at a descent resolution (see for instance Figure C2), higher dimensionality seems difficult to reach with present facilities without implementing a fully parallel version of the code.

3 AN APPLICATION: VALIDATING THE ZEL'DOVICH MAPPING

The scope of application of the algorithm presented in Sec. 2 is vast (see Sec. 4 for a discussion). Here we shall focus on a simple example which makes use of one of the clear virtues of the above implementation: it allows us to identify as physical objects the filaments present in the matter distribution on cosmological scales, and see how these objects evolve with time.

Specifically, we intend to show, using the skeleton as a diagnostic tool, that a relatively simple but powerful model, namely the truncated Zel'dovich approximation mapping (Zel'Dovich 1970), can capture the main features of the *cosmic evolution* of the web. Indeed predicting the evolution of matter distribution from the point of view of the topology and the geometry of the cosmic web has been a recurrent issue in cosmology (e.g. Bond & Myers (1996)) and is becoming critical as the geometry of the cosmic environment is now believed to play a key role in shaping galaxies (see, e.g. Ocvirk et al. (2008)).

Being able to carry such an extrapolation from the initial condition to the present day distribution of filaments should lead to a simplified and broader understanding of large scale structures in the Universe, in the same way the concept of clusters as important physical objects gave birth to the hierarchical model of structure formation. The fully connected skeleton encompasses both the geometry and the topology of the cosmic web: it is therefore the ideal tool to validate this mapping between the initial condition and the present day distribution of filaments. Understanding and partially correcting for the distorsion induced by the proper motions of the structures is also of prime importance when

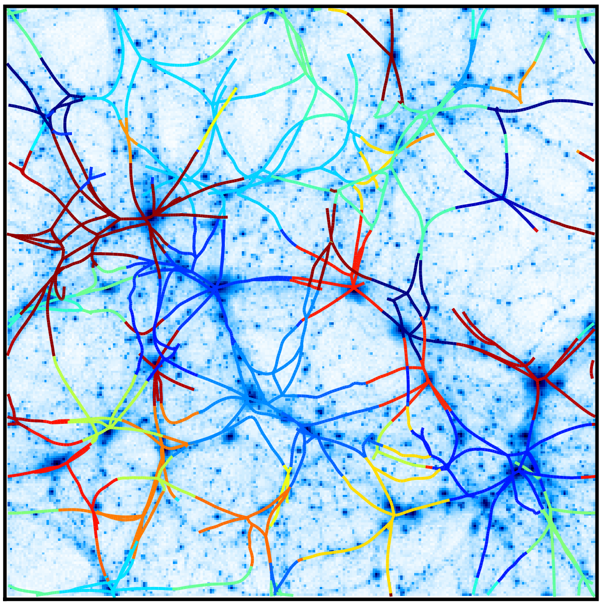

Figure 11. The 2D projection of a 3D skeleton computed on a simulation of the cosmological density density field in a $50h^{-1}$ Mpc box with `gadget-2`. This $20h^{-1}$ Mpc thick section of skeleton was computed from a 128^3 pixels sampling grid smoothed over 5 pixels ($\approx 2h^{-1}$ Mpc). The skeleton colour represents the index of the peak patch. Note that the 2D projection of a 3D skeleton differs from the skeleton of the 2D projection, hence the discrepancy between the skeleton and apparent filaments.

dealing with observationnal data sets (see e.g. Pichon et al. (2001)).

The principle of the Zel'dovich approximation (ZA hereafter) is to make a first order approximation, in Lagrangian coordinates, of the motion of the collisionless dark matter (DM) particles. The motion of these particles from the initial mass distribution in Lagrangian coordinates $\mathbf{q}$ to their Eulerian coordinates $\mathbf{x}$ can therefore be described as:

$$\mathbf{x}\left(z,t\right) = \mathbf{q} + D\left(z\right)/D\left(z_i\right)\mathbf{\Psi}_i\left(\mathbf{q}\right), \tag{11}$$

where z is the redshift, $D\left(z\right)$ the growth factor, and $\mathbf{\Psi}_i\left(\mathbf{q}\right)$ the displacement field, computed in the initial matter distribution as:

$$\mathbf{\Psi}_i\left(\mathbf{q}\right) = \nabla\Delta^{-1}\delta\left(z_i\right), \tag{12}$$

where $\delta\left(z_i\right) = (\rho - \bar{\rho})/\bar{\rho}$ is the density contrast in the initial conditions. The truncated Zel'dovich approximation simply consists in filtering short scale modes of the initial power spectrum before computing the displacement field in order to prevent shell crossing effects. It has been shown to improve the precision of the approximation (Coles et al. 1993). As we are mainly interested in the large scale behavior of the cosmic web, the smoothing scale, $L = L_{\rm NL} \approx 3.94$ Mpc, that we use hereafter to compute $\mathbf{\Psi}_i$ roughly corresponds to the scale of non linearity at $z = 0$, as the truncated Zel'dovich approximation has been shown to work best above this scale (Kofman et al. 1992). It was computed as the scale at which, in the simulation, the smoothed density field, $\rho(L)$, is such that $\sigma^2(L_{\rm NL}) = \left\langle(\rho(L_{\rm NL}) - \bar{\rho}(L_{\rm NL}))^2\right\rangle = 1$ at $z = 0$.

3.1 Simulation and skeletons

The numerical simulation that we use in this section was computed with the publicly available N-body code GADGET2 (Springel 2005). It corresponds to a dark matter only cosmological simulation of 512^3 particles within a $250h^{-1}$ Mpc cubic box, considering a ΛCDM concordant model ($H_0 = 70$, $\Omega_b = 0.05$, $\sigma_8 = 0.92$, $\Omega_\Lambda = 0.7$ & $\Omega_0 = 0.3$). In order to study the evolution of the cosmic web, a set of reference skeletons, $\mathcal{S}_{\rm simu}(z, L)$, were computed from different snapshots, at redshift $z = \{0, 0.15, 0.3, 0.5, 0.66, 1.15, 3, 5, 10\}$, where $z = z_i = 10$ corresponds to the redshift of the initial conditions of the simulation. These skeletons were computed on density fields generated by sampling the particle distribution of the respective snapshots on a 512^3 grid and after smoothing with a Gaussian kernel of size $L = L_{\rm NL} \approx 3.94$. In order to understand if the truncated Zel'dovich approximation is able to capture the essential features of cosmic web, these skeleton are compared to different sets of skeletons, generated using the truncated Zel'dovich approximation in different ways:

- $\mathcal{S}_{\rm ZA}(z, L_{\rm NL})$: This set of skeletons is generated by applying the Zel'dovich approximation to the DM particles of the simulation in the initial conditions. The displacement field is computed after smoothing over the scale $L_{\rm NL}$ and the resulting distribution is sampled and smoothed over the same scale to generate the skeletons.

- $\mathcal{S}_{\rm SZA}(z, L_{\rm NL})$: these skeletons are generated by applying the Zel'dovich approximation directly to the skeleton of the initial conditions. The initial condition simulation ($z_i = 10$) is sampled and smoothed over the scale $L_{\rm NL}$ to compute its skeleton. The displacement field is computed on the same field, but smoothed over a scale $L_{\rm l} \approx 8.81$ Mpc (such that $\sigma^2(L_{\rm l}) = 0.5$ at $z = 0$) and the Zel'dovich approximation is applied to each segment of the initial condition skeleton. We use a larger truncation scale for the Zel'dovich approximation here in order to prevent shell crossing, which can be tolerated when applied to particles but would result in a very fuzzy displaced skeleton.

- $\mathcal{S}_{\rm ZAL}(z, L_{\rm NL})$: same as $\mathcal{S}_{\rm ZA}(z, L_{\rm NL})$, but with a displacement field smoothed over the scale $L_{\rm l}$, in order to check the influence of this choice on $\mathcal{S}_{\rm SZA}(z, L_{\rm NL})$.

- $\mathcal{S}_{\rm ZA}(z, L_{\rm cor})$: same as $\mathcal{S}_{\rm ZA}(z, L_{\rm NL})$, but the sampled field is smoothed on a scale $L_{\rm cor}$ instead of $L_{\rm NL}$ to take into account that the Zel'dovich approximation introduces an artificial additional smoothing scale (see below).

3.2 Skeleton length

There exist many different ways to compare one dimensional sets of lines within a $3D$ space, but one of the simplest certainly involves comparing their lengths. Figure 13 presents the measured length per unit volume of the different sets of skeletons (described above) as a function of redshift. Let us first consider the length of $\mathcal{S}_{\rm simu}(z, L_{\rm NL})$ (*purple curve with discs symbols*). It was shown in Sousbie et al. (2008) and Sousbie et al. (2008) that, whereas for scale invariant fields such as the initial conditions of the simulation, the length of

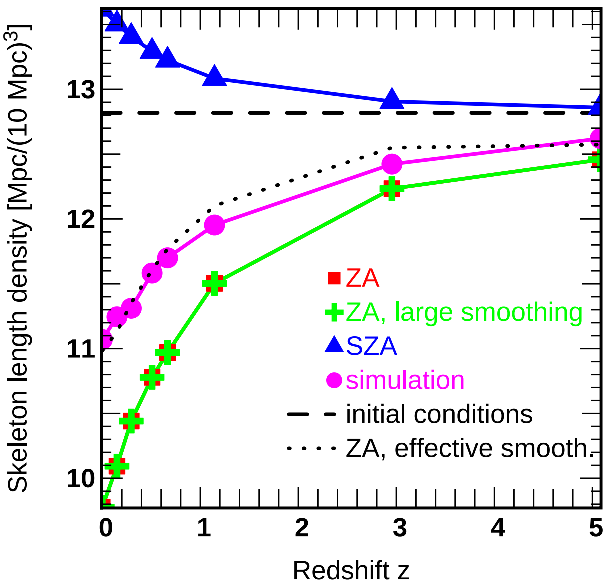

Figure 13. Measured length of the skeleton per unit volume as a function of redshift z. The length density was measured on the simulation (*purple discs*), its truncated Zel'dovich approximation whose displacement field was computed using a smoothing length $L \approx 3.94$ such that $\sigma(L, z = 0) = 1$ (*red squares*), or $L_l \approx 8.81$ such that $\sigma(L, z = 0) = 0.5$ (*green crosses*), and finally using the displacement field of the Zel'dovich approximation at scale L_l, applied directly to the skeleton of the initial condition, at $z = 10$ (*blue triangles*). The black dashed line stands for the length of the skeleton in the initial conditions (at $z = 10$), while the dotted line represents the length measured using the Zel'dovich approximation on the initial condition while taking into account the effective smoothing introduced by using the Zel'dovich approximation. This recipe yields the best match with the simulation. Except for this last case, the skeletons where computed after smoothing the density field with a Gaussian kernel of width L.

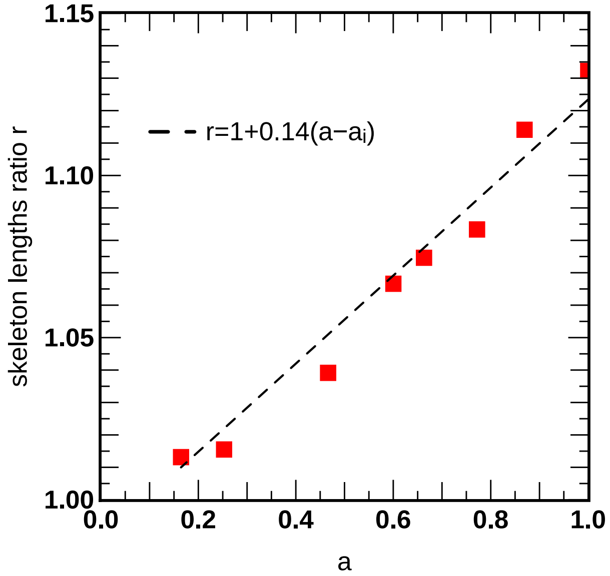

Figure 14. Ratio of the length of the skeleton measured in the simulation to the length of the skeleton of the Zel'dovich approximation as a function of time, a. The dashed line represents the best fit of the data (red squares).

the skeleton is expected to grow as L^2 (L being the smoothing length), it grows in fact as $\approx L^{-1.75}$ around $z = 0$ for ΛCDM simulation. This implies that the proportion of large scale filaments increases with time. The fact that the length of $\mathcal{S}_{\rm simu}(z, L_{\rm NL})$ decreases with time is consistent with this observation: while the long filaments detected on large scales grow (especially for $z < 1$ when the cosmological constant effect starts to dominate and expansion accelerates), the more numerous small filaments on smaller scales shrink and melt into each other as dark matter halos merge: the net result is a total length decrease.

This process seems to be well captured by the Zel'dovich approximation as the length of $\mathcal{S}_{\rm ZA}(z, L_{\rm NL})$ (*red curve, square markers*) exhibits the same time evolution as the length of $\mathcal{S}_{\rm simu}(z, L)$. The discrepancy between the measured length in the simulation and with Zel'dovich's approximation is nonetheless of the order of $\approx 10\%$ at $z = 0$. This disagreement should be explained in part by the fact that the Zel'dovich approximation uses a displacement field computed from a smoothed version of the initial condition density field, thus introducing an additional smoothing that one should take into account when computing $\mathcal{S}_{\rm ZA}$.

The measure of the ratio, r, of the length of $\mathcal{S}_{\rm simu}(z, L_{\rm NL})$ to the length of $\mathcal{S}_{\rm ZA}(z, L_{\rm NL})$ as a function of time, a, is displayed on Figure 14. It appears that r is a linear function of time, a, and can thus be fitted as

$$r = 1.00 + 0.14\,(a - a_i)\,, \tag{13}$$

where $a_i = 1/\,(1 + z_i) \approx 0.09$ is the time of the initial conditions from which the Zel'dovich approximation was computed. Moreover, the fact that the value of r is relatively close to unity confirms that the artificial smoothing introduced by the Zel'dovich approximation is small; we chose to model it as a convolution with a Gaussian kernel of size $L_{\rm ZA}$. The effective Gaussian smoothing used on Zel'dovich's approximation has scale $L_{\rm eff}$ and is thus the result of the composition of two Gaussian smoothing of scale $L_{\rm ZA}$ and $L_{\rm NL}$:

$$L_{\rm eff} = \sqrt{{L_{\rm ZA}}^2 + {L_{\rm NL}}^2}. \tag{14}$$

Using equations (13) and (14), and the fact that the skeleton length grows with smoothing scale as $\approx L^{1.75}$ (Sousbie et al. 2008), the value of $L_{\rm ZA}$ one should chose to get the best match with ΛCDM simulations is thus

$$L_{\rm ZA} \approx L_{\rm NL} \left(\frac{2 \cdot 0.14}{1.75}\,(a - a_i)\right)^{1/2} = 0.4 L_{\rm NL}\sqrt{a - a_i}. \tag{15}$$

In order to compute a skeleton that is comparable to $\mathcal{S}_{\rm simu}(z, L_{\rm NL})$, one should therefore smooth the distribution obtained using the Zel'dovich approximation on a scale $L_{\rm cor}$ such that

$$L_{\rm cor} = \sqrt{{L_{\rm NL}}^2 - {L_{\rm ZA}}^2} = L_{\rm NL}\sqrt{1.00 - 0.16\,(a - a_i)}. \tag{16}$$

On Figure 13, the dotted black curve represents the measure of the length of $\mathcal{S}_{\rm ZA}(z, L_{\rm cor})$, when the effective smoothing introduced by the Zel'dovich approximation is taken into account. The agreement with the measurements in the simulation is significantly improved compared to the naive approach; this suggest that the Zel'dovich approximation can be used to predict the shape of the evolved cosmic web from the initial conditions distribution only.

Of course, the length is only a global characteristic of the skeleton and it certainly does not fully constraint its shape. Higher order estimators that can compare the relative position and shapes of skeletons are needed to quantify how good an approximation the skeleton obtained by Zel'dovich's approximation is.

Before doing so, let us consider an alternative form of the Zel'dovich approximation, where, instead of displacing the particles from the initial conditions of the simulation to derive the evolved density field, we directly use the displacement field to evolve the skeleton of the initial conditions. This method will be called here the skeleton Zel'dovich approximation (SZA hereafter), and the resulting skeleton $\mathcal{S}_{\rm SZA}$. Studying the properties of $\mathcal{S}_{\rm SZA}$ is interesting as it should make it possible to distinguish between two different processes that affect the properties of the cosmic web: the simple deformation of the initial cosmic web on the one hand and the creation or annihilation of filaments on the other hand. Indeed, $\mathcal{S}_{\rm SZA}$ reflects only the modification of the skeleton due to its deformation while $\mathcal{S}_{\rm ZA}$ also takes into account the merging and annihilation of filaments. Note nonetheless that by definition, the locus of the skeleton for the SZA is biased toward higher density regions; in these regions, non-linear effects inducing shell-crossings in the Zel'dovich approximation are more likely. To be conservative, we thus use a larger smoothing length than $L_{\rm NL}$ to compute the displacement field. This smoothing length, $L_{\rm l} \approx 8.81h^{-1}$ Mpc, was chosen such that $\sigma(L_{\rm l}, z = 0) = 0.5$; the green curve (*cross markers*) of Figure 13 shows that using $L_{\rm l}$ or $L_{\rm NL}$ does not make any difference regarding the length of the skeleton. On this figure, the blue curve (*triangle markers*) depicts the evolution of the length of $\mathcal{S}_{\rm SZA}(z, L_{\rm NL})$: its behavior is clearly opposite to the $\mathcal{S}_{\rm ZA}$ case, as the length rises with time. Although surprising at first sight, this result only confirms our previous interpretation of the evolution of the cosmic web. In fact, if the SZA can nicely capture the large scale evolution of long filaments, the smaller ones cannot melt into each other, which induces several small scale filaments to be located at the same loci, where only one piece of filaments should have been measured. The disappearance of the smaller scale filaments does not compensate anymore for the expansion of large scale filament: the net result is thus an increase of the total measured length of $\mathcal{S}_{\rm SZA}$ with time.

3.3 Inter-skeleton pseudo-distance

Let us now define a way to compute a pseudo-distance between two different skeletons (see also Caucci et al. (2008)). In practice, a skeleton $\mathcal{S}$ is always computed from a sampled density and thus has a maximal resolution R_s. It can therefore be described, without loss of information, as the union of a set of N straight segments $\mathcal{S}^i$ of size R_s. We define a pseudo-distance from a skeleton $\mathcal{S}_a$ to a skeleton $\mathcal{S}_b$, $\mathcal{D}(\rm a, b)$, as the probability distribution function (PDF) of the minimal distance from the N^a segments $\mathcal{S}_a^i$ to any of the N^b segments $\mathcal{S}_b^j$. In practice, our algorithm applied to a density field sampled on a Cartesian grid naturally leads to a skeleton described as a set of segments of size the order of the sampling resolution. Hence we directly use these segments to compute inter-skeleton distances.

Note that there is no reason, in general, for $\mathcal{D}(\rm a, b)$ to be identical to $\mathcal{D}(\rm b, a)$; this discrepancy, together with the value of the different modes of the PDFs, do in fact quantify the differences between $\mathcal{S}_a$ and $\mathcal{S}_b$ (see appendix B for details on how to interpret pseudo-distances PDFs). The upper and lower panels of Figure 15 present the pseudo distance measurements obtained by comparing $\mathcal{S}_{\rm simu}$ to $\mathcal{S}_{\rm ZA}$ and $\mathcal{S}_{\rm SZA}$ respectively. A close examination of Figure 15(a) confirms the hypothesis we made in previous subsection. First, the high correlation of $\mathcal{S}_{\rm ZA}$ and $\mathcal{S}_{\rm simu}$ (*bold curves*) for any redshift, is demonstrated by the localization of the mode around $d \approx 600h^{-1}$ kpc, well below the smoothing length $L_{\rm NL} = 3.94$ Mpc. Second, the asymmetry between the PDFs of $\mathcal{D}(\rm ZA, simu)$ and $\mathcal{D}(\rm simu, ZA)$ follows from the fact that $\mathcal{S}_{\rm simu}$ has smaller scale filaments that have no counterpart in $\mathcal{S}_{\rm ZA}$ (the mode intensity is higher for $\mathcal{D}(\rm ZA, simu)$ than $\mathcal{D}(\rm simu, ZA)$). This is exactly what should happen if $\mathcal{S}_{\rm ZA}$ was effectively smoothed on a scale larger than $\mathcal{S}_{\rm simu}$. The thin curves, for which the effective Zel'dovich approximation smoothing was taken into account, confirms this, as the asymmetry is completely removed in that case.

It is also interesting to look at the distance PDFs between $\mathcal{S}_{\rm SZA}$ and $\mathcal{S}_{\rm simu}$ (see Figure 15(b)). Except for high redshifts ($z = 5$), the general intensity of the modes are lower for $\mathcal{D}(\rm SZA, simu)$ than for $\mathcal{D}(\rm ZA, simu)$, suggesting that the Zel'dovich approximation is a better description of the evolution of the filaments on large scales, and that filaments mergers and creation are important processes. The general position of the modes is still comparable, which means that SZA is nonetheless successful in describing the evolution of the general shape of the cosmic web. Also, the asymmetry between $\mathcal{D}(\rm SZA, simu)$ and $\mathcal{D}(\rm simu, SZA)$ suggests that $\mathcal{S}_{\rm SZA}$ has more small scale filaments than $\mathcal{S}_{\rm simu}$. These observations confirm our previous assumption that although the cosmic web evolves in a simple inertial way on larger scales (a process captured by SZA), the shrinking and fusion of the more numerous smaller scale filaments is the cause of the general length decrease of the cosmic web (as suggested by a simple visual examination of a $(50h^{-1})^3$ Mpc^3 subregion of $\mathcal{S}_{\rm simu}$, $\mathcal{S}_{\rm SZA}$ and $\mathcal{S}_{\rm ZA}$ on Figure 16).

The above investigation opens the prospect of correcting for the peculiar velocities of galaxies induced by gravitational clustering, and carry an Alcock-Paczynski (AP) test (Alcock & Paczynski 1979) on the skeleton of the large scale structures of the universe. In short, the AP test compares observed transverse and longitudinal distances to constrain the global geometry of the universe. Galaxy positions are usually observed in redshift space which induces an important distortion between the distances measured along and orthogonally to the line of sight, which plagues the regular AP-test. Our analysis suggests that it is in fact possible to correct through the Zel'dovich approximation for the distortions induced on the cosmic web. Having carried such a correction, we expect that the measure of the anisotropy of

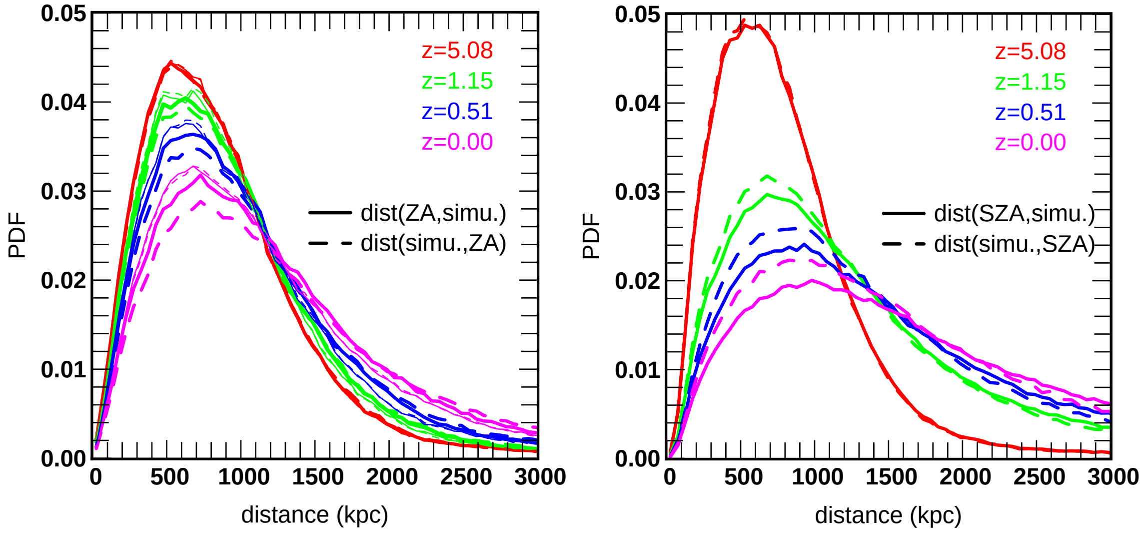

(a) ZA and simulation

(b) ZA applied to the skeleton (SZA) and simulation

Figure 15. The inter-skeleton distance as defined in the main text and appendix B, applied to the skeletons of the simulation and the Zel'dovich approximation (Figure 15(a)) and the skeletons of the simulation and displaced initial conditions skeleton, SZA (Figure 15(b)). The displacement fields and skeletons are computed after smoothing the field on a scale $L \approx 3.94$ such that $\sigma(L, z = 0) = 1$, except for SZA, where the displacement field was obtained after smoothing over $L_l \approx 8.81$ Mpc, such that $\sigma(L, z = 0) = 0.5$. The full lines represent the distance from the simulation's skeleton to the other, while the dotted lines represent the reciprocal distance. The thin lines on Figure 15(a) stand for the case where the effective smoothing introduced by the Zel'dovich approximation is taken into account. Note that SZA PDF is more skewed as the merging/annihilation of filaments is then not taken into account.

the observed skeleton length ratio could yield a good constraint on the value of the cosmological parameters.

The Zel'dovich mapping smoothed with $L_{\rm cor}$ (see Equation (16)) can be used to generate synthetically sets of extremely large cosmic skeletons probing exotic cosmologies using codes such as `mpgrafic` (Prunet et al. 2008) to generate the initial conditions and their Zel'dovich displacement. This construction could then be populated with halos and substructure using semi analytical models. Note finally that the total length and the skeleton's distance are two probes amongst many on how to characterize the difference between two skeleton. Moreover, there are other means to quantify the evolution of the cosmic web. For instance, an interesting statistics would be to find out how often does the reconnection of the skeleton occur as a function of redshift ?

4 DISCUSSION AND PROSPECTS

We have presented a method, based on an improved watershed technique, to efficicently compute the full hierarchy of critical subsets from a density field within spaces of arbitrary dimensions. Our algorithm uses a fast one pass probability propagation scheme that is able to improve significantly the quality of the segmentation by circumventing the discreteness of the sampling. We showed that, following Morse theory, a recursive segmentation of space yields, for a d-dimensional space, a succession of $d-1$ n-dimensional subspaces that characterize the topology of the density field. In 3D for cosmological matter density distribution, we particularly focused on the 3D subspaces which are the peak and void patches of the field (i.e. the attraction/repulsion pools) and the 1D critical lines which trace the filaments as well as the whole primary cosmic web structure (*i.e.* a *fully-connected*, non-local skeleton as defined in Novikov et al. (2006)). For the primary critical lines, we also demonstrated that it is possible to use the probabilities distribution from our algorithm to derive a smooth and differentiable skeleton with a sub-pixel level resolution. Thus this method allows us to consider the cosmic web as a precise physical object and makes it possible to compute any of its properties such as length, curvature, halos connectivity etc...

As an application, we used our algorithm to study the evolution of the cosmic web, while comparing the time evolution of the skeleton (a proxy to the cosmic web) of a simulation, to those corresponding to different versions of its Zel'dovich approximation. We first compared the evolution of the respective lengths of the different skeletons and then introduced a method to compute pseudo-distances between different skeletons. This pseudo distance makes it possible to compare different features of the skeleton such as the size of their filaments and the similarity of their locations. Using these measurements, we showed that two effects where competing, with net result a decrease of the cosmic length with time: a general dilation of the larger scales filaments that could be captured by a simple deformation of the skeleton of the initial conditions on the one hand, and the shrinking, fusion and disappearance of the more numerous smaller scales filaments on the other hand. We also showed that a simple Zel'dovich approximation could accurately capture most features of the evolution of the cosmic web for all scales larger than a few megaparsecs (provided an effective smoothing introduced by the approximation is taken into account). Hence in this context, the skeleton

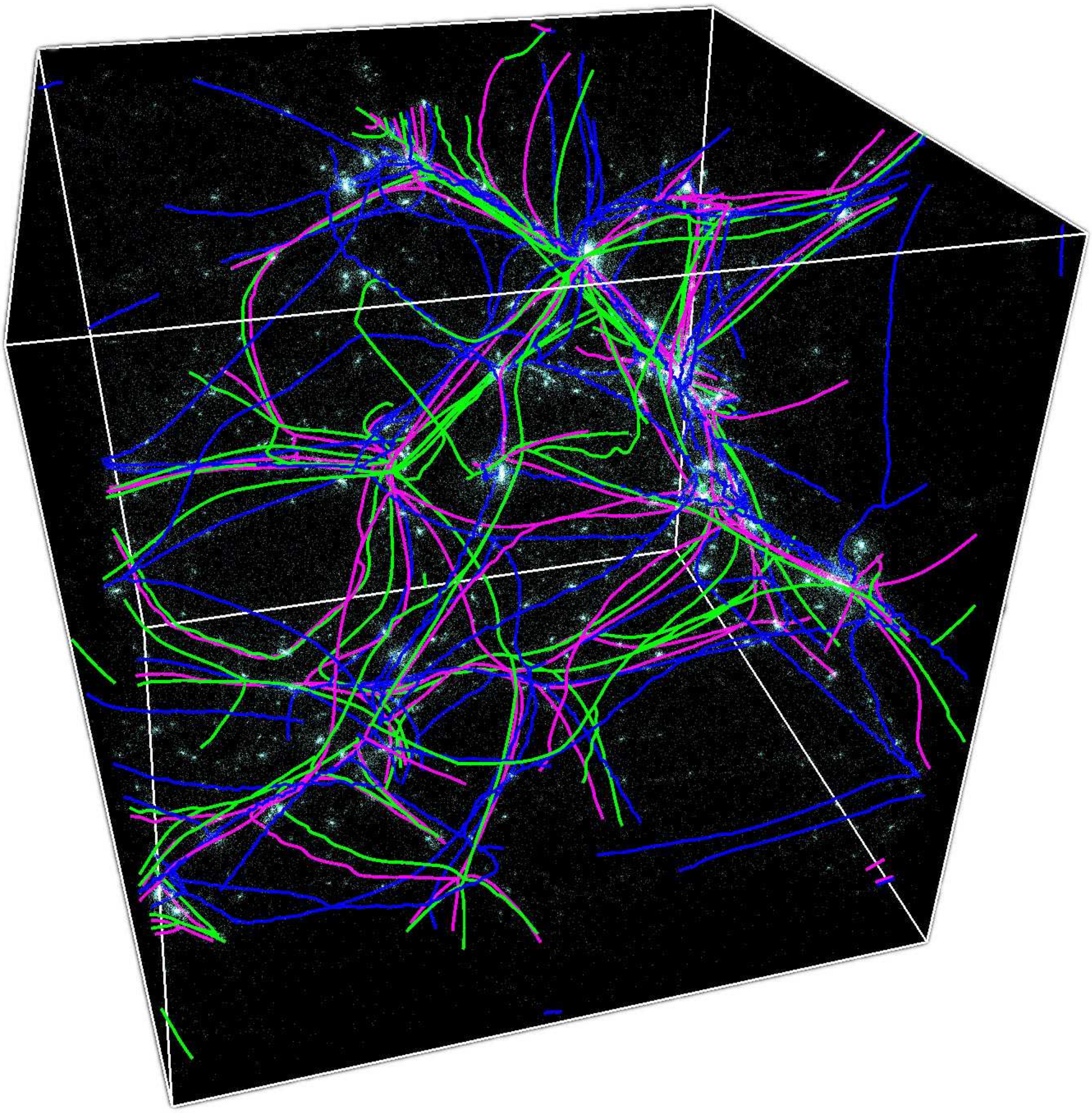

Figure 16. A $(50h^{-1})^3$ Mpc^3 section of the 512^3 particles simulation of a $250h^{-1}$ Mpc large box (only 1 particle every 8 is displayed). The purple skeleton is $\mathcal{S}_{\rm simu}(z, L)$ (computed from the simulation), the green one $\mathcal{S}_{\rm ZA}(z, L_{\rm cor})$ (computed on the Zel'dovich approximation using an effective smoothing length) and the blue one $\mathcal{S}_{\rm SZA}(z, L_{\rm NL})$ (computed by displacing the skeleton of the initial conditions). The simulation and corrected Zel'dovich approximation skeletons appear to be relatively close to each other and every individual filament has a counterpart in the other skeleton. The blue skeleton, computed from the skeleton Zel'dovich approximation, is more wiggly which reflects the small scale perturbation of the displacement field. Moreover, while many of its filaments have counterpart in the two other skeletons, others do not, as displacing the initial skeleton prevents the merging or disappearance of filaments. This results can be quantitatively measured, as shown on Figure 15 and explained in appendix B.

has proven to be a useful tool both for insight and as a quantitative probe and diagnostic. Conversely, the match between the simulated and the mapped skeleton confirms and extends geometrically the (point process elliptical) peak patch theory (Bond & Myers 1996) since both the peaks and their frontiers (the skeleton in 2D and the peak patch volumes in 3D) are well mapped by the Zel'dovich approximation.

The domain of interest of the skeleton is quite vast and offer the prospect of a number of applications.

From a theoretical point of view, using the points developed in this paper and in Sousbie et al. (2008), we are presently developing a general theory of the skeleton and its statistical properties (Pogosyan et al. in prep.) that aims to understand the properties of the critical lines of scale invariant Gaussian random fields as mathematical objects. In particular, this companion paper provides quantitative analytic predictions for the length per unit volume (resp. curvature) of the critical lines and its scaling with the shape parameter of the field, and checks successfully the current algorithm against these. In this paper we focussed on the skeleton. One could clearly investigate on the rest of the peak patch hierarchy and measure, say, the surface or volume of the

(hyper)-surfaces of the recursion (whose last intersection is given by the primary critical lines). Another interesting issue would be to estimate the fraction of special (degenerate) points which do not satisfy the Morse condition, where the fields behaves pathologically (Pogosyan et al. in prep.). For instance, one of the shortcoming of the present algorithm concerns special fields where critical lines disappear, a situation which occurs, say, in the context of tracing dendrites in a neural network, or blood vessels within a liver. Note also that the present network does not recover secondary critical lines, corresponding to say, lines of steepest ascent connecting directly minima to maxima. Indeed, neither set of lines are generically at the intersection of peak patches
In contrast, the algorithm is well suited to identify bifurcation points, and the connectivity of the network. In particular, in an astrophysical context, it would be worthwhile to make use of this feature and study statistically how the skeleton connects onto dark matter halos as a function of, say, they mass or spin, and investigate the details of local spin accretion in the context of the cosmic web superhighways, hence completing the spin alignment measurements of Sousbie et al. (2008) on smaller scales. More generally, the algorithm provides a neat bridge, via the provided connectivity, between the theory of continuous fields on the one hand, and graph theory for discrete networks on the other. This could prove to be of importance in the context of percolation theory. For instance, the percolation threshold can be explained in terms of the properties of the connectivity of the relevant nodes.
Here, as argued in section 2.4 we deliberately chose not to consider the issue of shot noise and its consequences on segmentation, for which no definitive solution yet exists, though many improvements have been proposed in the literature (see *e.g.* Roerdink (1995)). Instead, we followed the approach of Sousbie et al. (2008), that simply involves convolving the sampled density field with a large enough (in terms of sampling scale) Gaussian kernel so that the field can be considered smooth and differentiable; the probabilistic algorithm allows for the removal of sampling effects and small intensity residual shot noise. In appendix C we show that the corresponding fully connected skeleton is nonetheless quite robust (the core of the network remains quasi unchanged), so long as the SNR is above one. A possible drawback of this method is that it introduces a smoothing scale attached to the skeleton. This is not necessarily a problem in cosmology as the scaling of the skeleton properties with scale yields information on the distribution over these scales. Moreover, one is usually interested by the properties of the skeleton on a given scale (typically larger than the halo scale, a few megaparsecs). Nonetheless, there exist more complex multi-scale sampling and smoothing techniques such as the one presented in Platen et al. (2007) or Colberg (2007) that could straightforwardly be adapted to our implementation. All the algorithm requires is a structured sampling grid where one can recover a one to one pixel neighbourhood (*i.e.* one needs to be able to find the neighbouring pixels of any pixel and these pixels must have the former as neighbour as well). For instance, we already implemented the algorithm for an `Healpix` (Górski et al. 2005) pixelisation of the sphere (see Figure 17), while a direct implementation on a delaunay tesselation network is clearly an option[3].
A natural extension of the theoretical component of this work would be to investigate numerically the properties of the bifurcation points in abstract space or anisotropic settings (see Pogosyan et al. (in prep.) for a theoretical discussion for isotropic Gaussian random fields). For instance, in the context of cosmic structure formation, Hanami (2001), relied on the parallel between the skeleton of the density field in position-time 4D space and in position-scale 4D space to relate the two. In the former, the skeleton is a natural way of computing what is known as a halos merger tree, commonly used in semi-analytical galaxy formation models (see Hatton et al. (2003) for instance): the skeleton traces the evolution of the critical points of the density field in time. The peak theory (Bond & Myers 1996) tells us that the smoothing scale can be linked to time evolution on scales where gravitational effects remain weakly non-linear. A worthwhile goal is to establish the parallel between the properties of 4D skeleton in this position-smoothing scale space (which can be computed from the Gaussian initial conditions only) and the halo merger tree (see also Figure C2). Finally, note that classical bifurcation theory is concerned with the evolution of a critical point as a function of a control parameter. In the language of the skeleton, this evolution may correspond to the skeleton in the extended "phase space".

From the physical and observational point of view, beyond the above mentioned AP-test, an interesting venue would be to apply the skeleton to actual galaxy catalogs such as the SDSS (Adelman-McCarthy et al. 2008) to characterize the (universal) statistics of filaments as physical objects, like halos or voids, and describe them in terms of their thickness, length, curvature and environmental properties (galaxies types, halo proximity, color and morphology gradient...), both in virtual and observed catalogs. It could also be used as a diagnosis tool for inverse methods which aim at reconstructing the three dimensional distribution of the IGM from say QSO bundles (Caucci et al. 2008) or upcoming radio surveys (LOFAR, SKA etc...) Clearly the peak patch segmentation developed in this paper will also be useful in the context of the upcoming surveys such as the LSST, or the the SDSS-3 BAO surveys, for instance to identify rare events such as large walls or voids and study their shape. Its application to CMB related full sky data, such as WMAP or Planck should provide insight into, e.g. the level of non Gaussianity in these maps. Similarly, upcoming large scale weak lensing surveys (Dune, SNAP...) could be analysed in terms of these tools (see Pichon et al. (in prep.) for the validation of a reconstruction method in this context). Using the skeleton, the geometry of cold gas accretion that fuel stellar formation in the core of galaxies could be probed. The properties of the distribution of metals on smaller scales could be also investigated using peak patches, to see how they influence galactic properties; one could compare these statistical results to those obtained through WHIM detection by Oxygen emission lines (Aracil et al. (2004) Caucci et al. (2008)). Indeed it has been claimed (see e.g. Ocvirk et al. (2008) Dekel et al. (2008)) that the geometry of the cosmic inflow on a galaxy (its mass, temperature and entropy distribution, the

[3] for instance to segment regions on the surface of skull

connectivity of the local filaments network etc.) is strongly correlated to its history and nature.

In closing, let us emphasize again that the scope of application of the algorithm presented in this paper extends well beyond the context of the large scale structure of the universe: it could be used in any scientific of engineering context (medical tomography, geophysics, drilling ...) where the geometrical structure of a given field needs to be characterized.

Acknowledgements

We thank D. Pogosyan, D. Aubert, J. Devriendt, J. Blaizot and S. Peirani for fruitful comments during the course of this work, and D. Munro for freely distributing his Yorick programming language and opengl interface (available at `http://yorick.sourceforge.net/`*). This work was carried within the framework of the Horizon project, www.projet-horizon.fr.*

REFERENCES

Adelman-McCarthy, J. K., et al. 2008, *ApJ Sup.*, 175, 297
Alcock, C., & Paczynski, B. 1979, *Nature*, 281, 358
Aracil B., Petitjean P., Pichon C., Bergeron J., 2004, *A&A*, 419, 811
Aragón-Calvo, M. A., Jones, B. J. T., van de Weygaert, R., & van der Hulst, J. M. 2007, *A&A*, 474, 315
Aragón-Calvo, M. A., van de Weygaert, R., Jones, B. J. T., & van der Hulst, J. M. 2007, *ApJ Let.*, 655, L5
Aubert, D., & Pichon, C. 2006, EAS Publications Series, 20, 37
Aubert, D., Pichon, C., & Colombi, S. 2004, *MNRAS*, 352, 376
Barrow, J. D., Bhavsar, S. P., & Sonoda, D. H. 1985, *MNRAS*, 216, 17
Bertschinger, E. 1985, *ApJ Sup.*, 58, 1
Beucher S., Lantuejoul C., 1979, in Proceedings International Workshop on Image Processing, CCETT/IRISA, Rennes, France
Beucher S., Meyer F., 1993, Mathematical Morphology in Image Processing , ed. M. Dekker, New York, Ch. 12, 433
Bond, J. R., & Myers, S. T. 1996, *ApJ Sup.*, 103, 1
Bond, J. R., Cole, S., Efstathiou, G., & Kaiser, N. 1991, *ApJ*, 379, 440
Colberg, J. M. 2007, *MNRAS*, 375, 337
Coles, P., Melott, A. L., & Shandarin, S. F. 1993, *MNRAS*, 260, 765
Colless, M., et al. 2003, ArXiv Astrophysics e-prints, arXiv:astro-ph/0306581
Caucci S., Colombi S., Pichon C., Rollinde E., Petitjean P., Sousbie T., 2008, *MNRAS* in press, pp 000–000
Dekel A., Birnboim Y., Engel G., Freundlich J., Goerdt T., Mumcuoglu M., Neistein E., Pichon C., Teyssier R., Zinger E., 2008, ArXiv e-prints, 808
de Lapparent, V., Geller, M. J., & Huchra, J. P. 1986, *ApJ Let.*, 302, L1
El-Ad, H., & Piran, T. 1997, *ApJ*, 491, 421
Gottloeber, S. 1998, Large Scale Structure: Tracks and Traces, 43
Górski K. M., Hivon E., Banday A. J., Wandelt B. D., Hansen F. K., Reinecke M., Bartelmann M., 2005, *ApJ*, 622, 759
Graham, M. J., Clowes, R. G., & Campusano, L. E. 1995, *MNRAS*, 275, 790
Hahn, O., Carollo, C. M., Porciani, C., & Dekel, A. 2007, *MNRAS*, 381, 41
Hanami, H. 2001, *MNRAS*, 327, 721
Harker, G., Cole, S., Helly, J., Frenk, C., & Jenkins, A. 2006, *MNRAS*, 367, 1039
Hatton S., Devriendt J. E. G., Ninin S., Bouchet F. R., Guiderdoni B., Vibert D., 2003, *MNRAS*, 343, 75
Hoffman, Y., & Shaham, J. 1982, *ApJ Let.*, 262, L23
Huchra, J. P., & Geller, M. J. 1982, *ApJ*, 257, 423
Icke, V. 1984, *MNRAS*, 206, 1P
Jost , Jorgen., Riemannian Geometry and Geometric Analysis, Fourth Edition, 1995, Springer
Kirshner, R. P., Oemler, A., Jr., Schechter, P. L., & Shectman, S. A. 1981, *ApJ Let.*, 248, L57
Kofman, L., Pogosyan, D., Shandarin, S. F., & Melott0, A. L. 1992, *ApJ*, 393, 437
Lacey, C., & Cole, S. 1993, *MNRAS*, 262, 627
Martinez, V., & Saar, E. 2002, *Proc. SPIE*, 4847, 86
Merritt, D., Graham, A. W., Moore, B., Diemand, J., & Terzić, B. 2006, *AJ*, 132, 2685
Milnor, J., 1963, Morse Theory (Princeton University, Princeton, NJ)
Navarro, J. F., Frenk, C. S., & White, S. D. M. 1997, *ApJ*, 490, 493
Neyrinck, M. C. 2008, *MNRAS*, 386, 2101
Neyrinck, M. C., Gnedin, N. Y., & Hamilton, A. J. S. 2005, *MNRAS*, 356, 1222
Novikov, D., Colombi, S., & Doré, O. 2006, *MNRAS*, 366, 1201
Ocvirk P., Pichon C., Teyssier R., 2008, ArXiv e-prints, 803
Peebles, P. J. E. 1980, Research supported by the National Science Foundation. Princeton, N.J., Princeton University Press, 1980. 435 p.,
Peebles, P. J. E. 1993, Princeton Series in Physics, Princeton, NJ: Princeton University Press, —c1993,
Pichon C., Vergely J. L., Rollinde E., Colombi S., Petitjean P., 2001, *MNRAS*, 326, 597
Pichon C., Thiébaut E., Prunet S., Benabed K., Sousbie,T., Teyssier R., Colombi S. *in prep.*
Pogosyan D., Pichon C., Prunet S., Gay C., Sousbie,T., Colombi S. *in prep.*
Platen, E., van de Weygaert, R., & Jones, B. J. T. 2007, *MNRAS*, 380, 551
Prunet S., Pichon C., Aubert D., Pogosyan D., Teyssier R., Gottloeber S., 2008, ArXiv e-prints, 804
Jos, B. T. M., Roerdink & Arnold Meijster, 2001, *Fundamenta informaticae*, 41, 187-228
Sheth, R. K. 1998, *MNRAS*, 300, 1057
Sousbie, T., Pichon, C., Colombi, S., Novikov, D., & Pogosyan, D. 2008, *MNRAS*, 383, 1655
Sousbie, T., Pichon, C., Courtois, H., Colombi, S., & Novikov, D. 2008, *ApJ Let.*, 672, L1
Springel, V. 2005, *MNRAS*, 364, 1105
Springel, V., White, S. D. M., Tormen, G., & Kauffmann, G. 2001, *MNRAS*, 328, 726
Stoica, R. S., Martínez, V. J., Mateu, J., & Saar, E. 2005,

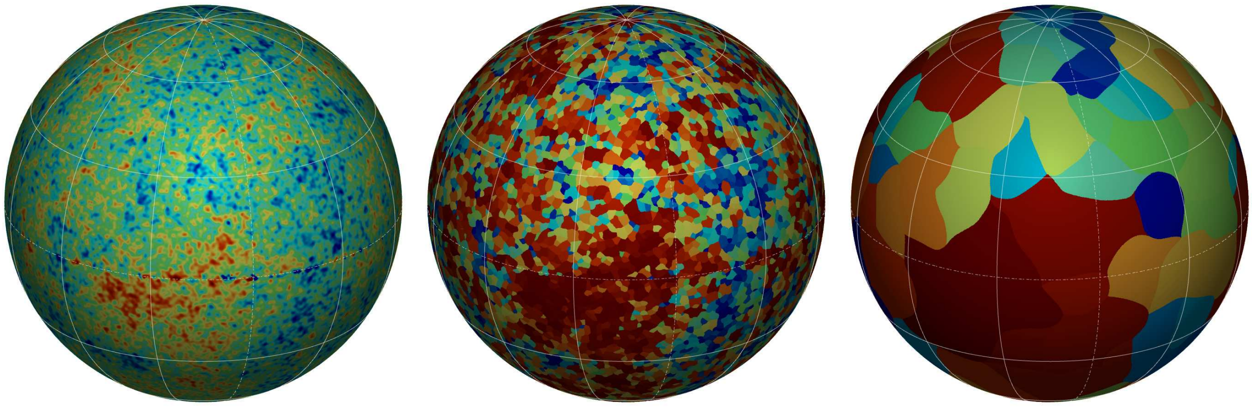

Figure 17. *from left to right*: the 5 year WMAP release of the CMB temperature map, the corresponding peak patches and the peak patches of the same field smoothed over a FHWM of 420 arcmin. Different colours represent different patches. The algorithm described in section 2 is implemented here on the `healpix` pixelisation.

A&A, 434, 423
Teyssier, R, Pires, S, Prunet, S, Aubert, D. Pichon, C Prunet, Amara, A Benabed, K Colombi, S Refregier, A. & Starck, J.L. 2008, submitted.
van de Weygaert, R., & Schaap, W. 2007, ArXiv e-prints, 708, arXiv:0708.1441
Wang, H. Y., Mo, H. J., & Jing, Y. P. 2007, *MNRAS*, 375, 633
Zel'Dovich, Y. B. 1970, A&A, 5, 84

APPENDIX A: A GENERIC MINIMIZATION ALGORITHM

In this appendix, we present a generic algorithm that aims at minimizing a multi-linear scalar function $f(x_1,..,x_d)$ of d variables within a polygonal volume, in a d-dimensional space, by reducing the problem to finding the respective minima of a set of polynomials of order d. It takes as input the location of the minima, M_i^0, of $f(x_1,..,x_d)$ on the edges of the square and simply consists in recursively minimizing the value of $f(x_1,..,x_d)$ along the lines joining them.

Let us first consider the 2D case illustrated by Figure A1, where the cell is a square. In this case, three minima, M_1^0, M_2^0 and M_3^0 (represented by red crosses) can be easily found on the edges of the square from the linearly interpolated value of f along them. One can then compute the location of the minima along the three lines linking them (the red triangle), noting that because of the multi-linearity of f, its value along a line can be expressed as a second order polynomial. One thus obtains 3 new points, M_1^1, M_2^1 and M_3^1, and the process can be repeated, as represented by the blue and black sets of lines, until convergence to the solution, represented by the blue cross (*i.e.* when the three points are close enough to each other).

This algorithm can be generalized to the case of the p-face of an n-cubic cell, $p \leqslant n$, thus providing the solution over the p-face from the k solutions, M_i^0 $i \in \{1,..,k\}$, over the sets of $(p-1)$-faces that are its edges. As explained in section 2.3.3, this algorithm is thus recursively applied to the edges of the cell, starting from the 1-faces, in the order of their increasing dimensionality. The j^{th} step of the algorithm thus goes as follows:

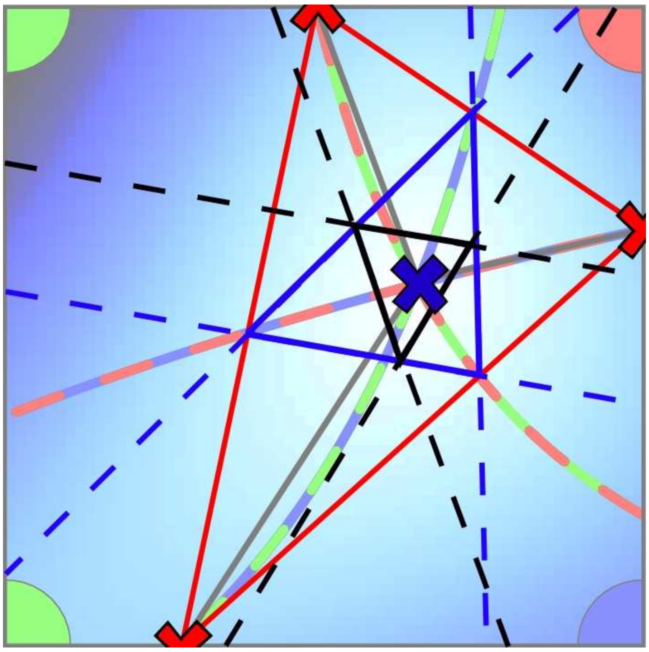

Figure A1. Illustration in the 2D case of the recursive minimization algorithm, applied to the case of Figure 5(b). The reader can refer to the legend of Figure 5 for more details. The scalar field to minimize is represented by the blue shading in the background while its minimum is located at the intersection of the 3 quadrics. The red crosses locate the field minima along the edges while the red, blue and black sets of lines result from the first three recursion steps.

(i) Compute the equations of the $(k)(k-1)/2$ lines joining pairs of M_i^{j-1}.
(ii) Evaluate the value of $f(x_1,..,x_d)$ at $p+1$ points along these lines using multi-linear interpolation, and fit a polynomial of order p.
(iii) Find the minima of these polynomials that belong to the cell and keep the k lowest among them, with coordinates M_i^j.

(iv) If these points are all contained in a sphere of radius a given fraction of the cell, stop, else start over.

Note that although only the case of a Cartesian sampling grid was presented here, the algorithm is easily transposable to any type of grid, such as the one produced by Voronoi tessellation on a manifold, which is composed of simplex shape cells.

APPENDIX B: INTER-SKELETON PSEUDO-DISTANCE

The inter-skeleton pseudo-distance from one skeleton $\mathcal{S}_a$ to another skeleton $\mathcal{S}_b$ was defined in the main text by the probability distribution function (PDF) of the minimum of the distance from each segment of $\mathcal{S}_a$ to any segments of $\mathcal{S}_b$. In this appendix, we show how this measure can be interpreted using realizations of scale invariant Gaussian random fields (GRFs) with different power spectrum index n (such that $P(k) \propto k^{-n}$) and different smoothing lengths L. All the skeletons that we use were computed from 512^3 pixels realizations of GRFs, smoothed over a scale $L = 8$ pixels or $L_L = 16$ pixels. These scales are defined as the width of the Gaussian kernel that we used to smooth the fields and the value of L roughly corresponds, in number of pixels, to the smoothing scale we used in the main text, $L_{\rm NL}$. A total of six different skeletons were computed:

- $\mathcal{S}_{\rm GRF0}$ and $\mathcal{S}_{\rm GRF0'}$: skeletons computed from two realizations (GRF0 and GRF0′) of GRFs with spectral index $n = 0$, smoothed over a scale $L = 8$ pixels.

- $\mathcal{S}_{\rm GRF3}$ and $\mathcal{S}_{\rm GRF3'}$: skeletons computed from two realizations (GRF3 and GRF3′) of GRFs with spectral index $n = 3$, smoothed over a scale $L = 8$ pixels.

- $\mathcal{S}_{\rm GRF0_T}$: this skeleton was computed from the field GRF0, smoothed on scale L. The resulting skeleton was then translated by $\mathbf{v} = (L/2, 0, 0)$.

- $\mathcal{S}_{\rm GRF0_L}$: this skeleton was computed from the field GRF0, smoothed on scale $L_L = 2L = 16$ pixels.

Figure B1 presents the different pseudo-distances between these skeletons, $\mathcal{D}(\rm a, b)$. Figures 1(a) and 1(b) present the results obtained when comparing uncorrelated fields (i.e. different realizations of GRFs). As expected in that case, $\mathcal{D}(\rm GRF0, GRF0') = \mathcal{D}(GRF0', GRF0)$ and $\mathcal{D}(\rm GRF3, GRF3') = \mathcal{D}(GRF3', GRF3)$ and the position of the mode is about the smoothing length. One should also note that the mode intensity differs between $n = 0$ and $n = 3$, which can be explained by the fact that in the latter case, small scale fluctuations are suppressed together with smaller scale filaments, thus making it less probable for a segment of one realization to be very close to one of the other realization. Figure 1(c) shows that these pseudo distance measurements make it possible to distinguish the different nature of two skeletons. In fact, whereas $\mathcal{S}_{\rm GRF0}$ has filaments on any scales, only the larger scales are present in $\mathcal{S}_{\rm GRF3}$, which translates into an asymmetry between $\mathcal{D}(\rm GRF0, GRF3)$ and $\mathcal{D}(\rm GRF3, GRF0)$. Whereas in the first case, there is no reason why every segment of $\mathcal{S}_{\rm GRF0}$ should be close to a segment of $\mathcal{S}_{\rm GRF3}$, the reciprocal is not true : $\mathcal{S}_{\rm GRF0}$ spreads on all scales and every segment of $\mathcal{S}_{\rm GRF3}$ should be as close as any other from a segment of $\mathcal{S}_{\rm GRF0}$ (hence the higher intensity of the mode for $\mathcal{D}(\rm GRF3, GRF0)$). When comparing a skeleton $\mathcal{S}_{\rm a}$ with less filaments to a skeleton $\mathcal{S}_{\rm b}$ with more filaments, the intensity of the mode is thus expected to be higher for $\mathcal{D}(\rm a, b)$ than for $\mathcal{D}(\rm b, a)$.

This observation is confirmed by Figure 1(e) where $\mathcal{S}_{\rm GRF0_L}$ is compared to $\mathcal{S}_{\rm GRF0}$, which has small scale filaments that $\mathcal{S}_{\rm GRF0_L}$ does not have. But in that case, the two skeletons are correlated as only the smoothing length changes. This results in a higher intensity of the mode of $\mathcal{D}(\rm GRF0_L, GRF0)$: the larger scale filaments are present in both skeletons. It also results in a shift in the position of the mode, located at a distance smaller than the smoothing length. Figure 1(d) illustrates the case of a simple translation of length half the smoothing length L: in that case, both PDFs are identical and a very asymmetric and high intensity mode is present at distance $L/2$. Finally, it is also interesting to note that the comparison of $\mathcal{S}_{\rm GRF0_L}$ to $\mathcal{S}_{\rm GRF0_T}$ almost gives the exact same result as the one for $\mathcal{S}_{\rm GRF0_L}$ to $\mathcal{S}_{\rm GRF0}$ and it is difficult to distinguish one from the other.

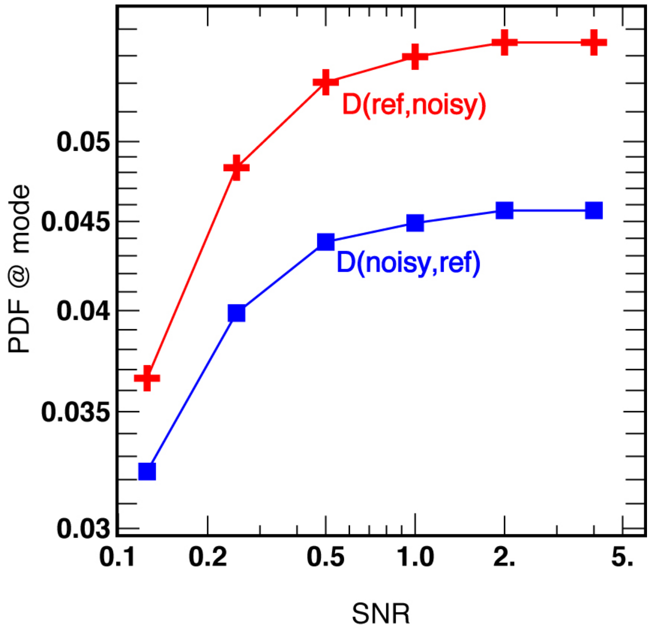

Figure C1. The evolution of the PDF of distances at the mode as a function of the SNR of a noisy field. Here the distance is computed between the reference skeleton and its noisy counter part. For SNR above one, only small differences between weak filaments account for the difference between the two distances. Conversely, for more noisy fields, the fraction of match between the two skeleton drops.

APPENDIX C: ROBUSTNESS OF FULLY CONNECTED SKELETON

In order to investigate the robustness of the fully connected skeleton with respect to small change in the underlying field, the following experiment is carried. A given 2D white ran-

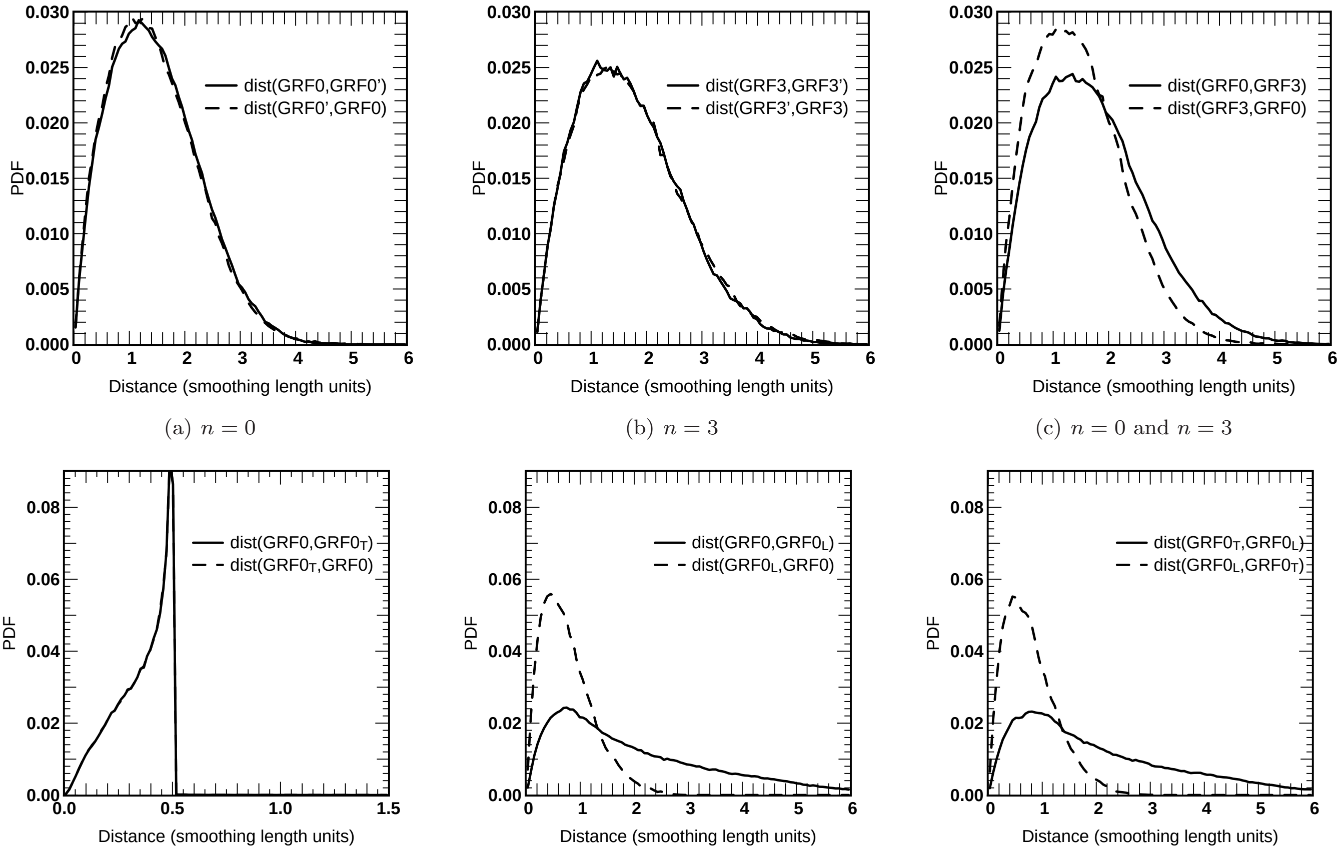

(a) $n = 0$

(b) $n = 3$

(c) $n = 0$ and $n = 3$

(d) $n = 0$ and its translation

(e) $n = 0$, different smoothing lengths

(f) $n = 0$, translation and different smoothing lengths

Figure B1. Measures of the inter-skeleton pseudo distances for Gaussian random fields with different power spectrum index n and smoothing length L. These plots show how the pseudo-distances measurements can be used to assess the discrepancies between two skeletons.

dom field of size 4096^2 is generated. It is then smoothed over 10 pixels, and its reference skeleton, $\mathcal{S}_{\rm ref}$ is computed. A white random field of amplitude SNR is added to the reference field, and the corresponding skeleton, $\mathcal{S}_{\rm SNR}$, is computed after smoothing over 10 pixels. The PDF of the distances $\mathcal{D}(\mathcal{S}_{\rm ref}, \mathcal{S}_{\rm SNR})$ and $\mathcal{D}(\mathcal{S}_{\rm SNR}, \mathcal{S}_{\rm ref})$ is then calculated (see Appendix B). The distance at the maximum (its mode) of both PDF remains unchanged for all the SNR considered $(1/8, 1/4, 1/2, 1, 2, 4)$, which demonstrates that the core of the skeleton is quite robust: the reference skeleton is always shadowed by its noisy counter part. The amplitude of the PDF at its maximum is plotted in Figure C1. This amplitude is sensitive to the high distance tail of mismatch between the two skeleton since the PDF is normalized. In short, within the network there is a small subset of filaments which are sensitive to any small variation of the field. For the vast majority of the network, the skeleton is globally only weakly affected by changes of the underlying field so long as the amplitude of the change has a SNR above one. When the SNR drops bellow one, spurious filaments occur more and more. The discrepancy between the two plateaux at larger SNR reflects the fact that weaker filaments will occur somewhat randomly from one realisation to another, depending on very small details in the field.

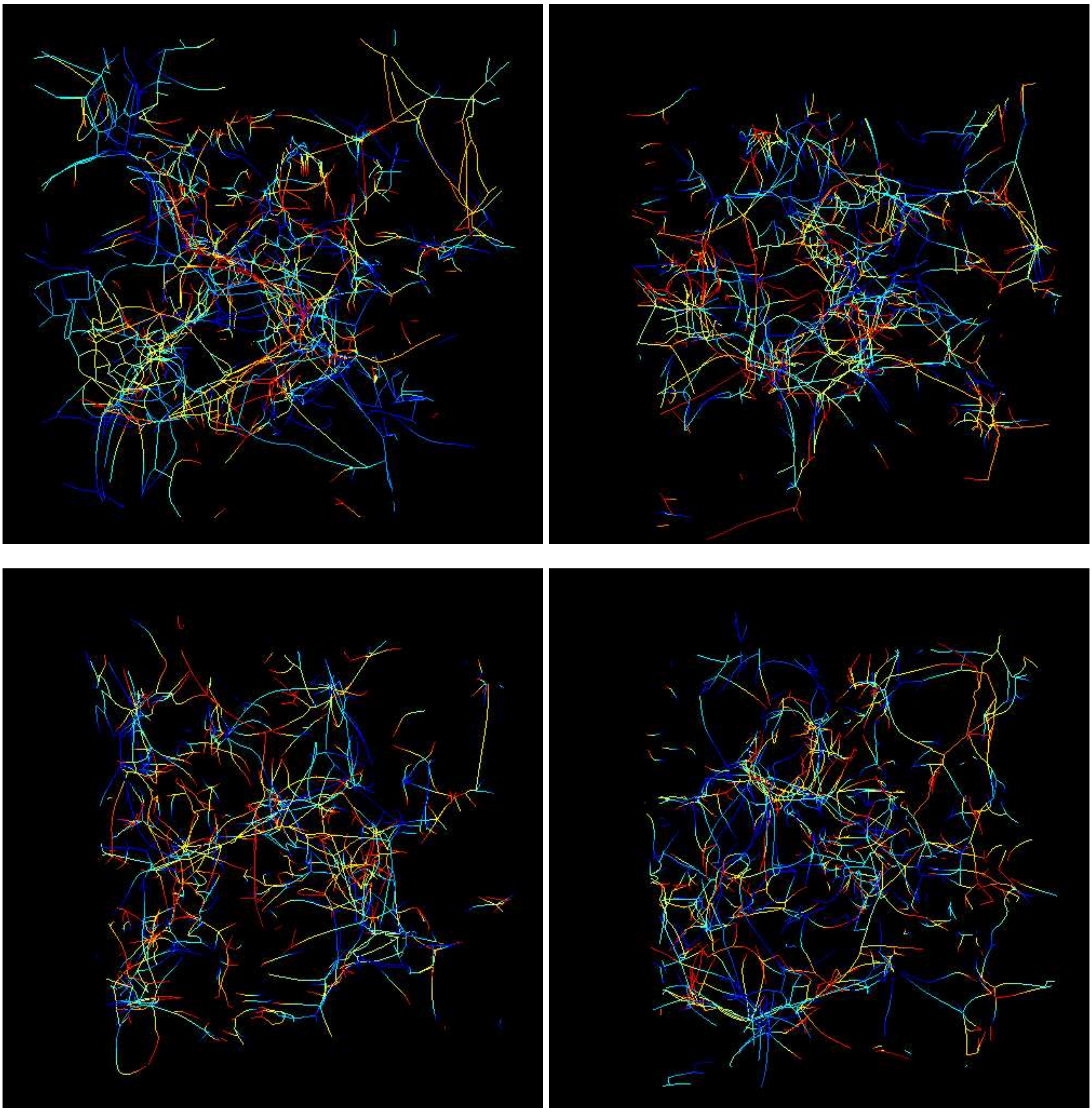

Figure C2. four consecutive thin slices of a 4D gaussian random field skeleton of width $1/8^{\text{th}}$ of the box size, colour coded according to the fourth dimension. The underlying field has 32^4 pixels. Note that for these sections, the skeleton is spitted into unconnected filaments. One could think of these short filaments as the traces of quantum particles corresponding to the maxima of their probability amplitude (which could randomly move forward and backwards in time, the fourth dimension).

Astron. Astrophys. 343, 663–681 (1999)

ASTRONOMY AND ASTROPHYSICS

Vorticity generation in large-scale structure caustics

C. Pichon[1,2,3] **and F. Bernardeau**[3,4]

[1] CITA, 60 St. George Street, Toronto, Ontario M5S 1A7, Canada
[2] Astronomisches Institut Universitaet Basel, Venusstrasse 7 CH-4102 Binningen, Switzerland,
[3] Institut d'Astrophysique de Paris, 98 bis Boulevard d'Arago, F-75014 Paris, France
[4] Centre d'étude de Saclay, Service de Physique Théorique, F-91191 Gif-sur-Yvette, France

Received 15 December 1997 / Accepted 2 December 1998

Abstract. A fundamental hypothesis for the interpretation of the measured large-scale line-of-sight peculiar velocities of galaxies is that the large-scale cosmic flows are irrotational. In order to assess the validity of this assumption, we estimate, within the frame of the gravitational instability scenario, the amount of vorticity generated after the first shell crossings in large-scale caustics. In the Zel'dovich approximation the first emerging singularities form sheet like structures. Here we compute the expectation profile of an initial overdensity under the constraint that it goes through its first shell crossing at the present time. We find that this profile corresponds to rather oblate structures in Lagrangian space. Assuming the Zel'dovich approximation is still adequate not only at the first stages of the evolution but also slightly after the first shell crossing, we calculate the size and shape of those caustics and their vorticity content as a function of time and for different cosmologies.

The average vorticity created in these caustics is small: of the order of one (in units of the Hubble constant). To illustrate this point we compute the contribution of such caustics to the probability distribution function of the filtered vorticity at large scales. We find that this contribution that this yields a negligible contribution at the 10 to 15 h^{-1}Mpc scales. It becomes significant only at the scales of 3 to 4 h^{-1}Mpc, that is, slightly above the galaxy cluster scales.

Key words: galaxies: formation – cosmology: theory – cosmology: dark matter – cosmology: large-scale structure of Universe

1. Introduction

The analysis of large-scale cosmic flows has become a very active field in cosmology (see Dekel 1994 for a recent review on the subject). The main reason is that it can in principle give access to direct dynamical measurements of various quantities of cosmological interest. There are now a very large number of methods and results for the comparison of the measured large–scale flows with the measured density fluctuations as observed in the galaxy catalogues. Most of these methods are sensitive to a combination of the density of the universe in units of the critical density, Ω, and the linear bias, b, associated to the mass tracers adopted to estimate the density fluctuations. The estimated values of $\beta = \Omega^{0.6}/b$ are about 0.3 to 1 depending on the method or on the tracers that are used. There are other lines of activities that aim to estimate Ω from only the *intrinsic* properties of the velocity field, (i.e., without comparison with the observed galaxy density fluctuations). All these methods exploit non-Gaussian features expected to appear in the velocity field, either the maximum expansion rate of the voids (Dekel & Rees 1994), non-Gaussian general features as expected from the Zel'dovich approximation (Nusser & Dekel 1993), or the skewness of the velocity divergence distribution (Bernardeau et al. 1995). Yet they all also assume that the velocity field is *potential*. This is indeed a necessary requirement for building the whole 3D velocity out of the line-of-sight informations in reconstruction schemes such as Potent (Bertschinger et al. 1990, Dekel et al. 1994). This is also a required assumption for carrying calculations in the framework of perturbation theory. It is therefore interesting to check the rotational content of the cosmic flows at scales at which they are considered in galaxy catalogues, that is at about 10 to 15h^{-1}Mpc. This investigation ought to be carried in the frame of the gravitational instability scenario with Gaussian initial conditions. It is known that in the single stream régime, primordial vorticity is diluted by the expansion and that the higher order terms in a perturbation expansion cannot create "new" vorticity. Hence it is natural to assume that the vorticity on larger scales originate from the (rare) regions where multi-streaming occurs. During the formation of large scale structures this happens first when the largest caustics cross the first singularity, creating a three-flow region where vorticity can be generated. As we argue in Sect. 2, analytical calculations of constrained random Gaussian fields suggest that the largest caustics that are created are sheet-like structures, in rough agreement with what is found in numerical simulations or in galaxy catalogues. It is therefore reasonable to use Zel'dovich's approximation to describe the subsequent evolution of those objects.

In order to estimate the large scales vorticity distribution we therefore proceed in five steps: first we evaluate the mean constrained random field corresponding to a local asymmetry of the deformation tensor on a given scale, R_L; secondly we

Send offprint requests to: C. Pichon (pichon@astro.unibas.ch) solve for the multi-flow régime within the generated caustic, using Zel'dovich's approximation throughout, even slightly beyond this first singularity. We then evaluate the vorticity field in that caustic. The next step involves modelling the variation of the characteristics of typical caustics as a function of time for different power spectra. Finally, we estimate the amount of vorticity expected at large scales arising from large scale flow caustics.

For the sake of simplicity and because is pedagologically more appealing, we present calculations carried out in two dimensions as well as in three dimensions. The former case is in particular easier to handle numerically.

The second section of this paper evaluates the characteristics of the typical caustics expected at large–scale in a 2D or 3D density field. The third section is devoted to the explicit calculation of the vorticity for the most typical caustics. The fourth section provides an estimate for the shape of the tail of the probability distribution function of the modulus of the vorticity in a sphere of a given radius. It is followed by a discussion on the validity and implications of these results.

2. Asymmetric constrained random fields

Since it is not our ambition to solve the problem of deriving the vorticity statistics in its whole generality the vorticity will be estimated only within specific but typical caustics in the framework of the Zel'dovich approximation.

The first step involves building an initial density field in which a caustic will eventually appear. The initial fluctuations are assumed to be Gaussian with a given power spectrum $P(k)$, characterizing the amplitude and shape of the initial fluctuations. No *a priori* assumptions about the values of Ω and Λ are made. It will be shown that the statistics has very straightforward dependences upon these parameters. The expectation values of the random variables, $\delta(\mathbf{k})$, corresponding to the Fourier transforms of the local density field,

$$\delta(\mathbf{x}) = \int \mathrm{d}^3\mathbf{k}\, \delta(\mathbf{k})\, \exp[\mathrm{i}\mathbf{k}\cdot\mathbf{x}], \tag{1}$$

are calculated once a local constraint has been imposed. This constraint will be chosen so that the caustic-to-be will have just gone through first shell crossing at the present time. It is expressed in terms of the *local* deformation matrix of the *smoothed* density field. The components of the local deformation tensor at the position $\mathbf{x}_0$ are given by

$$\Phi_{i,j}(\mathbf{x}_0) = \int \mathrm{d}^3\mathbf{k}\, \delta(\mathbf{k})\, W_D(k\,R_L)\exp[\mathrm{i}\mathbf{k}\cdot\mathbf{x}_0]\,\frac{\mathbf{k}_i\mathbf{k}_j}{k^2}, \tag{2}$$

where W_D is the adopted window function. In what follows, we will use the top-hat window function for which

$$W_2(k) \;=\; 2\,\frac{J_1(k)}{k^{1/2}} \quad \mathrm{in} \quad 2D,$$
$$W_3(k) \;=\; 3\sqrt{\pi/2}\,\frac{J_{3/2}(k)}{k^{3/2}} \;\; \mathrm{in} \;\; 3D, \tag{3}$$

where J_ν is the Bessel function of index ν. The scale R_L is the scale of the caustic in Lagrangian space. Here σ_0 stands for the *rms* density fluctuation at this scale:

$$\sigma_0^2 = \int \mathrm{d}^3k\, P(k)\, W_2^2(k\,R_L). \tag{4}$$

For the sake of simplicity a typical caustic is chosen to be characterized by the average local perturbation over a sphere of radius R_L for which the deformation tensor at its centre given point is fixed. We are aware that this is a somewhat drastic approximation but consider that, at large scales, the behaviour of caustics having the mean initial profile will be representative of the average behaviour. This is certainly not true at small scales where the complex interactions of structures at different scales and positions are expected to affect the global behaviour of any given caustic. For some rare enough objects however we expect the fluctuations around the mean profile to be small enough to affect only weakly the global properties of the caustics. This has been shown to be true in the early stages of the dynamics for spherically symmetric perturbations (Bernardeau 1994a). In the following we will, however, encounter properties (see Sect. 3.3) that we think are not robust against small scale fluctuations. Such properties will be ignored in the subsequent applications of our results.

Within the frame of this calculation, the values of $\delta(\mathbf{k})$ hence correspond to the expectation values of $\delta(\mathbf{k})$ for the power spectrum $P(k)$ when the constraints on the deformation tensor are satisfied. These solutions can be written as a linear combination of the values of the deformation tensor:

$$\delta(\mathbf{k}) = \sum_{i=1}^{D} -\frac{\left(C^{-1}\right)_{0,i}}{\left(C^{-1}\right)_{0,0}}\,\lambda_i \;\equiv \sum_{i=1}^{D}\,\alpha_i\,\lambda_i\,, \tag{5}$$

where the coefficients C is the matrix of the cross-correlations between the random Gaussian variables Φ_{ij} and $\delta(\mathbf{k})$ as shown in Appendix A. In Eq. (5) the summation is made only on the diagonal elements of the deformation tensor since it is always possible to choose the axis in such a way that the other elements are zero. In this instance, the diagonal elements are identified with the eigenvalues λ_i, of the matrix.

2.1. The 2D field

In 2D geometry, the two coefficients α_1 and α_2 defined by Eq. (5) are given by

$$\alpha_1 \;=\; (3I_1 - I_2)/\sigma_0^2\,,\;\; \alpha_2 = (3I_2 - I_1)/\sigma_0^2\,,\;\; \mathrm{where}$$
$$I_i \;=\; \left\langle \delta_k\,\Phi_{ii}\right\rangle = P(k)\,W_2(kR_L)\,\frac{\mathbf{k}_i^2}{k^2}. \tag{6}$$

The brackets, $\langle . \rangle$, denote ensemble averages over the initial (unconstrained) random density field. As a result, Eq. (5) reads

$$\delta(\mathbf{k}) \;=\; \frac{P(k)\,W_2(kR_L)}{\sigma_0^2} \times\left[2\,(\lambda_1+\lambda_2) + 4\,(\lambda_1-\lambda_2)\,\cos(2\theta)\right]\,; \tag{7}$$

λ_1 and λ_2 are the eigenvalues of the deformation tensor and where θ is the angle between $\mathbf{k}$ and the eigenvector associated with the first eigenvalue (see Appendix A for details). Consider the parameter a defined by

$$a = \frac{2(\lambda_1 - \lambda_2)}{\lambda_1 + \lambda_2}. \tag{8}$$

The coefficient a represents the amount of asymmetry in the fluctuation (thus $a = 0$ corresponds to a spherically symmetric perturbation). This parameter is similar to the eccentricity, e, that was used by Bardeen et al. (1986) and more specifically by Bond & Efstathiou (1987) for 2D fields. In these studies however investigations were made for the shape of the peaks around the maximum (i.e. eigenvalues of the second order derivatives of the local density), so a and e cannot be straightforwardly identified.

The formation time of the first singularity is determined by the maximum value of the eigenvalues, $\lambda_{\rm max}$. It is therefore relevant to calculate the distribution function of $\lambda_{\rm max}$, and the distribution function of a once $\lambda_{\rm max}$ is known. From the statistical properties of the matrix elements Φ_{ij} we derive the distribution function of the eigenvalues $\lambda_{\rm min}$ and $\lambda_{\rm max}$ (see Appendix B), which reads

$$P(\lambda_{\rm min}, \lambda_{\rm max}) \;=\; \frac{2^{3/2}}{\pi^{1/2}\,\sigma_0^3}\,(\lambda_{\rm max} - \lambda_{\rm min}) \times \exp\left[-\frac{1}{\sigma_0^2}\left(\frac{3}{2}J_1^2 - 4\,J_2\right)\right], \tag{9}$$

with

$$J_1 = \lambda_{\rm min} + \lambda_{\rm max}\,, \quad J_2 = \lambda_{\rm min}\,\lambda_{\rm max}. \tag{10}$$

The distribution function of $\lambda_{\rm max}$ follows by numerical integration over $\lambda_{\rm min}$. Fig. (1) shows the distribution function of $\lambda_{\rm max}$ in units of the variance. The dashed line corresponds to the approximation, valid at $\lambda_{\rm max}/\sigma_0 \gg 1$:

$$p_{\rm max}(\lambda_{\rm max})\,{\rm d}\lambda_{\rm max} \approx 1.5\,\frac{\lambda_{\rm max}}{\sigma_0}\exp\left[-\frac{4}{3}\left(\frac{\lambda_{\rm max}}{\sigma_0}\right)^2\right]\,\frac{{\rm d}\lambda_{\rm max}}{\sigma_0}. \tag{11}$$

The distribution function of a for different values of $\lambda_{\rm max}/\sigma_0$ is presented in Fig. (2). It turns out that the most significant value corresponds to $a \approx 1$. In the following this value is chosen as the typical value for the asymmetry in two dimensions.

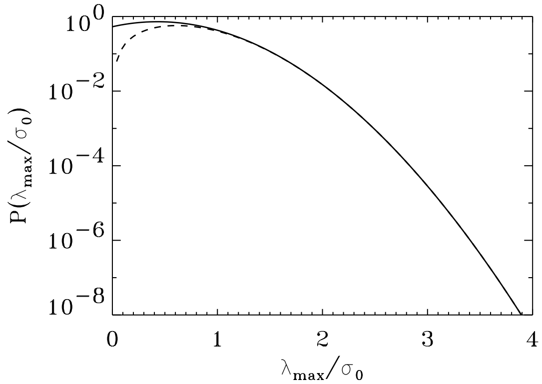

Fig. 1. The distribution function of $\lambda_{\rm max}/\sigma_0$ (solid line) in 2D dynamics. The dashed line is given by (Eq. (11)):

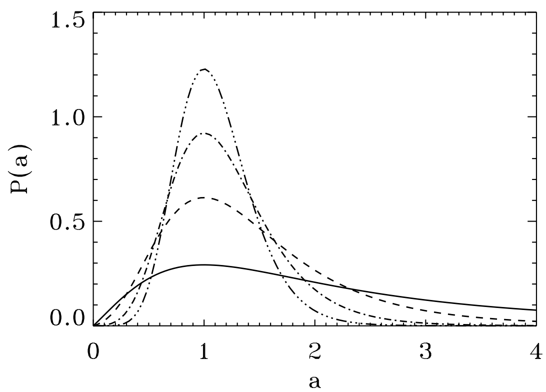

Fig. 2. The distribution functions of a for fixed values of $\lambda_{\rm max}/\sigma_0 = 1,\ 2,\ 3,\ 4$ (respectively the solid, long dashed, short dashed and long dotted dashed lines).

2.2. *The 3D field*

In three dimensions the geometry is slightly more complicated and yields for the constrained density field (see Appendix B for details)

$$\delta(\mathbf{k}) \;=\; \frac{3\,P(k)\,W_3(k\,R_L)}{8\sigma_0^2}\Big(\lambda_1\left[1 + 5\,\cos(2\phi_k) - 5\cos(2\theta_k) - 5\,\cos(2\phi_k)\,\cos(2\theta_k)\right] + \lambda_2\left[1 + 5\,\cos(2\phi_k) - 5\cos(2\theta_k) - 5\,\cos(2\phi_k) \times \cos(2\theta_k)\right] \,+\, 2\lambda_3\left[3 + 5\,\cos(2\,\theta_k)\right]\Big), \tag{12}$$

where θ_k and ϕ_k are polar angles of the vector $\mathbf{k}$ with respect to the basis of the eigenvectors associated to the three eigenvalues, $\lambda_1, \lambda_2, \lambda_3$. The asymmetry of the distribution is again characterized by the values of

$$a = 5\,\frac{2\lambda_3 - \lambda_1 - \lambda_2}{\lambda_1 + \lambda_2 + 6\lambda_3}\,,\ \text{ and }\ b = 5\,\frac{\lambda_1 - \lambda_2}{\lambda_1 + \lambda_2 + 6\lambda_3}. \tag{13}$$

When b only is zero Eq. (13) corresponds to a perturbation with axial symmetry, and when both a and b are zero it is a spherically symmetric perturbation. In terms of a and b Eq. (12) then becomes

$$\delta(\mathbf{k}) \;=\; \frac{3\,P(k)\,W_3(k\,R_L)}{8\,\sigma_0^2}\,(\lambda_1 + \lambda_2 + 6\lambda_3) \times \big(1 + a\,\cos(2\theta_k) + b\,\cos(2\phi_k)\left[1 + \cos(2\theta_k)\right]\big)\,. \tag{14}$$

Let us now evaluate the distribution of a and b from the distribution function of the eigenvalues $(\lambda_1, \lambda_2, \lambda_3)$ in 3D (assuming $\lambda_1 > \lambda_2 > \lambda_3$) in order to identify the shape of the most significant caustics. This distribution is given by (Doroshkevich 1970)

$$P(\lambda_1, \lambda_2, \lambda_3) \;=\; \frac{5^{5/2}\,27}{8\,\pi\,\sigma_0^6}\,(\lambda_1 - \lambda_2)\,(\lambda_1 - \lambda_3)\,(\lambda_2 - \lambda_3) \times \exp\left[-\frac{1}{\sigma_0^2}\left(3J_1^2 - \frac{15}{2}\,J_2\right)\right], \tag{15}$$

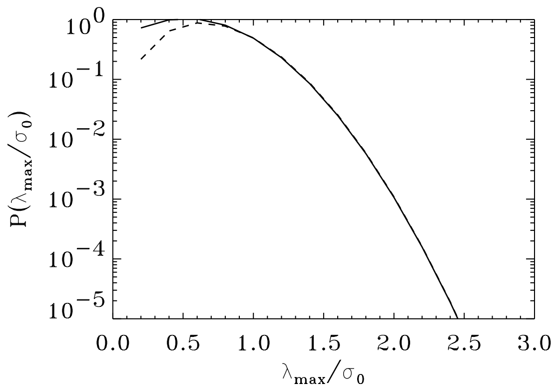

Fig. 3. The distribution function of $\lambda_{\max}/\sigma_0$ (solid line) in 3D dynamics. The dashed line is the analytical fit (17).

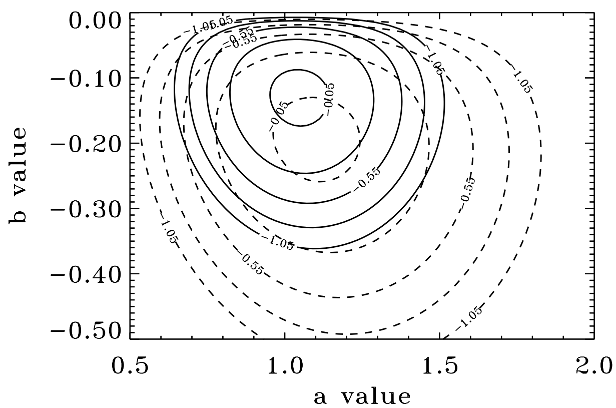

Fig. 4. The contour plot for the distribution of a and b for a fixed value of $\lambda_{\max}/\sigma_0 = 2$ (dashed lines) and $\lambda_{\max}/\sigma_0 = 3$ (solid lines). The lines are evenly distributed in a logarithmic scale.

with

$$J_1 = \lambda_1 + \lambda_2 + \lambda_3\,, \;\text{ and }\; J_2 = \lambda_1\lambda_2 + \lambda_2\lambda_3 + \lambda_3\lambda_1. \quad (16)$$

From this expression we compute numerically the distribution function of the maximum eigenvalue (Fig. (3)). An analytical fit of this distribution function is provided by its behaviour at large $\lambda_{\max}$

$$p_{\max}(\lambda_{\max})\,\mathrm{d}\lambda_{\max} \;\approx\; 6\,\left(\frac{\lambda_{\max}}{\sigma_0}\right)^2 \times \exp\left[-\frac{5}{2}\left(\frac{\lambda_{\max}}{\sigma_0}\right)^2\right]\frac{\mathrm{d}\lambda_{\max}}{\sigma_0}. \quad (17)$$

This fit is accurate for the rare event tail (as shown in Fig. (3)), which will be relevant for the derivation of Sect. 4.4. For a given value of $\lambda_{\max}$ we compute the distribution of the other eigenvalues, and thus the join distribution function of a and b.

The resulting contour plot corresponding to $\lambda_{\max}/\sigma_0 = 2$ and $\lambda_{\max}/\sigma_0 = 3$ is illustrated on Fig. (4). As for the distribution of a in the previous subsection in 2D it depends only weakly upon the adopted value of $\lambda_{\max}$ (although the position of the maximum varies a little), and it tends to be all the more peaked on its maximum as $\lambda_{\max}$ is large. This implies that a typical caustic will be given by $a \approx 1$ with a small b. For further simplifications we will assume that $b = 0$. Such a caustic then corresponds to a pancake-like structure with axial symmetry. Note that this result seems to differ from the results of Bardeen et al. (1986) who found that the shape of the rare peaks should be somewhat spherically symmetric or filamentary (this picture was recently sustained by Pogosyan et al. 1996, from the result of N-body simulations). This apparent discrepancy is due to the constraint under which the expectation values of a and b are calculated. In Bardeen et al.'s work the constraint is given by the value of the local density, i.e. the sum of the three eigenvalues, whereas in this paper we put a constraint on the largest eigenvalue. This is a natural assumption for this investigation since the multi-streaming occurs as soon as a singularity has been reached in one direction. Of course, this analysis assumes that the Zel'dovich approximation holds in order to predict the time at which this first singularity is reached. For oblate initial structures such as the ones obtained for the most likely values of a (see Figs. 5 and 6), we expect that this approximation is sufficiently accurate.

3. The geometry and vorticity of large-scale caustics

In this section we investigate the properties of the caustics that are induced by the initial density fluctuation profiles we found in the previous section. All the calculations are performed within the framework of the Zel'dovich approximation, even sightly after the first shell crossing.

3.1. The linear displacement field

In the framework of the Zel'dovich approximation the displacement field can be written

$$\mathbf{x} = \mathbf{q} + D(t)/D(t_0)\,\Psi(\mathbf{q})\,; \quad (18)$$

where $D(t)$ accounts for the time dependency of the linear growing mode (it is proportional to the expansion factor in case of an Einstein-de Sitter geometry only). An important simplification is that, at the order of the Zel'dovich approximation, this displacement field is separable in time and space, and its space dependence, $\Psi(\mathbf{q})$, is potential, i.e., there is a velocity potential $U(\mathbf{q})$ so that

$$\Psi(\mathbf{q}) = \nabla_{\mathbf{q}} \cdot U(\mathbf{q})\,. \quad (19)$$

This velocity potential is given by

$$U(\mathbf{q}) = \int \mathrm{d}^3\mathbf{q}\,\delta(\mathbf{k})\,\frac{1}{k^2}\,\exp[\mathrm{i}\mathbf{k}\cdot(\mathbf{q}-\mathbf{q}_0)]\,. \quad (20)$$

By construction the point $\mathbf{q}_0$ in Lagrangian space corresponds to the point $\mathbf{x}_0$ in real space (central position of the caustic). Both of them will be taken to be zero. For the calculation of the explicit expressions of $\delta(\mathbf{k})$ and $U(\mathbf{q})$ we will assume that the power spectrum follows a power law behaviour,

$$P(k) \propto k^n, \quad (21)$$

characterized by the power index n. From Eq. (21) the expression of the linear variance as a function of scale follows

$$\sigma(R_L) \propto R_L^{-(n+D)/2}. \tag{22}$$

This approximation is valid within a limited scale range as will be discussed in Sect. 5. At the scales of interest the index n is expected to be the range of $n \approx -1,\ -2$ from the constraints obtained with the large-scale galaxy catalogues, like the APM survey (Peacock 1991) the IRAS galaxy survey (Fisher et al. 1993) or from X-ray cluster number counts (Henry & Arnaud 1991, Eke et al. 1996, Oukbir & Blanchard 1997). In two dimensions there are of course no such observationally motivated values, but we will consider n of the order of -1 as an illustrative case.

3.1.1. The 2D potential

From the Eqs. (7),(20) it is possible to calculate the expression of the potential

$$\begin{aligned} U(\mathbf{q}) &= G(0, n-2, q) + a\,\cos(2\theta_q) \\ &\quad \times [G(0, n-2, q) - 2\,G(1, n-2, q)]\,, \quad \text{with} \\ G(\nu, n, q) &= \int \mathrm{d}^2\mathbf{k}\, k^n\, \frac{J_\nu(k\,q)}{(k\,q)^\nu}\, W_{2D}(k). \end{aligned} \tag{23}$$

The latter expression is given by

$$\begin{aligned} G(\nu, n, q) &= {}_2F_1(1 + n/2, n/2, 1 + \nu, q^2)\,, \\ &\quad \text{for} \quad q < 1\,, \quad \text{and} \end{aligned} \tag{24}$$

$$\begin{aligned} G(\nu, n, q) &= \frac{\Gamma(1+\nu)\,\Gamma(1-n/2)}{q^{n+2}\,\Gamma(\nu - n/2)}\ {}_2F_1(1 + n/2, 1 \\ &\quad -\nu + n/2, 2, q^{-2})\,, \ \text{for}\ q > 1. \end{aligned} \tag{25}$$

The expressions for the gradients of the potential involve similar hyper-geometric functions.

3.1.2. The 3D potential

The expression of the potential following from Eqs. (12),(20) becomes quite complicated, but involves here only "simple" functions. It reads

$$U(\mathbf{q}) = [V(q) - V(-q)]/q^3, \tag{26}$$

with

$$\begin{aligned} V(q) &= |1+q|^{2-n}\,\mathrm{sign}(1+q)\Big(A(q) - B(q)\,\big[b\,\cos(2\,\phi) \\ &\quad \times [1 - \cos(2\,\theta)] + a\,\cos(2\,\theta)\big]\Big)\,, \end{aligned} \tag{27}$$

$$\begin{aligned} A(q) &= -10\,q^2 + 7\,n\,q^2 - n^2\,q^2 + 5\,q^3 - n\,q^3 \\ &\quad + a\,\left(-1 + 2\,q - n\,q + 2\,q^2 - n\,q^2 - q^3\right)\,, \end{aligned} \tag{28}$$

$$\begin{aligned} B(q) &= 3 - 6\,q + 3\,n\,q + 4\,q^2 - 4\,n\,q^2 \\ &\quad + n^2\,q^2 - 2\,q^3 + n\,q^3 \end{aligned} \tag{29}$$

Note that the potentials in Eqs. (23) and (26) have discontinuous derivative at $q = 1$, which is an artifact of using a top-hat window function. Note also that the potentials given here have arbitrary normalizations. This is of no consequence for the derived results since the global normalization of the initial density profile is absorbed in the discussion for the value of $\lambda_{\max}$ (Sect. 4.4).

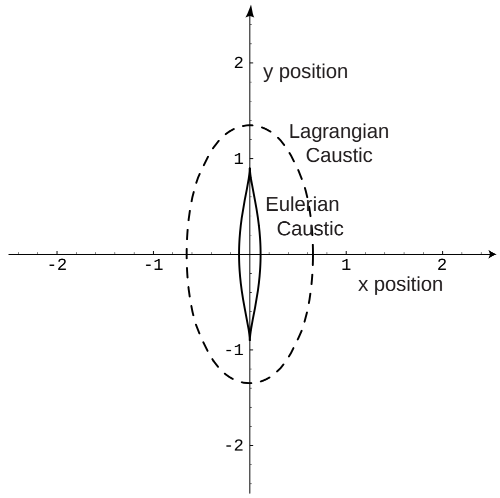

Fig. 5. The shape of the caustic for the 2D dynamics, $n = -1$, and $\lambda_{\max} \approx 1.3$. The dashed line is the shape in Lagrangian space and the solid line the shape in real space.

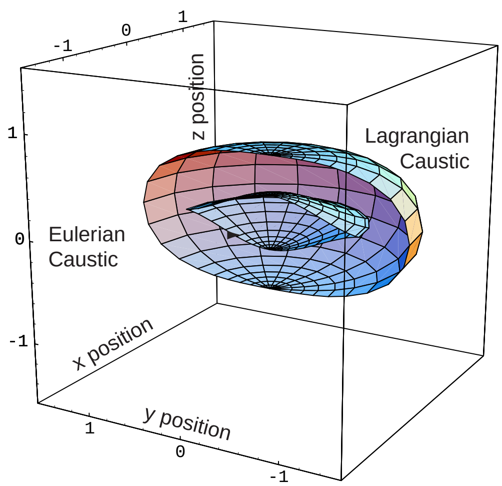

Fig. 6. The shape of the caustic for the 3D dynamics, $n = -1.5$ and $\lambda_{\max} \approx 1.5$. The external shell is the Lagrangian position of the caustic, the internal one its position in real space.

3.2. The shape of the caustics

A multi-flow region forms as soon as Eq. (18) has more than one solution. The corresponding region forms the so-called caustic. These regions are illustrated in Figs. (5) and (6) in respectively 2 and 3 dimensions for typical values of the parameters. The solid lines show in 2D the shape of the caustic in real space, and the dashed lines their shape in the original Lagrangian space.

For the chosen values of a and b and for the relevant $\lambda_{\max}$ the caustics form elongated structures. These figures are plotted in units of the smoothing scale R_L. They suggest that the largest dimension of the caustics are roughly of the order of magnitude of the initial Lagrangian scale. Note that the boundaries of the caustics correspond to surfaces (or lines in 2D) where the Jacobian of the transformation between Lagrangian space and real space vanishes, i.e.

$$J(\mathbf{q}) = |\frac{\partial \mathbf{x}}{\partial \mathbf{q}}| = 0. \tag{30}$$

The size and shape of these caustics are characterized, in 2D and 3D (although only approximately), by two lengths, the half-depth of the caustic, d, (that is the distance that has been covered by the shock front after the first singularity) and its half-extension e. For instance in Fig. (5) the value of d is about 0.1 and the value of e is about 0.9 in units of the Lagrangian size of the fluctuation R_L. In the case of the 3D dynamics e corresponds to the radius of the caustic since we restrict ourselves to cylindrical symmetry.

The density in each flow "s" is given by the inverse of the Jacobian of the transformation so that

$$\rho(\mathbf{q}_s) = 1/J(\mathbf{q}_s)\,. \tag{31}$$

The total density within the caustic is then given by the summation over each flow of each of their densities,

$$\rho(\mathbf{x}) = \sum_{\text{flow } s} \rho(\mathbf{q}_s). \tag{32}$$

3.3. The velocity field, and the generated vorticity

The velocity in each flow is given by

$$\mathbf{u}(\mathbf{q}) = \dot{D}(t)/D(t_0)\,\Psi(\mathbf{q}). \tag{33}$$

For a given Robertson Walker cosmology, $\dot{D}(t)$ obeys

$$\dot{D}(t) = f(\Omega)\,H_0\,D(t) \approx \Omega^{0.6}\,H_0\,D(t)\,. \tag{34}$$

where H_0 is the Hubble constant at the present time and $f(\Omega)$ is the logarithmic derivative of the growing factor with respect to the expansion factor. Eq. (34) is the only place where the Ω dependence (and Λ dependence though it is negligible) will come into play.

In general the velocity field, $\mathbf{u}(\mathbf{x})$, is defined as the density averaged velocities of each flow. Thus we have

$$\mathbf{u}(\mathbf{x}) = \frac{\sum_{\text{flow } s} \rho(\mathbf{q}_s)\,\mathbf{u}(\mathbf{q}_s)}{\sum_{\text{flow } s} \rho(\mathbf{q}_s)}\,, \tag{35}$$

where the summation is carried on all the flows that have entered the neighborhood of $\mathbf{x}$. The vorticity is then given by the antisymmetric derivatives of the total velocity with respect to $\mathbf{x}$:

$$\begin{aligned}\omega_k(\mathbf{x}) &= \sum_{i,j} \epsilon^{k,j,i}\,\frac{\partial \mathbf{u}_i(\mathbf{x})}{\partial \mathbf{x}_j} \\ &= \sum_{i,j} \epsilon^{k,j,i}\,\Bigg(\left[\sum_{\text{flow } s} \frac{\partial \rho(\mathbf{q}_s)}{\partial \mathbf{q}_{sl}}(D^{-1})_{j,l}\,\mathbf{u}_i(\mathbf{q}_s)\right] \\ &\quad\times\left[\sum_{\text{flow } s} \rho(\mathbf{q}_s)\right] - \left[\sum_{\text{flow } s} \rho(\mathbf{q}_s)\mathbf{u}_i(\mathbf{q}_s)\right] \\ &\quad\times\left[\sum_{\text{flow } s} \frac{\partial \rho(\mathbf{q}_s)}{\partial \mathbf{q}_{sl}}(D^{-1})_{j,l}\right]\Bigg) \\ &\quad\Bigg/\left[\sum_{\text{flow } s} \rho(\mathbf{q}_s)\mathbf{u}_i(\mathbf{q}_s)\right]^2\,,\end{aligned} \tag{36}$$

where $D_{i,j}$ is the matrix of the transformation between the Lagrangian space and the Eulerian space,

$$D_{i,j} = \frac{\partial \mathbf{x}_i}{\partial \mathbf{q}_j}\,, \tag{37}$$

and $\epsilon^{k,j,i}$ the totally antisymmetric tensor. The numerical expression of the local vorticity follows from the roots of Eq. (18) and the potentials Eqs. (23),(26).

3.3.1. The local vorticity

As illustrated in Fig. (7) (the 2D case) and (8) (the 3D case), the vorticity is null outside the caustic. First note that the vorticity sign changes from one quadrant to another, so that the global vorticity is zero (as it should be), and note that within each quadrant the vorticity is rather smooth. Note also that the vorticity is mainly located near the edges of the caustic. In fact the vorticity at the edge is unbounded and the behaviour of the vorticity close to the edges is easily estimated. Calling $\mathbf{q}_0$ and $\mathbf{x}_0$ the position of a point on the edge in respectively the Lagrangian space and the Eulerian space, we can expand $\mathbf{x}$ and $\mathbf{q}$ close to $\mathbf{x}_0$ and $\mathbf{q}_0$. Since the linear term in the expansion is singular in $\mathbf{q} = \mathbf{q}_0$ (by definition of the caustic), there is one direction, orthogonal to the edge and typeset with the subscript $_\perp$, for which

$$(\mathbf{x} - \mathbf{x}_0)_\perp \approx -\eta\,(\mathbf{q}_i - \mathbf{q}_0)_\perp^2\,, \tag{38}$$

where η is given by the second order expansion of the displacement field along this direction. The minus sign accounts here for the fact that $\mathbf{x}_{0\perp}$ has been assumed to be larger than $\mathbf{x}_\perp$. This equation is valid for two different flows (say 1 and 2) corresponding to the two roots of $\mathbf{q}_i$ in Eq. (38). The Jacobian for the first two flows is then

$$J(\mathbf{x}) \approx -2\eta\,(\mathbf{q}_i - \mathbf{q}_0)_\perp \approx 2\,\sqrt{\eta\,(\mathbf{x}_0 - \mathbf{x})_\perp}. \tag{39}$$

Note that on the edge of the caustic, $J(\mathbf{x})|\partial\,J(\mathbf{x})/\partial\mathbf{x}|$ has a finite value, η. There is also a third flow in the vicinity of $\mathbf{x}_0$ which is regular; let us call $\mathbf{q}_3$ the Lagrangian position of $\mathbf{x}_0$ in this flow. The velocity is then given by

$$\begin{aligned}\mathbf{u}(\mathbf{x}) \;\approx\; &\left((\mathbf{x}_0 - \mathbf{x})_\perp^{-1/2}/\sqrt{\eta}\,\mathbf{u}(\mathbf{q}_0) + \rho(\mathbf{q}_3)\,\mathbf{u}(\mathbf{q}_3)\right) \\ &\Big/\left((\mathbf{x}_0 - \mathbf{x})_\perp^{-1/2}/\sqrt{\eta} + \rho(\mathbf{q}_3)\right)\,.\end{aligned} \tag{40}$$

As a result we have

$$\mathbf{u}(\mathbf{x}) \approx \mathbf{u}(\mathbf{q}_0) + \rho(\mathbf{q}_3)\,\sqrt{\eta}\,(\mathbf{x}_0 - \mathbf{x})_\perp^{1/2}\,(\mathbf{u}(\mathbf{q}_3) - \mathbf{u}(\mathbf{q}_0)), \tag{41}$$

when $\mathbf{x}$ is within the caustic and

$$\mathbf{u}(\mathbf{x}) = \mathbf{u}(\mathbf{q}_3), \tag{42}$$

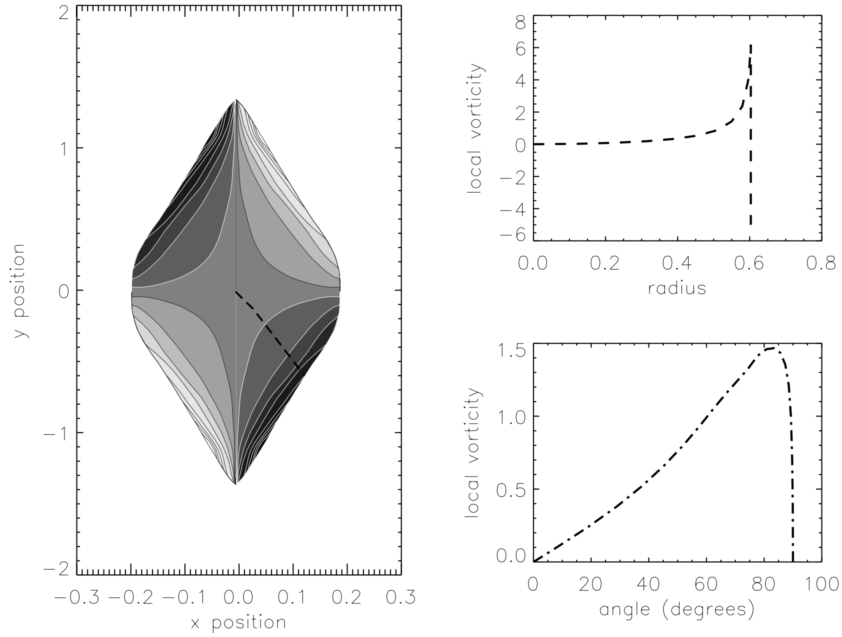

Fig. 7. The map of the vorticity in a typical 2D caustic ($n=-1$). *Left panel:* the local vorticity is anti-symmetric with respect to the centre of the caustic. It points along the Z-axis, and is positive in the second and fourth quadrant, and negative in the first and third. *Right panels:* behavior of the local vorticity along two different lines (thick dot-dashed line on the left panel). The top panel shows that the vorticity is singular near the edge of the caustic. It behaves as described by Eq. (43) and there is a non zero lineic vorticity located on the edges (represented here by a vertical line) due to the discontinuity of the local velocity field. The bottom panel shows that the local vorticity goes continuously to zero towards the axes.

when $\mathbf{x}$ has crossed the caustic boundary. The local velocity is thus discontinuous at the caustic boundary and the induced vorticity is consequently singular at $\mathbf{x}_0$ with

$$\omega(\mathbf{x}) \approx -\rho(\mathbf{q}_3)\,\sqrt{\eta}\,(\mathbf{x}_0-\mathbf{x})_\perp^{-1/2}\,(\mathbf{u}(\mathbf{q}_3)-\mathbf{u}(\mathbf{q}_0))_\parallel/2. \quad (43)$$

The direction $\parallel$ is a direction parallel to the caustic. There is only one such direction in 2D, two in 3D. There is however not only a surface (or volume) contribution within the caustic. Because of the discontinuity of the velocity field at the edges of the caustic, a vorticity field on the boundary of the caustic is created (see Fig. 7 for the 2D case), whose linear or surface density for respectively the 2D and 3D cases are given by

$$\omega_{\text{lin., surf}} = (\mathbf{u}(\mathbf{q}_3)-\mathbf{u}(\mathbf{q}_0))_\parallel. \quad (44)$$

It turns out that the two contributions tend to cancel each other. Indeed, as we have noticed previously, the velocity increases close to the edge of the caustic, and then has a discontinuity at the edge. This creates a sharp peak in the vicinity of the edge of the vorticity. The vorticity, which is obtained by differentiation of the local velocity is then expected to be opposite on both side of this peak. Realistically, the small scale perturbations are going to wash out these features, and to smooth the velocity peaks. As a result the quantities describing the behaviour of the vorticity near the edge of the caustic are not robust and should not be taken at face value. On the other hand, we expect the integrated vorticity to be a more robust quantity, since it is roughly independent of small scale fluctuations.

3.3.2. The integrated vorticity

In two dimensions, the integrated vorticity in each quadrant can be easily obtained numerically by simple one dimensional integrals which, from Stoke's theorem, can be expressed as

$$\omega_{\text{quad.}} = \int_{\text{quadran}} \mathrm{d}^2\mathbf{x}\,\omega(\mathbf{x}) = \int_{\text{edges}} \mathbf{u}\cdot\mathbf{dl}, \quad (45)$$

where $\mathbf{dl}$ describes the edge of the quadrant. One should bear in mind that, in Eq. (45) the velocities on the edge of the caustic are taken as the velocities of the third flow, $\mathbf{u}(\mathbf{q}_3)$, so that the singular part of the vorticity is taken into account.

In three dimensions and for (almost) spherically symmetric caustics the local vorticity is independent of the azimuthal angle, θ. It is then convenient to calculate the integrated vorticity per azimuthal angle in each quadrant,

$$\begin{aligned}\omega_{\text{quad.}}\,\mathrm{d}\theta &= \left(\int_{\text{quadran}} \mathrm{d}z\,r\,\mathrm{d}r\,\omega(\mathbf{x})\right)\mathrm{d}\theta \\ &= \left(\int_{\text{edges}} r\,\mathbf{u}\cdot\mathbf{dl} + \int_{\text{quadran}} \mathrm{d}^2\mathbf{x}\,u_z\right)\mathrm{d}\theta, \quad (46)\end{aligned}$$

where r is the distance of the running point to the symmetry axis, and u_z is the velocity component along this axis. Compared to the 2D case there is a further difficulty due to the surface integral of one component of the velocity. Note nonetheless that this contribution is not singular at the edge of the caustic as shown by Eq. (41), and can thus be safely computed numerically. We found that this second integral contributes typically to about 15% of the total for the relevant caustics.

3.3.3. Scaling laws

We now bring forward fits to describe the dependence of the integrated vorticity with the spectral index n and $\lambda_{\text{max.}}$ which will allow us to characterize the most significant caustics that contribute to the large–scales vorticity. We make explicit the dependence of those quantities with respect to the size of the perturbation R_L and the cosmological parameter Ω. Expressed in units of the expansion factor, the displacement, in the Zel'dovich approximation, is independent of Ω. Therefore a and b are independent of Ω, and are simply proportional to R_L. The total vorticity in each quadrant is on the other hand proportional to

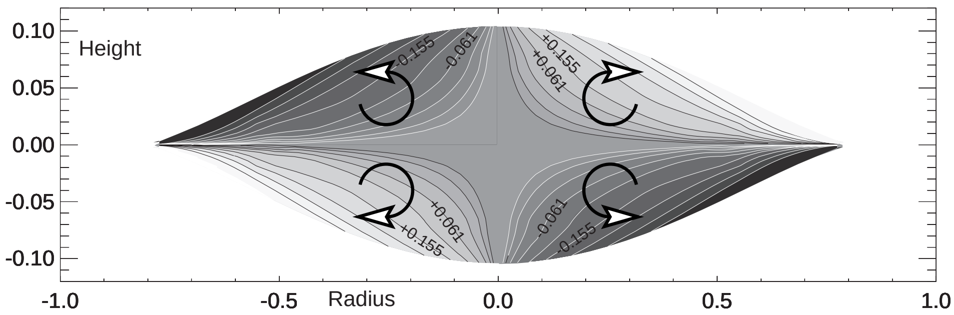

Fig. 8. Section of the vorticity field for the caustic of Fig. (6). The local vorticity is antisymmetric with respect to the centre of the caustic. In this $X-Z$ section, it points along the Y-axis, and is negative in the second and fourth quadrant, positive in the first and third.

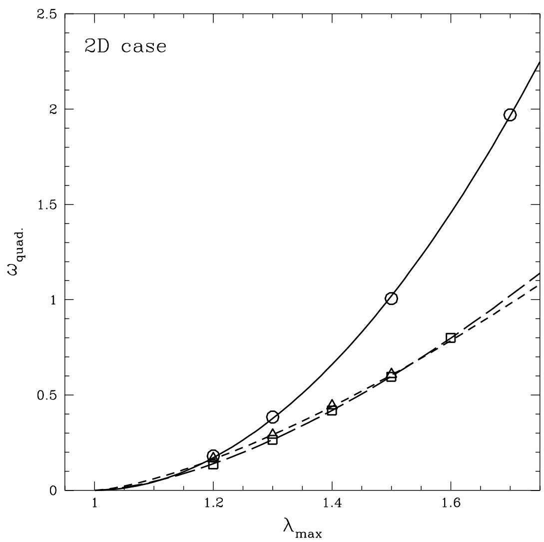

Fig. 9. $\omega_{\rm quad.}$ for 2D caustics as a function of $\lambda_{\max}$ and its corresponding fit for a $n=-1.5$ (circles, solid line), $n=-1$ (squares, long dash line), and $n=-0.5$ (triangles, short dashed line) power spectrum.

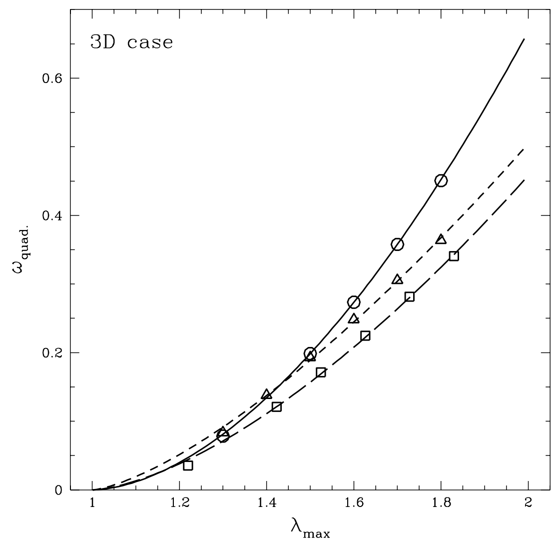

Fig. 10. $\omega_{\rm quad.}$ for 3D caustics as a function of $\lambda_{\max}$ and its corresponding fit for a $n=-2$ (circles, solid line), $n=-1.5$ (squares, long dash line), and $n=-1$ (triangles, short dashed line) power spectrum.

H_0 and $f(\Omega)$ (defined in Eq. (34)), given that it is proportional to the local velocity, and is clearly proportional to the volume of the perturbation. We thus have the following scalings,

$$\begin{aligned} d(R_L) &= R_L\, d_0\, (\lambda_{\max}-1)^{\alpha_d}, \\ e(R_L) &= R_L\, e_0\, (\lambda_{\max}-1)^{\alpha_e}, \\ \omega_{\rm quad}(R_L,\Omega) &= f(\Omega)\, R_L^D\, \omega_0\, (\lambda_{\max}-1)^{\alpha}\, H_0, \end{aligned} \quad (47)$$

where the parameters α, α_d, α_e, ω_0, d_0 and e_0 are given in Table (1) and (2) for respectively the 2D and the 3D geometry. The accuracy of these fits is illustrated on Figs. (9)–(10). These functions yield estimates of the geometry and vorticity generated by these large-scale caustics. From these tables one can see that the average vorticity (in units of H_0) is roughly one within the caustic. The amount of vorticity which is generated in the caustics is thus found to be somewhat limited. It is also interesting to note that $\omega_{\rm quad.}$ presents no singular behaviour when the caustic appears at $\lambda_{\max}\approx 1$ (i.e. $\alpha>1$).

Table 1. Fitting parameters in Eq. (47) for the 2D caustics. The quality of those fits for ω_0 and α are illustrated in Fig. (9).

n	ω_0	α	d_0	α_d	e_0	α_e
-1.5	3.94	1.95	0.8	1.3	2.7	0.6
-1	1.80	1.59	0.67	1.3	1.6	0.45
-0.5	1.63	1.43	0.75	1.3	1.3	0.32

Table 2. Fitting parameters in Eq. (47) for the 3D caustics. The quality of those fits are illustrated in Fig. (10).

n	ω_0	α	d_0	α_d	e_0	α_e
-2	0.67	1.76	0.57	1.31	1.61	0.49
-1.5	0.46	1.55	0.52	1.30	1.25	0.37
-1	0.49	1.37	0.53	1.30	1.13	0.30

4. The vorticity distribution at large scales

As argued previously, the calculation of the global shape of the vorticity distribution is beyond the scope of this paper. Indeed the low ω behaviour of the vorticity distribution is dominated by the small caustics that are not rare, and therefore not well described by the dynamical evolution of an isolated object. The aim of this section is to estimate *the shape and position of the cut-off in the probability distribution function of the local smoothed vorticity*. We will therefore estimate $P_{R_s}(>\omega_s)$, the probability that in a circular or spherical cell of radius R_s the mean vorticity exceeds ω_s. This estimation requires

(i) identifying the caustics that contribute mostly for each case;
(ii) estimating the contribution of each of those caustics.

In each case various approximations are used. In the main text we simply spell the major highlights of the derivation. A more detailed and explicit calculation of the vorticity distribution is presented in Appendix C.

4.1. Identification of the caustics

We assume in what follows that ω_s is large enough for the contribution to $P_{R_s}(>\omega_s)$ to be dominated by large and rare caustics. This assumption is the corner stone of the calculation: only a small fraction of the caustics with specific characteristics at some critical time will contribute.

The identification of the caustics contributing most results of a trade off between the amount of vorticity a given caustic can generate and its relative rarity: the higher $\lambda_{\rm max}$, the greater the internal vorticity is, according to Eq. (47) and given that α is positive, but the rarer those caustics are (Eqs. (11) and (17)). Obviously $\lambda_{\rm max}$ should be larger than unity for any vorticity at all to be generated. The calculation is slightly complicated by the fact that the Eulerian size of the caustics also depends of the value of $\lambda_{\rm max}$. Let us assume here that the Eulerian size of the caustics is substantially smaller than the smoothing length, so that the entire integrated vorticity in a quadrant can contribute (in Appendix C, this assumption is shown to be self-consistent). This implies a scaling relation between the smoothing cell, ω_s and $\lambda_{\rm max}$,

$$\omega_s\, R_s^D \propto R_L^D\, (\lambda_{\rm max}-1)^{\alpha}. \tag{48}$$

For a given smoothing length and a given ω_s, Eq. (48) yields a relation between the value of $\lambda_{\rm max}$ and the size of the caustic. The caustics which contribute most to the vorticity are then obtained by minimizing the ratio $\lambda_{\rm max}^2/\sigma^2(R_L)$ which appears in the exponential cutoff of the distribution function of $\lambda_{\rm max}$ (Eqs. (11) and (17)). Given that $\sigma^2(R_L)$ behaves like $R_L^{-(n+D)}$ this minimization yields for the extremum value of $\lambda_{\rm max}$,

$$\lambda_{\rm max}^{(0)} = \frac{2D}{2D-\alpha(n+D)}. \tag{49}$$

Note that for the values of α we have found, $\lambda_{\rm max}^{(0)}$ is always finite and positive. This means that the filtered vorticity is indeed expected to be dominated by caustics which have evolved for a finite time. This provides an a posteriori justification of the assumptions leading to this calculation.

The value of $\lambda_{\rm max}$ found in Eq. (49) is a robust result of our calculations, although it cannot be excluded that this value could be affected by the failure of the Zel'dovich approximation after the first shell crossing.

4.2. Estimation of the caustic contribution to the vorticity PDF

In order to estimate the contribution of those caustics to $P_{R_s}(>\omega_s)$ two other fundamental quantities have to be estimated:

(i) the number density of caustics;
(ii) the volume for which each of them contributes to $P_{R_s}(>\omega_s)$.

These quantities have been estimated for the specific caustics we have previously identified in Sect. 4.1.

4.2.1. The number density of caustics

Estimating the number density of caustics is, in general, a complicated problem. In the case of Gaussian fields the corresponding investigation was carried by Bardeen et al. (1986) for 3D fields, and by Bond & Efstathiou (1987) for 2D fields. The number of caustics is simply determined by the number of points at which the first derivatives of the local density vanishes. This defines accordingly the extrema of the local density field. The further requirements we have here on the second order derivatives of the potential ensures that such points are in fact maxima of density field. We refer here to Bardeen et al. (1986) for more details on how to carry the investigation. A critical step involves transforming the $\delta_{\rm Dirac}$ function in the value of the first derivatives into a $\delta_{\rm Dirac}$ function in the position, thus introducing the Jacobian of the second order derivatives of the density field. After some algebra we find:

$$\begin{aligned} n_{R_L}(\{\lambda_i\})\,{\rm d}^D\lambda_i \;&=\; p\left(\left\{\frac{\lambda_i}{\sigma(R_L)}\right\}\right) \\ &\quad\times\frac{{\rm d}^D\lambda_i}{\sigma^D(R_L)}\,\frac{|{\rm Jac}_2(\{\lambda_i\})|}{(2\pi\sigma_1^2)^{D/2}}\,, \end{aligned} \tag{50}$$

where the probability p is given either by Eq. (9) or (15) in respectively 2D and 3D, ${\rm Jac}_2(\{\lambda_i\})$ is the Jacobian of the second order derivatives of the density field for given eigenvalues of the deformation matrix and σ_1 is the variance of the derivatives of the local density field,

$$\sigma_1^2(R_L) = \int {\rm d}^D k\; P(k)\;\frac{\mathbf{k}^2}{2}\;W_D^2(R_L). \tag{51}$$

For a given geometry (*i.e.* given values of a and b) ${\rm Jac}_2$ is proportional to $\lambda_{\rm max}^3$, and it scales as $R_L^{-2\,D}$ due to the derivatives involved in the expression of the matrix elements. It is therefore appropriate to re-express Eq. (50) as

$$\begin{aligned} n_{R_L}(\{\lambda_i\})\,{\rm d}^D\lambda_i \;&=\; p\left(\left\{\frac{\lambda_i}{\sigma(R_L)}\right\}\right)\;\frac{{\rm d}^D\lambda_i}{\sigma^D(R_L)}\,\frac{n_0(\{\lambda_i\})}{R_L^D} \\ &\quad\times\left(\frac{\lambda_{\rm max}}{\sigma(R_L)}\right)^D \quad \text{where} \\ n_0(\{\lambda_i\}) \;&=\; \frac{|{\rm Jac}_2(\{\lambda_i\})|}{\lambda_{\rm max}^D\,(2\pi)^{D/2}}\;\left[\frac{\sigma}{\sigma_1}\right]^D\;R_L^D. \end{aligned} \tag{52}$$

Note that n_0, thanks to the prefactor R_L^D, is a dimensionless quantity in Eq. (52). A further simplification is provided by the fact that for large enough values of $\lambda_{\max}$, the distribution function $p(\{\lambda_i\})$, at fixed $\lambda_{\max}$, allows only a small range of possible values for the smaller eigenvalues. We therefore neglect the variations of $\mathrm{Jac}_2(\{\lambda_i\})$ with respect to those variables: it is viewed here as a function of $\lambda_{\max}$ only and calculated for fixed values of the a-symmetry parameters a and b. The ratio σ/σ_1 depends only on the value of the power law index. Recall however (see Bardeen et al. 1986) that this ratio is not well-defined for top-hat window functions because of spurious divergences for some values of n. To avoid this problem, we used the Gaussian window function to compute this ratio. As a result, for fixed values of a and b, n_0 is a dimensionless quantity that can be explicitly calculated in a straightforward manner. Relevant values of n_0 are given in tables in the Appendix C.

4.3. The contributing region

The region over which each caustic contributes is the surface (or volume in 3D) of space in the vicinity of a given caustic where, if one centers a cell in that location, the total vorticity induced by the caustic within the cell is above ω_s.

In general the contributing surface or volume can be written,

$$V_{\mathrm{caus.}}(R_L, R_s, \{\lambda_i\}, \omega_s) = \int \Theta\left[\omega_{\mathbf{c}}\left(\mathbf{c}, R_L, R_s, \{\lambda_i\}\right) - \omega_s\right] \mathrm{d}^D c\,, \tag{53}$$

where Θ is the Heaviside step function, $\mathbf{c}$ stands for the vector pointing to the center of the sampling sphere, while $\omega_{\mathbf{C}}$ is the vorticity found in that sphere intersecting the caustic with characteristics $R_s, \{\lambda_i\}$. In its full generality, $V_{\mathrm{caus.}}$ is a rather complex function of the scales R_L and R_s, and the eigenvalues λ_i through the shape of the caustics and of ω_s. Yet, since the functional form of the rare event tail in the probability distribution function is basically fixed by the exponential in Eq. (11), the only required ingredient for computing $P_{R_s}(>\omega_s)$ is the scaling behaviour of $V_{\mathrm{caus.}}$ at its takeoff – when reaching the critical time, $\lambda^{(0)}_{\max}$, at which a given caustic is large enough to start contributing. The detailed geometry of the caustic and its vorticity field accounts only for a correction in a multiplicative factor. Consequently we make approximations describing the distribution of the vorticity on the caustic in order to estimate the scaling properties of $V_{\mathrm{caus.}}$.

4.3.1. The 2D contributing surface

In two dimensions we make the radical assumption that the vorticity is entirely concentrated on four discrete points, which – consistently with the hypothesis of Sect. 3.3.2, have been taken to bear either the vorticity $+\omega_{\mathrm{quad.}}$ or $-\omega_{\mathrm{quad.}}$, depending on which quadrant is being considered. In practice the position of the points is chosen somewhat arbitrarily at a third of the depth and extension of the caustic. The corresponding area $V_{\mathrm{caus.}}$ is therefore identically null before a critical time corresponding to the chosen ω_s and R_s and then takes a constant value which can be deduced geometrically from the area of the loci of the center of the sampling disks. In Fig. (11) we show the shape of

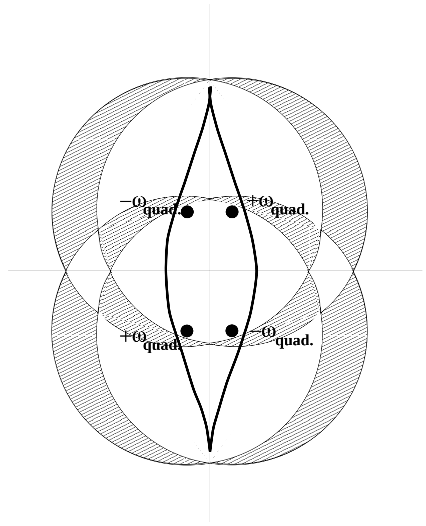

Fig. 11. Sketch showing the adopted simplification for describing a 2D caustic. Vorticity is assumed to be localized on the black dots having either $+\omega_{\mathrm{quad.}}$ or $-\omega_{\mathrm{quad.}}$. The dashed area represents $V_{\mathrm{caus.}}$ for $\omega_s > |\omega_{\mathrm{quad.}}|$.

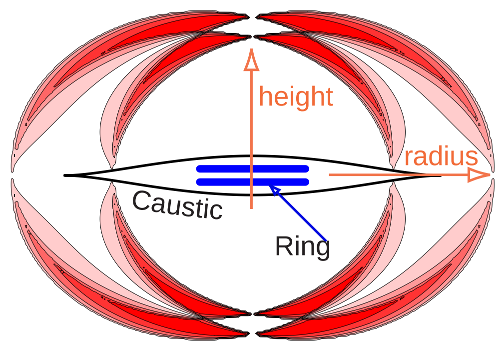

Fig. 12. Sketch showing the adopted simplification for describing a 3D caustic. Vorticity is assumed to be localized on two rings (that appear as two horizontal black segments) having a lineic vorticity of either either $+3\,\omega_{\mathrm{quad.}}/e$ or $-3\,\omega_{\mathrm{quad.}}/e$. The shaded area represents $\mathrm{d}V_{\mathrm{caus.}}/\mathrm{d}\omega_s$.

this location on a particular example. Under this assumption, the function $V_{\mathrm{caus.}}$ takes the form,

$$V_{\mathrm{caus.}} = V_0(R_L/R_s)\,\Theta(\lambda_{\max} - \lambda^{(0)}_{\max})\,R_L\,R_s\,, \tag{54}$$

where V_0 can be calculated for the values of interest of R_L and R_s.

4.3.2. The 3D contributing volume

In three dimensions, the vorticity will be assumed to be distributed uniformly along two *rings* which are taken to bear the linear vorticity $3\omega_{\mathrm{quad.}}/e$ – with respectively prograde and retrograde orientation. In practice these rings are also positioned at a third of the depth and extension of the caustic. The mean vorticity to be expected in a sampling sphere of radius R_s is then given by algebraic summation over the segments corresponding to the intersection of that sphere with the two rings. Maps of the sampled vorticity as a function of the centers of the sphere are derived to compute $V_{\rm caus.}$ which according to Eq. (53) corresponds to the volume in space defined by these centers yielding a vorticity larger than ω_s. Fig. (12) gives the shape of this location for a given caustic and sampling radius. The function $V_{\rm caus.}$ takes the form,

$$V_{\rm caus.} = V_0(R_L/R_s) R_L R_s^2\,(\lambda_{\rm max} - \lambda_{\rm max}^{(0)})^\gamma\,, \tag{55}$$

where V_0 and γ can be calculated for the values of interest of R_L and R_s at this critical values (see Appendix D, where it is in particular demonstrated that when $R_L \ll R_s$, V_0 asymptotes to a fixed value and $\gamma = 1/2$).

4.4. *Estimation of* $P_{R_s}(>\omega_s)$

The tail of the probability distribution for the vorticity is now estimated while integrating over all the caustics that might contribute, and assuming that, for a fixed caustic, the probability distribution is given by the number density of caustics times the volume associated with each caustic. There is however a further difficulty. The distribution of caustics n_{R_L} is well defined for a fixed value of R_L only, but there are actually caustics of all sizes. To circumvent this difficulty we simply choose R_L so that the result we obtain is maximal, i.e.,

$$P_{R_s}(>\omega_s)\ \simeq\ \max_{R_L}\left[\int \mathrm{d}^D\lambda_i\ n_{R_L}(\{\lambda_i\}) \times V_{\rm caus.}(R_L, R_s, \{\lambda_i\}, \omega_s)\right]. \tag{56}$$

Furthermore, it is fair to neglect the dependence of $n_0(\lambda_i)$ and $V_{\rm caus}$ on the initial asymmetry because the overall factor $p(\lambda_i)$ peaks in a narrow range of relevant values for the smaller eigenvalue(s). It is then possible to integrate over those variables introducing the probability distribution of $\lambda_{\rm max}$ in the expression of $P_{R_s}(>\omega_s)$,

$$P_{R_s}(>\omega_s)\ \simeq\ \max_{R_L}\left[\int \mathrm{d}\lambda_{\rm max}\ p_{\rm max}\,(\lambda_{\rm max})\ \frac{n_0(\lambda_{\rm max})}{R_L^D} \times \left(\frac{\lambda_{\rm max}}{\sigma(R_L)}\right)^D V_{\rm caus.}(R_L, R_s, \lambda_{\rm max}, \omega_s)\right]. \tag{57}$$

We show in Appendix C that the maximum of Eq. (56) is indeed given by caustics of size of the order of R_s at most. A detailed account of how to perform the sum in Eq. (56) is also given there for the two geometries. Repeated use of the rare event approximation together with the geometrical assumptions on the vorticity distribution sketched in Sect. 4.3.1 and Sect. 4.3.2 yields eventually an explicit expression for the tail of the probability distribution for the vorticity as a function of ω_s and R_s.

4.4.1. The two dimensional vorticity distribution

In two dimensions, the vorticity distribution is shown to obey (Eq. (C9))

$$P_{R_s}(>\omega_s)\ \simeq\ 0.56\, n_0\, V_0\, \left(\frac{\lambda_{\rm max}^{(0)}}{\sigma(R_s)}\right)^2\ f_s^{n+1}\,\omega_s^{(n+1)/2} \times\exp\left[-\frac{4}{3}\,\left(\frac{\lambda_{\rm max}^{(0)}}{\sigma(R_s)}\right)^2\ f_s^{n+2}\,\omega_s^{(n+2)/2}\right]. \tag{58}$$

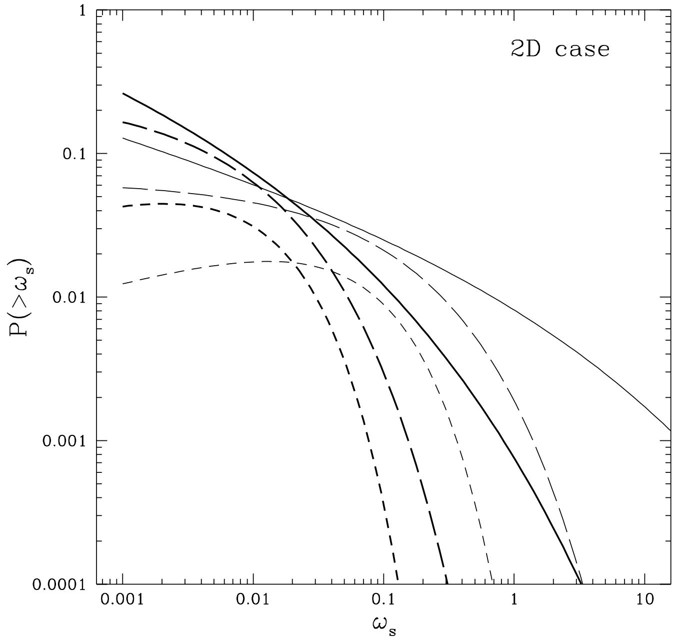

Fig. 13. $P_{R_s}(>\omega_s)$ in two dimensions for scales characterized by a $\sigma(R_s)$ of 0.5 (thick lines) and 1 (thin lines) and for a $n = -1.5$ (solid line), $n = -1$ (long dash line), and $n = -0.5$ (short dashed line) power spectrum.

In the rare event régime, the quantity that dominates Eq. (58) arises from the exponential cutoff. For $n = -1$ we find for instance that

$$\log\left[P_{R_s}(>\omega_s)\right] \simeq 3.5\,\frac{\omega_s^{1/2}}{\sigma^2(R_s)}. \tag{59}$$

The *r.h.s.* of Eq. (59) is roughly 0.5 when $\omega_s \approx 10^{-3}$, $\sigma(R_s) \approx 0.5$ or $\omega_s \approx 0.1$, $\sigma(R_s) \approx 1.5$, hence defining a threshold corresponding to a one sigma damping for $P_{R_s}(>\omega_s)$. Eq. p2Dfinalmt is illustrated on Fig. (13).

4.4.2. The three dimensional vorticity distribution

Similarly, the probability distribution is shown in the Appendix C (Eq. (C19)) to obey in 3D:

$$P_{R_s}(>\omega_s)\ =\ 0.48\, n_0\, V_0\, \left(\frac{\lambda_{\rm max}^{(0)}}{\sigma(R_s)}\right)^{7/2}\ f_s^{\frac{(13+7n)}{4}}\,\omega_s^{\frac{(13+7n)}{12}} \times\exp\left[-\frac{5}{2}\,\left(\frac{\lambda_{\rm max}^{(0)}}{\sigma(R_s)}\right)^2\ f_s^{n+3}\,\omega_s^{(n+3)/3}\right], \tag{60}$$

For $n = -1.5$, Eq. (60) gives for $\log\left[P_{R_s}(>\omega_s)\right]$

$$\log\left[P_{R_s}(>\omega_s)\right] \simeq 20.\,\frac{\omega_s^{1/3}}{\sigma^2(R_s)}. \tag{61}$$

yielding again at a one sigma level the range of relevant values for ω_s and $\sigma(R_s)$: $\omega_s \approx 5\,10^{-5}$, $\sigma(R_s) \approx 0.5$ or $\omega_s \approx 0.1$, $\sigma(R_s) \approx 3.5$. In both cases the caustics start to generate significant vorticity only at rather small scales. Equation (60) is also illustrated on Fig. (14). From this figure it is clear that the amount of vorticity that we derived is below what has been measured in N-body simulations (open and filled circles). Numerical measurements of this quantity are sparse, so we compared our estimations to measurements carried out by Bernardeau & Van de Weygaert (1996) in an adaptive $\mathrm{P^3M}$ simulation with CDM initial conditions (see Couchman 1991 for a description of these simulations). The typical amount of vorticity at the 10 to 15 h^{-1}Mpc scale for which the rms of the density is below 0.5 was found to be about 0.2 (in units of H_0). This is well above the values we have estimated in this paper. Though it is quite possible that these numerical measurements are spoiled by noise, we do not expect that it could account for all the discrepancy between the measured and the predicted vorticities (as suggested by the relative the scatter between the two methods suggested in Bernardeau & Van de Weygaert, 1996).

There are various possible explanations for such discrepancies. It could of course arise from the fact that the vorticity at large-scales does not spring from the rare and large caustics but from small scale multi-steaming events that cascade towards the larger scales. Such a scenario cannot be excluded but is difficult to investigate by means of analytic calculations. It is also possible that the N-body simulations do not address properly the physics of the large scales multi-streaming. In particular the two-body interactions should in principle be negligible, a property which seems to be hardly satisfied in current N-body simulations. This shortcoming has been raised by Suisalu & Saar (1995), Steinmetz & White (1997) and more specifically by Splinter et al. (1998), where they examine the outcome of the planar singularity in phase space. They have found in particular that in classical algorithms the particle's velocity dispersions are incorrectly large in all directions. These could turn out to be a major unphysical source of vorticity (since the Lagrangian time derivative of the vorticity scales like the curl of the divergence of the velocity anisotropies). Specific numerical experiments, that follow for instance the initial density profiles given in this paper, should be carried to address this problem more carefully.

5. Discussion and conclusions

We have estimated, within the framework of the gravitational instability scenario, the amount of vorticity generated after the first shell crossings in large-scales caustics. The calculations relied on the Zel'dovich approximation which yields estimates of the characteristics of the largest caustics and allows explicit calculation of their vorticity content. This analysis corresponds to one of the first attempts to investigate the properties of cosmological density perturbations beyond first shell-crossing. The previous investigations (Fillmore & Goldreich 1984, Bertschinger 1985) were carried out for spherically symmetric systems only, and obviously do not address the physics of vorticity generation. The only other means of investigation for this régime is numerical N-body simulations.

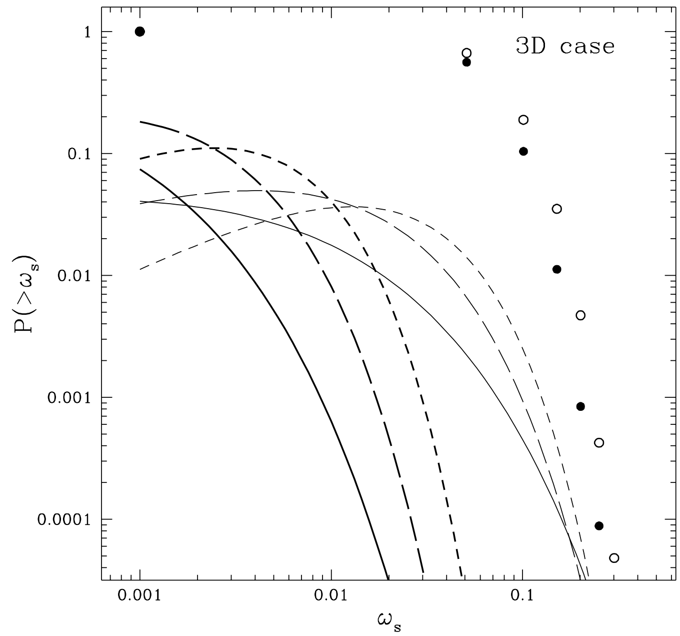

Fig. 14. $P_{R_s}(>\omega_s)$ in three dimensions for scales characterized by a $\sigma(R_s)$ of 0.5 (thick lines) and 1 (thin lines) and for a $n=-2$ (solid line), $n=-1.5$ (long dash line), and $n=-1$ (short dashed line) power spectrum. The filled and open circles correspond respectively to the measured integrated PDF in a CDM simulation at $15h^{-1}$Mpc scale with the "Delaunay" or "Voronoi" methods (see Bernardeau & Van de Weygaert 1996).

We found that large scales caustics can provide only an extremely low contribution to the vorticity at scales of 10 to $15h^{-1}\mathrm{Mpc}$. This contribution could be significant only at relatively small scales, when the variance reaches values of a few units. This effect is even more important in three dimensions, the difference arising mainly from the coefficient in the exponential cut-off. It is therefore unlikely that these caustics can have produced a significant effect on the velocity at large scales. In view of these results, it is amply justified to assume that the velocity remains potential down to very small scales, *i.e.* typically the cluster scale at which it is then more natural to expect the multi-streaming régime (not only three-flow régime) to play an important role.

This result provides a complementary view to the picture developed by Doroshkevich (1970) describing the emergence of galaxy angular momentum from small-scale torque interactions between protogalaxies (a prediction subsequently checked by White (1984), and examined in more detail by Catelan & Theuns, (1996 and 1997)). We rather explore here the large scale coherence of the vorticity field that may emerge in a hierarchical scenario from scale much larger than the galactic size. The effects we are exploring here does not originate from the two-body interaction of haloes as in the picture developed by Doroshkevich, but from the possible existence of large scale coherent vorticity field. The conclusion of our work is however that the efficiency with which the large-scale structure caustics generate vorticity is rather low. Therefore these results do not really challenge the fact that the small scales interactions should indeed be the dominant contribution to the actual galactic angular momenta.

As a consequence, we do not expect either a significant correlation of the angular momenta at large scale. In particular the vorticity field generated in caustics does not seem to be able to induce a significant large scale correlation of the galactic shapes which would have been desastruous for weak lensing measurements[1].

Let us reframe this calculation in the context of perturbation theory which has triggered some interest in the last few years as a tool to investigate the quasi-linear growth of structures. One key assumption in these techniques is that the velocity field is assumed to form a single potential flow. The detailed description of the properties of the first singularities is by essence not accessible to this theory: such singularities cannot be "seen" through Taylor expansions of the initial fields. In this context it was unclear whether the back reaction of the small scales multistreaming régime on the larger scales (which were thought to be adequately described by perturbation theory) could affect the results on those scales. Such effects are partially explored here where we find that the impact of the first multistreaming regions is rather low on larger scales. Our results therefore support the idea that the large scales velocity field can be accurately described by potential flows and support our views on the validity domain of perturbation theory calculations.

In the course of this derivation we have made various assumptions. We followed in essence the approach pioneered by Press & Schechter (1974) for the mass distribution of virialized objects by trying to identify in the initial density field the density fluctuations that contribute mostly to the large-scales vorticity. The calculations have been designed to be as accurate as possible in the rare event limit, an approximation which turned out to be crucial at various stages of the argument.

- The above estimation relies heavily on the assumption that the caustics only contribute to large-scale vorticity independently of each other. In other words it is assumed that the caustics do not overlap. Moreover the dynamical evolution of one caustic is taken to be well-described by the evolution of the caustic having the mean profile. This can be approximately true only in the rare event limit since otherwise it is likely that the substructures and its environment will change the dynamical evolution of the caustics. Although it is clear that, in the régime we investigated, the caustics are rare enough not to overlap, the effects of substructure are more difficult to investigate. In particular we have outlined some local features (3.3.1) of the vorticity maps that we think are unlikely to survive the existence of substructures.
- The typical caustics are characterized in this rare event limit. For instance the values of a and b were found to be all the more peaked to given values as the corresponding events are rare. We have then estimated the vorticity such caustics generate while assuming that slightly different geometries are unlikely to produce very different results. This assumption is somewhat suspicious, since it might turn out that slightly different geometries could produce more vorticities, and thus change the exact position of the cut-off. We do not expect however that the conclusions we have reached could be changed drastically in this manner.
- The contributions of each caustics to $P_{R_s}(>\omega_s)$ have also been calculated in the rare event limit. This is in practice a very useful approximation on large scales since it is then natural to expect the entire distribution to be dominated by a unique value of $\lambda_{\max}$.
- We have finally deliberately simplified the spatial distribution of the vorticity within the caustics. Since in the rare event limit it is natural to expect that the Lagrangian scales of the caustics are much smaller than the smoothing scale this detailed arrangement should be of little relevance. It certainly should not affect the scaling laws as only the value of the overall factor V_0 will change, and this has little bearing on our conclusions.

[1] In these measurements background galaxy shapes are assumed to be totally uncorrelated in the source plane, the observed correlation being interpreted as entirely due to gravitational lens effects.

On top of the rare event limit approximation, we have also made a dramatic simplification by using the Zel'dovich approximation throughout. This is certainly a secure assumption before the first shell-crossing since the geometries that we have investigated were rather sheet-like structures (and the Zel'dovich approximation is exact in 1D dynamics). After the first shell-crossing however, the back reaction of the large over-densities that are created could possibly affect the velocity field. However we do not expect that this effect should be very large so long as $\lambda_{\max}$ is moderately small (up to about 1.5), since before then the initial inertial movement should dominate. Later on, matter is expected to bounce back to the center of the caustics. Whether the vorticity content is then amplified or reduced remains an open question.

Acknowledgements. CP wishes to thank J.F. Sygnet, D. Pogosyan, S. Colombi and J.R. Bond for useful conversations. Funding from the Swiss NF is gratefully acknowledged.

Appendix A: average profile of an a-spherical constrained random field

A.1. General formula

Let us evaluate here the average profile of an a-spherical constrained random field in both 2 and 3D. Similar calculations as those presented in this Appendix have been investigated by Bardeen et al. (1986) for the 3D field and by Bond & Efstathiou (1987) for 2D fields. But, here, instead of the second order derivative of the density field, we consider instead the deformation tensor corresponding to second order derivatives of the potential. We also investigate the global properties that such constraints induce on the density field.

Consider a random density field, in either 2D or 3D, having fluctuations following a Gaussian statistics. It is then entirely determined, in a statistical sense, by the shape of its power spectrum, $P(k)$. Recall that $P(k)$ is defined from the Fourier transform of the density field,

$$\begin{aligned}\delta(\mathbf{k}) &= \int \mathrm{d}^3\mathbf{x}\,\exp(\mathrm{i}\mathbf{k}.\mathbf{x})\,\delta(\mathbf{x})\,, \quad \text{with}\\ \big\langle\delta(\mathbf{k})\,\delta(\mathbf{k}')\big\rangle &= \delta_{\mathrm{Dirac}}(\mathbf{k}+\mathbf{k}')\,P(k),\end{aligned} \tag{A1}$$

where the brackets $\langle.\rangle$ stands for the ensemble average of the random variables. Let us calculate the *expectation* value of $\delta(\mathbf{k})$ when a local constraint has been set in order to create an *a-spherical* perturbation. To set such a constraint, we have chosen to consider the deformation tensor of the density field smoothed at a given scale R_L. This tensor reads,

$$\phi_{i,j} = \int \mathrm{d}^3\mathbf{k}\,\delta(\mathbf{k})\,W_D(k\,R_L)\,\frac{\mathbf{k}_i\mathbf{k}_j}{k^2}. \tag{A2}$$

Note that the local smoothed density is given by the trace of this tensor. The chosen window function W_D in Fourier space corresponds to a top-hat filter in real space and it reads,

$$\begin{aligned}W_2(k) &= 2\,\frac{J_1(k)}{k^{1/2}} \quad \text{in} \quad 2D,\\ W_3(k) &= 3\sqrt{\pi/2}\,\frac{J_{3/2}(k)}{k^{3/2}} \quad \text{in} \quad 3D,\end{aligned} \tag{A3}$$

where J_ν are the Bessel functions of index ν. The matrix $\phi_{i,j}$ is now set to be equal to a given constraint. It is obviously possible to choose the axis so that this constraint is a diagonal matrix with eigenvalues $(\lambda_i), i=1,D$. The elements of the matrix $\phi_{i,j}$ and $\delta(\mathbf{k})$ form a *Gaussian* random vector,

$$\begin{aligned}V_c = \big(&\delta(\mathbf{k}),\phi_{1,1},\dots,\phi_{D,D},\phi_{1,2},\dots,\phi_{1,D},\\ &\phi_{2,2},\dots,\phi_{D,D-1}\big)\,,\end{aligned} \tag{A4}$$

and the desired expectation value of $\delta(\mathbf{k})$ is directly related to the cross-correlation matrix of the components of this vector. Consider the matrix $C_{a,b}$ with $a = 0,\cdots D(D+1)/2$ and $b = 0,\cdots D(D+1)/2$, so that

$$C_{0,0} = \big\langle\delta(\mathbf{k})\,\delta(\mathbf{k})\big\rangle = P(k)\,, \tag{A5}$$

$$C_{a,0} = \big\langle\delta(\mathbf{k})\,\phi_{i,j}\big\rangle = P(k)\,W_D(k\,R_L)\,\frac{\mathbf{k}_i\mathbf{k}_j}{k^2}\,, \tag{A6}$$

$$\begin{aligned}C_{a,b} &= \big\langle\phi_{i,j}\,\phi_{i',j'}\big\rangle\\ &= \int \mathrm{d}^3\mathbf{k}\,P(k)\,W_D^2(k\,R_L)\frac{\mathbf{k}_i\mathbf{k}_j\mathbf{k}_{i'}\mathbf{k}_{j'}}{k^4}\,,\end{aligned} \tag{A7}$$

where the indices i,j (respectively i',j') for the matrix elements ϕ_{ij} corresponds to the $(a+1)^{\mathrm{th}}$ (respectively $(b+1)^{\mathrm{th}}$) component of V_c. For a given spectrum these quantities are easily calculated and are given in the following subsections for power law spectrum in resp. 2 and 3 dimensions. The distribution function of the components of the vector V_c then reads in terms of Eq. (A7),

$$\begin{aligned}p(V_c)\,\mathrm{d}V_c = \exp&\left[-\frac{1}{2}\sum_{a,b}\left(C^{-1}\right)_{a,b}\,Vc_a\,Vc_b\right]\\ &\times\frac{\mathrm{d}V_c}{[2\pi\mathrm{Det}(C)]^{1/2+D(D+1)/4}}.\end{aligned} \tag{A8}$$

The expectation value of $\delta(\mathbf{k})$ is given by the ratio

$$\delta^{\mathrm{expec.}}(\mathbf{k}) = \frac{\int \mathrm{d}\delta(\mathbf{k})\,\delta(\mathbf{k})\,p(Vc)}{\int \mathrm{d}\delta(\mathbf{k})\,p(Vc)}\,, \tag{A9}$$

A straightforward calculation shows that this quantity is given by

$$\delta^{\mathrm{expec.}}(\mathbf{k}) = \sum_{i=1}^{D} -\frac{\left(C^{-1}\right)_{0,i}}{\left(C^{-1}\right)_{0,0}}\,\lambda_i\,. \tag{A10}$$

Note that the further constraint that the first derivative of the density field should be zero (so that the point x_0 is actually located on a maximum of the density field) would not change the resulting expression of $\delta^{\mathrm{expec.}}(\mathbf{k})$ since the cross correlation of the first order derivatives with any other involved quantities identically vanish.

A.2. The 2D profile

In 2 dimensions we have

$$C_{a,b} = \begin{pmatrix} C_{0,0} & C_{0,1} & C_{0,2} & C_{0,3}\\ C_{0,1} & 3\sigma_0^2/8 & \sigma_0^2/8 & 0\\ C_{0,2} & \sigma_0^2/8 & 3\sigma_0^2/8 & 0\\ C_{0,2} & 0 & 0 & \sigma_0^2/8\end{pmatrix}\,, \tag{A11}$$

with the variance of the smoothed density field, σ_0, given by

$$\sigma_0^2 = \int \mathrm{d}^3\mathbf{k}\,P(k)\,W_D^2(k\,R_L). \tag{A12}$$

The required elements of the inverse of this matrix are given by

$$\left(C^{-1}\right)_{0,0} = \frac{1}{64}\sigma_0^6/\mathrm{Det}(C)\,, \tag{A13}$$

$$\begin{aligned}\left(C^{-1}\right)_{0,1} &= -\begin{vmatrix} C_{0,1} & C_{0,2} & C_{0,3}\\ \sigma_0^2/8 & 3\sigma_0^2/8 & 0\\ 0 & 0 & \sigma_0^2/8\end{vmatrix}\,\frac{1}{64\,\mathrm{Det}(C)}\\ &= \frac{(C_{0,2}-3\,C_{0,1})\,\sigma_0^4}{64\,\mathrm{Det}(C)}\,,\end{aligned} \tag{A14}$$

$$\begin{aligned}\left(C^{-1}\right)_{0,2} &= \begin{vmatrix} C_{0,1} & C_{0,2} & C_{0,3}\\ \sigma_0^2/8 & \sigma_0^2/8 & 0\\ 0 & 0 & \sigma_0^2/8\end{vmatrix}\,\frac{1}{64\,\mathrm{Det}(C)}\\ &= \frac{(C_{0,1}-3\,C_{0,2})\,\sigma_0^4}{64\,\mathrm{Det}(C)}\,.\end{aligned} \tag{A15}$$

As a result, Eq. (A10) becomes here

$$\begin{aligned}\delta^{\mathrm{expec.}}(\mathbf{k}) &= \frac{P(k)\,W_2(k\,R_L)}{\sigma_0^2}\\ &\quad\times(\lambda_1+\lambda_2+2\cos(2\theta)[\lambda_1-\lambda_2])\,,\end{aligned} \tag{A16}$$

where the angle θ were chosen so that

$$k_1/k = \cos(\theta)\,, \quad k_2/k = \sin(\theta).$$

θ the angle between a given vector and the eigenvector associated to the first eigenvalue.

A.3. The 3D profile

In 3 dimensions the matrix C reads,

$$C=\begin{pmatrix} C_{0,0} & \dots & C_{0,6} \\ \vdots & D & \\ C_{0,6} & & \end{pmatrix}, \text{ with } D=\frac{\sigma_0^2}{15}\begin{pmatrix} 3 & 1 & 1 & & & \\ 1 & 3 & 1 & & 0 & \\ 1 & 1 & 3 & & & \\ & & & 1 & 0 & 0 \\ & 0 & & 0 & 1 & 0 \\ & & & 0 & 0 & 1 \end{pmatrix}. \tag{A17}$$

From this expression of the matrix of the cross correlations it is quite straightforward to re-express Eq. (A10) as

$$\delta^{\text{expec.}}(\mathbf{k}) = \frac{3P(k)\,W_3(k\,R_L)}{2}\left(\lambda_1[\mathbf{k}_2^2+\mathbf{k}_3^2-4\mathbf{k}_1^2]\right. \tag{A18}$$
$$\left.+\lambda_2[\mathbf{k}_1^2+\mathbf{k}_3^2-4\mathbf{k}_2^2]+\lambda_3[\mathbf{k}_1^2+\mathbf{k}_2^2-4\mathbf{k}_3^2]\right).$$

When the coordinates of the wave vector are expressed in terms of the angles θ_k and ϕ_k, defined by

$$k_1 = k\,\sin(\theta_k)\,\cos(\phi_k) \quad k_2 = k\,\sin(\theta_k)\,\sin(\phi_k) \quad \text{and}$$
$$k_3 = k\,\cos(\theta_k)\,.$$

Eq. (A18) becomes

$$\delta^{\text{expec.}}(\mathbf{k}) = \frac{3\,P(k)\,W_3(k\,R_L)}{8\,\sigma_0^2}\,(\lambda_1+\lambda_2+6\lambda_3)$$
$$\times(1+a\,\cos(2\theta_k)+b\,\cos(2\phi_k)$$
$$\times[1+\cos(2\theta_k)])\,, \tag{A19}$$

where a and b are specific combinations of the eigenvalues,

$$a=5\,\frac{2\lambda_3-\lambda_1-\lambda_2}{\lambda_1+\lambda_2+6\lambda_3}\,, \quad \text{and} \quad b=5\,\frac{\lambda_1-\lambda_2}{\lambda_1+\lambda_2+6\lambda_3}. \tag{A20}$$

Appendix B: the DF of the eigenvalues of the local deformation tensor

The derivation of the distribution function of the eigenvalues of the local deformation tensor was carried in 3D by Doroshkevich (1970). We extend here the calculation to the 2D case (for which the calculations are straightforward). Starting with equation (A11) – the cross-correlations between the elements of the deformation tensors, one can easily get the expression of the joint distribution function of the deformation tensor elements,

$$p(\phi_{1,1},\phi_{1,2},\phi_{2,2})\,\mathrm{d}\phi_{1,1}\,\mathrm{d}\phi_{1,2}\,\mathrm{d}\phi_{2,2}$$
$$=\frac{8}{(2\pi)^{3/2}}\,\frac{\mathrm{d}\phi_{1,1}\,\mathrm{d}\phi_{1,2}\,\mathrm{d}\phi_{2,2}}{\sigma_0^3}$$
$$\times\exp\left[-\frac{1}{2}\left(3\phi_{1,1}^2+8\phi_{1,2}^2+3\phi_{2,2}^2-2\phi_{1,2}\phi_{2,2}\right)\right] \tag{B1}$$

The change of variables,

$$\lambda_+ = \frac{\phi_{1,1}+\phi_{2,2}}{2}+\frac{\sqrt{\Delta}}{2},\ \lambda_- = \frac{\phi_{1,1}+\phi_{2,2}}{2}-\frac{\sqrt{\Delta}}{2}\,,\ \text{with}$$
$$\Delta = (\phi_{1,1}-\phi_{2,2})^2+4\phi_{1,2}^2, \tag{B2}$$

allows us to introduce the eigenvalues of the matrix. The Jacobian J of this transformation is given by

$$J^{-1} = \begin{vmatrix} \frac{1}{2}+\frac{\phi_{1,1}-\phi_{2,2}}{2\sqrt{\Delta}} & \sim & \frac{1}{2}-\frac{\phi_{1,1}-\phi_{2,2}}{2\sqrt{\Delta}} \\ \frac{1}{2}-\frac{\phi_{1,1}-\phi_{2,2}}{2\sqrt{\Delta}} & \sim & \frac{1}{2}-\frac{\phi_{1,1}+\phi_{2,2}}{2\sqrt{\Delta}} \\ 0 & 1 & 0 \end{vmatrix}$$
$$=\sqrt{1-4\,\phi_{1,2}/\Delta}\,. \tag{B3}$$

As a result we have

$$p(\lambda_+,\lambda_-,\phi_{1,2})\,\mathrm{d}\lambda_+\,\mathrm{d}\lambda_-\,\mathrm{d}\phi_{1,2}$$
$$=\frac{8\mathrm{d}\lambda_+\,\mathrm{d}\lambda_-\,\mathrm{d}\phi_{1,2}}{(2\pi)^{3/2}\sigma_0^3}\,\frac{1}{\sqrt{1-4\,\phi_{1,2}/\Delta}}$$
$$\times\exp\left[-\frac{1}{\sigma_0^2}\left(\frac{3}{2}J_1^2-4J_2\right)\right], \tag{B4}$$

with

$$J_1=\lambda_++\lambda_-\,,, \quad \text{and} \quad J_2=\lambda_+\,\lambda_-. \tag{B5}$$

The integration over $\phi_{1,2}$ yields

$$p(\lambda_+,\lambda_-)\,\mathrm{d}\lambda_+\,\mathrm{d}\lambda_- = \sqrt{\frac{2}{\pi}}\,\frac{\mathrm{d}\lambda_+\,\mathrm{d}\lambda_-}{\sigma_0^3}|\lambda_+-\lambda_-|$$
$$\times\exp\left[-\frac{1}{\sigma_0^2}\left(\frac{3}{2}J_1^2-4J_2\right)\right]. \tag{B6}$$

Note that if λ_+ is a priori assumed to be greater than λ_- the distribution should be multiplied by 2.

Appendix C: estimation of $P_{R_s}(>\omega_s)$

In this Appendix we estimate the probability $P_{R_s}(>\omega_s)$ that a sphere of radius R_s contains an integrated vorticity larger than ω_s. In order to account for caustics of all sizes we argued in the main text that $P_{R_s}(>\omega_s)$ was well approximated by

$$P_{R_s}(>\omega_s) \simeq \max_{R_L}\left[\int \mathrm{d}^D\lambda_i\,n_{R_L}(\lambda_i)\right.$$
$$\left.\times V_{\text{caus.}}(R_L,R_s,\{\lambda_i\},\omega_s)\right]. \tag{C1}$$

We will now show that the maximum is indeed given by caustics of size of the order of R_s and approximate this integral in 2 and 3D. To simplify further Eq. (C1), note first that the distribution function of the eigenvalues is peaked in a given geometry (i.e. $a=1$, and $b\simeq 0$ in 3D) for rare caustics (large values of $\lambda_{\max}$). Therefore the integral in Eq. (C1) will be dominated by caustics of this geometry and the factor $V_{\text{caus.}}$ can be taken at this point while carrying the integration over the other two eigenvalues. As a result we have

$$P_{R_s}(>\omega_s) \simeq \max_{R_L}\left[\int_1^\infty \mathrm{d}\lambda_{\max}\,p_{\max}(\lambda_{\max})\,\left(\frac{\lambda_{\max}}{\sigma(R_L)}\right)^D\right.$$
$$\left.\times\frac{n_0(\lambda_{\max})\,V_{\text{caus.}}(R_L,R_s,\lambda_{\max},\omega_s)}{R_L^D}\right]. \tag{C2}$$

This integral runs from 1 to infinity since the caustics exist only when $\lambda_{\max}$ is greater than 1. The evaluation of Eq. (C2) requires insights into the function $V_{\rm caus.}$. Although there are no real qualitative changes between the the 2D and 3D cases, we now proceed with the computation of Eq. (C2) by distinguishing the two geometries for the sake of clarity.

C.1. The 2D statistics

Recall that the integral Eq. (C1) will be dominated by the rare even tail, and thus by the lowest value of $\lambda_{\max}$ that contributes to the integral. In other words, when considering a given caustic characterized by its Lagrangian scale R_L, one should wait long enough so that it has grown sufficiently in order to contribute after sampling a vorticity larger than ω_s. For each R_L therefore corresponds $\lambda^{(0)}_{\max}(R_L)$, the lowest value of $\lambda_{\max}$ for which $V_{\rm caus.}$ is non zero:

$$P_{R_s}(>\omega_s) \;\simeq\; \max_{R_L}\left[\int_{\lambda^{(0)}_{\max}}^{\infty} {\rm d}\lambda_{\max}\, p_{\max}(\lambda_{\max})\;\left(\frac{\lambda_{\max}}{\sigma(R_L)}\right)^2 \times\frac{n_0(\lambda_{\max})\,V_{\rm caus.}(R_L,R_s,\lambda_{\max},\omega_s)}{R_L^2}\right]. \quad \text{(C3)}$$

The lower bound $\lambda^{(0)}_{\max}(R_L)$ is reached as soon as $\omega_{\rm quad.}$ is larger than $\pi\,R_s^2\,\omega_s$: the largest possible value of the integrated vorticity in a cell of a given radius. It is therefore implicitly defined by

$$\begin{aligned}\omega_s \;&=\; \frac{\omega_{\rm quad.}}{\pi\,R_s^2}\equiv\omega_M\\ &=\; f(\Omega)\,\frac{R_L^2}{\pi R_s^2}\omega_0\,(\lambda^{(0)}_{\max}(\omega_s,R_L)-1)^{\alpha}\,.\end{aligned} \quad \text{(C4)}$$

Assuming that $V_{\rm caus.}$ does not contain any exponential cutoff, and assuming that $\lambda_{\max}$ is in the rare event tail, Eq. (C2) can be approximatively re-expressed as

$$P_{R_s}(>\omega_s)\simeq\max_{R_L}\left[0.56\left(\frac{\lambda^{(0)}_{\max}}{\sigma(R_L)}\right)^2\exp\left[-\frac{4}{3}\left(\frac{\lambda^{(0)}_{\max}}{\sigma(R_L)}\right)^2\right] \times\frac{n_0\,V_{\rm caus.}(R_s,R_L,\lambda^{(0)}_{\max},\omega_s)}{R_L^2}\right], \quad \text{(C5)}$$

when using Eq. (11) for the distribution function of $\lambda_{\max}$, integrating by part and dropping the residual integral for large enough $\lambda^{(0)}_{\max}/\sigma(R_L)$ (see Appendix Appendix E: for details). This maximum with respect to R_L is then approximated by the minimum of the argument of the exponential, $\lambda^{(0)}_{\max}(R_L)/\sigma(R_L)$, where the minimum in the facto taken with respect to $\lambda^{(0)}_{\max}$ since $\sigma(R_L)$ can be thought of a function of $\lambda^{(0)}_{\max}$ via Eqs. (22) and (C4). This minimum can de facto be expressed independently of R_s. It reads

$$\lambda^{(0)}_{\max}=\frac{4}{4-\alpha(n+2)}. \quad \text{(C6)}$$

Table C1. Parameters of interest for the 2D caustics: the power index, n, the critical time $\lambda^{(0)}_{\max}$, the radial extension $e^{(0)}$, depth $d^{(0)}$ in units of R_L,scale factor $f_s^{(0)}$ as well as the values of n_0 and V_0 for the critical caustics.

n	$\lambda^{(0)}_{\max}$	$d^{(0)}$	$e^{(0)}$	f_s	n_0	V_0
−1.5	1.31	0.17	1.34	0.30	0.018	0.9
−1	1.67	0.40	1.33	0.95	0.023	1.8
−0.5	2.15	0.90	1.36	1.25	0.009	3.4

Once $\lambda^{(0)}_{\max}$ is fixed the geometry of the caustic which will contribute most to $P_{R_s}(>\omega_s)$ is entirely specified. The condition for the existence of a minimum defining $\lambda^{(0)}_{\max}$ is that $\alpha(n+2)<4$, and it is satisfied for all considered cases (see Table (1)). This implies that we are investigating a régime where the integral Eq. (C2) is not dominated by arbitrarily rare caustics – which would have been catastrophic given the assumptions (note that when n is too large $\lambda^{(0)}_{\max}$ tend to be quite large thus challenging the validity of quantitative results based upon the Zel'dovich approximation). The resulting value of R_L is

$$\begin{aligned}R_L \;&=\; R_s\,\sqrt{\frac{\pi\omega_s}{\omega_0\,f(\Omega)}}\;\left(\frac{4-\alpha\,(n+2)}{\alpha\,(n+2)}\right)^{\alpha/2}\\ &=\; f_s\,R_s\,\left(\frac{\omega_s}{f(\Omega)}\right)^{1/2}.\end{aligned} \quad \text{(C7)}$$

The scale factor f_s is given in Table (C1) for an Einstein-de Sitter universe ($f(\Omega)=1$) and different values of n. Completing the calculation of $P_{R_s}(>\omega_s)$ involves relating the shape and size of the caustic for the adopted value of $\lambda^{(0)}_{\max}$. These values are derived from the fits (Eq. (47)) and are given in Table (C1). Fig. (12) gives $V_{\rm caus.}$, in units of the square of R_L, as a function of the smoothing radius R_s. From Fig. (12) it is easy to see that

$$V_{\rm caus.}\simeq V_0\,R_s\,R_L\,, \quad \text{(C8)}$$

for any values and n; the corresponding values of V_0 are given in Table C1. Putting Eq. (C8) into Eq. (C3), using Eqs. (C6), (C7) yields for the sought distribution

$$P_{R_s}(>\omega_s)\;\simeq\;0.56\,n_0\,V_0\,\left(\frac{\lambda^{(0)}_{\max}}{\sigma(R_s)}\right)^2\,f_s^{n+1}\,\omega_s^{(n+1)/2} \times\exp\left[-\frac{4}{3}\,\left(\frac{\lambda^{(0)}_{\max}}{\sigma(R_s)}\right)^2\,f_s^{n+2}\,\omega_s^{(n+2)/2}\right], \quad \text{(C9)}$$

Note that the power of ω_s in the exponential is rather weak. The cut-off is nonetheless strong in the régime of interest because of the leading coefficient. Equation (C9) is illustrated on Fig. (13) and discussed in the main text.

C.2. The 3D statistics

The threshold on $\lambda_{\max}$, from which the caustics start to contribute at a given scale R_s depends on the adopted description for the local vorticity. We assume here as mentioned in Sect. 4.3.2 that the total vorticity is localized on two rings of radius $e/3$ each, distant of $2\,d/3$ of each other. They are assumed to bear opposite lineic (and uniformly distributed) vorticities; in order to get a consistent answer for the integrated vorticity in a quadrant, we should have

$$\omega_{\rm lin.} = \frac{3\omega_{\rm quad.}}{e}. \tag{C10}$$

The maximum vorticity that can be encompassed in a sphere then depends on its radius R_s. If R_s is larger than the radius of the rings $e/3$, it is possible to have half of a ring in a sphere (while the other ring does not intersect it at all), so that the values of $\lambda_{\rm max}$ (for which the maximum vorticity is sampled) is given by

$$\begin{aligned}\omega_s &= \frac{2\,e\,\omega_{lin.}}{3}\,\frac{1}{\frac{4\pi}{3}R_s^3} \equiv \omega_M^+ \\ &= \frac{3}{2\pi}\omega_0\,(\lambda_{\rm max}-1)^{\alpha} f(\Omega)\,\frac{R_L^3}{R_s^3}, \quad \text{if} \quad R_s > e/3. \end{aligned} \tag{C11}$$

If on the other hand R_s is smaller than $e/3$ then only a fraction of the half ring can be put in the sphere and we have instead

$$\begin{aligned}\omega_s &= 2\,R_s\,\omega_{lin.}\,\frac{1}{\frac{4\pi}{3}R_s^3} \equiv \omega_M^- \\ &= \frac{9}{2\pi}\,\frac{\omega_0}{e_0}\,(\lambda_{\rm max}-1)^{\alpha-\alpha_e} f(\Omega)\,\frac{R_L^2}{R_s^2}, \quad \text{if} \quad R_s < e/3. \end{aligned} \tag{C12}$$

Now the local behaviour of $V_{\rm caus.}$ near its takeoff value is well represented (as argued below and demonstrated in Appendix D for large enough R_s) as a function of $\lambda_{\rm max}$ by

$$\begin{aligned} & V_{\rm caus.}(R_L, R_s, \lambda_{\rm max}, \omega_s) \\ &\quad = \int \Theta\left[\omega_{\mathbf c}\left(\mathbf{c}, R_L, R_s, \lambda_{\rm max}\right) - \omega_s\right]\,{\rm d}^3c \\ &\quad \simeq R_L R_s^2 V_0 (\lambda_{\rm max} - \lambda_{\rm max}^{(0)})^{\gamma}\,, \end{aligned} \tag{C13}$$

Using Eq. (17) and (52) for the distribution function $p_{\rm max}(\lambda_{\rm max})$, changing integration variable from $u = \lambda_{\rm max}/\sigma$ to $\lambda_{\rm max}^{(0)} + u/\lambda_{\rm max}^{(0)}$ and dropping the residual integral for large enough $\lambda_{\rm max}^{(0)}/\sigma(R_L)$ (see Appendix Appendix E: for details) yields for Eq. (C3):

$$\begin{aligned} P_{R_s}(>\omega_s) \;\simeq\; \max_{R_L} & \left[\frac{6\,n_0\,V_0\Gamma(\gamma+1)}{5^{\gamma+1}}\left(\frac{\lambda_{\rm max}^{(0)}}{\sigma(R_L)}\right)^{4-\gamma}\right. \\ & \left.\times\,\exp\left[-\frac{5}{2}\left(\frac{\lambda_{\rm max}^{(0)}}{\sigma(R_L)}\right)^2\right]\frac{R_s^2}{R_L^2}\right], \end{aligned} \tag{C14}$$

From Eq. (22) and (C11), (C12), the minimum of the argument of the exponential corresponds to:

$$\begin{aligned} \lambda_{\rm max}^+ &\equiv \frac{6}{6-\alpha(n+3)} \quad \text{if} \quad R_s > e/3, \quad \text{and} \\ \lambda_{\rm max}^- &\equiv \frac{4}{4-(\alpha-\alpha_e)(n+3)} \quad \text{if} \quad R_s < e/3, \end{aligned} \tag{C15}$$

Table C2. Parameters of interest for the 3D caustics: the power index, n, the critical times $\lambda_{\rm max}^{\pm}$, the scale factor $f_s^{\pm}$ in the two régimes ($R_s < e/3$ in parentheses) with radial extension $e^{(0)}$, depth $d^{(0)}$ in units of R_L as well as the values of n_0 and V_0 that enter the final expressions.

n	$\lambda_{\rm max}^+$	$(\lambda_{\rm max}^-)$	f_s^+	(f_s^-)	$d^{(0)}$	$e^{(0)}$	n_0	V_0
$-2.$	1.41	(1.47)	2.46	(2.09)	0.18	1.04	0.18	0.96
-1.5	1.63	(1.79)	2.10	(1.58)	0.28	1.05	0.14	1.84
$-1.$	1.84	(2.15)	1.78	(1.17)	0.42	1.07	0.064	3.18

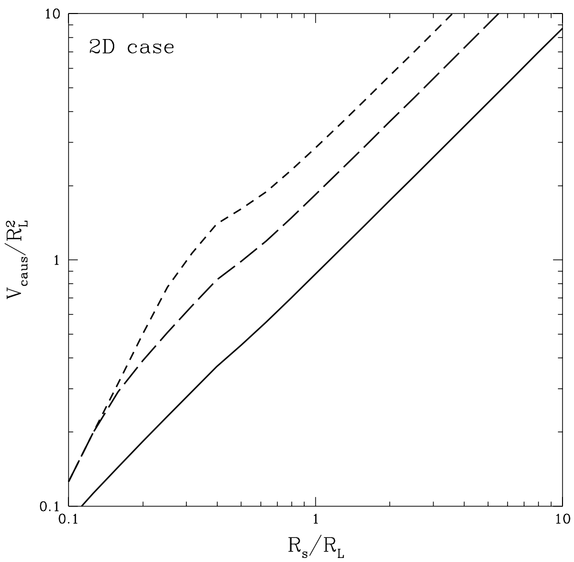

Fig. C1. The function $V_{\rm caus.}$, in units of the square of R_L, as a function of the smoothing radius in 2D. The solid line corresponds to the case $n = -1.5$, the dashed line to $n = -1$ and the long dashed line to $n = -0.5$. In all cases the geometry of the caustic is fixed by $\lambda_{\rm max} = \lambda_{\rm max}^{(0)}$.

which assumes that $\alpha(n+3) < 6$ (resp. $(\alpha-\alpha_e)(n+3) < 4$), both conditions being satisfied for all values of n considered. The corresponding scaling relations between R_L and R_s are given by

$$\begin{aligned} R_L &= f_s^+\,R_s\left(\frac{\omega_s}{f(\Omega)}\right)^{1/3} \quad \text{if} \quad R_s > e/3\,, \quad \text{or} \\ R_L &= f_s^-\,R_s\left(\frac{\omega_s}{f(\Omega)}\right)^{1/2} \quad \text{if} \quad R_s < e/3\,. \end{aligned} \tag{C16}$$

The scale factors $f_s^{\pm}$ – derived from the fits (Eq. (47)) – are given in Table (C2) for an Einstein-de Sitter universe ($f(\Omega) = 1$) and different values of n. Interestingly, as long as ω_s is not too large the condition $R_L > e/3$ is always satisfied. In practice at scales of about 10 to $15h^{-1}$Mpc the measured vorticity ω_s is expected to be indeed at most of a few tenth (Bernardeau & van de Weygaert, 1996). It is therefore always fair to assume that we are in the régime where $R_s > e/3$ which is the régime investigated hereafter.

Completing the calculation of $P_{R_s}(>\omega_s)$ requires evaluating the corresponding n_0, γ and V_0. The value of n_0 is entirely

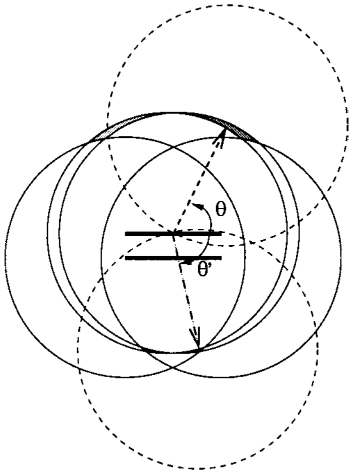

Fig. C2. The loci of the centres of spheres contributing ω_s in the range $[\omega_M^+(1-\epsilon^2/2), \omega_M^+[$. The dashed arrow points to a centre of such a sphere, and defines the running angle, θ, mentioned in Eq. (D2). The two (cylindrically symmetric) shaded regions correspond to the loci of the centre of spheres capturing almost half a ring and all or none of the other. Two examples of such spheres are displayed for either case.

determined by the geometry of the caustics and is given in the Tables 1 and 2. The behaviour of $V_{\rm caus.}$ as it departs from zero as a function of ω_s for the critical ratios of R_s, e and d is locally well fitted as a function of ω_s by a power law of the form

$$V_{\rm caus.}(\lambda_{\rm max}, \omega_s) \simeq U_0\, R_L\, R_s^2 \left(1 - \frac{\omega_s}{\omega_M^+(\lambda_{\rm max})}\right)^\gamma \, . \quad \text{(C17)}$$

where ω_M^+ is the threshold value of ω_s (Eq. (C11)). This expression is valid when ω_s is close to its threshold value. On the critical line, $\omega_s = \omega_M^+$, it is possible to relate the variation of $\lambda_{\rm max}$ to the variations of ω_s. We can then rewrite Eq. (C17) as a function of the difference between $\lambda_{\rm max}$ and the critical value $\lambda_{\rm max}^{(0)}$, assuming this departure is small,

$$\begin{aligned} V_{\rm caus.}(\lambda_{\rm max}, \omega_s) \;&\simeq\; R_L\, R_s^2 V_0\, (\lambda_{\rm max} - \lambda_{\rm max}^{(0)})^\gamma \, , \quad \text{with} \\ V_0 \;&=\; \frac{U_0\, \alpha^\gamma}{(\lambda_{\rm max}^{(0)} - 1)^\gamma} \, . \end{aligned} \quad \text{(C18)}$$

Since R_L/R_s is only a function of n and ω_s, so are V_0 and γ. In practice we take the asymptotic values of V_0 and γ given in Appendix D and corresponding to the limit $R_s \ll R_L$. Putting Eq. (C18) into Eq. (C14), using Eq. (C15) –(C17) and (D4) yields for the vorticity distribution

$$\begin{aligned} P_{R_s}(>\omega_s) = 0.48 n_0 V_0 \left(\frac{\lambda_{\rm max}^{(0)}}{\sigma(R_s)}\right)^{7/2} f_s^{\frac{(13+7n)}{4}}\, \omega_s^{\frac{(13+7n)}{12}} \\ \times \exp\left[-\frac{5}{2}\left(\frac{\lambda_{\rm max}^{(0)}}{\sigma(R_s)}\right)^2 f_s^{n+3} \omega_s^{(n+3)/3}\right] . \end{aligned} \quad \text{(C19)}$$

Equation (C19) is illustrated on Fig. (14) and discussed in the main text.

Appendix D: asymptotic behaviour of $V_{\rm Caust.}$ in 3D

For large enough R_s we derive here an asymptotic analytic expression for $V_{\rm Caust.}$. Let us first estimate geometrically the volume in space contributing almost ω_M^+ to $V_{\rm Caust.}$. The corresponding contribution is the sum of two volumes given by the shaded area in Fig. (C2), corresponding to the loci of the centers of spheres which capture almost half a ring and not the other, or which capture completely one ring and almost half of the other. In the asymptotic limit, as $e/R_s \to 0$, the element of volume is an infinitely thin strip and both contributions become equal since $\theta \to -\theta'$. The area corresponding to these loci can be evaluated algebraically as follow: let us call ϵ the projected ring segment by which a sampling sphere of radius R_s fails to encompass a ring diameter $2e/3$; it follows that the ratio of ω_s to ω_M^+, is given by

$$\frac{\omega_s}{\omega_M^+} = (1 - \frac{\epsilon^2}{2}) \, . \quad \text{(D1)}$$

On the other hand, for a given direction for the sphere centre given by $\cos(\theta) \equiv \mu$, within the solid angle $2\pi {\rm d}\mu$, the volume element (encompassed by the two shifted spheres capturing ω_s in the range $[\omega_M^+(1-\epsilon^2/2), \omega_M^+[$) is given by

$$\left(\frac{2e}{3}\right) 4\pi\, R_s^2 \epsilon \sin^2\theta {\rm d}\theta = 8\pi \frac{e}{3} R_s^2 \epsilon \sqrt{1-\mu^2}\, {\rm d}\mu \, . \quad \text{(D2)}$$

Summing over all possible directions (*i.e.* before intersecting the second ring) yields

$$8\pi \frac{e}{3} R_s^2 \epsilon \int_{\mu_0}^{1} \sqrt{1-\mu^2}\, {\rm d}\mu \;\equiv\; 8\,\pi\, \frac{e^{(0)}}{3} R_L\, R_s^2\, \epsilon \mathcal{J},$$

$$\text{where} \quad \mu_0 = \left[1 + \frac{4{d^{(0)}}^2}{{e^{(0)}}^2}\right]^{-1/2} . \quad \text{(D3)}$$

Accounting for the summation over the two configurations (half a ring captured or a full + one half ring captured), using Eq. (D1) to eliminate ϵ, we finally get for large enough R_s

$$V_{\rm Caust.} = 16\sqrt{2}\pi R_L\, R_s^2\, \frac{e^{(0)}}{3} \left(1 - \frac{\omega_s}{\omega_M^+}\right)^{1/2} ,$$

$$\text{therefore} \quad \gamma_\infty = \frac{1}{2} \quad \text{and} \quad U_0^\infty = 16\sqrt{2}\pi \frac{e^{(0)}}{3} \mathcal{J} \, . \quad \text{(D4)}$$

Appendix E: rare event approximation

Consider an integral of the form

$$\mathcal{I} = \int_a^\infty x^\beta (x-a)^\gamma \exp(-bx^2)\, {\rm d}x \, . \quad \text{(E1)}$$

Changing variable to $x = a + u/(2ab)$ Eq. (E1) reads

$$\begin{aligned} \mathcal{I} \;=\; \frac{1}{2ab} \exp(-ba^2) \int_0^\infty \left(\frac{u}{2ab}\right)^\gamma a^\beta \left[\left(1 + \frac{u}{2a^2 b}\right)^\beta \right. \\ \left. \times \exp\left(-\frac{u^2}{2ba^2}\right)\right] \exp(-u)\, {\rm d}u \, . \end{aligned} \quad \text{(E2)}$$

For large enough a the square brace in Eq. (E2) is well approximated by 1 yielding for Eq. (E2)

$$\mathcal{I} = \frac{a^{\beta-\gamma-1}}{(2b)^{\gamma+1}}\Gamma(\gamma+1)\,\exp(-ba^2)\,. \tag{E3}$$

Eq. (C5) is a special case of Eq. (E1) with $x = \lambda_{\max}/\sigma$, $a = \lambda_{\max}^{(0)}$, $\gamma = 0$, $\beta = 3$ and $b = 4/3$, while Eq. (C14) corresponds to $\beta = 5$, and $b = 5/2$. Note that the $\gamma = 0$ approximant can be deduced directly by integration by parts.

References

Bardeen J.M., Bond J.R., Kaiser N., et al., 1986, ApJ 304, 15
Bernardeau F., 1994a, ApJ 427, 51
Bernardeau F., Juszkiewicz R., Dekel A., Bouchet F.R., 1995, MNRAS 274, 20
Bernardeau F., Van de Weygaert R., 1996, MNRAS 279, 693
Bertschinger E., 1985, ApJS 58, 39
Bertschinger E., Dekel A., 1989, ApJ 336, L5
Bertschinger E., Dekel A., Faber S.M., et al., 1990, ApJ 364, 370
Bond J.R., Efstathiou G., 1987, MNRAS 226, 655
Catelan P., Theuns T., 1996, MNRAS 282, 455
Catelan P., Theuns T., 1997, MNRAS 292, 225
Couchman, H., 1991, ApJ 368, L23
Dekel A., 1994, ARA&A 32, 371
Dekel A., Rees M., 1994, ApJ 422, L1
Doroshkevich A.G., 1970, Astrofizika 6, 581
Eke V.R., Cole S., Frenk C.S., 1996, MNRAS 282, 263
Fillmore J.A., Goldreich P., 1984, ApJ 281, 1
Fisher K.B., Davis M., Strauss M.A., Yahil A., Huchra J.P., 1993, ApJ 402, 42
Henry J.P., Arnaud K.A., 1991, ApJ 372, 410
Juszkiewicz R., Weinberg D.H., Amsterdamski P., Chodorowski M., Bouchet F.R., 1995, ApJ 442, 39
Nusser A., Dekel A., 1993, ApJ 405, 437
Oukbir J., Blanchard A., 1997, A&A 317, 1O
Peacock J.A., 1991, MNRAS 253, 1p
Pogosyan D., Bond J.R., Kofman L., Wadsley J., 1996, A&AS 189, 1303
Press W.H., Schechter P.L., 1974, ApJ 187, 425
Splinter R.J., Melott A.L., Shandarin S., Suto Y., 1998, ApJ 497, 38
Steinmetz M., White S., 1997, MNRAS 288, 545
Suisalu I., Saar E., 1995, MNRAS 274, 287
White S.D.M., 1984, ApJ 286, 38

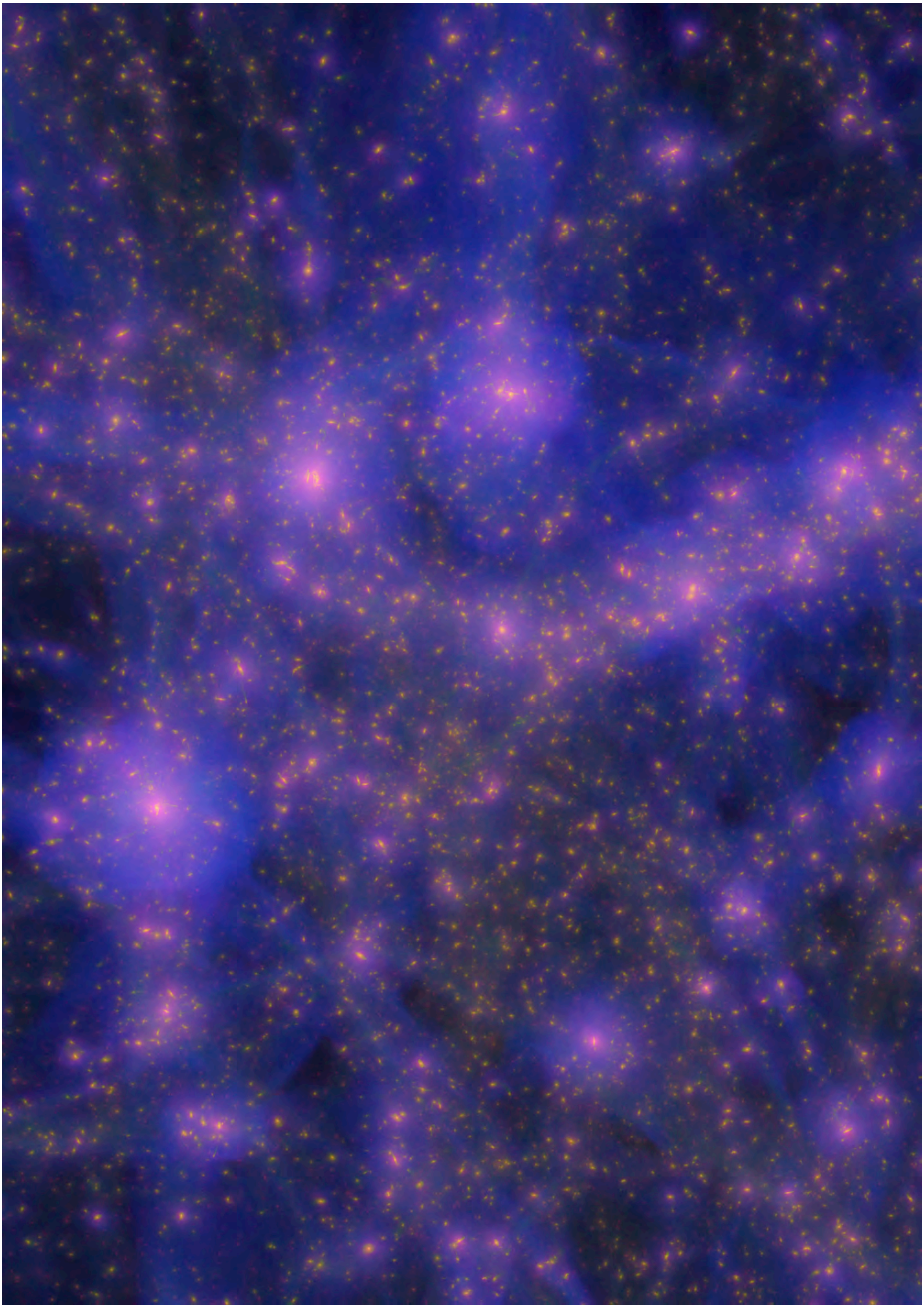

Lattice Melting and Rotation in Perpetually Pulsating Equilibria

C. Pichon[1], D. Lynden-Bell[1,2], J. Pichon[3] and R. Lynden-Bell[41]

[11] *Institut d'Astrophysique de Paris UMR 7595,*
UPMC, 98 bis boulevard d'Arago, 75014 Paris, France.
[2] *Institute of Astronomy and Clare College, Madingley Road, Cambridge CB3 0HA, United Kingdom,*
[3] *Lycée Blaise Pascal, 20, rue Alexandre Fleming, 91400 Orsay, France,*
[4] *University Chemical Laboratory, Lensfield Road,*
Cambridge CB2 1EW England, United Kingdom.

Systems whose potential energies consists of pieces that scale as r^{-2} together with pieces that scale as r^2, show no violent relaxation to Virial equilibrium but may pulsate at considerable amplitude for ever. Despite this pulsation these systems form lattices when the non-pulsational "energy" is low, and these disintegrate as that energy is increased. The "specific heats" show the expected halving as the "solid" is gradually replaced by the "fluid" of independent particles. The forms of the lattices are described here for $N \leq 20$ and they become hexagonal close packed for large N. In the larger N limit, a shell structure is formed. Their large N behaviour is analogous to a $\gamma = 5/3$ polytropic fluid with a quasi-gravity such that every element of fluid attracts every other in proportion to their separation. For such a fluid, we study the "rotating pulsating equilibria" and their relaxation back to uniform but pulsating rotation. We also compare the rotating pulsating fluid to its discrete counter part, and study the rate at which the rotating crystal redistributes angular momentum and mixes as a function of extra heat content.

PACS numbers:

I. INTRODUCTION

Astrophysics has provided several new insights into ways statistical mechanics may be extended to cover a wider range of phenomena. Negative heat capacity, bodies which get cooler when you heat them, were first encountered by [6] and when such bodies were treated thermodynamically by [1][13], what seemed natural to astronomers was seen as an apparent contradiction in basic physics to those from statistical mechanics background. Even after a physicist [16] first resolved this paradox and [8] gave an easily soluble example, there was considerable reluctance to accept the idea that micro canonical ensembles could give such different results to canonical ones. There was still some reluctance even in 1999 [9], though to those working on simulations of small clusters of atoms or molecules, the distinction was well understood by the early 1990s, see *e.g.* [3]. However by 2005, the broader statistical mechanics community had embraced these ideas, and emphasized this difference which had been with us for 30 years (see Pichon & Lynden-Bell 2006, where an early account of this work is given). Another area to which statistical mechanics might extend is that of collisionless systems which may be treated as "Vlasov" fluids in phase space. While early attempts at finding such equilibria gave interesting formulae reminiscent of a Fermi-Dirac distribution [7], there is ample evidence from astronomical simulations that these equilibria are not reached in gravitationnal systems. There are also different ways of doing the counting that lead to different results and recently, [2] gave an example that demonstrates that the concept of a unique final state determined by a few constants of motion found from the initial state is not realized. Thus the statistical mechanics of fluids in phase space remains poorly understood with theory and at best losely correlated with simulations and experiments (but see [4]).

This paper is concerned with a third area of non standard statistical mechanics which is restricted to very special systems, those for which the oscillation of the scale of the system separates off dynamically from the behaviour of the rescaled variables that are now scale free. These systems were found as a bi product of a study which generalized Newton's soluble N-body problem [10] [11] (papers I and II). A one dimensional model with exact solutions was found by [5] and the model considered here is a three dimensional generalisation of his combined with Newton's. A first skirmish with the statistical dynamics of the scale free variables despite the continuing oscillation of the scale was given there. Since then, [12], hereafter paper III, have showed that the peculiar velocities of the particles do indeed relax, as predicted, to a Maxwellian distribution, whose temperature continuously changes as $(\text{scale})^{-2}$. This occurs, whatever the ratio of the relaxation time to the pulsation period. The peculiar velocities are larger whenever the system is smaller. When the system rotates at fixed angular momentum, the resulting statistical mechanics leads again to Maxwell's distribution function *relative* to the rotating and expanding frame (see paper III, equation 17). It is then the distribution of the peculiar velocities after the "Hubble expansion velocity" and the time dependent rotation are removed that are distributed Maxwellianly; when the system is fluid, the density distribution is a Gaussian flattened according to the rotation that results from the fixed angular momentum.

The interest of this problem for those versed in statistical mechanics is that it is no longer an energy that is shared between the different components of the motion.

5	Two tetrahedra joined on a face
6	Two pyramids joined at their bases
7	Two pentagonal pyramids joined at their bases
8	A twisted cube
9	Three pyramids, each pair sharing the edge of a base
10	Skewed pyramid twisted
11	Two skewed pyramid twisted and one center
12	Icosahedron i.e. two skewed pentagonal pyramids
13	Icosahedron and one center
14	Hexagonal and pentagonal pyramids and one center
15	Two skewed hexagonal pyramids and one center
16	Pentagonal pyramid and an hexagon and a triangle and one center
17	Hexagonal pyramid over an hexagon over a triangle and one center
18	Two pentagonal pyramids and one twisted pentagon and one center

TABLE I: First 18 configurations of equilibria. A few of them are shown on Figure 1. Note that as the number of elements increases, the final configurations need not be unique.

The interest for astronomers lies in part because these systems suffer no violent relaxation to a size that obeys the Virial theorem. Nevertheless, despite the continual pulsation of such systems the rescaled variables within them do relax to a definite equilibrium.

The form of interaction potential ensures that neither the divergence of the potential energy at small separations nor the divergence of accessible volume at large separations which so plague systems with normal gravity occur for this model. Thus its interesting different statistical mechanics is simpler and free of any controversial divergences thanks to the small range repulsion and the harmonic long range attraction which extends to arbitrarily large separations.

Although the harmonic long range attraction is not realised in nature (with the possible exception of quarks), nevertheless, within homogeneous bodies of elipsoidal shape ordinary inverse square gravity does lead to harmonic forces analogous to those found here. Section 2.1.1 shows that only force laws with our particular scalings give such exact results.

In this paper, we demonstrate that such systems can form solids (albeit ones that pulsate in scale). We study in Section III their behaviour in the large N limits and show that they stratify into shells.

We show the phase transition as these structures melt and the corresponding changes in "specific heat". We also discuss the analogous a $\gamma = 5/3$ fluid system (corresponding to a classical white dwarf with an odd gravity, see below), we predict their equilibrium configuration and investigate their properties when given some angular momentum. Section II derives the basic formulae for the N-body system and its fluid analog.

II. DERIVATION

A. The discrete system

We consider N particles of masses m_i at $\mathbf{r}_i$, $i = N$ and set

$$\sum m_i = M, \qquad \sum m_i \mathbf{r}_i = M\overline{\mathbf{r}}\,, \tag{1}$$

and half the trace of the intertial tensor as

$$I = \sum m_i(\mathbf{r}_i - \overline{\mathbf{r}})^2 \equiv Ma^2, \tag{2}$$

which defines the scale a. In earlier work we showed both classically (paper I) and quantum mechanically [11] (paper II) that if the potential energy of the whole system was of the form

$$V = W(a) + a^{-2}W_2(\hat{\mathbf{a}})\,, \tag{3}$$

where $\hat{\mathbf{a}}$ is the 3N dimensional unit vector

$$\hat{\mathbf{a}} = \frac{N^{-1/2}}{a}(\mathbf{r}_1 - \overline{\mathbf{r}},\ \mathbf{r}_2 - \overline{\mathbf{r}}\ ....\ ,\ \mathbf{r}_N - \overline{\mathbf{r}})\,, \tag{4}$$

then the motion of the scaling variable a separates dynamically from the motions of both $\overline{\mathbf{r}}$ and the $\hat{\mathbf{r}}$ so those motions decouple. If we ask that V be made up of a sum of pairwise interactions then the hyperspherical potential, W, (independent of direction in the $3N-3$ dimensional space) has to be of the form:

$$W(a) = \frac{1}{2}\omega^2 Ma^2 = V_{-2}\,, \tag{5}$$

where ω^2 is constant but depends linearly on M, and

$$W_2(\hat{\mathbf{a}}) = a^2 V_2 = a^2 \sum\sum_{i<j} K_2|r_i - r_j|^{-2}\,. \tag{6}$$

Hence W_2 is a function of $\hat{\mathbf{a}}$ and is independent of the scale a.

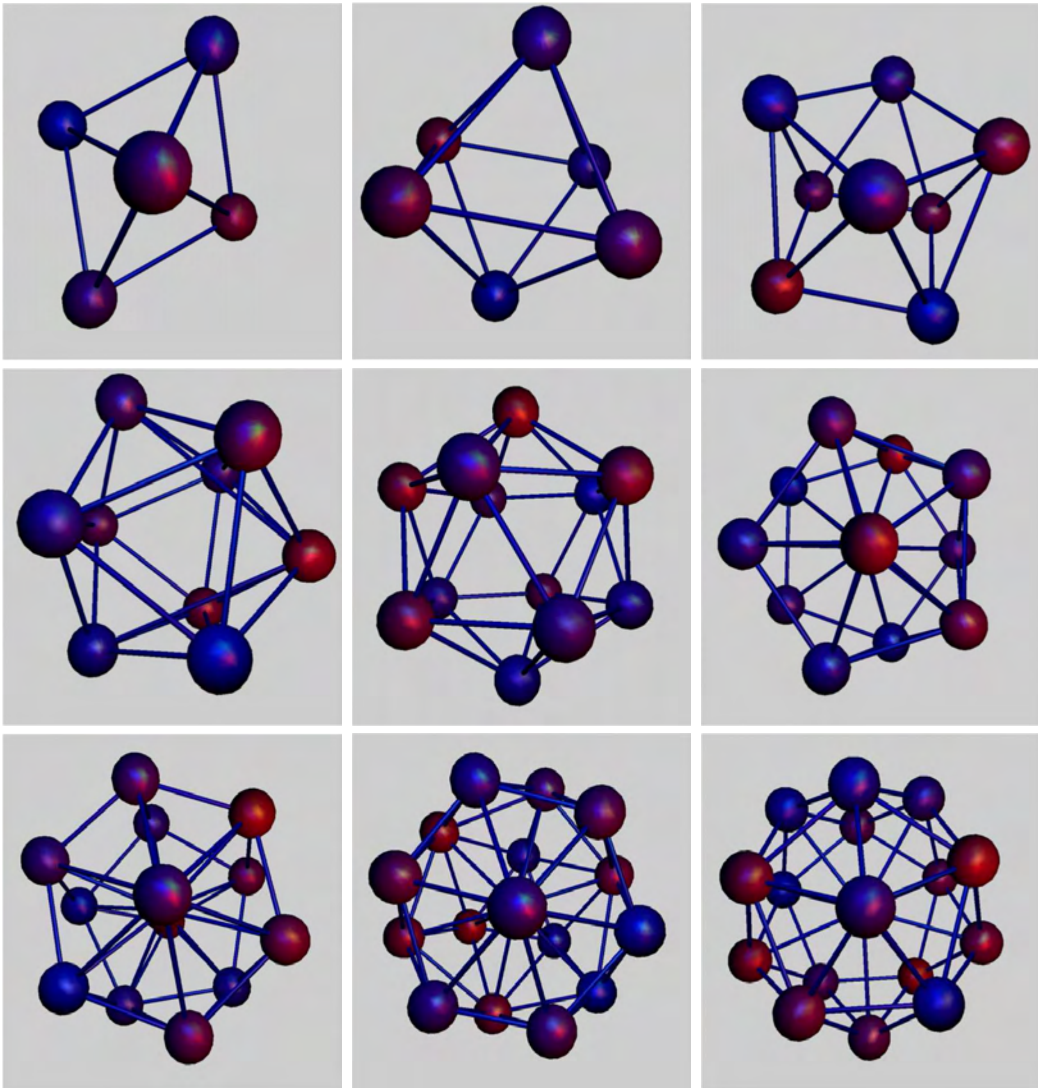

FIG. 1: (Color online) A small set of remarkable equilibria for low N; from left to right and top to bottom: N = [5] two tetrahedra joined at their bases, [6] two pyramids joined at their bases, [8] a twisted cube (three pyramids each pair sharing a base edge), [12] Icosahedron i.e. two skewed pentagonal pyramid, [13] Icosahedron+center, [14] hexagonal+ pentagonal pyramids+center, [17] hexagonal pyramid over hexagon over triangle+center, [18] two pentagonal pyramids+twisted pentagon center. Java animations describing theses oscillating crystals are found at `http://www.iap.fr/users/pichon/nbody.html`.

1. *Relationship to the Virial Theorem*

Let us now see why potentials of the for $V_2 + V_{-2}$ are so special by looking at the Virial Theorem and the condition of Energy conservation. Take the more general potential energy to be a sum of pieces V_n where each V_n scales as r^{-n} on a uniform expansion. n can be positive or negative. Then $V = \sum V_n$. For such a system the Virial Theorem reads:

$$\frac{1}{2}\ddot{I} = 2T + \sum nV_n = 2E + \sum(n-2)V_n \ .$$

Now we already saw that $V_{-2} \propto I$ and V_2 clearly drops out of the final sum because $n-2$ is zero. Thus for potentials of the form $V = V_{-2} + V_2$

$$\frac{1}{2}\ddot{I} = 2E - 4V_{-2} = 2E - 4\omega^2\left(\frac{1}{2}I\right) , \qquad (7)$$

so I vibrates harmonically with angular frequency 2ω about a mean value E/ω^2 and shows no Violent Relaxation (1). Multiplying by $4\dot{I}$ and integrating

$$\dot{I}^2 = 8EI - 4\omega^2 I^2 - 4M^2\mathcal{L}^2 ,$$

where the last term is the constant of integration chosen in conformity with Eq. (8). Now recall from Eq. (2) that $I = Ma^2$ so we find on division by $8M^2a^2$ that

$$\frac{\dot{a}^2}{2} + \frac{\mathcal{L}^2}{2a^2} + \frac{1}{2}\omega^2 a^2 = \frac{E}{M} , \qquad (8)$$

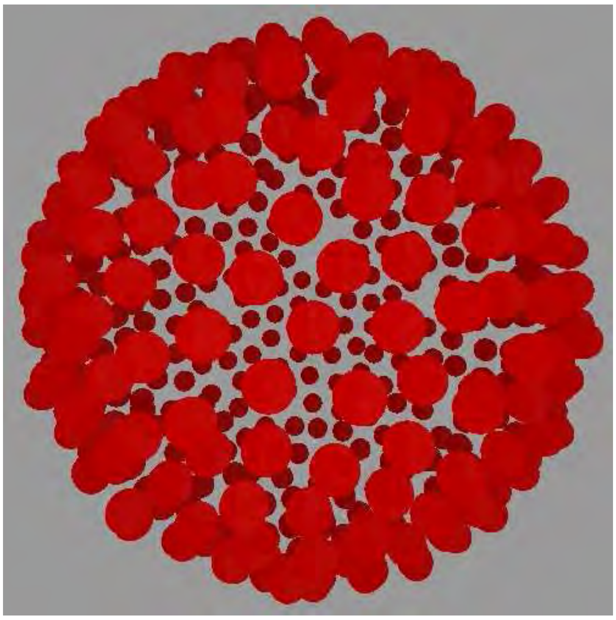

FIG. 2: (Color online) An example of large N static spherical equilibrium obeying Eq. (9); here only a given shell is represented for clarity.

which we recognise as the specific energy of a particle with specific "angular momentum" $\mathcal{L}$ moving in a simple harmonic spherical potential of 'frequency' ω. In such a potential a vibrates about its mean at 'frequency' 2ω.

Note here that the $\gamma = 5/3$ fluid also has a term $3(\gamma - 1)U = 2U$ in the virial theorem since its internal energy, U, scales like r^{-2} so it can be likewise absorbed into the total energy term. Thus if every elementary mass of such a fluid attracted every other with a force linearly proportional to their separation, then that system too would pulsate eternally, as described above in Eq. (7) (see Section II B below).

The aim of this paper is to demonstrate the existence of perpetually pulsating equilibrium lattices and to study the changes as the non-pulsational 'energy' $M\mathcal{L}^2/2$ is increased. We show that the part of the potential left in the equation of motion for the rescaled variables is the purely repulsive V_2. It is then not surprising that the lattice disruption at higher non-pulsational energy occurs quite smoothly and the solid phase appears to give way to the "gaseous" phase of half the specific heat without the appearance of a liquid with another phase transition. The hard sphere solid has been well studied and behaves rather similarly.

2. *The Equations of Motion and their separation*

Although the work of this section can be carried out when the masses m_i are different, (see paper I), we here save writing by taking $m_i = m$ and so $M = Nm$. We start with V of the form (3). The equations of motion are

$$m\ddot{\mathbf{r}}_i = -\partial V/\partial \mathbf{r}_i \quad . \tag{9}$$

Now V is a mutual potential energy involving only $\mathbf{r}_i - \mathbf{r}_j$ so $\sum_i \partial V/\partial \mathbf{r}_i = 0$ and summing the above equation for all i we have

$$d^2\overline{\mathbf{r}}/dt^2 = 0 \quad , \quad \overline{\mathbf{r}} = \overline{\mathbf{r}}_0 + \mathbf{u}t \quad .$$

Henceforth we shall remove the centre of mass motion and fix the centre of mass at the origin so $\overline{\mathbf{r}} = 0$. Now the $3N$-vector $\mathbf{a}$ can be rewritten in terms of its length a and its direction $\hat{\mathbf{a}} \equiv \mathbf{a}/a$ (a unit vector). Equation (9) takes the form

$$M\ddot{\mathbf{a}} = -\partial V/\partial \mathbf{a} = -W'\hat{\mathbf{a}} + 2a^{-3}W_2\hat{\mathbf{a}} - a^{-3}\partial W_2/\partial \hat{\mathbf{a}}\,, \tag{10}$$

where we have used the form (3) for V. Notice that when W_2 is zero (or negligibly weak) all the hyperangular momenta of the form $m(r_\alpha \dot{r}_\beta - r_\beta \dot{r}_\alpha)$ where $\alpha \neq \beta$ run from 1 to $3N$, are conserved!

Taking the dot product of (10) with $\mathbf{a}$ eliminates the $\partial W_2/\partial \hat{\mathbf{a}}$ term which is purely transverse so we get the Virial Theorem in the form:

$$\frac{1}{2}\frac{\mathrm{d}^2}{\mathrm{d}t^2}(Ma^2) = M\dot{\mathbf{a}}^2 - a\frac{\mathrm{d}W}{\mathrm{d}a} - \frac{2}{a^2}W_2 = 2E - \frac{1}{a}\frac{\mathrm{d}}{\mathrm{d}a}(a^2W)\,. \tag{11}$$

Multiplying by $\mathrm{d}(a^2)/\mathrm{d}t/2$ and integrating Eq. (11) yields

$$\frac{1}{2}Ma^2\dot{a}^2 = Ea^2 - Wa^2 - \frac{1}{2}M\mathcal{L}^2\,,$$

where the final term is the constant of integration. On division by a^2

$$\frac{M}{2}\left(\dot{a}^2 + \frac{\mathcal{L}^2}{a^2}\right) + W(a) = E\,, \tag{12}$$

which is the energy equation of a particle of mass M moving with angular momentum $\mathcal{L}$ and energy E in a hyperspherical potential $W(a)$. Now

$$\ddot{\mathbf{a}} = \frac{\mathrm{d}}{\mathrm{d}t}(\dot{a}\hat{\mathbf{a}} + a\dot{\hat{\mathbf{a}}}) = \ddot{a}\hat{\mathbf{a}} + \frac{1}{a}\frac{\mathrm{d}}{\mathrm{d}t}(a^2\dot{\hat{\mathbf{a}}}) \tag{13}$$

and from (12)

$$\ddot{a} = \frac{\mathcal{L}^2}{a^3} - \frac{1}{M}W'(a) \quad . \tag{14}$$

Inserting these values for $\ddot{\mathbf{a}}$ and $\ddot{a}$ into equation (10) we obtain on simplification, multiplying by a^3:

$$Ma^2\frac{\mathrm{d}}{\mathrm{d}t}\left(a^2\frac{\mathrm{d}\hat{\mathbf{a}}}{\mathrm{d}t}\right) = 2W_2\hat{\mathbf{a}} - \partial W_2/\partial\hat{\mathbf{a}} - M\mathcal{L}^2\hat{\mathbf{a}} \quad . \tag{15}$$

On writing $\mathrm{d}/\mathrm{d}\tau = a^2\mathrm{d}/\mathrm{d}t$ this becomes an autonomous equation for $\hat{\mathbf{a}}(\tau)$. Since $(\dot{\mathbf{a}})^2 = (a\dot{\hat{\mathbf{a}}} + \dot{a}\hat{\mathbf{a}})^2 = a^2\dot{\hat{\mathbf{a}}}^2 + \dot{a}^2$ we may write the energy in the form

$$E = \frac{1}{2}M\left[\frac{1}{a^2}\left(\frac{d\hat{\mathbf{a}}}{d\tau}\right)^2 + \dot{a}^2\right] + V = \frac{1}{2}M\left(\dot{a}^2 + \frac{\mathcal{L}^2}{a^2}\right) + W\,,$$

so

$$\frac{1}{2}M\left(\frac{\mathrm{d}\hat{\mathbf{a}}}{\mathrm{d}\tau}\right)^2 + W_2 = \frac{1}{2}M\mathcal{L}^2 \quad . \tag{16}$$

This shows that the only 'potential' in the hyper angular coordinates' motion is $W_2(\hat{\mathbf{a}})$ and that the effective hyper angular energy in that motion is $\frac{1}{2}M\mathcal{L}^2$ (which has the dimension of a^2 times an energy). In fact we showed in papers I and III that it was this quantity that was equally shared among the hyperangular momenta in the statistical mechanics of perpetually pulsating systems. (15) gives the equation of motion for $\hat{\mathbf{a}}$. In terms of the true velocities $\mathbf{v}_1,\ \mathbf{v}_2$ etc

$$\frac{\mathrm{d}\hat{\mathbf{a}}}{\mathrm{d}\tau} = \sqrt{N}a^2\frac{\mathrm{d}}{\mathrm{d}t}\left(\frac{\mathbf{r}_1}{a},\ \frac{\mathbf{r}_2}{a}\ ....\ \frac{\mathbf{r}_N}{a}\right) =$$

$$a\left(\mathbf{v}_1 - \frac{\dot{a}}{a}\mathbf{r}_1, \mathbf{v}_2 - \frac{\dot{a}}{a}\mathbf{r}_2\ ...\ \text{etc}\right) ,$$

so it is the peculiar velocities after removal of the Hubble flow $\dot{a}\mathbf{r}_i/a$ and after multiplication by a that constitute the kinetic components of the shared angular energy in the angular potential $W_2(\hat{\mathbf{a}})$.

When the $m(\mathrm{d}\hat{\mathbf{a}}/\mathrm{d}\tau)^2/2$ are large enough to escape the potential wells offered by W_2/N we get an almost free particle angular motion of these $3N-4$ components. The -4 accounts for the fixing of the centre of mass and the removal of $\dot{a}$ from the kinetic components. If we impose also a prescribed total angular momentum, the number of independent kinetic components would reduce by a further three components to $3N-7$. However the peculiar velocities are then measured relative to a frame rotating with angular velocity $\mathbf{\Omega}$ where $\mathbf{\Omega} = \mathcal{I}^{-1}\cdot\mathbf{J}$ where $\mathbf{J}$ is the angular momentum of the system. Here $\mathcal{I}$ is the inertial tensor, not to be confused with $I = \mathrm{trace}(\mathcal{I})/2$ introduced in Section II A 1. The constant Lagrange multiplier is no longer $\mathbf{\Omega}$, which is proportional to a^{-2} since the inertial tensor, has that dependence in pulsating equilibria. The Lagrange multiplier is $\tilde{\mathbf{J}} = \mathbf{\Omega}a^2$ which is constant during the pulsation and the peculiar velocity is $\mathbf{v}_{\mathrm{p}i} = (\mathbf{v}_i - \mathbf{u}_i)$ where $\mathbf{u}_i = \left(\dot{a}\mathbf{r}_i/a + \tilde{\mathbf{J}}\times\mathbf{r}_i/a^2\right)$ see paper III equation (17).[1] Hereafter we specialise to the requirements given by Eq. (5) and (6).

B. The $\gamma = 5/3$ analogous fluid system

When particles attract with both a long range force such as gravity or our linear law of attraction, and a short rage repulsion, the latter acts like the pressure of a fluid. Indeed short range repulsion forces only extend over a local region, and for large N their effect can be considered as pressure since only the particles close to any surface drawn through the configuration affect the exchange of momentum across that surface. In our case, the local r_{ij}^{-3} forces come from the r_{ij}^{-2} potential which scales as r^{-2}. A barotropic fluid with $p = \rho^\gamma$ has an internal energy that behaves as $\rho^{\gamma-1}$ scaling like $r^{-3(\gamma-1)}$. The required r^{-2} scaling gives a γ of $5/3$, *i.e.* a polytropic index of $n = 3/2$, the same as a non relativistic degenerate white dwarf. Thus we may expect *analogies* between a $\gamma = 5/3$ fluid with the linear long range attraction, and our large N particle systems. However an r_{ij}^{-3} repulsion between particles is not of very short range so this fluid is not the same as the large N limit of the particle system. The particle equilibria have the inverse cubic repulsion between particles balancing the long range linear attraction, which can be exactly replaced by a linear attraction to the barycentre proportional to the total mass. For the fluid, it is the pressure gradient that balances this long range force.

1. Mass profile of the static polytropic fluid

The equilibrium of such a fluid in the presence of a long range force, $-G^\star Mr$, (where $MG^\star \equiv \omega^2$) is given by

$$\frac{1}{\rho}\frac{\mathrm{d}p}{\mathrm{d}r} = -G^\star Mr\,. \tag{17}$$

Setting $p = \kappa\rho^{5/3}$, with $\xi \equiv r/r_{\mathrm{m}}$, this yields

$$\rho = \rho_0(1-\xi^2)^{3/2}, \tag{18}$$

where $\mathbf{r}$ is the 3D configuration space vector measured from the centre of mass of the system and r its modulus, with r_{m} its value at the edge.

Integrating the density gives a mass profile, $M(\xi)$,

$$M(\xi) = \frac{2M}{3\pi}\left(3\arcsin(\xi) - \xi(8\xi^4 - 14\xi^2 + 3)\sqrt{1-\xi^2}\right), \tag{19}$$

and M is the total mass. In practice for the discrete system of Section II A, there is a marked layering at equilibrium, and the "pressure" and the mass profiles depart from their predicted profiles as each monolayer of particles is crossed. See Section III and Fig. (3).

The relationship between the polytropic coefficient, κ, and K_2, the strength of the repulsion (entering W_2 in Eq. (6)) is found by identifying the internal energy of the corresponding fluid to the potential energy of the $1/r_{ij}^2$ coupling. In short, the former reads for a $\gamma = 5/3$ fluid with density profile Eq. (17):

$$V_2 = -\int_0^{r_{\mathrm{m}}}\frac{\kappa\gamma}{\gamma-1}\rho^{2/3}4\pi r^2\rho\mathrm{d}r = -\frac{25\pi^2}{128}\kappa\rho_0^{5/3}r_{\mathrm{m}}^3\,, \tag{20}$$

[1] The above definition of $\mathbf{u}$ is correct. That given under equation (18) of paper III has $-\mathbf{\Omega}$ for $\mathbf{\Omega}$ in error as may be seen from equation (17).

while the latter reads:

$$-\frac{K_2}{2}\iiint_0^{r_{\rm m}} \frac{8\pi r^2\rho(r)\pi r'^2\rho(r')\mathrm{d}\mu\,\mathrm{d}r\,\mathrm{d}r'}{r^2+r'^2-2\mu\, r\, r'} = -\frac{9\pi^4}{320}\rho_0^2 r_{\rm m}^4 K_2\,. \tag{21}$$

Identifying Eq. (20) and (21) gives (using $M = \pi^2\,\rho_0 r_{\rm m}^3/8$ consistant with the density profile, Eq. (18))

$$\kappa = \frac{36}{125}\pi^{4/3}M^{1/3}K_2. \tag{22}$$

Similarly, requiring that V_2 and V_{-2} balance at static equilibrium, where

$$V_{-2} = \int \rho(r)\,\frac{\omega^2\, r^2}{2}4\pi r^2 \mathrm{d}r = \frac{3\pi^2}{128}\omega^2\rho_0 r_{\rm m}^5\,, \tag{23}$$

yields

$$\rho_0 = \left(\frac{5G^\star}{3K_2}\right)^{3/4}\frac{M}{\pi^2}\,,\quad \text{and} \tag{24}$$

$$r_{\rm m} = 2\left(\frac{3K_2}{5G^\star}\right)^{1/4}\,. \tag{25}$$

Eqs. (18)-(25) allow us to relate the properties of the crystal to the properties of the analogous fluid system. Notice that $r_{\rm m}$ is independent of M and ρ_0 is proportional to M.

2. Figure of rotating configurations

Equilibrium in the rotating frame with the angular rate, $\mathbf{\Omega}$ (not to be confused with ω, the strength of the harmonic potential introduced in Eq. (5)), requires that:

$$\frac{1}{\rho}\nabla p = \nabla(\psi + \frac{1}{2}\Omega^2 R^2)\,,\quad \text{where}\quad \psi = -\frac{1}{2}G^\star M r^2\,, \tag{26}$$

where R is the distance off axis ($r^2 = R^2 + z^2$). Since $p = \kappa\rho^{5/3}$, it follows that, with $\Omega_\star^2 = \Omega^2/(G^\star M)$,

$$\frac{5}{2}\kappa\rho^{2/3} = -\frac{G^\star M}{2}(z^2 + (1-\Omega_\star^2)R^2) + \text{const.} \tag{27}$$

Let $\rho = 0$ at $z = z_0$ on axis, then

$$\frac{\rho}{\rho_0} = \left(1 - \frac{z^2}{z_0^2} - (1-\Omega_\star^2)\frac{R^2}{z_0^2}\right)^{3/2}\,. \tag{28}$$

From this we can derive the mass, M and the moment of inertia, $\mathcal{I}$ as functions of the z_0, ρ_0

$$M = \frac{\pi^2}{8}\frac{\rho_0 z_0^3}{1-\Omega_\star^2}\,,\quad \text{and}\quad \mathcal{I} = \frac{1}{4}\mathrm{M}R_0^2\,, \tag{29}$$

where $R_0^2 = z_0^2/(1-\Omega_\star^2)$ and $z_0^2 = 5\kappa/\rho_0^{2/3}/\mathcal{L}^2$. Eq. (28) generalizes Eq. (18) when the $\gamma = 5/3$ fluid is given some angular momentum. The ellipticity, ε, of the rotating configuration is given by

$$\varepsilon^2 = 1/(1-\Omega_\star^2) = 1/(1-\Omega^2/\omega^2)\,. \tag{30}$$

Fig. (6) displays the corresponding configuration for $N = 64$.

3. Dynamics of the rotating oscillating $\gamma = 5/3$ fluid

The basic pulsation of the $\gamma = 5/3$ fluid in rotation is given by a time dependent uniform expansion/contraction plus a rotation at constant angular momentum. Thus

$$\mathbf{u} = \frac{\dot a}{a}\mathbf{r} + \frac{1}{a^2}\tilde{\mathbf{J}}\times\mathbf{r}\,, \tag{31}$$

where $a(t)$ is the "expansion factor" of Section II A and $\tilde{\mathbf{J}}$ is the constant Lagrange multiplier associated with angular momentum conservation. The acceleration involved in this motion are

$$\frac{\mathrm{D}\mathbf{u}}{\mathrm{D}t} = \frac{\partial\mathbf{u}}{\partial t} + \mathbf{u}\cdot\nabla\mathbf{u} = \frac{\partial\mathbf{u}}{\partial t} + \nabla\left(\frac{1}{2}\mathbf{u}^2\right) - \mathbf{u}\times(\nabla\times\mathbf{u})\,. \tag{32}$$

Given that $\nabla\times\mathbf{u} = 2\tilde{\mathbf{J}}/a^2$, putting Eq. (31) into (32) yields

$$\frac{\mathrm{D}\mathbf{u}}{\mathrm{D}t} = \nabla\left(\frac{\ddot a}{a}\frac{r^2}{2} - \frac{1}{2a^4}(\tilde{\mathbf{J}}\times\mathbf{r})^2\right)\,. \tag{33}$$

Differentiating Eq. (8) yields:

$$\ddot a = \frac{\mathcal{L}^2}{a^3} - \omega^2 a\,, \tag{34}$$

while Euler's equation reads:

$$\frac{\mathrm{D}\mathbf{u}}{\mathrm{D}t} = -\nabla\left(\frac{5}{2}\kappa\rho^{2/3} + \frac{1}{2}\omega^2 r^2\right)\,. \tag{35}$$

Equating Eq. (35) and (33) together with Eq. (34) yields:

$$\nabla\left(\frac{5}{2}\kappa\rho^{2/3} + \frac{1}{2a^4}\mathcal{L}^2 r^2 - \frac{1}{2a^4}\left(\tilde{\mathbf{J}}\times\mathbf{r}\right)^2\right) = 0\,. \tag{36}$$

Now in the rescaled space, $\rho \equiv \tilde\rho/a^3$, $\mathbf{r} \equiv \tilde{\mathbf{r}}a$ and $\nabla \equiv \tilde\nabla/a$, Eq. (36) reads

$$\tilde\nabla\left(\frac{5}{2}\kappa\tilde\rho^{2/3} + \frac{1}{2}\mathcal{L}^2\tilde r^2 - \frac{1}{2}\left(\tilde{\mathbf{J}}\times\tilde{\mathbf{r}}\right)^2\right) = 0\,. \tag{37}$$

which is the equilibrium condition but with the time-dependently rescaled variables replacing the original ones. Hence it follows that in the comoving rotating frame, the $\gamma = 5/3$ fluid will stratify in the same manner as Eq. (28)[2] but in the rescaled variables ($\tilde R_0^2 = \tilde z_0^2/(1-\tilde J^2/\mathcal{L}^2)$ and $\tilde z_0^2 = 5\kappa/\tilde\rho_0^{2/3}/\mathcal{L}^2$). This maintains a *constant* ellipticity during the oscillation, since $\tilde R_0$ and $\tilde z_0$ are independent of $a(t)$.

[2] which follows from integrating Eq. (37) while evaluating the integration constant at $\tilde{\mathbf{r}} = 0$; this integration constant could in principle depend on time but because $\int\tilde\rho\mathrm{d}^3\tilde r \equiv M$ is independent of time, $5\kappa\tilde\rho_0^{2/3}$ is indeed constant

III. APPLICATIONS: CRYSTALLINE FORMS OF PULSATING EQUILIBRIA

Let us now study the discrete form of rotating pulsating equilibria that the systems described in Section II follow. Let us first ask ourselves what would the final state of equilibrium in which N particles obeying Eq. (9) would collapse to, if one adds a small drag force in order to damp the motions.

Numerical setup

A softening scale, s, of 0.05 was used[3] so that The effective interaction potential reads

$$\psi_{12} = G^{\star}\frac{r_{12}^2}{2} + \frac{K_2}{r_{12}^2 + s^2}\,. \tag{38}$$

We may escale both the repulsive, K_2 and the attractive strength, $G^{\star}$ of the potential to one by choosing appropriately the time units and the scale units. As a check, we compute the total energy of the cluster, together with the invariant, $m\mathcal{L}^2/2$ and check its conservation.

A. Static Equilibrium

The relaxation towards the equilibrium should be relatively smooth in order to allow the system to collapse into a state of minimal energy. We will consider here two different damping forces; first (in Section III A) an isotropic force, proportional to $-\alpha\mathbf{v}$ so that both the rotation and the radial oscillations are damped; or, in Section III B 1, a drag force so that the components of the velocity are damped until centrifugal equilibrium is reached.

1. Few particle Equilibria

Figure 1 displays the first few static equilibria, while Table I lists the first 18, which includes in particular the regular Icosahedron for $N = 12$. Strikingly, roughly beyond this limit of about $N = 20$, there exists more than one set of equilibria for a given value of N, and the configuration of lowest energy is not necessarily the most symmetric. The overall structure is not far from hexagonal close packed, but with a spherical layering at large radii. Java animations describing the crystals are found at `http://www.iap.fr/users/pichon/nbody.html`.

[3] we also checked that our results remained the same with $s = 0.01$

2. Larger N limit

Figure 3 displays both the mean mass profile and the corresponding section though $512 \leq N \leq 2048$ lattices; both the mass profile and the sections are derived while stacking different realisations of the lattice and binning the corresponding density. Note that the inner regions are more blurry as N increases; indeed, the inner layers are frozen early on by the infall of the outer layers.

Let us estimate the pressure profile in our crystal. In static equilibrium, given Eq. (17), we should have approximately

$$p(r) = \int \omega^2\rho(r)r\mathrm{d}r = \frac{\omega^2}{4\pi}\int_r^{r_\mathrm{m}} \frac{\mathrm{d}m}{r} \approx \frac{\omega^2}{4\pi}\sum_{r'>r}\frac{m}{r'}\,. \tag{39}$$

Eq. (39) is compared to Eq. (17) in Fig. (4).

3. Mean density profile

Fig. (5) shows the mean density within rescaled radius, $\xi = r/r_\mathrm{m}$ as a function of ξ for three different simulations. The shell structure is very obvious but at larger N values it is also clear that besides the oscillations due to shells the mean density falls off somewhat towards the outside. However such a fall off is far less pronounced than that predicted by the polytropic model which gave $\bar\rho(\xi) = M(\xi)/(4\pi r_\mathrm{m}^3\xi^{3/3})$ with $M(\xi)$ given by Eq. (19). On further inspection, it transpired that this is due to the longer range of the repulsion force which is not correctly represented by the pressure analogy.

Consider a continuum density distribution with a repulsive force between elements $\mathrm{d}m$ and $\mathrm{d}\bar m$ derived from the potential $K_2\mathrm{d}m\mathrm{d}\bar m/|\mathbf{r}-\bar{\mathbf{r}}|^2$. Then, for a spherical density distribution, $\rho(\bar r)$, the total potential reads

$$\psi(r) = K_2\iint\frac{2\pi\bar r^2\rho(\bar r)\mathrm{d}\mu\mathrm{d}\bar r}{r^2+\bar r^2 - 2\,r\bar r\mu} = 2\pi K_2\int\frac{\bar r\rho(\bar r)}{r}\log\left|\frac{r+\bar r}{r-\bar r}\right|\mathrm{d}\bar r$$

The condition of equilibrium balances against the harmonic attraction yields

$$-\frac{\mathrm{d}\psi}{\mathrm{d}r} = G^{\star}Mr\,,\quad r\leq r_\mathrm{m}\,. \tag{40}$$

Note that *all* the mass, not just that inside radius r, contributes to the attraction for the linear law. Eq. (40) generates a linear integral equation for $\rho(\bar r)$. A numerical solution to Eq. (40) shows that the mean density distribution agrees well with the simulations, once the shell structure is smoothed out (see Fig. (5)). The solution to the integral equation is well approximated by

$$\rho(r) = \rho_0\left(1-\frac{r^2}{6r_\mathrm{m}^2}\right)^3\,,\ \text{where } r\leq r_\mathrm{m}\,, \tag{41}$$

and 0 beyond. The corresponding mean density within

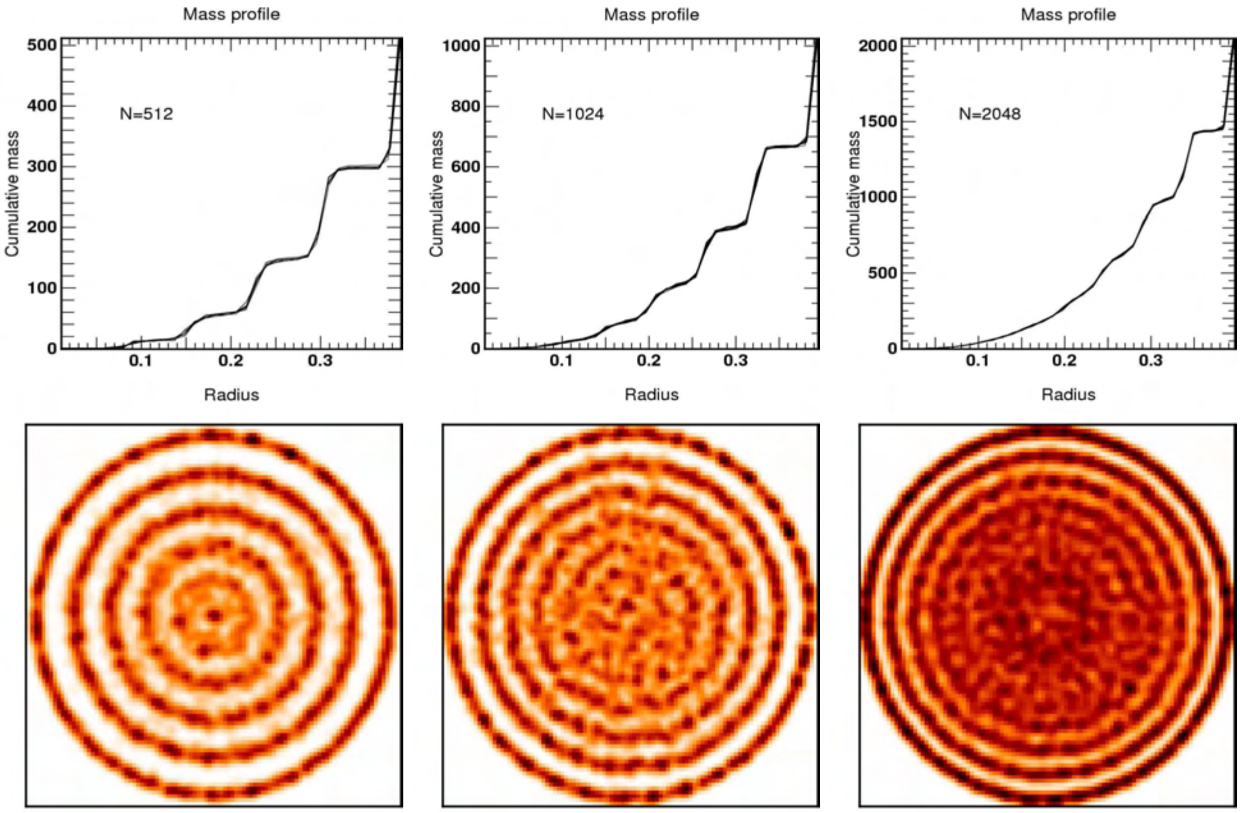

FIG. 3: *top*: (Color online) Mean mass profile and section (*top*) though a $N = 512$, $N = 1024$ and $N = 2048$ crystal; The mass profile is derived while stacking about 20 realisations of the lattice and binning the corresponding density. The shell structure (*bottom*) is clearly apparent on these sections. The number of shell, N, present is consistent with the prediction of Section III A 2. The ordering of the inner regions is lower as N increases since the inner shells do not settle gently as they are disturbed by the infall of the outer layers.

r, $\bar{n}$, scaled to one at the centre, reads

$$\bar{n}(\xi) = \frac{3}{\rho_0 \xi^3} \int^{\xi} \rho(r_{\rm m}\xi)\xi^2 {\rm d}\xi = \left(1 - \frac{3\,\xi^2}{10} + \frac{\xi^4}{28} - \frac{\xi^6}{648}\right), \tag{42}$$

with $\xi \equiv r/r_{\rm m}$, and $n(r) \equiv \rho(r)/m$, (see Fig. (5)) so that at $\xi = 1$, $\bar{n}(1) \equiv X = 16\,651/22\,680$. The simulations have been scaled so that ξ is one at the outermost particle. That will not be at the point at which the theoretical smooth density falls to zero which we have called $\xi = 1$ in our theoretical calculation. In practice this falls outside the last particle, hence we have to rescale the theory's ξ by a factor f which is determined to make the theoretical mean density profile, $\bar{n}$, fit the profile of the simulations' mean density. Once this scaling f has been determined the predicted mean density is given in terms of the observed ξ by the expression $X\bar{n}(f\xi)N/[4/3\pi(fr_{\rm m})^3]$.

4. *Stratification in spherical shells*

In atoms, the main gradient of the potential is towards the nucleus, so the shell structure is dominated by the inner shells which have large changes in energy. In our systems, the global potential gradient is proportional to r so the largest potential differences are on the outside. As a consequence, the system adjusts itself so that the outermost shell is almost full, and the central region is no longer shell dominated. Instead of counting shells outwards from the middle as in atoms, it is best to count shells inwards from the outside where they are best defined. For shells which are numbered from the outside, given that ${\rm d}r/n^{-1/3}(r)$ is the fractional increase in layer number, we have (using Eq. (41))

$$\int_{r_i}^{1} \frac{{\rm d}r}{n(r)^{-1/3}} = \frac{n_0^{1/3} r_{\rm m}}{X}\left[1 - \xi_i - \frac{1}{18}(1-\xi_i^3)\right] = i\,, \tag{43}$$

with $n_0 \equiv \rho_0/m = 3N/(4\pi r_{\rm m}^3)$. Conversely, the number of particles, $N(\leq i)$ within (and including) layer i is given by

$$N(\leq i) = \frac{N}{X}\,\xi_i^3\left[1 - \frac{3}{10}\xi_i^2 + \frac{1}{28}\xi_i^4 - \frac{1}{648}\xi_i^6\right]. \tag{44}$$

Solving the implicit Eq. (43) for the relative radius ξ_i of layer i and putting it into Eq. (44) yields the number of particles within layer i as a function its rank. The

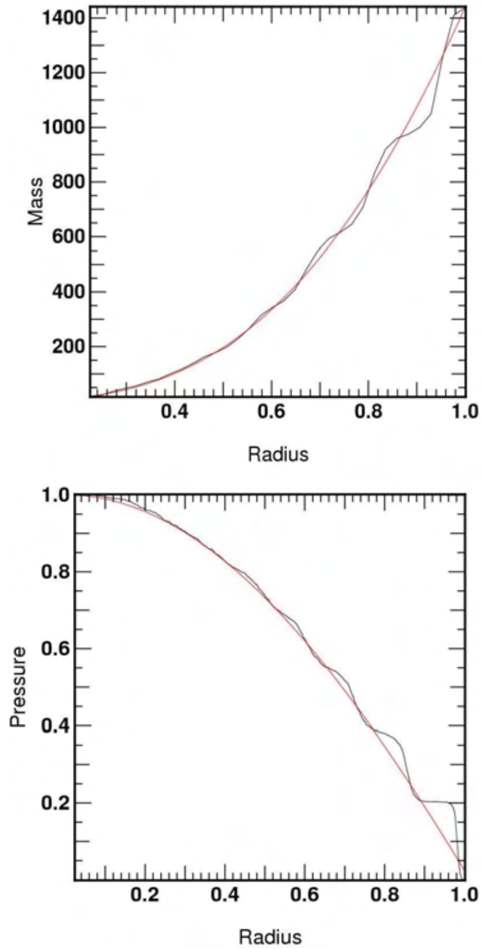

FIG. 4: (Color online) Mass profile and Pressure of an $N = 2048$ simulation together with *a fit of* its analytic prediction given by Eq. (18) and (19) (see Section III A 4 and Fig. (5) for a discussion of the accuracy of this fit). The mass profile is computed via the cumulative number of particles within a given shell, while the pressure profile is estimated via Eq. (39).

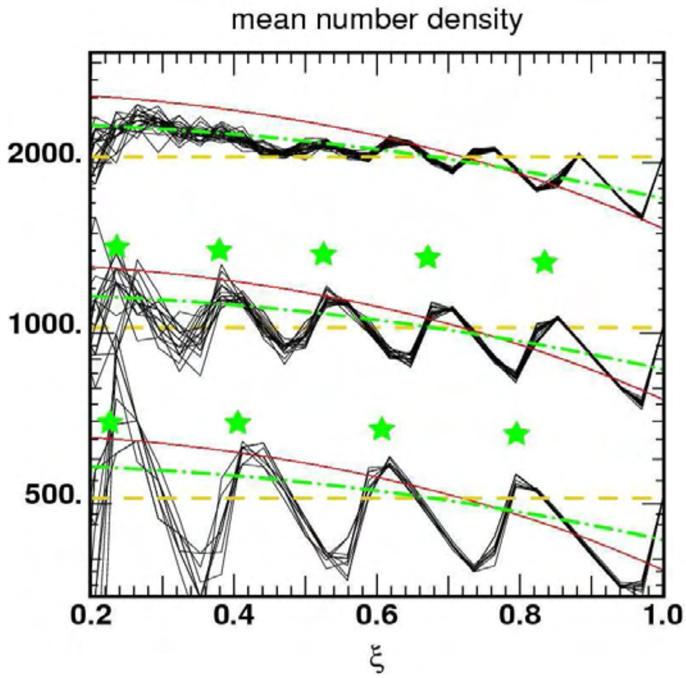

FIG. 5: (Color online) shows the mean number density profile, $N\,\bar{n}(\xi)$ for a set of about 10 $N = 512$, 1024 and 2048 simulations as a function of rescaled radius. The wiggles correspond to the shells seen in Fig. (3). The thin line corresponds to the prediction of Eq. (19) for the fluid system, but with an outer radius rescaled by the predicted radius, Eq. (25) divided by the measured outer radius, $r_{\rm m}$; the dashed line corresponds to a uniform density solid, while the dotted dashed line corresponds to the prediction of Eq. (42) (rescaled, see text). Clearly, this last model gives the best fit to the mean profile, which suggests that for those values of N, the crystal does behave according to the equilibrium Eq. (40), and neither like a pure solid nor as a fluid. The stars correspond to the predictions of the shell radii given by Eq. (43).

radii of the layers, $\xi_i r_{\rm m}$ follows from inverting Eq. (43) for ξ_i. Examples of such shells are shown in Fig. (2) and (3), while the corresponding mass profile checked against Eq. (19) in Fig. (4). The number of shell present in Fig. (3) is consistent with the prediction of Eq. (44).

B. Rotating Perpetually Pulsating Equilibria

1. *Rotating crystals*

The rotating crystal is achieved in steps; first, for each particle in the lattice, we added a velocity kick so that $\mathbf{v} \to \mathbf{v} + \mathbf{\Omega} \times \mathbf{r}$. We then rescale the z coordinate and the v_z (as defined along the momentum direction) of each particule by a constant factor. The system has then the ability to redistribute it momentum along the oscillating particles. We then add a drag force[4] proportional to $-\alpha\left(\mathbf{v} - \mathcal{I}^{-1}\cdot\tilde{\mathbf{J}}\right)$, so that the components of the velocity are damped until centrifugal equilibrium is reached. This defines the rotating spheroid equilibrium. An example of such a configuration is shown in Fig. (6) for $N = 64$. The properties of the corresponding analogous fluid system are described in Section II B 2.

2. *Rotating pulsating crystals*

In order to create a pulsating configuration which preserves the shape of the rotating spheroid, we rescaled all the positions by some factor, λ, and rescaled accordingly all velocities by the factor $1/\lambda$, so that angular momentum is preserved. When this special condition is met, the

[4] which can be shown to be truly dissipating energy

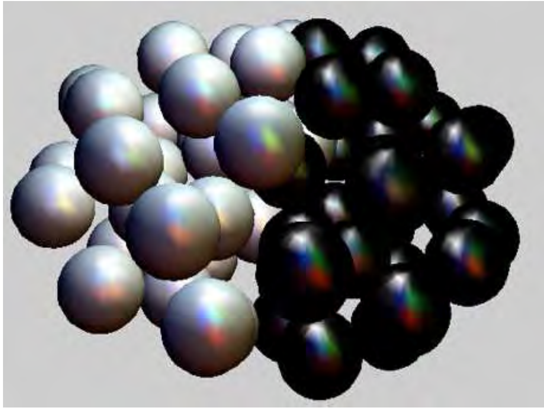

FIG. 6: (Color online) spheroidal crystal corresponding to the final state of a run of $N = 64$ with a damping force of the form $-\alpha\left(\mathbf{v} - \mathcal{I}^{-1}\cdot\tilde{\mathbf{J}}\right)$. Half of the particles was painted one color, while the other half was left some other color. The shape preserving oscillation is achieved by rescaling all position by some factor, λ, and rescaling all velocities by the factor $1/\lambda$. If the rescaling does not preserve momentum of each particle, some of the excess energy may go into heating the system and breaking its structure, which will induce mixing of the two populations (see Section III C 2 and paper III). Java animations corresponding to the corresponding oscillating rotating crystals are found at `http://www.iap.fr/users/pichon/nbody.html`.

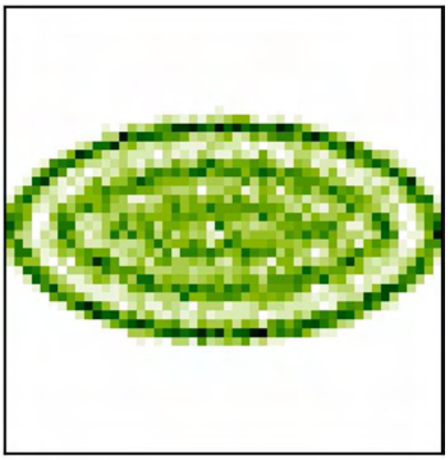

FIG. 7: (Color online) Same as Fig. (3), but for a set of 20 rotating configuration of $N = 256$ particles launched according to the prescription given in Section III B 1. The shell structure is also clearly apparent on this section. The ellipticity of the crystal is found to be in agreement with Eq. (30).

system oscillates and pulsates without *any* form of relaxation (*cf.* Section III C). Note that this situation differs from normal modes of more classical systems, which do preserve the shape of a given oscillation, but might not involve the same particles at all times. Java animations describing the pulsating and rotating crystals are found at `http://www.iap.fr/users/pichon/nbody.html`.

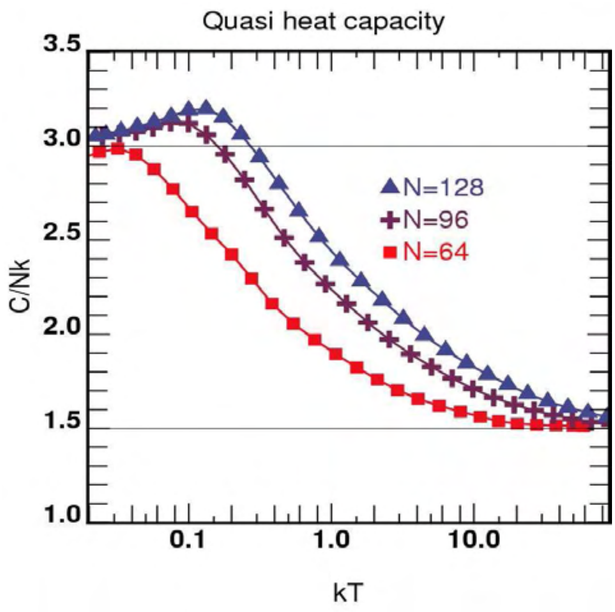

FIG. 8: (Color online) quasi specific heat measured by increase of quasi energy with quasi temperature in units of kN; the quasi temperature is a^2 times the kinetic energy relative to the time dependent "Hubble flow" divided by $3/2\,Nk$; the quasi energy is the sum of the quasi kinetic energy plus W_2; W_2 is a^2 times the repulsive part of the potential energy. During the large amplitude pulsation of the system, the quasi energy is conserved. It is the quasi energy that is shared between the different components in the statistical equilibrium. Since W_2 is only repulsive, the system displays characteristics similar to a hard sphere fluid. There is a continuous transition between the cold crystal lattice and the "free" fluid. Each point is derived over a set of about 20 independent runs. The initial condition is set up with some random motions above the lattice equilibrium.

C. Thermodynamics of dissolving crystal

1. *Specific heat & evaporation*

How does the shell structure disappear as a function of temperature increase ? Fig. 8 displays the quasi-specific heat measured by the increase of quasi energy with quasi temperature in units of kN; Here the quasi temperature is a^2 times the kinetic energy relative to the time dependent "Hubble flow" divided by $3/2\,Nk$; while the quasi energy is the sum of the quasi kinetic energy plus W_2 given by Eq. (6). During the large amplitude pulsation of the system, the quasi energy is shared between the different components in the statistical equilibrium. Since W_2 is only repulsive, the system displays characteristics similar to a hard sphere fluid. The quasi-heat capacity changes from the solid's $3Nk$ to the gaseous $3/2\,Nk$ as expected.

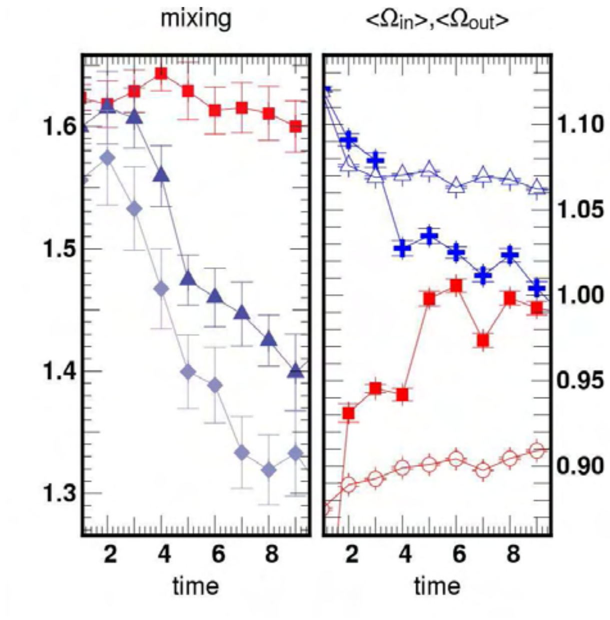

FIG. 9: (Color online) *left panel*: $\Delta n_{\rm WB}/\bar{n}_{\rm WB}$, the relative dispersion in mixing as a function of time for a set of $N = 64$ particles in a situation where the inner fraction of particles was rescaled along the rotation axis in order to induce some momentum exchange. Here three scalings (1.2, 1.6 and 2) were imposed (from top to bottom), corresponding to an increasing heat content which induce a faster relaxation. The initial condition corresponds to the prescription described in Section III B 1 and Fig. (6). *Right panel*: $\Omega_{\rm in}(t)/\bar{\Omega}(t)$ and $\Omega_{\rm out}(t)/\bar{\Omega}(t)$ as a function of time; again the hotter initial configuration (rescaled by 1.8 compared to 1.2) (full symbol) reaches a regime of uniform rotation more rapidly.

2. *Relaxation of the rotating pulsating configuration*

Let us split the particles within our spheroidal equilibrium in two sets as a function of axial radius, R, one corresponding to an inner ring, and one corresponding to an outer ring (which should initially rotate at the same angular rate) and rescale the z component of each inner particle by a factor of 2 so that it does not satisfy the equilibrium condition.

A measure of the thermalisation is given by the rate at which the system will redistribute momentum in order to achieve uniform rotation again. Fig. (9) (*right panel*) represents $\Omega_{\rm in}(t)/\bar{\Omega}(t)$ and $\Omega_{\rm out}(t)/\bar{\Omega}(t)$ as a function of time (with $\bar{\Omega}(t) = [\Omega_{\rm in}(t) + \Omega_{\rm out}(t)]/2$).

3. *Mixing of the rotating pulsating configuration*

A measure of mixing is given by the rate at which the system becomes uniform, when it is started as two distinct phases. Let us start by a configuration where half of the particles on one side of the spheroidal rotating equilibrium are colored in WHITE, and the other half, in BLACK, and rescale again the coordinate along the rotation axis by a factor of two. The redistribution of the excess energy in height will convert a fraction of it into heat. Fig. (9) (*left panel*) represents $\Delta n_{\rm WB}/\bar{n}_{\rm WB} \equiv {\rm RMS}(n_{\rm B}(t) - n_{\rm W}(t))/{\rm RMS}(n_{\rm B}(t) + n_{\rm W}(t))$, with $n_{\rm R}$ the density of WHITE particles, and $n_{\rm B}$ the density of BLACK particles as a function of time. In practice, we bin the x–y plane in the comoving coordinates and estimate $\Delta n_{\rm WB}/\bar{n}_{\rm WB}$ accordingly.

IV. CONCLUSION

In this paper, we have demonstrated that very special systems, those for which the oscillation of the system separates off dynamically from the beheaviour of the rescaled variables, can form (possibly spinning) solids (albeit ones that pulsate in scale). We studied their phase transition and the corresponding "specific heat" as these structures melt. As expected, we found that the heat capacity halve to that of a free fluid, but the phase transition appears to occur gradually even at large N. Although we expected a set or regular and semi regular solids, which we did find for small N, and an hexagonal close packing of most of the system at larger N, we did not foresee the strong shell structure found. Nevertheless, we constructed a theory that explained this shell structure once it had been recognized. We also investigated the evolution of the lattice, as some rotation was imposed on the structure and studied its relaxation under such circumstances, both in terms of mixing and for the redistribution of angular momentum. Another by-product of our study was that the internal energy of the corresponding barotropic fluid scales as $\rho^{\gamma-1}$, *i.e.* as $({\rm scale})^{-3(\gamma-1)}$ so that for $\gamma = 5/3$, it scales like $({\rm scale})^{-2}$. Thus our investigation applies equally to a $\gamma^{5/3}$ fluid with a quasi gravity such that every element of fluid attract every other in proportion to their separation. It is well known, since Newton, that such attractions are equivalent to every particle being attracted in proportion to its distance to the centre of mass as though the total mass were concentrated there. With such a law of interaction, we described the possible set of rotating pulsating equilibria it may reach, and found them is qualitative agreement with our simulations of the corresponding crystals, though the details of their mass profile differed: this fluid model failed to give the correct layering, while a more acurate model gives it correctly. Recently [14] used simulations of such systems to test their smooth particle hydrodynamics codes.

Acknowledgements *We thank David Wales for verifying our structures with his more thorough and well tested program. We would like to thank D. Munro for freely distributing his Yorick programming language and opengl interface (available at* `http://yorick.sourceforge.net`*) which we used to implement our N-body program. D. LB acknowledges support from EARA while working at the Insti-*

tut d'Astrophysique de Paris where this work was completed.

[1] Antonov V. A., 1961, SvA, 4, 859
[2] Arad I., Lynden-Bell D., 2005, MNRAS, 361, 385
[3] Bogdan, T.V. & Wales, 2004, D.J., J.Chem Phys 120, 11090,
[4] Binney J., 2004, MNRAS, 350, 939
[5] Calogero, F., 1971, JMP 12, 419.
[6] Eddington A. S., 1916, MNRAS, 76, 572
[7] Lynden-Bell, D. 1967 MNRAS 136, 101
[8] Lynden-Bell D., Lynden-Bell R. M., 1977, MNRAS, 181, 405
[9] Lynden-Bell D., 1999, PhyA, 263, 293
[10] Lynden-Bell, D. & Lynden-Bell, R.M. 1999 Proc R Soc A 455, 475 Paper I
[11] Lynden-Bell, D. & Lynden-Bell, R.M. 1999 Proc R Soc A 455, 3261 Paper II
[12] Lynden-Bell, D. & Lynden-Bell, R.M. 2004 J Stat Phys 117, 199 Paper III
[13] Lynden-Bell D., Wood R., 1968, MNRAS, 138, 495
[14] Price D.J. Monaghan J. J., MNRAS 365 (2006) 991-1006
[15] Pichon, C. & Lynden-Bell, D., Lattice Melting in Perpetually Pulsating Equilibria, in Statistical mechanics of non-extensive systems, NBS2005, Eds F. Combes, in press.
[16] Thirring W., 1970, Essays in physics 4
[17] Wales D.J. 2001 Science 293, 2067

Mon. Not. R. Astron. Soc. **280**, 1007–1026 (1996)

New sources for Kerr and other metrics: rotating relativistic discs with pressure support

C. Pichon[1,2]★† and D. Lynden-Bell[1]

[1]*Institute of Astronomy, Madingley Road, Cambridge CB3 0HA*
[2]*CITA, McLennan Labs, University of Toronto, 60 St. George Street, Toronto, Ontario M5S 1A7, Canada*

Accepted 1995 December 8. Received 1995 December 5; in original form 1995 March 17

ABSTRACT

Complete sequences of new analytic solutions of Einstein's equations which describe thin supermassive discs are constructed. These solutions are derived geometrically. The identification of points across two symmetrical cuts through a vacuum solution of Einstein's equations defines the gradient discontinuity from which the properties of the disc can be deduced. The subset of possible cuts which lead to physical solutions is presented. At large distances, all these discs become Newtonian but in their central regions they exhibit relativistic features such as velocities close to that of light, and large redshifts. Sections with zero extrinsic curvature yield cold discs. Curved sections may induce discs which are stable against radial instability. The general counter-rotating flat disc with planar pressure tensor is found. Owing to gravomagnetic forces, there is no systematic method of constructing vacuum stationary fields for which the non-diagonal component of the metric is a free parameter. However, all static vacuum solutions may be extended to fully stationary fields via simple algebraic transformations. Such discs can generate a great variety of different metrics, including Kerr's metric with any ratio of a to m. A simple inversion formula is given, which yields all distribution functions compatible with the characteristics of the flow, providing formally a complete description of the stellar dynamics of flattened relativistic discs. It is illustrated for the Kerr disc.

Key words: relativity – methods: analytical – celestial mechanics, stellar dynamics – quasars: general.

1 INTRODUCTION

The general-relativistic theory of rapidly rotating objects is of great intrinsic interest and has potentially important applications in astrophysics. Following Einstein's early work on relativistic collisionless sphericals shells, Fackerell (1968), Ipser & Thorne (1968) and Ipser (1969) have developed the general theory of relativistic collisionless spherical equilibria. The stability of such bodies has been further expanded by Katz, Horwitz & Klapish (1975). Here the complete dynamics of flat disc equilibria is developed and illustrated, extending these results to differentially rotating configurations with partial pressure support. A general inversion method for the corresponding distribution functions is presented, yielding a coherent model for the stellar dynamics of these discs. Differentially rotating flat discs in which centrifugal force almost balances gravity can also give rise to relatively long-lived configurations with large binding energies. Such objects may therefore correspond to possible models for the latest stage of the collapse of a protoquasar. Analytic calculations of their structure have been carried into the post-Newtonian regime by Chandrasekhar (1966). Strongly relativistic bodies have been studied numerically following the pioneering work on uniformly rotating cold discs by Bardeen (1970). An analytic vacuum solution to the Einstein equations, the Kerr metric (Kerr 1963), which is asymptotically flat and has the general properties expected of an exterior metric of a rotating object, has been known for 30 years, but attempts to fit an interior solution to its exterior metric have been unsatisfactory. A method for generating families of self-gravitating rapidly rotating discs purely by geometrical methods is pre-

★Present address: Astronomisches Institut, Universitat Basel, Venusstraße 7, CH-4102 Binningen, Switzerland.
†E-mail: pichon@astro.unibas.ch

sented. Known vacuum solutions of Einstein's equations are used to produce the corresponding relativistic discs. One family inlcudes interior solutions for the Kerr metric.

1.1 Background

Weyl (1917) and Levi-Civita (1919) gave a method for finding all solutions of the axially symmetric Einstein field equations after imposing the simplifying conditions that they describe a static vacuum field. Bičák, Lynden-Bell & Katz (1993, hereafter BLK) derived complete solutions corresponding to counter-rotating pressureless axisymmetric discs by matching exterior solutions of the Weyl–Levi-Civita type on each side of the disc. For static metrics, the vacuum solution was obtained via line superposition of fictitious sources placed symmetrically on each side of the disc by analogy with the classical method of images. The corresponding solutions describe two counter-rotating stellar streams. This method will here be generalized, allowing *true rotation* and radial pressure support for solutions describing self-gravitating discs. These solutions provide physical sources (interior solutions) for stationary axisymmetric gravitational fields.

1.1.1 *Pressure support via curvature*

In Newtonian theory, once a solution for the vacuum field of Laplace's equation is known, it is straightforward to build solutions to Poisson's equation for discs by using the method of mirror images. In general relativity, the overall picture is similar. In fact, it was pointed out by Morgan & Morgan (1969) that for pressureless counter-rotating discs in Weyl's coordinates, the Einstein equation reduces essentially to solving Laplace's equation. When pressure is present, no global set of Weyl coordinates exists. The condition for the existence of such a set of coordinates is that $T_{RR}+T_{zz}=0$. On the disc itself, this is satisfied only if the radial eigenvalue of the pressure tensor, p_R, vanishes (T_{zz} vanishes provided the disc is thin). When p_R is non-zero, vacuum coordinates of Weyl's type still apply both above and below the disc, but as two separate coordinate patches. Consider global axisymmetric coordinates (R', ϕ', z') with $z'=0$ on the disc itself. For $z'>0$, Weyl's coordinates R, ϕ, z may be used. In terms of these variables, the upper boundary of the disc $z'=0^+$ is mapped on to a given surface $z=f(R)$. On the lower patch, by symmetry, the disc will be located on the surface $z=-f(R)$. Thus, in Weyl coordinates, the points $z=f(R)$ on the upper surface of the disc must be identified with the points $z=-f(R)$ on the lower surface. The intrinsic curvature of the two surfaces that are identified match by symmetry. The jump in the extrinsic curvature gives the surface distribution of stress–energy on the disc. A given metric of Weyl's form is a solution of the empty-space Einstein equations, and does not give a complete specification of its sources (for example, a Schwarzschild metric of any given mass can be generated by a static spherical shell of any radius). With this method, all physical properties of the source are entirely characterized once it is specified that the source lies on the surface $z=\pm f(R)$ and the corresponding extrinsic curvature (i.e., its relative layout within the embedding vacuum space–time) is known (see Fig. 1). The freedom of choice of ν in the Weyl metric corresponds to the freedom to choose the density of the disc as a function of radius. The supplementary degree of freedom involved in choosing the surface of section $z=f(R)$ corresponds classically to the choice of the radial pressure profile.

1.1.2 *Rotating discs*

For rotating discs, the dragging of inertial frames induces strongly non-linear fields outside the discs which prohibit the construction of a vacuum solution by superposition of the line densities of fictitious sources. Nevertheless, in practice, quite a few vacuum stationary solutions have been given in the literature, the most famous being the Kerr metric. Hoenselaers, Kinnersley & Xanthopoulos (1979, hereafter HKX) and Hoenselaers & Dietz (1984) have also given a discrete method of generating rotating solutions from known static Weyl solutions. The discs are derived by taking a cut through such a field above all singularities or sources and identifying it with a symmetrical cut through a reflection of the source field. This method applies directly to the non-linear fields such as those generated by a rotating metric of the Weyl–Papapetrou type describing stationary axisymmetric vacuum solutions. The analogy with electromagnetism is then to consider the field associated with a known azimuthal vector potential $\boldsymbol{A}_\phi$, the analogue of $g_{t\phi}/g_{tt}$. The jump in the tangential component of the corresponding B-field gives the electric current in the plane, just as the jump in the t, ϕ component of the extrinsic curvature gives the matter current.

The procedure is then as follows. For a given surface embedded in curved space–time and a given field outside the disc, the jump in the extrinsic curvature on each side of the mirror images of that surface is determined in order to specify the matter distribution within the disc as illustrated in Fig. 1. The formal relationship between extrinsic curvatures and surface energy tensor per unit area was introduced by Israel, and is described in detail by Misner, Thorne & Wheeler (1973). Plane surfaces and non-rotating vacuum fields (i.e., the direct counterpart of the classical case) were investigated by BLK and led to pressureless counter-rotating discs. Any curved surface will therefore produce discs with some radial pressure support. Any vacuum metric with $g_{t\phi}\neq 0$ outside the disc will induce rotating discs.

In Section 2, the construction scheme for rotating discs with pressure support is presented. In Section 3, the properties of these discs are analysed, and a reasonable cut, $z=f(R)$, is suggested. Section 4 describes stellar equilibria which have the corresponding anisotropic stress–energy tensors, while Section 5 derives the properties of the limiting counter-rotating discs. This method is then first applied to warm counter-rotating discs in Section 6; the dominant energy condition given for Curzon discs by Chamorow et al. (1987), and the Lemos solution (Lemos 1989) for the self-similar Mestel disc with pressure support are recovered. In Section 7, the Kerr disc is studied, and the method for producing general HKX discs is sketched.

2 DERIVATION

The jump in extrinsic curvature of a given profile is calculated and related to the stress–energy tensor of the

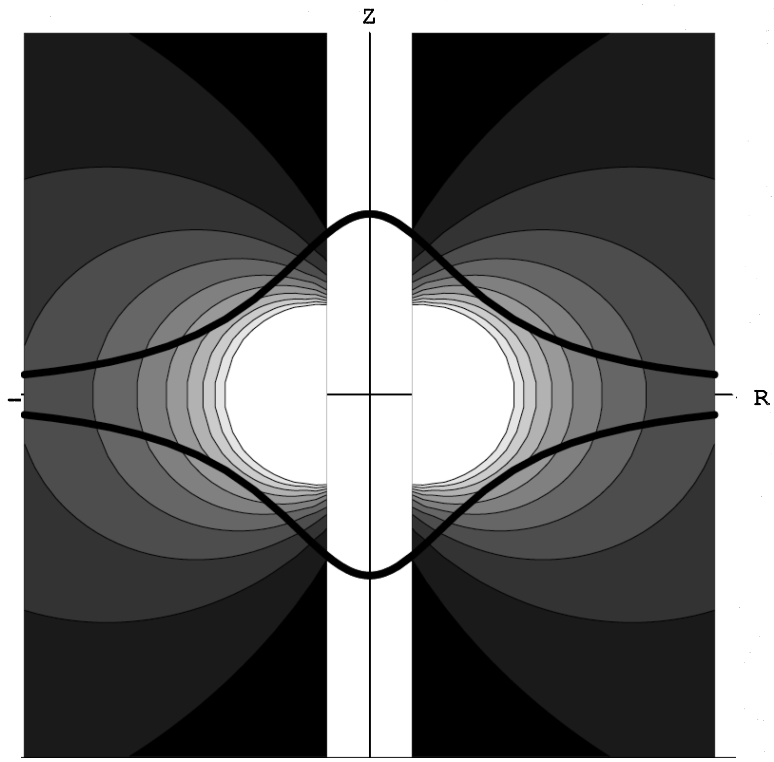

Figure 1. Symbolic representation of a section $z = \pm f(R)$ through the $g_{t\phi}$ field representing the upper and lower surface of the disc embedded in two Weyl–Papapetrou fields. The isocontours of $\omega(R, z)$ correspond to a measure of the amount of rotation in the disc.

matter distribution in the corresponding self-gravitating relativistic disc.

2.1 The extrinsic curvature

The line element corresponding to an axisymmetric stationary vacuum gravitational field is given by the Weyl–Papapetrou (WP) metric,

$$ds^2 = -e^{2\nu}(dt - \omega\, d\phi)^2 + e^{2\zeta - 2\nu}(dR^2 + dz^2) + R^2 e^{-2\nu}\, d\phi^2, \tag{2.1}$$

where (R, ϕ, z) are standard cylindrical coordinates, and ν, ζ and ω are functions of (R, z) only; geometric units $G = c = 1$ are used throughout this paper. Note that this form is explicitly symmetric under simultaneous change of ϕ and t. The vacuum field induces a natural metric on a 3-space-like $z = f(R)$ surface

$$d\sigma^2 = g_{\alpha\beta}\frac{\partial x^\alpha}{\partial x^a}\frac{\partial x^\beta}{\partial x^b}\, dx^a\, dx^b \equiv g_{ab} h^\alpha_a h^\beta_b\, dx^a\, dx^b \tag{2.2}$$

$$\equiv \gamma_{ab}\, dx^a\, dx^b,$$

where $\{x^a\}$ are the coordinates on the embedded hypersurface $z = f(R)$, $\{x^a\} = (t, R, \phi)$, and $\{x^\alpha\} = (t, R, z, \phi)$ are Weyl's coordinates for the embedding spacetime. Here, γ_{ab} stands for the embedded metric, and h^α_a is given by

$$h^\alpha_a = \frac{\partial x^\alpha}{\partial x^a} = \begin{bmatrix} 1 & 0 & 0 & 0 \\ 0 & 1 & 0 & f' \\ 0 & 0 & 1 & 0 \end{bmatrix}, \tag{2.3}$$

where hereafter a prime, ( )′, represents the derivative with respect to R. The line element is then

$$d\sigma^2 = -e^{2\nu}(dt - \omega\, d\phi)^2 + R^2 e^{-2\nu}\, d\phi^2 + e^{2\zeta - 2\nu}(1 + f'^2)\, dR^2. \tag{2.4}$$

Let the upward pointing normal N_μ to the surface $z = f(R)$ be

$$N_\mu = \frac{\partial}{\partial x^\mu}[z - f(R)] = (0, -f', 0, 1). \tag{2.5}$$

The normalized normal is therefore

$$n_\mu = \frac{N_\mu}{\sqrt{N_\alpha N^\alpha}} = \frac{N_\mu}{\sqrt{g^{\alpha\beta}N_\beta N_\alpha}} = \frac{N_\mu}{\sqrt{1 + f'^2}}\, e^{\zeta - \nu}. \tag{2.6}$$

The extrinsic curvature tensor K is given in its covariant form by

$$K_{ab} = n_\mu(\partial_a h^\mu_b + \Gamma^\mu_{\alpha\beta} h^\alpha_a h^\beta_b), \tag{2.7}$$

where $\partial_a h^\mu_b = \partial h^\mu_b / \partial x^a$. Equations (2.6) and (2.3) together with the Christoffel symbols for the Weyl metric lead to the computation of K, the extrinsic curvature of that surface embedded in the WP metric:

$$K_{tt} = -\frac{e^{\nu-\zeta}}{\sqrt{1+f'^2}}\left(\frac{\partial \nu}{\partial N}\right) e^{4\nu-2\zeta}, \tag{2.8a}$$

$$K_{RR} = -\frac{e^{\nu-\zeta}}{\sqrt{1+f'^2}}\left(\frac{f''}{1+f'^2}+\frac{\partial(\nu-\zeta)}{\partial N}\right)(1+f'^2), \tag{2.8b}$$

$$K_{\phi t} = -\frac{e^{\nu-\zeta}}{\sqrt{1+f'^2}}\left\{\frac{\partial[\nu+\frac{1}{2}\log(\omega)]}{\partial N}\right\}\omega e^{4\nu-2\zeta}, \tag{2.8c}$$

$$K_{\phi\phi} = -\frac{e^{\nu-\zeta}}{\sqrt{1+f'^2}}\left\{\left(\frac{f'}{R}+\frac{\partial \nu}{\partial N}\right)R^2 e^{-2\zeta} + e^{4\nu-2\zeta}\omega^2\frac{\partial[\nu-\log(\omega)]}{\partial N}\right\}, \tag{2.8d}$$

where the notation $\partial/\partial N \equiv (\partial/\partial z - f'\partial/\partial R)$ has been used.

2.2 The stress–energy tensor

The stress–energy tensor per unit surface τ^a_b is the integral of the stress–energy tensor carried along the normal to the surface $z=f(R)$. In a locally Minkowskian frame comoving with the mean flow of the disc, the corresponding orthonormal tetrad is

$$e^{(0)}_i = e^{\nu}(1, 0, -\omega), \tag{2.9a}$$

$$e^{(1)}_i = e^{\zeta-\nu}\sqrt{1+f'^2}\,(0, 1, 0), \tag{2.9b}$$

$$e^{(2)}_i = R e^{-\nu}(0, 0, 1), \tag{2.9c}$$

so that

$$ds^2 = \eta_{(a)(b)}(e^{(a)}_i\, dx^i)(e^{(b)}_j\, dx^j), \tag{2.10}$$

with $\eta_{(a)(b)} = \mathrm{Diag}(-1, 1, 1)$. In that frame,

$$[\tau^{(a)(b)}]_0 = \begin{bmatrix} \varepsilon & 0 & 0 \\ 0 & p_R & 0 \\ 0 & 0 & p_\phi \end{bmatrix}. \tag{2.11}$$

After a Lorentz transformation to a more general frame in which the flow is rotating with relative velocity V in the ϕ direction, this stress becomes

$$\tau^{(a)(b)} = \frac{1}{1-V^2}\begin{bmatrix} \varepsilon+p_\phi V^2 & 0 & (p_\phi+\varepsilon)V \\ 0 & (1-V^2)p_R & 0 \\ (p_\phi+\varepsilon)V & 0 & p_\phi+\varepsilon V^2 \end{bmatrix}. \tag{2.12}$$

2.3 The discontinuity equations

Israel (1964) has shown that Einstein's equations integrated through a given surface of discontinuity can be rewritten in terms of the jump in extrinsic curvature, namely

$$\tau^a_b = \frac{1}{8\pi}[K^a_b - K^a_a\delta^a_b]^+_- \equiv \mathscr{L}^a_b, \tag{2.13}$$

where $[\,]^+_-$ stands for ( ) taken on $z=f(R)$ minus ( ) taken on $z=-f(R)$. This tensor $\mathscr{L}^a_b$ is known as the Lanczos tensor.

In the tetrad frame (2.9), the Lanczos tensor given by equations (2.13) and (2.8) reads

$$\mathscr{L}(a)(b) = \frac{e^{\nu-\zeta}}{4\pi\sqrt{1+f'^2}} \times \begin{bmatrix} \frac{f''}{1+f'^2}+\frac{f'}{R}+\frac{\partial(2\nu-\zeta)}{\partial N} & 0 & \frac{\partial\omega}{\partial N}\frac{e^{2\nu}}{2R} \\ 0 & -\frac{f'}{R} & 0 \\ \frac{\partial\omega}{\partial N}\frac{e^{2\nu}}{2R} & 0 & -\frac{f''}{1+f'^2}+\frac{\partial\zeta}{\partial N} \end{bmatrix}. \tag{2.14}$$

Identifying the stress–energy tensor $\tau^{(a)(b)}$ with the tetrad Lanczos tensor $\mathscr{L}^{(a)(b)}$ according to equation (2.13), and solving for p_R, p_ϕ, ε and V yields

$$V = \frac{R e^{-2\nu}}{\partial\omega/\partial N}\left[\left(\frac{f'}{R}+2\frac{\partial\nu}{\partial N}\right)-Q\right], \tag{2.15a}$$

$$\varepsilon = \frac{e^{\nu-\zeta}}{4\pi\sqrt{1+f'^2}}\left\{\frac{Q}{2}+\left[\frac{f''}{1+f'^2}+\frac{f'}{2R}+\frac{\partial(\nu-\zeta)}{\partial N}\right]\right\}, \tag{2.15b}$$

$$p_\phi = \frac{e^{\nu-\zeta}}{4\pi\sqrt{1+f'^2}}\left\{\frac{Q}{2}-\left[\frac{f''}{1+f'^2}+\frac{f'}{2R}+\frac{\partial(\nu-\zeta)}{\partial N}\right]\right\}, \tag{2.15c}$$

$$p_R = \frac{e^{\nu-\zeta}}{4\pi\sqrt{1+f'^2}}\left(\frac{-f'}{R}\right), \tag{2.15d}$$

where

$$Q \equiv \sqrt{\left(\frac{f'}{R}+2\frac{\partial\nu}{\partial N}\right)^2-\frac{e^{4\nu}}{R^2}\left(\frac{\partial\omega}{\partial N}\right)^2}. \tag{2.16}$$

All quantities are to be evaluated along $z=f(R)$. Equation (2.15) gives the form of the most general solution to the relativistic rotating thin disc problem, provided that the expressions for ε, p_ϕ, p_R are physically acceptable.

3 PHYSICAL PROPERTIES OF THE WARM DISCS

Physical properties of interest for these discs are derived and related to the choice of profile $z=f(R)$ compatible with their dynamical stability.

Defining the circumferential radius R_c, proper radial length $\tilde{R}$, and a synchronized proper time τ_* by

$$R_c = R e^{-\nu}, \tag{3.1a}$$

$$\tilde{R} = \int \sqrt{1+f'^2}\, e^{\zeta-\nu}\, dR, \tag{3.1b}$$

$$\tau_* = \int_{(\mathscr{T})} e^{\nu}\left(1-\omega\frac{d\phi}{dt}\right)dt, \tag{3.1c}$$

where the integral over dR is performed at $z=f(R)$ and that over dt is performed along a given trajectory $(\mathscr{T})$, the line element on the disc (2.4) reads

$$d\sigma^2 = -đ\,\tau_*^2 + d\tilde{R}^2 + R_c^2\,d\phi^2. \tag{3.2}$$

For circular flows $[đ\,\tau_* = e^{\nu}(1-\omega\,d\phi/dt)\,dt]$, V may be rewritten as

$$V = R_c\frac{d\phi}{đ\,\tau_*}. \tag{3.3}$$

Equation (3.3) is inverted to yield the angular velocity of the flow as measured at infinity:

$$\Omega \equiv \frac{d\phi}{dt} = \frac{Ve^{\nu}/R_c}{1+\omega Ve^{\nu}/R_c}. \tag{3.4}$$

Similarly, the covariant specific angular momentum h of a given particle reads in terms of these variables

$$h \equiv \frac{p_\phi}{\mu} = \gamma_{t\phi}u^t + \gamma_{\phi\phi}u^\phi = \frac{1}{\sqrt{1-V^2}}(R_cV+\omega e^{\nu}), \tag{3.5}$$

where μ is the rest mass of the particle. The covariant specific energy ϵ of the particle reads

$$\epsilon \equiv -\frac{p_t}{\mu} = -\gamma_{t\phi}u^\phi - \gamma_{tt}u^t = \frac{e^{\nu}}{\sqrt{1-V^2}}. \tag{3.6}$$

which gives the central redshift, $1+z_c = \exp(-\nu)$. The velocity of zero angular momentum observers (so-called ZAMOs) follows from equation (3.5):

$$V_z = -\frac{\omega e^{\nu}}{R_c}. \tag{3.7}$$

With these observers, the cuts $z=f(R)$ may be extended inside ergoregions where the dragging of inertial frames induces apparent superluminous motions as measured by locally static observers. The circumferential radius R_z as measured by ZAMOs is Lorentz-contracted with respect to R_c, becoming

$$R_z \equiv \sqrt{g_{\phi\phi}} = R_c(1-V_z^2)^{1/2}, \tag{3.8}$$

while the velocity flow measured by ZAMOs is

$$V_{/z} = \frac{V-V_z}{1-VV_z}. \tag{3.9}$$

The total angular momentum of the disc H follows from the asymptotic behaviour of the vacuum field ω at large radii, $\omega \to -2H/r$. Define the binding energy of the disc ΔE as the difference between the baryonic rest mass M_0 and the total mass–energy of the disc M as measured from infinity given by $\nu \to -M/r$:

$$\Delta E = M_0 - M. \tag{3.10}$$

M is also given by the Tolman formula, but corresponds, by construction, to the mass of the line source for the vacuum field. The baryonic rest mass can be expressed as

$$M_0 \equiv \int \Sigma\sqrt{-g}\,U^\mu\,dS_\mu = \int \frac{(1-\omega\Omega)^{-1}}{\sqrt{1-V^2}}\Sigma 2\pi R_c\,d\tilde{R}, \tag{3.11}$$

where the baryonic energy density Σ can be related to the energy density ε through some yet unspecified equation of state or the knowledge of a distribution function.

3.1 Constraints on the internal solutions

The choice of the profile $z=f(R)$ is open, provided that it leads to meaningful physical quantities. Indeed, it must lead to solutions which satisfy $\varepsilon \geq 0$, $p_R \geq 0$, $p_\phi \geq 0$ and $V \leq 1$, while the dominant energy condition implies also that $\varepsilon \geq p_\phi$ and $\varepsilon \geq p_R$. These translate into the following constraints on f:

$$\varepsilon \geq 0 \Rightarrow \sqrt{\mathscr{N}^2-\mathscr{O}^2} + (\mathscr{N}-2\mathscr{Z}) \geq 0, \tag{3.12a}$$

$$0 \leq V \leq 1 \Rightarrow \mathscr{N} \geq \mathscr{O} \quad \text{and} \quad \mathscr{O} \geq 0, \tag{3.12b}$$

$$0 \leq p_\phi \leq \varepsilon \Rightarrow 4\mathscr{Z}\mathscr{N} \geq (\mathscr{O}^2 + 4\mathscr{Z}^2) \quad \text{and} \quad \mathscr{N} \geq 2\mathscr{Z}, \tag{3.12c}$$

$$0 \leq p_R \leq \varepsilon \Rightarrow f' \leq 0 \quad \text{and} \quad -2f'/R \leq \sqrt{\mathscr{N}^2 - \mathscr{O}} + (\mathscr{N}-2\mathscr{Z}), \tag{3.12d}$$

given

$$\mathscr{N} \equiv \frac{f'}{R} + 2\frac{\partial\nu}{\partial N}, \quad \mathscr{O} \equiv \frac{e^{2\nu}}{R}\frac{\partial\omega}{\partial N} \quad \mathscr{Z} \equiv \left(\frac{\partial\zeta}{\partial N} - \frac{f''}{1+f'^2}\right). \tag{3.13}$$

The existence of a solution satisfying this set of constraints can be demonstrated as follows: in the limit of zero pressure and counter-rotation (i.e., $\mathscr{O}\to 0$, $\mathscr{N}\to 2\partial\nu/\partial z$, and $\mathscr{Z}\to\partial\zeta/\partial z$), any cut $z=\text{constant}\equiv b \gg m$ satisfies equations (3.12). By continuity, there exist solutions with proper rotation and partial pressure support. In practice, all solutions given in Sections 6 and 7 satisfy the constraints (3.12). Note that in the limit of zero radial pressure, equation (3.12b) implies $\partial/\partial z\,[\omega/R + \exp 2\nu] \leq 0$.

3.2 Ansatz for the profile

In the following discussion, the section $z=f(R)$ is chosen so that the corresponding radial pressure gradient balances a given fraction of the gravitational field which would have occurred had there been no radial pressure within the disc. This choice 'bootstraps' calculations for all relevant physical quantities in terms of a single degree of freedom (i.e., this fraction η), rather than a complete functional. This gives

$$\frac{\partial p_R}{\partial\tilde{R}} = -\frac{\eta}{(1-V^2)}\frac{\partial\nu}{\partial\tilde{R}}[\varepsilon + p_R + V^2(p_\phi - p_R)]. \tag{3.14}$$

On the right-hand side of equation (3.14), p_R is put to zero and V, p_ϕ, ε are re-expressed in terms of ζ, ν, ω via equations (2.15) with $f' = f'' = 0$ and $z=\text{constant}$. On the left-hand side of equation (3.14), p_R is chosen according to equation (2.15d). In practice, this Ansatz for f is a convenient way to investigate a parameter space which is likely to be stable with respect to ring formation, as discussed in the next subsection. In principle, a cut, f, could be chosen so as to provide a closed, bounded symmetrical surface containing all fictitious sources. Indeed, by symmetry no flux then crosses the $z=0$ plane beyond the cut, and the energy distribution is therefore bound to the edge of that surface: this corresponds to a finite pressure-supported disc. It turns out that in general this choice is not compatible with all the constraints enumerated in the previous section. More specifically, the positivity of p_ϕ fails for all finite disc models constructed. The Ansatz described above gives, for instance, an upper bound on the height of that surface when assuming that all the support is provided by radial pressure. This height is in turn not compatible with positive azimuthal pressure at all radii.

3.3 Stability

To what extent are the equilibria studied in the previous sections likely to be stable under the action of disturbances? The basic instabilities can be categorized as follows:

(1) dynamical instabilities, which are intrinsic to the dynamical parameters of the discs, grow on an orbital time-scale, and typically have drastic effects on the structure of the system, and

(2) secular instabilities, which arise owing to dissipative mechanisms such as viscosity or gravitational radiation, grow on a time-scale which depends on the strength of the dissipative mechanism involved, and slowly drive the system along a sequence of dynamical equilibria.

Amongst dynamical instabilities, kinematical instabilities correspond to the instability of circular orbits to small perturbations, and collective instabilities arise from the formation of growing waves triggered by the self-gravity of the disc. Rings, for instance, will be generated spontaneously in the disc if the local radial pressure is insufficient to counteract the self-gravity of small density enhancements. Even dynamically stable non-axisymmetric modes may drive the system away from its equilibrium by radiation of gravitational waves which will slowly remove angular momentum from the disc. For gaseous discs, viscosity and photon pressure will affect the equilibria. Radiative emission may disrupt or broaden the disc if the radiation pressure exceeds the Eddington limit. The energy loss by viscosity may induce a radial flow in the disc. However, the discs discussed in this paper have anisotropic pressures inappropriate for gaseous discs and the accurate description of the latter two processes requires some prescription for the dissipative processes in the gas. The scope of this section is therefore restricted to a simple analysis of the dynamical instabilities.

Turning briefly to the corresponding Newtonian problem, Toomre (1963) gave the local criterion for radial collective instability of stellar discs,

$$\sigma_R \geq \frac{3.36 G\Sigma_0}{\kappa}, \tag{3.15}$$

where Σ_0 is the local surface density, σ_R^2 is the radial velocity dispersion, and κ is the epicyclic frequency of the unperturbed stars. This criterion is derived from the first critical growing mode of the dispersion relation for radial waves. The corresponding critical wavelength is the Jeans length $\sim 2\sigma_R^2/G\Sigma_0$.

For the relativistic discs described in this paper, space–time is locally flat, which suggests a direct translation of equation (3.15) term by term. The constraints that stability against ring formation places on these models will then be addressed at least qualitatively via the Newtonian approach. The proper relativistic analysis is left to further investigation. The relativistic surface density generalizing Σ_0 is taken to be the comoving energy density ε given by equation (2.15b). The radial velocity dispersion σ_R^2 is approximated by p_R/ε. The epicyclic frequency is calculated in Appendix D. Putting equations (D4) and (D5) into equation (3.15), we obtain another constraint on f for local radial stability of these discs. Note that the kinematical stability of circular orbits follows from equation (D3) by requiring κ^2 to be positive.

4 STELLAR DYNAMICAL EQUILIBRIA FOR ROTATING SUPERMASSIVE DISCS

The method described in Section 2 will generally induce rotating discs with anisotropic pressures ($p_\phi \neq p_R$). These objects may therefore be described in the context of stellar dynamics. It should then be checked that there exist stellar equilibria compatible with a given vacuum field and a given cut $z=f(R)$.

4.1 Distribution functions for rotating supermassive discs

Here a general procedure to derive all distribution functions corresponding to a specified stress–energy tensor is presented for discs with non-zero mean rotation (a more direct derivation for counter-rotating discs is given in Appendix B). The detailed description of the dynamics of the disc follows.

In Vierbein components, the stress–energy tensor reads

$$T^{(\alpha\beta)} = \int\int \frac{f_\star(\epsilon, h) P^{(\alpha)} P^{(\beta)}}{P^{(t)}} \,\mathrm{d}P^{(R)}\,\mathrm{d}P^{(\phi)}, \tag{4.1}$$

where $f_\star(\epsilon, h)$ is the distribution of stars at position R, ϕ with momentum $P^{(R)}$, $P^{(\phi)}$. For a stationary disc, it is a function of the invariant of the motion, ϵ, h. Now for the line element (2.4)

$$\mathrm{d}\sigma^2 = -\mathrm{e}^{2\nu}(\mathrm{d}t - \omega\,\mathrm{d}\phi)^2 + \mathrm{e}^{2\zeta-2\nu}(1+f'^2)\,\mathrm{d}R^2 + R^2\mathrm{e}^{-2\nu}\,\mathrm{d}\phi^2, \tag{4.2}$$

the Vierbein momenta read

$$P^{(\phi)} = \mathrm{e}^{\nu} R^{-1}(h - \omega\epsilon), \tag{4.3a}$$

$$P^{(t)} = \mathrm{e}^{-\nu}\epsilon, \tag{4.3b}$$

$$P^{(R)} = [\epsilon^2\mathrm{e}^{-2\nu} - \mathrm{e}^{2\nu}R^{-2}(h-\omega\epsilon)^2 - 1]^{1/2}. \tag{4.3c}$$

Calling $\chi = h/\epsilon$ and $\vartheta = 1/\epsilon^2$, equations (4.3) become

$$P^{(\phi)}=\mathrm{e}^{\nu}R^{-1}\vartheta^{-1/2}(\chi-\omega), \tag{4.4a}$$

$$P^{(t)}=\mathrm{e}^{-\nu}\vartheta^{-1/2}, \tag{4.4b}$$

$$P^{(R)}=\vartheta^{-1/2}[\mathrm{e}^{-2\nu}-\mathrm{e}^{2\nu}R^{-2}(\chi-\omega)^2-\vartheta]^{1/2}. \tag{4.4c}$$

In terms of these new variables, the integral element $\mathrm{d}P^{(\phi)}\,\mathrm{d}P^{(R)}$ becomes

$$\mathrm{d}P^{(\phi)}\,\mathrm{d}P^{(R)}=\left|\frac{\partial P^{(\phi)}\,\partial P^{(R)}}{\partial\chi\,\partial\vartheta}\right|\mathrm{d}\chi\,\mathrm{d}\vartheta$$

$$=\frac{\mathrm{e}^{-\nu}R^{-1}\vartheta^{-2}\,\mathrm{d}\chi\,\mathrm{d}\vartheta}{2\sqrt{\mathrm{e}^{-2\nu}-\mathrm{e}^{2\nu}R^{-2}(\chi-\omega)^2-\vartheta}}\ . \tag{4.5}$$

Given equations (4.5) and (4.3b), equation (4.1) may be rewritten as

$$T^{(\alpha\beta)}=\int\!\!\int P^{(\alpha)}P^{(\beta)}\frac{f_\star(\epsilon,h)R^{-1}\vartheta^{-3/2}\,\mathrm{d}\chi\,\mathrm{d}\vartheta}{2\sqrt{\mathrm{e}^{-2\nu}-\mathrm{e}^{2\nu}R^{-2}(\chi-\omega)^2-\vartheta}}\ . \tag{4.6}$$

In particular,

$$RT^{(tt)}\mathrm{e}^{2\nu}=\int\!\!\int\frac{f_\star(\epsilon,h)\vartheta^{-5/2}\,\mathrm{d}\chi\,\mathrm{d}\vartheta}{2\sqrt{\mathrm{e}^{-2\nu}-\mathrm{e}^{2\nu}R^{-2}(\chi-\omega)^2-\vartheta}}\ , \tag{4.7a}$$

$$R^2T^{(t\phi)}=\int\!\!\int(\chi-\omega)\frac{f_\star(\epsilon,h)\vartheta^{-5/2}\,\mathrm{d}\chi\,\mathrm{d}\vartheta}{2\sqrt{\mathrm{e}^{-2\nu}-\mathrm{e}^{2\nu}R^{-2}(\chi-\omega)^2-\vartheta}}\ , \tag{4.7b}$$

$$R^3T^{(\phi\phi)}\mathrm{e}^{-2\nu}=\int\!\!\int(\chi-\omega)^2\frac{f_\star(\epsilon,h)\vartheta^{-5/2}\,\mathrm{d}\chi\,\mathrm{d}\vartheta}{2\sqrt{\mathrm{e}^{-2\nu}-\mathrm{e}^{2\nu}R^{-2}(\chi-\omega)^2-\vartheta}}\ . \tag{4.7c}$$

Note that given equations (4.7), $T^{(RR)}$ follows from the equation of radial support. Note also that

$$R_{\mathrm{c}}[T^{(tt)}-T^{(\phi\phi)}-T^{(RR)}]=\int\!\!\int\frac{f_\star(\epsilon,h)\mathrm{e}^{-\mu}\vartheta^{-3/2}\,\mathrm{d}\chi\,\mathrm{d}\vartheta}{2\sqrt{\mathrm{e}^{-2\nu}-\mathrm{e}^{2\nu}R^{-2}(\chi-\omega)^2-\vartheta}}\ . \tag{4.8}$$

or, equivalently,

$$T^{(tt)}-T^{(\phi\phi)}-T^{(RR)}=\int\!\!\int\frac{f_\star(\epsilon,h)}{P^{(t)}}\,\mathrm{d}P^{(\phi)}\,\mathrm{d}P^{(R)}. \tag{4.9}$$

Equation (4.9) yields the total gravitating mass. It is known as Tolman's formulae and can be derived directly from the relation $P^{\mu}P_{\mu}=-1$ and equation (4.1).

Let

$$F(\chi,R)=\frac{1}{2}\int\frac{f_\star(\epsilon,h)\vartheta^{-5/2}\,\mathrm{d}\vartheta}{\sqrt{\mathrm{e}^{-2\nu}-\mathrm{e}^{2\nu}R^{-2}(\chi-\omega)^2-\vartheta}}$$

$$=\int_1^{\mathscr{Y}}\frac{f_\star(\chi,\vartheta)\,\mathrm{d}\vartheta}{2\sqrt{\mathscr{Y}-\vartheta}}\ , \tag{4.10}$$

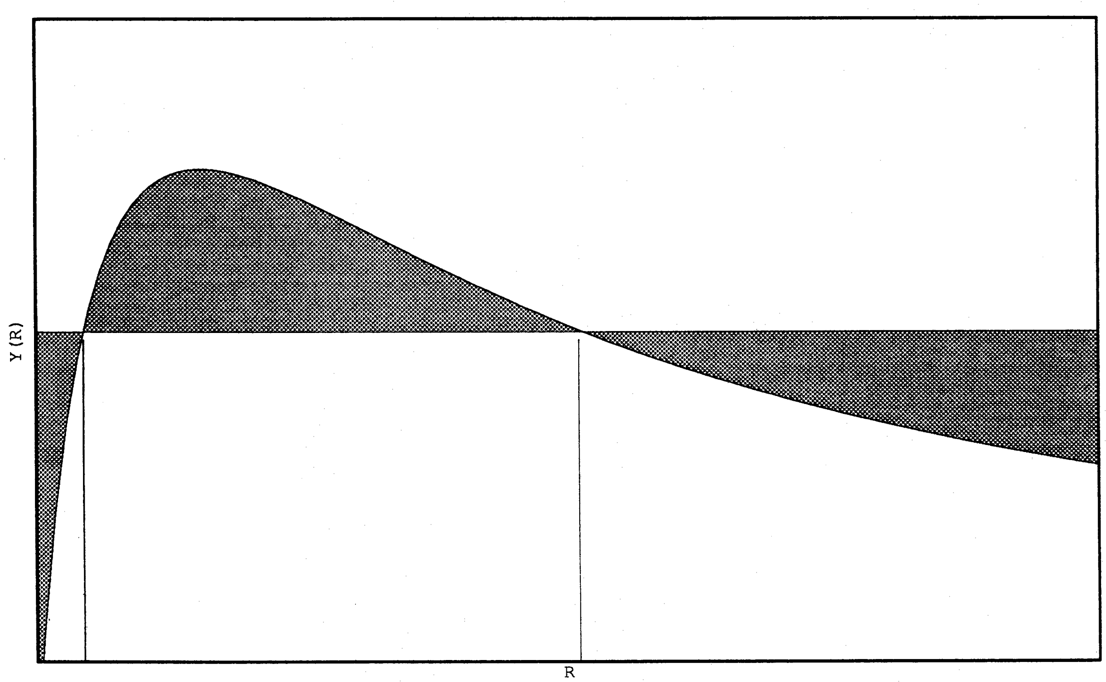

Figure 2. Sketch of the effective potential $Y(R)$ as a function of radius. The horizontal line corresponds to the energy level $1/\varepsilon^2$, the absissa line corresponds to the escape energy $1/\varepsilon^2=1$. The ordinate axis corresponds to $\mathscr{R}_{\mathrm{e}}(h,\varepsilon)$, the inner radius of a star on a 'parabolic' orbit with momentum h; the left vertical line corresponds to $\mathscr{R}_{\mathrm{p}}(h,\varepsilon)$, the perigee of a star with invariants (h,ε); the right vertical line corresponds to $\mathscr{R}_{\mathrm{a}}(h,\varepsilon)$, the apogee of a star with invariants (h,ε). The area between the curve $Y=Y(R)$ and the lines $Y=1/\varepsilon^2$ and $R=\mathscr{R}_{\mathrm{e}}$ is shaded, defining three regions from left to right. The middle region does not contribute to equation (4.14). The equation $Y=1/\varepsilon^2$ has two roots corresponding to $\mathscr{R}_{\mathrm{p}}(h,\varepsilon)$ and $\mathscr{R}_{\mathrm{a}}(h,\varepsilon)$, while $Y=1$ has two roots corresponding to infinity and $\mathscr{R}_{\mathrm{e}}$. The sign of the slope of $Y(R)$ gives the sign of the contribution for each branch in equation (4.14).

where

$$f_\star(\chi, \vartheta) = f_\star(\epsilon, h)\,\vartheta^{-5/2} \quad \text{and}$$
$$\mathscr{Y}(R, \chi) = \mathrm{e}^{-2\nu} - \mathrm{e}^{2\nu} R^{-2}(\chi - \omega)^2. \tag{4.11}$$

The set of equations (4.7) becomes

$$RT^{(tt)}\mathrm{e}^{2\nu} = \int F(\chi, R)\,\mathrm{d}\chi = R\mathrm{e}^{-2\nu}\int \bar{F}(v_\phi, R)\,\mathrm{d}v_\phi, \tag{4.12a}$$

$$R^2 T^{(t\phi)} = \int F(\chi, R)(\chi - \omega)\,\mathrm{d}\chi$$
$$= R^2\mathrm{e}^{-4\nu}\int v_\phi \bar{F}(v_\phi, R)\,\mathrm{d}v_\phi, \tag{4.12b}$$

$$R^3 T^{(\phi\phi)}\mathrm{e}^{-2\nu} = \int F(\chi, R)(\chi - \omega)^2\,\mathrm{d}\chi$$
$$= R^3\mathrm{e}^{-6\nu}\int v_\phi^2 \bar{F}(v_\phi, R)\,\mathrm{d}v_\phi, \tag{4.12c}$$

The right-hand side of equations (4.12) was re-expressed conveniently in terms of the new variable $v_\phi \equiv \mathrm{e}^{\nu}(\chi - \omega)/R_\mathrm{c}$ and the new function $\bar{F}(v_\phi, R) \equiv F(\chi = R_\mathrm{c} v_\phi \mathrm{e}^{-\nu} + \omega, R)$ in order to stress the analogy with the classical identities. Note that in the limit of zero pressures, v_ϕ reduces to V, the geodesic velocity of stars on circular orbits. In equation (4.12), the dragging of inertial frames requires to fix simultaneously three moments of the velocity distribution to account for the given energy density, pressures and rotation law. This third constraint does not hold in the corresponding Newtonian problem, nor for static relativistic discs as described in Appendix B. Any positive function $F(\chi, R)$ satisfying the moment constraints in equations (4.12) corresponds to a possible choice. For instance, the parametrization is carried in Appendix C for $\bar{F}$ distributions corresponding to powers of Lorentzians in azimuthal momenta. Let $\tilde{F}(\chi, \mathscr{Y}) = F(\chi, R)$, where $\mathscr{Y}(R, \chi)$ is given by equation (4.11). Written in terms of $\tilde{F}$, the integral equation (4.10) is solved for $f_\star$ by an Abel transform

$$f_\star(\chi, \vartheta) = \frac{2}{\pi}\int_1^{\vartheta}\left(\frac{\partial \tilde{F}}{\partial \mathscr{Y}}\right)_\chi \frac{\mathrm{d}\mathscr{Y}}{\sqrt{\vartheta - \mathscr{Y}}}. \tag{4.13}$$

The latter integration may be carried in R space and yields

$$f_\star(\epsilon, h) = \frac{2}{\epsilon^4\pi}\int_{\mathscr{R}_\mathrm{e}}^{\mathscr{R}_\mathrm{p}}\left(\frac{\partial F}{\partial R}\right)_\chi \frac{\mathrm{d}R}{\sqrt{-[P^{(R)}]^2}}$$
$$-\frac{2}{\epsilon^4\pi}\int_{\mathscr{R}_\mathrm{a}}^{\infty}\left(\frac{\partial F}{\partial R}\right)_\chi \frac{\mathrm{d}R}{\sqrt{-[P^{(R)}]^2}}, \tag{4.14}$$

where $P^{(R)}$ is given by equation (4.3c) as a function of R, ϵ and h. Here F is chosen to satisfy equation (4.12) which specifies the stress–energy components $T^{(\alpha\beta)}$. The integration limits correspond to two branches: the first branch is to be carried between $\mathscr{R}_\mathrm{e}(h)$, the inner radius of a star on a 'parabolic' orbit with momentum h, and $\mathscr{R}_\mathrm{p}(h, \epsilon)$, the perigee of a star with invariants (h, ϵ); the second branch contributes negatively to equation (4.14) and corresponds to radii larger than $\mathscr{R}_\mathrm{a}(h, \epsilon)$, the apogee of a star with invariants (h, ϵ) as illustrated in Fig. 2. Note that the derivative in equation (4.14) is taken at constant reduced momentum

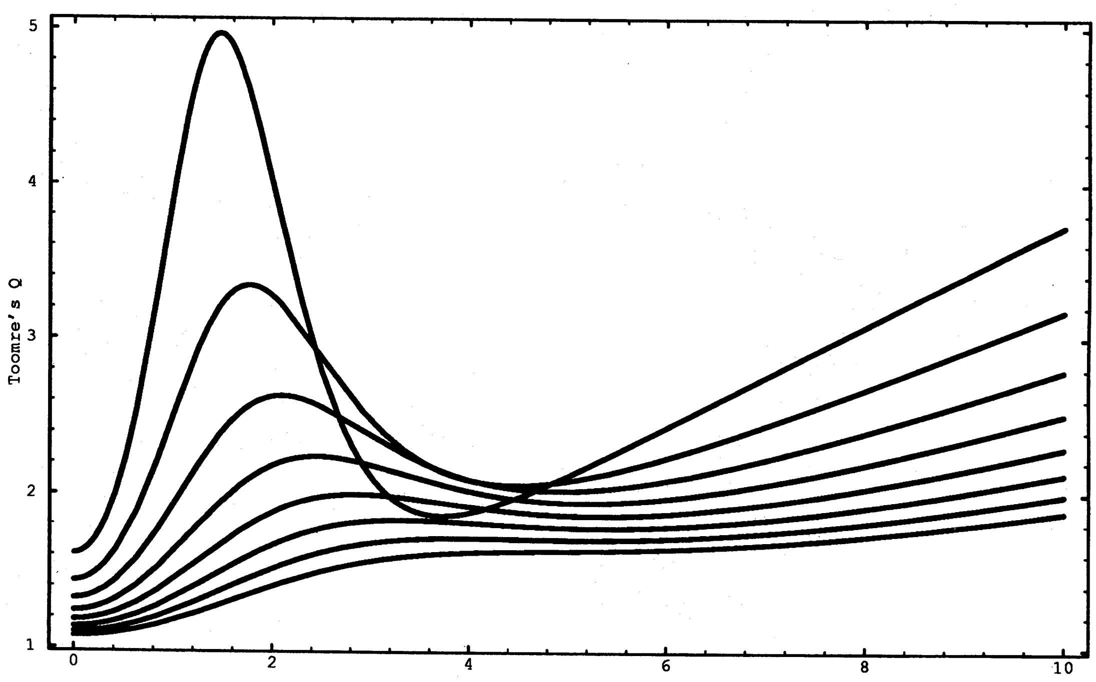

Figure 3. The 'Toomre Q number' $Q = \sigma_\mathrm{R}\kappa/(3.36\Sigma_0)$, is plotted here as a function of circumferential radius R_c for different compactness parameter $\alpha = b/M$ when $\eta = 1/25$.

$\chi = h/\epsilon$. This inversion procedure is illustrated in Fig. 9. All properties of the flow follow in turn from $f_\star(\epsilon, h)$. For instance, the rest-mass surface density, Σ, may be evaluated from the detailed 'microscopic' behaviour of the stars, leading to an estimate of the binding energy of the stellar cluster.

4.2 A simple equation of state

An equation of state for these rotating discs with planar anisotropic pressure tensors may alternatively be found directly by assuming (somewhat arbitrarily) that the fluid corresponds to the superposition of two isotropic flows going in opposite directions. In other words, the anistropy of the pressures measured in the frame comoving with the mean flow V is itself induced by the counter-rotation of two isotropic streams. (These counter-rotating streams are described in more detail in the next section.) In each stream, it is assumed that the pressure is isotropic and that the energy is exchanged adiabatically between each volume element. The detailed derivation of the corresponding relationship between the surface density and the pressure of each stream is given in Appendix A. The above set of assumptions yields the following prescription for Σ:

$$\Sigma = \frac{\varepsilon - p_\phi - p_R + \sqrt{(\varepsilon - p_\phi - p_R)(\varepsilon - p_\phi + 3p_R)}}{2\sqrt{1 - V_0^2}}, \tag{4.15}$$

where $V_0 = \sqrt{(p_\phi - p_R)/(\varepsilon + p_R)}$ is the counter-rotating velocity measured in the frame comoving with V which induces $p_\phi \neq p_R$. In the classical limit, $\Sigma \to (\varepsilon - p_\phi)/\sqrt{1 - V_0^2}$. The binding energy of these rotating discs is computed from equation (4.15) together with equations (3.11) and (2.15).

5 APPLICATION: WARM COUNTER-ROTATING DISCS

For simplicity, warm counter-rotating solutions are presented first, avoiding the non-linearities induced by the dragging of inertial frames. These solutions generalize those of BLK, while implementing partial pressure support within the disc. Formally, this is achieved by putting $\omega(R, z)$ identically to zero in equation (4.2); the metric for the axisymmetric static vacuum solutions given by Weyl is then recovered:

$$ds^2 = -e^{2\nu}\,dt^2 + e^{2\zeta - 2\nu}(dR^2 + dz^2) + R^2 e^{-2\nu}\,d\phi^2, \tag{5.1}$$

where the functions $\zeta(R, z)$ and $\nu(R, z)$ are generally of the form (cf. equation 2.21 in BLK)

$$\nu = -\int \frac{W(b)\,db}{\sqrt{R^2 + (|z| + b)^2}}, \tag{5.2a}$$

$$\zeta = \int\int W(b_1)W(b_2)Z(b_1, b_2)\,db_1\,db_2, \tag{5.2b}$$

with Z given by

$$Z = -\frac{1}{2r_1 r_2}\left[1 - \left(\frac{r_2 - r_1}{b_2 - b_1}\right)^2\right] \geq 0. \tag{5.3}$$

Here b_1 and b_2 are the distances of two points below the disc's centre, and r_1 and r_2 are the distances measured from these points to a point above the disc. Below the disc, Z is given by reflection with respect to the plane $z = 0$. When the line density of fictitious sources is of the form $W(b) \propto b^{-m}$ (Kuzmin–Toomre), or $W(b) \propto \delta^{(m)}(b)$ (Kalnajs–Mestel),

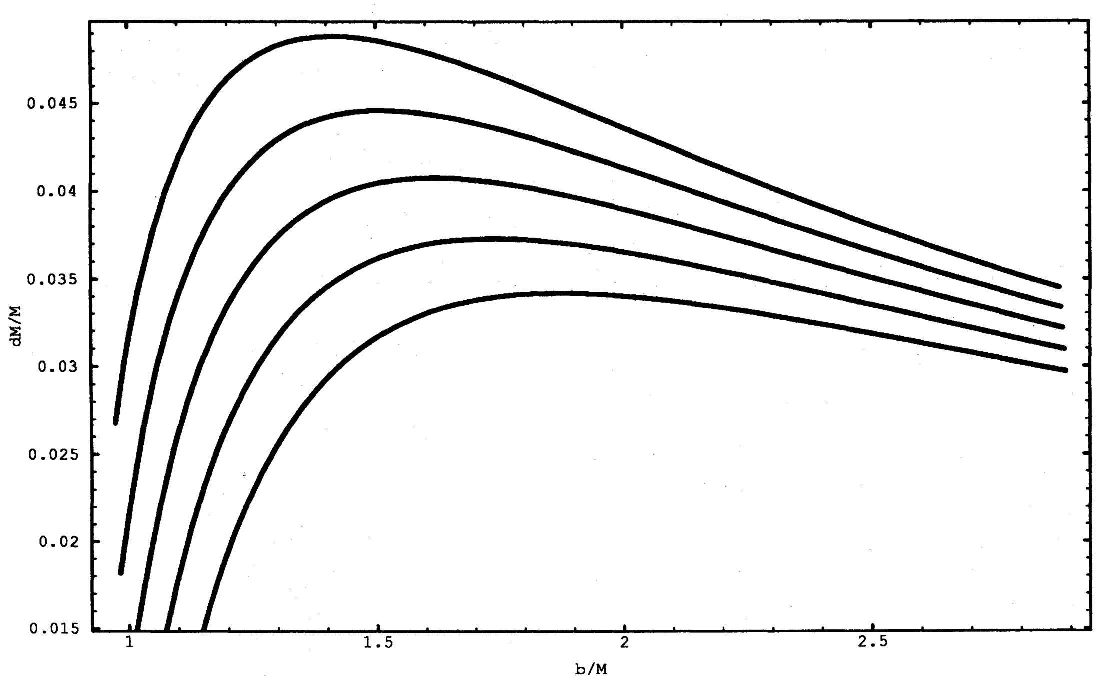

Figure 4. The binding energy over the rest mass $\Delta E/M_0$ for Curzon discs, plotted against the compactness parameter $\alpha = b/M$ for different ratios p_0/ε_0 fixed by $\eta = 0.01, 0.16, \ldots, 0.7$.

the corresponding functions ζ, ν have explicitly been given in Bìcák, Lynden-Bell & Pichon (1993). For the metric of equation (5.1), the Lanczos tensor (2.14) reads

$$\begin{bmatrix} \mathscr{L}^{(t)(t)} \\ \mathscr{L}^{(R)(R)} \\ \mathscr{L}^{(\phi)(\phi)} \end{bmatrix} = \frac{e^{\nu-\zeta}}{4\pi\sqrt{1+f'^2}} \begin{bmatrix} \dfrac{f''}{1+f'^2}+\dfrac{f'}{R}+\dfrac{\partial(2\nu-\zeta)}{\partial N} \\ \dfrac{-f'}{R} \\ \dfrac{-f''}{1+f'^2}+\dfrac{\partial\zeta}{\partial N} \end{bmatrix}. \tag{5.4}$$

Consider again counter-rotating discs made of two equal streams of stars circulating in opposite directions around the disc centre. The stress–energy tensor is then the sum of the stress–energy tensor of each stream:

$$\tau^{(a)(b)} = \begin{bmatrix} \varepsilon & 0 & 0 \\ 0 & p_R & 0 \\ 0 & 0 & p_\phi \end{bmatrix} = \frac{2}{1-V_0^2}$$

$$\times \begin{bmatrix} \varepsilon_0 + p_0 V_0^2 & 0 & 0 \\ 0 & (1-V_0^2)p_0 & 0 \\ 0 & 0 & p_0+\varepsilon_0 V_0^2 \end{bmatrix}, \tag{5.5}$$

the pressure p_0 in each stream being chosen to be isotropic in the plane. Subscript $(\,)_0$ represents quantities measured for one stream. Expressions for ε, p_ϕ and p_R follow from identifying equations (5.5) and (5.4) according to equation (2.13). Solving for ε_0, V_0, and p_0 in equation (5.5), given equations (5.4) and (2.13), we obtain

$$\varepsilon_0 = \frac{e^{\nu-\zeta}}{4\pi\sqrt{1+f'^2}}\left[\frac{f''}{1+f'^2}+\frac{\partial(\nu-\zeta)}{\partial N}\right], \tag{5.6a}$$

$$p_0 = \frac{e^{\nu-\zeta}}{8\pi\sqrt{1+f'^2}}\left[\frac{-f'}{R}\right], \tag{5.6b}$$

$$V_0^2 = \left(\frac{\partial\zeta}{\partial N}-\frac{f''}{1+f'^2}+\frac{f'}{R}\right)\left[\frac{f''}{1+f'^2}+\frac{\partial(2\nu-\zeta)}{\partial N}\right]^{-1}. \tag{5.6c}$$

The above solution provides the most general counter-rotating disc model with pressure support. Indeed, any physical static disc will be characterized entirely by its vacuum field ν and its radial pressure profile p_R, which in turn defines $W(b)$ and $f(R)$ uniquely according to equations (5.6) and (BLK 2.33). The other properties of the disc are then readily derived.

The angular frequency and angular momentum of these discs follow from equations (3.5) and (3.4) on putting ω to zero and V to V_0. The epicyclic frequency κ given by equation (D4) may be recast as

$$\kappa^2 = \frac{e^\nu}{R_c^3}\frac{dh^2}{d\tilde{R}}, \tag{5.7}$$

which relates closely to the classical expression $\kappa^2 = R^{-3}\, dh^2/dR$.

The Ansatz given by equation (3.14) for $z=f(R)$ becomes, after the substitutions $\varepsilon \to \varepsilon_0$, $V \to V_0$ and $p_\phi \to 0$,

$$(f'/R') = -\eta\frac{\partial\nu}{\partial R}\left(\frac{\partial\nu}{\partial z}-\frac{1}{2}\frac{\partial\zeta}{\partial z}\right), \tag{5.8a}$$

$$= \eta\frac{\partial\nu}{\partial R}\frac{\partial\nu}{\partial z}\left(R\frac{\partial\nu}{\partial R}-1\right), \tag{5.8b}$$

where z is to be evaluated at b. Equation (5.8b) follows from equation (5.8a), given the $\binom{R}{z}$ component of the Einstein equation outside the disc.

The equation of state for a relativistic isentropic 2D flow of counter-rotating identical particles is derived in Appendix A by relating the perfect-fluid stress–energy tensor of the flow to the most probable distribution function which maximizes the Boltzmann entropy. It reads

$$\varepsilon_0 = 2p_0 + \frac{\Sigma}{1+p_0/\Sigma}. \tag{5.9}$$

Solving for Σ, we obtain

$$\Sigma = \frac{1}{2}\left(\varepsilon_0 - 2p_0 + \sqrt{\varepsilon_0 - 2p_0}\,\sqrt{\varepsilon_0+2p_0}\right). \tag{5.10}$$

which in the classical limit gives $\Sigma \to \varepsilon_0 - p_0$. The binding energy of these counter-rotating discs is computed here from equation (5.10), together with equations (3.11) and (5.6). Alternatively, it could be computed by constructing distribution functions using the inversion described in Appendix B.

6 EXAMPLES OF WARM COUNTER-ROTATING DISCS

6.1 Example 1: the self-similar disc

The symmetry of the self-similar disc allows one to reduce the partial differential equations corresponding to Einstein's field equations to an ordinary differential equation with respect to the only free parameter $\theta = \arctan(R/z)$ (Lemos 1989). Lemos's solution may be recovered and corrected by the method presented in Sections 2 and 4. Weyl's metric in spherical polar coordinates (ρ, χ, ϕ), defined in terms of (R, z, ϕ), by $\rho = \sqrt{(R^2+z^2)}$ and $\cot(\chi) = z/R$, is

$$d\sigma^2 = -e^{2\nu}\,d\tau^2 + \rho^2\left[e^{-2\nu}\sin^2(\chi)\,d\phi^2 + e^{2\zeta-2\nu}\left(\frac{d\rho^2}{\rho^2}+d\chi^2\right)\right]. \tag{6.1}$$

A self-similarity argument led Lemos to the metric

$$ds^2 = -r^{2n}e^N\,dt^2 + r^{2k}\left[e^{2P-N}\,d\phi^2 + e^{Z-N}\left(\frac{dr^2}{r^2}+d\theta^2\right)\right], \tag{6.2}$$

where P, N, and Z are given by

$$P(\theta)=\log[\sin(k+n)\theta], \tag{6.3a}$$

$$N(\theta)=\frac{4n}{k+n}\log[\cos(k+n)\theta/2], \tag{6.3b}$$

$$Z(\theta)=\frac{8n^2}{(k+n)^2}\log[\cos(k+n)\theta/2]+2\log(k+n). \tag{6.3c}$$

Here the ϕs in both metrics have already been identified, since they should in both cases vary uniformly in the range $[0, 2\pi[$. The rest of the identification between the two metrics follows from the transformation

$$\chi=(n+k)\theta, \tag{6.4a}$$

$$\rho=r^{n+k}, \tag{6.4b}$$

$$\tau=t, \tag{6.4c}$$

with the result that ν and ζ take the form

$$2\nu=N+2n\log(t), \tag{6.5a}$$

$$2\zeta=Z-2\log(n+k). \tag{6.5b}$$

This can be written in terms of the new variables given in equations (6.4) as

$$\zeta=\frac{4n^2}{(k+n)^2}\log\left(\frac{\chi}{2}\right), \tag{6.6a}$$

$$\nu=\frac{2n}{(k+n)^2}\log\left(\frac{\chi}{2}\right)+\frac{n}{k+n}\log(\rho). \tag{6.6b}$$

The procedure described earlier may now be applied. In order to preserve the self-similarity of the solution and match Lemos's solution, $f(R)$ is chosen so that

$$f'(R)=\text{constant}=\cot(\bar{\eta}),\ \text{say.} \tag{6.7}$$

Then

$$\frac{\partial}{\partial N}\equiv\left(\frac{\partial}{\partial z}-f'\frac{\partial}{\partial R}\right)=-\frac{1}{\rho\sin(\bar{\eta})}\frac{\partial}{\partial\bar{\eta}}. \tag{6.8}$$

Putting equations (6.6) and (6.8) into equation (2.15) gives

$$\begin{bmatrix}\varepsilon\\ p_R\\ p_\phi\end{bmatrix}=\frac{r^{-k}}{4\pi}\left[\cos\left(\frac{\bar{\eta}}{2}\right)\right]^{\frac{2n(k-n)}{(k+n)^2}}\times\begin{bmatrix}\cot(\bar{\eta})+\dfrac{2nk}{(k+n)^2}\tan(\eta/2)\\ -\cot(\bar{\eta})\\ \dfrac{2n^2}{(k+n)^2}\tan(\bar{\eta}/2)\end{bmatrix}, \tag{6.9}$$

with $\bar{\eta}$ to be evaluated at $(n+k)\pi/2$. The above equations are in accordance with the solution found by Lemos by directly integrating the Einstein field equations.

6.2 Example 2: the Curzon disc

The Curzon (1924) disc is characterized by the following pair of Weyl functions:

$$\nu=-\alpha/r,\qquad \zeta=-\alpha^2R^2/(2r^4), \tag{6.10}$$

with $r=\sqrt{R^2+f^2}$, given the dimensionless parameter $\alpha=M/b$ (recall that $G\equiv c\equiv 1$), all lengths being expressed in units of b. This disc is the simplest example of the Kuzmin–Toomre family, where $W(b)\propto\delta(b)$. It also corresponds to the building block of the expansion given in equations (5.2). Equations (5.4) and (5.5) then imply

$$\begin{bmatrix}\varepsilon\\ p_R\\ p_\phi\end{bmatrix}=\exp\frac{\left[-\dfrac{\alpha}{r}\left(1-\dfrac{\alpha R^2}{2r^3}\right)\right]}{4\pi b\sqrt{1+f'^2}}\times$$

$$\begin{bmatrix}\dfrac{f''}{1+f'^2}+\dfrac{f'}{R}+\dfrac{\alpha}{r^6}\{2f(r^3-\alpha R^2)+[\alpha(R^2-f^2)-2r^3]Rf'\}\\ \dfrac{-f'}{R}\\ -\dfrac{f''}{1+f'^2}+\dfrac{\alpha^2}{r^6}[2R^2f-(R^2-f^2)Rf'\}\end{bmatrix}. \tag{6.11}$$

The weak energy conditions $\varepsilon\geq 0$, $\varepsilon+p_R\geq 0$, and $\varepsilon+p_\phi\geq 0$ which follow are in agreement with those found by Chamorow et al. (1987). Their solution was derived by direct integration of Einstein's static equations using the harmonic properties of the supplementary unknown needed to avoid the patch of Weyl metric above and below the disc. The cut $z=f(R)$ corresponds to the imaginary part of the complex analytic function, the existence of which follows from the harmonicity of that new function.

The Ansatz (3.14) leads here to the cut

$$f(R)-b+\frac{\eta}{2}\left[\frac{bm^2}{4(b^2+R^2)}-\frac{2bm^3(4b^2+7R^2)}{105(b^2+R^2)^{5/2}}\right]. \tag{6.12}$$

In Fig. 3, the ratio of the binding energy of these Curzon discs [which is derived from equations (3.11), (5.10), (6.11) and (6.12)] over the corresponding rest mass M_0 is plotted with respect to the compactness parameter b/M_0 for different ratios p_0/ε_0 measured at the origin. The relative binding energy decreases in the most compact configurations because these contain too many unstable orbits ($\kappa^2<0$). A maximum ratio of about 5 per cent is reached Fig. 3 gives the 'Toomre Q number' for these discs as described in Section 3.3.

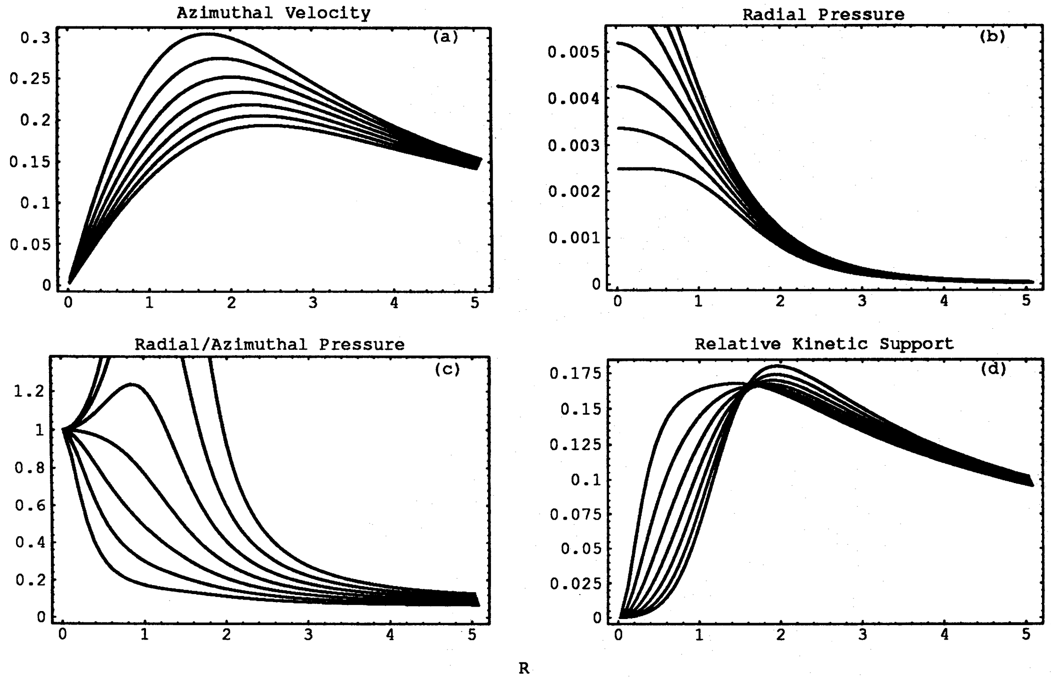

Figure 5. The azimuthal velocity (a), the radial pressure (b), the ratio of radial over azimuthal pressure (c) and the relative fraction of kinetic support (d), namely $\varepsilon V^2/(\varepsilon V^2+p_\phi+p_R)$ for the $a/m=0.5$ Kerr disc as a function of circumferential radius R_c, for a class of solutions with decreasing potential compactness, $b/m=1.1, 1.2, \ldots, 1.7$, and relative radial pressure support $\eta/m=1/5+2(b/m-1)/5$.

7 EXAMPLES OF ROTATING DISCS AND AN INTERNAL SOLUTION FOR THE KERR METRIC

The problem of constructing discs with proper rotation and partial pressure support is more complicated but physically more appealing than that of counter-rotating solutions. It is now illustrated on an internal solution for the Kerr metric, and a generalization of the solutions constructed by BLK and BLP to *warm rotating* solutions is sketched.

7.1 A Kerr internal solution

The functions (ν, ζ, ω) for the Kerr metric in WP form, expressed in terms of spheroidal coordinates $(R=s\sqrt{(x^2\mp 1)(1-y^1)}, z=sxy)$, are given by

$$e^{2\nu}=\frac{-m^2+s^2x^2+a^2y^2}{(m+sx)^2+a^2y^2}, \tag{7.1}$$

$$e^{2\zeta}=\frac{-m^2+s^2x^2+a^2y^2}{s^2(x^2\mp y^2)}, \tag{7.2}$$

and

$$\omega=-\frac{2am(m+sx)(1-y^2)}{-m^2+s^2x^2+a^2y^2}, \tag{7.3}$$

where $s=[\pm(m^2-a^2)]^{1/2}$. Here, $\pm$ corresponds to the choice of prolate $(+)$ or oblate $(-)$ spheroidal coordinates, corresponding to the cases $a<m$ and $a>m$ respectively. In this set of coordinates, the prescription given in Section 2 leads to completely algebraic solutions. The normal derivative to the surface $z=f(R)$ reads (when $a>m$)

$$(\partial/\partial N)=N(x,y)(\partial/\partial x)+N(y,x)(\partial/\partial y), \tag{7.4}$$

where

$$N(x,y)=(x^2-1)[y/s+x(y^2-1)f'/R]/(x^2-y^2).$$

Differentiation of equations (7.1) to (7.3) with respect to x and y, together with equation (7.4), leads via equations (2.15) to all physical characteristics of the Kerr disc in terms of the Kerr metric parameters m and a, and the function $z=f(R)$ which must be chosen so as to provide relevant pressures and energy distributions according to equations (3.12). (Bičák & Ledvinka 1993 have constructed independently a cold Kerr solution when $a<m$). On the axis $R=0$, $f\equiv b$, and $f''\equiv -c$, while equations (3.12) imply $f'=0$ at $(x=b/s, y=1)$. This in turn implies

$$(p_\phi)_0=(p_R)_0=\frac{c}{4\pi}\sqrt{\frac{a^2+b^2-m^2}{a^2+(b+m)^2}}, \tag{7.5a}$$

$$(\varepsilon)_0=\frac{1}{4\pi}\sqrt{\frac{a^2+b^2-m^2}{a^2+(b+m)^2}} \times\left\{\frac{2m[(b+m)^2-a^2]}{[a^2+(b+m)^2](a^2+b^2-m^2)}-c\right\}, \tag{7.5b}$$

where $(\,)_0$ stands for $(\,)$ taken at $R=0$. The constraint that all physical quantities should remain positive implies

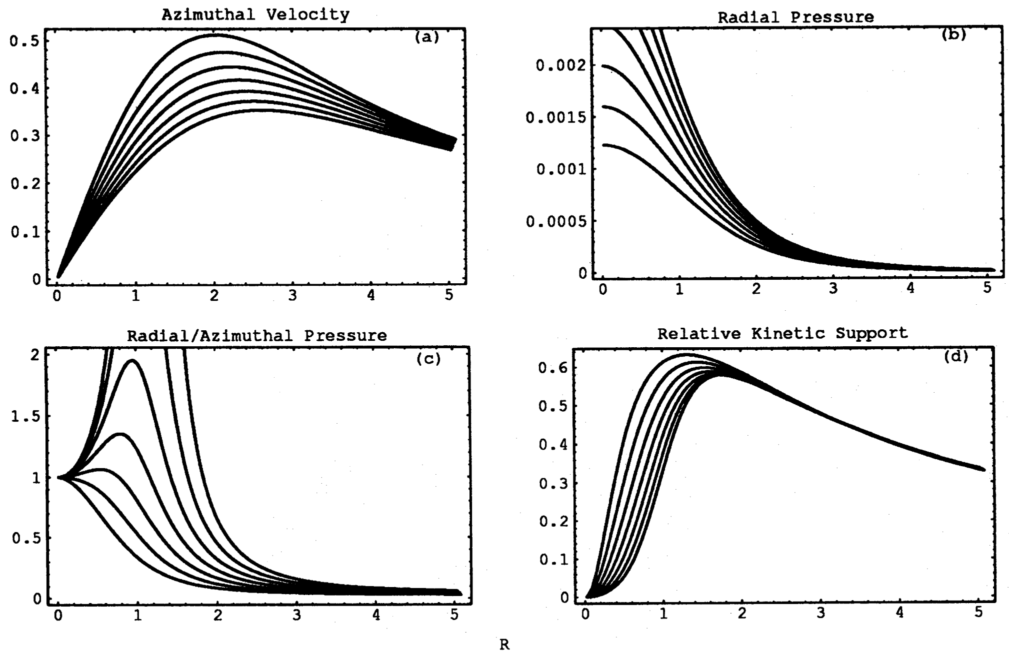

Figure 6. As in Fig. 5 with $a/m=0.95$, $\eta/m=1/15+(b-1)/5$. Note the large relative kinetic support.

$$b \geq \sqrt{m^2-a^2}, \tag{7.6a}$$

$$c \leq 2m \frac{(b+m)^2-a^2}{[a^2+(b+m)^2](a^2+b^2-m^2)}. \tag{7.6b}$$

Equation (7.6a) is the obvious requirement that the surface of the section should not enter the horizon of the fictitous source. Similarly, ergoregions will arise when the cut $z=f(R)$ enters the torus

$$\left(\frac{z}{m}\right)^2+\left(\frac{R}{m}-\frac{a}{m}+\frac{1}{2}\frac{m}{a}\right)^2=\left(\frac{1}{2}\frac{m}{a}\right)^2. \tag{7.7}$$

The analysis may be extended beyond the ergoregion via the ZAMO frame. The characteristics of these frames are given by equations (3.7), (3.8) and (3.9). The central redshift,

$$1+z_c=e^{-\nu}=\frac{(m+b)^2+a^2}{b^2+a^2-m^2}, \tag{7.8}$$

can be made very large for such models constructed when $b \rightarrow \sqrt{m^2-a^2}$. In Figs 5–7, some characteristics of these Kerr discs with both $a>m$ and $a<m$ are illustrated. For simplicity, pressure is implemented via the cut (6.12). These discs present anisotropy of the planar pressure tensor ($p_\phi \neq p_R$). The anisotropy follows from the properties of the ω vacuum field which gives rise to the circular velocity curve. Indeed, in the outer part of the disc, the specific angular momentum h tends asymptotically to a constant. The corresponding centrifugal force is therefore insufficient to counter-balance the field generated by the ν function. As this construction scheme generates such equilibria, the system compensates by increasing its azimuthal pressure away from isotropy. When $a>m$ and $\eta=0$, the height of the critical cut corresponding to the last disc with positive pressures everywhere scales like $a(a^2-m^2)^{1/2}$ in the range $2 \leq a/m \leq 20$. Note that this limit is above that of the highly relativistic motions which only occurs when b tends asymptotically to the Kerr horizon $(a^2-m^2)^{1/2}$. The binding energy which follows equation (4.15) reaches values as high as one-tenth of the rest mass for the most compact configurations. The inversion method described in Section 4.1 was carried for the Kerr discs and yields distribution functions which characterize completely the equilibria, as illustrated in Fig. 9. It was assumed that the velocity distribution of stars at radius R was a modified squared Lorentzian, as discussed in Appendix C and shown on Fig. 8. Note that discs with low rotation support present in their outer parts two distinct maxima, one of which is counter-rotating, in agreement with the assumptions yielding the equation of state, equation (4.15).

7.2 Other rotating solutions

The rotating disc models given in Section 2 require prior knowledge of the corresponding vacuum solutions. While studying the symmetry group of the stationary axially symmetric Einstein–Maxwell equations, HKX and Hoenselaers & Dietz (1984) found a method of generating systematically complete families of stationary WP vacuum metrics from known static Weyl solutions. Besides, the decomposition of the Weyl potential ν_0 into line densities provides a direct and compact method of finding solutions to the static field. The $N+1$ rank-zero HKX transform is defined as follows: let ν_0 and ζ_0 be the seed Weyl functions given by equations (5.2). HKX define the $N \times N$ matrix $\mathbf{\Gamma}$ parametrized by N twist parameters α_k and N poles, a_k, $k=1, \ldots, N$ as

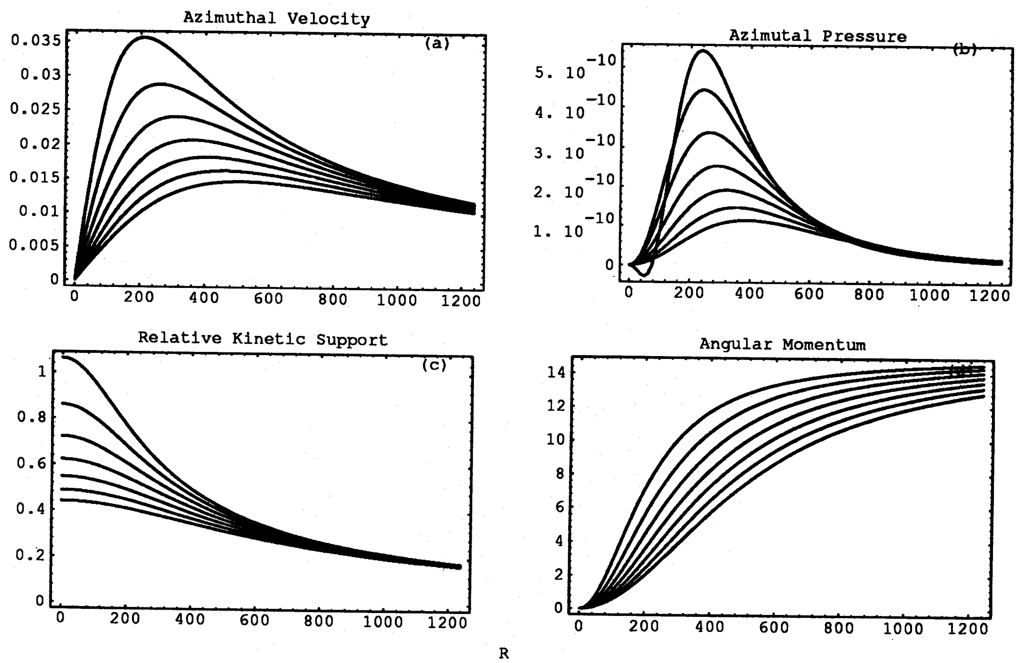

Figure 7. The azimuthal velocity (a), the azimuthal pressure (b), the relative fraction of kinetic support (c), namely $\varepsilon V^2/(\varepsilon V^2 + p_\phi)$ and the angular momentum (d) for the $a/m = 10$ zero radial pressure Kerr disc as a function of circumferential radius R_c, for a class of solutions with decreasing potential compactness $b/m = 210, 260, \ldots, 510$. The first curve corresponds to a cut which induces negative azimuthal pressure (tensions).

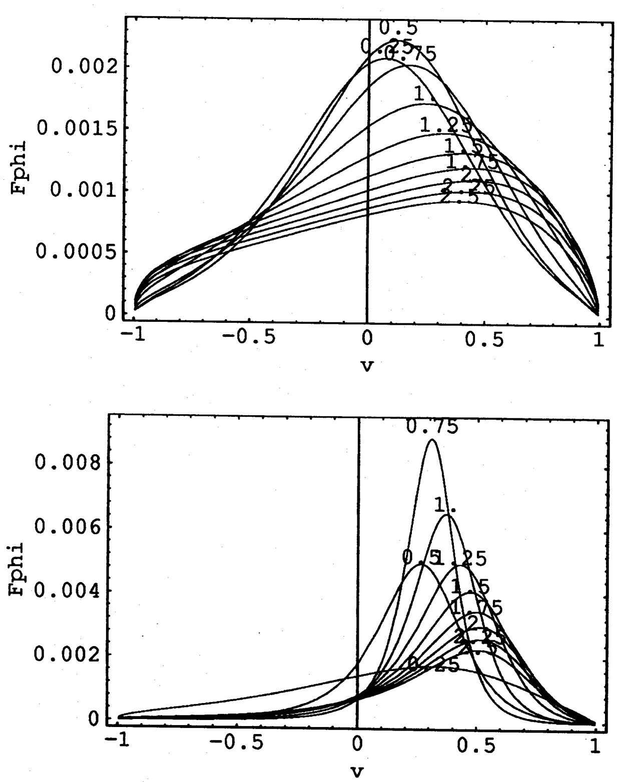

Figure 8. Parametrization of the number of stars with velocity v_ϕ at radius R as a squared Lorentzian (as discussed in Appendix C) for the Kerr disc. The corresponding radius is appended on each curve. The top panel correspond to $a = 0.2$, while the bottom panel corresponds to $a = 0.8$. The pressure law is given in the caption of Fig. 9, where the corresponding distribution function is illustrated.

$$(\Gamma^{\pm})_{k,k'} = \mathrm{i}\alpha_k \frac{e^{\beta_k}}{r_k}\left(\frac{r_k - r_{k'}}{a_k - a_{k'}} \pm 1\right), \tag{7.9}$$

with $r_k = r(a_k) = \sqrt{R^2 + (z - a_k)^2}$ and $\beta_k = \beta(a_k)$, β being a function satisfying equation (7.11a) below. Defining $\mathbf{r} = \mathrm{Diag}\,(r_k)$, they introduce the auxiliary functions

$D^{\pm} = |\mathbf{1} + \mathbf{\Gamma}^{\pm}|$, and $L_{\pm} = 2D^{\pm}\,\mathrm{tr}\,[(\mathbf{1} + \mathbf{\Gamma}^{\pm})^{-1}\mathbf{\Gamma}^{\pm}\mathbf{r}]$,

$\omega_{\pm} = D^{+} \pm e^{2\nu_0} D^{-}$, and $\mathcal{M}_{\pm} = \varpi\omega_{\pm} + 2(L_{+} \mp e^{2\nu_0} L_{-})$,

which lead to the WP potentials

$$e^{2\nu} = e^{2\nu_0}\mathcal{R}\left[\frac{D^{-}}{D^{+}}\right], \tag{7.10a}$$

$$e^{2\zeta} = k e^{2\zeta_0}\mathcal{R}[D^{-}D^{+*}], \tag{7.10b}$$

$$\omega = 2\mathcal{I}\left[\frac{\mathcal{M}^{*}_{+}(\omega_{+} + \omega_{-}) - \mathcal{M}_{-}(\omega_{+} + \omega_{-})^{*}}{|\omega_{+}|^2 - |\omega_{-}|^2}\right], \tag{7.10c}$$

where $\mathcal{R}$ and $\mathcal{I}$ stand respectively for the real part and the imaginary part of the argument, and ( )* represents the complex conjugate of ( ). Here k is a constant of integration which is fixed by the boundary conditions at infinity. The two as yet unspecified functions β and ϖ satisfy

$$\nabla\beta(a_k) = \frac{1}{r_k}[(z - a_k)\nabla + R\boldsymbol{e}_{\phi} \times \nabla]\,v_0, \tag{7.11a}$$

$$\nabla\varpi = R\boldsymbol{e}_{\phi} \times \nabla v_0, \tag{7.11b}$$

where $\nabla = (\partial/\partial R,\ \partial/\partial z)$ and $\boldsymbol{e}_{\phi}$ is the unit vector in the ϕ direction. The linearity of these equations suggests again that solutions should be sought in terms of the line density, $W(b)$, characterizing v_0, namely

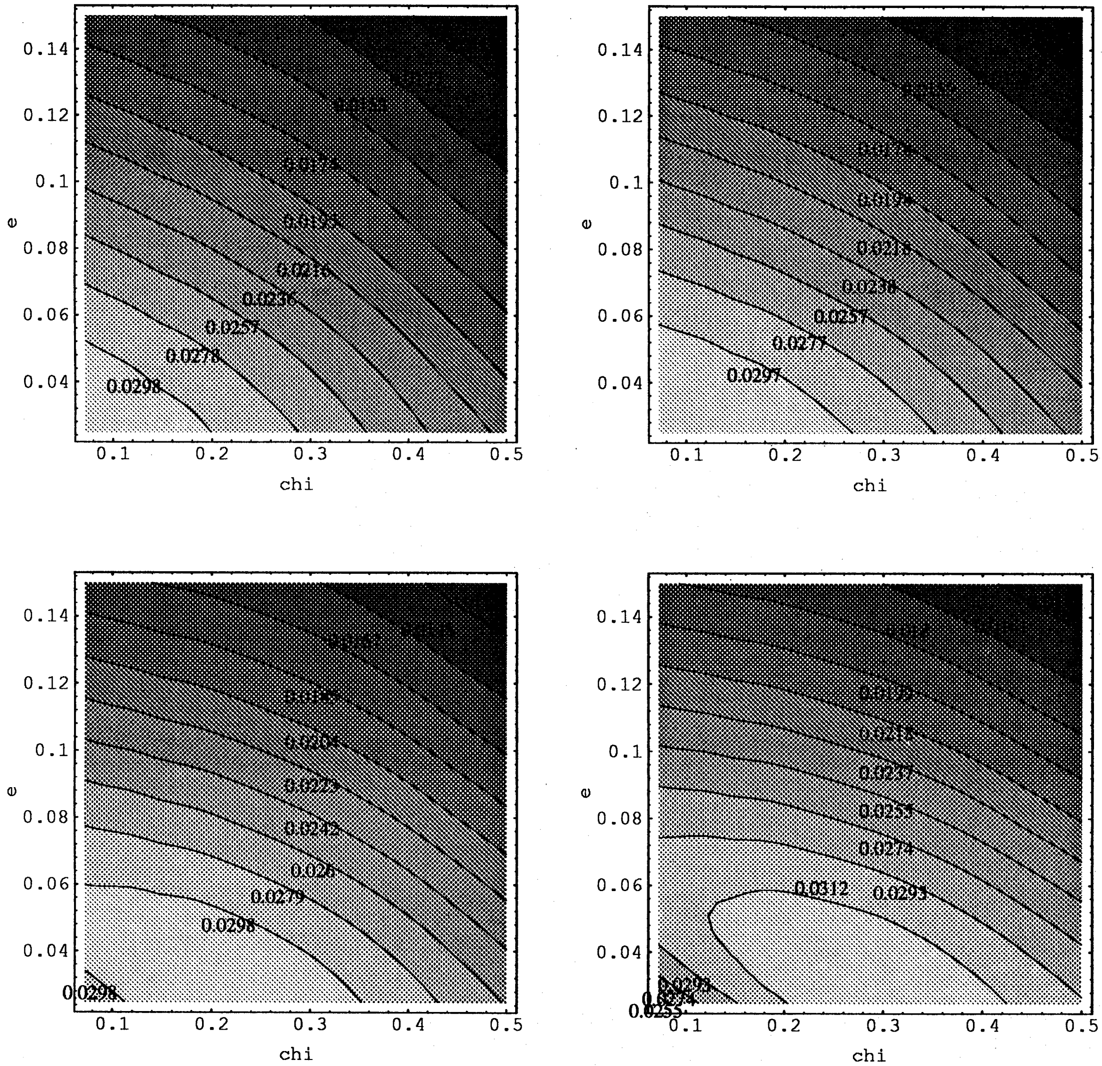

Figure 9. The isocontours of the distribution function for the Kerr disc as a function of the reduced momentum $\chi = h/\varepsilon$, and the relative eccentricity of the orbit $\bar{e}_c = (\varepsilon - \varepsilon_\chi)/(1-\varepsilon_\chi)$ where ε_χ is the energy of circular orbits with reduced momentum χ. The four panels correspond to $a = 0, 0.1, 0.2, 0.3, 0.4$ from left to right and top to bottom, while the pressure law was chosen to correspond to the cut $f(R) = -4(4+7R^2)/[525(1+R^2)^{5/2}] + (16+15R^2)/[10(1+R^2)]$ corresponding to a tepid disc. The figures are centred on the inner parts of the disc to illustrate the relative shift of the maximum number of stars towards larger angular momentum for faster rotating discs. The inversion assumed a squared Lorentzian for the distribution in angular velocity, as discussed in Appendix C and illustrated in Fig. 8.

$W(b)$, characterizing ν_0, namely

$$\beta(a_k) = \int \frac{W(b)}{a_k}\left[\frac{R^2 + (z-b-a_k)^2}{R^2+(z-b)^2}\right]^{1/2} \mathrm{d}b, \tag{7.12a}$$

$$\varpi = \int \frac{W(b)\,(b-z)}{\sqrt{R^2+(z-b)^2}}\,\mathrm{d}b. \tag{7.12b}$$

It is therefore a matter of algebraic substitution to apply the above procedure and construct all non-linear stationary vacuum fields of the Papapetrou form from static Weyl fields. Following the prescription described in Section 2, the corresponding disc in real rotation is then constructed. The requirement for the physical source to be a disc is in effect a less stringent condition on the regularity of the vacuum metric in the neighbourhood of its singularity, because only the half-space which does not contain these singularities is physically meaningful. A suitable Ehlers transformation on D_-/D_+ ensures asymptotic flatness at large distance from the source.

To illustrate this prescription, consider the vacuum field given by Yamazaki (1981). This field arises from 2 HKX rank-zero transformation on the Zipoy–Voorhess static metric (Voorhess 1970) given by

$$\nu_0 = \tfrac{1}{2}\delta \log\frac{(x-1)}{(x+1)}, \tag{7.13a}$$

$$\zeta_0 = \tfrac{1}{2}\delta^2 \log\frac{(x-1)}{(x^2-y^2)}, \tag{7.13b}$$

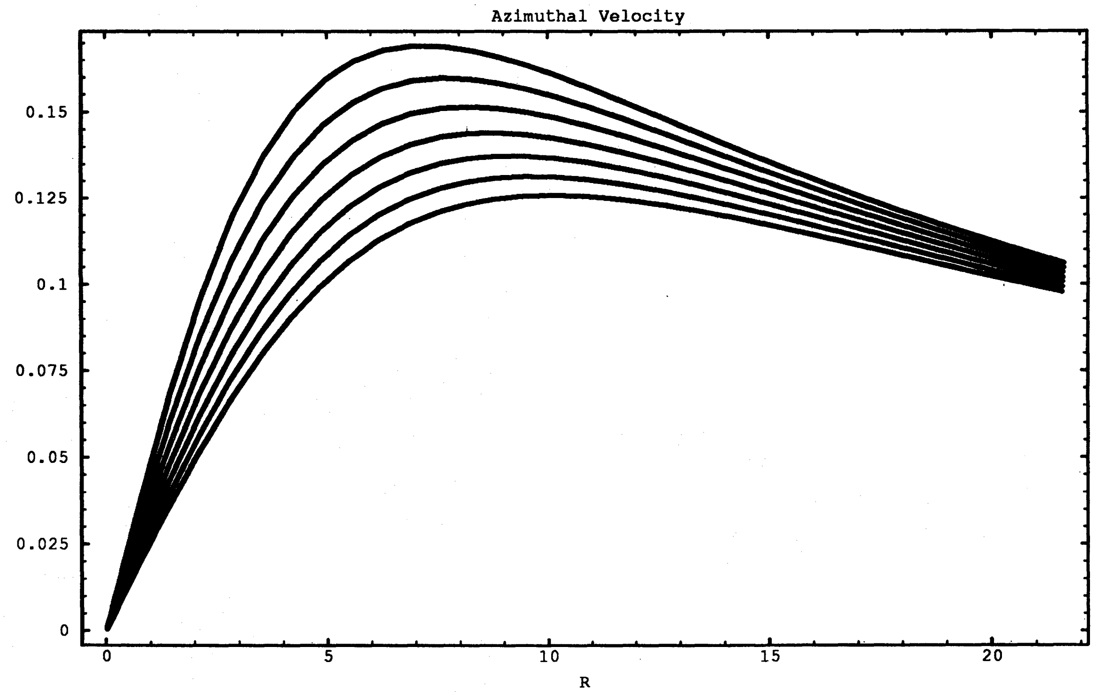

Figure 10. The azimuthal velocity for the a/κ_Y zero radial pressure Yamazaki disc as a function of circumferential radius R_c, for a class of solutions with decreasing potential compactness $b/\kappa_Y = 3.6, 3.8, \ldots, 5$. κ_Y is the natural unit of distance in these discs, as defined by Yamazaki's equation (Y-2) (Yamazaki 1981).

in prolate spheroidal coordinates. It corresponds to a uniform line density between $\pm\delta$. The functions β and ϖ follow from equations (7.12). Choosing poles a_k, $k=1, 2$ at the end of the rod $\pm\delta$, leads to

$$\beta(a_\pm) = \tfrac{1}{2}\delta \log \frac{x^2-1}{(x\mp y)^2}, \tag{7.14a}$$

$$\varpi = 2\delta y. \tag{7.14b}$$

Equations (7.10), together with equations (7.13) and (7.11), characterize completely the three WP metric functions ν, ζ and ω; all physical properties of the corresponding discs follow. For instance, Fig. 10 gives the zero radial pressure velocity curve of the Yamazaki disc spanning from the Schwarzschild ($\delta = 1/2$) metric when $\alpha_1 = \alpha_2$.

More generally, the extension of this work to the construction of discs with planar *isotropic* pressures should be possible by requiring that equation (2.15c) is identical to equation (2.15d), given equation (7.10).

8 CONCLUSION

The general counter-rotating disc with partial pressure support has been presented. The suggested method for implementing radial pressure support also applies to the construction of a stationary axisymmetric disc with rotation, but requires prior knowledge of the corresponding vacuum solution. In this manner, a disc-like source for the Kerr field has been constructed orbit by orbit. The corresponding distribution reduces to a Keplerian flow in the outer part of the disc and presents strong relativistic features in the inner regions such as azimuthal velocities close to that of light, large central redshift and ergoregions. The disc itself is likely to be stable against ring formation, and the ratio of its binding energy to rest mass can be as large as 1:10. The broad lines of how to construct all rotating discs arising from HKX-transforming the corresponding counter-rotating model into a fully self-consistent model with proper rotation and partial pressure support has been sketched. It should be a simple matter to implement this method with the additional requirement that the pressure remains isotropic with a sensible polytropic index. One could then analyse the fate of a sequence of gaseous discs of increasing compactness and relate it to the formation and evolution of quasars at high redshift. Alternatively, the inversion method described in Section 4.1 yields a consistent description of the detailed dynamics for all discs in terms of stellar dynamics.

REFERENCES

Bardeen J., 1970, ApJ, 162, 71
Bičák J., Ledvinka T., 1993, Phys. Rev. D, 71, 1669
Bičák J., Lynden-Bell D., Katz J., 1993, Phys. Rev. D, 47, 4334 (BLK)
Bičák J., Lynden-Bell D., Pichon C., 1993, MNRAS, 265, 126
Chamorow A. et al., 1977, Proc. R. Soc. Lond., 413, 251
Chandrasekhar, 1965, ApJ, 142, 1488
Curzon H., 1924, Proc. Lond. Math. Soc., 23, 477
Fackerell E., 1968, ApJ, 153, 643
Hoenselaers C., Dietz W., 1984, Gen. Relativ. Gravitation, 16, 71
Hoenselaers C., Kinnersley W., Xanthopoulos B., 1979, J. Math. Phys., 20, 2530 (HKX)

Ipser J., Thorne K., 1968, ApJ, 154, 251
Israel W., 1964, Nuovo Cimento, 33, 331
Katz J., Horwitz G., Klapish M., 1975, ApJ, 199, 307
Kerr R., 1963, Phys. Rev. Lett., 11, 237
Lemos J., 1989, Class. Q. Grav., 6, 1219
Levi-Civita T., 1919, Rend. Accad, Lincei, 28, 3
Misner C., Thorne K., Wheeler J., 1973, Gravitation. Freeman, p. 552
Morgan T., Morgan L., 1969, Phys. Rev., 183, 1097
Pichon C., Lynden-Bell D., 1996, MNRAS, in press
Synge J., 1957, The Relativistic Gas. North Holland
Tolman R., 1934, Relativity, Thermodynamics and Cosmology. Oxford Univ. Press, Oxford
Toomre A., 1964, ApJ, 139, 1217
Voorhess B., 1970, Phys. Rev. D, 2, 2119
Weyl H., 1917, Ann. Phys., 54, 117
Yamazaki M., 1981, J. Math. Phys., 22, 133

APPENDIX A: EQUATION OF STATE FOR A RELATIVISTIC 2D ADIABATIC FLOW

The equation of state of a planar adiabatic flow is constructed here by relating the perfect fluid stress–energy tensor of the flow to the most probable distribution function which maximizes the Boltzmann entropy. Synge (1957) gave an extensive derivation of the corresponding equation of state for a 3D flow. These properties are local characteristics of the flow. It is therefore assumed that all tensorial quantities introduced in this section are expressed in the local Vierbein frame.

Consider an infinitesimal volume element $\mathrm{d}\vartheta$ defined in the neighbourhood of a given event, and assume that the particles entering this volume element are subject to molecular chaos. The distribution function F of particles is defined so that $F(\boldsymbol{R}, \boldsymbol{P})\,\mathrm{d}\vartheta\,\mathrm{d}^2P$ gives the number of particles in the volume ϑ centred on $\boldsymbol{R}$ with 2-momentum pointing to $\boldsymbol{P}$ within d^2P.

The most probable distribution function $F^\star$ for these particles is then given by that which maximizes Boltzmann entropy S, subject to the constraints imposed by the conservation of the total energy momentum and by the conservation of the number of particles within that volume. This entropy reads in terms of the distribution $F^\star$

$$S=-\mathrm{d}\vartheta\int F^\star \log F^\star\,\mathrm{d}^2P. \tag{A1}$$

The stress–energy tensor corresponds to the instantaneous flux density of energy–momentum through the elementary volume $\mathrm{d}\vartheta$ (here a surface)

$$T^{ab}=\int F^\star P^\alpha P^\beta \frac{\mathrm{d}^2P}{|\mathscr{E}|}, \tag{A2}$$

where the $1/|\mathscr{E}|$ factor accounts for the integration over energy–momentum space to be restricted to the pseudo-sphere $P^\alpha P_\alpha=m^2$. Indeed, the detailed energy–momentum conservation requires the integration to be carried along the volume element

$$\int \delta(P^\alpha P_\alpha-m^2)\,\mathrm{d}^3P=\int \delta(P^{0^2}-\mathscr{E}^2)\,\mathrm{d}^2P\,\mathrm{d}P^0=\frac{\mathrm{d}^2P}{|\mathscr{E}|}, \tag{A3}$$

where $\mathscr{E}=\sqrt{m^2+\boldsymbol{P}^2}$. It is assumed here that momentum space is locally flat. Similarly, the numerical flux vector reads

$$\phi_\star^\alpha=\int F^\star P^\alpha \frac{\mathrm{d}^2P}{|\mathscr{E}|}. \tag{A4}$$

The conservation of energy–momentum of the volume element $\mathrm{d}\vartheta$ implies that the flux of energy–momentum across that volume should be conserved; this flux reads

$$T^{\alpha\beta}n_\beta\,\mathrm{d}\vartheta=\mathrm{d}\vartheta\int F^\star P^\alpha\,\mathrm{d}^2P=\text{constant}, \tag{A5}$$

where n_β is the unit time-axis vector. Keeping the population number constant provides the last constraint on the possible variations of S:

$$\phi_\star^\alpha n_\alpha\,\mathrm{d}^2P=\mathrm{d}\vartheta\int F^\star\,\mathrm{d}^2P=\text{constant}. \tag{A6}$$

Varying equation (A1) subject to the constraints (A5) and (A6), and putting δS to zero leads to

$$(\log F^\star+1)\,\delta F^\star=a\,\delta F^\star+\lambda_\alpha P^\alpha \delta F^\star, \tag{A7}$$

where a and λ_α are Lagrangian multipliers corresponding respectively to (A5) and (A6). These multipliers are independent of P^a but, in general, will be a function of position. The distribution which extremizes S therefore reads

$$F^\star=C\exp(\lambda_\alpha P^\alpha). \tag{A8}$$

The four constants $C=\exp(a)$ and λ_α, $\alpha=0,\ldots,2$ are, in principle, fixed by equations (A5) and (A6). The requirement for $F^\star$ to be Lorentz-invariant – that is, independent of the choice of normal n_α and self-consistent, is met instead by demanding that $F^\star$ obeys equations (A2) and (A4), namely

$$C\int P^\alpha \exp(\lambda_\mu P^\mu)\frac{\mathrm{d}^2P}{|\mathscr{E}|}=\phi_\star^\alpha, \tag{A9}$$

$$C\int P^\alpha P^\beta \exp(\lambda_\mu P^\mu)\frac{\mathrm{d}^2P}{|\mathscr{E}|}=T^{\alpha\beta}, \tag{A10}$$

where $\phi_\star^\alpha$ and $T^{\alpha\beta}$ satisfy in turn the covariant constraints

$$\frac{\partial T^{\alpha\beta}}{\partial x^\beta}=0 \tag{A11a}$$

and

$$\frac{\partial \phi_\star^\alpha}{\partial x^\alpha}=0. \tag{A11b}$$

Equations (A9)–(A11) provide a set of 13 equations to constraint the 13 functions C, λ_α, $\phi_\star^\alpha$, and $T^{\alpha\beta}$. Equations (A9) and (A10) may be rearranged as

$$\phi_\star^\alpha=C\frac{\partial\Phi}{\partial\lambda^\alpha},\qquad T^{\alpha\beta}=C\frac{\partial^2\Phi}{\partial\lambda^\alpha\partial\lambda^\beta}, \tag{A12}$$

where the auxiliary function Φ is defined as $\Phi=\int\exp(\lambda_\alpha P^\alpha)\,\mathrm{d}^2P/|\mathscr{E}|$; Φ is best evaluated using pseudopolar coordinates corresponding to the symmetry imposed by the energy-momentum conservation $P^\alpha P_\alpha - m^2 = 0$; these are

$$P^1 = m \sinh\chi \cos\phi,$$
$$P^2 = m \sinh\chi \sin\phi, \qquad \text{(A13)}$$
$$P^0 = im \cosh\chi,$$

where the coordinate χ is chosen so that the normal n_α lies along $\chi = 0$. In terms of these variables, $d^2P/|\mathscr{E}|$ then reads

$$d^2P/|\mathscr{E}| = dP^1\, dP^2/m \cosh\chi = m \sinh\chi\, d\chi\, d\phi. \qquad \text{(A14)}$$

Moving to a temporary frame in which λ^0 is the time axis ($\lambda^0 = i\lambda = i(-\lambda_\alpha\lambda^\alpha)^{1/2}$, $\lambda^k = 0$, $k = 1, 2$), Φ becomes

$$\Phi = 2\pi m \int_0^\infty \exp(-m\lambda\cosh\chi)\sinh\chi\, d\chi = \frac{2\pi}{\lambda}\exp(-\lambda). \qquad \text{(A15)}$$

From equations (A9), (A10) and (A15), it follows that

$$T^{\alpha\beta} = \frac{2\pi C}{\lambda^3}\exp(-\lambda)\left[(\lambda^2 + 3\lambda + 3)\frac{\lambda^\alpha}{\lambda}\frac{\lambda^\beta}{\lambda} + (\lambda+1)\,\delta^{\alpha\beta}\right], \qquad \text{(A16)}$$

$$\phi^\alpha_\star = \frac{2\pi C}{\lambda^3}\exp(-\lambda)(\lambda+1)\lambda^\alpha. \qquad \text{(A17)}$$

On the other hand, the stress–energy tensor of a perfect fluid is

$$T^{\alpha\beta} = (\varepsilon_0 + p_0)U^\alpha U^\beta + p_0\delta^{\alpha\beta}, \qquad \text{(A18)}$$

while the numerical surface density of particles measured in the rest frame of the fluid Σ is related to $\phi^\alpha_\star$ via

$$\Sigma = -\phi^\alpha_\star U_\alpha. \qquad \text{(A19)}$$

Equation (A16) has clearly the form of equation (A18) when identifying

$$U^\alpha = \lambda^\alpha/\lambda, \qquad \text{(A20a)}$$

$$\varepsilon_0 + p_0 = \frac{2\pi C}{\lambda^3}\exp(-\lambda)(\lambda^2 + 3\lambda + 3), \qquad \text{(A20b)}$$

$$p_0 = \frac{2\pi C}{\lambda^3}\exp(-\lambda)(\lambda+1). \qquad \text{(A20c)}$$

Eliminating λ, C between equations (A17)–(A20c) yields the sought-after equation of state:

$$\varepsilon_0 = 2p_0 + \frac{\Sigma}{1 + p_0/\Sigma}, \qquad \text{(A21)}$$

where $p_0 = \Sigma/\lambda$. This is the familiar gas law, given that $1/\lambda$ is the absolute temperature. The equation of state, equation (A21), corresponds by construction to an isentropic flow. Indeed, using the conservation equations (A11a) dotted with U^α, and equation (A11b) together with $U^\alpha U_\alpha = -1$ yields, after some algebra, to the identity

$$\lambda\frac{d}{ds}\left[\frac{(\lambda^2 + 3\lambda + 3)}{\lambda(\lambda+1)}\right] + \frac{1}{\lambda} = -\frac{\partial U^\alpha}{\partial x^\alpha} = \frac{1}{\Sigma}\frac{d\Sigma}{ds}, \qquad \text{(A22)}$$

where $d/ds = (dx^\alpha/dx^\alpha)(\partial/\partial x^\alpha)$ is the covariant derivative following the stream lines. Writing the right-hand side of equation (A22) as an exact covariant derivative leads to the first integral

$$\frac{d}{ds}\left[\frac{1}{1+\lambda} - 2\log(\lambda) + \log(1+\lambda) - \log(\Sigma)\right] = 0. \qquad \text{(A23)}$$

Given that $p_0 = \Sigma/\lambda$, it follows

$$\left(1 + \frac{p_0}{\Sigma}\right)\frac{p_0}{\Sigma}\exp\left(\frac{1}{1 + \Sigma/p_0}\right)\frac{1}{\Sigma} = \text{constant}, \qquad \text{(A24)}$$

which in the low-temperature limit gives $\Sigma^{-2}p_0 = \text{constant}$. This corresponds to the correct adiabatic index $\gamma = (2+2)/2$.

APPENDIX B: DISTRIBUTION FUNCTIONS FOR COUNTER-ROTATING RELATIVISTIC DISCS

For counter-rotating discs in the absence of gravomagnetic forces, the inversion for distribution functions given in Section 4.1 can be carried in close analogy to the Newtonian method given by Pichon & Lynden-Bell (1995), and is sketched here. The relativistic flow is characterized by its stress–energy tensor, $T^{(\alpha\beta)}$, which, in Vierbein components, reads

$$T^{(\alpha\beta)} = \int\!\!\int \frac{f_\star(\epsilon, h)P^{(\alpha)}P^{(\beta)}}{P^{(t)}}\, dP^{(R)}\, dP^{(\phi)}. \qquad \text{(B1)}$$

From the geodesic equation it follows that

$$P^\mu P_\mu = -1 \Rightarrow P^{(R)} = \frac{1}{\sqrt{\gamma_{tt}}}[\epsilon^2 - h^2\gamma_{tt}/\gamma_{\phi\phi} - g_{tt}]^{1/2}, \qquad \text{(B2)}$$

where the line element in the disc is taken to be

$$ds^2 = -\gamma_{tt}\, dt^2 + \gamma_{RR}\, dR^2 + \gamma_{\phi\phi}\, d\phi^2. \qquad \text{(B3)}$$

Differentiation of equation (B2) implies

$$\frac{dP^{(R)}}{P^{(t)}} = \frac{d\epsilon}{(\epsilon^2 - h^2\gamma_{tt}/\gamma_{\phi\phi} - \gamma_{tt})^{1/2}}, \quad \text{while } dP^{(\phi)} = \frac{dh}{\sqrt{\gamma_{\gamma\gamma}}}, \qquad \text{(B4)}$$

where the differentiation is done at constant R and h, and R and ϵ respectively. Combinations of equations (B1) lead to

$$\Lambda = \gamma_{\phi\phi}^{1/2}[T^{(tt)} - T^{(\phi\phi)} - T^{(RR)}]$$
$$= \int\!\!\int \frac{f_\star(\epsilon, h)\, dh\, d\epsilon}{\sqrt{\epsilon^2 - h^2\gamma_{tt}/\gamma_{\phi\phi} - \gamma_{tt}}}, \qquad \text{(B5a)}$$

$$\Delta = \gamma_{\phi\phi}^{3/2}T^{(\phi\phi)} = \int\!\!\int \frac{h^2 f_\star(\epsilon, h)\, dh\, d\epsilon}{\sqrt{\epsilon^2 - h^2\gamma_{tt}/\gamma_{\phi\phi} - \gamma_{tt}}}. \qquad \text{(B5b)}$$

Note that equation (B5a) corresponds to Tolman's formula (Tolman 1934), which yields by integration the total gravitating mass of the disc. Introducing

$$\mathscr{R}^2=\gamma_{\phi\phi}/\gamma_{tt}, \qquad e=\frac{1}{2}(\epsilon^2-1), \qquad \Psi=\frac{1}{2}(1-\gamma_{tt})$$

$$\text{and} \quad \hat{f}_\star(e,h)=\frac{f(\epsilon,h)}{\epsilon}, \tag{B6}$$

we obtain, for equations (B5):

$$\Lambda=\int\int\frac{\hat{f}_\star(e,h)\,\mathrm{d}h\,\mathrm{d}e}{[2(e+\psi)-h^2/\mathscr{R}^2]^{1/2}} \quad \text{and}$$

$$\Delta=\int\int\frac{h^2\hat{f}_\star(e,h)\,\mathrm{d}h\,\mathrm{d}e}{[2(e+\psi)-h^2/\mathscr{R}^2]^{1/2}}. \tag{B7}$$

Equation (B7) is formally identical to equation (2.9) of Pichon & Lynden-Bell (1996), replacing $(\Lambda, \Delta, \hat{f}_\star, \mathscr{R}, e, \Psi)$ by $(R\Sigma, R^3p_\phi, f, R, \epsilon, \psi)$. In fact, $(\Lambda, \Delta, \hat{f}_\star, \mathscr{R}, e, \Psi)$ tends to $(R\Sigma, R^3p_\phi, f, R, \epsilon, \psi)$ in the classical regime. Introducing the intermediate functions $\hat{F}(h,\mathscr{R})$, which is chosen so that its moments satisfy equations (B5), and following the classical prescription of Pichon & Lynden-Bell (1996), we obtain

$$\hat{f}(e,h)=\frac{1}{\pi}\int_{\mathscr{R}_c}^{\mathscr{R}_p}\frac{(\partial\hat{F}/\partial\mathscr{R})_h\,\mathrm{d}\mathscr{R}}{\sqrt{h^2/\mathscr{R}^2-2\Psi-2e}}$$

$$-\frac{1}{\pi}\int_{\mathscr{R}_a}^{\infty}\frac{(\partial\hat{F}/\partial\mathscr{R})_h\,\mathrm{d}\mathscr{R}}{\sqrt{h^2/\mathscr{R}^2-2\Psi-2e}}, \tag{B8}$$

where $\mathscr{R}_p(h,e)$, and $\mathscr{R}_a(h,e)$ are respectively the perigee and apogee of the star with invariants (h,e), and $\mathscr{R}_c(h)$ is the inner radius of a star on a 'parabolic' (zero e energy) orbit with momentum h. Equation (B8) provides direct and systematic means to construct families of distribution function for counter-rotating discs characterized by their stress–energy tensor in the plane. Note that, in contrast, the dragging of inertial frames required us to fix three moments of the velocity distribution to account for the given energy density pressure law and rotation law.

APPENDIX C: DISTRIBUTION FUNCTIONS FOR ROTATING DISCS: LORENTZIAN IN MOMENTUM

A possible choice for $\bar{F}$ is a Lorentzian parametrized in width, p_2, mean, p_1, and amplitude, p_0, such that

$$\bar{F}(v_\phi,R)\,\mathrm{d}v_\phi=\frac{p_0p_2\pi^{-1}\,\mathrm{d}p}{p_2^2+(p-p_1)^2},$$

$$\text{where } p=\frac{v_\phi}{\sqrt{1-v_\phi^2}} \quad \text{and} \quad v_\phi=\mathrm{e}^{\nu}(\chi-\omega)/R_c. \tag{C1}$$

The explicit function of v_ϕ is found using $\mathrm{d}p=\mathrm{d}v_\phi/(1-v_\phi^2)^{3/2}$. In this instance, equation (4.12) becomes

$$T^{(tt)}\mathrm{e}^{4\nu}=\frac{p_0p_2}{\pi}\int_{-\infty}^{\infty}\frac{\mathrm{d}p}{[p_2^2+(p-p_1)^2]}=p_0, \tag{C2a}$$

$$T^{(t\phi)}\mathrm{e}^{4\nu}=\frac{p_0p_2}{\pi}\int_{-\infty}^{\infty}\frac{p\,\mathrm{d}p}{\sqrt{1+p^2}[p_2^2+(p-p_1)^2]}$$

$$=\mathscr{G}(p_0,p_1,p_2), \tag{C2b}$$

$$T^{(\phi\phi)}\mathrm{e}^{4\nu}=\frac{p_0p_2}{\pi}\int_{-\infty}^{\infty}\frac{p^2\,\mathrm{d}p}{(1+p^2)^2[p_2^2+(p-p_1)^2]}$$

$$=\frac{p_0(p_2+p_2^2+p_1^2)}{(1+p_2)^2+p_1^2}, \tag{C2c}$$

where $\mathscr{G}(p_0,p_1,p_2)$ is given by equation (C4) below. The inversion of equations (C2) for (p_0,p_1,p_2), together with equations (C1), (4.14) and (4.3c), yields the distribution function of a Lorentzian flow compatible with the energy distribution imposed by the metric (ν,ζ,ω) and the cut $z=f(R)$. This inversion is always achievable provided the energy conditions equation (3.12) are satisfied.

More generally, families of distributions functions corresponding to azimuthal momentum distribution such as $2p_2^3p_0\pi^{-1}/[p_2^2+(p-p_1)^2]^2$, $8p_2^5p_0(3\pi)^{-1}/[p_2^2+(p-p_1)^2]^3\ldots$ are readily derived in a similar manner while differentiating the right-hand side of equation (C2) with respect to p_2^2. These higher order distributions all have vanishing numbers of stars with azimuthal velocity close to the velocity of light. This parametrization is illustrated for the Kerr disc in Fig. 9.

C1 The quadrature for $\mathscr{G}(p_0,p_1,p_2)$

Changing variables to u such that $p=(u-1/u)/2$, equation (C2b) becomes

$$\mathscr{G}(p_0,p_1,p_2)=\frac{2p_0p_2}{\pi}\int_0^{\infty}\frac{(u^2-1)\,\mathrm{d}u}{4p_2^2u^2+(u^2-1-2p_1u)^2} \tag{C3}$$

This integral is then carried and yields

$$\mathscr{G}(p_0,p_1,p_2)=$$

$$\frac{p_0(p_2+\mathrm{i}p_1)\log[-2\mathrm{i}p_2+2p_1-2\sqrt{1+(-\mathrm{i}p_2+p_1)^2}]}{2\sqrt{1+(-\mathrm{i}p_2+p_1)^2}\pi}$$

$$+\frac{p_0(\mathrm{i}p_2-p_1)\log[-2\mathrm{i}p_2+2p_1+2\sqrt{1+(-\mathrm{i}p_2+p_1)^2}]}{2\sqrt{1+(-\mathrm{i}p_2+p_1)^2}\pi}$$

$$+\frac{p_0(p_2-\mathrm{i}p_1)\log[2\mathrm{i}p_2+2p_1-2\sqrt{1+(\mathrm{i}p_2+p_1)^2}]}{2\sqrt{1+(\mathrm{i}p_2+p_1)^2}\pi}$$

$$+\frac{p_0(\mathrm{i}p_1-p_2)\log[2\mathrm{i}p_2+2p_1+2\sqrt{1+(\mathrm{i}p_2+p_1)^2}]}{2\sqrt{1+(\mathrm{i}p_2+p_1)^2}\pi} \tag{C4}$$

APPENDIX D: THE RELATIVISTIC EPICYCLIC FREQUENCY

The equation for the radial oscillations follows from the Lagrangian

$$\mathscr{L} = -\sqrt{e^{2\nu}(\dot{t}-\omega\dot{\phi})^2 - e^{2\zeta-2\nu}(1+f'^2)\dot{R}^2 - e^{-2\nu}\dot{\phi}^2R^2}, \quad \text{(D1)}$$

where $(\dot{\ })$ stands here for derivation with respect to the proper time τ for the star describing its orbit. In equation (D1), ϕ and t do not appear explicitly, which leads to the invariants

$$\frac{\partial \mathscr{L}}{\partial \dot{\phi}} = h, \qquad \frac{\partial \mathscr{L}}{\partial \dot{t}} = -\epsilon. \quad \text{(D2)}$$

The integral of the motion for the radial motion follows from equations (D2) and $U^\mu U_\mu = -1$, namely

$$e^{2\zeta-2\nu}(1+f'^2)\dot{R}^2 + \frac{e^{2\nu}}{R^2}(h-\epsilon\omega)^2 - \epsilon^2 e^{-2\nu} = -1.$$

This equation, together with its total derivative with respect to proper time, provides the radial equation of motion, having solved for the angular momentum h and the energy ϵ of circular orbits as a function of radius when equating both $\dot{R}$ and $\ddot{R}$ to zero. The relativistic generalization of the classical epicyclic frequency is defined here to be the frequency of the oscillator calling back linear departure from circular orbits. Hence the equation for radial perturbation reads

$$\delta\ddot{R} + \kappa^2 \delta R = 0, \quad \text{(D3)}$$

which gives for κ^2

$$\kappa^2 = e^{-2Z}(Z'' - 2Z'^2) - \epsilon^2 e^{-2L}(L'' - 2L'^2) - e^{2K}[(h-\epsilon\omega)^2(K'' + 2K'^2) - \epsilon(h-\epsilon\omega)(4K'\omega' + \omega'') + \epsilon^2\omega'^2], \quad \text{(D4)}$$

where $(\ )'$ stands in this appendix for $\mathrm{d}/\mathrm{d}R \equiv \partial/\partial R + f'\partial/\partial z$, and L, K, and Z are given in terms of the potential ζ and ν by

$$L = \zeta + \log\sqrt{1+f'^2}, \quad \text{(D5a)}$$

$$Z = \zeta + \log\sqrt{1+f'^2} - \nu, \quad \text{(D5b)}$$

$$K = 2\nu - \zeta - \log\sqrt{1+f'^2} - \log R. \quad \text{(D5c)}$$

Here ϵ and h are known functions of R, given by the roots of

$$\dot{R} = 0 \Rightarrow e^{-2L}\epsilon^2 = (h-\epsilon\omega)^2 e^{2N} + e^{-2Z}, \quad \text{(D6a)}$$

$$\ddot{R} = 0 \Rightarrow e^{-2Z}Z' = e^{-2L}L'\epsilon^2 + (h-\epsilon\omega)e^{2N}[(h-\epsilon\omega)N' - \epsilon\omega']. \quad \text{(D6b)}$$

APPENDIX E: CORRECTION TO LEMOS'S SELF-SIMILAR DISC

The result given in Section 6.1 agrees with that of Lemos (1989), having made the following agreed corrections to his solution.

(1) Equation (L3.14) should read: $(k+n)\cot\frac{1}{2}(k+n)\pi = -4\pi p_{*r}$ with a minus sign, because the integration of θ is carried downwards. This gives $n+k \geq 1$ for the discs with positive pressures.

(2) Lemos gives the stress–energy tensor integrated through the plane using coodinate increment rather than proper length. Our result gives the latter, which has an extra factor $\exp(\zeta-\nu)$ and gives the physical energy tensor per unit area.

(3) The exponent of $\cos[(n+k)\pi/2]$ is $2n(k-n)/(n+k)^2$ rather than $4n(1-2n)/(k+n)^2$.

Mon. Not. R. Astron. Soc. **000**, 000–000 (0000) Printed March 24, 2008 (MN LaTeX style file v2.2)

On the Onset of Stochasticity in ΛCDM Cosmological Simulations

J. Thiebaut[1], C. Pichon[1,2] , T. Sousbie[1], S. Prunet[1] & D. Pogosyan[3]
[1] *Institut d'astrophysique de Paris & UPMC (UMR 7095), 98, bis boulevard Arago , 75 014, Paris, France.*
[2] *Service d'Astrophysique, IRFU,(UMR) CEA-CNRS, L'orme des meurisiers, 91 470, Gif sur Yvette, France.*
[3] *Department of Physics, University of Alberta, 11322-89 Avenue, Edmonton, Alberta, T6G 2G7, Canada*

March 24, 2008

ABSTRACT
The onset of stochasticity is measured in ΛCDM cosmological simulations using a set of classical observables. It is quantified as the local derivative of the logarithm of the dispersion of a given observable (within a set of different simulations differing weakly through their initial realization), with respect to the cosmic growth factor. In an Eulerian framework, it is shown here that chaos appears at small scales, where dynamic is non-linear, while it vanishes at larger scales, allowing the computation of a critical transition scale corresponding to $\sim 3.5\mathrm{Mpc}/h$. This picture is confirmed by Lagrangian measurements which show that the distribution of substructures within clusters is partially sensitive to initial conditions, with a critical mass upper bound scaling roughly like the perturbation's amplitude to the power 0.15. The corresponding characteristic mass, $M_{\rm crit} = 2\,10^{13} M_\odot$, is roughly of the order of the critical mass of non linearities at $z = 1$ and accounts for the decoupling induced by the dark energy triggered acceleration.

The sensitivity to detailed initial conditions spills to some of the overall physical properties of the host halo (spin and velocity dispersion tensor orientation) while other "global" properties are quite robust and show no chaos (mass, spin parameter, connexity and center of mass position). This apparent discrepancy may reflect the fact that quantities which are integrals over particles rapidly average out details of difference in orbits, while the other observables are more sensitive to the detailed environment of forming halos and reflect the non-linear scale coupling characterizing the environments of halos.

Key words: Cosmology, Chaos, N-body, etc.

1 INTRODUCTION

Concerns regarding the predictability of cosmological measurements in simulations have been with us for some time. In the neighbouring field of secular galactic evolution, it has been known for a while (Sellwood and Wilkinson (1993)) that the significant undersampling of resonances could mislead the dynamical evolution of N-body systems when the evolution time becomes large compared to the local dynamical time. Over the course of the last decade, various "universal" relationships (Navarro et al. (1997), Zhang and Fall (1999), Richer et al. (1991)) have been extracted numerically from cosmological N-body simulations. In this context, significant efforts (Power et al. (2003)) have been invested in comparing different numerical schemes and codes, but, with the development of very high resolution "zoom" re-simulations (Weil et al. (1998), Diemand et al. (2004), Hansen and Moore (2006a) Sales et al. (2007), Strigari et al. (2007a)) one question remains: how sensitive is a given run with respect to its initial conditions? In particular, what set of observables is likely to be robust with respect to a specific choice in the "phases" of the draw (the whitened initial realization)? In the context of cosmology, the general assumption has been that, even though the detailed orbits of dark matter particles are likely to be poorly resolved by the numerical schemes implemented, the properties of structures would nevertheless be well represented *statistically*. In other words, so long as the simulated region was large enough to represent a fair sample of dynamically independent regions, the stochastic exponential departure from the unperturbed trajectories was expected to average out when considering such a statistical sample. The question remains for features specific to a given realization, such as the relative position of objects.

The sensitivity of the gravitational N-body problem to small changes in initial conditions has been investigated in details by Kandrup and collaborators in a series of papers (Kandrup and Smith (1991, 1992); Kandrup et al. (1992, 1994)) in the context of a Newtonian (time-independent) Hamiltonian. They have shown in particular that the growth of small perturbations in initial conditions is exponential, with a mean e-folding time that is asymptotically independent of the number of particles at large N, and a distribution of e-folding times that is reproducible from simulation to simulation for sufficiently large N. In the cosmological context, the N-body description is an approximation of the collisionless Boltzmann equation for the evolution of the dark matter, so that another related question is in which sense a limit to the continuum can be established as the number of particles increases. Indeed, it has been argued in the literature (Kandrup (1990); Goodman et al. (1993)) that the discretization of smooth, and possibly integrable potentials invariably leads to strongly chaotic orbits in the N-body framework, independently of the number of particles; this has been confirmed numerically (Kandrup and Sideris (2001); Sideris and Kandrup (2002)), both for integrable and non-integrable underlying distributions by evolving orbits in "frozen-N body" samplings of the smooth mass distributions. However, Kandrup and Sideris also showed that when one follows the deviation of orbits evolved in the frozen-N and smooth potentials with identical initial conditions, and when the deviation amplitude is allowed to reach large fractions of the system size (macroscopic view), a continuum limit can be well defined in the sense that these macroscopic departures from the orbits of the smooth potentials (which can be themselves either regular or chaotic) grow as a power law with time, and that the characteristic divergence time is growing with the number of particles. These results, together with the claim of universality (halo profiles (Navarro et al. (1997)), their shape (Hansen and Moore (2006b)), the mass functions (Zhang and Fall (1999), Richer et al. (1991))) that is widely used in the cosmology community, lead us to revisit the problem of the sensitivity of N-body simulations to slight changes in the initial conditions at fixed power spectrum in the cosmological context, and to numerically investigate the presence (or absence) of "chaotic" behaviour of different statistical quantities derived from N body simulations. Our focus will be on the transition between large scale linear dynamics and small scale stochastic properties (Strigari et al. (2007b)). A possible concern in this context is the development of stochasticity induced by the ill-conditioning/non-linearity of the estimator of the chosen set of observables. Another concern lies in the specificities of the numerical code used. Finally, numerical noise induced by round-off errors should also be kept at bay, since they by themselves will lead to some level of stochasticity. Since the topic of this paper is not optimal estimation, no attempt will be made to argue that the set of estimators used here is superior or offers a better trade-off in bias versus variance. Similarly, a standard integrator (Springel et al. (2001)) is used to carry the simulations with a set of conservative parameters. Round-off errors are assumed to be irrelevant. Specifically, this paper will investigate what scale and mass is expected to play a role and will identify which quantities are found to be robust with respect to such exponential divergence; it will also find out if stochasticity breaks in as soon as non linearities occur or if it is possible to identify two distinct time scales in the dynamics of large scale structures.

This paper is organized as follows: in Section 2 the method to characterize the statistical onset of stochasticity in numerical N-body simulations is presented. In Section 3 the corresponding Lyapunov exponents are computed for Eulerian quantities and (in Section 4) for Lagrangian ones. Section 5 discusses other issues and wraps up.

2 METHOD & SETTINGS

In this paper, we address the problem of the sensitivity of N-body simulations to initial conditions. To do so, we choose to study how slight changes in these initial conditions affect the evolution of the dispersion of a number of statistical quantities with time. This is achieved by generating several realizations of identical simulations where a small amount of random noise has been added to the initial realisation. The generic procedure goes as follows:

(i) Generate a cosmological simulation using $grafic$ (Bertschinger (1995)) and gadget (Springel et al. (2001)).

(ii) Start with the same noise file (i.e. the "phases"), but add a Gaussian white noise with RMS 1/30th of the previous white noise (except in Sections 3.2 and 4.4, where this amplitude is varied). This only affects the relative positions of clumps, not their spectral distribution (the expectation of the power spectrum remains unchanged).

(iii) Rerun the simulation with the new white noise;

(iv) Iterate the above two steps ~50 times;

(v) Compute a set of observables in each simulation;

(vi) Compute the RMS (or the relative RMS) of the distribution of observables for various expansion factors.

(vii) Fit the corresponding evolution of the $\log$ RMS vs the expansion factor.

(viii) Possibly find the scaling of its corresponding Lyapunov exponent (see below), with the smoothing scale associated with the observable (see Sec.3.2), or the corresponding mass (see Sec.4.4).

Let us define the "Lyapunov exponent", λ_X, as the rate of change of the logarithm of the fluctuation of the relevant quantity, X, as a function of the scale factor, a:

$$\lambda_X \equiv \frac{\mathrm{d}\ln\sigma_X}{\mathrm{d}a}\,. \tag{1}$$

This stochasticity parameter is not strictly speaking a Lyapunov exponent since it corresponds neither to an asymptotic limit at large time, nor to an asymptotic limit at small fluctuation. It is closer in spirit to the short time Lyapunov exponent defined by Kandrup et al. (1997).

In practice two distinct sets of simulations are considered in this paper, one composed of 65 realisations of 128^3 particles each (S_1 hereafter) and the other of 27 realisations with 256^3 particles each (S_2 hereafter). The box size is $100h^{-1}$Mpc, the cosmology a standard ΛCDM model ($\Omega_{\rm m} = 0.3$, $\Omega_\Lambda = 0.7$, $H_0 = 70$), the softening parameter is $39.5h^{-1}$kpc and the expansion factor ranges from 0.05 up to 1 for S_1 and from 0.05 up to 0.4 for S_2 . These two sets allow us to check the robustness of our finding with respect to resolution. Lyapunov exponents will also be expressed as characteristic timescales, τ, using the relationship between time and expansion factor in a CDM model (or equivalently in a ΛCDM model below $a \leqslant 0.5$), $a \propto \tau^{2/3}$. Note that the resolution in mass of FOF halos containing more than 100 particles corresponds here to $4\,10^{12}\,M_\odot$ for the set S_1 and $5\,10^{11}\,M_\odot$ for the set S_2 .

3 EULERIAN EXPONENTS

In this Section, we investigate the "global" chaos in the evolution of the Eulerian properties of the *density* field with respect to the expansion factor a, as opposed to chaos in the Lagrangian properties of *objects* which are specific to the matter distribution in the universe (such as halos and filaments). This will be addressed in Section 4.

3.1 Chaos in density fluctuations

In order to study the density fluctuations, the density fields of S_1 and S_2 are sampled on a 64^3 grid using a simple NGP (nearest grid point) method allowing the computation of statistical quantities on the resulting grid, such as the average density or the density fluctuations.[1] Within each set, for every pixel we compute the PDF of the realisations of the density values at that pixel and then average the individual pixel PDFs over all the pixels that have mean density value across realisations above the given threshold. The evolution of the width of this pixel-averaged PDF is then computed as a measure of the chaotic divergence amongst realisations with slightly different initial conditions. Specifically, Figure 1 presents the evolution of the mean relative dispersion of the density, $\delta\rho/\rho$ (where ρ is the mean density of the pixel over all the realisations and not the average density of the simulation), in identical pixels of the different realisations of S_1 (middle panel) and S_2 (bottom panel), considering regions where density is greater than given thresholds.[2]

As expected, these measurements show that this dispersion increases with time, as can easily be seen on the *top panel* of figure 1, where the PDF of $\delta\rho/\rho$ is plotted for different values of a. The fact that the growth rate of the dispersion increases when considering regions of higher densities may be explained by the higher level of nonlinearity of the evolution of matter distribution in these regions. In fact, in denser regions, the evolution becomes non-linear earlier, which favors the development of chaos. But at later times, non linearities have had time to develop at all considered overdensity levels, which explains the asymptotic merging of the curves. The exponential growth of the dispersions demonstrates that the evolution is chaotic as defined in the introduction and allows for the computation of Lyapunov exponents, λ_P, as the rate of change of the logarithm of the average relative density fluctuation as a function of the scale factor.

The fact that the non-linearity in the evolution increases chaos is illustrated by Figure 2, where maps of the average density (*top panel*) and the corresponding Lyapunov exponent λ_P (bottom panel) are plotted. Each map represents the projection of a $10h^{-1}$Mpc slice from a sample of S_2 at $a = 0.35$. The correlation between the two maps confirms the dependence of chaos on over density (see also the projections of different realisations of the same halos on Figure 6, where substructures are clearly different even though the shape of main halos remains mostly the same). These results must nonetheless be interpreted with care as the use of a finite sampling grid may bias the measurements. Indeed, considering higher density regions amounts to considering smaller scale regions, of order the size of the grid pixels ($\approx 1.5h^{-1}$ Mpc^3), which may affect the measured value of λ_P.

3.2 Chaos transition scale

Transition to chaotic behaviour of the density field that started with linear evolution is fundamentally linked to the development of the nonlinearity. Since different scales enter nonlinear regime at different epochs, one expects that at a given time there exist a transition scale, L_c, below which variation of the density in pixels of the sampled field is clearly chaotic. Figure 3 presents the behaviour of the average value of λ_P for different perturbation amplitudes A, as a function of the scale L. These measurements are derived by computing the average Lyapunov exponents in pixels on the sampled maps shown in figure 2, smoothed using a Gaussian kernel of

[1] we also considered a 128^3 grid and found no difference in the measured exponents.

[2] note that the number of pixels above a given threshold is going to depend on redshift, but for the contrasts considered here, the error on the dispersion due to shot noise is always negligible, as we have at least 8000 particles above the highest threshold, at the highest redshift.

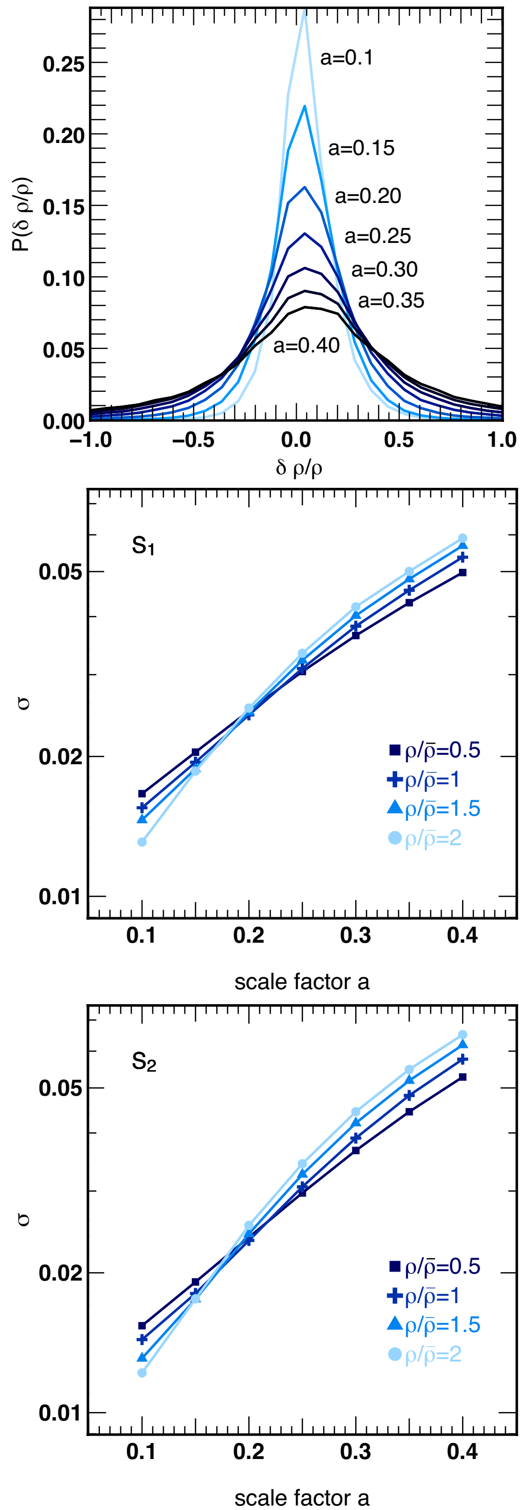

Figure 1. *top*: Evolution of the pixel-averaged PDF of the density values while sampling S_1 on a 64^3 grid for different values of $a \in [0.1(light), \cdots 0.4(dark)]$ (only the pixels where $\rho/\bar{\rho} > 2$ were considered, where $\bar{\rho}$ is the cosmic mean density). As expected the full width half max (FWHM) of the distribution increases exponentially with the expansion factor reflecting the chaotic behaviour of the PDF of the density field; *middle*: temporal evolution of the dispersion in the sampled density field per unit of the mean density, for sub regions of S_1 corresponding to thresholds in overdensity $\rho/\bar{\rho}$ of 0.5, 1, 1.5 and 2 respectively as labelled. The asymptotic merging for different thresholds reflects the fact that at later times, regions of different overdensity levels are all in the nonlinear regime; *bottom*: same as middle frame but for S_2.

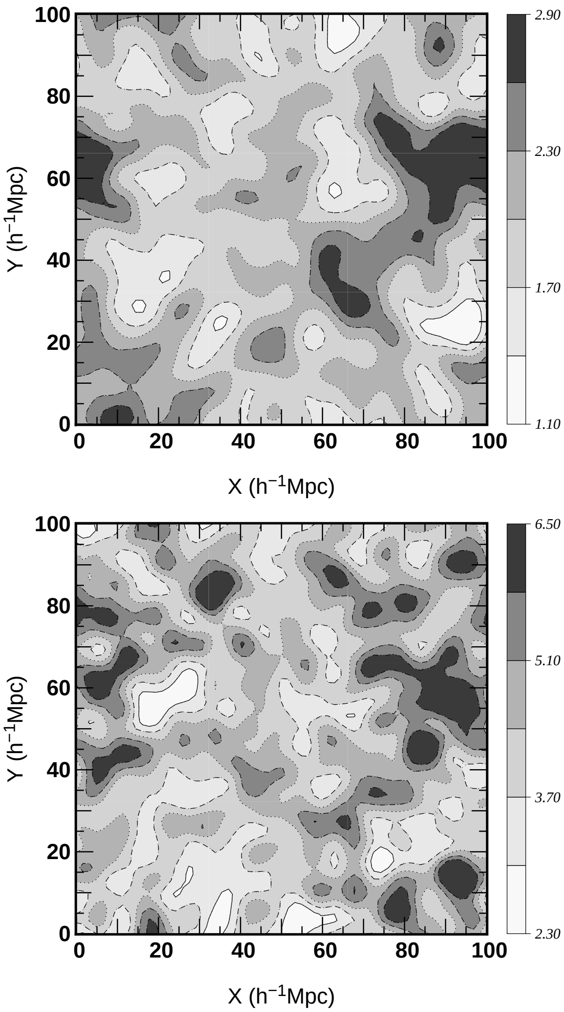

Figure 2. Logarithm of the projected density of the pixels (*top* frame) and their associated Lyapunov exponent (*bottom* frame), for a projected $10h^{-1}$Mpc slice S_2 at $a = 0.35$. The comparison of the two maps emphasizes the correlation of the two fields: denser regions have larger Lyapunov exponents. On closer inspection, one may argue that larger Lyapunov exponents lie in the outskirts of the denser regions.

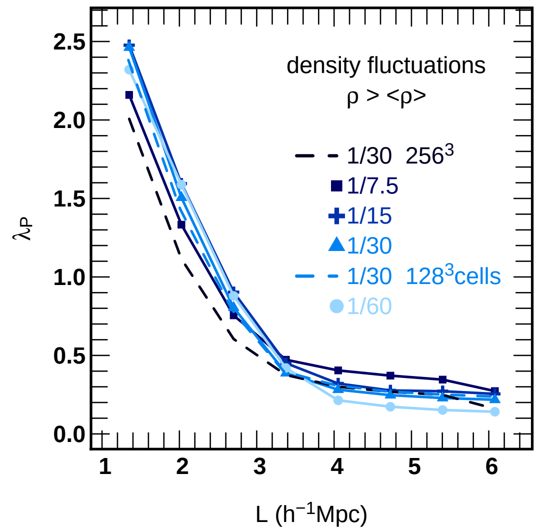

Figure 3. Evolution of the average Lyapunov exponent of the pixel density fluctuations, λ_P, as a function of the smoothing length L for regions where $\rho/\bar{\rho} > 1$ and for different amplitudes of the initial perturbations, A (expressed as a fraction of the initial dispersion amplitude) measured in the set S_1. The top dark dashed line corresponds to the set S_2 for $A = 1/30$. The sharp transition near $L_{\rm smooth} \approx 3.5{\rm Mpc}/h$ is exhibited in both resolutions. The perturbation amplitude does not affect the result significantly. The difference in time of measurement for the S_2 curve (slightly earlier than the freeze-out time around $z \sim 1$) may explain small the difference in the corresponding non linear scale. The bottom light dashed line corresponds also to $A = 1/30$ in S_1 but measured on a 128^3 grid; it shows that the exponent is not sensitive to the sampling resolution.

FWHM L, and considering only the overdense regions ($\rho/\bar{\rho} > 1$). Density is computed by making a histogram of particles in the grid using the NGP method, and by smoothing it with a Gaussian kernel afterwards. The measurements are performed at the present time, $a = 1$ in S_1 simulation and at $a = 0.4$ for S_2 set.

The plot demonstrates a rather sharp transition to chaotic behaviour at scales below the critical smoothing length $L_c \simeq 3.5h^{-1}$ Mpc with Lyapunov exponent increasing for ever smaller scales, whereas on larger scales the Lyapunov exponent is small and constant. This behaviour is indicative of the ΛCDM background cosmology of the standard model. Indeed, in the pure CDM cosmology with the critical density of the matter, the gravitational clustering would have continued to escalate to present time and one expect to see Lyapunov exponent falling smoothly to $L \simeq 8h^{-1}$Mpc, the present-day nonlinear scale [3]. In contrast, in ΛCDM cosmology the hierarchical clustering saturates when the dark energy begins to accelerate the expansion of the Universe. Numerical simulations show that in the standard ΛCDM model the clustering largely ceases by $z \sim 1$ ((Hatton et al. 2003)). The non-linear scale at this redshift is $L = 3.7h^{-1}$Mpc, which corresponds to the mass scale $M \approx 2 \times 10^{13} M_\odot$. The halos of smaller mass collapse en masse at earlier times passing by $z = 1$ through a period of hierarchical mergers with similar-mass halos as well as accretion that contributes to the formation of the chaotic features. Whereas the larger overdense patches, even the rare ones that turned around by $z \sim 1$ and will collapse by the present time, evolve in a quiescent environment of frozen hierarchy (van den Bosch 2002; Aubert and Pichon 2007). This argues for $L \approx 3.7h^{-1}$Mpc providing the fixed critical length between chaotic and regular regimes for all $z < 1$, which is in general agreement with our measurements.

4 LAGRANGIAN EXPONENTS

In the previous section, we studied the development of chaos in the density field of cosmological simulations. We measured the evolution of the variance of this density field on a grid (i.e. at peculiar *Eulerian* locations) and showed that chaos tends to be more pronounced in higher density regions as well as on smaller scales. Let us now focus instead on *Lagrangian* properties of peculiar objects with a physical significance such as dark matter halos or filaments.

[3] The nonlinear scale is usually defined with top-hat smoothing as $\sigma^2(R_{\rm TH}) = 1$. The FWHM of the Gaussian smoothing filter L that we use gives similar variance to the top-hat filter at $R_{\rm TH} \approx 0.9L$. Our simulations are normalized to $\sigma(8h^{-1}{\rm Mpc}) = 0.92$ which at $a = 1$ corresponds to nonlinear scale $R_{\rm TH} \approx 7.2h^{-1}$Mpc, i.e $L \approx 8h^{-1}$Mpc.

4.1 Inter skeleton distance

Filaments correspond to a central feature of the large scale distribution of matter: large void regions are surrounded by a filamentary web linking haloes together. Studying the properties of the filaments isn't an easy thing and one first needs to find a way of extracting their location from a simulation. The skeleton gives a mathematical definition of the filaments as the locus where, starting from the filament type saddle points (i.e. those where only one eigenvalue of the Hessian is positive), one reaches a local maximum of the field by following the gradient. This is equivalent to solving the equation:

$$\frac{d\mathbf{x}}{dt} \equiv \mathbf{v} = \nabla\rho\,, \tag{2}$$

for $\mathbf{x}$, where $\rho(\mathbf{x})$ is the density field, $\nabla\rho$ its gradient, and $\mathbf{x}$ the position. Although apparently simple, solving this equation is quite difficult which is why a local approximation was introduced in (Sousbie et al. (2006, 2007)): the *local* skeleton. One can show that, up to a second order approximation, solving Equation (2) is equivalent to finding the points in the field where the gradient is an eigenvector of the Hessian matrix together with a constraint on the sign of its eigenvalues. This approach leads to a system of two differential equations, solved by finding the intersection of two isodensity surfaces of some function of the density field and its first and second derivatives. This procedure is very robust and allows for a fair detection of the dark matter filaments. Figure 4 displays the skeleton of different realisations of S_2 at $a(t) = 0.1$ (*top*) and $a(t) = 0.4$ (*bottom*). Note that the dispersion of the skeleton location has increased with the scale factor. Using the method described in (Sousbie et al. (2006, 2007)), the *local* skeleton provides a list of small segments. In order to measure the distance between two skeletons, for each segment, the distance to the closest segment in the other skeleton is computed leading to the PDF of this distribution. The mean distance between the two skeletons is set to the position of the first mode of their inter-distance PDF (See also Caucci et al. (2008)). We then define a mean inter-skeleton distance among all the realisations within a set as the arithmetic average of their pairwise distances. This means that the normalized inter-skeleton distance, $\langle D\rangle/L_0$, is our measure of the dispersion in the skeleton location. It is a Lagrangian property since it follows the flow. Its evolution as a function of the scale factor is plotted on Figure 5 for different smoothing lengths L_0, for S_2 (*top*) and S_1 (*bottom*). The smoothing operation is achieved, as previously, by convolving the density field with a Gaussian kernel of FWHM L_0, ranging from $L_0 = 1.2\,h^{-1}$Mpc (3 pixels) up to $L_0 = 3.5\,h^{-1}$Mpc (9 pixels). It is clear that whatever the smoothing scale or the resolution used, the evolution of the dispersion is linear with the scale factor. A shift in the skeleton of the initial conditions will evolve linearly with time and not exponentially: the skeleton at present time won't be affected very much. There is no chaotic drift of the position of the skeleton and thus no chaos in the evolution of the cosmic web. Note nonetheless that the smaller the smoothing length, the stronger the increase of $\langle D\rangle/L_0$. This implies that smaller scales are more sensitive to initials conditions, which is confirmed by the fact that $\langle D\rangle/L_0$ is larger for lower values of L_0, whatever the value of a.

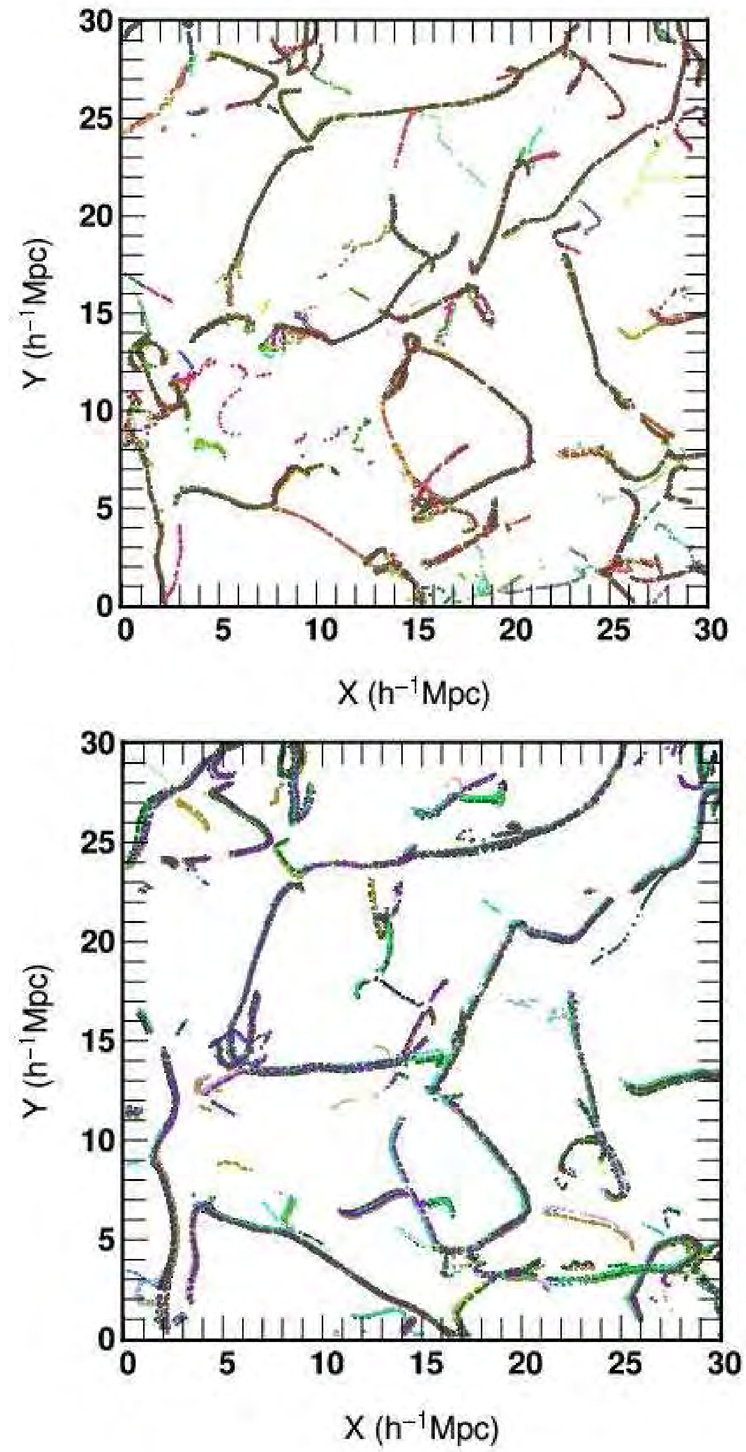

Figure 4. The *local* skeletons of the different realisations of S_2, computed at $a(t) = 0.1$ (*top*) and $a(t) = 0.4$ (*bottom*) and for a smoothing length $L_0 = 1.2h^{-1}$Mpc. Each figure corresponds to the projection of a $10h^{-1}$ Mpc thick slice. Each color represents a different realisation of the simulation, the color coding is not consistant between the top and the bottom panels. The dispersion in the position of the skeletons appears to have grown from $a(t) = 0.1$ to $a(t) = 0.4$.

4.2 Positions of halos

Turning to stochasticity on smaller scales in a Lagrangian framework (i.e. ignoring the absolute shift in position relative to a fixed

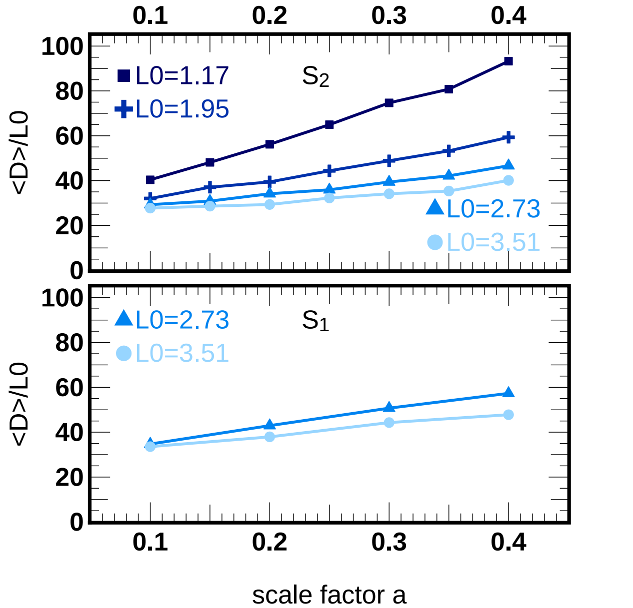

Figure 5. The normalized mean distance, $\langle D \rangle / L_0$, between the skeletons of S_2 (*top*) and S_1 (*bottom*) as a function of the scale factor and for different values of the smoothing length, L_0 in h^{-1} Mpc. Because of the lack of accuracy at smaller scales, only the larger smoothing lengths are represented for S_1. At these resolutions, the two sets agree. The cosmic web dispersion clearly evolves linearly with time, confirming that chaos is linked to non-linearities.

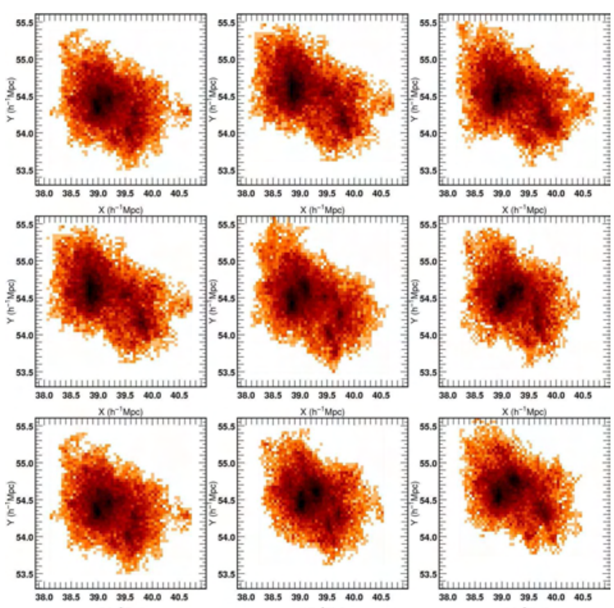

Figure 6. Heaviest cluster (in the X-Y plane in Mpc/h) of 9 realisations of S_2 at $z = 1.5$. The position and the global shape of the halo does not change from one simulation to another, but the substructures are quite different; this is confirmed via automated substructure identification using *ADAPTAHOP*.

frame), let us define a matching procedure to identify structures in different runs. haloes are first identified using the FOF algorithm (Davis et al. (1985); Suginohara and Suto (1992)) with a percolation length of $0.25h^{-1}$Mpc for S_1 and $0.5h^{-1}$Mpc for S_2 corresponding to $0.2\times$ mean interparticular distance. In order to tag different FOF haloes in different realisations as counterparts, all particles of a given halo are matched in another realisation using their initial index (Figure 6). The halo of the other simulation containing most of these particles is tagged as its counterpart. The procedure is carried over all pairs of simulations, allowing the measurement of the variation in the halo properties like their spins, their positions, their velocity dispersion tensors or their masses.

As shown on Figure 6, the haloes locations seem relatively insensitive to small changes in the initial conditions. The evolution of the mean distance between a halo in a given simulation and the same halo in another realisation is linear, as for the skeleton, which confirms the first impressions: no chaos is observed at linear scales and so λ_Q, the Lyapunov exponent of the inter halo distance, is null. But the most interesting results involve the substructures. The halo pictured in Figure 6 is a good example of the generic behaviour. The number of substructures changes from one realisation to another (here, 1 or 2 substructure(s)) and their positions also differ. These results are confirmed by an automated detection of the substructures using *ADAPTAHOP* (Aubert et al. (2004)). Both the locations and the number of substructures are possibly subject to chaos, but the lack of a cross identification procedure makes it difficult to quantify it and is somewhat beyond the resolution of these sets of simulations (Section 4.3 addresses this problem for the FOF halos). This trend confirms quantitatively the findings of section 3.1 from the point of view of Eulerian estimators which are sensitive to the detailed extension of the distribution of matter within halos: denser regions were found to be chaotic, and will be addressed in more details in Section 4.4 in terms of halo density and velocity moments.

4.3 Connexity and mass of clusters

The connexity of haloes can be defined as follows: considering the p^{th}halo, H_p^r, in the r^{th} realisation, its particles are spanned amongst n haloes in the r'^{th} realisation, and a fraction $f_{pk}^{rr'}$ $(k \in 1, .., n)$ of them belong to a halo k among n in the r'^{th} realisation. Hence, its relative connexity $C_p^{rr'}$ can be defined as:

$$C_p^{rr'} = \sum_{i=1}^{n} i \left(\prod_{j=1}^{i} \sum_{k=j}^{n} f_{pk}^{rr'} \right) , \tag{3}$$

where by construction $C_p^{rr'}$is equal to one if both haloes are identical in realisations r and r'; $C_p^{rr'}$ is equal to n if the halo p splits into n haloes with equal fractions $f_{pk}^{rr'} = 1/n$ in realisation r', while preserving continuity when the values of $f_{pk}^{rr'}$ differ, see Appendix A. The mean connexity, C, is obtained by averaging over all haloes containing more than 100 particles in every possible combinations of realisations and is a measure of the dispersion of the particles.

As shown on Figure 7, C increases with the scale factor, ranging from 1.17 (i.e., statistically, 90% of the particles belong to a unique halo in other realisations) to 1.37 (85%) from $a = 0.2$ up to $a = 1.0$. The connexity clearly does not vary exponentially with the scale factor : there are statistically no halo fission during evolution (thanks to the efficiency of dynamical friction). Moreover, two haloes marginally linked by FOF would almost always end up

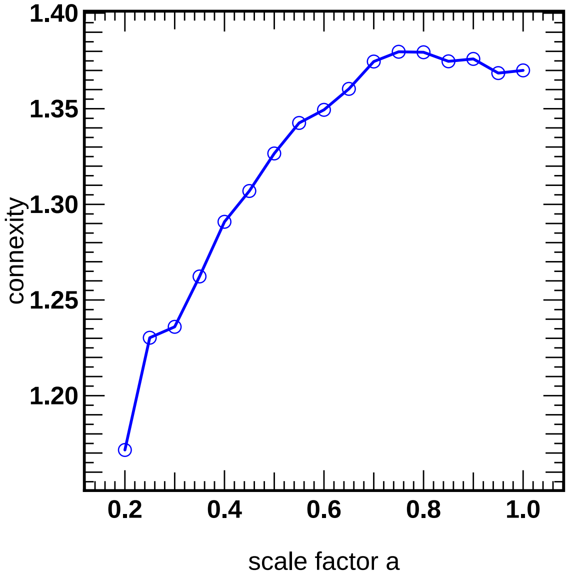

Figure 7. The haloes average connexity computed over all the realisations of S_1 as a function of the scale factor. While the connexity is not subject to chaos, its value increases with time. This result can be understood through the difference in merging time of the haloes.

merging sooner or later. More and more haloes merge at different times in different realisations which is in part due to the fact that some threshold is involved in the FOF algorithm: a precise linking length has to be chosen, inducing the possibility that small changes in particles position can induce significant changes in halo merging time (according to the FOF definition of a halo). At later times ($a > 0.7$), the connexity reaches a plateau, which suggests that when haloes are massive enough ($M \geqslant M_c$, see Section 4.4 below), they become insensitive to the merging of lighter ones, since equal mass merging rarely occur below $z = 1$. The analysis of the masses of the haloes shows that there is no sweeping change and so, no obvious evolution of the haloes mass distribution: the associated Lyapunov exponent, λ_M, is null. The number of different particles increases with time but the missing particles are replaced by new particles. Thus, the mass stays quite constant even as the connexity increases. It follows that the mass function extracted from the N-body simulations are found to be quite robust with respect to changes in the initial conditions. Although the masses of the haloes are similar in different realisations, some of the particles which compose them may be different, which may generate differences in the physical properties of the haloes. The substructures are different (Fig. 6) in their numbers and positions, which is responsible for the Eulerian chaos found in Section 3.2. Let us now re-explore this in a Lagrangian framework.

4.4 Spin Orientation of clusters

The influence of chaos on the spin of haloes is estimated by computing the cosine of the angle, θ_{pq}, between the spins $\boldsymbol{J}_p$ and $\boldsymbol{J}_q$ of corresponding haloes in two different realisations p and q:

$$\cos(\theta_{pq}) = \frac{\boldsymbol{J}_p \cdot \boldsymbol{J}_q}{\|\boldsymbol{J}_p\| \, \|\boldsymbol{J}_q\|}. \tag{4}$$

For every bin of mass, a measure of the dispersion, σ, of the orientation is given by the average angle:[4]

$$\sigma = \arccos\left(\frac{1}{N_c}\sum_{i=1}^{N_c}\cos\theta_{pq}\right), \tag{5}$$

where the sum is over all the N_c possible pairwise combinations of realisations. Note that only bins of masses containing more than 30 haloes have been retained.

Figure 8 displays the exponential growth of this dispersion with time, and shows that the precise value of its associated Lyapunov exponent λ_σ depends on the selected bin of mass. It also shows that the exponent does not seem to be sensitive to shot noise, as its value is left unchanged when resolution is increased between S_1 and S_2.

Also, as it is seen in Fig.6, the detailed distribution of satellites within a given cluster varies from one realisation to another; the angular momentum orientation (in contrast to say, its modulus or the halo mass) is quite sensitive to the outer region of the distribution. Recall that the spin parameter (i.e. the $\Lambda = J/(\sqrt{2}MV_{200}R_{200})$ (Bullock et al. (2001), Aubert et al. (2004)) of a halo displays no chaotic behaviour. It stays quite constant from a simulation to another and the evolution of its dispersion is not exponential.

The measured Lyapunov exponent ranges from 0 to 0.3. The value of the mean dispersion of the orientation of the spin for heavier haloes is about 35 degrees ($= \exp(3.55)$). Globally this suggests that the orientation of the spin varies with the tidal field, which in turn depends on the relative position of structures within the environment of the halo.

For lighter haloes, the measured value of λ_σ is higher than for heavier ones (Figure 8) which may be partly explained by the fact that a slight change in a few clumps within the haloes has a larger influence on its spin when they represent a significant fraction of it. Faltenbacher & al. (Faltenbacher et al. (2005)) showed that if the lightest halo has a mass less than 10% of the mass of the larger halo, the orientation of the resulting post merging halo will remain statistically the same. In contrast, if its mass is greater than 20% of the more massive halo, the final orientation of the merged halo depends on the speed vector of the two progenitors. Our results corroborate well their finding since the lightest haloes that are formed by merging of two substructures of comparable masses have chaotic spins (substructures being chaotic, see Section 3 and Figure 6), while heavier ones have spin that are relatively stable with time (they only merge with much smaller haloes). It emerges from these measurements that there is a critical mass, M_c, above which chaotic behaviour disappears. Haloes heavier than this mass are too heavy to feel the influence of incoming clumps and their spins are clearly defined. They are therefore not subject to chaos and their Lyapunov exponents are null at the one sigma level, in contrast to lighter ones whose spin are sensitive to the initial conditions and whose Lyapunov exponents are positive.

As for the critical smoothing length (see Section 3), we can study the evolution of this critical mass as a function of the amplitude, A, of the perturbations. Figure 9 shows this evolution. A good fit of this transition mass is given by $M_c = 2\,10^{13}\,M_\odot A^{0.15}$. The higher the amplitude of the perturbations, the higher the required time for haloes to have a spin clearly defined. Consequently, the critical mass increases with the perturbation amplitude, and haloes that can be considered stable are heavier. Note that it means that

[4] the estimator of the dispersion, Eq. (5) is robust since weighting the sum by the spin parameter yields the same results.

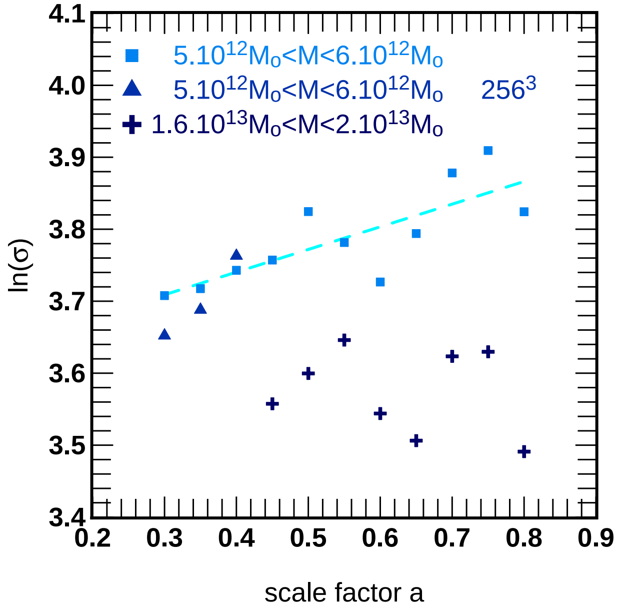

Figure 8. Logarithm of the dispersion of the angle between the spin of one halo of S_1 as a function of the scale factor. Results are computed for different ranges of masses, $5\,10^{12}\mathrm{M}_{\odot}$<M<$6\,10^{12}\mathrm{M}_{\odot}$ (*top*) and $1.6\,10^{13}\mathrm{M}_{\odot}$<M<$2\,10^{13}\mathrm{M}_{\odot}$ (*bottom*). For heavier halos the Lyapunov exponent vanishes. The triangles correspond to the first class of lighter mass, but measured in S_2; the exponent remains unchanged which suggests that particle shot noise is not an issue.

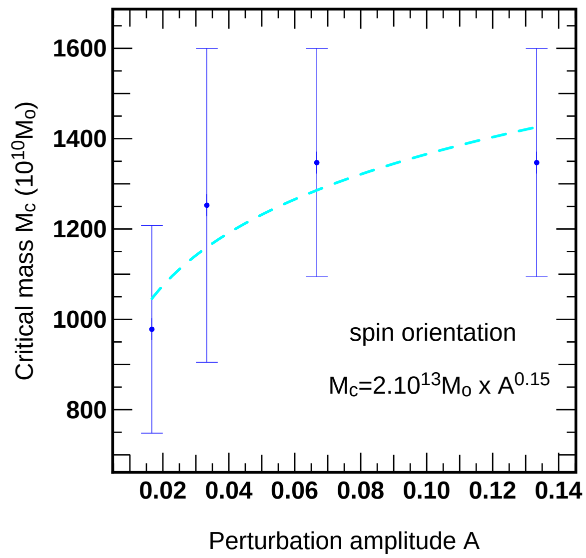

Figure 9. Critical mass, M_c, (in units of $10^{10}\mathrm{M}_{\odot}$) for the spin orientation as a function of the amplitude of the perturbations, A (in fraction of the initial dispersion amplitude). It appears that $M_c = 2\,10^{13} M_{\odot}\, A^{0.15}$. The larger the amplitude of the perturbation, the heavier the haloes that can be considered stable.

the spin is constant with time but not very reliable since its final orientation depends, in part, on the initial conditions.

4.5 Orientation of the velocity dispersion tensor

The orientation of the velocity dispersion tensor is also a quantity of interest from the point of view of stochasticity since it is related to the shape of the halo via the Virial theorem. The corresponding estimator involves computing the orientation of the eigenvector $\boldsymbol{V}$ associated to the largest eigenvalue of the velocity dispersion tensor. As for the orientation of the spin, (Sec. 4.4) the angle θ_{pq} between the eigenvector $\boldsymbol{V}_p$ of the halo in simulation p and its corresponding eigenvector $\boldsymbol{V}_q$ in a simulation q is computed as:

$$\cos(\theta_{pq}) = \frac{\boldsymbol{V}_p.\boldsymbol{V}_q}{\|\boldsymbol{V}_p\|\,\|\boldsymbol{V}_q\|}. \tag{6}$$

For every bin of mass, a measure of the dispersion, σ, is also given by Equation (5). Once again, only bins of masses containing more than 30 haloes were considered. As shown in Figure 10 this estimate is consistent with the exponents of the orientation of the spin: only the lightest masses are sensitive to the initial conditions, while the dispersion of the orientation for the heavier masses is constant (about 40 degrees). The measured Lyapunov exponent, λ_T, ranges from 0 up to 0.65 . These results corroborate well those for the spin axis, given that its orientation follows the third eigenvector of the dispersion matrix (i.e. the axis along which dispersion is the smallest). Faltenbacher et al. (2005) showed that the orientation of the principal axis of the halo is correlated with the vector linking the two mergers (i.e. their relative positions) particularly in the case where one of the mergers has a mass smaller than 10% of the second one. The chaos found at small scales (substructures scale) is once again responsible for the chaos in these geometrical properties of haloes since changing the initial conditions amounts to changing the relative positions of the substructures (see sec.3.1) and thus to changing the orientation of the resulting halo's dispersion tensor. As for the spin, there is evidence of a critical mass above which chaotic evolution disappears: more massive haloes only merge with lighter ones that do not affect their global properties.

5 CONCLUSION AND DISCUSSION

Let us first emphasize here again that the term chaos is used in this paper in the loose sense, as the age of the universe does not allow for many e-foldings on larger scales. Table 1 summarizes the different Lyapunov exponents computed in this paper. As shown in section 3.1 (Figure 3), chaos appears below a critical scale which corresponds roughly to cluster scales. The higher the density, the more chaotic is the corresponding region. We also found that both Lagrangian and Eulerian measurements are consistent: super clusters and filaments, whose dynamics is globally linear (large scale structures), are not stochastic: a shift in the initial conditions will increase linearly with the scale factor. By contrast, the distributions of substructures within clusters, whose characteristic size is smaller than $\sim 3.5h^{-1}$Mpc, are governed by non-linear dynamics and may undergo a stochastic evolution for some observables.

Nevertheless, this chaos at substructures scale does not occur for all physical characteristics of the cluster's halo. A main fraction of particles remains in the same halo from one realisation to another, while a difference arises (in part) from the delay in merging times of the substructures. These timing effects are however averaged out yielding, to first order, a constant halo mass. It follows that the mass function derived from a simulation is quite consistent from one realisation to another. Similarly, the dispersion of the amplitude of the total spin of haloes does not increase exponentially with time.

The mass of a given halo is an integrated quantity which does

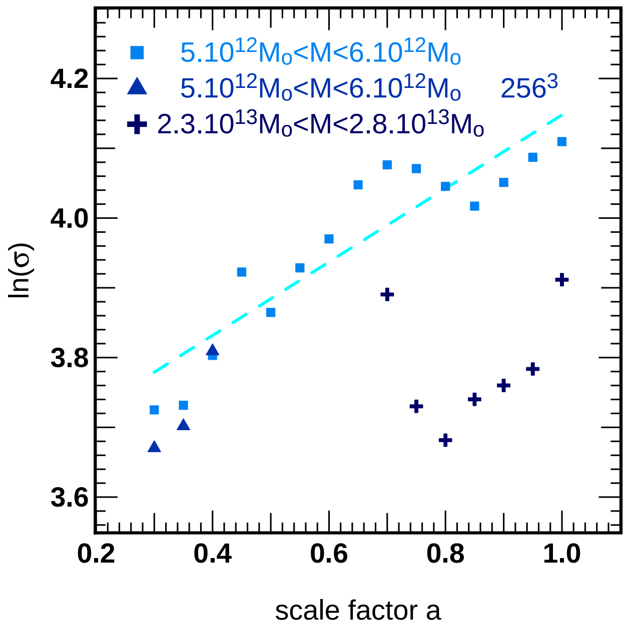

Figure 10. Logarithm of the dispersion of the angle between the first eigenvector of the velocity dispersion tensor of the haloes of S_1, as a function of the scale factor. Results are computed for different ranges of masses: $5\,10^{12}\mathrm{M}_\odot$<M<$6\,10^{12}\mathrm{M}_\odot$ (*top*) and $2.3\,10^{13}\mathrm{M}_\odot$<M<$2.8\,10^{13}\mathrm{M}_\odot$ (*bottom*). The less massive haloes are more sensitive to the initial conditions, the average angle being constant for the heavier ones, about a value of 40 degrees. The triangles correspond again to the S_2 set and shows not difference. The Lyapunov exponent, λ_T ranges from 0 to 0.65.

not trace which specific particle entered the FOF halo; similarly, the spin parameter is also an adiabatic invariant, and the trace of the dispersion tensor will relax rapidly to its virial expectation (which is mass dependent) in a few short dynamical times; in contrast, the spin orientation or the orientation of the dispersion tensor will depend precisely on the orientation of velocities of the entering particles and has no direct relation to the mass of the halo; it also reflects the initial environment of the proto halo. For instance it has been shown in Sousbie et al. (2007), Aubert et al. (2004) that the halos preferentially anti-align their spin with the axis of the filament in which they are embedded, while we have shown in Section 4.1 that the filament's locus was not stochastic.

It is possible to recast these interpretations in the context of the peak-patch (Bond and Myers (1996)) description of haloes. In this framework, massive haloes correspond to large quasi spherical patches around density peaks, which non-linear evolution will decouple from their neighbouring large patches thanks to the cosmic acceleration below $z \sim 1$. Conversely, small haloes correspond to small typically aspherical peak-patches, and will acquire tidal torques early on which depend specifically on the detailed white noise realisation (which fixes the shape of the peak-patches). In the tidal torque theory, the mass and the spin parameter are essentially integral functions over the volume of these patches, hence will not depend on the initial perturbations, whereas the spin orientation itself is sensitive to these perturbations, at least at the lower end of the mass spectrum. This is consistent with the low scatter relationship between the spin parameter and the mass (Aubert et al. (2004)).

Thanks to angular momentum leverage, the orientation of haloes is itself affected by stochasticity mostly at small scales, a result which seems insensitive to shot noise as the lyuponov exponents are consistent between sets S_1 and S_2. In fact, as long as the haloes merging together have similar sizes (masses), the orientation of both spin and velocity dispersion tensors is determined by the relative positions and velocities of the two mergers, whose dynamics is non-linear and whose characteristic size is below the critical scale (Figure 3). These results seem robust with respect to resolution.

	λ	τ(Gyear)
Pixels PDF, λ_P	0-2.5	3.4-∞
Velocity dispersion tensor, λ_T	0-0.65	25-∞
Spin orientation, λ_σ	0.-0.31	75-∞
Inter skeleton distance, λ_S	~ 0	∞
Connexity, λ_C	~ 0	∞
Position of the halos and substructures, λ_Q	~ 0	∞
Mass of the halos, λ_M	~ 0	∞
Spin parameter, λ_Λ	~ 0	∞
Mean dispersion of velocity, λ_V	~ 0	∞

Table 1. Lyapunov exponents of the different observables studied. Interestingly, many global properties of halos do not display chaotic behaviour.

When the halo is formed and well-isolated by cosmic acceleration, it merges only with satellites/substructures whose masses represent a small fraction of the host's mass. Consequently, their orientations are globally preserved after merging, and thus, the chaotic behaviour stops and the dispersion in the orientation remains at the same level (i.e. the resulting average angle is unchanged). Hence, a critical mass can be defined as the mass above which this chaotic behaviour of the orientation stops. The measured value of this critical mass, $M_c = 2\,10^{13} M_\odot A^{0.15}$, is just below the scale of non-linearity at $z \sim 1$ and shows weak dependence on the amplitude of the added perturbative noise: $M_c = 2\,10^{13} M_\odot A^{0.15}$. Although some slow increase of M_c with A is expected since adding power to inhomogeneities shifts the nonlinear scale to higher masses, the details of the dependence require further investigation.

This paper has concentrated on a realistic ΛCDM cosmology: it would also be interesting to rerun this investigation on scale-free power spectra to confirm that the dark energy is indeed responsible for the saturation of M_c. A natural extension of this work, clearly beyond its current scope, would also involve computing Lyapunov exponents for the properties of substructures within halos (see for instance Valluri et al. (2007)), and parameters corresponding to the inner structure of halos, such as NFW concentration parameter, the phase space density $Q = \rho_0/\sigma^3$ (Peirani et al. (2006)), the Gini index or the asymmetry (Conselice et al. (2007)) within the FOF.

In closing, the answer to our riddle is that chaos and non-linearities are very strongly linked, and both occur at small scales (substructures scales) though some non linear halo parameters (spin, mass etc...) do not seem to be subject to chaos. While the large scale structures in a simulation (filaments and haloes) are quite robust both in their locus and properties, the distribution of substructures is more sensitive to initial conditions since their numbers and positions vary when initial conditions vary. This in turn may prove to be a concern when generating zoomed resimulations.

Acknowledgments

We thank the anonymous referee for helpful suggestions, D. Aubert, S. Colombi, and R. Teyssier for fruitful comments during the course of this work, and D. Munro for freely distributing his Yorick programming language and opengl interface (available at `http://yorick.sourceforge.net/`*). This work was carried within the framework of the Horizon project,* `www.projet-horizon.fr`*.*

References

D. Aubert and C. Pichon. Dynamical flows through dark matter haloes - II. One- and two-point statistics at the virial radius. *MNRAS* , 374:877–909, January 2007.

D. Aubert, C. Pichon, and S. Colombi. The origin and implications of dark matter anisotropic cosmic infall on L* haloes. *MNRAS* , 352:376–398, August 2004.

E. Bertschinger. COSMICS: Cosmological Initial Conditions and Microwave Anisotropy Codes. *ArXiv Astrophysics e-prints*, June 1995.

J. R. Bond and S. T. Myers. The Peak-Patch Picture of Cosmic Catalogs. III. Application to Clusters. *ApJS* , 103:63–+, March 1996.

J. S. Bullock, A. Dekel, T. S. Kolatt, A. V. Kravtsov, A. A. Klypin, C. Porciani, and J. R. Primack. A Universal Angular Momentum Profile for Galactic Halos. *ApJ* , 555:240–257, July 2001.

S. Caucci, S. Colombi, C. Pichon, E. Rollinde, P. Petitjean, and T. Sousbie. The topology of the IGM. *MNRAS submitted*, 2008.

C. J. Conselice, S. Rajgor, and R. Myers. The Structures of Distant Galaxies I: Galaxy Structures and the Merger Rate to z˜3 in the Hubble Ultra-Deep Field. *ArXiv e-prints*, 711, November 2007.

M. Davis, G. Efstathiou, C. S. Frenk, and S. D. M. White. The evolution of large-scale structure in a universe dominated by cold dark matter. *ApJ* , 292:371–394, May 1985.

J. Diemand, B. Moore, and J. Stadel. Velocity and spatial biases in cold dark matter subhalo distributions. *MNRAS* , 352:535–546, August 2004.

A. Faltenbacher, B. Allgood, S. Gottlöber, G. Yepes, and Y. Hoffman. Imprints of mass accretion on properties of galaxy clusters. *MNRAS* , 362:1099–1108, September 2005.

J. Goodman, D. C. Heggie, and P. Hut. On the Exponential Instability of N-Body Systems. *ApJ* , 415:715–+, October 1993.

S. H. Hansen and B. Moore. A universal density slope Velocity anisotropy relation for relaxed structures. *New Astronomy*, 11: 333–338, March 2006a.

S. H. Hansen and B. Moore. A universal density slope Velocity anisotropy relation for relaxed structures. *New Astronomy*, 11: 333–338, March 2006b.

S. Hatton, J. E. G. Devriendt, S. Ninin, F. R. Bouchet, B. Guiderdoni, and D. Vibert. GALICS- I. A hybrid N-body/semi-analytic model of hierarchical galaxy formation. *MNRAS* , 343:75–106, July 2003.

H. E. Kandrup. Divergence of nearby trajectories for the gravitational N-body problem. *ApJ* , 364:420–425, December 1990.

H. E. Kandrup, B. L. Eckstein, and B. O. Bradley. Chaos, complexity, and short time Lyapunov exponents: two alternative characterisations of chaotic orbit segments. *AAP* , 320:65–73, April 1997.

H. E. Kandrup, M. E. Mahon, and H. J. Smith. On the sensitivity of the N-body problem toward small changes in initial conditions. 4. *ApJ* , 428:458–465, June 1994.

H. E. Kandrup and I. V. Sideris. Chaos and the continuum limit in the gravitational N-body problem: Integrable potentials. *PRE* , 64(5):056209–+, November 2001.

H. E. Kandrup and H. J. Smith. On the sensitivity of the N-body problem to small changes in initial conditions. *ApJ* , 374:255–265, June 1991.

H. E. Kandrup and H. J. Smith. On the sensitivity of the N-body problem to small changes in initial conditions. II. *ApJ* , 386: 635–645, February 1992.

H. E. Kandrup, H. J. Smith, and D. E. Willmes. On the sensitivity of the N-body problem to small changes in initial conditions. III. *ApJ* , 399:627–633, November 1992.

J. F. Navarro, C. S. Frenk, and S. D. M. White. A Universal Density Profile from Hierarchical Clustering. *ApJ* , 490:493–, December 1997.

S. Peirani, F. Durier, and J. A. de Freitas Pacheco. Evolution of the phase-space density of dark matter haloes and mixing effects in merger events. *MNRAS* , 367:1011–1016, April 2006.

C. Power, J. F. Navarro, A. Jenkins, C. S. Frenk, S. D. M. White, V. Springel, J. Stadel, and T. Quinn. The inner structure of ΛCDM haloes - I. A numerical convergence study. *MNRAS* , 338:14–34, January 2003.

H. B. Richer, G. G. Fahlman, R. Buonanno, F. Fusi Pecci, L. Searle, and I. B. Thompson. Globular cluster mass functions. *ApJ* , 381:147–159, November 1991.

L. V. Sales, J. F. Navarro, M. G. Abadi, and M. Steinmetz. Satellites of simulated galaxies: survival, merging and their relationto the dark and stellar haloes. *MNRAS* , 379:1464–1474, August 2007.

J. A. Sellwood and A. Wilkinson. Dynamics of barred galaxies . *Reports of Progress in Physics*, 56:173–256, February 1993.

I. V. Sideris and H. E. Kandrup. Chaos and the continuum limit in the gravitational N-body problem. II. Nonintegrable potentials. *PRE* , 65(6):066203–+, June 2002.

T. Sousbie, C. Pichon, S. Colombi, D. Novikov, and D. Pogosyan. The three dimensional skeleton: tracing the filamentary structure of the universe. *ArXiv e-prints*, 707, July 2007.

T. Sousbie, C. Pichon, H. Courtois, S. Colombi, and D. Novikov. The 3D skeleton of the SDSS. *ArXiv Astrophysics e-prints*, February 2006.

V. Springel, N. Yoshida, and S. D. M. White. GADGET: a code for collisionless and gasdynamical cosmological simulations. *New Astronomy*, 6:79–117, April 2001.

L. E. Strigari, J. S. Bullock, M. Kaplinghat, J. Diemand, M. Kuhlen, and P. Madau. Redefining the Missing Satellites Problem. *ApJ* , 669:676–683, November 2007a.

L. E. Strigari, J. S. Bullock, M. Kaplinghat, J. Diemand, M. Kuhlen, and P. Madau. Redefining the Missing Satellites Problem. *ApJ* , 669:676–683, November 2007b.

T. Suginohara and Y. Suto. Properties of galactic halos in spatially flat universes dominated by cold dark matter - Effects of nonvanishing cosmological constant. *ApJ* , 396:395–410, September 1992.

M. Valluri, I. M. Vass, S. Kazantzidis, A. V. Kravtsov, and C. L. Bohn. On Relaxation Processes in Collisionless Mergers. *ApJ* , 658:731–747, April 2007.

F. C. van den Bosch. The universal mass accretion history of cold dark matter haloes. *MNRAS* , 331:98–110, March 2002.

M. L. Weil, V. R. Eke, and G. Efstathiou. The formation of disc galaxies. *MNRAS* , 300:773–789, November 1998.

Q. Zhang and S. M. Fall. The Mass Function of Young Star Clusters in the "Antennae" Galaxies. *ApJL* , 527:L81–L84, December 1999.

APPENDIX A: CONNEXITY

Let us consider a halo, H, split into n parts, $P_i^n, i \leqslant n$, with a fraction, f_i, of its particles in each of them, the indices i being sorted following the decreasing values of f_i ($f_i \geqslant f_j$ if $i < j$). A measure C_n of the connexity of H should indicate the number of clumps into which it was split, this number does not necessarily have to be an integer, depending on the fraction of the mass of H that went into each P_i^n. For instance, if $n = 2$, we want to obtain $C_2 = 2$ when $f_1 = f_2 = 1/2$ and $C_2 \to 1$ when $f_1 \to 1$ and $f_2 = 1 - f_1 \to 0$; as the indices are sorted, $0 < f_2 < 1/2$. So, in this case, we could write the connexity of H as:

$$C_2 = 1 + 2f_2. \tag{A1}$$

Now, considering that H was split into 3 parts P_i^3, then $0 < (f_2 + f_3) < 2/3$ and $0 < f_3 < 1/3$. So $C_3' = 2 + 3f_3 \to 2$ if $f_3 \to 0$ and $C_3' \to 3$ when $f_3 \to 1/3$. It follows that $C_3'' = (f_2 + f_3)C_3' \to 2$ when $f_2 \to 1/3$ (which implies that $f_3 \to 1/3$) and that $C_3'' \to 0$ when $f_2 \to 0$ (which implies that $f_3 \to 0$ also). So

$$C_3 = 1 + (f_2 + f_3)(2 + 3f_3) \tag{A2}$$

has the right properties to represent the connexity of a halo split into 3 parts. Hence, by generalizing recursively this formula, we obtain:

$$\begin{aligned} C_n \quad = \quad & 1 + (f_2 + \cdots f_n)\left[2 + (f_3 + \cdots f_n)\left[\cdots\left[n - 2 + \right.\right.\right. & \text{(A3)} \\ & \left.\left.\left.(f_{n-1} + f_n)\left[(n-1) + nf_n\right]\right]\cdots\right]\right], & \text{(A4)} \end{aligned}$$

which can be developed as:

$$\begin{aligned} C_n &= 1 + 2(f_2 + \cdots f_n) + 3(f_2 + \cdots f_n)(f_3 + \cdots f_n) + & \text{(A5)} \\ & \qquad \cdots + n(f_2 + \cdots + f_n)(f_3 + \cdots + f_n)\cdots(f_n), & \text{(A6)} \\ &= \sum_{i=1}^{n} i \left(\prod_{j=1}^{i} \sum_{k=j}^{n} f_k \right), & \text{(A7)} \end{aligned}$$

which corresponds to Eq. (3). Note that by construction, the braket in Eq. (A7) is smaller than $1/i$, so that C_n is always smaller or equal to n.

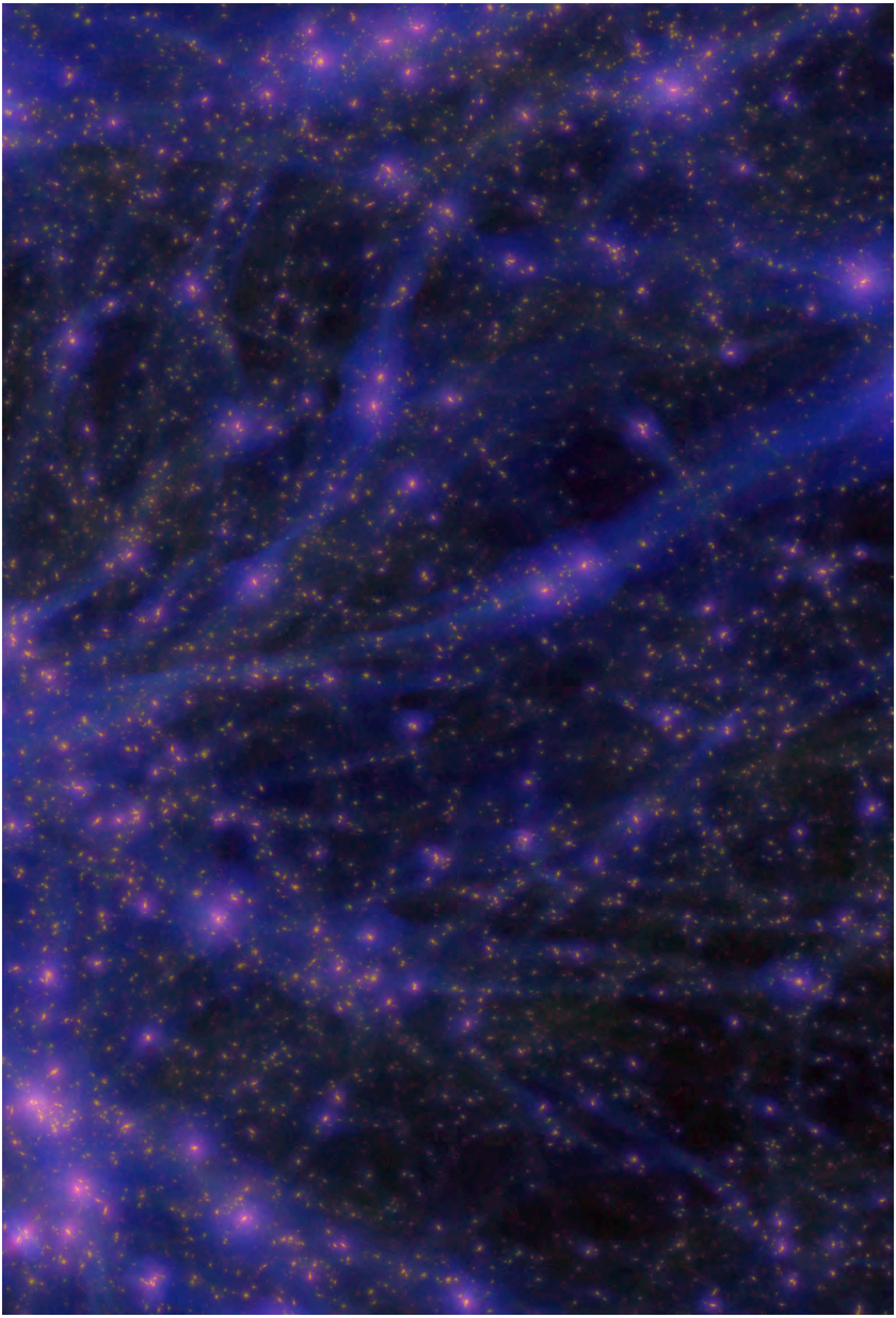

Mon. Not. R. Astron. Soc. **301,** 419–434 (1998)

Non-parametric reconstruction of distribution functions from observed galactic discs

C. Pichon[1,2,3]* and E. Thiébaut[4]

[1] CITA, 60 St George Street, Toronto, Ontario M5S 1A7, Canada
[2] Astronomisches Institut, Universitaet Basel, Venusstrasse 7, CH-4102 Binningen, Switzerland
[3] Institut d'Astrophysique de Paris, 98 bis boulevard d'Arago, 75014 Paris, France
[4] Centre de Recherches Astronomiques de Lyon, 9 avenue Charles André, F-69561 Saint Genis Laval Cedex, France

Accepted 1998 July 27. Received 1998 July 27; in original form 1997 April 14

ABSTRACT

A general inversion technique for the recovery of the underlying distribution function for observed galactic discs is presented and illustrated. Under the assumption that these discs are axisymmetric and thin, the proposed method yields a unique distribution compatible with all the observables available. The derivation may be carried out from the measurement of the azimuthal velocity distribution arising from positioning the slit of a spectrograph along the major axis of the galaxy. More generally, it may account for the simultaneous measurements of velocity distributions corresponding to slits presenting arbitrary orientations with respect to the major axis. The approach is non-parametric, i.e. it does not rely on a particular algebraic model for the distribution function. Special care is taken to account for the fraction of counter-rotating stars, which strongly affects the stability of the disc.

An optimization algorithm is devised – generalizing the work of Skilling & Bryan – to carry this truly two-dimensional ill-conditioned inversion efficiently. The performance of the overall inversion technique with respect to the noise level and truncation in the data set is investigated with simulated data. Reliable results are obtained up to a mean signal-to-noise ratio of 5, and when measurements are available up to $4R_e$. A discussion of the residual biases involved in non-parametric inversions is presented. The prospects of application of the algorithm to observed galaxies and other inversion problems are discussed.

Key words: methods: data analysis – methods: numerical – galaxies: general – galaxies: kinematics and dynamics.

1 INTRODUCTION

In years to come, accurate kinematical measurement of nearby disc galaxies will be achievable with high-resolution spectroscopy. Measurement of the observed line profiles will yield relevant data with which to probe the underlying gravitational nature of the interaction holding the galaxy together. Indeed the assumption that the system is stationary relies on the existence of invariants, which put severe constraints on the possible velocity distributions. This is formally expressed by the existence of an underlying distribution function which specifies the dynamics completely. The determination of realistic distribution functions which account for observed line profiles is therefore required in order to understand of the structure and dynamics of spiral galaxies.

Inversion methods have been implemented for spheroids (globular clusters or elliptical galaxies) by Merrifield (1991), Dejonghe (1993), Merritt (1996, 1997), Merritt & Tremblay (1993, 1994), Emsellem, Monnet & Bacon (1994), Dehnen (1995), Kuijken (1995) and Qian (1995). Indeed, for spheroids, the surface density alone yields access to the even component of a two-integral distribution function which may account for the internal dynamics (while the odd component can be recovered from the mean azimuthal flow). However, the corresponding recovered distribution might not be consistent with higher Jeans moments, since the equilibria may involve three (possibly approximate) integrals. The inversion problem corresponding to a flattened spheroid which is assumed to have two or three (Stakel-based) integrals has been addressed recently by Dejonghe et al. (1996) and is illustrated by NGC 4697. Non-parametric approaches have in particular been used with success by Merritt & Gebhardt (1994) and Gebhardt et al. (1996) to solve the dynamical inverse problem for the density in spherical geometry. If the spheroid is seen exactly edge on, Merritt (1996) has devised a method which allows one to recover simultaneously the underlying potential.

*E-mail: pichon@astro.unibas.ch

Here the inversion problem for thin and round discs is addressed for cases where symmetry ensures integrability. In this context, the inversion problem is truly two-dimensional and requires special attention for the treatment of quasi-radial orbits in the inner part of the galaxy.

By Jeans' theorem the steady-state mass-weighted distribution function describing a flat galaxy must be of the form $f=f(\varepsilon,h)$, where the specific energy, ε, and the specific angular momentum, h, are given by

$$\varepsilon=\tfrac{1}{2}(v_R^2+v_\phi^2)-\psi\,,\qquad h=R\,v_\phi\,. \tag{1}$$

Here v_R and v_ϕ are the star radial and angular velocities respectively of stars confined to a plane and $\psi(R)$ is the gravitational potential of the disc. The azimuthal velocity distribution, $F_\phi(R,v_\phi)$, follows from this distribution according to

$$F_\phi(R,v_\phi)=\int f(\varepsilon,h)\,\mathrm{d}v_R\,, \tag{2}$$

where the integral is over the region $1/2\times(v_R^2+v_\phi^2)<\psi$ corresponding to bound orbits. Pichon & Lynden-Bell (1996) demonstrated that, in the case of a thin round galactic disc, the distribution can be analytically inverted to yield a unique $f(\varepsilon,h)$ provided the potential $\psi(R)$ is known. The velocity distribution $F_\phi(R,v_\phi)$ can be estimated – within a multiplicative constant – from line-of-sight velocity distribution (LOSVD) data obtained by long-slit spectroscopy when the slit is aligned with the major axis of the galactic disc projected on to the sky. Similarly, the rotation curve observed in H I gives in principle access to the underlying potential. More generally, simultaneous measurements of velocity distributions are derived with slits presenting arbitrary orientations with respect to the major axis, as discussed in Appendix C.

The inversion of equation (2) is known to be ill-conditioned: a small departure in the measured data (e.g. caused by noise) may produce very different solutions since these are dominated by artefacts corresponding to the amplification of noise. Some kind of balance must therefore be found between the constraints imposed on the solution, in order to deal with these artefacts on the one hand and the degree of fluctuations consistent with the assumed information content of the signal on the other hand (i.e. the worse the data quality, the lower the informative content of the solution and the greater the constraint on the restored distribution so as to avoid an over-interpretation of the data). Finding such a balance is called the 'regularization' of the inversion problem (e.g. Wahba & Wendelberger 1979) and methods implementing adaptive level of regularization are described as 'non-parametric'.

Under the assumption that these discs are axisymmetric and thin, the proposed non-parametric methods described in this paper yield in principle a unique distribution: the smoothest solution consistent with all the available observables, the knowledge of the level of noise in each measurement and some objective physical constraints that a satisfactory distribution should fulfil.

Section 2 presents all relevant theoretical aspects of regularization and non-parametric inversion for galactic discs distributions. Section 3 present the various algorithms and the corresponding numerical techniques, which we implemented in steps to carry efficiently this two-dimensional minimization. It corresponds in essence to an extension of the work of Skilling & Bryan (1984) for maximum entropy to other penalizing functions that are more relevant in this context. All techniques are implemented in Section 4 on simulated data arising when the slit of the spectrograph is aligned with the long axis of the projected disc. A discussion follows.

2 NON-PARAMETRIC INVERSION FOR FLAT AND ROUND DISCS

The non-parametric inversion problem involves finding the best solution to equation (2) for the distribution function when only discretized and noisy measurements of $F_\phi(R,v_\phi)$ are available.

A distinction between *parametric* and *non-parametric* descriptions may seem artificial: it is only a function of how many parameters are needed to describe the model with respect to the number of independent measurements. In a parametric model there is a small number of parameters compared with the number of data samples. This makes the inversion for the parametric model somewhat regularized, i.e. well-conditioned. Once the model has been chosen, however, there is no way to control the level of regularization and the inversion will always produce a solution, whether the parametric model and its implicit level of regularization is correct or not. In a non-parametric model, as a result of the discretization, there is also a finite number of parameters but it is comparable to and usually larger than the number of data samples. In this case, the amount of information extracted from the data is controlled explicitely by the regularization. Here the latter non-parametric method is therefore preferred, because no particular unknown physical model for disc distributions is to be favoured.

2.1 The discretized kinematic integral equation

Since ε is an even function of v_R and since the relation between v_R and ε is one-to-one on the interval $v_R\in[0,\infty)$ and for given R and v_ϕ, equation (2) can be rewritten explicitly as

$$F_\phi(R,v_\phi)=\sqrt{2}\int\limits_{-Y(R,v_\phi)}^{0}\frac{f(\varepsilon,R\,v_\phi)}{\sqrt{\varepsilon+Y(R,v_\phi)}}\,\mathrm{d}\varepsilon\,, \tag{3}$$

where the effective potential is given by

$$Y(R,v_\phi)=\psi(R)-\frac{1}{2}v_\phi^2\,. \tag{4}$$

For a given angular momentum h the minimum specific energy is

$$\varepsilon_{\min}(h)=\min_{R\in[0,\infty)}\left\{\frac{h^2}{2R^2}-\psi(R)\right\}. \tag{5}$$

From equation (3), the generic ill-conditioning of equation (2) appears clearly, since the integral relation connecting the azimuthal velocity distribution and the underlying distribution is an Abel transform (i.e. a half derivative).

Given the error level in the measurements and the finite number of data points $N_{\rm data}$, $f(\varepsilon,h)$ is derived by fitting the data with some model. Since the number of physically relevant distributions $f(\varepsilon,h)$ is very large, a small number of parameters cannot describe the solution without further assumptions (i.e. other than the assumption that the disc is round and thin). A general approach must therefore be adopted; for instance, the solution can be described by its projection on to a basis of functions $\{e_k(\varepsilon,h);k=1,\ldots,N\}$:

$$f(\varepsilon,h)=\sum_{k=1}^{N}f_k\,e_k(\varepsilon,h)\,. \tag{6}$$

The parameters to fit are the weights f_k. In order to fit a wide variety of functions, the basis must be very large; consequently the description of $f(\varepsilon,h)$ is no longer parametric but rather non-parametric.

In order to account for the fact that the equilibrium should not incorporate unbound stars it is best to define the functions $e_k(\varepsilon,h)$ of equation (6) so that they are identically zero outside the interval $(\varepsilon, h) \in [\varepsilon_{\min}(h), 0] \times \mathbb{R}$. It is convenient to rectify this interval while replacing the integration over specific energy in equation (3) by an integration with respect to

$$\eta = 1 - \frac{\varepsilon}{\varepsilon_{\min}(h)} , \tag{7}$$

and to use a new basis of functions

$$\hat{e}_k(\eta, h) \equiv e_k\left[(1-\eta)\,\varepsilon_{\min}(h),\ h\right] ,$$

which are zero outside the interval $(\eta, h) \in [0, 1] \times \mathbb{R}$. Here η is some measure of the eccentricity of the orbit. Using these new basis functions, the distribution function becomes

$$\hat{f}(\eta, h) \equiv f\left[(1-\eta)\,\varepsilon_{\min}(h),\ h\right] = \sum_{k=1}^{N} f_k\ \hat{e}_k(\eta, h) . \tag{8}$$

Another important advantage of this reparametrization is that the distributions $\hat{f}(\eta, h)$ can be assumed to be smoother functions along η and h since these distributions correspond to the equilibia of relaxed and cool systems which have gone through some level of violent relaxation in their formation processes and where most orbits are almost circular. Note nonetheless that this assumption is somewhat subjective and introduces some level of bias corresponding to what is considered to be a good distribution function, as will be discussed in Section 5. Clearly the assumption that the distribution function should be smooth (i.e. without strong gradients) in the variable η yields different constraints on the sought solution from assuming that it should be smooth in the variable ε.

Real data correspond to discrete measurements R_i and $v_{\phi j}$ of R and v_ϕ respectively. Following the non-parametric expansion in equation (8), equation (3) now becomes

$$F_{i,j} \equiv F_\phi(R_i, v_{\phi j}) = \sum_{k=1}^{N} a_{i,j,k}\, f_k , \tag{9}$$

with

$$a_{i,j,k} = \sqrt{-2\varepsilon_{\min i,j}} \int_{\eta_{\mathrm{c}i,j}}^{1} \frac{\hat{e}_k(\eta, R_i\, v_{\phi j})}{\sqrt{\eta - \eta_{\mathrm{c}i,j}}}\, \mathrm{d}\eta , \tag{10}$$

where

$$\varepsilon_{\min i,j} \equiv \varepsilon_{\min}(R_i\, v_{\phi j}) , \quad \eta_{\mathrm{c}i,j} \equiv 1 + Y(R_i, v_{\phi j})/\varepsilon_{\min i,j} . \tag{11}$$

The implementation of this linear transformation for linear B-splines is given in Appendix A. Since the relations between $F_\phi(R, v_\phi)$ and $f(\eta, h)$ or $\hat{f}(\eta, h)$ are linear, equation (9) – the discretized form of the integral equation (2) – can be written in a matrix form by grouping index i with index j:

$$\mathbf{F} = \mathbf{a}{\cdot}\mathbf{f} . \tag{12}$$

The problem of solving equation (2) then becomes a linear inversion problem.

2.2 Maximum penalized likelihood

In order to model a wide range of distributions $\hat{f}(\eta, h)$ with good accuracy, the basis $\{\hat{e}_k(\eta, h); k = 1, \ldots, N\}$ must be sufficiently general (otherwise the solutions will be biased by the choice of the basis just as a parametric approach is biased by the choice of the model). The inversion should therefore be regularized and performed so as to avoid physically irrelevant solutions. Indeed, being a distribution, $\hat{f}(\eta, h)$ must for instance be positive and normalized. Finally, the inversion should provide some level of flexibility to account for the fact that the sought distribution might have a critical behaviour for some fraction of phase space, such as that corresponding to radial orbits. It should also cope with incomplete data sets and should yield some means of extrapolation.

In order to address these specificities let us explore techniques able to perform a reliable practical inversion of this ill-conditioned problem, and put the method described in this paper into context. The Bayesian description provides a suitable framework to discuss how the practical inversion of equation (12) should be performed.

2.2.1 Bayesian approach

When dealing with real data, noise must be accounted for: instead of the exact solution of equation (9), it is more robust to seek the *best* solution compatible with the data and, possibly, additional constraints. A criterion allowing us to select such a solution is provided by probability analysis. Indeed, given the measured data $\tilde{\mathbf{F}}$, one would like to recover the most probable underlying distribution $\mathbf{f}$. This is achieved by maximizing the probability of the distribution $\mathbf{f}$ given the data $\tilde{\mathbf{F}}$, $\Pr(\mathbf{f} \,|\, \tilde{\mathbf{F}})$, with respect to $\mathbf{f}$. According to Bayes' theorem, $\Pr(\mathbf{f} \,|\, \tilde{\mathbf{F}})$ can be rewritten as

$$\Pr(\mathbf{f} \,|\, \tilde{\mathbf{F}}) = \frac{\Pr(\tilde{\mathbf{F}} \,|\, \mathbf{f})\Pr(\mathbf{f})}{\Pr(\tilde{\mathbf{F}})} , \tag{13}$$

where $\Pr(\tilde{\mathbf{F}} \,|\, \mathbf{f})$ is the probability of the data $\tilde{\mathbf{F}}$ given that it should obey the distribution $\mathbf{f}$, while $\Pr(\tilde{\mathbf{F}})$ and $\Pr(\mathbf{f})$ are respectively the probability of the data $\tilde{\mathbf{F}}$ and the probability of the distribution $\mathbf{f}$. Since $\Pr(\tilde{\mathbf{F}})$ does not depend on $\mathbf{f}$, maximizing $\Pr(\mathbf{f} \,|\, \tilde{\mathbf{F}})$ with respect to $\mathbf{f}$ is equivalent to minimizing

$$Q(\mathbf{f}) = L(\mathbf{f}) + \mu R(\mathbf{f}) , \tag{14}$$

with

$$L(\mathbf{f}) = -\alpha \log\left[\Pr(\tilde{\mathbf{F}} \,|\, \mathbf{f})\right] + c , \tag{15}$$

$$\mu R(\mathbf{f}) = -\alpha \log\left[\Pr(\mathbf{f})\right] + c' , \tag{16}$$

with $\alpha > 0$ and where c and c' are constants that account for any contribution which does not depend on $\mathbf{f}$. Minimizing the likelihood, $L(\mathbf{f})$, enforces consistency of the model with the data while minimizing $R(\mathbf{f})$ tends to give the 'most probable solution' when no data is available, as discussed in Section 2.2.3.

2.2.2 Maximum likelihood

Minimization of $L(\mathbf{f})$ alone in equation (14) yields the maximum likelihood solution. The exact expression of $-\log\left[\Pr(\tilde{\mathbf{F}} \,|\, \mathbf{f})\right]$ can usually be derived and depends on the noise statistics. For instance, assuming that the noise in the measured data follows a normal law, maximizing the likelihood of the data is obtained by minimizing the χ^2 of the data:

$$-\log\left[\Pr(\tilde{\mathbf{F}} \,|\, \mathbf{f})\right] = \frac{1}{2}\chi^2 + c'' \quad \text{with} \quad \chi^2 \equiv \sum_{i,j} \frac{(F_{i,j} - \tilde{F}_{i,j})^2}{\mathrm{Var}\,(\tilde{F}_{i,j})} ,$$

where $F_{i,j}$ is the model of F_ϕ given by equation (9) and $\tilde{F}_{i,j}$ denotes the values of F_ϕ at (R_i, v_{ij}). Minimization of χ^2 is known as *chi-squared fitting*. Throughout this paper and for the sake of clarity, Gaussian noise is assumed, while defining the likelihood term by

$$L(\mathbf{f}) = \chi^2(\mathbf{f}) = \sum_{i,j} \frac{(F_{i,j} - \tilde{F}_{i,j})^2}{\mathrm{Var}\,(\tilde{F}_{i,j})} , \tag{17}$$

(which incidentally corresponds to the choice $\alpha = 2$ in equation 15). In the limit of a large number of independent measurements, N_{data}, χ^2 follows a normal law with an expected value and a variance given by

$$\mathrm{Expect}(\chi^2) = N_{\mathrm{data}} , \qquad \mathrm{Var}\,(\chi^2) = 2\, N_{\mathrm{data}} . \tag{18}$$

It follows that any distribution, **f**, yielding a value of χ^2 in the range $N_{\rm data} \pm \sqrt{2\,N_{\rm data}}$ is perfectly consistent with the measured data: none of these distributions can be said to be better than others on the basis of the measured data alone.

For a parametric description and provided that the number of parameters is small compared with $N_{\rm data}$, the region around the minimum of χ^2 is usually very narrow. In this case, χ^2 fitting may be sufficiently robust to produce a reliable solution (though this conclusion depends on the noise level and assumes that the parametric model is correct).

In a non-parametric approach, given the functional freedom left in the possible distributions, it is likely that the value of the χ^2 can be made arbitrarily small, i.e. much smaller than $N_{\rm data}$. Consequently, the solution that minimizes χ^2 is not reliable: it is too good to be true! In other words, solely minimizing χ^2 in a non-parametric description leads to an over-interpretation of the data: because of the ill-conditioned nature of the problem, many features in the solution are likely to be artefacts produced by amplification of noise or numerical rounding errors.

2.2.3 Regularization

Minimizing the likelihood term forces the model to be consistent with some objective information: the measured data. Nevertheless, this approach provides no means of selecting a particular solution from among all those which are consistent with the data [i.e. those for which $L(\mathbf{f}) = N_{\rm data} \pm \sqrt{2\,N_{\rm data}}$]. Taking into account $\mu R(\mathbf{f}) = -\alpha \log[\Pr(\mathbf{f})] + c''$ in equation (14) yields a natural procedure by which to choose between those solutions. At the very least, there are some objective properties of the distribution $\hat{f}(\eta, h)$ which are not enforced by χ^2 fitting (e.g. positivity) and which could be accounted for by the fact that $\Pr(\mathbf{f})$ must be zero [i.e. $R(\mathbf{f}) \rightarrow \infty$] for physically irrelevant solutions.

Unfortunately, e.g. for noisy data, taking into account those objective constraints alone is seldom sufficient: additional ad hoc constraints are needed to regularize the inversion problem. To that end, $R(\mathbf{f})$ is generally defined as a so-called *penalizing function* which increases with the discrepancy between **f** and those *subjective constraints*.

To summarise, the solution of equation (2) is found by minimizing the quantity $Q(\mathbf{f}) = L(\mathbf{f}) + \mu\, R(\mathbf{f})$ where $L(\mathbf{f})$ and $R(\mathbf{f})$ are respectively the likelihood and regularization terms and where the parameter $\mu > 0$ allows us to tune the level of regularization. The introduction of the Lagrange multiplier μ in equation (14) is formally justified by the fact that $Q(\mathbf{f})$ should be minimized subject to the constraint that $L(\mathbf{f})$ should be equal to some value, say $N_{\rm e}$. For instance, with $L(\mathbf{f}) = \chi^2(\mathbf{f})$ one would choose

$$N_{\rm e} \in [N_{\rm data} - \sqrt{2\,N_{\rm data}}, N_{\rm data} + \sqrt{2\,N_{\rm data}}]\,.$$

2.2.4 Definitions of the penalizing function

When data consist of samples of a continuous physical signal, uncorrelated noise will contribute to the roughness of the data. Moreover, noise amplification by an ill-conditioned inversion is likely to produce a forest of spikes or small-scale structures in the solution. As discussed previously, assuming that the 'probability' $\Pr(\mathbf{f})$ increases with the smoothness of $\hat{f}(\eta, h)$, the penalizing function should limit the effects of noise while not affecting (i.e. biasing) too much the range of possible shape of $\hat{f}(\eta, h)$. To that end, the penalizing function $R(\mathbf{f})$ should be defined so as to measure the roughness of **f**.

Many different penalizing functions can be defined to measure the roughness of $\hat{f}(\eta, h)$, for instance by minimizing (Wahba 1990)

$$R(\mathbf{f}) = \iint \left[\nabla^n \hat{f} \cdot \nabla^n \hat{f}\right] \mathrm{d}\eta\, \mathrm{d}h\,, \quad \text{with} \quad \nabla = \left(\frac{\partial \hat{f}}{\partial h}, \frac{\partial \hat{f}}{\partial \eta}\right) \tag{19}$$

(where $n > 1$) will enforce the smoothness of $\hat{f}(\eta, h)$. In the instance of a discretized signal for equation (8), such quadratic penalizing functions can be generalized by the use of a positive definite operator **K** (Titterington, 1985):

$$R_{\rm quad}(\mathbf{f}) = \mathbf{f}^{\perp} \cdot \mathbf{K} \cdot \mathbf{f}\,, \tag{20}$$

where $\mathbf{f}^{\perp}$ stands for the transpose of **f**.

Strict application of the Bayesian analysis implies that the penalizing function $R(\mathbf{f})$ is $-\log[\Pr(\mathbf{f})]$ (up to an additive constant and the factor μ) which is the negative of the entropy of **f**. This has led to the family of maximum entropy methods (hereafter MEM) which are widely used to solve ill-conditioned inverse problems. In fact MEM only differs from other regularized methods by the particular definition of the penalizing function, which provides positivity ab initio. A possible definition of the negentropy is (Skilling 1989)

$$R_{\rm MEM}(\mathbf{f}) = \sum_k \left[f_k \log \frac{f_k}{p_k} - f_k + p_k\right]\,, \tag{21}$$

where **p** is the a priori solution: the entropy is maximized when $\mathbf{f} = \mathbf{p}$. Although there are arguments in favour of that particular definition, there are many other possible options (Narayan & Nityananda 1986) that lead to similar solutions. Penalizing functions in MEM all share the property that they become infinite as **f** reaches zero, thus enforcing positivity. In order to enforce the smoothness of the solution further, Horne (1985) has suggested the use of a floating prior, defining **p** to be **f** smoothed by some operator **S**:

$$\mathbf{p} = \mathbf{S} \cdot \mathbf{f}\,. \tag{22}$$

For instance, along *each dimension* of $\hat{f}(\eta, h)$, the following monodimensional smoothing operator is applied:

$$p_i = \begin{cases} (1-\gamma) f_i + \gamma f_{i+1}\,, & \text{if } i = 1\,, \\ \gamma f_{i-1} + (1-2\gamma) f_i + \gamma f_{i+1}\,, & \text{if } 1 < i < n\,, \\ (1-\gamma) f_i + \gamma f_{i-1}\,, & \text{if } i = n\,, \end{cases}$$

with $0 \leq \gamma \leq 1/2$ (here $\gamma = 1/4$); here $i = 1, ..., n$ stands for the index along the dimension considered. This operator conserves energy, i.e. $\sum p = \sum f$.

The penalizing functions $R_{\rm quad}(\mathbf{f})$ or $R_{\rm MEM}(\mathbf{f})$ with a floating prior $\mathbf{p} = \mathbf{S} \cdot \mathbf{f}$ are implemented in the simulations to enforce the smoothness of the solution.

2.2.5 Adjusting the weight of the regularization

Thompson & Craig (1992) compared many different *objective methods* to fix the actual value of μ. Generally speaking, these methods consist of minimizing $Q(\mathbf{f})$ given by equation (14) subject to the constraints $L(\mathbf{f}) = N_{\rm e}$ where $N_{\rm e}$ is equivalent to the number of degrees of freedom of the model. Among those methods, two can be applied to non-quadratic penalizing functions (such as the negentropy).

The most simple approach is to minimize $Q(\mathbf{f})$ subject to the constraint that $L(\mathbf{f}) = \mathrm{Expect}[L(\mathbf{f})] = N_{\rm data}$. This yields an *over-regularized* solution (Gull 1989) since it is equivalent to assuming that regularization controls no degrees of freedom.

A second method is that of Gull (1989) who demonstrated that the Lagrange parameter should be tuned so that $Q(\mathbf{f}) = N_{\mathrm{data}}$, i.e. $N_{\mathrm{e}} = N_{\mathrm{data}} - \mu R(\mathbf{f})$. In other words, the sum of the number of degrees of freedom controlled by the data and by the entropy is equal to the number of measurements. This method is very simple to implement but can lead to *under-regularized* solutions (Gull 1989; Thompson & Craig 1992). Indeed if the subjective constraints pull $\mathbf{f}$ too far from the true solution then $R(\mathbf{f})$ takes a high value as soon as any structure appears in $\hat{f}(\eta, h)$. As a result, in order to meet $Q(\mathbf{f}) = N_{\mathrm{data}}$, the value of μ is found to be very small by this procedure. For instance, this occurs in MEM methods when choosing a uniform prior $\mathbf{p}$ since a uniform distribution is very far from the true distribution. Nevertheless, this kind of problem was not encountered with a floating prior (Horne 1985). In the algorithm described below this latter method (i.e. Gull plus Horne methods) is implemented to obtain a sensible value for μ.

Another potentially attractive way to find the value of μ is the cross-validation method (Wahba & Wendelberger 1979) since it relies solely on the data. Let $\dot{F}_{i,j}$ be the value at (i, j) of the model that fits the subset of data derived while excluding measurement (i, j) (in other words, $\dot{F}_{i,j}$ predicts the value of the assumed missing data point $\tilde{F}_{i,j}$); since the fit is achieved by minimizing $Q(\mathbf{f})$, the total prediction error, given by

$$\mathrm{TPE} = \sum_{i,j} \frac{[\dot{F}_{i,j} - \tilde{F}_{i,j}]^2}{\mathrm{Var}(\tilde{F}_{i,j})}$$

will depend on the sought value of μ. The so-called cross-validation method chooses the value of μ that minimizes TPE. When the number of data points is large this method becomes too CPU-intensive. Nonetheless, Wahba (1990) and also Titterington (1985) provide efficient means of choosing μ when the model is linear which involve constructing the so-called generalized cross-validation estimator for the TPE.

3 NUMERICAL OPTIMIZATION

In the previous section it was shown that the inversion problem reduces to the minimization of a multidimensional function $Q(\mathbf{f}) = L(\mathbf{f}) + \mu R(\mathbf{f})$ with respect to a great number of parameters (from a few 10^4 to 10^6) and subject to the constraints that (i) the likelihood term keeps some target value: $L(\mathbf{f}) = N_{\mathrm{e}}$, (ii) all parameters remain positive and (iii) special care is taken along some physical boundaries. Unfortunately there exists no general black-box algorithm able to perform this kind of optimization.

Let us therefore investigate in turn three techniques to carry the minimization, of increasing efficiency and complexity: direct methods, iterative minimization along a single direction (accounting for positivity at fixed regularization) and iterative minimization with a floating regularization weight.

3.1 Linear solution

Using quadratic regularization, the problem is solved by minimizing

$$Q_{\mathrm{quad}}(\mathbf{f}) = (\tilde{\mathbf{F}} - \mathbf{a}\cdot\mathbf{f})^{\perp}\cdot\mathbf{W}\cdot(\tilde{\mathbf{F}} - \mathbf{a}\cdot\mathbf{f}) + \mu\, \mathbf{f}^{\perp}\cdot\mathbf{K}\cdot\mathbf{f}, \tag{23}$$

where $\mathbf{W}$ is the inverse of the covariance matrix of the data. The solution $\mathbf{f}_{\mathrm{quad}}$ that minimizes Q_{quad} is

$$\mathbf{f}_{\mathrm{quad}} = (\mathbf{a}^{\perp}\cdot\mathbf{W}\cdot\mathbf{a} + \mu\,\mathbf{K})^{-1}\cdot\mathbf{a}^{\perp}\cdot\mathbf{W}\cdot\mathbf{F}. \tag{24}$$

This solution, which is linear with respect to the data, is clearly not constrained to be positive.

3.2 Non-linear optimization

Linear methods only provide raw, possibly locally negative, solutions. At the very least, enforcing positivity of the solution – more generally if the penalized function is not quadratic – requires non-linear minimization. In that case, the minimization of $Q(\mathbf{f})$ must be carried out by successive approximations.

At the n^{th} step, such iterative minimization methods usually proceed by varying the current parameters $\mathbf{f}^{(n)}$ along a direction $\delta\mathbf{f}^{(n)}$ so as to minimize Q; the new estimate of the parameters reads

$$\mathbf{f}^{(n+1)} = \mathbf{f}^{(n)} + \lambda^{(n)}\,\delta\mathbf{f}^{(n)}, \tag{25}$$

where the optimum step size $\lambda^{(n)}$ is the scalar

$$\lambda^{(n)} = \arg\{\min_{\lambda}[Q(\mathbf{f}^{(n)} + \lambda\,\delta\mathbf{f}^{(n)})]\}. \tag{26}$$

The problem is therefore to choose suitable successive directions of minimization.

3.2.1 Optimum direction of minimization

In principle, the optimum direction of minimization $\delta\mathbf{f}$ could be derived from the Taylor expansion,

$$Q(\mathbf{f} + \delta\mathbf{f}) \simeq Q(\mathbf{f}) + \sum_k \delta f_k \frac{\partial Q}{\partial f_k} + \frac{1}{2}\sum_{k,l} \delta f_k \delta f_l \frac{\partial^2 Q}{\partial f_k \partial f_l}, \tag{27}$$

that is minimized for the step

$$\delta\mathbf{f} = -\left(\nabla\nabla Q\right)^{-1}\cdot\nabla Q, \tag{28}$$

where ∇Q and $\nabla\nabla Q$ are respectively the gradient vector and the Hessian matrix of $Q(\mathbf{f})$:

$$\nabla Q_k = \frac{\partial Q}{\partial f_k}, \qquad \nabla\nabla Q_{k,l} = \frac{\partial^2 Q}{\partial f_k \partial f_l}.$$

The whole difficulty of multidimensional minimization lies in estimating the inverse of the Hessian matrix, which may typically be too large to be computed and stored. A further difficulty arises when $Q(\mathbf{f})$ is highly non-quadratic (e.g. in MEM) since the behaviour of $Q(\mathbf{f})$ can significantly differ from that of its Taylor expansion.

There exist a number of multidimensional minimization numerical routines that avoid the direct computation of the inverse of the Hessian matrix: e.g. steepest descent, conjugate gradient algorithm, Powell's method, etc. (Press et al. 1988). For the steepest descent method, the direction of minimization is simply given by the gradient: $\delta\mathbf{f}_{\mathrm{SD}} = -\nabla Q$. Other more efficient multidimensional minimization methods attempt to build information about the Hessian while deriving a more optimal direction, i.e. a better approximation of $-(\nabla\nabla Q)^{-1}\cdot\nabla Q$. For instance, the conjugate-gradient method builds a series of optimum conjugate directions $\delta\mathbf{f}_{\mathrm{CG}}$, each of which is a linear combination of the current gradient and the previous direction (Press et al. 1988). Among those improved methods and when the number of parameters is very large, the choice of conjugate gradient is driven by efficiency both in terms of convergence rate and memory allocation.

3.2.2 Accounting for positivity

Let us now examine the non-linear strategy leading to a minimization of $Q(\mathbf{f})$ with the constraint that $\hat{f}(\eta, h) \geq 0$ everywhere. We will assume that the basis of functions $\{\hat{e}_k(\eta, h)\}$ is chosen so that the positivity constraint is equivalent to enforcing that $f_k \geq 0$; $\forall k$ (see Appendix A for an example of such a basis).

When seeking the appropriate step size given by equation (26), it is possible to account for positivity by limiting the range of $\lambda^{(n)}$:

$$\mathbf{f}^{(n+1)} \geq 0 \quad \Leftrightarrow \quad -\min_{\delta f_k^{(n)}>0} \frac{f_k^{(n)}}{\delta f_k^{(n)}} \leq \lambda^{(n)} \leq -\max_{\delta f_k^{(n)}<0} \frac{f_k^{(n)}}{\delta f_k^{(n)}}.$$

In practice this procedure blocks the steepest descent method long before the right solution is found. It is in fact better to truncate negative values after each step:

$$f_k^{(n+1)} = \max\{0, f_k^{(n)} + \lambda^{(n)}\,\delta f_k^{(n)}\}\,.$$

Also, any of these methods to enforce positivity breaks conjugate gradient minimization because the latter assumes that the true minimum of $Q(\mathbf{f}^{(n)} + \lambda^{(n)}\,\delta\mathbf{f}^{(n)})$ is reached while varying $\lambda^{(n)}$.

Thiébaut & Conan (1995) circumvent this difficulty thanks to a reparametrization that enforces positivity. Following their argument, Q is minimized here with respect to a new set of parameters $\mathbf{x}$, such as

$$f_k = g(x_k)\,, \quad \text{with } g : \mathbb{R} \mapsto \mathbb{R}_+\,. \tag{29}$$

The following various reparametrizations meet these requirements:

$$f_k = \exp(x_k) \qquad \Rightarrow \qquad g'(x_k)^2 = f_k^2\,,$$
$$f_k = x_k^{2n} \quad (n \text{ positive integer}) \quad \Rightarrow \quad g'(x_k)^2 \propto f_k^{2-1/n}\,.$$

When $Q(\mathbf{f})$ is quadratic, $Q(\mathbf{f} + \lambda\delta\mathbf{f})$ is a second-order polynomial with respect to λ, the minimization of which can trivially be performed with a very limited number of matrix multiplications. One drawback of the reparametrization is that, since $g(\cdot)$ is non-linear, $Q \circ g(\mathbf{x})$ is necessarily non-quadratic. In that case the exact minimization of $Q \circ g(\mathbf{x} + \lambda\delta\mathbf{x})$ – mandatory in conjugate gradient or Powell's methods – requires many more matrix multiplications. Another drawback is that the direction of investigation derived by conjugate gradient or Powell's methods may no longer be optimal, requiring many more steps to obtain the overall solution. This latter point follows from the fact that these methods collect information about the Hessian while taking into account the previous steps, whereas for a non-quadratic functional this information becomes obsolete very soon since the Hessian (with respect to $\mathbf{x}$) is no longer constant (Skilling & Bryan 1984).

Consequently, instead of varying the parameters $\mathbf{x}$, we propose to derive a step $\delta\mathbf{f}$ for varying $\mathbf{f}$ from the reparametrisation that enforces positivity. Letting $\delta\mathbf{x}$ be the chosen direction of minimization for $\mathbf{x}$, the sought parameters reads $g(x_k + \lambda\,\delta x_k) \simeq f_k + \lambda\,\delta x_k\,g'(x_k)$. Identifying the right-hand side of this expression with $f_k + \lambda\delta f_k$ yields $\delta f_k = \delta x_k\,g'(x_k)$. Using the steepest descent direction,

$$\delta x_k = -\frac{\partial Q}{\partial x_k} = -\frac{\partial Q}{\partial f_k}\,g'(x_k)\,,$$

yielding finally

$$\delta f_k = -\frac{\partial Q}{\partial f_k}\,g'(x_k)^2 = -\frac{\partial Q}{\partial f_k} f_k^{\nu}\,, \tag{30}$$

with $1 \leq \nu \leq 2$ depending on the particular choice of $g(\cdot)$.

3.2.3 Algorithm for one-dimensional minimization: positivity at fixed μ

In Appendix B we show that other authors have derived a very similar optimum direction of minimization but in the more restrictive case of a regularization by R_{MEM}. Note that our approach is not limited to this type of penalizing function since positivity is enforced extrinsically. In short, the minimization step is derived from the unifying expression:

$$\delta f_k = -q_k \nabla Q_k\,, \tag{31}$$

where the gradient is scaled by (see Appendix B)

$$q_k = \begin{cases} f_k^{\nu}\,, & \text{this work (with } 1 \leq \nu \leq 2)\,, \\ f_k\,, & \text{Richardson–Lucy}\,, \\ f_k/\mu\,, & \text{classical MEM}\,, \\ \dfrac{f_k}{\mu + f_k \sum_{i,j} \frac{a_{i,j,k}^2}{\mathrm{Var}(\tilde{F}_{i,j})}}\,, & \text{Cornwell–Evans.} \end{cases}$$

The scheme of the one-dimensional optimization algorithm is illustrated in Fig. 1. Iterations are stopped when the decrement in $Q(\mathbf{f})$ becomes negligible, i.e. when

$$|Q(\mathbf{f} + \lambda\delta\mathbf{f}) - Q(\mathbf{f})| \leq \epsilon\,|Q(\mathbf{f})|\,,$$

where $\epsilon > 0$ is a small number which should not be smaller than the square root of the machine precision (Press et al. 1988). Lucy (1994) has suggested another stop criterion based on the value of the ratio

$$\rho = ||\delta\mathbf{f}|| / \left(||\delta\mathbf{f}_{\mathrm{L}}|| + ||\delta\mathbf{f}_{\mathrm{R}}||\right),$$

where $\delta\mathbf{f}_{\mathrm{L}}$ and $\delta\mathbf{f}_{\mathrm{R}}$ are the directions that minimize the likelihood and the regularization terms

$$\delta\mathbf{f}_{\mathrm{L}} = -\mathbf{q} \times \nabla L \quad \text{and} \quad \delta\mathbf{f}_{\mathrm{R}} = -\mu\mathbf{q} \times \nabla R\,,$$

where $\times$ denotes the element-wise product [in other words $\mathbf{q}$ stands loosely for $\mathrm{Diag}(q_1, \ldots, q_n)$]. In practice and regardless of the particular choice for $\mathbf{q}$, the algorithm makes no significant progress when ρ becomes smaller than 10^{-5}.

3.2.4 Performance issues

During the tests, it was found that the conjugate gradient method with reparametrization and the iterative method with direction given by equation (31) require roughly the same number of steps (one step involving minimization along a new direction of minimization). However, the non-linear reparametrization required to enforce positivity in the conjugate gradient method prevents interpolation and means that the method in effect spends much more time (a factor of 10 to 20) performing line minimization. Also, when the current estimate is far from the solution, the minimization direction following our prescription (30) (or that of classical MEM or Lucy) requires fewer steps than that of Cornwell & Evans to bring $\mathbf{f}$ near the true solution. When the current estimate is sufficiently close to the solution, Cornwell & Evans' method requires half as many steps as the other methods to reach the solution. The best compromise is to start with $\delta f_k \propto -f_k \nabla Q_k$, then after some iterations use $\delta\mathbf{f} = \delta\mathbf{f}_{\mathrm{CE}}$. As a rule of thumb, for low signal-to-noise ratios (SNR ~ 5) about as many steps as the number of parameters are required, while for high signal-to-noise ratios (SNR ≥ 30) fewer steps are needed (up to 10 times less). The fact remains that with these methods trial and error iterations are required to find the appropriate value for μ. The different implementations are illustrated and compared in Figs 2 and 3, as described in Section 4.

Accounting for positivity in multidimensional optimization therefore leads to a modified steepest descent algorithm for which the current gradient is locally rescaled. A faster convergence is achieved when some information from the Hessian is extracted appropriately. However, the above-described algorithm assumes that optimization is performed with a fixed value of the Lagrange parameter μ. Let us now turn to a more general minimization along

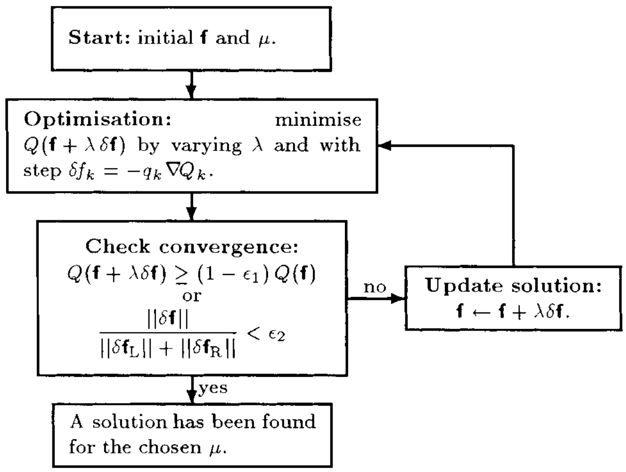

Figure 1. Synopsis of the single-direction minimization algorithm. Here $\epsilon_1 \simeq 10^{-8}$ and $\epsilon_2 \simeq 10^{-5}$.

several directions which allows μ to be adjusted 'on the fly' during the minimization.

3.3 Minimization along several directions

3.3.1 Skilling & Bryan method revisited

In the context of maximum entropy image restoration, Skilling & Bryan (1984) (hereinafter SB) have proposed a powerful method which is both efficient in optimizing a non-linear problem with a great number of parameters and able to vary automatically the weight of regularization so that the sought solution satisfies $L(\mathbf{f}) = N_{\mathrm{e}}$. Here their approach is further generalized to any penalizing function. In short, SB derive their method from the following remarks.

(i) To account for positivity, they suggest an appropriate 'metric' (or rescaling) which is equivalent to multiplying each minimization direction by $\mathbf{q} = \mathbf{f}$.

(ii) The regularization weight μ is adjusted at each iteration to meet the constraint $L(\mathbf{f}) = N_{\mathrm{e}}$. Therefore, instead of minimizing along the single direction $-\mathbf{q} \times (\nabla L + \mu \nabla R)$, at least two directions are considered: $-\mathbf{q} \times \nabla L$ and $-\mathbf{q} \times \nabla R$.

(iii) As the Hessian is not constant, for instance because μ is allowed to vary, no information is carried from the previous iterations. This clearly excludes conjugate gradient or similar optimization methods, but favours non-quadratic penalizing functions for which the Hessian is not assumed to be constant.

(iv) If the whole Hessian cannot be computed, it can nevertheless be applied to any vector $\mathbf{e}$ of the same size as $\mathbf{f}$ in a finite number of operations, e.g. two matrix multiplications for the likelihood term: $\nabla\nabla L \cdot \mathbf{e} = 2\,\mathbf{a}^{\perp} \cdot (\mathbf{a} \cdot \mathbf{e})$ (where, for the sake of simplicity, the diagonal weighting matrix was omitted here). This illustrates how this method provides a means to include some knowledge from the local Hessian while seeking the optimum minimization direction.

3.3.2 Local minimization subspace

In order to adjust the regularization weight, at least two simultaneous directions of minimization should be used: $-\mathbf{q} \times \nabla L$ and

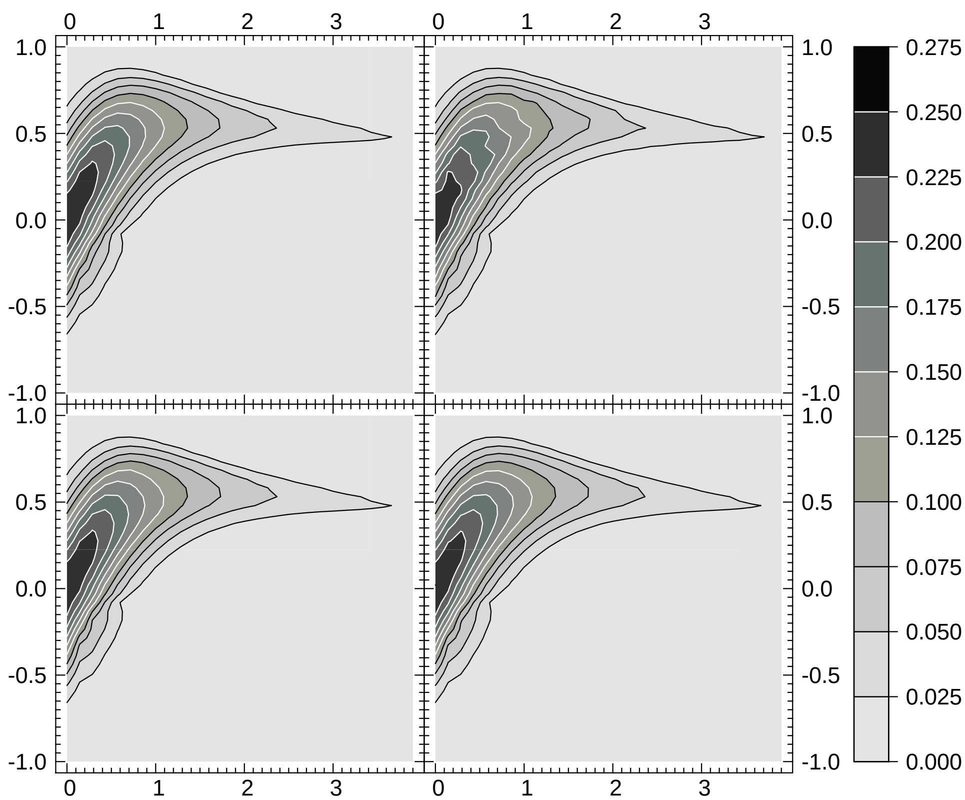

Figure 2. Fit of F_{ϕ} (as described in Section 4) with various penalizing functions. From top left to bottom right: (1) original F_{ϕ} and F_{ϕ} restored by (2) MEM with uniform prior, (3) MEM with floating smooth prior and (4) quadratic regularization, i.e. R_{quad} with $n = 1$ as defined in equation (19). As expected, no significant difference is to be found in the fits, though in panel (2), F_{ϕ} is slightly rougher. The SNR is 50.

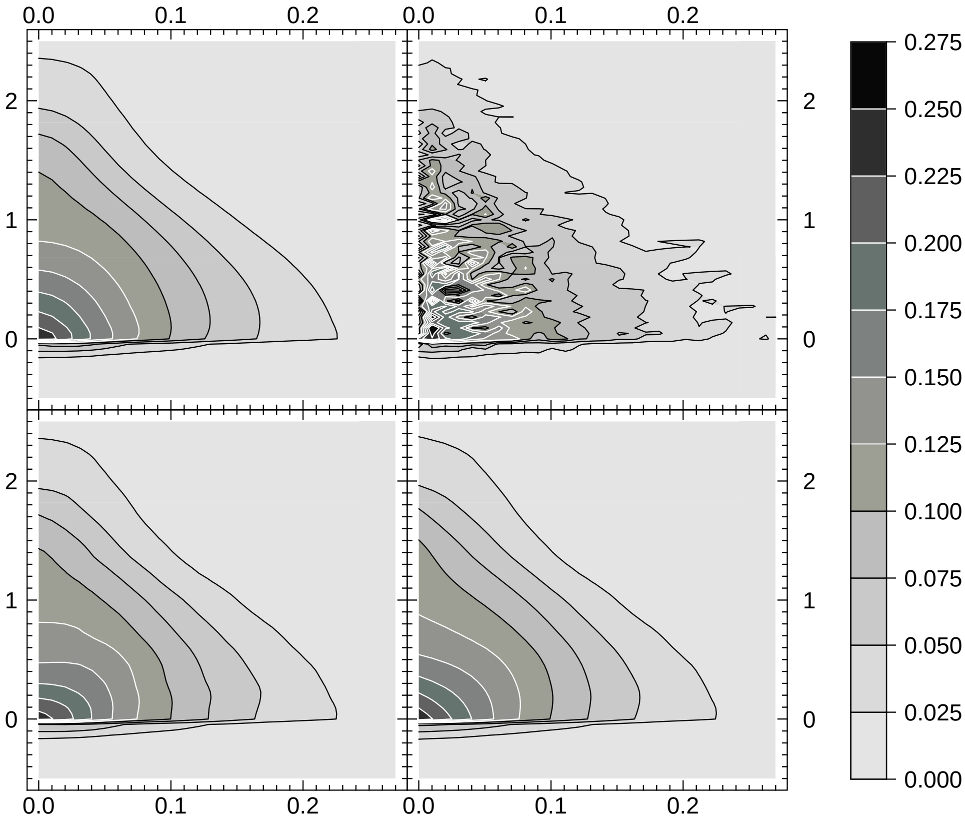

Figure 3. Restoration of $\hat{f}(\eta, h)$ from Fig. 2. From top left to bottom right: (1) true distribution and distributions restored by (2) MEM with uniform prior, (3) MEM with smooth floating prior and (4) quadratic regularization, i.e. $R_{\rm quad}$ with $n = 1$ as defined in equation (19). Note that MEM with a uniform prior yields a rather unsmooth solution, which is expected since no penalty is imposed by this method for lack of smoothness.

$-\mathbf{q} \times \nabla R$. Furthermore, the local Hessian provides other directions of minimization to increase the convergence rate. Using matrix notation, the Taylor expansion of $Q(\mathbf{f})$ for two simultaneous directions $\delta\mathbf{f}_1$ and $\delta\mathbf{f}_2$ reads

$$Q(\mathbf{f} + \delta\mathbf{f}_1 + \delta\mathbf{f}_2) \simeq Q(\mathbf{f}) + \delta\mathbf{f}_1^\perp \cdot \nabla Q + \frac{1}{2}\delta\mathbf{f}_1^\perp \cdot \nabla\nabla Q \cdot \delta\mathbf{f}_1 + \delta\mathbf{f}_2^\perp \cdot [\nabla Q + \nabla\nabla Q \cdot \delta\mathbf{f}_1] + \frac{1}{2}\delta\mathbf{f}_2^\perp \cdot \nabla\nabla Q \cdot \delta\mathbf{f}_2 \,,$$

where the Hessian and gradient are evaluated at $\mathbf{f}$. Given a first direction $\delta\mathbf{f}_1$, the optimal choice for a second direction is

$$\delta\mathbf{f}_{2,\rm opt} = -(\nabla\nabla Q)^{-1} \cdot (\nabla Q + \nabla\nabla Q \cdot \delta\mathbf{f}_1) \,.$$

In MEM, recall that positivity is enforced explicitly by the regularization penalty function while efficient minimization methods rely on the approximation of $(\nabla\nabla Q)^{-1}$ by a scaling vector $\mathbf{q}$. The optimum first two directions then become in MEM

$$\delta\mathbf{f}_{1,\rm opt} \simeq -\mathbf{q} \times \nabla Q \,, \quad \text{and} \quad \delta\mathbf{f}_{2,\rm opt} \simeq -\mathbf{q} \times (\nabla Q + \nabla\nabla Q \cdot \delta\mathbf{f}_1) \,.$$

Since the first term on the right-hand side of the expression for $\delta\mathbf{f}_{2,\rm opt}$ is $\delta\mathbf{f}_{1,\rm opt}$, the two near optimum directions sought are, finally,

$$\delta\mathbf{f}_1 = -\mathbf{q} \times \nabla Q \,, \quad \text{and} \quad \delta\mathbf{f}_2 = -\mathbf{q} \times (\nabla\nabla Q \cdot \delta\mathbf{f}_1) \,. \tag{32}$$

Similar considerations yield further possible directions:

$$\delta\mathbf{f}_n = -\mathbf{q} \times (\nabla\nabla Q \cdot \delta\mathbf{f}_{n-1}) \,. \tag{33}$$

If the rescaling, $\mathbf{q}$, provides too good an approximation of the inverse of the Hessian, then $\delta\mathbf{f}_1$ and $\delta\mathbf{f}_2$ will be almost identical (i.e. antiparallel); hence using only one is sufficient. In other words, since the local Hessian is accounted for by the use of additional directions of minimization, there is no need for $\mathrm{Diag}(\mathbf{q})$ to be an accurate approximation of $(\nabla\nabla Q)^{-1}$. The crude rescaling given by equation (B1) is therefore sufficient, i.e. taking $\mathbf{q} = \mathbf{f}$. This definition of $\mathbf{q}$ has the further advantage of warranting positive values of $\mathbf{f}$ and does not depend on the actual value of μ (which is obviously not the case for the Hessian).

If no term in $Q(\mathbf{f})$ enforced positivity, it was shown earlier that the reparametrization (29) would. From the Taylor expansion of $Q(\mathbf{x})$, the first two steepest descent directions with respect to the parameters $\mathbf{x}$ are given by

$$\delta x_{1,k} = -\frac{\partial Q}{\partial x_k} = -g'(x_k)\nabla Q_k \,,$$
$$\delta x_{2,k} = -\sum_l \frac{\partial^2 Q}{\partial x_k \partial x_l}\frac{\partial Q}{\partial x_l} = -g'(x_k)\sum_l \nabla\nabla Q_{k,l} g'(x_l)\delta x_{1,l} \,. \tag{34}$$

Since $\delta f_k \simeq g'(x_k)\delta x_k$, the two optimum directions of minimization for the parameters $\mathbf{f}$ are

$$\delta f_{1,k} = -g'(x_k)^2 \nabla Q_k \,, \tag{35}$$

$$\delta f_{2,k} = -g'(x_k)^2 \sum_l \nabla\nabla Q_{k,l} \delta f_{1,l} \,, \tag{36}$$

which are incidentally identical to those given by equation (32), provided that $q_k = g'(x_k)^2$.

For all the regularization penalizing functions considered here, clearly the best choice is to use directions given by the Hessian applied to equation (34) when other directions of minimization than those related to the gradient are considered. Since μ can vary, the

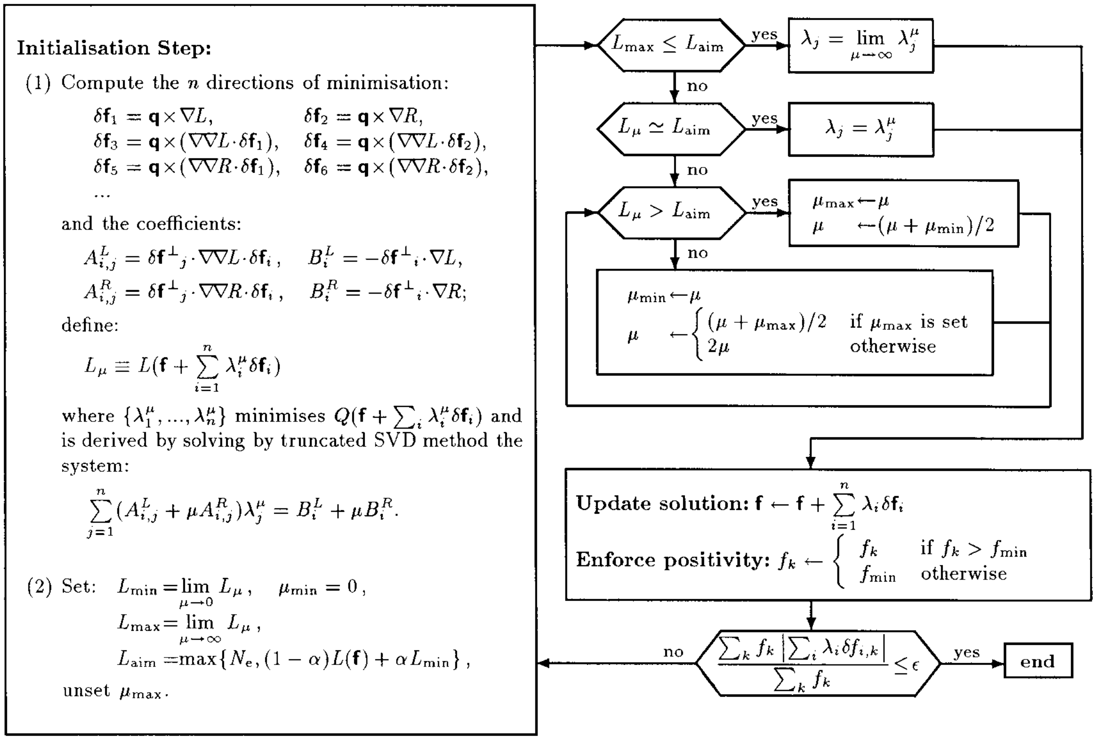

Figure 4. Synopsis of the multiple-direction multidimensional minimization algorithm with adjustment of the regularization weight. In this algorithm, $f_{\min} > 0$ is a small threshold used to avoid negative values, $0 \le \epsilon \ll 1$ is a small value used to check convergence.

Hessians of L and R have to be applied separately. At each step, the minimization is therefore performed in the $n = 3\times 2 = 6$ dimensional subspace defined by

$$\delta\mathbf{f}_1 = -\mathbf{q}\times\nabla L, \qquad \delta\mathbf{f}_2 = -\mathbf{q}\times\nabla R,$$
$$\delta\mathbf{f}_3 = -\mathbf{q}\times(\nabla\nabla L\cdot\delta\mathbf{f}_1), \quad \delta\mathbf{f}_4 = -\mathbf{q}\times(\nabla\nabla L\cdot\delta\mathbf{f}_2), \tag{37}$$
$$\delta\mathbf{f}_5 = -\mathbf{q}\times(\nabla\nabla R\cdot\delta\mathbf{f}_1), \quad \delta\mathbf{f}_6 = -\mathbf{q}\times(\nabla\nabla R\cdot\delta\mathbf{f}_2),$$

where

$$q_k = f_k^\nu \quad \text{with} \quad 1 \le \nu \le 2. \tag{38}$$

When $\nu = 1$, $\mathbf{q}$ is the same metric as that introduced by SB while relying on other arguments. Depending on the actual expression for $\nabla\nabla R$ (and in particular in MEM with a constant prior), a smaller number of directions need be explored (for instance, SB used only $n = 3$ simultaneous directions, because when $\mathbf{q} = \mathbf{f}$, $\nabla\nabla R = 1/\mathbf{f}$ so $\delta\mathbf{f}_5 = \delta\mathbf{f}_1$, $\delta\mathbf{f}_6 = \delta\mathbf{f}_2$; they also use a linear combination of $\delta\mathbf{f}_3$ and $\delta\mathbf{f}_4$). In this n-dimensional subspace, a simple second-order Taylor expansion of $Q(\mathbf{f} + \sum_{i=1}^n \lambda_i\delta\mathbf{f}_i)$ shows that the optimum set of weights sought, $\{\lambda_1, ..., \lambda_n\}$, is given by the solution of the n linear equations parametrized by μ and given by

$$\sum_{j=1}^{n}\lambda_j\delta\mathbf{f}^\perp{}_j\cdot(\nabla\nabla L + \mu\nabla\nabla R)\cdot\delta\mathbf{f}_i = -\delta\mathbf{f}^\perp{}_i\cdot(\nabla L + \mu\nabla R). \tag{39}$$

Now, in that subspace the optimization may be ill-conditioned (i.e. the set of linear equations is linearly dependent in a numerical sense). In order to deal with this degeneracy, truncated SVD decomposition (Press et al. 1988) is used to find a set of numerically independent directions. In practice, the rank of the six linear equations varies from 2 (very far from the solution or when convergence is almost reached) to typically 5 or 6. This method turns out to be much easier to implement than the bidiagonalization suggested by SB.

3.3.3 'On the fly' derivation of the regularization weight

At each iteration a strategy similar to that of SB was adopted here to update the value of μ.

(i) $L_{\min}$ and $L_{\max}$ are the values of the likelihood term in the subspace in the limits $\mu\to 0$ and $\mu\to\infty$ respectively. The corresponding solutions give what we call the maximum likelihood solution and the maximum regularized solution in the subspace.

(ii) If $L_{\max} < N_e$ the maximum regularized solution corresponding to $L_{\max}$ is adopted to proceed to the next iteration. Otherwise, in order to avoid relaxing the regularization and following SB, a modest reachable goal is fixed:

$$L_{\rm aim} = \max\{N_e, (1-\alpha)L_{\rm prev} + \alpha L_{\min}\},$$

where $L_{\rm prev}$ is the likelihood value at the end of the previous iteration, while $0<\alpha<1$ (say $\alpha = 2/3$). A simple bisection method is applied to seek the value of μ for which the solution of equation (39) yields $L = L_{\rm aim}$.

Following this scheme, the algorithm varies the value of μ so that at each iteration the likelihood is reduced until it reaches its target value; then the regularization term is minimized while the likelihood remains constant.

As a stop criterion, a measure of the statistical discrepancy between two successive iterations,

$$\sum_k f_k^{(n)}\left|f_k^{(n+1)} - f_k^{(n)}\right| \Big/ \sum_k f_k^{(n)},$$

is computed. In practice, in order to avoid over-regularization, N_e is taken to be $N_{\rm data} - \sqrt{2N_{\rm data}}$. The corresponding scheme of the n-dimensional optimization algorithm is illustrated in Fig. 4.

3.3.4 Performance and assessments

The optimization of $Q(\mathbf{f})$ in a multidimensional subspace yields many practical advantages.

(i) It provides faster convergence rates (about 10 times fewer overall iterations and even many fewer when accounting for the number of inversions required to derive the regularization weight) and less overall CPU time in spite of the numerous matrix multiplications involved in computing the n directions of minimization and their images by the Hessians.
(ii) It yields a more robust algorithm because it is less sensitive to local minima and also because the routine requires less tuning.
(iii) Since μ varies between iterations and since the local Hessian is always re-estimated, the solution can be modified 'on the fly', e.g. rescaled, without perturbing the convergence. Hence the normalization is no longer an issue.

This algorithm presents the following set of improvements over that of Skilling & Bryan:

(i) A more general penalizing function than entropy is considered (e.g. entropy with floating prior or quadratic penalizing function) which yields a different *metric*, derived heuristically. This yields almost the same optimization subspace but from a different approach.
(ii) Truncated SVD is implemented to avoid ill-conditioned problems in this minimization subspace.

4 SIMULATIONS

4.1 Specifics of stellar disc inversion

4.1.1 Models of azimuthal velocity distributions

Simulated azimuthal velocity distributions can be constructed via the prescription described in Pichon & Lynden-Bell (1996). The construction of Gaussian line profiles compatible with a given temperature requires specifying the mean azimuthal velocity of the flow, $\langle v_\phi \rangle$, on which the Gaussian should be centred, the surface density $\Sigma(R)$ and the azimuthal velocity dispersion σ_ϕ. The line profile F then reads

$$F_\phi(R, v_\phi) = \frac{\Sigma(R)}{\sqrt{2\pi}\,\sigma_\phi} \exp\left(-\frac{\left[v_\phi - \langle v_\phi \rangle\right]^2}{2\sigma_\phi^2} \right). \tag{40}$$

Here the azimuthal velocity dispersion is related to the azimuthal pressure, p_ϕ, by

$$\sigma_\phi^2 = p_\phi/\Sigma - \langle v_\phi \rangle^2 . \tag{41}$$

The azimuthal pressure p_ϕ follows from the equation of radial support,

$$\langle v_\phi^2 \rangle - R\frac{\partial \psi}{\partial R} = \frac{\partial\left(R\Sigma\sigma_R^2\right)}{\Sigma\,\partial R} , \tag{42}$$

and the kinematical 'temperature' of the disc with a given Toomre number Q (Toomre 1964),

$$Q = 0.298\, \sigma_R \kappa / \Sigma . \tag{43}$$

The expression of the average azimuthal velocity, $\langle v_\phi \rangle$, may be taken to be that which leads to no asymmetric drift equation:

$$\Sigma\langle v_\phi \rangle^2 = p_\phi - p_R(\kappa R / 2v_c)^2 , \tag{44}$$

where κ is the epicyclic frequency and v_c the velocity of circular orbits. Equations (40)–(44) provide a prescription for the Gaussian azimuthal line profile F_ϕ. These azimuthal velocity distributions are used throughout to generate simulated data corresponding to the iso-Q Kuzmin disc.

4.1.2 The counter-rotating radial orbits

As shown in Fig. 2, the azimuthal distributions of our models have Gaussian tails corresponding to stars on almost radial orbits with small negative azimuthal velocity. These few stars play a strong dynamical role in stabilizing the disc, and as such should not be overlooked since they significantly increase the azimuthal dispersion of inner orbits, effectively holding the inner galaxy against its self-gravity. Now this Gaussian tail translates in the momentum – reduced energy space as a small group of counter-rotating orbits introducing a cusp in the number of stars near $h = 0$ (this cusp is only apparent because the distribution is clearly continuous and differentiable across this line). In practice the regularization constraint across $h = 0$ is relaxed, in effect treating the two regions independently.

4.2 Validation and efficiency

4.2.1 Quality estimation

Clearly the quality level for the reconstructed distribution will depend upon the application in mind. For stability analysis, the relevant information involves, for instance, the gradient of the distribution function in action space. An acute quality estimator would therefore involve such gradients, although their computation requires some knowledge of the orbital structure of the disc, and is beyond the scope of this paper. Here the quality of the reconstruction is estimated while computing the mean distribution-weighted residual between the distribution sought and the model recovered. It is defined by

$$\mathrm{error}(\mathbf{f}) = \left\langle |f - f_{\mathrm{true}}| \right\rangle \simeq \frac{\sum_i f_{\mathrm{true},i}\, |f_i - f_{\mathrm{true},i}|}{\sum_i f_{\mathrm{true},i}} , \tag{45}$$

and measures the restored distribution error with respect to the true distribution $\hat{f}_{\mathrm{true}}(\eta, h)$ averaged over the stars (i.e. weighted by the distribution $\hat{f}_{\mathrm{true}}$). A set of simulations displaying this estimate for the quality of the reconstruction was carried while varying respectively the outer sampled edge of the disc, the signal-to-noise ratio, the sampling in the modelled distribution and the Q number of the underlying data set, and is described below.

4.2.2 Validation: zero noise level inversion

An inversion without any noise is first carried out in order to assess the accuracy of our inversion routine. This turned out to be more difficult than performing the inversion with some knowledge of the noise level since in this instance there is no simple assessment of a good value for the Lagrange multiplier μ. All the ill-conditioning arises because of round-off errors alone. The original distribution was eventually recovered in this manner with a mean distribution-weighted residual, error($\mathbf{f}$), smaller than one part in 10^4. From now on, the distribution $\hat{f}(\eta, h)$ derived from this noise-free inversion is taken in our simulations as the 'true' underlying distribution.

4.2.3 Choice of the penalizing function

Let us now investigate the penalizing functions corresponding to three methods of regularization, namely MEM with uniform prior (as advocated by SB), MEM with smooth floating prior (given by equations 21 and 22) and quadratic regularization (equation 20).

© 1998 RAS, MNRAS **301**, 419–434

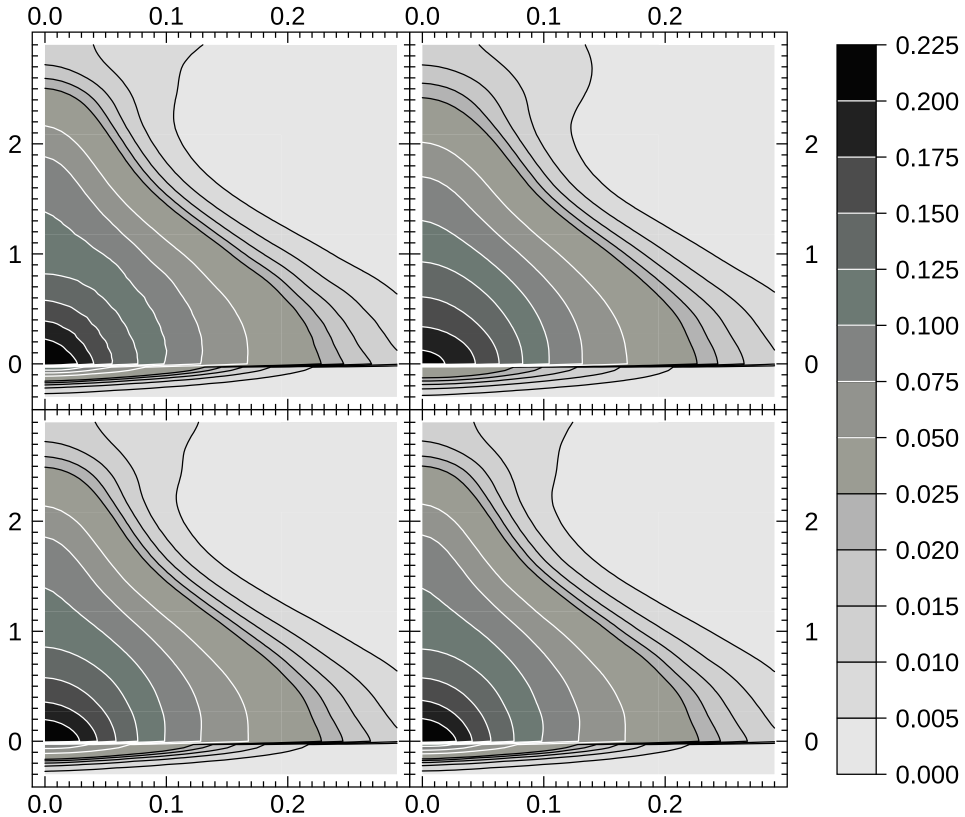

Figure 5. From top left to bottom right, (1) true distribution (approximately that of a disc with Toomre parameter $Q = 1.25$) and mean restoration of $\hat{f}(\eta, h)$ out of 40 iterations for a SNR of (2) 5, (3) 30 and (4) 100. Abscissa is normalized specific energy η and ordinate is specific angular momentum h. Note that the isocontours are not sampled uniformly in order to display counterrotating stars more acurately.

The corresponding modelled and recovered distribution functions are given in Figs 2 and 3. From these figures it is apparent that MEM with uniform prior is unsuitable in this context (this failure is expected, because here – in contrast to image reconstruction – no cut-off frequency forbids the roughness of the solution), while MEM with floating prior or quadratric penalizing function enforces smoothness, provides similar results and yields a satisfactory level of regularization. In particular, no qualitative difference occurs owing to the penalizing function alone, which is a good indication that the inversion is carried out adequately. Note that the apparent cusp at $h = 0$ is well accounted for by the inversion.

Regularization by negentropy with a floating smooth prior was used in the following simulations.

4.2.4 *Efficiency: the influence of the noise level*

In the second part of the simulations, the performance of the proposed algorithm with respect to noise level is investigated. The noise is assumed to obey a normal distribution with standard deviation given by

$$\sigma_{i,j} = \frac{F_{i,j}}{\mathrm{SNR}} + \max(\mathbf{F})\,\sigma_{\mathrm{bg}}\,. \tag{46}$$

In other words, the intrinsic data noise has a constant signal-to-noise ratio, SNR, and the detector adds a uniform readout noise. Three sets of runs corresponding respectively to a constant signal-to-noise ratio of SNR $= 5$, 30, and 100 are presented in Figs 5 (mean recovered $\mathbf{f}$), 6 (sample $\mathbf{f}$) and 7 (standard deviation). In all cases, the readout noise level is $\sigma_{\mathrm{bg}} = 10^{-4}$. The figures only display the inner part of the distribution while the simulation carries the inversion for h in the range $[-2, 3[$ and all possible energies.

The main conclusion to be drawn from these figures is that the main features – both qualitatively and quantitatively given the noise level – of the distribution are clearly recovered by this inversion procedure. Note that near the peak of the distribution at $h = 0$, $\eta = 0$, the recovered distribution is nonetheless slightly rounder than its original counterpart for the noisier (SNR $= 5$, panel 2) simulation. This is a residual bias of the reparametrization: the sought distribution is effectively undersampled in that region and the regularization truncates the residual high frequency in the signal while incorrectly assuming that it corresponds to noise. If the sampling had been tighter in that region, say using regular sampling in $\exp(-\eta)$, the regularization would not have truncated the restored distribution. Alternatively, in order to retain algebraic kernels, uneven logarithmic sampling in the spline basis is an option.

This point illustrates the danger of non-parametric inversions, which clearly provide the best approach to model fitting but leave open some level of model-dependent tuning and consequently can give rise to potential flaws when the wrong assumptions are made about the nature of the sought solution for low signal-to-noise ratio. For instance, the above-described procedure would inherently ignore any central cusp in the disc if the sampling in parameter space were too sparse in that region, even if the SNR level is adequate to resolve the cusp. Since in practice systematic over-sampling is computationally onerous, given the dimensionality of the problem, special care should be taken in deciding what an adequate sampling and parametrization involves.

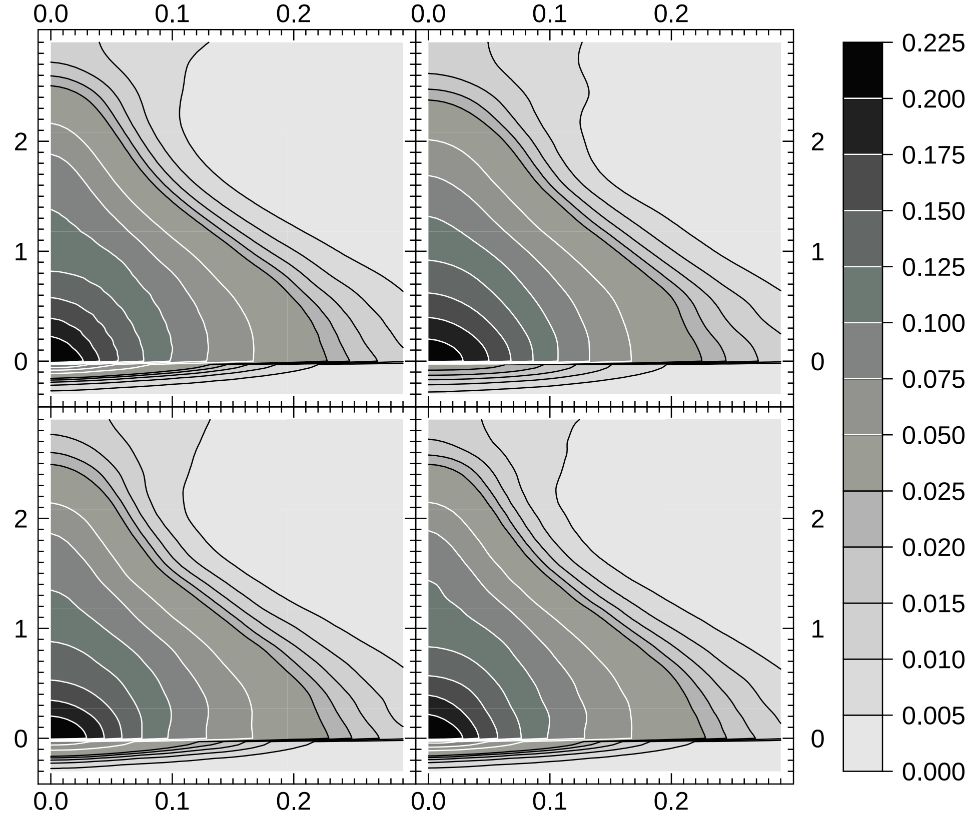

Figure 6. True distribution and one sample for each SNR out of the 40 restorations carried out, displayed as in Fig. 5. Abscissa is normalized specific energy η and ordinate is specific angular momentum h. Comparison with Fig. 5 shows that the inversion is successful both statistically and on a per sample basis.

Finally, Fig. 8 gives the evolution of the fit error signal-to-noise ratio for various Toomre parameters Q. This figure illustrates that the method is independent of the model disc, whether dynamically cold or hot.

4.2.5 *Efficiency: sampling in the model*

The best sampling of the phase space of f must be derived considering that two opposite criteria should be balanced: (i) using too few basis functions would bias the solution, (ii) using more basis functions consumes more CPU time. A simple and intuitive way to check that the sampling rate is sufficient is to ensure that the minimum likelihood reached without regularization is much smaller than the target likelihood, i.e. $\lim_{\mu\to 0} L(\mathbf{f}) \ll N_{\rm e}$. Unregularized inversions of noisy data with an increasing number of basis functions and signal-to-noise ratios was therefore performed. In practice, since completely omitting the regularization leads to a difficult minimization problem because of the large number of local minima, regularization was instead relaxed by using a target likelihood somewhat lower than the number of measurements ($N_{\rm e} \simeq 0.1 \times N_{\rm data}$). The results of these simulations are displayed in Fig. 9. It appears that $\sim 150 \times 150$ basis functions are sufficient to avoid the sampling bias. In all the other simulations, 150×150 or 200×200 basis functions are used.

4.2.6 *Efficiency: truncation in the measurements*

The inversion algorithm presented here makes no assumption about completeness of the input data set. Therefore, the recovered solution f can in principle be used to predict missing values in F_ϕ, in contrast to direct inversion methods which assume that F_ϕ is known everywhere. Real data will always be truncated at some maximum radius $R \leq R_{\rm max}$. There may also be missing measurements; caused for instance by dust clouds which hide some parts of the disc, or departure from axial symmetry corresponding to spiral structure. In order to check how extrapolation proceeds, various truncated data sets were simulated and the inversion was carried out. Fig. 10 shows the departure of the recovered distributions from the true one as a function of the outer radius $R_{\rm max}$ up to which data is measured. This figure also shows that our inversion allows some extrapolation, because, for all signal-to-noise ratios considered, the error reaches its minimum value as soon as $R_{\rm max} \geq 7$ (i.e. 4 half-mass radii, $R_{\rm e}$, compared with the true disc radius which was 10 half-mass radii in our simulations). Note that interpolation is likely to be more reliable than extrapolation; our method should therefore be much less sensitive to data 'holes'.

5 DISCUSSION AND CONCLUSION

This paper presented a series of practical algorithms to obtain the distribution function f from the *measured* distributions $F_\phi(R, v_\phi)$, compared these algorithms with existing algorithms and described in detail the best-suited algorithms to carry out efficient inversion of such ill-conditioned problems. It was argued that non-parametric modelling is best suited to describing the underlying distribution functions when no particular physical model is to be favoured. For these inversions, regularization is a crucial issue and its weight should be tuned 'on the fly' according to the noise level.

The mimimization algorithms described in Section 3 are fairly

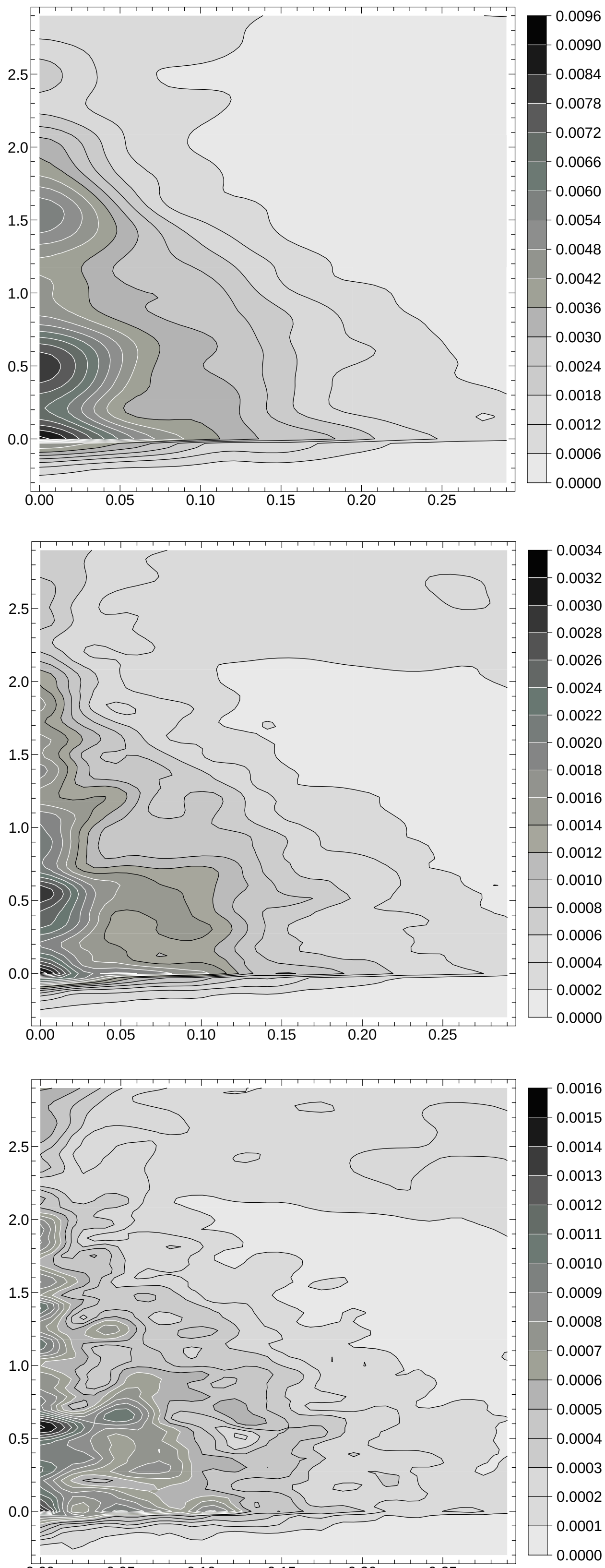

Figure 7. Standard deviation for each SNR out of the 40 restorations carried out displayed as in Fig. 5. From top to bottom: SNR $= 5$, 30 and 100. Abscissa is normalized specific energy η and ordinate is specific angular momentum h. Note that the maximum residual error is well below the signal amplitude and decreases with increasing SNR.

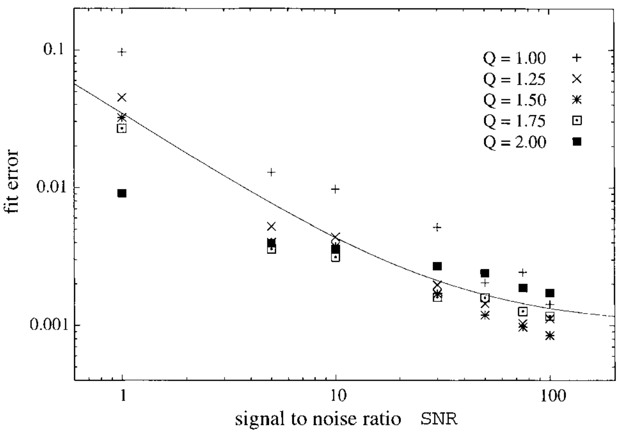

Figure 8. Fit error versus SNR for various Toomre parameters Q. The fit error approximatively decreases as: error $\simeq 1.0\times10^{-3} + 3.4\times10^{-2}/\mathrm{SNR}$ (solid curve).

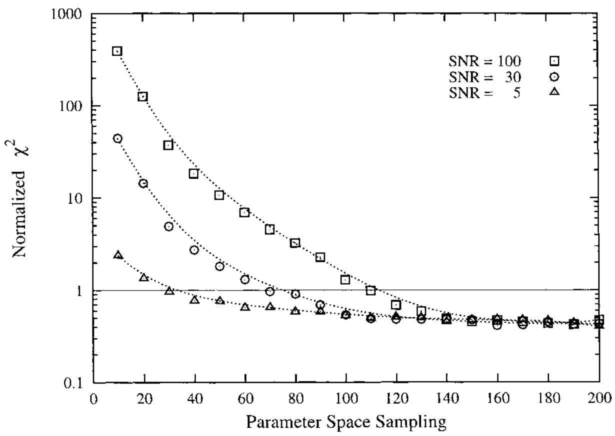

Figure 9. Minimum value of the normalized likelihood term χ^2/N_{data} that can be reached as the number of basis functions varies and for different signal-to-noise ratios. The abscissa is the number of samples along η and h, which is the square root of the number of basis functions used. The number of data measurements was 50×50 and the maximum disc radius was $R_{\max} = 7$. The curves are only here to clarify the figure: the simulation results are plotted as symbols.

general and could clearly be implemented for minimization problems corresponding to other geometries, such as that corresponding to the recovery of distributions for spheroid or elliptical galaxies explored by other authors (e.g. Merritt & Tremblay 1993). More generally, they could be applied to any linear inversion problem where positivity is an issue; this includes image reconstruction, all Abel deprojection arising in astronomy, etc. Applying this algorithm to simulated noisy data, it was found that the criteria of positivity and smoothness alone are sufficiently selective to regularize the inversion problem up to very low signal-to-noise ratios (SNR ~ 5) as soon as data is available up to $4R_{\mathrm{e}}$. The inversion method described here is directly applicable to published measurements.

Here the inversion assumed that the H I rotation curve gives access to an analytic (or spline) form for the potential. A more general procedure should provide a simultaneous recovery of the potential, although such a routine would be very CPU-intensive since changing the potential requires us to recompute the matrix $\mathbf{a}$. Nevertheless, it would be straightforward to extend the scope of this method to configurations corresponding to an arbitrary slit angle, such as those sketched in Appendix C, or to data produced by

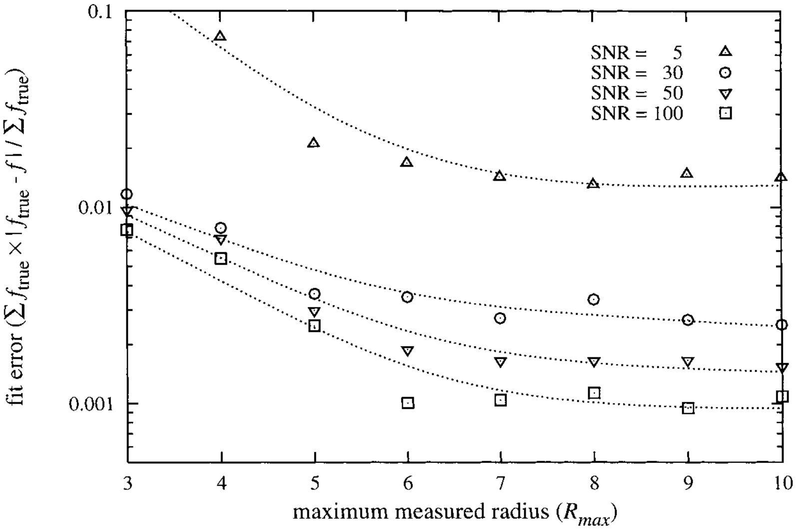

Figure 10. Evolution of the fit error as the data set is truncated in radius for different signal-to-noise ratios (in the simulations the disc outer edge was assumed to be 10). The curves are only here to guide the eye: the results of simulation are plotted as symbols.

integral field spectroscopy [such as TIGRE or OASIS (Bacon et al 1995)], where the redundancy in azimuth would lead to higher signal-to-noise ratios if the disc were still assumed to be flat and axisymmetric.

Once the distribution function has been characterized, it is possible to study quantitatively all departures from the flat axisymmetric stellar models. Indeed, axisymmetric distribution functions are the building blocks of all sophisticated stability analyses, and a good phase-space portrait of the unperturbed configuration is clearly needed in order to asses the stability of a given equilibrium state. Numerical *N*-body simulations require sets of initial conditions which should reflect the nature of the equilibrium. Linear stability analysis also relies on a detailed knowledge of the underlying distribution (Pichon & Cannon 1997).

ACKNOWLEDGMENTS

We thank R. Cannon and O. Gerhard for useful discussions and D. Munro for freely distributing his Yorick programming language (available at `ftp://ftp-icf.llnl.gov:/pub/Yorick)` which we used to implement our algorithm and perform simulations. Funding by the Swiss National Fund and computer resources from the IAP are gratefully acknowledged. Special thanks are due to J. Magorrian for his help with Appendix C.

REFERENCES

Bacon R. et al., 1995, A&AS, 113, 347
Cornwell T. J., Evans K. F., 1984, A&A, 143, 77
Dehnen W. 1995, MNRAS, 274, 919
Dejonghe H., 1993, in Dejonghe H., Habing H. J., eds, IAU Symp. 153, Galactic Bulges. Kluwer, Dordrecht, p. 73
Dejonghe H., De Bruyne V., Vauterin P., Zeilinger W. W., 1996, A&A, 306, 363
Emsellem E., Monnet G., Bacon R., 1994, A&A, 285, 723
Gebhardt K. et al., 1996, AJ, 112, 105
Gull F., 1989, in Skilling J., ed., Maximum Entropy and Bayesian Methods. Kluwer, Dordrecht, p. 53
Horne K., 1985, MNRAS, 213, 129
Kuijken K., 1995, ApJ, 446, 194
Lucy L.B., 1994, A&A, 289, 983
Merrifield M. R. 1991, AJ, 102, 1335
Merritt D.,1996, AJ, 112, 1085
Merritt D.,1997, AJ, 114, 228
Merritt D., Gebhardt K., 1994, in Durret F., Mazure A., Tran Thanh Van J., eds, Proc. XXIXth Rencontre de Moriond, Clusters of Galaxies. Editions Frontiere, Singapore, p. 11
Merritt D., Tremblay B., 1993, AJ, 106, 2229
Merritt D., Tremblay B., 1994, AJ, 108, 514
Narayan R., Nityananda R., 1986, ARA&A, 24, 127
Press et al., 1988, Numerical Recipes. Cambridge Univ. Press, Cambridge
Pichon C., Cannon R., 1997, MNRAS, 291, 616
Pichon C., Lynden-Bell D., 1996, MNRAS, 282, 1143
Qian E. E., de Zeeuw P. T., van der Marel R. P., Hunter C., 1995, MNRAS, 274, 602
Skilling J., 1989, in Skilling J., ed., Maximum Entropy and Bayesian Methods. Kluwer, Dordrecht, p. 45
Skilling J., Bryan R. K., 1984, MNRAS, 211, 111
Thiébaut E., Conan J.-M., 1995, J. Opt. Soc. Am. A, 12, 485
Thompson A. M., Craig I. J. D., 1992, A&A, 262, 359
Titterington D. M., 1985, A&A, 144, 381
Toomre A., 1964, AJ, 139, 1217
Wahba G., Wendelberger, J., 1979, Mon. Weather Rev., 108, 1122
Wahba G., 1990, CBMS-NSF Regional Conf. Ser. Appl. Math., Spline Models for Observational Data. Soc. Ind. Appl. Math., Philadelphia, p. 52

APPENDIX A: BILINEAR INTERPOLATION

In this non-parametric approach, the distribution $\hat{f}(\eta, h)$ is described by its projection on to a basis of functions. If we choose a basis for which the two variables η and h are separable then equation (8) becomes

$$\hat{f}(\eta, h) = \sum_k \sum_l f_{k,l}\, u_k(\eta)\, v_l(h)\,, \tag{A1}$$

where $u_k(\eta)$ and $v_l(h)$ are the new basis functions. This description of $\hat{f}(\eta, h)$ yields

$$\tilde{F}_\phi(R_i, v_{\phi j}) = \tilde{F}_{i,j} = \sum_k \sum_l a_{i,j,k,l} f_{k,l}\,, \tag{A2}$$

where $a_{i,j,k,l}$ are coefficients which only depend on R_i, $v_{\phi j}$ and ψ_i

[$\psi(R)$ in fact]:

$$a_{i,j,k,l} = v_l(R_i\, v_{\phi j})\sqrt{-2\varepsilon_{\min i,j}}\int_{\eta_{ci,j}}^{1}\frac{u_k(\eta)}{\sqrt{\eta-\eta_{ci,j}}}\,\mathrm{d}\eta\,. \tag{A3}$$

Bilinear interpolation is implemented in the simulations described in Section 4 to evaluate $\hat{f}(\eta,h)$ everywhere. In this case, the weights $f_{k,l}$ are the values of the distribution at the sampling positions $\{(\eta_k,h_l); k=1,\ldots,K; l=1,\ldots,L\}$,

$$f_{k,l} = \hat{f}(\eta_k,h_l)\,,$$

and the basis functions are linear splines,

$$u_k(\eta) = \begin{cases} 1-\left|\frac{\eta-\eta_k}{\Delta\eta}\right| & \text{if } \eta_{k-1}\le\eta\le\eta_{k+1},\\ 0 & \text{otherwise,}\end{cases}$$

$$v_l(h) = \begin{cases} 1-\left|\frac{h-h_l}{\Delta h}\right| & \text{if } h_{l-1}\le h\le h_{l+1},\\ 0 & \text{otherwise,}\end{cases}$$

with $\eta_{k+n}=\eta_k+n\,\Delta\eta$ and $h_{l+n}=h_l+n\,\Delta h$. The bilinear interpolation is a particular case of the general non-parametric description. It yields a very sparse matrix **a** which can significantly speed up matrix multiplications. The coefficients $a_{i,j,k,l}$ can be computed analytically, although since the basis functions are defined piecewise, the integration can be performed piecewise:

$$\int_{\eta_c}^{1}\frac{u_k(\eta)}{\sqrt{\eta-\eta_c}}\,\mathrm{d}\eta = \begin{cases}\alpha_k'' & \text{for } k=1,\\ \alpha_k'+\alpha_k'' & \text{for } k=2,\ldots,K-1,\\ \alpha_k' & \text{for } k=K,\end{cases}$$

with:

$$\alpha_k' = \int_{\max\{\eta_{k-1},\eta_c\}}^{\min\{\eta_k,1\}}\frac{u_k(\eta)}{\sqrt{\eta-\eta_c}}\,\mathrm{d}\eta$$

$$= \begin{cases} 0 & \text{if } \eta_k\le\eta_c,\\ \left[\frac{2\sqrt{\eta-\eta_c}}{3\Delta\eta}(\eta-3\eta_{k-1}+2\eta_c)\right]_{\eta=\max\{\eta_{k-1},\eta_c\}}^{\eta=\min\{\eta_k,1\}} & \text{otherwise,}\end{cases}$$

and

$$\alpha_k'' = \int_{\max\{\eta_k,\eta_c\}}^{\min\{\eta_{k+1},1\}}\frac{u_k(\eta)}{\sqrt{\eta-\eta_c}}\,\mathrm{d}\eta$$

$$= \begin{cases} 0 & \text{if } \eta_{k+1}\le\eta_c,\\ \left[\frac{2\sqrt{\eta-\eta_c}}{3\Delta\eta}(3\eta_{k+1}-\eta-2\eta_c)\right]_{\eta=\max\{\eta_k,\eta_c\}}^{\eta=\min\{\eta_{k+1},1\}} & \text{otherwise.}\end{cases}$$

Another useful feature of bilinear interpolation is that the positivity constraint is straightforward to implement:

$$\hat{f}(\eta,h) = \sum_{k,l} f_{k,l}u_k(\eta)v_l(h)\ge 0;\forall(\eta,h) \quad\Leftrightarrow\quad f_{k,l}\ge 0;\forall(k,l)\,.$$

There is no such simple relation for higher order splines.

APPENDIX B: SPECIFIC MINIMIZATION METHODS FOR MEM

Several non-linear methods have been derived specifically to seek the maximum entropy solution. Let us review those briefly so as to compare them with our method (Section 3.2.2). In MEM, assuming that (i) the prior **p** does not depend on the parameters and (ii) the Hessian of the likelihood term can be neglected, the Hessian of Q is then purely diagonal:

$$\nabla\nabla Q_{k,l}\simeq\mu\,\nabla\nabla R_{k,l} = \frac{\mu\delta_{k,l}}{f_k}\,.$$

The direction of minimization is therefore

$$\delta f_{\mathrm{MEM}k} = -\frac{f_k}{\mu}\,\nabla Q_k\,. \tag{B1}$$

Skilling & Bryan (1984) discussed further refinements to speed up convergence. Cornwell & Evans (1984) approximated the Hessian $\nabla\nabla Q$ by neglecting all non-diagonal elements:

$$\nabla\nabla Q_{k,l}\simeq\delta_{k,l}\frac{\mu}{f_k}+\delta_{k,l}\sum_{i,j}\frac{a_{i,j,k}^2}{\mathrm{Var}(\tilde{F}_{i,j})}\,,$$

which yields

$$\delta f_{\mathrm{CE}k} = -\frac{f_k\,\nabla Q_k}{\mu+f_k\sum_{i,j}a_{i,j,k}^2/\mathrm{Var}(\tilde{F}_{i,j})}\,. \tag{B2}$$

In fact, $\delta f_{\mathrm{CE}k}$ is equivalent to the steepest descent step in the preferred Levenberg–Marquart method (Press et al. 1988), which is the method to fit a parametric non-linear model. Extending the Richardson–Lucy method to the maximum penalized likelihood regime, Lucy (1994) suggests

$$\delta f_{\mathrm{Lucy}k} = -f_k\left[\nabla Q_k-\frac{\sum_l f_l\nabla Q_l}{\sum_l f_l}\right], \tag{B3}$$

which is almost the same as in classical MEM but for the term $\sum_l f_l\nabla Q_l/\sum_l f_l$ which accounts for the constraint that $\sum_k f_k$ should remain constant. Note that it is sufficient to replace ∇Q_k in equation (31) by $\nabla Q_k-\sum_l q_l\nabla Q_l/\sum_l q_l$ to apply a further constraint of normalization.

With all these non-linear methods, it may also be advantageous to seek the step size that minimizes $Q(\mathbf{f}+\lambda\delta\mathbf{f})$ (Cornwell & Evans 1984; Lucy 1994).

APPENDIX C: GENERAL MODEL WITH ARBITRARY SLIT ORIENTATION

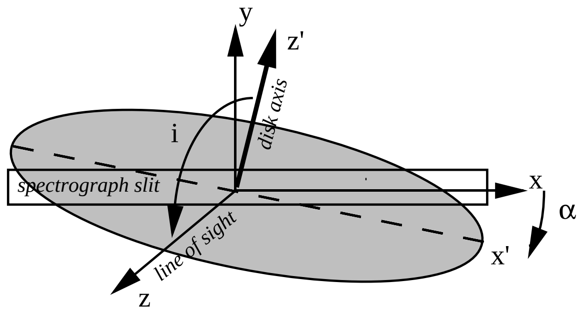

Figure C1. Angular notations.

Long-slit spectroscopic observations of a galactic disc provide the distribution

$$F_\alpha(R,v_{//}) = \int f(\varepsilon,h)\,\mathrm{d}v_\perp\,, \tag{C1}$$

where $v_{//}$ and $v_\perp$ are the star velocities (at intrinsic radius r and projected radius R) along and perpendicular to the line of sight respectively, which are related to the radial and azimuthal velocities by

$$v_R = c_1\,v_{//}+c_2\,v_\perp\,,\quad v_\phi = c_3\,v_{//}+c_4\,v_\perp \quad\text{and}\quad R = c_5\,r\,.$$

Here the c_k depend on the angle α between the slit and the major axis of the disc as measured in the plane of the sky and on the inclination i of the disc axis with respect to the line of sight (see Fig. C1). The case where the slit is parallel to the major axis of the disc, i.e. $\alpha=0$, has been examined in the main text. When $\alpha\neq 0$, the specific angular momentum $h = r\,v_\phi$ can be used as the variable of integration:

$$F_\alpha(R, v_{/\!/}) = \frac{c_5}{R\,c_4} \int_{-h_{\max}}^{h_{\max}} f(\varepsilon, h)\,\mathrm{d}h, \tag{C2}$$

where the specific energy and the integration bounds are

$$\varepsilon = \frac{1}{2} v_{/\!/}^2 + \frac{1}{2}\left(\frac{h\,c_5}{R\,c_4} - \frac{c_3}{c_4}\,v_{/\!/}\right)^2 - \psi\left(\frac{R}{c_5}\right),$$

$$h_{\max} = \frac{R}{c_5}\left(\frac{c_3}{c_4}\,v_{/\!/} + \sqrt{2\psi\left(\frac{R}{c_5}\right) - v_{/\!/}^2}\right).$$

In practice, straightforward trigonometry yields

$$c_1 = \sin(\beta)/\sin(i)\,,\ \ c_2 = \cos(\beta)\,,$$

$$c_3 = \cos(\beta)/\sin(i)\,,\ \ c_4 = \sin(\beta)\,,$$

$$c_5 = \sqrt{\cos^2(\beta) + \sin^2(\beta)\sin^2(i)}\,,$$

where β is the angle of the slit as measured in the plane of the disc, which obeys

$$\tan(\beta) = \tan(\alpha)/\sin(i)\,.$$

This paper has been typeset from a TEX/LATEX file prepared by the author.

Mon. Not. R. Astron. Soc. **000**, 000–000 (0000) Printed 26 December 2008 (MN LaTeX style file v2.2)

ASKI: towards a full-sky lensing map making pipeline

C. Pichon[1,2,3], E. Thiébaut[2,1], S. Prunet[1],
K. Benabed[1], S. Colombi[1], T. Sousbie[1,4], R. Teyssier[3,1,5]

[1] *Institut d'astrophysique de Paris & UPMC (UMR 7095), 98, bis boulevard Arago , 75 014, Paris, France.*
[2] *Observatoire de Lyon (UMR 5574), 9 avenue Charles André, F-69561 Saint Genis Laval, France.*
[3] *CEA/IRFU/SAP, l'Orme des Merisiers, 91170, Gif sur Yvette, France*
[4] *Tokyo University, Physics Dept 7-3-1 Hongo Bunkyo-ku,JP Tokyo 113-0033 Japan*
[5] *Institute für Theoretische Physik, Universität Zürich, Winterthurerstrasse 190 CH-8057 Zrich*

26 December 2008

ABSTRACT

Within the context of upcoming full-sky lensing surveys, the edge-preserving non-linear algorithm Aski (*All Sky κ Inversion*) is presented. Using the framework of Maximum A Posteriori inversion, it recovers the full-sky convergence map from noisy surveys with masks. It proceeds in two steps: (i) CCD images of possibly crowded galactic fields are deblurred using automated edge-preserving deconvolution; (ii) once the reduced shear is estimated, the convergence map is also inverted via an edge-preserving method. A feature of both components of the Aski algorithm is that the penalty can be applied in model space (i.e. *resp.* the Fourier and the harmonic coefficients of the corresponding sky brightness distribution and κ maps), while the optimization iterates back and forth between data space (i.e. *resp.* the pixels of the image and of the ellipticity map) and model space. It uses the variable metric limited memory algorithm OptimPack, which allows both optimizations to scale. The deblurring is implemented on Cartesian maps up to $16\,384^2$ pixels while the inversion is carried on the sphere for HEALPix resolutions up to $n_{\rm side} = 4096$.

For the deblurring, the quality of the deconvolution is measured using Sextractor to estimate the *relative* gain in the reduced shear achieved by the prior deblurring of the images. Cross validation as a function of the number of stars removed yields an automatic estimate of the optimal level of regularization for the deconvolution of the galaxies. It is found that when the observed field is crowded, this gain can be quite significant for realistic ground-based eight-metre class surveys. The most significant improvement occurs when both positivity and edge-preserving $\ell_1 - \ell_2$ penalties are imposed during the iterative deconvolution.

For the convergence inversion, the quality of the reconstruction is investigated on noisy maps derived from the horizon-4π N-body simulation with SNR within the range $\ell_{\rm cut} = 500 - 2500$, with and without Galactic cuts, and quantified using one-point statistics (S_3 and S_4), power spectra, cluster counts, peak patches and the skeleton. It is found that (i) the reconstruction is able to interpolate and extrapolate within the Galactic cuts/non-uniform noise; (ii) its sharpness-preserving penalization avoids strong biasing near the clusters of the map (iii) it reconstructs well the shape of the PDF as traced by its skewness and kurtosis (iv) the geometry and topology of the reconstructed map is close to the initial map as traced by the peak patch distribution and the skeleton's differential length (v) the two-points statistics of the recovered map is consistent with the corresponding smoothed version of the initial map (vi) the distribution of point sources is also consistent with the corresponding smoothing, with a significant improvement when $\ell_1 - \ell_2$ prior is applied. The contamination of B-modes when realistic Galactic cuts are present is also investigated. Leakage mainly occurs on large scales. The non-linearities involved in the model are significant on small scales near the peaks in the field.

1 INTRODUCTION

In recent years, weak shear measurements have become a major source of cosmological information. By measuring the bending of the rays of light emerging from distant galaxies, one can gain some knowledge of the distribution of matter between the emitter and ourselves, and thus probe the properties and evolution history of dark matter (Bartelmann & Schneider 2001). This technique has led to significant results in a broad spectrum of topics, from measurements of the projected dark matter power spectrum (for the latest results see Fu & et al. (2008)), 3D estimation of the dark matter spectrum (Kitching et al. 2006), studies of the higher order moments of the dark matter distribution, selection of source candidates for subsequent follow-ups (schirmer et al. 2007), and reconstruction of the mass distribution from small (Jee et al. 2007) to large scales (Massey et al. 2007). In view of these successes, numerous surveys have been planned specifically to use this probe either from ground-based facilities (eg VST-KIDS[1], DES[2] Pan-STARRS[3], LSST[4]) or space-based observatories (EUCLID/DUNE[5], SNAP[6] and JDEM[7]). More generally, it is clear that weak lensing will be a major player in the future, as it has been identified by different European and US working groups as one of the most efficient way of studying the properties of dark energy[8]. Data processing is an important issue in the exploitation of weak lensing of distant galaxies. The signal comes from the excess alignment of the ellipticities of the observed galaxies. Assuming one can ignore or deal with spurious alignments due to intrinsic effects (Hirata & Seljak 2004; Aubert et al. 2004; Pichon & Bernardeau 1999), or due to spurious lensing effects (Bridle & Abdalla 2007), the weak lensing signal will thus come from a small statistically coherent ellipticity on top of the random one of each object. Any result obtained with weak lensing on distant galaxies is thus conditioned by the quality with which shape parameters of the galaxies are recovered. This issue has of course been raised by the weak lensing community and tackled by the SHear Testing Program working group (Password 2007) whose effort have allowed for a fair comparison of the existing techniques. Schematically, the measurement of the shape parameters of the galaxies can be seen as a two-step process. First, one must correct for the non-idealities of the images due to atmospherical seeing (for ground-based telescopes), and telescope and camera aberrations. Indeed, these effects translate into an asymmetrical beam, which is varying between two images, and even possibly in the field of one image. Typically, the asymmetry induced by the instrumental response is much larger than the ellipticity to be measured. After this preprocessing step, a shape determination algorithm can be applied, and some estimation of the ellipticity of the object recovered. Stars, defects in the images, and objects too close to each other after deconvolution have to be removed from the final catalogue so as to avoid contamination from erroneous shape measurements.

After these operations, one obtains a catalogue of position and shape parameters. Many techniques exist for recovering the weak shear signal from this catalogue. For example, a lot of efforts have been devoted to the measurement of the shear two-point functions. The most used method is the measurement of the so called *Mass Aperture* averaged two-point functions, which is the result of the convolution of the shear two-point functions by a compensated filter (Schneider et al. 2002). This scheme includes the separation between the curl-free convergence-field two-point function, and the residual curl mode that can arise from incomplete PSF correction or intrinsic galaxy alignment (Crittenden et al. 2002). For three-point functions, different resummation schemes have been proposed, either using direct measurement of the shear (Bernardeau et al. 2002; Benabed & Scoccimarro 2005) or using the *Mass Aperture* filter (Takada & Jain 2003; Kilbinger & Schneider 2005).

Other applications (source detection and fit, some tomography algorithms) call for an estimation of the map of the convergence field. A convergence map can also be used to measure the two- and three-point functions as well, even if, as we will see later this is not the best way to do so. For this reason an important amount of work has already been devoted to the reconstruction of the convergence map. The problem in this reconstruction lies in the inversion of the non-local equations linking the convergence field κ, and the ellipticities of the galaxies, while controlling the noise and avoiding pollution from the spurious curl mode. Moreover, even assuming that the ellipticity catalogue was a noise free estimation of a curl-free underlying shear, the inversion could only be exact up to a global translation due to the form of the equation. Thus Bayesian techniques that use *a priori* on the solution properties to regularize the inversion problem are well suited to the reconstruction of κ. Previous works on the topic have explored different sets of *a priori* and regularization techniques (Starck et al. 2005; Marshall et al. 2002; Seitz et al. 1998; Bridle et al. 1998). The primary goal of those works being the measurement of the mass distribution in clusters, all of them are dealing only with small regions of the sky. For the same reason those works have been extended to include strong-lensing effects that can be observed around the cluster whose mass is being reconstructed using their lensing effect (Cacciato et al. 2006; Bradac et al. 2005; Halkola et al. 2006; Jee et al. 2007).

In this paper, we will focus on the reconstruction of the κ field from very large, and possibly full-sky maps, of the sky. We will thus only be interested in the weak lensing regime including the onset of the quasi-linear regime, where the non-linearities of the relation linking the ellipticities of the galaxies to the shear cannot be safely neglected. We will propose a new regularization technique that can be compared to multi resolution methods or wavelet approach (Starck et al. (2005)) and use a $\ell_1-\ell_2$ regularization scheme to perform a sharp feature preserving inversion. One of the biggest issues we will have to cope with is the incomplete coverage of the sky. We will show how our technique can deal with irregular coverage and masked portions of the sky.

Specifically, Section 2 shows how non-parametric $\ell_1-\ell_2$ deblurring can improve the construction of reduced shear, hence convergence maps. Section 3 describes the model for the reduced shear, the corresponding inverse problem, and the optimization procedure. Section 4 investigates the qual-

[1] `http://www.astro-wise.org/projects/KIDS/`
[2] `https://www.darkenergysurvey.org/`
[3] `http://pan-starrs.ifa.hawaii.edu/`
[4] `http://www.lsst.org/`
[5] `http://www.dune-mission.net/`
[6] `http://snap.lbl.gov/`
[7] `http://universe.nasa.gov/program/probes/jdem.html`
[8] see, on the European side `http://www.stecf.org/coordination/` and on the US side, `http://www.nsf.gov/mps/ast/aaac.jsp` and `http://www.nsf.gov/mps/ast/detf.asp`

ity of the global reconstruction; in particular, it probes the asymmetry/kurtosis of the recovered maps, its topology (total length and differential length of the skeleton), the recovered power spectra, the point source catalogue with and without galactic star cut. The leaking of B-modes induced by the Galactic cut is also investigated. Finally, Section 5 discusses implications for upcoming full-sky surveys and wraps up.
Appendix A describes the star removal algorithm (implemented for the cross validation estimation of the optimal level of smoothing required to deconvolve the crowded images), Appendix B details the κ inverse problem on the sphere while Appendix C derives the local plane corresponding approximation. Appendix D describes the construction of realistic κ maps.

2 DEBLURRING OF CROWDED FIELDS

The first step involved in reconstructing a full-sky map of the convergence on the sky requires estimating ellipticity and orientation maps from wide angle CCD images of large patches of the sky. Whether the experiment is ground-based, or space-born, it is advisable to correct for the effect of the instrumental response, in particular when mapping more crowded regions closer to the galactic plane. Indeed, the PSF-induced partial overlapping of galaxies within the field of view will bias the estimation of the reduced shear. As a first step towards building a full-sky map maker, let us therefore address the issue of deblurring crowded fields via regularized non parametric model fitting, and assess its efficiency in the weak lensing context.

2.1 Deblurring as an inverse problem

2.1.1 Regularized solution

Since observed objects are incoherent sources, the observed image depends linearly on the sky brightness distribution:

$$y(\boldsymbol{\omega}) = \int h(\boldsymbol{\omega}, \boldsymbol{\omega}')\, x(\boldsymbol{\omega}')\, \mathrm{d}\boldsymbol{\omega}' + e(\boldsymbol{\omega})\,,$$

where $y(\boldsymbol{\omega})$ is the observed distribution in the direction $\boldsymbol{\omega}$, $h(\boldsymbol{\omega}, \boldsymbol{\omega}')$ is the atmospheric and instrumental point spread function (PSF) which is the distribution of observed light in the direction $\boldsymbol{\omega}$ due to light coming from direction $\boldsymbol{\omega}'$, $x(\boldsymbol{\omega}')$ is the true sky brightness distribution and $e(\boldsymbol{\omega})$ is the noise. After discretization:

$$\boldsymbol{y} = \mathbf{H} \cdot \boldsymbol{x} + \boldsymbol{e}\,, \tag{1}$$

where $\boldsymbol{y}$ is the vector of pixel intensities in the observed image (the data), $\mathbf{H}$ is the matrix which accounts for the atmospheric and instrumental blurring, $\boldsymbol{x}$ is the (discretized or projected onto a basis of functions) object brightness distribution and $\boldsymbol{e}$ accounts for the errors (pixel-wise noise and modelisation approximations). Deblurring requires estimating the best sky brightness distribution given the data. Since the atmospheric and instrumental PSF results in a smoother distribution than the true one, it is well known that deblurring is an ill-conditioned problem ((Richardson 1972; Skilling et al. 1979; Tarantola & Valette 1982; Pichon & Thiébaut 1998; Pichon et al. 2001)). In other words, straightforward deblurring by applying $\mathbf{H}^{-1}$ to the data $\boldsymbol{y}$ would result in uncontrolled amplification of noise: a small change in the input data would yield unacceptably large artifacts in the solution. Regularization must be used to overcome ill-conditioning of this inverse problem. This is achieved by using additional prior constraints such as requiring that the solution be as smooth as possible, while being still in statistical agreement with the data and while imposing that the brightness distribution is positive. Following this prescription, the Maximum A Posteriori (MAP) solution $\boldsymbol{x}_\mu$ is the one which minimizes an objective function $\mathcal{Q}(\boldsymbol{x})$:

$$\boldsymbol{x}_\mu = \arg\min_{\boldsymbol{x} \geqslant 0} \mathcal{Q}(\boldsymbol{x})\,, \quad \text{with: } \mathcal{Q}(\boldsymbol{x}) = \mathcal{L}(\boldsymbol{x}) + \mu\, \mathcal{R}(\boldsymbol{x})\,, \tag{2}$$

where $\mathcal{L}(\boldsymbol{x})$ is a likelihood penalty which enforces agreement of the model with the data, $\mathcal{R}(\boldsymbol{x})$ is a *regularization* penalty which enforces prior constraints set on the model, and $\mu > 0$ is a so-called *hyper-parameter* which allow the tuning of the relative weight of the prior with respect to the data. Hence the MAP solution is a compromise between what can be inferred from the data alone and prior knowledge about the parameters of interest. Assuming Gaussian statistics for the errors $\boldsymbol{e}$ in equation (1), the likelihood penalty writes:

$$\mathcal{L}(\boldsymbol{x}) = (\mathbf{H} \cdot \boldsymbol{x} - \boldsymbol{y})^{\mathrm{T}} \cdot \mathbf{W} \cdot (\mathbf{H} \cdot \boldsymbol{x} - \boldsymbol{y})\,, \tag{3}$$

where the weighting matrix $\mathbf{W}$ is equal to the inverse of the covariance matrix of the errors: $\mathbf{W} \equiv \mathrm{Cov}(\boldsymbol{e})^{-1}$.

The most effective regularization for ill-conditioned problems such as deconvolution of blurred images consists in imposing a smoothness constraint (Thiébaut 2005). Then the regularization penalty writes:

$$\mathcal{R}(\boldsymbol{x}) = \sum_j \phi(\Delta x_j)\,, \tag{4}$$

where Δx_j is the local gradient of $\boldsymbol{x}$ and ϕ is some cost function. The local gradient of $\boldsymbol{x}$ can be approximated by finite differences: $\Delta \boldsymbol{x} = \mathbf{D} \cdot \boldsymbol{x}$ where $\mathbf{D}$ is a linear finite difference operator. For instance, in 1-D: $\Delta x_j = (\mathbf{D} \cdot \boldsymbol{x})_j = x_{j+1} - x_j$. To enforce smoothness, the cost function ϕ must be an increasing function of the magnitude of its argument. Very common choices for ϕ are: the ℓ_2 norm, the ℓ_1 norm, or an $\ell_1 - \ell_2$ norm. For our deblurring problem, we have considered different priors (quadratic or $\ell_1 - \ell_2$ smoothness) possibly with an additional positivity constraint. We have used generalized cross validation (GCV,(Wahba 1990)) applied to the circulant approximation of the quadratic problem to estimate the optimal regularization level μ. These different possibilities and their effects on the recovered images are discussed in details in what follows.

Finally, to solve for the constrained optimization problem (2), we used the VMLMB algorithm from OPTIMPACK (THIÉBAUT 2002). VMLMB (for *Variable Metric, Limited Memory, Bounded*) makes use of a BFGS (Nocedal & Wright 2006) update of the approximation of the Hessian (matrix of second partial derivatives) of $\mathcal{Q}(\boldsymbol{x})$ to derive a step to improve the parameters at every iteration. This strategy only requires computing the objective function, $\mathcal{Q}(\boldsymbol{x})$, and its gradient (partial derivatives) $\nabla_{\boldsymbol{x}} \mathcal{Q}(\boldsymbol{x})$ with respect to the parameters $\boldsymbol{x}$. The BFGS update is limited to a few last steps so that the memory requirements remains modest, that is a few times the number of sought parameters, and the algorithm can be applied to solve very large problems (in our case, there are as many parameters as the number of pixels in the sought image). Finally, VMLMB accounts

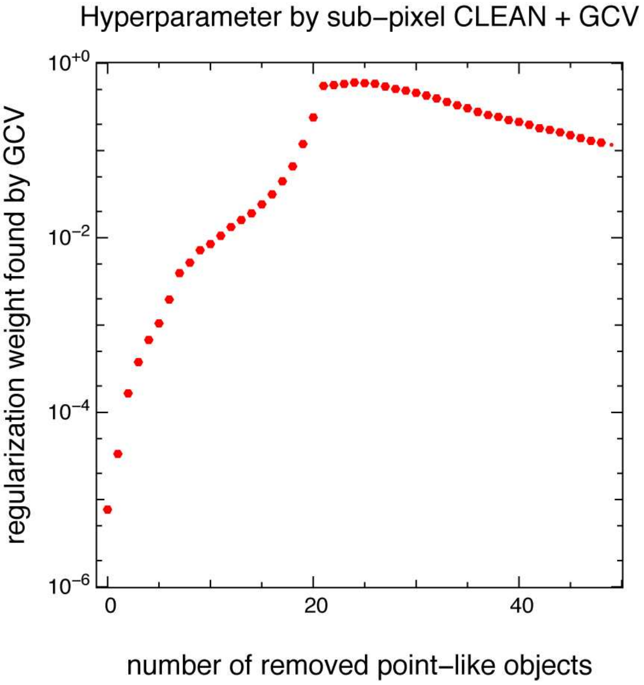

Figure 1. Hyper-parameter chosen by GCV as a function of the number of stars removed by our star removal algorithm (Appendix A). Note that this curve reaches a maximum corresponding to the moment when all the stars have been removed. Indeed stars correspond to high frequency correlated signal, while the wings of galaxies (for which the core has been erroneously removed) also give rise to such signal. In between, when all stars have been removed, while no galaxies has yet been deprived of its core, the amount of correlated high frequency signal reaches a minimum, or equivalently the GCV estimated value of μ reaches a maximum.

$n_{\rm side}$	128	256	512	1024	2048
time for one step (s)	0.13	0.59	2.13	8.48	34.3
number of steps (s)	13	12	9	13	24
total time (s)	2.6	10.4	33.4	171.1	1129.3

Table 1. the performance of the optimization of the linearized inversion problem $n_{\rm side} S_{\rm FS}^{\ell_{\rm cut}}$ as a function of $n_{\rm side}$ for an octo Opteron in OpenMP.

for bound constraints by means of gradient projections (Nocedal & Wright 2006). For a convex penalty $\mathcal{Q}(\boldsymbol{x})$, VmlmBis guaranteed to converge to the unique feasible minimum of $\mathcal{Q}(\boldsymbol{x})$ which satisfies the bound constraints; for a non-convex penalty, VmlmBbeing based on a descent strategy, it will find a local minimum depending on the initial set of parameters.

2.1.2 *Quadratic regularization and Wiener proxy*

Using the finite difference operator $\mathbf{D}$ and an ℓ_2 norm for the regularization and ignoring for the moment the positivity constraint, the MAP solution is the minimum of a quadratic penalty which simply involves solving a (huge) linear problem:

$$\begin{aligned}\boldsymbol{x}_\mu &= \arg\min_{\boldsymbol{x}} \Big\{ (\mathbf{H}\cdot\boldsymbol{x}-\boldsymbol{y})^{\rm T}\cdot\mathbf{W}\cdot(\mathbf{H}\cdot\boldsymbol{x}-\boldsymbol{y}) \\ &\qquad + \mu\,(\mathbf{D}\cdot\boldsymbol{x})^{\rm T}\cdot(\mathbf{D}\cdot\boldsymbol{x})\Big\} \\ &= \Big(\mathbf{H}^{\rm T}\cdot\mathbf{W}\cdot\mathbf{H}+\mu\,\mathbf{D}^{\rm T}\cdot\mathbf{D}\Big)^{-1}\cdot\mathbf{H}^{\rm T}\cdot\mathbf{W}\cdot\boldsymbol{y}\,, \qquad (5)\end{aligned}$$

providing the Hessian matrix $\mathbf{H}^{\rm T}\cdot\mathbf{W}\cdot\mathbf{H}+\mu\,\mathbf{D}^{\rm T}\cdot\mathbf{D}$ is non-singular, which is generally the case for $\mu > 0$. Owing to the large size of the matrices involved in this equation (there are as many unknown as the number of pixels), the linear problem has to be iteratively solved (by a limited memory algorithm such as vmlm) unless it can be diagonalized as explained below. The solution, equation (5), involves at least one parameter, μ, which needs to be set to the correct level of regularization: too low would give a solution plagued by lots of artifacts due to noise amplification, too high would result in an oversmoothed solution with small details blurred. The optimal level of smoothing can be computed by generalized cross validation (GCV) by minimizing with respect to μ the function (Golub et al. 1979; Wahba 1990):

$$\mathrm{GCV}(\mu) = \frac{(\mathbf{A}_\mu\cdot\boldsymbol{y}-\boldsymbol{y})^{\rm T}\cdot\mathbf{W}\cdot(\mathbf{A}_\mu\cdot\boldsymbol{y}-\boldsymbol{y})}{[1-\mathrm{tr}(\mathbf{A}_\mu)/N]^2}\,, \qquad (6)$$

where N is the number of data (size of $\boldsymbol{y}$) and $\mathbf{A}_\mu = \nabla_{\boldsymbol{y}}(\mathbf{H}\cdot\boldsymbol{x}_\mu)$ is the so-called *influence matrix*, in our case:

$$\mathbf{A}_\mu = \mathbf{H}\cdot\Big(\mathbf{H}^{\rm T}\cdot\mathbf{W}\cdot\mathbf{H}+\mu\,\mathbf{D}^{\rm T}\cdot\mathbf{D}\Big)^{-1}\cdot\mathbf{H}^{\rm T}\cdot\mathbf{W}\,. \qquad (7)$$

Computing the value of GCV(μ) involves: (i) solving the problem to find the regularized solution $\boldsymbol{x}_\mu$ and compute $\mathbf{A}_\mu\cdot\boldsymbol{y} = \mathbf{H}\cdot\boldsymbol{x}_\mu$; (ii) estimate the trace of $\mathbf{A}_\mu$ perhaps by using Monte Carlo methods (Girard 1989) since the influence matrix is very large. The computational cost of stages (i) and (ii) is similar to that of a few solvings of the quadratic problem. Since this has to be repeated for every different value of the regularization level, finding the optimal value of μ by means of GCV can be very time consuming unless the problem can be approximated by a diagonal quadratic problem (for which matrix inversions are both fast and trivial).

For this purpose, we introduce the proxy problem corresponding to white noise and circulant approximations of the operators $\mathbf{H}$ (convolution by the PSF) and $\mathbf{D}$ (finite differences). Then the weighting matrix becomes:

$$W_{i,j} = \delta_{i,j}/\sigma^2\,, \quad \text{where } \sigma^2 = \mathrm{Var}(n_i).$$

where $\sigma^2 = \mathrm{Var}(e_i)$ is the variance of the noise. In the special case where the PSF is *shift-invariant*, $\mathbf{H}$ is a convolution operator which can be approximated by a block Toeplitz with Toeplitz block matrix that can be coputed very quickly by means of FFT's:

$$\mathbf{H}\cdot\boldsymbol{x} \simeq \mathbf{F}^{-1}\cdot\mathrm{diag}(\mathbf{F}\cdot\boldsymbol{h})\cdot(\mathbf{F}\cdot\boldsymbol{x})\,, \qquad (8)$$

where $\boldsymbol{h}$ is the PSF (the first row of $\mathbf{H}$), $\mathbf{F}$ is the forward DFT operator, and diag($\boldsymbol{v}$) is the diagonal matrix with its diagonal given by the vector $\boldsymbol{v}$. This discrete convolution equation assumes that $F_{u,j} = \exp(-2\,\mathrm{i}\,\pi\,\sum_n u_n\,j_n/N_n)$ where N_n is the length of the $n^{\rm th}$ dimension, $j_n = 0,\ldots,N_n-1$ and $u_n = 0,\ldots,N_n-1$ are the indices of the position and discrete Fourier frequency along this dimension. In this case, the inverse DFT is simply $\mathbf{F}^{-1} = \mathbf{F}^{\rm H}/N_{\rm tot}$ with

$N_{\rm tot}$ the total number of elements in $\boldsymbol{x}$ and the H exponent standing for the conjugate transpose. With these approximations and definitions of the DFT, the likelihood term writes:

$$\mathcal{L}(\boldsymbol{x}) = \frac{1}{\sigma^2}\,\|\mathbf{H}\cdot\boldsymbol{x}-\boldsymbol{y}\|^2 \simeq \frac{1}{N_{\rm tot}\,\sigma^2}\sum_u |\hat{h}_u\,\hat{x}_u-\hat{y}_u|^2\,, \quad (9)$$

where $\hat{h}_u$ is the transfer function (the DFT of the point spread function) and $\hat{y}_u$ and $\hat{x}_u$ respectively the DFT of the data and of the sought image. Note that the exact normalization factor, here $1/N_{\rm tot}$, depends on the particular definition of the DFT.

Similarly, ignoring edges effects, the finite difference operator $\mathbf{D}$ along $n^{\rm th}$ direction can be approximated by:

$$\mathbf{D}_n\cdot\boldsymbol{x} \simeq \mathbf{F}^{-1}\cdot{\rm diag}(\hat{\boldsymbol{d}}_n)\cdot(\mathbf{F}\cdot\boldsymbol{x})\,, \quad (10)$$

where $\hat{\boldsymbol{d}}_n$ is the DFT of the first row of $\mathbf{D}_n$; then the quadratic regularization writes:

$$\mathcal{R}(\boldsymbol{x}) = \|\mathbf{D}\cdot\boldsymbol{x}\|^2 = \sum_n\|\mathbf{D}_n\cdot\boldsymbol{x}\|^2 \simeq \frac{1}{N_{\rm tot}}\sum_u r_u\,|\hat{x}_u|^2\,, \quad (11)$$

with:

$$r_u = \sum_n|\hat{d}_{n,u}|^2 = 4\sum_n\sin^2\left(\frac{\pi\,u_n}{N_n}\right)\,, \quad (12)$$

for first order finite differences and our choice for the DFT. Note that any $r_u \geqslant 0$ and being an increasing function of the length $|u|$ of the spatial frequency could be used instead and would result in imposong a smoothness constraint although with a different behaviour. Finally putting all these circulant approximations together, the quadratic problem to solve is diagonalized in the DFT space and trivially solved to gives the DFT of the MAP solution:

$$\hat{x}_{\mu,u} = \frac{\hat{h}_u^\star\,\hat{y}_u}{|\hat{h}_u|^2+\mu\,\sigma^2\,r_u}\,, \quad (13)$$

the asterisk exponent denoting the complex conjugate. Note that this circulant approximation of the solution is very fast to compute as it involves just a few FFT's. This expression of the MAP solution is very similar to what would give Wiener filter which would be exactly achieved by setting the term $\mu\,r_u$ equals to the reciprocal of the expected image powerspectrum in equation (13). Since, in our case, the image powerspectrum is unknown a priori, we have to choose the *regularization shape* r_u and derive the optimal level of smoothing, for instance, by means of GCV. Thanks to the circulant approximation made here, GCV criterion is now very easy to compute as:

$$\mathbf{A}_\mu \simeq \mathbf{F}^{-1}\cdot{\rm diag}(\hat{\boldsymbol{a}}_\mu)\cdot\mathbf{F}\,,\quad \text{with: } \hat{a}_{\mu,u} = \frac{|\hat{h}_u|^2}{|\hat{h}_u|^2+\mu\,\sigma^2\,r_u}\,,$$

and ${\rm tr}(\mathbf{A}_\mu) = \sum_u\hat{a}_{\mu,u}/N_{\rm tot}$, hence:

$${\rm GCV}(\mu) = \frac{N_{\rm tot}\sum_u t_{\mu,u}^2\,|\hat{y}_u|^2}{\sigma^2\,[\sum_u t_{\mu,u}]^2}\,, \quad (14)$$

with

$$t_{\mu,u} = 1-\hat{a}_{\mu,u} = \frac{\mu\,\sigma^2\,r_u}{|\hat{h}_u|^2+\mu\,\sigma^2\,r_u}\,. \quad (15)$$

In practice, for the optimization of equation (2), equation (13) is taken as a starting point together with the choice of μ given by the minimum of equation (14). Then the optimization of equation (2) is carried with possibly non stationary weights, while iterating back and forth between model and data space.

2.1.3 Crowded fields and star removal

Even though the estimation of the ellipticities does not require per se the deconvolution of the galaxies, it is shown below that this estimation is significantly improved by deconvolution when the fields of view are crowded and polluted by foreground stars: indeed galaxies and stars overlap less when deconvolved, which reduces the fraction of erroneous measurements. Unfortunately, when these stars are present, they significantly bias the estimation of the hyper parameter, μ, since stars correspond to high frequency correlated signal which leads to an underestimation of the optimal level of smoothing (for the galaxies) by cross validation. This is best seen in Figure 1 which displays the evolution of the hyper-parameter which minimizes GCV as a function of the number of stars removed by our star removal algorithm, see Appendix A. Interestingly, it suggests that GCV could be used as a classifier.

2.1.4 $\ell_1-\ell_2$ penalty and positivity

The drawback of using a quadratic (ℓ_2) norm in the regularization is that it tends to over-smooth the regularized map especially around sharp features as point-like sources (i.e. stars) and the core of galaxies. This is because the regularization prevents large intensity differences between neighboring pixels and result in damped oscillations (Gibbs effect). Such ripples hide any faint details in the vicinity of sharp structures. To avoid this, it would be better to use a regularization which smoothes out small local fluctuations of the sought distribution (here the deblurred image), presumably due to noise, but let larger local fluctuations arise occasionally. This can be achieved by using a $\ell_1-\ell_2$ cost function ϕ in equation (4). A possible $\ell_1-\ell_2$ cost function is (Mugnier et al. 2004):

$$\phi(r) \equiv 2\,\varepsilon^2\,\left[\left|\frac{r}{\varepsilon}\right|-\log\left(1+\left|\frac{r}{\varepsilon}\right|\right)\right]\,. \quad (16)$$

For a small, respectively large, pixel differences r, $\phi(r)$ has the following behavior

$$\phi(r)\sim\begin{cases} r^2 & \text{when } |r|\ll\varepsilon\,,\\ 2\,|\varepsilon\,r| & \text{when } |r|\gg\varepsilon\,,\end{cases}$$

which shows that, as required, the $\ell_1-\ell_2$ penalty behave quadratically for small *residuals* r's (in magnitude and w.r.t. ε) and only linearly for large r's. The derivative, needed for the optimization algorithm, of the $\ell_1-\ell_2$ penalty writes:

$$\phi'(r) = \frac{2\,\varepsilon\,r}{\varepsilon+|r|}\,.$$

An additional possibility to improve the restitution of faint details with level close to that of the background is to apply a strict positivity constraint. This is achieved by using VMLMB, a modified limited memory variable metric method (Thiébaut 2002), which imposes simple bound constraints by means of gradient projection. This yields a reduction of aliasing by bounding the allowed region of parameter space which can be explored during the optimization.

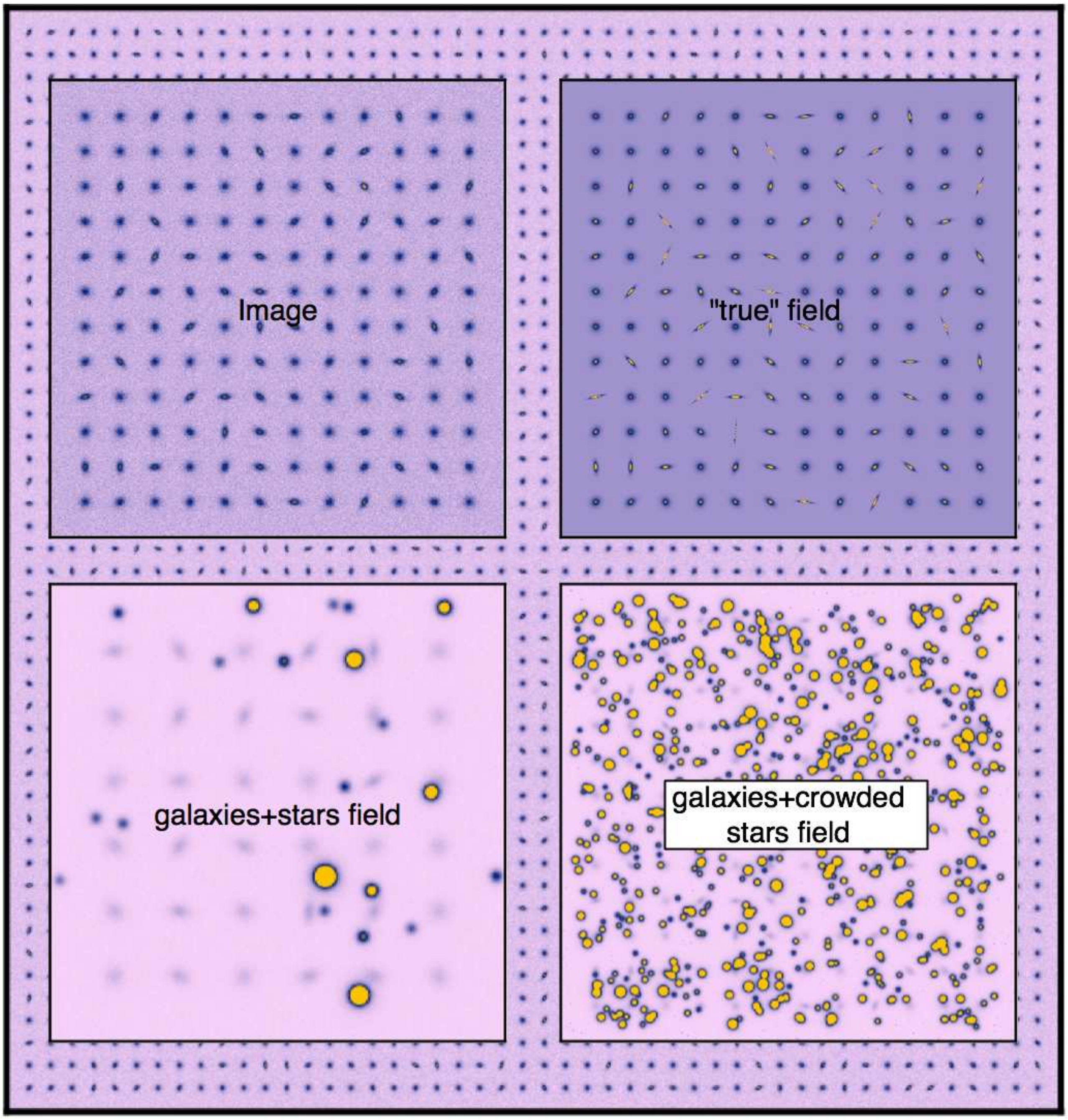

Figure 2. An example of virtual fields generated with SKYMAKER to be fed to SEXTRACTOR before and after deconvolution using the different regularizations described in the text. *From top to bottom and left to right,* a galaxy field image and the corresponding "true" field, a galaxies field with stars and a crowded galaxy field with stars (10^6 stars/arcmin^2). The exposure time is 10 seconds and the seeing is 1" for the VLT with VIMOS. The background field corresponds to the actual size of the corresponding images.

2.2 Numerical experiments

The public package SkyMaker (Erben et al. 2001) was used to generate galactic and stellar fields from ellipticity and magnitude catalogues. Table 2 summarizes the main parameter corresponding to the VLT with a VIMOS instrument, a worse case situation compared to upcoming space missions.

A regular grid of 12×12 galaxies of magnitude 20 with random orientation is produced twice (with the same random seed), one corresponding to a fixed seeing and a given exposure time, while the other assumes zero noise and zero seeing for a set of 512×512 pixels images, see Figure 2.

The background level and the amplitude of the background noise is first estimated automatically from the his-

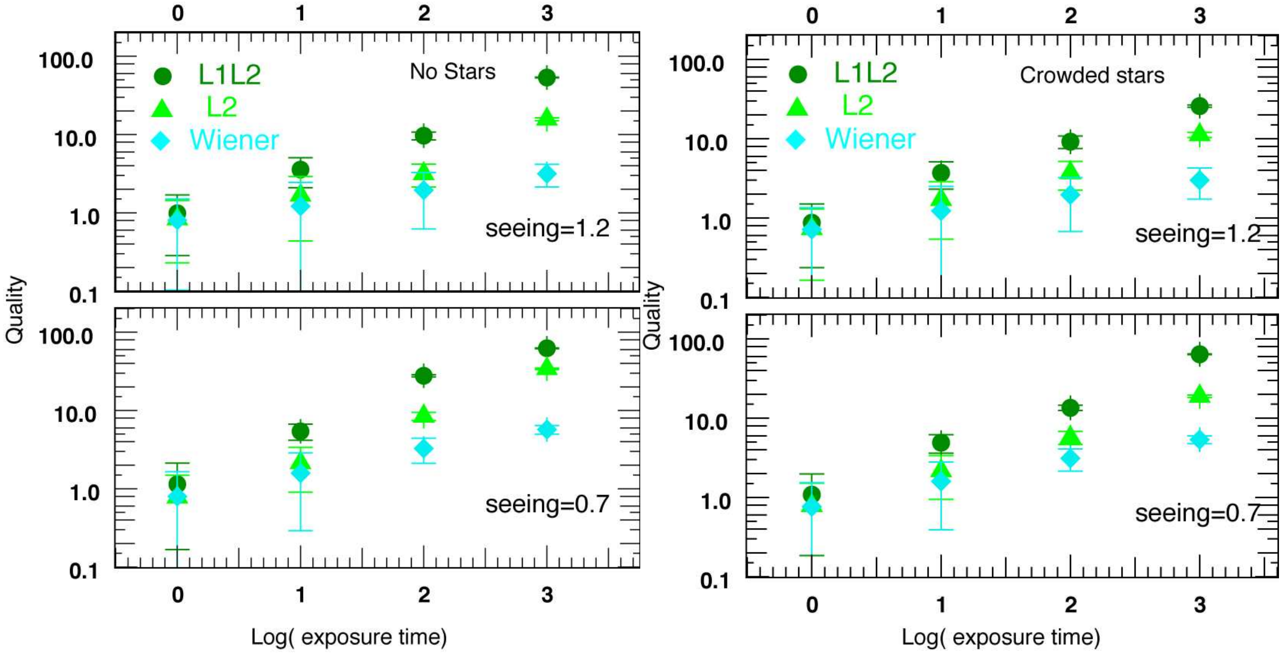

Figure 4. *Left panel*: the relative error quality factor (see main text) as a function of the log exposure time for the three methods, respectively Wiener filtering (*diamonds*), ℓ_2 gradient penalty function with enforced positivity (*triangles*) and $\ell_1 - \ell_2$ gradient penalty function with positivity (*circles*). Two seeing conditions are investigated, corresponding to a good (0.7") and a fair (1.2") seeing condition. These simulations assume that no star are present in the field, and correspond to a set of non overlapping galactic disks with random orientation and magnitude 20 in V (see Fig. 2). The telescope setting correspond to the VIMOS instrument on an 8 meter VLT. *Right panel*: the quality factor as a function of the log exposure time, but this time while allowing for stars in the field. The star count is 10^5 stars per arcmin^2. As discussed in the text, the penalty weight is estimated via generalized cross validation (GCV) on a temporary image where all stars are automatically removed via blind cleaning as describedin Appendix A. Here the removal of stars is essential since the GCV hyper-parameter (which sets the level of smoothing in the deconvolved image) varies by orders of magnitudes in the process (see Fig 1 for a discussion) and would be otherwise underestimated.

togram of the pixel values and fed to SEXTRACTOR (BERTIN & ARNOUTS 1996) which then estimates the position, the flux, the orientation and the ellipticity for all the galaxies in the field. This procedure is reproduced 50 times with different realizations. The measured and the recovered ellipticity are compared, together with flux and orientation for all the galaxies in the field. In this set of simulations the prior knowledge of the position of the galaxy is used to minimize errors which might arise while using SEXTRACTOR: the recovered galaxy is chosen to be that which is closest to the known position. The median and interquartile of the error (difference between the "true" and recovered) in ellipticity versus the ellipticity is computed for a range of exposure time; this procedure is iterated for the three deconvolution techniques used in this paper (Wiener, ℓ_2 with positivity, $\ell_1 - \ell_2$ with positivity). An example of such a plot is shown in Figure 3. Clearly the bias in the recovered ellipticity increases with the ellipticity and the amount of noise in the image (via poorer seeing or shorter exposure time). As expected, the Wiener deconvolution is the least efficient of the three methods, since the linear penalty does not avoid some level of Gibbs ringing. In contrast the ℓ_2 penalty with positivity avoids partially such ringing, while the $\ell_1 - \ell_2$ penalty works best at recovering the input eccentricity with a consistent level of bias below 10 % for an ellipticity in the range $[0.1, 0.8[$. Interestingly, there is also a residual bias (even for longer exposure times) for small ellipticity galaxies, which arises because noise induced departure from sphericity is amplified by the deconvolution. Note that the Wiener deconvolution is significantly faster than the iterative deconvolution with positivity (with ℓ_2 or $\ell_1 - \ell_2$ penalties). Positivity improves significantly the deconvolution, but will depend critically on the ability to estimate the background. In the present simulations, the level of background is automatically estimated while looking at the histogram of the pixels. Finally the $\ell_1 - \ell_2$ regularization significantly improves the restoration of fields of stars and galaxies, because the stars and the cores of galaxies are very sharp. These non-linear iterative methods are slower than the Wiener filtering, but can account at no extra cost for non uniform noise, or saturation and masking. Their convergence can be considerably boosted when they are initiated by the Wiener solution.

For any such plot, two numbers are defined which summarize the trend. The mean error (averaged over the various ellipticities) $\bar{\epsilon}$, and the mean of the interquartile, $\Delta\bar{\epsilon}$ were measured. The quality factor, QF is defined to be the ratio of the sum of this mean error and the mean interquartile for the image without deblurring, divided by the sum of the mean error and the mean interquartile for the deconvolved image for the three techniques (Wiener, ℓ_2 and $\ell_1 - \ell_2$). This reads

$$QF_{\text{method}} = \frac{\bar{\epsilon}_{\text{image}} + \Delta\bar{\epsilon}_{\text{image}}}{\bar{\epsilon}_{\text{method}} + \Delta\bar{\epsilon}_{\text{method}}} \,.$$

The evolution the quality of the ellipticity measurement is traced versus seeing conditions and signal to noise (exposure

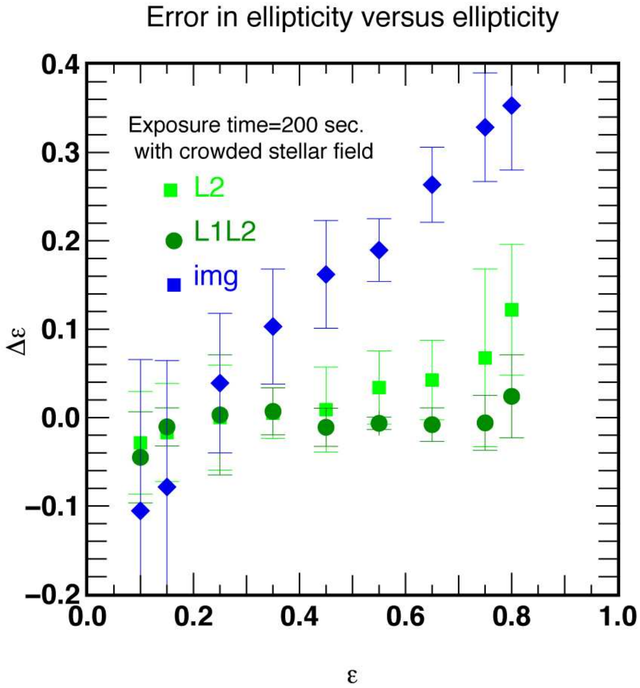

Figure 3. the error in ellipticity as a function of the ellipticity (measured by SEXTRACTOR) for a set of 50 images (such as those shown on Figure 2) either directly on the image (*medium squares*), deconvolved with ℓ_2 gradient penalty function with enforced positivity (*light diamonds*) and $\ell_1 - \ell_2$ gradient penalty function with positivity (*dark circles*). For each set, the ellipticity is also measured directly on the raw image. Note that, as expected, the error on the bias is largest for circular galaxies, since deconvolution will tend to over amplify departure from circular symmetry.

OBJECT	VALUE
Gain (e-/ADU)	30.11
Full well capacity in e-	300000
Saturation level (ADU)	60000
Read-out noise (e-)	1.3
Magnitude zero-point (ADU per second)	21.254
Pixel size in arcsec.	0.2
Number of microscanning steps	1
SB (mag/arcsec^2) at 1' from a 0-mag star	16.0
Diameter of the primary mirror (in meters)	8.0
Obstruction diam. from 2nd mirror in m.	2.385
Number of spider arms (0 = none)	4
Thickness of the spider arms (in mm)	5.0
Pos. angle of the spider pattern	45.0
Average wavelength analyzed (microns)	0.80
Back. surface brightness (mag/arcsec^2)	21.5
Nb of stars /$^\square$ brighter than MAG_LIMITS	1e5
Slope of differential star counts (dexp/mag)	0.3
Stellar magnitude range allowed	12.0,19.0

Table 2. SKYMAKER parameters used to generate the VIMOS/ VLT images

time) in two regimes: a galaxy-only field, and a galactic field with a crowded star content where the number of stars per square degree reaches 10^5 stars/arcmin^2. These two regime represent high and low Galactic region respectively. Figure 4 displays the evolution of $QF_{\rm Wiener}$ (*diamonds*), QF_{ℓ_2} (*squares*), and $QF_{\ell_1-\ell_2}$ (*circles*), as a function the exposure time of 1, 10, 100 and 1000 seconds respectively, and two seeing conditions of 1.2" and 0.7". No stars are present in the field on the left panel of Figure 4, whereas its right panel displays the three QF estimators for a field with a realistic 10^5 stars per square degree. Now that we have shown that state of the art edge-preserving deconvolution of deep sky images is mandatory to get good quality shear estimates, let us conclude this section by a leap forward, and assume from now on that we have access not only to discrete measurements of ellipticities over a significant fraction of the sky, but also that this point like process has been re-sampled. Indeed, since it is beyond the scope of this paper to carry out a full-sky deconvolution and reconstruction at the resolution of 0.7" (This would amount to about 10^{12} pixels!), it is assumed from now on that a full-sky catalogue of vector reduced shear exists and that the interpolation/re-sampling of the corresponding map on a uniform grid over the sphere has been done, together with an estimate of the corresponding shot noise. In this paper, we extract the virtual catalogue from a state of the art simulation (see below) we make use of the HEALPIX Pixelisation (Górski & et al. 1999), a hierarchical equi-surface and iso-latitude pixelisation of the sphere, which was developped to analyze polarized CMB type data.

3 A FULL-SKY MAP MAKER

3.1 The inverse problem

Our purpose is now to solve for the non-linear inverse problem of recovering the $\kappa(\hat{\boldsymbol{n}})$ map corresponding to a noisy incomplete measurement of the 2-D field $(g_1(\hat{\boldsymbol{n}}), g_2(\hat{\boldsymbol{n}}))^{\rm T}$ of the ellipticity and orientation on the sphere (in the local tangent plane):

$$g_k(\hat{\boldsymbol{n}}) = \frac{\gamma_k(\hat{\boldsymbol{n}})}{1-\kappa(\hat{\boldsymbol{n}})} + e_k(\hat{\boldsymbol{n}}) , \quad \text{for } k = 1 \text{ or } 2 , \qquad (17)$$

where $\hat{\boldsymbol{n}}$ is the sky direction, γ and κ are respectively the shear and the convergence, while $\mathbf{e}$ is a tensor field of the *errors* which accounts for the measurement noise (including the shot noise induced by the finite number of galaxies within that pixel) and model approximations.

3.1.1 *Spherical formulation*

On the sphere, the scalar field $\boldsymbol{\kappa}$ and the tensor field $\boldsymbol{\gamma}$ are linear functions of the *unknown* complex field $\boldsymbol{a} = \mathbf{Y} \cdot \boldsymbol{\kappa}$ whose coefficient are the spherical harmonic coefficients of $\boldsymbol{\kappa}$. After discretization and using matrix notation, $\boldsymbol{\kappa}$ and $\boldsymbol{\gamma}$

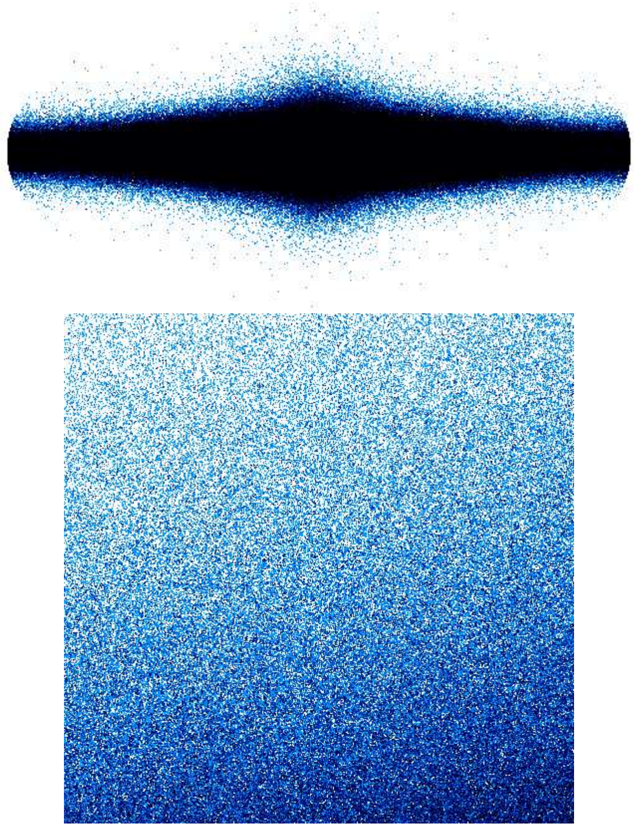

Figure 5. *Top panel*: full-sky view of the mask; *Bottom panel:* a zoom at coordinate $(l, b) = (30°, 30°)$ showing the distribution of stellar cuts. This cut corresponds to the inner central region of the reconstruction shown in Figure 12.

write

$$\kappa \equiv \mathbf{K}\cdot \boldsymbol{a} \quad \text{and} \quad \gamma \equiv \mathbf{G}\cdot \boldsymbol{a}\,, \tag{18}$$

where $\mathbf{K} = \mathbf{Y}$ and $\mathbf{G} = {}_p\mathbf{Y}\cdot\mathbf{J}$, denoting $\mathbf{Y}$ the scalar spherical harmonics and ${}_p\mathbf{Y} = ({}_E\mathbf{Y}, {}_B\mathbf{Y})$ the parity eigenstates based on spin 2 spherical harmonics. These eigenstates are defined in such a way that

$$\gamma_1 \pm i\gamma_2 = -\sum_{\ell m} (a_{\ell,m,E} \pm i a_{\ell,m,B})_{\pm 2}\,\mathbf{Y}_{\ell m}\,,$$

so that we have

$$\begin{pmatrix} \gamma_1 \\ \gamma_2 \end{pmatrix} = \sum_{\ell,m} \begin{pmatrix} -\mathbf{W}^{+}_{\ell,m} \\ +i\,\mathbf{W}^{-}_{\ell,m} \end{pmatrix} a_{\ell,m,E} + \sum_{\ell,m} \begin{pmatrix} -i\,\mathbf{W}^{-}_{\ell,m} \\ -\mathbf{W}^{+}_{\ell m} \end{pmatrix} a_{\ell,m,B}$$

with $\mathbf{W}^{\pm}_{\ell,m} = ({}_2\mathbf{Y}_{\ell,m} \pm {}_{-2}\mathbf{Y}_{\ell,m})/2$. Here $\mathbf{J}$ operates on $\boldsymbol{a}$ as

$$(\mathbf{J}\cdot\boldsymbol{a})_{\ell,m,E} \;=\; -\sqrt{\frac{(\ell+2)(\ell-1)}{(\ell+1)\ell}}\, a_{\ell,m}\,, \tag{19}$$

$$(\mathbf{J}\cdot\boldsymbol{a})_{\ell,m,B} \;=\; 0\,. \tag{20}$$

Appendix B gives more explicit formulations of the operators $\mathbf{K}$ and $\mathbf{G}$, using index notation on the sphere.

3.1.2 *Flat sky formulation*

The flat sky limits (corresponding to large ℓ's) of equations. (18)-(19) are (see Appendix C):

$$\mathbf{J} \approx (\mathbf{1}, \mathbf{0})\,, \quad \text{and} \quad \mathbf{Y} \approx \exp(i\boldsymbol{\ell}\cdot\hat{\boldsymbol{n}})\,, \tag{21}$$

while the parity eigenstates read locally, in the fixed copolar basis e_x, e_y:

$$\mathbf{W}^{+} \;\approx\; -\cos(2\,\phi_{\boldsymbol{\ell}})\exp(i\,\boldsymbol{\ell}\cdot\hat{\boldsymbol{n}}) = -\frac{l_x^2 - l_y^2}{l_x^2 + l_y^2}\exp(i\,\boldsymbol{\ell}\cdot\hat{\boldsymbol{n}})\,,$$

$$\mathbf{W}^{-} \;\approx\; -i\,\sin(2\,\phi_{\boldsymbol{\ell}})\exp(i\,\boldsymbol{\ell}\cdot\hat{\boldsymbol{n}}) = -i\,\frac{2\,l_x\,l_y}{l_x^2 + l_y^2}\exp(i\,\boldsymbol{\ell}\cdot\hat{\boldsymbol{n}})\,. \tag{22}$$

In this limit, the *unknowns*, $\boldsymbol{a}$, represent the Fourier coefficients of the convergence field, κ. Note that our definition of γ and κ warrants that they are consistent with the lens equation on the tangent plane — solving for κ in equation (18) and plugging the solution into equations (22) — which reads locally in real space:

$$\nabla^2\kappa(\hat{\boldsymbol{n}}) = \left(\partial_x^2 - \partial_y^2\right)\gamma_1(\hat{\boldsymbol{n}}) + 2\,\partial_x\partial_y\gamma_2(\hat{\boldsymbol{n}})\,, \tag{23}$$

where $\gamma_1(x, y)$ and $\gamma_2(x, y)$ are the two components of the E and B modes of the shear field. Also note that thanks to equation (20) the recovered map will *not* have B modes by construction. It can nevertheless be checked that the amplitude of the B modes in the residuals is small compared to the amplitude of the signal in the E modes, see Section 4.8.

3.1.3 *Cost function*

The considered problem can be stated as recovering $\boldsymbol{a}$ given the data $\boldsymbol{g}$ according to the model in equation (17). In the same way as what has been done for deblurring the images (section 2), finding the solution of this inverse problem in the Maximum a Posteriori (MAP) (Thiébaut (2005); Pichon & Thiébaut (1998)) sense involves minimizing a two-term cost function:

$$\mathcal{Q}(\boldsymbol{a}) = \mathcal{L}(\boldsymbol{a}) + \mu\,\mathcal{R}(\boldsymbol{a})\,, \tag{24}$$

with respect to the parameters $\boldsymbol{a}$. In the right hand side of equation (24), the term $\mathcal{L}(\boldsymbol{a})$ enforces agreement of the model with the data, whereas $\mathcal{R}(\boldsymbol{a})$ is a regularization term used to enforce our prior knowledge about the sought fields, and $\mu \geqslant 0$ is a Lagrange multiplier used to tune the relative importance of the prior with respect to the data.

For errors with a centered Gaussian distribution, the likelihood term writes:

$$\mathcal{L}(\boldsymbol{a}) = \sum_{j,k} W_{j_1,k_1,j_2,k_2}\, e_{k_1}(\hat{\boldsymbol{n}}_{j_1})\, e_{k_2}(\hat{\boldsymbol{n}}_{j_2})\,,$$

with $e_k(\hat{\boldsymbol{n}}_j) = g_k(\hat{\boldsymbol{n}}_j) - \gamma_k(\hat{\boldsymbol{n}}_j)/[1-\kappa(\hat{\boldsymbol{n}})]$ and $\mathbf{W} = \mathbf{C}^{-1}$ with $C_{j_1,k_1,j_2,k_2} = \langle e_{k_1}(\hat{\boldsymbol{n}}_{j_1})\, e_{k_2}(\hat{\boldsymbol{n}}_{j_2})\rangle$. If the errors are further uncorrelated, the likelihood simplifies to:

$$\mathcal{L}(\boldsymbol{a}) = \sum_{j,k} w_{j,k}\left[g_k(\hat{\boldsymbol{n}}_j) - \frac{\gamma_k(\hat{\boldsymbol{n}}_j)}{1-\kappa(\hat{\boldsymbol{n}}_j)}\right]^2\,, \tag{25}$$

where the sum is carried over the index j of the sampled sky directions $\hat{\boldsymbol{n}}_j$ (so called sky *pixels*) and index k of the two components of, say, the Q and U polarization fields respectively (see Appendix B for an explicit formulation with

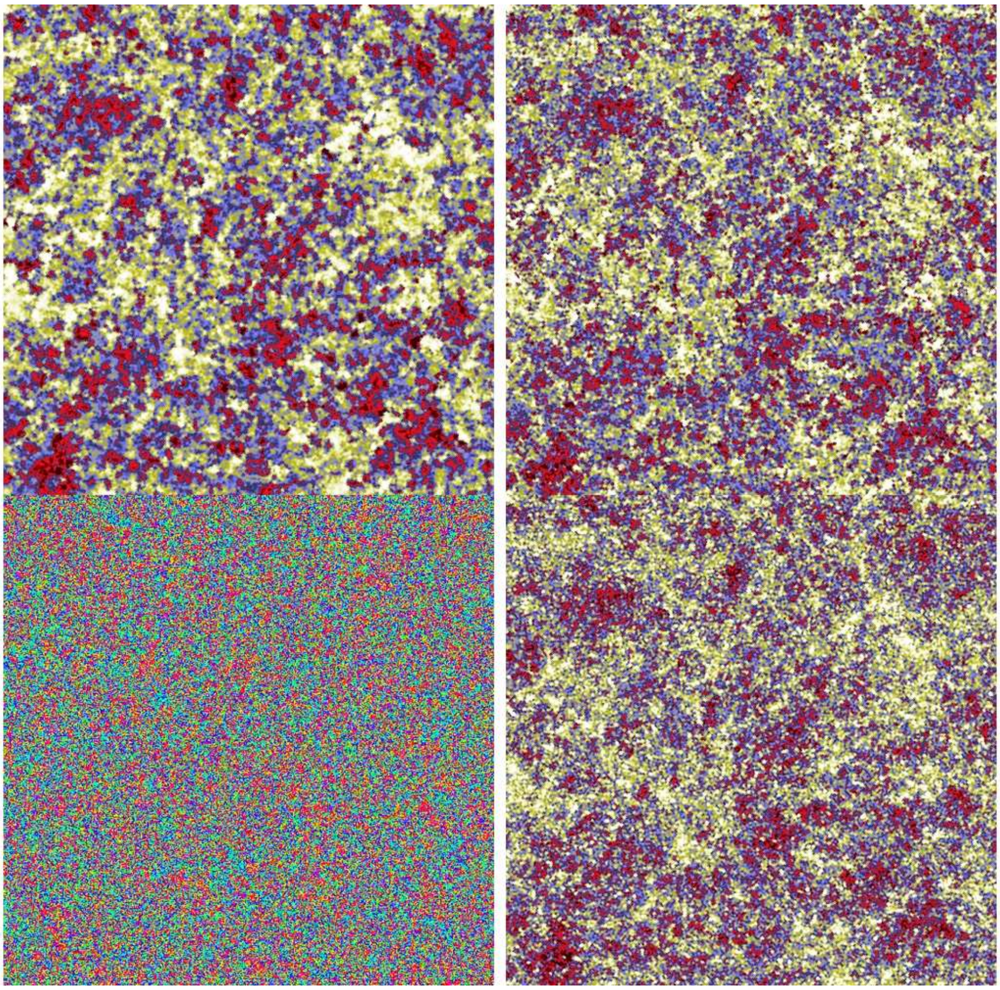

Figure 6. a zoom of the full-sky recovered κ maps of a simulation ${}_{2048}S_{\rm FS}^{\ell_{\rm cut}}$ with $\ell_{\rm cut} = 722$, *(top left panel) and* 1569, *(top right panel)* at coordinates $(\phi, \theta) = (0, 0)$. *(* the color table corresponds to a histogram equalization*) bottom left panel:* the corresponding data (the *hue* color table codes the polarization orientation); *bottom right panel* the corresponding underlying κ map.

all the relevant indices) and the weights are related to the variance of the noise:

$$w_{j,k} = \mathrm{Var}\left(e_k(\hat{\boldsymbol{n}}_j)\right)^{-1} . \tag{26}$$

This allow us to account for non uniform noise on the sky and also cuts (the galaxy, bright stars, *etc.*) for which the variance can be considered as infinite and thus the corresponding weights set to zero. Note that setting the weights in this statistically consistent way yields no such biases as those which would result from interpolation or inpainting methods used to replace missing data (Pires et al. (2008)).

For this recovery problem, our prior is that the field $\boldsymbol{\kappa}$ must be as smooth as possible in the limit that the model remains compatible with observables within the error bars, that is equation (17) must be valid. To that end, the regularization is written as a penalty based on the second order spatial derivatives (Laplacian) $\nabla^2\kappa$ of the field κ:

$$\mathcal{R}(\boldsymbol{a}) = \|\nabla^2 \boldsymbol{\kappa}\| . \tag{27}$$

Equation (B9) in Appendix B gives the expression of $\nabla^2\kappa$ as a function of the unknown $\boldsymbol{a}$. In order to enforces smoothness while preserving some sharp features in the κ map, quadratic and non quadratic norms of the Laplacian have been considered for the regularization, see Section B.

3.2 Generating the virtual data set

Let us first describe in turn the simulation used to model the full sky κ map, and the generation of the corresponding map.

3.2.1 The simulation

The Horizon 4Π (Teyssier et al. (2008), Prunet et al. (2008)) simulation was used, a ΛCDM dark matter simulation using the WMAP 3 cosmogony with a box size of $2h^{-1}$Gpc on a grid of 4096^3 cells. The 70 billions particles were evolved using the Particle Mesh scheme of the RAMSES code (Teyssier (2002)) on an adaptively refined grid (AMR) with about 140 billions cells, reaching a formal resolution of 262144 cells in each direction (roughly 7 kpc/h comoving). The simulation covers a sufficiently large volume to compute a full-sky convergence map, while resolving Milky-Way size halos with more than 100 particles, and exploring small scales deeply into the non-linear regime. The

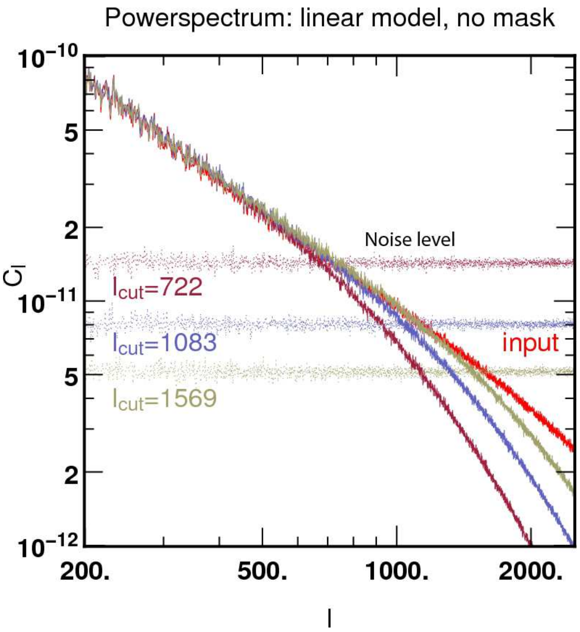

Figure 7. a zoom on the power spectra of the three reconstructions of ${}_{2048}S_{\rm FS}^{\ell_{\rm cut}}$ for $\ell_{\rm cut} = 722, 1083$, and 1569, together with the power spectra of the noise. Note that the level of smoothing decreases with increasing signal to noise, in parallel to the bias in the corresponding power spectrum.

dark matter distribution in the simulation was integrated in a light cone out to redshift 1, around an observer located at the center of the simulation box.

3.2.2 Mock data

This light cone was then used to calculate the corresponding full sky lensing convergence field, which is mapped using the HEALPIX pixelisation scheme with a pixel resolution of $\Delta\theta \simeq 0.74\,\mathrm{arcmin}^2$ ($n_{\rm side} = 4096$). Specifically, the convergence $\kappa(\hat{\boldsymbol{n}})$ at the sky coordinate $\hat{\boldsymbol{n}}$ is computed from the density contrast, $\delta(\boldsymbol{x}, z)$ in the Born approximation using:

$$\kappa(\hat{\boldsymbol{n}}) = \frac{3}{2}\Omega_m \int_0^{z_s} \frac{\mathrm{d}z}{E(z)} \frac{\mathcal{D}(z)\mathcal{D}(z,z_s)}{\mathcal{D}(z_s)} \frac{1}{a(z)} \delta(\frac{c}{H_0}\mathcal{D}(z)\hat{\boldsymbol{n}}, z)\,, \tag{28}$$

which is valid for sources at a single redshift $z_s = 1$, and $\mathcal{D}(z) = H_0\,\chi(z)/c$ is the adimensional comoving radial coordinate, hence $\mathrm{d}\mathcal{D} = \mathrm{d}z/E(z)$. The detailed procedure to construct such maps from the simulation using equation (28) is described in Appendix D1 (chosing the sampling strategy) and D2 and in Teyssier et al. (2008). In practice, a set of degraded maps of κ was generated from the full resolution, $n_{\rm side} = 4096$ down to $n_{\rm side} = 128$ in powers of 2, together with the corresponding masks (see Figure 5). Different levels of noise (corresponding to $700 \leqslant \ell_{\rm cut} < 2500$) and maps with/without Galactic masks are considered. The corresponding simulations are labeled as ${}_{n_{\rm nside}}S_{\rm FS/GC}^{\ell_{\rm cut}}$. Cartesian maps are also used, labeled as ${}_{n_{\rm pixel}}C_{\rm NL/lin}^{\rm SNR}$ corresponding to Cartesian sections of the full-sky maps, where for commodity, the experiments involving high resolution where calibrated. Here the flag NL/lin refers to whether or not the non-linear model is accounted for.

3.2.3 Penalty weight

In this paper, the weight of the penalty, μ, in equation (24) is chosen so that the ℓ_2 cutoff corresponds to the scale, $\ell_{\rm crit}$ at the intersection of the signal and the noise power spectra, see e.g. Figure 7. Specifically

$$\mu \propto 1/\ell_{\rm crit}^2\,.$$

In a more realistic situation, when the power spectrum of the signal is unknown, generalized cross validation could be used to find this scale. When $\ell_1 - \ell_2$ penalty is implemented (see Section 2.1.4), the ℓ_1 parameter ϵ entering equation (16) is chosen so that it cuts off the tail of the PDF of the Laplacian of the recovered field at the 3-σ level.

3.3 Optimization & Performance

Let us now turn to the optimization procedure and the performance of the algorithm.

3.3.1 Optimization

Recall that the procedure assumes here a sampling strategy, since the noisy $\mathbf{g}$ field is given on a pixelisation of the sphere. To solve the optimization problem, we used the algorithm VMLM from OPTIMPACK (THIÉBAUT 2002) which only involves computing the objective function $\mathcal{Q}(\boldsymbol{a})$ and its partial derivative with respect to the parameters $\boldsymbol{a}$. VMLM is an unconstrained version of VMLMB which has been used for the deblurring problem and which is described in some details in section 2.1. The optimization of equation (24) is carried by computing in turn equation (18) and Equations (28) and (B3) using HEALPIX (GÓRSKI & ET AL. (1999)) in OPENMP or MPI.

3.3.2 Overall Performance

Each back and forth transform takes respectively 0.1, 0.5, 2, 8, 32 and 128 seconds on an octo OPTERON for $n_{\rm side}$ equal to 128, 256, 512, 1024, 2048 and 4096, see Table 1. The linearized problem without mask converges typically in a dozen iterations (which typically only involve a back and forth transform, unless the convergence is poor). The linearized mask problem takes a few hundred iterations, see Table 3, and so does the non-linear problem (or the linearized problem with a non-linear $\ell_1 - \ell_2$ penalty function).

4 VALIDATION

Let us first investigate a few striking features of the method in turn: its ability to fill gaps, its ability to preserve the sharpness of clusters, its ability to impose strong prior on the two-points correlation.

4.1 Linear versus non-linear optimization

Figure 8 shows the effect of accounting for the non linearity in equation (17). Here a set of Cartesian simulations is used ${}_{256}C_{\rm NL/lin}^{1}$. This map represents (a 100 times) the difference between the recovered map while accounting for

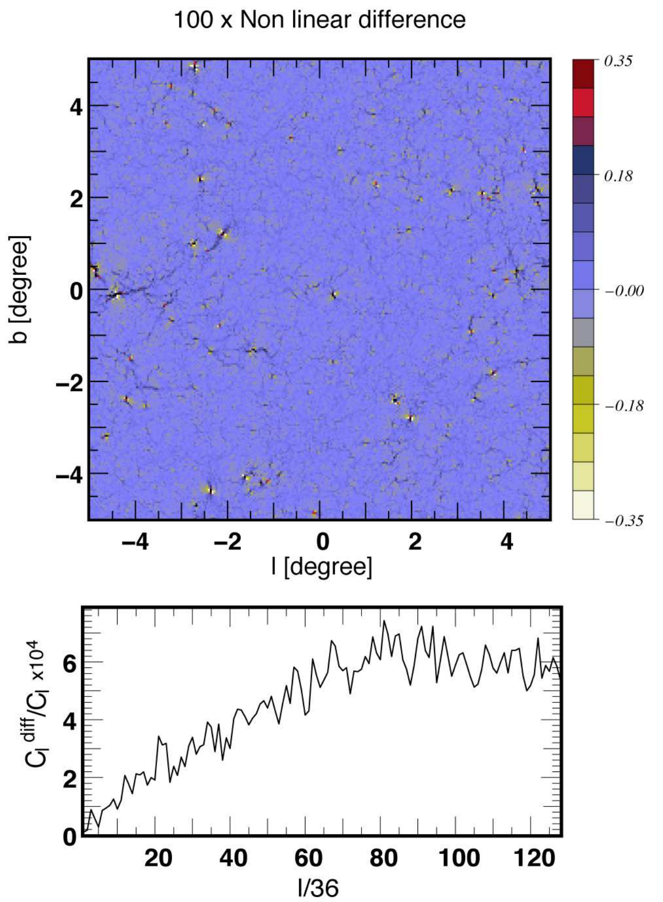

Figure 8. *Top panel*: a map of the 100 times difference between the recovered map with the non-linear model and $\ell_1 - \ell_2$ penalty, and the recovered map without accounting for the non-linearity. As expected the difference is largest at high frequencies near the cluster and along the filaments. *Bottom panel:* the power spectrum of the relative difference as a function of ℓ.

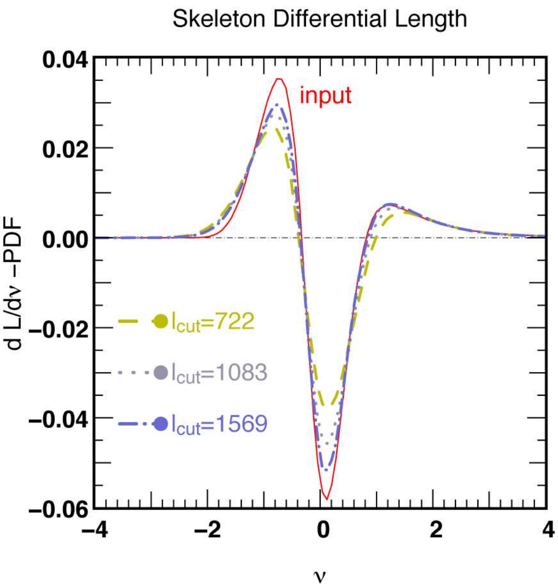

Figure 9. The input skeleton differential length with its recovered counterparts as a function of the normalized κ contrast, $\nu \equiv (\kappa - \bar{\kappa})/\sigma_\kappa$ for the set ${}_{2048}S_{\rm FS}^{\ell_{\rm cut}}$ with $\ell_{\rm cut} = 722, 1083$, and 1569. Here the PDF of the normalized κ contrast was subtracted to the differential length for clarity; As expected, the agreement is best at large convergence. This figure is complementary to Figure 12 which shows that the geometry of the field is well preserved on average.

$1-\kappa$ in equation (17) in the inversion, and the recovered map while neglecting this factor. The difference is small in amplitude, but shows as expected the strongest bias near the clusters and the filaments, where κ is largest. The bottom panel represents the corresponding relative power spectrum, $C_\ell[\mathrm{NL-lin}]/C_\ell[\mathrm{input}]$ as a function of ℓ. Again the larger discrepancy occurs at higher ℓ, corresponding to the sharp peaks at the positions of the clusters. Hence the non-linearity should be accounted for in the model if the shape of the cluster is an issue. For all practical purposes, at scales below $\ell_{\rm max} < 4096$ solving the linearized problem is de facto equivalent to the general non-linear problem when κ is neglected at the denominator in equation (17).

4.2 Topology & geometry: skeleton extraction

Let us now compare the shape of the recovered map to the initial map from the point of view of its topology and its geometry. For this purpose, the skeleton is used here (Novikov et al. (2006); Sousbie et al. (2007)). It is defined in 2D as the boundary of the void patches (See figure B1), which in turn are a segmentation of the map. The skeleton of the initial field and the recovered fields for simulation ${}_{2048}S_{\rm GC}^{\ell_{\rm cut}}$ is computed, and represented in Figure 12 The recovered skeletons are qualitatively fairly close to the original skeleton, which demonstrates that the local topology and geometry of the field is well recovered. Let us make this comparison more quantitative. The differential length per unit area of the recovered field (*the set* ${}_{2048}S_{\rm FS}^{\ell_{\rm cut}}$ with $\ell_{\rm cut} = 722, 1083$, and 1569 *as labeled*) over the initial κ map (*thin line*) as a function of density threshold is also shown in Figure 9. The agreement increases at larger density thresholds, which suggests that the topology of dense regions is well recovered. This quantity was shown (Sousbie et al. (2008), Pogosyan et al. (2009)) to trace well the underlying shape parameter of the powerspectrum and as been used in 3D to constaint the dark matter content of the universe (Sousbie et al. (2006)). An alternative to the differential length would be to measure the relative distance between the recovered and the input skeleton, see Caucci et al. (2008). Eventually, the skeleton could also be used to characterize the connectivity of clusters (i.e. the number of connected filaments), as it will depend on the cosmic energy content (Pichon & al. (2009)).

4.3 Skewness and Kurtosis

The simplest statistics to explore this transition is the skewness, S_3 and the kurtosis, S_4 of the PDF of the recovered maps. Furthermore, it has been shown that these parameters provide a powerful tool to measure the underlying cosmological parameter Bernardeau et al. (1997); Takada & Jain (2002, 2004). Figure 10 displays the evolution of these numbers as a function of scale in the initial and recovered maps, with and without galactic masking. Top hat filtering is used here of width $[2^i, 2^{i+1}]$, while the harmonic number of each

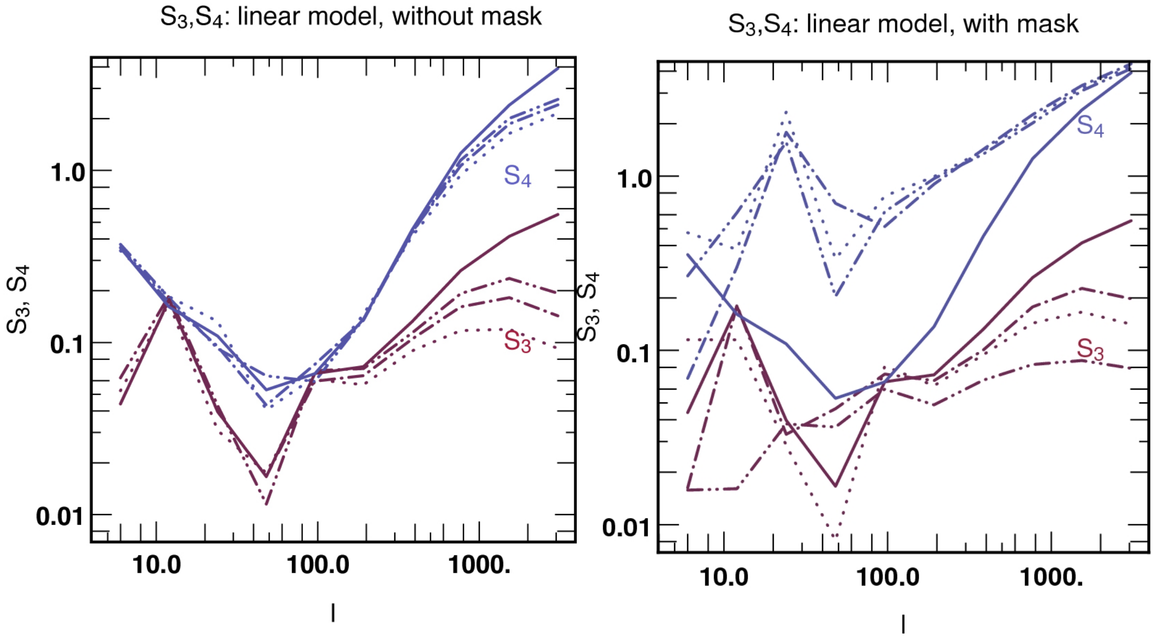

Figure 10. *left panel*: skewness, S_3 and kurtosis, S_4 as a function of scale (using sharp top hat filtering) for the model (*plane line*) and the recovered κ maps of a simulation ${}_{2048}S^{\ell_{\rm cut}}_{\rm FS}$ (*dotted, dot-dashed, dot-dot-dashed line* for $\ell_{\rm cut} = 722, 1083$, and 1569); *right panel*: same as top panel, but for the ${}_{2048}S^{\ell_{\rm cut}}_{\rm GC}$ set. Note that the kurtosis of the cut is significantly different at small ℓ.

$n_{\rm side}$	128	256	512	1024	2048
time for one step (s)	0.121	0.121	0.502	1.88	8.53
number of steps (s)	252	313	315	377	325
total time (s)	40.1	50.3	200	989	3340

Table 3. same as Table 1 with Galactic masks.

band is the mean of its boundary: $\bar{i} = (2^i + 2^{i+1})/2$. The recovery of skewness and kurtosis is good in the case of unmasked data. Of course it degrades with the scale as we reach ℓ_{cut}. Using the reconstructed map is not the optimal way of measuring the 3 and 4 point functions at small scale. However, an optimal dedicated estimator can be built upon the same regularization technique. The masked case is not as good. There, a dedicated estimator, acting only on small, clean, pieces of the sky will probably yield better results.

4.4 Point source extraction

A segmentation of both the initial and the recovered maps is carried using peak patch on the sphere (Novikov et al. (2006), Sousbie et al. (2008)). Within each peak patch (see Figure B1), the brightest pixel is assigned a mass corresponding to the enclosed mass within the peak patch. Figure 11 (*left panel*) displays the corresponding PDFs for resolutions corresponding to $n_{\rm side} = 256, 512, 1024$ before and after reconstruction. As expected, the recovered point source PDF has a shifted mode and is less skewed than the original distribution.

4.5 Filling gaps within masks

Let us compare the shape of the recovered map to the initial map from the point of view of masking. Figure 12 illustrates a feature of the penalized reconstruction: it allows for some level of interpolation which provides means to fill the gaps corresponding to the galactic cuts. The smoothing penalty also induces a level of extrapolation, best seen in the residuals, see Figure 18. The masking (or more generally, non uniform weights, w_i) nevertheless biases the reconstructed map, as seen on Figure 10 and 13. Note finally that when masks are accounted for, it is straightforward to correct for them when computing the powerspectrum as the harmonic transform of the autocorrelation, which in turn is derived by correcting for the autocorrelation of the masks (see Szapudi et al. (2001) for details).

4.6 Optimal Wiener filtering

Throughout this paper the prior $C_\ell \equiv \ell^{-1}(\ell+1)^{-1}$ for the Laplacian prior is used in equation (B8). Let us briefly investigate how a customized prior for C_ℓ improves the quality of the interpolation at frequencies beyond the cutoff frequency. Figure 14 shows the corresponding power spectra, and demonstrates that the match between the recovered powerspectrum with the correct prior and the initial powerspectrum is in this regime good, whereas the smoothing prior, equation (27), yields a κ whose power spectrum starts departing from the input power spectrum at the critical frequency, $\ell_{\rm cut}$ at which the signal and the noise match. Nevertheless in what follows, a smoothing prior which is not customized to the specific problem is preferred.

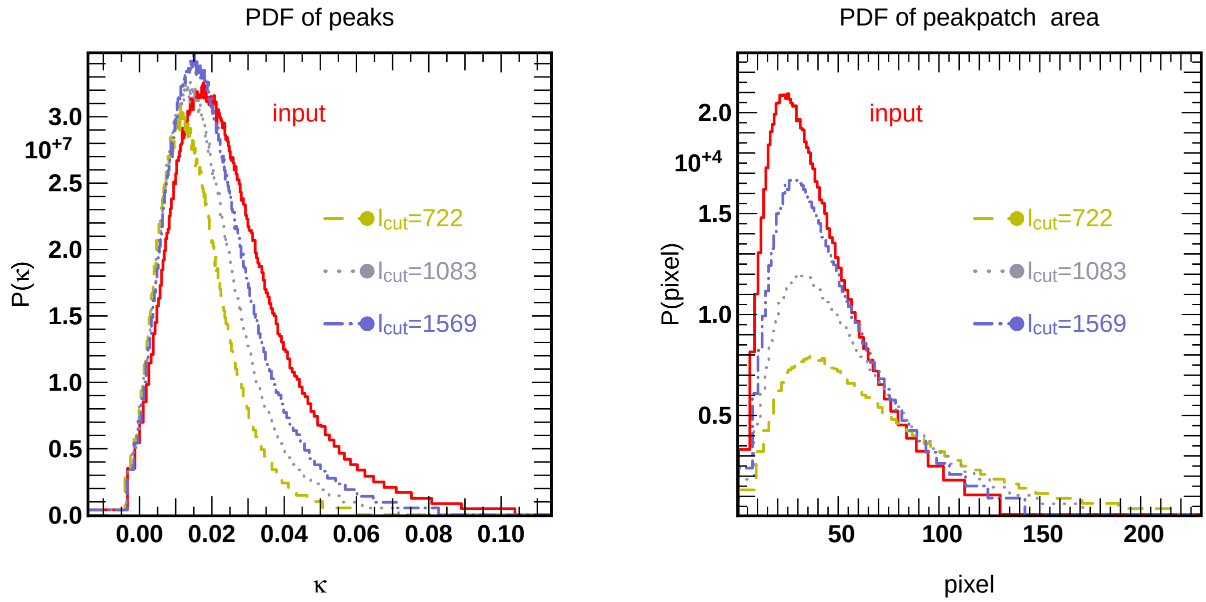

Figure 11. *left panel*: the PDFs of $\kappa_{\rm max}$ at point sources before and after reconstruction of set of simulations ${}_{2048}S_{\rm FS}^{\ell_{\rm cut}}$ (*dashed, dotted, dot-dashed line* for $\ell_{\rm cut} = 722, 1083$, and 1569); *right panel*: the PDFs of the area of peak patches (see Figure B1) before and after reconstruction for the same set of simulations. Note that, as expected, the recovered distribution of peaks is less skewed than the original, whereas conversely, PDF of the area of the peak patches for the low SNR reconstruction is more skewed towards larger patches.

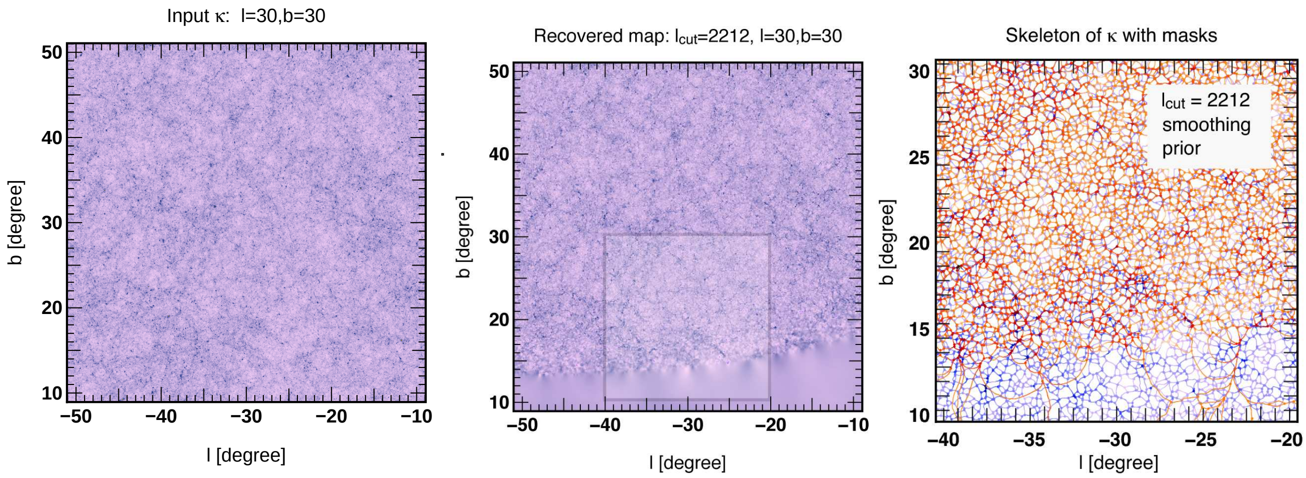

Figure 12. *left panel:* the initial κ map in the region with bright stars masking shown in Figure5 at coordinates $(l, b) = (30^\circ, 30^\circ)$; *middle panel:* the corresponding recovered κ map of a simulation ${}_{2048}S_{\rm GC}^{2212}$ Note that the gaps have been nicely filled up to the very edge of the mask; *right panel:* the corresponding two skeletons (*color coded by κ in purple:* input skeleton; *in orange:* recovered skeleton) for the inner region (marked as a square on the middle panel), when masking is present. Note the clear gradient away from the mask in the quality of the match between the two skeletons; Recall that most of the field is partially shielded by stars, as seen in Figure 5.

4.7 Sharpness preserving penalization

One of the main assets of high resolution full-sky lensing maps is to probe multiple scales: it then becomes possible to sample the non linear transition scale and, e.g. study the shape of clusters. Figure 15 illustrates this feature while displaying the result of the inversion with ℓ_2 and $\ell_1 - \ell_2$ penalties. For this experiment, a Cartesian subset at galactic coordinates $(l, b) = (0^\circ, 0^\circ)$ was extracted. The corresponding non-linear shear field $\mathbf{g}$ was generated via Fourier transform, and noised with a white additive noise of SNR of 1. This set was then inverted while assuming ℓ_2 (bottom right) and $\ell_1 - \ell_2$ (top right) penalties. The choice for the two penalty weights, μ and ϵ was made on the basis of least square residual in the inverted κ maps. The improvement of $\ell_1 - \ell_2$ over ℓ_2 penalty is significant. This statement is made more quantitative in Figure 16 which displays the PDF of the peaks within that image for the initial map (top left panel of Figure 15) computed following the peak patch prescription described in Section 4.4. The agreement between the input and the recovered distribution is significantly enhanced by the optimal $\ell_1 - \ell_2$ (top right) penalty.

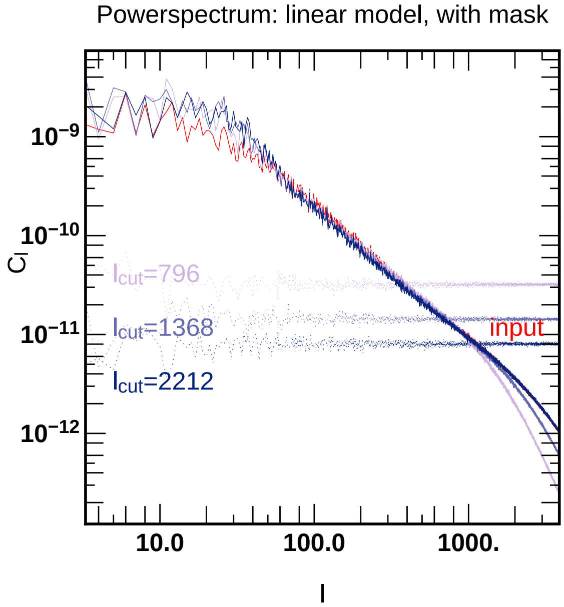

Figure 13. the power spectra of three reconstructions corresponding to Figure12 for $\ell_{\rm cut} = 796, 1368$, and 2212 together with the power spectra of the noise. Note that the the recovered power spectrum has extra power at large scales and less power at intermediate scales, an artifact of the mask which can be corrected for by accounting for the prior knowledge of the auto-correlation of the mask.

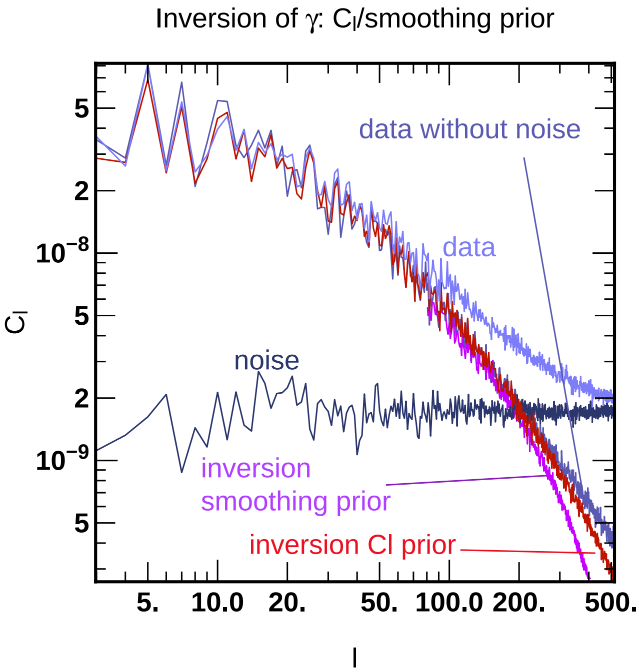

Figure 14. The power spectrum of the input and recovered κ, (with smoothing and C_ℓ prior, see equation (B5)) as a function of ℓ, together with the power spectrum of the noise and the noisy equivalent κ using a simulation, ${}_{512}S^{224}_{\rm FS}$. Note that the recovered power spectrum departs from the power spectrum of the input field roughly at the cutoff frequency when a quadratic smoothing penalty is applied. When the prior is constructed from the power spectrum, C_ℓ, of the sought field, a good extrapolation of the recovered power spectrum is achieved at ℓs well above the noise level.

4.8 Residual B modes

Let us investigate the effect of leaking of B modes with the following experiment: the noise in the transform of the B channel is boosted by some fixed amount over a map which has Galactic cuts. This corresponds to the case where the B is significantly larger than the noise, yet uncorrelated with the E mode, corresponding to e.g. a systematic bias in the ellipticity extraction for example. It is expected that, due to masks, this B mode will leak in E. An example of such leak, for B modes as large or up to 32 times larger than the noise, is shown in Figure 18. The power spectrum of the residuals in the corresponding κ map is computed while masking in the residual the exact regions corresponding to the cuts. When this boost is zero, (bottom curve in Figure 17) the power spectrum of these residuals is flat and corresponds to the noise powerspectrum. In contrast, the stronger the boost the larger the scale below which this power spectrum is colored. Note that it was checked that, as expected, these coherent residuals disappear completely if the galactic cuts are ignored. It would also be interesting to compare the distribution of the shape of dark matter in input/recovered clusters.

5 CONCLUSION & DISCUSSION

Weak lensing surveys require measuring statistical distributions of the morphological parameters (ellipticity, orientation, ...) of a very large number of galaxies. This paper demonstrated that these parameters can be measured with a better accuracy and strongly reduced bias if the deep sky images are properly deblurred prior to the shape measurements. Using a relative figure of merit (the recovered SExtractor ellipticity) we have shown that this deblurring could in crowded fields improve more than tenfold the accuracy of the recovered ellipticities. The deblurring is critical in crowded regions, where the overlapping of stars and galaxies otherwise prevents accurate morphological estimation. Henceforth dealing with such regions is important for a full-sky survey. Since such surveys will require the processing of a great number of large images, the calibration of these techniques is automated on the images themselves. In particular the level of regularization, μ and the $\ell_1 - \ell_2$ threshold are automatically tuned in order to deal with the noise level and the dynamics of the raw images. The gap-filling interpolation feature of the inversion would apply even more efficiently in this regime than in the map reconstruction regime described in Section 3. The algorithm described here scales well since it only relies on DFTs: hence it could be applied to very large images (say $16\,384^2$) such as those produced by modern surveys. Generalized cross validation was shown to yield a quantitative threshold in order to remove accurately the point sources within the field, hence imposing the optimal level of smoothing for the galaxies only. In this paper, the focus was put on blurred 8-meter ground-based observations, but the implementation for EUCLID-like space missions should be straightforward.

This paper also demonstrated that optimization in the context of Maximum A Posteriori provided a consistent

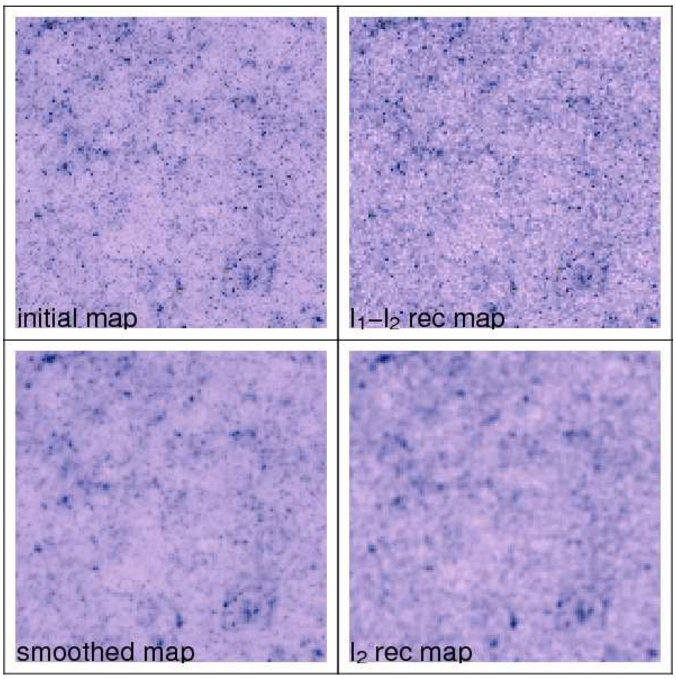

Figure 15. *top left panel:* a zoom of the original map at coordinates $(l, b) = (0^\circ, 0^\circ)$; *top right panel:* reconstruction with $\ell_1 - \ell_2$ penalty using the non-linear model. *bottom left panel:* input map smoothed at a FHWM of 1.5 pixels. *bottom right panel:* reconstruction with ℓ_2 penalty using the non-linear model. The color table is linear. The edge-preserving penalty appears qualitatively to preserve much better the amplitude and the number of high peaks in the κ map, as shown quantitatively in Figure16.

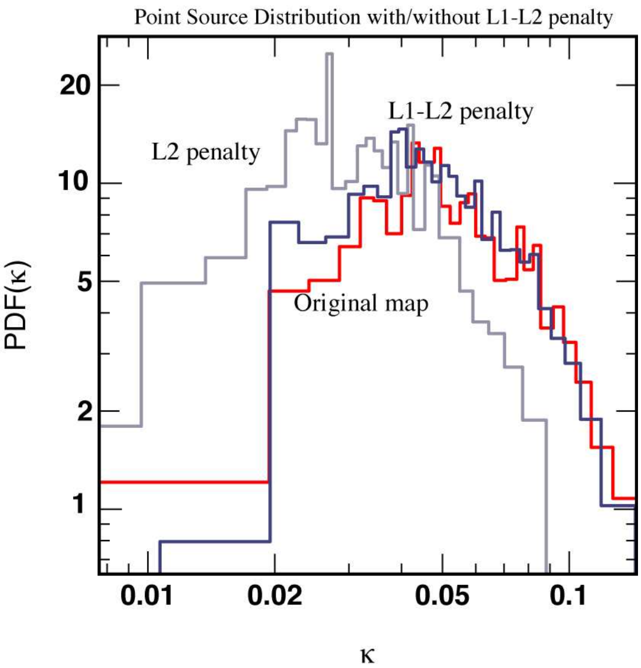

Figure 16. The PDF of point source as defined in Section 4.4 corresponding to the maps of Figure 15 recovered with $\ell_1 - \ell_2$ penalty, and ℓ_2 penalty respectively. The improvement with an edge-preserving penalty is significant.

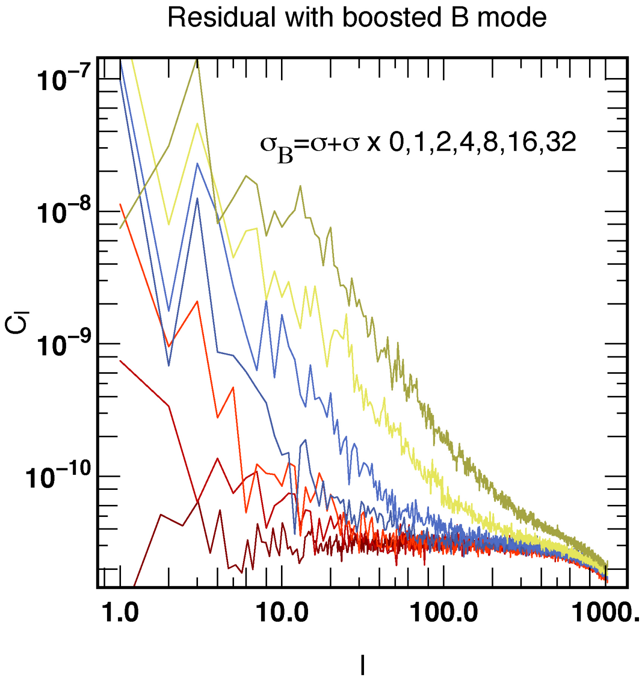

Figure 17. Power spectrum of the mask weighted residual error on κ as a function of the harmonic number,ℓ. The different curves correspond to boost of the B modes of increasing relative strength. The low order modes are polluted by leaks from the masks (see also Figure18); here $l_{\rm cut} = 752$.

framework for the reconstruction of κ maps on the sphere. Providing such maps is critical both in its own right, as it maps the dark matter distribution of our universe and gives access to the underlying powerspectrum at large scale. Such maps are also interesting when cross-correlated with other surveys (optical surveys, CMB maps, lensing reconstruction and distribution of SZ clusters from the Planck mission, X-ray sources etc..) in order to explore the evolution of the large-scale structure, and in the case of the surveys mapping the baryonic matter, to better understand biasing as a function of scale. Finally, though not optimally, it can be used to compute second and higher order statistics, and noticeably the three-point statistics or cluster counts, which constrain more efficiently the dark energy equation of state. It should be stressed once more that while the reconstructed κ maps yield biased estimates of the power-spectrum and higher order statistics, the technique described in this paper can be adapted to build dedicated optimal estimators for each of those observables.

This paper sketched possible solutions to issues that a full-sky weak-lensing pipeline will have to address, and also presented an inverse method implementing the map making step. Section 4 demonstrated the quality and limitations of the reconstruction using various statistical tools on a full-sky simulation of $\mathbf{g}$ with resolutions of up to $12 \times 4096^2 = 201\,326\,592$ pixels. In particular, it identified point sources of the fields and analyzed their PDF and showed that $\ell_1 - \ell_2$ penalty was critical at small scales. It also investigated the effect of leakage of B modes when Galactic cuts are present. Section 4.2 presented a method to probe the topology and geometry of a field on the sphere,

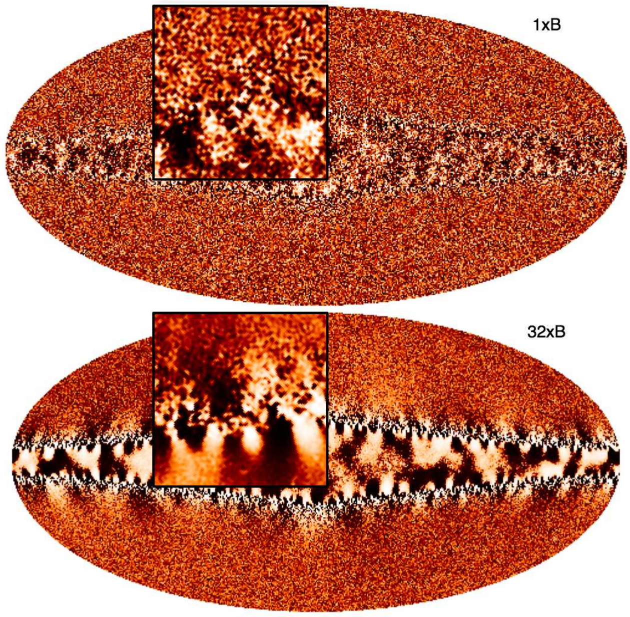

Figure 18. shows an example of full-sky leak of the B modes when masks are accounted for; *top panel*: the residuals corresponding to $\sigma_B = \sigma + \sigma$; the inner box corresponds to a zoom near the edge of the galactic cut at $(b, l) = (30, 20)$; *bottom panel*: same residual and box for $\sigma_B = \sigma + 32\sigma$. Note that for the latter case, the extend of the leakage is much larger and coherent.

the peak patches and the skeleton, and applied it to compare the recovered field to the initial field. The Cartesian dual formulation of ASKI was also implemented and may prove useful for surveys where sky coverage is sufficiently small. ASKI accounts for the possible building blocks that a full-scale pipeline aiming at sampling the dark matter distribution over the whole sky should provide. Specifically it allows for (i) automatically deblurring very large images using non-parametric self-calibrated edge-preserving $\ell_1 - \ell_2$ deconvolution with positivity; (ii) carrying the large *non-linear* inverse problem of reconstructing the convergence κ from the shear $\mathbf{g}$ using equation (17): the back and forth iterations between model and data are consistent with constraints in both spaces, and allow for an accurate recovery of cluster profiles and shapes; (iii) *non-uniform* weighting and masking: consistent with realistic Galactic cuts (and bright stars masking) and non-uniform sampling of the different regions of the sky, dealing transparently with the issue of the boundary; (iv) edge-preserving $\ell_1 - \ell_2$ penalty yielding quasi point-like cluster reconstruction. Finally (v) it introduced peak patches and the skeleton on the sphere as diagnosis for reconstruction, which acts as an efficient source extraction algorithm. Indeed, the degeneracy between the cosmological parameters $(\Omega_{\rm M}, \sigma_8)$ is for instance best lifted with cluster counts.

Possible improvements/investigation beyond the scope of this paper involve: (i) deblurring the images with a variable PSF within the field (ii) building optimal estimators for the power spectrum C_ℓ^κ, or the asymmetry S_3 (a possible option would be to rely on perturbation theory, and invert the non-linear problem for both C_ℓ^κ and S_3); (iii) inverting for γ *and* κ *simultaneously* and checking a posteriori the amplitude of the B modes (an alternative to the model described in equation (19); the issue of unicity of the solution will be a challenge); (iv) carrying the deprojection while assuming prior knowledge of a complete distribution of source planes in equation (28) (the corresponding inverse problem remains linear, with an effective kernel which depends on the optical configuration and the distribution of galaxies as a function of redshift); (v) moving away from the Born approximation, which involves solving Poisson's equation for each slice, and ray-tracing back to the source while solving for the lens equation though all the slices; (vi) implementing a more realistic noise modeling (which amounts to changing the cost function, equation (24)); (vii) studying the shape of dark matter distribution in clusters and groups: typically this would also involve cross-correlating the corresponding distribution with the light at various wavelengths and finally (viii) propagating the analysis up to the cosmic figure of merit for the dark energy parameters.

Acknowledgments

We thank Dominique Aubert, Eric Hivon, Martin Kilbinger and Yannick Mellier for comments and suggestions, the HORIZON 4Π *team and the staff at the CCRT for their help in producing the simulation, and D. Munro for freely distributing his* YORICK *programming language and* OPENGL *interface (available at* `http://yorick.sourceforge.net/`*) The galactic mask was provided to us by Adam Amara. This work was carried within the framework of the* HORIZON *project*: `www.projet-horizon.fr`.

REFERENCES

Aubert D., Pichon C., Colombi S., 2004, *MNRAS*, 352, 376
Bartelmann M., Schneider P., 2001, Phys. Rep., 340, 291
Benabed K., Scoccimarro R., 2005, Arxiv preprint astro-ph
Bernardeau F., Mellier Y., van Waerbeke L., 2002, Arxiv preprint astro-ph
Bernardeau F., van Waerbeke L., Mellier Y., 1997, Astronomy and Astrophysics, 322, 1
Bertin E., Arnouts S., 1996, aaps, 117, 393
Bradac M., Schneider P., Lombardi M., Erben T., 2005, arXiv, astro-ph
Bridle S., Abdalla F., 2007, The Astrophysical Journal
Bridle S., Hobson M., Lasenby A., Saunders R., 1998, Mon. Not. R. Astron. Soc.
Cacciato M., Bartelmann M., Meneghetti M., Moscardini L., 2006, arXiv, astro-ph
Caucci S., Colombi S., Pichon C., Rollinde E., Petitjean P., Sousbie T., 2008, *MNRAS* in press, pp 000–000
Crittenden R., Natarajan P., Pen U., Theuns T., 2002, The Astrophysical Journal
Erben T., Van Waerbeke L., Bertin E., Mellier Y., Schneider P., 2001, AAP , 366, 717
Fu et al. 2008, Astronomy & Astrophysics
Girard D. A., 1989, Numr. Math., 56, 1
Golub G. H., Heath M., Wahba G., 1979, Technometrics, 21, 215
Górski K. M., et al. 1999, in Banday A. J., Sheth R. K., da Costa L. N., eds, Evolution of Large Scale Structure : From Recombination to Garching Analysis issues for large CMB data sets. pp 37–+

Halkola A., Seitz S., Pannella M., 2006, arXiv, astro-ph
Hirata C., Seljak U., 2004, Physical Review D
Högbom J. A., 1974, A&AS , 15, 417
Hu W., 2000, *Phys. Rev. D*, 62, 043007
Jee M., Ford H., Illingworh G., White R., et al. 2007, The Astrophysical Journal
Kilbinger M., Schneider P., 2005, Arxiv preprint astro-ph
Kitching T., Heavens A., Taylor A., Brown M., et al. 2006, Arxiv preprint astro-ph
Marshall P., Hobson M., Gull S., Bridle S., 2002, Monthly Notices of the Royal Astronomical Society
Massey R., Rhodes J., Leauthaud A., Capak P., Ellis R., et al. 2007, Arxiv preprint astro-ph
Mugnier L. M., Fusco T., Conan J.-M., 2004, 21, 1841
Nocedal J., Wright S. J., 2006, Numerical Optimization, second edition edn. Springer Verlag
Novikov D., Colombi S., Doré O., 2006, *MNRAS*, 366, 1201
Password F., 2007, Monthly Notices of the Royal Astronomical Society
Pichon C., al. 2009, *MNRAS* in prep., pp 000–000
Pichon C., Bernardeau F., 1999, Astronomy and Astrophysics, 343, 663
Pichon C., Thiébaut E., 1998, *MNRAS*, 301, 419
Pichon C., Vergely J. L., Rollinde E., Colombi S., Petitjean P., 2001, *MNRAS*, 326, 597
Pires S., Starck J. ., Amara A., Teyssier R., Refregier A., Fadili J., 2008, ArXiv e-prints
Pogosyan D., Pichon C., Gay C., Prunet S., Cardoso J., Sousbie T., Colombi S., 2009, MNRAS, 0, 0
Prunet S., Pichon C., Aubert D., Pogosyan D., Teyssier R., Gottloeber S., 2008, *ApJ Sup.*, 178, 179
Richardson W. H., 1972, Journal of the Optical Society of America (1917-1983), 62, 55
schirmer M., Erben T., Hetterscheidt M., Schneider P., 2007, Astronomy & Astrophysics, 462
Schneider P., van Waerbeke L., Kilbinger M., Mellier Y., 2002, AAP , 396, 1
Schwarz U. J., 1978, AAP , 65, 345
Seitz S., Schneider P., Bartelmann M., 1998, Arxiv preprint astro-ph
Sheth R. K., Tormen G., 1999, *MNRAS*, 308, 119
Skilling J., Strong A. W., Bennett K., 1979, *MNRAS*, 187, 145
Soulez F., Denis L., Thiébaut E., Fournier C., Goepfert C., 2007, J. Opt. Soc. Am. A, 24, 3708
Sousbie T., Pichon C., Colombi 2008, *MNRAS* , pp 000–000
Sousbie T., Pichon C., Colombi S., Novikov D., Pogosyan D., 2007, ArXiv e-prints, 707
Sousbie T., Pichon C., Courtois H., Colombi S., Novikov D., 2006, ArXiv Astrophysics e-prints
Starck J., Pires S., Refregier A., 2005, Arxiv preprint astro-ph
Szapudi I., Prunet S., Colombi S., 2001, *ApJ Let.*, 561, L11
Takada M., Jain B., 2002, Monthly Notice of the Royal Astronomical Society, 337, 875
Takada M., Jain B., 2003, Monthly Notices of the Royal Astronomical Society
Takada M., Jain B., 2004, Monthly Notices of the Royal Astronomical Society, 348, 897
Tarantola A., Valette B., 1982, Reviews of Geophysics and Space Physics, 20, 219
Teyssier R., 2002, AAP , 385, 337
Teyssier R., Pires S., Prunet S., Aubert D., Pichon C., Amara A., Benabed K., Colombi S., Refregier A., Starck J.-L., 2008, ArXiv e-prints
Thiébaut E., 2002, in Starck J.-L., Murtagh F. D., eds, Astronomical Data Analysis II Vol. 4847, Optimization issues in blind deconvolution algorithms. pp 174–183
Thiébaut E., 2005, in Foy R., Foy F. C., eds, NATO ASIB Proc. 198: Optics in astrophysics Introduction to Image Reconstruction and Inverse Problems. pp 397–+
Wahba G., ed. 1990, Spline models for observational data

APPENDIX A: EFFICIENT STAR REMOVAL

We have observed that for realistic deep field images, generalized cross validation (GCV) yields an hyper-parameter value which is relevant to regularize the higher part of the dynamic (mainly due to stars, i.e. point-like objects which concentrate their luminous energy in a very small area) but which is much too low to regularize the lower parts ot the dynamic where galaxies remain. Indeed, when dealing with images with a large dynamical range, GCV yields a value of the regularization level μ which is necessarily a compromise between not smoothing too much the sharp features and sufficient smoothing of low contrasted structures to avoid noise amplification. The solution to the problem of underestimating the regularization weight can be solved by applying the GCV method onto the image with no stars. We want to find structures of known shape $s(x)$ but unknown position and intensity in the image $\boldsymbol{y}$. In our case, $s(x)$ is the PSF since we want to detect stars. This reasoning could however be generalized to other kind of objects. If a single object of this shape is present in the image, this could be achieved by considering the objective function:

$$\phi_{\rm full}(\alpha, t) = \sum_k w_k \left[\alpha\, s(x_k - t) - y_k\right]^2$$

to be minimized w.r.t. the weight α and the offset t, here a 2-D vector. In fact, since $\boldsymbol{y}$ may be crowded with similar structures (or with other fainter structures), a better strategy is to limit the local fit to a small region of interest (ROI) around the structure. This is achieved by minimizing:

$$\phi(\alpha, t) = \sum_k w_k\, r(x_k - t)\left[\alpha\, s(x_k - t) - y_k\right]^2$$

where $r(\delta\boldsymbol{x})$ is equal to 1 within the region of interest (ROI) and equal to 0 outside the ROI. Minimization of $\phi(\alpha, t)$ w.r.t. α yields the best intensity for a local fit around t:

$$\frac{\partial\phi}{\partial\alpha} = 0 \quad\Longleftrightarrow\quad \alpha^\star = \frac{\sum_k w_k\, r(x_k - t)\, s(x_k - t)\, y_k}{\sum_k w_k\, r(x_k - t)\, s(x_k - t)^2}\,. \tag{A1}$$

Inserting $\alpha^\star$ in the objective function yields:

$$\begin{aligned} \phi^\star(t) &\triangleq \phi(\alpha, t)\big|_{\alpha=\alpha^\star}\,, \\ &= \sum_k w_k\, r(x_k - t)\, y_k^2\,, \\ &\quad - \frac{\left(\sum_k w_k\, r(x_k - t)\, s(x_k - t)\, y_k\right)^2}{\sum_k w_k\, r(x_k - t)\, s(x_k - t)^2}\,. \end{aligned}$$

Since $r(\delta\boldsymbol{x})^2 = r(\delta\boldsymbol{x})$, by defining $s_{\rm ROI}(\delta\boldsymbol{x}) \equiv r(\delta\boldsymbol{x})\, s(\delta\boldsymbol{x})$, the local criterion and local best intensity can be rewritten as:

$$\begin{aligned}\phi^\star(t) &= \sum_k r(x_k - t)\, w_k\, y_k^2 - \frac{\left(\sum_k s_{\mathrm{ROI}}(x_k - t)\, w_k\, y_k\right)^2}{\sum_k s_{\mathrm{ROI}}(x_k - t)^2\, w_k}\,,\\ \alpha^\star(t) &= \frac{\sum_k s_{\mathrm{ROI}}(x_k - t)\, w_k\, y_k}{\sum_k s_{\mathrm{ROI}}(x_k - t)^2\, w_k}\,.\end{aligned}$$

These parameters can be computed for all shifts by an integer number of pixels by means of FFT's (cross-correlation product). Unfortunately, the overall minimum of $\phi^\star(t)$ is not the best choice for removing the brightest structures since there is no warranty that this minimum corresponds to a bright object. It is better to select the the location which yields the brightest structure, i.e. the maximum of $\alpha^\star(t)$. After removal of the contribution $\alpha^\star(t^\star)\, s(x - t^\star)$ from the data, this technique can be repeated to detect the second brightest source, and so on. The corresponding algorithm is very similar to the CLEAN method (Högbom 1974; Schwarz 1978) with the further refinement of accounting for non-stationary noise and missing data. It has been shown that it achieves sub-pixel precision (Soulez et al. 2007) and that it could be used to detect (and remove) out of field sources (Soulez et al. 2007).

APPENDIX B: DETAILED MODEL ON THE SPHERE

Let us describe in more details the model used for the inversion of Section 3.1.

B1 Discretization and Sampling

After discretization and using explicit indices, the model in equation (17) writes:

$$g_{j,k} = \frac{\gamma_{j,k}}{1 - \kappa_j} + e_{j,k}\,,$$

where the index j runs over the sky coordinates $\hat{\boldsymbol{n}}_j = (x_j, y_j)$, index k corresponds to the two components U and Q of the polarization, whereas ℓ and m are the harmonic indices and p refers to the two components of the spinned 2-harmonic. In words, the discretization yields:

$$g_{j,k} \equiv g_k(\hat{\boldsymbol{n}}_j),\;\; \gamma_{j,k} \equiv \gamma_k(\hat{\boldsymbol{n}}_j),\;\; \kappa \equiv \kappa(\hat{\boldsymbol{n}}_j),\;\; e_{j,k} \equiv e_k(\hat{\boldsymbol{n}}_j)\,.$$

Here the fields $\boldsymbol{\kappa}$ and $\boldsymbol{\gamma}$ are linear functions of the complex field $\boldsymbol{a}$ of the spherical harmonic coefficients of $\boldsymbol{\kappa}$. Using the matrix notation of the paper, $\boldsymbol{\kappa}$ and $\boldsymbol{\gamma}$ write:

$$\boldsymbol{\kappa} = \mathbf{K}\cdot\boldsymbol{a}\,,\quad \boldsymbol{\gamma} = \mathbf{G}\cdot\boldsymbol{a}\,,$$

where $\mathbf{K} = \mathbf{Y}$ and $\mathbf{G} = {}_p\mathbf{Y}\cdot\mathbf{J}$; with explicit index notations:

$$\kappa_j = \sum_{\ell,m} K_{j,\ell,m}\, a_{\ell,m} = \sum_{\ell,m} \mathbf{Y}_{j,\ell,m}\, a_{\ell,m}\,,$$

and

$$\gamma_{j,k} = \sum_{\ell,m} G_{j,k,\ell,m}\, a_{\ell,m} = \sum_{\ell,m,p} {}_p\mathbf{Y}_{j,k,\ell,m,p}\, (\mathbf{J}\cdot\boldsymbol{a})_{\ell,m,p}\,,$$

with

$$(\mathbf{J}\cdot\boldsymbol{a})_{\ell,m,1} = -\sqrt{\frac{(\ell+2)(\ell-1)}{(\ell+1)\ell}}\, a_{\ell,m}\,, \qquad \text{(B1)}$$

$$(\mathbf{J}\cdot\boldsymbol{a})_{\ell,m,2} = 0\,. \qquad \text{(B2)}$$

B2 Likelihood

The data related term in the cost function is

$$\mathcal{L} = \sum_{j,k} w_{j,k} \left(\frac{\gamma_{j,k}}{1 - \kappa_j} - g_{j,k}\right)^2\,.$$

The gradient of this term is needed to find the solution of the inverse problem:

$$\begin{aligned}\frac{\partial \mathcal{L}(\boldsymbol{a})}{\partial a_{\ell,m}} &= 2\sum_{j,k} H_{\ell,m,j,k}\,\frac{r_{j,k}}{1-\kappa_j} + \\ &\quad 2\sum_j \mathbf{Y}^*_{\ell,m,j}\,\frac{\sum_k \gamma^*_{j,k} r_{j,k}}{(1-\kappa_j)^2}\,,\end{aligned} \qquad \text{(B3)}$$

where

$$r_{j,k} = w_{j,k}\left(\frac{\gamma_{j,k}}{1-\kappa_j} - g_{j,k}\right)$$

are the weighted residuals, and where

$$H_{\ell,m,j,k} = -\sqrt{\frac{(\ell+2)(\ell-1)}{(\ell+1)\ell}}\; {}_p\mathbf{Y}^*_{\ell,m,1,j,k}\,. \qquad \text{(B4)}$$

B3 Regularization

The aim of the regularization is to avoid ill-conditioning and noise amplification in the inversion. Following Bayesian prescription, this can be achieved by requiring the field $\boldsymbol{\kappa}$ to obey some known *a priori* statistics.

B3.1 Wiener filter and ℓ_2 penalty

Assuming the field $\boldsymbol{\kappa}$ has Gaussian distribution with mean $\bar{\boldsymbol{\kappa}} = \langle\boldsymbol{\kappa}\rangle$ and covariance $\mathbf{C}_{\boldsymbol{\kappa}} = \langle(\boldsymbol{\kappa} - \bar{\boldsymbol{\kappa}})\cdot(\boldsymbol{\kappa} - \bar{\boldsymbol{\kappa}})^{\mathrm{T}}\rangle$, the prior penalty should write:

$$\mathcal{R} = (\boldsymbol{\kappa} - \bar{\boldsymbol{\kappa}})^{\mathrm{T}}\cdot\mathbf{C}_{\boldsymbol{\kappa}}^{-1}\cdot(\boldsymbol{\kappa} - \bar{\boldsymbol{\kappa}})\,.$$

For a field with zero mean ($\bar{\boldsymbol{\kappa}} = \mathbf{0}$) and stationary isotropic statistics, the regularization can be expressed in terms of the harmonic coefficients:

$$\mathcal{R}(\boldsymbol{a}) = \left\|\mathbf{C}^{-1/2}\cdot\boldsymbol{a}\right\|^2 = \sum_\ell \frac{\sum_m |a_{\ell,m}|^2}{C_\ell}\,, \qquad \text{(B5)}$$

with

$$C_\ell = \langle|a_{\ell,m}|\rangle^2\,, \qquad \text{(B6)}$$

where the angular brackets denote here the expected value taken over the index m of the harmonic coefficients. The gradient of the stationnary isotropic Gaussian regularization in equation (B5) is:

$$\frac{\partial \mathcal{R}(\boldsymbol{a})}{\partial a_{\ell,m}} = 2\,\frac{a_{\ell,m}}{C_\ell}\,.$$

Note that the regularization in equation (B5) with a known power spectrum C_ℓ for the field $\boldsymbol{\kappa}$ yields the so-called Wiener filter. When the power spectrum of $\boldsymbol{\kappa}$ is not exactly known, a quadratic prior can be used. For instance:

$$\mathcal{R}(\boldsymbol{a}) = \lambda\left\|\mathbf{R}^{-1/2}\cdot\boldsymbol{a}\right\|^2 = \lambda\sum_\ell \frac{\sum_m |a_{\ell,m}|^2}{R_\ell}\,, \qquad \text{(B7)}$$

where $\lambda \geqslant 0$ is a regularization parameter that must be properly tuned. In our framework, effective regularization is

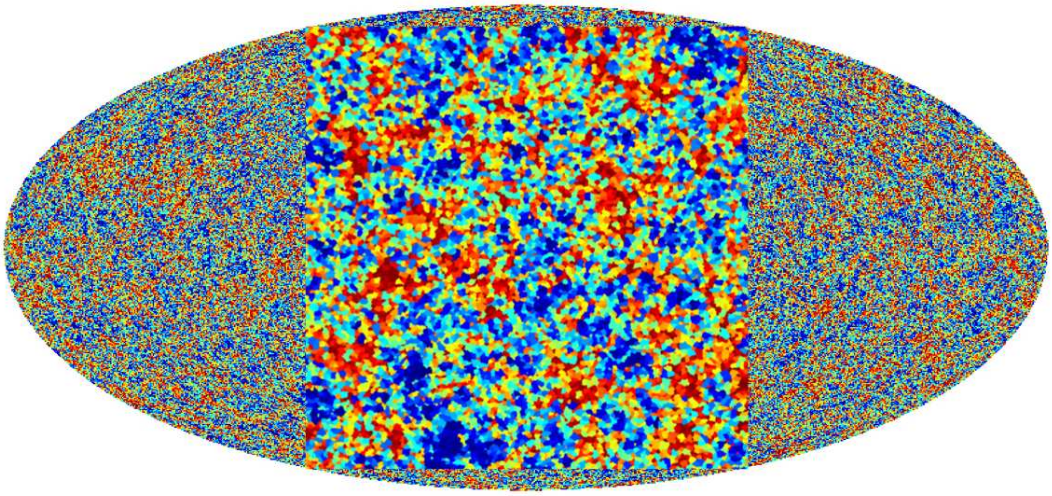

Figure B1. Peak patch of the recovered κ map. The inner box zooms the central region. The color coding corresponds loosely to the density of the different peak patches. The PDF of the area of these patches is described in Figure 11 while the maxima mentioned in this figure are found within each patch.

achieved by requiring the field $\boldsymbol{\kappa}$ to be somewhat smooth. In practice, this is obtained by requiring R_ℓ to be some positive non-decreasing function of the index ℓ. Note that, from a Bayesian viewpoint, the regularization in equation (B7) corresponds to the prior that$\boldsymbol{\kappa}$ is a stationary isotropic centered Gaussian field with mean power spectrum $C_\ell = R_\ell/\lambda$, which is similar to the Wiener filter except that the exact statistics is not known in advance (because some parameters of the regularization have to be tuned). The gradient of $\mathcal{R}$ in equation (B7) reads:

$$\frac{\partial \mathcal{R}(\boldsymbol{a})}{\partial a_{\ell,m}} = 2\,\lambda\,\frac{a_{\ell,m}}{R_\ell}\,.$$

The quadratic prior in equation (B7) can be expressed in terms of $\boldsymbol{\kappa}$:

$$\mathcal{R} = \lambda\,\left\|\mathbf{R}^{-1/2}\cdot\boldsymbol{a}\right\|^2 = \lambda\,\|\mathbf{D}\cdot\boldsymbol{\kappa}\|^2$$

where $\mathbf{D} = \mathbf{R}^{-1/2}\cdot\mathbf{Y}^{\#}$ is some finite difference operator which gives some estimate of the local fluctuation of the field, and $\mathbf{Y}^{\#}$is the (pseudo-)inverse of the scalar spherical harmonics matrix. In our framework, we choose to measure the amplitude of the local fluctuations of the field $\boldsymbol{\kappa}$ by its Laplacian $\nabla^2\boldsymbol{\kappa}$ and to express the regularization penalty as:

$$\mathcal{R}(\boldsymbol{a}) = \lambda\sum_j \phi\left(\left(\nabla^2\boldsymbol{\kappa}\right)_j\right) \tag{B8}$$

where the cost function $\phi(r)$ is an increasing function of $|r|$. When $\phi(r) = r^2$, our regulariztion is a quadratic penalty similar to equation (B7). Using matrix notation, the Laplacian of the field $\boldsymbol{\kappa}$ write :

$$\nabla^2\boldsymbol{\kappa} = \mathbf{Y}\cdot\mathbf{L}^{-1/2}\cdot\boldsymbol{a}\,, \tag{B9}$$

with

$$\left(\mathbf{L}^{-1/2}\cdot\boldsymbol{a}\right)_{\ell,m} = \frac{a_{\ell,m}}{\sqrt{L_\ell}}$$

where $L_\ell \equiv \ell^{-2}(\ell+1)^{-2}$. In order to perform the minimization, the gradient of the regularization must be computed. By the chain rule:

$$\begin{aligned}\frac{\partial \mathcal{R}(\boldsymbol{a})}{\partial a_{\ell,m}} &= \lambda\sum_j \phi'\left(\left(\nabla^2\boldsymbol{\kappa}\right)_j\right)\frac{\partial\left(\nabla^2\boldsymbol{\kappa}\right)_j}{\partial a_{\ell,m}}\,,\\ &= \lambda\sum_j \frac{\mathbf{Y}^*_{\ell,m,j}}{\sqrt{L_\ell}}\,\phi'\left(\left(\nabla^2\boldsymbol{\kappa}\right)_j\right),\end{aligned} \tag{B10}$$

where $\phi'(r)$ is the derivative of $\phi(r)$.

B3.2 $\ell_2 - \ell_1$ penalty

As for the image restoration, quadratic regularization yields spuriours ripples in the regularized $\boldsymbol{\kappa}$ map. To avoid them, we propose to use a $\ell_2 - \ell_1$ cost function ϕ applied to the Laplacian of $\boldsymbol{\kappa}$. The details of the $\ell_2 - \ell_1$ cost function are discussed in section 2.1.4.Taking $\mathcal{R}(\boldsymbol{a}) = \sum_j \phi\left(\left(\nabla^2\boldsymbol{\kappa}\right)_j\right)$, with ϕ given in equation (16), yields:

$$\begin{aligned}\frac{\partial \mathcal{R}(\boldsymbol{a})}{\partial a_{\ell,m}} &= \sum_j \frac{2\,\varepsilon\,\left(\nabla^2\boldsymbol{\kappa}\right)_j}{\varepsilon + \left|\left(\nabla^2\boldsymbol{\kappa}\right)_j\right|}\frac{\partial\left(\nabla^2\boldsymbol{\kappa}\right)_j}{\partial a_{\ell,m}}\,,\\ &= 2\,\varepsilon\sum_j \frac{\mathbf{Y}^*_{\ell,m,j}}{\sqrt{C_\ell}}\,\frac{\left(\nabla^2\boldsymbol{\kappa}\right)_j}{\varepsilon + \left|\left(\nabla^2\boldsymbol{\kappa}\right)_j\right|}\,.\end{aligned}$$

In practice, we use GCV to set the level of the regularization, possibly after stars removal (as explained in Appendix A) and the $\ell_1 - \ell_2$ threshold is set to be $\varepsilon = \alpha\,\sigma$ where $\alpha \sim 2-3$ and σ is the standard deviation of the histogram of spatial finite differences.

APPENDIX C: FROM THE SPHERE TO THE PLANE

Following closely Hu (2000), let us start with a scalar field on the sphere, and its decomposition on the usual spherical harmonics:

$$X(\hat{\mathbf{n}}) = \sum_{lm} X_{lm} Y_l^m\,, \tag{C1}$$

and let us define

$$X(\mathbf{l}) = \sqrt{\frac{4\pi}{2l+1}} \sum_m i^{-m} X_{lm} e^{im\phi_l} , \quad \text{(C2)}$$

together with the inverse relation

$$X_{lm} = \sqrt{\frac{2l+1}{4\pi}} i^m \int \frac{d\phi_l}{2\pi} X(\mathbf{l}) e^{-im\phi_l} ,$$

where ϕ_l is the polar angle of the $\mathbf{l}$ vector in Fourier space. Let us show, that $X(\mathbf{l})$ corresponds to the Fourier decomposition of the field in the flat-sky limit (small angles near the pole). Indeed, taking the asymptotic behavior of the spherical harmonics

$$Y_l^m \approx J_m(l\theta) \sqrt{\frac{l}{2\pi}} e^{im\phi} ,$$

together with the plane-wave expansion in terms of Bessel functions

$$e^{i\mathbf{l}.\hat{\mathbf{n}}} = \sum_m i^m J_m(l\theta) e^{im(\phi-\phi_l)} \approx \sqrt{\frac{2\pi}{l}} \sum_m i^m Y_l^m e^{im\phi_l} . \quad \text{(C3)}$$

We get from equation (C1)

$$\begin{aligned} X(\hat{\mathbf{n}}) &\approx \sum_l \frac{l}{2\pi} \int \frac{d\phi_l}{2\pi} X(\mathbf{l}) \sum_m J_m(l\theta) i^m e^{im(\phi-\phi_l)} , \\ &\approx \int \frac{d^2 l}{(2\pi)^2} X(\mathbf{l}) e^{i\mathbf{l}.\hat{n}} . \end{aligned}$$

For a spin-2 field, let us proceed likewise. We start from the all-sky definition of a spin-2 tensor field, and its decomposition in spin-2 spherical harmonics:

$$_{\pm}X(\hat{\mathbf{n}}) = \sum_{lm} {}_{\pm}X_{\{lm\}} {}_{\pm 2}Y_l^m , \quad \text{(C4)}$$

where $_{\pm}X(\hat{\mathbf{n}})$ is defined in the spherical tangent coordinates e_θ, e_ϕ. We define, as in equation (C2), the Fourier modes of the components of the spin-2 field as $_{\pm}X(\mathbf{l})$. We have in the flat-sky limit the following asymptotic form for the spin-2 spherical harmonics:

$$_{\pm 2}Y_l^m \approx \frac{1}{l^2} e^{\mp 2i\phi} (\partial_x \pm i\partial_y)^2 Y_l^m . \quad \text{(C5)}$$

Plugging equation (C4) into equation (C5) yields:

$$\begin{aligned} _{\pm}X(\hat{\mathbf{n}}) &\approx \sum_l \frac{l}{2\pi} \int \frac{d\phi_l}{2\pi} X(\mathbf{l}) e^{\mp 2i\phi} \frac{1}{l^2} (\partial_x \pm i\partial_y)^2 e^{i\mathbf{l}\cdot\hat{\mathbf{n}}} , \\ &\approx -\int \frac{d^2 l}{(2\pi)^2} {}_{\pm}X(\mathbf{l}) e^{\pm 2i(\phi_l-\phi)} e^{i\mathbf{l}\cdot\hat{\mathbf{n}}} . \end{aligned}$$

Redefining the spin-2 field in the fixed coordinate system such that the first axis (e_x) is aligned with $\phi = 0$, we obtain:

$$_{\pm}X'(\hat{\mathbf{n}}) \approx -\int \frac{d^2 l}{(2\pi)^2} {}_{\pm}X(\mathbf{l}) e^{\pm 2i\phi_l} e^{i\mathbf{l}\cdot\hat{\mathbf{n}}} , \quad \text{(C6)}$$

where $l_x + il_y = le^{i\phi_l}$. Expanding $_{\pm}X(\mathbf{l}) = -(E(\mathbf{l}) \pm iB(\mathbf{l}))$, we can relate these rotationally invariant quantities to the Fourier transforms of the spin-2 field individual components.

APPENDIX D: CONVERGENCE MAPS

The inversion technique described in the main text was validated using the mocks extracted from the HORIZON-4π simulation (Prunet et al. 2008). Let us briefly describe here how this simulation was used to generate mock slices and κ maps.

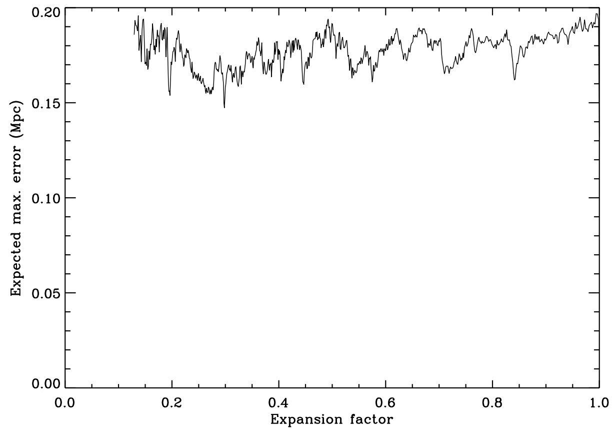

Figure D1. the expected maximum uncertainty on particle positions due to the method used to create the light cone as a function of the expansion factor. It is computed according to equation (D1) with a velocity v estimated to be 3 times the Virial velocity of the largest cluster in the simulation.

D1 Light cone generation

The generation of a light cone during run time can be performed easily at each coarse time step of the simulation. Given a choice of the observer position in the simulation box, that we suppose here for simplicity to be at the origin of coordinates, it is easy to select the particles that belong to the slice in between redshifts $z_2 < z_1$ corresponding to two successive coarse time steps: if (x, y, z) are the comoving coordinates of a particle, and $d = \sqrt{x^2 + y^2 + z^2}$ its comoving distance from the observer, we must have $d_{\rm dist}(z_2) < d \leqslant d_{\rm dist}(z_1)$ for the particle to be selected, where $d_{\rm dist}(z)$ is the comoving distance that a photon covers between redshift z and present time in the simulation box: $d_{\rm dist} = \int c\mathrm{d}t/\mathrm{a(t)}$, where c is the speed of light and a the expansion factor. The problem is that structures evolve during a coarse time step, so there are necessarily some discontinuities at the border between two successive light cone slices. These discontinuities are due to large scale motions of particles plus their thermal velocity within dark matter halos. Given the large size of the simulation considered here, thermal motion within the largest cluster are expect to bring the most significant effects of discontinuity. For a particle with peculiar velocity v, the largest discontinuity to be expected, i.e. the largest possible difference between expected and actual position of the particle is given by

$$\Delta = (v/c)[d_{\rm dist}(z_1) - d_{\rm dist}(z_2)]. \quad \text{(D1)}$$

In equation (D1), we performed a linear Lagrangian approximation, i.e. we neglected variations of the velocity of the particle during the coarse time step. Using Press & Schechter formalism, or the improved formula of Sheth & Tormen (1999), the mass of the largest cluster in the Horizon simulation solves approximately the implicit equation

$$\Omega_0 \rho_{\rm c} L^3 F[M_{\rm max}(z), z]/M_{\rm max}(z) = 1, \quad \text{(D2)}$$

where $\rho_{\rm c}$ is the critical density of the Universe and F is the fraction of mass in the Universe in objects of mass larger than M. Basically, this equation states that the mass in objects of mass larger than M is equal to M, which means that we are left with only one cluster of mass M, the largest detectable cluster in our cube of size L. We can compute $F(M,z)$ with the usual formula, e.g.

$$F(M,z) = \int_{\mu>\nu(M,z)} f(\mu)\mathrm{d}\mu, \tag{D3}$$

with $\nu = 1.686/\sigma(M,z)$ where $\sigma(M,z)$ is the linear variance at redshift z corresponding to mass scale M, and $f(\mu)$ is given by equation (10) of Sheth & Tormen (1999). Performing these calculations, we find that the largest cluster at present time in a cube of size $L = 2000h^{-1}$ Mpc should have a typical mass of $M_{\rm max}(z=0) \simeq 1.47\times10^{15}M_\odot$. With a standard Friend-of-friend algorithm using a linking parameter $b = 0.2$, we find that the most massive halo detected in the simulation presents a somewhat larger mass, $M = 5.4\times10^{15}M_\odot$. Yet, in that rare events regime, we cannot expect our theoretical estimate to be more accurate. What matters, though, is the thermal velocity rather than the mass. Applying the Virial theorem, we have (e.g., Peacock, 1999)

$$v^2 \simeq \frac{GM_{\rm max}}{R_{\rm vir}}, \tag{D4}$$

with

$$\frac{4}{3}\pi R_{\rm vir}^3\rho_{\rm vir} = M_{\rm max}, \quad \rho_{\rm vir} \simeq 178\Omega_0\rho_{\rm c}(1+z)^3/\Omega(z)^{0.7}, \tag{D5}$$

where $\Omega(z)$ is the density parameter as a function of redshift ($\Omega(0)\equiv\Omega_0$). These expressions are given in physical coordinates hence the factor $(1+z)^3$ in the expression of $\rho_{\rm vir}$. This reads, at $z = 0$, $v \simeq 1570$ km/s for $M_{\rm max}(z=0) \simeq 1.47\times10^{15}M_\odot$. In the largest cluster of the simulation, the overall velocity dispersion is of the order of 2100 km/s, a slightly larger value that reflects the actual value of the mass. To be conservative, we estimate the expected errors in equation (D1) with the Virial velocity rescaled by a factor 2100/1570, and with a further multiplication by a factor 3 to be in the 3σ regime. The corresponding maximal expected discontinuity displacement is shown in Mpc as a function of the expansion factor on Figure D1. As expected from the dynamically self-consistent calculation of the coarse time step (which is basically determined by a Courant condition using the velocity field), the comoving error does not change significantly with redshift and remains below the very conservative limit of 200 kpc. Obviously, we expect in practice the errors brought by discontinuities to be in general much smaller than that, as for $z = 0$ the present errors corresponds to unrealistic velocities as large as about 6000 km/s!

D2 From slices to κ maps

In the main text, the expression for κ as a function of the density contrast in the simulation is given in equation (28) in the geometric optic approximation. Let us rearrange this formula in a form that is more suited to integration over redshift slices in a simulation.

$$\kappa(\hat{\mathbf{n}}_{\rm pix}) \approx \frac{3}{2}\Omega_m \sum_b W_b \frac{H_0}{c}\int_{\Delta z_b}\frac{cdz}{H_0E(z)}\delta(\frac{c}{H_0}\mathcal{D}(z)\hat{\mathbf{n}}_{\rm pix}, z)\,,$$

where

$$W_b = \left(\int_{\Delta z_b}\frac{dz}{E(z)}\frac{\mathcal{D}(z)\mathcal{D}(z,z_s)}{\mathcal{D}(z_s)}\frac{1}{a(z)}\right)\Big/\left(\int_{\Delta z_b}\frac{dz}{E(z)}\right)\,,$$

is a slice-related weight, and the integral over the density contrast, δ, reads

$$\begin{aligned} I &= \int_{\Delta z_b}\frac{cdz}{H_0E(z)}\delta(\frac{c}{H_0}\mathcal{D}(z)\hat{\mathbf{n}}_{\rm pix}, z)\,, \\ &= \int_{\Delta\chi_b} d\chi\delta(\chi\hat{n}_{\rm pix},\chi)\,, \\ &\approx \frac{V(\text{simu})}{N_{\rm part}(\text{simu})}\left(\frac{N_{\rm part}(\theta_{\rm pix},z_b)}{S_{\rm pix}(z_b)} - 1\right)\,, \end{aligned}$$

where

$$S_{\rm pix}(z_b) = \frac{4\pi}{N_{\rm pix}}\frac{c^2}{H_0^2}\mathcal{D}^2(z_b)$$

is the comoving surface of the spherical pixel. Putting all together, we get the following formula for the convergence map:

$$\begin{aligned} \kappa(\theta_{\rm pix}) &= \frac{3}{2}\Omega_m\frac{N_{\rm pix}}{4\pi}\left(\frac{H_0}{c}\right)^3\frac{V(\text{simu})}{N_{\rm part}(\text{simu})}\times \\ &\quad \sum_b W_b\frac{N_{\rm part}(\theta_{\rm pix},z_b)}{\mathcal{D}^2(z_b)}\,. \end{aligned} \tag{D6}$$

Once the κ map is available it is straightforward to build the corresponding $\mathbf{g}$ using equation (17).

Mon. Not. R. Astron. Soc. **365,** 46–73 (2006) doi:10.1111/j.1365-2966.2005.09182.x

STECMAP: STEllar Content from high-resolution galactic spectra via Maximum A Posteriori

P. Ocvirk,[1]★ C. Pichon,[2] A. Lançon[1] and E. Thiébaut[3]

[1]*Observatoire de Strasbourg (UMR 7550), 11 rue de l'Université, 67000 Strasbourg, France*
[2]*Institut d'Astrophysique de Paris, 98 bis boulevard Arago, 75014 Paris, France*
[3]*Observatoire de Lyon, 9 avenue Charles André F-69561 Saint Genis Laval Cedex, France*

Accepted 2005 May 4. Received 2005 April 27; in original form 2005 March 17

ABSTRACT

In this paper we describe STECMAP (STEllar Content via Maximum A Posteriori), a flexible, non-parametric inversion method for the interpretation of the integrated light spectra of galaxies, based on synthetic spectra of single stellar populations (SSPs). We focus on the recovery of a galaxy's star formation history and stellar age–metallicity relation. We use the high-resolution SSPs produced by PÉGASE-HR to quantify the informational content of the wavelength range $\lambda\lambda = 4000$–6800. Regularization of the inversion is achieved by requiring that the solutions are relatively smooth functions of age. The smoothness parameter is set automatically via generalized cross validation.

A detailed investigation of the properties of the corresponding simplified linear problem is performed using singular value decomposition. It turns out to be a powerful tool for explaining and predicting the behaviour of the inversion, and may help designing SSP models in the future. We provide means of quantifying the fundamental limitations of the problem considering the intrinsic properties of the SSPs in the spectral range of interest, as well as the noise in these models and in the data. We demonstrate that the information relative to the stellar content is relatively evenly distributed within the optical spectrum. We show that one should not attempt to recover more than about eight characteristic episodes in the star formation history from the wavelength domain we consider. STECMAP preserves optimal (in the cross validation sense) freedom in the characterization of these episodes for each spectrum.

We performed a systematic simulation campaign and found that, when the time elapsed between two bursts of star formation is larger than 0.8 dex, the properties of each episode can be constrained with a precision of 0.02 dex in age and 0.04 dex in metallicity from high-quality data [$R = 10\,000$, signal-to-noise ratio (SNR) = 100 per pixel], not taking model errors into account. We also found that the spectral resolution has little effect on population separation provided low- and high-resolution experiments are performed with the same SNR per Å. However, higher spectral resolution does improve the accuracy of metallicity and age estimates in double-burst separation experiments. When the fluxes of the data are properly calibrated, extinction can be estimated; otherwise the continuum can be discarded or used to estimate flux correction factors.

The described methods and error estimates will be useful in the design and in the analysis of extragalactic spectroscopic surveys.

Key words: methods: data analysis – methods: statistical – techniques: spectroscopic – galaxies: abundances – galaxies: evolution – galaxies: stellar content.

1 INTRODUCTION

The diversity of shapes and colours of galaxies illustrates the wealth of physical mechanisms acting in these complex objects. Their formation history, including the building of their haloes, bulges, discs and disc patterns, is still controversial. Empirical constraints on the formation scenarios are engraved in the distribution of stellar ages, metallicities and kinematics. Unless the galaxies can be resolved into stars, this crucial information must be extracted from integrated spectra. This spectral energy distribution (SED) is a recording of the whole life of a galaxy: the condition of its birth, the

★E-mail: ocvirk@astro.u-strasbg.fr

formation and assembly of its first blocks, its passive evolution and the recycling of its material, or its active evolution through merging, all these determine the current stellar content. Yet, this information is embedded in a non-trivial manner in the light we receive.

While a wealth of such data is currently being gathered from spectroscopic surveys – for example, the Sloan Digital Sky Survey (SDSS) or the 2dF Galaxy Redshift Survey (2dFGRS) – using these to probe the general properties of stellar populations on a cosmological time-scale is an exciting perspective.

In the literature, the stellar content of a galaxy is often characterized by a luminosity weighted age, a luminosity weighted metallicity, a global velocity dispersion, and a parameter characterizing extinction. Since Worthey (1994), the Lick indices have been readily used in order to describe the nature of the stellar populations. Spectral indices are convenient because they are robust to a number of observational perturbations, but they exploit only small wavelength domains. The use of a larger fraction, and eventually of all the information in a spectrum must, at least in principle, help separate, age-date and characterize coexisting stellar components, the steps required to access the actual evolution of the galaxies under study. Individual spectral features with specific sensitivities to age or metallicity may add information to the Lick data points, and the redundancy provided by many lines spread over a wide spectral range reduces the sensitivity to noise. Recently, methods have emerged that use the whole available spectral range, relying on compression (Reichardt, Jimenez & Heavens 2001) or on non-negative least squares (Mateu, Magris & Bruzual 2001; Cid Fernandes et al. 2005).

The introduction of these methods has given birth to a field of research, whose goal is to measure the cosmic star formation history by summing the individual star formation histories of a large number of galaxies. This results in an estimate of the mean history of star formation (a so-called 'Madau plot') in principle free from the uncertainties related to pure emission-line diagnostics (Dopita 2005). Moreover, the distribution of individual star formation histories is even more constraining than a Madau plot alone. If feasible, this approach indeed constitutes a very powerful test for the current cosmological models. In fact, such techniques have been used recently to support the idea of galactic downsizing, i.e. to argue the stellar activity has shifted in the recent past towards less massive galaxies, something that some authors have presented as a problem for hierarchical clustering. As more results of this kind are published, it becomes clear that different authors have very different conceptions of what is a reasonable interpretation of a galactic spectrum (Heavens et al. 2004; Cid Fernandes et al. 2005). Indeed, the problem of characterizing star formation histories based on a spectrum is strongly ill-conditioned, as we will demonstrate extensively below (see also Moultaka & Pelat 2000; Moultaka et al. 2004). This remains true in the restrictive framework of evolutionary population synthesis, although this approach incorporates the simplifying assumption that the intrinsic spectra of monometallic, single-aged single stellar populations (SSPs) are known. Overinterpretation of the data is a common pitfall when ill-conditioning is misjudged or overlooked. A useful approach to ill-conditioned inverse problems is the maximum penalized likelihood, which is formally equivalent to a maximum a posteriori likelihood (MAP). It has been applied in the past in a variety of fields in astronomy such as light deprojection (Kochanek & Rybicki 1996), stellar kinematics (Saha & Williams 1994; Merritt 1997; Pichon & Thiébaut 1998), image deblurring (Thiébaut 2002, 2005) or the interpretation of low-resolution energy distributions of galaxies (Vergely, Lançon & Mouhcine 2002).

In this paper we discuss the interpretation of high-resolution optical spectra of galaxies. A maximum resolving power $R = 10\,000$ is considered, which is adequate, in particular, for the studies of low-mass galaxies or of massive star clusters in galaxy cores. We focus on the object's stellar content. The simultaneous extraction of the kinematical information with a direct extension of the adopted method is the subject of a companion paper. Our work is positioned at the interface between SSP models and observations. Its purpose is not to question the particular ingredients and assumptions of a specific population synthesis code, although some of the discussion will be specific to the model package PÉGASE-HR of Le Borgne et al. (2004), because it is the first package to have provided a similar spectral resolution (see Gonzalez Delgado et al. 2005 for a medium-resolution package). Rather, we intend to clarify how the intrinsic properties of a basis of SSP spectra can be used to infer consequences for the study of composite stellar populations.

The general problem, where additional constraints such as positivity of the star formation history are included, is a non-linear problem. Nevertheless, we give special importance to the linear problem because it provides a firm footing to explain the processes that determine the reliability of a recovered star formation history. It also clearly displays many of the features found in the more realistic inversions as well.

We also study the feasibility of the inversion in different observational regimes (in terms of spectral resolution and noise), and give simple scaling laws and error estimates to predict the accuracy and relevance of the results. The main characteristics of our approach are as follows.

(i) It is non-parametric, and thus provides properties such as the stellar age distribution with minimal constraints on their shape.

(ii) The ill-conditioning of the problem is taken into account through explicit regularization.

(iii) Optimal interpretation of the data is achieved by the proper setting of the smoothing parameter.

The organization of the paper is as follows. We start in Section 2 by describing the inversion problems that will be tackled. In Section 3, we provide a comprehensive investigation of the idealized linear problem of finding the stellar age distribution of a monometallic, reddening-free stellar population. In Section 4 we investigate the performance of these inversions in a set of simulations in terms of resolution and separability of bursts. In Section 5 we address the problem of the simultaneous study of stellar ages and metallicities, while allowing for extinction (or other transformations of the continuum). Conclusions are drawn in Section 6, while the paper closes with a discussion for prospects.

2 NON-PARAMETRIC MODELS OF SPECTRA

The SED that we measure for each spatial pixel of an observed galaxy results from light emitted by coexisting stellar populations of various ages, metallicities and kinematics, and from the interactions of the stellar light with the interstellar medium (ISM; reddening, nebular emission). The example of the Milky Way tells us that any given stellar population of a galaxy may consist of stars with non-trivial distributions in age, metallicity, or even relative abundances (Gratton et al. 2000; Prochaska et al. 2000; Feltzing, Holmberg & Hurley 2001). In principle, age, abundances and velocity distributions should thus be treated as independent parameters in a galaxy model meant for an exploration without preconceptions.

In the following, we restrict ourselves to simplified models that balance, in our view, technical feasibility (in view of current models and data) and scientific interest. We assume that metallicity describes the stellar abundances, mainly because our population synthesis model does not allow for abundance variations (Thomas, Maraston & Bender 2003 specifically address this issue). Except for the discussion of a more general case in Section 5, we restrict ourselves to the assumption of a one-to-one relationship between stellar ages and metallicities. This allows us to search for significant trends, as predicted by simple evolutionary scenarios for galaxies. We adopt a simple parametrized formulation for extinction. Finally, we deal with stellar populations at rest (or with known velocity distributions).

Emission lines are outside the aim of this study. They may be used in the future, in particular to obtain further constraints on the youngest stars and on obscuration by dust, or to constrain properties of the ISM.

2.1 Spectral basis

The basic building block to model the spectrum of an observed galaxy is the SED $S(\lambda, m, t, Z)$ of a star of initial mass m, age t and metallicity Z (mass fraction of metals at the formation of the star). Integrating over stellar masses yields the intrinsic spectrum $B^0(\lambda, t, Z)$ of the SSP of age t, metallicity Z and unit mass:

$$B^0(\lambda, t, Z) \triangleq \int_{M_{\min}}^{M_{\max}} \mathrm{IMF}(m)\, S(\lambda, m, t, Z)\, \mathrm{d}m, \tag{1}$$

where $\mathrm{IMF}(M)$ is the initial mass function and $M_{\min}$ and $M_{\max}$ are the lower and upper mass cut-offs of this distribution, respectively. Assuming that the metallicities of the stars can be described by a single-valued age–metallicity relation (AMR) $Z(t)$, it is possible to derive the unobscured SED of the galaxy at rest:

$$F_{\mathrm{rest}}(\lambda) = \int_{t_{\min}}^{t_{\max}} \mathrm{SFR}(t)\, B^0\,(\lambda, t, Z(t))\ \mathrm{d}t. \tag{2}$$

Here, $\mathrm{SFR}(t)$ is the star formation rate (i.e. mass of new stars born per unit of time, with the convention that $t = 0$ is today) and $t_{\max}$ is an upper integration limit, for instance the Hubble time. Similarly, $t_{\min}$ is a lower integration limit, ideally 0. Both $t_{\min}$ and $t_{\max}$ must in practice be set according to the validity domain of the SSP basis $B^0(\lambda, t, Z(t))$.

The luminosity weighted stellar age distribution (LWSAD) $\Lambda(t)$ gives the contribution to the total emitted light of stars of age $[t, t + \mathrm{d}t]$. It is related to the SFR by

$$\Lambda(t) \triangleq \frac{\mathrm{SFR}(t)}{\Delta\lambda} \int_{\lambda_{\min}}^{\lambda_{\max}} B^0\,(\lambda, t, Z(t))\ \mathrm{d}\lambda, \tag{3}$$

where $\Delta\lambda = \lambda_{\max} - \lambda_{\min}$ is the width of the available wavelength domain. In order to use the LWSAD, we define the flux-normalized SSP basis $B(\lambda, t, Z)$ where each spectrum is normalized to a unitary flux:

$$B(\lambda, t, Z) = \frac{B^0(\lambda, t, Z)}{(1/\Delta\lambda) \int_{\lambda_{\min}}^{\lambda_{\max}} B^0(\lambda, t, Z)\, \mathrm{d}\lambda}. \tag{4}$$

Using $\Lambda(t)$, $B(\lambda, t, Z)$ and $Z(t)$, the unobscured SED of any composite population at rest reads:

$$F_{\mathrm{rest}}(\lambda) = \int_{t_{\min}}^{t_{\max}} \Lambda(t)\, B\,(\lambda, t, Z(t))\ \mathrm{d}t. \tag{5}$$

For a given SSP basis, dealing with the star formation rate or the LWSAD is apparently equivalent. Yet, because of the strong dependence of the mass-to-light ratio of SSP fluxes on time, $\Lambda(t)$ is more directly related to observable quantities than $\mathrm{SFR}(t)$. We therefore prefer the formulation based on Λ (see also Section 4.1.2).

Many codes are available to construct $B(\lambda, t, Z)$. The SSP library adopted here is computed with PÉGASE-HR (Le Borgne et al. 2004), a version of PÉGASE[1] that provides optical spectra at high resolution ($R = 10\,000$), based on the ELODIE stellar library (Prugniel & Soubiran 2001). It consists of SSPs generated by single instantaneous starbursts with a set of metallicities $ZZ = [0.0001, 0.1]$. The wavelength range of the spectra is $\lambda\lambda = [4000, 6800]$, sampled in $\delta\lambda = 0.2$-Å steps. Fig. 1 shows example spectra of such SSPs, at fixed metallicity (Fig. 1a) and fixed age (Fig. 1b). The large number of lines is supposed to improve the accuracy of stellar content analysis. The IMF used is described in Kroupa, Tout & Gilmore (1993) and the stellar masses range from 0.1 to 120 $\mathrm{M}_{\odot}$. The IMF is an input of PÉGASE-HR, which we do not attempt to constrain. On the contrary, we assume it is universal and known a priori. The generated spectra are considered most reliable from $t_{\min} = 10$ Myr to $t_{\max} = 20$ Gyr (Le Borgne et al. 2004). The spectra of the different SSPs are computed for a set S_t of logarithmically spaced ages between $t_{\min}$ and $t_{\max}$. The set of monometallic SSPs obtained is referred to as the 'basis' or 'kernel' in the rest of the paper.

2.2 Extinction models

In most cases, the intrinsic emission of the stars of a galaxy is affected by dust. Both the composition and the spatial distribution of the dust determine the extinction. The ISM of galaxies is rarely homogeneous, and the stars may be seen through different amounts of dust. One could therefore envisage an age-dependent extinction law or extinction parameter. Indeed, there is evidence that the obscuration of an ensemble of stars varies systematically with age over the first $\sim 10^7$ yr of their evolution, while these young stars leave or destroy their parent molecular clouds (Charlot & Fall 2000, and references therein). However, the early epochs relevant to starbursts are currently slightly out of reach with PÉGASE-HR, although they will become accessible with improvements of the stellar library. Vergely et al. (2002) suggest that recovering such a trend with age is possible with high-quality data ranging from the ultraviolet to the infrared. In this paper, we have deliberately chosen not to search for an age dependence of extinction. The main reason is that we are considering only a limited section of the electromagnetic spectrum. We postpone a systematic study to future work. In the following, we adopt a unique extinction law $f_{\mathrm{ext}}(E, \lambda)$ parametrized by the colour excess $E \equiv E(B{-}V)$ and normalized to have a unit mean. Accounting for extinction, the model SED then reads:

$$F_{\mathrm{rest}}(\lambda) = f_{\mathrm{ext}}(E, \lambda) \int_{t_{\min}}^{t_{\max}} \Lambda(t) B\,(\lambda, t, Z(t))\ \mathrm{d}t. \tag{6}$$

Note that f_{ext} can be a function of more than one time-independent parameter, and may, for example, be a more complex attenuation law, a function of the distribution of dust in the galaxy and its mixing with the stars, or a low-order polynomial accounting for the instrumental spectrophotometric calibration error.

2.3 General properties and problems with single stellar populations

Synthetic spectra of SSPs are the building blocks involved in the interpretation of galaxy spectra. Their properties have a strong effect on the behaviour of the inversion problem.

[1] Projet d'Etude des GAlaxies par Synthèse Evolutive (see http://www.iap.fr/pegase).

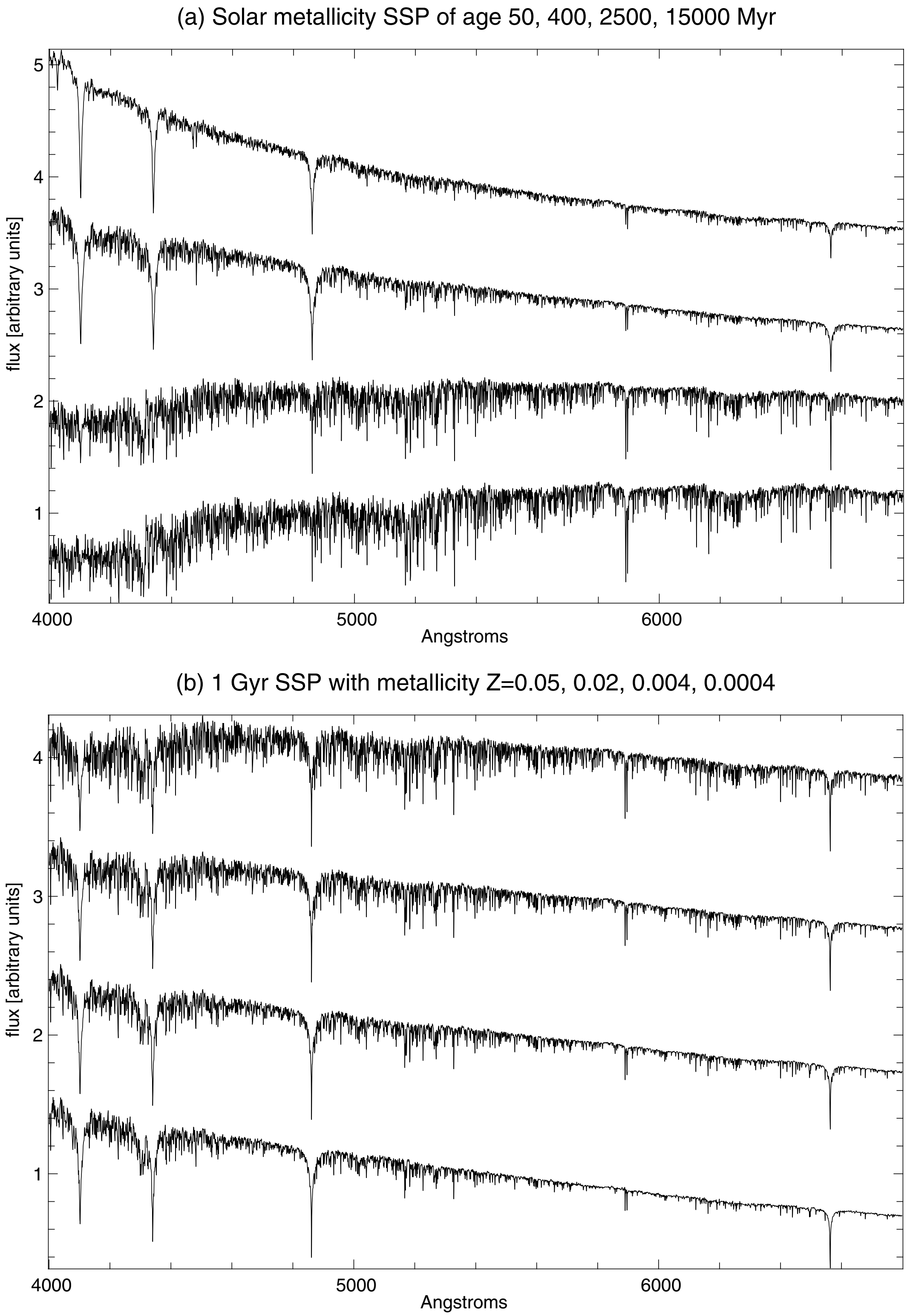

Figure 1. Example of high-resolution SSPs produced by PÉGASE-HR. (a) Solar metallicity SSPs of age 50, 400, 2500 and 15 000 Myr (from top to bottom). (b) 1-Gyr SSP for several metallicities, $Z = 0.05$, 0.02, 0.004 and 0.0004 (from top to bottom). The spectra are normalized to a common mean flux and offset for clarity.

Both the theory of stellar evolution and observations tell us that SSP evolution with time is fundamentally smooth in the optical except for a number of specific evolutionary transitions (e.g. helium flash, carbon flash, supernova explosion, envelope expulsion at the end of the asymptotic giant branch), and that it shows some linearity. This means, for instance, that a 500-Myr-old population looks very similar to the average between a 600- and 400-Myr-old one. Our ability to identify the differences depends strongly on the signal-to-noise ratio (hereafter SNR) of the models and data. Section 3 shows how to quantify this quasi-linearity and its consequences.

The synthetic spectra of SSPs are affected by uncertainties in the stellar evolutionary tracks and in the stellar library used to construct them. Despite permanent progress, some aspects of stellar evolution remain difficult to model (e.g. the horizontal branch, the asymptotic giant branch, the red supergiant phase; effects of convection, of rotation, of a binary companion). The errors propagate to the SSPs, resulting in unknown systematic errors in age and metallicity estimates. Some insight into the amplitude of these errors is given by the direct comparison between results obtained using different sets of tracks. Nevertheless, it is beyond the scope of this paper to discuss the pros and cons of the different set of tracks and the reader is referred to Charlot, Worthey & Bressan (1996) and Lejeune & Fernandes (2002) for an extensive discussion.

The input library of stellar spectra can be either empirical or theoretical. The latter situation has the advantage of providing spectra for any parameter set (T, g, Z) with no observational noise. However, these are not free of intrinsic uncertainties, due for instance to shortcomings of atomic and molecular data, to assumptions on partial thermodynamical equilibrium, or to inappropriate abundance ratios. Empirical spectra, on the other hand, are hampered by a number of issues, as follows.

(i) The library is discrete. Therefore, interpolation between existing stars is needed. This can be a tricky issue, especially on the borders of the grid and in underpopulated regions of (T, g, Z) space. Moreover, when stars are interpolated, the noise patterns are also carried along. We will see in Section 3.4 that this has noticeable effects on the behaviour of the inverse problem.

(ii) The library generally consists only of Milky Way or even Solar neighbourhood stars. Thus, the solar metallicity is the best populated region of parameter space, while other regions may be depleted, especially for extreme cases such as young metal-poor or old metal-rich stars. We also know that outer galaxies may involve abundance ratios that are not found within the Milky Way. One example is found in the metal-rich and α-enhanced populations of large elliptical galaxies. This difficulty is known as 'template mismatch' and results in biases that would be best studied using simulations based on theoretical spectra with various sets of abundances. The library used in PÉGASE-HR is known to be deficient in high-metallicity, high-α-element abundance red giants (Le Borgne et al. 2004), which may lead to an overestimate of age or metallicity in observed galaxies.[2]

(iii) Empirical stellar spectra have a finite SNR, and so do the averaged or interpolated spectra involved in the synthesis of a galaxy spectrum. It should then be considered useless to observe stellar populations at SNRs larger than those of the library.

(iv) The fundamental parameters of each star in the library are estimates, in the case of PÉGASE-HR based on a subset of standards and the automated code TGMET (Katz et al. 1998). Even though error bars on these parameters are provided, some glitches and outliers occur. The final error resulting from interpolating between correct and ill-parametered stars and summing is unknown.

Notwithstanding the above limitations of spectral synthesis, our purpose here is to investigate the behaviour of the inverse method for a given model. Hence, in this paper we will be restricted to one given SSP model.

[2] Work is being done to improve the underlying library.

3 A SIMPLIFIED INVERSE PROBLEM: THE AGE DISTRIBUTION RECOVERY

In this section we discuss the inverse problem of recovering the age distribution of a purely monometallic unobscured population at rest. This simplification is deliberate and yields a linear relationship between the observed SED $F_{\rm rest}(\lambda)$ and the stellar age distribution $\Lambda(t)$. It allows us to address its fundamental properties and behaviour, characterized by simple quantities and criteria. These turn out to be precious tools in the process of understanding and diagnosing the ill-conditioning and pathological behaviour of such a problem and their non-linear generalization. It also allows us to introduce the automated regularizing method required to solve the problem in practice.

3.1 Linear inverse problem

Our idealized monometallic unobscured model stellar population is characterized by its LWSAD $\Lambda(t)$ and its constant AMR $Z(t) = Z_0$. The SED of the emitted light $F_{\rm rest}(\lambda)$ then reads

$$F_{\rm rest}(\lambda) = \int_{t_{\rm min}}^{t_{\rm max}} \Lambda(t)\, B\,(\lambda, t, Z(t))\; {\rm d}t, \qquad (7)$$

where $B(\lambda, t, Z(t))$ is the flux-normalized SSP basis (cf. equation 4), which is just a function of the wavelength and time as the AMR $Z(t)$ is supposed to be known. Solving equation (7), where $B(\lambda, t, Z(t))$ and $F_{\rm rest}(\lambda)$ are given and $\Lambda(t)$ is the unknown, is as we will demonstrate, a classical example of a potentially ill-posed problem (Hansen 1994), i.e. it can be shown that small perturbations of the data can cause large perturbations of the solution. Hence, any noise in the data, $F_{\rm rest}(\lambda)$, or in the kernel, $B(\lambda, t, Z(t))$, can lead to a solution very far from the true solution.

3.2 Discretization: the matrix form

Intuitively, after discretization of the wavelength and age ranges, the linear integral equation (7) can be approximated by

$$s_i \approxeq \sum_{j=1}^{n} B_{i,j}\, x_j, \qquad i \in \{1, .., m\}, \qquad (8)$$

with

$$\begin{aligned} s_i &= \langle F_{\rm rest}(\lambda)\rangle_{\lambda\,\in\,\Delta\lambda_i}\,, \\ B_{i,j} &= \langle B\,(\lambda, t, Z(t))\rangle_{\lambda\,\in\,\Delta\lambda_i, t\,\in\,\Delta t_j}\,, \\ x_j &= \langle \Lambda(t)\rangle_{t\in\Delta t_j}\,, \end{aligned} \qquad (9)$$

where the notation, e.g. $\langle F_{\rm rest}(\lambda)\rangle_{\lambda\in\Delta\lambda_i}$, indicates some kind of weighted averaging or sampling of the argument $F_{\rm rest}(\lambda)$ over the ith wavelength interval $\Delta\lambda_i$ and similarly for the age interval.

More rigorously, let $\{g_i : [\lambda_{\rm min}, \lambda_{\rm max}] \mapsto \mathbb{R}; i = 1, \ldots, m\}$ and $\{h_j : [t_{\rm min}, t_{\rm max}] \mapsto \mathbb{R}; j = 1, \ldots, n\}$ be two orthonormalized bases of functions spanning the wavelength and age intervals, respectively. Then, the best approximation[3] of $\Lambda(t)$ is written

$$\Lambda(t) \approxeq \sum_{j=1}^{n} x_j\, h_j(t), \qquad \text{with } x_j = \int \Lambda(t)\, h_j(t)\, {\rm d}t. \qquad (10)$$

[3] In the sense of the ℓ_2 norm defined by the orthonormalized basis of functions.

Similarly, the best approximation of $F_{\mathrm{rest}}(\lambda)$ is written

$$F_{\mathrm{rest}}(\lambda) \approxeq \sum_{i=1}^{m} s_i\, g_i(\lambda), \quad \text{with } s_i = \int F_{\mathrm{rest}}(\lambda)\, g_i(\lambda)\, \mathrm{d}\lambda. \tag{11}$$

It is straightforward to obtain the coefficients of the matrix $\mathbf{B}$ in equation (8) by inserting these approximations in equation (7):

$$B_{i,j} = \int\!\!\int B\left(\lambda, t, Z(t)\right)\, g_i(\lambda)\, h_j(t)\, \mathrm{d}t\, \mathrm{d}\lambda. \tag{12}$$

In practice, we adopt equally spaced λ_i and equally spaced $\log(t_j)$ to sample the wavelength range and the evolutionary time-scales of SSPs. Then we simply use gate functions for g_i and h_j. In other words, s_i is the average flux received in $\lambda_i \pm \delta\lambda$ and x_j is the mean flux contribution of the subpopulation of age $[t_{j-1}, t_j]$; hence, the notation used in equation (9).

Note that if $t_j - t_{j-1}$ is too large, significantly different populations are already entangled in the sampled basis $B_j(\lambda) = \langle B(\lambda, t, Z(t))\rangle_{t\in\Delta t_j}$. For this reason, the number n of SSP elements in the basis should not be too small. The signatures of the populations of each age should be expressed in the adopted basis. On the other hand (see Section 3.4), we will sometimes want to use a small n, i.e. a basis that is coarser in time, and we will see that the overall adopted value strongly depends on the observational context (SNR, spectral resolution and range, etc.).

Using matrix notation and accounting for data noise, the observed SED reads

$$\boldsymbol{y} = \mathbf{B} \cdot \boldsymbol{x} + \boldsymbol{e}, \tag{13}$$

where $\boldsymbol{y} = (y_1, \ldots, y_m)^\top$ is the observed spectrum (including errors), i.e. y_i is the measured flux in the range $\lambda_i \pm \delta\lambda$, and $\boldsymbol{e} = (e_1, \ldots, e_m)^\top$ accounts for modelling errors and noise. The vector of sought parameter $\boldsymbol{x}$ is the discretized stellar age distribution, i.e. x_j is the luminosity contribution of the stars of age $[t_{j-1}, t_j]$ to the total luminosity, averaged over the available wavelengths. The vector $\boldsymbol{s} = \mathbf{B}\cdot\boldsymbol{x}$ is the model of the observed spectrum and $\mathbf{B}$ is the discrete model matrix, sometimes also referred to as the kernel.

3.3 Maximum a posteriori

In a real astrophysical situation, the data $\boldsymbol{y}$ are always contaminated by errors and noise. Following Bayes theorem, the a posteriori conditional probability density $f_{\mathrm{post}}(\boldsymbol{x}|\boldsymbol{y})$ for the realization $\boldsymbol{x}$ given the data $\boldsymbol{y}$ is written

$$f_{\mathrm{post}}(\boldsymbol{x}|\boldsymbol{y}) \propto f_{\mathrm{data}}(\boldsymbol{y}|\boldsymbol{x})\, f_{\mathrm{prior}}(\boldsymbol{x}), \tag{14}$$

where $f_{\mathrm{prior}}(\boldsymbol{x})$ is the a priori probability density of the parameters, and $f_{\mathrm{data}}(\boldsymbol{y}|\boldsymbol{x})$, sometimes referred to as the likelihood, is the probability density of the data given the model. For Gaussian noise, $f_{\mathrm{data}}(\boldsymbol{y}|\boldsymbol{x}) \propto \exp[-(1/2)\chi^2(\boldsymbol{y}|\boldsymbol{x})]$, with

$$\chi^2(\boldsymbol{y}|\boldsymbol{x}) = [\boldsymbol{y} - \boldsymbol{s}(\boldsymbol{x})]^\top \cdot \mathbf{W} \cdot [\boldsymbol{y} - \boldsymbol{s}(\boldsymbol{x})]\,, \tag{15}$$

where the weight matrix is the inverse of the covariance matrix of the noise: $\mathbf{W} = \mathrm{Cov}(\boldsymbol{e})^{-1}$. Maximizing the posterior probability (14) is equivalent to minimizing the penalty:

$$Q(\boldsymbol{x}) = \chi^2(\boldsymbol{y}|\boldsymbol{x}) - 2\,\log[f_{\mathrm{prior}}(\boldsymbol{x})]. \tag{16}$$

Without a priori information about the sought parameters, the probability density f_{prior} is uniformly distributed and this term can be dropped. In this case, $Q(\boldsymbol{x})$ simplifies to $\chi^2(\boldsymbol{y}|\boldsymbol{x})$, the traditional goodness-of-fit estimator for Gaussian noise.

When the errors are uncorrelated, the matrix $\mathbf{W}$ formally assigns a weight $1/\mathrm{Var}(y_i)$ to each pixel i of data. Practically, one may want to modify the variance–covariance matrix in order to use it as a mask. For example, a dead pixel can be assigned null weight. In the same way, we may also mask emission lines. Because of this particular usage of the matrix $\mathbf{W}$, it will often be called the weight matrix. It need not be exactly a variance–covariance matrix, even though it can be built upon one.

3.4 Ill-conditioning and noise amplification

As mentioned earlier, the linear problem corresponding to the recovery of the stellar age distribution $\boldsymbol{x}$ by maximizing the likelihood term only, qualifies as a discrete ill-conditioned problem, i.e. it might therefore be extremely sensitive to noise, both in the data and in the kernel. It thus will require some form of regularization in order to obtain physically meaningful solutions.

3.4.1 Noisy data

First, let us see how ill-conditioning arises, in the case of a noiseless kernel but with noisy data. We solve for $\boldsymbol{x}$ by maximizing the likelihood of the data $\boldsymbol{y}$ given the model; this is the same as minimizing

$$\chi^2(\boldsymbol{y}|\boldsymbol{x}) = (\boldsymbol{y} - \mathbf{B}\cdot\boldsymbol{x})^\top \cdot \mathbf{W} \cdot (\boldsymbol{y} - \mathbf{B}\cdot\boldsymbol{x}), \tag{17}$$

with respect to $\boldsymbol{x}$. The solution is the weighted least-squares solution:

$$\boldsymbol{x}_{\mathrm{ML}} = (\mathbf{B}^\top \cdot \mathbf{W} \cdot \mathbf{B})^{-1} \cdot \mathbf{B}^\top \cdot \mathbf{W} \cdot \boldsymbol{y}. \tag{18}$$

For the sake of simplicity, we consider stationary noise in this section. The results of this section, however, apply for non-stationary noise by replacing the model matrix $\mathbf{B}$ by $\mathbf{K}\cdot\mathbf{B}$ and the data vector $\boldsymbol{y}$ by $\mathbf{K}\cdot\boldsymbol{y}$ where $\mathbf{K}$ is the Choleski decomposition of the weight matrix, i.e. $\mathbf{W} = \mathbf{K}^\top\cdot\mathbf{K}$. For stationary noise, the weight matrix factorizes out

$$\chi^2(\boldsymbol{y}|\boldsymbol{x}) \propto (\boldsymbol{y} - \mathbf{B}\cdot\boldsymbol{x})^\top(\boldsymbol{y} - \mathbf{B}\cdot\boldsymbol{x}), \tag{19}$$

and the maximum-likelihood solution becomes the ordinary least-squares solution:

$$\boldsymbol{x}_{\mathrm{ML}} = (\mathbf{B}^\top \cdot \mathbf{B})^{-1} \cdot \mathbf{B}^\top \cdot \boldsymbol{y}. \tag{20}$$

In order to clarify the process of noise amplification, we introduce the singular value decomposition (SVD) of $\mathbf{B}$ as

$$\mathbf{B} = \mathbf{U} \cdot \boldsymbol{\Sigma} \cdot \mathbf{V}^\top, \tag{21}$$

where $\boldsymbol{\Sigma} = \mathrm{diag}(\sigma_1, \sigma_2, \ldots, \sigma_n)$ is a diagonal matrix carrying the singular values, sorted in decreasing order, of $\mathbf{B}$ on its diagonal. $\mathbf{U}$ contains the orthonormal data singular vectors $\boldsymbol{u}_i$ (data-size vectors), and $\mathbf{V}$ contains the orthonormal solution singular vectors $\boldsymbol{v}_i$ (solution-size vectors). Replacing $\mathbf{B}$ by its SVD in equation (20) yields

$$\boldsymbol{x}_{\mathrm{ML}} = \mathbf{V} \cdot \boldsymbol{\Sigma}^{-1} \cdot \mathbf{U}^\top \cdot \boldsymbol{y} = \sum_{i=1}^{n} \frac{\boldsymbol{u}_i{}^\top \cdot \boldsymbol{y}}{\sigma_i}\, \boldsymbol{v}_i. \tag{22}$$

The solution is obtained as the sum of n solution singular vectors $\boldsymbol{v}_i$ times the scalar $\boldsymbol{u}_i{}^\top \cdot \boldsymbol{y}/\sigma_i$. For real data, we have $\boldsymbol{y} = \overline{\boldsymbol{y}} + \boldsymbol{e}$, where the noiseless data $\overline{\boldsymbol{y}}$ are related to the true parameter vector $\overline{\boldsymbol{x}}$ via $\overline{\boldsymbol{y}} = \mathbf{B}\cdot\overline{\boldsymbol{x}}$. Instead of $\overline{\boldsymbol{x}}$, the solution recovered from the noisy data reads

$$\boldsymbol{x}_{\mathrm{ML}} = \sum_{i=1}^{n} \frac{\boldsymbol{u}_i^\top \cdot \overline{\boldsymbol{y}}}{\sigma_i}\, \boldsymbol{v}_i + \sum_{i=1}^{n} \frac{\boldsymbol{u}_i^\top \cdot \boldsymbol{e}}{\sigma_i}\, \boldsymbol{v}_i \equiv \overline{\boldsymbol{x}} + \boldsymbol{x}_e. \tag{23}$$

Thus, we recover the true unperturbed solution $\overline{\boldsymbol{x}}$ plus a perturbation, $\boldsymbol{x}_e$, related to the noise. Comparing $\overline{\boldsymbol{x}}$ and $\boldsymbol{x}_e$ is equivalent

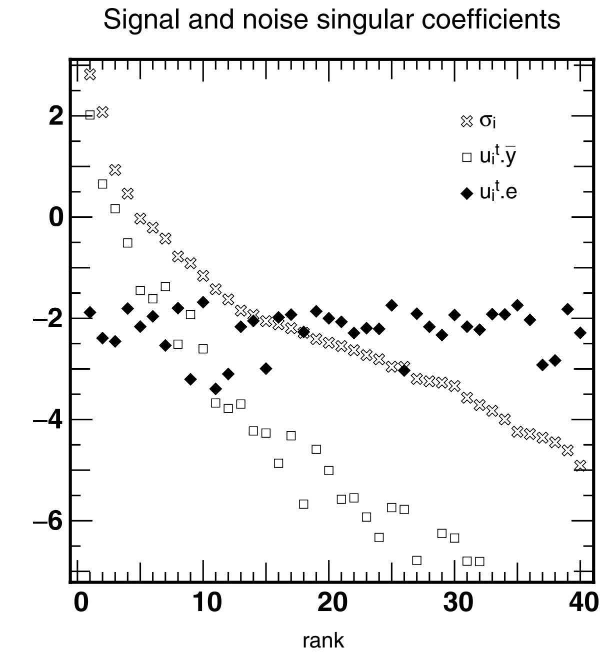

Figure 2. The decay of the singular values of the kernel (crosses) is the origin of the bad behaviour of the problem, through the amplification of the last singular vectors. In this example, the data $\boldsymbol{y}$ are perturbed by Gaussian noise of constant $\mathrm{SNR_d} = 100$ per pixel. The unperturbed singular coefficients (white squares) decay, while the noise singular coefficients (black diamonds) remain spread around $1/\mathrm{SNR_d}$ for any i (we chose $\langle\overline{\boldsymbol{y}}\rangle = 1$ in this example). The perturbed singular coefficients $\boldsymbol{u}_i^\top \cdot \boldsymbol{y}$ are thus noise-dominated as soon as $i \geqslant 7$–9, and so are the terms of the SVD solution (equation 22). The increasing difference between the true and noise singular coefficients is worsened by the division by smaller σ_i. The solution $\boldsymbol{x}$ is dominated by the last few solution singular vectors, and its norm is purely noise-dependent.

to comparing the unperturbed singular coefficients $\boldsymbol{u}_i^\top \cdot \overline{\boldsymbol{y}}$ and the noise singular coefficients $\boldsymbol{u}_i{}^\top \cdot \boldsymbol{e}$. Fig. 2 shows an example with 40 logarithmical age bins from 10 Myr to 20 Gyr, and where the data are perturbed by Gaussian noise and have constant $\mathrm{SNR_d} = 100$ per pixel (the subscript 'd' denotes data). The figure shows that the singular values decay very fast and span a large range, giving a conditioning number, defined by $\mathrm{CN} = \sigma_1/\sigma_n \approx 10^8$, characteristic of an ill-conditioned problem. Note that **B** is the flux-normalized SSP basis defined by equation (4), i.e. each spectrum of the basis has unitary flux, and the x_i are thus flux fractions and not mass fractions (see Section 4.1.2 for more details). The noise singular coefficients remain rather constant for any rank i. Indeed, $\boldsymbol{u}_i^\top \cdot \boldsymbol{e}$ involves a normalized vector times noise, and has a constant statistical expected value of $\langle\overline{\boldsymbol{y}}\rangle/\mathrm{SNR_d}$. On the contrary, the unperturbed singular coefficients decay. In this example, the model $\overline{\boldsymbol{x}}$ is a Gaussian centred on 1 Gyr, and we find that changing the mean age of the model does not significantly affect the decay of $\boldsymbol{u}_i^\top \cdot \overline{\boldsymbol{y}}$ (see Appendix A). We can thus define two regimes, with a transition for $i_0 \approx 7$–9 in this example:

(i) for $i \leqslant i_0$, we have $\boldsymbol{u}_i^\top \cdot \boldsymbol{y} \simeq \boldsymbol{u}_i^\top \cdot \overline{\boldsymbol{y}}$ and the singular coefficients and modes are set by the unperturbed signal $\overline{\boldsymbol{y}}$;

(ii) for $i > i_0$, we have $\boldsymbol{u}_i^\top \cdot \boldsymbol{y} \simeq \boldsymbol{u}_i^\top \cdot \boldsymbol{e} \simeq \langle\overline{\boldsymbol{y}}\rangle/\mathrm{SNR_d}$. The singular coefficients are set by the noise in the data and saturate.

The division by decreasing σ_i makes the high rank terms in $\boldsymbol{x}_e$ become very large. The solution $\boldsymbol{x}$ is thus dominated by the last few $\boldsymbol{v}_i$. Its norm is several orders of magnitude larger than the true solution. We see that, for such ill-conditioned problems, pure maximum-likelihood estimation results in huge noise amplification and useless solutions.

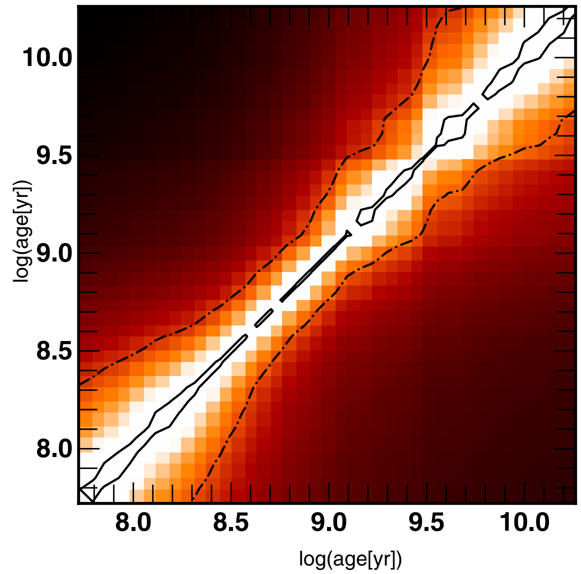

Figure 3. Distance map of the SEDs involved in the flux-normalized kernel **B**. The contours enclose a domain where the ith spectrum cannot be distinguished against the jth at a 90 per cent confidence level. The solid contour is for SNR = 100 per pixel and the dash-dotted one is for SNR = 10 per pixel. It is not possible to unambiguously disentangle two spectra in such regions, i.e. the resolution in age of any inversion method cannot be finer than the width of these regions (which is read on the axis), and it is not constant all along the age range. This resolution in age in data space has a counter part in the resolution defined in Section 4.2.

The origin of ill-conditioning is, in most part, physical: it lies in the evolution of the SSPs, which is dictated by stellar physics and the relevant stellar evolution models. One aspect of the situation is illustrated in Fig. 3. It shows a map of the χ^2 distances between the spectra (i.e. columns) of the kernel **B**, for different SNRs. In this figure, the time interval [50 Myr, 15 Gyr] was arbitrarily divided into 40 logarithmic age bins, and the SSP basis is flux normalized as in equation (4). This shows that for low SNRs (of order 10), one element of the basis cannot be quantitatively distinguished from its neighbours within a typical log age interval of ~0.5 dex. It also makes it clear that the logarithmic age-resolution of any inversion method will not be constant all over the time range.

3.4.2 Noisy correlated kernel

As discussed in Section 2.3, the models that are constructed from observed spectra are also contaminated by observational noise. Let us investigate the expected signature and basic properties of a noisy kernel.

PÉGASE-HR SSPs have a noise component estimated to $\mathrm{SNR_b} \approx 200$ per 0.2-Å pixel (the subscript 'b' denotes basis). From theoretical studies of random matrices (Hansen 1988), it is known that a hypothetical noiseless SSP basis perturbated by adding white noise of root mean square σ_0 should have its singular values settle around $\sqrt{m}\,\sigma_0$, where m is the number of samples in the observed SED. If the spectra are normalized to unitary flux, we have $\sigma_0 \simeq 1/\mathrm{SNR_b}$. Fig. 4 shows the singular values of the flux-normalized kernel **B** (thick line). The singular values clearly do not settle around the

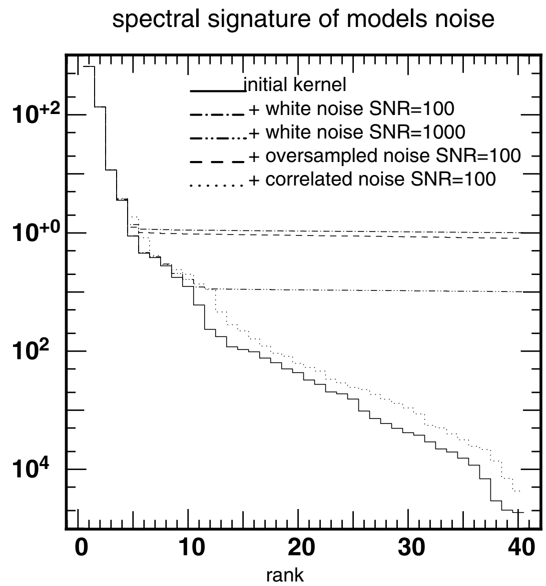

Figure 4. Investigation of the noise signatures of the kernel. For comparison, the kernel was noised in several different ways: with white noise, oversampled noise and finally noise correlated in the age direction of the kernel, each type of noise producing characteristic features in the singular values. The expected spectral signature of the noise in the initial basis (saturation of the singular values) does not occur. This is likely to be caused by the interpolation between the stars of the stellar library: the noise patterns are carried along in the interpolation, giving rise to noise patterns correlated in the direction of ages.

value expected for $m \simeq 10^4$, i.e. $\approx$1 for $\mathrm{SNR_b} = 100$ (dash-dotted line) and $\approx$0.1 for $\mathrm{SNR_b} = 1000$ (dash-double-dotted line). On the contrary, their decay is typical of an ill-conditioned noiseless kernel, as if the SSPs involved had infinite SNR. Let us investigate some details of the synthesis process, in an attempt to explain this unexpected property.

As every SSP is actually the weighted sum of p single stars from the library, the noise level of the synthetic SED should be lower (typically divided by $\sqrt{p}$). However, the singular values of the kernel plus white noise at a level SNR = 1000 (corresponding to summing $p = 100$ stars having SNR = 100) are still much larger than the initial kernel's singular values. Having more stars available would lower the saturation level, but one would need 10^{10} stars with SNR = 100 to make the saturation vanish.

In order to test for the effect of wavelength resampling of the individual stellar spectra, we added SNR = 100 per pixel smoothed noise (i.e. noise with a correlation between neighbouring wavelengths) to the kernel. The corresponding singular values are very similar to the former white noise case, except that they settle to a slightly smaller value. They still saturate high above the singular values of the initial kernel.

In contrast, when the added noise pattern is correlated in the direction of ages instead of wavelength, one obtains a non-saturated singular value spectrum very similar to the initial kernel, even with SNR as low as 100 (a larger SNR would make it look even more similar).

Indeed, such correlated noise arises in part in the kernel because individual stellar spectra are interpolated in (T, g, Z) space.

A single spectrum from the input stellar library can thus significantly contribute to several ages. For instance, the same limited number of red giants will be used (with slightly different weights) to represent the red giant branch stars over a range of ages and metallicities. Their noise patterns will show up in several consecutive synthetic SSPs, and can therefore not be properly discriminated against true physical signal. The expected saturation is washed out by the interpolation between spectra, resulting in a degraded signature. This correlation affects us in two ways: it prevents us from determining the precise SNR of the basis, and then from computing the conditioning number of the real problem (where $\mathrm{SNR_b} \to \infty$). Only a lower limit on the conditioning number is obtained, meaning the real problem could actually be worse.

Whatever process is responsible for degrading the noise signature, the properties of the problem in very high-quality data regimes cannot be inferred from the apparently noiseless initial kernel $\mathbf{B}$. Let us return to the case of white noise, with a noisy kernel $\mathbf{B} + \mathbf{E}$. Its singular values saturate at some rank i_B. The singular vectors of lower rank are identical to those of $\mathbf{B}$, but for higher rank they differ strongly. Thus, the number of free parameters we can recover cannot be larger than i_B. For PÉGASE-HR we estimate $i_B = 6$ for $\mathrm{SNR_b} \approx 200$. This means that high-frequency variations of the stellar age distribution are unreachable, no matter what the SNR of the data is. This is a fundamental limitation of the problem, related specifically to the SNR of the SSP models. When $\mathrm{SNR_d} \geqslant \mathrm{SNR_b}$, a pure maximum likelihood estimation actually uses noise patterns inside the kernel as if it was a true physical signal, and simulations will give results with an illusory accuracy. A useful technique, which explicitly accounts for modelling errors, is then total least squares (hereafter TLS). The TLS solution to our linear problem (for simplicity we set $\mathbf{W}$ to Identity here) is defined by

$$\boldsymbol{x}_{\mathrm{TLS}} = \arg\min_{\boldsymbol{x},\,\bar{\mathbf{B}}} (\|\boldsymbol{y} - \bar{\mathbf{B}} \cdot \boldsymbol{x}\|^2 + \|\bar{\mathbf{B}} - \mathbf{B}\|^2), \qquad (24)$$

where $\|\boldsymbol{x}\| = \sqrt{\boldsymbol{x}^{\top} \cdot \boldsymbol{x}}$ denotes the Euclidian (or ℓ_2) norm. More can be found in Hansen & O'Leary (1996) and Golub, Hansen & O'Leary (2000).

However, in the rest of the paper, we will most frequently explore regimes where the dominant error source is the data, so that the number of degrees of freedom of the problem is dictated by $\mathrm{SNR_d}$ rather than $\mathrm{SNR_b}$. It will also allow us to estimate what could be the best performance of the method, if the SSP models were taken as perfect. Thus, in the following sections, we focus exclusively on the treatment of noisy data, and will often drop the subscript 'd'.

3.5 Regularization and MAP

In this section we explain how adequate regularization allows us to improve the behaviour of the problem with respect to noise in the data. Perturbation of the solution arises from the noise-dominated higher rank terms of equation (22). In order to ensure that $\boldsymbol{x}_e$ remains small, one could reduce the effective number of age bins. Several criteria are applicable.

(i) The singular coefficients should always be dominated by the true signal. With plots such as Fig. 2, we find that i_0 is between 7 and 9 for $\mathrm{SNR_d} = 100$ per pixel with PÉGASE-HR SSPs. Nevertheless, in a real situation only $\boldsymbol{u}_i^{\top} \cdot \boldsymbol{y}$ is generally available, and i_0 is guessed from the rank for which the singular coefficients begin to saturate.

(ii) In the true signal dominated region, the singular coefficients decrease faster than the singular values. Inversely, singular coefficients decreasing faster than the singular values for any rank i guarantee the smallness of $\boldsymbol{x}_e$. This requirement is known as the discrete Picard condition. See Hansen (1994) for further details.

(iii) A useful criterion that does not require any plot involves choosing the number of age bins n so that the conditioning number of the resulting kernel satisfies

$$\mathrm{CN} = \sigma_1/\sigma_n \lesssim \sqrt{m}\,\mathrm{SNR_d}, \tag{25}$$

where m is the number of pixels. Note that this statement is SNR-dependent.

Another way to prevent the noise component from being amplified into the solution is to truncate the SVD expansion at some rank i_{trunc}:

$$\boldsymbol{x}_{\mathrm{TSVD}} = \sum_{i=1}^{i_{\mathrm{trunc}}} \frac{\boldsymbol{u}_i^{\top} \cdot \boldsymbol{y}}{\sigma_i}\,\boldsymbol{v}_i. \tag{26}$$

This technique is known as truncated SVD (hereafter TSVD). The use of this method dates back to Hanson (1971) and Varah (1973). The truncation rank i_{trunc} can be chosen with the help of plots such as Fig. 2

However, if the truncation is brutal, it will produce strong artefacts, known as aliasing, which reflects the fact that higher frequencies are projected on to a low-frequency basis; the best fit leads to a non-local alternated expansion which rings. Moreover, TSVD is best suited for problems where a clear gap in the singular values is seen because, in this instance, the lower modes are well represented by the truncated basis. Unfortunately, our kernel displays a smooth, continuously decreasing spectrum of singular values. This is very similar to the situation in image reconstruction. When deconvolution problems are addressed, the brutal truncation of the transfer function (which corresponds to the singular coefficients of the point spread function, hereafter PSF) results in the formation of strong artefacts known as Gibbs rings.

Moreover, here we have another degree of complexity arising from the property that our problem is not shift-invariant. As a consequence, the solution singular vectors are fairly unsmooth and even more artefacts are expected, as discussed in Section 4.1.2. In image deblurring, artefacts are reduced and reconstructions improved by apodizing the Fourier transformed PSF (i.e. making it smoothly decrease to 0), for example by Wiener filtering.[4] In a similar manner, we wish to apodize the singular value spectrum of the kernel $\mathbf{B}$.

We chose to regularize the problem by imposing the smoothness of the solution through a penalizing function. We define the objective function as

$$Q_\mu(\boldsymbol{x}) \equiv -\frac{1}{2}\log(f_{\mathrm{post}}) = \chi^2(\boldsymbol{s}(\boldsymbol{x})) + \mu\,P(\boldsymbol{x}), \tag{27}$$

which is a penalized χ^2, where P is the penalizing function; it has large (small) values for unsmooth (smooth) $\boldsymbol{x}$. Adding the penalization P to the objective function is exactly equivalent to injecting a priori information in the problem. We effectively proceed as if we have assumed a priori that a smooth solution was more likely than a rough one. This is in part justified by the fact that any unregularized inversion tends to produce rough solutions. If we identify Q_μ with the expression of the logarithm of the maximum a posteriori likelihood (16) we see that by building a penalization P we have built a prior distribution f_{prior}

$$f_{\mathrm{prior}}(\boldsymbol{x}) = \exp(-\mu P(\boldsymbol{x}))\,, \tag{28}$$

omitting the normalization constant. If $\mu = 0$, the prior distribution is uniform and contains no information. It is a pure maximum likelihood estimation. If $\mu > 0$, the prior probability density is larger for smooth solutions, and we are performing a maximum a posteriori likelihood estimation (MAP).

The smoothing parameter μ sets the smoothness requirement on the solution. There are several examples of such regularizations in the literature (Tikhonov, least squares with quadratic constraint, maximum entropy regularization, etc.; see Pichon, Siebert & Bienaymé 2002 for a discussion). Here, we define P as a quadratic function of $\boldsymbol{x}$, involving a kernel $\mathbf{L}$:

$$P(\boldsymbol{x}) = \boldsymbol{x}^{\top} \cdot \mathbf{L}^{\top} \cdot \mathbf{L} \cdot \boldsymbol{x}. \tag{29}$$

If $\mathbf{L}$ is the identity matrix $\mathbf{I}_n$, then $P(\boldsymbol{x})$ is just the square of the Euclidian norm of $\boldsymbol{x}$. To explicitly enforce a smoothness constraint, we can use a finite difference operator $\mathbf{D}_2 \equiv \mathrm{diag}_2[-1, 2, -1]$ that computes the Laplacian of $\boldsymbol{x}$, defined in Pichon et al. (2002) by

$$\mathbf{D}_2 \equiv \begin{bmatrix} -1 & 2 & -1 & 0 & 0 & 0 & 0 & \cdots \\ 0 & -1 & 2 & -1 & 0 & 0 & 0 & \cdots \\ 0 & 0 & -1 & 2 & -1 & 0 & 0 & \cdots \\ 0 & 0 & 0 & -1 & 2 & -1 & 0 & \cdots \\ \cdots & \cdots & \cdots & \cdots & \cdots & \cdots & \cdots & \cdots \end{bmatrix}. \tag{30}$$

The objective function Q_μ is then quadratic and has an explicit minimum

$$\boldsymbol{x}_\mu \stackrel{\Delta}{=} \widetilde{\mathbf{B}} \cdot \boldsymbol{y} = (\mathbf{B}^{\top} \cdot \mathbf{W} \cdot \mathbf{B} + \mu\,\mathbf{L}^{\top} \cdot \mathbf{L})^{-1} \cdot \mathbf{B}^{\top} \cdot \mathbf{W} \cdot \boldsymbol{y}, \tag{31}$$

where $\widetilde{\mathbf{B}}$ is defined here to be the regularized inverse model matrix, whose properties we investigate below.

We may now derive a more insightful expression for $\boldsymbol{x}_\mu$ while relying on the generalized singular value decomposition (hereafter GSVD) of $(\mathbf{B}, \mathbf{L})$ (assuming $\mathbf{W} = \mathbf{I}_m$ or using the Choleski square root of $\mathbf{W}$). According to Appendix C, the regularized solution is now written as

$$\begin{aligned} \boldsymbol{x}_\mu &= \arg\min_{\boldsymbol{x}}(\|\mathbf{B} \cdot \boldsymbol{x} - \boldsymbol{y}\|^2 + \mu\,\|\mathbf{L} \cdot \boldsymbol{x}\|^2)\,, \\ &= [\mathbf{B}^{\top} \cdot \mathbf{B} + \mu\,\mathbf{L}^{\top} \cdot \mathbf{L}]^{-1} \cdot \mathbf{B}^{\top} \cdot \boldsymbol{y}\,, \\ &= \mathbf{V} \cdot [\boldsymbol{\Sigma}^2 + \mu\,\boldsymbol{\Theta}^2]^{-1} \cdot \boldsymbol{\Sigma} \cdot \mathbf{U}^{\top} \cdot \boldsymbol{y}\,, \\ &= \sum_{i=1}^{n} \eta_i \left(\boldsymbol{u}_i^{\top} \cdot \boldsymbol{y}\right) \boldsymbol{v}_i, \end{aligned} \tag{32}$$

where the filter factors η_i

$$\eta_i = \frac{\sigma_i}{\sigma_i^2 + \mu\,\theta_i^2} \tag{33}$$

depend on the type of penalization and the smoothness parameter μ. For any quadratic penalization as in equation (29), the matrices $\mathbf{U}, \mathbf{V}, \boldsymbol{\Sigma} = \mathrm{diag}(\sigma_1, \sigma_2, \ldots, \sigma_n)$ and $\boldsymbol{\Theta} = \mathrm{diag}(\theta_1, \theta_2, \ldots, \theta_n)$ are given by the GSVD of the matrix pair $(\mathbf{B}, \mathbf{L})$ (see Appendix C for details). For the simple case of square Euclidian norm penalization, $\mathbf{L} = \mathbf{I}_n$, the filter factors becomes

$$\eta_i = \frac{\sigma_i}{\sigma_i^2 + \mu}. \tag{34}$$

We then have $\eta_i \approx 1/\sigma_i$ when $\sigma_i^2 \gg \mu$, and $\eta_i \to 0$ for higher ranks (i.e. smaller singular values), so that division by almost 0 is avoided in high rank terms. Thus, setting μ actually sets the rank where the weights of the SVD solution components begin to decrease. Note that the smooth cut-off (apodization) of the singular values should allow us to recover models similar to relatively high rank singular vectors provided that the weights associated to lower rank vectors are small enough. Small μ yield noise sensitive, possibly unphysical solutions, whereas very large μ lead to flat solutions whatever the

[4] Non-quadratic penalty functions, such as $\ell_1 - \ell_2$ penalties which accommodate rare sharp jumps in the sought field, can also significantly reduce the effect of ringing.

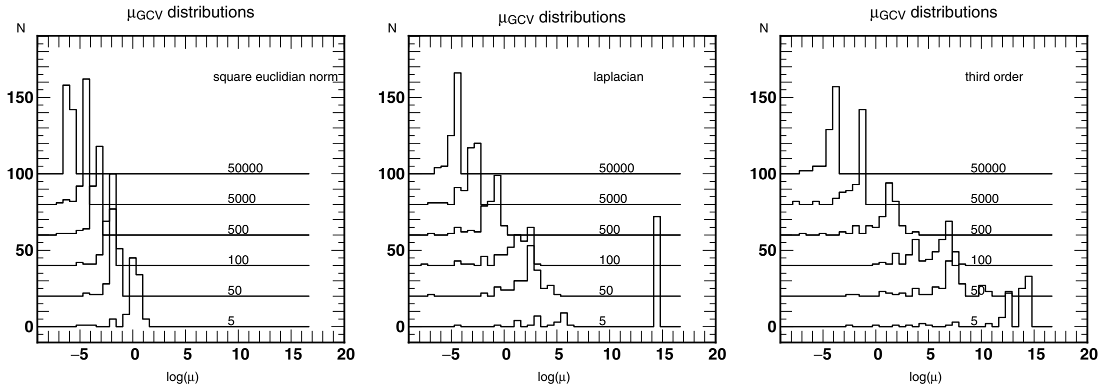

Figure 5. Histograms of the distribution of $\mu_{\rm GCV}$ for a linear stellar age distribution inversion with 60 age bins, and several SNR per pixel and penalizations. From left to right: Euclidian norm, Laplacian and $\mathbf{D}_3$ penalizations. The distributions are vertically offset for readability, and the SNR is given for each of them. The median of these distributions give the GCV-optimal smoothing parameter for each SNR and penalization. It is well defined in all cases except for very low SNR = 5 per pixel. The median parameter increases with the order of the penalization and decreasing SNR. Note the skewed distributions (this is quite generic in GCV).

data. The choice of μ thus appears as a critical step, and should give a fair balance between smoothness of the solution and sensitivity to the data.

3.6 Setting the weight for the penalty: μ

The optimal weighing between prior and likelihood is a central issue in MAP because it allows us to tailor the effective degree of freedom of each inversion to the SNR of the data. See, for example, Titterington (1985) for an extensive comparison between various methods for choosing the value of the hyper-parameter μ.

3.6.1 The automatic way: generalized cross validation

Generalized cross validation (GCV) is a function of the parameter μ, the data and the kernel $\mathbf{B}$, defined as

$$\mathrm{GCV}(\mu) = \frac{\|(\mathbf{I} - \mathbf{B}\cdot\tilde{\mathbf{B}})\cdot \boldsymbol{y}\|^2}{\mathrm{tr}^2(\mathbf{I} - \mathbf{B}\cdot\tilde{\mathbf{B}})}, \tag{35}$$

where $\tilde{\mathbf{B}}$ is the regularized inverse model, defined by equation (31) and $\mathrm{tr}(\cdot)$ is the trace of its argument. The minimum of GCV optimizes the predictive power of the solution (Wahba 1990), in the sense that if any pixel is left out of the data, this pixel's value should still be well predicted by the corresponding regularized solution. For quadratic penalizations, one may obtain very simple expressions for the GCV function, speeding up its computation, and therefore the determination of μ by several orders of magnitude. Using the GSVD of ($\mathbf{B}$, $\mathbf{L}$), we can derive

$$\mathrm{GCV}(\mu) = \frac{\sum_{i=1}^{n}\left(\rho_i\, \boldsymbol{u}_i{}^{\top}\cdot \boldsymbol{y}\right)^2}{\left(\sum_{i=1}^{n}\rho_i\right)^2}, \tag{36}$$

where

$$\rho_i = 1 - \frac{\sigma_i^2}{\sigma_i^2 + \mu\,\theta_i^2} = \frac{\mu\,\theta_i^2}{\sigma_i^2 + \mu\,\theta_i^2}. \tag{37}$$

Here, σ_i and θ_i are the singular values obtained from the GSVD of the matrix pair ($\mathbf{B}$, $\mathbf{L}$) (see Appendix C). Note that μ in the denominator of ρ_i factorizes out in the expression of GCV (μ).

When available, the minimum of GCV provides a good, data quality motivated value for μ. Moreover, GCV has been extensively tested and applied by a number of authors, in several fields of physics. Fig. 5 shows distributions of $\mu_{\rm GCV}$ for a monometallic inversion for several SNRs and penalizations. Each histogram results from 150 experiments. The GCV determination of the smoothing parameter is successful over a wide range of SNR, in the sense that the histogram shows a clear maximum. This maximum is best defined for the Tikhonov penalization (square of the Euclidian norm). With Laplacian and higher-order penalizations, especially for low SNR, the GCV values are more widely spread. Nevertheless, we can still obtain a useful value by extrapolating the higher SNR μ down to the desired SNR.

3.6.2 Empirical approach: trial and error

GCV and most of the automated smoothing parameter choice methods were designed for linear problems. In the case of non-linear problems, it can provide a useful value for μ to start with, but fine empirical tuning is also required (Craig & Brown 1986). For instance, when positivity is imposed through reparametrization or gradient clipping, μ should be smaller than $\mu_{\rm GCV}$. Indeed, because the positive problem has a better behaviour than the full linear one, it is expected that GCV overestimates μ. One can thus afford to lower it to some extent without threatening the relevance of the solution. As a consequence, finer structures can be recovered. To set μ for the positive problem, we used the simple following procedure. First, we set $\mu = \mu_{\rm GCV}$. We produce mock data, and perform successive inversions, while decreasing μ. As a consequence, finer structures are recovered. At some point, we will enter a regime where the structures of the solution can be identified as artefacts. This transition defines a lower limit above which μ should remain.

3.7 Where is the age information?

Which spectral domains or lines are most discriminative in terms of population age-dating? An answer to this can be given by inspecting the properties of the regularized inverse model matrix $\tilde{\mathbf{B}}(\mu)$ defined by equation (31). In effect, we expect the peak-to-peak amplitude of a column of $\tilde{\mathbf{B}}(\mu)$ to be largest for the most discriminatory wavelengths for age-dating. In Fig. 6, the inverse model matrix was computed for a Laplacian penalization with $\mu_{\rm GCV} = 10^2$ corresponding to SNR = 100 per pixel with 60 age bins from 10 Myr to 20 Gyr and half-solar metallicity. It shows that the Balmer lines $\mathrm{H}_{\alpha,\beta,\gamma,\delta}$, along with the spectral regions of the Lick index NaD, the magnesium

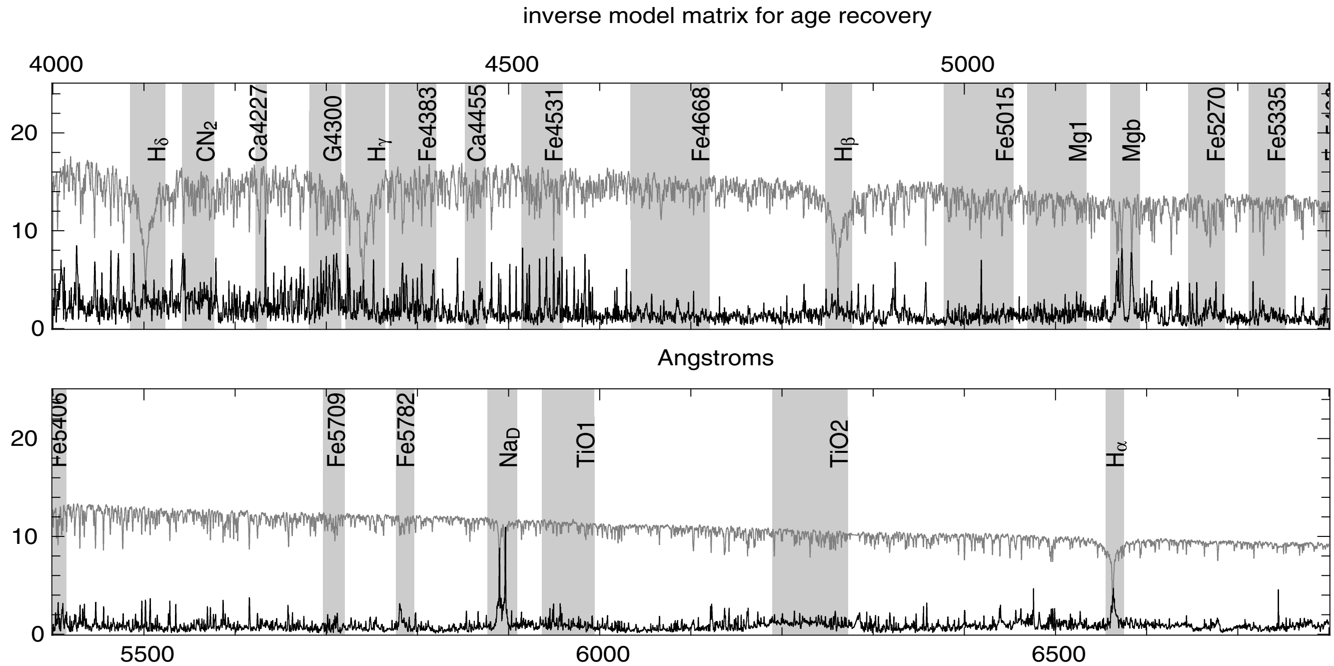

Figure 6. Black solid line: peak-to-peak variations of the inverse model matrix discussed in Section 3.7. In this example, we took 60 age bins and $\mu = 10^2$ corresponding to SNR = 100 per pixel with Laplacian penalization. Large values point at age-sensitive parts of the spectrum. A 500-Myr SSP with half-solar metallicity is shown as reference (grey solid line). The spectral domains corresponding to the Lick indices appear as grey-shaded areas. Many of the spectral domains involved in the Lick system seem to effectively carry more information than the rest of the spectrum. However, the information is still widely distributed along the whole optical range.

indices Mg_1, Mg_2, Mg_b and the calcium Ca $_{4227}$ have strong weight in the age-dating process. Note that the above analysis is clearly noise-dependent via $\tilde{\mathbf{B}}(\mu_{\mathrm{GCV}})$. The list of relevant lines will change with the SNR. Many of the wiggles and peaks of the inverse model remain so far uninterpreted, and many peaks hit spectral domains where no referenced index is known, but still contribute strongly to age separation. Another important feature of the inverse model is that most of its norm is in the form of low-value pixels. If some of the peaks were two or three orders of magnitude larger than the average value, we could conclude that most of the information is contained exclusively in the corresponding lines. Yet, Fig. 6 does not allow us to reach this conclusion. Even though the information seems denser in the strongest, well-known lines, most of it remains in the form of a large number of weaker lines, more concentrated in the blue part of our spectra. This supports the intuition that much information is left aside by looking exclusively at spectral indices, and that the constraints obtained therefrom are not optimal; hence, our effort to build a global spectrum fitting tool.

4 VALIDATION: BEHAVIOUR OF THE LINEAR INVERSION

Let us now apply STECMAP to mock data, to study the biases and the dispersion of the solutions, and to test for different penalizations. Producing mock data involves choosing a model age distribution, $\boldsymbol{x}_M$, and a noise model, $\boldsymbol{e}$. A mock spectrum is then obtained as $\boldsymbol{y} = \mathbf{B}\cdot\boldsymbol{x}_M + \boldsymbol{e}$. The corresponding astrophysical goal is the recovery of the star formation history of monometallic stellar populations (for example superimposed clusters) seen without extinction. The stellar age distribution models for these objects are single (Section 4.1) or multiple (Section 4.2) star formation episodes of approximately Gaussian shape. Recall that no assumption on the shape of the distribution is included in the inversion process. The only a priori is the smoothness of the solution, while the smoothing parameter is set by GCV. Here we relate the results of our simulations to the properties of the solution singular vectors, thereby explaining the generation of artefacts.

4.1 Single bump stellar age distribution

Let us discuss in turn the relationship between the artefacts of the reconstructions and the shape of the solution vectors (Section 4.1.1), the flux-averaging of the basis and the behaviour of the problem regarding the fiducial model (Section 4.1.2), the choice of penalization (Section 4.1.3), the requirement to impose positivity (Section 4.1.4), and the need for an extensive simulation campaign (Section 4.1.5).

4.1.1 Artefacts and the shape of the solution vectors

Because any solution is a linear combination of the solution vectors $\boldsymbol{v}_i$ (see equation 32), their shapes impose what kind of shape for $\boldsymbol{x}$ can or cannot be reconstructed, depending on what feature in the observed spectra is best matched by the corresponding data singular vectors.

Moreover, as regularizing the problem involves attenuating the high rank terms of equation (32), the detailed shape of the solution is in general given by the first few $\boldsymbol{v}_i$. Fig. 7 shows the stellar mass distribution reconstruction of an old population. It is actually a blow-up of the recovery of the oldest burst in the bottom right-hand panel of Fig. 8. The penalization is square Euclidian norm, so that the relevant singular vectors are given by the SVD of $\mathbf{B}$. The details of

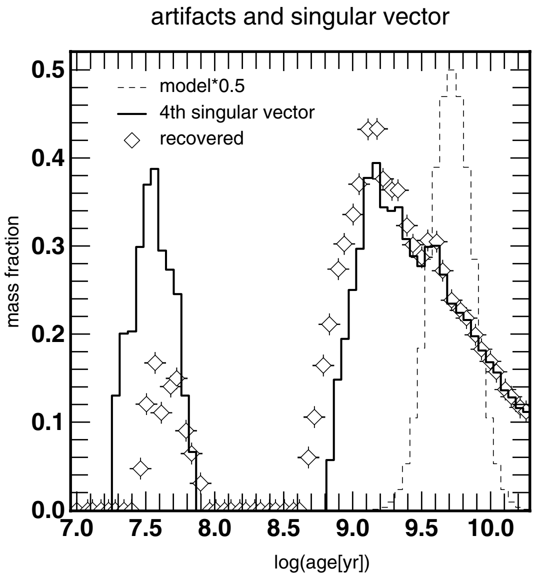

Figure 7. Blow-up of the bottom right-hand panel of Fig. 8 showing only the mass reconstruction of the oldest bump. The dashed line is the model distribution, and the diamonds show the median of the recovered age distributions for 10 realizations. The error bars showing the dispersion are smaller than the symbol itself. The details of the shape of the mass distribution reconstruction trace closely the fourth singular vector of the kernel **B**, with very little dispersion, showing that the artefacts and the fine structures of the reconstructions are closely related to the properties of the SSP models.

the solution are mostly those of the fourth solution singular vector, and appear as a systematic artefact (the diamonds are the median of 10 realizations, and the dispersion of the solutions is smaller than the symbol itself). The spurious young component between $10^{7.5}$ and 10^8 yr seems to be related to the fourth singular vector as well, and also appears systematically even though it has no physical reality. The fine structure and the artefacts of any solution thus rely most on the properties of the SSP basis rather than on the data or even the realization of the noise.

It is generally impossible to reconstruct accurately the shape of the distribution for ages where the singular vectors display no structure. The right-hand panel of Fig. 9 shows that the 10 first singular vectors of the absolute flux kernel have very little structure for ages larger than $\simeq 3$ Gyr. Correspondingly, the right-hand panels of Fig. 8 show that indeed, in this range of ages, the shape of the distribution is very poorly constrained.

For an inversion problem to be well behaved, the first solution singular vectors, $\boldsymbol{v}_k$, should be rather smooth. They should display more and more oscillations as the rank k increases (typically $k-1$ oscillations), but remain smooth and regular. The unsmooth aspect of our singular vectors arises from the temporal roughness in the spectral basis. This could also be related to physical fast evolution of the SSPs in some specific stages of stellar evolution, producing variable distance between the elements of the basis. It also reflects the non-shift-invariance of the problem, as is also illustrated by Fig. 3.

However, some further artefacts cannot be trivially explained by the solution singular vectors alone. For example, many of the displayed solutions, even with high SNR, show variations far away from the bulk of the signal, seen as misleading spurious secondary bumps. This artefact is the analogue of Gibbs rings in imaging. It arises because the higher-frequency modes needed to suppress these secondary oscillations are attenuated by regularization, and would be best identified by examining the GSVD of (**B**, **L**). It is the old age extension of the low-frequency mode involved in building the main bump. We deal with this by introducing positivity in Section 4.1.4

4.1.2 Flux-normalized basis and independence from the fiducial model

In practice, one can choose between a basis where the flux of each SSP is given for 1 $M_{\odot}$ (absolute flux basis or mass-normalized basis), and a basis where the flux of each SSP has been normalized to the same value (or flux-normalized basis; cf. Section 2.1). This choice has a physical meaning: in the first case, the unknown $\boldsymbol{x}$ will contain mass fractions, whereas in the latter case, it will contain flux fractions.

There are several reasons why we prefer to work with the flux-normalized basis.

It is more directly linked to the luminous properties of the observed population (and thus less directly linked to the mass); a component of a given flux cannot 'hide' behind another component of similar flux. This is not true for components of similar masses, due to the evolution of $M/L(t)$. For instance, in the upper-right plot of Fig. 8, the mass of the older components is poorly constrained when the model is a young burst. This is expected, because when a young component is present, adding the same mass of old stars will have very little effect on the integrated optical light. This is predictable from the lack of structure beyond 3 Gyr in the singular vectors of the right-hand panel of Fig. 9 (see also the discussion in Section 4.1.1). Modulations in this range of ages are seen in the vectors of the right-hand panel for the higher rank vectors only. On the other hand, the singular vectors of the flux-normalized basis (left-hand panel of Fig. 9) display structure in the large ages even for low ranks, indicating a better behaviour. Indeed, the upper-left plot of Fig. 8 shows that all the flux fractions are satisfactorily constrained no matter if the model population is young or old. In this respect, the 'separability' issues tackled later in the paper for superimposed populations (Section 4.2) are more easily discussed in terms of flux fractions. Note, however, that it is not expected that the mass fractions obtained by multiplying the flux fractions by $M/L(t)$ be accurate over the whole age range (positivity will improve this particular aspect significantly; see Section 4.1.4).

The difference of behaviour between the mass and flux fractions reconstructions is also reflected in the variation of the transition rank i_0 (see Section 3.4) between the noise- and signal-dominated regimes, as shown in Fig. A1. For a mass-normalized basis, the transition rank i_0 increases with the age of the fiducial model $\overline{\boldsymbol{x}}$ (as defined in Panter, Heavens & Jimenez 2003), from 5 to 20. On the other hand, for a flux-normalized basis, the transition rank remains around 7–9 in this pseudo-observational set-up, no matter the age of the fiducial model. Ideally, we would like to come up with a problem whose behaviour is fixed only by the SNR. In this respect, independence of the transition rank i_0 from the fiducial model is a welcome property. We have thus chosen to carry on with the flux-normalized basis for the rest of the paper.

4.1.3 Laplacian or square Euclidian norm penalty

Fig. 8 allows us to check which penalization gives the solutions with smallest distance to the model. First of all, it is quite clear that the square Euclidian norm penalization is worst, because it produces

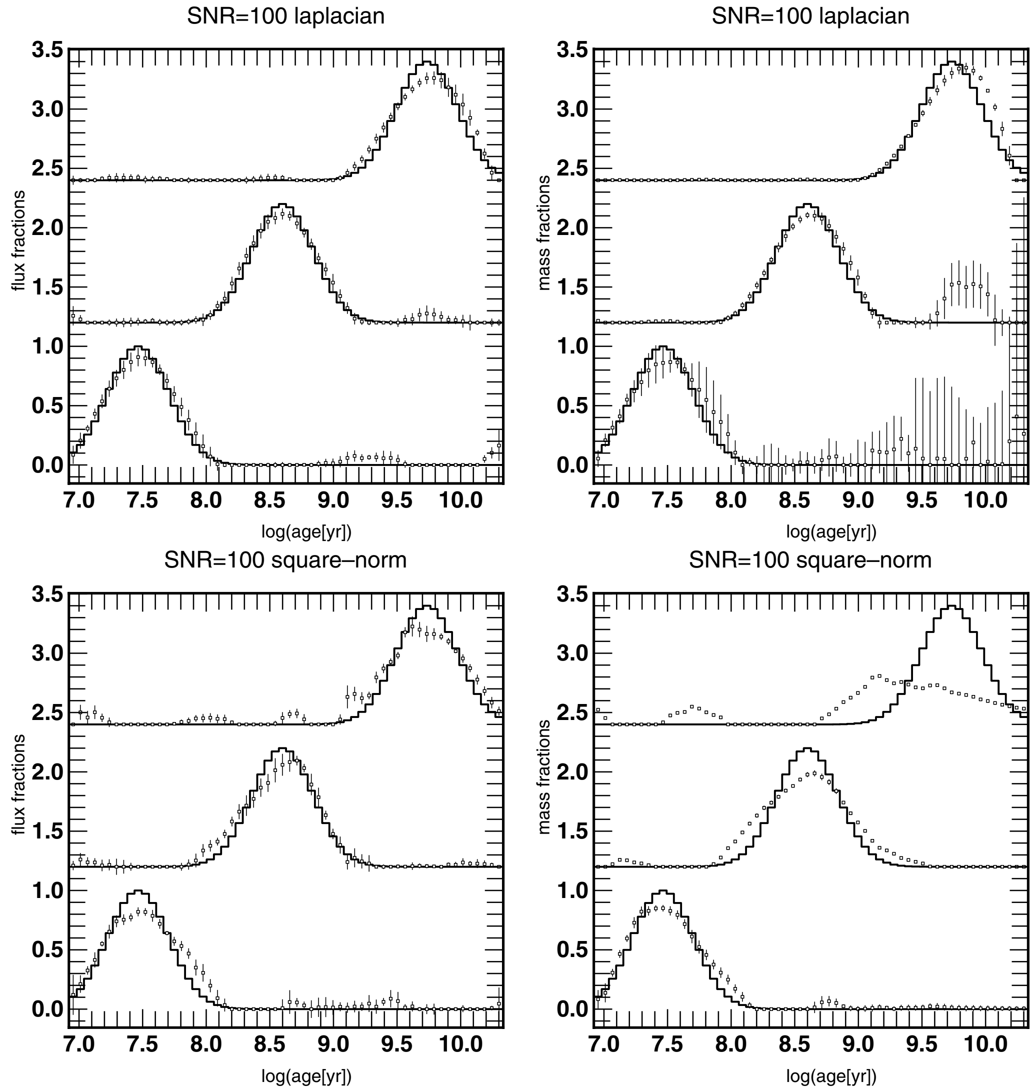

Figure 8. Simulations of the reconstruction of a young, intermediate and old single-burst populations. The thick histograms represent the models, while the symbols and vertical bars show the median and interquartiles of 10 inversions. Negative values in these reconstructions have been set to zero for clarity. Right: case of an absolute flux basis. The plots thus represent mass fractions. Left: case of a flux normalized basis. Thus are represented flux contributions. The SNR is fixed to 100 per pixel with $R = 10\,000$. The penalizations are square Euclidian norm (bottom) and Laplacian (top). In terms of distance to the model, the bumps are best reconstructed in flux fractions, and the best penalization is Laplacian. We checked that Laplacian penalization gave flux fraction reconstructions similar to the third-order penalization, showing that these do not strongly rely on the details of the smoothness a priori.

both flattened solutions and strong artefacts. Indeed, requiring the norm of the solution to be small does not explicitly have an effect on the smoothness of the solutions.

Laplacian penalizations give results very similar to the third-order penalization $\mathbf{D}_3 \equiv \mathrm{Diag}_3[-1, 3, -3, 1]$ defined as in equation (30). The latter are therefore not plotted, and perform equally well. Both produce moderately flattened solutions showing increasing dispersion with decreasing SNR, without systematic bias in age. The width of these bumps is a simple (but crude) measure of the time resolution of the reconstructions, because any bump narrower than the models displayed would be broadened by the inversion. The absence of significant difference between the results of the Laplacian and third-order penalizations shows that the inversion does not rely strongly on the details of regularization, as long as it involves a differential operator. We chose to carry on with the Laplacian penalization for the rest of the paper.

4.1.4 Positivity and Gibbs apodization

Positivity of the solution is a physically motivated requirement, but it also stabilizes the inversion by strongly reducing the explored parameter space. The maximum frequency (or best resolution in age) that would be obtained for infinite SNR is thus not only a matter of basis ill-conditioning but also has a methodological component. This is illustrated by the slightly better age resolution (and thus higher frequency) obtained while relying on positivity, as shown in Fig. 10. Unfortunately there is no simple extension of the analytical ill-conditioned problem diagnosis to the non-linear problem. Also, the minimization of Q_μ defined in equation (27) requires efficient algorithms, as described in Appendix B. As any regularization method, positivity will also introduce some bias. Indeed, the solutions in Fig. 10 seem to be slightly asymmetrical compared to the linear solutions. However, one strong advantage of positivity is its ability to reduce Gibbs ringing. Linear solutions with any penal-

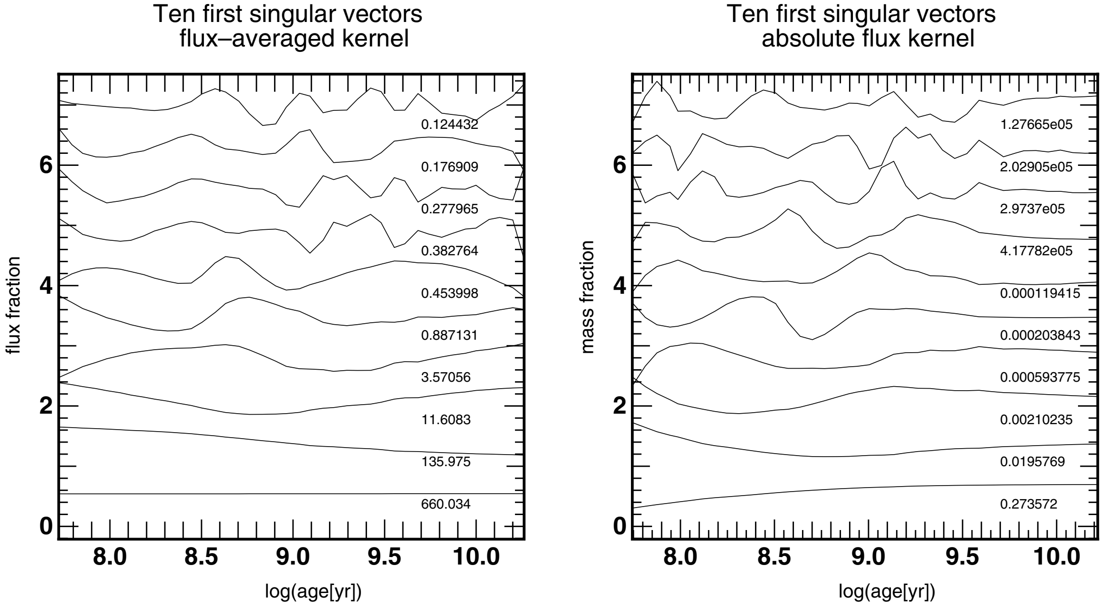

Figure 9. Solution singular vectors of the flux-normalized kernel (left) and the absolute flux basis (right). The vectors are vertically offset for visibility, and the associated singular values are given on the right. The low rank singular vectors of the absolute flux basis are very flat in the large ages, indicating that no information about these populations can be obtained unless we have very high SNR. On the contrary, fluctuations in large ages are already present in the low rank singular vectors of the flux-normalized basis, which indicates the better feasibility of reconstructing the age distribution in the older part.

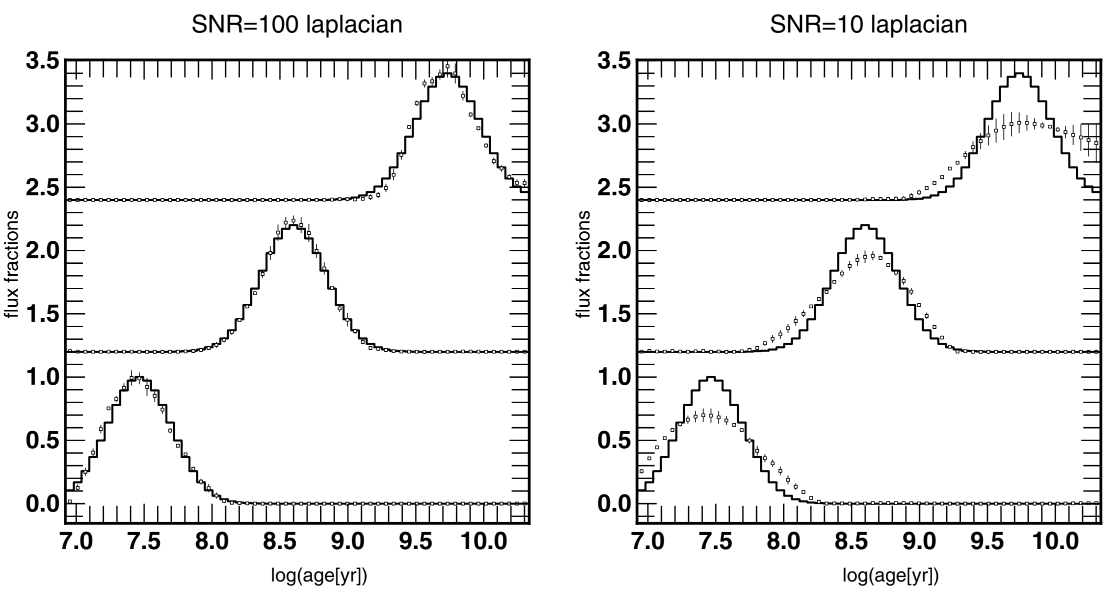

Figure 10. Same as Fig. 8 with a flux-normalized basis, positivity enforced by quadratic reparametrization and Laplacian penalization. Results of simulations for SNR = 100 and SNR = 10 per pixel at $R = 10\,000$ are shown. Even though some residual remains, the solution sticks to zero where it should, instead of displaying Gibbs rings.

ization exhibit spurious oscillations even far from the main bump, which can be interpreted as a superimposed component. These annoying artefacts do not appear in the positive solutions, as shown in Fig. 10. In many applications, this property turns out to be more important than the possible bias it might introduce in age estimation.

4.1.5 Why carry out an extensive simulation campaign?

An inversion method can perform very well for some specially chosen cases while performing poorly generally. As an example, we discuss the recovery of the age distribution of a complex population consisting in a superposition of young, intermediate, and old subpopulations. Each of these three components contributes equally to the total observed spectrum $\boldsymbol{y}$. The noise is Gaussian. Fig. 11 shows reconstructions of the age distribution by the equation (31), for 150 realizations, with a Laplacian penalization. The reconstruction seems to be satisfactory: it is unbiased and the interquartile intervals of the solutions shrink with increasing SNR. A naive reading of Fig. 11 would suggest that we are able to recover nearly any age distribution, without bias and with very small error for all the time bins, even with quite low SNR; however, there is a trick.

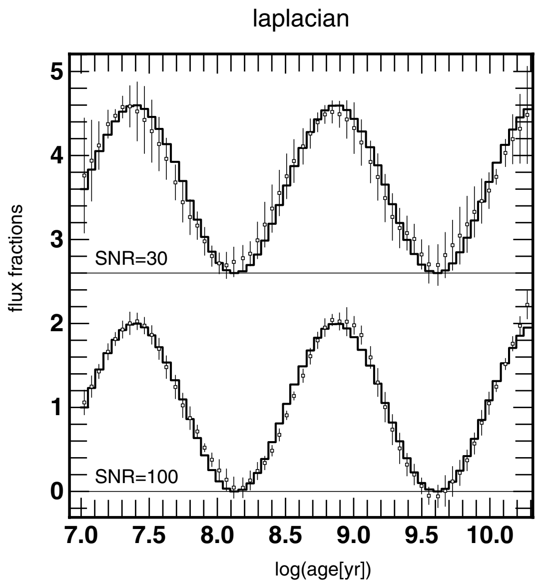

Figure 11. Same as Fig. 10, with a $1 + \sin$ model for the stellar age distribution. The SNR per pixel is given for each experiment (10 realizations), and the resolution is $R = 10\,000$. The smoothing parameter μ was adjusted by running several simulations and choosing the one providing the smallest distance to the model. The reconstruction is excellent, but there is a catch: it turns out that sine functions are intrinsically easier to recover than single bumps, given the shape of the solution vectors of the kernel. Hence, such reconstructions are very misguiding. More systematic simulations are required.

Why do the simulations in Fig. 11 look so good? First, the temporal frequency of the solution is lower than in the single bump simulations. Secondly, higher-frequency sine functions are needed to represent a single bump than to represent a sinusal curve (one is enough). Thus, as the first singular vectors roughly form a basis of sine functions, one needs fewer and lower-order solution singular vectors to represent a sine function than a bump, and lower SNR.

One simple (yet unadvisable) recipe to make good looking simulations even without regularization could involve the following steps:

(i) choose as model $\boldsymbol{x}$ one of the last few solution singular vectors $\boldsymbol{v}_k$ (or one of the first few if some penalization is implemented);
(ii) compute the corresponding pseudo-data $\boldsymbol{y} = \mathbf{B} \cdot \boldsymbol{x}$;
(iii) noise the data at chosen SNR;
(iv) invert and show how close the recovered solution lies to the initial model.

By doing so, we managed to produce apparently good looking simulations down to SNR = 0.1 per pixel. Thus, the requirement to assess and demonstrate the validity and efficiency of the MAP method carried out in this section.

4.2 Age separation versus *R* and SNR

We have already made clear that we cannot recover all the high-frequency oscillations of a given stellar age distribution even with very high SNR, but rather moderately slow variations, corresponding to smooth solutions. Let us none the less consider the special case where a composite population consists of two successive bursts, i.e. stellar age distributions with two bumps of same luminosity. This is one order of complexity above the classical characterization of a population through one unique age using Lick indices. Indeed, it applies to many astrophysically interesting cases. The ability to separate the two main populations would allow us, for example, to age-date respectively the disc and the bulge of unresolved spiral galaxies, or late stages of accretion and star-forming activity in ellipticals in surveys, such as the SDSS and 2dFGRS. It would also allow us to better constrain the mass-to-light ratio of such complex populations. We wish to investigate what observational specifications (spectral resolution, SNR) are required to reliably perform such a separation. We thus ran extensive simulations of reconstructions of double-burst populations. The spectral resolution, SNR and the age separation Δage between the two bursts were varied, and the recovered ages were studied as a function of R, SNR and Δage. Fig. 12 shows the recovered and model age couples (a_1, a_2) in several experiments of double-burst superpositions, for SNR = 20–200 per Å, at $R = 10\,000$ and $R = 2500$. The model age grid takes 13 values, separated by 0.2 dex, therefore defining 78 age couples.

These systematic simulations allow us to estimate the resolution in age achievable for a given (R, SNR) and the corresponding errors. It is a solid, systematic way for testing the method in different regimes. The smoothing parameter was set for each (R, SNR) by taking the GCV value as a guess and fine-tuning it in order to obtain stable reconstructions of close bumps. The quality of the reconstructions is assessed using the following two criteria.

(i) Because, in the model, the two bursts have exactly the same luminosity, we require that the areas of the two biggest bumps have a ratio smaller than 2.
(ii) The minimum between the two main bumps of the solution should be fairly low, otherwise it is difficult to state whether the populations are truly distinct or part of an extended star formation episode. Here, we required the minimum to be lower than 10 per cent of the mean height of the biggest bumps.

The solutions are required to satisfy these two criteria to be considered as 'good' in terms of age separation. Fig. 13 shows as an example an acceptable (well-defined bumps, minimum at 0) and a rejected solution (bumps and minimum unclear). In Fig. 12, we retained exclusively the cases satisfying these criteria, i.e. for the other age couples (not plotted), the recovered stellar age distributions failed one or both criteria. A common failure is the recovery of one wide bump instead of two, indicating that the subpopulations are not separated given the SNR and spectral resolution. Thus, the empty region between the successfully separated couples and the bisector (dashed line) is a region of 'inseparable' couples. The width of this region indicates the resolution in age that we can achieve. This region shrinks with increasing SNR, showing that we can separate two close subpopulations more accurately. We superimposed on the leftmost panel of Fig. 12 several vertical segments spanning the 'inseparable' region. We define the resolution in age as the median length of these segments. The statistical error on this quantity is of the order of 0.2 dex for SNR = 20 per Å.

In a realistic observational context, a separation of two subpopulations with an age difference lower than the computed resolution in age should not be attempted, or at least not trusted. The resolution in age achieved here is a lower limit because no error source other than Gaussian noise is considered. Other possible sources of noise are glitches, residual sky lines, non-sky-emission lines (when not masked in $\mathbf{W}$), spectrophotometric and wavelength calibration error, and model error, along with effects of the age–metallicity–extinction degeneracy (in this section the true metallicity of the observed system was known a priori).

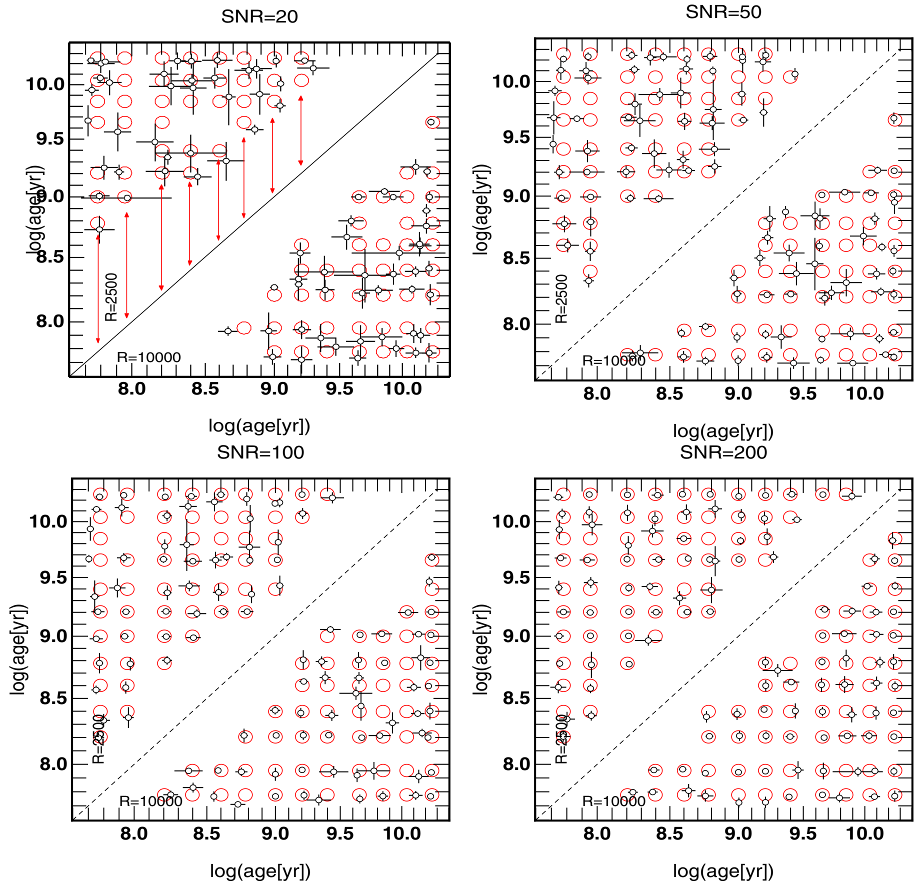

Figure 12. Recovery of double bursts for several SNR per Å. The large circles are the models. Their coordinates (a_1, a_2) are the ages of the two bursts. The smaller circles with error bars show the median and the interquartiles of the recovered ages in 10 reconstructions each. The dotted line represents the $a_1 = a_2$ limit. Solutions that do not satisfy the quality criteria illustrated in Fig. 14 are rejected and not plotted. The upper diagonal part of each panel shows $R = 2500$ results while the lower diagonal part shows $R = 10\,000$ results. Results for the other spectral resolutions down to $R \approx 1000$ are very similar and therefore are not shown. Our ability to separate close double bursts improves with increasing SNR, but does not significantly change with spectral resolution. The top left-hand panel illustrates the definition of the resolution in age as the median length of the segments. Note that the shape of the 'inseparable' zone and its evolution with SNR are similar to that shown in Fig. 3.

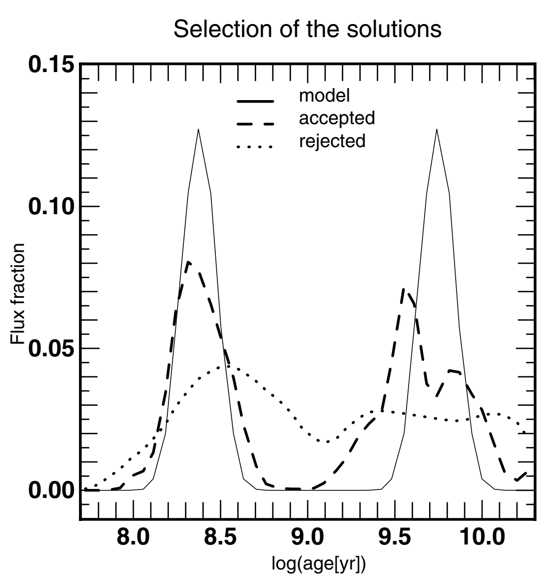

Figure 13. Selection criterion: the rejected solution shows no clear separation, while the accepted solution has two clear bumps of similar area with a well-defined minimum.

Fig. 12 also shows that the error on both ages of the couple of subpopulations decrease on average with increasing SNR, as expected. For small SNR, the figure is quite inconclusive, and the recovered age couples are more or less randomly spread all over the age domain, while for high SNR, every couple seems to be quite in place, even though some couples remain slightly offset. For other resolutions, the plots are quite similar, and therefore we do not reproduce them here. The left-hand panel of Fig. 14 gives a synthesis of all the experiments by showing the resolution in age, computed according to the given definition, versus the SNR per Å, for several spectral resolutions. The resolution in age improves with increasing SNR, from 0.9 dex at SNR = 20 per Å to 0.4 dex at SNR = 200 per Å. Given the small number of measurements of the width of the unseparable zone in each experiment, the variation of the resolution in age with spectral resolution is not highly significant. Thus, it seems that, as long as the SNR per Å is conserved, spectral resolution does not significantly improve our ability to separate subpopulations. The right-hand panel of Fig. 14 shows the error on recovered ages versus SNR for the successful separations, for several spectral resolutions. The error decreases with increasing SNR, as expected, and is about 10 times smaller than the resolution in age for the same SNR. Again, no strong trend is seen with spectral resolution.

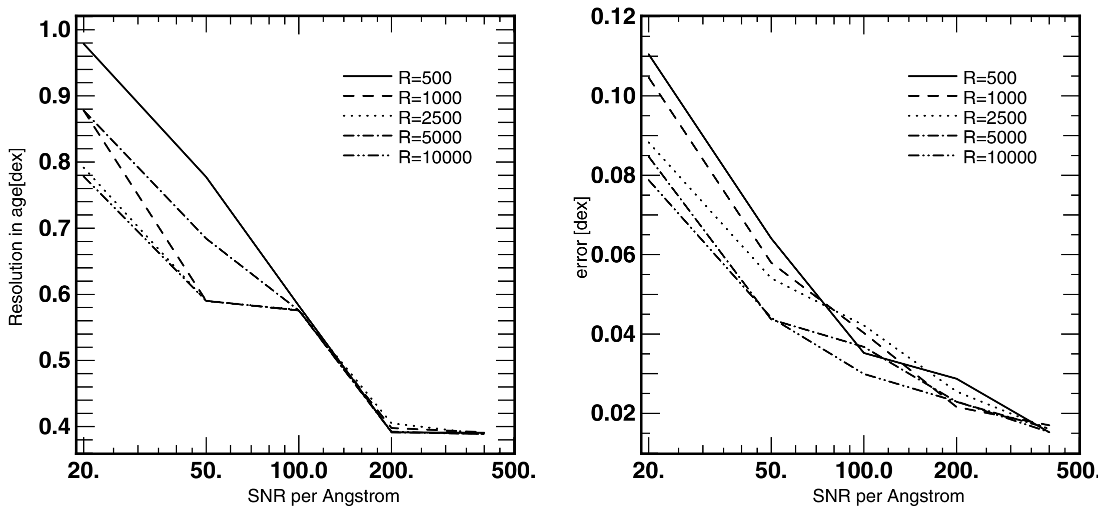

Figure 14. Left: resolution in age, in dex versus SNR per Å for various spectral resolutions. As expected, the age resolution improves with increasing SNR, and seems to settle around 0.4 dex for the highest SNR. No significant trend is seen with spectral resolution. Right: mean error of the age estimates for the successful cases (according to our criteria). The mean error is approximately one order of magnitude smaller than the resolution in age, and decreases with increasing SNR.

4.3 Compressed versus uncompressed data

In this section, we discuss the similarity between SVD and Gram–Schmidt othonormalization (GSO), the decomposition scheme adopted by MOPED's authors (Reichardt et al. 2001). This comparison is carried out in the monometallic, extinctionless regime. Data can be compressed by multiplying them by the n singular vectors to obtain n numbers containing the same information as the whole original spectrum. Appendix D shows that the fact that the singular vectors are provided by non-truncated SVD or GSO makes little difference in the linear regime. The compression can effectively be lossless, but the conditioning of the problem is unchanged, as shown by the inspection of the singular values in the left-hand panel of Fig. D1. The right-hand panel of Fig. D1 shows the result of a GSO (equation D2) and an SVD (equation 22) inversion for a composite population in a moderately ill-conditioned example. They are equal down to machine precision. Minimizing the χ^2 of the compressed data involves the issues discussed in Section 3.4, if the compression is provided via the SVD or GSO singular vectors.

4.4 Constraints on metallicity?

When attempting to reconstruct the stellar age distribution from real observations, one would still have to guess the metallicity of the population. A classical parametric way to proceed would be to perform a monometallic inversion for each of the available metallicities in the basis. If the dominant observational error is Gaussian, we expect χ^2 to be minimum when using the true metallicity. However, because of the age–metallicity degeneracy, it might not be so clear, and one could expect to reach a good χ^2 even with an erroneous metallicity guess, resulting in an error in age estimation. Fig. 15 shows a plot of the reduced χ^2 when inverting a population of metallicity $Z = 0.004$ with a basis of different metallicity for several SNR and $R = 10\,000$. The smoothing parameter was chosen using GCV with the $Z = 0.004$ kernel. The best fit is always obtained when the initial model metallicity is used. We computed the 90 per cent confidence level by taking as the number of degrees of freedom, the number of pixels in the spectrum minus the number of age bins (40 in this example). This choice could be discussed because the weights of adjacent time bins are correlated by the penalization. However, the number of time bins remains far smaller than the number of pixels and thus plays no critical role. For SNR = 10 per pixel (i.e. SNR = 20 per Å), we cannot reject fits with wrong metallicities $Z \in [0.002, 0.009]$. The error on metallicity can therefore reach 0.35 dex for SNR = 10. The range of acceptable metallicities, however, shrinks rapidly with increasing SNR, tightening the constraints. At SNR $\geqslant$ 30, it is possible to break the age–metallicity degeneracy, and thus to allow metallicity to be a free parameter of the inversion problem.

This closes our detailed investigation of the idealized problem of recovering the stellar age distribution of a monometallic, reddening-free stellar population.

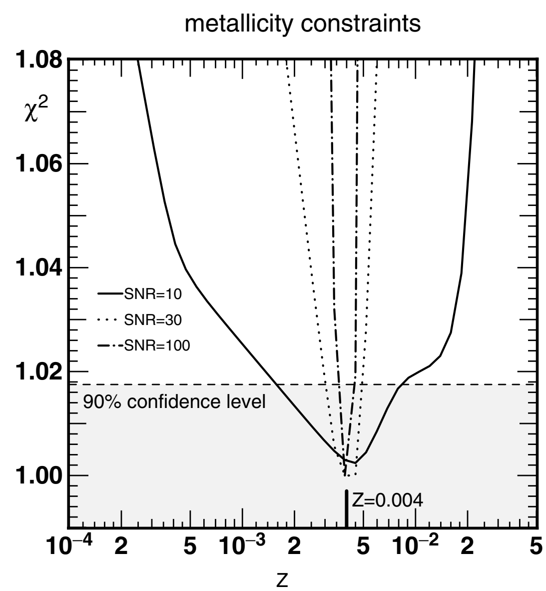

Figure 15. The high-resolution SED of model extinctionless monometallic population with $Z = 0.004$ is inverted using spectral bases with different metallicities for several SNR. For SNR = 10 per pixel, the metallicity is moderately well constrained ($\Delta Z \approx 1$ dex), while for SNR $\geqslant$ 30 per pixel all the metallicities other than 0.004 can be rejected at the 90 per cent confidence level.

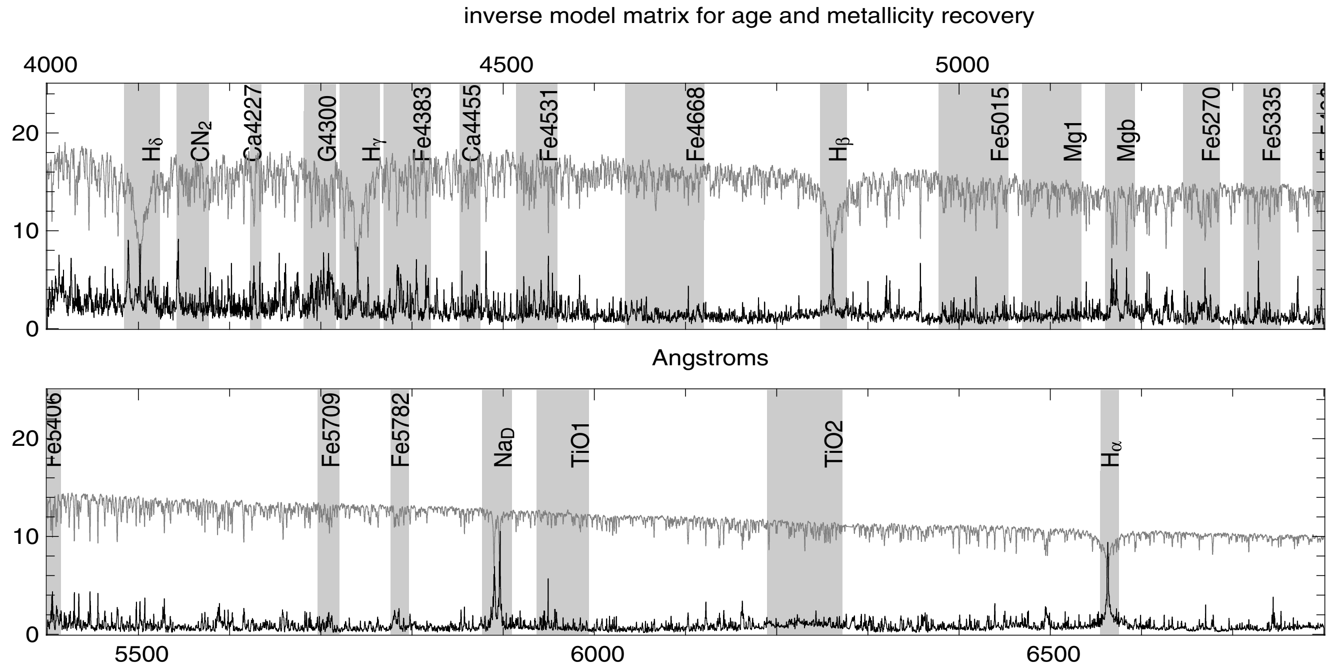

Figure 16. Same as in Fig. 6 for the linear age–metallicity distribution recovery. The dimensions of the inverse problem are 60 age bins and five metallicity bins. The smoothing parameter is set by GCV for SNR = 100 per pixel. The grey solid line is a 1-Gyr half-solar metallicity SSP for reference. Many of the spectral domains involved in the definition of the Lick indices system seem to carry more information than the rest of the spectrum. However, the information is still widely spread along the whole optical range in the form of medium depth lines, suggesting there is a large number of potential high-resolution indices.

5 STELLAR CONTENT AND REDDENING RECOVERY

In the previous section we have presented STECMAP in an idealized regime, which could only be applied to observations where both the metallicity and the extinction are known a priori, which is rarely the case in reality. We now present an extension of STECMAP accounting for these additional free parameters as well. In Section 5.1, the full linear age–metallicity problem is examined, where both metallicity mixing and age mixing are allowed, and we study its behaviour. Then, for simplicity, and given the extremely poor conditioning of this problem, the unknown metallicity will be handled specifically as an AMR. The technique for reconstructing the stellar age distribution, the AMR and the extinction will be presented in Section 5.2, along with a few example simulations in Section 5.3. Finally, its applicability and accuracy will be discussed while exploring several observational regimes in Section 5.4.

5.1 Two-dimensional linear age–metallicity problem

Here we consider a very composite population where several subpopulations with different ages and metallicities are superimposed. Let us define a two-dimensional (2D) stellar age and metallicity distribution $\Lambda(t, Z)$ yielding the fraction of optical flux emitted by stars with age $t \in [t, t + \mathrm{d}t]$ and metallicity $Z \in [Z, Z + \mathrm{d}Z]$. The model spectrum is the integral of Λ over age and metallicity space. Discretizing as in Section 3, we obtain the discrete model spectrum as the weighted sum of the SSPs for all the ages and all the metallicities in the basis. Here the parameter vector is a 2D map containing the weights x_{ij} of the SSP of age t_i and metallicity Z_j. The model matrix $\mathbf{B}$ is the concatenation of the monometallic bases described in Section 3, i.e. sequences of SSPs in age and metallicity. Its conditioning number is commonly of the order of 10^8, telling us that thorough regularization is required.

5.1.1 Where is the information on Z?

In a manner similar to Section 3.7 we can determine which spectral domains are important for age and metallicity determination. We compute the inverse model matrix $\tilde{\mathbf{B}}$ of the problem for a given $\mathrm{SNR_d}$ and look for large peak-to-peak variations in this matrix, indicating spectral features having strong discriminative power, as shown in Fig. 16. Most of the bands involved in the Lick indices carry much information. However, some of them, such as $\mathrm{TiO_2}$, seem to be unimportant, and a large number of medium- and high-resolution lines not involved in Lick indices actually carry most of the information.The comparison with Fig. 6 shows that several metallic lines, which were not important for a monometallic population age distribution recovery, turn out to carry a substantial part of the information when the metallicity is unknown. Again, the blue part of the spectrum seems to be more discriminative.

Because age sensitive and metallicity sensitive lines are spread along the whole optical wavelength range, any small section of the spectrum has good chances of containing such lines (see Le Borgne et al. 2004 for an example around H_γ). Thus, if the available data do not allow reliable full optical domain fitting, plots such as Fig. 16 are a good starting point for the search for new high-resolution indices. The use of the whole spectrum implies some redundancy, but considering the sensitivity of the inversion problem to noise, this redundancy is highly welcome.[5]

5.1.2 Age–metallicity degeneracy?

We carried out the following experiment illustrated in Fig. 17. We produced mock data corresponding to a 2D stellar age and

[5] The redundancy is also useful in oder to address in part problems induced by the poor modelling of some spectral lines.

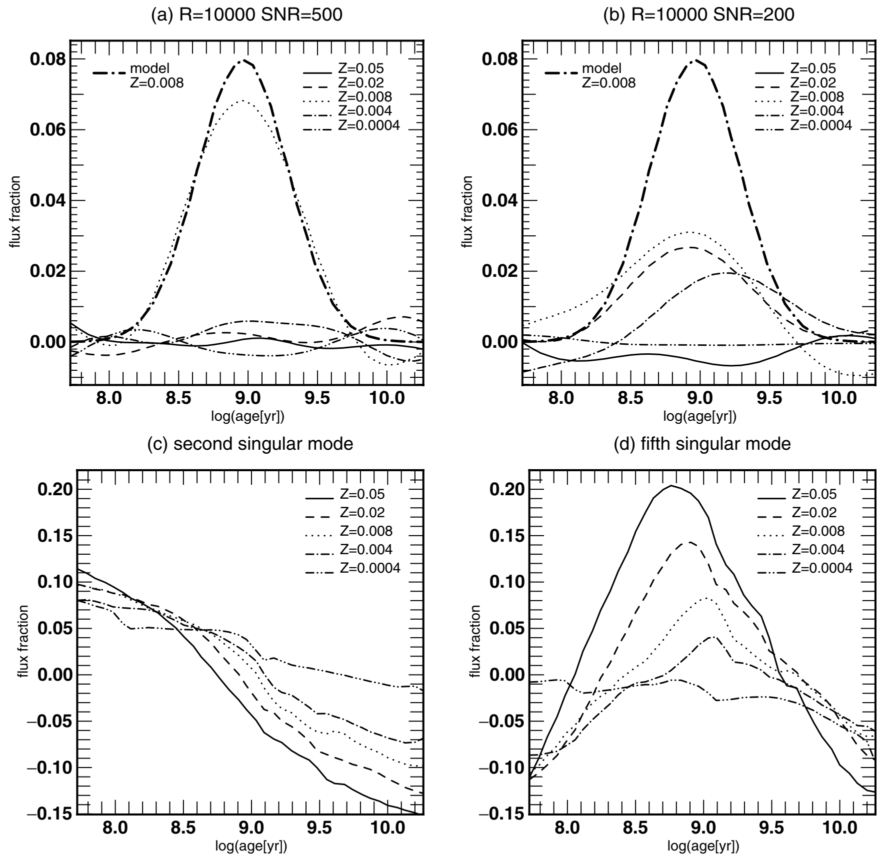

Figure 17. (a) and (b): free metallicity reconstructions of a monometallic population for SNR = 500 and SNR = 200 per pixel. For high SNR a monometallic population is unambiguously recovered, while at lower SNR, a multimetallic solution appears, indicating the degeneracy of the problem. (c) and (d): solution singular modes of the 2D age–metallicity reconstruction problem. The difficulty involved in such a reconstruction arises from the very bad conditioning number, and the lack of features of the first singular modes in the metallicity direction.

metallicity distribution map $\boldsymbol{x}$ and investigated how well we could reconstruct it for a given SNR. In the example of Fig. 17 (top panels), the model is a monometallic bump centred on 1 Gyr and $Z = 0.008$. The corresponding mock data are noised and then inverted as in equation (31) except that $\mathbf{B}$ is now the multimetallic SSP basis defined above. In this experiment, we focus on the broadening of the bump in the metallicity direction as a signature of the age–metallicity degeneracy.

The inspection of the first non-attenuated solution singular modes tells us about the properties of the regularized problem. Figs 17(c) and (d) show the second and fifth solution singular modes of the model matrix $\mathbf{B}$. Each of them is an age–metallicity map. The shapes of the stellar age distribution for each metallicity in the second singular mode are very similar, indicating bad separability between metallicities. Thus, if only the first singular modes are recovered, the solutions will have a strong tendency to be flat in the metallicity direction.

The fifth singular mode is the first to show a well-defined structure: a bump in age, elongated in the metallicity direction, with a slight shift to larger ages with decreasing metallicities. This traces the age–metallicity degeneracy: a pure monometallic population will be reconstructed in regularized regimes as a composite, mixing younger metal-rich SSPs with older metal-poor SSPs. Figs 17(a) and (b) show reconstructions of such age–metallicity maps for $R = 10\,000$, SNR = 500 and 200 per pixel. The model consists of a single bump centred on 1 Gyr and $Z = 0.008$, and the penalization is Laplacian. For SNR = 500 per pixel we see that the population is effectively reconstructed as a single bump in age and metallicity. The age–metallicity degeneracy is, in this example, explicitly broken. The same experiment with SNR = 200 per pixel gives a solution degenerate in metallicity: the monometallic population is seen as the sum of three monometallic subpopulations contributing nearly equally to the total light. The younger component is more metal-rich, while the older component is poorer, as is expected for age–metallicity degenerate solutions, and is similar to the trend seen in the solution singular modes. In this example, the smoothing parameter was chosen by GCV. More realizations of this experiment gave similar degenerate solutions. From the shape of the fifth solution singular mode, we can measure the slope of the age–metallicity degeneracy, i.e. the slope defined by the maxima of the bumps of the singular mode in the age–metallicity plane. We find it to be equal to 0.3, which is much smaller than the $3/2$ given in Worthey (1994). Smaller slopes indicate a better definition of age. This is expected because here we consider the whole optical range and the continuum as reliable.

As a conclusion, we found 2D age–metallicity map reconstructions to be feasible for only very high SNR $\geqslant 500$. Because this is comparable or larger than $\mathrm{SNR_b}$, we consider it strongly unphysical. Moreover, from an observational point of view, such a high (SNR, R) combination for an outer galaxy is generally unreachable in reasonable time with the present generation of instruments. Thus, inversions with this complexity and SNR are doubly challenging.

We now address a simplified version of this problem by reducing the metallicity parameters to a one-dimensional AMR.

5.2 Non-linear age–metallicity recovery

In the rest of the paper we assume that the chemical properties of the population are represented by an AMR $Z(t)$ of unknown shape. In contrast to Section 5.1, the subpopulation of age t_j is therefore assigned one and only one metallicity Z_j rather than a metallicity distribution. In addition, we now allow the SED to be affected by an extinction $f_{\mathrm{ext}}(E, \lambda)$ parametrized by the colour excess E. Finally, accounting for the age distribution $\Lambda(t)$, the observed SED at rest is then written as

$$F_{\mathrm{rest}}(\lambda) = f_{\mathrm{ext}}(E, \lambda) \int_{t_{\min}}^{t_{\max}} \Lambda(t)\, B\,(\lambda, t, Z(t))\, \mathrm{d}t. \tag{38}$$

This model is linear in age distribution Λ, and non-linear in metallicity Z and extinction E. Recall that f_{ext} may be replaced by other parametric functions of wavelength that could, for instance, describe flux calibration corrections.

5.2.1 Discretization and parameters

Following the same prescription as in Section 3, but accounting for extinction, we can derive the discretized version of equation (38). Provided the extinction law is very smooth compared to the size of the wavelength bins, the model of the sampled SED of the reddened composite stellar population in the ith spectral bin is written

$$\begin{aligned} s_i &= \int F_{\mathrm{rest}}(\lambda)\, g_i(\lambda)\, \mathrm{d}\lambda \\ &\approxeq f_{\mathrm{ext}}(E, \lambda_i) \int g_i(\lambda) \int_{t_{\min}}^{t_{\max}} \Lambda(t)\, B\,(\lambda, t, Z(t))\, \mathrm{d}t\, \mathrm{d}\lambda, \end{aligned} \tag{39}$$

which simplifies to

$$s_i = f_{\mathrm{ext}}(E, \lambda_i) \sum_{j=1}^{n} B_{i,j}\, x_j, \qquad i \in \{1, .., m\}, \tag{40}$$

or in matrix form

$$\boldsymbol{s} = \mathrm{diag}(\boldsymbol{f}_{\mathrm{ext}}(E)) \cdot \mathbf{B} \cdot \boldsymbol{x}. \tag{41}$$

Here, the kernel matrix $\mathbf{B}$ and the vector $\boldsymbol{x}$ of the age distribution $\Lambda(t)$ sampled upon time are defined as in Section 3, and $\mathrm{diag}(\boldsymbol{f}_{\mathrm{ext}})$ is the diagonal matrix formed from the extinction vector

$$\boldsymbol{f}_{\mathrm{ext}}(E) = (f_{\mathrm{ext}}(E, \lambda_1), \ldots, f_{\mathrm{ext}}(E, \lambda_m))^{\top}, \tag{42}$$

which contains the extinction law seen by the population and depends non-linearly on the colour excess E. Note that $\mathbf{B}$ contains the SSP basis for the AMR vector $\mathbf{Z}$ (the AMR $Z(t)$ sampled in time).

From a computational point of view, any matrix product involving $\mathrm{diag}(\boldsymbol{f}_{\mathrm{ext}}(E))$ is very expensive and can be profitably implemented using term-to-term product. However, in order to save the introduction of confusing operators, we will continue with the current notation.

5.2.2 Smoothness a priori with MAP

The model defined by equation (41) is non-linear because of the dependences of $\boldsymbol{f}_{\mathrm{ext}}$ and $\mathbf{B}$ on E and $\mathbf{Z}$, respectively. Therefore, we cannot refer to the classical definition of ill-conditioning. However, because the simpler problem solved in Section 3 is ill-conditioned, it is expected that the more complex problem treated here will be even more ill-conditioned, all the more because we now seek two fields plus one extinction parameter. We will thus add a priori information by implementing smoothness constraints, and allow the unknowns to have different smoothing parameters. We define the penalizing function P_{smooth} by

$$P_{\mathrm{smooth}}(\boldsymbol{x}, \mathbf{Z}) \equiv \mu_{\boldsymbol{x}} P(\boldsymbol{x}) + \mu_{\mathbf{Z}} P(\mathbf{Z}), \tag{43}$$

where P is the standard quadratic function defined by equation (29).

5.2.3 Metallicity bounds

The metallicity range $[Z_{\min}, Z_{\max}]$ for which models are available is bounded. We must therefore find a way to ensure that the solution lies in the desired metallicity range by making unwanted values of Z unattractive. To do this we use a binding function c (c denotes constraint) which is another kind of penalizing function. This technique was proposed by R. Lane (private communication). The function c must be flat inside $[Z_{\min}, Z_{\max}]$ in order not to influence the metallicity search and increase gradually outside. We define c piecewise by

$$c(Z) = \begin{cases} (Z - Z_{\min})^2 & \text{if } Z \leqslant Z_{\min}, \\ (Z - Z_{\max})^2 & \text{if } Z \geqslant Z_{\max}, \\ 0 & \text{else.} \end{cases} \tag{44}$$

The binding function C used in practice is defined by

$$C(\mathbf{Z}) = \sum_j c(Z_j). \tag{45}$$

The penalization function we finally adopt is

$$P_\mu(\boldsymbol{x}, \mathbf{Z}) \equiv P_{\mathrm{smooth}}(\boldsymbol{x}, \mathbf{Z}) + \mu_C\, C(\mathbf{Z}), \tag{46}$$

where a binding parameter μ_C allows us to set the repulsiveness of the exterior of $[Z_{\min}, Z_{\max}]$. The objective function

$$Q_\mu = \chi^2\,[\boldsymbol{s}(\boldsymbol{x}, \mathbf{Z}, E)] + P_\mu(\boldsymbol{x}, \mathbf{Z}),$$

is now fully characterized. Its derivatives are given in Appendix B.

5.3 Simulations of metal-dependent LWSAD

We applied the proposed inversion method to mock data for various stellar age distributions, AMRs, extinctions and SNRs. In this case, choosing an input model involves choosing the functions $\Lambda(t)$, $Z(t)$, and a colour excess E. The corresponding model spectrum is then computed following equation (41). Gaussian noise is added to obtain the pseudo-data.

Fig. 18 shows simulations of reconstructions in the case of high-quality pseudo-data: $R = 10\,000$ at 4000–6800 Å with SNR = 100 per pixel for 100 realizations. The left-hand panels show the stellar age distribution while the right-hand panels show the AMRs. The top row shows reconstructions of a double-burst population where the two bursts have different luminous contributions. The young component accounts for 75 per cent of the light, and its metallicity is a tenth of the old component's, which contributes only to 25 per cent of the total light. The imbalance between the young and old luminous contributions should make it more difficult to constrain the old component. Still, the reconstructions are good in the sense that the bumps are properly centred and scaled. Metallicities are also adequately recovered. The reconstructed stellar age distributions are smoothed versions of the model, as expected.

The bottom line plots illustrate the case of a continuous rather than bumpy stellar age distribution. All ages contribute equally to the light except the youngest and oldest. The model AMR yields a

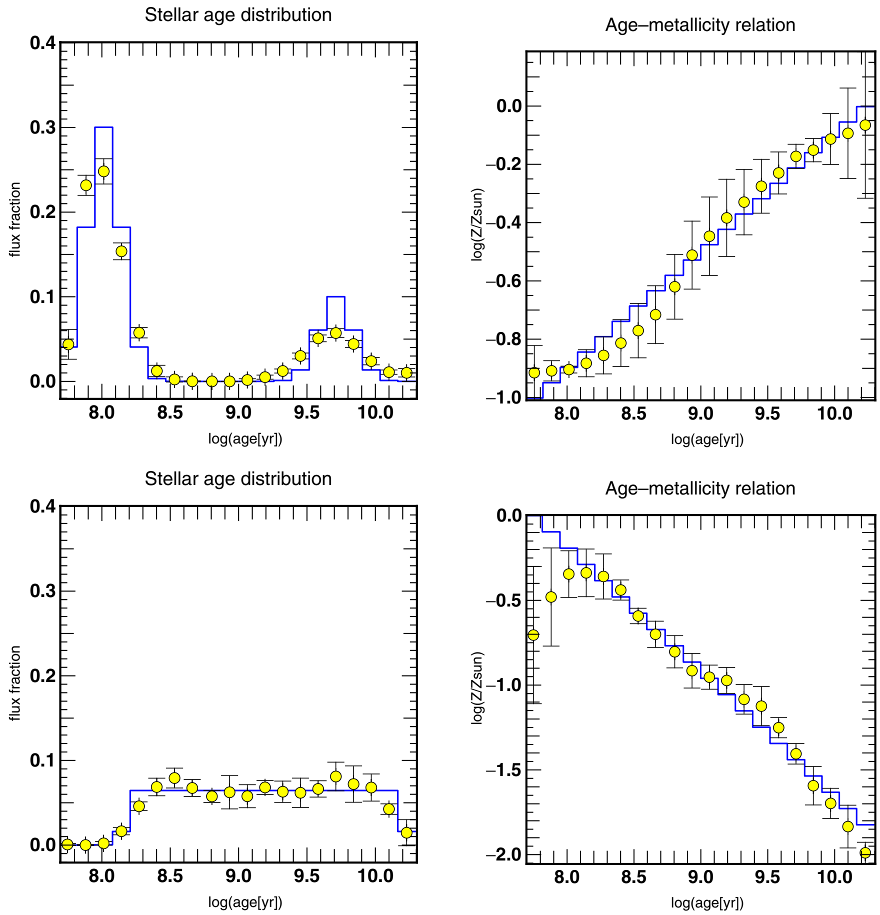

Figure 18. Reconstruction of the stellar age distribution (left) and AMR (right) for $R = 10\,000$ and SNR = 100 per pixel. The thick line is the input model. The circles and the bars show, respectively, the median and the interquartiles of the recovered solutions for 100 realizations. The metallicities and flux fractions of the populations with significant contributions are adequately recovered. In each experiment, the extinction parameter of the model was chosen randomly and recovered with good accuracy.

metallicity $Z(t)$ that increases with time. The rise and decay of the recovered age distribution are adequately located, and the metallicities have the correct trend. The metallicities of the youngest component are unconstrained simply because they do not contribute to the total light.

For each realization of these simulations, the colour excess was a random number between 0 and 1. In each case, it was recovered with an accuracy better than 10^{-2}.

5.4 Age separation of metal-dependent LWSAD

In a realistic observational setting, we would like to age-date superimposed populations. For such investigations, it is essential to have a good understanding of the limitations of the non-parametric method. We therefore investigated again how well we could reconstruct two superimposed bursts of unknown metallicities and extinction. We proceeded as in Section 4.2, and the grid of double-burst ages is the same. Both bursts contribute equally to the total light. In a first set of experiments, the model AMR is arbitrarily chosen as $\log(Z) = -9.95 + 0.85\,\log[\mathrm{age(yr)}]$, where the age ranges from 50 Myr to 15 Gyr. It is not supposed to be a physically motivated choice, but allows us to explore about two decades in metallicity. The allowed range for the solution AMR is $[Z_{\min} = 0.0004, Z_{\max} = 0.05]$. The extinction parameter was chosen randomly between 0 and 0.5. The reconstructions were performed without any a priori for the AMR, stellar age distribution or extinction parameter, apart from the requirement of smoothness. For each pseudo-observational context, the smoothing parameter was set using the GCV value for the monometallic case and fine-tuned for a small separation between two bursts. The smoothing parameter for the AMR was set to a large value (around 10^3) because we just wish to recover a global trend of the metallicity evolution in the reconstruction. A flat guess for all variables was the starting point. In every case we converged to a stable solution in less than 1500 iterations, corresponding to ≈1 min on a 1-GHz PC for a $R = 10\,000$ basis (i.e. 14 000 pixel of 0.2 Å) with 60 age bins. The distributions of the reduced χ^2 of the solutions were found to follow a Gaussian distribution law with unit mean, showing that each experiment had properly converged.

We are thus able to give an estimate of the resolution in age versus SNR and spectral resolution. Fig. 19 shows some of the results of our simulation campaign. On each panel we plotted the results obtained at $R = 2500$ (upper octan) and $R = 10\,000$ (lower octan). The results for $R = 1000$ and $R = 6000$ are very similar and are not shown. The number of successful inversions rises with increasing SNR, and the inseparable zone in the diagram shrinks. In the same way, the error bars and bias reduce with increasing SNR. We give the resolution in age for several SNR per Å and

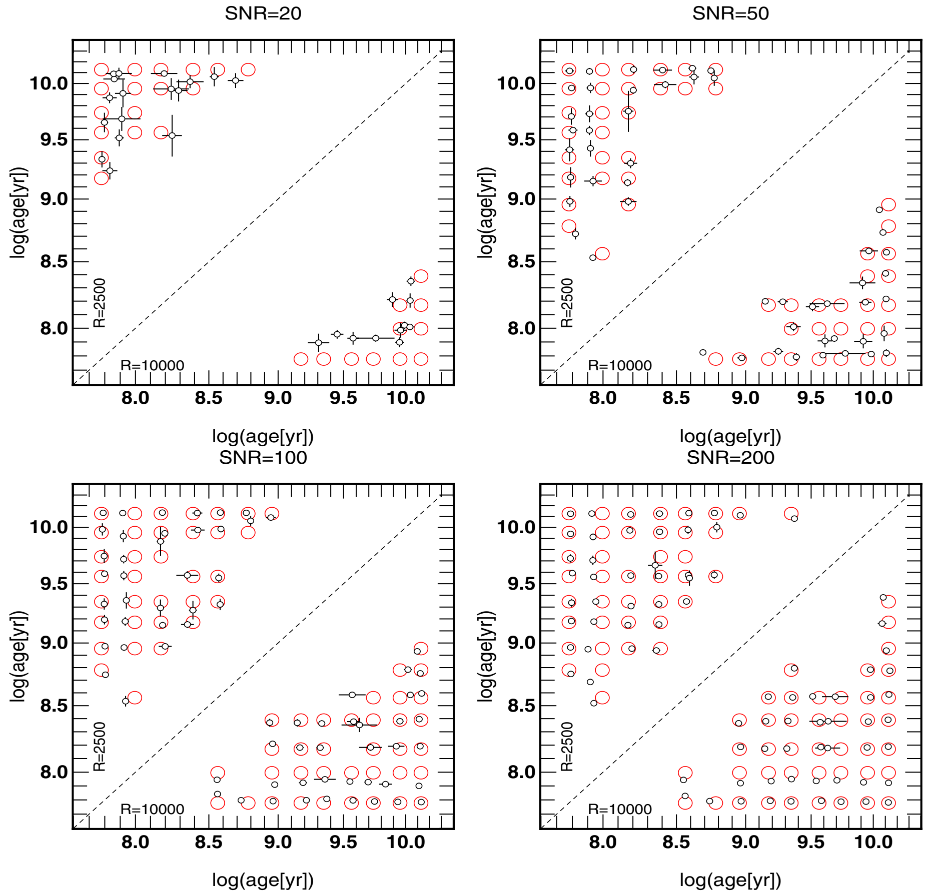

Figure 19. Same as Fig. 12 but the metallicities and the extinction are free parameters. The SNR is given per Å. The ability to separate close subpopulations improves with SNR, as does the accuracy of the age estimates.

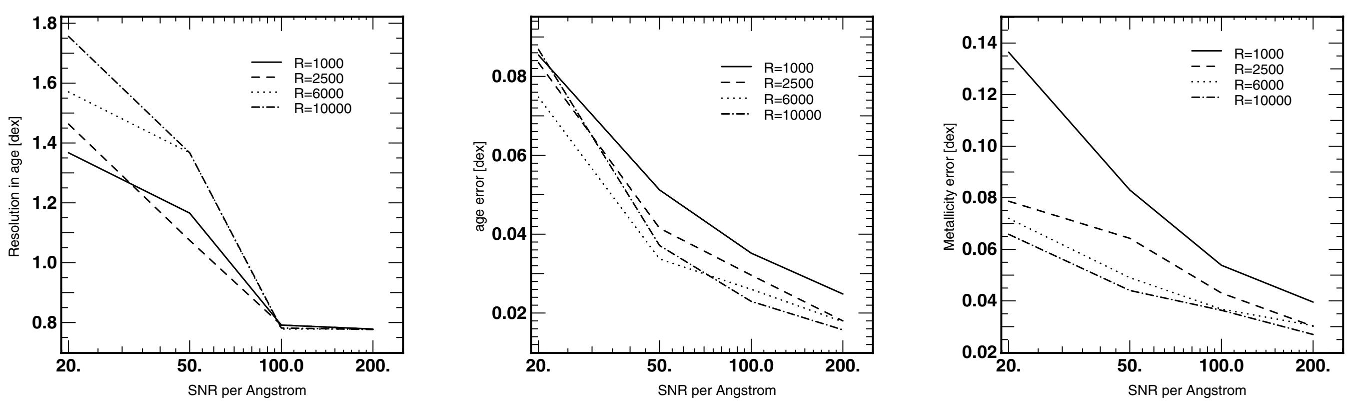

Figure 20. Left: resolution in age (dex) versus SNR per Å for various spectral resolutions. As expected, the resolution in age improves with increasing SNR. It settles around 0.8 dex for the highest SNR. No significant trend is seen with spectral resolution. Middle: median error on the age of the bursts (dex) in the successful separations versus SNR for several resolutions. High-resolution experiments give the smallest errors. Right: same as middle panel but for metallicity estimates. Again, the best accuracy is obtained at high spectral resolution, given the same total number of photons.

spectral resolutions in Fig. 20. It improves with increasing SNR, but settles around 0.8 dex for very high-quality data. The variation of the resolution in age with spectral resolution is not significant compared to the statistical error (≈0.25 dex), so that no trend with spectral resolution can clearly be deduced. The middle panel shows the median error on the luminous weighted ages of the two bursts for the successful separations. The error decreases with increasing SNR down to 0.02 dex for SNR = 200 per Å, and is significantly lower for the high-resolution experiments (the relative statistical error for this measure is smaller than 5 per cent). We see the same trend in the metallicity median errors of the double bursts, in the right-hand panel. The smallest error is obtained for the highest spectral resolution. The general smallness of these errors is partly explained by the severity of the selection, which rejects as non-separable any ambiguous solution.

Somewhat unexpectedly, the results do not depend on the slope of the AMR adopted for the double-burst models. With a negative slope, a young metal-rich population is added to an old metal-poor one. In view of the age–metallicity degeneracy, this should be the least favourable situation for a proper separation. We performed simulations with positive and negative slopes and obtained identical results considering the statistical errors given above. Thus, the age–metallicity degeneracy is not a limiting factor in our experiment.

6 CONCLUSIONS AND PROSPECTS

Let us sum up our findings relative to the diagnosis of the linear (monometallic) problem (Sections 3 and 4) and the more realistic non-linear problem of recovering simultaneously the LWSAD, the extinction and the AMR (Section 5) in turn, and close on the observational and methodological prospects of STECMAP.

6.1 Probing the linear problem: tricks of the trade

The idealized problem of recovering the non-parametric stellar age distribution of a monometallic population seen without extinction is linear. The conditioning number of the kernel is very large and accounts for the ill-conditioning of the problem, i.e. pathological sensitivity to noise in the data.

The noise in the SSP models also limits the number of free parameters that may be recovered robustly to describe the star formation history. In textbook inversion problems, this number can be estimated quantitatively from the sequence of singular values of the SSP basis. Here, however, this theoretical value is misleading because the expected signature of the model noise in the singular value spectrum is not apparent. We explained this by the correlations between the noise patterns in subsequent basis spectra. To obtain the number of free parameters, the singular values are used together with an independent estimate of the SNR of the basis. For the optical spectral range covered with PÉGASE-HR and ages ranging from 50 Myr to 15 Gyr, the corresponding number is 6. This makes high-frequency variations of the stellar age distribution unrecoverable, no matter the data quality, $\mathrm{SNR_d}$, and the inversion method.

When the dominant error source is the data, the problem may be regularized by truncating the SVD or reducing the number of age bins so that $\sigma_1/\sigma_n \leqslant \mathrm{SNR_d}\sqrt{m}$. This crude rule can be used to obtain a quick estimate of the performance expected for a given data set.

The problem can be more profitably regularized without reducing arbitrarily the number of age bins by imposing the smoothness of the solution, to obtain a penalized likelihood estimate. This constraint reduces the risk of overinterpreting the data. The smoothing parameter is set automatically by GCV for each $\mathrm{SNR_d}$, or/and by performing simulations in a suited pseudo-observational context.

For an adequately regularized problem, we defined the inverse model matrix and inspected it in order to find the wavelength ranges which are most discriminative for age determinations. We found that the information is widely distributed along the optical range (cf. Figs 6 and 16).

The behaviour of the inversion can be predicted by inspecting the SVD or GSVD of the kernel. The first non-attenuated solution vectors are responsible for the detailed shape of the regularized reconstructions, and thus for the generation of artefacts. The general shape of the solution vectors, and especially the presence/absence and location of their oscillations, gives an indication in which age ranges the inversion behaves worst.

In particular, the inspection of the SVD components revealed that the problem of recovering flux distributions was less pathological than the problem of recovering mass fractions. More specifically, the transition rank i_0 between signal- and noise-dominated regimes is independent from the fiducial model in the recovery of flux fractions.

Second- or third-order penalizations gave similarly good results, showing that the quality of the inversion does not rely strongly on the details of the regularization.

Requiring the solutions to be positive improves the results even further, and in particular reduces Gibbs ringing, as can be seen by comparing Figs 8 and 10.

One should be aware that the efficiency of the inverse method cannot be assessed on the basis of a small set of simulations. Indeed, it is easy to produce good-looking results down to $\mathrm{SNR_d} = 0.1$ per pixel by carefully choosing the model age distribution.

We performed an extensive simulation campaign by inverting a grid of double-burst models in several pseudo-observational regimes. If the age difference between the bursts was larger than 0.4 dex, we were able to separate the two components and recover their ages with a very small error from high-quality data ($\mathrm{SNR_d} =$ 200 per Å).

However, the high $\mathrm{SNR_d}$ regime for which we obtained the best results is questionable. Indeed, when $\mathrm{SNR_d}$ and $\mathrm{SNR_b}$ are comparable, the number of degrees of freedom is imposed by the noise in the basis rather than in the data. We therefore consider the extreme regimes with $\mathrm{SNR_d} \geqslant 200$ per Å unphysical: small oddities (of uncertain nature) in the basis are seen as physically discriminative information. Only an improvement of $\mathrm{SNR_b}$ could in principle increase the number of degrees of freedom. Assuming that the singular value spectrum of the initial kernel shown in Fig. 4 is representative of the basis even at higher $\mathrm{SNR_b}$, we can set the following rules of thumb.

(i) If, for example, $\mathrm{SNR_d} = 100$ per pixel, the maximum number of freedom degrees one may consider is of the order of 8 ($n = 8$ from criterion 25 or Fig. 2).

(ii) To ensure that no serious contamination of the singular values by noise in the basis happens for $i < 8$, one would need $\mathrm{SNR_b} \geqslant$ 1000 per pixel (estimated from Fig. 4) (2500 per Å). We caution that this is an extrapolation, and that the actual behaviour of SSP spectra at this kind of SNR is not known.

By comparing the solutions given by SVD and the GSO kernel we showed that ill-conditioning remains an issue when working with compressed data.

Finally, the mismatch observed when a monometallic population is fitted by a basis of different metallicity allowed us to constrain this additional metallicity parameter with a $\mathrm{SNR_d}$ as small as 10 per pixel, well enough to motivate a feasibility study of the recovery of the age distribution, the metallicities and the reddening of a composite stellar population.

6.2 Beyond the monometallic inversion?

The ill-conditioned problem of recovering a 2D age–metallicity distribution of a composite unreddened population can also be recast into a linear problem. A penalized likelihood estimate can be obtained by means of additional smoothness constraints. The inspection of the regularized inverse model matrix reveals that a large number of age and metallicity sensitive lines carrying discriminative information are located all along the optical range. The shape of the first solution singular modes shows that age–metallicity degenerate solutions are expected even for SNR_d as large as 200 per pixel. Notwithstanding the above caveat about high SNR, the inversions with such a complexity are thus infeasible in realistic regimes from optical integrated light only.

A natural simplification involves assuming that the metallicity of the population can be described by a one-to-one non-parametric AMR. The problem of recovering the stellar age distribution, the AMR and an extinction parameter then becomes tractable provided that adequate regularization (smoothness, bound and positivity) is implemented, and yields a penalized likelihood estimate.

A detailed simulation campaign allowed us to estimate the resolution in age that can be achieved from optical data in several pseudo-observational regimes. If the time elapsed between two instantaneous bursts is larger than 0.8 dex, they can be separated unambiguously by STECMAP from high-quality data (SNR_d = 100 per Å), and their ages and metallicities can be constrained with an accuracy of 0.02 and 0.04 dex, respectively. In such regimes, the age–metallicity degeneracy is effectively broken. For smaller separation, there is always a monoburst or smoother solution that fits the data equally well. Our experiments reveal no clear dependency of the resolution in age on the spectral resolution R ($\geqslant$1000) as long as the SNR per Å (or integration time) is conserved in the comparative experiments. As in the preliminary conclusion for the idealized monometallic unreddened problem, it is not clear whether the extreme SNR_d are physical or not, because in these regimes the noise in the basis is no longer negligible compared to the noise in the data. In any case, 0.8 dex should be considered as a lower-resolution limit, for any separation attempt in the range $\lambda\lambda = [4000, 6800]$.

The fact that free extinction does not hinder the inversions indicates that the continuum is not a critical constraint. Simulations with more complex corrections on the continuum (not described in this paper) confirm this point. The information on age and metallicities is carried in the line spectrum.

6.3 Discussion and prospective

Perhaps the most intriguing conclusions of this paper are the small number of degrees of freedom found in an optical SSP basis even with SNR_b as large as PÉGASE-HR, and the very anti-intuitive hint that significantly larger SNR is needed in the basis than in the data to be analysed. It highlights the need to study and quantify the influence of the models noise in linear and non-linear inversions, and to continue and improve the various steps involved in the construction of the model.

Several directions can be followed, on the basis of Section 2.3. Empirical libraries should improve with the combination of large collecting areas, and high-resolution, large coverage instruments with massive multi-object capacities, which should boost the construction of libraries by a significant factor. The library Ultraviolet and Visual Echelle Spectrograph (UVES) Paranal Observatory Project (POP; Bagnulo et al. 2003) is an example. With telescopes of the 10-m class or larger, stars in clusters and in Local Group galaxies can be observed to remedy in part the issue of completeness and some of the biases of solar neighbourhood libraries (e.g. more luminous metal-poor stars, or stars with modified α-element abundances).

On the theoretical side, one should investigate accurately and systematically what drives the shape of the singular value spectrum of the SSP basis. In this paper we have concentrated on a given SSP model, without tuning the basis to study the effect of, for example, sampling strategies on the conditioning. Because the behaviour of an inverse problem depends on the shape of the solution singular vectors as well, it is a key issue to understand what drives their shape. Making them smoother and more regular is a step towards reducing the generation of artefacts. Clearly, one would want to question the sampling strategy in (T, g, Z) space in terms of both the conditioning number of $\mathbf{B}$ and the roughness of its singular vectors. In particular, one would like for instance to apply an error-weighted regularized tomographic interpolation in (T, g, Z) space, in order to construct a noise-free spectral basis, which would by construction prevent from interpolating the noise from one spectrum to another. Even though the interpolation of the noise patterns of individual stars in the library may explain the vanishing of the saturation of the singular values, we still miss a quantitative relation between the density of library stars in (T, g, Z) space, their SNR, and the slope of the singular value spectrum.

Ultimately, one should aim at designing inverse methods where the errors in the models are explicitly taken into account (for instance, using TLS) in order to draw a consistent error budget.

The generally very limited separability of successive star formation episodes in most pseudo-observational settings is in strong contrast with the results of a number of more optimistic authors. In particular, if one is bound to draw cosmological constraints from the stacking of a large set of noisy star formation histories, it is still essential to check that individual star formation histories are well recovered, because otherwise the median solution is likely to be dominated by artefacts. Exhaustive testing of the method as we propose is in this case a mandatory step.

The SED matching procedures and parameter recovery presented here are absolutely not model-dependent and could be used in association with any other stellar population model as is.[6] It will thus be interesting and informative to perform the same kind of study (resolution in age, conditioning) with other existing evolutionary synthesis models, in order to quantify the amount of information and the constraints to be expected from observations in other wavelength domains, as the ultraviolet, near-infrared or far-infrared. It is expected that increasing the wavelength coverage should improve significantly the resolution in age and the behaviour of the problem in general. The possible discrepancies between the models are also a major matter of concern. For instance, are the metallicity constraints using a given set of SSPs robust to a change of the evolutionary synthesis code? It will be interesting to test this by producing mock data with one available code (Bruzual & Charlot 2003; Gonzalez Delgado et al. 2005) and interpreting them with another one. We expect misfits to arise from wavelength calibration error, small-scale flux calibration errors, and systematic deviations caused by the use of different evolutive tracks, IMFs, and stellar libraries. This exercise will allow us to investigate the amount of error introduced by the models themselves.

The methods we have described, together with the corresponding error and separability analysis, will be very useful for interpreting large sets of data from large surveys such as SDSS, 2DF-GRS, DEEP2, etc., and also for upcoming new generation instruments, especially high-resolution instruments with multi-object or field integral capacities, for instance FALCON (Puech & Sayede 2004) or MUSE (Henault et al. 2003). In this context, astronomers will want to extract kinematical information as well, and question the relationship between the kinematics and the nature of the stellar populations. The simultaneous recovery of the kinematical distribution and the corresponding stellar population via the

[6] We are preparing a public release of the inversion codes.

non-parametric interpretation of spectra is described in a companion paper.

ACKNOWLEDGMENTS

We thank the referee, Dr R. Jimenez, for criticisms. We are grateful to the PÉGASE-HR team for providing us with an early version of the models. We thank M. Fioc, R. Foy, S. Prunet, A. Siebert, D. LeBorgne and J. Blaizot for useful comments and helpful suggestions. We would like to thank D. Munro for freely distributing his YORICK programming language (available at http://www.maumae.net/yorick/doc/index.html), together with its message passing interface (MPI), which we used to implement our inversion algorithm in parallel. We thank the UK Astrophysical Fluids Facility (UKAFF) and the Max-Planck-Institut für Astrophysik (MPA) Garching for their hospitality. This work was partly supported by a European Association for Research in Astronomy (EARA) studentship.

REFERENCES

Bagnulo S., Jehin E., Ledoux C., Cabanac R., Melo C., Gilmozzi R., 2003, Messenger, 114, 10
Bruzual G., Charlot S., 2003, MNRAS, 344, 1000
Charlot S., Fall S. M., 2000, ApJ, 539, 718
Charlot S., Worthey G., Bressan A., 1996, ApJ, 457, 625
Cid Fernandes R., Mateus A., Sodre L., Stasinska G., Gomes J. M., 2005, MNRAS, 358, 363
Craig I. J. D., Brown J. C., 1986, Inverse Problems in Astronomy: A Guide to Inversion Strategies for Remotely Sensed Data. Adam Hilger, Bristol
Dopita M. A., 2005, in Popescu C. C., Tuffs R. J., eds, AIP Conf. Ser. Vol. 761, The Spectral Energy Distribution of Gas-Rich Galaxies: Confronting Models with Data. Am. Inst. Phys., New York, p. 203
Feltzing S., Holmberg J., Hurley J. R., 2001, A&A, 377, 911
Golub G. H., Hansen P. C., O'Leary D. P., 2000, SIAM Journal on Matrix Analysis and Applications, 21, 185
Gonzalez Delgado R. M., Cervino M., Pires Martins L., Leitherer C., Hauschildt P. H., 2005, MNRAS, 357, 945
Gratton R. G., Carretta E., Matteucci F., Sneden C., 2000, A&A, 358, 671
Hanson R. J., 1971, Numer. Anal., 8, 616
Hansen P. C., 1988, J. Comput. Appl. Math., 23, 117
Hansen P. C., 1994, Numer. Algorithms, 6, 1
Hansen P. C., O'Leary D. P., 1996, Technical Report CS-TR-3684, Regularization Algorithms Based on Total Least Squares (citeseer.ist.psu.edu/hansen96regularization.html)
Heavens A., Panter B., Jimenez R., Dunlop J., 2004, Nat, 428, 625
Henault F. et al., 2003, in Iye M., Moorwood A. F. M., eds, Proc. SPIE Vol. 4841, Instrument Design and Performance for Optical/Infrared Ground-based Telescopes. SPIE, Bellingham, p. 1096
Katz D., Soubiran C., Cayrel R., Adda M., Cautain R., 1998, A&A, 338, 151
Kochanek C. S., Rybicki G. B., 1996, MNRAS, 280, 1257
Kroupa P., Tout C. A., Gilmore G., 1993, MNRAS, 262, 545
Le Borgne D., Rocca-Volmerange B., Prugniel P., Lançon A., Fioc M., Soubiran C., 2004, A&A, 425, 881
Lejeune T., Fernandes J., eds, 2002, ASP Conf. Ser. Vol. 274, Observed HR Diagrams and Stellar Evolution. Astron. Soc. Pac., San Francisco
Mateu J., Magris G., Bruzual G., 2001, in Funes J. G. S. J., Corsini E. M., eds, ASP Conf. Ser. Vol. 230, Galaxy Discs and Disc Galaxies. Astron. Soc. Pac., San Francisco, p. 323
Merritt D., 1997, AJ, 114, 228
Moultaka J., Pelat D., 2000, MNRAS, 314, 409
Moultaka J., Boisson C., Joly M., Pelat D., 2004, A&A, 420, 459
Panter B., Heavens A. F., Jimenez R., 2003, MNRAS, 343, 1145
Pichon C., Thiébaut E., 1998, MNRAS, 301, 419
Pichon C., Siebert A., Bienaymé O., 2002, MNRAS, 329, 181
Prochaska J. X., Naumov S. O., Carney B. W., McWilliam A., Wolfe A. M., 2000, AJ, 120, 2513
Prugniel P., Soubiran C., 2001, A&A, 369, 1048
Puech M., Sayede F., 2004, in Moorwood A. F. M., Iye M., eds, Proc. SPIE Vol. 5492, UV and Gamma-Ray Space Telescope Systems. SPIE, Bellingham, p. 303
Reichardt C., Jimenez R., Heavens A. F., 2001, MNRAS, 327, 849
Saha P., Williams T. B., 1994, AJ, 107, 1295
Thiébaut E., 2002, in Starck J.-L., Murtagh F. D., eds, Proc. SPIE Vol. 4847, Astronomical Data Analysis II. SPIE, Bellingham, p. 174
Thiébaut E., 2005, in Foy R., Foy F.-C., eds, NATO ASI Series, Optics in Astrophysics. Kluwer Academic, Dordrecht
Thomas D., Maraston C., Bender R., 2003, MNRAS, 339, 897
Titterington D. M., 1985, A&A, 144, 381
Varah J. M., 1973, SIAM J. Numer. Anal., 10, 257
Vergely J. -L., Lançon A., Mouhcine 2002, A&A, 394, 807
Wahba G., ed. 1990, Spline Models for Observational Data. Soc. Industrial Appl. Math., Philadelphia, PA
Worthey G., 1994, ApJS, 95, 107

APPENDIX A: DEPENDENCE OF THE SIGNAL–NOISE TRANSITION ON THE FIDUCIAL MODEL

In this section we clarify the relation between the transition rank i_0 between the noise- and signal-dominated regimes (the intersection of $\boldsymbol{u}_i^\top \cdot \bar{\boldsymbol{y}}$ with $\boldsymbol{u}_i^\top \cdot \boldsymbol{e}$) and the fiducial model, as defined in Section 3.4 and Fig. 2. More specifically, we explore the shift of the transition by varying the age of the fiducial model, for a flux-normalized and a mass-normalized basis. The results are shown in Fig. A1. The fiducial models are given in the bottom of each column. Note that the y-axis is labelled 'flux fractions' on the left and 'mass fractions' on the right. This is to recall that the interpretation of the model curve differs, depending on the adopted normalization of the basis. Compared to Fig. 2, we added a third-order polynomial fit to the signal singular coefficients and a constant fit to the noise coefficients. This allows us to detect automatically and objectively the transition rank i_0, as the intersection of the two fits.

For the mass-normalized basis, the transition moves from the fifth rank (for the youngest fiducial model) up to the twentieth (for the oldest fiducial model). On the other hand, the location of the transition for the flux-normalized basis is rather unaffected by changes of the fiducial model and remains around rank 7–9.

APPENDIX B: GRADIENTS OF Q_μ

The direct linear solution which minimizes the objective function Q_μ can only be used in the case of a linear model (with respect to the parameters) and without constraints (such as positivity). For all other cases, the objective function Q_μ can only be minimized by means of an iterative method. The most efficient, and yet simple to use, of these methods require the computation of the objective function and of its gradient. These optimization methods are the conjugate gradients and variable metric methods (e.g. BFGS). In practice, for non-linear problems, variable metric methods have been found to require fewer iterations and fewer function evaluations than conjugate gradient ones (Thiébaut 2002). For this reason, we used the limited memory variable metric method VMLM-B implemented in the OPTIMPACK package written by E. Thiébaut for Yorick (http://www.maumae.net/yorick/doc/index.html).

Because the efficiency of these iterative optimization algorithms relies on the correctness of the gradient of Q_μ (i.e. partial derivatives of Q_μ with respect to the free parameters), we devote this appendix

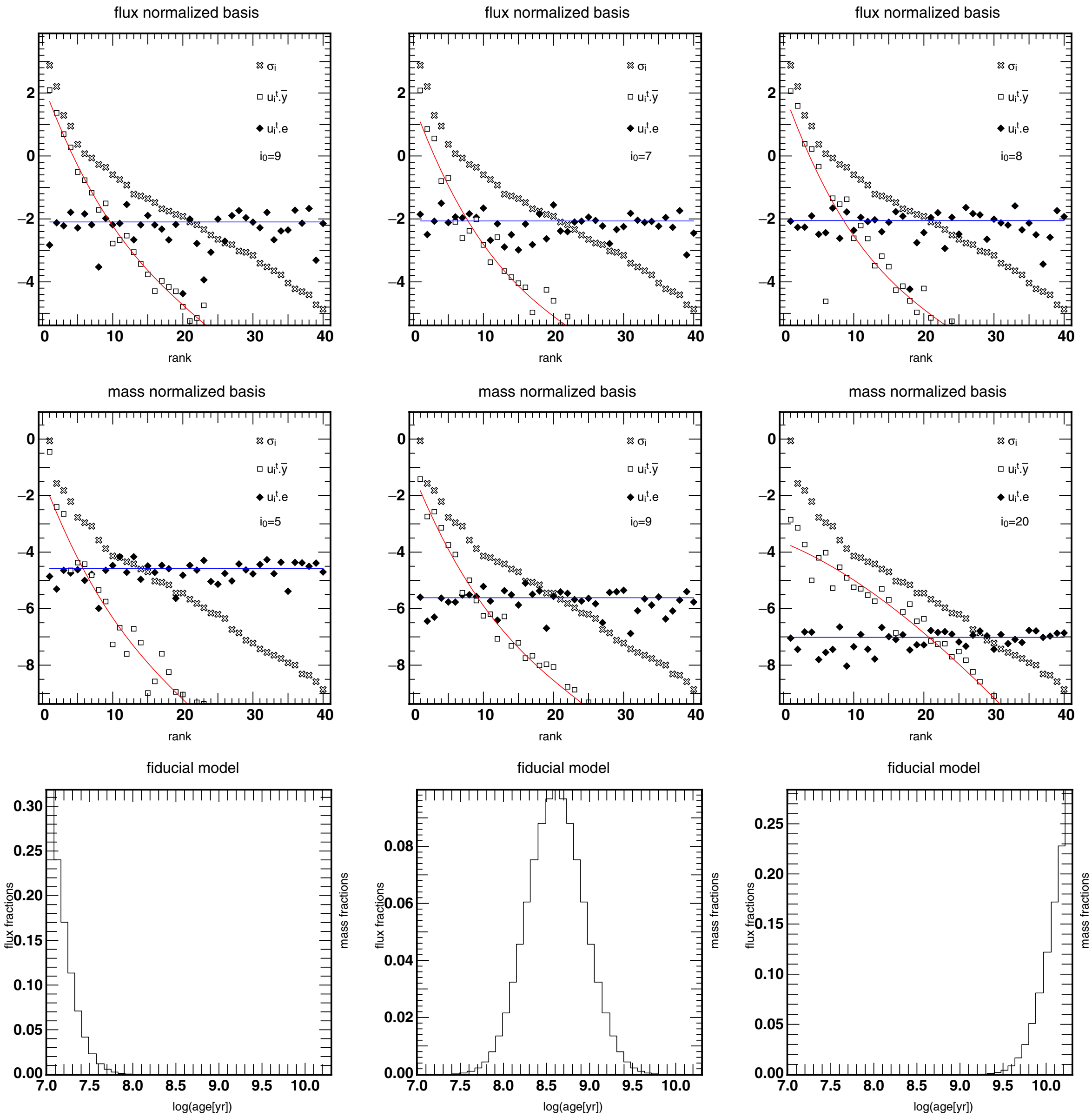

Figure A1. Study of the location of the signal–noise transition rank as a function of the fiducial model. The figures are the same as Fig. 2, with the same pseudo-observational setting (SNR = 100 per pixel), for a flux-normalized (top) and a mass-normalized basis (middle) respectively, for three different fiducial models $\overline{\boldsymbol{x}}$, given at the bottom of each column. Polynomial fits are given for the signal and noise singular coefficients. The transition rank i_0 is given in each figure as the intersection of these fits. For the mass-normalized basis, the rank of the transition between signal- and noise-dominated regimes spans a wide range of values depending on the fiducial model $\overline{\boldsymbol{x}}$. On the contrary, for the flux-normalized basis, the transition rank is rather constant with regard to modifications of the age of the fiducial model.

to the derivation of such partial derivatives for the different cases considered in this paper. Whenever it was possible (i.e. in the linear case), the iterative solutions were tested against the analytical solutions, and were found to be identical down to machine precision.

B1 Simple linear model

In the linear problem, the gradients of Q_μ have simple expressions:

$$\frac{\partial \chi^2}{\partial \boldsymbol{x}} = -2\,\mathbf{B}^\top \cdot \mathbf{W} \cdot (\boldsymbol{y} - \mathbf{B} \cdot \boldsymbol{x}), \tag{B1}$$

$$\frac{\partial P}{\partial \boldsymbol{x}} = 2\,\mathbf{L}^\top \cdot \mathbf{L} \cdot \boldsymbol{x}. \tag{B2}$$

B2 Age–metallicity–extinction gradients

For the resolution of the age–metallicity–extinction problem (Section 5), the objective function Q_μ is a χ^2 penalized by regularization terms and a binding function. The regularization terms being the same as in the linear case, their gradients are given by equation (B2). The gradient of the binding function C for a metallicity vector $\boldsymbol{Z}$ reads

$$\left(\frac{\partial \boldsymbol{C}}{\partial \boldsymbol{Z}}\right)_j = \begin{cases} 2\,(Z_j - Z_{\min}) & \text{for } Z_j < Z_{\min}, \\ 2\,(Z_j - Z_{\max}) & \text{for } Z_j > Z_{\max}, \\ 0 & \text{else.} \end{cases} \tag{B3}$$

In order to derive the gradients of the χ^2 term for more complex (non-linear) models, it is useful to rewrite it as

$$\chi^2 = \boldsymbol{r}^\top \cdot \mathbf{W} \cdot \boldsymbol{r}, \tag{B4}$$

where, for the sake of simplicity, we have introduced the vector of residuals $\boldsymbol{r}$ defined, in this case, by

$$\boldsymbol{r} \triangleq \boldsymbol{y} - \mathrm{diag}(\boldsymbol{f}_{\mathrm{ext}}) \cdot \mathbf{B} \cdot \boldsymbol{x}. \tag{B5}$$

Then the derivative of the χ^2 term with respect to any free parameter, say α, is written

$$\frac{\partial \chi^2}{\partial \alpha} = 2\,\frac{\partial \boldsymbol{r}^\top}{\partial \alpha} \cdot \mathbf{W} \cdot \boldsymbol{r}. \tag{B6}$$

Considering the different types of free parameters, we obtain

$$\frac{\partial \chi^2}{\partial \boldsymbol{x}} = -2\,\mathbf{B}^\top \cdot \mathrm{diag}(\boldsymbol{f}_{\mathrm{ext}}) \cdot \mathbf{W} \cdot \boldsymbol{r}, \tag{B7}$$

$$\frac{\partial \chi^2}{\partial \boldsymbol{Z}} = -2\,\boldsymbol{x}^\top \cdot \frac{\partial \mathbf{B}^\top}{\partial \boldsymbol{Z}} \cdot \mathrm{diag}(\boldsymbol{f}_{\mathrm{ext}}) \cdot \mathbf{W} \cdot \boldsymbol{r}, \tag{B8}$$

$$\frac{\partial \chi^2}{\partial E} = -2\,\boldsymbol{x}^\top \cdot \mathbf{B}^\top \cdot \mathrm{diag}\left(\frac{\partial \boldsymbol{f}_{\mathrm{ext}}}{\partial E}\right) \cdot \mathbf{W} \cdot \boldsymbol{r}. \tag{B9}$$

In the above expressions, $\partial \mathbf{B}/\partial \boldsymbol{Z}$ is derived directly from the SSP basis $B(\lambda, t, Z)$:

$$\left(\frac{\partial \mathbf{B}}{\partial \boldsymbol{Z}}\right)_{i,j} \triangleq \left(\frac{\partial B(\lambda, t, Z)}{\partial Z}\right)_{t=t_j, Z=Z_j, \lambda=\lambda_i}. \tag{B10}$$

Similarly, the term $\partial \boldsymbol{f}_{\mathrm{ext}}/\partial E$ derives directly from the chosen extinction law $f_{\mathrm{ext}}(E, \lambda)$:

$$\left(\frac{\partial \boldsymbol{f}_{\mathrm{ext}}}{\partial E}\right)_{i} \triangleq \left(\frac{\partial f_{\mathrm{ext}}(E, \lambda)}{\partial E}\right)_{E, \lambda=\lambda_i}. \tag{B11}$$

APPENDIX C: GENERALIZED SINGULAR VALUE DECOMPOSITION

In this section we introduce briefly the GSVD which is used in the main text to understand how regularization damps smoothly the singular vectors according to the SNR. In short, the GSVD of $(\mathbf{B}, \mathbf{L})$ is defined by

$$\mathbf{B} = \mathbf{U} \cdot \boldsymbol{\Sigma} \cdot \mathbf{V}^\top \quad \text{and} \quad \mathbf{L} = \mathbf{Q} \cdot \boldsymbol{\Theta} \cdot \mathbf{V}^\top, \tag{C1}$$

where $\mathbf{U}$ and $\mathbf{Q}$ are both orthogonal. The matrix $\mathbf{V}$ is non-singular and its columns $\boldsymbol{v}_i$ are $\mathbf{B}^\top{\cdot}\mathbf{B}$ and $\mathbf{L}^\top{\cdot}\mathbf{L}$ orthonormal, i.e. $\mathbf{V}^\top{\cdot}\mathbf{B}^\top{\cdot}\mathbf{B}{\cdot}\mathbf{V} = \boldsymbol{\Sigma}^2$ and $\mathbf{V}^\top{\cdot}\mathbf{L}^\top{\cdot}\mathbf{L}{\cdot}\mathbf{V} = \boldsymbol{\Theta}^2$. The matrices $\boldsymbol{\Sigma}$ and $\boldsymbol{\Theta}$ are diagonal: $\boldsymbol{\Sigma} = \mathrm{diag}(\sigma_1, \sigma_2, \ldots, \sigma_n)$ and $\boldsymbol{\Theta} = \mathrm{diag}(\theta_1, \theta_2, \ldots, \theta_n)$, with σ_i in increasing order and θ_i decreasing. See Hansen (1994) for a more detailed description of the GSVD and its properties.

APPENDIX D: GSO VERSUS SVD

In the main text, we claim that GSO amounts to SVD in the linear regime (monometallic and extinctionless populations) in the absence of truncation. Let us demonstrate and discuss this briefly.

In the monometallic extinctionless case, we can expand the kernel $\mathbf{B}$ as

$$\mathbf{B} = \mathbf{O} \cdot \boldsymbol{\Sigma} \cdot \mathbf{V}, \tag{D1}$$

where $\mathbf{O}$ is the GSO kernel obtained from $\mathbf{B}$, and $\boldsymbol{\Sigma} = \mathrm{diag}(\sigma_1, \ldots, \sigma_n)$ is a diagonal matrix such that $\boldsymbol{\Sigma} \cdot \mathbf{V} = \mathbf{O}^\top \mathbf{B}$ is the passage matrix from the initial coordinates of the kernel $\mathbf{B}$ to the orthonormalized basis. In this sense, σ_i are the norms of the vectors of the passage matrix. It is interesting to compare this expansion with the SVD: the kernel $\mathbf{O}$ is orthonormal and the matrix $\boldsymbol{\Sigma}$ is diagonal, but the matrix $\mathbf{V}$ is not orthogonal.

Thus, the expansion of equation (D1) is not exactly identical to that corresponding to the SVD. Still, as long as none of the σ_i is zero, the matrix $\mathbf{V}$ is inversible. As for the SVD, we can write the solution $\boldsymbol{x}$ as

$$\boldsymbol{x} = \mathbf{V}^{-1} \cdot \boldsymbol{\Sigma}^{-1} \cdot \mathbf{O}^\top \cdot \boldsymbol{y} = \sum_{i=1}^{n} \frac{\mathbf{O}_i^\top \cdot \boldsymbol{y}}{\sigma_i} (\boldsymbol{v}^{-1})_i, \tag{D2}$$

where $\boldsymbol{y} = \mathbf{B} \cdot \boldsymbol{x}$ is the data, and $(\boldsymbol{v}^{-1})_i$ are the columns of $\mathbf{V}^{-1}$. We will, in this section, by analogy with the SVD expansion, call σ_i the singular values, and $\mathbf{O}_i$ and $(\boldsymbol{v}^{-1})_i$ the data singular vectors and the solution singular vectors, respectively. The

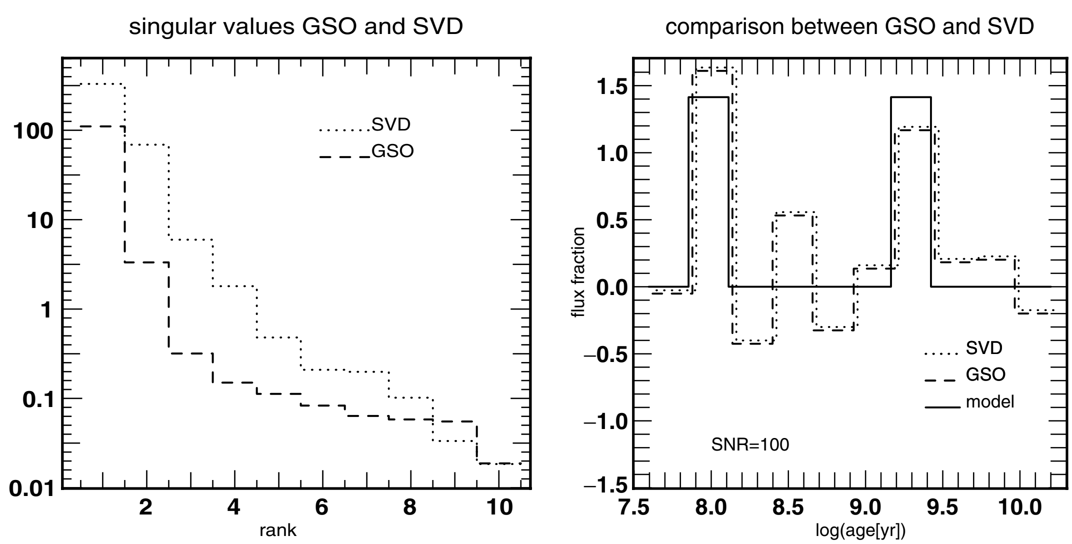

Figure D1. Left: singular values of the GSO and the SVD of the kernel. Both decays are characteristic of an ill-conditioned problem. Right: solutions found using the GSO and the SVD (slightly offset for clarity) for simulated data with SNR = 100 per pixel, $R = 10\,000$. They are identical down to machine precision, showing the similarity between both formulations.

solution $\boldsymbol{x}$ is the sum of the singular coefficients $\mathbf{O}_i{}^{\top} \cdot \boldsymbol{b}$ (the 'compressed datum' proposed by MOPED's authors) divided by the singular values σ_i times the solution singular vector $(\boldsymbol{v}^{-1})_i$. The left-hand panel of Fig. D1 shows the singular values of the SVD and the GSO expansion of the kernel. Their very similar decay indicates similar behaviour of the inverse problem. The right-hand panel of Fig. D1 shows for a moderately ill-conditioned example ($R = 10\,000$, $\mathrm{SNR_d} = 100$, 10 age bins, solar metallicity, $\sigma_1/\sigma_{10} = 2\sqrt{m}\,\mathrm{SNR_d}$) the solutions found by applying equations (D2) and (22) corresponding to the two expansions. As expected from the conditioning number and $\mathrm{SNR_d}$, both are fairly noisy, but the important point is that they are actually equal down to machine precision. Thus, even though there is a slight formulation difference between these two expansions, they practically give the same solutions.

This paper has been typeset from a TEX/LATEX file prepared by the author.

Mon. Not. R. Astron. Soc. **365,** 74–84 (2006) doi:10.1111/j.1365-2966.2005.09323.x

STECKMAP: STEllar Content and Kinematics from high resolution galactic spectra via Maximum A Posteriori

P. Ocvirk,[1⋆] C. Pichon,[2] A. Lançon[1] and E. Thiébaut[3]

[1]*Observatoire de Strasbourg (UMR 7550), 11 Rue de l' Université, F-67000 Strasbourg, France*
[2]*Institut d' Astrophysique de Paris (UMR 7095), 98 bis Boulevard Arago, F-75014 Paris, France*
[3]*Observatoire de Lyon, 9 Avenue Charles André, F-69561 Saint Genis Laval, France*

Accepted 2005 June 14. Received 2005 May 10

ABSTRACT

We introduce STECKMAP (STEllar Content and Kinematics via Maximum A Posteriori likelihood), a method for recovering the kinematic properties of a galaxy simultaneously with its stellar content from integrated light spectra. It is an extension of STECMAP (presented recently by Ocvirk et al.) to the general case where the velocity distribution of the underlying stars is also unknown. The reconstructions of the stellar age distribution, the age–metallicity relation and the line-of-sight velocity distribution (LOSVD) are all non-parametric, i.e. no specific shape is assumed. The only a priori conditions that we use are positivity and the requirement that the solution is smooth enough. The smoothness parameter can be set by generalized cross-validation according to the level of noise in the data in order to avoid overinterpretation.

We use single stellar populations (SSPs) from PÉGASE-HR ($R = 10\,000$, $\lambda = 4\,000$–$6\,800$ Å, from Le Borgne et al.) to test the method through realistic simulations. Non-Gaussianities in LOSVDs are reliably recovered with signal-to-noise ratio (SNR) as low as 20 per 0.2 Å pixel. It turns out that the recovery of the stellar content is not degraded by the simultaneous recovery of the kinematic distribution, so that the resolution in age and error estimates given in Ocvirk et al. remain appropriate when used with STECKMAP.

We also explore the case of age-dependent kinematics (i.e. when each stellar component has its own LOSVD). We separate the bulge and disc components of an idealized simplified spiral galaxy in integrated light from high-quality pseudo-data (SNR = 100 per pixel, $R = 10\,000$), and constrain the kinematics (mean projected velocity, projected velocity dispersion) and age of both components.

Key words: methods: data analysis – methods: statistical – techniques: spectroscopic – galaxies: abundances – galaxies: kinematics and dynamics – galaxies: stellar content.

1 INTRODUCTION

For decades now, the spectral indices from the Lick group have been used to study the properties of stellar populations (Faber et al. 1985; Worthey 1994; Trager et al. 1998). Since the profile and depth of the lines involved in these spectral indices are affected by the line-of-sight velocity distribution (LOSVD) of the stars, it is necessary to correct the measured depths by a factor depending on the moments of the velocity distribution (Davies, Sadler & Peletier 1993; Kuntschner 2000, 2004). The latter moments must be determined using specialized code (Bender 1990; Kuijken & Merrifield 1993; van der Marel & Franx 1993; Saha & Williams 1994; Merritt 1997; Pinkney et al. 2003). These kinematic deconvolution routines have been used for some time and have undergone two major mutations. First, thanks to the increasing power of computers, it became affordable to swap back and forth from direct space to Fourier space, so that many disturbances such as border effects and saturation could be avoided. It became straightforward to mask problematic regions of the data, such as dead pixels, emission lines, etc. The second evolution of these codes allowed the use of multiple superimposed stellar templates to match best the observed spectrum (Rix & White 1992; Cappellari & Emsellem 2004). It has also been proposed to use single stellar populations (SSPs) as synthetic templates, and this approach has proved to be useful in addressing the template mismatch problem (Falcón-Barroso et al. 2003). Moreover, this technique can save precious telescope time, since it circumvents the need for observing template stars.

In Ocvirk et al. (2005, hereafter Paper I), we introduced STECMAP, a method for recovering non-parametrically the stellar

⋆ocvirk@pleiades5.u-strasbg.fr

content of a given galaxy from its integrated light spectrum. Using STECMAP requires, as a preliminary, convolving the data or models with the proper point spread function (PSF), which can be of both physical (i.e. the stellar LOSVD) and instrumental (the instrument's PSF) origin. Adjusting the LOSVD to fit the data not only constrains the kinematics of the observed galaxy but will also reduce the mismatch due to errors in the determination of the redshift or anomalous PSF, which is ultimately a necessary step when fitting galaxy spectra.

Here we propose to constrain the velocity distribution simultaneously with the stellar content, by merging the kinematic deconvolution and the stellar content reconstruction into one global maximum a posteriori likelihood inversion method. Hence, STECMAP becomes STECKMAP (STEllar Content and Kinematics via Maximum A Posteriori likelihood). In this respect, STECKMAP resembles the method proposed by, for example, Falcón-Barroso et al. (2003), except that it takes advantage of the treatment of the stellar content by STECMAP. Together with the stellar age distribution and the age–metallicity relation, the LOSVD is described non-parametrically and the only a priori conditions we use are smoothness and positivity.

We also tentatively address the case of age-dependent kinematics, i.e. we try to recover the individual LOSVDs and ages of several superimposed kinematic subcomponents. This approach is motivated by the fact that galaxies often display several kinematic components. Ellipticals and dwarf ellipticals, for instance, are known often to harbour kinematically decoupled cores (Balcells & Quinn 1990; Bender & Surma 1992; De Rijcke et al. 2004), and spiral galaxies are usually assumed to be constituted of a thin and a thick disc, a bulge and a halo (Freeman & Bland-Hawthorn 2002). The variety of the dynamical properties of the components has a counterpart in their stellar content, as a signature of the formation and evolution of the galaxy. For instance, the halo of the Milky Way is believed to consist mainly of old, metal-poor stars, while the bulge is more metal-rich, and the thin disc is mainly younger than the bulge (Freeman & Bland-Hawthorn 2002). It is thus natural to let any stellar subpopulation have its own LOSVD. This possibility has been recently addressed by De Bruyne et al. (2004a,b), in a slightly different framework. They use individual stars as templates for the different components, while we propose to use synthetic SSP models. Such a method would allow us to separate the several kinematic components of galaxies from integrated light spectra, and to constrain, for example, their age–velocity dispersion and age–metallicity relation. The highly detailed stellar content and kinematic information that can be obtained for the Milky Way or for nearby galaxies that can be resolved into stars, such as M31 (Ferguson et al. 2002; Ibata et al. 2004), could be extended to a larger sample of more distant galaxies. This technique could also be useful in detecting and characterizing major stellar streams in age and velocity from integral field spectroscopy of galaxies.

In this paper we use the PÉGASE-HR SSP models (Le Borgne et al. 2004) in order to illustrate and investigate the behaviour of the problems through simulations and inversions of mock data. Indeed, PÉGASE-HR, with its high spectral resolution ($R = 10\,000$), is an adequate choice for testing the recovery of detailed kinematic information in the form of non-parametric LOSVDs. The problems and methods we describe are, however, by no means specific to PÉGASE-HR (and its wavelength coverage), and STECKMAP could be used with any possible SSP model, depending on the type of data that is being analysed.

We will start with the modelling of the kinematics. Then, we will address the idealized linear problem of recovering the LOSVD when the stellar content is known, i.e. the template is assumed to be perfect. Section 4 deals with simultaneous age and LOSVD reconstruction of composite populations. Finally, Section 5 investigates the case of age-dependent kinematics in a simplified context where the metallicity and extinction are known a priori.

2 MODELS OF GALAXY SPECTRA

In this section we present the modelling of galaxy spectra, taking into account the composite nature of the stellar population, in age, metallicity and extinction, and finally its kinematics.

2.1 The composite reddened population at rest

We model the spectral energy distribution (SED) of the composite reddened population at rest using the ingredients defined in Paper I:

$$F_{\rm rest}(\lambda) = f_{\rm ext}(E,\lambda) \int_{t_{\rm min}}^{t_{\rm max}} \Lambda(t) B(\lambda, t, Z(t))\, \mathrm{d}t, \tag{1}$$

where $f_{\rm ext}(E,\ \lambda)$ is the extinction law, $\Lambda(t)$ is the luminosity-weighted stellar age distribution, $Z(t)$ is the age–metallicity relation, and $B(\lambda, t, Z)$ is the flux-averaged SSP basis of an isochrone population of wavelength λ, age t and metallicity Z. We recall briefly the main properties of the PÉGASE-HR SSP basis that we use in this paper. As mentioned earlier, spectral resolution is $R = 10\,000$ over the full optical domain $\lambda = [4000,\ 6800]$ Å, sampled in steps of 0.2 Å. The models are available for metallicities $Z \in [0.0001,\ 0.1]$ and considered reliable between $t_{\rm min} = 10$ Myr and $t_{\rm max} = 15$ Gyr. The initial mass function (IMF) used is described in Kroupa, Tout & Gilmore (1993), and the stellar masses range from 0.1 $\mathrm{M}_\odot$ to 120 $\mathrm{M}_\odot$. The extinction law $f_{\rm ext}$ was taken from Calzetti (2001).

2.2 Model kinematics

Stellar motions in galaxies define a LOSVD corresponding to projected local velocity distributions integrated along the line of sight and across one resolved spatial element.

2.2.1 Global kinematics

The motion of the stars can to first approximation be accounted for by assuming that the velocities of all stars of all ages along the line of sight are taken from the same velocity distribution (hence 'global'). The model SED, $\phi(\lambda)$, is the convolution of the assumed normalized LOSVD, $g(v)$, defined for $v \in [v_{\rm min}, v_{\rm max}]$ with the model spectrum at rest $F_{\rm rest}(\lambda)$. The convolved spectrum $\phi(\lambda)$ reads

$$\phi(\lambda) = \int_{v_{\rm min}}^{v_{\rm max}} F_{\rm rest}\left(\frac{\lambda}{1+v/c}\right) g(v) \frac{\mathrm{d}v}{1+v/c}, \tag{2}$$

where c is the velocity of light. The above expression reads as a standard convolution

$$\widetilde{\phi}(w) = c \int_{u_{\rm min}}^{u_{\rm max}} \widetilde{F}(w-u)\widetilde{g}(u)\, \mathrm{d}u, \tag{3}$$

with the following reparametrization:

$$w \equiv \ln(\lambda), \qquad u \equiv \ln\left(1+\frac{v}{c}\right), \tag{4}$$

$$\widetilde{F}(w) \equiv F_{\rm rest}(\mathrm{e}^w) = F_{\rm rest}(\lambda), \tag{5}$$

$$\widetilde{g}(u) \equiv g(c(\mathrm{e}^u - 1)) = g(v), \qquad \widetilde{\phi}(w) \equiv \phi(\mathrm{e}^w) = \phi(\lambda), \tag{6}$$

$$u_{\rm min} = \ln\left(1+\frac{v_{\rm min}}{c}\right), \qquad u_{\rm max} = \ln\left(1+\frac{v_{\rm max}}{c}\right). \tag{7}$$

2.2.2 Age-dependent kinematics

We now allow the LOSVD to depend on the age of the stars. For simplicity, we consider here only unreddened monometallic populations, i.e. $f_{\rm ext}(E, \lambda) = 1$ and $Z(t) = Z_0$. We introduce the age–velocity distribution, $\Xi(v, t)$, defined in $[v_{\min}, v_{\max}] \times [t_{\min}, t_{\max}]$, which gives the contribution of stars of velocity and age in $[v, v + \mathrm{d}v] \times [t, t + \mathrm{d}t]$ to the total observed light. Thus, for a given age t, $\Xi(v, t)$ is the LOSVD of the SSP of age t. The age–velocity distribution, $\Xi(v, t)$, is related to the stellar age distribution, $\Lambda(t)$, by

$$\int_{v_{\min}}^{v_{\max}} \Xi(v, t)\,\mathrm{d}v = \Lambda(t). \tag{8}$$

The model spectrum of such a population thus reads

$$\phi(\lambda) = \int_{t_{\min}}^{t_{\max}}\int_{v_{\min}}^{v_{\max}} B\left(\frac{\lambda}{1+v/c},\ t,\ Z_0\right)\Xi(v, t)\,\frac{\mathrm{d}v\,\mathrm{d}t}{1+v/c}. \tag{9}$$

The above expression can be rewritten more conveniently as

$$\widetilde{\phi}(w) = c\int_{u_{\min}}^{u_{\max}}\int_{t_{\min}}^{t_{\max}} \widetilde{B}(w-u, t)\widetilde{\Xi}(u, t)\,\mathrm{d}t\,\mathrm{d}u, \tag{10}$$

using the same reparametrization as in Section 2.2.1 and

$$\widetilde{B}(w, t) \equiv B(\mathrm{e}^{w}, t, Z_0) = B(\lambda, t, Z_0), \tag{11}$$

$$\widetilde{\Xi}(u, t) \equiv \Xi(c(\mathrm{e}^{u} - 1), t) = \Xi(v, t). \tag{12}$$

In the rest of this paper, we will use exclusively the standard (i.e. reparametrized) convolutions as in equations (3) and (10). For readability, we will drop the superscript $\widetilde{\ }$ and set the speed of light to unity.

3 KINEMATIC DECONVOLUTION

Section 2.2.1 shows that, with proper reparametrization, the convolution of a model spectrum at rest, $F(w)$, with the stellar LOSVD, $g(u)$, reads as a standard convolution, given by equation (3). Finding the LOSVD when the observed spectrum, $\phi(w)$, and the template spectrum, $F(w)$, are given is a classical deconvolution problem. Our goal here is not to discuss the respective qualities of the many different methods available in the literature to solve this problem. Most rely on fitting the data while imposing some a priori constraint on the LOSVD, i.e. they provide maximum a posteriori (MAP) estimates of the LOSVD. Let us describe briefly our method to obtain such a solution with the purpose of coupling it in a later step with STECMAP.

3.1 The convolution kernel

Here we discretize equation (3) to obtain a matrix form defining the convolution kernel. We use an evenly spaced set

$$\left\{u_j = u_{\min} + \left(j - \tfrac{1}{2}\right)\delta u;\quad j = 1, 2, \ldots, p\right\}$$

spanning $[u_{\min}, u_{\max}]$ with constant step $\delta u \equiv (u_{\max} - u_{\min})/p$. We expand the LOSVD as a sum of p gate functions:

$$g(u) = \frac{1}{\delta u}\sum_j g_j\,\theta\left(\frac{u - u_j}{\delta u}\right),$$

where

$$\theta(x) = \begin{cases} 1 & \text{if } -\frac{1}{2} < x \leqslant \frac{1}{2}, \\ 0 & \text{otherwise.}\end{cases}$$

Inserting this expansion into equation (3) leads to

$$\phi(w) = \frac{1}{\delta u}\sum_{j=1}^{j=p} g_j \int_{u_{\min}}^{u_{\max}} F(w-u)\,\theta\left(\frac{u-u_j}{\delta u}\right)\mathrm{d}u, \\ \simeq \sum_{j=1}^{j=p} g_j F(w - u_j). \tag{13}$$

Similarly, we now sample along the wavelengths by integrating over a small δw:

$$\phi_i \equiv \frac{1}{\delta w}\int \phi(w)\,\theta\left(\frac{w - w_i}{\delta w}\right)\mathrm{d}w, \\ \simeq \sum_{j=1}^{j=p} g_j F(w_i - u_j), \tag{14}$$

where $\{w_j\ ;\ j = 1, 2, \ldots, m\}$ is a set of *logarithmic* wavelengths spanning the spectral range with a constant step.

Using matrix notation and accounting for data noise, the observed SED reads

$$\boldsymbol{y} = \mathbf{K}\cdot\boldsymbol{g} + \boldsymbol{e}, \tag{15}$$

where $\mathbf{y} = (\phi_1, \phi_2, \ldots, \phi_m)^{\rm T}$ is the measured spectrum, and $\boldsymbol{e} = (e_1, e_2, \ldots, e_m)^{\rm T}$ accounts for modelling errors and noise. The vector of sought parameters $\boldsymbol{g} = (g_1, g_2, \ldots, g_p)^{\rm T}$ is the discretized LOSVD. The vector $\boldsymbol{s} = \mathbf{K}\cdot\boldsymbol{g}$ is the *model* of the observed spectrum, and the matrix $\mathbf{K}$,

$$K_{ij} = F(w_i - u_j),\ \ \forall\,(i, j) \in \{1, \ldots, m\} \times \{1, \ldots, p\}, \tag{16}$$

is called the convolution kernel.

The convolution theorem (Press et al. 2002) states that the Fourier transform of the convolution of two functions is equal to the frequency-wise product of the individual Fourier transforms of the two functions. Applying this theorem yields another equivalent expression for the model spectrum $\mathbf{s}$:

$$\boldsymbol{s} = \mathcal{F}^{-1}\cdot \mathrm{diag}(\mathcal{F}\cdot\boldsymbol{F})\cdot\mathcal{F}\cdot\boldsymbol{g}, \tag{17}$$

where $\mathcal{F}$ is the discrete Fourier operator defined in Press et al. (2002) as

$$\mathcal{F}_{ij} = \exp\left[\frac{2\mathrm{i}\pi}{m}(i-1)(j-1)\right],\ \ \forall\,(i, j) \in [1, \ldots m]^2, \tag{18}$$

$$\mathcal{F}^{-1} = \frac{1}{m}\mathcal{F}^{*}. \tag{19}$$

Note that, since m is the size of the template spectrum $\boldsymbol{F}$, the discretized LOSVD $\boldsymbol{g}$, which is initially of size p, needs to be symmetrically padded with zeros to the size m in order to transform the Toeplitz matrix into a circulant one. The diagonal matrix $\mathrm{diag}(\mathcal{F}\cdot\boldsymbol{F})$ carries the coefficients of the Fourier transform of the model spectrum at rest, $\boldsymbol{F}$. This notation involving the Fourier operator, $\mathcal{F}$, will be very useful for a number of algebraic derivations in the rest of the paper. In practice, from a computational point of view, it is more efficient to implement any forward or inverse Fourier transform through a fast Fourier transform (FFT). Similarly, the product $\mathrm{diag}(\mathcal{F}\cdot\boldsymbol{F})\cdot\mathcal{F}\cdot\boldsymbol{g}$ is in practice implemented as a frequency-wise product of the individual FFTs.

3.2 Regularization and MAP

A number of earlier publications have shown that the maximum-likelihood solution to equation (15) is very sensitive to the noise in the data, $\boldsymbol{e}$. Hence, in the spirit of Paper I, we choose to regularize the problem by requiring the LOSVD to be smooth. To do so, we use the quadratic penalization $P(\boldsymbol{g})$ as defined by equation (29) in Paper I:

$$P(\boldsymbol{g}) = \boldsymbol{g}^{\mathrm{T}} \cdot \mathbf{L}^{\mathrm{T}} \cdot \mathbf{L} \cdot \boldsymbol{g}. \tag{20}$$

In the rest of the paper, the penalization is Laplacian, i.e. $\mathbf{L} = \mathbf{D}_2$, where $\mathbf{D}_2$ is the discrete second-order difference operator, as defined in Pichon, Siebert & Bienaymé (2002). The objective function, Q_μ, to be minimized is given by

$$Q_\mu(\boldsymbol{g}) = \chi^2(\boldsymbol{y} \mid \boldsymbol{g}) + \mu P(\boldsymbol{g}), \tag{21}$$

where the χ^2 is defined by

$$\chi^2(\boldsymbol{y} \mid \boldsymbol{g}) = (\boldsymbol{y} - \boldsymbol{s}(\boldsymbol{g}))^{\mathrm{T}} \cdot \mathbf{W} \cdot (\boldsymbol{y} - \boldsymbol{s}(\boldsymbol{g})). \tag{22}$$

The vector $\mathbf{y}$ is the observed spectrum, and the weight matrix is the inverse of the covariance matrix of the noise: $\mathbf{W} = \mathrm{Cov}(\boldsymbol{e})^{-1}$. The parameter μ controls the smoothness of the LOSVD through its coefficients, $\boldsymbol{g}$. It can be set on the basis of simulations (as described in Paper I) or automatically by generalized cross validation (GCV) (Wahba 1990), according to the signal-to-noise ratio (SNR) of the data. In the latter case, the properties of the convolution kernel can be used to speed up the computation of the GCV function. Further regularization is provided by the requirement of positivity, implemented through quadratic reparametrization. Minimizing Q_μ yields the regularized solution $\boldsymbol{g}_\mu$. Efficient minimization procedures require the analytical expression of the gradients of Q_μ, given in Appendix Section A1.

3.3 Simulations

We applied this deconvolution technique to mock data, created from PÉGASE-HR SSPs of several ages and metallicities, with $R = 10\,000$ at 4000–6800 Å. In a first set of experiments, the model spectrum at rest was a solar-metallicity 10-Gyr SSP. It was convolved with various LOSVDs, both Gaussian and non-Gaussian, with velocity dispersions ranging from 30 to 500 km s^{-1}. It was then perturbed with Gaussian noise at levels ranging from SNR = 5 to 100 per pixel, and deconvolved using the model spectrum at rest as template (i.e. no template mismatch). In all cases, the LOSVDs are adequately recovered. Fig. 1 shows the reconstruction of a Gaussian LOSVD, for SNR = 10 per pixel. However, there are necessarily some biases in the reconstruction of the sharp features of the LOSVD. This is expected since we introduced regularization via smoothing. To illustrate the relationship between regularization and bias, we performed a new set of similar simulations for a non-Gaussian LOSVD (sum of two Gaussians) with SNR = 20 per pixel and varied the smoothing parameter μ. The results are shown in Fig. 2. Panels (a) and (b) correspond to $\mu = 10$, while panels (c) and (d) correspond to $\mu = 1000$. The model, median and interquartiles of 500 reconstructions are displayed. We also plotted the whole set of 500 recovered solutions, in order to show the locus of the solutions. One can see that the biases of the median reconstruction are reduced when lowering μ. The highest bump is correctly reproduced for $\mu = 10$, while it is not for $\mu = 1000$. On the other hand, the solutions are much more widely spread when $\mu = 10$. This means that most solutions taken from the set of low-μ simulations can be very far from the model, while all the large-μ solutions lie reasonably close to the model.

The regularization acts as a Wiener filter in the sense that it damps the high-frequency components of the solution. Regularization improves the significance of an individual reconstruction (it will nearly always lie reasonably close to the model), at the cost of introducing a bias.

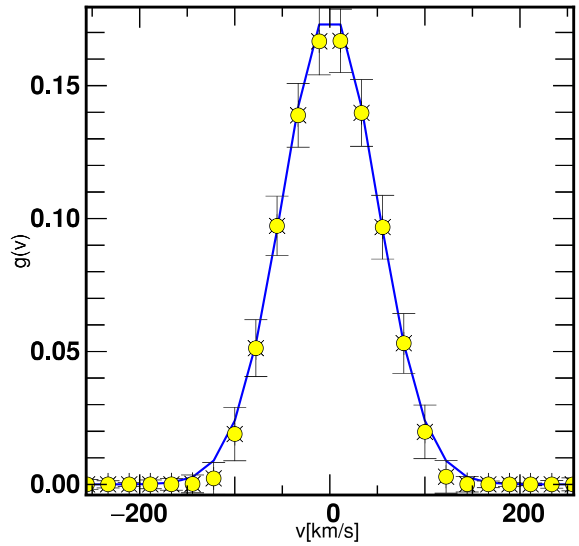

Figure 1. Non-parametric reconstruction of a Gaussian LOSVD for simulated data, $\sigma_v = 100$ km s^{-1}, SNR = 10 per pixel. The model spectrum at rest is a 10 Gyr old solar-metallicity SSP with $R = 10\,000$ at 4000–6800 Å. The template spectrum is identical, so that no template mismatch is allowed here. The curve is the input model. The circles and the bars show respectively the median and the interquartiles of the recovered solutions for 500 realizations of the noise.

3.4 Age and metallicity mismatch

We take advantage of the large range of ages and metallicities of SSPs covered by PÉGASE-HR to illustrate briefly the effects of template mismatch on LOSVD determinations. In this section we show the results of a large number of simulations aimed at characterizing the error made when a wrong template is chosen for the kinematic inversion of data. For this purpose, mock data were created by convolving an SSP of age a_0 and metallicity Z_0 with a centred Gaussian LOSVD of dispersion $\sigma_v = 50$ km s^{-1}. It was perturbed by Gaussian noise corresponding to SNR = 100 per pixel and then deconvolved, using as template an SSP of age a_1 and metallicity Z_1. The spectral resolution and wavelength range are the same as in Section 3.3. Fig. 3 shows the error on the measured velocity dispersion. The latter is measured as the rms of the reconstructed LOSVD. If the parameters of the template are different from those of the model, the velocity dispersion error increases very quickly. The age–metallicity degeneracy is visible as a valley of smaller error, following the upper left to bottom right diagonal of the figures. Of course, the χ^2 distance between the model and the mock data follows a similar 2D distribution, and will lead to the rejection of highly mismatched LOSVD estimates. However, in practice, it is usually not straightforward to quantify all the sources of error. It is thus somewhat arbitrary to set an upper limit of χ^2 for the admissible solutions, and the error on the kinematics is thus hard to quantify. This experiment illustrates in this context the long known issue that, when the correct model is not available, large errors on the determination of kinematics are expected. In order to reduce the error in the estimates of the kinematic properties of a stellar assembly, it is necessary to allow for a wide range of modulations of the template. This is naturally achieved by making the non-parametric stellar content account for the changes of the template, as discussed in the next section.

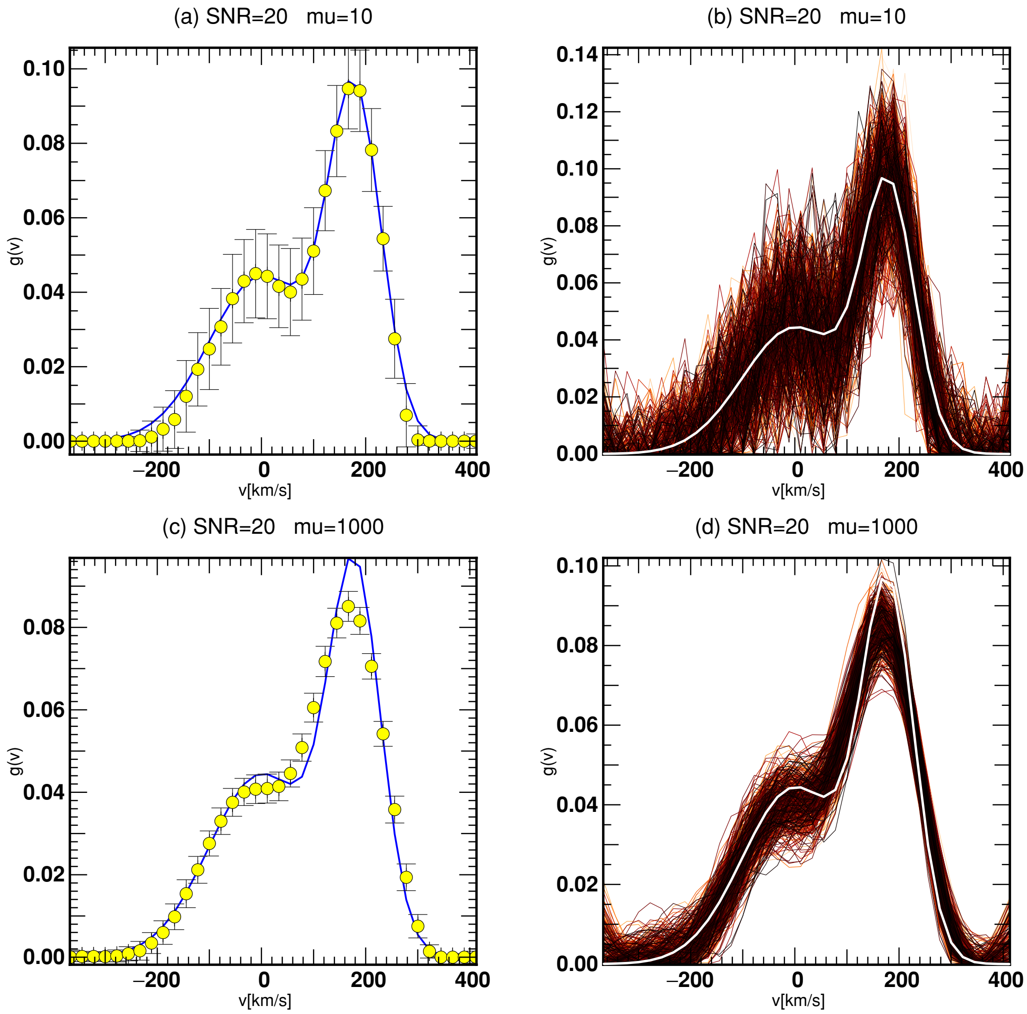

Figure 2. Impact of the smoothing parameter. Reconstruction of a non-Gaussian LOSVD for simulated data with SNR = 20 per pixel for $\mu = 10$ (top) and $\mu = 1000$ (bottom). Left: The curve is the input model LOSVD. The circles and the bars show respectively the median and interquartiles of the reconstructed LOSVDs for 500 realizations of the experiment. Right: The whole set of 500 solutions is displayed, with the model as a thick white line, in order to give the reader a sense of what individual solutions look like. The figures show the trade-off between bias and reliability of the reconstruction. For small μ, the median reconstruction is unbiased but the individual reconstructions are very noisy. For large μ, the median reconstruction is slightly biased but all the reconstructions are reasonable. Hence, the significance of an individual reconstruction is improved by regularization at the cost of introducing a bias.

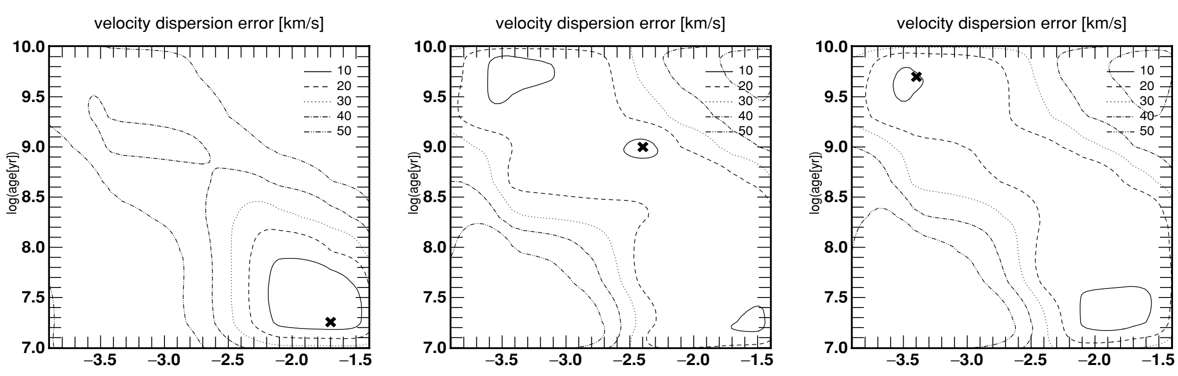

Figure 3. Velocity dispersion error as a function of the age and metallicity of the template SSP. Contours show regions of increasing velocity dispersion error. In each experiment, the age and metallicity of the original model template are shown as a thick cross, and the model LOSVD is a Gaussian with zero mean and 50 km s^{-1} dispersion. The velocity dispersion error is minimum when the template' s age and metallicity are similar to those of the model. The error increases quickly when the template parameters differ from the model parameters, also in the age–metallicity degeneracy direction (upper left to bottom right diagonal). It increases even faster in the direction orthogonal to the age–metallicity degeneracy.

4 RECOVERING STELLAR CONTENT AND GLOBAL KINEMATICS

The mixed inversion described in this section couples the recovery of both the stellar content and the kinematics, thereby turning STECMAP into STECKMAP. Proper application of this method provides an interpretation of the observed object in terms of stellar content and kinematics.

4.1 Inverse problem

For a given model spectrum at rest, $F_{\rm rest}(\lambda)$, and an LOSVD, $g(v)$, the emitted SED, $\phi(\lambda)$, is given by equation (2). We now wish to account also for the additional variables involved in $F_{\rm rest}$, given by equation (1), namely the stellar age distribution, $\Lambda(t)$, the age–metallicity relation, $Z(t)$, and the colour excess, $E(B-V)=E$. Inserting equation (1) into the convolution equation (3) yields the emitted SED

$$\phi(w)=\iint f_{\rm ext}(E,w-u)\Lambda(t)B(w-u,t,Z(t))g(u)\,\mathrm{d}t\,\mathrm{d}u. \quad (23)$$

Solving equation (23) for Λ, Z, E and g when $\phi, f_{\rm ext}$ and B are given is the inverse problem we are tackling here.

4.2 Discretization and parameters

Expanding the two time-dependent unknowns $\Lambda(t)$ and $Z(t)$ as a sum of n gate functions and inserting into equation (1) yields the discrete model spectrum at rest:

$$\boldsymbol{F}=\mathrm{diag}(\boldsymbol{f}_{\rm ext}(E))\cdot\mathbf{B}\cdot\boldsymbol{x}, \quad (24)$$

This discretization is explained in detail in section 5 of Paper I. Similarly, we develop the LOSVD $g(u)$ as a sum of p gate functions as in Section 3. Note that the reddened model at rest plays the role of the stellar template in a classical kinematic convolution. Inserting equation (24) into equation (17) thus allows us to express the model spectrum, $\boldsymbol{s}$, as

$$\boldsymbol{s}=\mathcal{F}^*\cdot\mathrm{diag}(\mathcal{F}\cdot\mathrm{diag}(\boldsymbol{f}_{\rm ext}(E))\cdot\mathbf{B}\cdot\boldsymbol{x})\cdot\mathcal{F}\cdot\boldsymbol{g}, \quad (25)$$

However, here, the template is this time modulated by the unknowns describing the stellar content.

4.3 Smoothness and metallicity constraints

The discrete problem of finding the stellar age distribution $\boldsymbol{x}$, the age–metallicity relation $\boldsymbol{Z}$, the extinction E and the LOSVD $\boldsymbol{g}$ for an observed spectrum $\boldsymbol{y}$ and given an extinction law $f_{\rm ext}$ and an SSP basis $\mathbf{B}$ is of course likely to be very ill-conditioned since it arises as the combination of several ill-conditioned problems. It therefore requires regularization. We also want the metallicity of the components to remain in the model range. We use the standard penalization P and the binding function C defined in Paper I to build the penalization P_μ for this problem:

$$P_\mu=\mu_x P(\boldsymbol{x})+\mu_Z P(\boldsymbol{Z})+\mu_C C(\boldsymbol{Z})+\mu_v P(\boldsymbol{g}), \quad (26)$$

where $\boldsymbol{\mu}\equiv(\mu_x,\mu_Z,\mu_C,\mu_v)$. Again, we choose $\mathbf{L}=\mathbf{D}_2$ as defined in Pichon et al. (2002), so that the penalization P is actually Laplacian. The objective function, Q_μ, is now defined as

$$Q_\mu=\chi^2(\boldsymbol{s}(\boldsymbol{x},\boldsymbol{Z},E,\boldsymbol{g}))+P_\mu(\boldsymbol{x},\boldsymbol{Z},E,\boldsymbol{g}), \quad (27)$$

and its partial derivatives are given in Appendix Section A2. Note that there is in principle an additional formal degeneracy for this inverse problem. If the set $(\boldsymbol{x},\boldsymbol{Z},E,\boldsymbol{g})$ is a solution to (23), then $(\alpha\boldsymbol{x},\boldsymbol{Z},E,\boldsymbol{g}/\alpha)$ is also a solution for any scalar α, because the age distribution $\boldsymbol{x}$ and the LOSVD $\boldsymbol{g}$ are not explicitly normalized in this formulation. However, the adopted regularization lifts this degeneracy. The penalization function P is quadratic $[P(\alpha\boldsymbol{x})=\alpha^2P(\boldsymbol{x})]$. Thus, if $\boldsymbol{x}$ or $\boldsymbol{g}$ is too large in norm, the solution is unattractive. Practically, the algorithm reaches a solution where $\boldsymbol{x}$ and $\boldsymbol{g}$ are similar in norm. In any case, this degeneracy would easily be remedied by adding a normalizing term to the penalization P_μ of the form $\|\boldsymbol{x}\|-1$, which would force the discretized stellar age distribution $\boldsymbol{x}$ to have unitary norm. Following the same principle, one could equivalently choose to normalize the LOSVD rather than the stellar age distribution.

4.4 Simulations

Let us now test the behaviour of STECKMAP by applying it to mock data. The latter were produced using an arbitrary stellar age distribution $\boldsymbol{x}$, an age–metallicity relation $\boldsymbol{Z}$, an LOSVD $\boldsymbol{g}$ and an extinction parameter E. Several simulations were performed with various input models: bumpy age distributions, increasing or decreasing age–metallicity relation and extinctions, Gaussian and non-Gaussian wide or narrow LOSVDs, in various pseudo-observational contexts. Fig. 4 shows the results of two of these experiments. In the top line, the model is a young metal-poor population superimposed on to an older metal-rich population. In the bottom panels, the model has a rather constant stellar age distribution, a non-monotonic age–metallicity relation and a strongly non-Gaussian LOSVD. In both cases the three unknowns are correctly recovered. In these examples, the data quality mimics that of the best Sloan Digital Sky Survey galaxies: the resolution is $R\approx 2000$ and SNR $=30$ per ≈ 1 Å pixel. The wavelength domain of PÉGASE-HR is however narrower than that of the SDSS. These simulations simply aim to demonstrate the generally good behaviour of the method, and show that accounting for the kinematics does not fundamentally weaken the constraints on the stellar content. For a more thorough study of the informational content of the PÉGASE-HR wavelength range, the reader can refer to the systematic double burst simulations with variable spectral resolution and SNR per Å performed in Paper I.

5 RECOVERY OF AGE-DEPENDENT KINEMATICS

In this section we present an implementation of the recovery of age-dependent kinematics, i.e. the situation when each subpopulation has its *own* LOSVD. In this experiment, we restrict ourselves to the case where the stellar populations have a known metallicity and are seen without extinction. This choice is mainly motivated by the numerical cost of such a large inversion procedure. The modelling is given by equation (10). Finding the age–velocity distribution $\Xi(u, t)$ when the monometallic basis $\mathbf{B}$ and the observed spectrum ϕ are given is the inverse problem. It arises as the combination of a linear age inversion and a kinematic deconvolution.

5.1 A sum of convolutions

The age–velocity distribution, $\Xi(u,t)$, is expanded as a linear combination of normalized 2D gate functions $\theta_{ij}(u,t)$:

$$\theta_{ij}(u,t)\equiv\frac{1}{\delta u\,\delta t}\,\theta\left(\frac{u-u_i}{\delta u}\right)\theta\left(\frac{t-t_j}{\delta t}\right).$$

In other words, $\Xi(u,t)$ is represented by a 2D array $\mathbf{v}$ of size (p,n), i.e. p is the size of each LOSVD and n is the number of age bins. The linear step in u is δu and the step in t is δt.

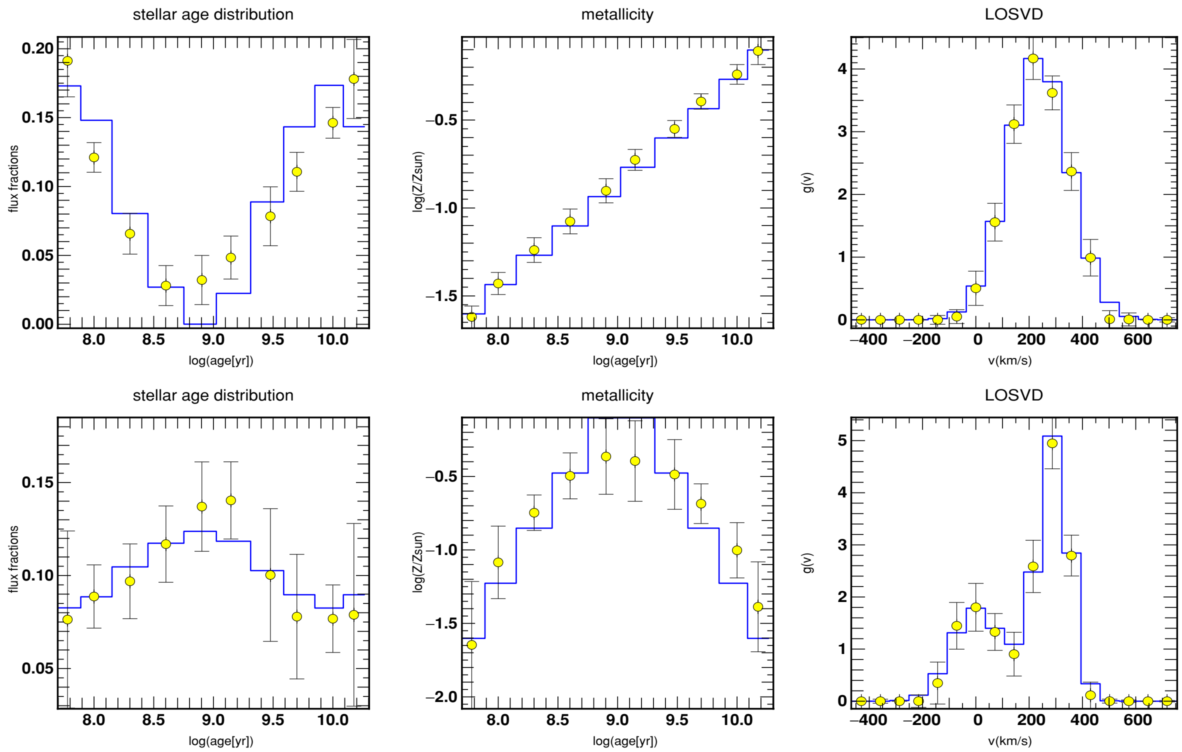

Figure 4. Reconstruction of the stellar age distribution, age–metallicity relation and LOSVD for simulated SDSS-like data with SNR = 30 per pixel. The histogram is the input model. The circles and the bars show respectively the median and the interquartiles of the recovered solutions for 50 realizations.

By inserting the expansion into equation (10) we obtain

$$\phi(w) = \int\!\!\int \sum_{i=1}^{p}\sum_{j=1}^{n} v_{ij}\theta_{ij}(u,t)B(w-u,t)\,\mathrm{d}t\,\mathrm{d}u,$$

$$\simeq \sum_{i=1}^{p}\sum_{j=1}^{n} v_{ij}B_j(w-u_i). \tag{28}$$

As in the previous sections, $B_j\ (u)$ is a time-averaged SSP of age $t_j \pm \frac{1}{2}\delta t$. We then discretize along wavelengths by averaging over small δw:

$$\phi_k = \frac{1}{\delta w}\sum_{i=1}^{p}\sum_{j=1}^{n} v_{ij}\int B_j(w-u_i)\,\theta\left(\frac{w-w_k}{\delta w}\right)\mathrm{d}w,$$

$$\simeq \sum_{i=1}^{p}\sum_{j=1}^{n} v_{ij}B_j(w_k-u_i), \tag{29}$$

where $(w_j)_{j\in\{0,\ldots,m\}}$ is a set of constant step logarithmic wavelengths. The above expression also reads in matrix form as a sum of kernel convolutions. Finally, the model SED of the emitted light reads

$$\boldsymbol{s} = \sum_{j=1}^{n}\mathbf{K}_j\cdot\boldsymbol{v}_j, \tag{30}$$

where $\boldsymbol{s} = (\phi_1, \phi_2, \ldots, \phi_m)$, $\boldsymbol{v}_j = (v_{1j}, v_{2j}, \ldots, v_{pj})$ and

$$\mathbf{K}_j = \begin{bmatrix} K_{11j} & K_{12j} & \ldots & K_{1pj} \\ K_{21j} & K_{22j} & \ldots & K_{2pj} \\ \vdots & \vdots & \ddots & \vdots \\ K_{m1j} & K_{m2j} & \ldots & K_{mpj} \end{bmatrix}, \tag{31}$$

with

$$K_{ikj} \equiv B_j(w_k - u_i). \tag{32}$$

With this notation, $\mathbf{K}_j$ and $\boldsymbol{v}_j$ are respectively the convolution kernel and the LOSVD of the subpopulation of age t_j, and the model spectrum $\boldsymbol{y}$ is the sum of the convolution of the kernel of each subpopulation with its own LOSVD.

5.2 2D age–velocity smoothness constraints

In the previous sections, the unknowns were 1D functions of time or velocity. Here, the unknown is a 2D distribution, and we thus have to implement a 2D smoothing constraint. We wish to allow the smoothness in age to be distinct from the smoothness in velocity. We thus construct two penalizing functions, P_a and P_v, relying on the standard function P. P_a computes the sum of the Laplacians of the columns of $\mathbf{v}$ while P_v computes the sum of the Laplacians of the lines of $\mathbf{v}$. The smoothness in the direction of the velocities (respectively ages) is set by μ_v (respectively μ_a). We define the vectors $\boldsymbol{v}_j = (v_{1j}, v_{2j}, \ldots, v_{pj})$ as the columns of $\mathbf{v}$, i.e. the LOSVDs of the subpopulations. We similarly define the vectors $\boldsymbol{v}^i = (v_{i1}, v_{i2}, \ldots, v_{in})$ as the lines of $\mathbf{v}$. With this notation, the penalization P_μ reads

$$P_\mu(\mathbf{v}) \equiv \mu_a P_a(\mathbf{v}) + \mu_v P_v(\mathbf{v}),$$

$$\equiv \mu_a \sum_{i=1}^{p} P(\boldsymbol{v}^i) + \mu_v \sum_{j=1}^{n} P(\boldsymbol{v}_j). \tag{33}$$

The objective function, Q_μ, is now fully specified as $Q_\mu = \chi^2 + P_\mu$. Its gradients are given in Appendix Section A3. Here we choose the smoothing parameters, $\boldsymbol{\mu} \equiv (\mu_a, \mu_v)$, on the basis of simulations.

5.3 Simulations of a bulge–disc system

We studied the feasibility of separating two age-dynamically distinct populations, i.e. two components that do not overlap in an

Table 1. Projected kinematic parameters and age of the model bulge–disc system used to produce the simulations of Figs 5 and 6. V_c (respectively σ_v) is the rotation velocity (respectively, the velocity dispersion) projected on the line of sight.

	V_c (km s^{-1})	σ_v (km s^{-1})	Age (Gyr)
Case 1			
Bulge	0	100	8
Disc	120	30	0.5
Case 2			
Bulge	0	150	8
Disc	0	50	0.5

age–velocity distribution diagram, in a regime of very high-quality model and data. We performed simulations in the idealized case of a very simplified spiral galaxy consisting of a bulge–disc system of solar metallicity seen without extinction at some intermediate inclination, in two observational contexts. The corresponding ages and projected kinematic parameters are given in Table 1. The resolution of the pseudo-data is $R = 10\,000$ at 4000–6800 Å, and the SNR is 100 per 0.2 Å pixel.

Case 1: The galaxy is resolved, and the fibre aperture is small compared to the angular size of the galaxy. The line of sight is offset by a couple of kiloparsecs from the centre along the major axis. The projected model age–velocity distribution involves two superimposed components: an old, non-rotating, kinematically hot population representing the bulge; and a young, rotating, kinematically cold component. The model and the median of 30 reconstructions are shown in Fig. 5. The separation of the components is clear and their parameters can be recovered with good accuracy, considering the difficulty of the task.

Case 2: The galaxy is unresolved. The difference from the former situation is that, because of the spatial integration, both age–velocity distributions are centred. For a given dynamical model, the projected dispersion of the disc component depends on its inclination. Fig. 6 shows that the separation is successful and that the ages and integrated kinematic properties of both components can be measured.

6 CONCLUSIONS AND OUTLOOK

6.1 Conclusions

The non-parametric kinematic deconvolution of a galaxy spectrum is efficiently performed using a MAP formalism (Section 3). Regularization through smoothness requirements and positivity significantly improve the behaviour of the inversion with respect to noise in the data. This improvement occurs at the cost of introducing some bias in the reconstructed LOSVD, but this bias remains reasonable. Strong non-Gaussianities of LOSVDs are reliably detected from mock data generated using PÉGASE-HR SSPs for SNR down to 20 per 0.2 Å pixel.

When the template does not exactly match the model spectrum at rest, i.e. there is some template mismatch, the error on the velocity dispersion increases very quickly (Section 3.4). For example, in our experiments, where $\sigma_v = 50$ km s^{-1} with $R = 10\,000$ data, the error on the measured velocity dispersion amounts to 10–20 per cent if the template differs from the model by more than 0.3 dex in age and metallicity, perpendicular to the age–metallicity degeneracy.

The formal similarity between the non-parametric kinematic deconvolution and the recovery of the stellar content allows us to merge both processes in a 'mixed' inversion where the observed spectrum is fitted by determining the stellar content and the kinematics simultaneously (Section 4). This circumvents the need for iterations where kinematic and stellar content analyses are carried out one after the other, until convergence is reached; this provides an efficient method to analyse large sets of data.

Satisfactory reconstructions of the stellar age distribution, the age–metallicity relation, the extinction and the global LOSVD were obtained from mock data down to $R = 2000$, SNR $= 30$ per 1 Å pixel in the 4000–6800 Å range (simulating SDSS data in the PÉGASE-HR range), indicating the good behaviour of the method. Since, in our simulations, the introduction of the kinematics into STECMAP did not affect the recovery of the stellar content, we consider that the

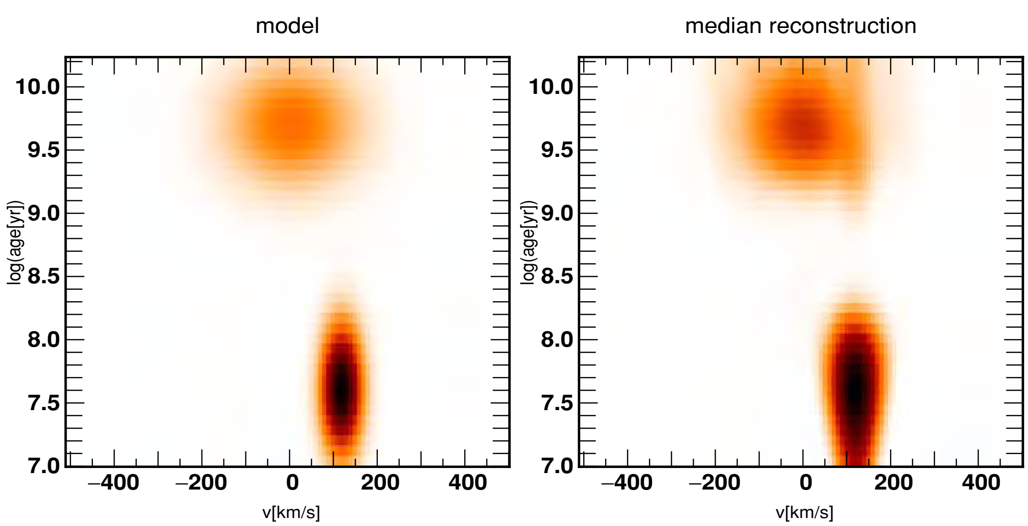

Figure 5. Model (left) and median reconstruction (right, ≈30 realizations) of a stellar age–velocity distribution from SNR = 100 per 0.2 Å pixel pseudo-data at 4000–6800 Å. The model stellar age–velocity distribution mimics that of a simplified spiral galaxy seen with intermediate inclination. The old, broad component can account for the bulge population, while the young, narrow, rotating component represents a thin disc population. The projected kinematic parameters of the model are given in Table 1 (Case 1). The different kinematic components are well separated and clearly identifiable.

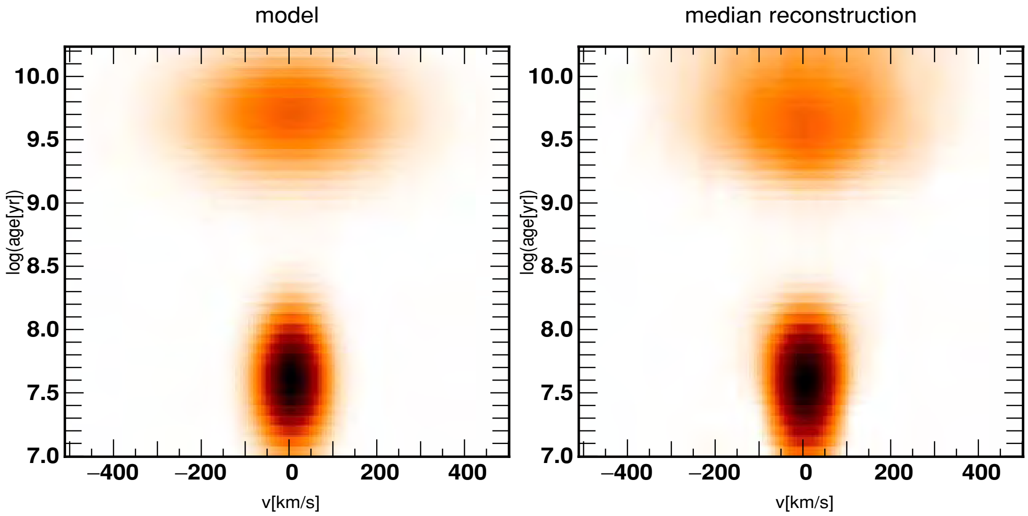

Figure 6. Same as Fig. 5 but for an unresolved simplified spiral galaxy with projected and spatially integrated kinematic parameters given in Table 1 (Case 2). The velocity dispersion of the integrated young disc component depends on the inclination angle. The bulge and the disc are well separated and clearly identifiable. Their respective velocity dispersions and ages are reliably recovered.

error estimates and separability analysis given in Paper I remain valid.

In a more exploratory part of this work, we showed the feasibility of recovering age-dependent kinematics in a simplified monometallic unreddened context (Section 5). We were able to separate the bulge and disc components of a simplified model spiral galaxy in integrated light provided very high-quality data (SNR = 100 per 0.2 Å pixel in the optical domain) and models are available, i.e. we constrain both components in velocity dispersion and age. This separation was also carried out successfully in the setup corresponding to an unresolved galaxy.

Further investigations are needed to extend this technique to a regime where the metallicity and extinction are unknown. We expect that letting the metallicity be a free parameter would certainly lead to a more degenerate problem, as shown by the degradation of the resolution in age found in Paper I compared to fixed metallicity problems. On the contrary, we do not expect the addition of the extinction as a free parameter or a more complex form of extinction law or flux calibration correction, possibly non-parametric, to deteriorate the conditioning of the problem. The results are encouraging, and the feasibility of such age-dependent kinematics reconstructions deserves to be tackled in realistic specific pseudo-observational regimes in the future.

As mentioned in Paper I, the SSP models were considered to be perfect and noiseless. It still has to be investigated how instrumental error sources such as flux and wavelength calibration error, additive noise, contamination by adjacent objects and, equally important, model errors can affect the robustness of such sophisticated interpretations.

6.2 Outlook

STECKMAP will be very useful to interpret data of large spectroscopic surveys, complete or in progress, such as 2DFGRS,[1] SDSS,[2] DEEP2,[3] or VVDS,[4] especially where constraints on both the stellar content and the dynamics are required. STECKMAP' s analysis of the spectroscopic survey data or of an SNR-selected subsample, combined with survey photometry, could provide estimates of the stellar and dynamical masses (which must be corrected for fibre aperture though), thereby allowing astronomers the prospect of investigating the dark matter content in galaxies on a statistically significant sample, in the spirit of Padmanabhan et al. (2004).

The application of age-dependent kinematics to integral field spectroscopy data from, for example, SAURON (Bacon et al. 2001; de Zeeuw et al. 2002), OASIS (McDermid et al. 2004a), MUSE (Henault et al. 2003) or MPFS (Chilingarian et al. 2004) could significantly boost the amount of information extracted from these data.

The inner parts of elliptical or dwarf elliptical galaxies have shown via adaptive optics new kinematically decoupled structures (cores or central discs), which were previously unresolved (McDermid et al. 2004b; Bacon et al. 2001). Similarly, if decoupled structures are unresolved and remain so, even with adaptive optics, it may still be possible to separate components in age–velocity space. Hence, the technique presented in Section 5 extends the range of investigation for the inner components of galaxies even further in redshift and distance with the current generation of instruments. The faint, generalized counterparts of kinematically decoupled cores, i.e. stellar streams generated by minor merging and accretion of satellites, may also be detectable by an age-dependent kinematics reconstruction in systems that cannot be resolved into stars, provided that they are sufficiently distinct from the bulk stars of the galaxy in the age–velocity space. This will enlarge the sample of galaxies for which such detailed information is available, and may make it statistically significant.

ACKNOWLEDGMENTS

We are grateful to A. Siebert for useful comments and helpful suggestions. We would like to thank D. Munro for freely distributing

[1] http://www.mso.anu.edu.au/2dFGRS/
[2] http://www.sdss.org/
[3] http://www.deep.berkeley.edu/
[4] http://www.oamp.fr/virmos/vvds.htm

his Yorick programming language,[5] together with its MPI interface, which we used to implement our algorithm in parallel. PO thanks the MPA for their hospitality and funding from a Marie Curie studentship.

REFERENCES

Bacon R. et al., 2001, MNRAS, 326, 23
Bacon R., Emsellem E., Combes F., Copin Y., Monnet G., Martin P., 2001, A&A, 371, 409
Balcells M., Quinn P. J., 1990, ApJ, 361, 381
Bender R., 1990, A&A, 229, 441
Bender R., Surma P., 1992, A&A, 258, 250
Calzetti D., 2001, PASP, 113, 1449
Cappellari M., Emsellem E., 2004, PASP, 116, 138
Chilingarian I., Prugniel P., Silchenko O., Afanasiev A., 2004, astro-ph/0412293
Davies R. L., Sadler E. M., Peletier R. F., 1993, MNRAS, 262, 650
De Bruyne V., De Rijcke S., Dejonghe H., Zeilinger W. W., 2004a, MNRAS, 349, 440
De Bruyne V., De Rijcke S., Dejonghe H., Zeilinger W. W., 2004b, MNRAS, 349, 461
De Rijcke S., Dejonghe H., Zeilinger W. W., Hau G. K. T., 2004, A&A, 426, 53
de Zeeuw P. T. et al., 2002, MNRAS, 329, 513
Faber S. M., Friel E. D., Burstein D., Gaskell C. M., 1985, ApJS, 57, 711
Falcón-Barroso J., Balcells M., Peletier R. F., Vazdekis A., 2003, A&A, 405, 455
Ferguson A. M. N., Irwin M. J., Ibata R. A., Lewis G. F., Tanvir N. R., 2002, AJ, 124, 1452
Freeman K., Bland-Hawthorn J., 2002, ARA&A, 40, 487
Henault F. et al., 2003, in Iye M., Moorwood A. F. M., eds, Proc. SPIE 4841, Instrument Design and Performance for Optical/Infrared Ground-Based Telescopes. SPIE, Bellingham, WA, p. 1096
Ibata R., Chapman S., Ferguson A. M. N., Irwin M., Lewis G., McConnachie A., 2004, MNRAS, 351, 117
Kroupa P., Tout C. A., Gilmore G., 1993, MNRAS, 262, 545
Kuijken K., Merrifield M. R., 1993, MNRAS, 264, 712
Kuntschner H., 2000, MNRAS, 315, 184
Kuntschner H., 2004, A&A, 426, 737
Le Borgne D., Rocca-Volmerange B., Prugniel P., Lançon A., Fioc M., Soubiran C., 2004, A&A, 425, 881
McDermid R. et al., 2004a, Newsl. Isaac Newton Group Telescopes, No 8, p. 3
McDermid R. et al., 2004b, Astron. Nachr., 325, 100
Merritt D., 1997, AJ, 114, 228
Ocvirk P., Pichon C., Lançon A., Thiébaut E., 2005, MNRAS, in press (Paper I, this volume)
Padmanabhan N. et al., 2004, New Astron., 9, 329
Pichon C., Siebert A., Bienaymé O., 2002, MNRAS, 329, 181
Pinkney J. et al., 2003, ApJ, 596, 903
Press W. H., Teukolsky S. A., Vetterling W. T., Flannery B. P., 2002, Numerical Recipes in C++: The Art of Scientific Computing, 2nd edn. Cambridge Univ. Press, Cambridge
Rix H., White S. D. M., 1992, MNRAS, 254, 389
Saha P., Williams T. B., 1994, AJ, 107, 1295
Trager S. C., Worthey G., Faber S. M., Burstein D., Gonzalez J. J., 1998, ApJS, 116, 1
van der Marel R. P., Franx M., 1993, ApJ, 407, 525
Wahba G., ed., 1990, Spline Models for Observational Data (CBMS-NSF Regional Conf. Ser. Appl. Math., Vol. 59). SIAM, Philadelphia
Worthey G., 1994, ApJS, 95, 107

[5] Available at http://www.maumae.net/yorick/doc/index.html

APPENDIX A: GRADIENT COMPUTATIONS

A1 Kinematic deconvolution

In this section we derive the gradient of Q_μ with respect to the LOSVD $\boldsymbol{g}$. First, we rewrite the χ^2 term as

$$\chi^2 = \boldsymbol{r}^{\mathrm{T}} \cdot \mathbf{W} \cdot \boldsymbol{r}, \tag{A1}$$

where the residuals vector $\boldsymbol{r}$ is defined by

$$\boldsymbol{r} = \boldsymbol{y} - \mathcal{F}^{-1} \cdot \mathrm{diag}(\mathcal{F} \cdot \boldsymbol{F}) \cdot \mathcal{F} \cdot \boldsymbol{g}. \tag{A2}$$

The derivative of the χ^2 then reads

$$\frac{\partial \chi^2}{\partial \boldsymbol{g}} = -2\mathcal{F}^* \cdot \mathrm{diag}(\mathcal{F} \cdot \boldsymbol{F})^* \cdot \mathcal{F} \cdot \mathbf{W} \cdot \boldsymbol{r}, \tag{A3}$$

where the asterisk * denotes the complex conjugate. Since the stellar template and the LOSVD can play symmetrical roles in equation (17), we can also write the derivative of χ^2 relatively to the stellar template:

$$\frac{\partial \chi^2}{\partial \boldsymbol{F}} = -2\mathcal{F}^* \cdot \mathrm{diag}(\mathcal{F} \cdot \boldsymbol{g})^* \cdot \mathcal{F} \cdot \mathbf{W} \cdot \boldsymbol{r}. \tag{A4}$$

This expression will be useful for later derivations of gradients for more complex problems in the following appendices.

A2 Gradients of the mixed inversion

Here we show how to obtain the partial derivatives of $Q_\mu = \chi^2 + P_\mu$ as defined in Section 4. Given that writing the derivatives of the penalizing functions P_μ is straightforward, in this appendix we will focus on the gradients of χ^2. In the mixed inversion, the reddened model spectrum at rest plays the role of the stellar template $\boldsymbol{F}$ in the classical kinematic deconvolution of equation (15). Thus $\partial\chi^2/\partial\boldsymbol{g}$ can be obtained by replacing $\boldsymbol{F} \leftarrow \mathrm{diag}(\boldsymbol{f}_{\mathrm{ext}}(E)) \cdot \mathbf{B} \cdot \boldsymbol{x}$ in equation (A3):

$$\frac{\partial \chi^2}{\partial \boldsymbol{g}} = -2\mathcal{F}^* \cdot \mathrm{diag}(\mathcal{F} \cdot \mathrm{diag}(\boldsymbol{f}_{\mathrm{ext}}(E)) \cdot \mathbf{B} \cdot \boldsymbol{x})^* \cdot \mathcal{F} \cdot \mathbf{W} \cdot \boldsymbol{r}, \tag{A5}$$

where $\boldsymbol{r} = \boldsymbol{y} - \boldsymbol{s}$ is the residuals vector, with $\boldsymbol{s}$ as given by equation (25). To obtain the other partial derivatives, we use the following relation. For any parameter α we have

$$\frac{\partial \chi^2}{\partial \alpha} = \left(\frac{\partial \chi^2}{\partial \boldsymbol{F}}\right)^{\mathrm{T}} \cdot \frac{\partial \boldsymbol{F}}{\partial \alpha}. \tag{A6}$$

The first term $\partial\chi^2/\partial\boldsymbol{F}$ is given by equation (A4), while the second term reads, considering each unknown,

$$\frac{\partial \boldsymbol{F}}{\partial \boldsymbol{x}} = \mathrm{diag}(\boldsymbol{f}_{\mathrm{ext}}) \cdot \mathbf{B}, \tag{A7}$$

$$\frac{\partial \boldsymbol{F}}{\partial \boldsymbol{Z}} = \mathrm{diag}(\boldsymbol{x}) \cdot \frac{\partial \mathbf{B}}{\partial \boldsymbol{Z}} \cdot \mathrm{diag}(\boldsymbol{f}_{\mathrm{ext}}), \tag{A8}$$

$$\frac{\partial \boldsymbol{F}}{\partial E} = \mathrm{diag}\left(\frac{\partial \boldsymbol{f}_{\mathrm{ext}}}{\partial E}\right) \cdot \mathbf{B} \cdot \boldsymbol{x}, \tag{A9}$$

with the same notation as in the appendix of the STECMAP paper.

A3 Gradients for the age-dependent kinematics recovery

Again, we focus on the partial derivatives of χ^2. Using equation (17), the model can be rewritten using the Fourier operator

$$\boldsymbol{s} = \sum_{j=1}^{n} \mathcal{F}^* \cdot \mathrm{diag}(\mathcal{F} \cdot \boldsymbol{B}_j) \cdot \mathcal{F} \cdot \boldsymbol{v}_j, \tag{A10}$$

where $\boldsymbol{B}_j$ is the discretized time-averaged SSP of age $[t_{j-1}, t_j]$. The derivatives of χ^2 relative to $\mathbf{v}$ can be derived directly from equation (A3) since the model is just a sum of convolutions. Replacing $\boldsymbol{F} \leftarrow \boldsymbol{B}_j$ and $\boldsymbol{g} \rightarrow \boldsymbol{v}_j$ yields the gradient of χ^2:

$$\frac{\partial \chi^2}{\partial \boldsymbol{v}_j} = -2\mathcal{F}^* \cdot \mathrm{diag}(\mathcal{F} \cdot \boldsymbol{B}_j)^* \cdot \mathcal{F} \cdot \mathsf{W} \cdot \boldsymbol{r}, \tag{A11}$$

with the residuals vector $\boldsymbol{r} = \boldsymbol{y} - \boldsymbol{s}$. Finally, the derivative of Q_μ relative to $\mathbf{v}$ is the matrix defined by

$$\frac{\partial Q_\mu}{\partial \mathbf{v}} = \left(\frac{\partial Q_\mu}{\partial \boldsymbol{v}_1}, \frac{\partial Q_\mu}{\partial \boldsymbol{v}_2}, \ldots, \frac{\partial Q_\mu}{\partial \boldsymbol{v}_n} \right). \tag{A12}$$

This paper has been typeset from a TEX/LATEX file prepared by the author.

Mon. Not. R. Astron. Soc. **329,** 181–194 (2002)

On the kinematic deconvolution of the local neighbourhood luminosity function

C. Pichon,[1,2]★ A. Siebert[1] and O. Bienaymé[1]
[1]*Observatoire de Strasbourg, 11 rue de l'Université, 67000 Strasbourg, France*
[2]*Institut d'Astrophysique de Paris, 98 bis boulevard d'Arago, 75014 Paris, France*

Accepted 2001 August 31. Received 2001 July 5; in original form 1999 December 29

ABSTRACT

A method for inverting the statistical star counts equation, including proper motions, is presented; in order to break the degeneracy in that equation, it uses the supplementary constraints required by dynamical consistency. The inversion gives access to both the kinematics and the luminosity function of each population in three régimes: the singular ellipsoid, the constant ratio Schwarzschild ellipsoid plane-parallel models and the epicyclic model. This more realistic model is tailored to account for the local neighbourhood density and velocity distribution.

The first model is fully investigated, both analytically and by means of a non-parametric inversion technique, while the second model is shown to be formally its equivalent. The effect of noise and incompleteness in apparent magnitude is investigated. The third model is investigated by a 5D + 2D non-parametric inversion technique where positivity of the underlying luminosity function is explicitly accounted for.

It is argued that its future application to data such as the Tycho catalogue (and in the upcoming satellite *GAIA*) could lead – provided that the vertical potential and or the asymmetric drift or $w_\odot$ are known – to a non-parametric determination of the local neighbourhood luminosity function without any reference to stellar evolution tracks. It should also yield the proportion of stars for each kinematic component and a kinematic diagnostic to split the thin disc from the thick disc or the halo.

Key words: methods: data analysis – Hertzsprung–Russell (HR) diagram – stars: luminosity function, mass function – Galaxy: kinematics and dynamics – Galaxy: stellar content – Galaxy: structure.

1 INTRODUCTION

Most of our knowledge of the global structure of the Galaxy relies on the comparison of magnitude and colour star counts in different Galactic directions. Star counts alone do not allow us to solve the dilemma that a star of a given apparent magnitude can be either intrinsically faint and close by, or bright and distant. This problem may be addressed statistically by using the century-old equation of stellar statistics (von Seeliger 1898):

$$A_\lambda(m, \ell, b) = \int_0^\infty \Phi_\lambda(M)\rho(r, \ell, b) r^2 \,\mathrm{d}r, \tag{1}$$

where $A_\lambda(m, \ell, b)\,\mathrm{d}m\,\mathrm{d}\ell\,\mathrm{d}(\sin b)$ is the number of stars that have an apparent magnitude in the range $[m, m + \mathrm{d}m]$, $\Phi_\lambda(M)$ is the luminosity function (LF), which depends on the intrinsic magnitude, M, and the colour band λ, while $\rho(r, \ell, b)$ is the density at radius r (within $\mathrm{d}r$) along the line of sight in the direction given by the Galactic longitudes and latitudes (ℓ, b) [within the solid angle $\mathrm{d}\ell \cos(b)\,\mathrm{d}b$].

This equation cannot be solved or inverted (i.e., by determining both the stellar LF and the density law) except for a few simplified cases. For instance, with a 'homogeneous' stellar sample for which the absolute magnitudes of stars or, more precisely, their LFs are known, the density law along the line of sight can be recovered. A classical numerical technique (Mihalas & Binney 1981) has been proposed – the Bok (1937) diagram – while more rigorous treatments are required for small samples to stabilize the inversion so as to produce smooth solutions (Binney & Merrifield 1998). The converse situation is the determination of the LF assuming a known density law (see, for instance, recent studies of the faint end of the disc or halo main sequence based on deep star counts (Reid et al. 1996; Gould, Flynn & Bahcall 1998).

★E-mail: pichon@astro.u-strasbg.fr

A simple approach, developed largely in the 1980s, was to integrate equation (1) assuming some prior information concerning the stellar populations (see, e.g., Pritchet 1983, Bahcall, Soneira & Schmidt 1983, Buser & Kaeser 1985 and Robin & Crézé 1986). A frequent assumption is, for instance, to assume that the halo stars have the same LF as some low-metallicity globular clusters. Another approach consists in building a stellar LF from stellar evolution tracks and isochrones of various ages. This has been used to put constraints on the Galactic disc star formation rate (Haywood, Robin & Crézé 1997a,b).

Stronger a priori constraints may also be derived by requiring dynamical consistency, since the vertical kinematics of stars is related to the flattening of stellar discs or spheroidal components.

Since star counts alone, $A_\lambda(m, \ell, b)$, are not sufficient to constrain uniquely the Galactic stellar population models, it is expected that two (or more) distinct models will reproduce the same apparent star counts. However, this is not a real worry, since it is likely that adding some relevant extra a priori information must help to lift partially the degeneracy of the models.

In this paper it is shown that the degeneracy is lifted altogether when we consider, in addition to the star counts in apparent magnitude, the proper motions, μ_ℓ and μ_b. For a relatively general dynamically consistent model (stationary, axisymmetric and fixed kinematic radial gradients), the statistical equation counts may be formally inverted, giving access to *both* the vertical density law of each stellar population *and* their LFs. This is developed in Section 2, where we show how the vertical motions are related to the thickness of stellar components. The remaining degeneracy occurs only for a quadratic vertical potential. Otherwise – when the vertical component of the potential is known – the departures from quadratic behaviour define a characteristic scale that allows us to transform statistically the magnitudes into distances and proper motions into velocities. Similarly, the asymmetric drift and/or the vertical velocity component of the Sun provide a natural scale in energy, leading to the same inversion procedure.

For ideal star counts (infinitely deep and for an infinite number of stars), the inversion gives exactly the proportion of stars in each kinematic component, providing a direct diagnostic to split the thin disc from the thick disc or the halo, and its luminosity function $\Phi_\lambda(M)$ is recovered for each kinematic stellar component. This is a direct consequence of the supplementary constraints introduced by the requirement for dynamical consistency.

Section 2 presents the generalized stellar statistic equation which accounts for proper motions, and demonstrates the uniqueness of the inversion for two families of plane-parallel distribution functions: the singular velocity ellipsoid (Section 2.1) and a constant ratio velocity ellipsoid (Section 2.2), while Section 2.3 presents a basic description of the epicyclic model. Section 3 illustrates the inversion procedure on a fictitious superposition of four kinematically decoupled populations with distinct main-sequence turn-off magnitudes for the constant ratio velocity ellipsoid and the epicyclic models. Section 4 discusses the effects of truncation in apparent magnitude (i.e., completeness of the catalogue) in the recovered LF, as well as noise in the measurements. Finally, Section 5 discusses the applicability of the method to the Tycho-2 catalogue and to external clusters, and concludes the paper.

2 DERIVATION

The number of stars, dN, that have an apparent luminosity in the range $[L, L + \mathrm{d}L]$ in the solid angle defined by the Galactic longitudes and latitudes (ℓ, b) [within $\mathrm{d}\ell\,\mathrm{d}(\sin b)$], with proper motions μ_ℓ and μ_b (within $\mathrm{d}\mu_b$ and $\mathrm{d}\mu_\ell$) is given by

$$\begin{aligned}\mathrm{d}N \equiv\ & A_\lambda(L, \mu_l, \mu_b; l, b)\,\mathrm{d}\mu_\ell\,\mathrm{d}\mu_b\,\mathrm{d}\ell\cos b\,\mathrm{d}b\,\mathrm{d}L\\ =\ & \left\{\int\!\!\int\!\!\int \Phi_\lambda^{\star}[L_0, \beta]\left[\int f_\beta(\boldsymbol{r}, \boldsymbol{u})\,\mathrm{d}u_r\right] r^4\,\mathrm{d}r\,\mathrm{d}\beta\right\}\\ & \times \mathrm{d}\mu_\ell\,\mathrm{d}\mu_b\,\mathrm{d}\ell\cos b\,\mathrm{d}b\,\mathrm{d}L, \end{aligned} \tag{2}$$

where we have introduced the LF per unit bandwidth, $\Phi_\lambda^{\star}[L_0, \beta]$, which is here taken to be a function of the absolute luminosity, L_0, and of a continuous kinematic index, β. The variables $\boldsymbol{r}$, $\boldsymbol{u}$ are the vector position and velocity coordinates (u_r, u_ℓ, u_b) in phase-space relative to the local standard of rest, while $\boldsymbol{R}$ and $\boldsymbol{V}$ are those relative to the Galactic Centre. The relationship between $A_\lambda(L, \mu_l, \mu_b; l, b)$ and $\Phi_\lambda^{\star}[L_0, \beta]$ involves a double summation over β, and distance, r, along the line of sight. Here $f_\beta(\boldsymbol{r}, \boldsymbol{u})$ represents the β component of the distribution function of the assumed stationary axisymmetric equilibrium, i.e.,

$$f(\boldsymbol{r}, \boldsymbol{u}) = \int_0^\infty f_\beta(\boldsymbol{r}, \boldsymbol{u})\,\mathrm{d}\beta, \tag{3}$$

where f is decomposed over the basis of isothermal solutions f_β of the Boltzmann equation for the assumed known potential ψ. Equation (3) corresponds to a decomposition over isothermal populations of different kinematic temperatures, $\sigma^2 = 1/\beta$. Apart from this restriction, the shape of the distribution $f(E_z)$ could be anything. Note that equation (2) is a direct generalization of equation (1), since

$$\rho_\beta(r, \ell, b, \mu_\ell, \mu_b) \equiv r^2 \int f_\beta(\boldsymbol{r}, \boldsymbol{u})\,\mathrm{d}u_r$$

is by definition the density of stars (belonging to population β) which are at position $\boldsymbol{r} \equiv (r, \ell, b)$ within $\mathrm{d}r\,\mathrm{d}\ell\,\mathrm{d}(\sin b)$, with proper motion μ_b (within $\mathrm{d}\mu_b$) and μ_ℓ(within $\mathrm{d}\mu_\ell$). The extra summation on β which arises in equation (2) accounts for the fact that stars in the local neighbourhood come from a superposition of different kinematic populations which, as is shown later, can be disentangled. Note that $\Phi_\lambda^{\star}$ is defined here per unit absolute luminosity, L_0, and therefore

$$\begin{aligned}\Phi_\lambda[M(L_0)] &= \frac{2\log(10)}{5} L_0 \int \Phi_\lambda^{\star}[L_0, \beta]\,\mathrm{d}\beta, \quad \text{where}\\ M(L_0) &= -\frac{5}{2}\frac{1}{\log 10}\log\left(\frac{L_0}{\mathrm{L}_\odot}\right) + \mathrm{M}_\odot. \end{aligned}$$

Since there is no convolution on λ (which is mute), it will be omitted from now on in the derivation. In Section 3, $B - V$ colours are reintroduced to demonstrate the inversion for a fictitious HR diagram. We shall also drop the ☆ superscript, but will keep in mind that the LF is expressed as a function of the absolute luminosity, L_0.

This paper is concerned with the inversion of equation (2). We proceed in three steps. First, a simplistic Ansatz for the distribution function is assumed (corresponding to a stratification in height of uniform discs with a pin-like singular velocity ellipsoid), leading to a proof that, in this context, equation (2) has a well-defined unique solution which can be made formally explicit. A more realistic model is then presented, accounting for the measured anisotropy of the velocity ellipsoid. It is shown that, in the direction of the Galactic Centre, and if the velocity dispersions ratios are constant for all populations, this model is formally invertible following the same route. Away from the Galactic Centre direction, the velocity components of the Sun are also accounted for to recover statistically distances via another inversion procedure related to secular parallaxes. Finally, we illustrate the inversion on a fully seven-dimensional epicyclic model. The detailed investigation of this model is postponed to a companion paper (Siebert, Pichon & Bienaymé, in preparation).

2.1 A toy model: parallel sheet model with singular velocity ellipsoid

Let us assume here a sheet-like model for the distribution function of kinematic temperature β:

$$f_\beta(\boldsymbol{r},\boldsymbol{u}) = \sqrt{\frac{\beta}{2\pi}}\exp(-\beta E_z)\delta(v_R)\delta(v_\phi), \tag{4}$$

which corresponds to a stratification in height with a pin-like singular velocity ellipsoid that is aligned with the rotation axis of the Galaxy. Calling $\mu_b \equiv u_b/r$, the energy reads in terms of the heliocentric coordinates

$$E_z = \frac{v_z^2}{2} + \psi_z(z) = \frac{r^2\mu_b^2}{2\cos^2(b)} + \alpha\sin^2(b)r^2 + \chi[r\sin(b)], \tag{5}$$

where the harmonic component of the z potential (αz^2) was made explicit while leaving unspecified the non-harmonic residual, χ.

Putting equation (4) into equation (2) leads to

$$A\,[b,\mu_b,L] = \iint \sqrt{\frac{\beta}{2\pi}}\frac{\Phi[Lr^2,\beta]}{\cos(b)} \times \exp\left\{-\beta\alpha r^2\sin^2(b) - \beta r^2\frac{\mu_b^2}{2\cos^2(b)} - \beta\chi[r\sin(b)]\right\} r^3\,\mathrm{d}r\,\mathrm{d}\beta, \tag{6}$$

given the relationship $L_0 = Lr^2$ relating apparent and absolute luminosities. Introducing $\zeta = L^{1/2}r$,

$$x = \alpha\frac{\sin^2(b)}{L} + \frac{\mu_b^2}{2L\cos^2(b)}, \quad \text{and} \quad y = \frac{\sin(b)}{L^{1/2}}. \tag{7}$$

Equation (6) then reads

$$L^2\cos(b)A[b,\mu_b,L] = \iint \sqrt{\frac{\beta}{2\pi}}\Phi[\zeta^2,\beta] \times \exp[-\beta\zeta^2 x - \beta\chi(\zeta y)]\zeta^3\,\mathrm{d}\zeta\,\mathrm{d}\beta. \tag{8}$$

2.1.1 Harmonic degeneracy

Suppose for now that the z-potential is purely harmonic, so that χ is identically null. Calling $s = \beta\zeta^2$, the inner integral over ζ in equation (8) can be rewritten as an integral over β and s:

$$\iint \sqrt{\frac{\beta}{2\pi}}\Phi[\zeta^2,\beta]\exp(-\beta\zeta^2 x)\zeta^3\,\mathrm{d}\zeta\,\mathrm{d}\beta = \frac{1}{2\sqrt{2\pi}}\int\left(\int \Phi[s/\beta,\beta]\beta^{-3/2}\,\mathrm{d}\beta\right)\exp(-sx)s\,\mathrm{d}s. \tag{9}$$

Equation (9) shows that for a purely harmonic potential the *mixture* of populations (integrated over β) is recovered from $A[b,\mu_b,L]$, which is effectively a function of x only (given by equation 7). In this instance, the inversion does not allow us to disentangle the different kinematic populations. In physical terms, there is a degeneracy between the distance, luminosity and proper motion. In contrast, when the data set extends far enough to probe the anharmonic part of the potential, we now demonstrate that equation (8) has formally a unique exact solution, before exploring non-parametric means of inverting it in a more general framework.

2.1.2 Uniqueness?

Let us assume that not too far from the Galactic plane, $\chi(z)$ is well approximated by $\chi(z) = \gamma z^\nu$, so that equation (8) becomes

$$L^2\cos(b)A[b,\mu_b,L] = \iint \sqrt{\frac{\beta}{2\pi}}\Phi[\zeta^2,\beta] \times \exp(-\beta\zeta^2 x - \beta\gamma\zeta^\nu y^\nu)\zeta^3\,\mathrm{d}\zeta\,\mathrm{d}\beta. \tag{10}$$

Calling

$$\Phi_1[U,B] = \frac{1}{\sqrt{2\pi}}\Phi[\exp(2U),\exp(B)] \times \exp\{4U + 3/2B - c[(2+\nu)U + 2B]\},$$
$$K_0(z) = \exp[cz - \exp(z)], \tag{11}$$

and $\quad A_1[X,Y] = L^2\cos b A[b,\mu_b,L]\exp[c(X+Y)], \qquad (12)$

where

$$B = \log(\beta), \quad Z = \log(\zeta),$$
$$X = \log(x) = \log\left[\alpha\frac{\sin^2(b)}{L} + \frac{\mu_b^2}{2L\cos^2(b)}\right],$$
$$Y = \log\left|\frac{\gamma\sin^\nu(b)}{L^{\nu/2}}\right|, \tag{13}$$

Equation (10) becomes

$$A_1[b,\mu_b,L] = A_1[X,Y] = \iint \Phi_1[Z,B]K_0(B+2Z+X) \times K_0(B+\nu Z+Y)\,\mathrm{d}Z\,\mathrm{d}B. \tag{14}$$

The positive scalar c is left to our discretion and can be chosen so as to yield a narrow kernel, K_0 (in practice, c should be close to one). Since r runs from zero to infinity and so does β, the integration over B and Z will run from $-\infty$ to ∞. Similarly, X and Y span $]-\infty,\infty[$ as b goes from zero to $\pi/2$. Let

$$w = -(B+\nu Z), \quad \varpi = -(B+2Z); \tag{15}$$

Equation (14) then reads

$$A_1[X,Y] = |\nu-2|^{-1}\iint \Phi_1[\varpi,w]K_0(X-\varpi) \times K_0(Y-w)\,\mathrm{d}\varpi\,\mathrm{d}w. \tag{16}$$

The *unique* solution of equation (16) reads formally

$$\Phi_1[\varpi,w] = |\nu-2|FT^{-1}\left(\frac{\hat{A}_1[k_\varpi,k_w]}{\hat{K}_0(k_\varpi)\hat{K}_0(k_w)}\right), \tag{17}$$

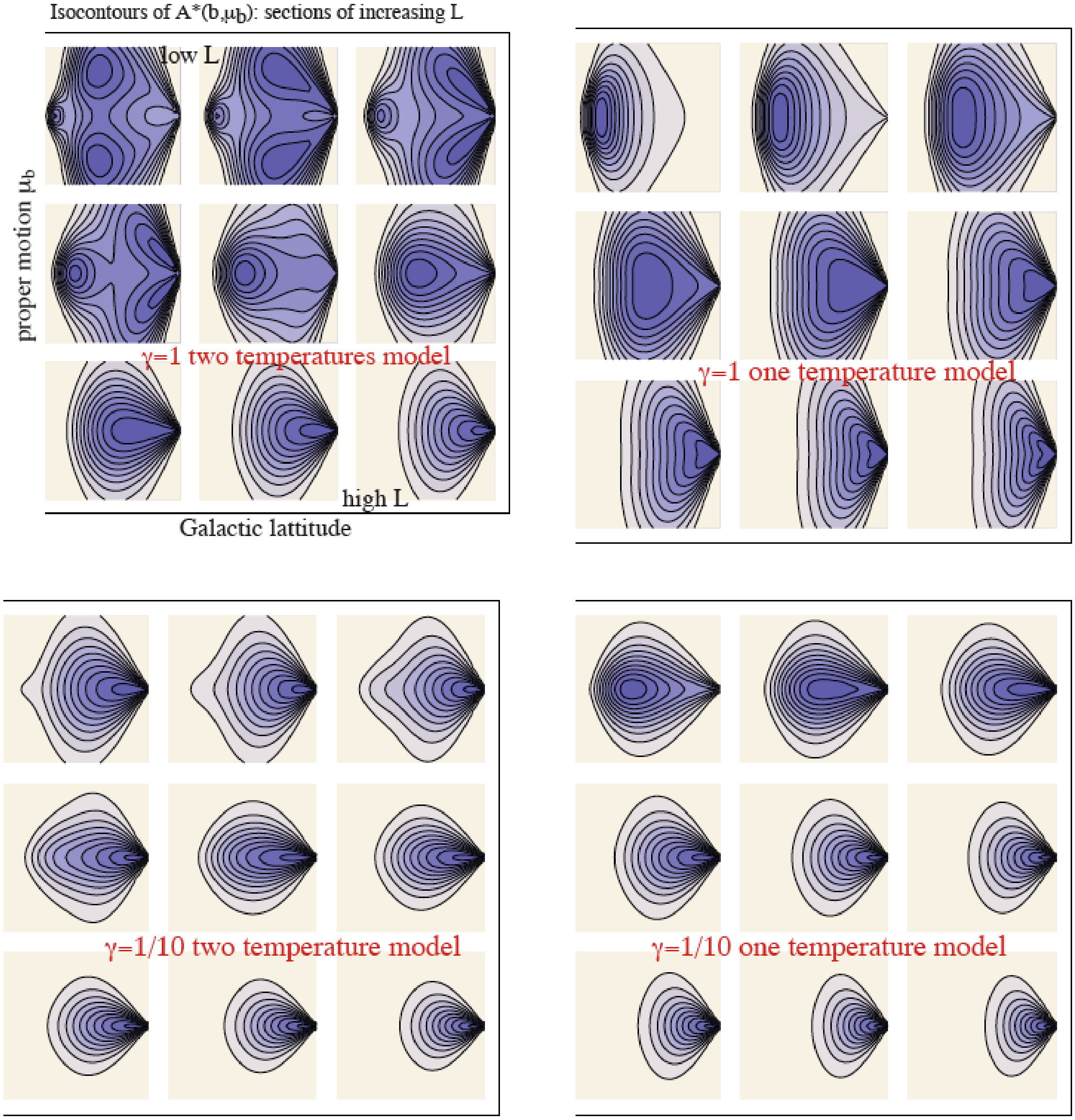

Figure 1. *In each panel:* Isocontour of $A^*(b,\mu_b)$ (defined by equation 48) in the b,μ_b plane (b ranging from $-\pi/2$ to $\pi/2$ and μ_b from -1 to 1): sections of increasing apparent magnitude (from left to right and top to bottom) *Top left:* two-temperature models [$\log\beta = -2$ and $\log\beta = 2$, $\log(L_0) = 0$] *Top right:* same as top left, but for a unique temperature ($\beta = 1$) model. The observed star counts enable us to distinguish between the one- and two-temperature models, especially at the faint end (top left section) for significantly non-zero $\gamma(=1)$. *Bottom left:* Shows that even the faint end (top left section) of the observed star counts are barely distinguishable from the two-temperature model (*Bottom right:*) for small $\gamma(=1/10)$. This demonstrates graphically the requirement to access the break radius, $\ell_0 \propto 1/\gamma$, of the potential to derive statistical distances to the stars.

where

$$\hat{A}_1[k_\varpi, k_w] = \iint \exp[+\mathrm{i}(k_w X + k_\varpi Y)] A_1[X, Y]\,\mathrm{d}X\,\mathrm{d}Y \quad \text{and}$$

$$\hat{K}_0[k] = \int \exp[+\mathrm{i}(kX)] K_0(X)\,\mathrm{d}X,$$

while

$$FT^{-1}[f(k_x, k_y)] = \frac{1}{4\pi^2}\iint \exp[-\mathrm{i}k_x\varpi - \mathrm{i}k_y w] f(k_x, k_y)\,\mathrm{d}k_x\,\mathrm{d}k_y.$$

Both Fourier transforms are well-defined, given the span of ϖ, w and X, Y. Approximating both K_0 and A_1 by a Gaussian of width respectively $1/\ell_K$ and $1/\ell_N^2$, equation (17) shows that Φ_1 will be a Gaussian of width $1/(\ell_N - \ell_K)^2$.

This procedure is therefore a *true* deconvolution: the luminosity function $\Phi_\lambda[L, \beta]$ is effectively recovered at arbitrary resolution (in effect fixed by the signal-to-noise ratio of the data). In practice, equation (17) is impractical for noisy finite data sets, so we shall investigate non-parametric regularized solutions to equation (8) in Section 3.1.1.

There is a natural scale $\ell_0 = (\alpha/\gamma)^{1/(\nu-2)}$, given by the break in the potential, which provides us with a means to lift the degeneracy between faint close stars moving slowly and bright stars moving faster farther out. This scale reflects the fact that statistically the dynamics (i.e., the velocities) gives us a precise indication of distances in units of ℓ_0. We can therefore reassign a posteriori distances to stars in the statistical sense and deconvolve the colour–magnitude diagram. Fig. 1 graphically demonstrates the requirement to access the break radius of the potential in order to derive statistical distances to the stars. It shows sections of increasing apparent magnitude in the b, μ_b plane for a two-temperature model and for a one-temperature model (corresponding to a unique absolute luminosity). The observed star counts enable us to distinguish between the one- and two-temperature models, especially at the faint end for significantly non-zero γ.

Turning back to equation (8), it remains true that for more general χ the equation can still be inverted in the least-squares sense, but this involves a less symmetric kernel, $K_1(x, y|u, \beta)$, whose functional form depends explicitly on χ:

$$K_1(x, y|u, \beta) = \sqrt{\frac{\beta}{2\pi}} \exp\left[-\beta u^2 x - \beta\chi(uy)\right] u^3.$$

The inversion procedure, which will be described in Section 3, still applies to such kernels.

2.2 A Schwarzschild model: accounting for the local velocity ellipsoid anisotropy

Let us now move to more realistic models with a fully triaxial Schwarzschild ellipsoid. Its distribution function is given in terms of the kinematic inverse dispersions β_R, β_ϕ and β_z by

$$f_\beta(\boldsymbol{r}, \boldsymbol{u}) = \sqrt{\frac{\beta_R\beta_z\beta_\phi}{8\pi^3}} \exp[-(\beta_z E_z + \beta_R E_R + \beta_\phi E_\phi)], \tag{18}$$

where

$$E_z = \tfrac{1}{2}v_z^2 + \psi_z(z), \quad E_R = \tfrac{1}{2}v_R^2 \quad \text{and} \quad E_\phi = \tfrac{1}{2}(v_\phi - \bar{v}_\phi)^2. \tag{19}$$

Here $\bar{v}_\phi$ measures the mean azimuthal velocity in the local neighbourhood (which is assumed not to depend on β), and $\boldsymbol{V} = (v_R, v_\phi, v_z)$ are respectively the radial, azimuthal and vertical velocities of a given star measured in a direct cylindrical system of coordinates centred at the Galactic Centre. These velocities are given as a function of the velocities measured in the frame of the Sun by

$$v_\Phi = \frac{1}{R}\{r_\odot \sin(b)\sin(\ell)u_b - r_\odot\cos(b)\sin(\ell)u_r - r_\odot\cos(\ell)u_\ell + r\cos(b)[u_\ell - \sin(\ell)u_\odot] + [r_\odot + r\cos(b)\cos(\ell)]v_\odot\}, \tag{20}$$

$$v_R = \frac{1}{R}\{[r\cos(b) - r_\odot\cos(\ell)]\sin(b)u_b - r_\odot\sin(\ell)u_\ell - \cos(b)[r\cos(b) - r_\odot\cos(\ell)]u_r + r_\odot u_\odot - r\cos(b)\cos(\ell)u_\odot + r\cos(b)\sin(\ell)v_\odot\}, \tag{21}$$

$$v_z = \sin(b)u_r + \cos(b)u_b + w_\odot, \tag{22}$$

where

$$R = \sqrt{r_\odot^2 - 2r_\odot r\cos(b)\cos(\ell) + r^2\cos(b)^2} \quad \text{and}$$

$$z = r\sin(b). \tag{23}$$

R measures the projected distance (in the meridional plane) to the Galactic Centre, while z is the height of the star. Here $u_\odot, v_\odot, w_\odot$ and $r_\odot$ are respectively the components of the Sun's velocity and its distance to the Galactic Centre. The argument of the exponential in equation (18) is a quadratic function in u_r via equations (20)–(22), so the integration over that unknown velocity component is straightforward.

In short, we show in Appendix A that equation (2) has solutions for families of distributions obeying equation (18). Those solutions are unique, and can be made explicit for a number of particular cases which are discussed there. They are shown to be formally equivalent to those found for equation (4). For instance, at large distances from the Galactic Centre ($r_\odot \to \infty$), equation (6) along the plane $\mu_b = 0$ can be recasted into

$$L^2 \cos(b)A_2[b, \ell, \mu_b = 0, L] = \iint \sqrt{\frac{\beta}{2\pi}}\Phi[u^2, \beta] \times \exp(-\beta u^2 x_3 - \beta z_2)u^3 \,\mathrm{d}u\,\mathrm{d}\beta, \quad \text{with} \quad x_3 = \alpha\frac{\sin^2(b)}{L}, \tag{24}$$

and

$$z_2 = \frac{[w_\odot\cos b - (v_\odot - \bar{v}_\phi)\sin b\sin\ell]^2}{2\cos^2(b) + 2\sin^2(b)[\xi_R\cos^2(\ell) + \xi_\phi\sin^2(\ell)]},$$

$$\xi_R = \frac{\beta_z}{\beta_R}, \quad \xi_\phi = \frac{\beta_z}{\beta_\phi}, \tag{25}$$

which is of the form described in Section 2.1.2 with $\nu = 0$, x_3 replacing x, and z_2 replacing y. With the exception of the special cases also described in Appendix A, the solution can be found via χ^2 minimization, as shown below in Section 3.

2.3 Epicyclic model: accounting for density gradients

The above models do not account for any density or velocity dispersion gradients, which is a serious practical shortcoming. Let us therefore construct an epicyclic model for which the radial variation of the potential and the kinematic properties of the Galaxy are accounted for.

A distribution function solution of Boltzmann equation with two integrals of motion (energy and angular momentum) can be written according to Shu (1969) as

$$f_\beta(\boldsymbol{r}, \boldsymbol{u}) = \Theta(H)\frac{\Omega\beta^{3/2}\rho_D}{\sqrt{2}\pi^{\frac{3}{2}}\kappa\sigma_R^2\sigma_z}\exp\left(-\beta\frac{E_R - E_\mathrm{c}}{\sigma_R^2} - \beta\frac{E_z}{\sigma_z^2}\right), \tag{26}$$

where Θ is the Heaviside function, while

$$\Omega = \frac{\kappa}{\sqrt{2\alpha + 2}}, \quad \rho_D = \rho_\odot \exp\left(\frac{R_\odot - R_\mathrm{c}}{R_\rho}\right), \quad \text{with}$$

$$R_\mathrm{c} = H^{\frac{1}{\alpha+1}}R_\odot^{\frac{\alpha}{\alpha+1}}V_\odot^{-\frac{1}{\alpha+1}}, \tag{27}$$

α being the slope of the rotation curve, Ω the angular velocity, κ the epicyclic frequency, ρ_D the density, R_c the radius of the circular orbit of angular momentum H, σ_R^2 and σ_z^2 the square of the radial and vertical velocity dispersion, and β the kinematic index

$$\sigma_R^2 = \sigma_{R_\odot}^2 \exp\left(\frac{2R_\odot - 2R_\mathrm{c}}{R_{\sigma_R}}\right),$$

$$\sigma_z^2 = \sigma_{z\odot}^2 \exp\left(\frac{2R_\odot - 2R_\mathrm{c}}{R_{\sigma_z}}\right),$$

$$E_\mathrm{c} = \frac{\alpha + 1}{2\alpha}H^{\frac{2\alpha}{\alpha+1}}R_\odot^{-\frac{2\alpha}{\alpha+1}}V_\odot^{\frac{2}{\alpha+1}}. \tag{28}$$

Here $\rho_0, \Omega, \kappa, \sigma_R, \sigma_z$ and E_c are known functions of momentum H given by

$$H = r_\odot\cos(b)\sin(\ell)u_r - r_\odot\sin(b)\sin(\ell)u_b - [r\cos(b) - r_\odot\cos(\ell)]u_\ell + r\cos(b)\cos(\ell)u_\odot + [r_\odot - r\cos(b)\cos(\ell)]v_\odot. \tag{29}$$

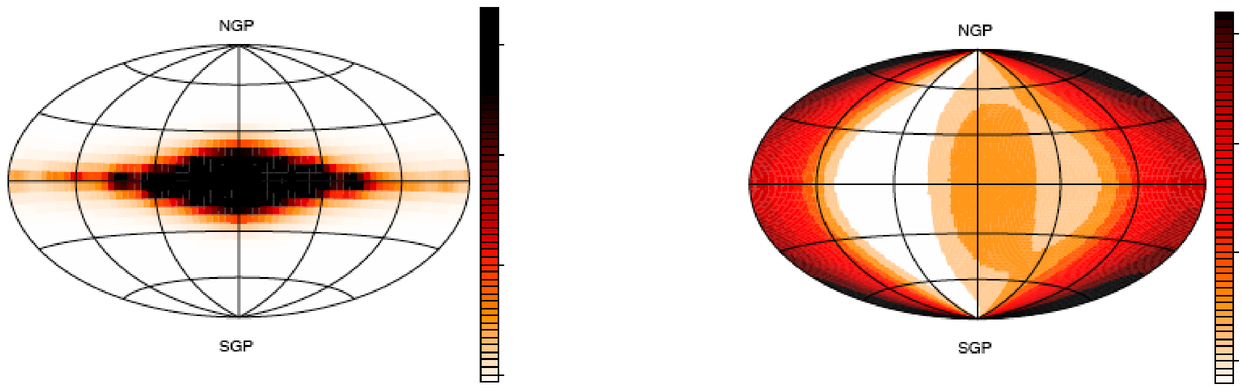

Figure 2. *Left:* Aitoff projection of the normalized density distribution for the epicyclic Shu model. *Right:* Distribution of the maximum of the proper motion along the galactic longitude (in arcsec yr^{-1}). The Galactic Centre is at the centre of the plot, and longitude is increasing from the centre to the left. The asymmetry along the Galactic longitude derives from the peculiar motion of the Sun.

In the case of a separable potential given by

$$\psi(R,z) = \psi_R(R) + \psi_z(z), \quad \text{where} \quad \psi_R(R) = \frac{R^{2\alpha}V_\odot^2 R_\odot^{-2\alpha}}{2\alpha},$$

$$\psi_z(z) = \frac{1}{2\pi G}\left[\Sigma_0\left(\sqrt{z^2+D^2}-D\right) + \rho_{\mathrm{eff}}z^2\right], \tag{30}$$

where G is the universal gravity constant, while Σ_0, ρ_{eff} and D are constants, the energies E_z and E_R obey

$$E_z = \frac{[\sin(b)u_r + \cos(b)u_b + w_\odot]^2}{2} + \psi_z(z), \tag{31}$$

$$E_R = \frac{[\cos(b)u_r - \sin(b)u_b]^2 + u_\ell^2 + u_\odot^2 + v_\odot^2}{2}$$
$$+ \psi_R(R) - \sin(\ell)\{u_\ell u_\odot - [\cos(b)u_r - \sin(b)u_b]v_\odot\}$$
$$+ \cos(\ell)\{[\cos(b)u_r - \sin(b)u_b]u_\odot + u_\ell v_\odot\},$$

while R and z are given by

$$R = \sqrt{r_\odot^2 - 2r_\odot r\cos(b)\cos(\ell) + r^2\cos(b)^2} \quad \text{and}$$

$$z = r\sin(b). \tag{33}$$

Note that the integration over u_r in equation (2) must now be carried numerically, since ρ_0, Ω, κ, $\sigma_\|$ and σ_z are all functions of u_r via equation (29).

This model, based on the epicyclic theory, accounts for density and velocity dispersion gradients, and is therefore more realistic than the Schwarzschild ellipsoid model presented in Section 2.2. The density distribution together with the distribution of the maximum of the proper motion along the ℓ coordinate are presented in Fig. 2 projected on to the sphere. The asymmetry along the Galactic longitude is produced by the solar motion.

3 SIMULATIONS

3.1 Method

We have chosen to implement a non-parametric inversion technique to invert equation (2) or (8). The non-parametric inversion problem is concerned with finding the best solution to equation (2) or (8) for the underlying LF indexed by kinematic temperature when only discrete and noisy measurements of $[Ab, \mu_b, L]$ are available (e.g. Titterington 1985; Dejonghe 1993; Lucy 1994; Merritt, 1996; Fadda, Slezak & Bijaoui 1998, Pichon & Thiébaut 1998; and references therein), and most importantly when we have little prejudice regarding what the underlying LF should be. In short, the non-parametric inversion corresponds to model-fitting in a regime where we do not want to impose (say via stellar evolution tracks) what the appropriate parametrization of the model is. It aims at finding the best compromise between noise and bias; in effect, it correlates the parameters so as to provide the smoothest solution amongst all possible solutions compatible with a given likelihood.

An optimal approach should involve a maximum-likelihood solution parametrized in terms of the underlying six-dimensional distribution. In practice, such an approach turns out to be vastly too costly for data sets involving 10^6 measurements. Binning is therefore applied to our ensemble of $(\ell, b, \mu_\ell, \mu_b, L, B-V)$ measurements.

3.1.1 Non-parametric inversion

The non-parametric solutions of equations (8) and (14) are then described by their projection on to a complete basis of $p \times p$ functions

$$\{e_k(\zeta)e_l(\beta)\}_{k=1,\ldots,p\, l=1,\ldots,p}$$

of finite (asymptotically zero) support, which could be cubic B-splines (i.e., the unique C^2 function, which is defined to be a cubic over four adjacent intervals and zero outside, with the extra property that it integrates to unity over that interval) or Gaussians:

$$\Phi(\zeta,\beta) = \sum_{k=1}^{p}\sum_{l=1}^{p}\Phi_{kl}e_k(\zeta)e_l(\beta), \tag{34}$$

The parameters to fit are the weights Φ_{kl}. Calling $\mathbf{x} = \{\Phi_{kl}\}_{k=1,\ldots p, l=1,\ldots p}$ (the parameters) and $\tilde{\mathbf{y}} = \{L^2\cos(b)\, A(x_i,y_j)\}_{i=1,\ldots n, j=1,\ldots n}$ (the $n\times n$ measurements, with $L^2\cos(\beta)$ a function of x_i, y_i via equation (7)), equation (8) then becomes formally

$$\tilde{\mathbf{y}} = \mathbf{a} \cdot \mathbf{x}, \tag{35}$$

where $\mathbf{a}$ is an $(n, n) \times (p, p)$ matrix with entries given by

$$a_{i,j,k,l} = \left\{ \iint e_k(u^2) e_l(\beta) \exp[-\beta u^2 x_i - \beta \chi(u y_j)] u^3 \, \mathrm{d}u \, \mathrm{d}\beta \right\}_{i,j,k,l}. \tag{36}$$

For the epicyclic model the measurements are $\tilde{\mathbf{y}} = \{A_{ijklm} = A(\ell_i, b_j, \mu_{\ell_k} \mu_{b_l}, L_m)\}_{i=1,\ldots n_1, j=1,\ldots n_2, k=1,\ldots n_3, l=1,\ldots n_4, m=1,\ldots n_5}$ and $\mathbf{a}$ is an $(n_1, n_2, n_3, n_4, n_5) \times (p_1, p_2)$ matrix with entries given by

$$a_{i,j,k,l,m,q,s} = \left\{ \iiint e_q(L_m r^2) e_s(\beta) f_\beta(\ell_i, b_j, \mu_{\ell_k} \mu_{b_l}, r, u_r) r^4 \times \mathrm{d}r \, \mathrm{d}u_r \, \mathrm{d}\beta \right\}_{i,j,k,l,m,q,s}, \tag{37}$$

with f_β given by equation (26).

Assuming that we have access to discrete measurements of A_{ij} (or A_{ijklm} via binning as discussed above), and that the noise in A can be considered to be normal, we can estimate the error between the measured star counts and the non-parametric model by

$$L(\mathbf{x}) \equiv \chi^2(\mathbf{x}) = (\tilde{\mathbf{y}} - \mathbf{a} \cdot \mathbf{x})^\perp \cdot \mathbf{W} \cdot (\tilde{\mathbf{y}} - \mathbf{a} \cdot \mathbf{x}), \tag{38}$$

where the weight matrix $\mathbf{W}$ is the inverse of the covariance matrix of the data (which is diagonal for uncorrelated noise, with diagonal elements equal to one over the data variance).

The decomposition in equation (34) typically involves many more parameters than constraints, such that each parameter controls the shape of the function only locally. The inversion problem corresponding to the minimization of equation (38) is known to be ill-conditioned: Poisson noise induced by the very finite sample of stars may produce drastically different solutions, since these solutions are dominated by artefacts due to the amplification of noise. Some trade-off must therefore be found between the level of smoothness imposed on the solution in order to deal with these artefacts on the one hand, and the level of fluctuations consistent with the amount of information in the data set on the other hand. Finding such a balance is called the 'regularization' of the inversion problem, and in effect implies that between two solutions yielding equivalent likelihood, the smoothest is chosen. In short, the solution of equation (35) is found by minimizing the quantity

$$Q(\mathbf{x}) = L(\mathbf{x}) + \lambda R(\mathbf{x}),$$

where $L(\mathbf{x})$ and $R(\mathbf{x})$ are, respectively, the likelihood and regularization terms given by equation (38) and

$$R(\mathbf{x}) = \mathbf{x}^\perp \cdot \mathbf{K} \cdot \mathbf{x}, \tag{39}$$

where $\mathbf{K}$ is a positive definite matrix, which is chosen so that R in equation (39) should be non-zero when $\mathbf{x}$ is strongly varying as a function of its indices. In practice, we use here

$$\mathbf{K} = \mathbf{K}_3 \otimes \mathbf{I} + \mathbf{I} \otimes \mathbf{K}_3 + 2\mathbf{K}_2 \otimes \mathbf{K}_2,$$

where $\otimes$ stands for the outer product, $\mathbf{I}$ is the identity matrix, and $\mathbf{K_2} = \mathbf{D_2^\perp} \cdot \mathbf{D_2}$, $\mathbf{K_3} = \mathbf{D_3^\perp} \cdot \mathbf{D_3}$. Here $\mathbf{D}_2$ and $\mathbf{D}_3$ are finite difference second-order operators [of dimensions $(p-2) \times p$ and $(p-3) \times p$ respectively] defined by

$$\mathbf{D}_2 = \mathrm{Diag}_2[-1, 2, -1] \equiv \begin{bmatrix} -1 & 2 & -1 & 0 & 0 & \ldots \\ 0 & -1 & 2 & -1 & 0 & \ldots \\ 0 & 0 & -1 & 2 & -1 & \ldots \\ 0 & 0 & 0 & -1 & 2 & \ldots \\ \ldots & \ldots & \ldots & \ldots & \ldots & \ldots \end{bmatrix},$$

$$\mathbf{D}_3 = \mathrm{Diag}_3[1, -3, 3, -1] \equiv \begin{bmatrix} 1 & -3 & 3 & -1 & 0 & \ldots \\ 0 & 1 & -3 & 3 & -1 & \ldots \\ 0 & 0 & 1 & -3 & 3 & \ldots \\ 0 & 0 & 0 & 1 & -3 & \ldots \\ \ldots & \ldots & \ldots & \ldots & \ldots & \ldots \end{bmatrix}, \tag{40}$$

This choice corresponds a quadratic operator whose kernel include planes and paraboloids. The operator $\mathbf{K}$ is typically non-zero [and therefore penalizes the minimization of $Q(\mathbf{x})$] for unsmooth solutions (i.e., those leading to strong variations in the coefficients Φ_{kl}).

The Lagrange multiplier $\lambda > 0$ allows us to tune the level of regularization. The introduction of the Lagrange multiplier λ is formally justified by the fact that we want to minimize $Q(\mathbf{x})$, subject to the constraint that $L(\mathbf{x})$ should be in the range $N_{\mathrm{data}} \pm \sqrt{2N_{\mathrm{data}}}$. In practice, the minimum of

$$Q(\mathbf{x}) = (\tilde{\mathbf{y}} - \mathbf{a} \cdot \mathbf{x})^\perp \cdot \mathbf{W} \cdot (\tilde{\mathbf{y}} - \mathbf{a} \cdot \mathbf{x}) + \lambda \mathbf{x}^\perp \cdot \mathbf{K} \cdot \mathbf{x} \tag{41}$$

is

$$\mathbf{x} = (\mathbf{a}^\perp \cdot \mathbf{W} \cdot \mathbf{a} + \lambda \mathbf{K})^{-1} \cdot \mathbf{a}^\perp \cdot \mathbf{W} \cdot \tilde{\mathbf{y}}. \tag{42}$$

The last remaining issue involves setting the level of regularization. The so-called cross-validation method (Wahba 1990) adjusts the value of λ so as to minimize residuals between the data and the prediction derived from the data. Let us define

$$\tilde{\mathbf{a}}(\lambda) = \mathbf{a} \cdot (\mathbf{a}^\perp \cdot \mathbf{W} \cdot \mathbf{a} + \lambda \mathbf{K})^{-1} \cdot \mathbf{a}^\perp \cdot \mathbf{W}. \tag{43}$$

We make use of the value for λ given by generalized cross validation (GCV) (Wahba & Wendelberger 1979) estimator corresponding to the minimum of

$$\lambda_0 \equiv GCV(\lambda) = \min_\lambda \left\{ \frac{\|(\mathbf{1} - \tilde{\mathbf{a}}) \cdot \tilde{\mathbf{y}}\|^2}{[\mathrm{trace}(\mathbf{1} - \tilde{\mathbf{a}})]^2} \right\}. \tag{44}$$

Note that the model equation (35) is linear and so is equation (42), but this need not be the case when positivity is required. We would then resort to non-linear minimization of equation (41).

3.1.2 Positivity

When dealing with noisy data sets, the non-parametric inversion technique presented above (Section 3.1.1) may produce negative coefficients in the reconstructed LF. In order to avoid such effects, positivity can be imposed on those coefficients Φ_{kl} in equation (34). A simple way to achieve positivity is to use an exponential

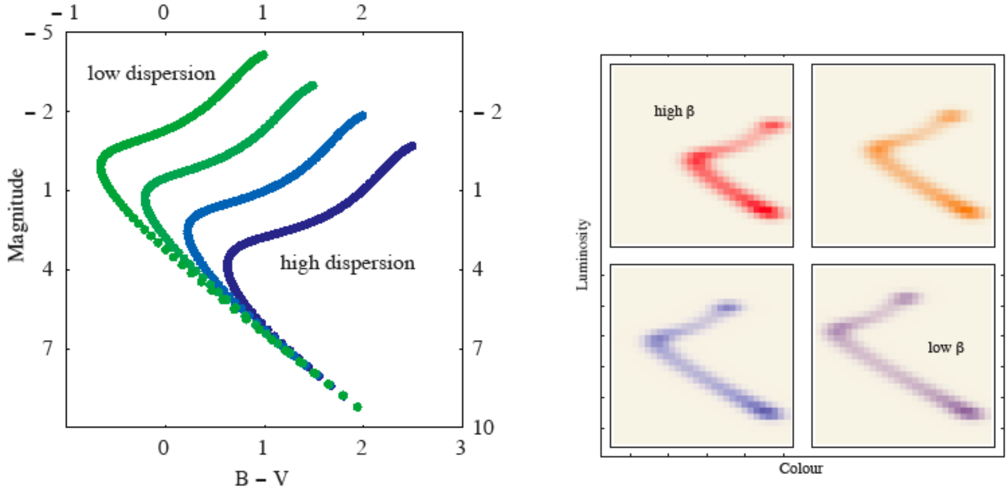

Figure 3. *Left:* Fictitious tracks corresponding to increasing (from left to right) kinematic temperature. *Right:* Decomposition of corresponding colour magnitude diagram into its four components, weighted by the IMF on each track. The image in the observed plane $(\mu_b, b, L, B-V)$ of these tracks is shown in Fig. 4.

transform and introduce φ so that

$$\Phi \equiv \Phi_0 \exp(\varphi), \tag{45}$$

where Φ_0 corresponds to our first guess for Φ (here $\Phi_0{\equiv}10^3$). A first-order Taylor expansion of equation (45), together with equation (35), yields

$$\tilde{\mathbf{y}}'{\equiv}\tilde{\mathbf{y}} - \mathbf{a}\cdot\Phi_0 = \mathbf{a}\cdot\Phi_0\cdot\varphi{\equiv}\mathbf{a}\cdot\mathbf{x}', \tag{46}$$

which defines $\tilde{\mathbf{y}}'$ and $\mathbf{x}'$. We first invert equation (46) for $\mathbf{x}'$. The algorithm is then iterative, and we invert in turn for $\mathbf{x}_n'$

$$\tilde{\mathbf{y}}_n' = \mathbf{a}\cdot\mathbf{x}_n', \quad \text{where} \quad \tilde{\mathbf{y}}_n' = \tilde{\mathbf{y}} - \mathbf{a}\cdot\Phi_{n-1} \quad \text{and} \quad \mathbf{x}_n' = \Phi_{n-1}\cdot\varphi_n;$$

the LF is expressed as

$$\Phi_n = \Phi_{n-1}\exp(\eta_{\rm conv}\mathbf{x}_n'/\Phi_{n-1}) \tag{47}$$

in equation (46) for the iteration number n. In practice, convergence is controlled via a parameter, $\eta_{\rm conv} \in [0, 1]$, which fixes the amplitude of the correction in equation (47) in order to remain within the régime of the Taylor expansion. It should be emphasized that using equation (46) together with equation (42) (replacing $\mathbf{x}$ by $\mathbf{x}'$) does not lead directly to the expected LF but to a correction that has to be applied to Φ_0.

We will now proceed to invert equation (10) in two régimes: the Schwarzschild model described by equation (18), and the epicyclic model given by equation (26). The former model is dimensionally less demanding, while the latter is more realistic, since it accounts for density and velocity dipsertion gradients.

3.2 Simulated Schwarzschild models

We will first focus on the inversion of equation (8), rather than (A5) or (A8) (which were shown to be equivalent in the zero asymmetric drift approximation) and (24) (which was also shown to be of the same form). Special emphasis is put on the toy model described in Section 2.1 while carrying the inversion on a superposition of four kinematically decoupled populations with distinct main sequence turn-off magnitudes. These are illustrated in Fig. 3, which displays the four fictitious tracks corresponding to increasing kinematic temperature weighted by some IMF on each track. The image in the observed plane $(\mu_b, b, L, B-V)$ of these tracks is shown in Fig. 4, which shows isocontours of A^* defined by (corresponding to equation 12 with $c = 3/4$)

$$A^*[b, \mu_b, L] = A[b, \mu_b, L]\cos(b)$$
$$\times \left\{\frac{\gamma\sin^\nu(b)[\mu_b^2\sec^2(b) + 2\alpha\sin^2(b)]}{2L^{\nu/2-5/3}}\right\}^{3/4} \tag{48}$$

in the b,μ_b plane for increasing $B-V$ at a fixed apparent magnitude $L = 1/10$. The multiple kinematic components of the redder sections display distinct extrema for opposite values of μ_b at fixed Galactic latitude, b, and also as a function of b at fixed proper motions. In all figures, γ is chosen equal to 1 (unless specified

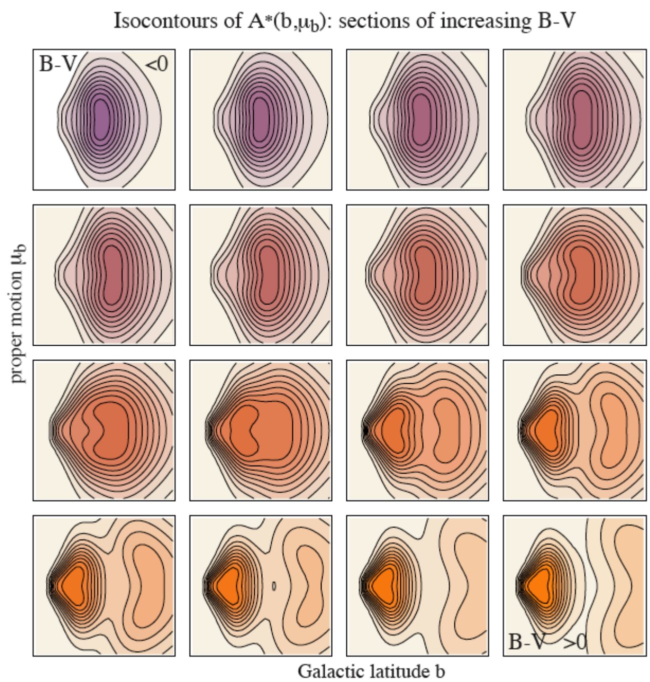

to right and top to bottom) at a fixed apparent magnitude $L = 1/10$ of the model described in Fig. 3. Interestingly, the multiple kinematic components of the redder sections display distinct extrema for opposite values of μ_b at fixed Galactic latitude, b, and also as a function of b at fixed proper motions.

Table 1. Parameters used for the epicyclic model described in Section 2.3.

Distribution function	Potential	Solar motion
$R_\rho = 2.5\,\mathrm{kpc}$	$D = 240\,\mathrm{pc}$	$R_\odot = 8.5\,\mathrm{kpc}$
$R_\rho = 2.5\,\mathrm{kpc}$	$\Sigma_0 = 48\,\mathrm{M_\odot\,pc^{-2}}$	$V_{\mathrm{LSR}} = 220\,\mathrm{km\,s^{-1}}$
$R_{\sigma_R} = 10\,\mathrm{kpc}$	$\rho_{\mathrm{eff}} = 0.0105\,\mathrm{M_\odot\,pc^{-3}}$	$U_\odot = 9\,\mathrm{km\,s^{-1}}$
$R_{\sigma_z} = 5\,\mathrm{kpc}$	$\alpha = -0.1$	$V_\odot = 5.2\,\mathrm{km\,s^{-1}}$
$\sigma_{R_\odot} = 48\,\mathrm{km\,s^{-1}}$		$W_\odot = 7\,\mathrm{km\,s^{-1}}$
$\sigma_{z_\odot} = 24\,\mathrm{km\,s^{-1}}$		
$\rho_\odot = 0.081\,\mathrm{M_\odot\,pc^{-3}}$		

otherwise) and ν equal to 3. For simplicity, we also numerically approximate K_0 in equation (11) by a Gaussian, since the matrix elements in equation (37) are then analytic.

3.3 Simulated epicyclic models

In order to test the inversion procedure, a set of four HR diagrams with different turn-off luminosity was constructed, assuming a mass–luminosity relation (MLR) and a Salpeter initial mass function (IMF). The LF of each population scales like

$$\Phi_0 \propto L^{-\frac{\sigma}{\tau}}, \qquad (49)$$

where τ (the slope of the MLR on a logarithmic scale) was set to 3.2, which is characteristic of the main sequence, and σ to 2.35 (the IMF slope). The scaling factor fixes the number of stars in the simulated galaxy. The tracks associated with those HR diagrams were then binned on a $20 \times 20 \times 4$ grid in the [$L_0, B-V$, *beta*] space; those HR diagrams represent the absolute luminosity function, $\Phi_{B-V}(L_0, \beta)$. The *observed* counts were then computed assuming that each track corresponds to a given kinematic index, and that its distribution can be reproduced by the epicyclic model of the same kinematic index, i.e.,

$$\mathrm{d}N\,(\ell_i, b_j, \mu_{\ell,k}, \mu_{b,l}, L_m, B-V) = a_{i,j,k,l,m,q,s} \times [\Phi_0(B-V)]_{q,s}\,\mathrm{d}\mu_\ell\,\mathrm{d}\mu_b\,\mathrm{d}\ell \cos b\,\mathrm{d}b\,\mathrm{d}L\,\mathrm{d}(B-V), \qquad (50)$$

where $a_{i,j,k,l,m,q,s}$ is given by equation (37). Poisson noise was introduced in corresponding histograms used as input for the inversion procedure. It should be emphasized that constructing such HR diagrams does not challenge the relevance of our physical model, equation (26), but only our ability to recover a given LF. The model LF need not be very realistic at this stage. The parameters of the epicyclic model given in Table 1 were set so as to reproduce the local neighbourhood according to Bienaymé & Séchaud (1997) and Vergely et al. (2001). Fig. 8 shows the assumed and reconstructed HR diagrams for the four populations in the $[L_0, B-V]$ plane for this model, while Fig. 9 shows the reconstruction error in per cent for those two figures.

4 RESULTS

4.1 The Schwarzschild models

The above non-parametric inversion technique was implemented on $19 \times 19 \times 19$ data sets (and up to $41 \times 41 \times 41$) corresponding to measurements in $X, Y, B-V$ (equation 13). For each $B-V$ section, we recover 19×19 (respectively 41×41) coefficients $\mathbf{x}_{ij}$ corresponding to values of U,B, which implies that our resolution in kinematic dispersion is logarithmic. Fig. 5 shows isocontours of the assumed and reconstructed HR diagram as its decomposition in kinematic dispersion. In this zero-noise, no-bias régime, the relative discrepancy between the data and the projection of the model is less than one part in 10^3, while that between the model and the inversion is lower than 10 per cent (the corresponding loss in accuracy is characteristic of non-parametric deconvolution). Note that the wiggly structures are a property of the model, and are well recovered by the inversion procedure. Fig. 6 shows the actual deprojection overlaid on top of the expected contour of the model in the (logarithmic) (β, L) plane for increasing values of $B-V$ (the projection of the fit in data space is not displayed, because residuals of the fit would be too small to be seen). Errors in the deprojection are largest for lower contours. Note that the contours in Fig. 5 correspond to sections of the cube shown in Fig. 6 that are orthogonal to those displayed in Fig. 6.

4.1.1 Errors in measurements and finite sample

The above results were achieved assuming infinite numbers of stars and no truncation in apparent magnitude. The Poisson noise induced by the finite number of stars (for which accurate photometric and kinematic data are available), as well as the actual error in those measurements, are likely to make the inversion of equation (8) troublesome.

Fig. 7 shows how the error in the recovered HR diagram decreases as a function of the signal-to-noise ratio in the data which, for the sake of simplicity, was assumed to be constant while the noise was taken to be Gaussian (corresponding to the large number of stars per bin). Note that in reality the signal-to-noise ratio will clearly be apparent-magnitude-dependent, and distance-dependent (because of extinction and proper motion errors). Fig. 7 also shows how the truncation in apparent magnitude induces a truncation in absolute magnitude (here we truncate in *Y*, since a truncation in *L* induces a truncation in *Y* but none in *X*, given equation 13).

4.2 The epicyclic models

The inversion technique has been implemented over a $36 \times 9 \times 7 \times 7 \times 10 \times 20 \times 4$ model which corresponds to a bin size projected on to the sphere of 10×10 degrees in position sampled linearly, seven bins in proper motion ranging from -0.2 to $0.2\,\mathrm{mas\,yr^{-1}}$, and 20 bins in apparent and absolute luminosity corresponding to an integration over the line of sight from 0.1 pc to 4 kpc (those are also linear bins in luminosity, which correspond to a logarithmic binning in radius). The four kinematic indexes (ranging from 0.8 to 120) were set to reproduce a series of discs with density scaleheights ranging from nearly 200 pc to 1 kpc (i.e., corresponding to thin and thick discs). The mean signal-to-noise ration for these simulation is 2000, ranging from 20 on the giant branches to 70 000 at the bottom of the main sequence.

Fig. 9 shows the reconstruction error in the $[B-V, L_0]$ plane corresponding to the HR diagram shown in Fig. 8. The main sequence and the different turn-off are well reconstructed (the error lies well below 1 per cent for the faint part of the main sequence, and is less than 10 per cent at the turn-offs). The red giant branch (RGB) is also well reproduced, even though it strongly depends on the age of the population (via β). This can be understood if we look at the number of stars in the different regions on the $[B-V, L_0]$ plane. Older (younger) populations have larger (lower) number of stars on the RGB, and the signal-to-noise ratio is increasing (decreasing) correspondingly. We note that the four tracks are recovered without creating any spurious structure. The LFs $\Phi_\beta(L_0)$

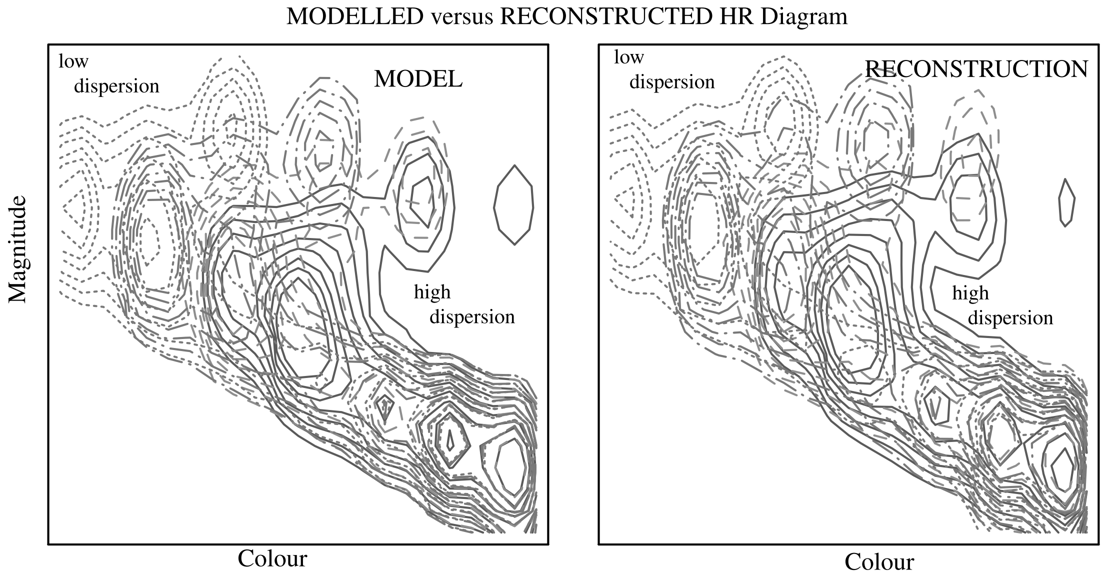

Figure 5. *Left:* assumed and *Right:* reconstructed HR diagram together with its decomposition in kinematic temperature. Note that the wiggly structures are a property of the model, and are well recovered by the inversion procedure. The plain, dashed, dot-dashed, short-dashed curves correspond to the four dispersions associated with the four populations with distinct main-sequence turn-off radii shown in Fig. 3.

are recovered within 1 per cent uncertainty (in mean value) for the oldest population, and within 20 per cent for the youngest (note that sometimes the reconstruction error increases up to 100 per cent when no stars are recovered on the RGB).

5 DISCUSSION AND CONCLUSION

The main result of this paper is a demonstration that the generalized stellar statistic equation including proper motions, equation (2), can be inverted, giving access to both the kinematics and the luminosity function. The inversion was carried for two rather specific functional decompositions of the underlying distribution (namely, constant ratio and possibly singular Schwarzschild ellipsoids plane-parallel models) and a more realistic physical model (the epicyclic Shu model) which accounts for gradients. The inversion assumes that the departure from harmonicity of the vertical potential, and/or the asymmetric drift or the Sun's vertical velocity, $w_\odot$, are known. Indeed, the break in the potential yields a scale which reflects the fact that statistically the dynamics (i.e., the velocities) gives a precise indication of distances in units of that scale. The asymmetric drift or vertical component of the Sun's velocity provides another energy scale (and therefore a distance scale). The existence of more than one distance scale is mathematically redundant, but practically of interest for the purpose of accounting for local and remote stars.

In a nutshell, it was shown in Section 2 that equation (2) has solutions for families of distributions obeying equation (4) (singular ellipsoid) or equation (18) (Schwarzschild ellipsoid). Those solutions are unique, and can be made explicit for a number of particular cases: equation (17) (pin-like velocity ellipsoid), equation (A5) (constant ratio β_R/β_z, $w_\odot \approx 0$), equation (A8) (constant ratio β_R/β_z and β_ϕ/β_z, either with $v_\odot \approx \bar{v}_\phi, w_\odot \approx 0$, or with $v_\odot - \bar{v}_\phi \neq 0$, $w_\odot \neq 0$ and $\chi \approx 0$: statistical secular parallaxes). In all other instances, the solution can be found via the general non-parametric inversion procedure described in Section 3.1.1, the only constraint being the computation of the model matrix generalizing equation (37) (which might require numerical integration, as shown for instance in Section 2.3); in this more general framework it remains also to demonstrate that the inversion will converge towards a solution which is *unique*. For instance, in the régime where the epicyclic model has been tested (Section 3.3) a unique solution seems to be well defined. The LF of each kinematical component is well recovered throughout the HR diagram.

More tests are required before applying the method to real data, and are postponed to a companion paper (Siebert et al., in preparation). For a given vertical potential, it appears that the modelling of star counts indexed by proper motion $A_\lambda(m, \mu_l, \mu_b;$

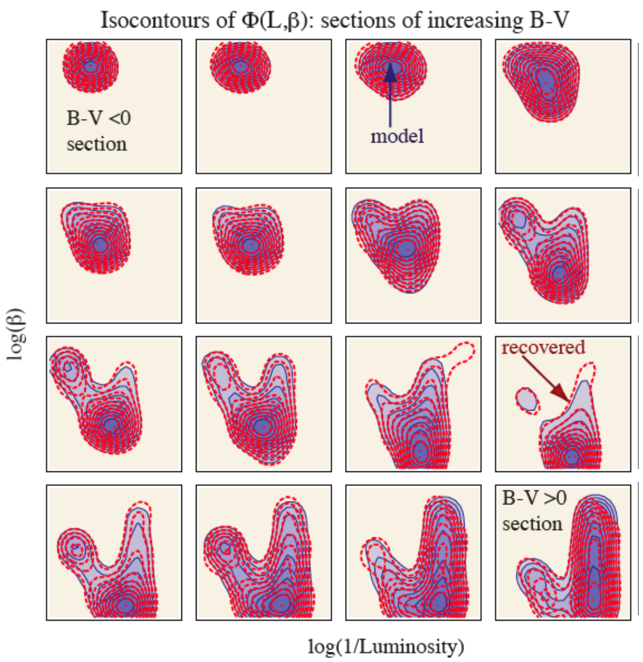

Figure 6. Assumed model (plain line, filled contour) and non-parametric deprojection (dashed line) overlaid on top of the expected contours in the $(\log 1/L, \log \beta)$ plane for increasing $B-V$ sections. Errors in the deprojection are largest for lower contours. Note that these sections are orthogonal to those superposed in Fig. 5.

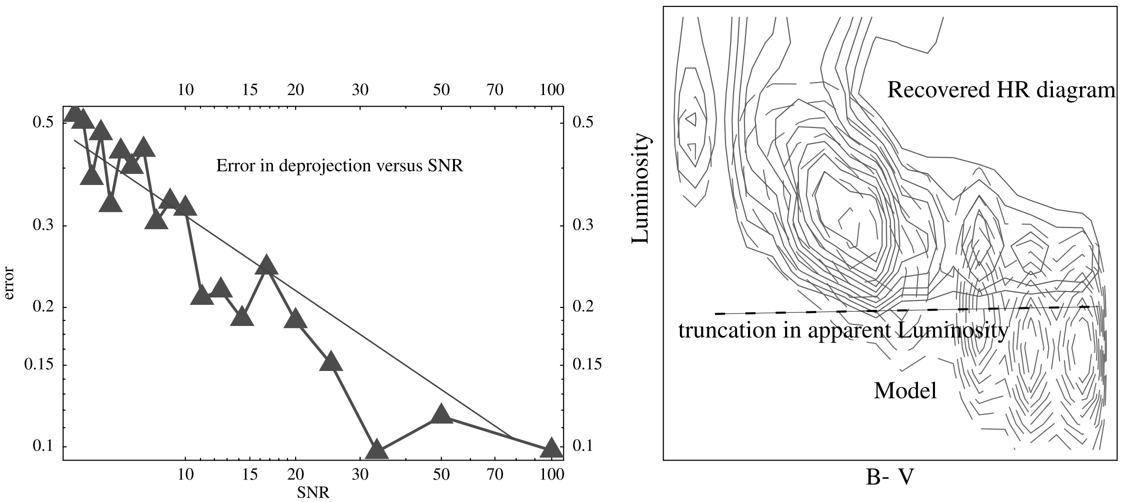

Figure 7. *Left panel:* The mean absolute residual of the luminosity function, $\sum_{ij}|\Phi_{ij}^{\mathrm{recov}} - \Phi_{ij}^{\mathrm{input}}|/\sum_{ij}|\Phi_{ij}^{\mathrm{input}}|$ versus the signal-to-noise ratio in logarithmic coordinates. This graph demonstrates that the non-parametric inversion sketched in Section 3.1.1 is robust with respect to sampling or measurement noise. *Right panel:* The effect of truncation in magnitude on the main sequence: plain line: recovered HR diagram with a truncated data set; dashed line: recovered HR diagram without truncation. As expected, the truncation in apparent magnitude removes the information at the bottom of the main sequence.

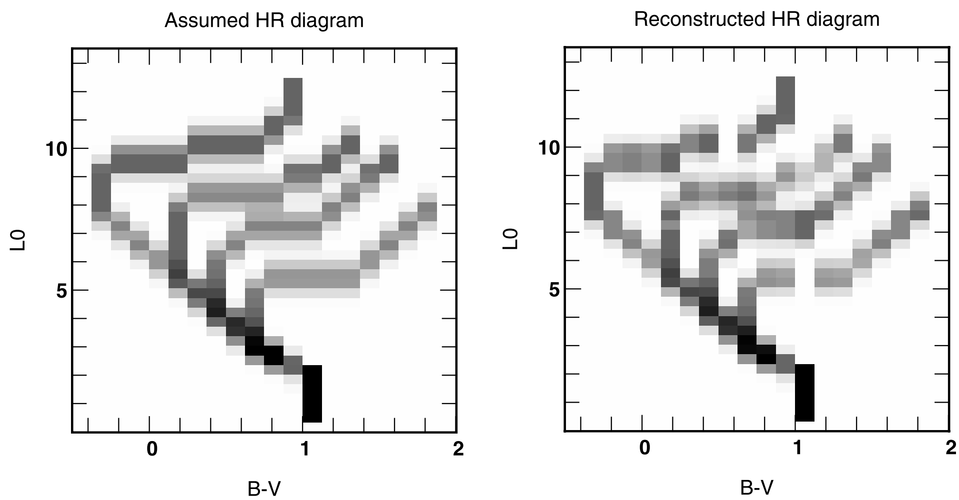

Figure 8. *Left:* Assumed HR diagram for the epicyclic model. The four populations have distinct turn-off point and kinematic index. *Right:* Reconstructed HR diagram. L_0 is expressed in unit of $L_\odot$. Note that all four populations are well recovered. The main sequence and turn-off are reconstructed within 10 per cent error (less than 1 per cent for the lower part of the main sequence due to the large number of stars in that part of the HR diagram). The giant branch is also recovered, although the reconstruction error is higher.

l, b) has a solution for most model parameters. Many different models based on distinct *priors* have produced realistic magnitude and colour star counts, but failed to predict proper motion measurements accurately [for instance, note that the Besançon model – which relies on a nearly dynamical consistent model – produces a good fit to proper motion surveys (Ojha et al. 1994), while dynamically inconsistent models are more problematic (Ratnatunga, Bahcall & Casertano 1989)].

It should be emphasized that the inversion method presented in Section 3.1.1 is a true deconvolution, and should give access to a kinematically indexed HR diagram. Together with some model of the time evolution of the different kinematic components (via, say, a disc-heating mechanism), the indexing could be translated into one on a cosmological time, hence providing a non-parametric measurement of the local neighbourhood LF which is complementary to that obtained by evolutionary track fitting with an assumed IMF and star formation rate (see, e.g., Hernandez, Valls-Gabaud & Gilmore 1999). Note that, conversely, the agreement between the standard direct method to predict the local LF and the method presented here could be used to measure the Galactic potential.

The deepest photometric and proper motion of whole sky survey available is the Tycho-2 catalogue (Høg et al. 2000), which is a new reduction of the Tycho data (Høg et al. 1998). Many Tycho stars are disc giants and subgiants covering a large range of distances; the method developed here can be applied to these stars, and will allow us to recover their LF without any prior information from stellar evolution tracks. We intend in a forthcoming paper to apply the method presented here to the Tycho-2 catalogue (Høg et al. 1998) and to other proper motion catalogues in order to determine the LF of stars in the solar neighbourhood. We will investigate the limitations introduced by a magnitude-limited catalogue, by the finite size of catalogues, and also by our limited knowledge of the Galactic potential. Reddening is also bound to be a concern, since it will bias apparent luminosities as a function of ℓ and b. If

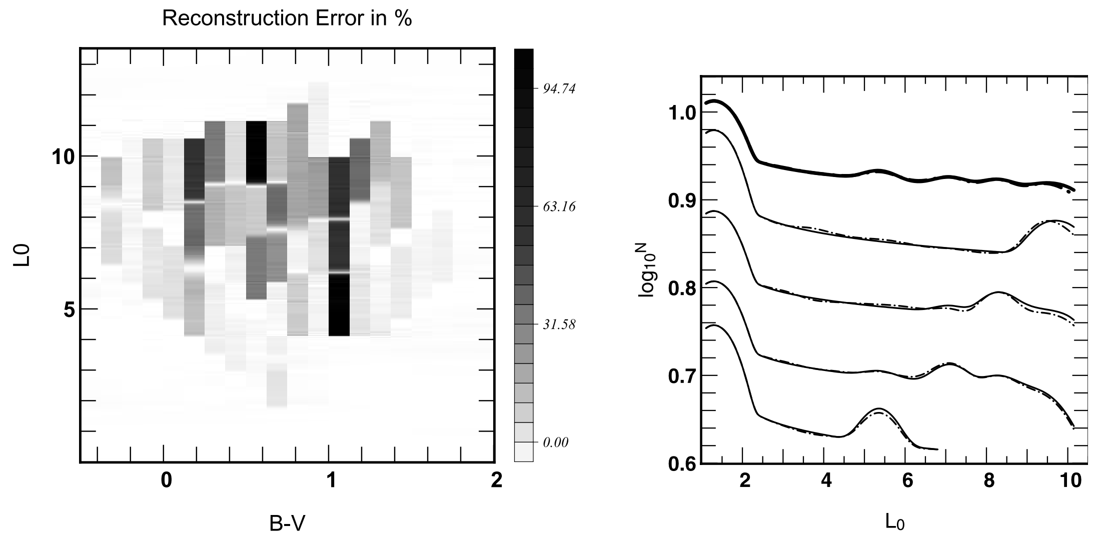

Figure 9. *Left panel:* Reconstruction error in the $[B-V, L_0]$ plane for the epicyclic model shown in Fig. 8. *Right panel:* Model versus recovered luminosity function $\Phi_\beta(L_0)$ for the four kinematic indexes corresponding to the oldest population (lower curve) to the youngest (upper curve). The LFs are plotted on a logarithmic scale and arbitrary normalized. The curves corresponding to the two kinematic index where shifted along the *y*-axis. Plain lines correspond to the model LF, while dot-dashed lines are the reconstructed LF. Note that the LF is well reconstructed for the main sequence (at low luminosity) and for the turn-off. The total LF summed over the kinematic index is also displayed as the top thick lines. The bumps at low and high luminosity are properties of the model and correspond to the lower part of the main sequence and to the subgiant branch of each population.

the reddening is diffuse and the absorbing component law is known, the kernel of e.g., equation (10) will simply be modified accordingly. Alternatively, multicolour photometry could be sufficient to constrain the spatial extinction law. Of course, the dimensionality of the problem is increased by the number of colour bands used, since the analysis must be carried while accounting for all colours simultaneously.

The final error on the recovered LFs will depend on the photometric errors of the observational catalogue (~ 0.1 for the Tycho-2 catalogue down to 0.013 for $V_T < 9$, ~ 0.05–0.10 for photographic surveys). It will also depend on the relative proper motion accuracy [$\delta(m) \sim 2\delta(\mu)/\sigma_\mu$, with σ_μ the typical dispersion for a stellar group at a given distances]. With the Tycho-2 catalogue completed by proper motions (with an accuracy of $2.5\,\mathrm{mas\,y^{-1}}$), and for disc giants with velocity dispersions from 10 to $50\,\mathrm{km\,s^{-1}}$ and proper motion dispersions from 2 to $10\,\mathrm{mas\,y^{-1}}$, the accuracy on the recovered LF will be limited to about 0.5 mag. Closer (and fainter) stars with proper motions from photographic catalogues will constrain the lower part of the LF with a higher accuracy.

In the next decade, sky surveys by the *Fame*, *Diva* and *GAIA* satellites will probe the Galactic structure in superb detail, giving directly access to larger volumes of the 6D stellar phase space of the Galaxy. It will remain that farther out, only proper motions and photometry will have sufficient accuracy and generalization of methods such as that derived here will be used to extrapolate our knowledge of the kinematic and LFs of the Galaxy and its satellites. For instance, Appendix B sketches the possible inversion of an external globular cluster LF with *GAIA*-quality photometry.

ACKNOWLEDGMENTS

We thank J. L. Vergely for early stimulating discussions on this project, and E. Thiébaut for fruitful comments.

REFERENCES

Bahcall J. N., Soneira R. M., Schmidt M., 1983, ApJ, 265, 730
Bienaymé O., Séchaud N., 1997, A&A, 323, 781
Binney J., Merrifield M., 1998, Galactic Astronomy. Princeton Series in Astronomy, Princeton Univ. Press, Princeton
Bok B. J., 1937, The Distribution of Stars in Space. Univ. Chicago Press, Chicago
Buser R., Kaeser U., 1985, A&A, 145, 1
Dejonghe H., 1993, in Dejonghe H., Habing H. J., eds, Proc. IAU Symp. 153, Galactic Bulges. Kluwer, Dordrecht, p. 73
Fadda D., Slezak E., Bijaoui A., 1998, A&AS, 127, 335
Gould A., Flynn C., Bahcall J. N., 1998, ApJ, 508, 798
Haywood M., Robin A. C., Crézé M., 1997a, A&A, 320, 428
Haywood M., Robin A. C., Crézé M., 1997b, A&A, 320, 444
Hernandez X., Valls-Gabaud D., Gilmore G., 1999, MNRAS, 304, 705
Høg E., Kuzmin A., Bastian U., Fabricius C., Kuimov K., 1998, A&A, 335, L65
Høg E. et al., 2000, A&A, 355, L27
Lucy L., 1994, A&A, 289, 983
Merritt D., 1996, AJ, 112, 1085
Mihalas D., Binney J., 1981, Galactic Astronomy: Structure and Kinematics. W. H. Freeman & Company
Ojha D. K., Bienaymé O., Robin A. C., Mohan V., 1994, A&A, 290, 771
Pichon C., Thiébaut E., 1998, MNRAS, 301, 419
Pritchet C., 1983, AJ, 88, 1476
Ratnatunga K. U., Bahcall J. N., Casertano S., 1989, ApJ, 339, 106
Reid I. N., Yan L., Majewski S., Thompson I., Smail I., 1996, AJ, 112, 1472
Robin A., Crézé M., 1986, A&AS, 64, 53
Shu F. H., 1969, ApJ, 158, 505
Titterington D. M., 1985, A&A, 144, 381
Vergely J.-L., Egret D., Köeppen J., Bienaymé O., 2001, A&A, submitted
von Seeliger H. H., 1898, Abh. K. Bayer Akad Wiss Ser II Kl, 19, 564
Wahba G., 1990, Spline models for Observational Data. CBMS-NSF Regional Conf. Ser. App. Mathematics Soc. Industrial and Applied Mathematics, Philadelphia
Wahba G., Wendelberger J., 1979, Monthly Weather Review, 108, 1122

APPENDIX A: ASYMPTOTIC ANALYTIC SOLUTIONS FOR THE SCHWARZSCHILD MODEL

Let us demonstrate that equation (2) has explicit analytic solutions for families of distributions obeying (18), using the inversion procedure sketched in Section 2.1.

A1 Slices towards the Galactic Centre

For the sake of simplicity, let us first restrict the analysis to $u_\odot = v_\odot = w_\odot = 0$ and assume first that we have measurements only in the direction $\ell = 0$. The integration over u_r then yields

$$\int f_\beta(\boldsymbol{r}, \boldsymbol{u})\,\mathrm{d}u_r = \sqrt{\frac{\beta_b \beta_\phi}{4\pi^2}} \times \exp\{-\tfrac{1}{2}[\beta_\phi(u_\ell - \bar{v}_\phi)^2 + \beta_b u_b^2] - \beta_z \psi_z(z)\}, \tag{A1}$$

where

$$\beta_b^{-1} = \beta_R^{-1}\sin^2(b) + \left[\frac{r_\odot - r\cos(b)}{R}\right]^2 \beta_z^{-1}\cos^2(b). \tag{A2}$$

Without loss of generality, let us integrate over u_ℓ:

$$\int\int f_\beta(\boldsymbol{r}, \boldsymbol{u})\,\mathrm{d}u_r\,\mathrm{d}u_\ell = \sqrt{\frac{\beta_b}{2\pi}} \exp[-\tfrac{1}{2}\beta_b u_b^2 - \beta_z \psi_z(z)]. \tag{A3}$$

At large distances from the Galactic Centre, both R and $r_\odot$ are large compared to r, and equation (A2) becomes

$$\bar{\beta}_b^{-1} = \beta_R^{-1}\sin^2(b) + \beta_z^{-1}\cos^2(b). \tag{A4}$$

Let us now also assume that β_R and β_z are known monotonic functions of a unique parameter β. We may now convolve equation (A3) with the LF sought, $\Phi[Lr^2, \beta]$, so that

$$A[b, \mu_b, L] = \int\int \sqrt{\frac{\bar{\beta}_b}{2\pi}} \Phi[Lr^2, \beta] \times \exp\{-\tfrac{1}{2} r^2 \bar{\beta}_b \mu_b^2 - \beta_z \psi_z[r\sin(b)]\} r^3\,\mathrm{d}r\,\mathrm{d}\beta. \tag{A5}$$

Equation (6) appears now as a special case of equations (A4) and (A5) corresponding to $\beta_R \to \infty$. Even though the convolution in equation (A5) is less straightforward than that of equation (8), and so long as ψ_z is not purely harmonic, equation (A5) will have a non-trivial solution for Φ. In particular, if the ratio of velocity dispersions β_R/β_z is assumed constant, equation (8) still holds but with $\beta = \beta_z$, and x replaced by x' defined by

$$x' = \alpha \frac{\sin^2(b)}{L} + \frac{\mu_b^2}{2L\cos^2(b) + \xi 2L\sin^2(b)}, \quad \text{where} \quad \xi = \frac{\beta_z}{\beta_R},$$

with $A'[b, \mu_b, L] = A[b, \mu_b, L]\sqrt{1 + \xi \tan^2(b)}$.

Note that if $v_\odot$ and $w_\odot$ are not negligible, equation (A5) becomes

$$A[b, \mu_b, L] = \int\int \sqrt{\frac{\bar{\beta}_b}{2\pi}} \Phi[Lr^2, \beta] \exp\{-\tfrac{1}{2}\bar{\beta}_b[u_b + \cos(b) w_\odot]^2 - \beta_z \psi_z[r\sin(b)]\} r^3\,\mathrm{d}r\,\mathrm{d}\beta, \tag{A6}$$

and is of the form discussed below as equation (A8) with $\ell = 0$.

A2 Slices away from the Galactic Centre

For any direction $\ell \neq 0$ when $r_\odot \to \infty$, the kinetic dispersion (replacing in equation A4) along Galactic latitude is given by

$$\hat{\beta}_b^{-1} = (\beta_R^{-1}\cos^2\ell + \beta_\Phi^{-1}\sin^2\ell)\sin^2 b + \beta_z^{-1}\cos^2 b,$$

and equation (6) is replaced by

$$A\,[b, \ell, \mu_b, L] = \int\int \sqrt{\frac{\hat{\beta}_b}{2\pi}} \Phi[Lr^2, \beta] \exp\{-\hat{\beta}_b[r\mu_b + \cos(b) w_\odot - \sin(b)\sin(l)(v_\odot - \bar{v}_\phi)]^2 - \beta_z \psi_z[r\sin(b) r^3\,\mathrm{d}r\,\mathrm{d}\beta]\}, \tag{A7}$$

which can be rearranged as (again with $\beta = \beta_z$)

$$L^2\cos(b) A_2[b, \ell, \mu_b, L] = \int\int \sqrt{\frac{\beta}{2\pi}} \Phi[u^2, \beta] \times \exp[-\beta u^2 x_2 + \beta u y_2 - \beta z_2 - \beta\chi(uy)] u^3\,\mathrm{d}u\,\mathrm{d}\beta, \tag{A8}$$

with z_2 given by equation (25),

$$x_2 = \alpha \frac{\sin^2(b)}{L} + \frac{\mu_b^2}{2L\cos^2(b) + 2L\sin^2(b)[\xi_R\cos^2(\ell) + \xi_\phi\sin^2(\ell)]}, \tag{A9}$$

$$y_2 = \frac{\mu_b[(v_\odot - \bar{v}_\phi)\sin b \sin\ell - w_\odot \cos b]}{\sqrt{L}\cos^2(b) + \sqrt{L}\sin^2(b)[\xi_R\cos^2(\ell) + \xi_\phi\sin^2(\ell)]}, \tag{A10}$$

$$A_2[b, \ell, \mu_b, L] = A[b, \mu_b, L] \times \sqrt{1 + \tan^2(b)[\xi_R\cos^2(\ell) + \xi_\phi\sin^2(\ell)]},$$

$$\text{where} \quad \xi_R = \frac{\beta_z}{\beta_R}, \quad \xi_\phi = \frac{\beta_z}{\beta_\phi}. \tag{A11}$$

In the region where the asymmetric drift and the z-component of the Sun's velocity can be neglected, $v_\odot \approx \bar{v}_\phi$ and $w_\odot \approx 0$, y_2 and z_2 vanish and equation (A8) is formally identical to equation (10); once again the solution of equation (A8) is given by equation (17) with the appropriate substitutions. Alternatively, in the regions where either $w_\odot$ or $v_\odot - \bar{v}_\phi$ cannot be neglected, equation (A8) has a unique solution even if $\chi \equiv 0$, which can be found along the section $\mu_b = 0$ (note that when $r_\odot \to \infty$, we can always assume $u_\odot = 0$ by changing the origin of Galactic longitude, ℓ). Indeed, equation (A8) becomes equation (24), which is of the form described in Section 2.1.2 with $\nu = 0$, x_3 replacing x, and z_2 replacing y; the corresponding solution is found by following the same route. It is analogous to statistical secular parallaxes (note, none the less, that the section $\mu_b = 0$ might not be sufficient to carry the inversion without any truncation bias, since $\log(z_2)$ spans $]-\infty, Z[$ when b and ℓ vary with Z as a function of ξ_R, ξ_Φ, $w_\odot$ and $(v_\odot - \bar{v}_\phi)$.

Turning back to equation (A8), it remains true that for more general χ the equation can still be inverted via the kernel, $K_2(x_2, y_2, z_2, y|u, \beta)$, which depends explicitly on χ:

$$K_2\,(x_2, y_2, z_2, y|u, \beta) = \sqrt{\frac{\beta}{2\pi}} \times \exp[-\beta u^2 x_2 + \beta u y_2 - \beta z_2 - \beta\chi(uy)] u^3.$$

Note that the multidimensionality of the kernel, K_2, is not a problem from the point of view of a χ^2 non-parametric minimisation described in Section 3.

APPENDIX B: EXTERNAL SPHERICAL ISOTROPIC CLUSTERS

Consider a satellite of our Galaxy assumed to be well described as a spherical isotropic cluster with an LF indexed by this kinematic temperature. Let $4\pi^2 A_\lambda(\mu_b, L, R)\mu\, d\mu\, dLR\, dR$ be the number of stars which have proper motions, $\mu^2 = \mu_b^2 + \mu_\ell^2$, and apparent luminosity L at radius R from the centre at the wavelength λ. This quantity is a convolution of the distribution function $f(\varepsilon, \beta)$ (a function of energy, ε, and $\beta \equiv 1/\sigma^2$) and the luminosity function, $g_\lambda(L_0, \beta)$, a function of the intrinsic luminosity, L_0, the population, β, and wavelength λ:

$$A_\lambda(\mu, L, R) = \iiint f(\varepsilon, \beta) g_\lambda(\beta, Lr'^2)\, d\beta\, dz\, dv_z, \tag{B1}$$

which can be rearranged as

$$A_\lambda(\mu, L, R) = 4\iiint f(\varepsilon, \beta) g_\lambda(\beta, Lr'^2) \times \frac{r\, dr}{\sqrt{r^2 - R^2}} \frac{d\varepsilon}{\sqrt{2(\psi + \varepsilon) - v^2}} d\beta, \tag{B2}$$

where $v^2 = \mu^2 r'^2$ is the velocity in the plane of the sky, $r'^2 = (r^2 - R^2 + r_\odot^2)$ the distance to the observer, $r_\odot$ the distance to the cluster, and r the distance to the cluster centre. The potential can be derived non-parametrically from the projected density (using Jeans's equation). Indeed, the mass enclosed within a sphere of radius r reads

$$M_{\rm dyn}(< r) = r^2 \frac{d\psi}{dr} = -\frac{r^2}{\rho} \frac{d(\rho\sigma^2)}{dr}, \tag{B3}$$

where $\psi(r)$ is the gravitational potential, $\rho(r)$ the density, and $\sigma(r)$ the radial velocity dispersion. The surface density is related to the density via an Abel transform:

$$\Sigma(R) = \int_{-\infty}^{\infty} \rho(r)\, dz = 2\int_R^\infty \rho(r) \frac{r\, dr}{\sqrt{r^2 - R^2}} \equiv \mathcal{A}_R(\rho), \tag{B4}$$

where $\Sigma(R)$ is the projected surface density, and R the projected radius as measured on the sky. Similarly, the projected velocity dispersion σ_p^2 is related to the intrinsic velocity dispersion, $\sigma^2(r)$, via the *same* Abel transform (or projection)

$$\Sigma(R)\sigma_p^2(R) = 2\int_R^\infty \rho(r)\sigma^2(r) \frac{r\, dr}{\sqrt{r^2 - R^2}} \equiv \mathcal{A}_R(\rho\sigma^2). \tag{B5}$$

Note that $\Sigma(R)\sigma_p^2$ is the projected kinetic energy density divided by 3 (corresponding to one degree of freedom), and $\rho(r)\sigma^2$ the kinetic energy density divided by 3. Inserting equations (B4) and (B5) in equation (B3) yields

$$M_{\rm dyn}(< r) = -\frac{r^2}{\mathcal{A}_r^{-1}(\Sigma)} \frac{d\mathcal{A}_r^{-1}(\Sigma\sigma_p^2)}{dr},$$

$$\text{while} \quad \rho(r) = \frac{1}{4\pi r^2}\frac{d}{dr} M_{\rm dyn}(< r) \quad \text{and} \quad \nabla^2\psi = -4\pi G\rho. \tag{B6}$$

The underlying isotropic distribution is given by an inverse Abel from the density:

$$f(\varepsilon) = \frac{1}{\sqrt{8}\pi^2} \int \frac{d^2\rho}{d\psi^2} \frac{d\psi}{\sqrt{\varepsilon - \psi}} \equiv \int_0^\infty F(\beta) \exp(-\beta\varepsilon)\, d\beta, \tag{B7}$$

where an isothermal decomposition over temperature β was assumed for the distribution function (this assumption is not required: any parametrized decomposition is acceptable). So

$$F(\beta) = \mathcal{L}^{-1}[f(\varepsilon)] = \mathcal{L}^{-1}\{\mathcal{A}^{-1}[\mathcal{A}^{-1}(\Sigma)]\}, \tag{B8}$$

where $\mathcal{L}$ is the Laplace operator.

Calling

$$G[Y] = \int_0^Y \frac{\exp(-X)\, dx}{\sqrt{Y - X}} = \sqrt{\pi}\, \mathrm{Erfi}(\sqrt{Y})\, e^{-Y},$$

$$g_1(\beta, Lr'^2) = g_\lambda(\beta, Lr'^2) F(\beta) \beta^{-3/2}, \tag{B9}$$

equation (B2) becomes

$$A_\lambda(\mu, L, R) = 2\sqrt{2}\int_0^\infty \left[\int_R^\infty G\left\{\beta\left[\frac{\mu^2(r^2 - R^2 + r_\odot^2)}{2} - \psi(r)\right]\right\} \times g_1[\beta, L(r^2 - R^2 + r_\odot^2)] \frac{r\, dr}{\sqrt{r^2 - R^2}}\right] d\beta \tag{B10}$$

where G is a known kernel, while g_λ is the unknown LF sought. Equation (B10) is the direct analogue of equation (8). It will be invertible following the same route with *GAIA* photometry. (With today's accuracy in photometry, for a typical globular cluster at a distance $r_\odot$ of, say, 10 kpc, the relative positions within the cluster are negligible with respect to $r_\odot$: $r^2 - R^2 \ll r_\odot^2$; therefore

$$A_\lambda(\mu, L, R) = 2\sqrt{2}\int_0^\infty \left[\int_R^\infty G\left\{\beta\left[\frac{\mu^2 r_\odot^2}{2} - \psi(r)\right]\right\} \frac{r dr}{\sqrt{r^2 - R^2}}\right] \times g_1(\beta, Lr_\odot^2) d\beta.$$

L is then also mute, and the inversion problem shrinks to one involving finding the relative weights, $g_L[\beta]$ of a known distribution.

This paper has been typeset from a TEX/LATEX file prepared by the author.

Mon. Not. R. Astron. Soc. **326,** 597–620 (2001)

Inversion of the Lyman α forest: three-dimensional investigation of the intergalactic medium

C. Pichon,[1,2,3]★ J. L. Vergely,[1,4] E. Rollinde,[2] S. Colombi[2,3] and P. Petitjean[2,5]

[1]*Observatoire de Strasbourg, 11 rue de l'Université, 67000 Strasbourg, France*
[2]*Institut d'Astrophysique de Paris, 98 bis boulevard d'Arago, 75014 Paris, France*
[3]*Numerical Investigations in Cosmology (NIC), CNRS, France*
[4]*Institute of Astronomy, Madingley Road, Cambridge CB3 0HA*
[5]*UA CNRS 173 – DAEC, Observatoire de Paris-Meudon, F-92195 Meudon Cedex, France*

Accepted 2001 April 17. Received 2001 March 22; in original form 2000 August 7

ABSTRACT

We discuss the implementation of Bayesian inversion methods in order to recover the properties of the intergalactic medium from observations of the neutral hydrogen Lyman α absorptions observed in the spectra of high-redshift quasars (the so-called Lyman α forest). We use two complementary schemes: (i) a constrained Gaussian random field linear approach, and (ii) a more general non-linear explicit Bayesian deconvolution method, which offers in particular the possibility to constrain the parameters of the equation of state for the gas.

The interpolation ability of the first approach is shown to be equivalent to the second one in the limit of negligible measurement errors, low-resolution spectra and null mean prior.

While relying on prior assumption for the two-point correlation functions, we show how to recover, at least qualitatively, the three-dimensional topology of the large-scale structures in redshift space by inverting a suitable network of adjacent, low-resolution lines of sight. The methods are tested on regular bundles of lines of sight using *N*-body simulations specially designed to tackle this problem.

We also discuss the inversion of single lines of sight observed at high spectral resolution. Our preliminary investigations suggest that the explicit Bayesian method can be used to derive quantitative information on the physical state of the gas when the effects of redshift distortion are negligible. The information in the spectra remains degenerate with respect to two parameters (the temperature scale factor and the polytropic index) describing the equation of state of the gas.

Redshift distortion is considered by simultaneous constrained reconstruction of the velocity and the density field in real space, while assuming statistical correlation between the two fields. The method seems to work well in the strong prior régime where peculiar velocities are assumed to be the most likely realization in the density field. Finally, we investigate the effect of line-of-sight separation and number of lines of sight. Our analyses suggest that multiple low-resolution lines of sight could be used to improve the most likely velocity reconstruction on a high-resolution line of sight.

Key words: methods: data analysis – methods: *N*-body simulations – methods: statistical – intergalactic medium – quasars: absorption lines – dark matter.

1 INTRODUCTION

It has been realized recently that the cosmological mass density of the baryons located in the intergalactic medium (IGM) at high redshift is similar to the total cosmological mass density of baryons predicted by primordial nucleosynthesis theories (Meiksin & Madau 1993; Petitjean

★E-mail: pichon@astro.u-strasbg.fr

hydrogen density, $n_{\mathrm{H\,I}}$, by

$$\tau_\ell(w) = \frac{c\sigma_0}{H(\bar{z})\sqrt{\pi}} \int\int\left[\int_{-\infty}^{+\infty} \frac{n_{\mathrm{H\,I}}(x, \boldsymbol{x}_\perp)}{b(x, \boldsymbol{x}_\perp)} \exp -\left\{-\frac{[w - x - v_{\mathrm{p}}(x, \boldsymbol{x}_\perp]^2}{b(x, \boldsymbol{x}_\perp)^2}\right\} \mathrm{d}x\right] \delta_{\mathrm{D}}(\boldsymbol{x}_\perp - \boldsymbol{x}_{\perp,\ell})\, \mathrm{d}^2\boldsymbol{x}_\perp, \quad \ell = 1 \ldots L, \tag{1}$$

where σ_0 is the effective cross-section for resonant line scattering, $H(\bar{z})$ is the Hubble constant at mean redshift $\bar{z}$, and $v_{\mathrm{p}}(x)$ is the projection of the peculiar velocity along the LOS. The double sum over $\boldsymbol{x}_\perp$ corresponds to the integration in the directions perpendicular to the LOSs. δ_{D} is the 2D Dirac distribution. The Doppler parameter $b(\boldsymbol{x})$ is considered a function of the local temperature of the IGM at point $\boldsymbol{x} \equiv (x, \boldsymbol{x}_\perp)$ where x is the real-space coordinate expressed in km $^{-1}[= rH(\bar{z})]$.

This work is concerned with assessing the inversion of equation (1) with the aim of constraining the 3D fields, $n_{\mathrm{H\,I}}(x, \boldsymbol{x}_\perp)$, $b(x, \boldsymbol{x}_\perp)$ and $v_{\mathrm{p}}(x, \boldsymbol{x}_\perp)$, from the knowledge of a bundle of LOSs, $\ell = 1 \ldots L$.

2.1 The model

To relate the gas density, the dark matter (DM) density and the temperature, we follow the prescriptions of Hui & Gnedin (1997). We refer to this paper for a detailed derivation of the relations given below. We assume that baryons trace DM potential (Bi & Davidsen 1997) and are in ionization equilibrium. Therefore

$$n_{\mathrm{H\,I}} \propto \rho_{\mathrm{DM}}^2 T^{-0.7}, \tag{2}$$

where $n_{\mathrm{H\,I}}$ is the neutral hydrogen particle density, and ρ_{DM} the dark matter density.

Considering that shock heating is unimportant for the thermal budget of the intergalactic gas (Hui & Gendin 1997), an effective equation of state describes the physical state of the gas,

$$T(\boldsymbol{x}) = \bar{T}\left[\frac{\rho_{\mathrm{DM}}(\boldsymbol{x})}{\bar{\rho}_{\mathrm{DM}}}\right]^{2\beta}. \tag{3}$$

The parameter β is in the interval $0 < \beta < 0.31$ (this upper bound corresponds to the asymptotic value at $z = 0$ far from re-ionization). Therefore

$$n_{\mathrm{H\,I}}(\boldsymbol{x}) = \bar{n}_{\mathrm{HI}}\left[\frac{\rho_{\mathrm{DM}}(\boldsymbol{x})}{\bar{\rho}_{\mathrm{DM}}}\right]^{\alpha} \quad \text{with a scaling} \quad \alpha = 2 - 1.4\beta. \tag{4}$$

If there is no turbulence, then the Doppler parameter $b(x)$ at each position is due to thermal broadening only,

$$b(\boldsymbol{x}) = 13\,\mathrm{km\,s^{-1}}\sqrt{\frac{\bar{T}}{10^4\,\mathrm{K}}\left[\frac{\rho_{\mathrm{DM}}(\boldsymbol{x})}{\bar{\rho}_{\mathrm{DM}}}\right]^{\beta}}, \tag{5}$$

and equation (1) becomes

$$\tau_\ell(w) = A(\bar{z})c_1 \int\int\int_{-\infty}^{+\infty} \left[\frac{\rho_{\mathrm{DM}}(x, \boldsymbol{x}_\perp)}{\bar{\rho}_{\mathrm{DM}}}\right]^{\alpha-\beta} \exp\left\{-c_2 \frac{[w - x - v_{\mathrm{p}}(x, \boldsymbol{x}_\perp)]^2}{[\rho_{\mathrm{DM}}(x, \boldsymbol{x}_\perp)/\bar{\rho}_{\mathrm{DM}}]^{2\beta}}\right\} \mathrm{d}x\, \delta_{\mathrm{D}}(\boldsymbol{x}_\perp - \boldsymbol{x}_{\perp,\ell})\, \mathrm{d}^2\boldsymbol{x}_\perp. \tag{6}$$

The parameters c_1 and c_2 depend on the characteristic temperature of the IGM:

$$c_1 = \left(13\sqrt{\pi}\sqrt{\frac{\bar{T}}{10^4}}\right)^{-1}, \quad c_2 = \left(13^2 \frac{\bar{T}}{10^4}\right)^{-1} \quad \text{and} \quad A(\bar{z}) = \bar{n}_{\mathrm{H\,I}} \frac{c\sigma_0}{H(\bar{z})} \propto \frac{\bar{T}^{-0.7}}{J}, \tag{7}$$

where J is the ionizing flux, assumed to be uniform. Here the temperatures are given in Kelvin. The value of $A(\bar{z})$ is fixed by matching the observed average optical depth ($\simeq 0.2$ at $\bar{z} = 2$).

2.2 The régimes of interest for the reconstruction

Several régimes will be considered in Section 5 when performing the inversion.

(i) *Small scales or high resolution* ($\ell \lesssim 0.1$ Mpc) : In this régime, and although it might not necessarily be a good approximation (e.g. Hui et al. 1997), we simply assume that redshift distortion is negligible ($v_{\mathrm{p}} = 0$ in equation 6), and reconstruct the density field in redshift space while constraining the equation of state.

(ii) *Large scales or low resolution* ($\ell \gtrsim 1$ Mpc) : In this régime, applicable to low-resolution spectra, thermal broadening can be neglected and equation (1) simply becomes

$$\tau_\ell(w) = A(\bar{z}) \int\int \left[\frac{\rho_{\mathrm{DM}}\{w - v_{\mathrm{p}}[x(w, \boldsymbol{x}_\perp)], \boldsymbol{x}_\perp\}}{\bar{\rho}_{\mathrm{DM}}}\right]^{\alpha} \delta_{\mathrm{D}}(\boldsymbol{x}_\perp - \boldsymbol{x}_{\perp,\ell})\, \mathrm{d}^2\boldsymbol{x}_\perp, \quad \text{for } \ell = 1 \ldots L, \tag{8}$$

et al. 1993; Press & Rybicki 1993; Rauch et al. 1997; Valageas, Schaeffer & Silk 1999). Therefore there is probably a close interplay between galaxy formation and IGM evolution. The IGM acts as the baryonic reservoir for galaxy formation, while star formation activity in forming galaxies should influence the physical state of the IGM through metal enrichment and emission of ionizing radiation. Hence it would be of primary interest to be able to correlate the spatial distribution of intergalactic gas with that of galaxies.

Neutral hydrogen in the IGM is revealed by the numerous absorption lines seen in QSO spectra (the so-called Lyman α forest). The physics of the gas is remarkably simple: its thermal state is governed by photoionization heating and adiabatic cooling (e.g. Hui & Gnedin 1997; Weinberg 1999), and its dynamics results from the effects of gravity on large scales and pressure smoothing on small scales (Reisenegger & Miralda-Escudé 1995; Bi & Davidsen 1997; Hui, Gnedin & Zhang 1997). Dark matter and baryons trace each other quite well, and the Lyman α forest is due to mildly overdense fluctuations in a pervasive medium with density contrasts of the order of 1 to 10. The gas should be distributed along filaments and/or sheets of significant extension.

This is supported by observations of multiple lines of sight (LOSs) showing that the gaseous complexes producing the Lyman α forest have large sizes. Indeed, in the spectra of multiple images of lensed quasars with separations of the order of a few arcsec (Smette et al. 1995; Impey et al. 1996), the Lyman α forests appear nearly identical, implying that the absorbing objects have sizes $> 50\,h_{75}^{-1}$ kpc.[1] Pairs with separation up to $500\,h_{75}^{-1}$ kpc show an excess of absorptions common to both LOSs compared to what is expected for an uncorrelated distribution of absorption lines (Dinshaw et al. 1995; Crotts & Fang 1998; D'Odorico et al. 1998; Petitjean et al. 1998). This suggests rather large dimensions or better coherence length and a non-spherical geometry of the absorbing structures (Rauch & Haehnelt 1995).

Recent *N*-body simulations have provided a consistent theoretical framework for the description of the IGM (Cen et al. 1994; Petitjean, Mücket & Kates 1995; Zhang, Anninos & Norman 1995; Hernquist et al. 1996; Miralda-Escudé et al. 1996; Mücket et al. 1996; Bond & Wadsley 1998). The simulations are very successful at reproducing the main characteristics of the Lyman α forest: the column density distribution, the Doppler parameter distribution, the flux decrement distribution and the redshift evolution of absorption lines. It has become clear that the Lyman α forest is a powerful tool to investigate key cosmological issues such as the re-ionization of the Universe (Abel & Haehnelt 1999; Schaye et al. 1999; Ricotti, Gneden & Shull 2000), the density fluctuation power spectrum (Croft et al. 1998; Gnedin & Hui 1998; Hui 1999; Nusser & Haehnelt 1999a), the geometry of the Universe (Hui, Stebbins & Burles 1999) or cosmological parameters (Weinberg et al. 1999).

Applications to real data have led to interesting constraints on the fluctuation power spectrum (Croft et al. 1999; Nusser & Haehnelt 1999b), cosmological parameters (Weinberg et al. 1999; Theuns, Schaye & Haehnelt 2000) or the physical characteristics of the gas (Schaye et al. 1999). However, these studies are presently limited by the amount of information available, and show that it is important to increase current LOS data sets.

Two approaches can be considered: (i) increasing the number of LOSs observed at intermediate and high spectral resolution in order to improve the precision of the above measurements; large redshift surveys in progress or in preparation such as the Sloan Digital Sky Survey (SDSS; e.g. Szalay 2000) the Two degree Field (2dF; e.g. Folkes et al. 1999) or the VIRMOS redshift survey (e.g. Le Fèvre et al. 1998) should dramatically increase the number of low spectral resolution QSO spectra available for analysis; (ii) using groups of QSOs to constrain the three-dimensional (3D) distribution of the gas and to study redshift-space distortion effects, taking into account peculiar velocities in the reconstruction; the ultimate goal would be to increase the density of LOSs so that the reconstructed 3D spatial distribution of the gas can be correlated with galaxies observed in the same field; the deep imaging surveys planned with MEGACAM (e.g. Boulade et al. 1998) at the Canada-France-Hawaii Telescope and follow-up spectroscopy should provide data for such projects.

It is thus of first importance to prepare the tools needed for the interpretation of the wealth of data that will be provided by the planned surveys. Nusser & Haehnelt (1999a) have described a method for the recovery of the real-space density distribution along one LOS. Using an analytical model of the IGM, they propose a direct inversion of the Lyman α forest seen in the QSO spectra using an iterative scheme based on Lucy's deconvolution method (Lucy 1974). This method yields fields for the density in contrast to Voigt profile decomposition.

Here we show that these techniques can be generalized to multiple LOSs to reconstruct the 3D density field (see Vergely et al. 2001 for a similar application to the 3D mapping of the local interstellar medium). This should help for characterizing the structures (filaments, sheets…), determining physical properties of the gas (temperature, peculiar velocity) and discussing the cosmological evolution of the IGM.

This paper is organized as follows. In Section 2 we present basic equations describing the relationship between absorption along LOSs and properties of the IGM. Section 3 is concerned with sketching the basis for the inversion technique; two methods are described, a Bayesian regularized inverse method and a constrained random Gaussian field reconstruction, which can actually be seen as a particular case of the first method.Section 4 describes two *N*-body simulations from which we construct simulated data. Section 5 discusses the use of inversion techniques implemented here (i) to recover the 3D spatial distribution of the IGM from Lyman α forest absorption lines on large scales while neglecting thermal broadening, (ii) to address the issue of thermal broadening on small scales, and (iii) to take into account peculiar velocities and correction for the induced redshift distortions.

2 THE LYMAN-α OPTICAL DEPTH ALONG A LINE OF SIGHT

The optical depth, $\tau_\ell(w)$, along the LOS ℓ, at projected position $\boldsymbol{x}_{\perp,\ell} \equiv (y_\ell, z_\ell)$ on the sky, and in velocity space, w, is related to neutral

[1] where h_{75} is the Hubble constant expressed in units of $75\,\mathrm{km\,s^{-1}\,Mpc^{-1}}$.

where $x(w, \boldsymbol{x}_\perp)$ is defined implicitly by the equation $x = w - v_\mathrm{p}(x, \boldsymbol{x}_\perp)$. Our efforts in this régime will focus on 3D reconstruction of the density in redshift space, i.e., with $v_\mathrm{p} = 0$ in equation (8) and known equation of state for the gas. In principle, redshift distortion should not be neglected, but this does not change significantly the topology of large-scale structures, at least at weakly non-linear scales, thus making such simplified analysis still relevant.

(iii) *Intermediate scales or intermediate resolution* ($0.1 \lesssim \ell \lesssim 1\,\mathrm{Mpc}$) : Redshift distortion will not be neglected anymore, and equation (6) will be used to determine simultaneously the density and velocity fields, assuming that the effective equation of state is known.

Note that we neglect here the statistical scatter away from equation (3) and in particular the departure from a unique power law for larger overdensities.

3 DECONVOLUTION OF THE IGM

The basic idea is to interpolate between adjacent LOSs the fields which are measured along the LOSs. This first requires assumptions on the nature of the fields. In fact, strictly speaking, our ability to say anything away from the LOSs could be questioned, since to the best of our unbiased knowledge, space between the LOSs could well be empty. Moreover, the inversion of equation (1) is obviously not unique, and additional assumptions must be made in order to reduce the parameter space. For example, the Doppler parameter and/or the peculiar velocity fields are taken to be described by a simple function of the sought density field, $n_{\mathrm{H\,I}}$. Indeed, dynamical considerations supported by numerical simulations suggest there exists a statistical relationship between overdensities and the corresponding projected velocity field, while temperature and density are also statistically related by an equation of state.

This paper addresses these issues via two techniques.

(i) A general, explicit Bayesian deconvolution method (Section 3.1), capable of dealing with fields and priors such as a given equation of state. This method should allow one to deconvolve thermal broadening non-linearly, while accounting for peculiar velocities, and therefore to reconstruct the density/velocity field along a LOS and constrain the equation of state of the gas. With several LOSs, it should simultaneously be possible to obtain the 3D density field.

(ii) A constrained Gaussian random field linear approach (Section 3.2), which relates the peculiar velocities projected along the LOS to the 3D density field, or directly the 3D density field to the LOS density in redshift space. It requires prior knowledge of the logarithm of density in redshift space along each LOS, but can be used after applying method (i) to each LOS.

In fact, method (i) is very general and can be applied in many ways, which differ mainly in the priors taken for the statistical properties of the density and velocity fields. Method (ii) corresponds to a given choice of strategy for the 3D density/velocity reconstruction step: like Wiener filtering, it is a particular case of method (i) (Section 3.3).

3.1 A non-parametric explicit Bayesian regularized inverse method

We aim to invert equation (1), i.e., reconstruct the density field $n_{\mathrm{H\,I}}$ and the velocity field $v_\mathrm{p}(x, \boldsymbol{x}_\perp)$. To that end, we take a *model*, g, such as equations (3)–(5), which basically relate the Doppler parameter b and the gas density $n_{\mathrm{H\,I}}$ to the dark matter density, ρ_{DM}, and obtain equation (6). In this equation, there are a certain number of *parameters* to be determined, which can be continuous fields such as the DM density or the velocity field, or discrete parameters such as α and β. This set of parameters can be formally described as a vector, $\boldsymbol{M}$. The goal here is to determine $\boldsymbol{M}$ by fitting the data, $\boldsymbol{D}$, i.e., the absorption spectra along the N LOSs.

Since the problem is underdetermined, we use a Bayesian technique described in Tarantola & Valette (1982a; see also, e.g., Craig & Brown 1986 and Pichon & Thiébaut 1998). In order to achieve regularization, this method requires a prior guess for the parameters, or in statistical terms, their probability distribution function, $f_{\mathrm{prior}}(\boldsymbol{M})$.

Using Baye's theorem, the conditional probability density $f_{\mathrm{post}}(\boldsymbol{M}|\boldsymbol{D})$ for the realization $\boldsymbol{M}$ given the observed data $\boldsymbol{D}$ then writes:

$$f_{\mathrm{post}}(\boldsymbol{M}|\boldsymbol{D}) = \mathcal{L}(\boldsymbol{D}|\boldsymbol{M}) f_{\mathrm{prior}}(\boldsymbol{M}), \tag{9}$$

where $\mathcal{L}$ is the likelihood function of the data given the model.

If we assume that both functions $\mathcal{L}$ and f_{prior} are Gaussian, we can write

$$f_{\mathrm{post}}(\boldsymbol{M}|\boldsymbol{D}) = \mathcal{A} \exp\left\{ -\frac{1}{2}[\boldsymbol{D} - g(\boldsymbol{M})]^\perp \cdot \mathbf{C}_\mathrm{d}^{-1} \cdot [\boldsymbol{D} - g(\boldsymbol{M})] - \frac{1}{2}(\boldsymbol{M} - \boldsymbol{M}_0)^\perp \cdot \mathbf{C}_0^{-1} \cdot (\boldsymbol{M} - \boldsymbol{M}_0) \right\}, \tag{10}$$

with $\mathbf{C}_\mathrm{d}$ and $\mathbf{C}_0$ being respectively the covariance 'matrix'[2] of the observed noise and of the prior guess for the parameters, $\boldsymbol{M}_0$. $\mathcal{A}$ is a normalization constant. The superscript, $\perp$, stands for transposition. The first argument of the exponential in equation (10) corresponds to the likelihood of the data, given the model and the parameters,[3] while the last corresponds to the likelihood of the parameters, given the prior $\boldsymbol{M}_0$. Note that the assumption of a Gaussian field for f_{prior} could be lifted, in particular to account for the presence of contrasted filaments (i.e., we could introduce three-point correlation functions, or higher order statistics to account for the fact that, say, the prior likelihood of aligned

[2]Formally defined on continuous + discrete fields, as is the vector $\boldsymbol{M}$.

[3]Note that the model g taken here would correspond to equation (6) instead of equations (3)–(5) as said earlier.

overdensities is higher). A possible method for maximizing the posterior probability given in equation (10) is sketched in Appendix A. In a nutshell, the minimum, $\langle \boldsymbol{M} \rangle$, of the argument of the exponential in equation (10) is shown by a simple variational argument (Tarantola & Valette 1982a,b) to obey the implicit equation

$$\langle \boldsymbol{M} \rangle = \boldsymbol{M}_0 + \mathbf{C}_0 \cdot \mathbf{G}^{\perp} \cdot (\mathbf{C}_\mathrm{d} + \mathbf{G} \cdot \mathbf{C}_0 \cdot \mathbf{G}^{\perp})^{-1} \cdot (\boldsymbol{D} + \mathbf{G} \cdot (\langle \boldsymbol{M} \rangle - \boldsymbol{M}_0) - g(\langle \boldsymbol{M} \rangle)), \tag{11}$$

where $\mathbf{G}$ is the matrix (or, more rigorously, the functional operator) of partial derivatives of the model $g(\boldsymbol{M})$ with respect to the parameters. Note that, under the assumption of Gaussianity, the extremum $\langle \boldsymbol{M} \rangle$ is at the same time the most likely constrained value of the parameters vector and its mean value. The posterior covariances of the parameters, $\mathbf{C}_{\boldsymbol{M}}$, can be computed from equation (A6).

The method can in principle be iterated, taking in equation (11) $\boldsymbol{M}_0 = \boldsymbol{M}$ and $\mathbf{C}_0 = \mathbf{C}_{\boldsymbol{M}}$ to compute a new value of $\boldsymbol{M}$ until possible convergence. However, in this paper we did not test this procedure.

We might then wonder how the choice of the prior for the parameters, $\boldsymbol{M}_0$ and their covariance matrix, $\mathbf{C}_0$, affect the final result, $\langle \boldsymbol{M} \rangle$. We will show in Section 3.3 that for null prior, $\boldsymbol{M}_0 = 0$, the method proposed here is equivalent to Wiener filtering if the model is linear [$g(\boldsymbol{M}) = \mathbf{G}.\boldsymbol{M}$]. However, we may include more prior information when possible. For instance, if in the field of interest, redshifts of galaxies and clusters, gravitational lensing or SZ data, etc., is available, we may explicitly incorporate these additional constraints in the prior $\boldsymbol{M}_0$ instead of extending the data set, $\boldsymbol{D}$. More realistic expressions accounting for the statistical scatter around equation (3) and a possible slope break are also possible. Additional information about our prejudice on the evolution of large-scale structures can also be incorporated in the description of the prior probability distribution function to account for, say, dynamically induced non-Gaussianity.

3.2 Constrained mean field reconstruction

In principle, the explicit Bayesian method described above can be applied to the data to reconstruct along each LOS the density field in redshift space while constraining the equation of state, as illustrated in Section 5.3. When dealing with the large-scale régime of Section 2.2, equation (8) applies, and the density contrast, defined by

$$\delta(x) \equiv \log(\rho_\mathrm{DM}/\bar{\rho}_\mathrm{DM}) \approx (\rho_\mathrm{DM} - \bar{\rho}_\mathrm{DM})/\bar{\rho}_\mathrm{DM}, \tag{12}$$

reads, along each LOS and in redshift space ($x = w$),

$$\delta_\ell(x, \boldsymbol{x}_\perp) = \frac{1}{\alpha} \log\left[\frac{\tau_\ell(x)}{A(\bar{z})}\right]. \tag{13}$$

This section focuses on recovering the 3D density field in redshift space or in real space, the latter case requiring treatment of peculiar velocities. To achieve that, we use a constrained mean field method (e.g. Hoffman & Ribak 1992). Broadly speaking, such a method assumes that part of a model (here the density in redshift space along the LOSs) is fixed by the observations. It then provides the relation between these 'data' and the most likely value of the remaining part of the parameters (here the density between the LOSs and the full 3D velocity field). This method requires some assumptions on the statistical properties of the searched fields. The idea is to consider large enough scales so that non-linear effects have not driven the system dynamically too far away from its initial conditions, which we assume to be Gaussian-distributed.[4] The theory of constrained random Gaussian fields is well known (e.g. Rice 1944, 1945; Longuet-Higgins 1957; Adler 1981; Bardeen et al. 1986, and references therein), and application to our problem is detailed in Appendix B.

We assume that the constraints are distributed along a bundle of L LOSs, i.e., that the density contrast (defined above in equation 12) takes the values $[\delta_\ell(x)]_{\ell=1\ldots L}$ along the LOSs. Then, using linear perturbation theory and the Gaussian nature of underlying fields, we can write the probability distribution function of the 3D velocity or density field in redshift space in terms of these constraints and of the 3D power spectrum of the density field, $P_\mathrm{3D}(\boldsymbol{k})$. A prior is thus required for $P_\mathrm{3D}(\boldsymbol{k})$, but an iterative procedure can in principle be implemented, using the $P_\mathrm{3D}(\boldsymbol{k})$ measured in the reconstructed data after redshift distortion deconvolution as a new prior.

We demonstrate that the most likely velocity $\langle v_\mathrm{p} \rangle_\ell$ along the LOS ℓ is given by the linear relationship (equation B14)

$$\langle v_\mathrm{p} \rangle_\ell(x) = \sum_{\ell'} \int K_{\ell\ell'}(x, x') \delta_{\ell'}(x')\, \mathrm{d}x', \quad \text{or discretely} \quad \langle \boldsymbol{v}_\mathbf{p} \rangle = \mathbf{C}_{v\delta} \cdot \mathbf{C}_{\delta\delta}^{-1} \cdot \boldsymbol{\delta}, \tag{14}$$

where the kernel, $K_{\ell\ell'}(x, x')$, is a simple function of the assumed 3D power spectrum given by equation (B14), while $\mathbf{C}_{\delta\delta}$ and $\mathbf{C}_{v\delta}$ are respectively the log density autocorrelation, and the mixed log density–velocity correlation given by

$$\mathbf{C}_{\delta\delta} \equiv (\langle \delta_i \delta_j \rangle)_{i=1\ldots n, j=1\ldots n}, \quad \mathbf{C}_{v\delta} \equiv (\langle v_i \delta_j \rangle)_{i=1\ldots p, j=1\ldots n}, \tag{15}$$

assuming we know the log-density at n points in space (p stands for the number of points at which we seek the velocity).

To obtain the density in real space along one LOS, it is possible to rely on the explicit Bayesian method once more, by using for the model, g, equation (6) or equation (8) with v_p given by equation (14). This 'strong prior' régime will be tested against simulations in Section 5.4.2. Of course, the Bayesian method could as well allow us to perform the simultaneous 3D reconstruction of the density field.

The constrained mean field machinery can also be used to reconstruct the 3D density field in redshift space (or in real space once the

[4]Hence we do not address here possible non-Gaussianity due to topological defects.

density along each LOS is deconvolved from redshift distortion), $\langle\delta^{(3D)}\rangle(\boldsymbol{x})$. This is particularly relevant at low spectral resolution which corresponds to the large-scale régime, where equation (13) can be directly used for $\delta_\ell(x)$. One obtains (equation B15)

$$\langle\delta^{(3D)}\rangle(\boldsymbol{x}_\lambda) = \sum_\ell \int K_{\lambda\ell}^{(3D)}(\boldsymbol{x}_\lambda, \boldsymbol{x}'_\ell)\delta_\ell(x')\,\mathrm{d}x', \quad \text{or} \quad \langle\boldsymbol{\delta}^{(3D)}\rangle = \mathbf{C}_{\delta^{(3D)}\delta}\cdot\mathbf{C}_{\delta\delta}^{-1}\cdot\boldsymbol{\delta}, \tag{16}$$

where the kernel, $K_{\lambda\ell}^{(3D)}(\boldsymbol{x}_\lambda, \boldsymbol{x}'_\ell)$, is also a function of the assumed 3D power spectrum given by equation (B15). $\mathbf{C}_{\delta\delta}$ is given by equation (15), $\mathbf{C}_{\delta^{(3D)}\delta}$ is the mixed LOS-3D overdensity correlation given by $\mathbf{C}_{\delta^{(3D)}\delta} \equiv (\langle\delta_i^{(3D)}\delta_j\rangle)_{i=1\ldots p, j=1\ldots n}$.

3.3 Overlap between the two methods and connection with Wiener filtering

The above extrapolation technique is restricted to quasi-linear analysis in redshift space and unsaturated absorption lines, since it assumes a priori that the density is *known* along each LOS and that it is Gaussian distributed. As such, constrained mean fields methods cannot be applied directly to equation (1) which involves a double non-linear convolution over the underlying density both explicit (via $n_{\mathrm{H\,I}}$) and implicit (via v_p). The Bayesian approach sketched in Section 3.1 is more general and makes less stringent assumptions. In particular, it should provide means of applying redshift distortion correction on the fly while accounting for temperature-induced blending. We none the less show that, for linear models, when the prior dominates, the extrapolation ability of equation (10) reduces to constrained mean field extrapolation, while, in contrast, in the zero prior limit, it reduces to Wiener filtering. We also show how the covariance of the prior log-density and velocity can be adjusted to fix a unique linear relationship between the sought density field and its redshift distortion.

Let us start from the explicit Bayesian method. If the prior is null, $\boldsymbol{M}_0 \equiv 0$, the error in the measurements negligible, $\mathbf{C}_\mathrm{d} \approx 0$, the model linear, $g(\boldsymbol{M}) = \mathbf{G}\cdot\boldsymbol{M}$, equation (11) becomes

$$\langle\boldsymbol{M}\rangle = \mathbf{C}_0\cdot\mathbf{G}^\perp\cdot(\mathbf{G}\cdot\mathbf{C}_0\cdot\mathbf{G}^\perp)^{-1}\cdot\boldsymbol{D}. \tag{17}$$

When recovering the 3D density field from the measured density along the LOSs, $\mathbf{C}_0 \equiv \mathbf{C}_{\delta^{(3D)}\delta^{(3D)}}$, the linear operator $\mathbf{G}$ operates then simply like a Dirac comb on a field η:

$$\mathbf{G}_\ell\cdot\eta \equiv \int \delta_\mathrm{D}(\boldsymbol{x}_\perp - \boldsymbol{x}_{\perp\ell})\eta(\boldsymbol{x})\,\mathrm{d}\boldsymbol{x}_\perp, \tag{18}$$

so that

$$\mathbf{C}_0\cdot\mathbf{G}^\perp = \mathbf{C}_{\delta^{(3D)}\delta} \quad \text{and} \quad \mathbf{G}\cdot\mathbf{C}_0\cdot\mathbf{G}^\perp = \mathbf{C}_{\delta\delta}, \;\; \text{which implies for equation (17)}: \langle\boldsymbol{\delta}^{(3D)}\rangle = \mathbf{C}_{\delta^{(3D)}\delta}\cdot(\mathbf{C}_{\delta\delta})^{-1}\cdot\boldsymbol{\delta}. \tag{19}$$

Equation (19) is identical to equation (16). Note incidentally that if the prior is null and the model linear, but if the errors in the measurements are accounted for, equation (11) becomes

$$\langle\boldsymbol{M}\rangle = \mathbf{C}_0\cdot\mathbf{G}^\perp\cdot(\mathbf{G}\cdot\mathbf{C}_0\cdot\mathbf{G}^\perp + \mathbf{C}_\mathrm{d})^{-1}\cdot\boldsymbol{D} = (\mathbf{G}^\perp\cdot\mathbf{C}_d^{-1}\cdot\mathbf{G} + \mathbf{C}_0^{-1})^{-1}\cdot\mathbf{G}^\perp\cdot\mathbf{C}_d^{-1}\cdot\boldsymbol{D}, \tag{20}$$

which corresponds to Wiener filtering (Wiener 1949; Zaroubi et al. 1995). In other words, when the model is linear, our method is equivalent to Wiener filtering applied to $\boldsymbol{M} - \boldsymbol{M}_0$. When we seek to invert for both δ and v_p (hence imposing a weak prior on the field),

$$\boldsymbol{M} \equiv (\boldsymbol{\delta}, \boldsymbol{v}_\mathbf{p}), \tag{21}$$

The penalty function (corresponding to the log of the prior in equation 10) can be re-arranged (cf. equation B2):

$$(\boldsymbol{M} - \boldsymbol{M}_0)^\perp\cdot\mathbf{C}_0^{-1}\cdot(\boldsymbol{M} - \boldsymbol{M}_0) = (\boldsymbol{v}_\mathbf{p} - \mathbf{C}_{v\delta}\cdot\mathbf{C}_{\delta\delta}^{-1}\cdot\delta)^\perp\cdot(\mathbf{C}_{vv} - \mathbf{C}_{v\delta}\cdot\mathbf{C}_{\delta\delta}^{-1}\cdot\mathbf{C}_{v\delta}^\perp)^{-1}\cdot(\boldsymbol{v}_\mathbf{p} - \mathbf{C}_{v\delta}\cdot\mathbf{C}_{\delta\delta}^{-1}\cdot\boldsymbol{\delta}). \tag{22}$$

The strong prior régime, mentioned in Section 3.2 and tested in Section 5.4.2, is therefore a subcase of equation (22) where

$$\mathbf{C}_{vv} \approx \mathbf{C}_{v\delta}\cdot\mathbf{C}_{\delta\delta}^{-1}\cdot\mathbf{C}_{v\delta}^\perp, \;\; \text{implying} \quad \boldsymbol{v}_\mathbf{p} \approx \mathbf{C}_{v\delta}\cdot\mathbf{C}_{\delta\delta}^{-1}\cdot\boldsymbol{\delta},$$

i.e., $\boldsymbol{v}_\mathbf{p}$ will take its most likely value, as was assumed in equation (14).

Both the explicit Bayesian method and the constrained mean field reconstruction require detailed description of a *prior* model for the large-scale structure of the IGM in order to fix $\boldsymbol{M}_0$, $\mathbf{C}_0$, $P_{3\mathrm{D}}(\boldsymbol{k})$, plus additional relationships such as those sketched in Section 2. As mentioned earlier, these methods can be iterated with new priors measured in the reconstructed data, but we have not tested the convergence of such a scheme, and leave that to future work.

4 NUMERICAL SIMULATIONS

To test our methods we use two standard cold dark matter (CDM) *N*-body simulations. The gas distribution is derived from the DM distribution, using simple recipes described in Section 2 and based on previous works (e.g. Hui & Gnedin 1997; Nusser & Haehnelt 1999a). As discussed in the analysis of more realistic numerical simulations, taking fully into account the details of the gas dynamics is left for future work. Many aspects of the reconstruction problem do not strongly depend on the detail of the gas dynamics.

The simulations were run with a particle-mesh (PM) code, fully vectorized and parallelized on SGI-CRAY architecture with shared

Table 1. Characteristics of the *N*-body experiments.

Model	Ω_0	Λ	h	Γ	σ_8	$N_{\rm p}$	L
S	1.0	0.0	0.5	0.5	0.51	$512\times256\times256$	$50\times25\times25$
B	1.0	0.0	0.5	0.5	0.51	$1024\times128\times128$	$800\times100\times100$

Model: 'S' and 'B' stand for 'small' and 'big' respectively.
Ω_0: value of the density parameter of the Universe.
Λ: value of the cosmological constant.
h: parametrizes the Hubble constant, $H_0 = 100\,h\,\mathrm{km\,s^{-1}\,Mpc^{-1}}$.
Γ: shape parameter of the initial power spectrum (see, e.g. Jenkins et al. 1998 for details). σ_8^2 : the linear variance in the dark matter at the present time in a sphere of radius $8\,h^{-1}$ Mpc (to fix the normalization). $N_{\rm p}$: size of the grid used to compute the potential and the forces; also the number of particles. L: dimensions of the rectangular periodic box in comoving Mpc.

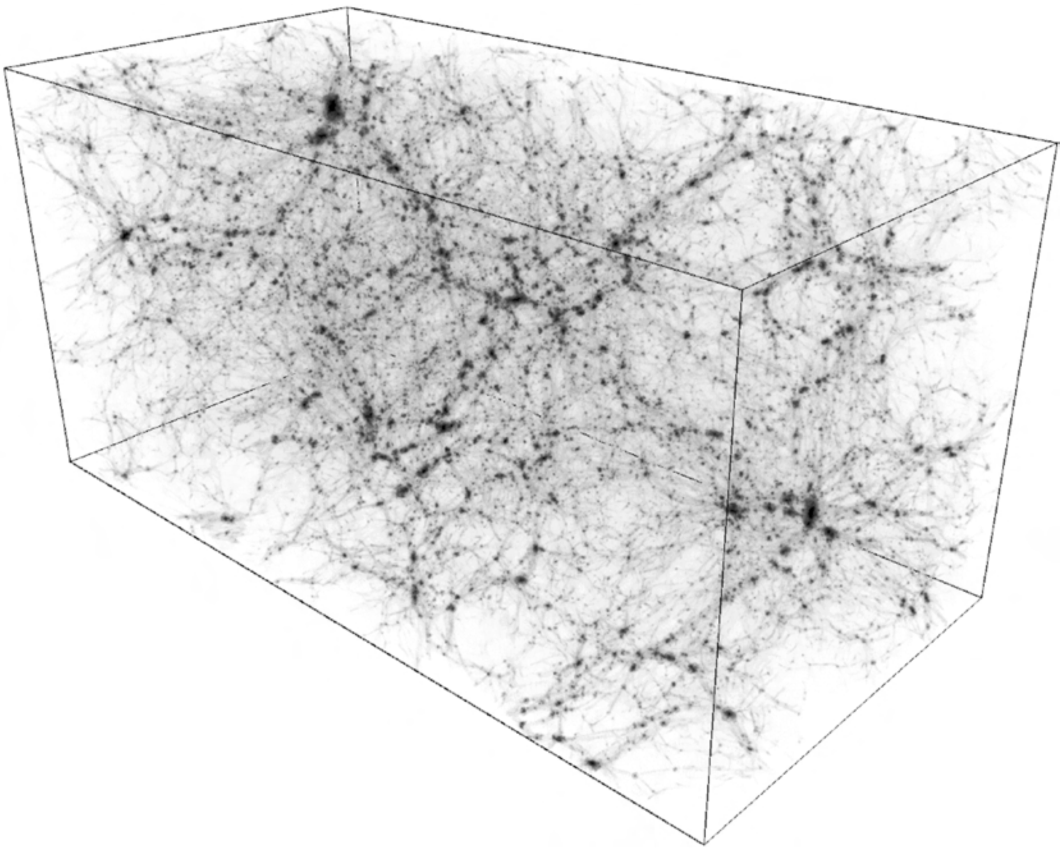

Figure 1. The dark matter distribution in the small simulation box, S, at $z = 2$ (see Table 1 and text). The colour scales roughly logarithmically with the projected density. Darker regions are denser.

memory.[5] The characteristics of the simulations, S and B, which involve respectively ~ 32 and ~ 16 millions particles, are given in Table 1. The cosmological parameters are inspired from Jenkins et al. (1998). The particles were laid down on a mesh with the same shape as the grid used to compute the forces. Then the Zel'dovich (1970) approximation was used to perturb the positions of the particles and to set up Gaussian initial conditions with the appropriate power spectrum for standard CDM. This was done in a similar way as in the COSMICS package of Bertschinger (1995). To avoid effects of transients (e.g. Scoccimarro 1998), the simulations were started at high redshift $z = 255$ and evolved until the desired redshift, $z = 2$. Figs 1 and 2 display the corresponding DM distribution. A detailed analysis of the power spectrum and the variance of the density field measured in the simulations is presented in Appendix C.

The spatial comoving resolutions of simulations S and B are $\lambda_{\rm g} \simeq 4.9$ and $40\,\mathrm{km\,s^{-1}}$ respectively, which correspond to physical resolutions ~ 8.5 and $68\,\mathrm{km\,s^{-1}}$ at $z = 2$. This is to be compared with the maximum possible pixel resolutions of the instruments available on

[5]This program is an improved version of an older code (Bouchet, Adam & Pellat 1985; Alimi et al. 1990; Moutarde et al. 1991; Hivon 1995). It uses for better performances a 'predictor-corrector' (e.g. Rahman 1964) implementation of the time-step (instead of the traditional 'leapfrog', e.g. Hockney & Eastwood 1981). It is still in construction, but available on request by e-mail at nic@iap.fr.

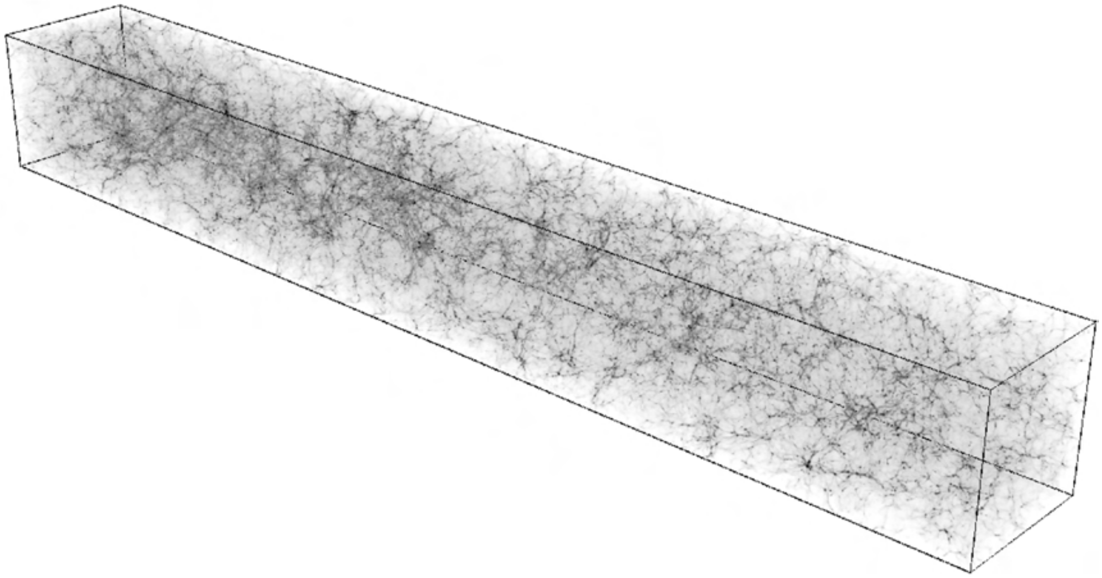

Figure 2. Same as Fig. 1, but for the large simulation box, B.

the VLT: UVES, $\lambda \simeq 3\,\mathrm{km}^{-1}$, and FORS, $\lambda \simeq 100\,\mathrm{km}^{-1}$. However, the actual resolution of the simulation depends on the physical parameter of interest, and is always worse than the mesh resolution. For density-related processes, we can expect the PM simulation to be sufficiently accurate at scales as small as $\sim 2\lambda_{\mathrm{g}}$, although the dynamics can actually be contaminated by softening of the forces on scales as large as $6\lambda_{\mathrm{g}}$ (Bouchet et al. 1985). For velocities, which are quite sensitive to resolution, numerical comparisons between PM simulations and higher resolution codes show that results are correct to within ~ 25 per cent at scales close to λ_{g} (e.g. Colombi 1996). Concerning the gas dynamics, density fluctuations are expected to be damped out below the Jeans length, and therefore it is not necessary to have a spatial resolution much better than this cut-off scale. For example, the thorough analysis of Gnedin & Hui (1998) shows that this scale is of the order of 50–100 h^{-1} comoving kpc, i.e., 5–10 comoving $\mathrm{km\,s^{-1}}$. This roughly corresponds to the spatial resolution of the S simulation (at least for density-related quantities). In this respect, the resolution of the B simulation is not high enough, and this simulation is only used to test reconstruction of weakly non-linear structures.

In addition to small-scale softening and limited resolution, discreteness effects represent another source of concern, particularly in underdense regions. We apply adaptive Gaussian smoothing to the particle distribution as follows. The mean quadratic distance, d_i, between each particle, i, and its six nearest neighbours is computed. This sets a smoothing length, $\ell_i = d_i$, i.e., the Gaussian filter associated to particle i is $W_{\ell_i}(r) \propto \exp(-r^2/2\ell_i^2)$ within $3\ell_i$ after appropriate renormalization. In practice, the smoothed density (or mass-weighted velocity) is computed on a grid chosen here to be the same as the simulation grid. Each cell, j, is subdivided in N^3 subpixels, k_j, corresponding to positions x_{k_j}, with $N = 3$. The contribution of particle i to the grid site j writes

$$C_{j,i} \propto \sum_{k_j, |r - x_{k_j}| \leq 3\ell_i} W_{\ell_i}(|r - x_{k_j}|), \tag{23}$$

with the appropriate normalization $\sum_j C_{j,i} = m_i$, where m_i is the mass of particle i.

5 APPLICATION

In this section we apply the methods discussed in Section 3 to simulated Lyman-α spectra extracted from the N-body simulations (using equation 6).

Our preliminary analyses are organized as follows. In Section 5.1 we give some details on the models and the priors used for both the Bayesian method and the constrained mean field reconstruction. Section 5.2 deals with 3D reconstruction of the density field. We first test the constrained mean field method in a régime where the density along each LOS is supposed to be known. Next, we test the Bayesian approach. The latter method does not rely on such a strong prior for the density, and is first applied to the large-scale régime discussed in Section 2.2, where thermal broadening can be neglected. Moreover, redshift distortion is not taken into account. In Section 5.3 we apply the Bayesian method to constrain the equation of state of the gas. We consider the small-scale régime as discussed in Section 2.2, but neglect redshift distortion again for the sake of simplicity, although peculiar velocity effects should realistically be accounted for. These velocities are dealt with in Section 5.4, which assume in turn that the equation of state of the IGM is well constrained. We analyse the efficiency of velocity reconstruction versus number of LOSs, and test Bayesian reconstruction in the frameworks of strong and floating priors.

The reader will notice that for each problem considered, we neglect in turn either redshift distortion or thermal broadening. Accounting simultaneously for both effects can in principle be achieved with the explicit Bayesian method or a combination with the constrained mean field reconstruction. However, our main goal here was to illustrate the method and to pin down various effects at each step of the reconstruction, concentrating on one particular property of the IGM, such as the structures of the 3D density field, the equation of state, or redshift distorsion. More general applications will be developed in future work.

5.1 The priors

5.1.1 *Explicit Bayesian method*

The Gaussian Bayesian prior (equation 10) is fully described by the first two moments: the prior choice for the parameters of the model, $\boldsymbol{M}_0$, and its covariance, $\mathbf{C}_0$.

For the model we choose the following combination of fields and discrete parameters:

$$\boldsymbol{M} = [\gamma(x, \boldsymbol{x}_\perp), v_\mathrm{p}(x, \boldsymbol{x}_\perp), \bar{T}, \beta]. \tag{24}$$

Function $\gamma(x, \boldsymbol{x}_\perp)$ is defined as

$$\frac{\rho_\mathrm{DM}(x, \boldsymbol{x}_\perp)}{\bar{\rho}_\mathrm{DM}} = D_0(x, \boldsymbol{x}_\perp) \exp[\gamma(x, \boldsymbol{x}_\perp)], \tag{25}$$

so that positivity of density is insured. Here, $D_0(x, \boldsymbol{x}_\perp)$ is an arbitrary function (specified later) which fixes the value of the prior for $\rho_\mathrm{DM}(x, \boldsymbol{x}_\perp)/\bar{\rho}_\mathrm{DM}$, when $\gamma(x, \boldsymbol{x}_\perp) = \gamma_0 \equiv 0$. Note that $A(z)$ is assumed to be known throughout the paper.

For the prior, we take

$$\boldsymbol{M}_0 = [0, 0, \bar{T}_0, \beta_0], \tag{26}$$

where the values of $\bar{T}_0$ and β_0 will be given in Section 5.3.

We derive the prior covariance operator $\mathbf{C}_0$ either in an ad hoc manner (Sections 5.2.2, 5.3 and 5.4.2) or from the simulations (Section 5.4.3). In the first case, $\mathbf{C}_{\gamma\gamma}$, is chosen to obey

$$\mathbf{C}_{\gamma\gamma}(x, x', \boldsymbol{x}_\perp, \boldsymbol{x}_\perp') \equiv \sigma_\gamma^2 \exp\left(-\frac{|x - x'|}{\xi_x}\right) \exp\left(-\frac{|\boldsymbol{x}_\perp - \boldsymbol{x}_\perp'|}{\xi_T}\right), \tag{27}$$

where ξ_x and ξ_T are natural lengths in the inversion and govern the level of smoothness of the reconstruction. Typically, ξ_T will be of order of the mean transverse distance between two LOSs. The optimal choice for ξ_x depends on the problem considered. If peculiar velocity effects are neglected, ξ_x can be taken as small as the maximum scale between spectral resolution and Jeans length (Sections 5.2.2 and 5.3). In that case, no small-scale information is lost along the LOSs. However, when redshift distortion is to be taken into account (e.g. Section 5.4.2), it is necessary to have a smoother prior to stabilize the inversion, typically the length marking the transition toward the non-linear régime (in other words, the typical size of clumps).

The parameter σ_γ may, if required, depend on position. On average, it corresponds roughly to the variance of γ in a rectangle of volume $\xi_x \xi_T^2$. It governs indirectly by how much the reconstructed field, $\langle \boldsymbol{M} \rangle$, is allowed to float around the prior $\boldsymbol{M}_0$ while solving equation (11) with the iterative method detailed in Appendix A. When peculiar velocity effects are neglected, this parameter can be taken to be rather large, of the order of 0.2. Otherwise, the inversion process is more complicated: details will be given in Section 5.4.2. Exponential correlation functions turned out to be more appropriate than Gaussian ones in order to recover filamentary structures: the covariance kernel given in equation (27) is steeper, which allows us to take into account high-density fluctuations.

5.1.2 *Constrained mean field reconstruction priors*

The constrained mean field reconstruction method, applied in Sections 5.2.1, 5.4.1 and 5.4.2, also requires values for the prior covariance matrix $\mathbf{C}_0$, which is taken to be those measured in the simulations, as detailed in Appendix B. Some of the biases involved in this choice are discussed in Section 5.2.3.

5.2 Large-scale structures: tomography of the IGM

We apply the two methods described in Section 3 to recover the large-scale structures in simulation B. For this purpose, we use a network of equally separated LOSs, along which we simulate spectra in accordance with equation (6) (as shown in Fig. 5) while varying the separation. We proceed in two steps: we first ignore all issues related to finite signal-to-noise ratios (S/N), thermal broadening or line saturation, and use constrained mean fields to extrapolate the density away from the LOSs, assuming that this latter is fully determined along the LOSs (Section 5.2.1); we then illustrate the Bayesian technique, which does not suppose that the density along the LOSs is known (Section 5.2.2). In the latter case, only the large-scale régime is considered [i.e., the régime (ii) discussed in Section 2.2], and redshift distortion is neglected ($v_\mathrm{p} = 0$). Section 5.2.3 discusses shortcomings of the two methods and realistic extensions.

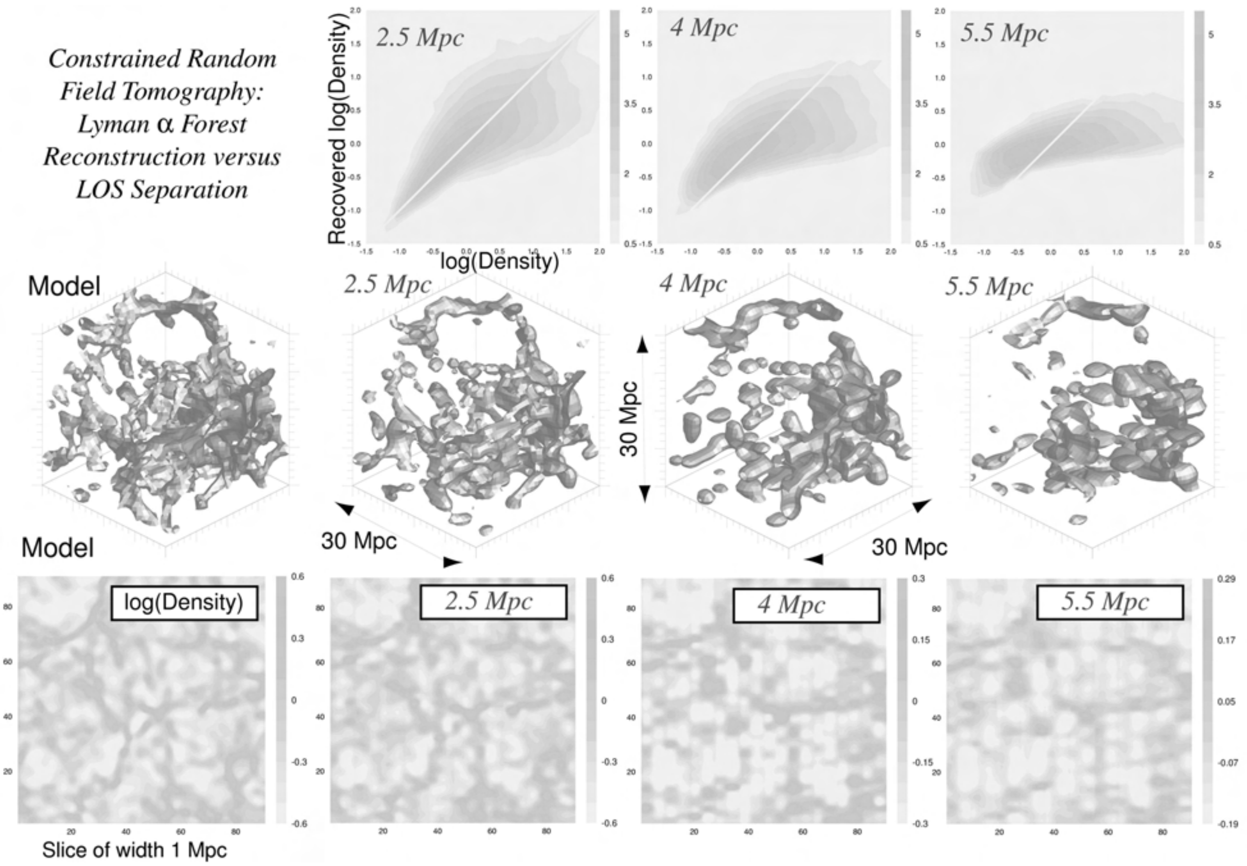

Figure 3. *Top panels, from left to right:* The recovered log density versus the real (simulated) log density as a function of the distance between the LOSs, $L_{\rm LOS}$, as labelled: as expected, the bias increases with $L_{\rm LOS}$; *Middle panels, from left to right:* the model and the reconstructed density for $L_{\rm LOS} = 2.5, 4$ and 5.5 Mpc comoving; *Bottom panels, from left to right:* a slice of $1 \times 80 \times 80$ Mpc across the simulation and the reconstructed fields (the scale on the panels is in pixels). Most of the small-scale structures are lost in the reconstructed field. The large-scale topology is, however, recovered. The rounded features in the reconstructed density are an artefact of the interpolation method.

5.2.1 Constrained mean field

Let us first consider redshift space and assume that we have derived the density on each LOS using for example equation (13). Recall that the most likely 3D density away from the LOS obeys equation (16). The covariance matrix of the prior, $\mathbf{C}_0 = \mathbf{C}_{\delta\delta}$, is shown on the top of the bottom right panel of Fig. 6. We present the results of a reconstruction of part of simulation B in Fig. 3. For this figure, we used the discrete form of equation (16), on a regular network of overlapping subgrids of size $20 \times 20 \times 20$ pixels such that the centres of adjacent subgrids are separated from each other by 10 pixels. The value of the reconstructed density on one pixel is obtained by a weighted interpolation of the recovered density on each subgrid containing this pixel, the weight being inversely proportional to the distance of the pixel from the centre of the subgrid considered. This procedure ensures smoothness of the reconstruction, while keeping the size of the matrices reasonable. The top panels of Fig. 3 illustrate the bias in the extrapolation procedure as we vary the distances between LOSs, the middle panels display the 3D reconstructed iso-log densities corresponding to $\delta = 0.2$, while the bottom panels show a slice through this field. The large-scale filaments are recovered for all separations investigated, but small-scale structures disappear beyond 2.5 Mpc comoving of separation. The topography of the structures is well described. As expected, the density is poorly recovered for the largest separations.

5.2.2 Bayesian reconstruction: line saturation and finite signal-to-noise ratio (S/N)

Choosing simply $D_0 \equiv 1$ in equation (25), our model g, on pixelized data, reads (equation 8 with $v_{\rm p} = 0$; see also Appendix D1.2)

$$g_{i\ell}(\gamma) = A(\bar{z}) \exp[\alpha\gamma(w_{i\ell}, x_{\perp\ell})], \tag{28}$$

with α fixed equal to 1.7 Here, $w_{i\ell}$ is the velocity at bin i corresponding to the LOS labelled ℓ, and $\gamma(x, \boldsymbol{x}_\perp)$ is the only parameter for which the prior covariance is given by equation (27). The parameters σ_γ, ξ_x and ξ_T are respectively chosen equal to 1, twice the resolution and 1.5 times the distance between LOSs. The matrix $\mathbf{G}$ is given in Appendix D1.2. Errors in the simulated data are modelled as follows. We assume that they are uncorrelated, so that the covariance error matrix $\mathbf{C}_{\rm d}$ is diagonal, with elements given by

$$\sigma_\tau^2 \equiv \frac{\sigma_F^2}{F^2} \simeq \frac{1}{(S/N)^2} + \frac{\sigma_0^2}{F^2} = \frac{1}{(S/N)^2} + \sigma_0^2 \exp(2\tau), \tag{29}$$

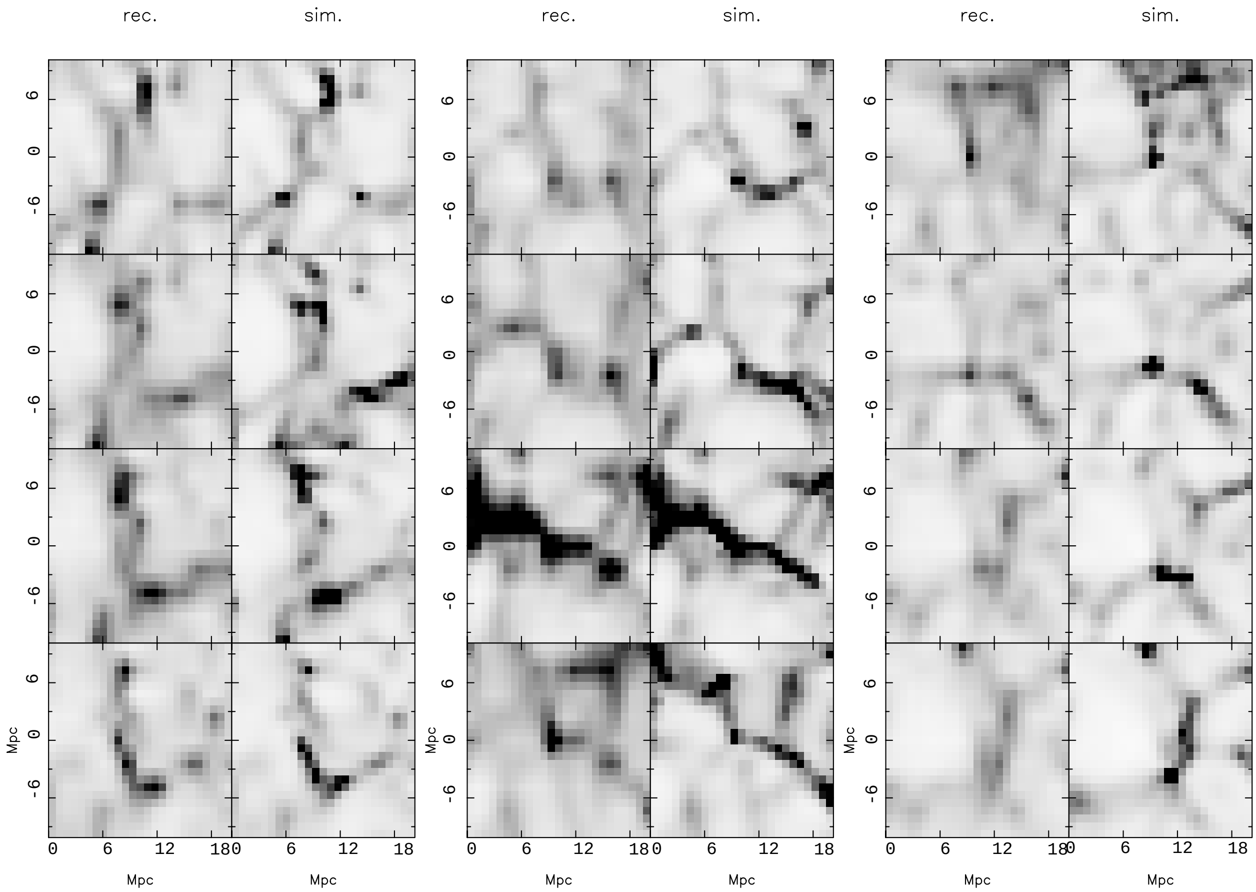

Figure 4. Density contrast reconstruction using the Bayesian algorithm from a set of 9×9 lines of sight taken through simulation B. The distance between two adjacent lines of sight is equal to 2.4 Mpc comoving. Each panel represents respectively on the left the reconstruction and on the right the simulation. Dark regions correspond to overdense regions. The filaments are well recovered.

since the observed flux is simply: $F(w) = \exp[-\tau(w)]$. Equation (29) states that the error on the flux has two origins: a constant S/N component and a residual instrumental noise, σ_0, which dominates at large optical depth. In the inversion illustrated in Fig. 4, we use an S/N of 25 and a residual error of magnitude 0.01.

The reconstruction of filamentary structures is effective only in the régime where the distance between LOSs is of the order of 1–3 Mpc comoving. Beyond this limit, the isotropic method presented here is insufficient to recover the structure of the IGM (such anisotropic features may be described by higher order correlation functions and stronger assumptions relying on a prior different from equation 10). Inherent to the method is the limitation that density fluctuations at scales smaller than the separation between LOSs are damped out by the reconstruction. Also, the probability to intersect a given strong overdensity is inversely proportional to the amplitude of the overdensity. In other words, the information regarding rare high overdensities is simply not sampled enough by the LOSs. A related effect is induced by flux saturation in the spectra depending on the spectral resolution and the S/N. For instance, optical depths of $\tau = 5$ or 10 will correspond to very different overdensities but very similar (≈ 0) fluxes. Note finally that for simplicity we have made use of Gaussian line profiles, when Lorentzian would have been more appropriate.

5.2.3 Discussion

In the reconstruction of Section 5.2.1, the density is assumed to be known along the LOSs, together with the covariance matrix of the 3D log-density field. At low spectral resolution, we may neglect both thermal broadening and peculiar velocities, and use equation (13) to determine directly the density in redshift space from the Lyman α forest along each LOS. At high spectral resolution, thermal debroadening and redshift distortion deconvolution could in principle be achieved simultaneously with the explicit Bayesian method or a combination of the Bayesian method with the constrained mean field reconstruction, as discussed in Section 3.2 and shown below.

Note also that our prior for the 3D covariance matrix in Section 5.2.1 is optimal: it is measured directly in the simulation. In that sense, our reconstruction is biased, since we use part of the correct answer in advance. Moreover, we go beyond Gaussian linear approximation, since we work on *log*-density, which contributes to improve the reconstruction even more. In real observations, we would not have a prior as good as that chosen here at our disposal. However, as shown in Section 5.2.2, the results from the explicit Bayesian reconstruction, which rely

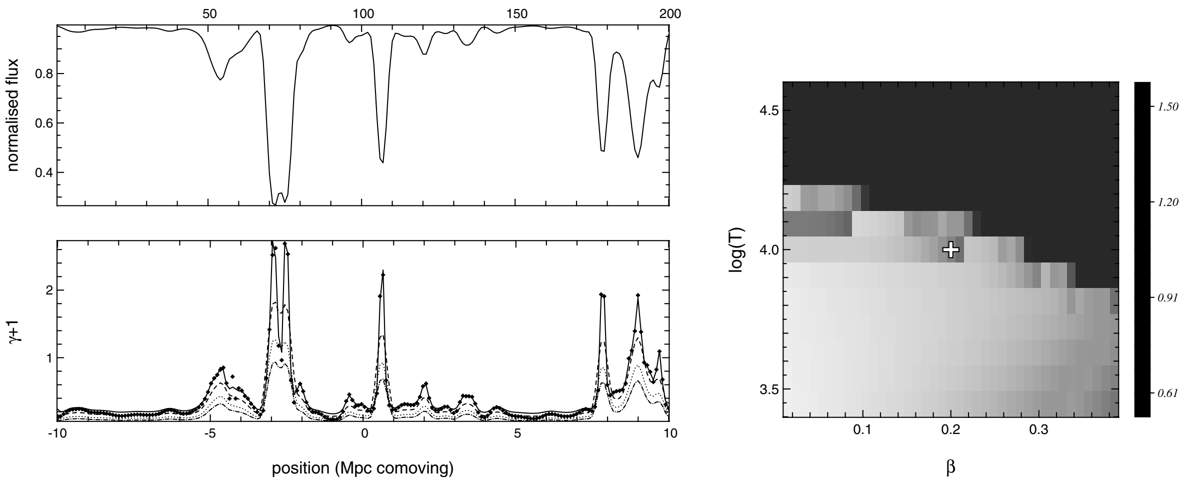

Figure 5. *Left-hand panels:* Inversion using different equations of state. The upper panel shows a portion of simulated spectrum through S. The equation of state used corresponds to equation (3) with $\bar{T} = \bar{T}_t \equiv 10^4$ K, $\beta = \beta_t \equiv 0.2$. Peculiar velocities are not considered. The lower panel shows the simulated density as black dots. The density recovered using the same equation of state is plotted as a solid line; it is apparent that even the internal structure of absorption blends is recovered. Other curves correspond to the results of inversions using various lower values of $\bar{T}$ at fixed $\beta = 0.2$. The effect of lowering $\bar{T}$ is to give smaller values for reconstructed density with a reduced $\chi^2 < 1$. If, on the contrary, $\bar{T} > T_t$, one obtains $\chi^2 \gg 1$. *Right-hand panel:* Map of convergence ($\chi^2 < 1$) or divergence ($\chi^2 \gg 1$) for inversions using equation (30) with different values of $\bar{T}$ and β. The LOS is the same as in the left-hand panels.

on a much weaker prior, equation (27), give very similar results to the constrained mean field reconstruction. This shows that the non-linear features present in the measured correlations do not play an important role in our ability to carry out the inversion on the scales explored here. Finally, it may be worth mentioning again that the methods should be iterated, using for new priors and covariance matrixes the measured ones in the reconstructed field.

5.3 Small scales: the IGM temperature

We now aim to determine the equation of state of the IGM by considering the inversion of a single LOS observed at high spectral resolution [régime (i) in Section 2.2]. The inversion of the density, velocity and temperature fields from a single LOS is not unique (Hui & Rutledge 1999; Theuns et al. 1999). Indeed, the same spectrum can be reconstructed with different equations of state and density distributions, as illustrated by Fig. 5. Neglecting peculiar velocities for the sake of simplicity ($v_p = 0$), the problem reduces to the determination of two parameters $\bar{T}$ and β and one unknown field, γ. The simultaneous determination of these parameters *and* the field remains a degenerate problem. As detailed in Appendix D1.1, our model, g, on pixelized data reads, from equation (6),

$$g_{i\ell}(\gamma) = A(\bar{z})c_1 \int\!\!\int \left(\int_{-\infty}^{+\infty} \{D_0(x,\boldsymbol{x}_\perp)\exp[\gamma(x,\boldsymbol{x}_\perp)]\}^{\alpha-\beta} \exp\left[-c_2 \frac{(w_{i\ell}-x)^2}{\{D_0(x,\boldsymbol{x}_\perp)\exp[\gamma(x,\boldsymbol{x}_\perp)]\}^{2\beta}}\right] \mathrm{d}x \right) \delta_\mathrm{D}(\boldsymbol{x}_\perp - x_{\perp\ell})\, \mathrm{d}^2\boldsymbol{x}_\perp . \tag{30}$$

Here, $A(\bar{z})$ is arbitrarily fixed to $A(\bar{z}) = 0.7$ as explained in Section 5.1.1, $\alpha = 2 - 1.4\beta$ (equation 4), and c_1 and c_2 are functions of $\bar{T}$ (equation 7). The function $D_0(x, \boldsymbol{x}_\perp)$ is chosen to be

$$D_0(x, x_\perp) = \left[\frac{\tau_\ell(w \equiv x)}{A(\bar{z})}\right]^{1/\alpha}. \tag{31}$$

The prior covariance matrix $\mathbf{C}_{\gamma\gamma}$ is given by equation (27) with $\xi_T \to \infty$. Here ξ_x and σ_γ are chosen equal to 0.2 Mpc comoving and 0.2.

We conduct our analyses as follows. We first simulate a spectrum along one LOS with a given *real* pair (β_t, $\bar{T}_t$). The noise matrix $\mathbf{C}_d$ is the same as in Section 5.2.2 with a $(S/N, \sigma_0) = (50, 0.05)$. We then invert this LOS for $\gamma(x)$, while varying (β, $\bar{T}$) over a given range of realistic values. In that sense, the only *effective* parameter in the inversion is the field γ. For each value of (β, $\bar{T}$), we compute the reduced χ^2, i.e., $[\boldsymbol{D} - g(\boldsymbol{M})]^\perp \cdot \mathbf{C}_d^{-1} \cdot [\boldsymbol{D} - g(\boldsymbol{M})]$ in equation (10), as shown in the right-hand panel of Fig. 5. The value of (β_t, $\bar{T}_t$) is shown by a white cross. The (β, $\bar{T}$) plane is divided into two regions separated by a straight borderline, one with $\chi^2 \gg 1$ (corresponding to large values of $\bar{T}$) and the other one with $\chi^2 \leq 1$. This arises because the absorption lines are indeed thermally broadened and resolved. When $\bar{T} > \bar{T}_t$, the absorption features in the data are narrower than the model and cannot be fitted anymore.

As expected, the real parameters stand on the borderline between convergence and divergence: these parameters correspond to a good fit. We cannot however distinguish – using a χ^2 criterion – between pairs of (β, $\bar{T}$) on this borderline. Even though the degeneracy is not completely lifted, this analysis provides a complementary method to the standard techniques of Voigt profile fitting (see Schaye et al. 1999 and Ricotti et al. 2000) to measure the mean properties of the IGM and its cosmological evolution. The application of our method to real data is developed to a companion paper (Rollinde, Petitjean & Pichon, submitted).

Note finally that, for close enough LOSs (e.g., multiple lensed QSO images) we might in theory be able to investigate the small-scale 3D properties of the IGM, while accounting for thermal broadening.

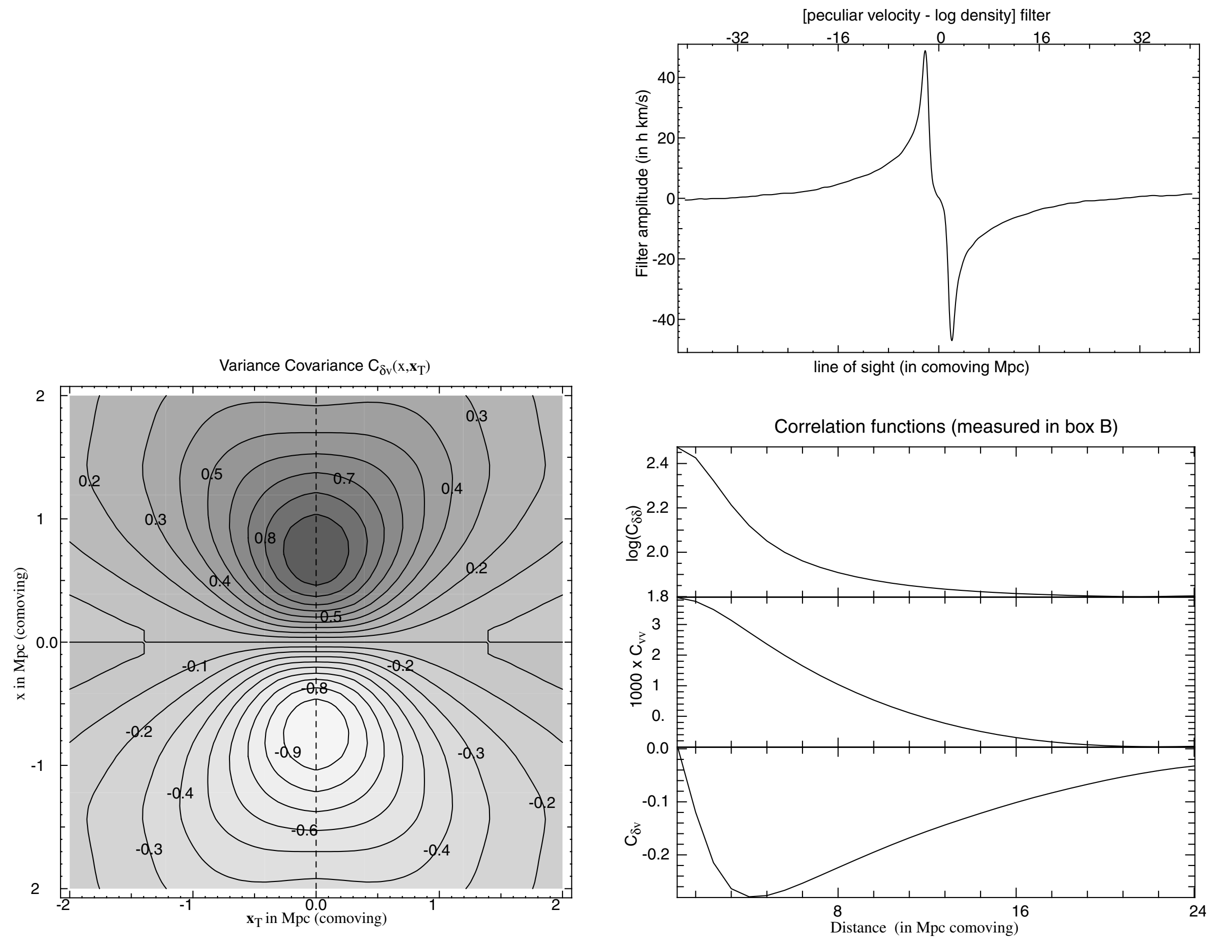

Figure 6. *Left-hand panel:* the 3D correlation function, $\mathbf{C}_{v\delta}(x,\boldsymbol{x}_\perp)$, measured in simulation S. *Top right panel:* the filter $K^{(v)}$ required to compute the most likely velocities along one LOS (equation 14 with $\ell = \ell' = L = 1$). The width of the filter shows that the peculiar velocity has two natural scales, as discussed in the main text. *Bottom right panel:* the 1D LOS correlation functions: top subpanel: $\log(\mathbf{C}_{\delta\delta})$; middle subpanel: $\mathbf{C}_{vv}$; bottom subpanel: $\mathbf{C}_{\delta v}$.

5.4 Redshift distortion

Recall that in this section, for the sake of simplicity, we assume that the equation of state of the IGM is known.

There are several issues to address here. The optical depth along a bundle of LOSs does not constrain uniquely the corresponding velocity field. This would require the knowledge of the full 3D density distribution, together with the assumption that linear dynamics applies. Thus we first investigate how increasing the number of measured LOSs, or changing the mean separation between them, improves the likelihood of the corresponding realization of the constrained velocity field for a given density field along the bundle (Section 5.4.1). We then turn to the problem of deconvolving the optical depth in real space, but conduct a preliminary analysis on *a single* LOS. We test two approaches. The first approach is a strong prior inversion (Section 5.4.2), i.e., it relies on the Bayesian formalism, while assuming that the velocity field takes its most likely value. The second method allows the velocity field to float around this most likely value (Section 5.4.3). Finally, we discuss the limitations of the present work and possible improvements (Section 5.4.4).

Let us briefly describe the filters and correlation function involved. Fig. 6 (left-hand panel) displays the 3D correlation function, $\mathbf{C}_{v\delta}(x,\boldsymbol{x}_\perp)$, measured in simulation S. It is antisymmetric along the LOS, and symmetric orthogonally. The top right panel shows the 1D filter, $K^{(v)}(x, y)$ (equation 14 with $\ell = \ell' = L = 1$), which was in practice computed according to the prescription sketched in Appendix B. This antisymmetric filter presents two characteristic scales: a strong peak at ≈ 2 Mpc (comoving) and broad wings up to ≈ 20 Mpc. This implies that the most likely velocity at a given point will depend on the local density *and also significantly* on the density further away (up to ≈ 20 Mpc). Transversally, the shape of the 3D cross-correlation function, $\mathbf{C}_{v\delta}(x, \boldsymbol{x}_\perp)$, which vanishes near the line $x = 0$, implies that the density away from a given point will dominate the local velocity field.

5.4.1 *Most likely velocity versus LOS separation and the number of LOSs*

In this subsection we assume temporarily that the log-density field is known along a bundle of LOSs. In the framework of constrained mean field (Section 3.2), equation (14) gives the relationship between the most likely velocity along a given bundle of LOSs and the corresponding log-density.

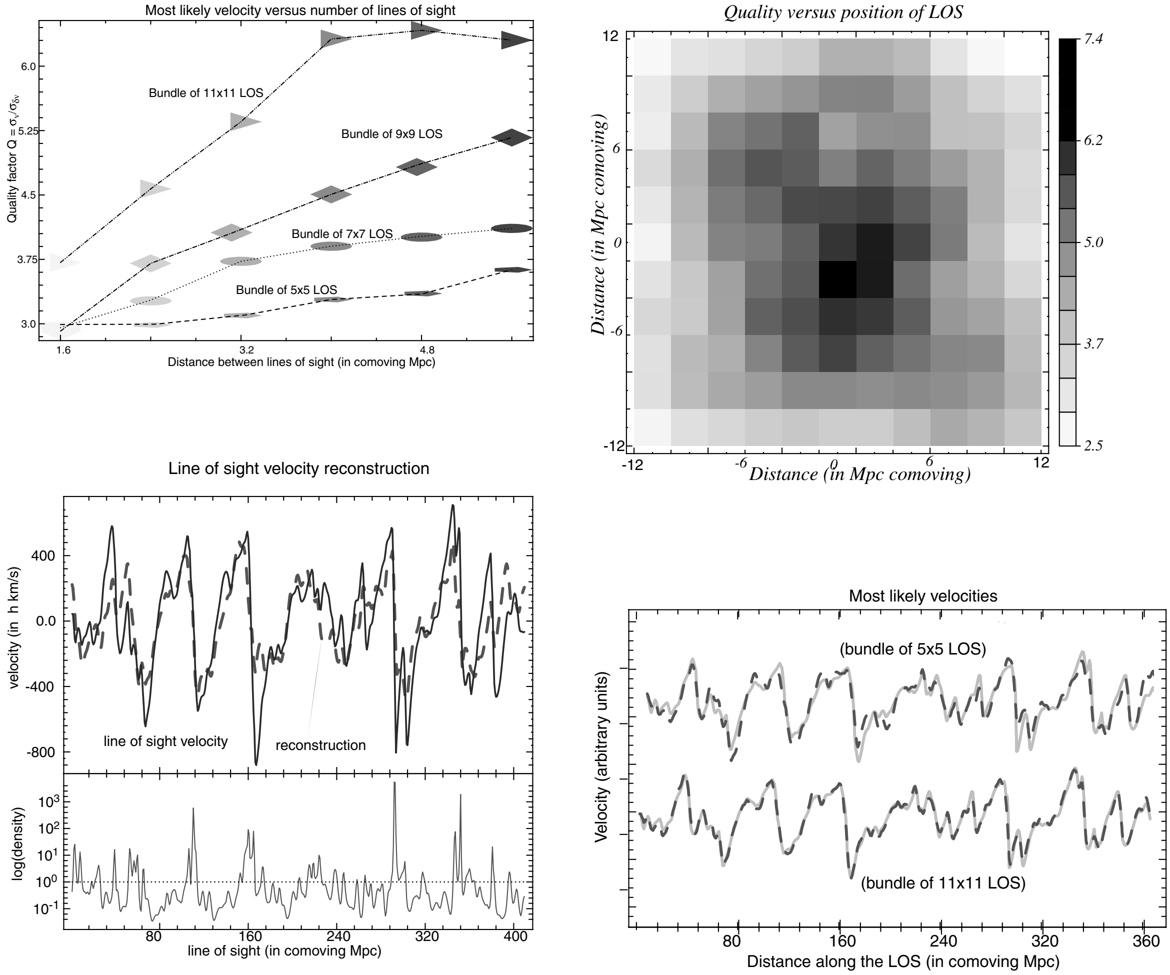

Figure 7. *Top left panel:* quality of the reconstruction (equation 32) versus LOS separation and the number of LOSs. Increasing the sampling on the sky decreases the dispersion between the constrained most likely velocity and the measured velocity as discussed in the text. Note the saturation for 11×11 LOSs at a separation of $\simeq 5$ Mpc. *Top right panel:* isocontour for the quality of the reconstruction projected on the sky for a bundle of 11×11 LOSs, separated by 2.4 Mpc comoving. Note that the reconstruction obviously works better for the central LOSs. *Bottom left panel:* in simulation B, most likely velocity constrained by a single LOS. The solid line on the upper subpanel corresponds to simulated velocity, and the dashed one to the reconstructed velocity. The simulated density is displayed in the lower subpanel. *Bottom right panel:* solid lines: simulated velocities along the centre of a bundle of 5×5 LOSs or 11×11 LOSs; dashed lines: corresponding recovered velocities.

Let us define the quality factor, Q, as

$$Q \equiv \frac{\sigma_{v_{\rm p}}}{\sigma_{\delta v_p}} = \sqrt{\frac{\langle v_p^2 \rangle}{\langle (v_{\rm p} - v_{\rm rec})^2 \rangle}}, \tag{32}$$

where $v_{\rm rec}$ is the reconstructed velocity. Parameter Q measures the inverse residual misfit in units of the variance for the velocity. We show in Fig. 7 (top left panel) that this number increases with the number of LOSs sampling the sky, as expected. However, Q increases as well with the distance between LOSs until it reaches a maximum, which might sound confusing. This can be easily understood by examining the left-hand panel of Fig. 6. In fact, a bundle of LOSs constrains the transverse 3D velocity distribution *at intermediate scales*, as a result of a competition between short-range and long-range correlations.

(i) High-frequency structures are read from the LOS through the two strong peaks along the x coordinate axis in the left-hand panel of Fig. 6 (at approximately ± 0.8 Mpc). Other LOSs can in principle contribute to small scales, but only if they are found very close to the LOS of interest (i.e., with $\boldsymbol{x}_\perp \simeq 0$).

(ii) Low 3D frequency features are mainly sampled by LOSs away from the LOS of interest, due to the significant tails present on $\mathbf{C}_{v\delta}$ at scales as large as ~ 20 Mpc, as illustrated by the top right panel of Fig. 6. This effect is three-dimensional, i.e., in *all directions*: it thus provides information on the structures transverse to the LOS.

(Note that in this discussion, we implicitly assumed that $\mathbf{C}_{\delta\delta} \simeq$ identity in equation 14. Taking into account the real contribution of matrix $\mathbf{C}_{\delta\delta}^{-1}$ would simply boil down to smoothing the density with an isotropic filter, which has no effect on our qualitatives conclusions.)

The competition between effects (i) and (ii) fixes an optimal separation between the LOSs as a function of their number. From the top left panel of Fig. 7, we see, for example, that the optimal separation is 5 Mpc for a bundle of 11×11 LOSs. For a bundle with a smaller number of LOSs, the optimal separation becomes larger, so that the tails of $\mathbf{C}_{v\delta}$ are still fully sampled (but with a sparser binning and thus a smaller quality factor).

The bottom right and left panels of Fig. 7 compare the velocity along one LOS measured in the simulation to the reconstructed one by applying equation (14) to bundles of various sizes (1×1, 5×5 and 11×11) distributed uniformly on the sky (from simulation B), with a mean separation of 2.5 Mpc. With only one LOS, the reconstructed velocity does not account in detail for small structures, although it seems to match well large-scale flows in the example studied here. Increasing the number of LOSs significantly improves the reconstruction: with a bundle of 11×11 LOSs, the reconstruction almost perfectly matches the simulation.

An important outcome of this analysis is that since the optimal separation between LOSs is rather large (a few Mpc), the small-scale information in the reconstruction is only contained in the LOS of interest. Therefore, having high-resolution spectra on all the LOSs is not required: a survey dedicated to real-space reconstruction should provide a high-resolution spectrum together with a set of low-resolution spectra separated by distances smaller than or of the order of $\approx$ 4–5 Mpc comoving. Note that Q was computed while averaging over the whole bundle: the quality of the reconstruction in fact depends on the position of the LOS in the bundle, as illustrated in the top right panel of Fig. 7. Obviously, the quality factor is optimal at the centre of the bundle: the high-resolution spectrum should be located there.

We assumed here that the 3D covariance matrices needed for the reconstruction were known. In fact, we used the best possible guess for them, since they were derived from direct measurement in the simulation. In reality, we would have to proceed iteratively: for a given power spectrum, we could recover the 3D density, compute perturbatively the corresponding 3D velocity field, and derive a new covariance matrix until convergence is achieved. We have not demonstrated here that this procedure is convergent. This is certainly a possible shortcoming of the procedure.

5.4.2 *Strong prior inversion*

Let us now try to deconvolve the density in real space along *one* LOS. A combination of the general Bayesian method and the constrained mean field technique is implemented: the constrained mean field method allows us to relate the unknown field v_{p} to γ, imposing that the peculiar velocity takes its most likely value, but the recovery of γ is still based on the Bayesian method. Our model, $g_i(\gamma)$, is now

$$g_i(\gamma) = A(\bar{z})c_1 \int_{-\infty}^{+\infty} \{D_0(x)\exp[\gamma(x)]\}^{\alpha-\beta} \exp\left[-c_2 \frac{[w_i - x - v_{\mathrm{p}}(x)]^2}{\{D_0(x)\exp[\gamma(x)]\}^{2\beta}}\right] \mathrm{d}x, \tag{33}$$

with the supplementary assumption that the peculiar velocity in equation (33) equals the most likely velocity (Appendix B):

$$v_{\mathrm{p}}(x) = \langle v \rangle \equiv \int K^{(v)}(x,y)\gamma(y)\,\mathrm{d}y, \quad \text{where} \quad K^{(v)}(x,y) \equiv \frac{1}{2\pi}\int \mathrm{e}^{\mathrm{i}k_x(x-y)} \frac{P_{v\delta,\mathrm{1D}}(k_x)}{P_{\delta\delta,\mathrm{1D}}(k_x)}\mathrm{d}k_x. \tag{34}$$

The unknown parameter remains the density contrast. The prior for the density is chosen as $D_0 \equiv 1$ so that $\gamma = \delta$. For the filter $K^{(v)}(x, y)$ we use a simple analytic fit of the function $K^{(v)}(x, y)$ measured in the simulation as explained in Appendix B1.1. The derivation of the different vectors and matrices involved in this case is sketched in Appendix D2.1. The practicalities involves fixing appropriately the parameters (σ_γ, ξ_x) in equation (27) ($\xi_T \equiv \infty$ for a single LOS) for the minimization procedure detailed in Appendix A to converge while providing as accurate reconstruction as possible. To stabilize the inversion, we need to take for ξ_x a value close to the correlation length, $\xi_x = 1$ Mpc. With a larger value of ξ_x, the inversion is still stable but makes the reconstructed density field too smooth, while a smaller value of ξ_x makes the inversion unstable. The choice of σ_γ, which fixes the amount of variations allowed around the prior, is more delicate. A small value of σ_γ makes convergence easier, but does not leave enough freedom for the reconstructed density to float around the prior: voids tend to be filled, and high density peaks are not saturated. On the contrary, a large value for σ_γ allows significant deviations from the prior but makes the iteration procedure less stable. For this reason, the reconstruction is carried out in two steps. We first take a small value for $\sigma_\gamma = 0.0175$, and reconstruct the density while using equation (34) to determine accurately the most likely velocity. Because of our choice of σ_γ, the reconstructed density is not as contrasted as it should be, but this does not affect significantly the corresponding most likely velocity: it just makes it smoother. In the second step, we *fix* the most likely velocity at the value obtained from the first step. Thus equation (34) is disregarded, and we iterate once more on the density with a larger value of σ_γ, $\sigma_\gamma = 0.2$, allowing more variations of the density around the new prior – the reconstructed density obtained from the first step. The fact that the most likely velocity is fixed indeed makes the inversion more stable and allows larger values of σ_γ.

Fig. 8 illustrates how the method performs on two unsaturated LOSs: the first isolated and the latter nearby a cluster. The simulated spectra assume $A = 0.39$, $\beta = 0.4$, $\bar{T} = 10^4$ K, and were calculated after smoothing the density and velocity fields with a cube of size ~ 200 kpc (2 cells). The errors in the data are modelled as described in Section 5.2.2 with $(S/N, \sigma_0) = (100, 0.05)$ in equation (29). As expected, the reconstructed velocity matches the original only when there is no significant structure close to the LOS, likely to induce large-scale infall contamination. The bottom panels of Fig. 7 show that the reconstructed density reproduces well the shape of most structures, except that they are not correctly located along the velocity axis in the bottom right panel.

Note that our two-step procedure is similar in spirit to that proposed by Nusser & Haehnelt (1999a), although we use same smoothing length ξ_x in both steps, which allows more small-scale features on the reconstructed density. Also, our method is not yet able to deal with spectra containing significantly saturated absorption lines: in that case, the inversion is much less stable and the reconstructed most likely velocity is often unrealistic, even if the LOS is isolated. Finally, we assumed that the kernel function $K^{(v)}(x, y)$ was known, which should not

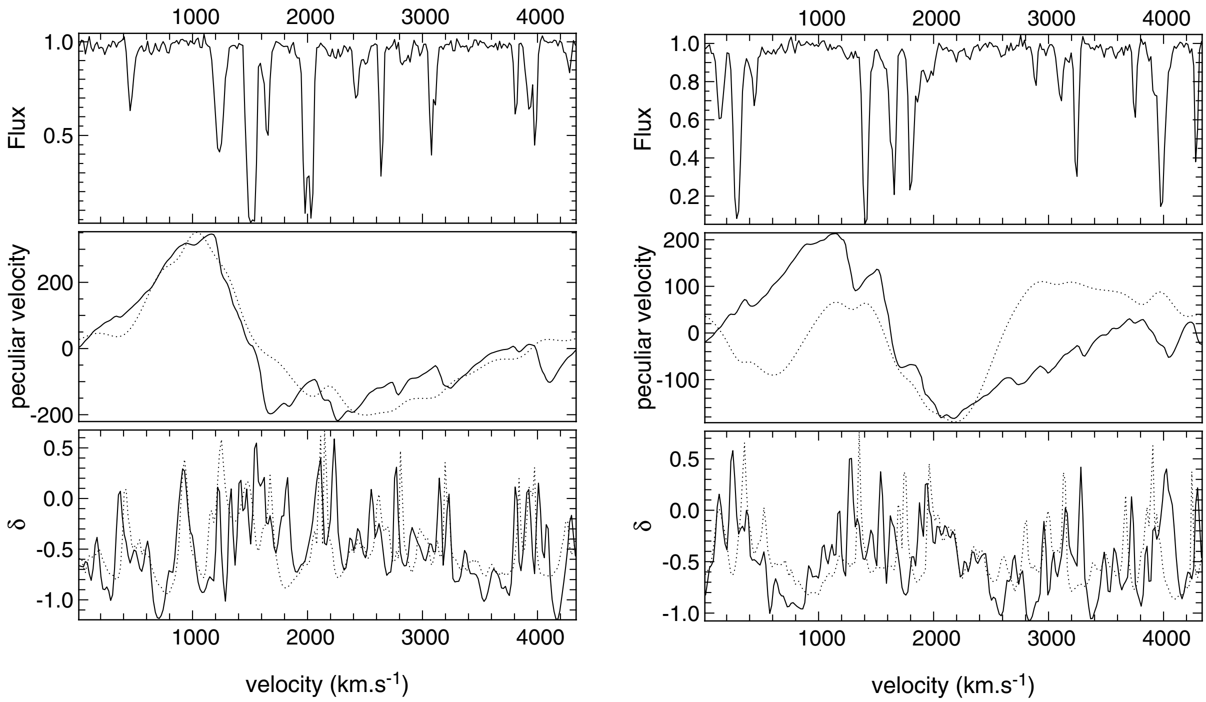

Figure 8. *Inversion while accounting for peculiar velocity with strong prior.* Simulation S is used to test the method. Two examples are considered, according to whether there is a large structure near the LOS or not (respectively right and left panels). *Top panels:* the simulated spectra. *Middle panels:* the simulated (solid line) and most likely (dotted line) peculiar velocity along the LOS. *Bottom panels:* the simulation (solid line) and reconstructed (dotted line) log-density (in $\log_{10}$ units).

be the case in reality: a more detailed study of the effects of the assumed shape for this function will be needed in the future to fully qualify the method.

5.4.3 Floating prior for the velocities

A less biased representation of the underlying field would be to assume that γ and v_p are two fields which are statistically correlated (by the dynamics) but whose realizations are independent. The model is formally identical to equation (33), with the restriction that v_p does *not* obey equation (34) anymore. The vector of the model parameters is: $\boldsymbol{M} = [\gamma(x), v_\mathrm{p}(x)]$. The correlation between γ and v_p, $\mathbf{C}_{v\gamma}$, is considered to be linear. Recall that the prior variance–covariance matrix, $\mathbf{C}_0$, has three independent terms, shown in the bottom right panel of Fig. 6:

$$\mathbf{C}_0 = \begin{pmatrix} \mathbf{C}_{\gamma\gamma} & \mathbf{C}_{v\gamma} \\ \mathbf{C}_{v\gamma}^{\perp} & \mathbf{C}_{vv} \end{pmatrix}. \tag{35}$$

The penalty function then obeys equation (22), and realizations of the velocity field are entitled to float around their most likely values, equation (14). The corresponding model, g, is sketched in Appendix D2.2. The iterative procedure presented in Appendix A brings the reduced χ^2 down from values of about a 100 to $1 \pm \sqrt{2/N}$ in a few iterations, but does not converge if peculiar velocities induce displacements larger than the effective width of the absorption lines. Even though the weak prior inversion is more elegant and easier to implement than the strong prior approach (cf. Appendix D2.2), it seems to fail to constrain sufficiently our model when redshift distortion is important. This arises because the effective correlation in equation (22) is too weak to induce convergence.

5.4.4 Discussion

A priori, the best approach for reconstructing the density in redshift space would be to use the explicit Bayesian method with a floating prior for the velocity described in Section 5.4.3. However, our preliminary analyses show that this method fails to converge when applied to *one* LOS if redshift distortion becomes of the order of the width of absorption lines, which is unfortunately the case in realistic situations. The strong prior inversion of Section 5.4.2, tested again on one LOS, seems to be more reliable, but gives accurate reconstruction only if the considered LOS is unsaturated and is isolated from large structures. The only reliable way to improve the reconstruction is therefore to have more information on the 3D structure of the IGM through bundles of LOSs, as studied in Section 5.4.1. The difference between Sections 5.4.3 and 5.4.2 would then vanish, since the discrepency between the most likely velocity and the actual field becomes smaller and smaller, while the correlation between the density and the velocity becomes simultaneously tighter and tighter. However, we have not explicitly tested the methods of Sections 5.4.2 and 5.4.3 on several LOSs: this is left for future work.

6 CONCLUSIONS

In this paper an explicit Bayesian technique and a constrained mean field method have been proposed to recover various properties of the intergalactic medium from observations of the Lyman α forest along LOSs to quasars. In particular, our preliminary analyses suggest that these methods may be used (i) to recover the large-scale 3D topology of the IGM from inversion of a network of adjacent LOSs observed at low spectral resolution, (ii) to constrain the physical characteristics of the gas from inversion of single LOSs observed at high spectral resolution, (iii) to investigate how the number of, and the distance between, LOSs constrain the projected peculiar velocities, and (iv) to correct in part for redshift distortions induced by these velocities using either strong or weak priors.

Both approaches rely on prior assumptions on the covariance of the log-density field and the cross-correlation between the log-density field and the peculiar velocity field.

These methods are used in various régimes: as extrapolation tools to recover the 3D structure of the IGM, as non-linear deconvolution tools to correct for blending, as non-parametric field extractors, and as model fitting routines to constrain the parameters of the equation of state.

We have demonstrated (Section 3.3) that as far as extrapolation is concerned the standard constrained mean field interpolation scheme could be viewed as a specific linear subcase of the Bayesian inversion scheme presented in Section 3.1. The method presented in Section 3.1 is therefore complementary to, and more general than, standard constrained mean field techniques: it can also cope with thermal broadening and finite S/N, in a manner similar to Wiener filtering, but allows for non-linear models and non-zero mean priors. The correlation functions required for the prior need not be measured in the simulations, and can be postulated. It is more flexible, since some level of redshift distortion can in principle be corrected for using the full 3D information along the bundle (although we did not demonstrate it explicitly in this paper). It is well suited for this kind of problems, since it deals directly with unknown continuous fields (i.e., the parameter space is the Hilbert space L2; see, e.g. equation D16). In contrast with the Lucy–Richardson algorithm, regularization is built in.

We have shown that temperature inversion is degenerate with respect to two parameters describing the equation of state of the gas, the temperature scalefactor $\bar{T}$ and the effective polytropic index β.

Recall that we have assumed in this paper the correlation matrices of the log density to be fixed a priori, together with the cross-correlation of the log density and the velocities when dealing with peculiar velocities. When the method is applied to real data, we will proceed iteratively and recompute these (cross-)correlations once the 3D reconstruction is achieved. We expect this procedure to converge, and that the convergence limit will not depend too strongly on the initial prior.

A thorough analysis of the various biases involved in the methods presented here is postponed to a companion paper, which will investigate statistically the properties of the reconstructed fields and the degeneracies involved in recovering the density and the temperature, while relying on numerical hydrodynamical simulations. Since this inversion method relies on existing cross-correlation between the density and the velocity fields, it should still be applicable on scales where dark matter dynamics is less relevant, so long as such correlations exist. We have left aside for now the simultaneous true 3D deconvolution of both the temperature and the peculiar velocities.

ACKNOWLEDGMENTS

We thank F. Bernardeau, E. Thiébaut and D. Pogosyan for many discussions and an introduction to constrained mean field theory. JLV and PP also thank Bob Carswell for useful discussions. JLV was supported in part by the EC TMR network ‘Galaxy Formation and Evolution’ and the Centre de Données Astronomique de Strasbourg. This work was supported by the Programme National de Cosmologie.

REFERENCES

Abel T., Haehnelt M., 1999, ApJ, 520, L13
Adler R. J., 1981, The Geometry of Random Fields. Wiley, Chichester
Alimi J.-M., Bouchet F. R., Pellat R., Sygnet J.-F., Moutarde F., 1990, ApJ, 354, 3
Backus G., Gilbert F., 1970, Phil. Trans. R. Soc. London, 266, 123
Bardeen J. M., Bond J. R., Kaiser N., Szalay A. S., 1986, ApJ, 304, 15
Bertschinger E., 1995, A&AS, 186, 2602
Bi HongGuang, Davidsen A. F., 1997, ApJ, 477, 579
Bond J. R., Wadsley J. W., 1998, in Petitjean P., Charlot S. eds, Proc. 13th IAP meeting, Structure et Evolution du Milieu Inter-Galactique Revele par Raies D’Absorption dans le Spectre des Quasars. Editions Frontières, Paris, p. 143
Bouchet F. R., Adam J.-C., Pellat R., 1985, A&A, 144, 413
Boulade O. et al., 1998, in D’Odorico S. ed., Optical Astronomical Instrumentation. Proc. SPIE 3355, p. 614
Cen R., Miralda-Escudé J., Ostriker J. P., Rauch M., 1994, ApJ, 437, L9
Colombi S., 1996, in Ansari, Giraud-Héraud, Trân Thanh Vân eds, Dark Matter in Cosmology, Quantum Measurements, Experimental Gravitation, Proc. of the XXXIst Rencontres de Moriond. Editions Frontières, Gif-sur-Yvette, France, p. 199
Colombi S., Bouchet F. R., Schaeffer R., 1994, A&A, 281, 301
Craig I. J. D., Brown J. C., 1986, Inverse Problems in Astronomy. Adam Hilger Ltd., Bristol and Boston
Croft R. A. C., Weinberg D. H., Katz N., Hernquist L., 1998, ApJ, 495, 44
Croft R. A. C., Weinberg D. H., Pettini M., Hernquist L., Katz N., 1999, ApJ, 520, 1
Crotts A. P. S., Fang Y., 1998, ApJ, 502, 16

Dinshaw N. et al., 1995, Nat, 373, 223
D'Odorico V. et al., 1998, A&A, 339, 678
Folkes S. et al., 1999, MNRAS, 308, 459
Gnedin N., Hui L., 1998, MNRAS, 296, 44
Hamilton A. J. S., Kumar P., Lu E., Matthews A., 1991, ApJ, 374, L1
Hernquist L., Katz N., Weinberg D. H., Miralda-Escudé J., 1996, ApJ, 457, L51
Hivon E., 1995, PhD thesisUniversité Paris XI
Hockney R. W., Eastwood J. W., 1981, Computer Simulation Using Particles. McGraw Hill, New York
Hoffman Y., Ribak E., 1992, ApJ, 384, 448
Hui L., 1999, ApJ, 516, 519
Hui L., Gnedin N. Y., 1997, MNRAS, 292, 27
Hui L., Rutledge R. E., 1999, ApJ, 517, 541
Hui L., Gnedin N. Y., Zhang Y., 1997, ApJ, 486, 599
Hui L., Stebbins A., Burles S., 1999, ApJ, 511, L5
Impey C. D., Foltz C. B., Petry C. E., Browne I. W. A., Patnaik A. R., 1996, ApJ, 462, L53
Jenkins A. et al., 1998, ApJ, 499, 20
Le Fèvre O. et al., 1998, in Colombi S., Mellier Y., Rabban B. eds, Proc. 14th IAP meeting. Wide Field Surveys in Cosmology. Editions Frontières, Paris, p. 327
Longuet-Higgins M. S., 1957, Phil. Trans. Roy. Soc. London A, 249, 321
Lucy L., 1974, AJ, 79, 745
Meiksin A., Madau P., 1993, ApJ, 412, 34
Miralda-Escudé J., Cen R., Ostriker J. P., Rauch M., 1996, ApJ, 471, 582
Moutarde F., Alimi J.-M., Bouchet F. R., Pellat R., Ramani A., 1991, ApJ, 382, 377
Mücket J. P., Petitjean P., Kates R., Riediger R., 1996, A&A, 308, 17
Nusser A., Haehnelt M., 1999a, MNRAS, 303, 179
Nusser A., Haehnelt M., 1999b, astro-ph/9906406
Peacock J. A., Dodds S. J., 1996, MNRAS, 280, 19, P
Peebles P. J. E., 1980, The Large-Scale Structure of the Universe. Princeton Univ. Press, Princeton, p. 153
Petitjean P. et al., 1993, MNRAS, 262, 499
Petitjean P., Mücket J., Kates R. E., 1995, A&A, 295, L9
Petitjean P., Surdej J., Smette A., Shaver P., Mücket J., Remy M., 1998, A&A, 334, L45
Pichon C., Thiébaut E., 1998, MNRAS, 301, 419
Press W. H., Rybicki G. B., 1993, APJ, 418, 585
Rahman A., 1964, Phys. Rev. A., 136, 405
Rauch M., Haehnelt M., 1995, MNRAS, 275, 76
Rauch M. et al., 1997, ApJ, 489, 7
Reisenegger A., Miralda-Escudé J., 1995, ApJ, 449, 476
Rice S. O., 1944, Bell System Tech J., 23, 282
Rice S. O., 1945, Bell System Tech J., 24, 41
Ricotti M., Gnedin N., Shull J. M., 2000, ApJ, 534, 41
Schaye J., Theuns T., Leonard A., Efstathiou G., 1999, MNRAS, 310, 57
Scoccimarro R., 1998, MNRAS, 299, 1097
Smette A. et al., 1995, A&AS, 113, 199
Szalay A., 2000, Proc. IAU Symp. 204, The Extragalactic Infrared Background and its Cosmological Implications. Astron. Soc. Pac., San Francisco, p. 16
Tarantola A., Valette B., 1982a, J. Geophys., 50, 159
Tarantola A., Valette B., 1982b, Reviews of Geophysics and Space Physics, 20, 219
Theuns T., Leonard A., Schaye J., Efstathiou G., 1999, MNRAS, 303, L58
Theuns T., Schaye J., Haehnelt M., 2000, MNRAS, 315, 600
Valageas P., Schaeffer R., Silk J., 1999, A&A, 345, 691
Vergely J. L., Freire Ferrero R., Siebert A., Valette B., 2001, A&A, 366, 1016
Weinberg D. H., 1999, in Banday A. J., Sheth R. K., da Costa L. N. eds, Proc. of ESO/MPA conf. Evolution of Large Scale Structure: from Recombination to Garching. ESO, Garching, p. 346
Weinberg D. H., Croft R. A. C., Hernquist L., Katz N., Pettini M., 1999, ApJ, 522, 563
Wiener N., 1949, Extrapolation and Smoothing of Stationary Time Series. Wiley, New York
Zaroubi S., Hoffman Y., Fisher K. B., Lahav O., 1995, ApJ, 449, 446
Zel'dovich Ya. B., 1970, A&A, 5, 84
Zhang Yu., Anninos P., Norman M. L., 1995, ApJ, 453, L57

APPENDIX A: MINIMIZATION PROCEDURE

In this section we sketch an iterative procedure leading to the optimization of the posterior probability of the model for a given data set in equation (10). The minimum of the argument of the exponential in equation (10) is shown by a simple variational argument (Tarantola & Valette, 1982a,b) to obey the implicit equation

$$\langle \boldsymbol{M} \rangle = \boldsymbol{M}_0 + \mathbf{C}_0 \cdot \mathbf{G}^{\perp} \cdot (\mathbf{C}_\mathrm{d} + \mathbf{G} \cdot \mathbf{C}_0 \cdot \mathbf{G}^{\perp})^{-1} \cdot [\boldsymbol{D} + \mathbf{G} \cdot (\langle \boldsymbol{M} \rangle - \boldsymbol{M}_0) - g(\langle \boldsymbol{M} \rangle], \qquad \text{(A1)}$$

with $\mathbf{G}$, the matrix of partial derivatives:

$$\mathbf{G} = \left(\frac{\partial g}{\partial \boldsymbol{M}}\right). \tag{A2}$$

This minimum is found using an iterative procedure:

$$\boldsymbol{M}_{[k+1]} = \boldsymbol{M}_0 + \mathbf{C}_0 \cdot \mathbf{G}_{[k]}^{\perp} \cdot (\mathbf{C}_\mathrm{d} + \mathbf{G}_{[k]} \cdot \mathbf{C}_0 \cdot \mathbf{G}_{[k]}^{\perp})^{-1} \cdot [\boldsymbol{D} + \mathbf{G}_{[k]} \cdot (\boldsymbol{M}_{[k]} - \boldsymbol{M}_0) - g(\boldsymbol{M}_{[k]}], \tag{A3}$$

where subscript $[k]$ refers to the iteration order. In this scheme the minimum corresponds to $\tilde{\boldsymbol{M}} = \boldsymbol{M}_{[\infty]}$, and in practice is found via a convergence criterion on the relative changes between iteration $[k]$ and $[k+1]$. For the sake of numerical efficiency, rather than inverting $(\mathbf{C}_\mathrm{d} + \mathbf{G}_{[k]} \cdot \mathbf{C}_0 \cdot \mathbf{G}_{[k]}^{\perp})$, we solve for the vector $\boldsymbol{W}_{[k]}$ satisfying

$$\mathbf{S}_{[k]} \cdot \boldsymbol{W}_{[k]} = [\boldsymbol{D} + \mathbf{G}_{[k]} \cdot (\boldsymbol{M}_{[k]} - \boldsymbol{M}_0) - g(\boldsymbol{M}_{[k]}), \quad \text{where} \quad \mathbf{S}_{[k]} = \mathbf{C}_\mathrm{d} + \mathbf{G}_{[k]} \cdot \mathbf{C}_0 \cdot \mathbf{G}_{[k]}^{\perp}, \tag{A4}$$

and iterate:

$$\boldsymbol{M}_{[k+1]} = \boldsymbol{M}_0 + \mathbf{C}_0 \cdot \mathbf{G}_{[k]}^{\perp} \cdot \boldsymbol{W}_{[k]}. \tag{A5}$$

From now on, we drop the subscript $[k]$. Once the maximum of equation (10) has been reached, an approximation of the internal error made on the parameter estimation is derived from a second-order development of the posterior distribution function in the vicinity of the solution:

$$\mathbf{C}_{\boldsymbol{M}} = \mathbf{C}_0 - \mathbf{C}_0 \cdot \mathbf{G}^{\perp} \cdot \mathbf{S}^{-1} \cdot \mathbf{G} \cdot \mathbf{C}_0. \tag{A6}$$

The high spatial frequency fluctuations are lost in the inverse process because of limited resolution and finite S/N. The *prior* correlation function therefore plays an important role to transform an ill-posed problem into an invertible one. How is the density information degraded in the spectra? This question can be addressed via the resolving kernel, $\boldsymbol{R}$, introduced for the first time by Backus & Gilbert (1970) and which gives the spread of the density estimation at a given position. Suppose that we know the true model, $\boldsymbol{M}_\mathrm{true}$. The data can be written: $\boldsymbol{D} = \boldsymbol{g}(\boldsymbol{M}_\mathrm{true})$. Approximating locally operator g near its minimum as a linear operator, equation (A1) yields:

$$\langle \boldsymbol{M} \rangle - \boldsymbol{M}_0 = \mathbf{C}_0 \cdot \mathbf{G}^{\perp} \cdot \mathbf{S}^{-1} \cdot \mathbf{G} \cdot (\boldsymbol{M}_\mathrm{true} - \boldsymbol{M}_0) \equiv \boldsymbol{R} \cdot (\boldsymbol{M}_\mathrm{true} - \boldsymbol{M}_0), \tag{A7}$$

which defines the resolving kernel $\boldsymbol{R}(x, x')$ as a low-bandpass filter.

APPENDIX B: CONSTRAINTS, MEAN FIELDS AND MULTIPLE LINE OF SIGHTS

As a thought experiment, let us assume that we know the density contrast δ on n points and ask what the corresponding most likely velocity (or density) at points labelled $k = 1 \ldots p$, ϖ_k is. We shall not assume that the densities $\delta_1, \ldots, \delta_n$ are necessarily along the same LOS, nor that the quantity ϖ_k is sought along any of these. Let $X = [\varpi_1, \ldots, \varpi_p, \delta_1, , \delta_n]$. We define

$$\mathbf{C} \equiv \begin{bmatrix} \langle \varpi_1 \varpi_1 \rangle & \ldots & \langle \varpi_1 \varpi_p \rangle & \langle \varpi_1 \delta_1 \rangle & \ldots & \langle \varpi_1 \delta_n \rangle \\ \vdots & \ddots & \vdots & \vdots & \ddots & \vdots \\ \langle \varpi_1 \varpi_p \rangle & \ldots & \langle \varpi_p \varpi_p \rangle & \langle \varpi_p \delta_1 \rangle & \ldots & \langle \varpi_p \delta_n \rangle \\ \langle \varpi_1 \delta_1 \rangle & \ldots & \langle \varpi_p \delta_1 \rangle & \langle \delta_1 \delta_1 \rangle & \ldots & \langle \delta_1 \delta_n \rangle \\ \vdots & \ddots & \vdots & \vdots & \ddots & \vdots \\ \langle \varpi_1 \delta_n \rangle & \ldots & \langle \varpi_p \delta_n \rangle & \langle \delta_1 \delta_n \rangle & \ldots & \langle \delta_n \delta_n \rangle \end{bmatrix} \equiv \begin{bmatrix} \mathbf{C}_{ww} & \mathbf{C}_{w\delta} \\ \mathbf{C}_{w\delta}^{\perp} & \mathbf{C}_{\delta\delta} \end{bmatrix}, \tag{B1}$$

so that $\mathbf{C}_{ww}$ is the $p \times p$ autocorrelation matrix of the sought field, $\mathbf{C}_{\delta\delta}$ is the $n \times n$ autocorrelation matrix of the known density field, and $\mathbf{C}_{w\delta}$ is the $p \times n$ cross-correlation matrix of the sought field with the density field. The joint probability of achieving velocity ϖ_k and density profile $\delta_1, \ldots, \delta_n$ is given by

$$p(X)\, \mathrm{d}^{n+p} X = p(\varpi_1, \ldots, \varpi_p, \delta_1, \ldots, \delta_n)\, \mathrm{d}\varpi_1 \ldots \mathrm{d}\varpi_p\, \mathrm{d}\delta_1 \ldots \mathrm{d}\delta_n = \exp\left\{ -\frac{1}{2} \left[\sum_{a,b=1 \ldots n+p} (C^{-1})_{a,b} X_a X_b \right] \right\} \frac{\mathrm{d}^{n+p} X}{\sqrt{(2\pi)^{n+p} \det|C|}}.$$

The argument of the exponential can be rearranged as

$$(\boldsymbol{\varpi}, \delta)^{\perp} \cdot \begin{bmatrix} \mathbf{C}_{ww} & \mathbf{C}_{w\delta} \\ \mathbf{C}_{w\delta}^{\perp} & \mathbf{C}_{\delta\delta} \end{bmatrix}^{-1} \cdot (\boldsymbol{\varpi}, \delta) = (\boldsymbol{\varpi} - \mathbf{C}_{w\delta} \cdot \mathbf{C}_{\delta\delta}^{-1} \cdot \delta)^{\perp} \cdot (\mathbf{C}_{ww} - \mathbf{C}_{w\delta} \cdot \mathbf{C}_{\delta\delta}^{-1} \cdot \mathbf{C}_{w\delta}^{\perp})^{-1} \cdot (\boldsymbol{\varpi} - \mathbf{C}_{w\delta} \cdot \mathbf{C}_{\delta\delta}^{-1} \cdot \delta) + \text{ rest} \tag{B2}$$

where 'rest' stands for terms independent of $\boldsymbol{\varpi} \equiv (\varpi_1 \ldots \varpi_p)$. Applying Bayes's theorem, the conditional probability of $\boldsymbol{\varpi}$, given the density profile $(\delta_1, \ldots, \delta_n)$, obeys

$$p(\varpi_1, \ldots, \varpi_p|\delta_1, \ldots, \delta_n)\,\mathrm{d}\varpi_1\ldots\mathrm{d}\varpi_p = p(\varpi_1, \ldots\varpi_p, \delta_1, \ldots, \delta_n)/p(\delta_1, \ldots, \delta_n)\,\mathrm{d}\varpi_1\ldots\mathrm{d}\varpi_p,$$

which in turns implies that

$$p(\varpi_1, \ldots, \varpi_p|\delta_1, \ldots, \delta_n) \propto \exp\left[-\frac{1}{2}\left\{(\boldsymbol{\varpi} - \mathbf{C}_{w\delta}\cdot\mathbf{C}_{\delta\delta}^{-1}\cdot\delta)^{\perp}\cdot(\mathbf{C}_{ww} - \mathbf{C}_{w\delta}\cdot\mathbf{C}_{\delta\delta}^{-1}\cdot\mathbf{C}_{w\delta}^{\perp})^{-1}\cdot(\boldsymbol{\varpi} - \mathbf{C}_{w\delta}\cdot\mathbf{C}_{\delta\delta}^{-1}\cdot\delta)\right\}\right],$$

since $p(\delta_1, \ldots, \delta_n)$ is independent of $\boldsymbol{\varpi}$. The maximum of the conditional probability is therefore reached for $\langle\boldsymbol{\varpi}\rangle$ given by

$$\langle\boldsymbol{\varpi}\rangle = \mathbf{C}_{w\delta}\cdot\mathbf{C}_{\delta\delta}^{-1}\cdot\delta. \tag{B3}$$

Appendix B1 Peculiar velocity–density relation

Let us now be more specific about ϖ_k and assume, in this subsection, that we are seeking the most likely peculiar velocity field, v_k, where we dropped the subscript p referring to 'peculiar'.

Appendix B1.1 One line of sight

Recall that nothing has been said about the relative position of the δ_i and the v_k at this stage. Let us now assume for a while that the subscript i refers to a regular ordering along the LOS, so that $\delta_i = \delta(i\Delta x)$, and $v_i = v(i\Delta x)$. Let us also introduce the intermediate field, $\boldsymbol{u} = (u_i)_{i=1\ldots n} \equiv \mathbf{C}_{\delta\delta}^{-1}\cdot\boldsymbol{\delta}$, so that equation (B3) reads

$$\langle\boldsymbol{v}\rangle = \mathbf{C}_{v\delta}\cdot\boldsymbol{u}, \quad \boldsymbol{\delta} = \mathbf{C}_{\delta\delta}\cdot\boldsymbol{u}. \tag{B4}$$

Multiplying both sides of equation (B4) by Δx, we get

$$\sum_j (C_{v\delta})_{i,j} u_j \Delta x = \sum_j u[j\Delta x]\langle v[j\Delta x]\delta[(i-j)\Delta x]\rangle\Delta x = \langle v[i\Delta x]\rangle\Delta x,$$

$$\sum_j (C_{\delta\delta})_{i,j} u_j \Delta x = \sum_j u[j\Delta x]\langle \delta[j\Delta x]\delta[(i-j)\Delta x]\rangle\Delta x = \delta[i\Delta x]\Delta x. \tag{B5}$$

In the limit of Δx going to zero, equation (B5) reads

$$\int\langle\delta(x-x')v(x')\rangle u(x')\,\mathrm{d}x' = \langle v(x)\rangle\Delta x \quad \text{and} \quad \int\langle\delta(x-x')\delta(x')\rangle u(x')\,\mathrm{d}x' = \delta(x)\Delta x. \tag{B6}$$

Transforming equation (B6) in Fourier space leads to

$$\langle\tilde{v}\rangle(k_x) = \frac{P_{v\delta,1\mathrm{D}}(k_x)}{P_{\delta\delta,1\mathrm{D}}(k_x)}\tilde{\delta}(k_x), \tag{B7}$$

where $P_{\delta\delta,1\mathrm{D}}(k_x)$ and $P_{v\delta,1\mathrm{D}}(k_x)$ are respectively the 1D density power spectrum and the 1D mixed velocity density power spectrum, while $\tilde{\delta}(k_x)$ and $\langle\tilde{v}\rangle(k_x)$ are the Fourier transform of $\delta(x)$ and $\langle v\rangle(x)$ respectively. Here the 1D power spectra satisfy

$$P_{\delta\delta,1\mathrm{D}}(k_x) = \int P_{3\mathrm{D}}(\boldsymbol{k})W_{\mathrm{J}}(\boldsymbol{k})\,\mathrm{d}^2k_{\perp} \quad \text{and} \quad P_{v\delta,1\mathrm{D}}(k_x) = \int\frac{P_{3\mathrm{D}}(\boldsymbol{k})k_x}{k_x^2 + k_{\perp}^2}W_{\mathrm{J}}(\boldsymbol{k})\,\mathrm{d}^2k_{\perp}, \tag{B8}$$

where $P_{3\mathrm{D}}(\boldsymbol{k})$ is the 3D power spectrum of the density contrast, while $W_{\mathrm{J}}(\boldsymbol{k})$ is a window function whose characteristic scale R_{J} should be the Jeans length, but is chosen here to be the maximum of the Jeans length and the sampling scale. Indeed, below this latter scale no information is to be derived from the data. Note that the direct inversion of equation (B3) may lead to significant aliasing if the power spectrum has energy beyond the cut-off frequency $1/R_{\mathrm{J}}$. The power spectrum ratio in equation (B7) is an antisymmetric filter which relates the most likely velocity field to a given density field in linear theory.

Equation (B7) can be transformed back into real space as

$$\langle v\rangle(x) = \int K^{(v)}(x,x')\delta(x')\,\mathrm{d}x', \quad \text{where} \quad K^{(v)}(x,x') \equiv \frac{1}{2\pi}\int \mathrm{e}^{\mathrm{i}k_x(x-x')}\frac{P_{v\delta,1\mathrm{D}}(k_x)}{P_{\delta\delta,1\mathrm{D}}(k_x)}\mathrm{d}k_x. \tag{B9}$$

This filter is illustrated in Fig. 6. Equation (B9) could be used to derive $K^{(v)}(x,x')$ from perturbation theory in the weakly non-linear régime given an initial power spectrum. In practice, this filter is constructed here from the simulation in the following manner: for each LOS in the simulation, we compute the FFT of the overdensity and of the velocity; we multiply one by the complex conjugate of the other, and repeat the operation on the whole box; we then average over the box (using a bundle of 60×60 LOSs) and FFT-transform back in real space: this yields equation (B9).

Appendix B1.2 Multiple lines of sight

Let us now turn to the more general problem of multiple LOSs. How can we take advantage of larger scale information on multiple LOSs to constrain the velocity *along* the measured LOSs ?

To conduct the calculation which follows, we order the $\delta_1, \ldots, \delta_n$, where $n = Lp$, so that the first p corresponds to the first LOS, the next p to the second LOS, and so on for the $\ell = 1 \ldots L$ LOSs. Our purpose here is to account for the fact that in realistic situations, the LOSs distribution on the sky is not necessarily uniform and that the volume covered by all LOSs is rather elongated (i.e., $L \ll p$). For the sake of numerical efficiency, we Fourier-transform along the longitudinal direction and are left with a matrix representation for the two transverse dimensions. We write each block in Fourier space in terms of the corresponding 1D power spectra (this is possible since both Fourier transform and matrix multiplication are linear operations, which therefore commute when applied on different directions); following the derivation of equation (B7) we find

$$\langle \tilde{\boldsymbol{v}} \rangle = \tilde{\boldsymbol{\Xi}} \cdot \tilde{\boldsymbol{\Delta}}^{-1} \cdot \tilde{\boldsymbol{\delta}}, \tag{B10}$$

where

$$\tilde{\boldsymbol{\Delta}} \equiv \begin{bmatrix} P^{11}_{\delta\delta}(k_x) & \ldots & P^{1L}_{\delta\delta}(k_x) \\ \vdots & \ddots & \vdots \\ P^{1L}_{\delta\delta}(k_x) & \ldots & P^{LL}_{\delta\delta}(k_x) \end{bmatrix}, \quad \tilde{\boldsymbol{\Xi}} \equiv \begin{bmatrix} P^{11}_{v\delta}(k_x) & \ldots & P^{1L}_{v\delta}(k_x) \\ \vdots & \ddots & \vdots \\ P^{1L}_{v\delta}(k_x) & \ldots & P^{LL}_{v\delta}(k_x) \end{bmatrix}, \tag{B11}$$

and $\langle \tilde{\boldsymbol{v}} \rangle = [\tilde{v}^1(k_x), \ldots \tilde{v}^L(k_x)]$, $\tilde{\boldsymbol{\delta}} = [\tilde{\delta}^1(k_x), \ldots \tilde{\delta}^L(k_x)]$, where the superscript refers to the L LOSs. Here

$$P^{\ell\ell'}_{\delta\delta}(k_x) = \int \exp\left(\mathrm{i}\boldsymbol{k}_\perp \cdot \{\boldsymbol{x}_{\perp,\ell} - \boldsymbol{x}_{\perp,\ell'}\}\right) P_{3\mathrm{D}}(\boldsymbol{k}) W_{\mathrm{J},\bar{R}}(\boldsymbol{k})\, \mathrm{d}^2\boldsymbol{k}_\perp, \tag{B12}$$

$$P^{\ell\ell'}_{v\delta}(k_x) = \int \exp\left(\mathrm{i}\boldsymbol{k}_\perp \cdot \{\boldsymbol{x}_{\perp,\ell} - \boldsymbol{x}_{\perp,\ell'}\}\right) W_{\mathrm{J},\bar{R}}(\boldsymbol{k}) \frac{P_{3\mathrm{D}}(\boldsymbol{k}) k_x}{k_x^2 + \boldsymbol{k}_\perp^2}\, \mathrm{d}^2\boldsymbol{k}_\perp. \tag{B13}$$

The window function, $W_{\mathrm{J},\bar{R}}(k_x, \boldsymbol{k}_\perp)$ involves two scales: the longitudinal Jeans length and the transverse mean inter-LOS separation, $\bar{R}$. The latter filtering is required to apodize the inversion. Note that $P^{\ell\ell}_{\delta\delta}(k_x) = P_{\delta\delta,1\mathrm{D}}(k_x)$ and $P^{\ell\ell}_{\delta v}(k_x) = P_{\delta v,1\mathrm{D}}(k_x)$ are given by equation (B8). Equation (B10) reads back into real space:

$$v_{\ell'}(x) = \sum_\ell \int K_{\ell'\ell}(x, x') \delta_\ell(x')\, \mathrm{d}x', \quad \text{where} \quad K_{\ell'\ell}(x, x') \equiv \frac{1}{2\pi} \int \mathrm{e}^{\mathrm{i}k_x(x-x')} (\tilde{\boldsymbol{\Xi}} \cdot \tilde{\boldsymbol{\Delta}}^{-1})_{\ell'\ell}\, \mathrm{d}k_x, \tag{B14}$$

where the matrix $\tilde{\boldsymbol{\Xi}} \cdot \tilde{\boldsymbol{\Delta}}^{-1}$ is given in equation (B11). In practice, this filter is also constructed here from the simulation following the prescription sketched above: for each bundle of LOSs in the simulation, we compute the FFT of the log density and of the velocity; we multiply one bundle by the complex conjugate of the other, and repeat the operation on the whole box; we then average over the box (using a bundle of 20×20 LOSs): this yields the matrix (B11). The matrix multiplication in equation (B14) is carried Fourier mode by Fourier mode, while the inverse Fourier transform is done by FFT.

Appendix B2 3D density–LOSs density relation

Let us now assume that ϖ_k refers to the 3D density on a grid of P points at the point $\boldsymbol{x}_\lambda = (\boldsymbol{x}_{\perp,\lambda}, x_\lambda)_{\lambda=1\ldots P}$. No restriction on the location of $\boldsymbol{x}_\lambda$ along the LOSs applies here. Under these assumptions, the above section translate as:

$$\langle \delta^{(3\mathrm{D})} \rangle(\boldsymbol{x}_\lambda) = \sum_\ell \int K^{(3\mathrm{D})}_{\lambda\ell}(\boldsymbol{x}_\lambda, \boldsymbol{x}'_\ell) \delta_\ell(x')\, \mathrm{d}x', \quad \text{where} \quad K^{(3\mathrm{D})}_{\lambda\ell}(\boldsymbol{x}_\lambda, \boldsymbol{x}_\ell{}') \equiv \frac{1}{(2\pi)^3} \int \exp[\mathrm{i}\boldsymbol{k} \cdot (\boldsymbol{x}_\lambda - \boldsymbol{x}_\ell{}')] (\tilde{\boldsymbol{\Xi}}_{3\mathrm{D}} \cdot \tilde{\boldsymbol{\Delta}}^{-1})_{\lambda\ell}\, \mathrm{d}^3\boldsymbol{k} \tag{B15}$$

with $\tilde{\boldsymbol{\Delta}}$ obeying equation (B11) and

$$\tilde{\boldsymbol{\Xi}}_{3\mathrm{D}} = \begin{bmatrix} P^{11}_{3\mathrm{D}}(k_x) & \ldots & P^{L1}_{3\mathrm{D}}(k_x) \\ \vdots & \ddots & \vdots \\ P^{1P}_{3\mathrm{D}}(k_x) & \ldots & P^{LP}_{3\mathrm{D}}(k_x) \end{bmatrix}, \quad \text{given} \quad P^{\ell\lambda}_{3\mathrm{D}}(k_x) = \int \exp\left(\mathrm{i}\boldsymbol{k}_\perp \cdot \{\boldsymbol{x}_{\perp,\ell} - \boldsymbol{x}_{\perp,\lambda}\}\right) P_{3\mathrm{D}}(\boldsymbol{k}) W_{\mathrm{J},\bar{R}}(\boldsymbol{k})\, \mathrm{d}^2\boldsymbol{k}_\perp. \tag{B16}$$

We check that when we consider a point on the LOSs, $\boldsymbol{x} = (\boldsymbol{x}_{\perp,\ell}, x)$, $K^{(3\mathrm{D})}_{\lambda\ell}(\boldsymbol{x}, x') = \delta_\mathrm{D}(x - x') \tilde{\delta}^\lambda_\ell$, where $\tilde{\delta}^\lambda_\ell$ stands for the Kronecker symbol.

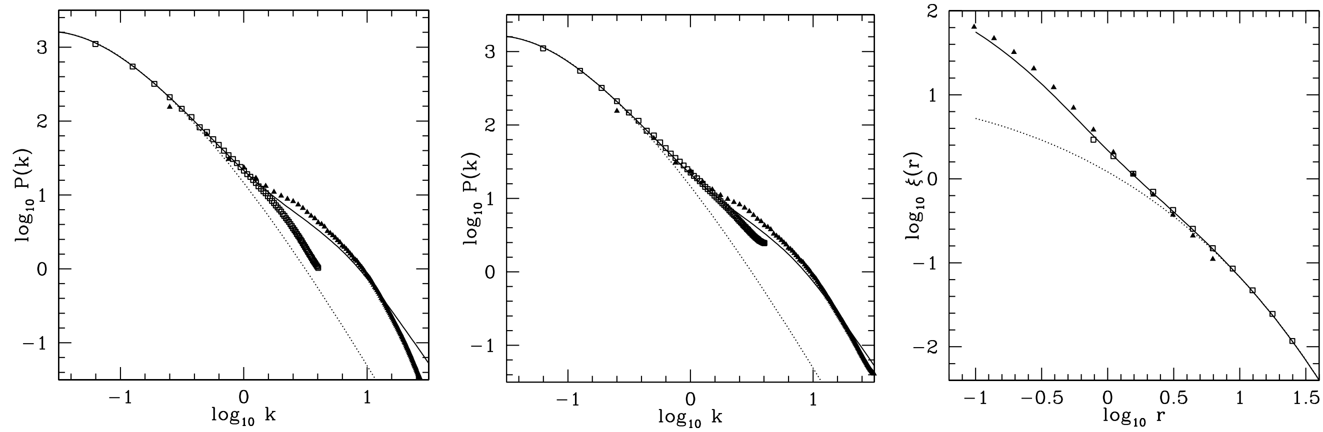

Figure C1. *Left-hand panel:* the power spectrum measured at $z = 2$ in the S (filled triangles) and B (open squares) simulations after adaptive smoothing, in logarithmic coordinates (wavenumber k is expressed in Mpc^{-1}). It is compared to linear theory (dots) and to non-linear Ansatz of Peacock & Dodds (1996, solid curve). *Middle panel:* same as left-hand panel, except that a correction for NGP damping was applied to the data prior to measurement of $P(k)$. *Right-hand panel:* the variance of the smoothed density field with a spherical cell of radius r is shown in logarithmic coordinates as a function of r, as explained in the text.

APPENDIX C: PROPERTIES OF THE SIMULATION

Note from Table 1 that the simulation boxes are rectangular. This long-box technique might be questionable. Indeed, the number of modes available in Fourier space is different along each coordinate axis. This anisotropic mode sampling contaminates the simulation, and the effect augments with the ratio between the largest and the smallest side of the box.

One way to test, at least partly, the quality of our N-body experiments is to compare second-order statistics measured in the simulations to theoretical predictions, as illustrated by Fig. C1. The left-hand panel shows the measured power spectrum, $P(k) = \langle|\delta_k|^2\rangle$, in the density field smoothed with the procedure described in Section 4. Agreement with linear theory is appropriate at large scales, as expected. For comparison, we also plot the result obtained from the non-linear Ansatz of Hamilton et al. (1991) optimized for the power spectrum by Peacock & Dodds (1996). The overall agreement between measurements and non-linear theory is quite good, except at large values of k in both simulations. This is mainly the effect of the grid, and to a lesser extent a consequence of the adaptive Gaussian smoothing. Indeed, any procedure inferring on a grid a density from a particle distribution implies some smoothing with a window of approximately the mesh cell size. This induces large-k damping of the power spectrum. Here, the smoothing is not well defined, but most of the particles are in dense regions, due to non-linear clustering, and therefore the corresponding smoothing length, ℓ, is likely to be much smaller than the grid size. Thus, for most particles, all the contribution to the density is given to the nearest grid point (NGP). As a result, the Gaussian adaptive smoothing has a damping effect quite close, though slightly larger, to top-hat smoothing with a mesh cell (at least for sufficiently evolved stages). This is illustrated by middle panel of Fig. C1, which shows the power spectrum after correction for damping due to NGP assignment. Most of the missing power is recovered, as expected, and the agreement with theory is much improved. Note that the triangles tend to be slightly above the solid curve in the neighbourhood of $\log_{10}k \simeq 0.4$. This irregularity is not surprising, given the small physical size of simulation S. It is probably associated with a rare event, for example an atypical cluster, although this does not show up significantly in Fig. 1.

The right-hand panel of Fig. C1 shows the real-space counterpart of the power spectrum. More precisely, it displays the variance of the smoothed density field with a sphere of radius ℓ as a function of ℓ. To measure it, we computed the density from the particle distribution on a grid twice thinner than the one used to do the simulation, using the cloud-in-cell method (CIC) (e.g. Hockney & Eastwood 1981). Then we corrected for CIC damping and smoothed with the top-hat window of size ℓ in Fourier space. Finally, back in real space, the variance of the density field was computed with the appropriate corrections for discreteness (e.g. Peebles 1980), i.e., $\sigma^2 = \langle\delta^2\rangle - 1/\bar{N}$, where $\bar{N}$ is the average particle count in a cell of radius ℓ. The scale range considered was $\lambda_{\mathrm{g}} \leq \ell \leq L/4$, where L is the smallest dimension of the box and λ_{g} the spatial resolution of the simulation. As can been seen in Fig. C1, the agreement with theoretical predictions is quite good, even at $\ell \simeq \lambda_{\mathrm{g}}$, although the effect of softening of the forces is slightly felt at this point. Note also that the triangles are somewhat shifted up compared to the non-linear Ansatz (except at very large scales, where finite-volume-effect contamination reduces the value of σ^2; e.g. Colombi, Bouchet & Schaeffer 1994), as already noticed for the power spectrum.

APPENDIX D: IMPLEMENTATION OF THE INVERSE METHOD

Appendix D1 Neglecting peculiar velocities

Appendix D1.1 High-resolution spectra

When the spectral resolution is higher than $100\,\mathrm{km}^{-1}$, thermal broadening cannot be neglected and our model reads

$$g_{i\ell}(\gamma) = A(\bar{z})c_1 \int\!\!\int \left(\int_{-\infty}^{+\infty} \{D_0(x, \boldsymbol{x}_\perp)\exp[\gamma(x, \boldsymbol{x}_\perp)]\}^{\alpha-\beta} \exp\left[-c_2 \frac{(w_{i\ell} - x)^2}{\{D_0(x, \boldsymbol{x}_\perp)\exp[\gamma(x, \boldsymbol{x}_\perp)]\}^{2\beta}} \right] \mathrm{d}x \right) \delta_{\mathrm{D}}(\boldsymbol{x}_\perp - \boldsymbol{x}_{\perp\ell})\, \mathrm{d}^2\boldsymbol{x}_\perp, \tag{D1}$$

where α, $A(\bar{z})$, c_1, c_2, β, $D_0(x, \boldsymbol{x}_\perp)$ and $w_{i\ell}$ are defined in equations (3)–(7) and equation (25). Since the model, $\boldsymbol{M} \equiv \gamma(x, \boldsymbol{x}_\perp)$ is a continuous field, we need to interpret equation (6) in terms of convolutions, and functional derivatives. In particular, the matrix of partial functional (Fréchet) derivatives, $\mathbf{G}$, has the following kernel:

$$(\mathbf{G})_{i\ell}(x, \boldsymbol{x}_\perp) \equiv \left(\frac{\partial g_{i\ell}}{\partial \gamma}\right)(x, \boldsymbol{x}_\perp) = A(\bar{z}) c_1 D_0^{\alpha-\beta}(x, \boldsymbol{x}_\perp) \exp\left[(\alpha - \beta)\gamma(x, \boldsymbol{x}_\perp)\right] B_{i\ell}(x, \boldsymbol{x}_\perp) \delta_{\mathrm{D}}(\boldsymbol{x}_\perp - \boldsymbol{x}_{\perp,\ell}), \tag{D2}$$

with $\delta_{\mathrm{D}}(\boldsymbol{x}_\perp - \boldsymbol{x}_{\perp,\ell})$ the Dirac delta function accounting for the singular distribution of LOSs, and

$$B_{i\ell}(x, \boldsymbol{x}_\perp) = \{(\alpha - \beta) + c_2 2\beta (w_{i\ell} - x)^2 D_0^{-2\beta}(x, \boldsymbol{x}_\perp) \exp[-2\beta\gamma(x, \boldsymbol{x}_\perp)]\} \mathcal{B}_{i\ell}(x, \boldsymbol{x}_\perp), \tag{D3}$$

where

$$\mathcal{B}_{i\ell}(x, \boldsymbol{x}_\perp) = \exp\left[-c_2 \frac{(w_{i\ell} - x)^2}{\{D_0(x, \boldsymbol{x}_\perp) \exp[\gamma(x, \boldsymbol{x}_\perp)]\}^{2\beta}}\right]. \tag{D4}$$

The operator, $\mathbf{G}$, defined by equation (D2) contracts over a given field, η, as:

$$(\mathbf{G})_{il} \cdot \eta = \int A(\bar{z}) c_1 D_0^{\alpha-\beta}(x, \boldsymbol{x}_\perp) \exp[(\alpha - \beta)\gamma(x, \boldsymbol{x}_\perp)] B_{i\ell}(x, \boldsymbol{x}_{\perp,\ell}) \eta(x, \boldsymbol{x}_{\perp,\ell})\, \mathrm{d}x. \tag{D5}$$

Appendix D1.2 Low-resolution spectra

At low spectral resolution, the model spells

$$g_{i\ell}(\gamma) = A(\bar{z}) \int\int\int (D_0(x, \boldsymbol{x}_\perp) \exp[\gamma(x, \boldsymbol{x}_\perp)])^\alpha \delta_{\mathrm{D}}(x - w_{i\ell}) \delta_{\mathrm{D}}(\boldsymbol{x}_\perp - \boldsymbol{x}_{\perp,\ell})\, \mathrm{d}x\, \mathrm{d}^2\boldsymbol{x}_\perp, \tag{D6}$$

which corresponds to the limit $c_2 \rightarrow \infty$ in equation (D1). The kernel of partial functional derivatives $\mathbf{G}$ obeys

$$(\mathbf{G})_{i\ell}(x, \boldsymbol{x}_\perp) = A(\bar{z}) \alpha D_0^\alpha(x, \boldsymbol{x}_{\perp,\ell}) \exp[\alpha\gamma(x, \boldsymbol{x}_{\perp,\ell})] \delta_{\mathrm{D}}(x - w) \delta_{\mathrm{D}}(\boldsymbol{x}_\perp - \boldsymbol{x}_{\perp,\ell}). \tag{D7}$$

For instance, $(\mathbf{G} \cdot \mathbf{C}_0 \cdot \mathbf{G}^\perp)_{i\ell,jm}$ in equation (A1) reads

$$A(\bar{z})^2 \alpha^2 C_{\gamma\gamma}(w_{i\ell}, w_{jm}, \boldsymbol{x}_{\perp,\ell}, \boldsymbol{x}_{\perp,m}) D_0^\alpha(w_{i\ell}, \boldsymbol{x}_{\perp,\ell}) D_0^\alpha(w_{jm}, \boldsymbol{x}_{\perp,m}) \exp[\alpha\gamma(w_{i\ell}, \boldsymbol{x}_{\perp,\ell}) + \alpha\gamma(w_{jm}, \boldsymbol{x}_{\perp,m})]. \tag{D8}$$

Appendix D2 Implementation of the inverse method with peculiar velocities

Appendix D2.1 Strong prior: peculiar velocity equals most likely velocity

Restricting ourselves to a unique LOS, our model reads

$$g_{i\ell}(\gamma) = A(\bar{z}) c_1 \int_{-\infty}^{+\infty} \{D_0(x) \exp[\gamma(x)]\}^{\alpha-\beta} \exp\left[-c_2 \frac{[w_{i\ell} - x - v_{\mathrm{p}}(x)]^2}{\{D_0(x) \exp[\gamma(x)]\}^{2\beta}}\right] \mathrm{d}x, \tag{D9}$$

where the peculiar velocity, $v_{\mathrm{p}}(x)$, equals the most likely velocity

$$\langle v_{\mathrm{p}}(x) \rangle = \int K^{(v)}(x, y) \gamma(y)\, \mathrm{d}y. \tag{D10}$$

The matrix of partial functional derivatives, $\mathbf{G}_i$ is defined by its contraction over a given field, η, as:

$$(\mathbf{G})_i \cdot \eta \equiv \int G_i(x) \eta(x)\, \mathrm{d}x = \int \mathcal{A}_i(x) \eta(x)\, \mathrm{d}x + \int \mathcal{D}_i(x) \left[\int K^{(v)}(x, y) \eta(y)\, \mathrm{d}y\right] \mathrm{d}x, \tag{D11}$$

with

$$\mathcal{A}_i(x) = A(\bar{z}) c_1 D_0^{\alpha-\beta}(x) \exp\left[(\alpha - \beta)\gamma(x)\right] \{\alpha - \beta + 2\beta c_2 D_0^{-2\beta} \exp\left[-2\beta\gamma(x)\right][w_i - x - v_{\mathrm{p}}(x)]\} E_i(x), \tag{D12}$$

$$\mathcal{D}_i(x) = A(\bar{z}) c_1 D_0^{(\alpha-3\beta)}(x) \exp\left[(\alpha - 3\beta)\gamma(x)\right] 2c_2 [w_i - x - v_{\mathrm{p}}(x)] E_i(x), \tag{D13}$$

$$E_i(x) = \exp\left\{-c_2 \frac{[w_i - x - v_{\mathrm{p}}(x)]^2}{D_0^{2\beta}(x) \exp\left[2\beta\gamma(x)\right]}\right\}. \tag{D14}$$

The double integration in the last term of equation (D11) arises because g is effectively a double convolution.

Appendix D2.2 Weak prior: floating peculiar velocity

We aim to determine directly the density and the velocity, while assuming the correlations between these two quantities are known. The model is identical to equation (D9), but the peculiar velocity does not obey equation (D10). The matrix of partial functional derivatives is $\mathbf{G} = (\partial g/\partial\gamma, \partial g/\partial v_p)$. The first component of $\mathbf{G}$ is given by equation (D2). The kernel of the second component is computed as follows:

$$\frac{\partial g}{\partial v_p} = A(\bar{z})c_1 D_0^{\alpha-3\beta}(x)\exp\left[(\alpha-3\beta)\gamma(x)\right]2c_2[w_i - x - v_\mathrm{p}(x)]E_i(x) \equiv \mathcal{E}_i(x), \tag{D15}$$

where $E_i(x)$ is given by equation (D14). The matrix $\mathbf{G}\cdot\mathbf{C}_0\cdot\mathbf{G}^\perp$ (where MC_0 is given by equation (35) is computed as follows:

$$\int\int[\mathcal{A}_i(x)\mathcal{A}_j(y)C_{\gamma\gamma}(x,y) + \mathcal{A}_i(x)\mathcal{E}_j(y)C_{\gamma v}(x,y) + \mathcal{E}_i(x)\mathcal{A}_j(y)C_{v\gamma}(x,y) + \mathcal{E}_i(x)\mathcal{E}_j(y)C_{vv}(x,y)]\,\mathrm{d}x\,\mathrm{d}y. \tag{D16}$$

Note that this is a double integral to be compared to the quadruple integral involved in the computation of the equivalent term in the strong prior method (where contraction already involves a double convolution).

This paper has been typeset from a TEX/LATEX file prepared by the author.

Mon. Not. R. Astron. Soc. **365,** 615–637 (2006) doi:10.1111/j.1365-2966.2005.09753.x

The sources of intergalactic metals

E. Scannapieco,[1★] C. Pichon,[2,3] B. Aracil,[4] P. Petitjean,[2,5] R. J. Thacker,[6] D. Pogosyan,[7] J. Bergeron[2] and H. M. P. Couchman[8]

[1] *Kavli Institute for Theoretical Physics, Kohn Hall, University of California Santa Barbara, Santa Barbara, CA 93106, USA*
[2] *Institut d'Astrophysique de Paris, 98 bis Boulevard d'Arago, F-75014 Paris, France*
[3] *Observatoire de Strasbourg, 11 Rue de l'Université, F-67000 Strasbourg, France*
[4] *Department of Astronomy, University of Massachusetts, Amherst, MA 01003, USA*
[5] *LERMA, Observatoire de Paris, 61 Avenue de l'Observatoire, F-75014 Paris, France*
[6] *Department of Physics, Queen's University, Kingston, Ontario, K7L 3N6, Canada*
[7] *Department of Physics, University of Alberta, 412 Avadh Bhatia Physics Laboratory, Edmonton, Alberta, T6G 2J1, Canada*
[8] *Department of Physics and Astronomy, McMaster University, 1280 Main Street West, Hamilton, Ontario, L8S 4M1, Canada*

Accepted 2005 October 12. Received 2005 August 20; in original form 2004 December 13

ABSTRACT

We study the clustering properties of metals in the intergalactic medium (IGM) as traced by 619 C IV and 81 Si IV absorption components with $N \geqslant 10^{12}\,\mathrm{cm}^{-2}$ and 316 Mg II and 82 Fe II absorption components with $N \geqslant 10^{11.5}\,\mathrm{cm}^{-2}$ in 19 high signal-to-noise ratio (60–100 pixel^{-1}), high-resolution ($R = 45\,000$) quasar spectra. C IV and Si IV trace each other closely and their line-of-sight correlation functions $\xi(v)$ exhibit a steep decline at large separations and a flatter profile below $\approx$150 km s^{-1}, with a large overall bias. These features do not depend on absorber column densities, although there are hints that the overall amplitude of $\xi_{\mathrm{C\,IV}}(v)$ increases with time over the redshift range detected (1.5–3). Carrying out a detailed smoothed particle hydrodynamic simulation (2×320^3, 57 Mpc^3 comoving), we show that the C IV correlation function cannot be reproduced by models in which the IGM metallicity is constant or a local function of overdensity ($Z \propto \Delta^{2/3}$). However, the properties of $\xi_{\mathrm{C\,IV}}(v)$ are generally consistent with a model in which metals are confined within bubbles with a typical radius R_{s} about sources of mass $\geqslant M_{\mathrm{s}}$. We derive best-fitting values of $R_{\mathrm{s}} \approx 2$ comoving Mpc and $M_{\mathrm{s}} \approx 10^{12}\,\mathrm{M}_{\odot}$ at $z = 3$. Our lower-redshift (0.5–2) measurements of the Mg II and Fe II correlation functions also uncover a steep decline at large separations and a flatter profile at small separations, but the clustering is even higher than in the $z = 1.5$–3 measurements, and the turnover is shifted to somewhat smaller distances, $\approx$75 km s^{-1}. Again, these features do not change with column density, but there are hints that the amplitudes of $\xi_{\mathrm{Mg\,II}}(v)$ and $\xi_{\mathrm{Fe\,II}}(v)$ increase with time. We describe an analytic 'bubble' model for these species, which come from regions that are too compact to be accurately simulated numerically, deriving best-fitting values of $R_{\mathrm{s}} \approx 2.4$ Mpc and $M_{\mathrm{s}} \approx 10^{12}\,\mathrm{M}_{\odot}$. Equally good analytic fits to all four species are found in a similarly biased high-redshift enrichment model in which metals are placed within 2.4 comoving Mpc of $M_{\mathrm{s}} \approx 3 \times 10^9$ sources at $z = 7.5$.

Key words: galaxies: formation – intergalactic medium – quasars: absorption lines – cosmology: observations

1 INTRODUCTION

Pollution is ubiquitous. Even in the tenuous intergalactic medium (IGM), quasar (QSO) absorption-line studies have encountered heavy elements in all regions in which they were detectable (Tytler et al. 1995; Songaila & Cowie 1996). Such analyses were limited at first to somewhat overdense regions of space, traced by Lyman α clouds with column densities $N_{\mathrm{H\,I}} \geqslant 10^{14.5}\,\mathrm{cm}^{-2}$. Here measurements of $N_{\mathrm{C\,IV}}/N_{\mathrm{H\,I}}$ indicated that typically [C/H] $\simeq -2.5$ at $z \simeq 3$, with an order-of-magnitude scatter (Hellsten et al. 1997; Rauch, Haehnelt & Steinmetz 1997a).

Pushing into more tenuous regions, statistical methods have shown that unrecognized weak absorbers must be present in order to reproduce the global C IV optical depth (Ellison et al. 2000), and that a minimum IGM metallicity of approximately $3 \times 10^{-3}\,\mathrm{Z}_{\odot}$

★E-mail: evan@kitp.ucsb.edu

was already in place at $z = 5$ (Songaila 2001, hereafter S01). While the filling factor of metals in such tenuous structures is an object of intense investigation and debate (Schaye et al. 2000, 2003; Petitjean 2001; Bergeron et al. 2002; Carswell, Schaye & Kim 2002; Simcoe, Sargent & Rauch 2002; Pettini et al. 2003; Aracil et al. 2004), their very existence has profound cosmological implications.

As the presence of metals increases the number of lines available for radiative cooling, even modest levels of enrichment can greatly enhance the cooling rate (e.g. Sutherland & Dopita 1993), which has the potential to accelerate the formation of massive ($\gtrsim 10^{12}$ M$_\odot$) galaxies (e.g. Thacker, Scannapieco & Davis 2002). Furthermore, significant pre-enrichment is necessary to reproduce the abundances of G-dwarf stars in the Milky Way (e.g. van den Bergh 1962; Schmidt 1963) and nearby galaxies (e.g. Thomas, Greggio & Bender 1999).

Similarly, the violent events that propelled heavy elements into the space between galaxies have important implications for the thermal and velocity structure of the IGM (e.g. Tegmark, Silk & Evrard 1993; Gnedin & Ostriker 1997; Cen & Bryan 2001). Outflows energetic enough to eject metals from the potential wells of dwarf galaxies, for example, would have exerted strong feedback effects on nearby objects (Thacker et al. 2002). In this case the winds impinging on pre-virialized overdense regions would have been sufficiently powerful to strip the baryons from their associated dark matter, greatly reducing the number of $\lesssim 10^{10}$ M$_\odot$ galaxies formed (Scannapieco, Ferrara & Broadhurst 2000; Sigward, Ferrara & Scannapieco 2005).

Yet despite their many consequences, the details of how metals came to enrich the IGM are unclear. While numerous starburst-driven outflows have been observed at $z = 3$ (Pettini et al. 2001) and in lensed galaxies at $4 \lesssim z \lesssim 5$ (Frye, Broadhurst & Benitez 2002), it is unclear whether these objects are responsible for the majority of cosmological enrichment. In fact, a variety of theoretical arguments suggest that such galaxies represent only the tail end of a larger population of smaller 'pre-galactic' starbursts that mostly formed at much higher redshifts (Madau, Ferrara & Rees 2001; Scannapieco, Ferrara & Madau 2002). On the other hand, active galactic nuclei are observed to host massive outflows (Begelman, Blandford & Rees 1984; Weymann 1997), whose contribution from less luminous objects at intermediate redshifts remains unknown (e.g. Fan et al. 2001). The impact of such lower-redshift events on the IGM is also hinted at by the 'stirring' of C IV systems observed in studies of lensed QSO pairs (Rauch, Sargent & Barlow 2001). Finally, a number of theoretical studies suggest that primordial, metal-free stars may have been very massive (e.g. Bromm et al. 2001; Schneider et al. 2002), resulting in a large number of tremendously powerful pair-production supernovae, which distributed metals into the IGM at extremely early redshifts $\gtrsim 15$ (Bromm, Yoshida & Hernquist 2003; Norman, O'Shea & Paschos 2004).

While perhaps the main feature shared by such scenarios is their dependence on a poorly understood population of presently undetectable objects, this assessment paints an overly bleak picture. Regardless of which objects enriched the IGM, it is clear that they must have formed in the densest regions of space, regions that are far more clustered than the overall dark matter distribution. Furthermore this 'geometrical biasing' is a systematic function of the masses of these structures, an effect that has been well studied analytically and numerically (e.g. Kaiser 1984; Jing 1999). Thus the observed large-scale clustering of metal absorbers encodes valuable information about the masses of the objects from which they were ejected. Likewise, as the maximal extent of each enriched region is directly dependent on the velocity at which the metals were dispersed, measurements of the small-scale clustering of these absorbers are likely to constrain the energetics of their sources.

Previous studies of the two-point correlation function of C IV components have shown that they cluster strongly on velocity scales up to 500 km s^{-1} (Sargent et al. 1980; Steidel 1990; Petitjean & Bergeron 1994; Rauch et al. 1996). It has often been suggested that this clustering signal reflects a combination of (i) relative motions of clouds within a galactic halo and (ii) clustering between galaxies. More recently Boksenberg, Sargent & Rauch (2003, hereafter BSR03) have gathered a sample of 908 C IV absorber components clumped into 199 systems in the redshift range $1.6 < z < 4.4$ identified in the Keck spectra of nine QSOs. They conclude that most of the signal is due to the clustering of components within each system, where a system is defined as a set of components that is 'well separated' from its neighbours as identified by the observer. In this case almost all the systems extend less than 300 km s^{-1} and most extend less than 150 km s^{-1}. They did not observe clustering between systems on the larger scales expected for galaxy clustering, although they concluded from their measurements of component clustering and ionization balance that each system was closely associated with a galaxy.

In Pichon et al. (2003, hereafter Paper I) we used 643 C IV and 104 Si IV absorber components, measured by an automated procedure in 19 high signal-to-noise ratio quasar spectra, to place strong constraints on the number and spatial distribution of intergalactic metals at intermediate redshifts ($2 \leqslant z \leqslant 3$). In this work, we showed that the correlation functions of intergalactic C IV and Si IV could be understood in terms of the clustering of metal bubbles of a typical comoving radius R_s around sources whose biased clustering was parametrized by a mass M_s. A similar picture was also put forward in BSR03, but in our case significant large-scale clustering, similar to that seen in galaxies, was observed.

In this paper we extend the analysis in Paper I in three important ways. First we carry out a more detailed study of the physical properties of C IV and Si IV absorbers and the relationship between local quantities and the overall spatial distribution. Secondly, we carry out a similar analysis of Mg II and Fe II absorbers in our observational sample, which probe the IGM in a somewhat lower redshift range. Finally, we replace our dark-matter-only modelling of Paper I with a full-scale smoothed particle hydrodynamic simulation. We then generate simulated metal-line spectra by painting bubbles of metals directly on to the gas distribution at $z \geqslant 2$. By analysing the resulting spectra with the same automated procedure applied to the measured data set, we are able to place our models and observations on the same footing, drawing important constraints on the sources of metals. Motivated by measurements of the cosmic microwave background, the number abundance of galaxy clusters and high-redshift supernovae (e.g. Spergel et al. 2003; Eke, Cole & Frenk 1996; Perlmutter et al. 1999), we adopt cosmological parameters of $h = 0.7$, $\Omega_m = 0.3$, $\Omega_\Lambda = 0.7$ and $\Omega_b = 0.044$ throughout this investigation, where h is the Hubble constant in units of 100 km s^{-1} Mpc^{-1} and Ω_m, Ω_Λ and Ω_b are the total matter, vacuum and baryonic densities in units of the critical density, ρ_{crit}.

The structure of this work is as follows. In Section 2 we summarize the properties of our data set and reduction methods. In Section 3 we present the number densities of C IV, Si IV, Mg II and Fe II, and estimate the cosmological densities of these species. In Section 4 we study the spatial clustering of these species and how it is related to local quantities such as column density and abundance ratios. In Section 5 we describe our numerical model for the distribution of neutral hydrogen in the IGM and compare it with observations. In Section 6 we extend our model to include various histories of cosmological enrichment; and in Section 7 we compare these to the observed distribution of C IV to derive constraints on the sizes and properties of sources of cosmological metals. In Section 8 we discuss an analytic model that is particularly suitable for comparisons with the distribution of Mg II and Fe II, as numerical analyses of these species are beyond the capabilities of our simulation. Conclusions are given in Section 9.

2 DATA SET AND ANALYSIS METHODS

2.1 Data and reduction

The ESO Large Programme 'The Cosmic Evolution of the IGM' was devised to provide a homogeneous sample of QSO sightlines suitable for studying the Lyα forest in the redshift range 1.7–4.5. High-resolution ($R \approx 45\,000$), high signal-to-noise ratio (60–100 pixel^{-1}) spectra were taken over the wavelength ranges 3100–5400 and 5450–10 000 Å, using the UVES spectrograph on the Very Large Telescope (VLT). Emphasis was given to lower redshifts to take advantage of the very good sensitivity of UVES in the blue and the fact that the Lyα forest is less blended. The distribution of redshifts and the resulting coverage of various metal-line absorbers are given in Table 1. In all cases we consider only metal absorption lines redward of the Lyα forest, to avoid the extensive blending in this region, and blueward of 8110 Å, to avoid contamination from sky lines. The regions 5750–5830, 6275–6323, 6864–6968, 7165–7324 and 7591–7721 Å were also excluded from our sample because of sky-line contamination. The C IV, Si IV, Mg II and Fe II metal lines discussed in this paper were well detected over the redshift ranges of 1.5–3.0, 1.8–3.0, 0.4–1.8 and 0.5–2.4, respectively.

Observations were performed in service mode over a period of 2 yr. The data were reduced using the UVES context of the ESO MIDAS data reduction package, applying the optimal extraction method, and following the pipeline reduction step by step. The extraction slit length was adjusted to optimize sky background subtraction. While this procedure systematically underestimates the sky background signal, the final accuracy is better than 1 per cent. Wavelengths were corrected to vacuum heliocentric values and individual 1D spectra were combined using a sliding window and weighting the signal by the total errors in each pixel.

The underlying emission spectrum of each quasar was estimated using an automated iterative procedure that minimizes the sum of a regularization term and a χ^2 term that was computed from the difference between the quasar spectrum and the continuum estimated during the previous iteration. Finally the spectrum was divided by this continuum, leaving only the information relative to absorption features.

2.2 Metal-line identification

Metal-line absorbers were identified using an automated two-step procedure. For each species that has multiple transitions, we estimated the minimal flux compatible with the data for all pixels of the spectrum. This was done by first finding the pixels associated with the transition wavelengths w_i of a given species and then taking the maximum of the flux values in these pixels, scaled by $w_i f_i$, where f_i is the oscillator strength associated with each of the transitions.

A standard detection threshold was then applied to these spectra, such that only absorption features with equivalent widths (EWs) larger than five times the noise rms were accepted, giving a first list of possible identifications. This list was cleaned, using the similarity of the profiles of the transitions of a species and applying simple physical criteria that correlate the detection of two different species. For instance, one criterion implies that the detection of a Si IV system at a given redshift should be associated with the detection of a C IV system.

Next, each system was fitted with Voigt profiles, taking care of their identification and possible blends with other systems. The first guess and the final Voigt profile decomposition were carried out using the VPFIT software (Carswell et al. 1987). Our decomposition of saturated systems is conservative, in that it introduces additional unsaturated components only if there is some structure in the 1551-Å line that reveals their presence. This fitting procedure is described in detail in Aracil (in preparation) and has been tested on simulated spectra, doing well for all components with realistic values of N and b.

Table 1. List of lines of sight. Here $z_{\rm em}$ is the quasar redshift, while Lyα forest is used only redward of the Lyβ transition at 1025.7 Å, and metal absorption lines are used only redward of the Lyα forest and blueward of 8130 Å.

Name	$z_{\rm em}$	Coverage				
		Forest	C IV	Si IV	Mg II	Fe II
PKS 2126−158	3.280	2.61–3.28	2.36–3.28	2.74–3.28	0.85–1.89	1.03–2.42
Q 0420−388	3.117	2.47–3.12	2.23–3.12	2.59–3.12	0.79–1.89	0.95–2.42
HE 0940−1050	3.084	2.45–3.08	2.21–3.08	2.56–3.08	0.77–1.89	0.93–2.42
HE 2347−4342	2.871	2.27–2.87	2.04–2.87	2.38–2.87	0.68–1.89	0.83–2.42
HE 0151−4326	2.789	2.20–2.79	1.97–2.79	2.31–2.79	0.64–1.89	0.79–2.42
Q 0002−422	2.767	2.18–2.77	1.96–2.77	2.29–2.77	0.64–1.89	0.78–2.42
PKS 0329−255	2.703	2.13–2.70	1.91–2.70	2.23–2.70	0.61–1.89	0.75–2.42
Q 0453−423	2.658	2.09–2.66	1.87–2.66	2.19–2.66	0.59–1.89	0.73–2.42
HE 1347−2457	2.611	2.05–2.61	1.83–2.61	2.15–2.61	0.57–1.89	0.70–2.42
HE 1158−1843	2.449	1.91–2.45	1.71–2.45	2.01–2.45	0.50–1.89	0.63–2.42
Q 0329−385	2.435	1.90–2.44	1.70–2.44	2.00–2.44	0.49–1.89	0.62–2.42
HE 2217−2818	2.414	1.88–2.41	1.68–2.41	1.98–2.41	0.48–1.89	0.61–2.41
Q 1122−1328	2.410	1.87–2.41	1.68–2.41	1.98–2.41	0.39–1.89	0.61–2.41
Q 0109−3518	2.404	1.87–2.40	1.67–2.40	1.97–2.40	0.48–1.89	0.61–2.40
HE 0001−2340	2.263	1.75–2.26	1.56–2.26	1.84–2.26	0.42–1.89	0.54–2.26
PKS 0237−23	2.222	1.72–2.22	1.53–2.22	1.81–2.22	0.40–1.89	0.53–2.22
PKS 1448−232	2.220	1.72–2.22	1.53–2.22	1.81–2.22	0.40–1.89	0.52–2.22
Q 0122−380	2.190	1.70–2.19	1.50–2.19	1.78–2.19	0.38–1.89	0.51–2.19
HE 1341−1020	2.135	1.65–2.14	1.46–2.14	1.74–2.14	0.36–1.89	0.48–2.14

Finally we applied a set of five cuts to the automated list generated by VPFIT: $\log N(\mathrm{cm}^{-2}) \geqslant 12$ for C IV and Si IV, and $\log N(\mathrm{cm}^{-2}) \geqslant 11.5$ for Mg II and Fe II, owing to the detection limit of our procedure; $b \geqslant 3$ km s^{-1} to avoid false detections due to noise spikes; $\log N(\mathrm{cm}^{-2}) \leqslant 16$ to remove very badly saturated components; and $b \leqslant 45$ km s^{-1} to avoid false detections due to errors in continuum fitting. For the analyses presented here, we removed all associated components within 5000 km s^{-1} of the quasar redshifts. These cuts resulted in a final data set of 619 C IV (1548, 1551 Å), 81 Si IV (1394, 1403 Å), 316 Mg II (2796, 2803 Å) and 82 Fe II (2344, 2473, 2382 Å) components, drawn from 688, 102, 320 and 88 components, respectively, if we include the associates. These numbers differ slightly from those presented in Paper I as a result of further refinements in our detection procedure.

3 NUMBER DENSITIES

We first used our sample to compute the column density distribution function, $f(N)$, again working in the above assumed cosmology. Following Tytler (1987), $f(N)$ is defined as the number of absorbing components per unit column density and per unit redshift absorption path, $\mathrm{d}X$. In this paper, we adopt a definition

$$\mathrm{d}X \equiv (1+z)^2 \left[\Omega_\Lambda + \Omega_\mathrm{m}(1+z)^3\right]^{-1/2} \mathrm{d}z$$

such that at all redshifts $f(N)$ does not evolve for a population whose physical size and comoving space density are constant. Note that this definition is slightly different from that used in Paper I and in S01, namely

$$\mathrm{d}X' \equiv (1+z)^{1/2}\,\mathrm{d}z,$$

although when $z > (\Omega_\Lambda/\Omega_\mathrm{m})^{1/3} - 1 = 0.32$, as is appropriate for our sample, $\mathrm{d}X'$ can be very closely approximated as $\Omega_\mathrm{m}^{1/2}\,\mathrm{d}X$ for comparison with previous analyses.

In Fig. 1 we plot $f(N)$ for both C IV and Si IV components, as was presented in Paper I. The mean redshifts of C IV and Si IV in our sample were 2.16 and 2.38, respectively, and so in this plot we divide the data into two redshift bins from $1.5 \leqslant z \leqslant 2.3$ and $2.3 \leqslant z \leqslant 3.1$. Both species are consistent with a lack of redshift evolution, as found by previous lower-resolution studies of C IV and Si IV (S01; Pettini et al. 2003), and pixel-by-pixel analyses of intergalactic C IV (Schaye et al. 2003). The overall density distribution of C IV is also consistent with a power law of the form $f(N) = BN^{-\alpha}$ with $\alpha = 1.8$ and $\log_{10} f = -12.7$ at 10^{13} cm^{-2} as fitted by S01. Finally, we compare our results with the data set collected in BSR03 from nine QSO spectra with a signal-to-noise ratio ≈50 pixel^{-1}. Here and below we use the *full data set* taken by BSR03, to which we apply exactly the same cuts as we do to our data. For components with columns ≈10^{13} cm^{-2} these data sets are quite similar. However, a significant difference between this sample and our own is the fit to the saturated C IV components with $\log(N_{\mathrm{C\,IV}}) \geqslant 14$. These have been decomposed into a large number of smaller $\log(N_{\mathrm{C\,IV}}) \leqslant 12.5$ systems in the BSR03 analysis, while our decomposition only introduces additional unsaturated components if there is structure in the 1551-Å line. Extrapolating the results of S01 to column depths below 10^{13} cm^{-2} also yields a distribution similar to ours.

While fewer in total, the Si IV components in the lower panel of Fig. 1 are also consistent with a lack of evolution, following a similar power law with a lower overall magnitude. Note that in this figure the error bars are purely statistical, estimated as the reciprocal of the square root of the number of components in each bin. Again, for comparison, we include the number densities computed from the full BSR03 sample, with our cuts applied. While this comparison

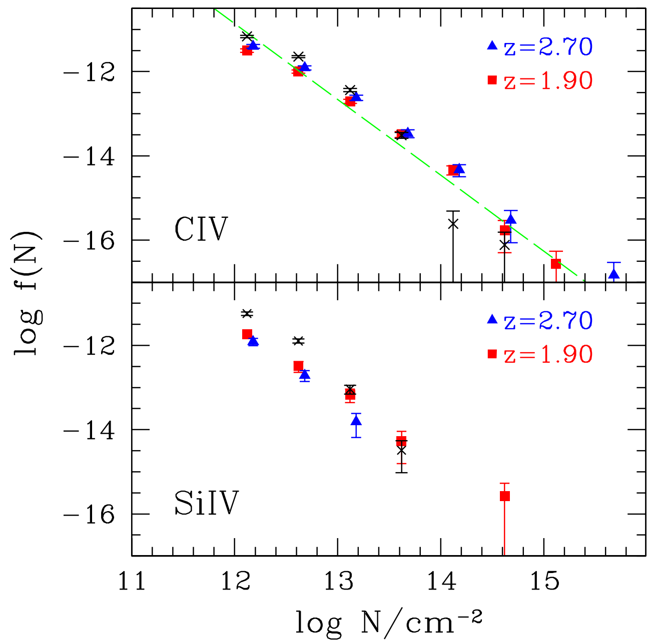

Figure 1. Column density distributions of C IV (upper panel) and Si IV (lower panel) absorption components. In each panel, components are divided into two redshift bins: $1.5 \leqslant z \leqslant 2.3$ (squares) and $2.3 \leqslant z \leqslant 3.1$ (triangles). The column density bins are $10^{0.5}$ N cm^{-2} wide and error bars in this and all further plots are 1σ. The dashed line is the power-law fit measured in S01. Finally the small crosses are the full set of C IV and Si IV components identified by BSR03, with our cuts imposed.

is noisier, the overall trends are the same: at 10^{13} cm^{-2} the number densities are similar, while saturated components are decomposed into a larger number of smaller systems in the BSR03 data set.

In Fig. 2 we plot $f(N)$ for both Mg II and Fe II, now going down to a minimum column density of $10^{11.5}$ cm^{-2}, which corresponds to roughly the same optical depth as 10^{12} cm^{-2} for C IV and Si IV. For Mg II and Fe II the relevant doublets are at substantially longer rest-frame wavelengths, and therefore our UVES detections primarily occur at lower redshifts. Thus the mean redshifts of Mg II and Fe II are only 1.05 and 1.38, and we divide our data into bins from $0.4 \leqslant z \leqslant 1.15$ and $1.15 \leqslant z \leqslant 1.9$. These lines arise in lower-ionization gas and are often thought of as tracers of quiescent clouds, probably associated with galaxies (e.g. Petitjean & Bergeron 1990; Churchill et al. 1999; Churchill, Vogt & Charlton 2003).

Like its higher-ionization counterparts, Mg II is consistent with a lack of evolution in number densities over the observed redshift range. In the Fe II case, however, a significant excess of intermediate column density components is found at lower redshifts. A closer inspection of the data indicates that this feature is caused by a single large system in Q 0002−422, at $z = 0.836$, which spans over 560 km s^{-1}. The removal of this system results in the third set of points in the lower panel of Fig. 2, which are consistent with the higher-redshift values. The large impact of this system in our measurements suggests that simple $\sqrt{N}$ estimates may somewhat underpredict the statistical error on our measurement. This hints at strong clustering between Fe II components, which is in fact measured, as we discuss in detail below.

Statistical fluctuations aside, the overall density distributions of Mg II and Fe II are largely consistent with the power-law fits obtained from previous measurements, apart from showing only a weak deviation in the lowest $N_{\mathrm{Fe\,II}}$ bin, probably due to incompleteness.

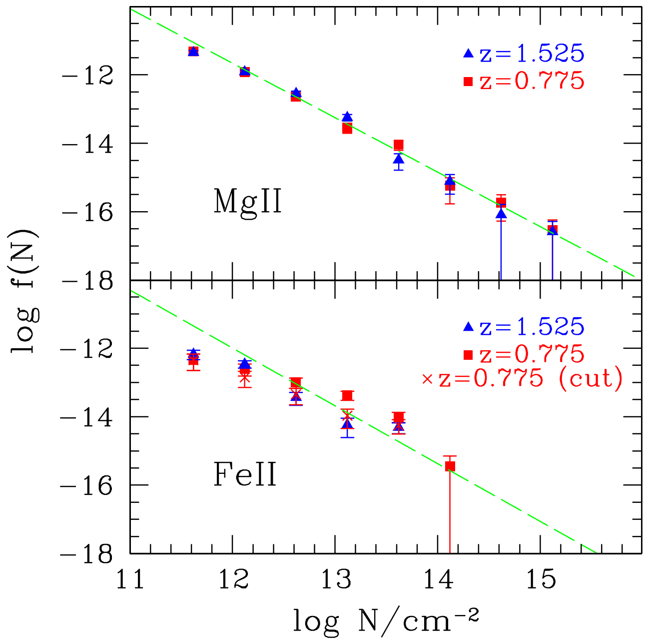

Figure 2. Column density distributions of Mg II (upper panel) and Fe II (lower panel) absorption components. In each panel, components are divided into two redshift bins: $0.4 \leqslant z \leqslant 1.15$ (squares) and $1.15 \leqslant z \leqslant 1.9$ (triangles). As in Fig. 1, the column density bins are $10^{0.5}$ N cm^{-2} wide. The dashed lines correspond to the power-law fits described in the text, and in the lower panel we also include f values when the large $z = 0.836$ system in Q 0002−422 is removed (crosses; see text).

In this case, the dashed-line fits in Fig. 2 are $f(N) = BN^{-\alpha}$ with $\alpha = 1.6$ and $\log_{10} f = -13.2$ at 10^{13} cm^{-2} for Mg II, and $\alpha = 1.7$ and $\log_{10} f = -13.4$ at 10^{13} cm^{-2} for Fe II. While some flattening of $f_{\rm Mg\,II}(N)$ at even higher columns is necessary to match observations at column densities $\geqslant 10^{16.5}$ cm^{-2} (Prochter, Prochaska & Burles 2004), for the column densities in our sample our measured slopes are identical to those determined by previous studies. In particular our α fits match those of Churchill et al. (2003), although our B values are different, as these authors did not attempt to normalize their results by the total redshift path observed.

In summary, our automatic identification procedure produces a set of components whose column density distributions are consistent with previous measurements, complete to $N \gtrsim 10^{12}$ cm^{-2} for C IV and Si IV, and complete to $N \gtrsim 10^{11.5}$ cm^{-2} for Mg II and Fe II. No evolution in f is seen for any species over the full redshift range probed, indicating that the majority of IGM enrichment is likely to have occurred before the redshifts observed in our sample.

Finally, our number densities allow us to compute the total cosmological densities of each of the detected species. Following S01, we express these in terms of a mass fraction relative to the critical density, which can be computed as

$$\Omega_{\rm ion} = \frac{H_0 m_{\rm ion}}{c\rho_{\rm crit}} \frac{\sum N_{\rm ion}}{\Delta X} = 1.4 \times 10^{-23} A \frac{\sum N_{\rm ion}}{\Delta X}, \qquad (1)$$

where H_0 is the Hubble constant, $m_{\rm ion}$ is the mass of the given ion, A is its atomic number, and ΔX is the total redshift path over which it is measured. The results of this analysis are given in Table 2. Note that these values are *species* densities, and no ionization corrections have been applied to estimate the corresponding element densities. Again, these values are broadly consistent with previous measurements, although there is a significant scatter due to the fact that most of the material lies in the largest, rarest components. Thus previous studies have found $\Omega_{\rm C\,IV}$ values as disparate as 6.8×10^{-8} at $z = 2.5$ (S01), $(3.8 \pm 0.7) \times 10^{-8}$ (BRS03), and between 3.5×10^{-8} and 7.9×10^{-8} depending on the method of analysis (Simcoe, Sargent & Rauch 2004).

Table 2. Cosmological densities of detected species.

Species	$\langle z \rangle$	$\log N$ (cm^{-2})	Ω	$\Delta\Omega$
C IV	2.2	12–16	7.54×10^{-8}	$\pm 2.16 \times 10^{-8}$
Si IV	2.4	12–16	6.00×10^{-9}	$\pm 1.21 \times 10^{-9}$
Mg II	1.1	11.5–16	5.95×10^{-8}	$\pm 2.23 \times 10^{-8}$
Fe II	1.4	11.5–16	1.87×10^{-8}	$\pm 0.36 \times 10^{-8}$

4 SPATIAL DISTRIBUTION

4.1 C IV and Si IV

Having constructed a sample of well-identified metal absorption components, we then computed their two-point correlation function in redshift space, $\xi(v)$. This quantity was previously studied in Rauch et al. (1996), who noted a marked similarity between $\xi(v)$ of C IV and Mg II, in BSR03, who carried out a two-Gaussian fit (see also Petitjean & Bergeron 1990, 1994), and in Paper I. For each quasar, we computed a histogram of all velocity separations and divided by the number expected for a random distribution. Formally, the correlation function for a QSO ℓ is

$$\xi^{\ell}(v_k) + 1 = \frac{n_k^{\ell}}{\langle n_k^{\ell} \rangle}, \qquad (2)$$

where n_k^{ℓ} is the number of pairs separated by a velocity difference corresponding to a bin k, and $\langle n_k^{\ell} \rangle$ is the average number of such pairs that would be found in the redshift interval covered by QSO ℓ, given a random distribution of redshifts with an overall density equal to the mean density in the *sample*. Alternatively, we may consider all QSOs at once and compute

$$\xi(v_k) + 1 = \frac{\sum_{\ell} n_k^{\ell}}{\sum_{\ell} \langle n_k^{\ell} \rangle}, \qquad (3)$$

or equivalently

$$\xi(v_k) + 1 = \sum_{\ell} w_k^{\ell} \left[\xi^{\ell}(v_k) + 1 \right] \qquad (4)$$

with

$$w_k^{\ell} \equiv \frac{\langle n_k^{\ell} \rangle}{\sum_{\ell} \langle n_k^{\ell} \rangle},$$

that is weighting the correlation found for each QSO by the number of random pairs that are expected given the redshift coverage of that QSO. The statistical variance in this measurement is given by

$$\sigma_k^2 = \sum_{\ell} \left(w_k^{\ell} \right)^2 \sigma_k^{2,\ell}, \qquad (5)$$

where $\sigma_k^{2,\ell}$ is the variance associated with bin k of quasar ℓ. In Paper I, we estimated this quantity according to the usual formula

$$\sigma_k^{2,\ell} = \frac{n_k^{\ell}}{\langle n_k^{\ell} \rangle^2}, \qquad (6)$$

which gives the Poisson error in our measurement. In the results presented here, however, we adopt a more conservative approach, and also include the additional scatter caused by the finite sample

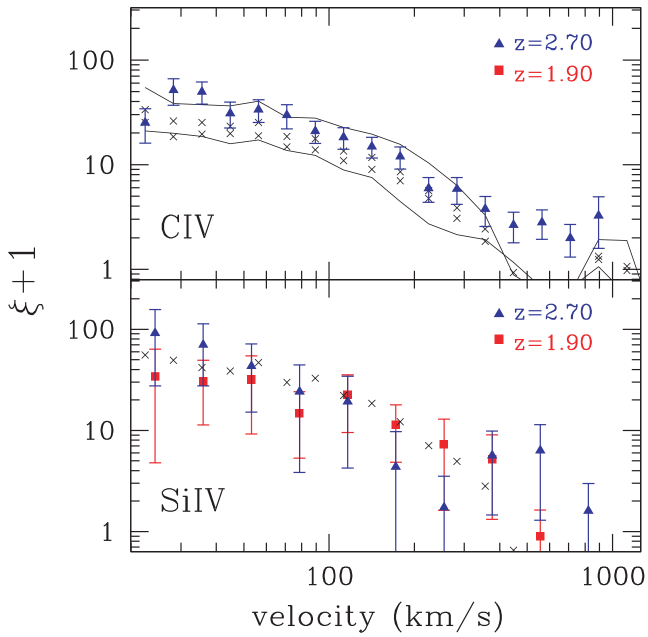

Figure 3. Two-point correlation function of C IV (upper panel) and Si IV (lower panel) absorption components. In each panel the components have been divided into two redshifts bins, with symbols as in Fig. 1. The upper panel also includes a number of comparisons with previous measurements. In particular: the lower set of crosses corresponds to the full set of components defined in BSR03, normalizing each QSO individually; the upper set of crosses corresponds to imposing a column density cut of 10^{12} cm^{-2}, normalizing each QSO by its expected number of pairs; and the solid lines correspond to dividing the BSR03 data into a subsamples with $z \geqslant 3.1$ (lower line) and $z < 3.1$ (upper line), as described in the text. In the lower panel, the crosses corresponds to imposing a column density cut of 10^{12} cm^{-2} on the Si IV components observed in BSR03 and normalizing each QSO by its expected number of pairs.

size used to construct the correlation function (Mo, Jing & Börner 1992). In this case

$$\sigma_k^{2,\ell} = \frac{1}{\left\langle n_k^\ell \right\rangle^2} \left[n_k^\ell + 4\frac{\left(n_k^\ell\right)^2}{N^\ell} \right], \tag{7}$$

where N^ℓ is the total number of components detected in QSO ℓ. Note that the presence of this additional scatter highlights the strength of our high signal-to-noise ratio data set, as it allows us to work in the limit in which the number of C IV components detected in *each quasar* is large.

The resulting correlation functions are shown in Fig. 3, again split into two redshift bins. Interestingly, in the better measured C IV case, there are hints that the $z \leqslant 2.3$ correlation function may be enhanced with respect to the high-redshift one. Furthermore, this growth is consistent with a population of absorbers that ‘passively’ evolves by following the motion of the IGM during the formation of structure, as we discuss in further detail in Section 8.

In the upper panel of Fig. 3 we also plot correlation functions computed from the sample defined in BSR03, which is drawn from the spectra of nine QSOs with a mean redshift of 3.1 and a signal-to-noise ratio per pixel of ≈50. In this case we show results obtained both from using the full data set, normalizing each quasar individually (as was carried out in BSR03), and from imposing a lower cut-off at $N_{\rm C\,IV,min} = 10^{12}$ cm^{-2}, normalizing each quasar by the *expected* number of pairs (as was carried out in our analysis). In both cases the resulting $\xi_{\rm C\,IV}(v)$ values are similar and somewhat lower in amplitude than our measurements. Rauch et al. (1996) similarly have found a lower amplitude. Dividing the BSR03 data into a $z < 3.1$ bin with a mean redshift of 2.5 and a $z > 3.1$ bin with a mean redshift of 3.6 resulted in correlation functions given by the solid curves (again calculated according to our method). Furthermore, the amplitude of the $z = 2.5$ BSR03 correlation function is similar to our measurements, which are drawn from a sample with a mean redshift of 2.3. However, the higher-redshift curve is substantially lower, again indicating that $\xi_{\rm C\,IV}(v)$ is likely to evolve with redshift. This was also suggested by the analysis in fig. 14 of BSR03, although they point out that the changing ionizing background may also be an issue. Finally we note that the BSR03 sample shows a relative lack of components at ≈500 km s^{-1}. This is very near the C IV doublet separation.

Moving to the bottom panel of Fig. 3, we see that the overall shape and amplitude of the C IV and Si IV correlation functions are similar and are consistent to within the Si IV measurement errors, as was discussed in Paper I. Both functions exhibit a steep decline at large separations and a flatter profile at small separations, with an elbow occurring at ≈150 km s^{-1}. Both functions are also consistent with the correlation one obtains from the full BSR03 Si IV sample, after applying our cuts. Finally, as was noted in Paper I, there is a weak low-redshift feature at ≈500 km s^{-1} in $\xi_{\rm C\,IV}(v)$, the origin of which we explore in Section 4.2.

In Fig. 4 we study the dependence of the C IV spatial distribution on column density, by computing the correlation function over the full redshift range but selecting components within a fixed range of column density. In the upper panel we apply a cut on the maximum column density component, while holding the minimum $N_{\rm C\,IV}$ fixed at our detection limit of 10^{12} cm^{-2}. Apart from a weak shift in the 500–630 km s^{-1} bin, $\xi_{\rm C\,IV}(v)$ remains practically unchanged by this threshold. As the majority of the detected components are relatively weak, this indicates that our signal is determined by the bulk of the

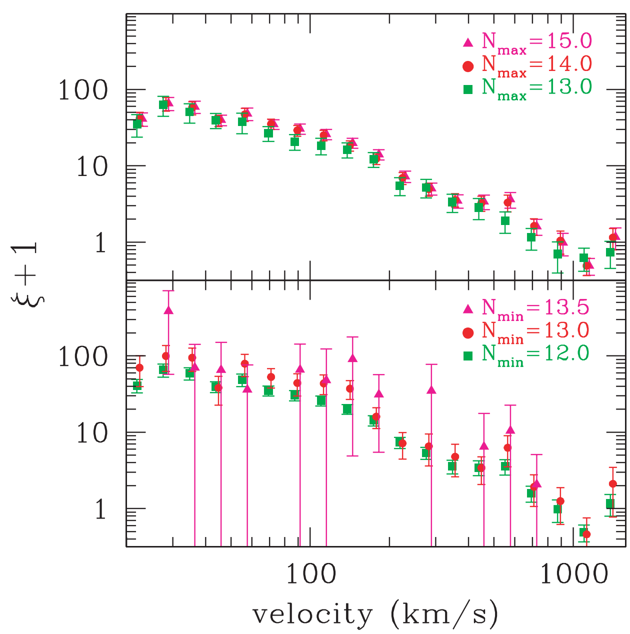

Figure 4. Dependence of the C IV correlation function on column density threshold. Upper panel: Effect of applying a cut on the maximum column density of C IV components used to calculate $\xi_{\rm C\,IV}(v)$. In all cases $N_{\rm C\,IV,min} = 10^{12}$ cm^{-2}. Lower panel: Effect of applying a cut on the minimum C IV column density, with $N_{\rm C\,IV,max}$ fixed at 10^{16} cm^{-2}.

components in our sample, rather than by the properties of individual strong absorbers.

The results of a more drastic test are shown in the lower panel of Fig. 4. Here we hold $N_{\mathrm{C\,IV,max}}$ fixed at 10^{16} cm^{-2} and apply a cut on the minimum column density, which greatly reduces the number of components in the sample. Nevertheless, moving from $N_{\mathrm{C\,IV,min}} = 10^{12}$ cm^{-2} to $N_{\mathrm{C\,IV,min}} = 10^{13.5}$ cm^{-2} results only in a very weak enhancement of $\xi_{\mathrm{C\,IV}}(v)$ at small separations, while the rest of the correlation function remains unchanged. Thus, unlike Lyα absorption systems (Cristiani et al. 1997), the correlation of C IV does not depend strongly on absorption column densities. Instead, the spatial distribution seems to be a global property of the population of C IV components.

A question that immediately arises is whether the features observed in the C IV and Si IV correlation functions are intrinsic to the underlying distribution of metals, or perhaps arise from variations in the ultraviolet (UV) background at somewhat shorter wavelengths. In fact, analyses of the He II distribution due to ionization by 54.4-eV photons suggest that the second reionization of hydrogen may still have been quite patchy at $z = 2.3$–2.9 (Shull et al. 2004), with He II found preferentially in 'void' regions where H I is weak or undetected.

On the other hand, the ionization potentials of C III and Si III are 47.5 and 33.5 eV, respectively, somewhat lower than that of He II, but well beyond the ionization potential of hydrogen. Thus if the suggested patchiness of He II is due primarily to changes in the IGM opacity at wavelengths shortward of 54.4 eV, then the distribution of C IV and Si IV is likely to trace the underlying distribution of metals more closely. If He II inhomogeneities exist and are caused by a sparsity of hard sources, however, it is possible that background variations may also play a role in the distribution of triply ionized regions of carbon and silicon.

As the ionization potentials of C III and Si III differ by 12 eV, each is sensitive to a slightly different range of UV photons. Thus if the features seen in Fig. 3 were produced by changes in the ionizing background, one might expect to see systematic changes in the ratio of these species as a function of separation. As a simple test of this possibility, we considered the average log $(N_{\mathrm{C\,IV}}/N_{\mathrm{Si\,IV}})$ as a function of separation. In order to make the sample included in this average as large as possible, we computed this as

$$\left\langle \log\left(\frac{N_{\mathrm{C\,IV}}}{N_{\mathrm{Si\,IV}}}\right)\right\rangle_k = \sum_{i,j\in \mathrm{bin}\,k}\sum_{\ell} \log\left(\frac{N_{\mathrm{C\,IV},i}}{N_{\mathrm{Si\,IV},\ell}}\right)\theta(5-|v_\ell - v_i|) \times \left\{\sum_{i,j\in \mathrm{bin}\,k}\sum_{\ell}[1\times\theta(5-|v_\ell - v_i|)]\right\}^{-1}, \tag{8}$$

where $\theta(v)$ is the Heaviside step function, i and j are indices of C IV components, ℓ is an index over all Si IV components, and k is a given bin in velocity separation used to calculate the correlation function. In other words, for each bin in the correlation function, we average $\log(N_{\mathrm{C\,IV}}/N_{\mathrm{Si\,IV}})$ over all C IV components i that are found at the appropriate separation from another C IV component j and within 5 km s^{-1} of a Si IV component ℓ.

The results of this analysis are found in Fig. 5, which shows no correlation between separation and species abundances. Furthermore, our average value of log $(N_{\mathrm{C\,IV}}/N_{\mathrm{Si\,IV}}) \approx 0.7$ is similar to that seen in previous analyses of 10^{12} cm^{-2} $\leqslant N_{\mathrm{C\,IV}} \leqslant 3\times10^{14}$ cm^{-2} absorbers (Kim, Cristiani & D'Odorico 2002; BSR03), as well as the weaker

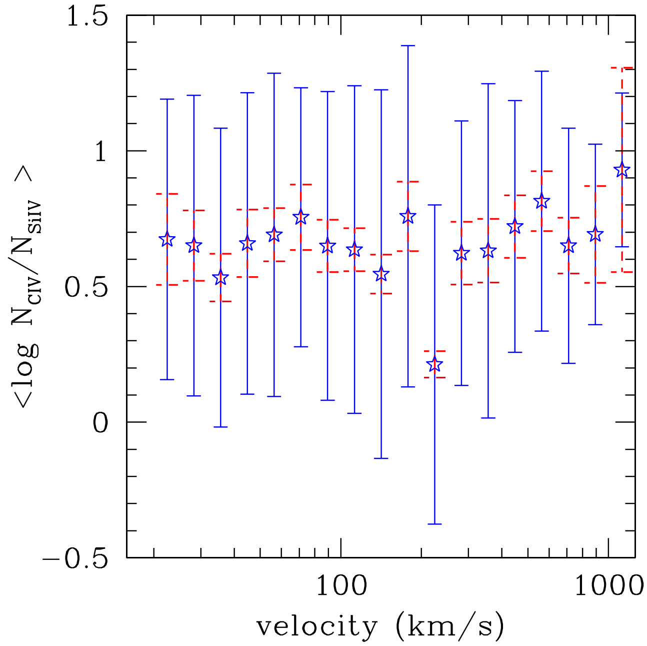

Figure 5. The average $\log(N_{\mathrm{C\,IV}}/N_{\mathrm{Si\,IV}})$ ratio for C IV components contributing to the correlation function at various separations. At each separation the dashed error bars are the statistical errors, while the solid error bars are the intrinsic scatter.

C IV and Si IV lines detected by Aguirre et al. (2004) using the pixel optical depth method. Thus there is nothing particularly unusual about the subset of absorbers selected by our procedure. Although this is clearly not an exhaustive test, it nevertheless suggests that the features in the correlation functions are not imprinted in a straightforward way by the UV background itself, and are more likely to be caused by the spatial distribution of metals. However, a much more detailed analysis is necessary to settle this issue definitively.

4.2 Peculiar systems at low redshift

The C IV correlation functions in Figs 3 and 4 hint at a secondary bump at large separations. It is important to try to understand if this comes from the presence of a few peculiar systems or if this is a generic feature of the C IV distribution. To this end, we computed the correlation function for different samples, each time excluding one of the lines of sight, and discovered that the signal comes from three QSOs, namely, PKS 0237−23, HE 0001−2340 and Q 0122−380.

The first of these has long been known to be very peculiar. Indeed, a huge C IV complex is seen towards PKS 0237−23 at 11 different redshifts over the range 1.596–1.676 (more than 10 000 km s^{-1}) with three main subcomplexes at $z_{\mathrm{abs}} = 1.596$, 1.657 and 1.674 (Boroson et al. 1978; Sargent et al. 1988). Furthermore Foltz et al. (1993) searched the field around PKS 0237−23 for other QSOs to provide background sources against which the presence of absorption at the same redshifts could be investigated. They concluded that the complex can be interpreted as a real spatial overdensity of absorbing clouds with a transverse size comparable to its extent along the line of sight, that is of the order of 30 Mpc. The correlation function without this line of sight is shown in Fig. 6.

Two other lines of sight display peculiar systems. At $z_{\mathrm{abs}} = 2.1851$ towards HE 0001−2340 there is a sub-damped Ly α (sub-DLA) system and the associated C IV system is spread over ≈450 km s^{-1}. It is therefore difficult to know if the structure there is due to large scales or more probably to the internal structure of the halo

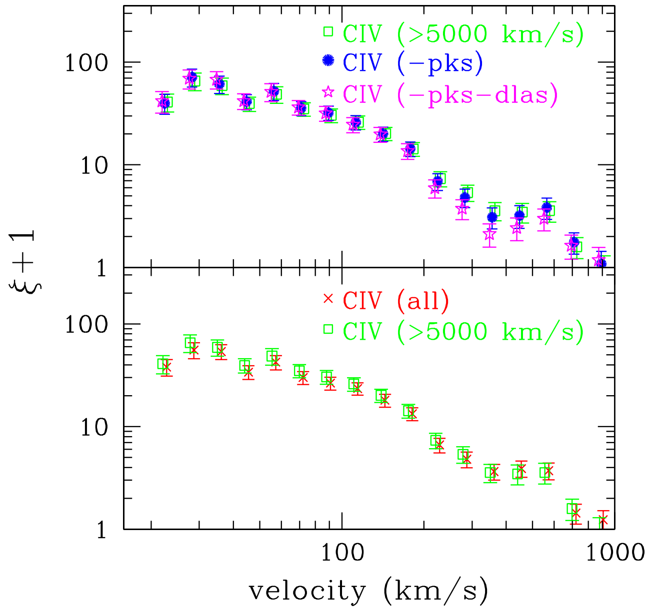

Figure 6. Upper panel: Impact of peculiar systems on the C IV correlation function. Here the square points are computed from the full sample, the circles are computed excluding the sightline towards PKS 0237−23, and the stars are computed excluding both PKS 0237−23 and the two sub-DLA systems, as described in the text. Lower panel: Comparison between $\xi_{\rm C\,IV}(v)$ for the full sample, including associated absorbers (crosses), and excluding C IV components with 5000 km s^{-1} of the quasar redshifts (squares).

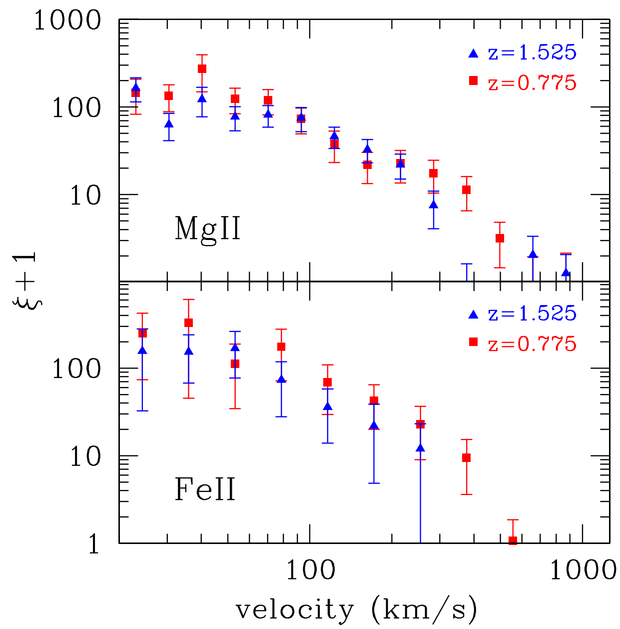

Figure 7. Upper panel: Two-point correlation function of Mg II, divided into two redshift bins as in Fig. 2. Lower panel: Two-point correlation function of Fe II, divided into the same redshift bins.

associated with this high-density peak. At $z_{\rm abs} = 1.9743$ towards Q 0122−380, there is a double strong system spread over more than 500 km s^{-1}. It is again difficult to know whether these absorptions reflect internal motions of highly disturbed gas.

After these are removed, the most significant excess at large separations is found in the 500–630 km s^{-1} bin. This velocity difference corresponds to the difference in wavelengths of the C IV doublet itself. In fact, it is interesting to note that this bin is the only one that is significantly reduced by applying a cut to eliminate the larger $N_{\rm C\,IV}$ components, as was seen in Fig. 4.

As a further test of large-separation correlations, we have also computed $\xi_{\rm C\,IV}(v)$ including the associated systems, found within 5000 km s^{-1} of the redshifts of the QSOs in this sample. This is compared with the C IV correlation function for our standard sample in the lower panel of Fig. 6. At all separations, $\xi_{\rm C\,IV}(v)$ remains unchanged, thus indicating that associated systems are not distributed in a particularly unusual way, and do not contribute any significant features to $\xi_{\rm C\,IV}(v)$ at ≈500 km s^{-1}, or any other separation.

4.3 Fe II and Mg II

We now turn our attention to the distribution of lower-redshift metals, as traced by Mg II and Fe II. Splitting the data into two redshift ranges yields the line-of-sight correlation functions shown in Fig. 7, where again we have included both the Poisson and sample-size errors in our estimate of the variances. Like their high-redshift counterparts, Mg II and Fe II are found to trace each other closely. Their correlation functions are both relatively shallow at small separations and fall off more steeply at large separations. Also, like $\xi_{\rm C\,IV}(v)$, both $\xi_{\rm Mg\,II}(v)$ and $\xi_{\rm Fe\,II}(v)$ exhibit slight enhancements at lower redshifts, although again these excesses fall within the errors.

Next we examine the dependence of the Mg II spatial distribution on column density. Removing the strongest absorbers in our sample before calculating $\xi_{\rm Mg\,II}(v)$ results in the values plotted in the upper panel of Fig. 8. As in the C IV case, the Mg II correlation function is not dominated by the clustering of large components, but rather remains almost unchanged as a function of $N_{\rm max}$, even when it is reduced to $10^{12.5}$ cm^{-2}, excluding over a third of the systems. Similarly, raising the minimum column density from $10^{11.5}$ to $10^{12.5}$ cm^{-2}

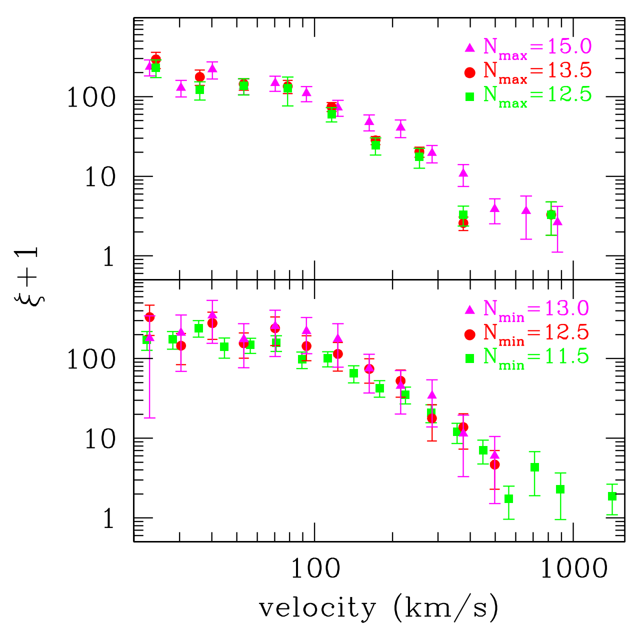

Figure 8. Dependence of Mg II correlation function on column density threshold. Upper panel: Effect of applying a cut on the maximum column density of Mg II subcomponents used to calculate $\xi_{\rm Mg\,II}(v)$. In all cases $N_{\rm Mg\,II,min} = 10^{11.5}$ cm^{-2}. Lower panel: Effect of applying a cut on the minimum Mg II column density, with $N_{\rm Mg\,II,max}$ fixed at 10^{16} cm^{-2}.

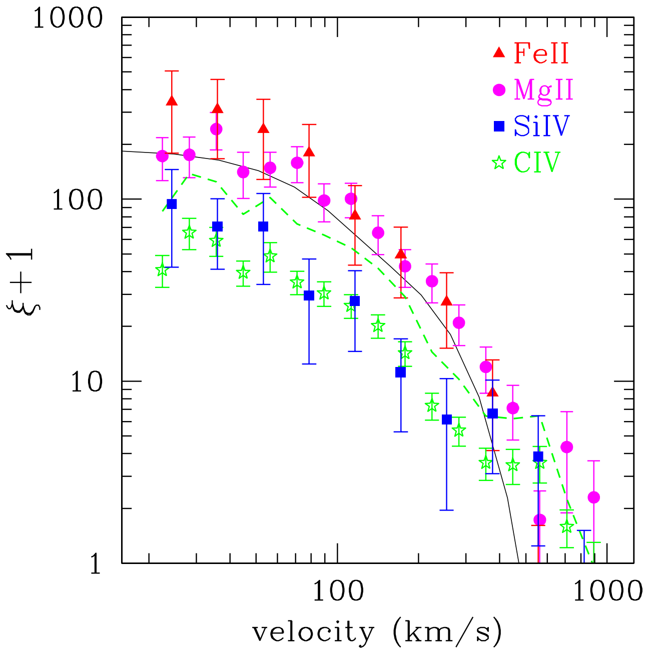

Figure 9. Measured correlation function of all metal-line components. Points are measurements from our sample, while the solid line is the Mg II fit by Churchill et al. (2003), arbitrarily normalized. The dashed line is the C IV correlation function, shifted upwards by a factor of 2.1 to provide a simple estimate of the impact of structure formation from $z = 2.2$ to 1.1 on a fixed population of absorbers.

does not boost $\xi_{\mathrm{Mg\,II}}(v)$, even though this excludes approximately two-thirds of the sample.

In Fig. 9 we compare the correlation functions of C IV and Si IV with those of Mg II and Fe II. Note that the mean redshift z_{mean} of these lower-ionization species is ≈1.2, while for C IV and Si IV it is ≈2.3. Thus our sample contains very few objects in which all four species can be directly compared. Nevertheless, a comparison of their redshift-space correlation functions reveals a number of important parallels. While $\xi(v)$ of all species decline steeply at large separations and exhibit a turnover at smaller velocity differences, the transition between these two regimes is pushed to slightly smaller separations in the Mg II and Fe II case, and the fall-off at higher densities is more abrupt.

Interestingly, the features seen in this distribution can be inferred from the original fitting to the distribution of velocity separations of Mg II absorbers by Petitjean & Bergeron (1990), using a remarkably small number of systems. Their data were fitted with the sum of two Gaussian distributions with similar overall weights and velocity dispersions of $\sigma_v = 80$ and 390 km s^{-1}, which the authors interpreted as due to the kinematics of clouds bound within a given galaxy halo, and the kinematics of galaxy pairs, respectively. Working at higher spectral resolution and higher signal-to-noise ratio, Churchill et al. (2003) also obtained a good two-component Gaussian fit to the two-point clustering function of Mg II components, although they did not attempt to normalize this function to obtain $\xi_{\mathrm{Mg\,II}}(v) + 1$. In this case the best-fitting values were $\sigma_v = 54$ and 166 km s^{-1}, where the relative amplitude of the narrow component was twice that of the broad component. This fit has been added to Fig. 9, adopting an arbitrary normalization. Although our data set has an overall signal-to-noise ratio that is higher than that of Churchill et al. (2003), and thus is more complete at lower column densities, their two-Gaussian model also provides a good match to our data at $\Delta v \lesssim 400$ km s^{-1}. However, it falls short of the observed correlation at larger separations.

To contrast the correlation functions in more detail, we have added a simple estimate of 'passive' evolution to Fig. 9, that is, the evolution if the metals detected at $z \approx 2.3$ as C IV absorbers were to move along with the formation of structure before appearing as Mg II absorbers at $z = 1.2$. To first approximation, the overall bias of such a metal tracer field would remain fixed, but its correlation function would be enhanced by a factor of $D^2(1.2)/D^2(2.3) = 2.1$, where $D(z)$ is the linear growth factor. Surprisingly, simply shifting $\xi_{\mathrm{C\,IV}}(v)$ by a factor of 2.3 provides us with an accurate match for the Mg II correlation function over a large range of separations, although it underpredicts the clustering of Mg II and Fe II at smaller distances. This is discussed in further detail in Section 8.

To facilitate future comparisons, in Table 3 we give the correlation function and errors for each of the four species averaged over our full

Table 3. Summary of measured metal-component correlation functions. Note that there is likely to be significant redshift evolution of these functions. The mean redshifts of C IV and Si IV are ≈2.3. The mean redshifts of Mg II and Fe II are ≈1.15.

Bin (km s^{-1})	$\xi_{\mathrm{C\,IV}}$	$\xi_{\mathrm{Mg\,II}}$	Bin (km s^{-1})	$\xi_{\mathrm{Si\,IV}}$	$\xi_{\mathrm{Fe\,II}}$
20–25	41 ± 8	170 ± 50	20–30	94 ± 52	310 ± 150
25–32	66 ± 13	170 ± 40	30–43	71 ± 30	280 ± 130
32–40	59 ± 11	240 ± 60	43–65	71 ± 36	220 ± 100
40–50	40 ± 6	140 ± 40	65–100	30 ± 17	160 ± 70
50–63	49 ± 9	145 ± 30	100–140	27 ± 13	74 ± 34
63–79	35 ± 5	155 ± 40	140–200	11 ± 6	45 ± 19
79–100	30 ± 5	96 ± 23	200–300	6.2 ± 4.2	25 ± 11
100–125	26 ± 4	98 ± 21	300–450	6.6 ± 3.5	7.8 ± 4.1
125–160	20 ± 3	64 ± 15	450–670	3.9 ± 2.6	0.88 ± 0.58
160–200	14 ± 2	42 ± 10	670–1000	0.8 ± 0.7	0 ± 1
200–250	7.3 ± 1.2	35 ± 8			
250–320	5.4 ± 1.0	20 ± 5			
329–400	3.6 ± 0.7	12 ± 3			
400–500	3.5 ± 0.7	6.9 ± 2.3			
500–630	3.6 ± 0.8	1.7 ± 0.8			
630–790	1.6 ± 0.4	4.2 ± 2.4			
790–1000	0.98 ± 0.32	2.2 ± 1.3			

sample. Note that the small number of Si IV and Fe II components forces us to use a smaller number of bins to beat down the statistical noise in our measurements.

Finally, we carry out a test to determine if the spatial distribution of metals as traced by $\xi_{\rm C\,IV}(v)$ may be affected by our VPFIT decomposition into components. Previous studies have attempted to trace the distribution of intergalactic metals by grouping together components into 'systems', which are likely to have a common physical origin, and computing the correlation function of these systems (e.g. Petitjean & Bergeron 1990; BSR03). While, typically, system identifications have been carried out by eye, here we attempt a more objective approach, which parallels the friends-of-friends technique (Davis et al. 1985) widely used for group finding in cosmological simulations. In this case, we define a velocity linking length ($v_{\rm link}$) and group together all components whose separation from their nearest neighbour is less than $v_{\rm link}$ into a system at a redshift equal to the average over all its components. Note that this procedure does not involve simply linking together pairs within $v_{\rm link}$, but rather forms collections of many components, each within a linking length of its neighbours and grouped together into a single entity. It is therefore equivalent to partitioning a set of components into two systems whenever they are separated by a gap wider than $v_{\rm link}$.

In the upper panel of Fig. 10 we plot $\xi_{\rm C\,IV}(v)$ computed for the resulting C IV systems, for three different choices of $v_{\rm link}$. In all cases, within our measurement errors, combining components into systems has no appreciable impact at separations much larger than the linking length. Thus while BSR03 report a lack of clustering of systems as identified by eye, we are unable to reproduce this behaviour with our automatic method. Perhaps this is not surprising, as the clustering of $\xi_{\rm C\,IV}(v)$ is very strong, and thus many pairs of 'systems' are likely to be closely spaced and easily tagged as a single object. However, our results show that fixing a pre-specified definition of systems does not remove large-scale correlations in this way.

In the lower panel of Fig. 10, we see that grouping Mg II components into systems has no clear impact at larger separations if

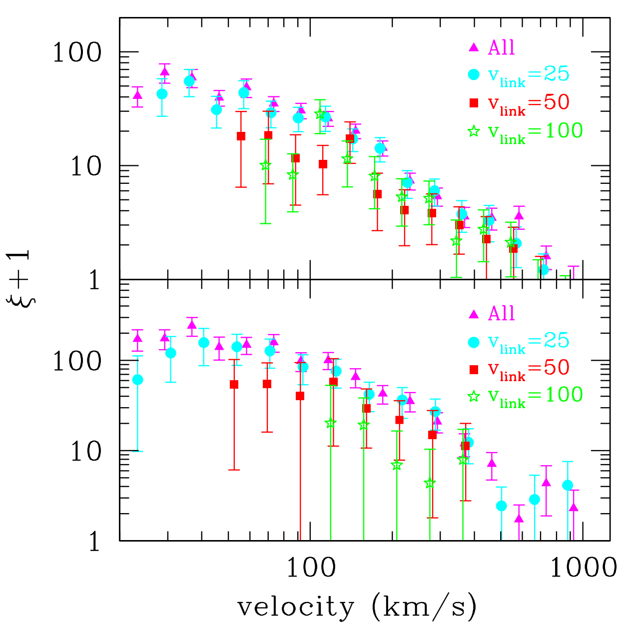

Figure 10. Upper panel: Impact of linking together C IV components into systems. Lower panel: Impact of linking together Mg II components into systems. Details described in the text.

$v_{\rm link} = 25$ or 50, and while there are hints of weak larger-scale damping if $v_{\rm link} = 100$; these changes are within our errors. Similar results were obtained if each group was assigned the redshift of its largest component, leading us to conclude that the $\xi(v)$ features observed in both the high-redshift and low-redshift species are not related to division into components, but rather reflect the underlying distribution of intergalactic metals.

5 NUMERICAL SIMULATION

5.1 Overall properties

For a better interpretation of the features seen in metal absorption-line systems, we conducted a detailed smoothed particle hydrodynamic (SPH) simulation of structure formation. Our goal here is to apply the same automated procedure used to identify metal absorbers in the ESO Large Programme (LP) data set to a detailed simulation, drawing conclusions as to what constraints our measurements place on the underlying distribution of IGM metals. For this purpose we focus our attention on a cold dark matter (CDM) cosmological model with the same general cosmological parameters as above, and the additional parameters $\sigma_8 = 0.87$ and $n = 1$, where σ_8^2 is the variance of linear fluctuations on the $8\,h^{-1}$ Mpc scale and n is the 'tilt' of the primordial power spectrum. The Bardeen et al. (1986) transfer function was used with an effective shape parameter of $\Gamma = 0.2$, and the ionizing background flux was taken to be (Haardt & Madau 1996):

$$J(\nu, z) = 2.2 \times 10^{-22} \left(\frac{\nu}{\nu_{\rm H\,I}}\right)^{-1} (1+z)^{0.73} \exp\left[-\frac{(z-2.3)^2}{1.9}\right]$$
$$\text{erg s}^{-1}\ \text{Hz}^{-1}\ \text{cm}^{-2}\ \text{sr}^{-1},$$

corresponding to a photoionization rate of

$$6.8 \times 10^{-13}\,(1+z)^{0.73} \exp[-(z-2.3)^2/1.9]\ \ \text{s}^{-1}.$$

We simulated a box of size $40/h$ comoving Mpc on a side, using 320^3 dark matter particles and an equal number of gas particles. The mass of each dark matter particle was $2.0 \times 10^8\,{\rm M}_\odot$, and the mass of each gas particle was $3.4 \times 10^7\,{\rm M}_\odot$. This yields a nominal minimum mass resolution for our (dark matter) group finding of $1.0 \times 10^{10}\,{\rm M}_\odot$. The run was started at an initial redshift of $z = 99$, and a fixed physical S2 (Hockney & Eastwood 1988) softening length of 6.7 kpc was chosen, which is equivalent to a Plummer softening length of 2.8 kpc. The simulation was conducted using a parallel MPI2-based version of the HYDRA code (Couchman, Thomas & Pearce 1995) developed by the Virgo Consortium (Thacker et al. 2003).

We used the SPH algorithm described in Thacker et al. (2000), although, in an improvement upon earlier work, the maximum SPH search radius now allows us to resolve the mean density of the box accurately. Photoionization was implemented using the publicly available routines from our serial HYDRA code. Radiative cooling was calculated using the Sutherland & Dopita (1993) collisional ionization equilibrium tables, and a uniform 2 per cent solar metallicity was assumed for all gas particles for cooling purposes. Integration to $z = 2.0$ required 9635 (unequal) steps, and four weeks of wall clock time on 64 processors. Outputs for post-processing were saved at redshifts of $z = 8.0$, 5.0, 4.0, 3.0, 2.5 and 2.0.

From each of the final three outputs, we interpolated to extract two-dimensional slices of overdensity, temperature and line-of-sight peculiar velocities on 24 equally spaced planes. By extracting random sightlines from each of these three fields, we were then able to generate simulated metal-line spectra, which could be processed in an identical fashion as the observed data. Before turning our attention to this issue, however, we first address the more basic concern of the overall hydrogen distribution, which serves as both a check of our simulation methods, and a way of fine-tuning the assumed ionizing background to reproduce the observed properties of the IGM.

5.2 Calculation of neutral hydrogen fraction

Once the baryon density, temperature and line-of sight velocity are extracted along a line of sight, constructing a simulated spectrum is relatively straightforward. One obtains the neutral hydrogen fraction, $f_{\mathrm{H\,I}}$, in the IGM by solving the ionization equilibrium equation (Black 1981)

$$\alpha(T) n_{\mathrm{p}} n_{\mathrm{e}} = \Gamma_{\mathrm{ci}}(T) n_{\mathrm{e}} n_{\mathrm{H\,I}} + J_{22} G_1 n_{\mathrm{H\,I}}, \tag{9}$$

where $\alpha(T)$ is the radiative recombination rate, $\Gamma_{\mathrm{ci}}(T)$ is the rate of collisional ionization, J_{22} is the UV background intensity in units of 10^{-22} erg s^{-1} Hz^{-1} cm^{-2} sr^{-1}, $J_{22}G_1$ is the rate of photoionization, and n_{p}, n_{e} and $n_{\mathrm{H\,I}}$ are the number densities of protons, electrons and neutral hydrogen, respectively. For the Haardt & Madau (2001) spectrum assumed below, $G_1 = 2.7 \times 10^{-13}$ s^{-1}; for the original Haardt & Madau (1996) spectrum, $G_1 = 3.2 \times 10^{-13}$ s^{-1}; and for the $(\nu/\nu_{\mathrm{H\,I}})^{-1}$ spectrum used in our simulation, $G_1 = 3.1 \times 10^{-13}$ s^{-1}. For comparison, $G_1 J_{22}$ is equal to J_{-12} as defined in Choudhury, Srianand & Padmanabhan (2001) and to 10 G_1 J_{21} as defined in Bi & Davidsen (1997).

If we assume that the neutral fraction of hydrogen is $\ll$1 and all the helium present is in the fully ionized form, we find

$$f_{\mathrm{H\,I}}(x, z) = \frac{\alpha(T(x, z))}{\alpha(T(x, z)) + \Gamma_{\mathrm{ci}}(T(x, z)) + G_1 J_{22} n_{\mathrm{e}}^{-1}(z)}, \tag{10}$$

where the collisional ionization rate is

$$\Gamma_{\mathrm{ci}}(T) = 5.85 \times 10^{-11}\, T^{1/2} \exp(-157\,809.1/T)\ \ \mathrm{cm^3\ s^{-1}},$$

with T in kelvin, and Black (1981) gives an approximate form for the radiative recombination rate as

$$\frac{\alpha(T)}{\mathrm{cm^3\ s^{-1}}} = \begin{cases} 4.36 \times 10^{-10}\, T^{-0.7573} & \text{if } T \geqslant 5000\ \mathrm{K}, \\ 2.17 \times 10^{-10}\, T^{-0.6756} & \text{if } T < 5000\ \mathrm{K}. \end{cases} \tag{11}$$

With these expressions we can compute the neutral hydrogen density, $n_{\mathrm{H\,I}}(x, z(x))$, along a line of sight. Here x and z are related by $c\,\mathrm{d}z = \mathrm{d}x\ H(z)$, where the Hubble constant as a function of redshift is $H(z) = H_0\sqrt{\Omega_\Lambda + \Omega_{\mathrm{m}}(1+z)^3}$. We choose a coordinate system such that $x = 0$ at the front of the box and define $\Delta z(x, z_0)$ as the change in redshift from $x = 0$. We then construct the Lyα optical depth as

$$\tau_\alpha(z_0 + \Delta z) = \frac{c\sigma_\alpha}{(1+z_0)\sqrt{\pi}} \int \mathrm{d}x\ \frac{n_{\mathrm{H\,I}}(x, z_0)}{b(x, z_0)} \times \exp\left\{-\left[\frac{xH(z_0) + v(x, z_0)(1+z_0) - c\Delta z}{(1+z_0)b(x, z_0)}\right]^2\right\}, \tag{12}$$

where

$$b(x, z_0) \equiv \sqrt{2k_{\mathrm{B}}T(x, z_0)/m_{\mathrm{p}}}$$

(with k_{B} the Boltzmann constant),

$$n_{\mathrm{H}}(z) = 1.12 \times 10^{-5}\,(1 - Y)\Omega_{\mathrm{b}}(1+z)^3 h^2\ \ \mathrm{cm^{-3}} = 1.83 \times 10^{-7}\,(1+z)^3\ \ \mathrm{cm^{-3}}$$

(with Y the helium mass fraction), and σ_α is the Lyα cross-section, which can be calculated as

$$\sigma_\alpha = (3\pi\sigma_{\mathrm{T}}/8)^{1/2} f \lambda_0, \tag{13}$$

where λ_0 is the rest-frame wavelength of the transition, f is the appropriate oscillator strength, and $\sigma_{\mathrm{T}} = 6.25 \times 10^{-25}$cm^2 is the Thomson cross-section. For Lyα, we have $\lambda_0 = 1215$ Å and $f = 0.4162$, which gives $\sigma_\alpha = 4.45 \times 10^{-18}$ cm^2. With equation (13) in hand, we are able to construct simulated UVES spectra of the Lyα forest by stacking vectors of optical density computed from randomly extracted sightlines. These are then convolved with a Gaussian smoothing kernel with a width of 4.4 km s^{-1} (corresponding to the UVES resolution) and rebinned on to a 205 000 array of wavelengths, using the UVES pixelization from 3050 to 10 430 Å. Rather than interpolate between simulation outputs, however, we first turn our attention to a careful comparison between observations and limited segments of spectra at fixed redshifts, concentrating on two main quantities: the probability distribution function, a single-point quantity that is sensitive to the overall temperature and J_{22} evolution background; and the two-point correlation function, a measure of the spatial distribution of the gas.

5.3 Tests of the numerical hydrogen distribution

The probability distribution function (PDF) of the transmitted flux was first used to study the Lyα forest by Jenkins & Ostriker (1991) and since then has been a widely used tool for quantifying the mean properties of the IGM (e.g. Rauch et al. 1997b; McDonald et al. 2000). In the upper panels of Fig. 11 we compare the PDF as measured by McDonald et al. (2000) to that generated from 20 simulated spectra at representative redshifts of 2.5 and 3.0. In order to obtain the good agreement seen in this figure, it was necessary to adjust the assumed J_{22} values to 4.7 at $z = 2.5$ and to 3.7 at $z = 3$ (corresponding to photoionization rates of 1.3×10^{-12} s^{-1} and 1.0×10^{-12} s^{-1}), down from the values of 5.4 and 4.7 (corresponding to photoionization rates of 1.7×10^{-12} s^{-1} and 1.5×10^{-12} s^{-1}), respectively, that were assumed in the simulations.

This results in a slight inconsistency between the simulated ρ–T relation and the one that would have arisen if we had repeated the simulation with our fitted values of J_{22}. In practice, however, this difference is unimportant in relation to our primary goal of constructing simulated metal lines. It is dwarfed by effects due to the uncertain evolution of the UV background at higher redshifts (e.g. Hui & Gnedin 1997; Hui & Haiman 2003), uncertainties in the normalization of the quasar spectra (e.g. McDonald et al. 2000), and the extrapolation of the UV background from 912 Å to the shorter wavelengths relevant for C IV and Si IV (e.g. Haardt & Madau 2001). Thus our approach is more than adequate for the purposes of this study. With our assumed background values, the mean fluxes at $z = 2.5$ and 3.0 are 0.794 and 0.692, respectively, while the observed values are 0.818 ± 0.012 and 0.684 ± 0.023.

As a second test of our simulations, we constructed the Lyα flux correlation function $\xi(\Delta v) = \langle \delta F(v)\, \delta F(v + \Delta v)\rangle$, which primarily provides a validation of our assumed primordial power spectrum $P(k)$ and its evolution in our simulation. Beginning with Croft et al. (1998), the direct inversion of the one-dimensional power spectrum of the Lyα flux has been seen as one of the best constraints on the shape of the mass power spectrum on intermediate scales (e.g. Hui

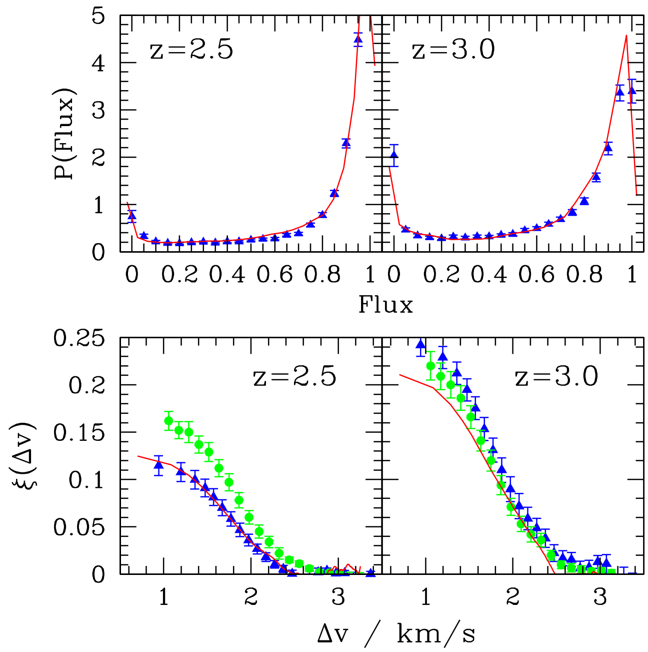

Figure 11. Top: Measured and simulated flux PDFs of the Lyα forest at two representative redshifts. Measurements are taken from McDonald et al. (2000) over redshift ranges of $2.09 \leqslant z \leqslant 2.67$ (left panel) and $2.67 \leqslant z \leqslant 3.39$ (right panel), respectively, while simulations are at fixed redshifts of 2.5 (left panel) and 3 (right panel). Bottom: Measured and simulated flux two-point correlation functions of the Lyα forest: $\xi(\Delta v) = \langle \delta F(v)\, \delta F(v + \Delta v)\rangle$, where $\delta F = F/\bar{F} - 1$, at two representative redshifts. The triangles are measurements by McDonald et al. (2000) over redshift ranges of $2.09 \leqslant z \leqslant 2.67$ (left panel) and $2.67 \leqslant z \leqslant 3.39$ (right panel), respectively, and the circles are measurements by Croft et al. (2002) over redshift ranges of $2.31 \leqslant z \leqslant 2.62$ (left panel) and $2.88 \leqslant z \leqslant 3.25$ (right panel). Again, the simulations, represented by the solid lines, are at fixed redshifts of 2.5 (left panel) and 3 (right panel).

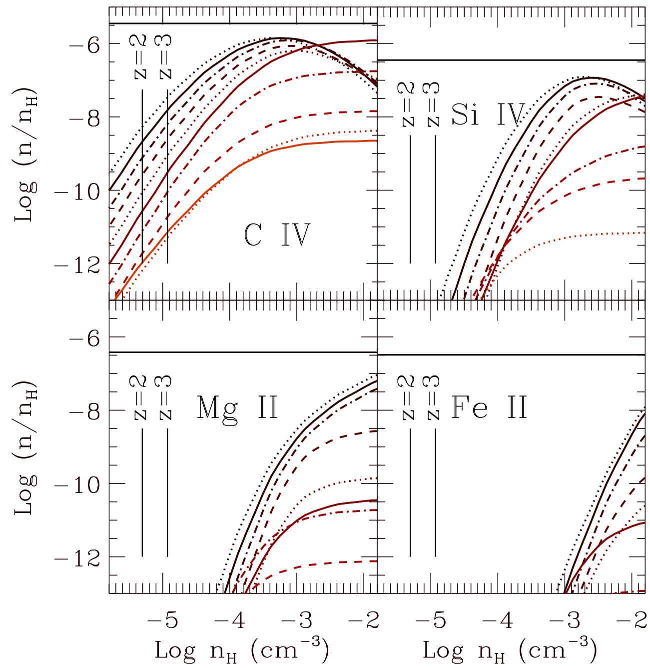

Figure 12. Abundances of various species as a function of total hydrogen number density for a $10^{-2}\,\mathrm{Z}_{\odot}$ gas exposed to a Haardt & Madau (2001) background at $z = 2.5$. In the upper left panel, the temperatures corresponding to each of the curves are, from top to bottom, $10^{3.75}$ K (dotted), 10^{4} K (solid), $10^{4.25}$ K (dot-dashed), $10^{4.5}$ K (dashed), $10^{4.75}$ K (dotted), $10^{5.0}$ K (solid), $10^{5.25}$ K (dot-dashed), $10^{5.5}$ K (dashed), $10^{5.75}$ K (dotted) and $10^{6.0}$ K (solid). Similar labelling is used in the other panels. The vertical lines give the mean hydrogen number density at $z = 3$ and 2, while the horizontal lines give the total abundance of each of the elements.

1999; McDonald et al. 2000; Pichon et al. 2001; Croft et al. 2002; Viel, Haehnelt & Springel 2004).

Again, this quantity is straightforward to extract from our simulated spectra. The resulting values are shown in the lower panels of Fig. 11, in which we compare them to measurements by McDonald et al. (2000) as well as Croft et al. (2002). As in the single-point case, our simulations are generally in good agreement with the observed values. In fact, at $z = 2.5$, our simulated values are well within the range of values bracketed by the weakly disagreeing observational results. At $z = 3.0$, our simulated values provide a slight underprediction at small separations, although this is only just outside the 1σ error in the current measurements. In summary, then, the gas properties of our numerical simulation are more than adequate to provide a firm basis for the construction of Lyα spectra, while at the same time containing sufficient resolution to allow us to push towards the denser regions associated with metal-line absorption systems.

6 MODELLING METAL ENRICHMENT

6.1 Calculation of observed metal lines

Extending the methods of Section 5.2 to construct the spatial distribution of metal lines requires us to adopt an overall spectral shape for the ionizing background, as well as a more detailed calculation of the densities of various species. Here we assume a UV spectrum as predicted by the updated models of Haardt & Madau (2001, see also Haardt & Madau 1996) at $z = 2.5$, but shifted such that J_{22} is consistent with the levels found in Section 5. Assuming local thermal equilibrium, we then make use of CLOUDY94 (Ferland et al. 1998; Ferland 2000) to construct tables of the relevant species as a function of temperature and density at each of these redshifts, for a characteristic metallicity of $10^{-2}\,\mathrm{Z}_{\odot}$. Self-shielding in optically thick regions was not taken to account. The resulting species densities are shown as a function of hydrogen number density and temperature in Fig. 12, which is modelled after fig. 2 of Rauch et al. (1997a).

In this figure, we see that, roughly speaking, C IV traces the widest range of environments, while Si IV, Mg II and Fe II probe progressively denser regions. Thus while an appreciable level of C IV is found in only a few times overdense $z = 3$ gas, comparable levels of Si IV are achieved only in denser regions with $\Delta \equiv \rho(x)/\bar{\rho} \approx 10$; and while Mg II is found at similar densities to Si IV, Fe II is only detectable in $\Delta \geqslant 100$ regions, orders of magnitude denser than most C IV regions.

Similarly, C IV is detectable over a large temperature range, covering from 10^{4} up to $\approx 10^{6}$ K. While Si IV is also relatively stable with respect to temperature changes, Mg II and Fe II are much more fragile, and their abundances fall away quickly above $\approx 10^{5}$ K. From these results, we see that the correct modelling of Si IV requires simulations that probe to densities ≈ 10 times higher than those most relevant to CIV, although $\xi_{\mathrm{C\,IV}}(v)$ and $\xi_{\mathrm{Si\,IV}}(v)$ trace each other closely. Thus while our numerical modelling was carried out at the

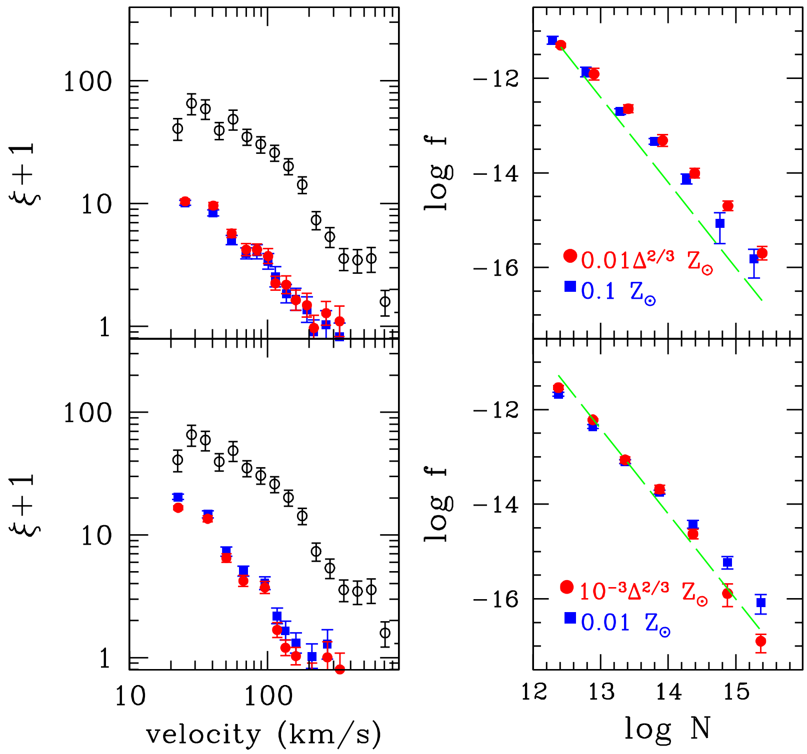

Figure 13. Correlation functions and column density distributions for models in which metallicity is assumed to be constant throughout the simulation, or a simple function of density. The filled points in the upper panels show high-metallicity models in which $Z = 10^{-1}\,Z_\odot$ and $Z = \Delta^{2/3}\,10^{-2}\,Z_\odot$, while the filled points in the lower panels show lower-metallicity models in which $Z = 10^{-2}\,Z_\odot$ and $Z = \Delta^{2/3}\,10^{-3}\,Z_\odot$. Fifty-seven simulated QSO sightlines were averaged in the high-metallicity models, and 114 were averaged in the lower-metallicity cases. The open circles give the measured C IV correlation function, and the dashed lines give the fit to the column density distribution as in Fig. 1.

highest resolution possible, we nevertheless limit our comparisons to C IV to minimize any remaining numerical effects.

6.2 A non-local dependence

Having determined the number densities of each of the species of interest as a function of temperature and density in a $10^{-2}\,Z_\odot$ medium, we then applied these calculations to extract simulated metal absorption spectra from our simulations. As a first step, following Rauch et al. (1997a), we assumed a constant metallicity across the simulation volume and extracted sightlines of $\tau_{\rm C\,IV}$ using an appropriately modified version of equation (12):

$$\tau_{{\rm C\,IV},i}(z_0+\Delta z) = \frac{c\sigma_{{\rm C\,IV},i}}{(1+z_0)\sqrt{\pi}}\int {\rm d}x\,\frac{n_{\rm C\,IV}(x,z_0)}{b_{\rm C\,IV}(x,z_0)} \times \exp\left\{-\left[\frac{xH(z_0)+v(x,z_0)(1+z_0)-c\Delta z}{(1+z_0)b_{\rm C\,IV}(x,z_0)}\right]^2\right\}, \quad (14)$$

where now

$$b_{\rm C\,IV}(x,z_0) \equiv \sqrt{2k_{\rm B}T(x,z_0)/12m_{\rm p}},$$

$n_{\rm C\,IV}(z)$ is the mean C IV density, and $\sigma_{{\rm C\,IV},i}$ is the cross-section corresponding to the ith absorption line of the C IV doublet. These we compute directly from equation (13), taking $(\lambda_{0,{\rm C\,IV},1},\,\lambda_{0,{\rm C\,IV},2}) = (1548.2,\,1550.8)$ and $(f_{\rm C\,IV,1},\,f_{\rm C\,IV,2}) = (0.1908,\,0.09522)$. For the low metallicities relevant for the IGM, the effects of changing metallicity can be modelled as a simple linear shift in the species under consideration.

In contrast with the fixed-redshift comparisons described in Section 5, our goal was to construct simulated data sets that corresponded as closely as possible to the full LP data set. In this case, instead of stacking together spectra drawn from a single output, we instead allowed for redshift evolution: drawing slices from the output that most closely corresponded to the redshift in question, taking $n \propto (1+z)^3$, and interpolating between CLOUDY tables with appropriate J_{22} values. Finally, we applied Poisson noise corresponding to a signal-to-noise ratio of 100 pixel^{-1}.

Each spectrum generated by this method was subject to the same two-step identification procedure that was applied to the real data, and the resulting fits were subject to the same N and b cuts as described in Section 2.2. The line lists compiled in this way were then used to generate correlation functions and column density distributions that directly parallel those calculated from the LP data set.

These are shown in Fig. 13, in which we explore a low-metallicity model ($10^{-2}\,Z_\odot$) roughly consistent with previous estimates (e.g. Rauch et al. 1997a; Schaye et al. 2003) as well as a higher-metallicity model ($10^{-1}\,Z_\odot$). Note that, at these metallicities, changes in Z can be modelled simply by boosting the C IV density derived from the CLOUDY tables by a linear factor. Increasing the metallicity by a factor of 10 in this way has very little effect on the correlation function: decreasing $\xi_{\rm C\,IV}(v)$ in the 20 and 35 km s^{-1} bins by roughly a factor of 1.5, while leaving the rest of the correlation function largely unchanged. In all cases these values fall far short of the clustering levels seen in our observational data, and they lack the conspicuous bend observed at ≈150 km s^{-1}.

However, changing metallicity has a large effect on the column density distribution. The low-metallicity model is consistent with observations over the range of $12.5 \leqslant \log N(\mathrm{cm}^{-2}) \leqslant 13.5$, and slightly overpredicts the number of large components (which have a negligible impact on the correlation function). The high-metallicity model, on the other hand, overpredicts the number of components for all column densities $\log N(\mathrm{cm}^{-2}) \geqslant 13.0$.

The poor fit to the correlation function is perhaps not surprising given the known inhomogeneity of the IGM metal distribution (e.g. Rauch et al. 1997a). Most recently, this has been quantified by Schaye et al. (2003), who applied a pixel optical depth method to derive a non-linear relation between the local overdensity Δ of hydrogen and the local carbon abundance. Over a large range of environments, they found $[\mathrm{C/H}] \propto \Delta_{\mathrm{H}}^{2/3}$ with a large variance. Is it possible that accounting for this relationship would be able to resolve the discrepancy in $\xi_{\mathrm{C\,IV}}(v)$? In order to address this question, we repeated our experiment, assuming that the local density followed the best-fitting relationship derived by Schaye et al. (2003). Again we considered both high- and low-metallicity models, resulting in correlation functions and column density distributions that are shown in Fig. 13.

As our results, which depend on a line-fitting procedure, are biased to the densest regions, the 'zero-point' metallicities of these models are naturally shifted to lower values. Thus, the $\Delta^{2/3}\,10^{-2}\,\mathrm{Z}_{\odot}$ and the $\Delta^{2/3}\,10^{-3}\,\mathrm{Z}_{\odot}$ models shown in these figures yield similar numbers of components as the single-metallicity $10^{-1}\,\mathrm{Z}_{\odot}$ and $10^{-2}\,\mathrm{Z}_{\odot}$ models, respectively. In particular, the lower-metallicity model allows us to obtain good agreement with the observed column density distribution, while assuming mean metallicity values more in line with previous estimates (e.g. Hellsten et al. 1997; Rauch et al. 1997a; Schaye et al. 2003).

Introducing a Δ dependence has almost no effect, however, on the correlation function, neither boosting it at low separations nor introducing a feature at $\approx$150 km s^{-1}. Thus it appears that this relationship is not the source of the clustering properties of the metal-line components, and rather that the large variance seen in the pixel-by-pixel results hides a third parameter that determines these features. In fact, in Paper I, we described just such a key parameter, the separation from a large dark-matter halo.

7 SOURCES OF INTERGALACTIC C IV

7.1 Distribution of metals and identification of sources

While the observed features in the C IV correlation function cannot be understood in terms of a local non-linear relationship between the metal and density distributions, we saw in Paper I that these features could be easily explained in terms of the distribution of metal *sources*. In that work we used a pure dark matter model to describe C IV components as contained within bubbles centred around sources, and we interpreted the amplitude and the knee in the C IV correlation function in terms of the source mass and bubble size, respectively. In this investigation we develop a similar model, but make use of the full gas and CLOUDY modelling described in Sections 5 and 6.

Following Paper I, we adopt a parametrization in which all metals are found within a comoving radius R_{s} of a dark matter halo whose mass is above a fixed value, M_{s}. To facilitate comparison with our previous modelling, as well as to allow for future comparisons with analytic approaches, we identified all sources at a fixed redshift of $z = 3$. In particular, halo detection was performed using the HOP algorithm (Eisenstein & Hut 1998) with parameters $\delta_{\mathrm{peak}} = 160$, $\delta_{\mathrm{saddle}} = 140$ and $\delta_{\mathrm{outer}} = 80$. The centres of these groups were then traced forwards in time to the $z = 2.5$ and 2.0 slices such that exactly the same groups could be selected from all the simulation slices, accounting for appropriate peculiar motions.

As in Paper I, our choice of $z = 3$ is not meant to imply that enrichment occurred at this redshift, but rather that it occurred at an unknown redshift higher than the observed range, centred on groups whose large-scale clustering was equivalent to $z = 3$ objects of mass M_{s}. For each choice of R_{s} and M_{s}, we then painted bubbles of metals on our simulations, as illustrated in Fig. 14. While increasing R_{s} has the obvious effect of increasing the volume filling factor of metals, increasing M_{s} not only lowers this filling factor, but also clusters the bubbles more strongly. This can be most easily seen by comparing models with similar filling factors. For example, comparing the $M_{\mathrm{s}} = 1 \times 10^{11}\,\mathrm{M}_{\odot}$, $R_{\mathrm{s}} = 1.6$ comoving Mpc slice to the $M_{\mathrm{s}} = 5 \times 10^{11}\,\mathrm{M}_{\odot}$, $R_{\mathrm{s}} = 2.4$ comoving Mpc slice indicates that a similar fraction is enriched with metals in both cases, but these regions are spread over a considerable area in the lower-mass case and concentrated into dense knots in the higher-mass case.

7.2 Properties of C IV

From slices such as those shown in Fig. 14 we were able to generate simulated QSO absorption spectra, in a manner exactly parallel to that described in Section 6.2: drawing lines of sight for the various time outputs, piecing them together by evolving the mean density, interpolating between CLOUDY tables, and applying realistic levels of Poisson noise. In this case the metallicity was assumed to be at a fixed value Z_{b} within each bubble, and zero everywhere else. Note, however, that our measurements are insensitive to C IV components with columns below 10^{12} cm^{-2}, and thus a more widely dispersed, lower-level contribution to IGM metals (e.g. Schaye et al. 2003; Bergeron & Herbert-Fort 2005) cannot be excluded.

In Paper I, our modelling made use of a parameter $\tilde{b}$ that controlled the impact parameter associated with each subclump within a bubble. In our more physical modelling, this role is played by Z_{b}, which we fixed at an initial value of $1/20\,\mathrm{Z}_{\odot}$. These spectra were analysed by our automated procedure, and in Figs 15 and 16 we compare the resulting correlation functions and column density distributions with those measured in the LP data set.

These plots reflect the trends seen in the slices. Increasing the mass concentrates the metal into fewer regions, boosting the correlation function, particularly at large separations. Increasing R_{s}, on the other hand, impacts the correlation function primarily at smaller separations, and has a strong impact on the total number of C IV components detected per spectrum. From Fig. 15, the best-fitting models are the $M_{\mathrm{s}} = 5 \times 10^{11}\,\mathrm{M}_{\odot}$ and $R_{\mathrm{s}} = 2.4$ Mpc, the $M_{\mathrm{s}} = 10^{12}\,\mathrm{M}_{\odot}$ and $R_{\mathrm{s}} = 2.4$ Mpc, and the $M_{\mathrm{s}} = 10^{12}\,\mathrm{M}_{\odot}$ and $R_{\mathrm{s}} = 3.2$ Mpc cases, with filling factors of 5.5, 8.6 and 11.6 per cent, respectively, although several of the lower filling factor cases produce so few lines as to be difficult to evaluate in detail. Similar filling factors have been advocated by Pieri & Haehnelt (2004) on the basis of O VI measurements. The large M_{s} values we derive are also suggestive of the regions around Lyman-break galaxies (LBGs), which are observed to be clustered like $\approx 10^{11.5}\,\mathrm{M}_{\odot}$ haloes at $z = 3$ (Porciani & Giavalisco 2002), and for which a strong cross-correlation with C IV absorbers has been measured (Adelberger et al. 2003, 2005; see also Chen et al. 2001). It is also reminiscent of the association between galaxies and C IV absorbers put forward in BSR03.

In Fig. 16 we better quantify the number of components in each model by constructing simulated column density distributions as discussed in Section 3.1. Here we see that, regardless of our choice

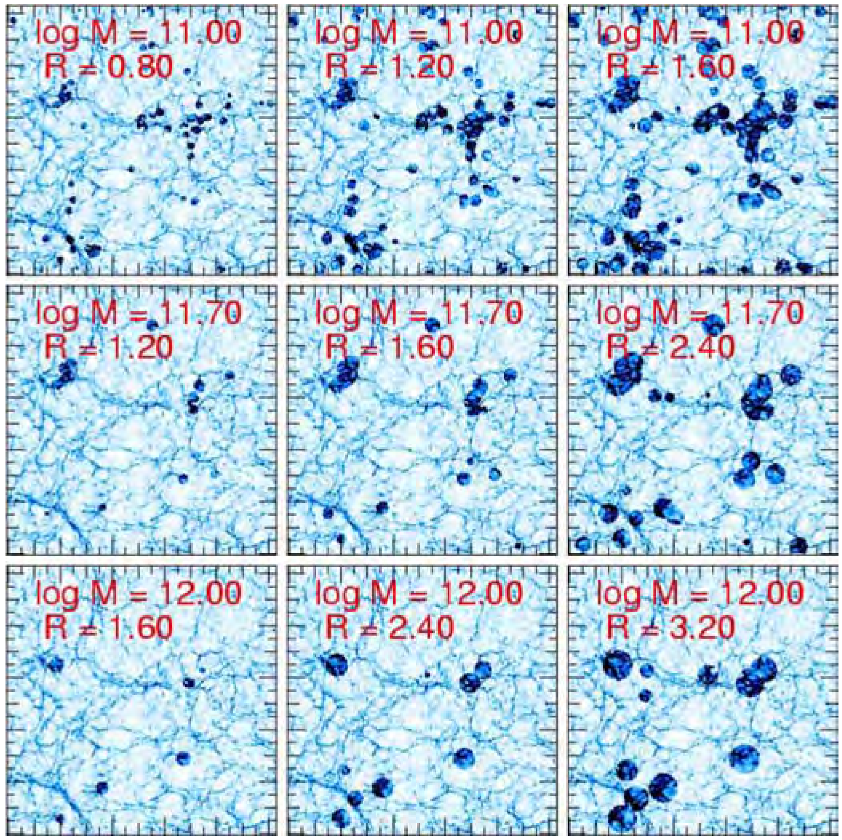

Figure 14. The C IV distribution of a $z = 3$ slice in the simulation. Dark regions are those contained within a distance R_s of a dark matter halo of mass M_s, with parameters as labelled in the panels. These regions are used in constructing simulated spectra, while all gas outside them is considered to be metal-free. From left to right, and then top to bottom, the overall volume filling factors (per cent) of these models are: 3.3, 8.6, 16.1; 3.4, 8.6, 16.7; and 1.7, 5.5, 11.6.

of source mass and bubble radius, all these models fall short of reproducing the observations. Owing to the relatively small filling factors of such bubble models, our choice of $Z_b = 1/20\,\mathrm{Z}_\odot$ is not able to generate the relatively large number of C IV absorbers seen in the data.

In order to improve this agreement we considered a model in which we assume a higher bubble metallicity of $Z_b \approx 0.2\,\mathrm{Z}_\odot$, generating the $\xi_{\mathrm{C\,IV}}(v)$ and $\log f(N)$ values seen in Figs 17 and 18. As was the case for our $\tilde{b}$ parameter in Paper I, varying Z_b has relatively little impact on the C IV correlation function, although the increased number of components does result in less noise.

Thus the high-metallicity simulations display the same trends and best-fitting models as were seen in the lower Z_b case. However, the improved signal allows us to distinguish the $M_s = 10^{12}\,\mathrm{M}_\odot$ and $R = 2.4$ Mpc model as a somewhat better match to the data than the $M_s = 5 \times 10^{11}\,\mathrm{M}_\odot$ and $R = 1.6$ Mpc model and the $M_s = 10^{12}\,\mathrm{M}_\odot$ and $R = 3.2$ Mpc model. The improved signal in Fig. 17 also enables us to reject cases with very low filling factors. In particular, we see that the models with the smallest bubble sizes do not reproduce the observed $\approx$150 km s^{-1} elbow, exceeding the measured $\xi_{\mathrm{C\,IV}}(v)$ at small separations. Furthermore, models with $M_s = 10^{11}\,\mathrm{M}_\odot$ are now seen to fall far short of the observed correlation function at large separations, particularly if we consider the models with $R_s \geqslant 0.8$, which are not overly peaked at small distances.

Finally, assuming a mean bubble metallicity of $1/5\,\mathrm{Z}_\odot$ has a large impact on the column density distribution, approximately doubling the number of detected components and bringing our best-fitting model into rough agreement with the data, although perhaps even this value is slightly low in our best-fitting cases. It is clear that we are forced towards these values because much of the gas around $\approx 10^{12}\,\mathrm{M}_\odot$ is heated by infall above $\approx 10^{5.5}$ K, and thus it is largely in the outskirts of our bubbles in which C IV absorbers are found.

While, at face value, this metallicity is widely discrepant with other estimates, there are nevertheless two reasons to take it seriously. First, the dense metal-rich regions in our model are observed to be enriched to similar levels at $z = 1.2$. At this point, the LBG-scale haloes around which we have placed our metals are expected to have fallen into clusters, and thus the IGM gas is detectable through X-ray emission in the intracluster medium (ICM). In fact, detailed *Chandra* and *XMM–Newton* observations indicate ICM iron levels of $Z = 0.20^{+0.10}_{-0.05}$ at $z = 1.2$ (Tozzi et al. 2003), implying that at even higher redshifts these metals have been efficiently mixed into the diffuse gas that forms into clusters. Secondly, we note that more than enough star formation has occurred by $z = 2.3$ to enrich these regions to our assumed values. Indeed, comparisons between the integrated star formation history and more standard estimates of IGM metallicity have shown that a large fraction of $z \approx 2$ metals have so far escaped detection (Pettini 1999). Thus, we find no compelling reason to dismiss this high metallicity value as spurious, although we emphasize that it has no direct impact on our derived clustering masses and bubble sizes.

8 AN ANALYTIC MODEL

While our simulated bubble model provides a compelling picture of the C IV and Si IV distribution at $z \approx 2$–3, it leaves open the question

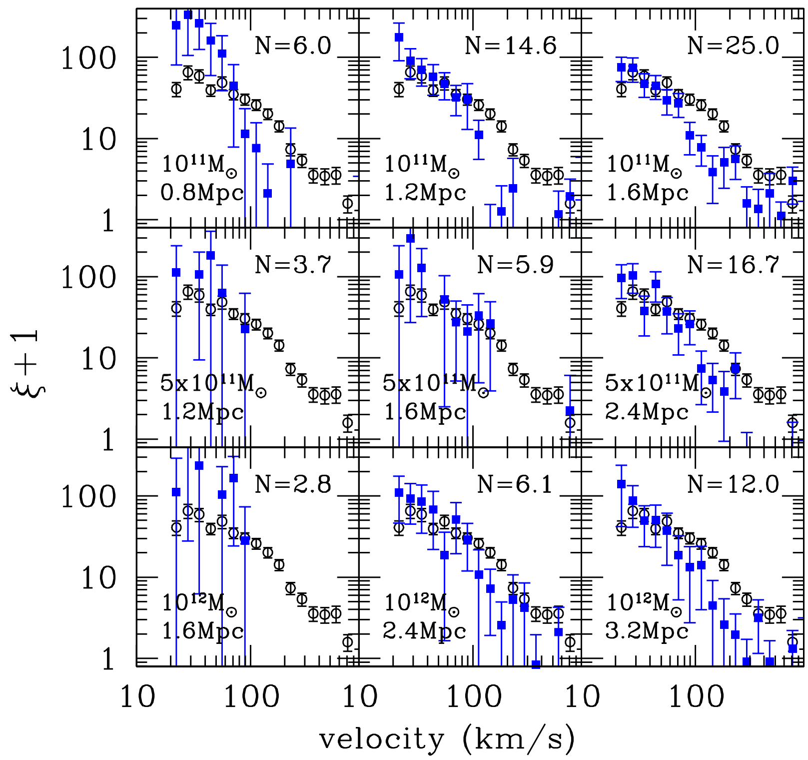

Figure 15. Correlation functions of simulated C IV components, with an assumed bubble metallicity of $1/20\,Z_{\odot}$. Panels are labelled by their assumed M_s in units of $M_{\odot}$ and R_s in units of comoving Mpc. In each panel the open circles summarize the observational results, while the filled squares represent the experimental results, as averaged over 114 spectra. Each panel is also labelled by the average number of C IV components detected per simulated spectrum.

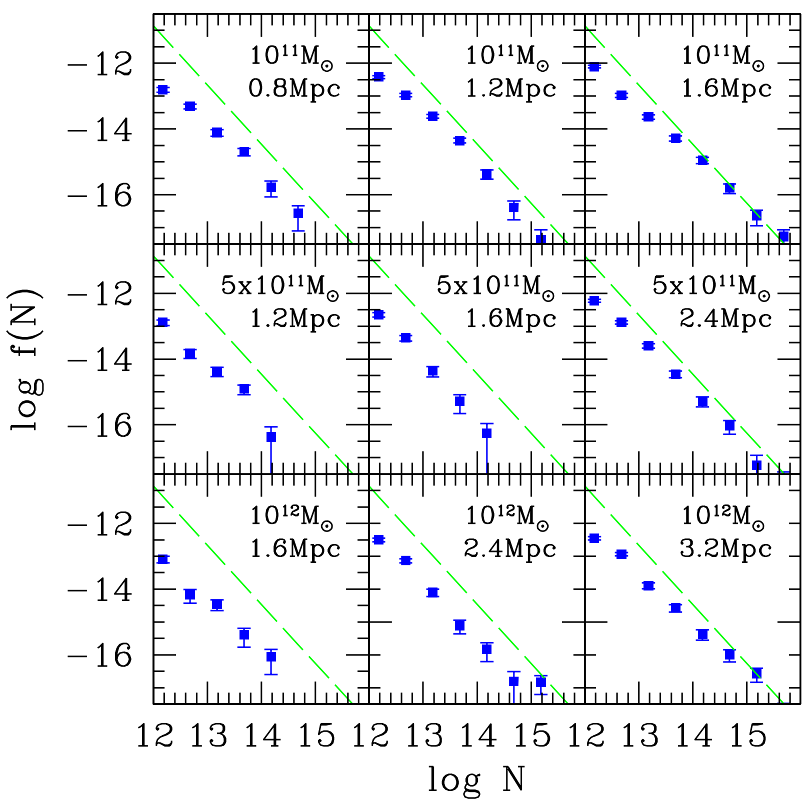

Figure 16. Column density distributions of simulated C IV absorption components, with an assumed bubble metallicity of $1/20\,Z_{\odot}$. Models are as in Fig. 15, and in each panel the filled points represent the simulation results, while the dashed line is the fit given in Fig. 1.

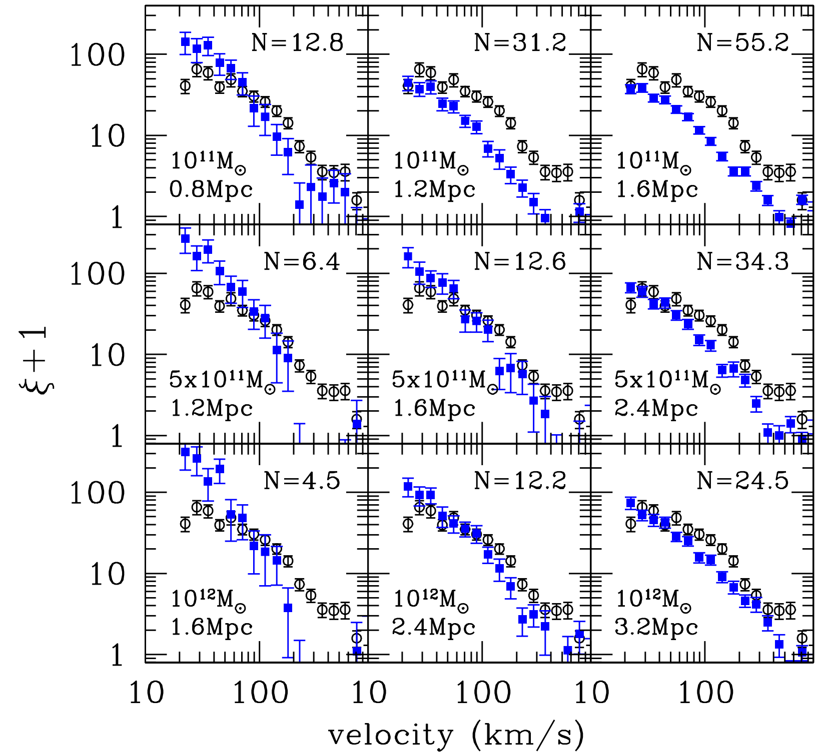

Figure 17. Correlation function of simulated C IV components, with an assumed bubble metallicity of $1/5\,Z_{\odot}$. Panels and symbols are as in Fig. 16.

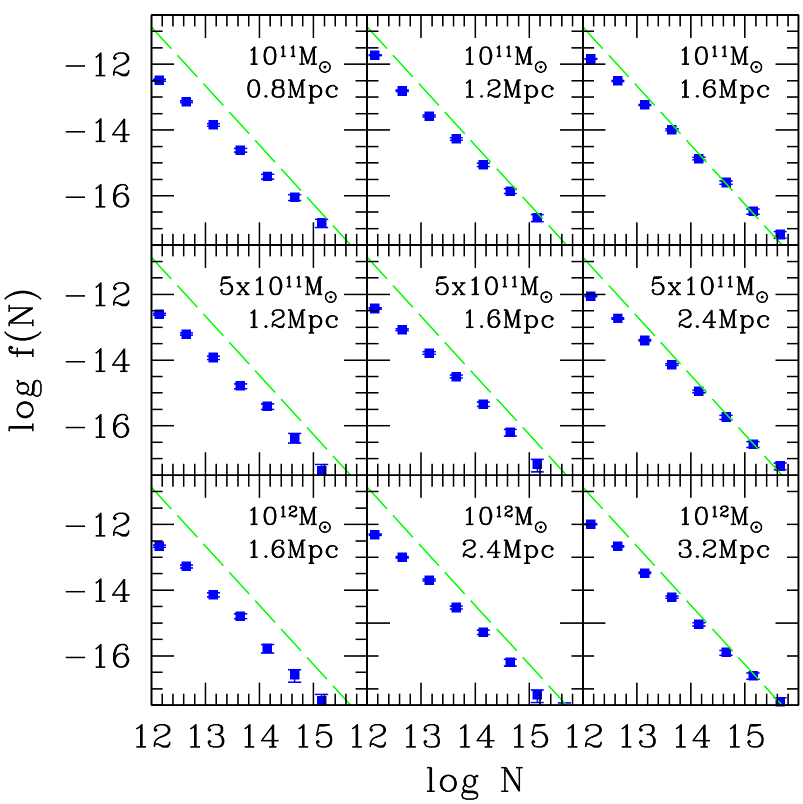

Figure 18. Column density distributions of simulated C IV absorption components, with an assumed bubble metallicity of $1/5\,Z_{\odot}$. Panels and symbols are as in Fig. 16.

as to properties of Mg II and Fe II. Yet the detailed modelling of these species is beyond the capabilities of our simulation. As we saw in Section 6.1, the environments of Mg II and Fe II are denser than C IV and Si IV, particularly in the case of Fe II. Even more constraining is the fact that almost all our detections of these systems fall well below our final simulated redshift of 2, with the majority lying in the $0.5 \lesssim z \lesssim 1.5$ redshift range.

In Fig. 9 we saw that, while the overall shape and correlation function of these species is comparable to that observed in C IV and Si IV, the magnitude and long separation tail of $\xi(v)$ are shifted upwards by a factor associated with the cosmological growth of structure. While reproducing these trends is beyond the capabilities of our simulation, they can nevertheless be studied from an approximate analytic perspective.

8.1 Derivation

In Section 7 we found good agreement between our observations and a model in which we painted metals around biased regions in our simulation. Analytically this corresponds to a picture in which the metal lines observed at $z_{\rm obs}$ come from clumps that are within a fixed radius of the sources of IGM metals. These pollution sources are associated with relatively rare objects of mass $M_{\rm p}$ that ejected metals into surroundings at a high redshift $z_{\rm p} > z_{\rm obs}$. After enrichment, these components continue to cluster gravitationally to $z_{\rm obs}$.

In the numerical simulations, these pollution centres are identified with the galaxies of mass $M_{\rm s}$ at a redshift of $z = 3$. However, this mass and redshift were intended only to quantify the bias of sources, and it is more probable that they are really related to less massive, higher-redshift objects, which exhibit similar clustering properties (Porciani & Madau 2005; Scannapieco 2005).

Let us consider, then, four points: the centres of two clumps (1 and 2), which we observe as metal-line components, and the centres of two bubbles (3 and 4), which correspond to the sources of pollution. We require that the pollution sources correspond to peaks [i.e. linear overdensities with a contrast larger than $\delta_{\rm cr} \equiv 1.68 D(z_{\rm p})^{-1}$] at a redshift $z_{\rm p} > z_{\rm obs}$ and at a mass scale $M_{\rm p}$. The clumps, on the other hand, are associated with the C IV absorbers themselves, and correspond to peaks at a mass scale $M_{\rm c}$. In the linear approximation, these fields satisfy a joint Gaussian probability distribution, which is specified by the block correlation matrix

$$\mathbf{M} = \begin{bmatrix} \xi_{\rm cc}(0) & \xi_{\rm cc}(r_{12}) & \xi_{\rm cp}(r_{13}) & \xi_{\rm cp}(r_{14}) \\ \xi_{\rm cc}(r_{12}) & \xi_{\rm cc}(0) & \xi_{\rm cp}(r_{23}) & \xi_{\rm cp}(r_{24}) \\ \xi_{\rm cp}(r_{13}) & \xi_{\rm cp}(r_{23}) & \xi_{\rm pp}(0) & \xi_{\rm pp}(r_{34}) \\ \xi_{\rm cp}(r_{14}) & \xi_{\rm cp}(r_{24}) & \xi_{\rm pp}(r_{34}) & \xi_{\rm pp}(0) \end{bmatrix} \equiv \begin{bmatrix} \mathbf{M}_{\rm cc} & \mathbf{c}_{\rm cp} \\ \mathbf{c}_{\rm pc} & \mathbf{M}_{\rm pp} \end{bmatrix}, \tag{15}$$

where $r_{ij} \equiv ||\boldsymbol{r}_i - \boldsymbol{r}_j||$, and $\xi_{\rm pp}$, $\xi_{\rm cc}$ and $\xi_{\rm cp}$ refer to the correlation between pollution centres, the correlation between satellite clumps, and the cross-correlation between satellite clumps and pollution centres, respectively. The joint probability of having a peak of an amplitude larger than $\delta_{\rm cr}$ at the four points is given by

$$p(1,2,3,4) = \frac{1}{4\pi^2\sqrt{\det|\mathbf{M}|}} \int_{\delta_{\rm cr}}^{\infty} {\rm d}\delta_1 \int_{\delta_{\rm cr}}^{\infty} {\rm d}\delta_2 \int_{\delta_{\rm cr}}^{\infty} {\rm d}\delta_3 \int_{\delta_{\rm cr}}^{\infty} {\rm d}\delta_4 \times \exp\left[-\frac{(\delta_1,\delta_2,\delta_3,\delta_4)^{\rm T} \cdot \mathbf{M}^{-1} \cdot (\delta_1,\delta_2,\delta_3,\delta_4)}{2}\right]. \tag{16}$$

We will evaluate this expression, assuming that the threshold that defines the object is high relative to the corresponding rms densities and taking the correlation between the metal-line clumps and the centres of pollution to be small. We shall not assume the smallness of the centre–centre nor clump–clump correlations, the first of which is the most important. In this limit

$$\mathbf{M}^{-1} \approx \begin{bmatrix} \mathbf{M}_{\rm cc}^{-1} & -\mathbf{M}_{\rm cc}^{-1}\mathbf{c}_{\rm cp}\mathbf{M}_{\rm pp}^{-1} \\ -\mathbf{M}_{\rm pp}^{-1}\mathbf{c}_{\rm pc}\mathbf{M}_{\rm cc}^{-1} & \mathbf{M}_{\rm pp}^{-1} \end{bmatrix}, \tag{17}$$

$$\det|\mathbf{M}| \approx \det|\mathbf{M}_{\rm cc}| \cdot \det|\mathbf{M}_{\rm pp}| \tag{18}$$

and

$$\begin{aligned} p(1,2,3,4) &\approx \frac{1}{4\pi^2\sqrt{\det|\mathbf{M}_{\rm cc}|}\sqrt{\det|\mathbf{M}_{\rm pp}|}} \\ &\times \int_{\delta_{\rm cr}}^{\infty} {\rm d}\delta_1 \int_{\delta_{\rm cr}}^{\infty} {\rm d}\delta_2 \exp\left[-\tfrac{1}{2}(\delta_1,\delta_2)^{\rm T} \cdot \mathbf{M}_{\rm cc}^{-1} \cdot (\delta_1,\delta_2)\right] \\ &\times \int_{\delta_{\rm cr}}^{\infty} {\rm d}\delta_3 \int_{\delta_{\rm cr}}^{\infty} {\rm d}\delta_4 \exp\left[-\tfrac{1}{2}(\delta_3,\delta_4)^{\rm T} \cdot \mathbf{M}_{\rm pp}^{-1} \cdot (\delta_3,\delta_4)\right] \\ &\times \exp\left[(\delta_1,\delta_2)^{\rm T} \cdot \mathbf{M}_{\rm cc}^{-1}\mathbf{c}_{\rm cp}\mathbf{M}_{\rm pp}^{-1} \cdot (\delta_3,\delta_4)\right]. \end{aligned} \tag{19}$$

In the high peak limit, the last cross-correlation term can be factored out from the integrals (see Appendix), yielding

$$p(1,2,3,4) \approx p(1,2)p(3,4) \exp\left[(\delta_{\rm cr},\delta_{\rm cr})^{\rm T} \cdot \mathbf{M}_{\rm cc}^{-1}\mathbf{c}_{\rm cp}\mathbf{M}_{\rm pp}^{-1} \cdot (\delta_{\rm cr},\delta_{\rm cr})\right], \tag{20}$$

where $p(1, 2)$ and $p(3, 4)$ are computed from equation (A12), or, explicitly,

$$\begin{aligned} p(1,2,3,4) &\approx \frac{1}{4\pi^2}\nu_{\rm cc}^{-2}\nu_{\rm pp}^{-2} C(c_{cc}(r_{12}),\nu_{\rm cc}) C(c_{pp}(r_{34}),\nu_{\rm pp}) \\ &\times \exp\left\{-\frac{\nu_{\rm cc}^2}{1+c_{\rm cc}(r_{12})} - \frac{\nu_{\rm pp}^2}{1+c_{\rm pp}(r_{34})} \right. \\ &\left. + \nu_{\rm cc}\nu_{\rm pp} \frac{c_{\rm cp}(r_{13}) + c_{\rm cp}(r_{24}) + c_{\rm cp}(r_{14}) + c_{\rm cp}(r_{23})}{[1+c_{\rm pp}(r_{34})][1+c_{\rm cc}(r_{12})]}\right\}, \end{aligned} \tag{21}$$

where the function $C(x, \nu)$ is defined in the Appendix, and we define the cross-correlation coefficients[1] as

$$c_{\rm cc} \equiv \xi_{\rm cc}(r)/\xi_{\rm cc}(0),$$

$$c_{\rm pp} \equiv \xi_{\rm pp}(r)/\xi_{\rm pp}(0),$$

$$c_{\rm cp} \equiv \xi_{\rm cp}(r)/\sqrt{\xi_{\rm cc}(0)\xi_{\rm pp}(0)},$$

and the normalized density thresholds as

$$\nu_{\rm cc} \equiv \delta_{\rm cr}/\sqrt{\xi_{\rm cc}(0)},$$

$$\nu_{\rm pp} \equiv \delta_{\rm cr}/\sqrt{\xi_{\rm pp}(0)}.$$

[1] The cross-correlation coefficients $\xi_{\rm cc}(r)/\xi_{\rm cc}(0)$ and $\xi_{\rm pp}(r)/\xi_{\rm pp}(0)$ reach unity at $r = 0$ and thus cannot be assumed small everywhere. At the same time $\xi_{\rm cp}(r)/\sqrt{\xi_{\rm cc}(0)\xi_{\rm pp}(0)}$ is always less than unity if $M_{\rm c}$ and $M_{\rm p}$ do not coincide (Schwartz inequality). In particular, the smaller its maximum value, achieved at $r = 0$, the larger the difference between the scales describing the clumps and the pollution centres.

Note that in equation (21) the correlation functions in the denominator are not assumed to be small, which allows for proper accounting of the case when two clumps or two pollution centres are the same. For example, setting $r_{12} = r_{34} = 0$ properly recovers the bivariant joint probability $p(1, 3)$ to find a clump at a separation r_{13} from the centre of pollution (equal in this case to $r_{14} = r_{23} = r_{24}$).

In our model only those clumps that lie within the spherical bubble around some pollution centre are observed to have metals. The correlation function of clumps of mass $M_{\rm c}$ that are within spherical bubbles around peaks corresponding to the mass $M_{\rm p}$ is defined as

$$p(\delta_1, \delta_3)p(\delta_2, \delta_4)[1 + \bar{\xi}(r_{12})] \equiv \bar{p}(\delta_1, \delta_2, \delta_3, \delta_4), \tag{22}$$

where the bar denotes averaging over the position of pollution centres within a distance $R_{\rm s}$ around two metal-rich clumps at a fixed separation r_{12}. Note that our definition of the correlation function, $\bar{\xi}(r_{12})$, is not equivalent to the estimator of the underlying correlation function of all the clumps of mass $M_{\rm c}$, $\xi(r_{12})$, nor is it equivalent to the conditional correlation function if there were a source of metals (a high peak of the scale $M_{\rm p}$) in the vicinity of *every* small halo, $\bar{\xi}_{\rm c}(r_{12})$, which would be given by

$$p(\delta_1)p(\delta_2)\bar{p}(\delta_3, \delta_4)[1 + \bar{\xi}_{\rm c}(r_{12})] \equiv \bar{p}(\delta_1, \delta_2, \delta_3, \delta_4). \tag{23}$$

Furthermore, $\bar{\xi}(r_{12})$ depends on the underlying two-point correlation of small clumps, the correlation of the sources, and the cross-correlation between clumps and sources. This last term is subject to the most modification should the physics of metal dispersal change. However, it mostly affects the biased density of small clumps in the vicinity of the sources relative to the cosmological mean, which is precisely the excess factored out in equation (22).

Thus equation (22) describes the correlation of metal components at the redshift of pollution, which is dominated by the clustering of the pollution sources. Subsequent gravitational clustering of enriched metals then leads to further amplification of the correlation in the linear approximation as

$$\bar{\xi}(r, z_{\rm obs}) = [D(z_{\rm obs})/D(z_{\rm p})]^2\bar{\xi}(r, z_{\rm p}), \tag{24}$$

where $D(z)$ is the linear density growth factor. This growth is suggestive of the difference between the C IV and Mg II correlation functions, as we saw in Fig. 9, as well as the hints of evolution seen in $\xi_{\rm C\,IV}(v)$ and $\xi_{\rm Mg\,II}(v)$ in Figs 3 and 7.

8.2 Application to observed metal absorbers

In Fig. 19 we fit our analytic model to the data. In the left panel we adopt the parameters used in our numerical simulations, identifying metal pollution centres with $M_{\rm p} = 10^{12}\,{\rm M}_\odot$ objects at a redshift $z_{\rm p} = 3$ and metal-rich clumps with collapsed objects of $M_{\rm c} = 10^9\,{\rm M}_\odot$, with $R_{\rm s} = 2.4$ comoving Mpc. At $z_{\rm obs} = 2.3$, the analytic fit reproduces the measured $\xi_{\rm C\,IV}(v)$ at large velocity separations, where it is dominated by the correlation between pollution centres, but it falls short at small velocities, where $\xi_{\rm C\,IV}(v)$ is dominated by the clump distribution within each bubble.

This is because the smoothing imposed by choosing $M_{\rm p} \approx 10^{12}\,{\rm M}_\odot$ is similar to the 2.4 Mpc bubble size, and thus our linear formalism is insufficient to describe distances less than $R_{\rm s}$. In reality, the non-linear collapse of $M_{\rm p}$ would have moved in new material to fill in this region. To mimic such non-linear effects at small radii, we apply the prescription $\delta_{\rm cr} \longrightarrow \delta_{\rm cr} + (1 - 1/\delta_{\rm cr})\xi$ (Mo & White 1996), resulting in the dashed curve. This correction, while crude, is seen to recover a $\xi_{\rm C\,IV}(v)$ that is similar to our simulated $10^{12}\,{\rm M}_\odot$ and $R_{\rm s} = 2.4$ Mpc case (and thus the observed correlation function), confirming that the discrepancy at small distances is caused by our neglect of non-linear motions.

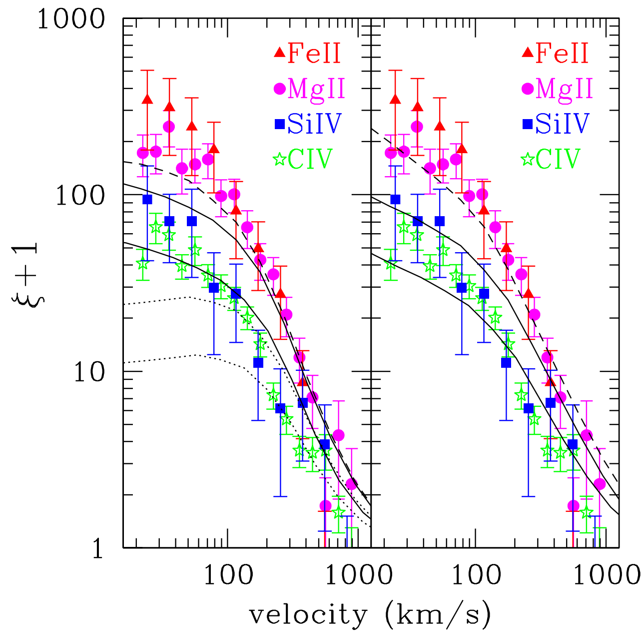

Figure 19. Comparison of our analytic model with the data. Left panel: Low-redshift model for metal sources. Dotted lines represent the linear clustering at $z_{\rm obs} = 2.3$ (lower) and $z_{\rm obs} = 1.15$ (upper) of clumps observed in the vicinity of the pollution centres, with $M_{\rm p} = 10^{12}\,{\rm M}_\odot$, $M_{\rm c} = 10^9\,{\rm M}_\odot$ and $z_{\rm p} = 3$. Solid lines show the effect of applying a non-linear correction to these models. Finally, the dashed curve shows a non-linear $z_{\rm obs} = 1.15$ model in which $M_{\rm p} = 10^{12}\,{\rm M}_\odot$ and $z_{\rm p} = 3$, but now $M_{\rm c} = 10^{10}\,{\rm M}_\odot$. Right panel: The lower solid curve corresponds to $M_{\rm p} = 3 \times 10^9\,{\rm M}_\odot$, $M_{\rm c} = 10^8\,{\rm M}_\odot$, $z_{\rm pol} = 7.5$, $z_{\rm obs} = 2.3$, with no non-linear correction applied. The upper solid line is a further linear extrapolation of this model to $z_{\rm obs} = 1.15$. The dashed line is a linear model again with $z_{\rm obs} = 1.15$, $M_{\rm p} = 3 \times 10^9\,{\rm M}_\odot$, $z_{\rm pol} = 7.5$, but with $M_{\rm c}$ raised to $10^9\,{\rm M}_\odot$. For all curves the comoving size of the bubble is 2.4 Mpc.

Next we turn our attention to Mg II and Fe II, which are observed at lower redshifts $z \approx 1.2$. As we saw in Fig. 9, the rise of the correlation amplitude of these species relative to C IV and Si IV is generally in agreement with the hypothesis of linear growth of gravitational clustering of a fixed population of objects from $z = 2.3$ to $z = 1.15$, although there are significant discrepancies at small radii. Again we plot both a linear $z_{\rm pol} = 3$, $M_{\rm p} = 10^{12}\,{\rm M}_\odot$, $M_{\rm c} = 10^9\,{\rm M}_\odot$ model observed at $z_{\rm obs} = 1.15$ and a similar model in which a non-linear correction has been applied. While the non-linear curve does well at most radii, a shortfall is seen at $z \lesssim 100$ km s^{-1}, similar to the discrepancy between the 'shifted' $\xi_{\rm C\,IV}(v)$ curve and the $\xi_{\rm Mg\,II}(v)$ curves in Fig. 9. Based on our plots of the species fraction as a function of environment, an important difference between these species is clear. As Mg II can only survive in regions with a low ionization parameter, it is biased towards much denser regions than C IV, which corresponds in our analytic models to higher clump masses. Raising $M_{\rm c}$ to $10^{10}\,{\rm M}_\odot$ to account for this effect leads to the dashed curve in the left panel, which again agrees well with the data.

As discussed above, however, it is likely that the origin of metal pollution lies at higher redshift from sources of a lower mass, whose comoving clustering properties are identical to $M \approx 10^{12}\,{\rm M}_\odot$ galaxies identified at $z = 3$. Indeed, these biased high-redshift sources may be the progenitors that later grew into large $z = 3$ galaxies. In the right panel of Fig. 19 we explore such a high-redshift model, in which we take $z_{\rm pol} = 7.5$ and $M_{\rm p} = 3 \times 10^9\,{\rm M}_\odot$, so that the bias of our sources is the same as for $M_{\rm p} = 10^{12}\,{\rm M}_\odot$, objects forming at $z_{\rm p} = 3$. Adopting a similar $\nu_{\rm c}$ as in the $z_{\rm p} = 3$ case results in the solid curves. As the smoothing due to the Lagrangian radius associated with $M_{\rm p} = 3 \times 10^9$ is minimal, no non-linear correction is necessary and our simple model provides a reasonable fit to the C IV and Si IV components observed at $z = 2.3$.

Similarly, extrapolation of the same objects to $z = 1.15$, the mean redshift for Mg II and Fe II systems, matches their large-scale ($v > 300$ km s^{-1}) correlations quite well, although the data at these separations are sparse. At small velocities the difference between the environments of the two species becomes important, and linear scaling does not completely explain the enhancement of correlation amplitude in Fe II and Mg II relative to C IV and Si IV. As in the low-redshift case, if we associate these species with larger clumps, the fit is much improved at small radii, resulting in the dashed curve.

In summary, our simple analytic model generally reproduces the features seen in our simulations of the C IV and Si IV correlation functions, although a non-linear correction is necessary in the $z_{\rm p} = 3$ model. Linearly extrapolating these models to lower redshift results in a good fit to Mg II and Fe II at large distances, although a fit at smaller distances requires us to use larger clump masses, associated with denser environments. Finally, we find that there is a strong degeneracy between $M_{\rm p}$ and $z_{\rm pol}$, with a family of sources with similar biases producing acceptable fits.

9 CONCLUSIONS

While intergalactic metals are ubiquitous, the details of how these elements made their way into the most tenuous regions of space remains unknown. In this study we have used a uniquely large, homogeneous and high signal-to-noise ratio sample of QSO sightlines to pin down the spatial distribution of these metals and combined this with advanced automated detection techniques and a high-resolution SPH simulation to pin down just what we can learn from this distribution. Our study has been focused on four key species: C IV and Si IV, which serve as tracers of somewhat overdense regions from redshifts 1.5 to 3.0, and Mg II and Fe II, which trace dense, lower-redshift ($z = 0.5$–2.0) environments. No evolution in the column density distributions of any of these species is detected.

In the high-redshift case, C IV and Si IV trace each other closely. For both species, $\xi(v)$, exhibits a steep decline at large separations, which is roughly consistent with the slope of the ΛCDM matter correlation function and the spatial clustering of $z \approx 3$ Lyman-break galaxies. At separations below ≈150 km s^{-1}, this function flattens out considerably, reaching a value of $\xi(v) \approx 50$, if $v \lesssim 50$ km s^{-1}. Our data also suggest that $\xi_{\rm C\,IV}(v)$ evolves weakly with redshift, at a level consistent with the linear growth of structure.

The distribution of metals as traced by $\xi_{\rm C\,IV}(v)$ is extremely robust. We find that it remains almost completely unchanged when minimum or maximum column density cuts are applied to our sample, even if they are so extreme as to eliminate over two-thirds of the components. We have also linked together C IV components into systems, using a one-dimensional friends-of-friends algorithm, with linking lengths of $v_{\rm link} = 25$, 50 and 100 km s^{-1}. In all cases, the line-of-sight correlation function of the resulting systems matches the original component correlation function (within measurement errors) at separations above $v_{\rm link}$. Finally, the Si IV/C IV ratio shows no clear dependence when binned as a function of separation, suggesting that the features seen in $\xi_{\rm C\,IV}(v)$ and $\xi_{\rm Si\,IV}(v)$ do not result from fluctuations in the ionizing background.

Thus none of our tests indicate that the observed distributions of C IV and Si IV represent anything but the distribution of intergalactic metals at $z = 1.5$–3.0. This motivated us to carry out a confrontation between our C IV observations and detailed simulations of IGM metal enrichment, which paralleled previous comparisons for the Lyα forest. Furthermore, the advanced automatic detection procedures described in Section 2.2 (see also Aracil, in preparation) allowed us not only to compare simulated and observed spectra, but also to generate simulated line lists in a manner that exactly paralleled the observations.

Using these tools, we found that the observed features of the C IV line-of-sight correlation function cannot be reproduced if the IGM metallicity is constant. Rather, any such model falls far short of the observed $\xi_{\rm C\,IV}(v)$ amplitude and fails to reproduce flattening seen below ≈150 km s^{-1}. Furthermore, adopting a local relation between overdensity and metallicity, as observed by Schaye et al. (2003), has little or no effect on these results.

On the other hand, rough agreement between simulated and observed C IV correlation functions is obtained in a model in which only a *fraction* of the IGM is enriched. Emulating the simple model in Paper I, we explored a range of models in which metals were confined within bubbles of radius $R_{\rm s}$ about $z = 3$ sources of mass $M_{\rm s}$, where these quantities are not meant literally as source redshifts and masses, but rather as tracers of the *bias* of the $z_{\rm pol} \geqslant 3$ source population. Varying these quantities, we derived parameters that suggest large metal bubbles, $R_{\rm s} \approx 2$ comoving Mpc, around highly biased sources, with $M_{\rm s} \approx 10^{12}\,{\rm M}_\odot$.

These results are suggestive of the association between galaxies and C IV absorbers put forward in BSR03, and the high cross-correlation between LBGs and C IV absorbers measured by Adelberger et al. (2003, 2005). Yet this does not mean that LBGs are the sources of intergalactic metals, only that the $z_{\rm pol} \geqslant 3$ sources were biased like LBGs. In fact, the case for outflows escaping lower-redshift starbursts is much more convincing for dwarfs (Martin 2005). Similarly, $R_{\rm s}$ need not be interpreted as the ejection radius of each source, but instead as the distance at which bubbles from multiple sources overlap. Our best-fitting $M_{\rm s}$ and $R_{\rm s}$ values are independent of the assumed bubble metallicity, although the low ($\lesssim$10 per cent) volume filling factors of these models forces us to use large ($\approx 1/5\,{\rm Z}_\odot$) values to reproduce the observed C IV column density distribution. Note, however, that given the high bias of our enriched regions, such metallicities may be necessary to reconcile $z \approx 2.3$ measurements with $z \approx 1.2$ observations of the iron content of the ICM in high-redshift galaxy clusters (Tozzi et al. 2003).

At lower redshifts, the line-of-sight correlation functions of Mg II and Fe II are consistent with the same enriched regions seen in C IV and Si IV, but now 'passively' evolved down to $z \approx 1.2$. Again both $\xi_{\rm Mg\,II}(v)$ and $\xi_{\rm Fe\,II}(v)$ trace each other closely, and exhibit the same steep decline at large separations and flattening at small separations as were seen in $\xi_{\rm C\,IV}(v)$ and $\xi_{\rm Si\,IV}(v)$. Also, as in the higher-redshift case, the Mg II correlation function remains unchanged when minimum and maximum column density cuts are applied, and linking together Mg II components into systems has no strong impact on $\xi_{\rm Mg\,II}(v)$ outside separations corresponding to the linking length.

Although Mg II and Fe II are detected in regions that cannot be simulated numerically, we are nevertheless able to develop an analytic model that allows for a simple analysis of these species. Testing our model against $\xi_{\rm C\,IV}(v)$ and $\xi_{\rm Si\,IV}(v)$, we find generally good agreement with the data for similar values of mass and $R_{\rm s}$ as in the numerical case. Pushing the model to lower redshift, we find that the same parameters do well at reproducing the clustering properties of Mg II and Fe II, especially when we account for the fact that these species are found in denser environments. Finally, we also find agreement with the observed $\xi_{\rm C\,IV}(v)$ and $\xi_{\rm Si\,IV}(v)$ at $z = 2.3$ and $\xi_{\rm Mg\,II}(v)$ and $\xi_{\rm Fe\,II}(v)$ at $z = 1.15$, and a high-redshift analytic model in which $z_{\rm p} = 7.5$ and $M_{\rm p} = 3 \times 10^9\,{\rm M}_{\odot}$, illustrating the strong degeneracy between $M_{\rm p}$ and $z_{\rm p}$ for similarly biased sources.

Taken together, our $z \approx 2.3$ and $z \approx 1.2$ measurements, numerical simulations and analytic modelling paint a consistent picture of IGM enrichment. The distribution of intergalactic metals does not appear uniform, nor simply dependent on the local density, but rather it bears the signature of the population from which it came. While the $z \geqslant 3$ redshift of metal ejection is unknown, a joint constraint on the masses and redshifts of the objects responsible for IGM pollution remains compelling. Models of IGM enrichment must come to terms with the observed biased sources of intergalactic metals.

ACKNOWLEDGMENTS

We are grateful to K. Adelberger, A. Aguirre, D. Aubert, M. Davis, A. Ferrara, M. Haehnelt, J. Heyvaerts, C. Martin, C. Mallouris, E. Rollinde, J. Schaye, R. Teyssier and E. Thiébaut for useful comments and helpful suggestions. We thank the anonymous referee for a careful reading of our paper, which greatly improved it. ES was supported in part by an NSF MPS-DRF fellowship. RJT acknowledges funding from the Canadian Computational Cosmology Consortium and use of the SHARCNET computing facilities. This work greatly benefited from the many collaborative discussions made possible by visits by ES and DP, hosted by the Observatoire de Strasbourg. We would like to thank D. Munro for freely distributing his YORICK programming language,[2] which we used to implement our algorithm, and F. Haardt and P. Madau for providing us with an updated version of their UV background models. This work is based on observations collected through ESO Project ID No. 166.A-0106. We acknowledge partial support from the Research and Training Network 'The Physics of the Intergalactic Medium' set up by the European Community under the contract HPRN-CT2000-00126 RG29185. This work was supported by the National Science Foundation under grant PHY99-07949.

REFERENCES

Adelberger K. L., Steidel C. C., Shapley A. E., Pettini M., 2003, ApJ, 584, 45
Adelberger K. L., Shapley A. E., Steidel C. C., Pettini M., Erb D., Reddy N. A., 2005, ApJ, 629, 636
Aguirre A., Schaye J., Kim T.-S., Theuns T., Rauch M., Sargent W. L. W., 2004, ApJ, 602, 38
Aracil B., Petitjean P., Pichon C., Bergeron J., 2004, A&A, 419, 811
Bardeen J. M., Bond J. R., Kaiser N., Szalay A., 1986, ApJ, 304, 15
Begelman M. C., Blandford R. D., Rees M. J., 1984, Rev. Mod. Phys., 56, 255
Bergeron J., Herbert-Fort S., 2005, in Williams P. R., Shu C., Ménard B., eds, IAU Colloq. 199, Probing Galaxies through Quasar Absorption Lines. Cambridge Univ. Press, Cambridge, p. 265
Bergeron J., Aracil B., Petitjean P., Pichon C., 2002, A&A, 396, L11
Bi H., Davidsen A. F., 1997, ApJ, 479, 523
Black J. H., 1981, MNRAS, 197, 553
Boksenberg A., Sargent W. L. W., Rauch M., 2003, ApJS, submitted (astro-ph/0307557) (BSR03)
Boroson T., Sargent W.L.W., Boksenberg A., Carswell R.F., 1978, ApJ, 220, 772
Bromm V., Ferrara A., Coppi P. S., Larson R. B., 2001, MNRAS, 328, 969
Bromm V., Yoshida N., Hernquist L., 2003, ApJ, 596, L135
Carswell R. F., Webb J. K., Baldwin J. A., Atwood B., 1987, ApJ, 319, 709
Carswell R. F., Schaye J., Kim T. S., 2002, ApJ, 578, 43
Cen R., Bryan G., 2001, ApJ, 546, 81
Chen H. W., Lanzetta K. M., Webb J. K., 2001, ApJ, 556, 158
Choudhury T. R., Srianand R., Padmanabhan T., 2001, ApJ, 559, 29
Churchill C. W., Rigby J. R., Charlton J. C., Vogt S. S., 1999, ApJS, 120, 51
Churchill C. W., Vogt S. S., Charlton J. C., 2003, AJ, 125, 98
Couchman H. M. P., Thomas P. A., Pearce F. R., 1995, ApJ, 452, 797
Cristiani S., D'Odorico S., D'Odorico V., Fontana A., Giallongo E., Savaglio S., 1997, MNRAS, 285, 209
Croft R. A. C., Weinberg D. H., Katz N., Herquist L., 1998, ApJ, 495, 44
Croft R. A. C., Weinberg D.H., Bolte M., Burles S., Hernquist L., Katz N., Kirkman D., Tytler D., 2002, ApJ, 581, 20
Davis M., Efstathiou G., Frenk C. S., White S. D. M., 1985, ApJ, 292, 371
Eisenstein D. J., Hut P., 1998, ApJ, 498, 137
Eke V. R., Cole S., Frenk C. S., 1996, MNRAS, 282, 263
Ellison S. L., Songaila A., Schaye J., Pettini M., 2000, AJ, 120, 1175
Fan X. et al., 2001, AJ, 121, 54
Ferland G. J., 2000, Rev. Mex. Astron. Astrophys., 9, 153
Ferland G. J., Korista K. T., Verner D. A., Ferguson J. W., Kingdon J. B., Verner E. M., 1998, PASP, 100, 761
Foltz C. B., Hewett P. C., Chaffee F. H., Hogan C. J., 1993, AJ, 105, 22
Frye B., Broadhurst T., Benitez N., 2002, ApJ, 568, 558
Gnedin N. Y., Ostriker J. P., 1997, ApJ, 486, 581
Haardt F., Madau P., 1996, ApJ, 461, 20
Haardt F., Madau P., 2001, in Neumann D.M., Van J.T.T., eds, XXIst Moriond Astrophy. Meet., Clusters of galaxies and the high redshift universe observed in X-rays. (online publication only, astro-ph/0106018)
Hellsten U., Davé R., Hernquist L., Weinberg D., Katz N., 1997, ApJ, 487, 482
Hockney R. W., Eastwood J. W., 1988, Computer simulation using particles. Adam Hilger, Bristol
Hui L., 1999, ApJ, 516, 519
Hui L., Gnedin N., 1997, ApJ, 586, 581
Hui L., Haiman Z., 2003, ApJ, 596, 9
Jenkins E. B., Ostriker J. P., 1991, ApJ, 376, 33
Jing Y. P., 1999, ApJ, 515, L45
Kaiser N., 1984, ApJ, 284, L9
Kim T.-S., Cristiani S., D'Odorico S., 2002, A&A, 383, 747
Madau P., Ferrara A., Rees M. J., 2001, ApJ, 555, 9
McDonald P., Miralda-Escudé J., Rauch M., Sargent W. L. W., Barlow T. A., Cen R., Ostriker J. P., 2000, ApJ, 543, 1
Martin C. L., 2005, ApJ, 621, 227
Mo H. J., White S. D. M., 1996, MNRAS, 282, 348
Mo H. J., Jing Y. P., Börner G., 1992, ApJ, 392, 452
Norman M., O'Shea B., Paschos P., 2004, ApJ, 601, L115
Perlmutter S. et al., 1999, ApJ, 517, 565
Petitjean P., 2001, Ap&SS, 277, 517
Petitjean P., Bergeron J., 1990, A&A, 231, 309
Petitjean P., Bergeron J., 1994, A&A, 283, 759
Pettini M., 1999, in Walsh J., Rosa M., eds, Proc. ESO Workshop, Chemical Evolution from Zero to High Redshift. Springer, Berlin, p. 233
Pettini M., Shapley A. E., Steidel C. C., Cuby J.-G., Dickinson M., Moorwood A. F. M., Adelberger K. L., Giavalisco M., 2001, ApJ, 554, 981
Pettini M., Madau P., Bolte M., Prochaska J. X., Ellison S., Fan X., 2003, ApJ, 594, 695
Pichon C., Vergely J. L., Rollinde E., Colombi S., Petitjean P., 2001, MNRAS, 326, 597
Pichon C., Scannapieco E., Aracil B., Petitjean P., Aubert D., Bergeron J., Colombi S., 2003, ApJ, 597, L97 (Paper I)
Pieri M. M., Haehnelt M. G., 2004, MNRAS, 347, 985
Porciani C., Giavalisco M., 2002, ApJ, 565, 24
Porciani C., Madau P., 2005, ApJ, 625, L43
Prochter G. E., Prochaska J. X., Burles S. M., 2004, ApJ, in press (astro-ph/0411776)
Rauch M., Sargent W. L., Womble D. S., Barlow T. A., 1996, ApJ, 467, L5

[2] Available at http://www.maumae.net/yorick/doc/index.html

Rauch M., Haehnelt M. G., Steinmetz M., 1997a, ApJ, 481, 601
Rauch M. et al., 1997b, ApJ, 489, 7
Rauch M., Sargent W. L., Barlow T. A., 2001, ApJ, 554, 823
Sargent W. L. W., Young P. J., Boksenberg A., Tytler D., 1980, ApJS, 42, 41
Sargent W. L. W., Steidel C. C., Boksenberg A., 1988, ApJS, 68, 539
Scannapieco E., 2005, ApJ, 624, L1
Scannapieco E., Ferrara A., Broadhurst T., 2000, ApJ, 536, L11
Scannapieco E., Ferrara A., Madau P., 2002, ApJ, 574, 590
Schaye J., Rauch M., Sargent W. L. W., Kim T.-S., 2000, ApJ, 551, L1
Schaye J., Aguirre A., Kim T.-S., Theuns T., Rauch M., Sargent W. L. W., 2003, ApJ, 596, 768
Schmidt M., 1963, ApJ, 137, 758
Schneider R., Ferrara A., Natarajan P., Omukai K., 2002, ApJ, 571, 30
Shull J. M., Tumlinson J., Giroux M. L., Kriss G. A., Reimers D., 2004, ApJ, 600, 570
Sigward F., Ferrara A., Scannapieco E., 2005, MNRAS, 358, 755
Simcoe R. A., Sargent W. L. W., Rauch M., 2002, ApJ, 578, 737
Simcoe R. A., Sargent W. L. W., Rauch M., 2004, ApJ, 606, 92
Songaila A., 2001, ApJ, 561, L153 (S01)
Songaila A., Cowie L. L., 1996, AJ, 112, 335
Spergel D. N. et al., 2003, ApJS, 148, 175
Steidel C. C., 1990, ApJS, 72, 1
Sutherland R. S., Dopita M. A., 1993, ApJS, 88, 253
Tegmark M., Silk J., Evrard A., 1993, ApJ, 417, 54
Thacker R. J., Tittley E. R., Pearce F. R., Couchman H. M. P., Thomas P. A., 2000, MNRAS, 319, 619
Thacker R. J., Scannapieco E., Davis M., 2002, ApJ, 202, 581
Thacker R. J., Pringle G., Couchman H. M. P., Booth S., 2003, in Senechal D., ed., HPCS 2003, Proc. Performance Computing Systems and Applications 2003. NRC Research Press, Ottawa
Thomas D., Greggio L., Bender R., 1999, MNRAS, 302, 537
Tozzi P., Rosati P., Ettori S., Borgani S., Mainieri V., Norman C., 2003, ApJ, 593, 705
Tytler D., 1987, ApJ, 321, 49
Tytler D., Fan X. M., Burles S. M., Cottrell L., Davis C., Kirkman D., Zuo L., 1995, in Meylan G., ed., Proc. ESO Workshop, QSO Absorption Lines. Springer, Berlin, p. 289
van den Bergh S., 1962, AJ, 67, 486
Viel M., Haehnelt M. G., Springel V., 2004, MNRAS, 354, 684
Weymann R. J., 1997, in Arav N., Shlosman I., Weymann R. J., eds, ASP Conf. Ser. Vol. 128, Mass Ejection from AGN. Astron. Soc. Pac., San Francisco, p. 3

APPENDIX A: TWO-POINT JOINT PROBABILITY DISTRIBUTION OF HIGH PEAKS IN GAUSSIAN FIELDS

In this section we present formulae for the joint two-point probability for the peaks in the Gaussian field that are used in our analytic model. These allow for the pair of peaks to have different scales and improve on the asymptotic results for the high peaks.

In the standard cosmological picture one identifies a collapsed object of mass M with a peak of height $\delta > \delta_{\rm cr}$ in the density field $\delta(x)$, smoothed with a top-hat window function $W(R)$ with the scale $R = (3M/4\pi\bar{\rho})^{1/3}$. In the limit of large height the geometrical peaks of the Gaussian field can be approximately described as just the regions of high field values. This is the approximation that we adopt.

We shall need, first, the variance of the smoothed density field

$$\sigma^2 = \int P(k) W^2(kR) k^2 \, {\rm d}k, \tag{A1}$$

where $P(k)$ is the power spectrum of the density field and the Fourier image of the top-hat window is

$$W(kR) \equiv 4\pi R^3 \left[\frac{\sin(kR)}{(KR)^3} - \frac{\cos(kR)}{(KR)^2}\right], \tag{A2}$$

and, secondly, the correlation function between the values of the field at two positions, separated by the distance $r_{12} = x_1 - x_2$,

$$\xi(r_{12}) = \int P(k) \frac{\sin(kr_{12})}{kr_{12}} W(kR_1) W(kR_2) k^2 \, {\rm d}k, \tag{A3}$$

where the value at point 1 is taken after the field is smoothed on a scale R_1, while at point 2 the field is evaluated after smoothing on a scale R_2. If $R_1 = R_2$, then $\xi(0) = \sigma^2$, while in general $\xi(0) \leqslant \sigma_1 \sigma_2$.

To evaluate the probability distribution functions used in Section 8, we begin with the well-known result for the one-point probability of the field height to exceed $\delta_{\rm cr}$:

$$p(1) = \frac{1}{\sqrt{2\pi}\sigma} \int_{\delta_{\rm cr}}^{\infty} {\rm d}\delta_1 \, \exp\left(-\frac{\delta_1^2}{2\sigma_1^2}\right) \sim \frac{1}{\sqrt{2\pi}} \frac{\sigma_1}{\delta_{\rm cr}} \exp\left(-\frac{\delta_{\rm cr}^2}{2\sigma_1^2}\right) = \frac{1}{\sqrt{2\pi}} \nu_1^{-1} \exp\left(-\frac{\nu_1^2}{2}\right), \tag{A4}$$

where $\nu_1 \equiv \delta_{\rm cr}/\sigma_1$. Here 1 refers both to the (arbitrary) point where the field is evaluated, as well as to the scale it was smoothed with, R_1.

Next we evaluate the asymptotic behaviour at large $\delta_{\rm cr} \gg \sigma$ for the joint two-point probability

$$p(1,2) = \frac{1}{2\pi\sqrt{\sigma_1^2\sigma_2^2 - \xi(r_{12})}} \int_{\delta_{\rm cr}}^{\infty} {\rm d}\delta_1 \int_{\delta_{\rm cr}}^{\infty} {\rm d}\delta_2 \, \exp\left[-\frac{1}{2} \frac{\delta_1\sigma_2^2 + \delta_2\sigma_1^2 - 2\xi(r_{12})\delta_1\delta_2}{\sigma_1^2\sigma_2^2 - \xi^2(r_{12})}\right], \tag{A5}$$

paying attention to the prefactors of the exponential terms. In general, $\sigma_1 \neq \sigma_2$, but when δ_1 and δ_2 represent the same field smoothed with the same filter taken at two different points (the case that we mostly need in this paper), then $\sigma_1 = \sigma_2$. Introducing uncorrelated variables

$$x = \frac{\delta_1\sigma_2 + \delta_2\sigma_1}{\delta_{\rm cr}\sigma_2 + \delta_{\rm cr}\sigma_1} \qquad \text{and} \qquad y = \frac{\delta_1\sigma_2 - \delta_2\sigma_1}{\sigma_1\sigma_2},$$

we obtain

$$p(1,2) = \frac{\delta_{\rm cr}(\sigma_1+\sigma_2)}{4\pi\sqrt{\sigma_1^2\sigma_2^2 - \xi^2(r_{12})}} \int_1^{\infty} {\rm d}x \, \exp\left[-\frac{1}{4}\frac{\delta_{\rm cr}^2}{\sigma_1\sigma_2}\frac{(\sigma_1+\sigma_2)^2}{\sigma_1\sigma_2 + \xi(r_{12})} x^2\right] \int_{\delta_{\rm cr}[2\sigma_2 - x(\sigma_1+\sigma_2)]/\sigma_1\sigma_2}^{\delta_{\rm cr}[x(\sigma_1+\sigma_2)-2\sigma_1]/\sigma_1\sigma_2} {\rm d}y \, \exp\left[-\frac{1}{4}\frac{\sigma_1\sigma_2}{\sigma_1\sigma_2 - \xi(r_{12})} y^2\right]. \tag{A6}$$

This integral is of Laplace type,

$$I = \int_1^\infty \mathrm{d}x\ \mathrm{e}^{-\alpha\phi(x)} f(x) \qquad \text{with} \qquad \alpha = \delta_{\rm cr}^2/\sigma_1\sigma_2,$$

which for large α asymptotically accumulates at the lower integration boundary over the interval $x \in [1, 1 + \Delta x]$, with

$$\Delta x = 2\frac{\sigma_1\sigma_2}{\delta_{\rm cr}^2}\frac{\sigma_1\sigma_2 + \xi(r_{12})}{(\sigma_1+\sigma_2)^2}.$$

Asymptotic expansion is straightforward if one can expand $f(x)$ in a Taylor series near $x = 1$,

$$f(x) \equiv \int_{\delta_{\rm cr}[2\sigma_2 - x(\sigma_1+\sigma_2)]/\sigma_1\sigma_2}^{\delta_{\rm cr}[x(\sigma_1+\sigma_2)-2\sigma_1]/\sigma_1\sigma_2} \mathrm{d}y\ \exp\left[-\frac{1}{4}\frac{\sigma_1\sigma_2}{\sigma_1\sigma_2 - \xi(r_{12})}y^2\right] \approx 2(x-1)\frac{\delta_{\rm cr}(\sigma_1+\sigma_2)}{\sigma_1\sigma_2}\ \exp\left[-\frac{1}{4}\frac{\delta_{\rm cr}^2}{\sigma_1\sigma_2}\frac{(\sigma_1-\sigma_2)^2}{\sigma_1\sigma_2 - \xi(r_{12})}\right], \tag{A7}$$

in which case we get

$$p(1,2) \approx \frac{2}{\pi}\frac{\sigma_1\sigma_2}{\delta_{\rm cr}^2}\frac{[\sigma_1\sigma_2 + \xi(r_{12})]^{3/2}}{(\sigma_1+\sigma_2)^2[\sigma_1\sigma_2 - \xi(r_{12})]^{1/2}}\ \exp\left[-\frac{1}{2}\delta_{\rm cr}^2\frac{\sigma_1^2+\sigma_2^2-2\xi(r_{12})}{\sigma_1^2\sigma_2^2 - \xi^2(r_{12})}\right]. \tag{A8}$$

Two things are notable: First is the prefactor $(\sigma_1\sigma_2)/\delta_{\rm cr}^2$. Secondly, we find that for small correlations the effect in the exponent where small $\xi/\sigma_1\sigma_2$ is multiplied by $\delta_{\rm cr}/\sigma_1\sigma_2$ dominates the correction from the prefactor. Thus, as a leading-order approximation, we can account for small correlations by factoring out the exponential correlation term from the original expression, with the values of the field replaced by the threshold values.

In reality, the asymptotics in equation (A8) do not give an accurate approximation if correlations are strong, $\xi(r_{12}) \to \sigma_1\sigma_2$, especially since our threshold parameter $\delta_{\rm cr}/\sigma$ may not be very large. This is definitely the case for a distribution of identical objects at short distances, since then $\xi(r \to 0) = \sigma^2$. More accurately, the Taylor expansion of $f(x)$ in equation (A7) is not suitable when the width of the relevant integration range $\Delta y = \delta_{\rm cr}\ \Delta x\ (\sigma_1+\sigma_2)/(\sigma_1\sigma_2)$ exceeds the width of the Gaussian $\sqrt{[\sigma_1\sigma_2 - \xi(r_{12})]/(\sigma_1\sigma_2)}$. In this case, however, the integration over y can be extended to $\pm\infty$. With subsequent asymptotic analysis of the integral over x, this gives

$$p(1,2) \approx \frac{1}{\sqrt{\pi}}\frac{\sqrt{\sigma_1\sigma_2}}{\delta_{\rm cr}}\frac{\sqrt{\sigma_1\sigma_2+\xi(r_{12})}}{\sigma_1+\sigma_2}\ \exp\left[-\frac{1}{4}\frac{\delta_{\rm cr}^2}{\sigma_1\sigma_2}\frac{(\sigma_1+\sigma_2)^2}{\sigma_1\sigma_2+\xi(r_{12})}\right],\ \text{with}\ \frac{2}{\sqrt{\sigma_1\sigma_2 - \xi(r_{12})}}\frac{\sigma_1\sigma_2+\xi(r_{12})}{\sigma_1+\sigma_2} \gg \frac{\delta_{\rm cr}}{\sqrt{\sigma_1\sigma_2}} \gg 1. \tag{A9}$$

The general equations (A8) and (A9) are much simpler in the case when variances are identical, $\sigma_1^2 = \sigma_2^2 = \xi(0)$. Defining the cross-correlation coefficient $c(r_{12}) = \xi(r_{12})/\xi(0)$ and specifying accurately the range of validity of equation (A8) gives

$$p(1,2) \approx \frac{1}{2\pi}\nu^{-2}A(c(r_{12}))\ \exp\left[-\frac{\nu^2}{1+c(r_{12})}\right], \qquad \text{for} \qquad \nu \gg \max\left(1,\ \frac{1+c(r_{12})}{\sqrt{1-c(r_{12})}}\right), \tag{A10}$$

$$p(1,2) \approx \frac{1}{\sqrt{2\pi}}\nu^{-1}B(c(r_{12}))\ \exp\left[-\frac{\nu^2}{1+c(r_{12})}\right], \qquad \text{for} \qquad \frac{1+c(r_{12})}{\sqrt{1-c(r_{12})}} \gg \nu \gg 1, \tag{A11}$$

where smooth functions

$$A(x) \equiv \sqrt{\frac{(1+x)^3}{1-x}} \xrightarrow{x\to 0} 1 \qquad \text{and} \qquad B(x) \equiv \sqrt{\frac{1+x}{2}} \xrightarrow{x\to 1} 1.$$

As expected,

$$p(1,2) \xrightarrow{c\to 0} p(1)p(2) \qquad \text{and} \qquad p(1,2) \xrightarrow{c\to 1} p(1).$$

It is important to note that the probability is additionally enhanced by $\nu = \delta_{\rm cr}/\sigma$ when correlations are strong.

Finally, we combine (A10) and (A11) into the uniform approximation

$$p(1,2) \approx \frac{1}{2\pi}\nu^{-2}C(c(r_{12}),\nu)\ \exp\left[-\frac{\nu^2}{1+c(r_{12})}\right], \qquad \text{for} \qquad \nu \gg 1, \tag{A12}$$

with the help of an interpolating function, $C(x, \nu)$, such that $C(0, \nu) = 1$, $C(1, \nu) = \nu\sqrt{2\pi}$. The choice

$$C(x,\nu) = \frac{\nu\sqrt{\pi}\sqrt{(1+x)^3}}{(\nu\sqrt{\pi}-1)\sqrt{1-x}+(1+x)} \tag{A13}$$

reflects both the details of the functions $A(x)$ and $B(x)$ and of the transition between (A10) and (A11).

In the weak correlation regime, the formula (A12) coincides with the classic result of Kaiser (1984). At the same time, in the strong correlation regime, the result (A12) shows that the correlation between regions of high density is additionally enhanced by the factor $\sqrt{2\pi}\nu$. Although our result is rigorous for the points of high excursions of the field at all separations r, the interpretation of the last regime in terms of peak, or object, correlation is questionable at $r < R_1 + R_2$ when the two high-density points probably belong to the same peak.

This paper has been typeset from a TEX/LATEX file prepared by the author.

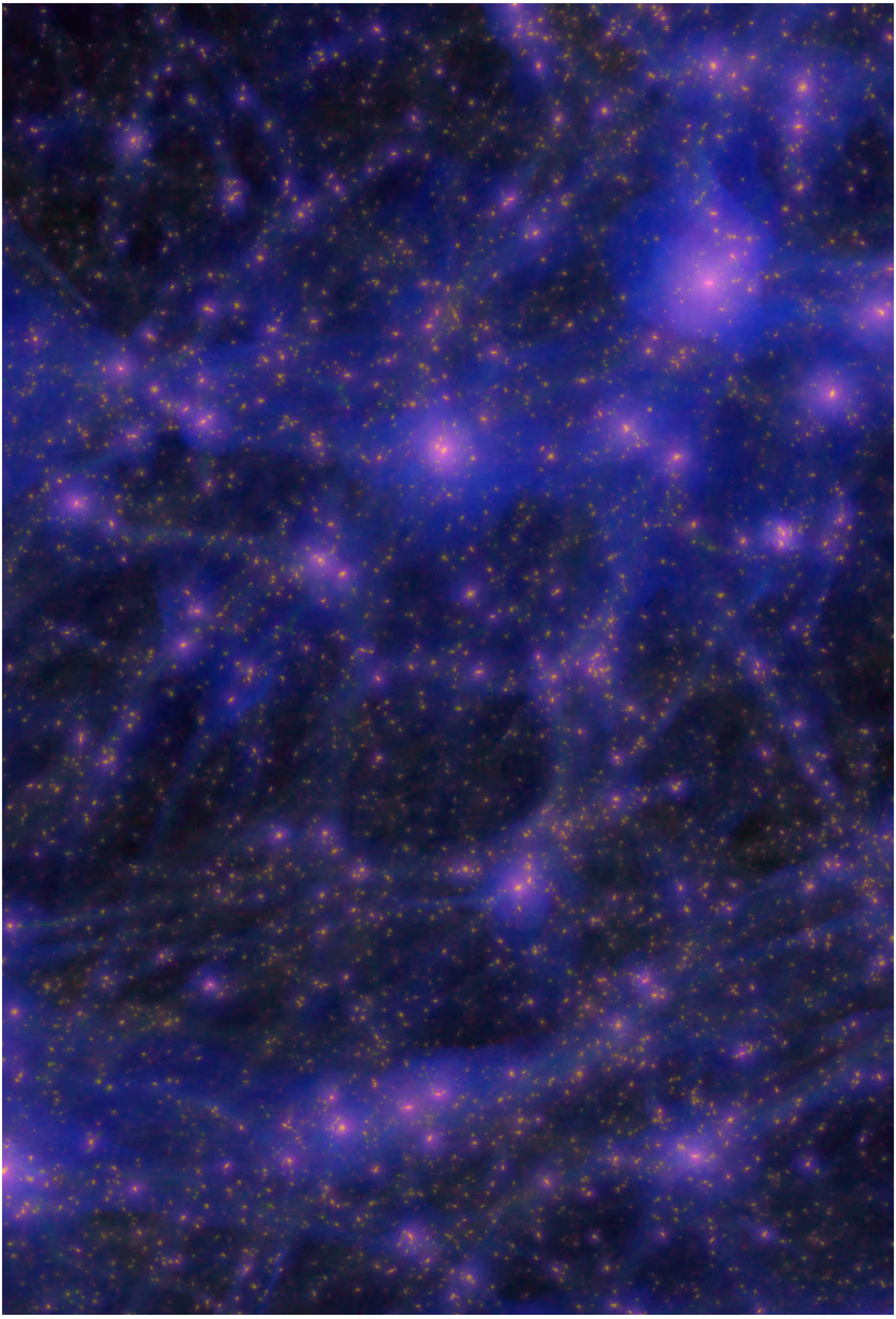

Mon. Not. R. Astron. Soc. **317**, 348–374 (2000)

Stellar dynamics in the Galactic Centre: proper motions and anisotropy

R. Genzel,[1★] C. Pichon,[2,3] A. Eckart,[1] O. E. Gerhard[2] and T. Ott[1]

[1]*Max-Planck Institut für Extraterrestrische Physik, D-85740 Garching bei München, Germany*
[2]*Astronomisches Institut, Universität Basel, Switzerland*
[3]*Observatoire de Strasbourg, 11 rue de l'Observatoire, Strasbourg, France*

Accepted 2000 March 20. Received 2000 February 2; in original form 1999 November 8

ABSTRACT

We report a new analysis of the stellar dynamics in the Galactic Centre, based on improved sky and line-of-sight velocities for more than 100 stars in the central few arcseconds from the black hole candidate SgrA*. The main results are as follows.

(1) Overall, the stellar motions do not deviate strongly from isotropy. For those 32 stars with a determination of all three velocity components, the absolute, line-of-sight and sky velocities are in good agreement, consistent with a spherical star cluster. Likewise the sky-projected radial and tangential velocities of all 104 proper motion stars in our sample are also consistent with overall isotropy.

(2) However, the sky-projected velocity components of the young, early-type stars in our sample indicate significant deviations from isotropy, with a strong radial dependence. Most of the bright He I emission-line stars at separations from 1 to 10 arcsec from SgrA* are on tangential orbits. This tangential anisotropy of the He I stars and most of the brighter members of the IRS 16 complex is largely caused by a clockwise (on the sky) and counter-rotating (line of sight, compared to the Galaxy), coherent rotation pattern. The overall rotation of the young star cluster may be a remnant of the original angular momentum pattern in the interstellar cloud from which these stars were formed.

(3) The fainter, fast-moving stars within ≈ 1 arcsec of SgrA* may be largely moving on radial or very elliptical orbits. We have so far not detected deviations from linear motion (i.e., acceleration) for any of them. Most of the SgrA* cluster members are also on clockwise orbits. Spectroscopy indicates that they are early-type stars. We propose that the SgrA* cluster stars are those members of the early-type cluster that happen to have small angular momentum, and thus can plunge to the immediate vicinity of SgrA*.

(4) We derive an anisotropy-independent estimate of the Sun–Galactic Centre distance between 7.8 and 8.2 kpc, with a formal statistical uncertainty of ± 0.9 kpc.

(5) We explicitly include velocity anisotropy in estimating the central mass distribution. We show how Leonard–Merritt and Bahcall–Tremaine mass estimates give systematic offsets in the inferred mass of the central object when applied to finite concentric rings for power-law clusters. Corrected Leonard–Merritt projected mass estimators and Jeans equation modelling confirm previous conclusions (from isotropic models) that a compact central mass concentration (central density $\geq 10^{12.6}\,M_\odot\,pc^{-3}$) is present and dominates the potential between 0.01 and 1 pc. Depending on the modelling method used, the derived central mass ranges between 2.6×10^6 and $3.3 \times 10^6\,M_\odot$ for $R_\odot = 8.0$ kpc.

Key words: celestial mechanics, stellar dynamics – stars: kinematics – Galaxy: centre – Galaxy: kinematics and dynamics.

1 INTRODUCTION

High spatial resolution observations of the motions of gas and stars have in the past decade substantially strengthened the evidence that central dark mass concentrations reside in many (and perhaps most) nuclei of nearby galaxies (Kormendy & Richstone 1995; Magorrian et al. 1998; Richstone et al. 1998). These dark central masses are very likely to be massive black

★ E-mail: genzel@mpe-garching.mpg.de

Mon. Not. R. Astron. Soc. **000**, 1–13 (2007)   Printed 30 April 2008   (MN LATEX style file v2.2)

Numerical investigation of lens models with substructures using the perturbative method.

S. Peirani[1*], C. Alard[1], C. Pichon[1], R. Gavazzi[1] and D. Aubert[2]
[1] *Institut d'Astrophysique de Paris, 98 bis Bd Arago, 75014 Paris, France -*
Unité mixte de recherche 7095 CNRS - Université Pierre et Marie Curie.
[2] *Observatoire Astronomique de Strasbourg, 11 Rue de l'Université, 67000 Strasbourg, France.*

30 April 2008

ABSTRACT

We present a statistical study of the effects induced by substructures on the deflection potential of dark matter halos in the strong lensing regime. This investigation is based on the pertubative solution around the Einstein radius (Alard 2007) in which all the information on the deflection potential is specified by only a pair of one-dimensional functions on this ring.

Using direct comparison with ray-tracing solutions, we found that the iso-contours of lensed images predicted by the pertubative solution is reproduced with a mean error on their radial extension of less than 1% — in units of the Einstein radius, for reasonable substructure masses. It demonstrates the efficiency of the approximation to track possible signatures of substructures.

We have evaluated these two fields and studied their properties for different lens configurations modelled either through massive dark matter halos from a cosmological N-body simulation, or via toy models of Monte Carlo distribution of substructures embedded in a triaxial Hernquist potential.

As expected, the angular power spectra of these two fields tend to have larger values for larger harmonic numbers when substructures are accounted for and they can be approximated by power-laws, whose values are fitted as a function of the profile and the distribution of the substructures.

Key words: methods: Gravitational lensing-strong lensing; N-body simulations

1 INTRODUCTION

The cold dark matter (CDM) paradigm (Cole et al. 2005 and references therein) has led to a successful explanation of the large-scale structure in the galaxy distribution on scales $0.02 \leq k \leq 0.15$h Mpc^{-1}. The CDM power spectrum on these scales derived from large redshift surveys such as, for instance, the Anglo-Australian 2-degree Field Galaxy Redshift Survey (2dFGRS), is also consistent with the Lyman-α forest data in the redshift range $2 \leq z \leq 4$ (Croft et al. 2002; Viel et al. 2003; Viel, Haehnelt & Springel 2004).

In spite of these impressive successes, there are still discrepancies between simulations and observations on scales ≤ 1 Mpc, extensively discussed in the recent literature. We may mention the sharp central density cusp predicted by simulations in dark matter halos and confirmed by the rotation curves of low surface brightness galaxies (de Blok et al. 2001) or in bright spiral galaxies (Palunas & Williams 2000; Salucci & Burkert 2000; Gentile et al. 2004). Moreover, deep surveys ($z \geq 1-2$), such as the Las Campanas Infrared Survey, HST Deep Field North and Gemini Deep Deep Survey (GDDS) are revealing an excess of massive early-type galaxies undergoing "top-down" assembly with high inferred specific star formation rates relative to predictions of the hierarchical scenario (Glazebrook et al. 2004; Cimatti, Daddi & Renzini 2006).

One problem that requires closer examination concerns the large number of sub-L_* subhalos present in simulations but not observed (Kauffmann, White & Guiderdoni 1993; Moore et al. 1999; Klypin et al. 1999). This is the case of our Galaxy or M31, although there is mounting evidence for a large number of very low mass dwarfs (Belokurov et al. 2006). However, it is still unclear whether the CDM model needs to be modified to include self-interacting (Spergel & Steinhardt 2000) or warm dark matter (Bode, Ostriker & Turok 2001; Colín, Avila-Reese & Valenzuela 2000) or whether new physical mechanisms can dispel such discrepancies with the observations. For instance, gas cooling can be partly prevented by photoionization process which may

* E-mail: peirani@iap.fr

Astronomy & Astrophysics manuscript no. paper2˙v8 April 10, 2008
(DOI: will be inserted by hand later)

Cosmic Star-formation History from the Infrared

Star-formation rate density and Luminosity Functions from direct and inverse methods

D. Le Borgne[1], D. Elbaz[1], P. Ocvirk[1,2], C. Pichon[3]

[1] CEA/Saclay, DSM/IRFU/SAp, F-91191 Gif-sur-Yvette, France
[2] Astrophysikalisches Institut Potsdam, An der Sternwarte 16, D-14482 Potsdam, Germany
[3] Institut d'Astrophysique de Paris, UMR7095 CNRS, UPMC, 98bis boulevard Arago, F-75014 Paris, France

Received...; accepted...

Abstract. The shape and the decomposition of the Lilly-Madau diagram representing the evolution of the cosmic star-formation rate density (hereafter SFRD) is still subject to vigorous debates, both on observational and modeling grounds. We address here this issue with two complementary empirical approaches. First, using the deepest data available today at $24\,\mu$m ($24\,\mu$Jy), we present the evolution of the SFRD probed by infrared light and of the infrared luminosity functions, complementing previous similar works on this subject, which were 4 times shallower, with a luminosity gain of 0.6 dex in the faint-end. We then use an original non-parametric inversion technique to derive the range of all possible evolving luminosity functions able to reproduce simultaneously the available multi-wavelength infrared counts from 15 to $850\,\mu$m. The redshifts of the sources are not needed as an input for this inversion: the only constraints we impose are that the limits from measurements of the cosmic infrared background are respected, and that the evolution of the LF is smooth both in redshift and in luminosity. We find that the range of possible LFs is in remarkable agreement with the direct measurements at low redshift. The cosmic SFRD inferred by these luminosity functions are also in agreement with direct observations; the uncertainties in the contribution of LIRGs and ULIRGS are tightened at high redshift. When accounting for stellar lifetimes and remnants, the integral of the SFRD is consistent with the stellar density per unit comoving volume from $z = 0$ to 3, in contrast with previous claims. Since these SFRD are measured from completely independent datasets (old-cold stars from optical-NIR for the stellar density, and young massive warm stars from UV radiation reprocessed by dust in the FIR), the consistency between the SFR and stellar mass histories in that redshift range should now be considered to be a robust constraint for theoretical models and numerical simulations. A particular difficulty for these models will be to explain this "IR downsizing", i.e. the fact that the average IR luminosity of the galaxies, which dominate the SFR density, increases with redshift. Finally, we make predictions for the number of sources to be seen in future infrared missions such as HERSCHEL and SCUBA2.

Key words. Galaxies: high-redshift– Galaxies: evolution – Galaxies: formation – Infrared: galaxies – Submillimeter – Galaxies: luminosity function

1. Introduction

Some key questions remain concerning the cosmic formation of galaxies, such as when and how galaxies formed their stars over the last 13 Gyr. However, thanks to recent ultra-deep surveys at various wavelengths, some phenomena are now quite accurately measured and described, at least at relatively low redshift. For instance, it is well established that massive galaxies have experienced most of their star formation (SF) activity at early epochs whereas the SF activity in small galaxies keeps on average a more constant level. This so-called "downsizing" has been subject to many studies over the last few years (Madau et al. 1996; Lilly et al. 1996; Steidel et al. 1999; Juneau et al. 2005; Le Floc'h et al. 2005) and various signs of this downsizing are now seen. But precise measurements of the SF occurring at high redshift are still needed to challenge efficiently the latest models of galaxy formation. Hence additional constraints on the modeling of the evolution of the cosmic star-formation history must come from observations.

Recently, very deep surveys were designed to probe SF in the distant universe. The GOODS survey (PI. Dickinson, see also Giavalisco et al. 2004), with its very

Send offprint requests to: Damien Le Borgne, e-mail: damien.leborgne@cea.fr

Mon. Not. R. Astron. Soc. **282,** 1143–1158 (1996)

Equilibria of flat and round galactic discs

C. Pichon[1,2]★ and D. Lynden-Bell[1]

[1] *Institute of Astronomy, The Observatories, Cambridge CB3 0HA*
[2] *CITA, 60 St George Street, Toronto, Ontario M5S 1A7, Canada*

Accepted 1996 May 20. Received 1996 May 20; in original form 1994 December 30

ABSTRACT

A general method is presented for constructing distribution functions for flat systems whose surface density and Toomre Q number profile are given. The purpose of these functions is to provide plausible galactic models and assess their critical stability with respect to global non-axisymmetric modes. The derivation may be carried out for an azimuthal velocity distribution (or a given specific energy distribution) which may either be observed or be chosen to match a specified temperature profile. Distribution functions describing stable models with realistic velocity distributions for power-law discs, the isochrone and the Kuzmin discs are provided. Specially simple inversion formulae are also given for finding distribution functions for flat systems the surface densities of which are known.

Key words: methods: numerical – galaxies: formation.

1 INTRODUCTION

Over the next decade, ample and accurate observational data on the detailed kinematics of nearby disc galaxies will become available. It will be of great interest to link these observations with theoretical models for the underlying dynamics. The problem of finding the distribution function for an axially symmetrical system may formally be solved by using Laplace transforms (Lynden-Bell 1960) or by using power series (Fricke 1952 or, more recently, Vauterin & Dejonghe 1995). Kalnajs (1976), followed by Miyamoto (1974) chose specific forms of distribution function because the flat problem has no unique solution. Distribution functions for the power-law discs were also derived recently by Evans (1993), while Hunter & Qian (1993) presented an inversion scheme which can be applied for thickened discs with two integrals. For flat discs, it is desirable to use the functional freedom left in f in order to constuct a distribution function that accounts for all the kinematics, either observed or desired (i.e. which accounts for the line profiles observed, or which are marginally stable to radial modes). Independent measurement of the observed radial and azimuthal velocity distribution functions could, for instance, be contrasted with predictions arising from the gravitational nature of the interaction. Indeed the laws of the motion and the associated conserved quantities together with the assumption that the system is stationary put strong constraints on the possible velocity distributions. This is formally expressed by the existence of an underlying distribution function that characterizes the dynamics completely Binney & Tremaine (1987). The determination of realistic distribution functions which could account for observed line profiles is therefore an important project *vis-à-vis* the understanding of galactic structure. Producing theoretical models that account globally for the observed line profiles of a given galaxy provides a unique opportunity to inspect the current understanding of the dynamics of disc galaxies. It should then be possible to study quantitatively all departures from the flat axisymmetric stellar models. Indeed, axisymmetric distribution functions are the building blocks of all sophisticated stability analyses, and a good phase-space portrait of the unperturbed configuration is often needed in order to assess the stability of a given equilibrium state. Numerical N-body simulations also require sets of initial conditions which reflect the nature of the equilibrium.

For a flat galaxy all the stellar orbits are confined to a plane and by Jeans' theorem the steady state mass-weighted distribution function must be of the form $f=f(\varepsilon, h)$, where the specific energy, ε, and the specific angular momentum, h, are

★Present address: Astronomisches Institut, Universitat Basel, Venusstrasse 7, CH-4102 Binningen, Switzerland.

Mon. Not. R. Astron. Soc. **265,** 126–144 (1993)

Relativistic discs and flat galaxy models

J. Bičák,* D. Lynden-Bell and C. Pichon
Institute of Astronomy, The Observatories, Madingley Road, Cambridge CB3 0HA

Accepted 1993 May 12. Received 1993 April 17; in original form 1993 February 18

ABSTRACT

Recent progress in Newtonian potential theory of infinitesimally thin discs enables one to generate the potential–density pairs of axisymmetric discs in closed forms. We show that these results can be used to construct infinite sequences of new solutions of Einstein's equations which describe counter-rotating static discs of finite mass. At large distances these discs become Newtonian, but in their central regions they exhibit relativistic features such as velocities close to that of light and large redshifts. In particular, we construct space–times representing relativistic Kuzmin–Toomre discs and Kalnajs–Mestel discs; the second family includes also the relativistic generalization of the isochrone discs. The properties of the discs are discussed and illustrated.

Key words: relativity – celestial mechanics, stellar dynamics – galaxies: kinematics and dynamics.

1 INTRODUCTION

Recently, Evans & de Zeeuw (1992) constructed the potential–density pairs of an infinite number of families of non-axisymmetric discs by superposing 'elliptic discs'. Their approach also advances the theory of axisymmetric discs: it shows that any axially symmetric disc can be analysed into a superposition of simple Kuzmin discs with different weights. Unlike classical methods, theirs yields potentials in closed, compact forms.

The potential of the Kuzmin discs in cylindrical coordinates (R, z) is given by

$$\nu = -GM/r_b, \qquad \text{where} \qquad r_b^2 = R^2 + (|z| + b)^2; \tag{1.1}$$

the corresponding classical surface density of mass is

$$\Sigma(R) = (4\pi G)^{-1}\left[\frac{\partial \nu}{\partial z}\right]_{0-}^{0+} = (2\pi)^{-1}Mb/(R^2+b^2)^{3/2}. \tag{1.2}$$

The total mass of the disc is M.

Kuzmin (1956) constructed the potential (1.1) by considering a point mass placed at a distance b *below* the centre $R=0$ of a plane $z=0$, and its gravity field *above* the plane $z=0$. By reflecting this potential with respect to $z=0$ he arrived at a symmetrical solution (1.1) of Poisson's equation everywhere, which has a discontinuous normal derivative on $z=0$ (cf. equation 1.2).

Employing Kuzmin's idea, we see that a general axially symmetric classical disc has a potential above its plane equal to that of a line distribution of mass along the negative z-axis below the plane. The potential is thus given by

$$\nu = -G\int_{b_1}^{b_2}\frac{W(b)\,\mathrm{d}b}{[R^2+(|z|+b)^2]^{1/2}}, \tag{1.3}$$

where the integration limits are determined by the interval $\langle b_1, b_2\rangle$ along the negative z-axis, in which the line density $W(b)$ – or the 'weight function' – is non-zero. The corresponding surface density of mass on the disc is

*Permanent address: Department of Theoretical Physics, Faculty of Mathematics and Physics, Charles University, V Holešovičkách 2, 18000 Prague 8, Czech Republic.

Mon. Not. R. Astron. Soc. **000**, 000–000 (0000) Printed 29 January 2008 (MN LaTeX style file v2.2)

Recovering the topology of the IGM at z∼2

S. Caucci[1], S. Colombi[1], C. Pichon[1,2], E. Rollinde[1], P. Petitjean[1], T. Sousbie[1,2]
[1] *Institut d'Astrophysique de Paris & UPMC, 98 bis boulevard Arago, 75014 Paris, France*
[2] *Centre de Recherche Astrophysique de Lyon, 9 avenue Charles Andre, 69561 Saint Genis Laval, France*

29 January 2008

ABSTRACT

We investigate how well the 3D density field of neutral hydrogen in the Intergalactic Medium (IGM) can be reconstructed using the Lyman-α absorptions observed along lines of sight to quasars separated by arcmin distances in projection on the sky. We use cosmological hydrodynamical simulations to compare the topologies of different fields: dark matter, gas and neutral hydrogen optical depth and to investigate how well the topology of the IGM can be recovered from the Wiener interpolation method implemented by Pichon et al. (2001). The *global* statistical and topological properties of the recovered field are analyzed quantitatively through the power-spectrum, the probability distribution function (PDF), the Euler characteristics, its associated critical point counts and the filling factor of underdense regions. The *local* geometrical properties of the field are analysed using the local skeleton by defining the concept of inter-skeleton distance.

As a consequence of the nearly lognormal nature of the density distribution at the scales under consideration, the tomography is best carried out on the logarithm of the density rather than the density itself. At scales larger than $\sim 1.4\langle d_{\rm LOS}\rangle$, where $\langle d_{\rm LOS}\rangle$ is the mean separation between lines of sight, the reconstruction accurately recovers the topological features of the large scale density distribution of the gas, in particular the filamentary structures: the inter-skeleton distance between the reconstruction and the exact solution is smaller than $\langle d_{\rm LOS}\rangle$. At scales larger than the intrinsic smoothing length of the inversion procedure, the power spectrum of the recovered HI density field matches well that of the original one and the low order moments of the PDF are well recovered as well as the shape of the Euler characteristic. The integral errors on the PDF and the critical point counts are indeed small, less than 20% for a mean line of sight separation smaller than ∼2.5 arcmin. The small deviations between the reconstruction and the exact solution mainly reflect departures from the log-normal behaviour that are ascribed to highly non-linear objects in overdense regions.

Key words: methods: statistical, hydrodynamical simulations – cosmology: large-scale structures of universe, intergalactic medium – quasars: absorption lines

1 INTRODUCTION

The structure and composition of the intergalactic medium (IGM) has long been studied using the Ly-α forest in QSO absorption spectra (Rauch 1998). The progress made in high resolution Echelle-spectrographs has led to a consistent picture in which the absorption features are related to the distribution of neutral hydrogen through the Lyman transition lines of HI. Hydrogen in the IGM is highly ionized (Gunn & Peterson, 1965). Its photoionization equilibrium in the expanding IGM establishes a tight correlation between neutral and total hydrogen density and numerical simulations have confirmed the existence of this correlation. They have also shown that the gas density traces the fluctuations of the DM density on scales larger than the Jeans length (see for example Cen et al. 1994, Petitjean et al. 1995, Miralda-Escudé et al. 1996, Theuns et al. 1998, Viel, Haehnelt & Springel 2004).

As we will show in the first part of this work, the statistical and topological properties of the IGM and of the dark matter distributions are the same, so that recovering the three-dimensional distribution and inferring the topological properties of the IGM allows us to constrain the properties of the dark matter distribution as well.

Although topological tools have been introduced only relatively recently in cosmological analysis, they have been used extensively to characterize the topology of large scales structures as revealed by the three-dimensional distribution of galaxies in the local universe (see for exemple Gott et al. (1986), Vogeley et al. (1994), Protogeros & Weinberg (1997), Trac et al. (2002), Park et al.(2005) and Sousbie et al. (2006) for the topological analysis of

A&A 376, 28–42 (2001)
DOI: 10.1051/0004-6361:20010901

Astronomy & Astrophysics

Physical properties and small-scale structure of the Lyman-α forest: Inversion of the HE 1122–1628 UVES spectrum[⋆,⋆⋆]

E. Rollinde[1], P. Petitjean[1,2], and C. Pichon[3,1]

[1] Institut d'Astrophysique de Paris, 98bis boulevard d'Arago, 75014 Paris, France
[2] UA CNRS 173 – DAEC, Observatoire de Paris-Meudon, 92195 Meudon Cedex, France
[3] Observatoire de Strasbourg, 11 rue de l'Université, 67000 Strasbourg, France

Received 19 February 2001 / Accepted 31 May 2001

Abstract. We study the physical properties of the Lyman-α forest by applying the inversion method described by Pichon et al. (2001) to the high resolution and high S/N ratio spectrum of the $z_{\rm em} = 2.40$ quasar HE 1122–1628 obtained during Science Verification of UVES at the VLT. We compare the column densities obtained with the new fitting procedure with those derived using standard Voigt profile methods. The agreement is good and gives confidence in the new description of the Lyman-α forest as a continuous field as derived from our method. We show that the observed number density of lines with $\log N > 13$ and 14 is, respectively, 50 and 250 per unit redshift at $z \sim 2$. We study the physical state of the gas, neglecting peculiar velocities, assuming a relation between the overdensity and the temperature, $T = \overline{T}(\rho(x)/\bar{\rho})^{2\beta}$. There is an intrinsic degeneracy between the parameters β and $\overline{T}$. We demonstrate that, at a fixed β, the temperature at mean density, $\overline{T}$, can be uniquely extracted, however. While applying the method to HE 1122–1628, we conclude that for $0.2 < \beta < 0.3$, $6000 < \overline{T} < 15\,000$ K at $z \sim 2$. We investigate the small-scale structure of strong absorption lines using the information derived from the Lyman-β, Lyman-γ and C IV profiles. Introducing the Lyman-β line in the fit allows us to reconstruct the density field up to $\rho/\bar{\rho} \sim 10$ instead of 5 for the Lyman-α line only. The neutral hydrogen density is of the order of $\sim 2 \times 10^{-9}$ cm^{-3} and the C IV/H I ratio varies from about 0.001 to 0.01 within the complexes of total column density N(H I) $\sim 10^{15}$ cm^{-2}. Such numbers are expected for photo-ionized gas of density $n_{\rm H} \sim 10^{-4}$ cm^{-3} and [C/H] ~ -2.5. There may be small velocity shifts ($\sim$10 km s^{-1}) between the peaks in the C IV and H I density profiles. Although the statistics is small, it seems that C IV/H I and $n_{\rm HI}$ are *anti-correlated*. This could be a consequence of the high sensitivity of the C IV/H I ratio to temperature. The presence of associated O VI absorption, with a similar profile, confirms that the gas is photo-ionized and at a temperature of $T \sim 10^5$ K.

Key words. methods: data analysis – methods: N-body simulations – methods: statistical – galaxies: intergalactic medium – galaxies: quasars: absorption lines – cosmology: dark matter

1. Introduction

The numerous absorption lines seen in the spectra of distant quasars (the so-called Lyman-α forest) reveal the intergalactic medium (IGM) up to redshifts larger than 5. It is believed that the space distribution of the gas traces the potential wells of the dark matter. Indeed, recent numerical N-body simulations have been successful at reproducing the observed characteristics of the Lyman-α forest (Cen et al. 1994; Petitjean et al. 1995; Hernquist et al. 1996; Zhang et al. 1995; Mücket et al. 1996; Miralda-Escudé et al. 1996; Bond & Wadsley 1998). The IGM is therefore seen as a smooth pervasive medium which can be used to study the spatial distribution of the mass on scales larger than the Jeans' length. This idea is reinforced by observations of multiple lines of sight. It is observed that the Lyman-α forest is fairly homogeneous on scales smaller than 100 kpc (Smette et al. 1995; Impey et al. 1996) and highly correlated on scales up to one megaparsec (Dinshaw et al. 1995; Fang et al. 1996; Petitjean et al. 1998; Crotts & Fang 1998; D'Odorico et al. 1998; Young et al. 2001). The number of known suitable multiple lines of sight is

Send offprint requests to: E. Rollinde,
e-mail: `rollinde@iap.fr`

⋆ Based on data collected during Science Verification of the Ultra-violet and Visible Echelle Spectrograph at the European Southern Observatory on the 8.2 m KUEYEN telescope operated on Cerro Paranal, Chile.

⋆⋆ Table A.1 is only available in electronic form at the CDS via anonymous ftp to `cdsarc.u-strasbg.fr` (130.79.128.5) or via `http://cdsweb.u-strasbg.fr/cgi-bin/qcat?J/A+A/376/28`

A&A 419, 811–819 (2004)
DOI: 10.1051/0004-6361:20034346

Astronomy & Astrophysics

Metals in the intergalactic medium*

B. Aracil[1], P. Petitjean[1,2], C. Pichon[3], and J. Bergeron[1]

[1] Institut d'Astrophysique de Paris – CNRS, 98bis Boulevard Arago, 75014 Paris, France
[2] LERMA, Observatoire de Paris-Meudon, 61 avenue de l'Observatoire, 75014 Paris, France
e-mail: petitjean@iap.fr
[3] Observatoire de Strasbourg, 11 rue de l'Université, 67000 Strasbourg, France

Received 18 September 2003 / Accepted 15 February 2004

Abstract. We use high spectral resolution (R = 45 000) and high signal-to-noise ratio ($S/N \sim$ 35−70 per pixel) spectra of 19 high-redshift ($2.1 < z_{\rm em} < 3.2$) quasars to investigate the metal content of the low-density intergalactic medium using pixel-by-pixel procedures. This high quality homogeneous survey gives the possibility to statistically search for metals at H I optical depths smaller than unity. We find that the gas is enriched in carbon and oxygen for neutral hydrogen optical depths $\tau_{\rm H\,I} > 1$. Our observations strongly suggest that the C IV/H I ratio decreases with decreasing $\tau_{\rm H\,I}$ with $\log \tau_{\rm C\,IV} = 1.3 \times \log \tau_{\rm H\,I} - 3.2$. We do not detect C IV absorption statistically associated with gas of $\tau_{\rm H\,I} < 1$. However, we observe that a small fraction of the low density gas is associated with strong metal lines as a probable consequence of the IGM enrichment being highly inhomogeneous. We detect the presence of O VI down to $\tau_{\rm H\,I} \sim 0.2$ with $\log \tau_{\rm O\,VI}/\tau_{\rm H\,I} \sim -2.0$. We show that O VI absorption in the lowest density gas is located within ∼300 km s^{-1} of strong H I lines. This suggests that this O VI phase may be part of winds flowing away from overdense regions. This effect is more important at the largest redshifts ($z > 2.4$). Therefore, at the limit of present surveys, the presence of metals in the underdense regions of the IGM is still to be demonstrated.

Key words. cosmology: observations – galaxies: halos – galaxies: ISM – quasars: absorption lines

1. Introduction

One of the key issues in observational cosmology is to understand how and when star formation took place in the high redshift universe. In particular, it is not known when the first stars appeared or how they were spatially distributed. The direct detection of these stars is challenging but the intergalactic medium (IGM) provides at least a record of stellar activity at these remote times. Indeed, metals are produced in stars and expelled into the IGM by supernovae explosions and subsequent winds and/or by galaxy interactions. It is therefore crucial to observe the distribution of metals present in the IGM at high redshifts.

The high-redshift intergalactic medium (IGM) is revealed by numerous H I absorption lines observed in the spectra of remote quasars (the so-called Lyman-α forest). It is believed that the gas in the IGM traces the potential wells of the dark matter and its spatial structures: overdense sheets or filaments and underdense voids (e.g. Cen et al. 1994; Petitjean et al. 1995; Hernquist et al. 1996; Bi & Davidsen 1997). In the course of cosmic evolution, the gas is most likely metal enriched by winds flowing out from star-forming regions that are located preferentially in the centre of massive halos. It is therefore not surprising to observe C IV absorption associated with most of the strong H I lines with $\log N$(H I) > 14.5 as these lines most likely trace filaments in which massive halos are embedded (Cowie et al. 1995; Tytler et al. 1995). The question of whether the gas filling the underdense space (the so-called voids) delineated by these overdense structures also contains metals or not is crucial. Indeed, it is improbable that winds from star-forming regions located in the filaments can pollute the voids entirely (Ferrara et al. 2000). Therefore, if metals are found in the gas filling the voids, then they must have been produced in the very early Universe by objects more of less uniformly spatially distributed.

Absorptions arising through voids are mostly of low-column densities (typically of the order or less than N(H I) = 10^{13} cm^{-2}). Given the expected low metalicities (typically [C/H] < −2.5 relative to solar), direct detection of metals at such low neutral hydrogen optical depth is currently impossible due to the weakness of the expected metal absorption and statistical methods should be used instead. Lu et al. (1998) used the stacking method to increase the signal-to-noise ratio at the place where metal absorptions are expected and did not find any evidence for metals in the range $10^{13} < N$(H I) $< 10^{14}$ cm^{-2}. Although uncertainties in the position of the lines can lead to underestimate the absorption, they conclude that

Send offprint requests to: B. Aracil, e-mail: aracil@iap.fr

* Based on observations collected at the European Southern Observatory (ESO), under the Large Programme "The Cosmic Evolution of the IGM" ID No. 166.A-0106 with UVES on the 8.2 m KUEYEN telescope operated at the Paranal Observatory, Chile.

Mon. Not. R. Astron. Soc. **341,** 1279–1289 (2003)

The correlation of the Lyman α forest in close pairs and groups of high-redshift quasars: clustering of matter on scales of 1–5 Mpc

E. Rollinde,[1⋆] P. Petitjean,[1,2] C. Pichon,[1,3,4] S. Colombi,[1,4] B. Aracil,[1]
V. D'Odorico[1] and M. G. Haehnelt[5]

[1] *Institut d'Astrophysique de Paris, 98 bis boulevard d'Arago, 75014 Paris, France*
[2] *LERMA, Observatoire de Paris, 61 Avenue de l'Observatoire, F-75014 Paris, France*
[3] *Observatoire de Strasbourg, 11 Rue de l'Université, 67 000 Strasbourg, France*
[4] *Numerical Investigations in Cosmology (NIC), CNRS, France*
[5] *Institute of Astronomy, Madingley Road, Cambridge CB3 0HA*

Accepted 2003 February 5. Received 2003 January 28; in original form 2002 May 8

ABSTRACT

We study the clustering of matter in the intergalactic medium from the Lyman α forests seen in the spectra of pairs or groups of $z \sim 2$ quasars observed with FORS2 and UVES at the VLT-UT2 Kueyen ESO telescope. The sample consists of five pairs with separation of 0.6, 1, 2.1, 2.6 and 4.4 arcmin and a group of four quasars with separations from 2 up to 10 arcmin. This unprecedented data set allows us to measure the transverse flux correlation function for a range of angular scales. Correlations are clearly detectable at separations smaller than 3 arcmin. The shape and correlation length of the transverse correlation function on these scales are in good agreement with those expected from absorption by the photoionized warm intergalactic medium associated with the filamentary and sheet-like structures predicted in cold dark matter-like models for structure formation. At larger separation no significant correlation is detected. Assuming that the absorbing structures are randomly orientated with respect to the line of sight, the comparison of transverse and longitudinal correlation lengths constrains the cosmological parameters (as a modified version of the Alcock & Paczyński test). The present sample is too small to have significant constraints. Using N-body simulations, we investigate the possibility of constraining Ω_Λ from future larger samples of quasistellar object pairs with similar separations. The observation of a sample of 30 pairs at 2, 4.5 and 7.5 arcmin should constrain the value of Ω_Λ at ±15 per cent (2σ level). We also use the observed spectra of the group of four quasars to search for underdense regions in the intergalactic medium. We find a quasi-spherical structure of reduced absorption with radius 12.5 h^{-1} Mpc, which we identify as an underdense region.

Key words: methods: data analysis – methods: N-body simulations – methods: statistical – intergalactic medium – quasars: absorption lines – dark matter.

1 INTRODUCTION

The intergalactic medium (IGM) is revealed by the numerous H I absorption lines seen in the spectra of distant quasars, the so-called Lyman α forest. For a long time these absorption lines have been believed to be the signature of discrete and compact intergalactic clouds photoionized by the ultraviolet (UV) background (e.g. Sargent et al. 1980). However, N-body simulations (Cen et al. 1994; Petitjean, Mücket & Kates 1995; Zhang, Anninos & Norman 1995; Hernquist et al. 1996; Mücket et al. 1996; Miralda-Escudé et al. 1996; Bond & Wadsley 1998; Theuns et al. 1998) and analytical works (e.g. Bi & Davidsen 1997; Hui & Gnedin 1997) together with the first determination of the approximate size of the absorbing structures from observation of quasistellar object (QSO) pairs (Bechtold et al. 1994; Dinshaw et al. 1994) established a new paradigm. The Lyman α forest is now generally believed to arise instead from spatially extended density fluctuations of moderate amplitude in the continuous intergalactic medium. The baryons thereby follow the dark matter distribution on scales larger than the Jeans length. Observations of the Lyman α forest can thus be used to constrain structure formation models and cosmological parameters. Croft et al. (2002), for example, used hydrodynamic simulations to investigate the relation between the flux power spectrum along the line of sight and the

⋆E-mail: rollinde@ast.cam.ac.uk

A&A 396, L11–L15 (2002)
DOI: 10.1051/0004-6361:20021611

Astronomy & Astrophysics

The warm-hot intergalactic medium at $z \sim 2.2$: Metal enrichment and ionization source*

J. Bergeron[1], B. Aracil[1], P. Petitjean[1,2], and C. Pichon[3]

[1] Institut d'Astrophysique de Paris - CNRS, 98bis Boulevard Arago, 75014 Paris, France
[2] LERMA, Observatoire de Paris, 61 Avenue de l'Observatoire, 75014 Paris, France
[3] Observatoire Astronomique de Strasbourg, 11 rue de l'Université, 67000 Strasbourg, France

Received 10 October 2002 / Accepted 31 October 2002

Abstract. Results are presented for our search for warm-hot gas towards the quasar Q 0329−385. We identify ten O VI systems of which two are within 5000 km s^{-1} of $z_{\rm em}$ and a third one should be of intrinsic origin. The seven remaining systems have H I column densities $10^{13.7} \le N(\rm H\,I) \le 10^{15.6}$ cm^{-2}. At least ∼1/3 of the individual O VI sub-systems have temperatures $T < 1 \times 10^5$ K and cannot originate in collisionally ionized gas. Photoionization by a hard UV background field reproduces well the ionic ratios for metallicities in the range $10^{-2.5}$–$10^{-0.5}$ solar, with possibly sub-solar N/C relative abundance. For [O/C] = 0, the sizes inferred for the O VI clouds are in some cases larger than the maximum extent implied by the Hubble flow. This constraint is fulfilled assuming a moderate overabundance of oxygen relative to carbon. For a soft UV ionizing spectrum, an overabundance of O/C is required, [O/C] ≈ 0.0−1.3. For a hard(soft) U spectrum and [O/C] = 0(1), the O VI regions have overdensities $\rho/\overline{\rho} \approx 10$−40.

Key words. cosmology: observations – intergalactic medium – galaxies: halos – quasars: absorption lines

1. Introduction

Numerical simulations suggest the existence of a warm-hot phase in the intergalactic medium, $10^5 < T < 10^7$ K, which comprises a fraction of the baryons increasing with time. This phase should be mostly driven by shocks, at least at low redshift z (Cen & Ostriker 1999; Davé et al. 2001). Possible signatures of the warm-hot intergalactic medium (WHIM) are absorptions by high ionization species such as O V, O VI and O VII. These absorptions are difficult to detect as they either fall in the Lyα forest (below the atmospheric cut-off for $z < 1.92$) or in the soft X-ray range. Successful observations of the WHIM at low z were made with the FUSE, HST and Chandra satellites (e.g. Tripp et al. 2001; Savage et al. 2002; Nicastro et al. 2002).

At $z \sim 2$–2.5, an analysis of the O IV/O V ratio from HST stacked spectra favors a hard UV background spectrum (thus a small break at 4 Ryd) and the inferred metallicity is [O/H] ≃ −2.2 to −1.3 together with an enhanced oxygen abundance relative to carbon (Telfer et al. 2002). Detection of individual O VI absorbers has been recently reported: for systems at $z \sim 2.5$ with $N(\rm H\,I) \sim 10^{14.0}$ to $10^{15.0}$ cm^{-2}, the inferred metallicity is [O/H] ∼ −3 to −2 (Carswell et al. 2002) and for $N(\rm H\,I) \ge 10^{15.5}$ cm^{-2} the metallicity is higher, [O/H] ≥ −1.5 (Simcoe et al. 2002). The main heating process of the high z WHIM is still unclear: the more tenuous regions of the Lyα forest could be ionized by a hard UV background spectrum, whereas the high column density population could be shock heated.

A systematic, large survey of quasar absorption lines at high S/N and high spectral resolution is being completed at ESO for a sample of about 20 quasars of which half are at $z \le 2.6$. In this paper, we present the results of our search for O VI absorbers towards one quasar of the ESO large programme, Q 0329−385, with several unambiguous cases of narrow, strong and weak O VI absorptions. The observations, the selection procedure for O VI systems and our O VI sample are presented in Sect. 2. The constraints derived from the line widths are given Sect. 3. Our modelling of the O VI absorbers is presented in Sect. 4. The summary and conclusions are given in Sect. 5.

2. Observations and the O VI sample

The quasar Q 0329−385 ($z_{\rm em}$ = 2.423) was observed at the VLT with the UVES spectrograph. The full wavelength coverage 3050–10 400 Å was obtained in two settings, using dichroics, with an exposure time of 6 hr per setting. The S/N ratio is about 30 and 100 at 3300 and 5000 Å respectively. The resolution is b = 6.6 km s^{-1}. A modified version of the ESO-UVES pipeline was used, better adapted to quasar spectra. A full description of the data reduction

Send offprint requests to: J. Bergeron, e-mail: bergeron@iap.fr

* Based on observations made at the European Southern Observatory (ESO), under prog. ID No. 166.A-0106(A), with the UVES spectrograph at the VLT, Paranal, Chile.

Astron. Astrophys. 329, 920–936 (1998)

ASTRONOMY AND ASTROPHYSICS

The distribution of nearby stars in phase space mapped by Hipparcos*

I. The potential well and local dynamical mass

M. Crézé[1,2], E. Chereul[1], O. Bienaymé[1], and C.Pichon[3]

[1] Centre de Données astronomique de Strasbourg, CNRS URA1280 11 rue de l'Université, F-67000 Strasbourg, France
[2] IUP de Vannes, 8 rue Montaigne, BP 561, F-56017 Vannes Cedex, France
[3] Astronomisches Institut Universität Basel, Venusstrasse 7, CH-4102 Binningen, Switzerland

Received 6 May 1997 / Accepted 29 July 1997

Abstract. Hipparcos data provide the first, volume limited and absolute magnitude limited homogeneous tracer of stellar density and velocity distributions in the solar neighbourhood. The density of A-type stars more luminous than M_v = 2.5 can be accurately mapped within a sphere of 125 pc radius, while proper motions in galactic latitude provide the vertical velocity distribution near the galactic plane. The potential well across the galactic plane is traced practically hypothesis-free and model-free. The local dynamical density comes out as $\rho_0 = 0.076 \pm 0.015\ M_\odot\ \mathrm{pc}^{-3}$ a value well below all previous determinations leaving no room for any disk shaped component of dark matter.

Key words: Galaxy: kinematics and dynamics – Galaxy: fundamental parameters – Galaxy: halo – solar neighbourhood – Galaxy: structure – dark matter

1. Introduction

All the data used here were collected by the Hipparcos satellite (ESA, 1997). Individual stellar distances within more than 125 pc were obtained with an accuracy better than 10% for almost all stars brighter than m_v = 8., together with accurate proper motions. Based on these data, a unique opportunity is offered to revisit stellar kinematics and dynamics; any subsample of sufficiently luminous stars is completely included within well defined distance and luminosity limits, providing a tracer of the local density-motion equilibrium in the galaxy potential: a snapshot of the phase space. We have selected a series of A-F dwarf samples ranging from $M_v = -1.0$ down to M_v = 4.5. Completeness is fixed within 50 pc over the whole magnitude range and within 125 pc at the luminous end ($M_v \leq 2.5$). In this series of papers we shall investigate such samples in terms of density and velocity distribution small scale inhomogeneities addressing the problem of cluster melting and phase mixing.

The expected first order departure to homogeneity is the potential well across the galactic plane. This problem is well known in galactic dynamics; it is usually referred to as "the K_z problem", where K_z means the force law perpendicular to the galactic plane. The K_z determination and subsequent derivation of the local mass density ρ_0 has a long history, nearly comprehensive reviews can be found in Kerr & Lynden-Bell (1986) covering the subject before 1984 and in Kuijken (1995) since 1984. Early ideas were given by Kapteyn (1922), while Oort (1932) produced the first tentative determination.

The essence of this determination is quite simple: the kinetic energy of stellar motions in the z direction when stars cross the plane fixes their capability to escape away from the potential well. Given a stellar population at equilibrium in this well, its density law $\nu(z)$ and velocity distribution at plane crossing $f(w_0)$ are tied to each other via the K_z or the potential $\phi(z)$. Under quite general conditions the relation that connects both distributions is strictly expressed by Eq. (1).

$$\nu(\phi) = 2 \int_{\sqrt{2\phi}}^{\infty} \frac{f(|w_0|)\ w_0\ \mathrm{d}w_0}{\sqrt{w_0^2 - 2\phi}} \tag{1}$$

This integral equation and its validity conditions are established and discussed in detail by Fuchs & Wielen (1993) and Flynn & Fuchs (1994). There is no specification as to the form of distribution functions f and ϕ except smoothness and separability of the z component.

Given $\nu(z)$ and $f(w_0)$, $\phi(z)$ can be derived. Then according to Poisson equation, the local dynamical density comes out as

$$\rho_0 = \frac{1}{4\pi G}(\mathrm{d}^2\phi/\mathrm{d}z^2) \tag{2}$$

Send offprint requests to: M. Crézé

* Based on data from the Hipparcos astrometry satellite

Mon. Not. R. Astron. Soc. **370,** 1804–1816 (2006) doi:10.1111/j.1365-2966.2006.10601.x

Transverse and longitudinal correlation functions in the intergalactic medium from 32 close pairs of high-redshift quasars⋆

F. Coppolani,[1]† P. Petitjean,[2,3] F. Stoehr,[2] E. Rollinde,[2,4] C. Pichon,[2] S. Colombi,[2] M. G. Haehnelt,[5] B. Carswell[5] and R. Teyssier[6]

[1] *European Southern Observatory, Alonso de Córdova 3107, Casilla 19001, Vitacura, Santiago, Chile*
[2] *Institut d'Astrophysique de Paris, UMR 7095 CNRS & Université Pierre et Marie Curie, 98 bis boulevard d'Arago, 75014 Paris, France*
[3] *LERMA, Observatoire de Paris, 61, avenue de l'observatoire F-75014 Paris, France*
[4] *IUCAA, Post Bag 4, Ganesh Khind, Pune 411 007, India*
[5] *Institute of Astronomy, Madingley Road, Cambridge CB3 0HA*
[6] *DAPNIA, CEA Saclay, Bat 709, 91191 Gif-sur-Yvette, France*

Accepted 2006 May 19. Received 2006 May 19; in original form 2005 September 12

ABSTRACT

We present the transverse flux correlation function of the Lyα forest in quasar absorption spectra at $z \sim 2.1$ from VLT-FORS and VLT-UVES observations of a total of 32 pairs of quasars; 26 pairs with separations in the range $0.6 < \theta < 4$ arcmin and six pairs with $4 < \theta < 10$ arcmin. Correlation is detected at the 3σ level up to separations of the order of $\sim$4 arcmin (or $\sim$4.4 h^{-1} Mpc comoving at $z = 2.1$ for $\Omega_{\rm m} = 0.3$ and $\Omega_\Lambda = 0.7$). We have, furthermore, measured the longitudinal correlation function at a somewhat higher mean redshift ($z = 2.39$) from 20 lines of sight observed with high spectral resolution and high signal-to-noise ratio with VLT-UVES. We compare the observed transverse and longitudinal correlation functions to that obtained from numerical simulations and illustrate the effect of spectral resolution, thermal broadening and peculiar motions. The shape and correlation length of the correlation functions are in good agreement with those expected from absorption by the filamentary and sheet-like structures in the photoionized warm intergalactic medium predicted in cold dark matter (CDM)-like models for structures formation. Using a sample of 139 C IV systems detected along the lines of sight towards the pairs of quasars we also investigate the transverse correlation of metals on the same scales. The observed transverse correlation function of intervening C IV absorption systems is consistent with that of a randomly distributed population of absorbers. This is likely due to the small number of pairs with separation less than 2 arcmin. We detect, however, a significant overdensity of systems in the sightlines towards the quartet Q 0103−294A&B, Q 0102−2931 and Q 0102−293 which extends over the redshift range $1.5 \leqslant z \leqslant 2.2$ and an angular scale larger than 10 arcmin.

Key words: methods: data analysis – methods: *N*-body simulations – methods: statistical – intergalactic medium – quasars: absorption lines – dark matter.

1 INTRODUCTION

The numerous H I absorption lines seen in the spectra of distant quasars, the so-called Lyα forest, contains precious information on the spatial distribution of neutral hydrogen in the Universe. Unravelling this information from individual spectra has for a long time proven difficult and ambiguous (see Rauch 1998, for a review). Studies of the correlation of the Lyα forests observed in the two spectra of QSO pairs have been instrumental in measuring the spatial extent of absorbing structures. The Lyα forests in the spectra of multiple images of lensed quasars or pairs of quasars with separations of a few arcsec (Bechtold et al. 1994; Dinshaw et al. 1994; Smette et al. 1995; Impey et al. 1996; Rauch et al. 1999; Becker, Sargent & Rauch 2004) appear nearly identical implying that the absorbing structures have sizes $>50\,h_{70}^{-1}$ kpc. Significant correlation between absorption spectra of adjacent lines of sight towards quasars

⋆Based on observations carried out at the European Southern Observatory with UVES (ESO programme no. 65.O-299 and the Large Programme 'The Cosmic Evolution of the IGM' no. 166.A-0106), FORS2 (ESO programme no. 66.A-0183) and FORS1 (ESO programmes nos 69.A-0457 and 70.A-0032) on the 8.2-m VLT telescopes Antu, Kuyen and Melipal operated at Paranal Observatory, Chile.
†E-mail: fcoppola@eso.org

Astron. Astrophys. 343, 760–774 (1999)

ASTRONOMY AND ASTROPHYSICS

The rich cluster of galaxies ABCG 85

IV. Emission line galaxies, luminosity function and dynamical properties*

F. Durret[1,2], **D. Gerbal**[1,2], **C. Lobo**[3], **and C. Pichon**[1,4,5]

[1] Institut d'Astrophysique de Paris, CNRS, 98bis Bd Arago, F-75014 Paris, France
[2] DAEC, Observatoire de Paris, Université Paris VII, CNRS (UA 173), F-92195 Meudon Cedex, France
[3] Osservatorio Astronomico di Brera, via Brera 28, I-20121 Milano, Italy
[4] Observatoire de Strasbourg, 11 rue de l'Observatoire, F-67000 Strasbourg, France
[5] Astronomisches Institut, Universitaet Basel, Venusstrasse 7, CH-4102 Binningen, Switzerland

Received 6 November 1998 / Accepted 22 December 1998

Abstract. This paper is the fourth of a series dealing with the cluster of galaxies ABCG 85. Using our two extensive photometric and spectroscopic catalogues (with 4232 and 551 galaxies respectively), we discuss here three topics derived from optical data. First, we present the properties of emission line versus non-emission line galaxies, showing that their spatial distributions somewhat differ; emission line galaxies tend to be more concentrated in the south region where groups appear to be falling onto the main cluster, in agreement with the hypothesis (presented in our previous paper) that this infall may create a shock which can heat the X-ray emitting gas and also enhance star formation in galaxies. Then, we analyze the luminosity function in the R band, which shows the presence of a dip similar to that observed in other clusters at comparable absolute magnitudes; this result is interpreted as due to comparable distributions of spirals, ellipticals and dwarfs in these various clusters. Finally, we present the dynamical analysis of the cluster using parametric and non-parametric methods and compare the dynamical mass profiles obtained from the X-ray and optical data.

Key words: methods: analytical – methods: numerical – galaxies: clusters: general – galaxies: clusters: individual: ABCG 85 – galaxies: luminosity function, mass function

1. Introduction

As the largest gravitationally bound systems in the Universe, clusters of galaxies have attracted much interest since the pioneering works of Zwicky, who evidenced the existence of dark matter in these objects, and later of Abell (1958), who achieved the first large catalogue of clusters. Clusters of galaxies are now studied through various complementary approaches, e.g. optical imaging and spectroscopy, which allow in particular to derive the distribution and kinematical properties of the cluster galaxies, and to estimate the luminosity function, and X-ray spectral imaging, which gives informations on the physical properties of the X-ray gas embedded in the cluster, and with some hypotheses can lead to estimate the total cluster binding mass.

As a complementary approach to large cluster surveys at small redshifts such as the ESO Nearby Abell Cluster Survey (ENACS, Katgert et al. 1996), we have chosen to analyze in detail a few low-z clusters of galaxies, by combining optical data (imaging and spectroscopy of a large number of galaxies) and X-ray data from the ROSAT archive. We present here complementary results on ABCG 85, which our group has already analyzed under various aspects (see references below).

ABCG 85 has a redshift of z$\sim$0.0555, corresponding to a spatial scale of 97.0 kpc/arcmin (for $H_0 = 50\,\mathrm{km\,s^{-1}Mpc^{-1}}$, value that will be used hereafter, together with q_0=0). Its center is defined hereafter as the center of the diffuse X-ray component: $\alpha_{\rm J2000} = 0^{\rm h}41^{\rm mn}51.9^{\rm s}$, $\delta_{\rm J2000} = -9^\circ18'17''$ (Pislar et al. 1997). A wealth of data is now available for this cluster: a photometric catalogue of 4232 galaxies obtained by scanning a b_J band photographic plate in a square region $\pm1^\circ$ (5.83 Mpc at the cluster redshift) from the cluster center, calibrated with V and R band CCD imaging taken in the very center (Slezak et al. 1998) and a spectroscopic catalogue of 551 galaxies in a roughly circular region of 1° radius in the direction of ABCG 85, among which 305 belong to the cluster (Durret et al. 1998a). As discussed in our previous papers (Pislar et al. 1997, Lima-Neto et al. 1997, Durret et al. 1998b), there exists in fact a complex of clusters ABCG 85/87/89 in this direction. In X-rays, ABCG 85 shows a homogeneous body, onto which are superimposed various structures: an excess towards the north-west and south-west, a south region superimposed on it, and several blobs forming a long filament towards the south-east; the velocity data confirm the existence of groups and clusters superimposed along the line of sight (see a complete description in Durret et al. 1998b) and show that this X-ray filament seems to be made of blobs falling onto the main cluster.

Send offprint requests to: F. Durret (durret@iap.fr)

* Based on observations collected at the European Southern Observatory, La Silla, Chile

Mon. Not. R. Astron. Soc. **000**, 000–000 (0000) Printed 13 May 2008 (MN LATEX style file v2.2)

Recovering the topology of the IGM at z∼2

S. Caucci[1], S. Colombi[1], C. Pichon[1,2], E. Rollinde[1], P. Petitjean[1], T. Sousbie[1,2]
[1] *Institut d'Astrophysique de Paris & UPMC, 98 bis boulevard Arago, 75014 Paris, France*
[2] *Centre de Recherche Astrophysique de Lyon, 9 avenue Charles Andre, 69561 Saint Genis Laval, France*

13 May 2008

ABSTRACT

We investigate how well the 3D density field of neutral hydrogen in the Intergalactic Medium (IGM) can be reconstructed using the Lyman-α absorptions observed along lines of sight to quasars separated by arcmin distances in projection on the sky. We use cosmological hydrodynamical simulations to compare the topologies of different fields: dark matter, gas and neutral hydrogen optical depth and to investigate how well the topology of the IGM can be recovered from the Wiener interpolation method implemented by Pichon et al. (2001). The *global* statistical and topological properties of the recovered field are analyzed quantitatively through the power-spectrum, the probability distribution function (PDF), the Euler characteristics, its associated critical point counts and the filling factor of underdense regions. The *local* geometrical properties of the field are analysed using the local skeleton by defining the concept of inter-skeleton distance.

As a consequence of the nearly lognormal nature of the density distribution at the scales under consideration, the tomography is best carried out on the logarithm of the density rather than the density itself. At scales larger than $\sim 1.4\langle d_{\rm LOS}\rangle$, where $\langle d_{\rm LOS}\rangle$ is the mean separation between lines of sight, the reconstruction accurately recovers the topological features of the large scale density distribution of the gas, in particular the filamentary structures: the inter-skeleton distance between the reconstruction and the exact solution is smaller than $\langle d_{\rm LOS}\rangle$. At scales larger than the intrinsic smoothing length of the inversion procedure, the power spectrum of the recovered HI density field matches well that of the original one and the low order moments of the PDF are well recovered as well as the shape of the Euler characteristic. The integral errors on the PDF and the critical point counts are indeed small, less than 20% for a mean line of sight separation smaller than ∼2.5 arcmin. The small deviations between the reconstruction and the exact solution mainly reflect departures from the log-normal behaviour that are ascribed to highly non-linear objects in overdense regions.

Key words: methods: statistical, hydrodynamical simulations – cosmology: large-scale structures of universe, intergalactic medium – quasars: absorption lines

1 INTRODUCTION

The structure and composition of the intergalactic medium (IGM) has long been studied using the Ly-α forest in QSO absorption spectra (Rauch 1998). The progress made in high resolution Echelle-spectrographs has led to a consistent picture in which the absorption features are related to the distribution of neutral hydrogen through the Lyman transition lines of HI. Hydrogen in the IGM is highly ionized (Gunn & Peterson, 1965). Its photoionization equilibrium in the expanding IGM establishes a tight correlation between neutral and total hydrogen density and numerical simulations have confirmed the existence of this correlation. They have also shown that the gas density traces the fluctuations of the DM density on scales larger than the Jeans length (see for example Cen et al. 1994, Petitjean et al. 1995, Miralda-Escudé et al. 1996, Theuns et al. 1998, Viel, Haehnelt & Springel 2004).

As we will show in the first part of this work, the statistical and topological properties of the IGM and of the dark matter distributions are the same, so that recovering the three-dimensional distribution and inferring the topological properties of the IGM allows us to constrain the properties of the dark matter distribution as well.

Although topological tools have been introduced only relatively recently in cosmological analysis, they have been used extensively to characterize the topology of large scales structures as revealed by the three-dimensional distribution of galaxies in the local universe (see for exemple Gott et al. (1986), Vogeley et al. (1994), Protogeros & Weinberg (1997), Trac et al. (2002), Park et al.(2005) and Sousbie et al. (2006) for the topological analysis of

Mon. Not. R. Astron. Soc. **000**, 000–000 (0000) Printed 2 October 2008 (MN LaTeX style file v2.2)

Phase-space structures I: A comparison of 6D density estimators

M. Maciejewski[1,2], S. Colombi[1], C. Alard[1] , F. Bouchet[1], C. Pichon[1] ⋆
[1] *Institut d'Astrophysique de Paris, CNRS UMR 7095 & UPMC, 98 bis boulevard Arago, 75014 Paris, France*
[2] *Max-Planck-Institut für Astrophysik, Garching, Karl-Schwarzschild-Straße 1, 85741 Garching bei München, Germany*

2 October 2008

ABSTRACT

In the framework of particle-based Vlasov systems, this paper reviews and analyses different methods recently proposed in the literature to identify neighbours in six dimensional space (6D) and estimate the corresponding phase-space density. Specifically, it compares Smooth Particle Hydrodynamics (SPH) methods based on tree partitioning to 6D Delaunay tessellation. This comparison is carried out on statical and dynamical realisations of single halo profiles, paying particular attention to the unknown scaling, $S_{\rm G}$, used to relate the spatial dimensions to the velocity dimensions.

It is found that, in practice, the methods with local adaptive metric provide the best phase-space estimators. They make use of a Shannon entropy criterion combined with a binary tree partitioning and with subsequent SPH interpolation using 10 to 40 nearest neighbours. We note that the local scaling $S_{\rm L}$ implemented by such methods, which enforces local isotropy of the distribution function, can vary by about one order of magnitude in different regions within the system. It presents a bimodal distribution, in which one component is dominated by the main part of the halo and the other one is dominated by the substructures of the halo.

While potentially better than SPH techniques, since it yields an optimal estimate of the local softening volume (and therefore the local number of neighbours required to perform the interpolation), the Delaunay tessellation in fact generally poorly estimates the phase-space distribution function. Indeed, it requires, prior to its implementation, the choice of a global scaling $S_{\rm G}$. We propose two simple but efficient methods to estimate $S_{\rm G}$ that yield a good global compromise. However, the Delaunay interpolation still remains quite sensitive to local anisotropies in the distribution.

To emphasise the advantages of 6D analysis versus traditional 3D analysis, we also compare realistic six dimensional phase-space density estimation with the proxy proposed earlier in the literature, $Q = \rho/\sigma^3$, where ρ is the local three dimensional (projected) density and $3\sigma^2$ is the local three dimensional velocity dispersion. We show that Q only corresponds to a rough approximation of the true phase-space density, and is not able to capture all the details of the distribution in phase-space, ignoring, in particular, filamentation and tidal streams.

Key words: methods: data analysis, methods: numerical, galaxies: haloes, galaxies: structure, cosmology: dark matter

1 INTRODUCTION

There are many methods to analyse dark matter haloes structures. A standard approach involves investigating spherically averaged density profiles, such as the Hernquist profile (Hernquist 1990), the NFW profile (Navarro, Frenk and White 1997), the Moore profile (Moore et al. 1998; Moore et al. 1999) and the Stoehr profile (Stoehr 2006). More sophisticated methods developed recently involve different elliptical density profiles (Jing & Suto 2002; Hayashi et al. 2007). An other alternative consists of analysing velocity profiles, e.g., Romano-Diaz & van de Weygaert (2007), for a review.

Other investigations look in more details at halo detection as well as their internal substructures, the subhaloes. They usually use a two steps procedure: they first find haloes

⋆ E-mail: maciejewski.michal@gmail.com (MM); colombi@iap.fr (SC); alard@iap.fr (CA); bouchet@iap.fr (FB); pichon@iap.fr (CP)

Mon. Not. R. Astron. Soc. **000**, 000–000 (0000) Printed 3 November 2008 (MN LaTeX style file v2.2)

Accurate estimators of power spectra in N-body simulations

Stéphane Colombi,[1⋆] Andrew Jaffe,[2⋆] Dmitri Novikov,[2⋆] Christophe Pichon,[1⋆]

[1] *Institut d'Astrophysique de Paris, UMR7095 CNRS, Univ. P. & M. Curie, 98 bis Boulevard Arago, 75014 Paris, France*
[2] *Astrophysics, Blackett Laboratory, Imperial College London, London SW7 2AZ*

3 November 2008

ABSTRACT

A method to rapidly estimate the Fourier power spectrum of a point distribution is presented. This method relies on a Taylor expansion of the trigonometric functions. It yields the Fourier modes from a number of FFTs, which is controlled by the order N of the expansion and by the dimension D of the system. In three dimensions, for the practical value $N = 3$, the number of FFTs required is 20.

We apply the method to the measurement of the power spectrum of a periodic point distribution that is a local Poisson realization of an underlying stationary field. We derive explicit analytic expression for the spectrum, which allows us to quantify—and correct for—the biases induced by discreteness and by the truncation of the Taylor expansion, and to bound the unknown effects of aliasing of the power spectrum. We show that these aliasing effects decrease rapidly with the order N. For $N = 3$, they are expected to be respectively smaller than $\sim 10^{-4}$ and 0.02 at half the Nyquist frequency and at the Nyquist frequency of the grid used to perform the FFTs. The only remaining significant source of errors is reduced to the unavoidable cosmic/sample variance due to the finite size of the sample.

The analytical calculations are successfully checked against a cosmological N-body experiment. We also consider the initial conditions of this simulation, which correspond to a perturbed grid. This allows us to test a case where the local Poisson assumption is incorrect. Even in that extreme situation, the third-order Fourier-Taylor estimator behaves well, with aliasing effects restrained to at most the percent level at half the Nyquist frequency.

We also show how to reach arbitrarily large dynamic range in Fourier space (*i.e.*, high wavenumber), while keeping statistical errors in control, by appropriately "folding" the particle distribution.

Key words: methods: analytical, data analysis, numerical, statistical, N-body simulations – cosmology: large-scale structure of Universe

1 INTRODUCTION

The power spectrum, $P(k)$, represents the primary tool to characterize the clustering properties of the large scale structure of the universe. Most of major constraints on cosmological models and on cosmological parameters have been derived from measuring $P(k)$ or its Fourier transform, the two-point correlation function. For instance, the tight constrains derived from WMAP experiment rely on measurements of the power spectrum in spherical harmonic space (*e.g.*, Dunkley et al., 2008); the most significant results from weak lensing analysis come from measurements of the two-point correlation function of the cosmic shear (*e.g.*, Benjamin et al., 2007; Fu et al., 2008); the analysis of the power spectrum of absorption lines of lyman-α forest allowed one to infer drastic constraints on the clustering properties of the matter distribution at small scales (*e.g.*, Croft et al., 1999); and, last but not least, the two-point correlation function and the power spectrum have been used extensively to analyse directly the clustering properties of 2 and 3 dimensional galaxy catalogs (*e.g.*, Peebles, 1980; Baumgart & Fry, 1991; Martinez, 2008, for a recent general review on the subject).

To be able to derive predictions from models of large scale structure formation, there has been successful attempts to find universal dynamical laws, partly phenomenological, that lead to semi-analytical expressions of the non linear power spectrum (or the two-point correlation function) of the matter distribution. Among them, one can cite the nonlinear ansatz of Hamilton et al. (1991), later improved by Peacock & Dodds (1996, see also Smith et al., 2003). Such a non-linear ansatz has been used to constrain models against observations, particularly in weak lensing surveys (*e.g.*, Benjamin et al. 2007; Fu et al. 2008). Another well known phenomenological description is the so called halo model, which proposes not only some insights on the clustering properties of the dark matter distribution, but also of the galaxy distribution itself (see, *e.g.*, Ma &

⋆ E-mails: colombi@iap.fr (SC), a.jaffe@imperial.ac.uk (AJ), d.novikov@imperial.ac.uk (DN), pichon@iap.fr (CP).

Vol 000|00 Month 2008|doi:10.1038/nature07648 nature

LETTERS

1 Cold streams in early massive hot haloes as the main
2 mode of galaxy formation

A. Dekel[1], Y. Birnboim[1,2], G. Engel[1], J. Freundlich[1,3], T. Goerdt[1], M. Mumcuoglu[1], E. Neistein[1,4], C. Pichon[5], R. Teyssier[6,7] & E. Zinger[1]

Massive galaxies in the young Universe, ten billion years ago, formed stars at surprising intensities[1,2]. Although this is commonly attributed to violent mergers, the properties of many of these galaxies are incompatible with such events, showing gas-rich, clumpy, extended rotating disks not dominated by spheroids[1–5]. Cosmological simulations[6] and clustering theory[6,7] are used to explore how these galaxies acquired their gas. Here we report that they are 'stream-fed galaxies', formed from steady, narrow, cold gas streams that penetrate the shock-heated media of massive dark matter haloes[8,9]. A comparison with the observed abundance of star-forming galaxies implies that most of the input gas must rapidly convert to stars. One-third of the stream mass is in gas clumps leading to mergers of mass ratio greater than 1:10, and the rest is in smoother flows. With a merger duty cycle of 0.1, three-quarters of the galaxies forming stars at a given rate are fed by smooth streams. The rarer, submillimetre galaxies that form stars even more intensely[2,12,13] are largely merger-induced starbursts. Unlike destructive mergers, the streams are likely to keep the rotating disk configuration intact, although turbulent and broken into giant star-forming clumps that merge into a central
3 **spheroid[4,10,11].**

It appears that the most effective star formers in the Universe were galaxies of stellar and gas masses of $\sim 10^{11} M_\odot$ at redshifts $z = 2-3$, when the Universe was ~3 Gyr old. ($M_\odot$, solar mass.) The common cases[1,3] show star-formation rates (SFRs) of $100M_\odot - 200M_\odot\,\mathrm{yr}^{-1}$. These include ultraviolet-selected galaxies termed BX/BM galaxies (ref. 14) and rest-frame optically selected galaxies termed sBzK galaxies (ref. 15), to be referred to collectively as 'star-forming galaxies' (SFGs). Their SFRs are much higher than the $4M_\odot\,\mathrm{yr}^{-1}$ in today's Milky Way, although their masses and dynamical times are comparable. The co-moving space density of SFGs is $n \approx 2\times10^{-4}\,\mathrm{Mpc}^{-3}$, implying, within the standard cosmology (termed ΛCDM), that they reside in dark matter haloes of mass $\lesssim 3.5\times10^{12}M_\odot$. The most extreme star formers are dusty submillimetre galaxies (SMG)[12,13], with SFRs of up to $\sim 1{,}000 M_\odot\,\mathrm{yr}^{-1}$ and $n \approx 2\times10^{-5}\,\mathrm{Mpc}^{-3}$. Whereas most SMGs could be starbursts induced by major mergers, the kinematics of the SFGs indicate extended, clumpy, thick rotating disks that are incompatible with the expected compact or highly perturbed kinematics of ongoing mergers[1,3,4]. The puzzle is how massive galaxies form most of their stars so efficiently at early times through a process other than a major merger. A necessary condition is a steady, rapid gas supply into massive disks.

It is first necessary to verify that the required rate of gas supply is compatible with the cosmological growth rate of dark matter haloes. The average growth rate of halo mass, M_v, through mergers and smooth accretion, is derived[6] on the basis of the extended Press–Schechter (EPS) theory of gravitational clustering (Supplementary Information, section 1) or from cosmological simulations[16,17]. For ΛCDM, the corresponding growth rate of the baryonic component is approximately

$$\dot{M} \approx 6.6 M_{12}^{1.15}(1+z)^{2.25} f_{0.165} M_\odot\,\mathrm{yr}^{-1} \qquad (1)$$

where $M_{12} \equiv M_\mathrm{v}/10^{12}M_\odot$ and $f_{0.165}$ is the baryonic fraction in the haloes in units of the cosmological value, $f_\mathrm{b} = 0.165$. Thus, at $z = 2.2$, the baryonic growth rate of haloes of mass $2\times10^{12}M_\odot$ is $\dot{M} \approx 200 M_\odot\,\mathrm{yr}^{-1}$, sufficient to maintain the SFR in SFGs. However, the margin by which this is sufficient is not large, implying that (1) the incoming material must be mostly gaseous, (2) the cold gas must efficiently penetrate into the inner halo and (3) the SFR must closely follow the gas supply rate.

The deep penetration is not a trivial matter, given that halo masses of $M_\mathrm{v} > 10^{12}M_\odot$ are above the threshold for virial shock heating[8,9,18–21], $M_\mathrm{shock} \lesssim 10^{12}M_\odot$. Such haloes are encompassed by a stable shock near their outer radius, R_v, inside which gravity and thermal energy are in virial equilibrium. Gas falling in through the shock is expected to heat up to the virial temperature and stall in quasi-static equilibrium before it cools and descends into the inner galaxy[22]. However, at $z \gtrsim 2$, these hot haloes are penetrated by cold streams[8,9,20]. Because early haloes with $M_\mathrm{v} > M_\mathrm{shock}$ populate the massive tail of the distribution, they are fed by dark matter filaments from the cosmic web that are narrow in comparison with R_v and denser than the mean within the halo[8]. The enhanced density of the gas along these filaments makes the flows along them unstoppable; in particular, they cool before they develop the pressure to support a shock, and thus avoid shock heating (Supplementary Information, section 2).

To investigate the penetration of cold streams, we study the way gas feeds massive high-z galaxies in the cosmological MareNostrum simulation—an adaptive-mesh hydrodynamical simulation in a co-moving box of side length 71 Mpc and a resolution of 1.4 kpc at the galaxy centres (Supplementary Information, section 3). The gas maps in Figs 1 and 2 demonstrate how the shock-heated, high-entropy, low-flux medium that fills most of the halo is penetrated by three narrow, high-flux streams of low-entropy gas (Supplementary Figs 3–6). The penetration is evaluated from the profiles of gas inflow rate, $\dot{M}(r)$, through shells of radius r (Fig. 3, Supplementary Fig. 7). The average profile reveals that the flow rate remains constant from well outside $R_\mathrm{v} \approx 90$ kpc to the disk inside $r \approx 15$ kpc.

To relate the feeding by streams to the observed abundance of galaxies as a function of SFR, we use the MareNostrum inflow-rate profiles to evaluate $n(>\dot{M})$, the co-moving number density of galaxies with an inflow rate $>\dot{M}$. We first extract the conditional probability distribution $P(\dot{M}\,|\,M_\mathrm{v})$ by sampling the $\dot{M}(r)$ profiles

[1]Racah Institute of Physics, The Hebrew University, Jerusalem 91904, Israel. [2]Harvard Smithsonian Center for Astrophysics, 60 Garden St, Cambridge, Massachusetts 02138, USA. [3]Department de Physique, ENS, 24 rue Lhomond, 75231 Paris cedex 05, France. [4]Max Planck Institute for Astrophysics, Karl-Schwarzschild-Strasse 1, 85741 Garching, Germany. [5]Institut d'Astrophysique de Paris and UPMC, 98bis Boulevard Arago, Paris 75014, France. [6]CEA Saclay, DSM/IRFU, UMR AIM, Batiment 709, 91191 Gif-sur-Yvette cedex, France. [7]Institute for Theoretical Physics, University of Zurich, CH-8057 Zurich, Switzerland.

Mon. Not. R. Astron. Soc. **000**, 1–9 (2006) Printed 21 January 2009 (MN LaTeX style file v2.2)

DRAFT

On the environment of galaxies: bimodal spectral properties at intermediate redshifts

C. Gay[1], C. Pichon[1,2], D. Le Borgne[1,2], R. Teyssier[2,1] & T. Sousbie[1]
[1] *Institut d'Astrophysique de Paris (UMR 7095 et UPMC), 98 bis boulevard Arago, 75014 Paris, France.*
[2] *Service d'Astrophysique, IRFU, CEA-CNRS, L'orme des meurisiers, 91 470, Gif sur Yvette, France*

Typeset 21 January 2009; Received / Accepted

ABSTRACT
The effect of the environment of galaxies on their spectroscopic properties is investigated in 3D using the skeleton and the Horizon MareNostrum cosmological simulation. Galactic winds, chemical enrichment, UV background heating and radiative cooling are taken into account in this high resolution simulation, which over the course of 4 Gyrs (before $z = 1.5$) produced 2×10^7 "star" like particles with a given age, metallicity and mass . Spectral synthesis is applied to these single stellar populations to generate spectra and colors for all "galaxies", defined here as a set of at least 10 stars which are embedded within a given dark halo subclump. All galaxies are labelled according to their euclidian distance to the closest filament (using the skeleton as a tracer of the cosmic web), which are split in two equal groups (dense and diffuse), according to the the relative density of dark matter underneath that filament.

The evolution of the age, metallicity, star formation rate, and rest-frame and observed colours of galaxies as a function of the distance to the filaments are investigated. It is found that both physical, and spectroscopic properties of galaxies show strong spatial gradient as a function of the environment. Denser filaments are redder, older, more metal rich, a trend which increases with cosmic time. These features reflect the dynamical flow of galaxies within the cosmic network. This is found both in 3D and in projection over $50h^{-1}$Mpc using the 2D skeleton, which opens the prospect of using photometric redshifts. Preliminary analysis of the SDSS catalogue using slightly different tools at lower redshift show similar features. Other environments estimators such as the fifth neighbour confirmed this bias but are less sensitive than the skeleton.

For denser filaments, a bimodality also appears below redshift two and close to the skeleton, involving red, old, metal rich galaxies on the one hand and blue, young, metal poor galaxies on the other hand, whereas for more diffuse filaments no such bimodality occurs. It is conjectured that this bimodality is induced by the tidal stipping of satellites within the more massive clusters of the simulation.

The corresponding catalogs (spectroscopical properties of the MareNostrum galaxies) are available online*.

Key words: methods: Numerical simulations, N-body, hydrodynamical, adaptive mesh refinement galaxies: formation

1 INTRODUCTION

It is nowadays admitted that the ΛCDM theory provides a framework where a large number of observed galaxy properties can be interpreted. It is referred to as the "hierarchical scenario of galaxy formation". Most importantly, this framework explains why many of these properties (physical sizes, black hole mass, bulge mass...) are found to correlate simply with galaxy mass (Kauffmann & Haehnelt 2000). Beyond these simple correlations, it is of interest to investigate how the interplay between galaxies and with the intergalactic medium affect these findings. The environment of the galaxies is known to influence the properties of the galaxies. Dressler (1980) showed the existence of the morphology-density relation (MDR): the denser regions tends to contain more elliptical galaxies (Postman & Geller 1984). This suggests that the environment strongly influences the formation and evolution of galaxies and therefore their spatial repartition (Davis & Geller 1976), as well as their physical properties (Balogh et al. 1998). This feature is expected in the

Mon. Not. R. Astron. Soc. **000**, 000–000 (0000) Printed January 6, 2009 (MN LaTeX style file v2.2)

DRAFT

Probing magnetic fields with multi-frequency polarized synchrotron emission.

J. Thiébaut[1], S. Prunet[1⋆], C. Pichon[1,3] and E. Thiébaut[2]
[1]*Institut d'astrophysique de Paris (UMR 7095), 98 bis boulevard Arago , 75014 Paris, France.*
[2]*Centre de Recherche Astronomique de Lyon (UMR 5574), 9 avenue Charles André, 69561 Saint Genis Laval Cedex, France.*
[3]*Service d'Astrophysique, IRFU, CEA-CNRS, L'orme des meurisiers, 91 470, Gif sur Yvette, France.*

January 6, 2009

ABSTRACT

We investigate the problem of probing the spatial structure of the magnetic field of our Galaxy using multi-frequency polarized maps of the synchrotron emission at radio wavelengths. More specifically, we focus in this paper on the three-dimensional reconstruction of the largest scales of the magnetic field, relying on the internal depolarisation (due to differential Faraday rotation) of the emitting medium as a function of electromagnetic frequency. We argue that multi-band spectroscopy in the radio wavelengths, developped mostly nowadays in the context of the search of high-redshift extragalactic HI lines, could be very useful probe of the magnetic field structure of our Galaxy. We show here that starting from a quite good approximation of the magnetic field, we are able to recover the true one by using a linearized version of the inverse problem considered. We show that the statistical and topological properties of the fields can be refound and how apply our method to realistic galactic magnetic field (GMF).

1 INTRODUCTION

The problem of studying the magnetic field structure of our Galaxy using measurements of the synchrotron emission of high energy electrons in the Galactic magnetic field is an old one (e.g. (Ginzburg and Syrovatskii(1965)), (Ruzmaikin et al.(1988)Ruzmaikin, Sokolov, and Shukurov), (Beck et al.(1996)Beck, Brandenburg, Moss, Shukurov, and Sokoloff)). The fact that the emitting medium is itself magnetized induces a differential Faraday rotation of the different emission planes transverse to the line of sight, resulting in a well known depolarisation effect of the integrated emission that depends strongly on the electromagnetic frequency. This effect, described in the first place by (Burn(1966)) in the case of a constant magnetic field, has been further studied in detail semi-analytically for given functional forms of the magnetic field; it has also been studied from the statistical point of view in some asymptotic regimes (see e.g. (Sokoloff et al.(1998)Sokoloff, Bykov, Shukurov, Berkhuijsen, Beck, and Poezd)). In the present work, we want to consider the (ambitious) problem of using this depolarization effect, together with the solenoidal character of the magnetic field, to *reconstruct* the magnetic field structure from a set of polarized maps of the synchrotron emission of an ionized medium at different electromagnetic frequencies. A statistical inference of the measurement of the Galactic magnetic field correlator as a function of scale from multi-frequency polarization measurements has already been successfully achieved by (Vogt and Enßlin(2005)) in the case of the Faraday rotation of the polarized light from background objects by the intra-cluster magnetized plasma. In this case, there is no depolarization effect due to differential Faraday rotation, and the relationship between the measured polarization at a given frequency and the polarization of light in the source plane is linear in the (longitudinal) magnetic field strength. The linearity of the problem makes the statistical analysis tractable in the former case. In the case that we investigate, the emitting and the rotating medium are the same, which results in depolarization effects of the emitted light. Moreover, the synchrotron emissivity itself depends in a non-linear way on the field strength transverse to the line of sight. The reconstruction of the magnetic field structure from the polarization data is in this case a non-linear inverse problem. Finally, we must note that to address the full problem of reconstruction of the magnetic field from the depolarized synchrotron emission we need in principle knowledge of both the thermal electron spatial distribution n_e*and* the spatial distribution of cosmic ray electrons n_{cr}, when, in comparison, the inference of the magnetic energy spectrum from the rotation measures of background sources only requires knowledge of the thermal electron distribution. In a first attempt at reconstructing the magnetic field, we will make the assumption that the fluctuations of the thermal and cosmic ray electrons can be neglected compared to the fluctuations in the magnetic field itself. This article is organized as follows: in the following section 2, we consider the electronic distribution as constant, and discuss the reconstruction of the magnetic field on large scales using only the leading coupling coefficient in the equation of radiative transfer. In the (thin medium, strong rotativity) limit that we assume for this work, this leading term is the usual Faraday term, responsible for the rotation of the plane of polarization. We will assume that the Faraday coefficient is dominated by the thermal electrons, which is a reasonable assumption in non-relativistic astrophysical plasmas. We will discuss in particular when we solve the linearized problem corresponding to a small fluctuating field added to a dominant "mean" field (Section 3). In section 4.6, we will deal with the statistical and topological properties of the reconstructed field and then in section 5 we will apply our reconstruction method to a realistic galactic magnetic field (GMF). Finally, we will present our

DRAFT

First galaxies: UV dark or sensitive to cosmology?

Julien Devriendt[1,2], Christopher Rimes[2], Christophe Pichon[3], Romain Teyssier[4], Damien Leborgne[3], Dominique Aubert[5], Edouard Audit[4], Stéphane Colombi[3], Simon Prunet[3], Adrianne Slyz[1], Dylan Tweed[2]

[1]*Astrophysics, University of Oxford, Keble Road, Oxford OX1 3RH, UK.*

[2]*Observatoire de Lyon, 9 Avenue Charles André, F69561 Saint-Genis-Laval Cedex, France.*

[3]*IAP, 98[bis] Boulevard Arago, F75014 Paris, France.*

[4]*IRFU, CEA Saclay, Bat 141, F91191 Gif-sur-Yvette Cedex, France.*

[5]*Observatoire de Strasbourg, 11 rue de l'Université, F67000 Strasbourg, France.*

The current concordance cosmological model provides us with a successful framework to understand large scale structure formation in a universe dominated by dark energy and cold dark matter. On galaxy scales however, the complex interplay between cold dark matter and baryons has prevented us to convincingly validate this model one step further. This article reports on state-of-the-art numerical efforts undertaken to achieve this goal. More specifically, we calculate the basic properties of galaxies which form during the first couple of billion years after the Big Bang, using the most resolved cosmological simulation including hydrodynamics ever performed to date. The evolution of an expanding cubic fragment of the Universe 230 billion light years on a side containing dark matter and gas is followed numerically, solving the coupled Vlazov and Euler-Poisson equations. Key physical processes for galaxy formation such as radiative heating and cooling, star formation, supernovae feedback and dust extinction are also implemented self-consistently using the latest subgrid algorithms. It is shown that these calculations yield galaxies whose luminosities closely match those measured in the deepest observational surveys available. This agreement is surprisingly good considering our admittedly simplistic modelling of the subgrid physics: ultra-violet luminosity functions can be reconciled with the data over the whole redshift range from 3 to 7, which strongly suggests that their evolution with time is correctly reproduced. Arguably the most interesting conclusion we draw from this study is the existence of a major degeneracy between dust extinction and cosmological parameters. Indeed, this will require that astronomers detect the far infrared counterparts of primordial galaxies in order to be broken should it turn out that extinction strongly affects galaxies across their entire luminosity range.

Over the past couple of decades, the cold dark matter (CDM) model, recently complemented with dark energy[5aa], has established itself as the theoretical framework of choice to describe the formation of structures in the Universe. In such a paradigm, density fluctuation seeds of quantum origin will eventually grow into galaxies after they are stretched to a macroscopic size and amplified by gravitational instability. Whereas it is certainly true[16], that critical aspects of the baryonic physics of galaxy formation are still poorly understood and beyond the reach of direct numerical simulation, the

Mon. Not. R. Astron. Soc. **000**, 000–000 (0000) Printed 21 January 2009 (MN LaTeX style file v2.2)

DRAFT

The connection of the Universe traced by the skeleton

C. Pichon[1,2], T. Sousbie[3], D. Pogosyan[4], C. Gay,
S. Colombi[1], J. F. Sygnet[1], D. Aubert[5]

[1] *Institut d'Astrophysique de Paris & UPMC, 98 bis boulevard Arago, 75014 Paris, France*
[2] *Service d'Astrophysique, IRFU, CEA-CNRS, L'orme des merisiers, 91 470, Gif sur Yvette, France,*
[3] *Tokyo University, Physics Dept 7-3-1 Hongo Bunkyo-ku,JP Tokyo 113-0033 Japan*
[4] *Department of physics, University of Alberta, 412 Avadh Bhatia Physics Laboratory, Edmonton, Alberta, T6G 2J1, Canada*
[5] *Observatoire astronomique de Strasbourg, UMR 7550 & ULP, 11 rue de l'Universite, 67000 Strasbourg, France*

21 January 2009

ABSTRACT
The connection of the cosmic web down to galactic scales is investigated via the skeleton. This tool produces a set of vertex (the critical points of the field), together with the corresponding list of edges (the skeleton segments connecting the critical points together) which allow us to relate the properties of the field to those of the corresponding graph.
When applied to N Dimensional Gaussian random fields, it is found that the most likely degree of the vertices (connected edges) of peakpatches is 3 in 2D and 6 in 3D. Correspondingly, the mean degree is 4 and 12 respectively, a value which does not depend on the scale invariant powerspectrum. In contrast, the mean degree of maxima is 3 and 4 in 2 and 3D respectively.

When investigating the connectivity of cosmological dark matter simulations this paper analyses what is the statistics of the degree of cosmic nodes, how the skeleton connects onto dark matter halos as a function of they mass or spin versus cosmic time, and investigates the details of local spin accretion in the context of the cosmic web superhighways. As a function of redshift the mean connectivity decreases both in 2D projection and in 3D from 4 to about 3.6 (on scales below 20 h^{-1}Mc) and from 12 to 8 for a ΛCDM cosmogony. The lower the scale the stronger the departure from the linear Gaussian result.

1 INTRODUCTION

Over the course of the last decades, our understanding of the extragalactic universe has undergone a paradigm shift: the description of its components has evolved from from being (totally) isolated to being multiply connected both on large scale, cluster scales and galactic scales. This interplay between large and small scales is driven in part by the scale invariance of gravity which tends to couple dynamically different scales, but also by a the strong theoretical prejudice associated with the so-called concordant cosmological model (de Bernardis 2000). This model predicts a certain shape for the initial conditions, leading to a hierarchical formation scenario, which produces the so called cosmic web, the most striking feature of matter distribution on megaparsecs scale in the Universe. This distribution confirmed more than twenty years ago by the first CfA catalog (de Lapparent et al. 1986) and the more recent catalogs such as SDSS (Adelman-McCarthy 2008) or 2dFGRS (Cole 2005). On these scales, the "Cosmic Web" picture relates the observed clusters of galaxies, and filaments that link them, to the geometrical properties of the initial density field that are enhanced but not yet destroyed by the still mildly non-linear evolution (Zel'Dovich 1970) (Bond et al. 1996). The analysis of the connectivity of this filamentary structures is critical to map the very large scale distribution of our universe to establish, in particular, the percolation properties of the Web (Colombi et al. 2000).

On intermediate scales, the paradigm shift is sustained by pan chromatic observations of the environment of galaxies which illustrate sometimes spectacular merging processes, following the pioneer work of e.g. Schweizer (1982) (motivated by theoretical investigations such as Toomre & Toomre (1972)). The importance of anisotropic accretion on cluster and dark matter halo scales (Aubert et al. (2004),Aubert & Pichon (2007) Bailin & Steinmetz (2005)) is now believed to play a crucial role in regulating the shape and spectroscopic properties of galaxies. Indeed it has been claimed (see e.g. Ocvirk et al. (2008) Dekel et al. (2008)) that the geometry of the cosmic inflow on a galaxy (its mass, temperature and entropy distribution, the connectivity of the local filaments network etc.) is strongly correlated to its history and nature. One of the puzzle of galaxy formation

6. Remerciements

Je voudrais avant tout remercier chaleureusement mes rapporteurs, Steve Balbus, Ed Bertschinger, James Binney, Jean-François Giovannelli et Jean Heyvaerts pour avoir pris le temps d'examiner ce document.

Je voudrais remercier les personnes qui ont encadré mon activité de recherche : Donald Lynden-Bell, Renaud Foy, Ortwin Gerhard, Agris Kalnajs, Scott Tremaine, Simon White, Jean-François Sygnet, François Bouchet, Michel Tagger, Dick Bond, Jiri Bicak, Françoise Combe et Pierre Encrenaz qui ont été une source d'inspiration continuelle et d'aide pour mener ce travail.

Je voudrais aussi remercier mes étudiants Dominique Aubert, Arnaud Siebert, Thierry Sousbie, Bastien Aracil, Pierre Ocvirk, Sara Caucci, Jean-Luc Vergely, Emmanuel Rollinde, Jérome Thiébaut, Christophe Gay, Damien Chapon, Myriam Fischer, Isabelle Paris et Florence Brault qui ont su contribuer activement à ces travaux, supporter un encadrement souvent chaotique et stimuler notre recherche par leurs critiques.

Un grand merci à mes collaborateurs et amis Eric Thiébaut, Stephane Colombi, Simon Prunet, Dmitry Pogosyan, Robert Cannon, Francis Bernardeau, Romain Teyssier, Karim Benabed, Jim Collett, Evan Scannapieco, Julien Devriendt, Damien Le Borgne, Sébastien Peirani, Adrianne Slyz, John Magorrian, Michel Tallon, Hélène Courtois, Felix Stoehr, Richard Lane, Pierre Fernique, Francois Bonnarel, David Munro, James Murray, Olivier Bienaymé, Ariane Lançon, Martin Haehnelt, Patrick Petitjean, Anaïs Oberto, Stéphane Rouberol, Didier Vibert, Thomas Keller, Bruno Moya et Sandrine Langenbacher pour leur aide précieuse et leurs encouragements.

Toutes ces personnes m'ont toujours proposé une autre façon de voir les choses, et ont contribué à donner une dimension humaine à une activité qui parfois en manque à mon avis. Interagir avec eux a toujours été un plaisir et une joie : le sentiment d'être plus intelligent à plusieurs !

Je voudrais aussi remercier l'ensemble de mes collègues de l'observatoire de Strasbourg et de l'institut d'astrophysique de Paris pour le cadre de travail agréable où cette recherche a été conduite.

Je tiens à remercier mes enfants, Jean, Héloïse, Iris et Eric, et mes parents pour leur patience durant les épreuves qui leur furent imposées par cette passion souvent (trop) envahissante. Enfin, merci à toi Brigit pour tout.